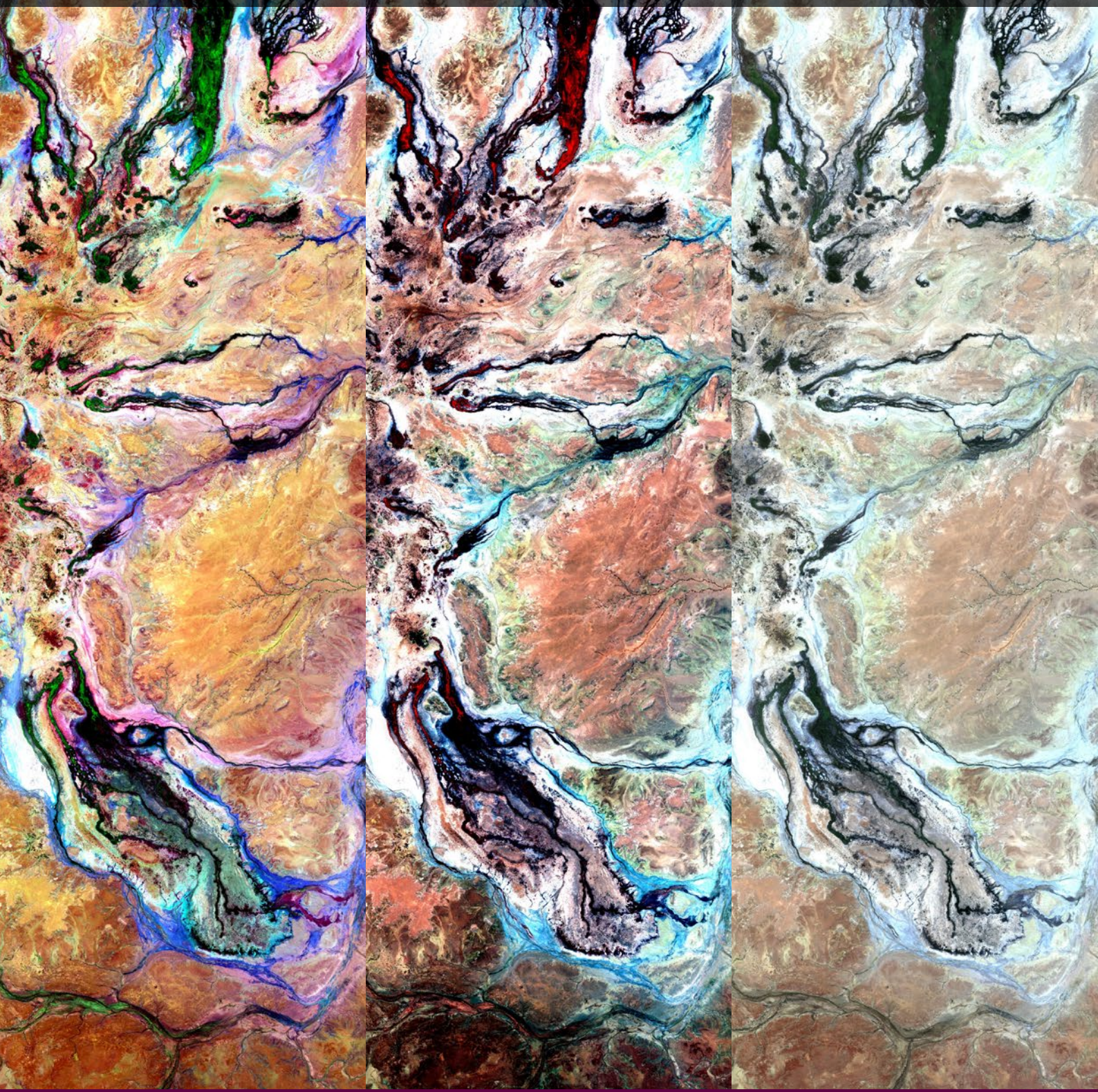
Earth Observation:
Data, Processing and Applications

Volume 1: Data



This publication is available in PDF format at *eopublications.au*.
We welcome your comments regarding the readability and usefulness of this report.
To provide feedback, please contact us at *feedback@eopublications.au*.

Publisher:
Australia and New Zealand CRC for Spatial Information

ISBN [ONLINE]:
Volume 1A 978-0-9943019-2-5
Volume 1B 978-0-9943019-3-2
Volume 1X 978-0-9943019-6-3

Copyright:
All material in this publication is licensed under a Creative Commons Attribution 4.0 Australia Licence, save for content supplied by third parties, and logos. Creative Commons Attribution 4.0 Australia Licence is a standard form licence agreement that allows you to copy, distribute, transmit and adapt this publication provided you attribute the work. The full licence terms are available from *https://creativecommons.org/licenses/by/4.0/legalcode*. A summary of the licence terms is available from *https://creativecommons.org/licenses/by/4.0/*.



Disclaimer:
While every effort has been made to ensure its accuracy, the CRCSI does not offer any express or implied warranties or representations as to the accuracy or completeness of the information contained herein. The CRCSI and its employees and agents accept no liability in negligence for the information (or the use of such information) provided in this report.

Recommended Citation for Volume 1:
CRCSI (2018) *Earth Observation: Data, Processing and Applications. Volume 1: Data*. (Eds: Harrison, B.A., Jupp, D.L.B., Lewis, M.M., Forster, B.C., Mueller, N., Phinn, S., Coppa, I., Hudson, D., Smith, C., Grant, I., Anstee, J., Dekker, A.G., Ong, C., and Lau, I.) CRCSI, Melbourne.

Latest Revision:
October 2025

Cover Image: This HyMap airborne hyperspectral image mosaic was acquired in 2009 over the Dalhousie Springs Complex, in far-northern South Australia. Three colour composite strips are juxtaposed using bands 2.22 μm, 0.833 μm, 0.444 μm as RGB on the left, bands 0.833 μm, 0.666 μm, 0.559 μm as RGB in the centre and bands 0.636 μm, 0.544 μm, 0.467 μm as RGB on the right. This region features extensive wetlands in an arid environment, fed by Great Artesian Basin spring flows.
This imagery was acquired by HyVista Corporation for *Allocating Water and Maintaining Springs of the Western Great Artesian Basin* project, 2009.
Source: Megan Lewis, University of Adelaide

About this Series

This text, *Earth Observation: Data, Processing and Applications*, is an Australian Earth Observation (EO) community undertaking, which has been jointly sponsored by the Cooperative Research Centre for Spatial Information (CRCSI), the Commonwealth Scientific and Industrial Research Organisation (CSIRO), Geoscience Australia (GA) and the Bushfire and Natural Hazards Cooperative Research Centre (BNHCRC). This publication describes EO data, processing and applications in an Australian context, and includes a wide range of local case studies. It aims to:

- Consolidate EO teaching resources in Australia;
- Encourage a greater number of tertiary courses involving EO in Australia; and
- Promulgate Australia's growing dependence on EO data.

This new text substantially revises and updates two previous books published by CSIRO, namely *Introduction to Remotely Sensed Data* and *Introduction to Image Processing*[1], which were written to support users of the microBRIAN Image Processing system and used as tertiary texts throughout Australasia for over a decade. The new series comprises multiple volumes, with the option to expand into the future. Unlike the previous publications, the new text is envisaged as an ongoing, community resource, involving a broader range of professionals from academia, government and industry, with relevance to a wider audience. Each volume has been prepared by an editorial panel of local experts, supported by contributing authors who have written and/or reviewed application chapters and case studies. Planning and production of the series has been overseen by advisors from the sponsor organisations.

This series currently comprises three volumes:

Volume 1: Data

This volume outlines the basics of EO in terms of energy sources, data acquisition, sampling characteristics, and image availability. Discussion focuses on the scientific foundations of EO. This volume also considers the interactions of electromagnetic radiation with various targets and media, as relevant to understanding optical, thermal, passive microwave and radar imagery. Volume 1 comprises three sub-volumes:

- 1A—Basics and Acquisition
- 1B—Image Interpretation
- 1X—Appendices

Volume 2: Processing

Volume 2 describes the various options involved with image representation, analysis, transformation, integration and modelling, including details of relevant algorithms, with emphasis on their underlying mathematical and statistical principles. It comprises six sub-volumes:

- 2A—Basic Image Operations
- 2B—Image Rectification
- 2C—Image Transformations
- 2D—Image Integration
- 2E—Image Classification
- 2X—Appendices

1. Harrison, B.A., and Jupp, D.L.B. (1989) Introduction to Remotely Sensed Data: Part ONE of the microBRIAN Resource Manual. CSIRO, Melbourne. 156pp.
Harrison, B.A., and Jupp, D.L.B. (1990) Introduction to Image Processing: Part TWO of the microBRIAN Resource Manual CSIRO, Melbourne. 256pp

Volume 3: Applications

This final volume introduces the Australian environment in terms of topography, climate, ecoregions, land use and vegetation dynamics, then covers a broad range of application areas reliant on EO data. Specific case studies are included to demonstrate individual applications as appropriate. Volume 3 currently comprises two sub-volumes:

- 3A—Terrestrial Vegetation
- 3B—Surface Waters

This structure has been designed to easily enable expansion of volumes in the future.

The resulting publication aims to be both comprehensive and current. It will also enable consistent definitions to be established within the Australian EO sector. Ongoing inclusion of methods, applications and case studies, which utilise a wide range of data sources, will enhance its value to our whole community.

About this Volume

The term 'Earth Observation' (EO) embraces a wide range of technologies that derive valuable information about planet Earth by detecting different types of energy. It should be stressed that, while EO is a unique and irreplaceable dataset for our planet, its value can only be realised through informed interpretation and analysis. EO technologies rely on the physical properties of matter, an understanding of which is essential to appropriate use and interpretation of the acquired data. The data itself merely provides an interesting view of Earth; the real benefits of the data are derived by extracting timely, reliable and repeatable measurements about Earth surface features and processes.

The first volume, Data, introduces sources, characteristics, uses and limitations of EO data. Several introductory sections provide an overview of relevant information from physics, geography and ecology.

Volume 1 in this series comprises three sub-volumes:

Volume 1A — Basics and Acquisition

Volume 1A introduces EO, and is structured into four parts:

- Background—presents relevant foundational concepts that underpin remote sensing:
  - Scientific Foundations—reviews basic physical principles (see Section 2);
  - Planet Earth—summarises established facts about our planet and its processes (see Section 3);
  - Energy pathways—describes thermal, biochemical, photosynthetic and carbon cycles (see Section 4);
- Energy Sources used for EO—includes electromagnetic radiation (EMR; see Section 5); radioactivity (see Section 6), magnetism (see Section 7), gravity (see Section 8), and vibrations (see Section 9);
- Platforms used for EO—describes ground-based (see Section 10), airborne (see Section 11) and spaceborne (see Section 12); and
- Sensors used for EO that detect EMR—covers sensing principles (see Sections 13) plus passive imaging sensors (see Section 14), active imaging sensors (see Section 15) and non-imaging and sounding sensors (Section 16).

Volume 1B—Image Interpretation

Volume 1B focuses on characteristics and interpretation of EO imagery:

- Image Characteristics—discusses spectral, spatial, radiometric and temporal dimensions of data resolution, density and extent (Section 1) and imaging artefacts (Section 2);
- EMR Interactions—reviews interactions between EMR and the target surface (Section 3) and atmosphere (Section 4), plus radiative transfer modelling (Section 5);
- Interpreting EO imagery—includes interpretation of optical (Section 6), thermal (Section 7), and microwave imagery (Section 8); and
- Using EO imagery—overviews aspects of image availability including communication, processing and legal issues (Section 9), and also looks ahead to future developments in this field (Section 10).

Volume 1X — Appendices

Volume 1X provides additional information about:

- Recommended Reading (Appendix 1);
- Professional Societies (Appendix 2);
- EO Data and Information Sources (Appendix 3);
- Photographic Products (Appendix 4); and
- Measuring Reflectance (Appendix 5).

Preface

It has been suggested that business schools do three things for students[2]:

- provide them with a vocabulary that enables them to talk with authority about subjects they do not understand;
- transmit to them a set of principles that have demonstrated an ability to withstand any amount of disconfirming evidence; and
- provide a ticket of admission to a job where they can learn something about these subjects.

Some would say that these characteristics apply to current approaches to education in many other disciplines, including Earth Observation.

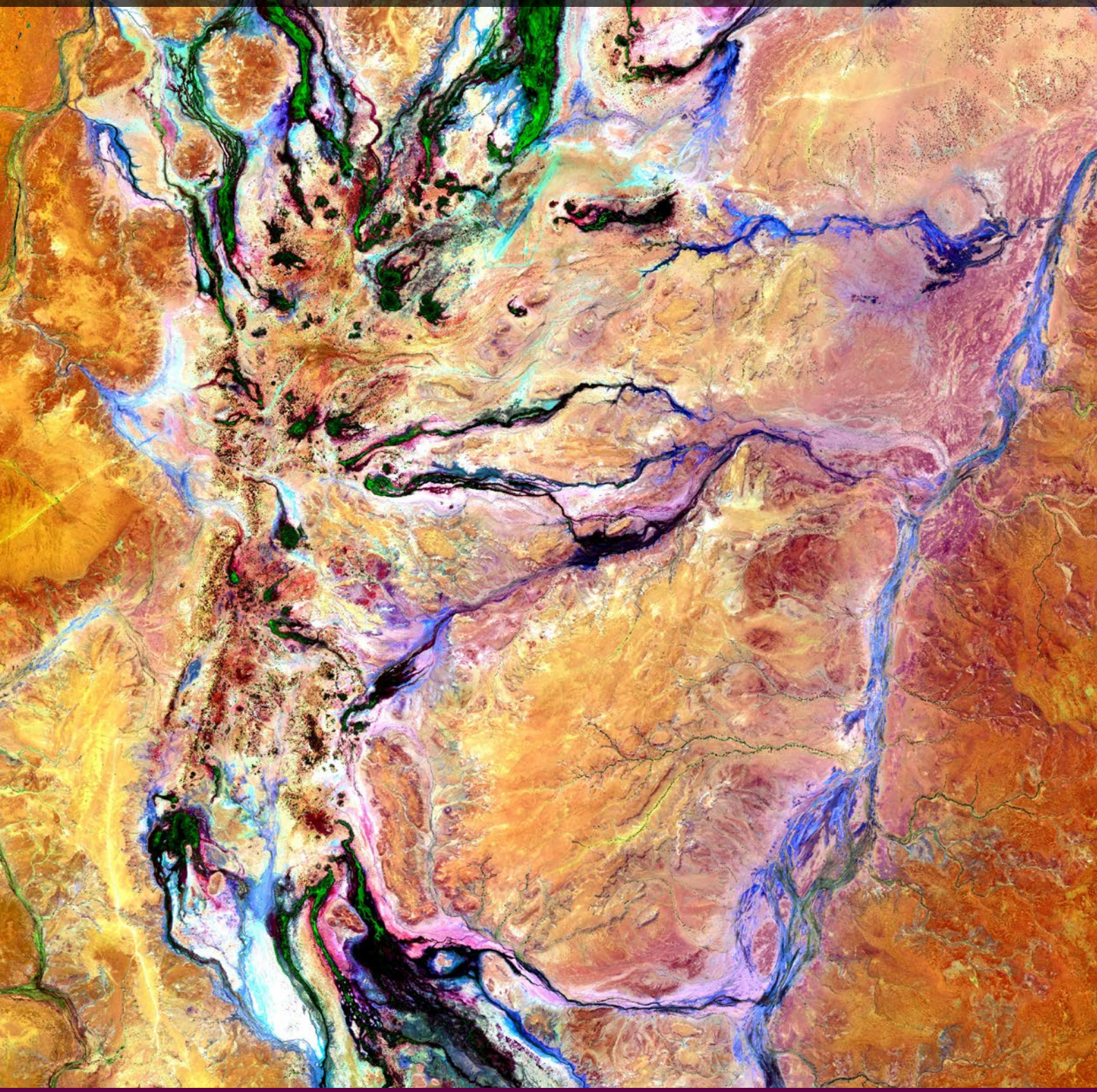
It is the aspiration of the authors of this text that students will learn more than the vocabulary of Earth Observation from these pages; hopefully they will acquire the knowledge to develop robust analytical and synthetic skills that will enable this field to advance and expand with insight and integrity.

A range of additional resources to assist readers is compiled in various Appendices. In particular, numerous online tutorials are now available from a range of sources to complement the material presented in this series.

2. Comments by Russell L. Ackoff in an interview with Robert J. Allio as reported in: Allio, R.J., and Ackoff, R.L. (2003). Iconoclastic management authority, advocates a 'systematic' approach to innovation. Strategy and Leadership 31 (3), 19–26.

Earth Observation:
Data, Processing and Applications

Volume 1A: Data—Basics and Acquisition



This publication is available in PDF format at *eopublications.au*.
We welcome your comments regarding the readability and usefulness of this report.
To provide feedback, please email *feedback@eopublications.au*.

Publisher:
Australia and New Zealand CRC for Spatial Information

ISBN [ONLINE]:
978-0-9943019-2-5

Copyright:
All material in this publication is licensed under a Creative Commons Attribution 4.0 Australia Licence, save for content supplied by third parties, and logos. Creative Commons Attribution 4.0 Australia Licence is a standard form licence agreement that allows you to copy, distribute, transmit and adapt this publication provided you attribute the work. The full licence terms are available from *https://creativecommons.org/licenses/by/4.0/legalcode*. A summary of the licence terms is available from *https://creativecommons.org/licenses/by/4.0/*.



Disclaimer:
While every effort has been made to ensure its accuracy, the CRCSI does not offer any express or implied warranties or representations as to the accuracy or completeness of the information contained herein. The CRCSI and its employees and agents accept no liability in negligence for the information (or the use of such information) provided in this report.

Recommended Citation for Volume 1A:
CRCSI (2018) *Earth Observation: Data, Processing and Applications. Volume 1A: Data—Basics and Acquisition*. (Eds. Harrison, B.A., Jupp, D.L.B., Lewis, M.M., Forster, B.C., Mueller, N., Smith, C., Phinn, S., Hudson, D., Grant, I., Coppa, I.) CRCSI, Melbourne.

Latest Revision:
October 2025

Background image on previous page: This HyMap airborne hyperspectral image mosaic over the Dalhousie Springs Complex, in far-northern South Australia, is displayed using the 2.22 μm band as red, the 0.833 μm band as green and the 0.444 μm band as blue. This region features extensive wetlands in an arid environment, fed by Great Artesian Basin spring flows. This imagery was acquired by HyVista Corporation for the *Allocating Water and Maintaining Springs of the Western Great Artesian Basin* project in 2009. **Source:** Megan Lewis, University of Adelaide

Acknowledgements

Production of this series of texts would not have been possible without the financial support of CSIRO, CRCSI, GA, and BNHCRC, direction from members of the advisory panel (Peter Woodgate, Adam Lewis, Alex Held and Arnold Dekker) and input from reviewers and contributors.

Volumes 1 and 2 of this series are based on text originally published in Harrison and Jupp (1989, 1990, 1992 and 1993)[1]. Many illustrations and some text from these publications have been reproduced with permission from CSIRO. Selected tables and text have been reproduced (with amendments) from GA (2011), GA (2013a, 2013b)[2] and CSIRO (2012)[3].

Other contributors are gratefully acknowledged:

- Chapter 15 authors: Glenn Newnham, John Armston, Bruce Forster and Catherine Ticehurst;
- reviewers: Clive Fraser (Sections 1, 2, 10, 11 and 12), John Richards (Section 13), Terry Cocks (Sections 13 and 14), Daniel Jaksa (Section 3, including Excursus), Alan Marks (Sections 6 to 9), Murray Richardson (Sections 6 to 8), Andrew Lewis (Section 7), Steve Tatham (Section 9), Zheng-Shu Zhou (Section 15), and Alfredo Huete and Laurie Chisholm (various sections);
- illustrations: Norman Mueller kindly supplied most of the lovely images; other contributors of graphical material include: Chris Roelfsema, Cheryl Brown, Christopher Griffin, Matthew Paget, Megan Lewis, Murray Richardson, Andrew Lewis, Darius Culvenor, Michael Schaefer, Thomas Schroeder, Arnold Dekker, David Lamb, Nina Putica, Arko Lucieer, Robert Norman, Ian Grant, James Prior, Graham Donald, Gary Shaw, John Le Marshall, Antoni Rogalski, Gail Kelly, Svetla Hristov-Veleva, Dave Winker, Kim Richardson;
- Paul Cockram and Matej Hrcek, who 'translated' the Harrison and Jupp (1989, 1990) files from Quark Express 2.0;
- Joost Kuckartz for meticulous formatting of references and equations, plus general editing;
- Daniel Rawson (Accessible Publication & Template Design) for layout and formatting;
- Carl Davies (CMDphotographics) for bespoke graphical illustrations; and
- last, but not least, Pete Harrison for last minute graphical updates.

We thank those owners of copyrighted illustrative material for permission to reproduce their work: Geoscience Australia, CHARIM, UNSW, CNES, Airbus D&S, Planet, ESA, IPCC, Lawrence Braille and MIT Lincoln Laboratory. Credits for individual illustrations are provided below the relevant graphic.

1. Harrison, B.A., and Jupp, D.L.B. (1989) Introduction to Remotely Sensed Data: Part ONE of the microBRIAN Resource Manual. CSIRO, Melbourne. 156pp.
   Harrison, B.A., and Jupp, D.L.B. (1990) Introduction to Image Processing: Part TWO of the microBRIAN Resource Manual CSIRO, Melbourne. 256pp.
   Harrison, B.A., and Jupp, D.L.B. (1992) Image Rectification and Registration: Part FOUR of the microBRIAN Resource Manual. MPA, Melbourne.
   Harrison, B.A., and Jupp, D.L.B. (1993) Image Classification and Analysis: Part THREE of the microBRIAN Resource Manual. MPA, Melbourne.
2. Geoscience Australia (2011) Continuity of Earth Observation Data for Australia: Operational Requirements to 2015 for Lands, Coasts and Oceans. Geoscience Australia, Canberra.
   Geoscience Australia (2013a) GA Earth Observation Product Description Framework and Templates. Unpublished report by Barbara Harrison, February 2013.
   Geoscience Australia (2013b) Draft Report on the National Dynamic Land Cover Dataset (Version 2). Unpublished report by Barbara Harrison, June 2013.
3. CSIRO (2012) Continuity of Earth Observation Data for Australia: Research and Development Dependencies to 2020. CSIRO, Canberra.

Table of Contents

Acknowledgements i

1 Introduction **1**

1.1 Why Observe the Earth? 1

1.2 What is Earth Observation? 1

1.2.1 Platforms and sensors 1

1.2.2 Indirect observations 3

1.2.3 A philosophical interlude 6

1.3 Observing the Earth 8

1.3.1 Historical background 8

1.3.2 EO data characteristics 10

1.4 Using Earth Observations 14

1.4.1 Detecting and mapping features 15

1.4.2 Monitoring changes 15

1.4.3 Modelling processes 17

1.5 The Global Picture 18

1.5.1 The Global Earth Observation System of Systems 18

1.5.2 Essential climate variables 18

1.6 Key Terms 21

1.7 Further Information 22

1.8 References 23

Background 25

2 Scientific Foundations **27**

2.1 Energy, Mass and Fundamental Forces 27

2.2 Matter 28

2.3 Measurement 28

2.3.1 Scales of measurement 29

2.3.2 International System of Units (SI) 29

2.3.3 SI metric prefixes 30

2.3.4 SI units for measuring waves 30

2.3.5 Angles 31

2.4 Force Fields 32

2.5 Waves 33

2.5.1 Wave types and characteristics 33

2.5.2 Reflection, refraction and diffraction 34

2.5.3 Polarisation 36

2.5.4 The Doppler effect 36

2.5.5 Coherence 36

2.6 Properties of EMR 36
2.6.1 Radiometric terms 36
2.6.2 Spectral terms 38
2.6.3 Photometric terms 38
2.7 Colour and Human Vision 38
2.7.1 Human visual system 38
2.7.2 Perception of colour and brightness 39
2.7.3 Colour models 40
2.8 Optics 41
2.8.1 Theories 41
2.8.2 Lenses 41
2.9 Radiation laws 43
2.9.1 Inverse-square law 43
2.9.2 Beer-Lambert law 45
2.10 Heat and Temperature 45
2.10.1 Thermal properties of matter 45
2.10.2 Latent heat 46
2.10.3 Thermodynamics 47
2.11 Blackbody Radiation 47
2.11.1 Stefan-Boltzmann's law 47
2.11.2 Kirchhoff's law 48
2.11.3 Wien's displacement law 48
2.11.4 Planck's law 48
2.11.5 Other bodies 48
2.12 Further Information 49
2.13 References 50

3 Planet Earth **51**
3.1 The Earth in Space 51
3.2 Structure of the Earth 53
3.3 Shape of the Earth 56
3.4 Further Information 61
3.5 References 61

4 Earth Systems and Processes **63**
4.1 Earth System Science 63
4.1.1 Atmosphere 64
4.1.2 Hydrosphere 66
4.1.3 Geosphere 66
4.1.4 Biosphere 67
4.2 Earth System Processes 67
4.2.1 Energy 67
4.2.2 Water 72
4.2.3 Earth 73
4.2.4 Carbon 75
4.3 Further Information 76
4.4 Reference 76

5 Electromagnetic Radiation **79**
5.1 The EM Spectrum 79
5.2 Reflectance and Emission 81
5.2.1 Reflected energy 81
5.2.2 Emitted energy 83
5.3 Spectral Regions 84
5.4 Atmospheric Interactions 90
5.5 Further Information 93
5.6 References 93

6 Radioactivity **95**
6.1 Introducing Radioactivity 95
6.2 Gamma Rays 96
6.3 Further Information 100
6.4 References 100

7 Magnetism **101**
7.1 Introducing Magnetism 101
7.2 Magnetic Field 102
7.3 The Earth's Magnetic Field 103
7.4 Geomagnetics 106
7.5 Further Information 109
7.6 References 109

8 Gravity **111**
8.1 The Earth's Gravitational Field 111
8.2 Measuring Gravity 113
8.3 Gravity Applications 115
8.4 Further Information 115
8.5 References 115

9 Vibrations **117**
9.1 Sound Waves 117
9.2 Seismic Waves 119
9.2.1 What are earthquakes? 119
9.2.2 Types of seismic waves 121
9.2.3 Using seismic waves to determine the structure of Earth 122
9.2.4 Detecting seismic waves 123
9.3 Further Information 125
9.4 References 125

Platforms for Earth Observation 127

10 Ground-based Platforms **129**
10.1 In situ 129
10.2 Mobile Sensors 134
10.3 Citizen Science and Crowdsourcing 136
10.4 Further Information 137
10.5 References 137

11 Airborne Platforms **139**
11.1 Manned Aircraft 140
11.2 Remotely Operated Aircraft 143
11.3 Further Information 144
11.4 References 144

12 Spaceborne Platforms **145**
12.1 Manned Spacecraft 145
12.2 Satellites 146
12.2.1 Geostationary 148
12.2.2 Polar orbiting 156
12.3 Further Information 164
12.4 References 164

EMR Sensors for Earth Observation 167

13 Sensing Electromagnetic Radiation **169**
13.1 Measuring Electromagnetic Radiation 169
13.2 Earth Observation Sensors 170
13.2.1 Passive sensors 171
13.2.2 Active sensors 172
13.2.3 Sounders 172
13.3 Sensor Design Constraints 172
13.4 Sensor Performance Metrics 173
13.5 CEOS Sensor Categories 175
13.6 Further Information 178
13.7 References 178

14 Passive Imaging Systems **179**
14.1 Optical and thermal sensor components 180
14.2 Image formation 183
14.2.1 Electromechanical 184
14.2.2 Linear array 185
14.2.3 Central perspective 186
14.3 Optical 186
14.3.1 Panchromatic 188
14.3.2 Multispectral 190
14.3.3 Hyperspectral 195

14.4 Thermal infrared 197
14.5 Passive microwave 201
14.6 Further Information 201
14.7 References 202

15 Active Imaging Systems 203
15.1 Lidar 203
15.2 Radar 207
15.2.1 Side-Looking Airborne Radar (SLAR) or Real Aperture Radar (RAR) 209
15.2.2 Synthetic Aperture Radar (SAR) 210
15.3 Further Information 213
15.4 References 213

16 Non-imaging and Sounding Systems 215
16.1 Non-imaging systems 217
16.1.1 Passive 217
16.1.2 Active 217
16.2 Sounding Systems 219
16.2.1 Passive 219
16.2.2 Active 220
16.3 Further Information 226
16.4 References 226

List of Figures

Figure 1.1 Earth from space 2

Figure 1.2 Space photo of Berlin at night 3

Figure 1.3 Median mosaic of Landsat-8 OLI 4

Figure 1.4 From observation domain to attribute domain 5

Figure 1.5 Data-Information-Knowledge-Wisdom triangle 7

Figure 1.6 MODIS global composite image 8

Figure 1.7 Historical development of remote sensing 9

Figure 1.8 Nanosatellite imagery 10

Figure 1.9 CubeSat 11

Figure 1.10 Scales of EO 13

Figure 1.11 Monthly composite 15

Figure 1.12 Lake Disappointment 15

Figure 1.13 Construction of Elizabeth Quay, Perth 16

Figure 1.14 Modelling photosynthetically active radiation 17

Figure 1.15 The global picture 19

Figure 2.1 Planar and solid angles 32

Figure 2.2 Force field example 32

Figure 2.3 Longitudinal and transverse waves 33

Figure 2.4 Components of waves 34

Figure 2.5 Longitudinal or compression waves 34

Figure 2.6 Law of reflection 35

Figure 2.7 Specular and diffuse reflectors 35

Figure 2.8 Refraction and diffraction 35

Figure 2.9 Radiometric measurements 37

Figure 2.10 Relative light absorption of human cones 39

Figure 2.11 Perception of light intensity changes 39

Figure 2.12 Additive and subtractive colour mixing 40

Figure 2.13 Relationship between additive and subtractive primary colours 41

Figure 2.14 Convex and concave lenses 42

Figure 2.15 Field of view 42

Figure 2.16 Object more than twice focal length from convex lens 42

Figure 2.17 Inverse-square law 44

Figure 2.18 Beer-Lambert law 45
Figure 2.19 Blackbody radiation 48
Figure 2.20 Spectral emissivity and spectral radiant exitance of various bodies 49
Figure 3.1 Our solar system 51
Figure 3.2 Earth's axis of rotation 52
Figure 3.3 Variation in solar radiation due to Earth's elliptical orbit 53
Figure 3.4 Cross-section of Earth 54
Figure 3.5 Tectonic plates 55
Figure 3.6 Tectonic plate boundaries 55
Figure 3.7 Modelling the shape of the Earth 56
Figure 3.8 Local versus geocentric datums 57
Figure 3.9 Average number of visible satellites across all planned constellations 59
Figure 3.10 Satellite Laser Ranging 60
Figure 4.1 Earth System Science 63
Figure 4.2 Processes and interactions within Earth System Science 64
Figure 4.3 Interrelationship between atmosphere and ionosphere 65
Figure 4.4 Impact of ionosphere on radio frequency waves 65
Figure 4.5 Global ionospheric foF2 map 66
Figure 4.6 Energy distribution and net radiation 68
Figure 4.7 Earth's energy budget 68
Figure 4.8 Solar illumination angle variation with latitude 70
Figure 4.9 Variations in insolation with latitude and annual cycle 70
Figure 4.10 Typical daily insolation cycle on equinox days 71
Figure 4.11 Annual cycle of total daily solar irradiance 71
Figure 4.12 Reflected solar radiation 72
Figure 4.13 Outgoing radiation 72
Figure 4.14 Net radiation 72
Figure 4.15 Hydrological cycle 73
Figure 4.16 Rock cycle 74
Figure 4.17 Carbon cycle 75
Figure 5.1 Electromagnetic wave 79
Figure 5.2 Electromagnetic spectrum 80
Figure 5.3 Common remote sensing systems 81
Figure 5.4 Incident energy components 82
Figure 5.5 Albedo of different materials 83

Figure 5.6 Solar radiation at top of atmosphere and at sea level 84
Figure 5.7 Refraction of polychromatic light through a prism 84
Figure 5.8 Reflectance characteristics of typical green leaf structure 85
Figure 5.9 Idealised spectral reflectance curves 86
Figure 5.10 Seeing water from space—Kerang, Victoria 87
Figure 5.11 Mapping permanent water 88
Figure 5.12 WOfS continental map 89
Figure 5.13 Atmospheric layers 90
Figure 5.14 Atmospheric opacity 92
Figure 6.1 Stable nuclei 95
Figure 6.2 Gamma ray ionisation 97
Figure 6.3 Gamma spectroradiometry 98
Figure 6.4 Radiometric map of Australia 99
Figure 7.1 Magnetic fields 101
Figure 7.2 Magnetic vector components 102
Figure 7.3 Magnetosphere 103
Figure 7.4 Southern Aurora 103
Figure 7.5 Geomagnetic observation network for Australia 104
Figure 7.6 Magnetic time series 104
Figure 7.7 Total intensity variability over Australia 105
Figure 7.8 AGRF 2010 model at epoch 2010.0 106
Figure 7.9 Aeromagnetic imagery 107
Figure 7.10 Australian Magnetic Anomaly Grid 108
Figure 8.1 Gravity, gravity variations, mass transport and distribution 112
Figure 8.2 Geoid surface 112
Figure 8.3 Global gravity field anomalies 113
Figure 8.4 Global gravity derived from GOCE 113
Figure 8.5 Isostatic Residual Gravity Anomaly Map of Australia 114
Figure 9.1 Speed of sound with varying water depth 118
Figure 9.2 Decibel range 118
Figure 9.3 Shock waves and sonic booms 119
Figure 9.4 Global earthquake occurrence 120
Figure 9.5 Earthquake focus and epicentre 120
Figure 9.6 Body waves 121
Figure 9.7 Surface waves 122

Figure 9.8 Shadow zones for seismic waves 123
Figure 9.9 Global earthquake frequency and energy 124
Figure 10.1 Dual wavelength Echidna™ LIDAR (DWEL) 130
Figure 10.2 VEGNET scanner 131
Figure 10.3 Marine in situ sensors 131
Figure 10.4 Flux Tower Function 132
Figure 10.5 NEON flux tower measurements 132
Figure 10.6 TERN OzFlux flux towers 133
Figure 10.7 Mobile sensors for Earth Observation 134
Figure 10.8 Hand-held sensors for Earth Observation 134
Figure 10.9 UNETracker 135
Figure 10.10 Livestock pasture usage compared with pasture productivity 135
Figure 11.1 Effect of wide scan angle 140
Figure 11.2 Nearmap imagery 141
Figure 11.3 Some manned airborne platforms 141
Figure 11.4 Urban development 142
Figure 11.5 Port operations 142
Figure 11.6 Monitoring construction projects 142
Figure 11.7 Mining operations 142
Figure 11.8 Remotely piloted aircraft systems 143
Figure 12.1 Comparison of satellite orbits 147
Figure 12.2 Some orbital inclinations 147
Figure 12.3 Satellite density around Earth 148
Figure 12.4 Geostationary orbit 149
Figure 12.5 Network of geostationary satellites 150
Figure 12.6 Himawari-8 disks 151
Figure 12.7 The launch of the first weather satellite, TIROS-1, in 1960 152
Figure 12.8 Early meteorological satellite imagery 152
Figure 12.9 A Himawari-8 colour image 154
Figure 12.10 Wind vectors over GMS-5 image of the Tasman Sea 155
Figure 12.11 Himawari-8 Atmospheric Motion Vectors (AMVs) 155
Figure 12.12 Orbit parameters 156
Figure 12.13 Daily acquistions for MODIS/Aqua and MODIS/Terra 157
Figure 12.14 Landsat satellites 158
Figure 12.15 Polar orbiting satellites provide a variety of spatial scales 159

Figure 13.1 Information acquired by sensors 173
Figure 13.2 Sensor performance terms 174
Figure 13.3 Spectral response function of Hyperion SWIR band 174
Figure 13.4 Relative spectral variation across Hyperion image line 174
Figure 14.1 Simple example of monochromatic sensor 181
Figure 14.2 Spectral response functions 183
Figure 14.3 Scanning mechanisms 183
Figure 14.4 Operation of electromechanical aircraft scanner 184
Figure 14.5 MSS measurements along one scan line 184
Figure 14.6 Whiskbroom versus pushbroom scanners 185
Figure 14.7 Panchromatic imagery from Landsat-7 ETM+ and Landsat-8 OLI 188
Figure 14.8 Decommissioned Landsat-5 satellite visible from Landsat-8 189
Figure 14.9 Image sharpening 189
Figure 14.10 Comparison of bands acquired by Landsat-7, Landsat-8 and Sentinel-2 190
Figure 14.11 Differentiation within spectral regions 191
Figure 14.12 Colour composites 192
Figure 14.13 Landsat ETM+ optical channels 193
Figure 14.14 Gross Annual Pasture Production (GAPP) from 2007 to 2010 for southwestern WA 194
Figure 14.15 Compilation of hyperspectral data cube 195
Figure 14.16 Hyperspectral image interpretation 196
Figure 14.17 Simulated Landsat TM spectral signature 197
Figure 14.18 Detectivity of IR detectors 198
Figure 14.19 Spectral response of Landsat thermal bands 199
Figure 14.20 Thermography 200
Figure 15.1 Lidar operation 204
Figure 15.2 Perspective view of classified point cloud 205
Figure 15.3 Enlarged perspective view showing details of towers and power lines 205
Figure 15.4 Terrain model 206
Figure 15.5 The microwave and radio wave spectra 207
Figure 15.6 Radar wavelengths 208
Figure 15.7 Interaction of radar wavelengths with vegetation 208
Figure 15.8 Operation of side-looking airborne radar 209
Figure 15.9 Radar image distortions 210
Figure 15.10 Impact of radar distortions in imagery 210
Figure 15.11 Operation of synthetic aperture radar 211

Figure 15.12 Comparing SAR and Optical imagery 211

Figure 16.1 1 500 hPa height anomaly correlations 216

Figure 16.2 Laser altimeter 217

Figure 16.3 Radar altimetry 218

Figure 16.4 Cryosat radar altimeter 218

Figure 16.5 Wind estimates derived from SeaWinds observations 219

Figure 16.6 Profile of LITE observations over Sahara Desert 221

Figure 16.7 Profiles of CALIOP observations over Sahara Desert 221

Figure 16.8 TRMM Precipitation Radar 222

Figure 16.9 Cloudsat Cloud Profiling Radar 223

Figure 16.10 Spectral resolution of HIRS/2 compared with simulated AIRS spectra 225

List of Tables

Table 1.1 Logical stages in EO data use 5

Table 1.2 Data-information-knowledge-wisdom hierarchy 6

Table 1.3 Observations, measurements and attributes 11

Table 1.4 GCOS essential climate variables 20

Table 2.1 Base Units in the International System of Units (SI) 29

Table 2.2 Derived Units in the International System of Units (SI) 29

Table 2.3 SI metric prefixes 30

Table 2.4 SI units of length 31

Table 2.5 SI units of frequency 31

Table 2.6 Radiometric terms 37

Table 2.7 SI units 37

Table 2.8 Spectral terms defined in terms of wavelength 38

Table 2.9 Equivalent photometric terms 38

Table 2.10 Energy required to convert 10 g ice to steam 46

Table 3.1 Comparison of planetary features 52

Table 4.1 Composition of planet Earth 66

Table 5.1 Sample albedo values 83

Table 5.2 Atmospheric layers 91

Table 5.3 Global cloud properties 91

Table 5.4 EMR spectral regions and atmospheric windows 92

Table 6.1 Isotope properties 97

Table 7.1 Magnetic components 102

Table 12.1 Satellite orbital characteristics 146

Table 12.2 Types of satellite orbits 147

Table 12.3 Geostationary meteorological satellites 150

Table 12.4 JMA Australasian coverage satellites 151

Table 12.5 Some Important Series of Weather Satellites 153

Table 12.6 Polar orbiting satellites 162

Table 13.1 Spectral regions observed by EO sensors 170

Table 13.2 Common sensor performance metrics 173

Table 13.3 CEOS sensor categories[49] 175

Table 13.4 EO sensors commonly used in Australia 177

Table 14.1 Potential components of generic passive sensor 181

Table 14.2 SWIR detector categories 182

Table 14.3 EMR sensitive materials 182

Table 14.4 Examples of satellite optical sensors 187

Table 14.5 Landsat TM/ETM+ channels 190

Table 14.6 Landsat OLI/TIRS channels 191

Table 14.7 Examples of hyperspectral imagers 197

Table 14.8 Commonly used thermal imaging sensors 200

Table 14.9 Examples of satellite passive microwave sensors 201

Table 15.1 Standard radar frequency and wavelength letter bands. 207

Table 15.2 Polarisation options for radar signals 209

Table 15.3 Examples of active and future satellite SAR sensors 212

Table 16.1 Characteristics of AIRS and HIRS sounding instruments 224

List of Excurses

Excursus 1.1—Observing Australia 4

Excursus 1.2—How do EO sensors identify healthy vegetation? 5

Excursus 1.3—EO processing stages 12

Excursus 3.1—Datums and Geoids 57

Excursus 3.2—Space Geodesy and Reference Frames 59

Excursus 4.1—Insolation 70

Excursus 5.1—Water Observations from Space (WOfS) 86

Excursus 6.1— Australian Radiometric Map 99

Excursus 7.1—Australian Geomagnetic Reference Field Model 106

Excursus 7.2—Australian Magnetic Anomaly Grid 108

Excursus 8.1—Australian Gravity Anomaly Map 114

Excursus 10.1—GPS tracking in Precision Agriculture 135

Excursus 11.1—High resolution aerial imagery 142

Excursus 12.1—Meteorological Satellites 152

Excursus 14.1—Pastures from Space 194

Excursus 15.1—Airborne Lidar Applications 205

Excursus 16.1—Value of EO to Numerical Weather Prediction 215

Excursus 16.2—Meteorological Sensors and Applications 224



1 Introduction

1.1 Why Observe the Earth?

The Earth is our home. Our livelihood—past, present and future—is inextricably bound to the diversity and integrity of our planet. Our survival will inevitably depend on prudent management of its resources.

For several millennia, human civilisations have conducted a wide variety of inventories of Earth's resources. This information has allowed societies to understand their environment, and also to plan and monitor their opportunities for development and sustainability.

Mapping and monitoring the Earth's resources is a fundamental activity for governments, industries and communities at global, national, regional and now local scales. As the demands of growing populations emphasise the finite nature of our natural resources, their accurate and timely assessment has become essential to land and water managers for both development and conservation purposes. Frequent, consistent and accurate information over large areas is needed to fully understand ecosystem processes and functions before we can reliably monitor and predict the composition and condition of the lands, coasts, oceans and atmosphere of planet Earth. Fortunately, the technology available to provide this information, as well as insight into the characteristics and impact of our celestial neighbours, has also become more sophisticated in the form of Earth Observation (EO; see Figure 1.1).

1.2 What is Earth Observation?

Gathering information about the Earth using remote sensing technologies is called Earth Observation (EO). Remote sensing refers to making observations of an object using a device that is physically remote from it. This term is most frequently used to describe imagery of the Earth and its atmosphere recorded by airborne and satellite-borne sensors (see Figure 1.2), but can also encompass observations from ground-based sensors.

1.2.1 Platforms and sensors

EO sensors basically detect energy from Earth, which may be either reflected from another source or intrinsic to our own planet. Remote sensing devices have been designed to detect various types of energy, including electromagnetic radiation (EMR), radioactivity, magnetism, gravity, and sound and seismic waves (see Sections 1 to 9 respectively). By definition, these sensors generally do not have direct contact with the Earth, so they need to be carried by an elevated platform. (An exception to this is ground-penetrating radar antennae, which achieve a stronger signal when in contact with the ground.) Three broad groups of platforms are used to carry EO sensors:

- spaceborne—satellites, shuttles, or space stations;
- airborne—manned aircraft, unmanned aerial vehicles, balloons or blimps; and
- ground-based—in situ, mobile devices, or animals (including humans).

Background image: Landsat-8 image of Rockhampton, Queensland, and nearby reefs acquired on 6 July 2016 (displayed using bands 6, 5, 3 as RGB).
Source: Norman Mueller, Geoscience Australia

Remote sensing devices are either passive, that is, the sensor detects energy from other sources such as the Sun, or active, in that the sensor emits pulses of energy then records a response. Some common examples of passive EO sensors include:

- eyes—detecting reflected light waves from ambient lighting;
- ears—detecting sound waves from ambient sounds; and
- digital cameras and sensors—measuring reflected or emitted visible and non-visible energy from ambient sources, e.g. mobile phone cameras, or satellite based imaging sensors.

Examples of active EO sensors include:

- digital camera with flashlight—measuring reflected light waves from both flashlight and ambient lighting;
- sonar—measuring echoes of sound waves generated by the sensor;
- lidar —measuring reflected light waves generated by the sensor; and
- radar—measuring reflected radio waves generated by the sensor.

Various sources of EO data are detailed in subsequent sections of this volume. One of the most commonly used sources of EO imagery is acquired by the Landsat series of satellites (see Excursus 1.1).

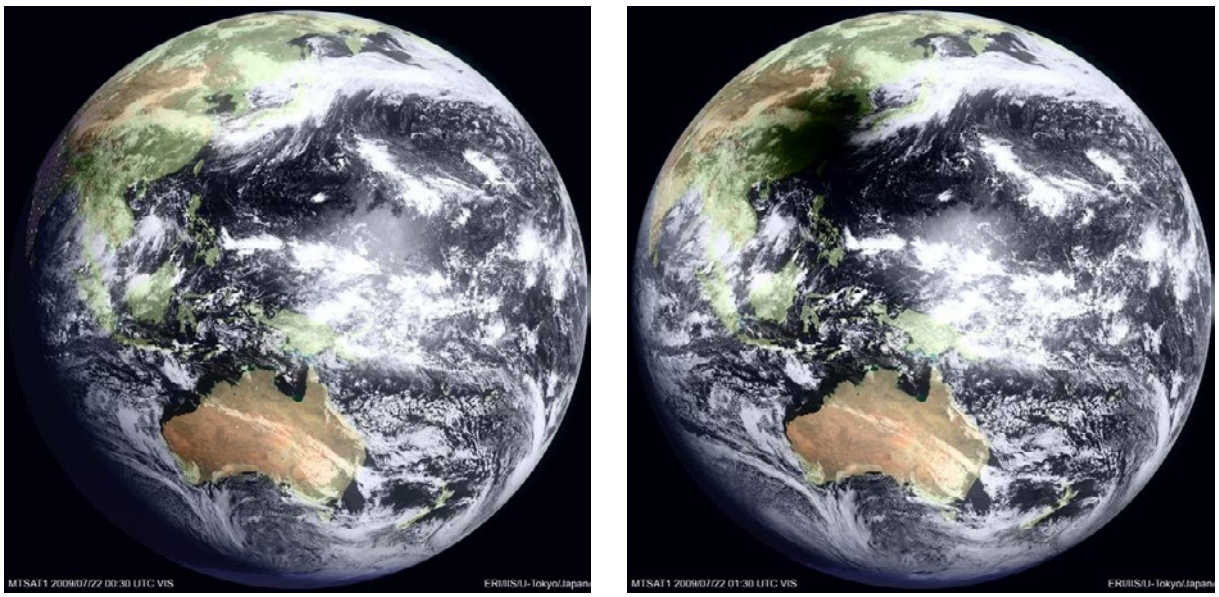
In the fields of observation chance favours the prepared mind
(Louis Pasteur)

Figure 1.1 Earth from space

The Japanese geostationary satellite (MTSAT) imaged the solar eclipse on 22 July 2009 over eastern China, when the Moon's shadow completely overlapped the Sun's disk and plunged Taiwan and southeast China into darkness.

a. MTSAT image taken at 8:30 am, combined with night lights background (from NASA Blue Marble Collection).

b. MTSAT image taken at 9:30 am showing locations in the centre of this shadow (the umbra) experiencing a total eclipse, while locations on the edge (penumbra) experienced a partial eclipse.



Source: NASA. Retrieved from *http://earthobservatory.nasa.gov/IOTD/view.php?id=39520*

Figure 1.2 Space photo of Berlin at night

This photo, taken from the International Space Station (ISS) in April 2013, differentiates between East and West Berlin on the basis of night lighting. Lighting with sodium-vapour lamps in East Berlin is more yellow than the predominantly fluorescent (mercury arc and gas lamp) lighting in West Berlin.



Source: Chris Hadfield, NASA. Retrieved from *http://eol.jsc.nasa.gov/DatabaseImages/ESC/large/ISS035/ISS035-E-17210.JPG*

1.2.2 Indirect observations

The key characteristic that distinguishes remote sensors from other sensing devices is that their observations are indirect. Being remote, their sensing mechanism does not rely on contact with the object being observed, but rather detects some form of energy from the object. Use of remote sensing technologies assumes that the detected energy is indicative of properties of the object. Before observations from remote sensors can be used with confidence, their relationship with known properties of the Earth must be established using some form of reference data.

Interpretation of observations from EO sensors thus involves at least one level of inference (or indirection). The energy detected by an EO sensor is related to properties of the Earth's features and/or its physical, chemical or biological processes (see Excursus 1.2). The generalised process of using remotely sensed observations could be described in terms of three logical stages:

- acquisition—observations are made of the object or surface;
- processing—observed data is modified to represent a property of the object or surface; and
- interpretation—processed data is analysed with reference data for a specific end use or application.

These stages are implicitly linked by models that rely on prior knowledge of the:

- object (or surface) and its properties—observation domain;
- sensor and its properties—measurement domain; and
- intended end use of the remotely sensed data—attribute domain.

The relationships between stages, prior knowledge, and the underlying models are further developed in Table 1.1.

Excursus 1.1—Observing Australia

Source: Norman Mueller, Geoscience Australia
Further information: Geoscience Australia: *http://www.ga.gov.au/*

The Landsat series of satellites has been observing Australia for several decades. The first Landsat satellite was launched in 1972 and quickly proved its value for global monitoring. Since then, a total of eight Landsat satellites have been launched (but Landsat-6 failed to reach orbit after launch). In some years, two Landsat satellites have been acquiring imagery.

The Landsat-1 to -5 satellites carried various sensors, with its multispectral scanner (MSS) being most commonly used for EO applications. Landsat-4 to Landsat-8 have carried a higher resolution MSS (originally called Thematic Mapper (TM), with successive improvements called ETM—enhanced TM— and ETM+). The MSS on board Landsat-8 is called the Operational Land Imager (OLI). A thermal sensor also acquires imagery on Landsat-5, -7, and -8, which is used to observe variations in surface temperature.

Australia established its own receiving station in 1979. In the current Landsat acquisition grid (WRS-2), 369 image scenes cover the Australian mainland and Tasmania. The current satellites, Landsat-7 and Landsat-8, fly over Australia every 16 days (8 days apart), creating 23 sets of scenes each year. Each satellite completes over 5,000 lapses around Earth each year, acquiring over 200,000 image scenes globally. Since the launch of Landsat-1, over half a million image scenes have been acquired over Australia, creating an unprecedented environmental record of our landscape and waterscape.

The mosaic shown in Figure 1.3 is a 'synthetic image', cleverly created by collecting all observations of Landsat-8 OLI over the less cloudy months (April to September) in 2014 and 2015, and calculating the median value of every pixel in those observations. This creates a 'synthetic' view of Australia, since each pixel is not a true observed value, but a statistical median value derived from a set of observations.

Figure 1.3 Median mosaic of Landsat-8 OLI

All Landsat-8 OLI images acquired from April to September in 2014 and 2015 were selected, then the median value for each pixel was computed. This continental mosaic shows spatial variaton in those median values.



Source: Norman Mueller, Geoscience Australia

Table 1.1 Logical stages in EO data use

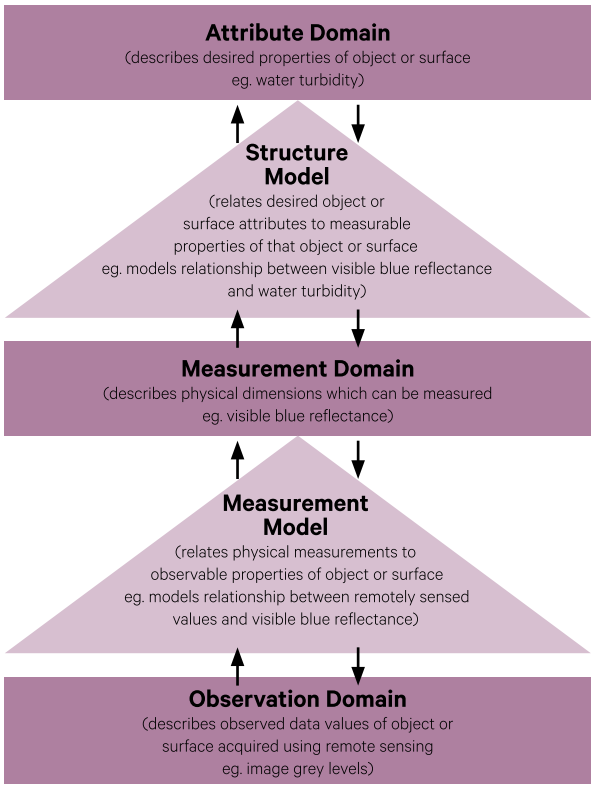
Stage	Description	Domain
Acquisition	Observe object or surface using remote sensing	Observation
Processing	Convert remote sensing observation to measurable property of object or surface using pre-defined measurement model	Measurement
Interpretation	Interpret measured properties of object or surface (that is, the converted remote sensing observation) in terms of a specific application using pre-defined structure model	Attribute

The indirect relationships between observation, measurement and variable domains are illustrated in Figure 1.4. An additional limitation, which must be considered, is that the observations we collect using a remote sensor only provide discrete samples of the potentially continuous range of measurements in any 'measurement domain'. The measurement model also implicitly separates relevant information in the observations from 'noise', where the definitions of both relevant information and noise can differ for different applications. These concepts are further developed in Volume 1B—Sections 1 and 2.

While an individual image analysis exercise would progress from observations to attributes, the interconnections between these domains and models are invariably two-way. Improved understanding of attributes feeds back to improved tools and methods for acquisition and analysis. This ongoing cycle should form the basis of all scientific enquiry and is further considered in Volume 1B.

Figure 1.4 From observation domain to attribute domain

Interpreting imagery from EO sensors is an indirect process, whereby a measurement model is used to transform remotely sensed observations to measurements of some measurable property, and a structure model is used to relate those measurements to application-specific attributes.



Adapted from: Harrison and Jupp (1989) Figure 33

Excursus 1.2—How do EO sensors identify healthy vegetation?

Healthy vegetation appears green because green wavelengths of light are reflected, not absorbed, by photosynthesising foliage. Since the process of photosynthesis absorbs blue and red wavelengths, and the leaf structure reflects near infrared (NIR) wavelengths, green vegetation is characterised by high NIR reflectance and low visible red reflectance. Thus, identification of healthy vegetation using remote sensing relies on measuring NIR and visible red reflectance from the Earth's surface, then analysing the relative difference between these two measurements.

Before vegetation can be declared as healthy or otherwise on the basis of remotely sensed data, reference data is required to determine the threshold at which the relative difference between red and NIR reflectance measurements is significant. In this context, measurement necessarily implies that observations are calibrated to some defined standard, which enables them to be compared with other measurements that are calibrated to a comparable scale (see Section 2.3).

Table 1.2 Data-information-knowledge-wisdom hierarchy

Zeleny (1987)		Ackoff (1989)				Bellinger *et al.* (2004)	
Concept	**Definition**	**Concept**	**Definition**	**Timeframe**	**% Human Mind**	**Concept**	**Transition Process**
Enlightenment	Sense of truth						
Wisdom	Know-why	Wisdom	Ability to see long-term consequences and evaluate them	Permanent	~0	Wisdom	
		Understanding	Ability to assess and correct for errors; Requires diagnosis and prescription	Aura of permanence	~10		Understanding Principles
Knowledge	Know-how	Knowledge	Refines information; Allows information to be transformed into instructions	Longer life span	~20	Knowledge	Understanding Patterns
Information	Know-what	Information	Data processed to be useful; Answers 'who', 'what', 'where', and 'when' questions	Ages rapidly	~30	Information	Understanding relations
Data	Know-nothing	Data	Product of observations; Symbols with no inherent structure or meaning	Transient	~40	Data	

1.2.3 A philosophical interlude

The three logical stages involved with using EO data directly correspond to the first three transitions outlined in the Data-Information-Knowledge-Wisdom (DIKW) hierarchy popularised by Ackoff (1989), and summarised in Table 1.2. The concepts of data, information, knowledge and wisdom are widely viewed as the building blocks of library and information science (Bernstein, 2009), and knowledge management (Zeleny, 1987).

While the following terms are sometimes used interchangeably in EO literature, the three equivalents below, and their definitions, are recommended for clarity:

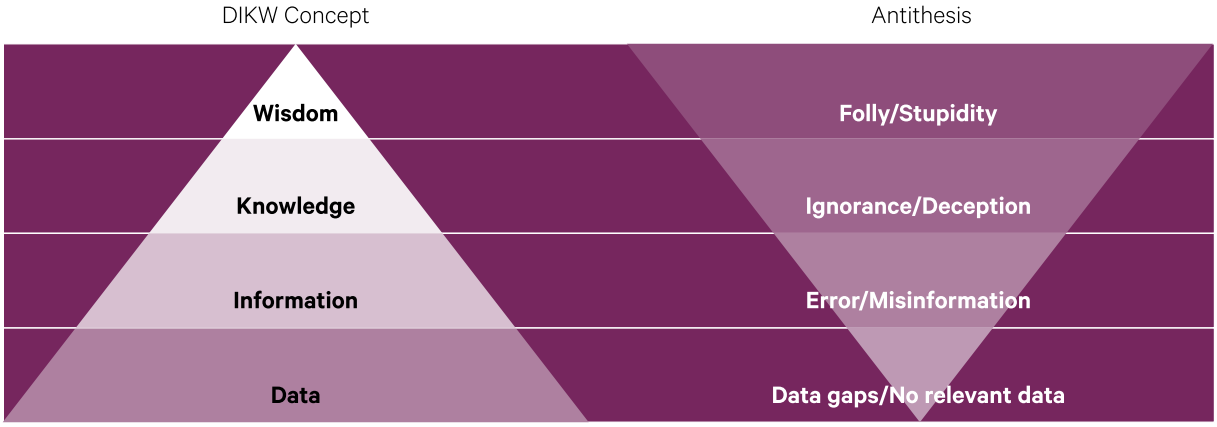
- data ~ observations—raw representation(s) of a quantity;
- information ~ measurements—self-describing representation of a quantity, with defined scale and metadata; and
- knowledge ~ attributes—represents a quantity in terms of the application domain, and reflects the process that the interpreter is attempting to model.

We will not presume to suggest an equivalence for wisdom.

Where is the wisdom we have lost in knowledge?
Where is the knowledge we have lost in information?
(Eliot, 1934)

Figure 1.5 Data-Information-Knowledge-Wisdom triangle

The Data-Information-Knowledge-Wisdom (DIKW) triangle represents the relative abundance of each type of 'intelligence' and the progression from data to wisdom. This sequence from data to wisdom is characterised by both decreasing volume and variety, and increasing control, understanding and connection. As a snapshot in time, It could also be argued that data is inherently relevant to the past, while derived wisdom should be relevant to the future. The antithesis of the DIKW hierarchy, the progression from folly to wisdom, reverses these relationships.



As illustrated in Figure 1.5a, the DIKW hierarchy is often represented as a triangle or pyramid in which the area or volume of each layer is indicative of the variety and volume of examples that exist for that layer. For example, the Data layer has the largest area, indicating the greatest number of data sources and the greatest number of data types. Conversely, in the smallest layer, Wisdom, there exist the fewest varieties and the smallest number of instances. Progression through this hierarchy has also been linked to increasing control, understanding and connectedness, as well as relevance to the passage of time.

Also of relevance to EO is the antithesis of the DIKW hierarchy discussed by Bernstein (2009) and illustrated in Figure 1.5b, where the extent of each antithesis layer is inversely proportional to its corresponding DIKW layer. For example, while there are few instances of wisdom, there are many of folly.

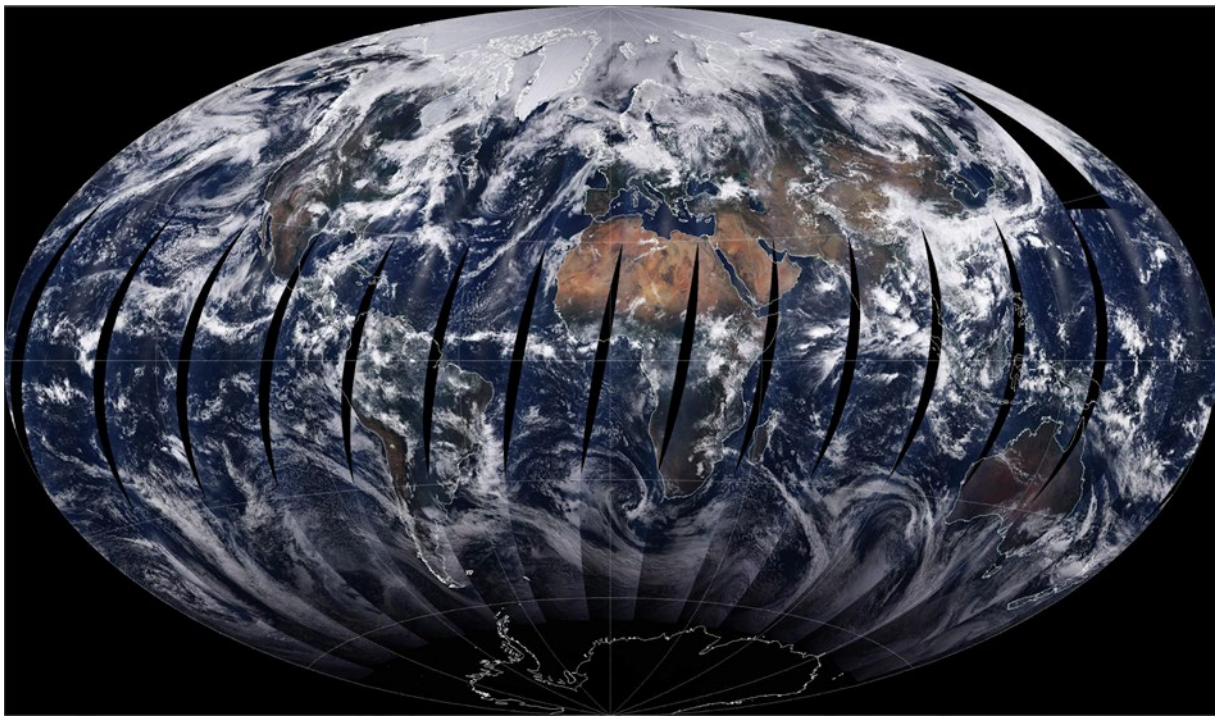
Science involves systematic enquiry into the structure and behaviour of the world using the tools of observation and experiment. This process should result in a base of knowledge and understanding about the world that is defensible. While the DIKW triangle implies that the process of moving from data to wisdom is one-directional, the resulting knowledge and wisdom also feed back to improved methods of data acquisition, processing and interpretation. The antithesis of the DIKW triangle could be attributed to a lack of enquiry.

Obviously, the goal of every EO project should be to increase our knowledge and understanding of the Earth. This task becomes more important and more difficult as both the volumes of available data sources and the expectations for instant answers increase at unprecedented rates. To maintain the integrity of EO it is imperative that its users remain focussed on attaining relevant and defensible knowledge outcomes—and understanding them.

One can survive without understanding, but not thrive. Without understanding one cannot control causes; only treat effect, suppress symptoms. With understanding one can design and create the future… people in an age of accelerating change, increasing uncertainty, and growing complexity often respond by acquiring more information and knowledge, but not understanding.
(Gharajedaghi and Ackoff, 1984)

Figure 1.6 MODIS global composite image

This composite image demonstrates an example of the volume of data collected by one satellite sensor, MODIS, on 28 May 2001.



Source: Marc Imhoff, NASA

1.3 Observing the Earth

Remotely sensed data provide a synoptic or regional view of the Earth as well as the opportunity to observe and identify particular features and processes of interest. EO offers a unique perspective on our planet and delivers observations that are consistent and repeatable at a range of specific spatial and temporal scales. Sensing forms of energy that are outside the human visual range also allows early detection of many forms of environmental stress and degradation. These features combine to create a robust, flexible and cost-effective data source for mapping, monitoring and modelling Earth's resources (see Figure 1.6).

Relevant characteristics of the Earth are reviewed in Section 3. Many of these characteristics have been discovered or refined using remote sensing, including:

- precise measurements of distances to, and radiation from, other celestial bodies;
- more accurate models for the changing shape of the Earth;
- better models of the Earth's magnetic and gravitational fields;
- enhanced knowledge of the structural and chemical composition of the Earth's interior;
- global information concerning the extent and condition of land cover;
- detailed mapping of ocean colour, temperature and extent; and
- improved observations and models of the Earth's atmospheric processes.

1.3.1 Historical background

The origin of remote sensing of the Earth's surface (using sensors rather than eyes) can be traced back to the first photograph, which was taken in 1826 by Joseph Nicéphore Niépce looking onto the French countryside. The first aerial photograph was taken over Paris in 1858, by balloonist Gaspard-Félix Tourmachon Nadar, from an altitude of around 400 m. In 1908, the first photographs were taken from an aircraft being piloted by Wilbur Wright. Aerial photography was being used for civilian mapping, topography and cartography before World War 1, but its reconnaissance value was only realised and further developed during the two World Wars. Aerial photography and/or imagery can now be acquired using a range of platforms, including Remotely Piloted Aircraft Systems (RPAS) (which are also known as Unmanned Aerial Vehicles or UAV; see Section 11.2).

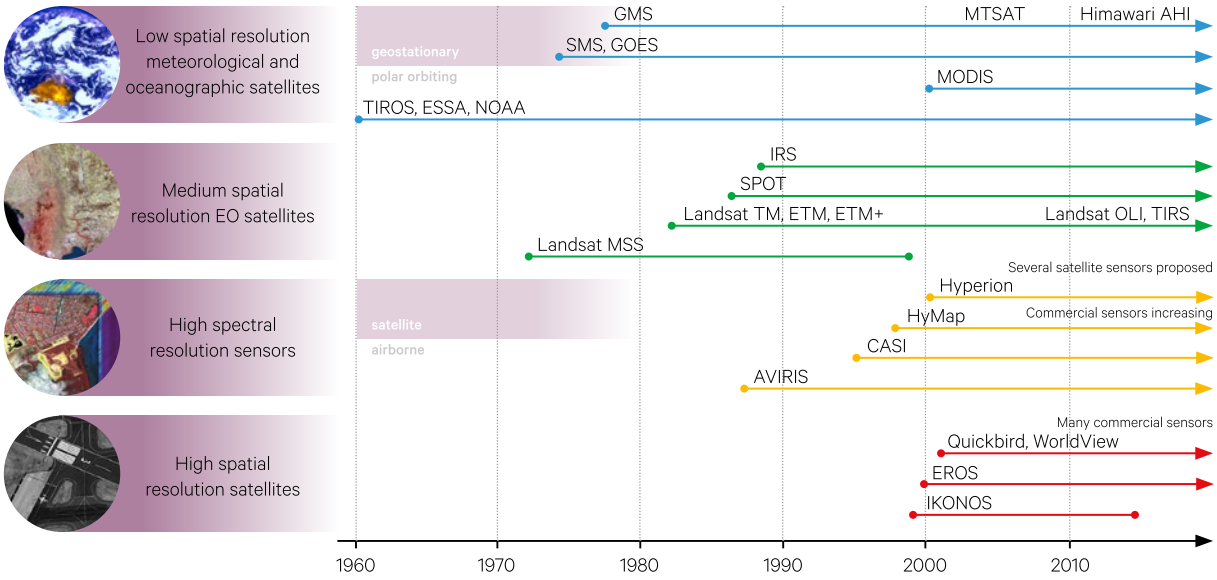
The first space photographs were taken from V-2 rockets in 1946. The first satellite, Sputnik, was launched in 1957 by the Soviet Union and was quickly followed by the US Corona Project in 1960, which demonstrated the vast potential of space photography. The first polar-orbiting meteorological satellite, TIROS-1, was also launched by the USA in 1960 and delivered operational weather imagery with global coverage from 1966 (see Excursus 12.1). The first of the Landsat series of satellites, originally called the Earth Resources Technology Satellite (ERTS), was launched in 1972 to map characteristics relating to land cover. This satellite has been followed by hundreds of spacecraft that routinely collect EO imagery at a range of scales for a wide variety of applications. Skylab, the first space station, was launched by the USA in 1973 as part of the Apollo program, and carried a range of remote sensing devices. The historical development of space-based EO is summarised in Figure 1.7.

Both the quality and quantity of EO imagery has greatly increased since the initial EO satellites were launched, with an estimated 70 operational EO satellites currently providing public good (that is, non-commercial) imagery and several hundred more satellites planned to become operational before 2025 (ATSE, 2009). The extent of operational usage of space-based EO data has enabled an increasing number of commercial companies to manage satellite platforms, with several dozen commercial satellites now supplying EO data internationally.

Recent advances in hardware and software, often borrowed from other industry sectors such as video games, mobile phones and medical technology, have enabled a new approach to satellite development. Variously labelled as microsatellites or nanosatellites (nanosats) these platforms are significantly smaller and cheaper than the traditional EO satellites, both to build and launch, making them affordable for a range of businesses and users. By April 2025[4], thousands of nanosats had been placed in orbit. These miniaturised satellites are often networked into larger constellations that enable multiple images of a selected location to be acquired each day (see Figure 1.8). Frequent imagery is particularly valuable for observing a range of disaster events, monitoring crop condition, and surveillance activities.

Figure 1.7 Historical development of remote sensing

While the origins of remote sensing can be traced back to balloons, kites, pigeons and aeroplanes, this diagram illustrates the rapid advances in airborne and spaceborne remote sensors in recent decades.



Source: Megan Lewis, University of Adelaide

4. http://www.nanosats.eu

Figure 1.8 Nanosatellite imagery

Image of Sydney acquired by Flock-1 satellites on 29 November 2015 showing the city centre, Port Jackson and Bondi Beach.



Source: Planet Labs. Inc. (CC BY SA 4.0). Retrieved from *https://www.planet.com/gallery/sydney-20151130/*

Another nanosatellite constellation is QB50, an international network of 36 CubeSats launched in 2017 to study Earth's largely unexplored thermosphere. Each Cubesat weighs about 1 kg and is expected to have a short lifespan (1 to 2 years).

Three of these satellites were developed in Australia—the first Australian satellites to be launched since 2002. The UNSW-EC0 CubeSat, for example, was developed by the Australian Centre for Space Engineering Research at the University of NSW (UNSW) to observe the thermosphere's atomic composition (see Figure 1.9).

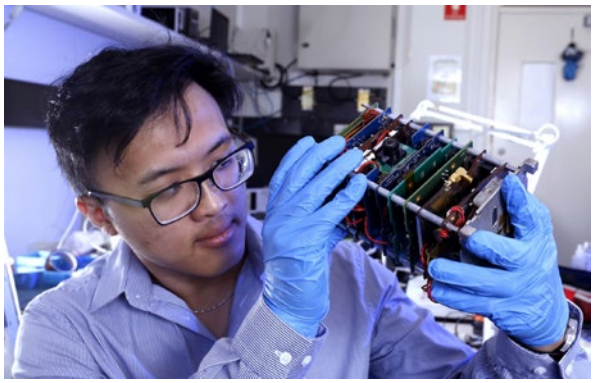
The volume and variety of EO data that is currently available, either as archives or ongoing acquisitions, is enormous. One of the major challenges for EO users is to select the most appropriate data for each specific application.

1.3.2 EO data characteristics

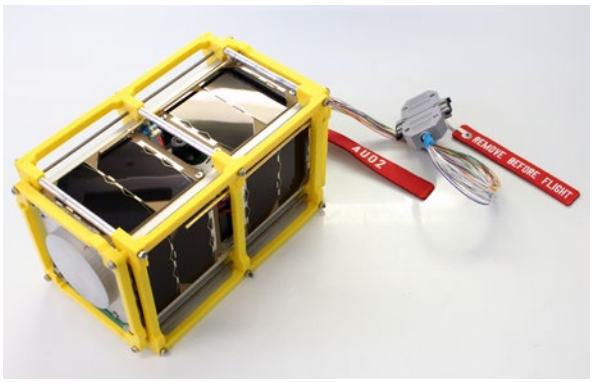
As introduced in Section 1.2.2, EO sensors acquire data in the form of observations. This data may be processed to become measurements then interpreted to become information. The initial observations of most remote sensing devices are quantitative, but only calibrated relative to a sensor-specific sensitivity range. The processing stage converts the initial observations so that they are comparable with a standard measurement scale and/or other data sources. This initial conversion is often undertaken by the data distributor, so may not be apparent to many data users. Nonetheless, when EO data is being used to underpin environmental monitoring and modelling activities, it is essential that its provenance can be verified and satisfies the expectations of end users. It should be noted that some forms of EO data, for which metadata and/or appropriate models do not exist, cannot be converted into measurements or variables so, in this context, can only be considered as observations.

Figure 1.9 CubeSat

a. Dr Joon Wayn Cheong, Technical Lead, examining the UNSW-EC0 QB50 CubeSat prior to the external solar panels and antennae being fitted. Photo Credit: Grant Hausler, UNSW



b. UNSW-EC0 QB50 satellite in its protective 3D printed yellow frame, ready for shipment Photo Credit: John Lam, UNSW



Source: Cheryl Brown, University of New South Wales

The interrelationships between these terms and their relevance to remote sensing are summarised in Table 1.3. These stages and processes are most easily understood in the context of specific examples. The EO example traces the stages, or processes, involved with detecting potential fire hotspots using imagery from sensors that detect energy in visible, near infrared, middle infrared and thermal infrared wavelengths. The non-EO example relates the stages of acquisition, processing and interpretation, and their resulting observation, measurement and attribute, to the operation of a traffic speed camera. As this example demonstrates, there are many uses of remote sensing technology that are not directly related to EO, however this book focuses on those that do.

Another example of the stages that can be involved with processing EO imagery is shown in Excursus 1.3 where features of interest are corrected, isolated then classified. In this example, Quickbird imagery is selected to classify benthic cover of coral reefs along the Queensland coast.

Table 1.3 Observations, measurements and attributes

Process	Result	Description	EO Example	Non-EO Example
Acquisition		Using sensors carried on platforms	Remote sensor records radiance of land area	Traffic speed camera photographs speeding vehicle
	Observation	Detect energy from an object or feature of interest	Images of visible and infrared radiation	Photograph vehicle number plate
Processing		Using pre-defined algorithms and prior knowledge about the sensor and/or platform	Land temperature computed from infrared images	Sharpen photograph to match standard clarity
	Measurement	Represent known properties of feature of interest	Brightness temperature image	Clear licence number of vehicle
Interpretation		Using reference information about feature of interest and measurements	Use visible and near infrared channels to exclude bright, non-fire pixels or cloud	Use registration records to link licence number to owner details
	Attribute	Relate directly to feature of interest	Hotspot imagery showing potential locations of active fires	Identification of vehicle owner

Excursus 1.3—EO processing stages

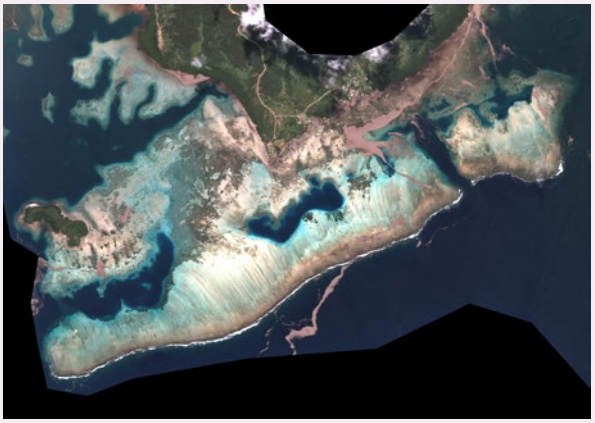
Source: Chris Roelfsema, University of Queensland

Processing of EO imagery involves a number of stages. The example below uses an image acquired by the Quickbird satellite on 17 October 2006 to map 21 benthic cover classes in Navakavu, Vanua Levu, Fiji (Phinn *et al*., 2010).

a. Selected data with no corrections may not show the best contrast or geometry



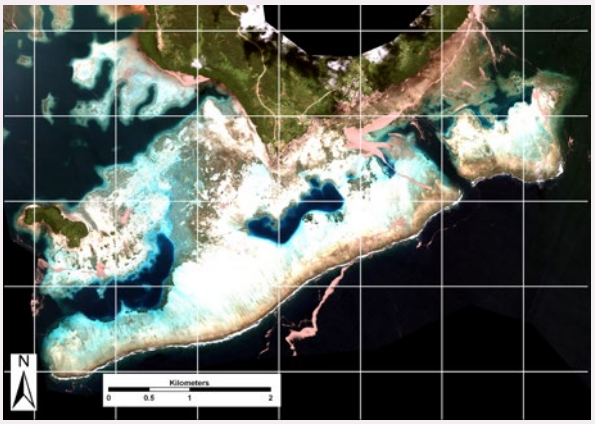
b. Correct distortions in image values due to atmospheric factors



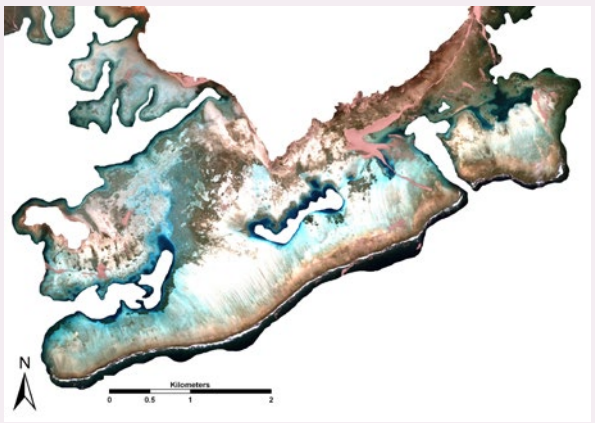
c. Correct distortions in image values due to water factors



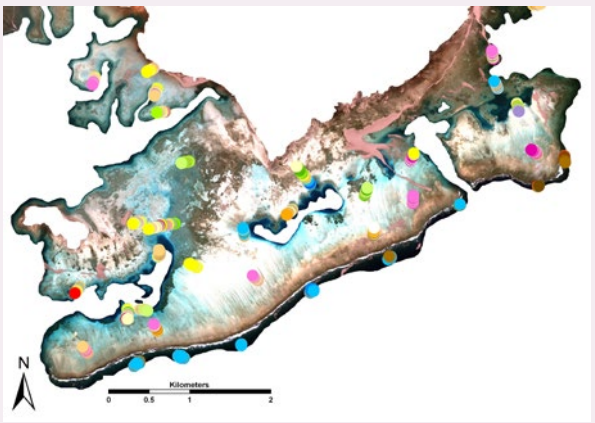
d. Correct geometric distortions



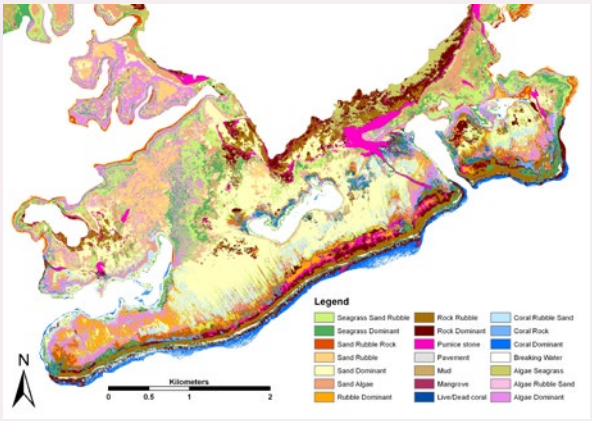
e. Remove features not related to the analysis, in this case land and deep water



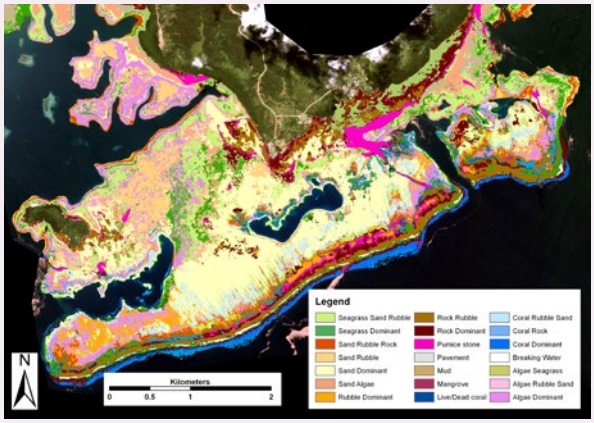
f. Compare image data with field information for this site



g. Classify image data to match field categories



h. Overlay final image classes on corrected image



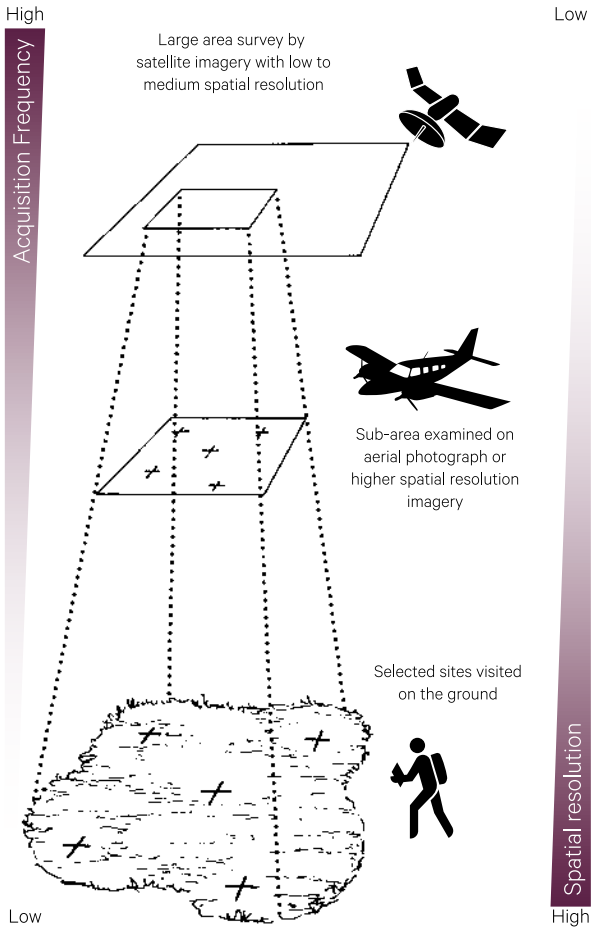
Thus, considering the logical stages involved with using remotely sensed data, the ability to relate objects, or features, and/or physical processes on the Earth's surface to data acquired by remote sensors rests on two underlying, but interrelated, considerations, namely the:

- intrinsic ability of the features to be resolved in the type of measurements being made—that is, the accuracy and precision of the sensing device; and the
- effectiveness of the models that relate features or physical processes to these measurements.

The issue of measurement is both fundamental and vital to planning EO data acquisition and its subsequent processing. The usual measurement space for EO data has a variety of measurement 'dimensions', such as intensity, wavelength and position. These can be considered as providing a coordinate framework in space and time. A data set is usually a sample in this coordinate framework. The objective of any data analysis exercise is to distinguish effects and/or events in the data. To achieve this objective, a data set must be sufficiently resolved, appropriately dense and cover an adequate extent.

Figure 1.10 Scales of EO

Analysis of low and medium resolution imagery can be more easily related to ground data through high resolution imagery. Low resolution imagery tends to be acquired more quickly and cover a larger extent, so is most appropriate for large area surveys. Selected locations within the surveyed area would typically be checked using data with higher spatial resolution, such as aerial photography. Some of these locations would then be visited in the field to verify the image analysis. This scaled approach enables the results of expensive and time-consuming field work to be extended to a larger area.



Adapted from: Harrison and Jupp (1989) Figure 39

Resolution refers to level of detail, density refers to the intensity or rate of sampling, and extent refers to the overall coverage of a data set. Extent can be seen as relating to the largest object or feature, or range of features, which can be observed, while resolution relates to the smallest. Density indicates the continuity and frequency of sampling. For a feature to be distinguishable in the data, the resolution, density, and extent of the measurement dimensions of the data need to be appropriate to the measurable properties of the feature. For a feature to be separable from other features, these measurements must also be able to discriminate between the differences in reflectance from those features.

EO projects, however, do not need to be limited to a single source of imagery. Two or more sources of data, imaged at different scales, can be integrated, as discussed in Volume 1B—Section 9 and Volume 2D.

A further characteristic of EO data that impacts its value to particular applications is latency, or the time interval between acquisition of data and its dissemination to users. The EO data distribution process typically involves multiple data handling steps including reception, processing, quality assurance, and delivery. As EO data becomes increasingly important to a growing number of application areas, the demand for reduced latency is also growing, especially for disaster management. The inverse relationship between data acquisition (and dissemination) rates and spatial resolution are shown in Figure 1.10. Resolution, extent, and density of remotely sensed data are further discussed in Volume 1B—Section 1.

1.4 Using Earth Observations

As summarised in Section 1.3.1 above, EO data have been available from airborne platforms for over a century while imagery from spaceborne platforms have been available internationally for over five decades. Space-based imagery, in particular, offers a unique source of data about the Earth by recording:

- accurate geo-locations for contiguous target areas;
- objective, consistent measurements of physical properties of the Earth and its atmosphere that can be interpreted to define its features and condition; and
- repeated coverage to enable detection of changes in features and/or their condition.

No other source of data for the Earth provides comparable consistency, repeatability and coverage. Additionally, EO offers the least expensive form of environmental data acquisition. One example of the volume of data that is acquired in one day by a single sensor is illustrated in Figure 1.6. A monthly composite derived from such imagery is shown in Figure 1.11.

The results from EO analyses are now routinely used for a wide range of applications such as land use planning, agricultural management, land rehabilitation, transport planning, surveillance, disaster management, mineral exploration, geodesy, water resources management, and weather and climate forecasting (see Volume 3 for a detailed discussion of EO applications and case studies). Current usage of EO data can be considered in terms of three broad functions, namely:

- detecting and mapping specific features of interest, such as determining the spatial distribution of crop health on a particular date (see 1.4.1);
- monitoring changes in specific features, such as quantifying the spatial variations in crop health over a season (see Section 1.4.2); and
- modelling environmental processes, such as identifying the relationship between crop health and management practices (see Section 1.4.3).

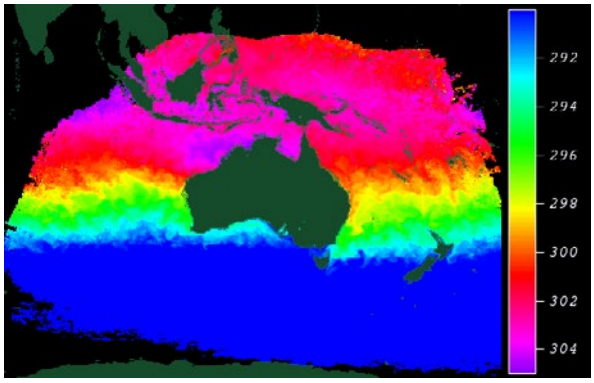
To ensure that the attributes derived from EO datasets are accurate, consistent and relevant, each of these three functions incorporates two fundamental processes:

- calibration—relates EO observations to standard measurement scales to ensure traceability both between sensors and through time. This process is a component of the measurement model introduced in Section 1.2 and is considered in greater detail in Volume 2A—Section 3; and
- validation—assesses the quality of derived attributes relative to independent datasets. This process is a component of the structure model introduced in Section 1.2 and is considered in greater detail in Volume 3.

Facilities and activities relevant to calibration and validation of satellite data in Australia are reviewed by Malthus and Li (2014).

Figure 1.11 Monthly composite

Sea Surface Temperature (SST) from AVHRR mosaic of thermal images calibrated using measurements from ships and drifting buoys. This one-month composite was compiled from night-time data during April 2016. Scale units in K.



Source: Christopher Griffin, Bureau of Meteorology

1.4.1 Detecting and mapping features

For several decades, EO data has been used to map features associated with the Earth for a range of environmental and scientific applications. Relevant features being mapped include vegetation condition and extent, crop productivity and health, habitats, urban and rural land use, evapotranspiration, soil moisture, erosion, salinity, paleovalleys, archaeological sites, terrain and vegetation height, mineral deposits, surface deformation, potential fire locations, fire scars, snow cover and extent, ocean colour and temperature, water turbidity, flood events, and atmospheric composition, temperature and water vapour content (see Figure 1.12). EO data is also used for geodetic surveys, cartography, navigation and border surveillance.

As detailed in Volumes 2 and 3, procedures for mapping such features using specific EO data sources are now well established and yield reliable results on an operational basis. The resulting maps show the location and spatial distribution of the target feature at a particular point in time.

1.4.2 Monitoring changes

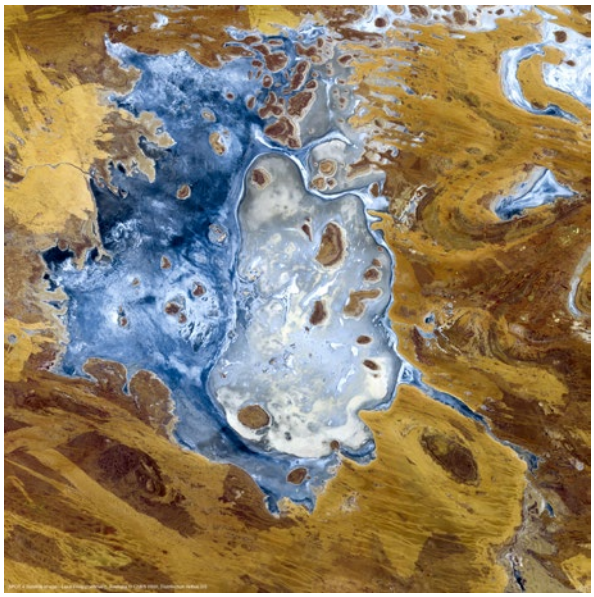
In many instances, Earth's features can be mapped from a single image and validated using appropriate reference data. To maximise the value of the recurrent imagery available from EO however, multiple images from one or more sources can be used to monitor changes in particular features and assess the extent of change within a selected time period. Given the dynamic nature of the Earth, EO offers an invaluable monitoring tool especially for early detection of various forms of environmental degradation.

EO data sources are used to quantify changes in a range of activities and resources including deforestation, agricultural production, city growth, land use change, wind erosion, waterlogging, remnant vegetation, rangelands, desertification, wetlands, sea floor topography, ocean currents, climatic indicators and pollution. For example, the construction of Elizabeth Quay, Perth, is monitored by a sequence of Nearmap aerial images in Figure 1.13.

Recent environmental legislation has further reinforced dependency on EO to monitor the ongoing status of various resources including inland water quality and carbon sequestration. The growing archive of EO data enables changes in environmental resources to be carefully tracked and correlated with potential drivers. This archive also offers the opportunity for time series analysis of relevant imagery and thus the separation of seasonal from longer-term trends.

Figure 1.12 Lake Disappointment

Lake Disappointment is a salt lake in the Little Sandy Desert (Pilbara region, northern WA), mostly surrounded by sand dunes. This lake only contains water after heavy rain or floods and thus proved to be a disappointment when encountered by early explorers. The image below was acquired by SPOT-4 in March 2002 during a rare inundation event.



Source: © CNES (2016). Distribution Airbus DS.

Figure 1.13 Construction of Elizabeth Quay, Perth

Elizabeth Quay, named after Queen Elizabeth II, is a major mixed-use development in Perth's CBD, spanning 10 ha on the northern shore of the Swan River. The development included construction of an artificial inlet, with 1.5 km of boardwalks and promenades, and will ultimately comprise office, retail and residential buildings, and recreational facilities. This sequence of Nearmap high-resolution aerial images monitors the development from the original Esplanade Reserve before the project commencement date of 26 April 2012, to after its official opening on 29 January 2016. Construction of buildings associated with the site is expected to be complete by 2018.

22 February 2012



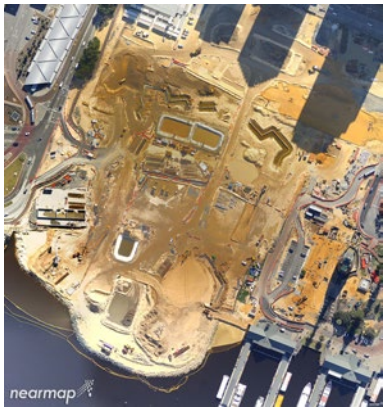
30 June 2013



20 February 2014



8 August 2014



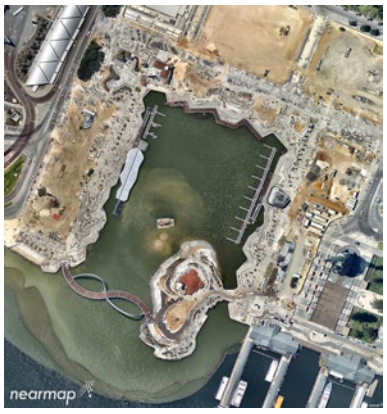
28 June 2015



7 September 2015



22 November 2015



4 March 2016



10 May 2016



Source: © Nearmap

1.4.3 Modelling processes

The Earth is a dynamic planet. All aspects of Earth—its surface, water, air and interior—are continuously changing in terms of their biology, chemical composition, physical form, and energy. EO data have allowed these changes to be quantified and modelled. The elevated perspective of most EO sensors provides an ideal view of the Earth to observe its physical, chemical and biological processes. The fundamental goal of any EO analysis is to increase our understanding of Earth's dynamic processes and, in consequence, our management of the planet.

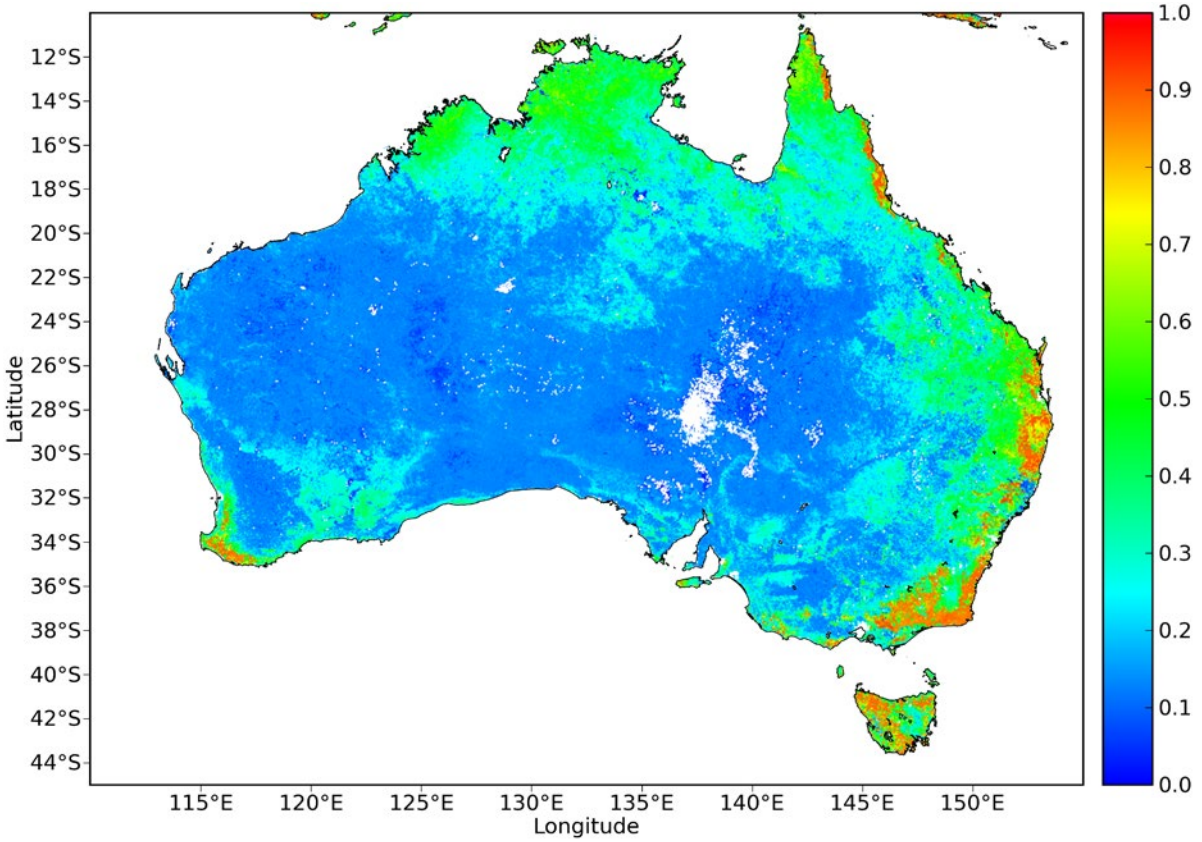
Monitoring changes using EO is a first step in quantifying these processes. However, we need to model the processes themselves in order to predict future states and/or determine their interdependence on other factors, such as management practices.

Reliable EO-based models already exist for weather forecasting and, in conjunction with other data sources, are being developed to better predict the dynamics of climate, vegetation, salinity, oceans, and natural disasters. Processes for modelling indicators of photosynthetic activity are well established and underpin a wide range of environmental and agricultural activities (see Figure 1.14).

By understanding the rate of change that is occurring in key environmental variables, land managers are better equipped to evaluate the impact of particular management strategies and modify management practices if appropriate. Improved efficiency in urban planning, agricultural production, freshwater management, natural resource utilisation and pollution control will undoubtedly benefit all inhabitants of planet Earth.

Figure 1.14 Modelling photosynthetically active radiation

Fraction of Photosynthetically Active Radiation (fPAR) derived from MODIS/Terra imagery (LPDAAC MOD15A2 mosaic) acquired between 1 and 8 January 2016 (inclusive). This gridded 8-day composite shows fPAR on a scale from 0 to 1.



Source: TERN AusCover. Retrieved from *http://www.auscover.org.au/purl/lpdaac-mosaic-mod15a2-v5*
AusCover is the remote sensing data products facility of the Terrestrial Ecosystem Research Network (TERN; *http://www.tern.org.au*).

1.5 The Global Picture

EO is the only technology that offers the luxury of truly seeing the global picture (see Figure 1.15).

1.5.1 The Global Earth Observation System of Systems

The Group on Earth Observations (GEO) is an international body established in 2002 to encourage its member governments to coordinate projects, strategies and investments for EO. Since 2005, GEO has been implementing the Global Earth Observation System of Systems (GEOSS) ten year plan to advance and demonstrate the societal benefits of EO in nine Societal Benefit Areas (SBA):

- **Agriculture**—support local, national and regional activities for agriculture, rangelands, forestry and fisheries, including famine early warning, food security prediction, drought forecasting, agriculture production and forecasting, aquaculture production, timber, fuel and fibre management, forest perturbations and protection, and carbon and biomass estimation;
- **Biodiversity**—assess condition and extent of ecosystems, distribution and status of species, and genetic diversity in key populations, as well as tracking invasive species;
- **Climate**—model, mitigate, adapt and assess risks of climate change for atmosphere, lands and oceans;
- **Disasters**—predict and monitor earthquakes, floods, landslides, cyclones, volcanic eruptions, and wildfires;
- **Ecosystems**—monitor and evaluate ecosystem health, function and change in coastal and near-shore marine systems, forests, inland waters, oceanic islands and archipelagos, tundra, and watersheds;
- **Energy**—assess viability of renewable energy sources, including hydropower, wind power, bioenergy, solar power, geothermal power;
- **Health**—monitor aeroallergens, air quality, and infectious diseases, and provide early warning for public health risks such as heat waves and epidemic pre-conditions;
- **Water**—monitor terrestrial hydrology of surface waters, ground waters, forcings, water quality, and water usage; and
- **Weather**—improve weather information, forecasting and warning using numerical weather prediction (global and regional), synoptic, aeronautical and agricultural meteorology, and atmospheric chemistry.

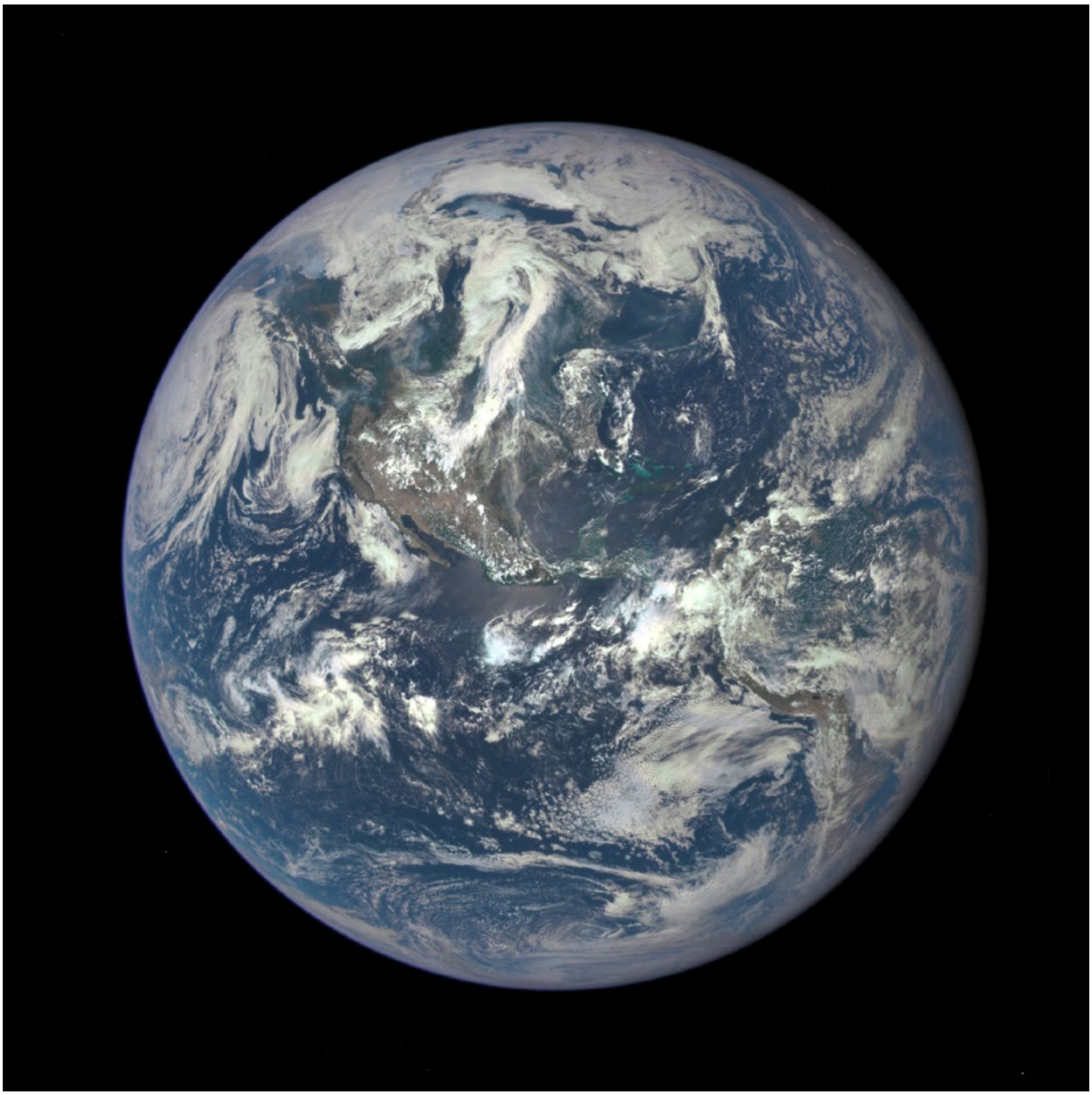
GEOSS aims to increase knowledge and understanding of Earth systems by continuous monitoring of its state and dynamics (van Zyl *et al.*, 2009). Realisation of this goal will require new, autonomous infrastructure, as envisioned by the Sensor Web Concept (Botts *et al.*, 2006; Botts *et al.*, 2007), to collate and disseminate relevant data. Such developments, and other global monitoring systems, are further discussed in Volume 3.

1.5.2 Essential climate variables

The Global Climate Observing System (GCOS) has defined a set of derived climate variables that are deemed essential for monitoring Earth's climate. These Essential Climate Variables (ECV) are listed in Table 1.4 (GCOS, 2010). Measurement of over half of the recognised ECVs is largely or exclusively dependent on EO data acquired from satellite platforms (see underlined entries). This list exemplifies the importance of EO data for a wide range of environmental monitoring and modelling applications.

Figure 1.15 The global picture

This is the first view of the entire sunlit side of the globe from 'one million miles' (1.6 million km) away. It was taken by NASA's Earth Polychromatic Imaging Camera (EPIC) on 6 July 2015 from the Deep Space Climate Observatory (DSCOVR). This image uses the red, green and blue channels.



Source: NASA. Retrieved from *http://www.nasa.gov/press-release/nasa-satellite-camera-provides-epic-view-of-earth*

As a former astronaut who's been privileged to view the Earth from orbit,
I want everyone to be able to see and appreciate our planet as an integrated, interacting system.
DSCOVR's observations of Earth, as well as its measurements and early warnings of space weather
events caused by the sun, will help every person to monitor the ever-changing Earth,
and to understand how our planet fits into its neighbourhood in the solar system.
(Charlie Bolden, NASA)

Table 1.4 GCOS essential climate variables

Measurement of underlined ECVs can be derived from EO.

Domain	Type of Measurement	Essential Climate Variables
Atmospheric	**Surface** (includes measurements at standardized, but globally varying, heights in close proximity to the surface)	Air temperature Wind speed and direction Water vapour Pressure Precipitation Surface radiation budget
	Upper-air (up to the stratopause)	Temperature Wind speed and direction Water vapour Cloud properties Earth radiation budget (including solar irradiance)
	Composition	Carbon dioxide Methane and other long-lived greenhouse gases (including nitrous oxide (N_2O), chlorofluorocarbons (CFCs), hydrochlorofluorocarbons (HCFCs), hydrofluorocarbons (HFCs), sulphur hexafluoride (SF_6), and perfluorocarbons (PFCs) Ozone and Aerosol properties, supported by their precursors (in particular nitrogen dioxide (NO_2), sulphur dioxide (SO_2), formaldehyde (HCHO) and carbon monoxide (CO))
Oceanic	**Surface** (includes measurements within the surface mixed layer, usually within the upper 15m)	Sea-surface temperature Sea-surface salinity Sea level Sea state Sea ice Surface current Ocean colour Carbon dioxide partial pressure Ocean acidity Phytoplankton
	Sub-surface	Temperature Salinity Current Nutrients Carbon dioxide partial pressure Ocean acidity Oxygen Tracers
Terrestrial		River discharge Water use Groundwater Lakes Snow cover Glaciers and ice caps Ice sheets Permafrost Albedo Land cover (including vegetation type) Fraction of absorbed photosynthetically active radiation (FAPAR) Leaf area index (LAI) Above-ground biomass Soil carbon Fire disturbance Soil moisture.

Adapted from: CEOS (2016) at *http://database.eohandbook.com/climate/gcosecvindex.aspx*

1.6 Key Terms

Terminology can be confusing in EO literature. To ensure consistency with terminology (and with reference to Ackoff, 1989; Rowley, 2007; OGC, 2012), this book assumes the meanings listed below for some basic terms. The reader is also referred to the glossary of photogrammetric terms compiled by Newby (2012).

Accuracy—degree to which information on a map or in a digital database [or remotely sensed image] matches true or accepted values. Accuracy pertains to the quality of data and the number of errors contained in a dataset or map.

Acquisition—process of observing an object or surface using a remote sensor.

Application—specific area of interest, or field of study, that will use the results from an EO analysis. Examples of applications include water quality, desertification, agriculture and climate studies.

Attribute—represents measured properties of object or surface in terms of a specific application using a pre-defined structure model. In the context of EO, end users are interested in attributes that directly relate to their application areas. Examples of attributes that might be derived from EO imagery include water turbidity, rate of erosion, crop yield, and rainfall variability.

Attribute domain—describes properties of an object or surface that are relevant to an end user (see Figure 1.4).

Calibration—process of defining the relationship between observations and physical measurement standards. In the context of EO, calibration relates remotely sensed observations to absolute references and standards to ensure consistency between sensors and through time[5]. Calibration is a component of the measurement model.

Data—symbols; discrete, unorganised and unprocessed objective facts or observations that represent properties of objects, events and environments. Data do not convey any specific meaning and are of no use until they are processed into a form relevant to a particular application.

End user—person or persons that will use the processed, interpreted EO data for a specific application.

Feature—starting point for modelling of geographic information; a digital representation of a real world entity or an abstraction of the real world. The terms feature and object are often used synonymously.

Geographic Feature—feature associated with a location relative to the Earth.

Image—collection of contiguous coverage data, usually from sampling at regular, discrete locations.

Information—data that are processed to be useful, contained in descriptions, and answers to questions that begin with such words as 'who', 'what', 'when' and 'how many'. The difference between data and information relates to function rather than structure. Information is inferred from data and frequently includes metadata. Information contains tags to context. In the context of EO, information relates to application areas, implying interpretation via established models that link calibrated measurements to end user requirements.

Interpretation—process of understanding the measurable properties of an object or surface in terms of a specific application using a pre-defined structure model.

Knowledge—application of data and information; answers 'how' questions.

Map—two-dimensional visual portrayal of geospatial data as opposed to the data itself.

Measurement—a 'self-describing' observation associated with scale and metadata. A measurement usually refers to the measuring device and procedure used to determine the value, such as a sensor, analytical procedure, simulation or other numerical process. In the context of EO, this should imply calibrated observations.

Measurement domain—describes physical dimensions that can be measured, such as visible blue reflectance, relative to known scale and metadata as defined by associated measurement model (see Figure 1.4).

Measurement model—relates physical measurements to observable properties of an object or surface. For example, measurement models are used to relate remotely sensed observations to calibrated reflectance measurements (see Figure 1.4).

Metadata—appended information that describes other data, such as the coordinate framework in space and time for measurement dimensions. This involves documentation of data to enable managers or users to understand, compare and interchange the content of a dataset[6].

Noise—part of observation considered irrelevant to the end-use of observations and, as a consequence, often removed in conversion to the measurement space.

5. See also: *http://calvalportal.ceos.org/cal/val-wiki/-/wiki/tag/terms+and+definition?p_p_auth=04F08ThF*
6. See also *https://www.e-education.psu.edu/geog486/node/1882*

Object—feature (on, or associated with, the Earth) that is being observed by a remote sensor.

Observation—an event that estimates an observed property of some feature of interest using a specified procedure and generates a result (Cox *et al*., 2010; OGC, 2012). This can also be viewed as a raw representation of a quantity or attribute. In the context of EO, raw (that is, uncalibrated) image data can be viewed as observations.

Observation domain—describes observed data values of an object or surface acquired using remote sensing. For example, in the context of EO, uncalibrated image values can be viewed as observations (see Figure 1.4).

Precision—minimum level of differentiation in dataset, which is related to the limit of resolution in measurements and exactness of descriptions. Statistically, precision relates to the level of dispersion in observations (such as standard deviation), and thus to the repeatability of a measurement process. Measurements may be precise, but not accurate, due to errors in data acquisition or handling.

Processing—process of converting remote sensing observations to a measurable property of the observed object or surface using a pre-defined measurement model.

Reference data—reliable, independent data used to calibrate or validate primary data. In the context of EO, reference data may be derived from ground measurements and other EO sensors.

Sensor Web—networked collection of sensors that can be remotely read and/or controlled.

Structure model—relates desired object or surface attributes to measurable properties of that object or surface. In the context of EO, structure models link measurement domains to attribute domains. One example of a structure model allows visible blue reflectance measurements to be interpreted in terms of water turbidity (see Figure 1.4).

Validation—process of testing an application or system to ensure that it conforms to a specification. In the context of EO, validation compares attributes derived from calibrated EO measurements with reference data to determine the quality and limitations of those attributes. Validation is a component of the structure model.

Variable—attribute or physical characteristic of the object or surface being observed that is required by the end user. A variable is the result of moving from the measurement domain to the attribute domain and reflects the process an interpreter is attempting to model. In this context, the term 'variable' is used interchangeably with 'attribute'.

Wisdom—evaluated understanding, up to the present time...

1.7 Further Information

Earth Observation:

Geoscience Australia (GA): *http://www.ga.gov.au/scientific-topics/earth-obs*

European Space Agency (ESA): *http://www.eo-miners.eu/earth_observation/eo_introduction.htm*

National Aeronautical and Space Agency (NASA): *http://neo.sci.gsfc.nasa.gov/*

Please also see Volume 1X—Appendices 1 to 3 for recommended reading and professional societies relevant to EO, plus sources of EO data and products.

Image Galleries:

NASA Worldview: *https://worldview.earthdata.nasa.gov*

ESA Image pairs: *https://earth.esa.int/web/earth-watching/image-of-the-week/content*
(Note that some of these image pairs are from different seasons, which can accentuate the extent of change—see Volume 2D).

Astronaut photographs of Earth: *http://eol.jsc.nasa.gov/SearchPhotos/*

EOPortal Images: *https://eoportal.org/web/eoportal/images*

Airbus Defence and Space: *http://www.geo-airbusds.com/satellite-image-gallery/*

1.8 References

Ackoff, R. L. (1989). From Data to Wisdom: Presidential Address to ISGSR, June 1988. Journal of Applied Systems Analysis, 16(1), pp. 3-9.

ATSE (2009). An Australian Strategic Plan for Earth Observation from Space. Australian Academy of Technological Sciences and Engineering and Australian Academy of Science, Canberra.

Bellinger, G., Castro, D., and Mills, A. (2004). Data, Information, Knowledge, and Wisdom. Retrieved from *http://www.systems-thinking.org/dikw/dikw.htm*.

Bernstein, J. (2009). The Data-Information-Knowledge-Wisdom Hierarchy and its Antithesis. Journal of Information Science, 35(2), pp. 68-75.

Botts, M., Percivall, G., Reed, C., and Davidson, J. (2007). OGC® Sensor Web enablement: Overview and high level architecture (OGC White Paper OGC 07-165, Version 3).

Botts, M., Robin, A., Davidson, J., and Simonis, I. (2006). OpenGIS® Sensor Web Enablement Architecture Document (OGC 06–021r1, Version 1). OpenGIS® Discussion Paper.

Cox, S., Botts, M., Robin, A., Atkinson, R., Falke, S., Woolf, A., and Portele, C. (2010). Geographic Information: Observations and Measurements OGC Abstract Specification Topic 20 (OGC 10-004r3 and ISO 19156, Version 2.0.0). Open Geospatial Consortium. Retrieved from *https://portal.opengeospatial.org/files/?artifact_id=41579*.

Eliot, T. S. (1934). The Rock. Faber and Faber, London, United Kingdom.

Gharajedaghi, J., and Ackoff, R. L. (1984). Mechanisms, Organisms and Social-Systems. Strategic Management Journal, 5(3), pp. 289-300. doi:*http://dx.doi.org/10.1002/smj.4250050308*.

Harrison, B. A., and Jupp, D. L. B. (1989). Introduction to Remotely Sensed Data. Part ONE of the microBRIAN Resource Manual (156 pages). CSIRO Australia, Melbourne.

Malthus, T. J., and Li, F. (2015). Calibration of Optical Satellite and Airborne Sensors. Chapter 4 in 'AusCover Good Practice Guidelines:A technical handbook supporting calibration and validation activities of remotely sensed data products' (Eds: A. Held, S. Phinn, M. Soto-Berelov, and S. Jones). TERN AusCover, Australia. ISBN 978-0-646-94137-0.

Newby, P. R. T. (2012). Photogrammetric Terminology: Second Edition. The Photogrammetric Record, 27(139), pp. 360-386. doi:*http://dx.doi.org/10.1111/j.1477-9730.2012.00693.x*.

OGC (2012). Earth Observation Metadata profile of Observations and Measurements (OGC 10-157r3) (J. Gasperi, F. Houbie, A. Woolf, and S. Smolders Eds.). Open Geospactial Consortium.

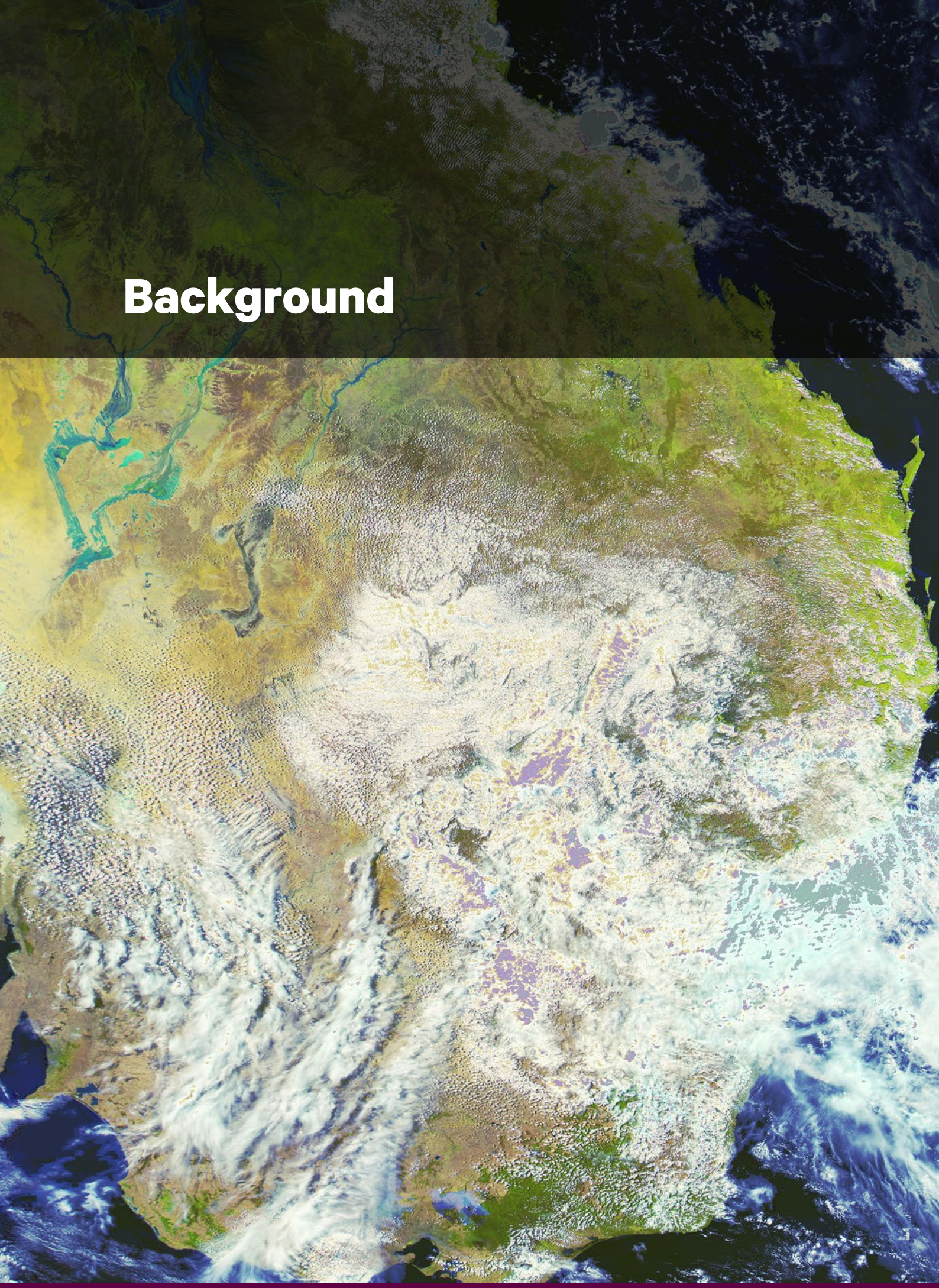
Phinn, S. R., Roelfsema, C. M., and Stumpf, R. (2010). Remote sensing: Discerning the promise from the reality. Chapter 15 in 'Integrating and applying science: A handbook for effective coastal ecosystem assessment' (Eds: B. J. Longstaff, T. J. B. Carruthers, W. C. Dennison, T. R. Lookingbill, J. M. Hawkey, J. E. Thomas, E. C. Wicks, and J. Woerner), pp. 201-222. IAN Press, Cambridge, Maryland, USA.

Rowley, J. (2007). The wisdom hierarchy: representations of the DIKW hierarchy. Journal of Information Science, 33(2), pp. 163-180. doi:*http://dx.doi.org/10.1177/0165551506070706*.

van Zyl, T. L., Simonis, I., and McFerren, G. (2009). The Sensor Web: systems of sensor systems. International Journal of Digital Earth, 2(1), pp. 16-30. doi:*http://dx.doi.org/10.1080/17538940802439549*.

Zeleny, M. (1987). Management Support Systems - Towards Integrated Knowledge Management. Human Systems Management, 7(1), pp. 59-70.

Background



The following three sections provide background information to review our current understanding of some basic principles that underlie remote sensing for Earth Observation (EO), including:

- scientific concepts and principles that are used to design remote sensing instruments and the algorithms that are used to transform these data into information about the Earth's environments (see Section 2);
- current knowledge about our planet—including its relative position in the universe and its structure, shape and life forms (see Section 3); and
- recycling pathways—thermal, hydrological, rock and carbon cycles (see Section 4).

These principles are referenced in subsequent sections and volumes. They are fundamental to understanding how remote sensing instruments operate, what they observe and how their observations are converted to measurements and information about the biological, chemical and physical properties and processes of the Earth.

Contents

2 Scientific Foundations 27

3 Planet Earth 51

4 Earth Systems and Processes 63

Background image on previous page: MODIS image acquired on 15 February 2009 during the Black Saturday bushfires, the most devastating fires on record for Australia. Concurrently, in the gulf region of northern Australia, vast areas were experiencing severe flooding. This image is displayed using bands 5, 2, 4 as RGB. **Source:** Norman Mueller, Geoscience Australia



2 Scientific Foundations

The scientific principles and concepts that enable and underpin remote sensing are summarised in this section, including:

- energy, mass and fundamental forces (see Section 2.1);
- matter (see Section 2.2);
- measurement (see Section 2.3)
- force fields (see Section 2.4);
- waves (see Section 2.5);
- properties of EMR (see Section 2.6);
- colour and human vision (see Section 2.7);
- optics (see Section 2.8);
- radiation laws (see Section 2.9);
- heat and temperature (see Section 2.10); and
- blackbody radiation (see Section 2.11).

All of these topics provide background information that is relevant to the acquisition and interpretation of Earth Observation (EO) data. Readers who are familiar with these concepts may prefer to simply refer to them as needed from subsequent sections. For those who do not have training in science, we have chosen to start with the basics and briefly include all topics that underpin the broad field of remote sensing.

True science teaches, above all,
to doubt and to be ignorant
(Miguel de Unamuno)

2.1 Energy, Mass and Fundamental Forces

Energy is traditionally defined as the capacity to do work. Note that this defines what energy can do, not what it is. Energy is one of those fundamental entities that we rely upon, but don't completely understand. We do know that it can take many forms—heat, light, sound, electrical, chemical, or nuclear—and that life wouldn't exist without it.

Mass is another fundamental property of objects. It measures the amount of matter in an object and thus its inertia, that is, its tendency to stay in its current state of motion, whether resting or moving. Weight, the force of gravity on an object, is used as a surrogate for mass in most practical applications on Earth.

Our understanding of energy and mass has developed over millennia, based on observations of how different types of matter move and interact. Modern physics recognises four fundamental interactions, or forces, listed in order of increasing strength and decreasing range of influence:

- gravitation—attraction between objects due to their mass;
- weak nuclear—responsible for radioactive decay of sub-atomic particles;
- electromagnetism—holds atoms and molecules together; and
- strong nuclear—holds together the nucleus of each atom.

Background image: Landsat-5 image of Gascoyne River in flood, acquired on 22 December 2010. The Gascoyne River is the longest river in WA (760km) but only flows above the surface for about one third of each year. The Gascoyne River stretches from the Robinson Ranges, west of the Gibson Desert to the Indian Ocean near Carnarvon. This image is displayed using bands 5, 4, 2 as RGB. **Source:** Norman Mueller, Geoscience Australia

External forces acting on an object can change the energy of that object. If the external forces acting on an object are balanced, it is in equilibrium, or a resting position. The laws of thermodynamics state that the mass-energy of the universe is constant, but is continually being changed from one form to another, or moved from one place to another. Energy and mass are related by the famous mass-energy equivalence equation:

$$E = mc^2$$

where

E is energy;
m is the mass of the object; and
c is speed of light.

Potential demonstrations of mass changing into energy include radioactivity; the mass of the Sun, for example, is constantly decreasing as it radiates energy (see Section 6).

Energy is further differentiated as either kinetic, due to actual motion and being dependent on mass, or potential, due to possible motion and reliant on physical position and/or chemical composition.

2.2 Matter

Atoms are regarded as the basic building blocks of matter. According to current understanding, each atom can be visualised as a positively charged nucleus surrounded by small, negatively charged electrons. Each nucleus contains at least one positively charged proton. The nuclei of most atoms also contain uncharged neutrons, which stabilise the positive charges.

An element is distinguished by the number of protons in the nuclei of its atoms, which is also known as its unique atomic number. In a neutral state, the number of protons in an atom equals the number of electrons. Atoms combine in myriad different configurations to create molecules. These have distinct chemical properties and are characterised in terms of their atomic structure. Most matter exists as molecules rather than individual atoms.

The spatial distribution of electrons around a nucleus is described by atomic and molecular orbitals. Electrons are viewed to exist in probability shells or orbitals around the nucleus of an atom. Each orbital is associated with a discrete energy level, or quantum, such that the energy associated with an electron is that of its orbital. Electrons move between orbitals by absorbing or emitting a precise quantum of energy (such as a photon—see Section 2.11.4). The lowest energy level is referred to as the electron's ground state and higher energy levels are called excited states. This is the mechanism by which EM energy in the ultraviolet to visible wavelengths is absorbed by materials (see Section 5).

An atom with a different number of electrons than protons is referred to as an ion of that element. When atoms of an element have different numbers of neutrons, they are called isotopes. The nuclei of some isotopes are unstable, so release energy to achieve internal stability. This mechanism forms the basis of radioactivity and will be further discussed in Section 6.

Matter can exist in any one of four fundamental states:

- solid—molecules vibrate about fixed locations, often within crystal lattices, and cannot change position within a substance. Solids have defined shapes and volumes;
- liquid—molecules that can move but are bound loosely by intra-molecular forces. Liquids do not have a fixed shape, but can flow and maintain a near-constant volume with changes in pressure;
- gas—molecules in constant random motion without a fixed volume or shape; and
- plasma—ionised gas comprising charged particles, namely positive ions and negative electrons or ions.

The precise interaction between energy from an external energy source, such as the Sun, and matter depends on many factors, including the state and temperature of matter, its atomic composition and structure, and the intensity, frequency and proximity of the energy source.

2.3 Measurement

Measurement records numeric values to describe observations or events, where:

- an observation notes the state or condition of an object or relationship; and
- an event relates to a change in state or condition.

Recorded measurements allow the association(s) between multiple observations or events to be determined.

2.3.1 Scales of measurement

Four scales of measurement can be used to define numeric variables (Anderberg, 1973):

- nominal—assigns categories which define different states, in which case relationships between measurements are limited to their being the same or not, and no ordering can be inferred;
- ordinal—involves an implied ordering between different states, which allows relationships to imply rank, but the interval between different values does not imply distance;
- interval—measures the extent of difference between states, which allows measurements to be ordered and separation to be treated as distance; and
- ratio—uses a scaled measure with a meaningful zero. Like interval variables, ratio variables can be ordered and differenced, but given that they additionally have a true zero point, fractions can also be computed for ratio variables.

These distinctions are relevant when interpreting remotely sensed measurements to ensure that appropriate processes are selected for image enhancement and analysis (see Volume 2).

2.3.2 International System of Units (SI)

The International Bureau of Weights and Measures (Bureau International des Poids et Mesures: BIPM) is one of three international standards organisations that ensures the use of uniform weights and measures around the globe[7]. In particular, it maintains the International System of Measurement (Système International d'Unités: SI), which defines the seven base units of measurement summarised in Table 2.1.

Other quantities can be derived from these base units using standardised quantity equations. Some of the derived units that are relevant to EO are summarised in Table 2.2.

Table 2.1 Base Units in the International System of Units (SI)

Measures	Unit	Abbreviation	Defined as
length	metre	m	length of the path travelled by light in vacuum during a time interval of 1/299,792,458 of a second
mass	kilogram	kg	mass of the international prototype of the kilogram
time	second	s	duration of 9,192,631,770 periods of the radiation corresponding to the transition between the two hyperfine levels of the ground state of the cesium 133 atom
electric current	ampere	A	constant current which, if maintained in two straight parallel conductors of infinite length, of negligible circular cross-section, and placed 1 meter apart in a vacuum, would produce between these conductors a force equal to 2×10^{-7} newton per metre of length
thermodynamic temperature	kelvin	K	1/273.16 of the thermodynamic temperature of the triple point of water
amount of substance	mole	mol	amount of substance of a system which contains as many elementary entities as there are atoms in 0.012 kilogram of carbon 12
luminous intensity	candela	cd	luminous intensity, in a given direction, of a source that emits monochromatic radiation of frequency 540×10^{12} hertz and that has a radiant intensity in that direction of 1/683 watts per steradian

Source: National Institute of Standards and Technology (NIST) at *http://physics.nist.gov/cuu/Units/current.html*

Table 2.2 Derived Units in the International System of Units (SI)

Measures		Unit	Abbreviation	Expressed in terms of
angle	plane	radian	rad	$m \cdot m^{-1} = 1$
	solid	steradian	sr	$m^2 \cdot m^{-2} = 1$
frequency		hertz	Hz	s^{-1}
force		newton	N	$m \cdot kg \cdot s^{-2}$
energy		joule	J	$m^2 \cdot kg \cdot s^{-2}$ (or N · m)
power, radiant flux		watt	W	$m^2 \cdot kg \cdot s^{-3}$ (or J / s)
Celsius temperature		degrees Celsius	°C	K (0°C = 273.15K)
luminous flux		lumen	lm	$m^2 \cdot m^{-2}$ cd = cd
luminance		lux	lx	$m^2 \cdot m^{-4}$ cd = $m^{-2} \cdot$ cd

Source: National Institute of Standards and Technology (NIST) at *http://physics.nist.gov/cuu/Units/units.html*

7. For further information, visit *http://www.bipm.org/en/publications/si-brochure/*

In the context of EO, relevant units based on these derived units include:

- Heat flux density, irradiance (W/m^2);
- Specific heat capacity ($J/(kg \cdot K)$);
- Specific energy (J/kg);
- Radiant intensity (W/sr); and
- Radiance ($W/(sr \cdot m^2)$).

2.3.3 SI metric prefixes

Standard prefixes are used to define multiples and submultiples of SI units. Prefixes adjoin the SI base units names and abbreviations to modify the size of the base unit. There are currently 20 prefixes used to represent powers of 10, as listed in Table 2.3.

As shown in Tables 2.3 and 2.4, it is convenient to use scientific notation for particularly large and small numbers. For example, a quantity with the value 1,900,000, can be written in terms of its factors:

$1.9 \times 1{,}000{,}000$

or

1.9×10^6

Similarly, a microscopic quantity of 0.0000019 can be expressed as:

1.9×0.000001

or

1.9×10^{-6}

This notation both simplifies arithmetic operations and emphasises the order of magnitude associated with a measurement.

2.3.4 SI units for measuring waves

Commonly used measurement units in EO relate to measuring the wavelengths or frequencies of different forms of radiation. SI units of length are based on the metre as summarised in Table 2.4. SI units for frequency are based on the hertz as listed in Table 2.5. In this text, units of length are generally used to distinguish different forms of EMR.

Table 2.3 SI metric prefixes

Prefix	Abbreviation	Decimal value	Scientific Notation	Colloquial Name
yocto	y	0.000 000 000 000 000 000 000 001	10^{-24}	septillionth
zepto	z	0.000 000 000 000 000 000 001	10^{-21}	sexillionth
atto	a	0.000 000 000 000 000 001	10^{-18}	quntillionth
femto	f	0.000 000 000 000 001	10^{-15}	quadrillionth
pico	p	0.000 000 000 001	10^{-12}	trillionth
nano	n	0. 000 000 001	10^{-9}	billionth
micro	m	0.000 001	10^{-6}	millionth
milli	m	0.001	10^{-3}	thousandth
centi	c	0.01	10^{-2}	hundredth
deci	d	0.1	10^{-1}	tenth
---	---	1	10^{0}	one
deka	da	10	10^{1}	ten
hecto	h	100	10^{2}	hundred
kilo	k	1,000	10^{3}	thousand
mega	M	1,000,000	10^{6}	million
giga	G	1,000,000,000	10^{9}	billion
tera	T	1,000,000,000,000	10^{12}	trillion
peta	P	1,000,000,000,000,000	10^{15}	quadrillion
exa	E	1,000,000,000,000,000,000	10^{18}	quintillion
zetta	Z	1,000,000,000,000,000,000,000	10^{21}	sextillion
yotta	Y	1,000,000,000,000,000,000,000,000	10^{24}	septillion

Source: Astronomy Education at the University of Nebraska-Lincoln at *http://astro.unl.edu/classaction/tables/intro/si_prefixes.html*

Table 2.4 SI units of length

Unit		Distance	
Name	**Abbreviation**	**In metres (decimal value)**	**In metres (scientific notation)**
Kilometre	km	1,000	10^{3}
Metre	m	1	10^{0}
Centimetre	cm	0.01	10^{-2}
Millimetre	mm	0.001	10^{-3}
Micrometre[10]	µm	0.000 001	10^{-6}
Nanometre	nm	0.000 000 001	10^{-9}
Angstrom	Å	0.000 000 000 1	10^{-10}

Table 2.5 SI units of frequency

Unit		Frequency	
Name	**Abbreviation**	**In cycles per second (decimal value)**	**In cycles per second (scientific notation)**
Hertz	Hz	1	10^{0}
Kilohertz	kHz	1,000	10^{3}
Megahertz	MHz	1,000,000	10^{6}
Gigahertz	GHz	1,000,000,000	10^{9}

2.3.5 Angles

On a (two-dimensional) plane, the angle between two intersecting lines can be readily conceived and illustrated. The SI unit for planar angles is the radian (see Section 2.3.2), such that a full circle equates to 2π radians (or 360°). A reference circle can be used to define any angle (θ) formed by two lines radiating from its centre (see Figure 2.1a):[8]

$$\theta = \frac{s}{R}$$

where

s is the length of the arc formed by angle θ along the circumference of the circle; and
R is the radius of the circle.

In geometrical terms, the angle θ is said to be subtended by the arc of length s. By definition the perimeter of a circle equals $2\pi R$, so for a unit circle (radius = 1), the perimeter subtends an angle of 360° or 2π radians.

Solid angles occur in three-dimensional structures, such as cones, and are quantified in terms of reference spheres. The SI unit for solid angles is the steradian (see Section 2.3.2). A solid angle (Ω) represented by the apex of a cone originating at (or radiating from) the centre of a sphere can be computed from the radius of the sphere (R) and the area on the sphere's surface that it intersects (A; see Figure 2.1b), such that (in steradians):

$$\Omega = \frac{A}{R^2}$$

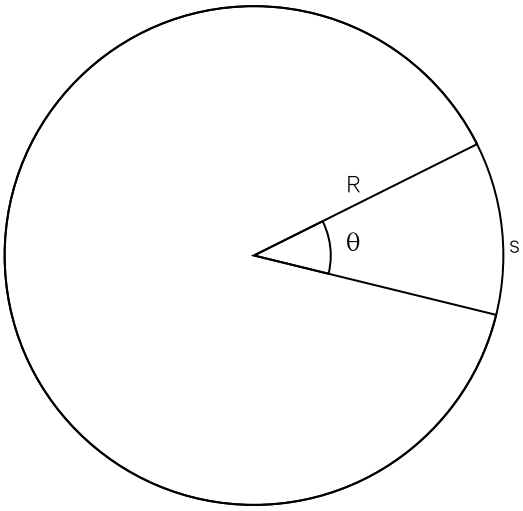
As with planar angles, Ω is described as the angle subtended by the area A. Since the surface area of a sphere equals $4\pi R^2$ radians, the solid angle subtended by a whole unit sphere (radius = 1) is 4π radians.

8. Formerly micron.

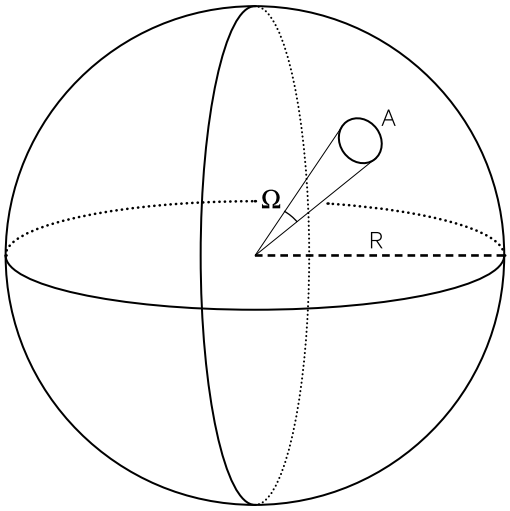
Figure 2.1 Planar and solid angles

Planar angles define the angular separation between two intersecting lines (vectors) in two dimensions, while solid angles define the three-dimensional equivalent, and are often represented as cones.

a. Plane angle $\theta = \frac{s}{R}$ radians, where s is the length of an arc on a circle of radius R.



b. Solid angle $\Omega = \frac{A}{R^2}$ steradians, where A is the area on the surface a sphere of radius R that is intersected by a cone originating from the centre of the sphere.



A solid angle effectively quantifies how large an object appears to an observer. An understanding of solid angles is essential for many aspects of remote sensing, including measurement of radiation (see Sections 2.6 and 13) and mapping projections (see Volume 2B).

2.4 Force Fields

Work involves force and motion, such as pushing or pulling an object some distance. Since energy is neither created nor destroyed, work can be viewed as an energy transfer mechanism:

work = *force* × *distance*

where

work is measured in newton-metres;
force is measured in newtons; and
distance is measured in metres.

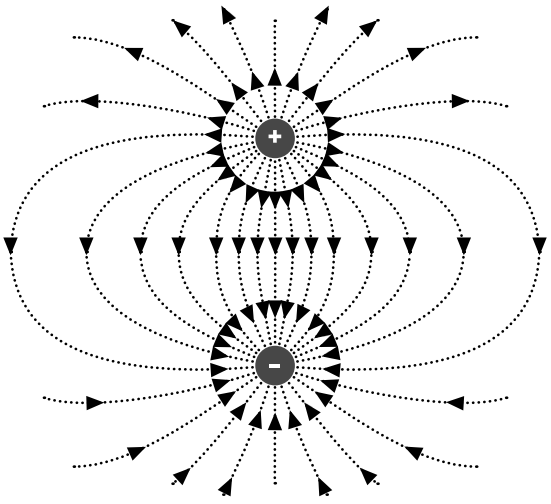
A force field defines the region in space within which an object would experience that force. Examples of force fields include:

- gravitational field—region where an object would feel a gravitational pull;
- electric field—region where an object would feel an electric force;
- magnetic field—region where an object would feel a magnetic force; or
- electromagnetic field—region where an object would feel an electromagnetic force.

All force fields are associated with a source, such as an electric charge. A force field is generally depicted by a set of imaginary field lines that indicate the direction of the force (see Figure 2.2).

Figure 2.2 Force field example

Direction of force in a dipole electric field is shown by a set of imaginary field lines away from a positive charge to a negative charge.



An electric charge is a fundamental property of certain sub-atomic particles. Electric charges are generated by a flow of electrons between atoms, such as occurs in static electricity. The electric charge associated with an object is the sum of its component charged particles.

Every charged object is surrounded by an electric field. Charged objects also experience the electric field created by other charged objects. Charges may be positive or negative. Objects with different charges are attracted to each other while those with the same charge (both positive or both negative) repel each other.

Charged particles that are moving create and experience an additional force, called a magnetic force. Every moving charged object is surrounded by a magnetic field. Moving charged objects also experience the magnetic fields created by other moving charged objects.

An oscillating electric field will induce an oscillating magnetic field and, conversely, an oscillating magnetic field will induce an oscillating electric field. Together these oscillating fields form electromagnetic (EM) waves, which travel at 300,000 km/s (or 3×10^8 m/s). Since visible light is a form of EMR, this velocity is better known as the speed of light.

Maxwell's equations integrate studies of electricity, magnetism and optics into a unified theory (Maxwell, 1873; Signell, 2001). This set of four partial differential equations combine the work of Coulomb, Oersted, Ampere and Faraday to describe the propagation of electric and magnetic fields, their interaction, and their impact on objects. EMR is further discussed in Sections 1 and 13.

2.5 Waves

Many forms of energy are transported by waves. A wave can be viewed as a disturbance that allows energy to travel through a medium without transporting matter. Wave propagation may result in temporary displacement of particles of the medium, but these particles then (theoretically) return to their original position.

Mechanical waves, such as sound waves, carry energy through a medium—solid, liquid, gas or plasma—without transporting any of the matter of the medium (see Section 9.1). EM waves are produced by the vibration of charged particles, such as electrons and protons, and can be transmitted without a medium so can travel through a vacuum. Since EM waves exhibit behaviours characteristic of both particles and waves, they are considered to have a dual nature (see Section 5).

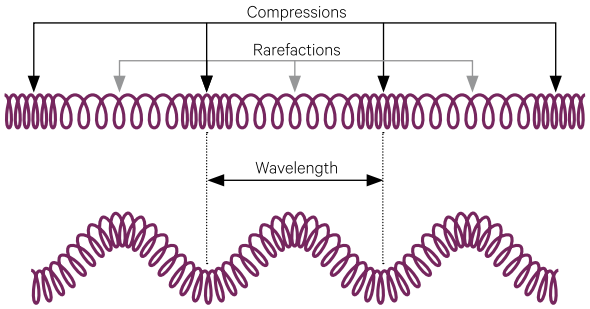
2.5.1 Wave types and characteristics

Waves are further characterised by the orientation of oscillations relative to their direction of travel (see Figure 2.3):

- transverse waves, such as EM waves and secondary seismic waves, oscillate in a plane that is perpendicular to the direction the waves are travelling; these are often pictured as a sinusoidal waveform and, when travelling through a medium, move particles of matter up and down;
- particles associated with compression or longitudinal waves, such as sound waves in air or seismic waves through the Earth, move in the same plane as the wave; these are most simply viewed as the back and forth movement that occurs through the length of 'slinky' toys; and
- surface or circular waves, such as occur in water bodies, carry particles of the medium in a circular motion and diminish with depth.

Figure 2.3 Longitudinal and transverse waves

a. Longitudinal or compression wave—energy moves particles of medium in the direction of wave propagation. This is comparable to pushing a slinky toy at one end, which causes the coils to compress and dilate as the energy moves to the other end.
b. Transverse wave—energy moves particles of medium in a direction that is orthogonal to wave propagation. This is comparable to shaking a slinky toy at one end, which move the coils up and down or side to side as the energy is transferred to the other end.



The energy of a transverse wave is determined by its repeat cycle, that is the distance it travels from one crest to the next trough and back to the next crest. The wavelength (λ) is the length of one complete wave cycle from crest to crest. The period of a wave (T) is the time taken to travel one wavelength. The frequency (ν) is the inverse of the period, that is the number of complete wave cycles in a given time unit, such as per second. For energy forms with constant velocity, such as light, as wavelength increases, frequency decreases and vice versa (see Figure 2.4). These components are related by the wave equation:

$$velocity = \nu\lambda$$

where

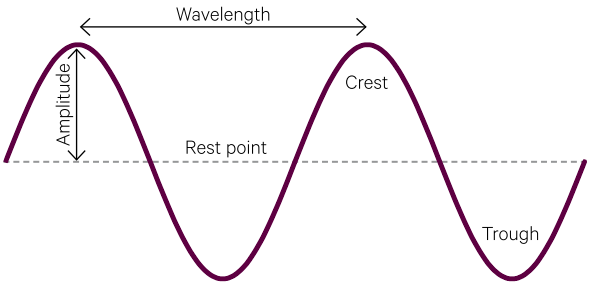
ν is frequency of the wave; and
λ is the wavelength.

The amplitude of a longitudinal wave increases as the pressure difference between compressions and dilations (or rarefactions) increases. Figure 2.5 compares longitudinal wave representations with the more common sine wave representations of waves with different amplitudes. As the amplitude increases, the compressions of longitudinal waves become more dense (darker in Figure 2.5) and the rarefactions less dense (lighter in Figure 2.5).

While the power and the intensity of a wave are related, they are not the same. Power is the term used to define the energy at the source of a disturbance, while intensity is the energy at any particular point on the wave front. The two are related by the equation:

$$intensity = \frac{power}{area}$$

Figure 2.4 Components of waves



Source: Langlopress (2016)

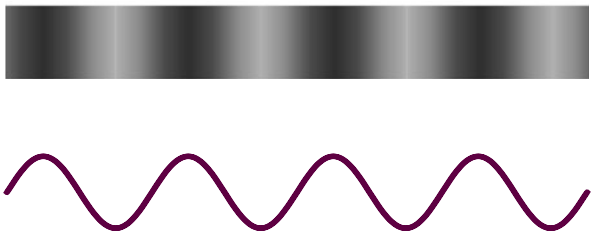
Figure 2.5 Longitudinal or compression waves

Three waves are represented as both compressions and sine waves:

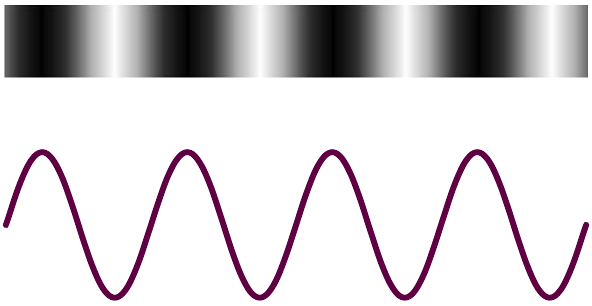
a. No signal



b. Low amplitude wave



c. High amplitude wave



Source: Langlopress (2016)

2.5.2 Reflection, refraction and diffraction

It is of relevance to remote sensing that all waves obey physical laws involved with reflection, refraction and diffraction. Waves are reflected when they encounter a surface. Regardless of the angle at which a wavefront approaches a barrier, the law of reflection (see Figure 2.6) applies:

angle of incidence = angle of reflection

The extent to which a surface obeys the law of reflection depends on its physical structure relative to the wavelength of the wave (see Volume 1B—Section 3). A totally smooth surface, or specular reflector, will reflect all incoming energy without any scattering (see Figure 2.7a). Diffuse or 'Lambertian' reflectance occurs when the surface is rough relative to the wavelength(s) of the incoming radiation and causes the energy to be reflected in many directions (see Figure 2.7b).

Waves also change direction when they pass from one medium to another, such as from air to water. This type of change is called refraction and varies with the 'refractive index' of the medium as described by Snell's law (see Figure 2.8a):

$$n_1 \sin\theta_1 = n_2 \sin\theta_2$$

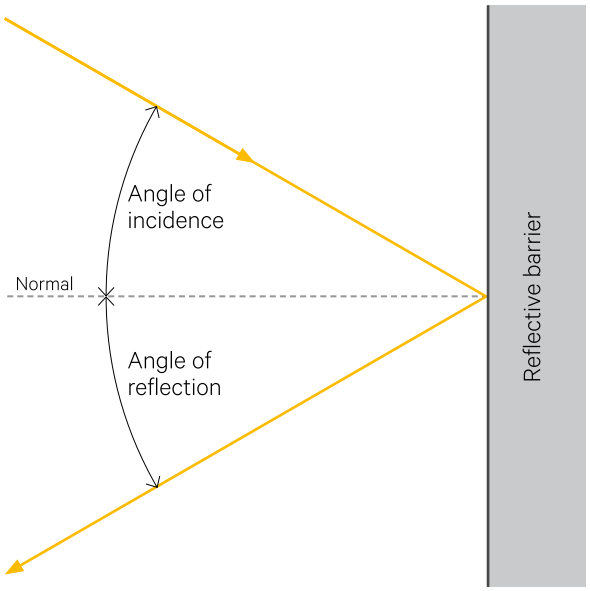
where

n is the refractive index; and
θ is the angle of incidence.

Waves can also change direction, or are diffracted, as they pass through an opening or around a barrier (see Figure 2.8b). This effect is most obvious when the size of the barrier is comparable to the wavelength. Transverse waves, such as EM and gravitational waves, can oscillate with multiple orientations whereas longitudinal waves, such as sound waves, only oscillate in the direction of travel.

Figure 2.6 Law of reflection

When a light wave encounters a reflectance barrier it is reflected such that the angle of incidence equals the angle of reflection

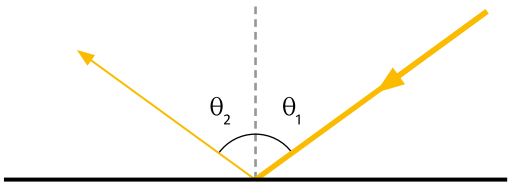


Source: Langlopress (2016)

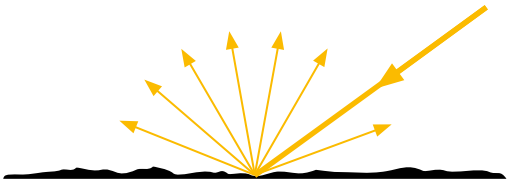
Figure 2.7 Specular and diffuse reflectors

The extent to which a surface obeys the law of reflection depends on its surface texture relative to the wavelength of incident radiation.

a. Specular reflection from a smooth surface—angle of incidence θ_1 equals angle of reflection θ_2.



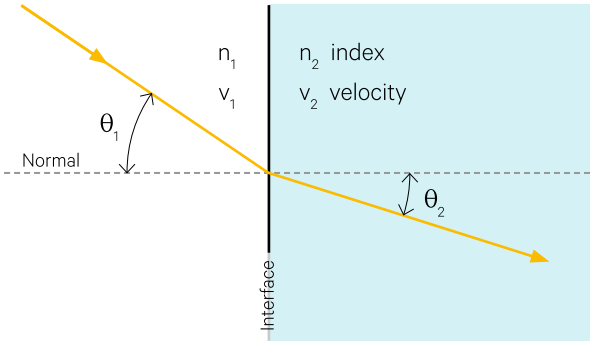
b. Diffuse reflection from a rough surface—light is scattered in many directions



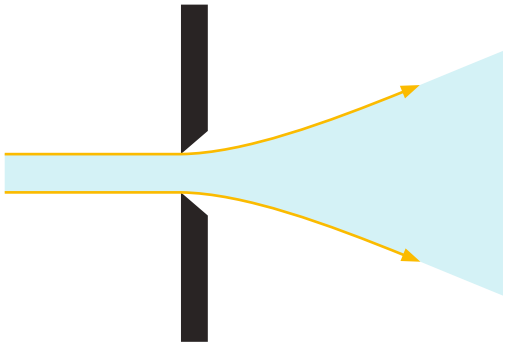
Source: Harrison and Jupp (1989) Figure 7

Figure 2.8 Refraction and diffraction

a. Refraction through an interface between two media



b. Diffraction through a narrow opening



Source: Langlopress (2016)

2.5.3 Polarisation

Each EM wave comprises an electric force field and a magnetic force field, which are perpendicular to each other, and transverse to the direction of travel. Maxwell's equations (see Section 2.4) allow the direction and magnitude of one of these fields to be derived from knowledge of the direction and magnitude of the other (Suits, 1983).

Polarisation describes the orientation of the electric field (or its electric vector) relative to a reference plane. Horizontal (or plane) polarisation applies when the wave's plane of incidence and vertical polarisation is perpendicular to the horizontal polarisation, that is, the electric vector is aligned with the plane of incidence and also the direction of travel. Other types of polarisation include circular, when the electric field spirals to the right or left, and elliptical, when plane and circular polarisations combine to form an electric field with an elliptical cross-section (Elachi and van Zyl, 2006).

Transverse waves can be polarised to restrict their vibrations to a single plane. By contrast, randomly polarised energy vibrates in all potential orientations that are perpendicular to the direction of energy propagation. Light waves can be polarised using specially aligned filters, while microwaves and radio waves are polarised by orienting the antenna to transmit and receive specific wave planes (see Volume 1B—Section 8).

2.5.4 The Doppler effect

The Doppler Effect is observed whenever the wave source is moving relative to the observer such that a change in frequency is perceived. For example, when an observer is approaching an energy source, the wave frequency will be observed to be higher than when the observer is moving away. This perception is in fact due to the relative motion of the observer rather than an actual change in frequency of the wave. This effect can be observed with sound and light waves and is particularly of interest to astronomy for determining the radial velocity of stars and galaxies relative to Earth. Several forms of remote sensing using radar sensors are based on the Doppler Effect (see Sections 14 and 15).

2.5.5 Coherence

Two waves with a systematic relationship between their amplitudes are called coherent, that is, they oscillate in phase. In terms of EMR, which comprises two three-dimensional vectors, definition of the underlying physics of coherence is complex, but this characteristic can be simply viewed as their relationship in time. Lasers, for example, generate coherent radiation. Conversely, waves are 'incoherent' when their amplitudes are randomly related, that is, their waves oscillate out of phase. Sunlight, candles, and incandescent light globes generate incoherent radiation.

2.6 Properties of EMR

The energy properties of EMR that are most commonly detected and quantified can be described in terms of:

- radiometric terms—describe the energy radiated per unit time (see Section 2.6.1);
- spectral terms—focus on the energy of specific wavelength(s) (see Section 2.6.2); and
- photometric terms—consider those wavelengths detected by the human visual system (see Section 2.6.3).

For a more detailed treatment of these topics, readers are referred to the *Manual of Remote Sensing* (Colwell, 1983), *The Light Measurement Handbook* (Ryer, 1997), *ASPRS Manual of Remote Sensing* (Morain and Budge, 1998), or Elachi and van Zyl (2006).

2.6.1 Radiometric terms

In physics, the term 'power' describes the rate of energy flow, that is, energy per unit time. Radiometry is concerned with measuring power and radiometric terms define specific quantities related to power. In SI units, power is measured in Watts (W; see Section 2.3.2). CIE regulations denote radiometric quantities with the subscript *e* (for energy). The most commonly encountered radiometric terms in EO are defined in Table 2.6 and ground measurement of these quantities is detailed in Volume 1X—Appendix 5. Definitions of relevant standard SI units (see Section 2.3.2) are provided in Table 2.7.

Table 2.6 Radiometric terms

Term	Symbol	Definition	Unit
Radiant Energy	Q_e	Energy carried by EMR	J
Radiant Energy Density	W_e	Energy per unit volume	J/m^3
Radiant Flux (or Radiant Power)	Φ_e	Radiant energy per unit time	W
Irradiance	E_e	Density of radiant flux incident upon a unit area of a plane surface	W/m^2
Radiant exitance (or Radiant emittance)	M_e	Density of radiant flux radiated from a unit area of a plane surface	W/m^2
Radiant Intensity	I_e	Radiant flux radiated from a point source per unit solid angle in a specified direction	W/sr
Radiance	L_e	Radiant flux radiated from a unit projected area per unit solid angle in a specified direction	$W/(sr \cdot m^2)$

Adapted from: Suits (1983)

Table 2.7 SI units

Unit	Symbol	Measures	Definition
Candela	Cd	luminous intensity	One candela is the luminous intensity, in a given direction, of a source that emits monochromatic radiation of frequency 540×10^{12} Hz and has a radiant intensity in that direction of $^1/_{683}$ watts per steradian.
Joule	J	work or energy	Work done by a force of one newton when its point of application moves one meter in the direction of action of the force, equivalent to one 3600th of a watt-hour
Lumen	lm	luminous flux	Amount of light emitted per second in a unit solid angle of one steradian from a uniform source of one candela
Radian	rad	planar angle	Angle at the centre of a circle whose arc is equal in length to the radius
Steradian	sr	solid angle	Angle at the centre of a sphere subtended by a part of the surface equal in area to the square of the radius
Watt	W	power	One joule per second, corresponding to the power in an electric circuit in which the potential difference is one volt and the current one ampere

Source: BIPM (2016)

For a constant flow of energy in time t,

$$Q = \Phi t$$

where

Q is radiant energy; and
Φ is radiant flux.

For a point source, the radiant intensity (I) in a given direction can be computed as:

$$I = \frac{\Phi}{\Omega}$$

where the solid angle $\Omega = \frac{A}{R^2}$, for surface area A at distance R (see Figure 2.1).

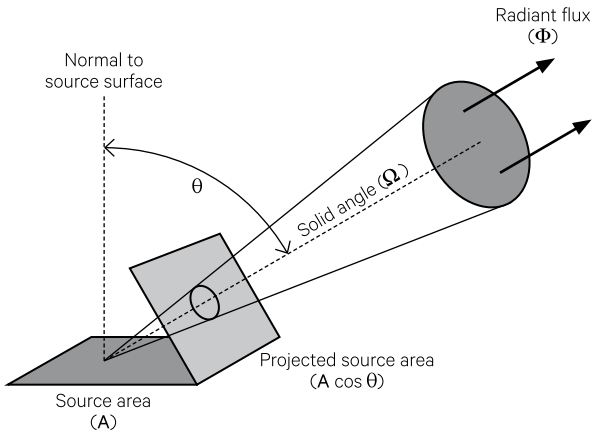
Remote sensors measure radiance (L) from a source area in a particular direction within a defined solid angle (see Figure 2.9). Radiance can be defined as:

$$L = \frac{\Phi / \Omega}{A\cos\theta}$$
$$= \frac{I}{A\cos\theta}$$

where θ indicates the direction from the source.

Figure 2.9 Radiometric measurements

The radiance L from a source surface area A is measured in terms of the radiant flux Φ within a specified solid angle Ω in a given direction θ and computed as $L = \frac{\Phi / \Omega}{A\cos\theta}$



Adapted from: Elachi and van Zyl (2006) Figure 2-10

2.6.2 Spectral terms

Spectral terms describe radiometric quantities as a function of wavelength. These terms are generally prefixed by the word 'spectral'. Their symbols either use the subscript λ to indicate relevant wavelengths or the subscript ν to indicate relevant frequencies.

For example, spectral intensity may be defined as the radiant intensity per unit wavelength or the radiant intensity per unit frequency. Relevant spectral terms are summarised in Table 2.8. For simplicity, the 'e' subscript is often omitted, and the specific range of wavelengths or frequencies may be appended in parentheses.

Table 2.8 Spectral terms defined in terms of wavelength

Term	Symbol	Definition	Unit
Spectral Flux	$\Phi_{e,\lambda}$	Radiant flux per unit wavelength	W/m
	$\Phi_{e,\nu}$	Radiant flux per unit frequency	W/Hz
Spectral irradiance	$E_{e,\lambda}$	Irradiance of a surface per unit wavelength	W/m^3
	$E_{e,\nu}$	Irradiance of a surface per unit frequency	W/(m^2·Hz)
Spectral exitance (or Spectral emittance)	$M_{e,\lambda}$	Radiant exitance per unit wavelength	W/m^3
	$M_{e,\nu}$	Radiant exitance per unit frequency	W/(m^2·Hz)
Spectral Intensity	$I_{e,\lambda}$	Radiant intensity per unit wavelength	W(/sr·m)
	$I_{e,\nu}$	Radiant intensity per unit frequency	W/(sr·Hz)
Spectral radiance	$L_{e,\lambda}$	Radiance of a surface per unit wavelength	W/(sr·m^3)
	$L_{e,\nu}$	Radiance of a surface per unit frequency	W/(sr·m^2·Hz)

2.6.3 Photometric terms

For visible wavelengths, EMR can be measured both in terms of electrical and optical properties (see Section 5). Various quantities are used to represent the amount of light associated with EMR[9]. As introduced in Section 2.6.1, flux measures the amount of radiation, or number of photons, incident on an area in a given time. While EO scientists working with visible wavelength data generally describe EMR in radiometric or spectral quantities, colour scientists use photometric (light) units (see Table 2.9). The term 'luminous' implies that the wavelengths being referenced are within the human visual range (400 to 700 nm), and the subscript n is sometimes used in conjunction with relevant radiometric symbols to denote this qualification (WMO, 2008).

Table 2.9 Equivalent photometric terms

Quantity	Radiometric		Photometric	
	Attribute	Unit	Attribute	Unit
Flux	Power	W	Luminous Flux	lm
Flux/Area	Irradiance	W/m^2	Illuminance	lm/m^2
Flux/Solid Angle	Radiant Intensity	W/sr	Luminous Intensity	lm/sr
Flux/Area/Solid Angle	Radiance	W/(sr·m^2)	Luminance	lm/(sr·m^2)

2.7 Colour and Human Vision

2.7.1 Human visual system

Human vision relies on the detection of light by two types of photochemical receptors in the retina of the eye: rods and cones. It has been estimated that each human eye contains approximately:

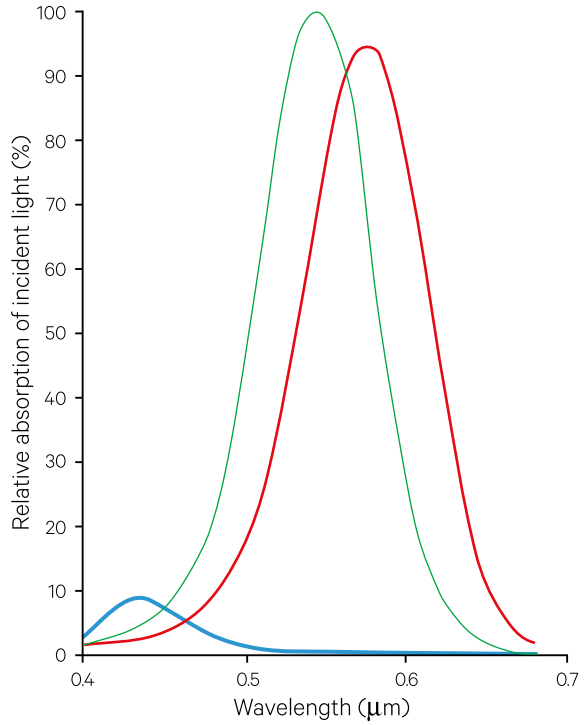
- seven million cones—which differentiate colours; and
- 120 million rods—which essentially respond to luminance (the amount of intercepted light) and are particularly important for night vision (Padgham and Saunders, 1975).

9. See also tutorials on light measurements: *http://light-measurement.com/tutorials-on-light-measurement/*

The human sensation of colour is considered to be due to the sensitivities of three types of neurochemical sensors to different wavelengths in the visible region of the EM spectrum. Each sensor is associated with one type of cone and responds with varying sensitivity to a range of wavelengths as shown in Figure 2.10. One type of sensor is maximally sensitive to short wavelengths with a peak response at approximately 0.44 μm. This is often referred to as the blue sensor and is insensitive to wavelengths longer than 0.52 μm. The second sensor has peak sensitivity at 0.53 μm, or green light. The third is referred to as the red sensor although peak sensitivity actually occurs at 0.57 μm, which is the wavelength of yellow light. However, of the three, this third sensor still has the highest absorption of red light and its sensitivity avoids responding to near infrared wavelengths (which would be rather undesirable in vegetated landscapes).

Figure 2.10 Relative light absorption of human cones

In the human eye, the relative absorption of light differs for different cones, with blue cones (a) being significantly less responsive than green or red cones.



Source: Harrison and Jupp (1989) Figure 9 [Adapted from Cornsweet (1970)]

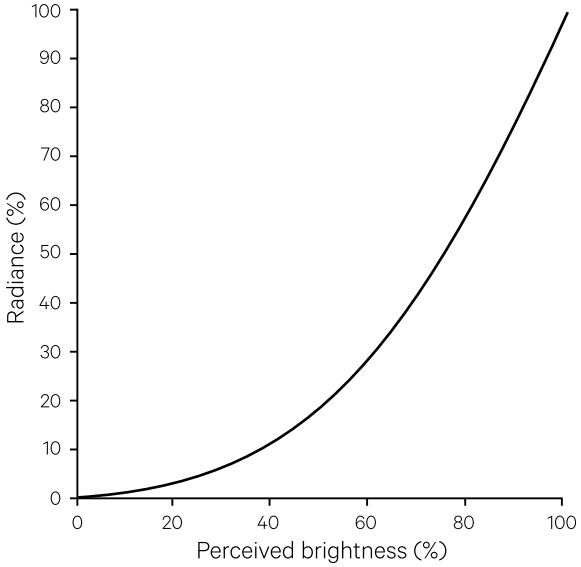
The human colour response is determined by the relative ratios of neural activities in these three sensors, which change with the wavelength of perceived light. For example, a single wavelength light at 0.45 μm produces a strong response from the blue sensor, a weaker response from the green sensor and a still weaker response from the red sensor. Similarly, red radiation produces strongest response from the red sensor and much weaker responses from the other two sensors. Yellow light will also invoke a strong response from the red sensor but the green and blue responses will be stronger than for red light, hence allowing the two colours to be differentiated.

2.7.2 Perception of colour and brightness

However, our final perception of the colour of an object is influenced by the ambient light intensity, its size and proximity to other objects, and the peculiar sensitivities of each human eye. As illustrated in Figure 2.11, small differences in dark colours (lower radiance) are better discriminated than comparable differences in brighter colours (with higher radiance). Because of the variable relationship between visual sensitivity and wavelength, it is difficult to classify colours in terms of brightness. Accordingly, while luminance measures physical brightness in photopic terms (see Section 2.6.3), luminosity, a scale on which the energy of light is corrected for the human eye's sensitivities, is used as a rough approximation for perceived brightness (Padgham and Saunders, 1975).

Figure 2.11 Perception of light intensity changes

The human eye does not differentiate between high intensities (brighter shades or colours) as well as between low intensities (darker colours).



Source: Harrison and Jupp (1990) Figure 39 [Adapted from Land (1977)]

Although the eye has a remarkable capacity for detecting light, it is not a good discriminator in terms of perceived brightness (see Figure 2.11). Drury (1987) reports that for objects with visual angles which are similar to those typically found in remotely sensed imagery, only 20–30 different brightness steps are discernible. Perception of colour is a different matter, however, with hundreds of thousands, or even millions, of colours being distinguishable to the human eye. These human factors have considerable relevance to visual interpretation of remotely sensed imagery. While photointerpretation of EO image products yields valuable information about Earth surface features, it should be remembered that human colour perception is not implicitly related to the physical measurement of spectral colour. Notwithstanding the complexities of human colour perception, however, a trained interpreter can derive significant detail from both colour and panchromatic imagery.

2.7.3 Colour models

Colour spaces, or models, attempt to describe the colours perceived by human beings. The three peak sensitivity wavelengths described above (blue, green and red) form a natural basis or coordinate system for describing colour measurement. In colour science, these peak-sensitivity wavelengths are referred to as the additive primaries, since they add together to give white light, or the RGB (red-green-blue) system (see Figures 2.12 and 2.13). As shown in Figure 2.12, the brighter, secondary colours may be formed by combining different pairs of primary colours. In the additive system:

- red and green combine to produce yellow;
- blue and red combine to produce magenta; and
- green and blue combine to produce cyan.

Various colour representation devices such as projectors and display screens utilise this additive property of radiation. Colour display screens use various technologies based on red, green and blue 'sub-pixels', each of which can be activated separately, to achieve a mixture of coloured light at the screen's surface (see Volume 2A—Section 7).

Colour mixing for film dyes and print media uses the subtractive primaries of yellow, magenta and cyan (YMC). These coloured pigments are mixed to produce a range of colours by being 'subtracted' from a white background. In the subtractive colour system:

- magenta and cyan combine to produce blue;
- yellow and cyan combine to produce green; and
- yellow and magenta combine to produce red.

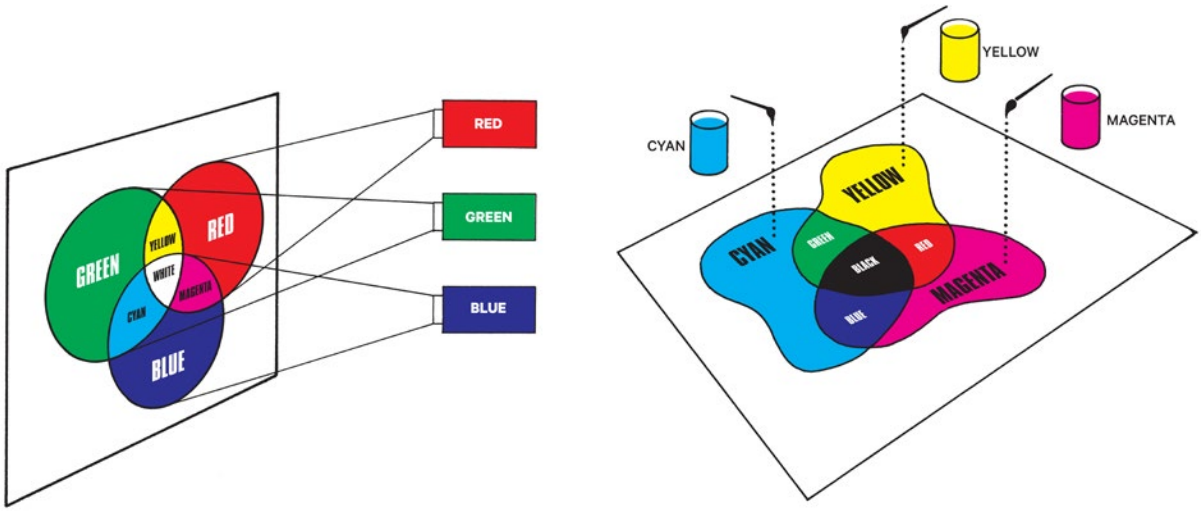
As illustrated in Figure 2.12, these subtractive primaries produce secondary colours by removing their complementary colours from white. The relationship between additive and subtractive primaries is illustrated in Figure 2.13.

Other models order colours in terms of their hue (apparent colour), saturation (purity or chroma) and intensity (brightness), or on the basis of chromaticity. The use of colour in image processing, interpretation and presentation is further discussed in Volume 2A—Sections 5 and 6 and Volume 2X—Appendix 3.

Figure 2.12 Additive and subtractive colour mixing

a. Red, green and blue primaries are added to a black background to give other colours

b. Yellow, magenta and cyan primaries subtract from a white background to produce other colours

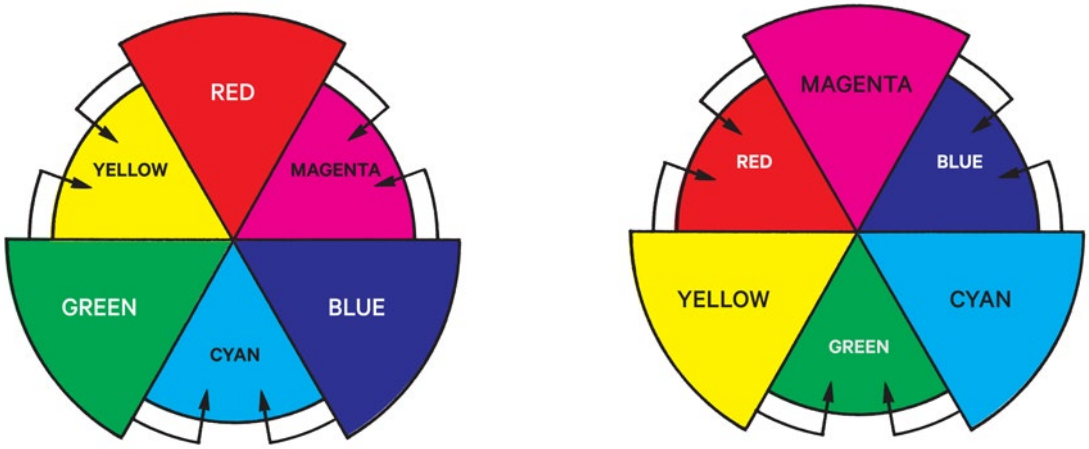


Source: Harrison and Jupp (1989) Figures 10 and 11

Figure 2.13 Relationship between additive and subtractive primary colours

a. Additive primaries—can be combined to form brighter, secondary colours; added all together they give white light

b. Subtractive primaries—produce secondary colours by removing their complementary colours from white; added all together they produce black



Source: Harrison and Jupp (1989) Figure 12

2.8 Optics

As a branch of physics, optics is concerned with the way light is generated, propagated and detected.

2.8.1 Theories

Three major theories have been proposed to describe the behaviour of light:

- geometric or ray optics, based on the Newtonian view of an EM wave comprising a stream of particles (now called photons), simply considers light in terms of 'rays' that reflect and refract as described in Section 2.5.2;
- physical or wave optics, based on "Huygens' Principle" (which visualised light as a wave vibrating vertically and perpendicular to the direction of propagation), which was also able to model non-geometric wave behaviours such as diffraction and interference; and
- quantum optics, based on the work of Planck and Einstein, which applies quantum mechanics to optical systems and accounts for the dual wave-particle nature of light (Ditchburn, 1952).

While the term 'optical' implies the wavelengths of visible light, in this context it is generally applied to those wavelengths whose behaviour is best described by ray optics. This includes wavelengths that are small relative to the lenses and sensors that interact with them and applies to those EMR wavelengths that are shorter than visible (ultraviolet—UV) and longer (near infrared (NIR), short wave infrared (SWIR) and thermal infrared (TIR)).

2.8.2 Lenses

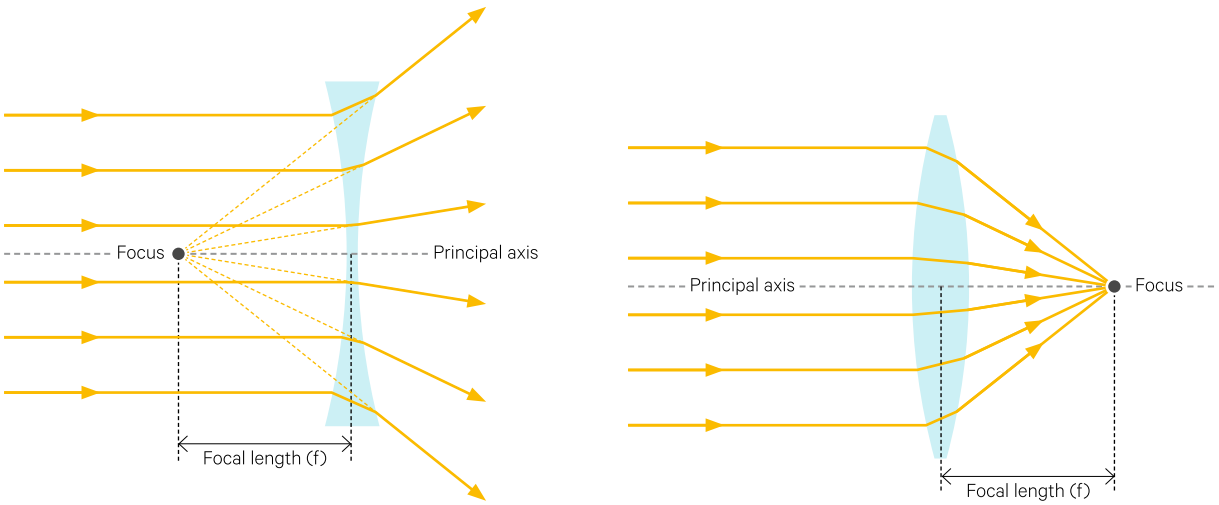
The surface of a lens is designed to make the rays of incident light converge or diverge. A beam of light travelling parallel to the optical (principal) axis of a convex lens will be focused to a single point on the axis beyond the lens (see Figure 2.14a). This point is known as the focus of the lens. The distance from the centre of the lens to the focus is known as the focal length of the lens. The same beam of light will diverge when passing through a concave lens (see Figure 2.14b). The divergent beam will appear to be emanating from a particular point on the axis on the other side of the lens. This point is also known as the focus, and the distance from the centre of the lens is called the focal length, although in this case the focal length is usually negative.

We must be mindful of the fact that our sense of vision is limited to only a narrow band of vibration within the spectrum, and the colours as we perceive them are not necessarily real, in a definitive and absolute sense.
(Ark Redwood, The Art of Mindful Gardening)

Figure 2.14 Convex and concave lenses

a. Convex lens—a beam of light travelling parallel to the optical (principal) axis will be focused to a single point (or focus) on the axis beyond the lens

b. Concave lens—a beam of light will diverge when passing through a concave lens, with the divergent beam appearing to be emanate from a particular point (the focus) on the axis on the other side of the lens



Source: Langlopress (2016)

The field of view (FOV) for any optical system is the extent of the world it can observe (see Figure 2.15). An increase in focal length would result in a decrease in field of view. The field of view can be computed as:

$$FOV = 2 \cdot \arctan\left(\frac{1}{2}\frac{image\,dimension}{focal\,length}\right)$$

When the object is further than twice the focal length from a convex lens, as occurs in EO, the image optics can be represented as in Figure 2.16.

Figure 2.15 Field of view

The field of view (FOV) for an optical system is inversely proportional to the focal length. The FOV defines how much of the world can be observed by the optical system.

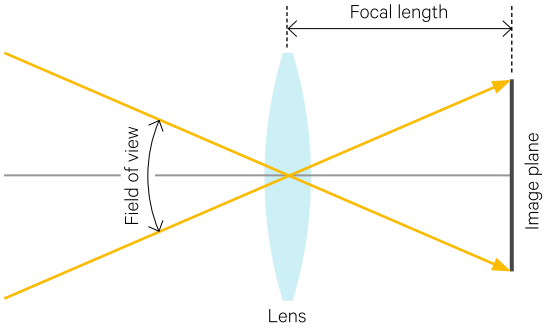
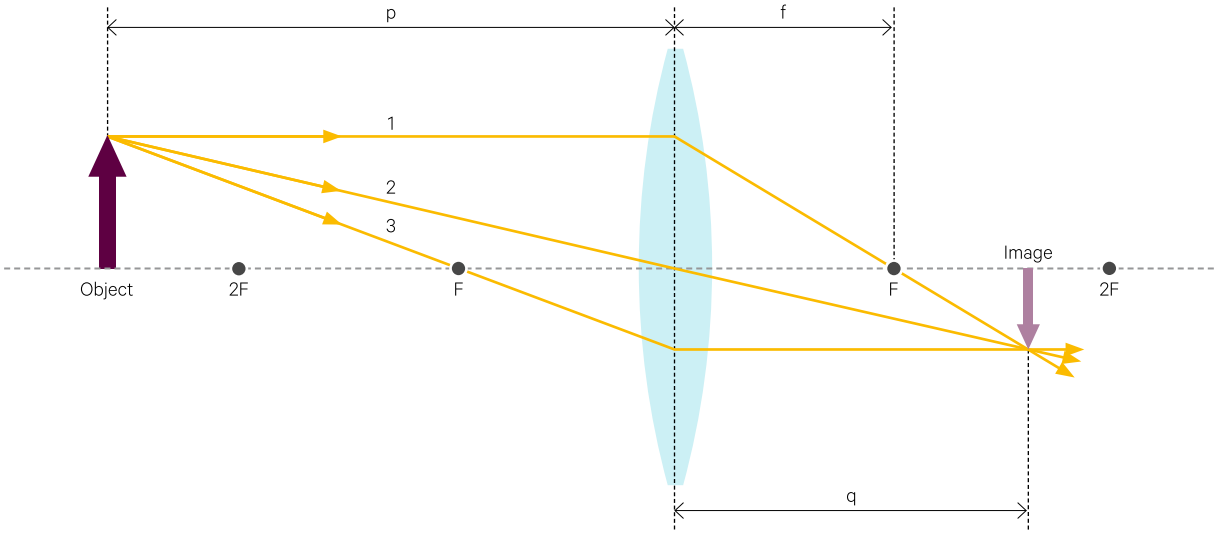


Figure 2.16 Object more than twice focal length from convex lens



Source: Langlopress (2016)

A thin lens is defined as one whose thickness is much less than its focal length. Given the altitude of most EO systems, this lens model is an appropriate one to use when calculating scaling parameters. The thin lens approximation relates the object distance (p), image distance (q) and focal length (f) by the equation:

$$\frac{1}{p}=\frac{1}{q}+\frac{1}{f}$$

A compound lens comprises an array of simple convex and concave lenses sharing a common axis. While simple convex lenses are used in some photographic cameras, compound lenses are used in high quality photographic cameras, telescopes, microscopes and other optical instruments.

2.9 Radiation laws

A number of physical laws apply to EMR. Two laws that are particularly relevant to EO are the:

- inverse-square law, which quantifies the radiant intensity of EMR emanating from a point source as a function of distance from the source (see Section 2.9.1); and
- Beer-Lambert law, which quantifies attenuation of energy through an absorbing medium (see Section 2.9.2).

2.9.1 Inverse-square law

The inverse-square law in physics describes how an omnidirectional point source spreads its 'influence' into three-dimensional space. This physical law applies to many natural phenomena, including EMR, gravity, and sound. Using simple geometric relationships, the intensity of an influence at a given distance from the source is inversely proportional to the square of the distance from the source (see Figure 2.17a). When applied to EMR, radiant intensity from a point source of radiation can be seen to decrease as a function of the square of the distance from the source (see Figure 2.17c). Thus, for a target area, A, if the radiant intensity at distance r from the source is x, then the radiant intensity at distance 2r is x/4. As a target of constant area moves further from the source, the solid angle it subtends at the source reduces in proportion to $1/r^2$ (see Figure 2.17b). Likewise, the radiant intensity reaching the target at increasing distances is reduced in the same proportion (see Figure 2.17c).

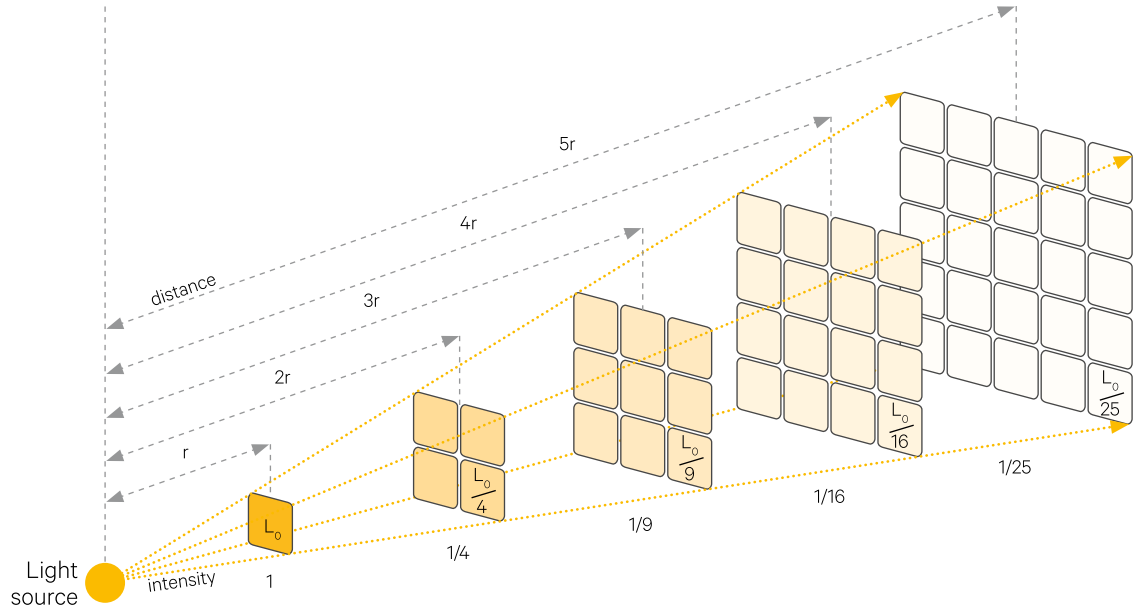
Science operates according to a law of conservation of difficulty.
The simplest questions have the hardest answers;
to get an easier answer, you need to ask a more complicated question.
(George Musser)

Figure 2.17 Inverse-square law

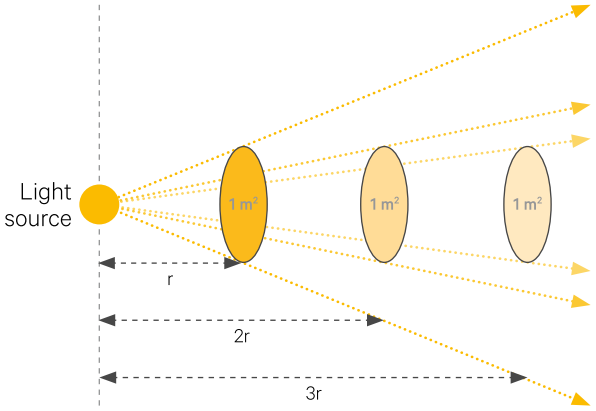
The intensity of a constant point source can be seen to decrease with increasing distance from the source by the relationship:

$$intensity = \frac{1}{distance^2}$$

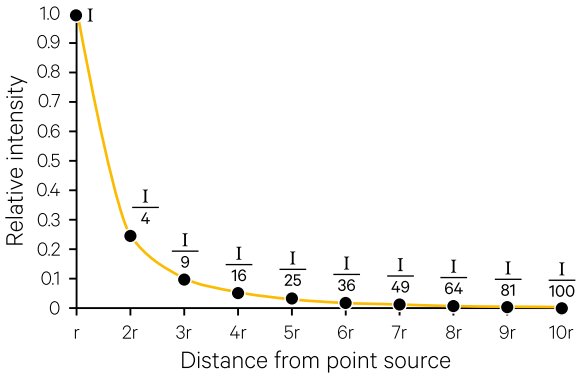
a. At a distance r from the source, the energy is spread over area A, but at distance 2r the same energy is spread over four times the area (4A). Accordingly, the resulting intensity of the energy at distance 2r is only ¼ of its intensity at distance r.



b. As a target of constant area moves further from the source, the solid angle it subtends at the source reduces in proportion to the square of the distance such that at twice a given distance, the target detects a quarter of the energy.



c. The radiant intensity from a point source decreases in proportion to the square of distance from the source.



2.9.2 Beer-Lambert law

It has been observed that the radiant intensity of light is reduced, or attenuated, as it passes through a medium. This is due to some light being absorbed by the medium. The rate of attenuation is described by the Beer-Lambert law:

$$A = a(\lambda) b c$$

where

A is the measured absorbance;
$a(\lambda)$ is a wavelength-dependent absorptivity coefficient (rate of attenuation per unit distance);
b is the length travelled by the light through the medium (or path length); and
c is the concentration of the homogeneous medium.

This is commonly expressed in terms of radiant intensities of incident and transmitted light, that is, the intensity of light before and after travelling through the medium:

$$A = \log_{10} \frac{\Phi_t}{\Phi_0}$$

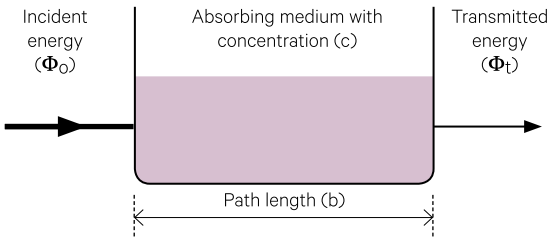
where

Φ_o is the radiant intensity of the incident light; and
Φ_t is the radiant intensity of the transmitted light (see Figure 2.18).

Non-linear attenuation can also occur due to chemical and instrumental factors.

Figure 2.18 Beer-Lambert law

This law quantifies how much light is absorbed as it passes through a medium. Absorption is dependent on both the concentration of the medium (assumed to be homogeneous) and its thickness (or the path length of light through it).



2.10 Heat and Temperature

The energy of particles in random motion is called kinetic energy or kinetic heat. The temperature of an object is indicative of its internal energy, that is, the average kinetic energy of its particles. The particles of all matter with a temperature above 0K exhibit the random motion of kinetic heat. The temperature of an object can be expressed in terms of:

- internal temperature—kinetic motion of particles; and
- external temperature—emitted EMR resulting from internal kinetic energy (see Section 2.11).

Heat can be described as the thermal energy that is transferred from matter with a higher temperature to matter with a lower temperature. Heat is transferred between materials via one of three fundamental processes:

- conduction—adjacent molecules of a solid material are agitated without visible motion of the solid, resulting in the transfer of heat along the material. Conduction of heat from one material to another requires materials to be in physical contact. Metals are good conducting materials due to the presence of free electrons.
- convection—circulating currents within fluids resulting from a temperature gradient. Heat is transferred by convection due to movement of the heated material.
- radiation—EM energy that is transferred through a medium or vacuum. On Earth, emission of EM energy generally only occurs after shorter wave EMR from the Sun has been absorbed (see Section 5.1). Radiation is the only mechanism by which energy can be transmitted through a vacuum.

2.10.1 Thermal properties of matter

The heat of a material that can be sensed or measured is called its *Sensible Heat*. *Heat (or thermal) capacity* (c) defines the amount of heat required to increase the temperature of matter by 1°C (or 1K):

$$c = \frac{Q}{\Delta T}$$

where

T is temperature.

Heat is measured in joules (J) or calories (cal), where 1 calorie represent the amount of heat needed to increase the temperature of 1 gm of water by 1°C and 1 cal = 4.184 J (see Section 2.3).

Specific Heat (c_p) is the ratio of the heat capacity of an object to its mass and represents the energy required to increase the temperature of 1 gm of matter by 1°C (or 1K) in an environment of constant pressure. For example, the specific heat of water is 4.184 kJ/(kg·K), while the specific heat of carbon

is 0.71 kJ/(kg·K). This implies that over 4 times the energy is required to increase the temperature of water compared to the energy required to heat carbon. Water has a higher heat capacity than any other substance on Earth, which is the reason that waterbodies heat and cool more slowly than nearby land surfaces. By comparison, gold, which heats up and cools down rapidly, has a specific heat capacity of 0.13 kJ/(kg·K).

Thermal conductance and thermal conductivity describe the rate at which heat can pass through matter. Thermal conductance measures the energy that flows through a unit area in unit time, where opposite faces of the area maintain a constant difference in unit temperature, with units of $J/(m^2 \cdot s \cdot K)$. Thermal conductivity (k) measures the energy that flows through a unit length in unit time, where opposite faces of the area or length maintain a constant difference in unit temperature. The SI unit for measuring thermal conductivity is W/(m·K). Thermal conductivity varies with moisture content and particle size. For example, the thermal conductivity of fresh water, with slow heat transfer, is 0.6 W/(m·K), whereas the thermal conductivity of gold, with rapid heat transfer, is 300 W/(m·K).

Thermal inertia (P) measures the thermal response of matter to changes in ambient temperature in the units of $J\ m^{-2}\ K^{-1}\ s^{-1/2}$:

$$P = \sqrt{k \rho c}$$

where

k is thermal conductivity ($W\ m^{-1}\ K^{-1}$);
ρ is the density ($g\ cm^{-3}$); and
c is specific heat capacity ($J\ kg^{-1}\ K^{-1}$).

Thermal inertia of a material generally increases proportionally with increasing density. Apparent thermal inertia can be derived from EO by comparing registered images of a particular location that were acquired at different times during the diurnal cycle (see Sections 14.1.3 and Volume 1B—Section 7).

2.10.2 Latent heat

When a substance changes state, such as from solid to liquid, additional energy is required to overcome cohesion between molecules. The heat required for this process is called *Latent Heat*. Thus, heat can either increase the kinetic energy of molecular vibrations in a substance or break the bonds between its molecules. Latent heat effectively changes the potential energy of the molecules. The Latent Heat of Fusion converts a solid to a liquid without a temperature change. In the case of ice, most of the energy involved in this melting process rearranges the molecules from crystal lattice to the weaker bonds between liquid water molecules. The Latent Heat of Vaporisation refers to the energy required to convert a liquid to a gas without a change in temperature. Again using the example of water, this energy completely separates the water molecules so that they can move freely as a gas. The energy requirements corresponding to changing the states of water are summarised in Table 2.10.

Table 2.10 Energy required to convert 10 g ice to steam

Temperature (ºC)	State	Temperature	Energy Transfer (J)	Heat Function
-25 – 0	Ice	increasing	522	Increase kinetic energy of molecules
0	melting	same	3,330	Latent heat of fusion
0 – 100	water	increasing	4,190	Increase kinetic energy of molecules
100	boiling	same	22,600	Latent heat of vaporisation
100–125	steam	increasing	502	Increase kinetic energy of molecules

Adapted from: Holt Physics, Table 10-5

2.10.3 Thermodynamics

Thermodynamics is a field of physics that examines the impact of heat and work energy on the temperature, volume and pressure of 'systems'. In this context, a system refers to a specific area of study with a defined boundary and a finite volume. Transfers of energy across a system boundary (between the system and its surroundings) are the focus of thermodynamics. Open systems permit exchanges of energy and matter, closed systems only allow exchanges of energy but not matter, and isolated systems exchange neither. The planet Earth most nearly approximates a closed system in which matter cycles between the lithosphere, hydrosphere, atmosphere and biosphere, and solar energy enters the system through the atmosphere.

The first law of thermodynamics relates to conservation of energy within a system:

$$\Delta E = Q + W$$

where

E is internal energy of a system;
Q is heat added to the system; and
W is work done to the system.

This is equivalent to the statement that the energy in the universe is constant—it cannot be created or destroyed but changes from one form to another. A cyclic process is one that enables a system to return to its initial state so that its internal energy does not change. When heat flows into a system (Q is positive in the equation above), the process in endothermic; when heat flows out of the system (Q is negative), the process is exothermic.

The second law of thermodynamics states that the disorder, or entropy, of the universe is always increasing. This law allows for the reality of converting heat energy into work. Since it is not possible to attain complete efficiency in any energy transfer, some amount of heat is also transferred outside of the system. Thermodynamic efficiency indicates the proportion of heat that is transferred out of a system during the process of energy conversion.

2.11 Blackbody Radiation

Radiation transfers EM energy by emission from a source through a medium or a vacuum. EMR emitted by an object is called the radiant flux (Φ; measured in watts—see Section 2.6.1). EM energy is continuously being emitted at all wavelengths by every material with a temperature above absolute zero (-273.15°C or 0K). With no other objects in the universe, a material would gradually cool to 0K by radiating all of its energy. Absorption of energy increases both the temperature and rate of emission of a material.

A blackbody is a theoretical object or system that absorbs all incident EMR, hence has an apparent colour of black. The wavelengths of energy emitted by a blackbody are determined by the temperature of the blackbody, rather than either its chemical composition or the incident radiation. While no blackbodies actually exist, this concept is valuable for describing the radiative properties of matter.

Four physical laws have been derived to characterise blackbody behaviour:

- Stefan-Boltzmann's law (see Section 2.11.1;
- Kirchof's law (see Section 2.11.2);
- Wien's displacement law (see Section 2.11.3); and
- Planck's law (see Section 2.11.4).

These laws are used to derive apparent temperature estimates from measurements of thermal IR emission (see Volume 1B—Section 7).

2.11.1 Stefan-Boltzmann's law

The total radiation (across the full EM spectrum) emitted from a blackbody is proportional to the fourth power of its absolute temperature:

$$W_b = \sigma T^4$$

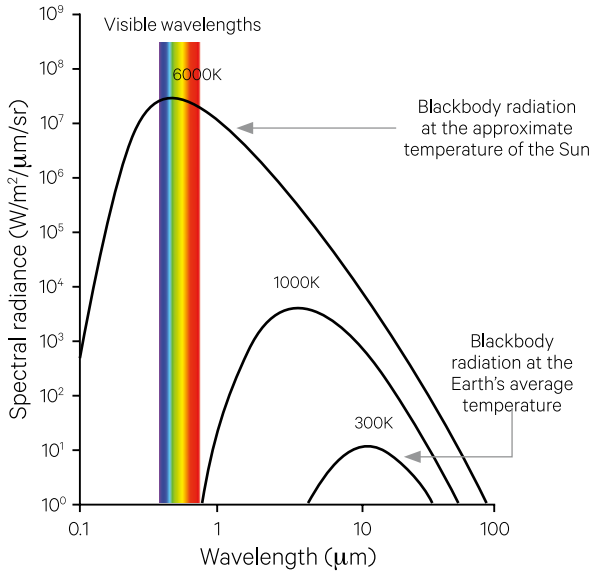
where

W_b is total emitted radiation, or emitted radiance, from the blackbody;
T is the absolute temperature of the blackbody; and
σ is the Stefan-Boltzmann constant = 5.670373 × 10^{-8} W/(m^2·K^4).

Thus, per unit area, more energy is emitted from hot objects than from cool ones.

Figure 2.19 Blackbody radiation

The wavelength of peak radiant exitance for a blackbody decreases as its temperature increases (Note: Scales are logarithmic)



Adapted from: NASA/USGS Astrogeology Science Center Radiance Calculator at *http://astrogeology.usgs.gov/tools/thermal-radiance-calculator/*

2.11.2 Kirchhoff's law

The *emissivity* of a target object (ε) is quantified relative to the behaviour of a blackbody at a given wavelength by comparing their emitted radiances at a selected wavelength, λ:

$$\varepsilon = \frac{emitted\,radiance\,at\,\lambda}{blackbody\,radiance\,at\,\lambda}$$

This law is more commonly written as:

$$W = \varepsilon W_b$$

where

ε is emissivity of target object (scaled 0–1);
W_b is total emitted radiation, or emitted radiance, from the blackbody; and
W is the total emitted radiation from the target object.

The emissivity index can be viewed as a measure of radiating efficiency across the whole spectrum.

2.11.3 Wien's displacement law

The wavelength of peak radiant exitance of a blackbody is inversely proportional to its absolute temperature:

$$\lambda_{max} T = constant = 2897.756\,\mu m\,K$$

where

λ_{max} is the wavelength of peak radiant exitance; and
T is the absolute temperature of the target object.

This law quantifies the observation that the wavelength corresponding to the peak radiance of a target object decreases as its temperature increases (see Figure 2.19).

2.11.4 Planck's law

The frequency distribution of energy emitted by a blackbody is explained by the Planck Hypothesis (see Figure 2.19). This states that energy exists in discrete quanta, called photons, in proportion to the energy's frequency:

$$L_\lambda(T) = \frac{2hc^2}{\lambda^5} \times \frac{1}{e^{\frac{hc}{\lambda k_B T}} - 1}$$

where

L_λ is the spectral radiance at wavelength λ and temperature T (energy per unit time per unit surface area per solid angle per unit wavelength);
h is the Planck constant = 6.6206896×10^{-34} J s (Joule seconds);
c is the speed of light; and
k_B is the Boltzmann constant = 1.38065156×10^{-23} J/K.

Planck's law allows the proportion of radiation within specific wavelength intervals to be determined.

2.11.5 Other bodies

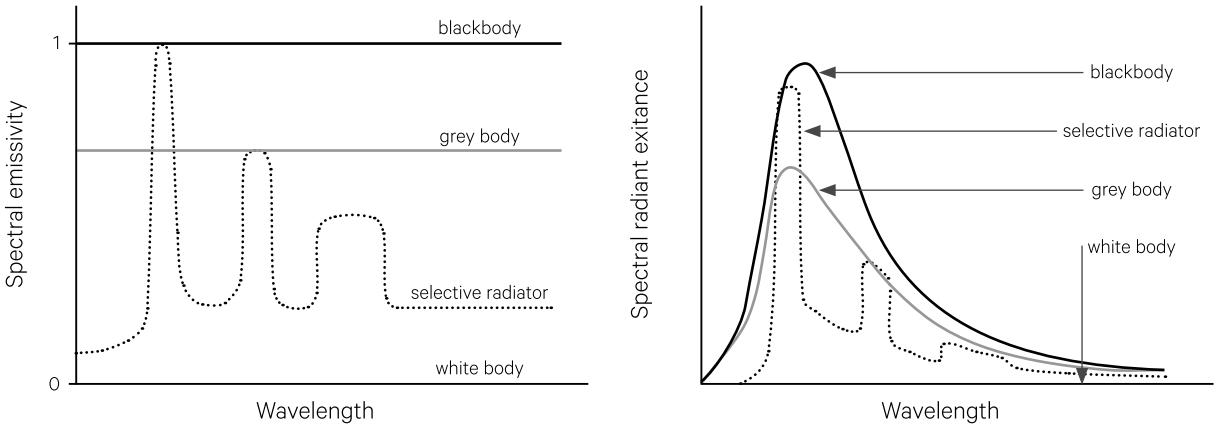
In contrast with blackbodies, a white body has zero emissivity across all wavelengths. A greybody is a theoretical energy source that reflects some incident radiation equally across all wavelengths, thus has an apparent colour of grey and emissivity less than one. This property is also expressed as constant emissivity over all wavelengths. Greybodies are used to approximate the emission properties of real world materials.

The term selective radiator describes an object whose emissivity varies with wavelength. A selective radiator with higher emissivity but the same temperature as another selective radiator will have a higher radiance, that is, it will radiate more strongly. The emissivity differences between blackbodies, greybodies, white bodies and selective radiators are illustrated in Figure 2.20.

Figure 2.20 Spectral emissivity and spectral radiant exitance of various bodies

a. By definition, the emissivity (e) for a blackbody equals 1 and for a white body equals zero. A greybody both reflects and emits energy equally over all wavelengths, so has a constant emissivity value which is less than 1. Emissivity from a selective radiator, however, varies with wavelength.

b. Spectral radiant exitance for blackbody, greybody, selective radiator and white body.



Adapted from: Remote Sensing lectures by Wataru Takeuchi, University of Tokyo at *http://wtlab.iis.u-tokyo.ac.jp/~wataru/lecture/rsgis/rsnote/cp1/1-7-2.gif*

2.12 Further Information

Basic Physics Topics:

http://hyperphysics.phy-astr.gsu.edu/hbase/hph.html

http://www.physnet.de/PhysNet/education.html

http://www.olympusmicro.com/primer/lightandcolor/index.html

http://langlopress.net/homeeducation/resources/science/index.php?op=scienceoutline

Basic Chemistry Topics:

http://www.chem.ucla.edu/~gchemlab/

http://teaching.shu.ac.uk/hwb/chemistry/tutorials/

http://langlopress.net/homeeducation/resources/science/index.php?op=scienceoutline

Thermal Remote Sensing lectures:

http://topex.ucsd.edu/rs/Lec06.pdf

http://wgbis.ces.iisc.ernet.in/envisrs/?q=node/40

Measurement:

http://physics.nist.gov/cuu/Units/index.html

http://www.cleavebooks.co.uk/dictunit/

http://www.bipm.org/en/publications/si-brochure/

Wave Motion:

http://www.acs.psu.edu/drussell/Demos/waves/wavemotion.html

Blackbody Radiation:

https://www.e-education.psu.edu/astro801/content/l3_p5.html

http://astrogeology.usgs.gov/tools/thermal-radiance-calculator/

Light:

Ryer (1997)

http://www.livescience.com/50678-visible-light.html

https://optics.synopsys.com/lighttools/pdfs/illuminationfund.pdf

Solid angles:

http://marine.rutgers.edu/dmcs/ms552/2009/solidangle.pdf

2.13 References

Anderberg, M. A. (1973). Cluster Analysis for Applications. Academic Press, New York.

BIPM (2016). Bureau International de Poids et Mesures. Retrieved from *http://www.bipm.org/en/about-us/*.

Colwell, R. N. (1983). Manual of Remote Sensing, Second Edn. American Society of Photogrammetry, Falls Church, Virginia.

Cornsweet, T. N. (1970). Visual Perception. Academic Press, New York.

Drury, S. A. (1987). Image Interpretation in Geology. Allen and Unwin, London.

Elachi, C., and van Zyl, J. (2006). Introduction to the Physics and Techniques of Remote Sensing, Second Edn. Wiley Interscience, New Jersey.

Harrison, B. A., and Jupp, D. L. B. (1989). Introduction to Remotely Sensed Data. Part ONE of the microBRIAN Resource Manual (156 pages). CSIRO Australia, Melbourne.

Harrison, B. A., and Jupp, D. L. B. (1990). Introduction to Image Processing. Part TWO of the microBRIAN Resource Manual (256 pages). CSIRO Australia, Melbourne.

Land, E. (1977). The retinex theory of colour vision. Scientific American, 237(6), pp. 108-128.

Langlopress (2016). Scientific Illustrations. Retrieved from *http://langlopress.net/homeeducation/resources/science/index.php?op=sciencethumbs*.

Maxwell, J. C. (1873). A Treatise on Electricity and Magnetism, Vol. 1 and 2, Clarendon Press Series. Macmillan and Co, London.

Morain, S. A., and Budge, A. M. (1998). Earth Observing Platforms and Sensors, Vol. 1, Third Edn., Ed: R. A. Ryerson, Manual of Remote Sensing. American Society for Photogrammetry and Remote Sensing (ASPRS); John Wiley & Sons, Inc., New York.

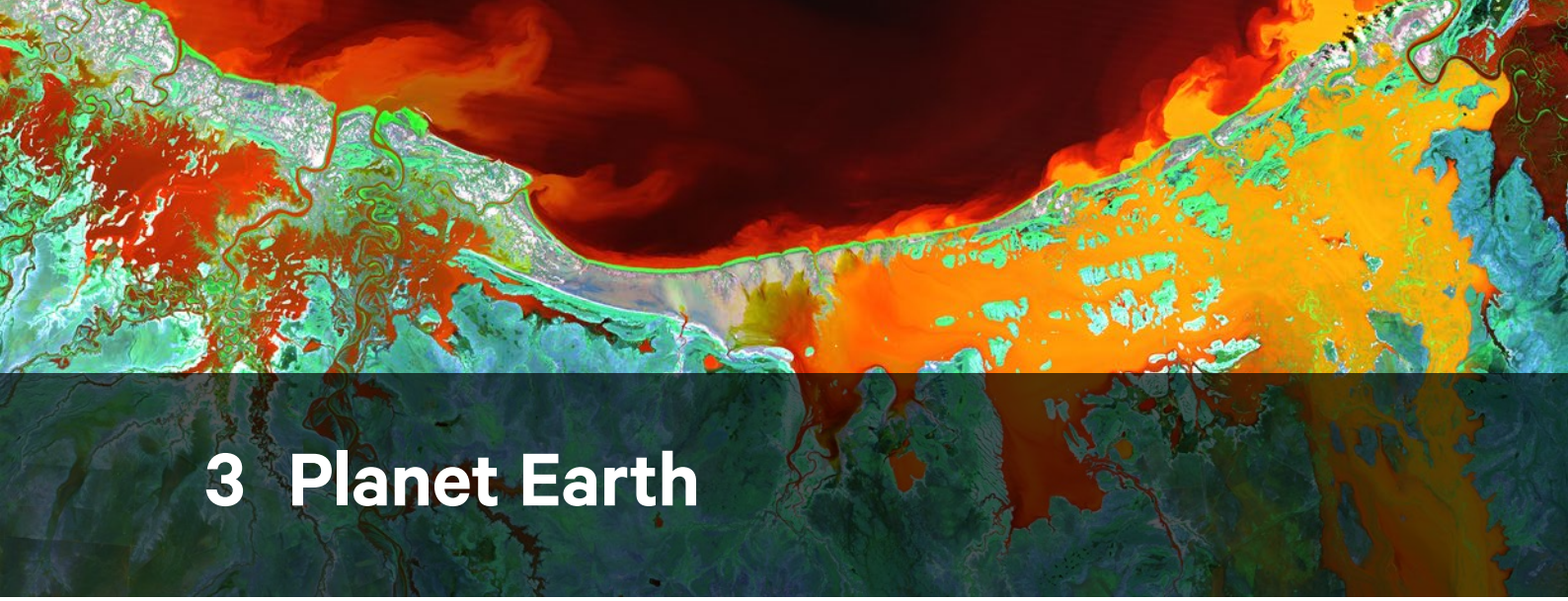
Padgham, C. A., and Saunders, J. E. (1975). The Perception of Light and Colour. Academic Press, New York.

Ryer, A. (1997). Light Measurement Handbook. Retrieved from *http://www.intl-lighttech.com/services/ilt-light-measurement-handbook*.

Signell, P. (2001). Electromagnetic Waves from Maxwell's Equations. Retrieved from *http://www.physnet.org/modules/pdf_modules/m210.pdf*.

Suits, G. H. (1983). The Nature of Electromagnetic Radiation. Chapter 2 in 'Manual of Remote Sensing' (Ed: R. N. Colwell), pp. 27-60. ASPRS, Falls Church, Virginia.

WMO (2008). Nomenclature of Radiometric and Photometric Quantities. Chapter 7A in 'Guide to Meterological Instruments and Methods of Observation', Vol. 8. 7th Edn. World Meteorological Organisation, Geneva.



3 Planet Earth

As the name implies, Earth Observation (EO) is about observing the Earth. An understanding of the target is invaluable for any investigative exercise and this is especially true for one that is as large, varied and unique as our own planet.

Before discussing EO in more detail, this section will review our current understanding of planet Earth in terms of:

- its place in space (see Section 3.1);
- its structure (see Section 3.2);
- its shape (see Section 3.3); and
- its life forms (see Section 3.4).

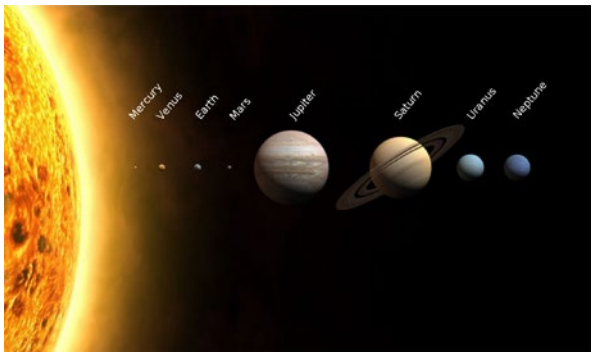
It should be emphasised that much of our current knowledge of each of these aspects of the Earth has been derived and/or refined using EO, especially at global and regional scales. Indeed, EO offers a unique perspective for observing changes in features and processes on the Earth, integrating multiple observations with ground-based validation measurements, and testing models that attempt to describe the observed changes.

3.1 The Earth in Space

The Earth is the third of eight planets that revolve around the Sun[10] (see Figure 3.1).

Figure 3.1 Our solar system

The Earth is the third of eight planets in our solar system. Note: that distances are not to scale.



Source: NASA. Retrieved from *https://commons.wikimedia.org/wiki/File:Planets2013.svg*

Planets move according to Kepler's three laws:

- Law of ellipses—planets move in ellipses with the Sun at one focus, that is, the elliptical orbit is anchored on one side by the Sun;
- Law of Equal Areas—the radius vector describes equal areas in equal times, that is, a line between the planet and the Sun would sweep the same area in equivalent time intervals; and
- Law of Harmonies—the square of the periodic times are to each other as the cubes of the mean distance, that is, the orbit period squared is proportional to the cube of the semi-major axis of the orbit (NASA, 2015).

What's the use of a fine house if you haven't got a tolerable planet to put it on?
(Henry David Thoreau)

Background image: This Landsat-5 image was acquired on 18 February 2009 and shows the rivers flowing into the Gulf of Carpentaria in flood conditions (displayed using bands 2, 4, 5 as RGB). **Source:** Norman Mueller, Geoscience Australia

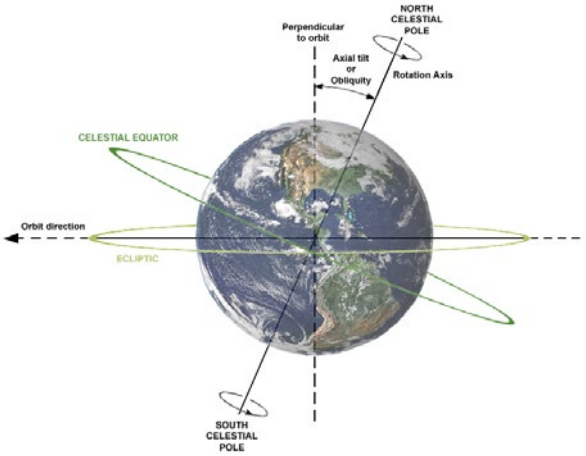
10. Pluto was demoted from full planetary status in 2006, and it now considered a dwarf planet.

All planets do not share a common axial tilt, or obliquity (the angle between the rotational axis and the orbital axis; see Table 3.1). This is equivalent to the angle between the equatorial and orbital planes of the planet (see Figure 3.2), or solar declination, and equals 23.4º for planet Earth. The plane of Earth's orbit around the Sun is called the elliptic plane (Iqbal, 1983). The plane that is orthogonal to Earth's rotational axis is the plane of the celestial equator, which can be used to track the position of the Sun relative to Earth. On two days each year, these planes coincide so that the Sun is positioned directly over Earth's equator. On these equinox days[11] all locations on Earth experience 12 hours of daylight and 12 hours of night (20/21 March and 22/23 September). The solstices[12] occur on days of maximum solar declination (21/22 June and 21/22 December, when there is maximum difference between the length of day and night (Iqbal, 1983).

Based on spherical geometry principles, irradiance decreases with the square of the distance from a radiation source (see Section 2.9.1). Accordingly, the total solar irradiance reaching Earth is about half that reaching Venus and more than twice that reaching Mars. Features of Earth are compared with other planets in Table 3.1.

Figure 3.2 Earth's axis of rotation

Relationship between axial tilt (or obliquity), rotation axis, plane of orbit, celestial equator and ecliptic (plane of Earth's orbit). Earth is shown as viewed from the Sun, with the orbit direction counter-clockwise (to the left).



Source: Dennis Nilsson (CC BY 3.0). Retrieved from *https://en.wikipedia.org/wiki/Earth%27s_rotation#/media/File:AxialTiltObliquity.png*

Table 3.1 Comparison of planetary features

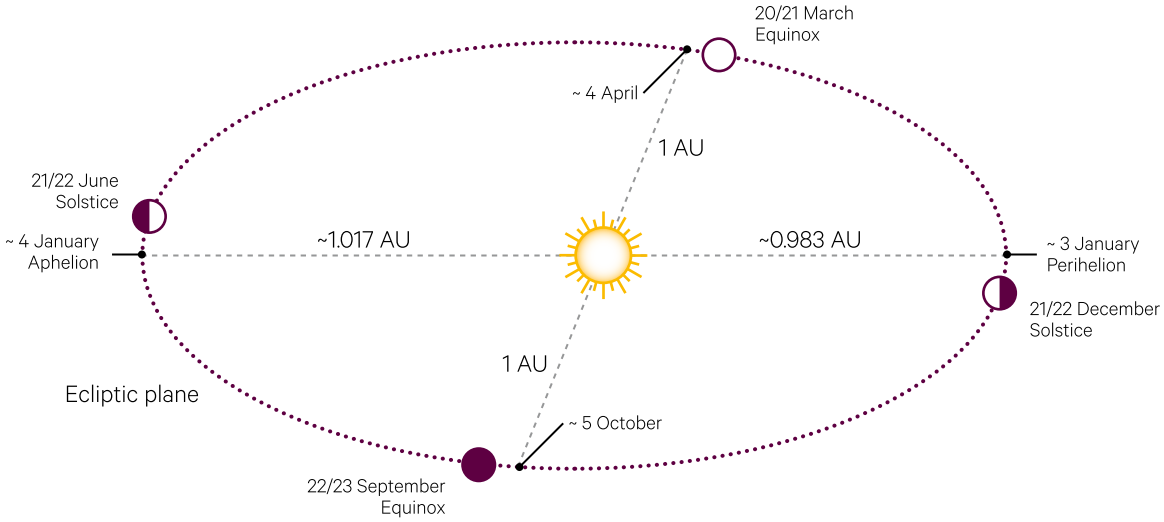
Planet Characteristic	Mercury	Venus	Earth	Mars	Jupiter	Saturn	Uranus	Neptune
Mass (10^{24}kg)	0.33	4.87	5.97	0.642	1898	568	86.8	102
Equatorial diameter (km)	4879	12,104	12,756	6792	142,984	120,536	51,118	49,528
Average density (kg/m^3)	5427	5243	5514	3933	1326	687	1271	1638
Equatorial gravity (m/s^2)	3.7	8.9	9.8	3.7	23.1	9	8.7	11
Rotation period (hours)	1407.6	-5832.5	23.9	24.6	9.9	10.7	-17.2	16.1
Length of day (hours)	4222.6	2802	24	24.7	9.9	10.7	17.2	16.1
Distance from Sun (10^6 km)	57.9	108.2	149.6	227.9	778.6	1433.5	2872.5	4495.1
Astronomical Units (AU)[15]	0.387	0.723	1	1.52	5.20	9.58	19.20	30.05
Solar irradiance (W/m^2)	9,000	2,640	1,370	590	50	15	3.7	1.5
Perihelion (10^6 km)	46	107.5	147.1	206.6	740.5	1352.6	2741.3	4444.5
Aphelion (10^6 km)	69.8	108.9	152.1	249.2	816.6	1514.5	3003.6	4545.7
Orbital Period (days)	88	224.7	365.2	687	4331	10,747	30,589	59,800
Average orbital velocity (km/s)	47.4	35	29.8	24.1	13.1	9.7	6.8	5.4
Orbital inclination (degrees)	7	3.4	0	1.9	1.3	2.5	0.8	1.8
Orbital Eccentricity	0.205	0.007	0.017	0.094	0.049	0.057	0.046	0.011
Obliquity to orbit (degrees)	0.01	177.4	23.4	25.2	3.1	26.7	97.8	28.3
Mean temperature (°C)	167	464	15	-65	-110	-140	-195	-200
Number of moons	0	0	1	2	67	62	27	14

Source: NASA (2015)[13]

11. From Latin/Old French: equi = equal, nox = night
12. From Latin/Old French: sol = Sun, stit = stationary or stopped
13. Measurement unit equaling 149,597,870.7 km (mean distance from the Earth to the Sun). (Source: *http://neo.jpl.nasa.gov/glossary/au.html*)

Figure 3.3 Variation in solar radiation due to Earth's elliptical orbit

Seasonal characteristics of Earth's orbit. Note: Distances are not to scale.



Adapted from: Iqbal (1983) Figure 1.2.1

The Earth rotates once around its own axis each day and completes one revolution around the Sun each year. Its solar orbit is elliptical, which results in variations in the distance from the Sun to Earth within each annual orbit. The combination of an elliptical orbit and a tilted axis of rotation change the amount of solar radiation reaching each part of the Earth's surface during each year, and this differential heating cycle produces our seasons.

The approximate distance from Earth to our moon is 384,000 km and its mean diameter is around one quarter the diameter of Earth (NASA, 2015). The synchronous rotation of the moon around Earth exerts enough gravitational force on the waters of the Earth to create tides. While the surface area on Earth is over 510 million km^2, the surface area of the Moon spans 37.9 million km^2—less than the Asian continent—and 7.4% of the surface area of Earth (Cain, 2016).

The Earth's elliptical orbit around the Sun brings it closest to the Sun in early January. This point is called the periapsis (smallest radial distance of an ellipse) or the perihelion (smallest radial distance in an elliptical orbit around the Sun). The point of greatest distance is called the apoapsis (greatest radial distance of an ellipse) or aphelion (furthest distance from the Sun in an elliptical orbit; see Figure 3.3). The Earth is furthest from the Sun in early July and closest in January, with the actual dates varying from year to year. This configuration varies the amount of solar radiation reaching the top of Earth's atmosphere throughout the year, such that around 6.7% more radiation is received at periapsis than at apoapsis (see also Section 5).

3.2 Structure of the Earth

Current knowledge of Earth's internal structure is heavily reliant on remote sensing techniques. Our understanding of the internal structure of Earth is based on investigations relating to:

- earthquake waves and how they travel through the Earth;
- geology of surface rocks;
- Earth's movement in the Solar System;
- Earth's gravity and magnetic fields; and
- heat transfer from inside the Earth.

On the basis of these observations, geophysicists have inferred the structure of the Earth in terms of both compositional and mechanical layers as illustrated in Figure 3.4. Traditionally the Earth has been viewed as being composed of three layers: the innermost and densest core, an intermediate mantle layer, and a surface crust, on which we live. Our knowledge of these compositional layers has recently been expanded by new data relating to their mechanical properties. The density transitions between layers are stepped, rather than continuous, with a marked change occurring at the boundary between the mantle and the outer core (Dziewonski and Anderson, 1981).

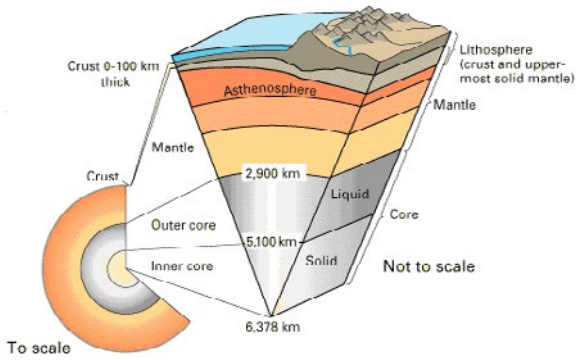
According to Dynamo Theory, the Earth's magnetic field derives from properties of fluid in the outer core, spurred into motion by the Coriolis Effect, which results from Earth's rotation. While the inner solid core appears to be too hot to retain a magnetic field, the average magnetic field strength in the outer core is believed to be 50 times stronger than at the surface (Buffett, 2010).

The theory of Plate Tectonics views the crust and the upper mantle as forming a rocky mosaic called the lithosphere (Kious and Tilling, 1996). Averaging at least 80 km in thickness over much of the Earth, the lithosphere has been broken up into large, slowly moving, plates that contain the world's continents and oceans. Pangaea is believed to be the most recent supercontinent, which started to fragment some 175 million years ago to ever so slowly form the current land masses on Earth (see Figure 3.6). The boundaries between tectonic plates have been classified into four groups, according to the relative movement of their plates (see Figure 3.6):

- divergent boundaries—plates pull apart allowing magma to be pushed up from the mantle to form new lithosphere; these boundaries are characterised by chains of volcanoes, which form oceanic ridges, or rift valleys;
- convergent boundaries—plates push together so that one plate slides under another, causing some lithosphere to be consumed into the mantle. This process is called subduction and occurs under oceans (to form deep ocean trenches) or along coastlines. Volcanoes, earthquakes and orogenesis occur in these zones;
- transform boundaries—adjacent plates slide in opposite directions, resulting in fault lines; these zones are characterised by earthquakes; and
- plate boundary zones—boundaries and their interaction are not clearly defined (Kious and Tilling, 1996).

Figure 3.4 Cross-section of Earth

The structure of layers comprising Earth can be viewed in terms of composition or mechanics. This cutaway diagram shows the Earth's internal structure (to scale), with an inset showing the breakdown in terms of mechanical layers (not to scale)



Source: USGS (CC BY). Retrieved from *https://commons.wikimedia.org/wiki/File:Earth_internal_structure.png*

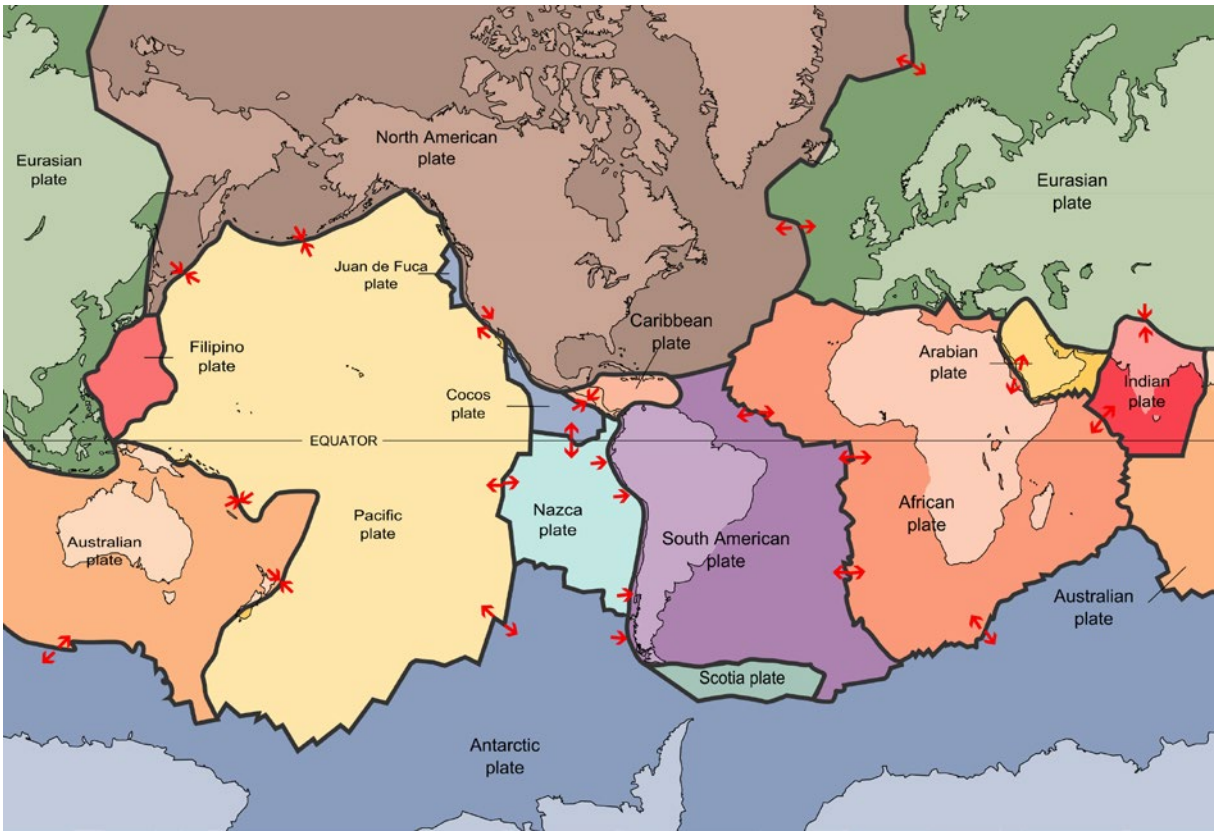
Below the lithosphere is a narrow zone called the asthenosphere, which appears to be composed of hot, mobile material. Movement of the rigid lithospheric plates appears to be driven by convection within the asthenosphere. Most of the movement of tectonic plates occurs along boundaries, where plates can separate, collide, or slide. Most earthquakes and active volcanoes can be observed to occur along these boundaries and records of such geodynamic events were used to locate them.

For further information on the interior of the Earth, please refer to Rencz (1999) and Robertson (2001). Specific EO applications to geology are discussed in Volume 3.

It suddenly struck me that that tiny pea, pretty and blue, was the Earth.
I put up my thumb and shut one eye, and my thumb blotted out the planet Earth.
I didn't feel like a giant. I felt very, very small.
(Neil Armstrong)

Figure 3.5 Tectonic plates

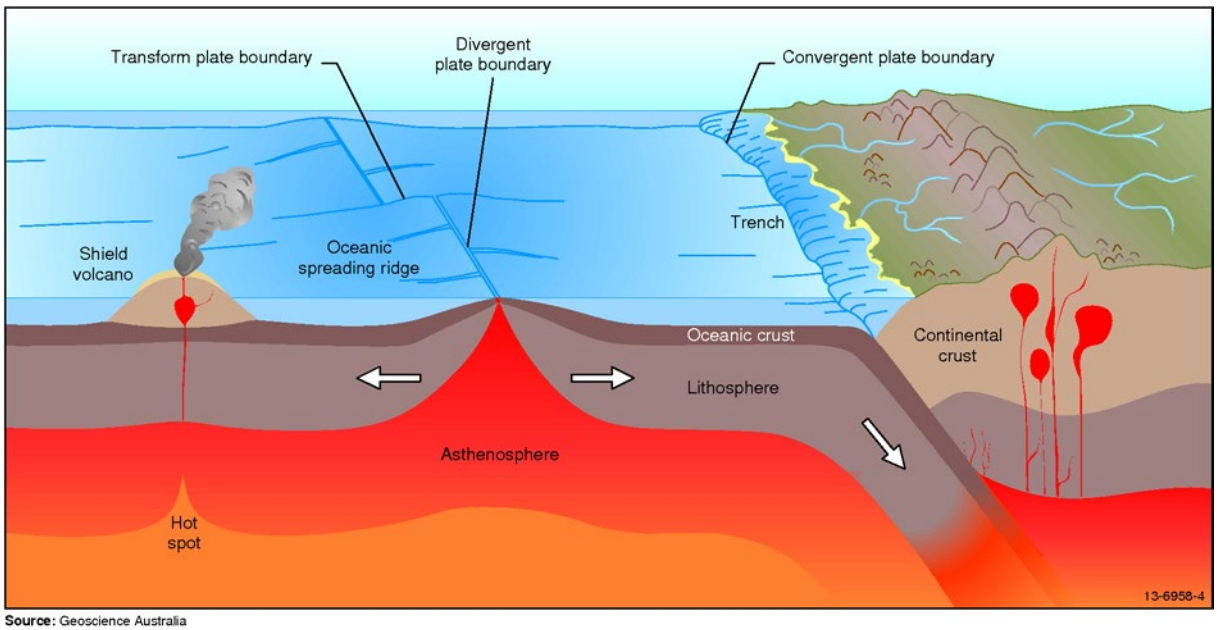
The layer of the Earth we inhabit comprises several rigid plates. These tectonic plates are moving in relatively different directions as indicated by the red arrows.



Source: Wikimedia Commons (CC BY) from USGS original. Retrieved from *https://commons.wikimedia.org/wiki/File:Plates_tect2_en.svg*

Figure 3.6 Tectonic plate boundaries

The tectonic plates comprising the lithosphere 'float' and move on the slowly flowing asthenosphere. Tectonic plates are constantly moving towards, away from or past each other resulting in three major types of boundaries—divergent, convergent and transform—as illustrated below.



Source: Geoscience Australia

Source: Lewis and Collins (2014), Geoscience Australia

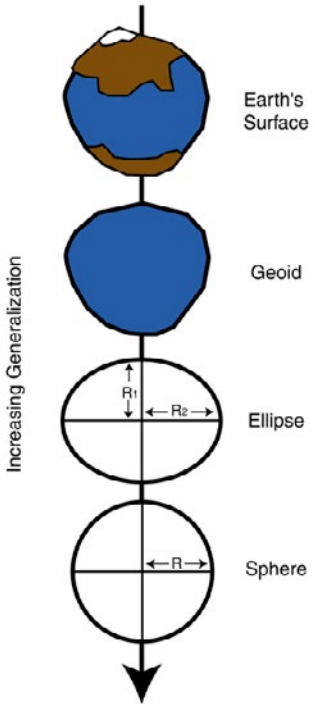
3.3 Shape of the Earth

Geodesy allows locations and elevations on the Earth's surface to be defined precisely. This branch of applied mathematics measures the size and shape of the Earth, and its gravity field, and quantifies changes in these attributes. It also defines frames of reference to locate the Earth in space and monitor its movements relative to other celestial bodies.

Earth is not a sphere (see Figure 3.7). It approximates the shape of an ellipsoid, being slightly flattened at the poles and widest at the equator. A reference ellipsoid is a mathematical model of the Earth's size and shape, which is used to derive coordinate systems that precisely define unique locations on the Earth's surface. This underpins all cartographic and positioning activities.

Figure 3.7 Modelling the shape of the Earth

The shape of Earth is irregular. With increasing accuracy, it can be modelled by a sphere, an ellipse or a geoid.



Source: ©The Pennsylvania State University (CC BY-NC-SA 3.0). Retrieved from *https://www.e-education.psu.edu/geog486/node/1883*

Multiple ellipsoids have been derived to best fit the curvature of particular regions of the Earth, but in recent years satellite positioning measurements have allowed development of global ellipsoids for large area mapping. Sets of permanent reference locations, or horizontal datums, have been established around the globe to define coordinates on an ellipsoid. Similarly, networks of precise elevation measurements define vertical datums for mapping topography.

However, the Earth is not an ellipsoid either but has a highly irregular surface that is continuously changing. Surface elevation on Earth varies from a maximum at Mt Everest (8,850 m above mean sea level) to a minimum in the Mariana Trench (10,924 m below mean sea level).

A geoid attempts to model the topographic shape of the Earth more accurately than an ellipsoid (see Excursus 3.1). This interpolated model can be viewed as a surface on which every point is perpendicular to gravity and experiences the force of gravity at mean sea level. This shape has been likened to that which would result if the globe were covered by water, unaffected by tides, and only impacted by gravity. The geoid is the most logical reference surface for measuring and mapping heights.

Detailed geodetic models have been made possible using accurate distance measurements from satellites (see Excursus 3.2). The use of geodetic models to improve the geometry of EO imagery is discussed in Volume 2B.

We live at the bottom of a deep gravity well, on the surface of a gas-covered planet going around a nuclear fireball 90 million miles away
(Douglas Adams)

Excursus 3.1—Datums and Geoids

Source: Geoscience Australia: GA: *http://www.ga.gov.au/*
Further information: Intergovernmental Committee on Surveying and Mapping (ICSM): *http://www.icsm.gov.au/mapping/index.html*

A map represents features on Earth and shows the spatial relationship between different features. Global maps require:

- a reference system to describe the locations of points on Earth' s surface, eg. latitude/longitude or local grids;
- a datum to mathematically define how the reference system is placed on the Earth's surface,
- a measurement system to calculate coordinates of locations on Earth;
- a projection to convert three-dimensional coordinates onto a two-dimensional map;
- additional information such as metadata, legends, scale, and annotation.

Datums

There are many datums and projections to best suit particular regions on the Earth's surface and/or specific mapping purposes. Horizontal datums define spatial locations and vertical datums define the surface height above a fixed reference point.

While a datum is intended to map to the surface of the Earth, this is very difficult given the variations in shape that occur. Also, we now know that the surface of Earth is moving on a system of tectonic plates. Accordingly, datums map to a three-dimensional surface that models the shape of the Earth, such as a spheroid, an ellipsoid or a geoid.

Datums can be either:

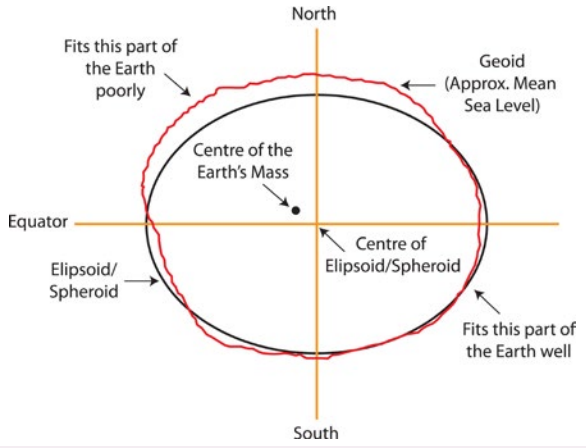
- plate-fixed—relative to a tectonic plate so that coordinates are unchanged by plate movement. Traditional mapping datums have been plate-fixed; or
- Earth-fixed—move over time with tectonic plate movement. GNSS coordinates are Earth-fixed.

Datums can also be:

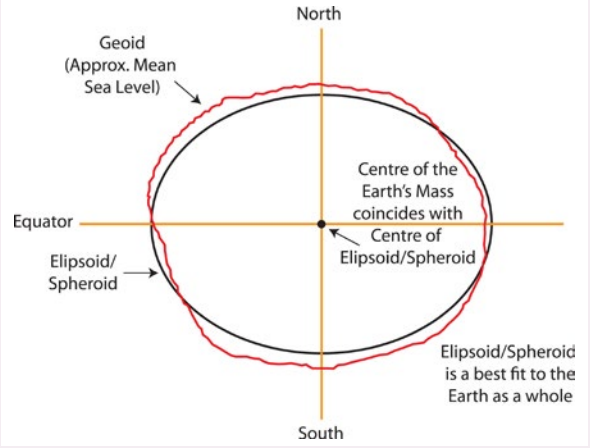
- local or regional—defined to fit a specific region of the Earth but may be a poor fit for other regions (see Figure 3.8a); or
- geocentric—defined to achieve best fit over the whole globe (see Figure 3.8b).

Figure 3.8 Local versus geocentric datums

a. Local or regional datum suits a specific region only



b. Geocentric datum is best suits the whole globe



Source: © Commonwealth of Australia 2014—on behalf of the Intergovernmental Committee on Surveying & Mapping (ICSM). Retrieved from *http://www.icsm.gov.au/mapping/datums1.html#difference*

Australian Horizontal Datums

Australia has used three plate-fixed datums:

- Australian Geodetic Datum of 1966 (AGD66), which used the Australian National Spheroid for geodetic computations, relative to the Johnston Geodetic Station in central Australia. Coordinates in this regional datum were derived from classical triangulation, traversing and astrogeodetic and aero observations.
- Australian Geodetic Datum of 1984 (AGD84), which added refinements to AGD66 that were derived from space-based geodetic techniques, such as Doppler satellite measurements, Very Long Baseline Interferometry and Satellite Laser Ranging (see Section 8).
- Geocentric Datum of Australia (GDA94), which was based on the internationally recognised Geodetic Reference System 1980 (GRS80).

While these datums work well for a single continent, they are not compatible with global positioning satellite technology. Our tectonic plate is moving north-north-east at around 7 cm per year, resulting in more than 1.5 m difference between GDA94 coordinates and GNSS devices in 2016.

The National Positioning Infrastructure (NPI) Plan is working towards a precise, Earth-fixed system to ensure Australian spatial information is totally compatible with GNSS (see Volume 1B—Section 10: Excursus 10.1).

Australian Vertical Datum

The Australian Height Datum (AHD) was adopted in 1971 as the national reference for vertical control of elevation mapping. This datum surface passes through mean sea level at 32 defined tide gauges around the coastline of Australia.

Our Dynamic Earth

The structure and shape of Earth changes constantly both in terms of horizontal and vertical motion. While we are aware of some rapid crustal shape changes, such as earthquakes and subsidence, the tectonic plates are also slowly moving. Australia, for example, is moving in a north-north-easterly direction at a rate of around 7 cm per year, and this slow movement becomes highly significant for locational accuracy over time.

The horizontal and vertical motion of the Australian landmass is monitored by Geoscience Australia (GA) as part of an international effort to monitor the changing shape and motion of Earth. This work integrates continuous measurements from a system of ground stations with various EO data sets to provide a uniform and accurate foundation for all spatial data in Australia (see Section 8).

Geoids

A geoid is a three-dimensional level surface representing equal gravitational potential. By definition, this surface is perpendicular to the direction of the gravity vector at all points. However, as the mass and density distribution of the Earth are not uniform or constant, the direction of gravity varies (see Section 8). As a result, the shape of the geoid is both irregular and dynamic.

While there are an infinite number of possible equipotential surfaces for the Earth, the term 'geoid' is most commonly used to describe the equipotential surface that most closely approximates mean sea level.

Across Australia, mean sea level and its onshore model, the Australian Height Datum (AHD), correspond to within approximately ±0.5 m of the geoid. This discrepancy is due to differences in temperature and density of coastal waters in northern and southern Australia, with the warmer water being about one metre higher off the northern coast.

Global Navigation Satellite System (GNSS)

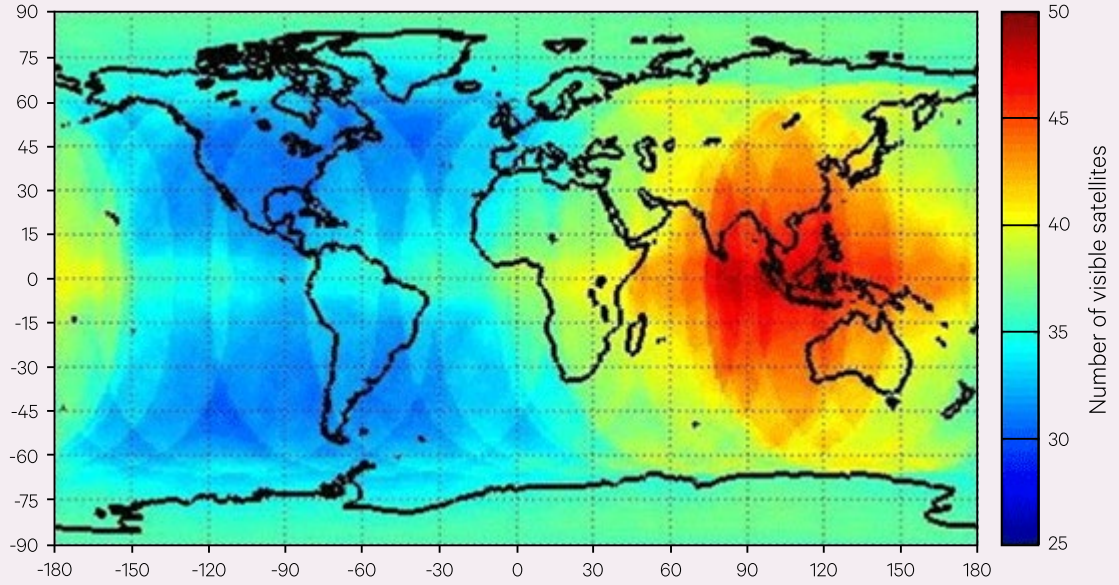
Satellite systems that provide geospatial positioning on Earth are collectively called the Global Navigation Satellite System (GNSS). This system currently comprises over 100 operational satellites, owned and managed by six national and regional jurisdictions, namely:

- USA (GPS),
- Russia (GLONASS),
- China (BeiDou),
- EU (Galileo),
- India (Navic) and
- Japan (QZSS).

The average number of satellites that will be visible from the planned constellations is mapped in Figure 3.9. As well as providing precise location and time, these satellites enable the movement of tectonic plates to be measured accurately (see Volume 1B—Section 10).

Figure 3.9 Average number of visible satellites across all planned constellations

The average number of current and planned GNSS satellites visible from different locations over a 24 hour period is shown as a colour scale from blue (25 satellites) to red (50 satellites). Australia and Southeast Asia are well situated for good GNSS coverage.



Source: Dempster and Rizos (2009) **Adapted from:** Dempster and Hewitson (2007). Used with permission.

Excursus 3.2—Space Geodesy and Reference Frames

Source: Geoscience Australia (GA): *http://www.ga.gov.au*
Further information: International Earth Rotation and Reference Systems Service (IERS) : *http://www.iers.org*
International Astronomical Union (IAU) *http://www.iau.org*
International GNSS Service (IGS): *https://www.iers.org/IERS/EN/Organization/TechniqueCentres/IGS/igs.html*
International DORIS Service: *http://ids-doris.org*
NASA Space Geodesy Project: *http://space-geodesy.nasa.gov/techniques/VLBI.html*
International Laser Ranging Service (ILRS): *http://ilrs.gsfc.nasa.gov*
Global Geodetic Observing System (GGOS) *http://www.ggos.org*

Just as the shape and structure of Earth are dynamic, so are its placement, orientation and motion in space. Earth's rotational vector does not have a fixed axis and the rate of rotation is not uniform. Its surface shape and energy fields are also affected by the gravitational influence of other celestial bodies.

While datums are required to measure positions on Earth relative to a standard referencing system, accurate reference frames are required to monitor the changes in Earth's position, orientation and movement in space. These are defined as the Geocentric Celestial Reference Frame (GCRF) and the International Terrestrial Reference Frame (ITRF).

The International Earth Rotation and Reference Systems Service (IERS) maintains procedures and models to transform between the GCRF and the ITRF. These transformations require continuous monitoring of several fundamental parameters that quantify irregularities in Earth's rotation (known as Earth Orientation Parameters: EOP):

- Universal time difference (UT1)—based on Earth's rotation—variations indicate changes in Earth's rotational speed;
- Pole Coordinates—show the movement of Earth's rotational axis relative to its crust; and
- Celestial Pole Offsets—show changes in the orientation of the Earth's rotational axis (such as precession, nutation, obliquity).

Reference system—specifies how a celestial coordinate system is defined, including origin and axes, plus models, constants and algorithms to convert between conformal observations and reference data

Reference frame—set of identifiable fiducial points, and their coordinates, that realise the reference system.

Celestial Reference Frame

The International Celestial Reference Frame (ICRF) realizes an ideal reference system, the International Celestial Reference System (ICRS), by precise equatorial coordinates of extragalactic radio sources observed in Very Long Baseline Interferometry (VLBI) programs. (IERS, 2013)[14]

The GCRF is the geocentric equivalent of the ICRS.

Terrestrial Reference Frame

A Terrestrial Reference System (TRS) is a spatial reference system co-rotating with the Earth in its diurnal motion in space. In such a system, positions of points attached to the solid surface of the Earth have coordinates which undergo only small variations with time, due to geophysical effects (tectonic or tidal deformations). (Ch. 4 in Petit and Luzum, 2010)

ITRF

The International Terrestrial Reference System (ITRS) constitutes a set of prescriptions and conventions, together with the modeling required to define origin, scale, orientation and time evolution of a Conventional Terrestrial Reference System (CTRS). The ITRS is an ideal reference system, ... realised by the International Terrestrial Reference Frame (ITRF). ...The ITRS can be connected to the International Celestial Reference System ICRS by use of the IERS EOP (IERS, 2013)[15]

The ITRF2014 (released in early 2016) is viewed as the most accurate terrestrial reference frame available for geodesy, in both global and regional applications. The ITRF2014 is based on data from 1,499 ground stations at 975 sites, often co-located with space geodetic instruments:

- Global Navigation Satellite Systems (GNSS; see Volume 1B—Section 10);
- Satellite Laser Ranging (SLR; see Volume 1A—Sections 8 and 16.1.2.1);
- Lunar Laser Ranging (LLR);
- Very Long Baseline Interferometry (VLBI); and
- Doppler Orbitography Radio Positioning Integrated by Satellite (DORIS; see Section 16.1.2.2).

Laser Ranging

The International Laser Ranging Service (ILRS) provides global satellite and lunar laser ranging data and products. SLR (see Figure 3.10) and LLR actually measure the distance (based on two-way time interval) between ground stations and retroreflector arrays on orbiting satellites and the Moon using short-pulse lasers. Such measurements highlight variations in Earth's centre of mass, which is the origin of geocentric reference systems.

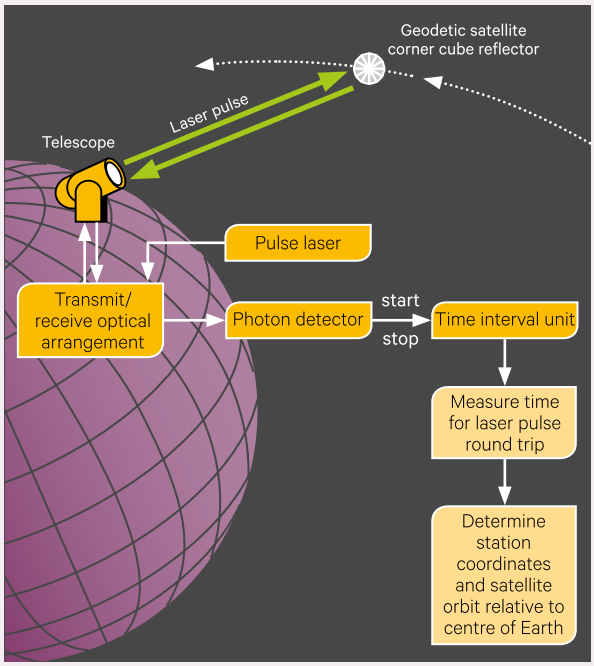
DORIS

The DORIS (Doppler Orbitography Radio Positioning Integrated by Satellite) system relies the Doppler shift between transmitted and received signals between a ground station and a member satellite to determine orbital information. A radio signal is transmitted from a ground beacon to a passing satellite then, based on the observed frequency shift of the signal, the relevant positions of the satellite and ground beacon can be computed. Two Australian ground stations (managed by Geoscience Australia) are part of an international network. These measurements have also been valuable for highlighting changes in the Earth's crust.

VLBI

VLBI is a geometric technique that collects signals from distant astronomical radio sources, such as quasars, at multiple radio antennae on Earth. Since these measurements are precise to picoseconds (with hydrogen maser clock accuracy of one second in one million years), the positions of the antennae relative to the quasars can be determined accurately. These measurements have been invaluable for defining the inertial reference frame for our planet and tracking crustal and surface water changes. Australia operates three VLBI observatories, located near Hobart, Perth and Darwin.

Figure 3.10 Satellite Laser Ranging



Adapted from: Geoscience Australia

14. International Earth Rotation and Reference Systems Service: *https://www.iers.org/IERS/EN/DataProducts/ICRF/icrf.html*
15. International Earth Rotation and Reference Systems Service: *https://www.iers.org/IERS/EN/DataProducts/ITRS/itrs.html*

3.4 Further Information

International Earth Rotation and Reference Systems Service (IERS):

https://www.iers.org/IERS/EN/Home/home_node.html

Geodesy:

Geoscience Australia: *http://www.ga.gov.au/scientific-topics/positioning-navigation/geodesy*

International Committee on Surveying and Mapping (ICSM): *http://www.icsm.gov.au/index.html*

Earth Structure:

Robertson (2001)

Windows to the Universe (NESTA): *http://www.windows2universe.org/earth/Interior_Structure/interior.html*

3.5 References

Buffett, B. A. (2010). Tidal dissipation and the strength of the Earth/'s internal magnetic field. Nature, 468(7326), pp. 952-954. doi:*http://dx.doi.org/10.1038/nature09643*.

Cain, F. (2016). The Moon compared to Earth. Universe Today. Retrieved from *http://www.universetoday.com/20489/moon-compared-to-earth/*.

Dempster, A. G., and Hewitson, S. (2007). The 'System of Systems' Receiver: an Australian Opportunity? Paper presented at the International Global Navigation Satellite System Society IGNSS Symposium 2007, Sydney, Australia.

Dempster, A. G., and Rizos, C. (2009). Implications of a "system of systems" receiver. Paper presented at the Surveying & Spatial Sciences Institute Biennial International Conference, Adelaide, Australia.

Dziewonski, A. M., and Anderson, D. L. (1981). Preliminary reference Earth model. Physics of the Earth and Planetary Interiors, 25(4), pp. 297-356. doi:*http://dx.doi.org/10.1016/0031-9201(81)90046-7*.

Iqbal, M. (1983). An Introduction to Solar Radiation. Academic Press, Toronto.

Kious, W. J., and Tilling, R. I. (1996). This Dynamic Earth: The Story of Plate Tectonics. USGS, Washington, DC. Retrieved from *http://pubs.usgs.gov/gip/dynamic/dynamic.html*.

Lewis, G., and Collins, C. (2014). Earthquakes - Teacher notes and student activities (2014/06). Geoscience Australia, Canberra. Retrieved from *https://d28rz98at9flks.cloudfront.net/76611/Rec2014_006.pdf*. doi:*http://dx.doi.org/10.11636/Record.2014.006*.

NASA (2015). Lunar and Planetary Science. Retrieved from *http://nssdc.gsfc.nasa.gov/planetary/*.

Petit, G., and Luzum, B. (2010). Verlag des Bundesamts für Kartographie und Geodäsie. IERS Conventions, Frankfurt am Main.

Rencz, A. N. (1999). Remote Sensing for the Earth Sciences, Vol. 3, Third Edn., Ed: R. A. Ryerson, Manual of Remote Sensing. American Society for Photogrammetry and Remote Sensing (ASPRS); John Wiley & Sons, Inc., New York.

Robertson, E. C. (2001). The Interior of the Earth. Retrieved from *http://pubs.usgs.gov/gip/interior/*.



4 Earth Systems and Processes

This section introduces the integrated systems (see Section 4.1) and processes (see Section 4.2) that keep our planet alive. Much of this information has been derived using Earth Observation (EO) technologies. Volume 3 describes some of the specific applications of EO that have been used to monitor Earth System processes.

4.1 Earth System Science

The Earth can be viewed as an integrated system comprising four spheres (Lindsey, 2009):

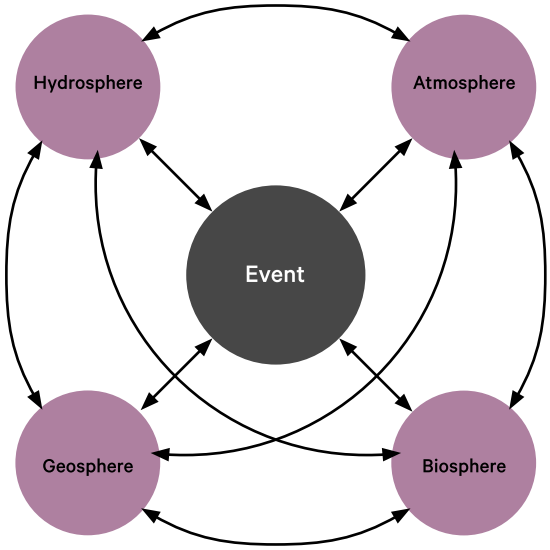
- atmosphere—gaseous, protective layer around the Earth (see Section 4.1.1).
- hydrosphere—all surface waters, groundwater and atmospheric water in any state (see Section 4.1.2);
- geosphere—solid components of Earth on land and under water (see Section 4.1.3); and
- biosphere—all forms of life on Earth (see Section 4.1.4).

This multi-disciplinary approach assumes a holistic perspective, such that individual events on Earth can be related to all four spheres (see Figure 4.1).

Earth System Science analyses the dynamic geochemical processes and interactions occurring between these spheres to better understand the Earth—its past, present and future—at global to local scales (see Figure 4.1). Some of these processes and interactions are illustrated in Figure 4.2.

Figure 4.1 Earth System Science

Events on Earth can be interpreted in the context of four, integrated spheres: Biosphere, geosphere, hydrosphere and atmosphere.

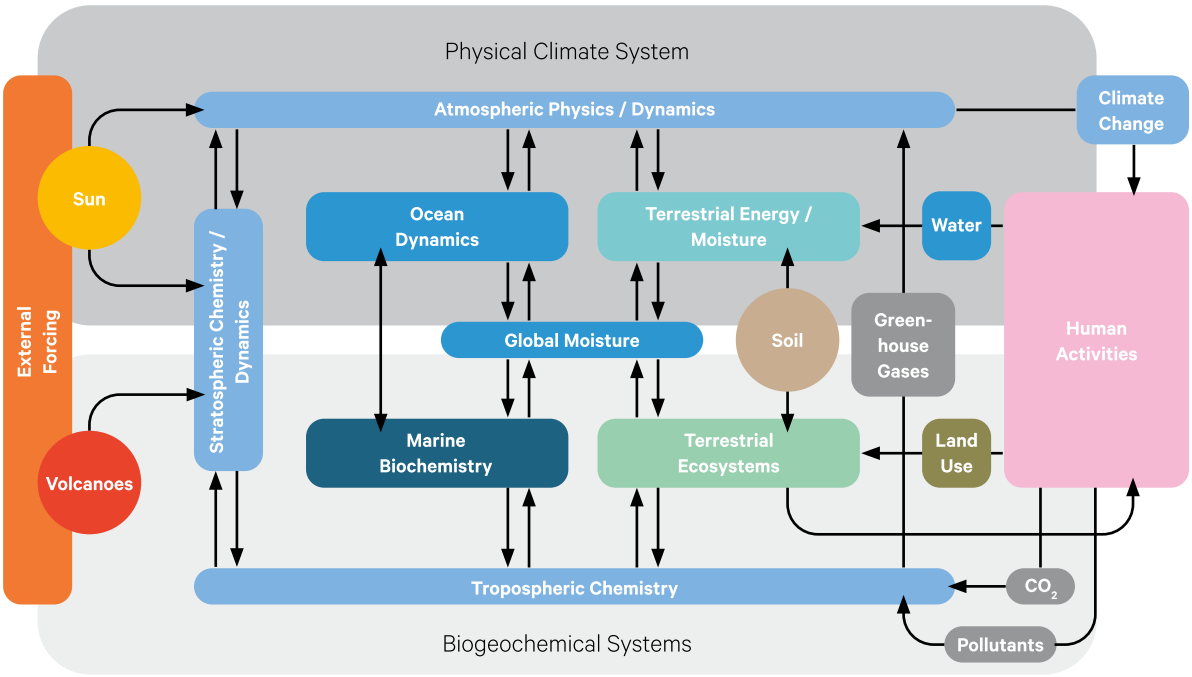


The history of life on Earth has been a history of interaction between living things and their surroundings. To a large extent, the physical form and habits of the Earth's vegetation and its animal life have been moulded by the environment. Considering the whole span of earthly time, the opposite effect, in which life actually modifies its surroundings, has been relatively slight. Only within the moment of time represented by the [last] century has one species – man – acquired significant power to alter the nature of his world.
(Rachel Carson, Silent Spring)

Background image: Landsat-5 image of the Georgina River, northern SA, which ultimately feeds into Lake Eyre. This image, acquired on 28 March 2011 after a rare rainfall event, is displayed using bands 2, 4, 5 as RGB. **Source:** Norman Mueller, Geoscience Australia

Figure 4.2 Processes and interactions within Earth System Science

All processes on Earth are interrelated and impacted by human activities. This conceptual framework was proposed by Francis Bretheton (NASA Bretheton) to link major components with the processes that impact them.



Adapted from: NASA at *http://education.gsfc.nasa.gov/experimental/all98invproject.site/pages/trl/inv4-3.abstract.html*

4.1.1 Atmosphere

Atmosphere (from) Greek, atmos meaning 'vapour' and sphaira meaning 'sphere'

The atmosphere is a gaseous layer surrounding the Earth that protects the planet from the solar wind and high-energy solar radiation (cosmic rays, X-rays and some UV rays) as well as most meteors. It has been divided vertically into four layers, defined by the way air temperature changes with increasing altitude: the troposphere, stratosphere, mesosphere, and thermosphere (see Section 5.4). Most major weather and climate activity occurs in the troposphere. These layers vary in terms of temperature, barometric pressure and chemical composition. A fifth layer, the exosphere, forms the boundary with space.

The ionosphere, where solar radiation ionises the upper atmosphere, lies approximately 80–600 km above the Earth (NOAA, 2016). During the daytime, three distinct layers of the ionosphere layers are ionized by solar radiation (see Figure 4.3):

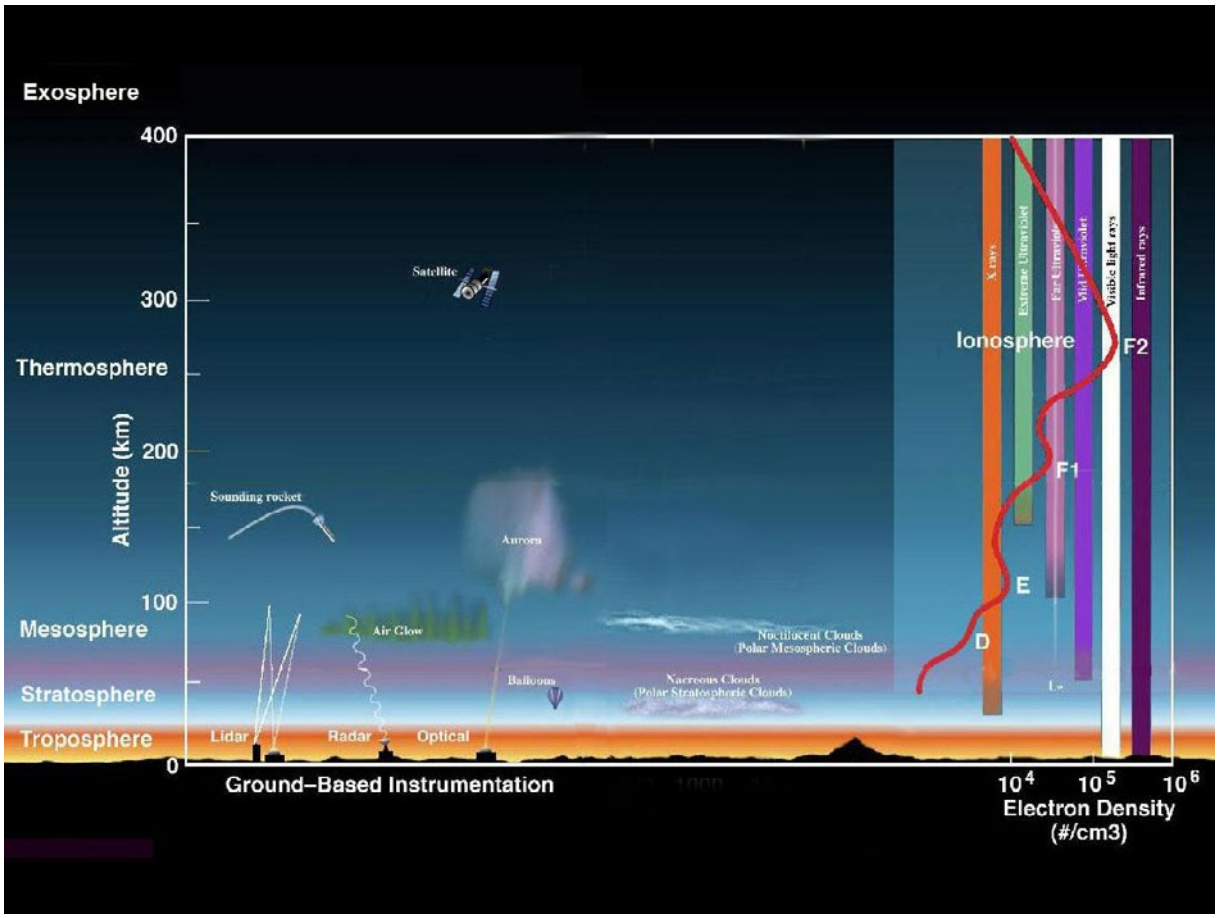
- D layer—highest frequency ionisation of NO and hard X-ray ionisation of N_2 and O_2;
- E layer—soft X-ray and UV ionisation of O_2; and
- F layer—extreme UV ionisation of atomic O. This layer deforms to a second layer during the day. The lower of these layers, F_2, faciliates long distance HF communication.

At night, the weaker cosmic rays only ionize the E and F layers (see Figure 4.4). The ionosphere is particularly significant for telecommunications and remote sensing since it influences the propagation of radio waves away from Earth. The Space Weather Network (SWN) updates global ionospheric maps on a regular basis as shown in Figure 4.5.

The saddest aspect of life right now is that science gathers knowledge faster than society gathers wisdom.
(Isaac Asimov)

Figure 4.3 Interrelationship between atmosphere and ionosphere

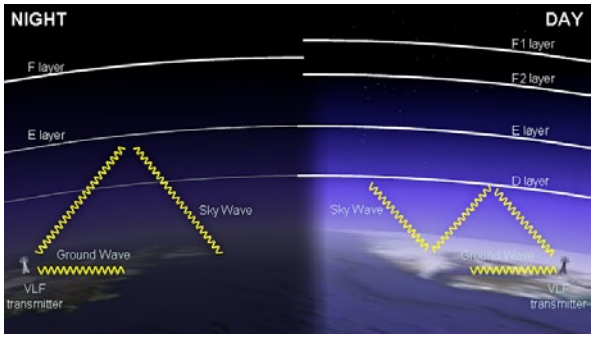
Approximate altitudes of atmospheric and ionospheric layers. The structure of ionospheric layers changes with the diurnal cycle (see Excursus 4.1).



Source: NASA. Retrieved from *http://www.nasa.gov/sites/default/files/images/463940main_atmosphere-layers2_full.jpg*

Figure 4.4 Impact of ionosphere on radio frequency waves

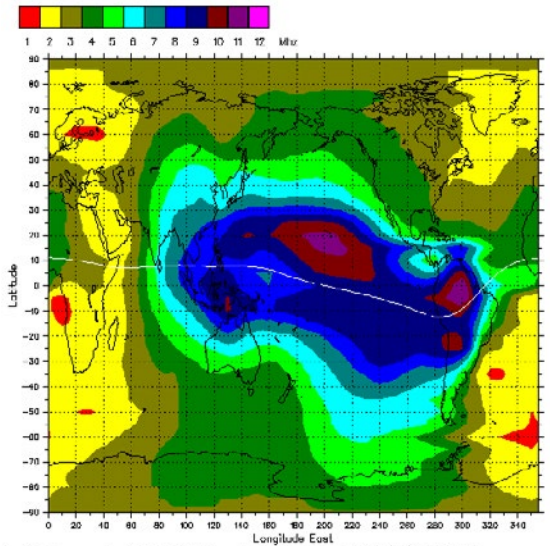
Very low frequency (VLF) waves bounce off the ionophere. During the daytime, all three layers of the ionosphere are ionized by solar radiation, enabling 'over the horizon' communication.



Source: SID Monitoring Station (CC-BY-NC-SA 3.0). Retrieved from *http://sidstation.loudet.org/ionosphere-en.xhtml*

Figure 4.5 Global ionospheric foF2 map

As part of the Space Weather Network (SWN), global ionospheric foF2 maps are updated hourly based on the previous two hours of data (acquired at half hour intervals). This map was created at 01:00 UT on 29 September 2016. The geomagnetic equator (where magnetic dip equals zero) is shown as a white line (see Section 7).



Source: © Bureau of Meteorology. Retrieved from *http://www.sws.bom.gov.au/HF_Systems/6/5*

4.1.2 Hydrosphere

Hydrosphere (from) Greek, hydro meaning 'water' and sphaira meaning 'sphere'

The hydrosphere includes all surface waters, both liquid and frozen, as well as groundwater stored in soil and rocks, and water vapour in the atmosphere. The oceans cover over 70% of the Earth's surface and provide most of the water vapour in the atmosphere. Oceans also act as a heat source and sink, or storage medium. The hydrologic cycle, or water cycle, involves vertical and horizontal movement of water (in vapour, liquid or solid form) between the Earth's surface, atmosphere and oceans (see Section 4.2.2).

The total volume of water of Earth has been estimated as 1,386 million km^3, 97.5% are saline (Shiklomanov, 1998). Of the 2.5% freshwater, nearly 69% is frozen in permanent ice and glaciers and around 30% exists as groundwater, leaving only 0.26% for use in lakes, reservoirs and rivers. These routinely available freshwater sources total around 93,000 km^3 or 0.023% of the Earth's mass. Components of the hydrosphere are described in greater detail in Volume 3.

The fact that a cloud from a minor volcanic eruption in Iceland— a small disturbance in the complex mechanism of life on the Earth— can bring to a standstill the aerial traffic over an entire continent is a reminder of how, with all its power to transform nature, humankind remains just another species on the planet Earth. (Slavoj Žižek)

4.1.3 Geosphere

Geosphere (from) Greek, geo meaning 'earth' and sphaira meaning 'sphere'

Solid Earth, both on land and under water, is called the geosphere. The structure of the geosphere is illustrated in Figure 3.4 in terms of mechanical and compositional layers. The compositional layers are summarised in Table 4.1.

As introduced in Section 3.2, the upper part of the geosphere is the lithosphere, which rests on the asthenosphere and comprises moving tectonic plates. The topography of the geosphere is shaped by the various dynamic processes associated with the rock cycle (see Section 4.2.3), often occurring over very long time periods. Soil, the focus of many studies using remote sensing, is one of the outputs from the rock cycle.

Table 4.1 Composition of planet Earth

Layer	Thickness (km)	Density (g/cm^3)	Composition
Crust	30 (5-50) Thinner under ocean basins and rift valleys and thicker under mountain ranges	2.2–2.9	Predominately silicates at surface, basalt at base
Upper mantle	720	3.4–4.4	Molten (500–900°C)
Lower mantle	2,171	4.4–5.6	More dense (~4,000°C)
Outer core	2,259	9.9–12.2	Molten
Inner core	1,221	12.8–13.1	Solid

Source: Robertson (2001), *http://pubs.usgs.gov/gip/interior/* from Anderson (1989)

4.1.4 Biosphere

Biosphere (from) Greek, bios meaning 'life' and sphaira meaning 'sphere'

Biosphere was first defined as 'the place on Earth's surface where life dwells' (Suess, 1875). This has been expanded to include all parts of the planet that can support life, including land, sea and air. The biosphere comprises all living organisms and has been sub-divided into biomes on the basis of climate and geography. Since all organic compounds contain the element carbon, it is considered to be the foundation for all forms of life on Earth.

While all spheres are involved in the carbon cycle, carbon is primarily recycled within the biosphere. The transfer of energy within the biosphere generally involves the exchange of carbon, water and air—principally via photosynthesis, which is part of the carbon cycle (see Section 4.2.4). All plants photosynthesise, that is, produce oxygen and sugar from carbon dioxide, water and sunlight. This photochemical reaction occurs in chloroplasts, specialised organelles that contain the pigment chlorophyll. Pores on the leaf surface open and close, as required, to exchange carbon dioxide and oxygen with the atmosphere. The sugar product stores energy and provides raw materials for synthesising other compounds. Photosynthesis is the ultimate primary energy production mechanism on Earth, enabling plant growth and providing food and shelter for other life forms. More details on photosynthesis in leaves are provided in Volume 3A.

4.2 Earth System Processes

Almost all energy on Earth ultimately derives from the Sun (with a relatively minor component originating from the Earth's interior). The solar radiation that reaches the Earth's surface is called solar irradiance, or insolation (and measured in W/m^2, or accumulated over time as solar exposure in MJ/m^2 or Wh/m^2—see Section 2.3). At any single point on the globe, variations in insolation can result from solar output fluctuations, atmospheric transmission, and seasonal and diurnal cycles. Around the globe, insolation also varies with latitude, altitude, and aspect.

Energy and matter are transferred between the geosphere, hydrosphere, atmosphere and biosphere via a number of ongoing pathways. These can be considered in terms of four broad areas, namely:

- energy—heat transfer and storage (see Section 4.2.1);
- water—cycling of matter and some energy with the movement of water (see Section 4.2.2);
- earth—transfer of matter and energy in the rock cycle (see Section 4.2.3); and
- carbon—slow and fast cycling of carbon between the spheres (see Section 4.2.4).

An understanding of these transfers provides insight into the broader concerns of efficient energy consumption and storage, and conservation of fundamental ecological resources.

4.2.1 Energy

The Earth is commonly viewed as a closed system, that is, a unit with defined boundaries that permit the exchange of energy but not matter (see Section 2.10.3). Exceptions to this definition include the entry of meteorites and journeys of spacecraft, but most of Earth's processes do not exchange matter with the rest of the universe.

Solid matter on Earth absorbs solar energy as:

- sensible heat, leading to a change in temperature, or
- latent energy, leading to a change in state (see Section 2.10.2).

The flow, or flux, of thermal energy on Earth is driven by two major factors:

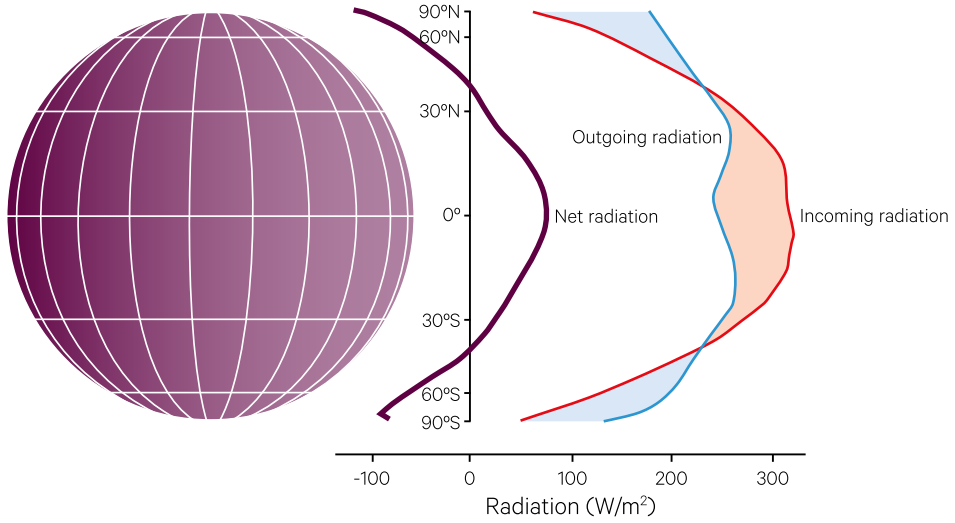
- amount of solar energy that reaches the surface; and
- how Earth surface materials interact with that energy (see Sections 2.10 and 2.11).

Minor sources of heat also originate within Earth due to its material composition, friction resulting from internal changes, and radioactivity.

As a consequence of the inclination, revolution and rotation of the Earth relative to the Sun, insolation around the globe varies markedly with latitude, season and time of day (see Excursus 4.1). These variations result in differential heating around the globe. To balance global energy, heat is moved from the tropics to the poles via large-scale circulation of air and water, our two most mobile and ubiquitous fluids (see Figure 4.6, plus Volume 3). Overall, this 'meridional' circulation allows the 'surplus' solar energy received between 40°N and 38°S to balance the 'deficit' of energy nearer the poles. Heat is also transferred out of Earth's system into space (see Figure 4.7 and Volume 3).

Figure 4.6 Energy distribution and net radiation

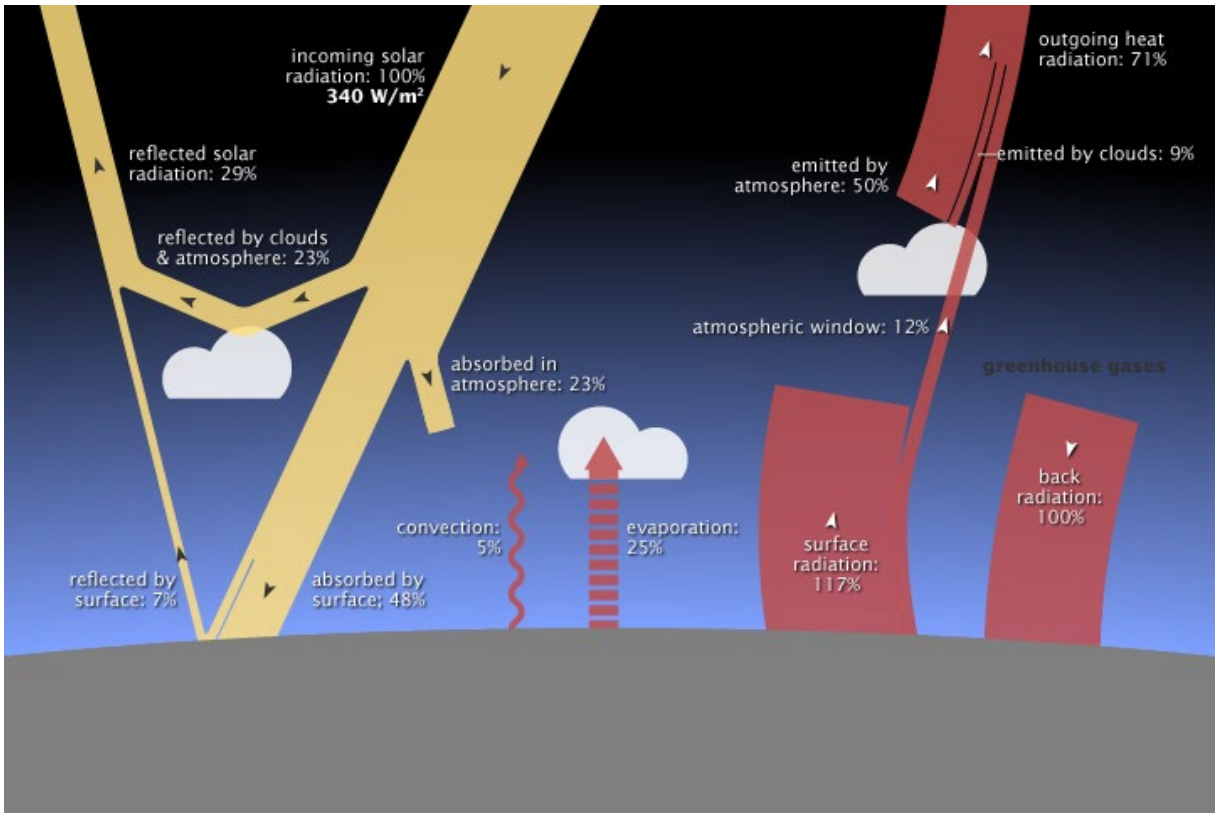
Between around 40°N and 38°S, there is more incoming than outgoing energy, resulting in a net energy gain (pink). At higher latitudes this relationship is reversed, causing a net energy loss (blue). Overall, the surplus energy moves from the warmer equatorial latitudes to the poles via atmospheric and ocean circulation patterns.



Adapted from: Adapted from: RAPID/NOC at SEOS Ocean Currents (CC-BY-SA). Retrieved from *http://www.seos-project.eu/modules/oceancurrents/oceancurrents-c03-p02.html*

Figure 4.7 Earth's energy budget

Of the 340 W/m² of solar energy that reaches the top of Earth's atmosphere, an equal amount of energy is returned to space as either reflected or emitted energy. This balance is essential to maintain a stable temperature on Earth.



Source: Lindsey (2009). Retrieved from *http://earthobservatory.nasa.gov/Features/EnergyBalance/page6.php*

Three processes facilitate this circulation:

- sensible heat flux—conduction and convection of energy from the surface to the atmosphere, which then moves warm equatorial air to the poles by advection, then colder air returns to the equator (see Section 2.10);
- latent heat flux—vertical and horizontal energy transfer due to evaporation of solid and liquid water (see Section 2.10.2);
- surface heat flux:
  - into oceans—warm surface water is circulated vertically within the water column by conduction and convection and horizontally by ocean currents; or
  - into soil and solid surfaces.

Water surfaces have a high specific heat capacity so heat and cool slowly, can readily cool by evaporation, and can transfer heat to a greater depth than land. Land surfaces thus experience a greater seasonal temperature range, especially on larger continents. Land is cooled more slowly by evapotranspiration. Air temperatures above land and water surfaces vary in a similar way to those of their underlying surface.

The flow of energy into and out of the Earth's system is referred to as the Earth's energy or radiation budget (see Figure 4.7 and Excursus 4.1). This considers both the solar energy reaching Earth and the energy being radiated from Earth back to space, that is:

net radiation = incoming radiation – outgoing radiation

where

incoming radiation is short wave direct and indirect solar radiation plus long wave radiation from the atmosphere; and

outgoing radiation is short wave reflection and long wave emission from Earth.

Indirect radiation includes radiation that has been scattered by atmospheric particles and other surfaces.

It is estimated that around:

- 29% of the solar energy that reaches the top of Earth's atmosphere is returned to space by reflection primarily from the atmosphere and water vapour (clouds), or highly reflective surface features such as ice or snow;
- 23% of solar radiation is absorbed in transit through the atmosphere;
- 48% is absorbed by the Earth's surface.
- Thus, the Earth's surface and atmosphere together absorb approximately 71% of the incoming radiation (Lindsey, 2009).

For any system to stay in equilibrium there needs to be a long-term balance between energy inputs and outputs. The Earth's energy budget can be compartmentalised into three sub-budgets:

- at the surface;
- within the atmosphere; and
- at the top of the atmosphere.

To maintain equilibrium, each of these sub-budgets also needs to balance incoming and outgoing energy levels. At the surface, of the 48% of net solar radiation absorbed, approximately:

- 25% is transferred into the atmosphere by evaporation (latent heat);
- 5% is transferred via convection of air in direct contact with warmed surfaces; and
- 17% is emitted as thermal infrared energy (Lindsey, 2009); see Volume 1B—Section 7 and Volume 3).

Seldom if ever does nature operate in closed and separate compartments, and she has not done so in distributing the earth's water supply. Rain, falling on the land, settles down through pores and cracks in soil and rock, penetrating deeper and deeper until eventually it reaches a zone where all pores of the rock are filled with water, a dark, subsurface sea, rising under hills, sinking beneath valleys. This ground water is always on the move, sometimes at a pace so slow that it travels no more than 50 feet [17 m] a year, sometimes rapidly, by comparison, so that it moves nearly a tenth of mile [160 m] a day. It travels by unseen waterways until here and there it comes to the surface as a spring, or perhaps it is tapped to feed a well. But mostly it contributes to streams and so to rivers. Except for what enters streams directly as rain or surface run-off, all the running water of the earth's surface was at one time ground water.
(Rachel Carson, Silent Spring)

Excursus 4.1—Insolation

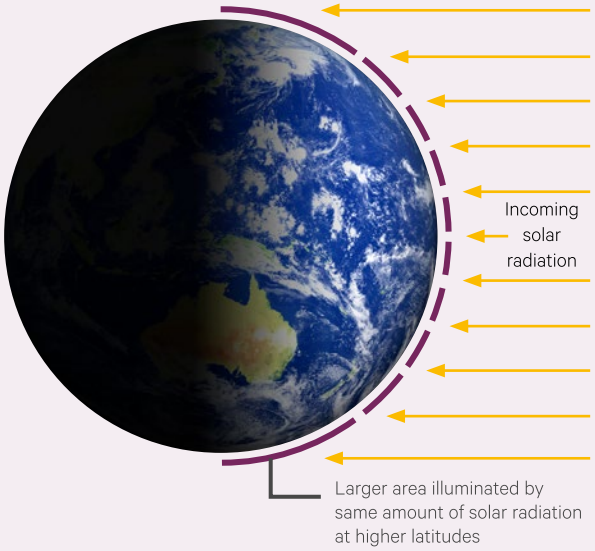
Further information: Lindsey (2009)

The total solar irradiance is defined as the average intensity of solar energy at the top of Earth's atmosphere (TOA). This is based on the average distance between the Earth and the Sun (around 150 million km) and was previously believed to be constant, but is now known to vary with solar activity (see Section 3).

The Total Irradiance Monitor (TIM) on the Solar Radiation and Climate Experiment (SORCE) determined total solar irradiance as 1360.8±0.5 W/m^2 during the 2008 solar minimum (NASA, 2016)[16]. This estimate only applies to surfaces that are perpendicular to incoming radiation (namely midday at the equator) and decreases towards the poles (see Figure 4.8). The average solar irradiance at TOA over the whole globe reduces to 340 W/m^2.

Figure 4.8 Solar illumination angle variation with latitude

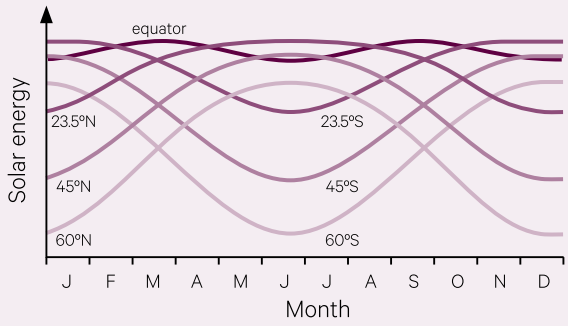
At higher latitudes, the Sun angle (measured as elevation) decreases. Accordingly the average solar irradiance reaching the surface of Earth decreases, and the area being irradiated increases.



Adapted from: Lindsey (2009)

Figure 4.9 Variations in insolation with latitude and annual cycle

Insolation at solar noon for different latitudes through the year. Peak energy shows little annual variation at the equator, but significant seasonal variations nearer the poles.



Adapted from: Lindsey (2009)

The actual solar irradiance intercepted by the Earth's surface varies significantly with latitude, season and time of day (see Figure 4.9). This variation results from the inclination, revolution and rotation of Earth relative to the Sun (see Section 3).

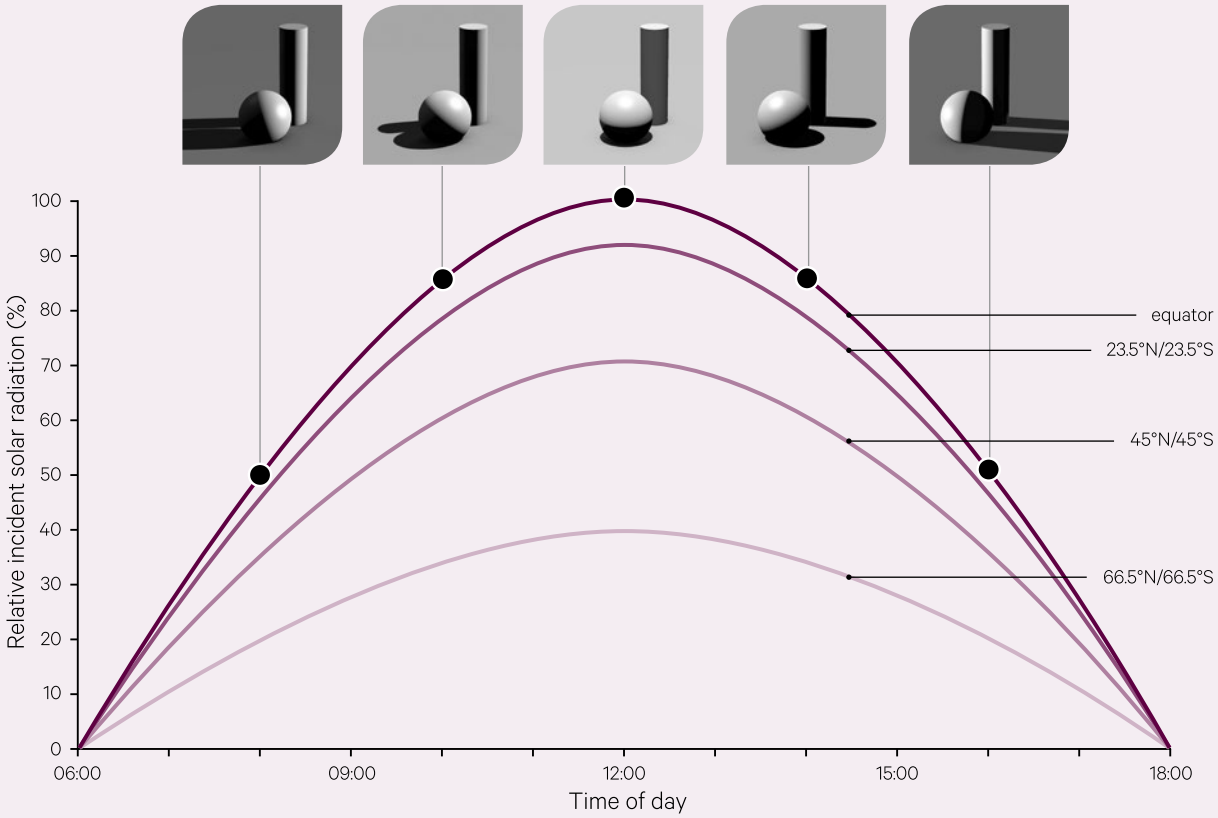
Moving away from the equator, the angle of solar illumination (relative to the horizon) decreases, which both decreases the average solar irradiance reaching the surface through the atmosphere and increases the area of its effective footprint (see Figures 4.8 and 4.10). At each latitude, both the length and intensity of insolation varies each day of the year (see Figure 4.10), with the number of sunlight hours per day ranging from 0 in winter to 24 in summer for polar regions, compared with 12 hours throughout the year at the equator.

Asymmetry in the Earth's orbit also introduces differences in peak solar radiation between hemispheres. Since the Earth is closer to Sun during summer in the southern hemisphere, that hemisphere receives more summer energy overall (see Figure 4.11).

16. For more details, please see: *http://atmospheres.gsfc.nasa.gov/climate/?section=136*

Figure 4.10 Typical daily insolation cycle on equinox days

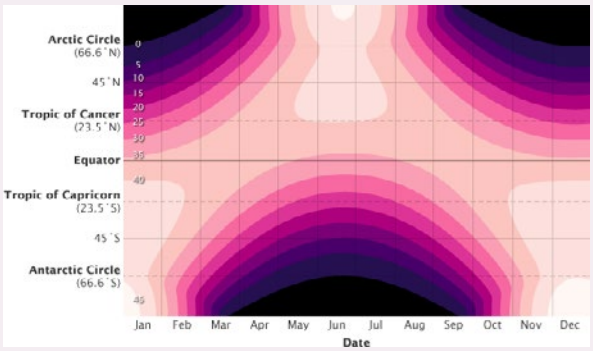
Typical solar radiation reduces with increasing latitude



Adapted from: Lindsey (2009)

Figure 4.11 Annual cycle of total daily solar irradiance

Shown on a colour scale from dark (low) to pale (high), the total solar irradiance at TOA varies with latitude and season. High latitudes receive the highest levels of incoming energy during long summer days.



Source: Lindsey (2009)

CERES

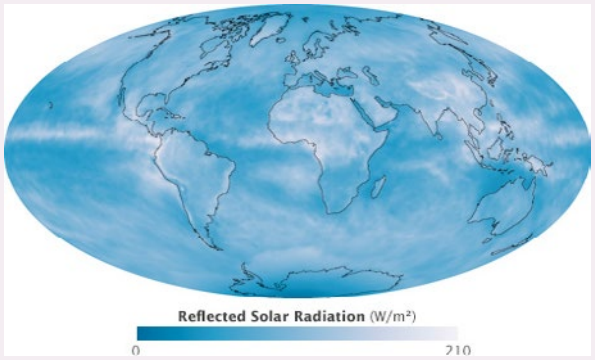
The Clouds and the Earth's Radiant Energy System (CERES) includes instruments on several NASA satellite missions. This mission measures two types of outgoing energy from Earth:

- reflected solar radiation (short wave EMR; see Figure 4.12); and
- emitted radiation (long wave EMR; see Figure 4.13).

The difference between the incoming solar radiation and total outgoing radiation is called the net radiation (see Figure 4.14). These global imbalances in energy drive circulation of the atmosphere and oceans to create our weather and climate.

Figure 4.12 Reflected solar radiation

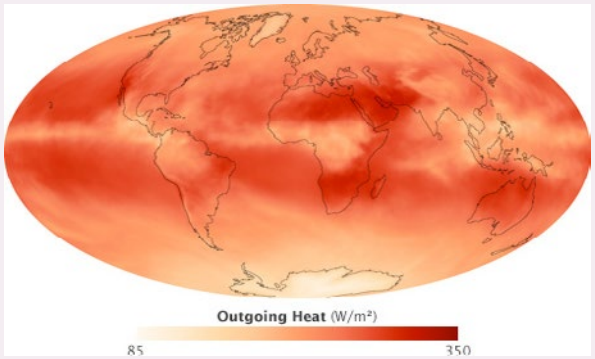
Clouds and bright surfaces reflect more solar radiation. Derived from CERES data for September 2008, averaged over one month.



Source: Robert Simmon, NASA. Retrieved from *http://earthobservatory.nasa.gov/Features/EnergyBalance/page3.php*

Figure 4.13 Outgoing radiation

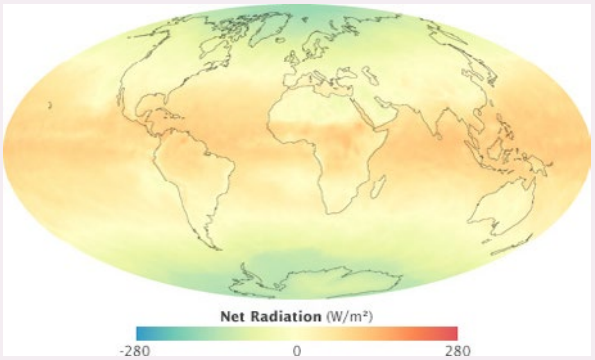
Distribution of thermal infrared emission derived from CERES data during the month of September 2008. Clouds around the equator reduce heat loss, with maximum loss occurring in the warm, relatively cloud-free middle latitudes.



Source: Robert Simmon, NASA. Retrieved from *http://earthobservatory.nasa.gov/Features/EnergyBalance/page4.php*

Figure 4.14 Net radiation

This global image shows the difference between incoming solar radiation and outgoing radiation during September 2008, an equinox month. In areas with positive net radiation (orange and red—such as near the equator) there was more incoming than outgoing radiation, that is, they absorbed more energy. In areas with negative net radiation (green and blue—such as the poles) more radiation was outgoing than incoming.



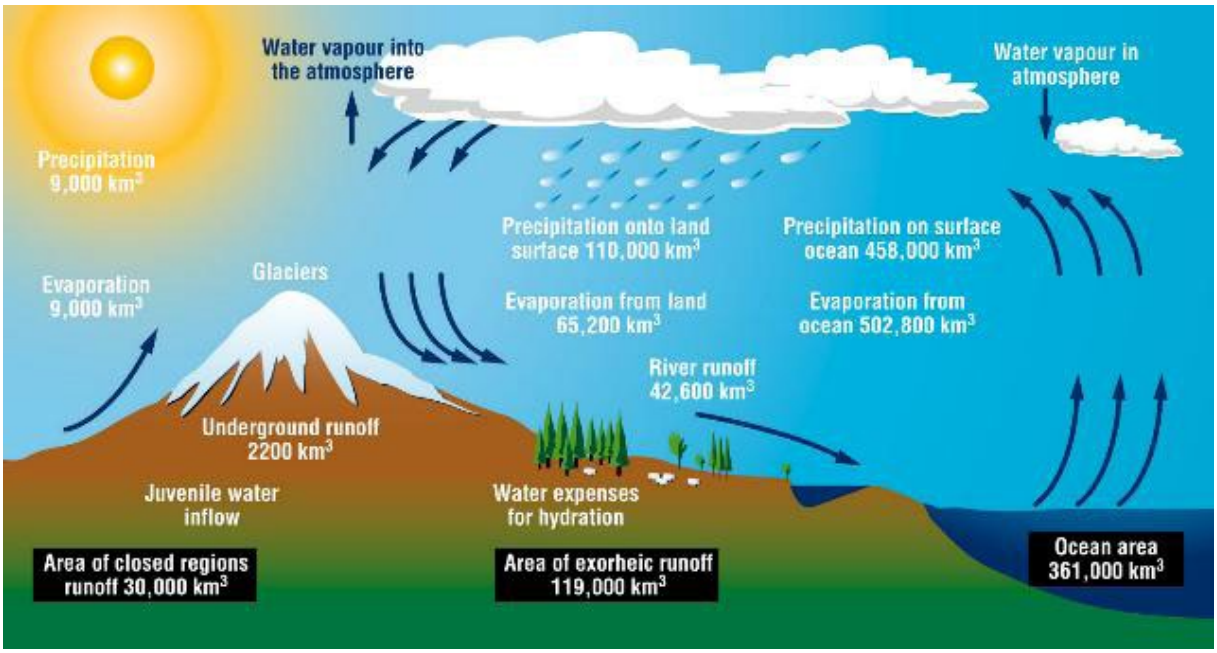
Source: Robert Simmon, NASA. Retrieved from *http://earthobservatory.nasa.gov/Features/EnergyBalance/page3.php*

4.2.2 Water

Each year, more than half a million cubic kilometres of water moves between locations on the Earth's surface, between the surface and sub-surface storage, and between the surface and the atmosphere (Shiklomanov, 1998). This constant movement can occur in the form of liquid water, steam, ice or snow and may be close to pure or contain dissolved and/or suspended substances see Figure 4.15.

Figure 4.15 Hydrological cycle

More than half a million cubic kilometres of water is moved around the Earth's surface, between the surface and sub-surface storage, and between the surface and the atmosphere each year.



Source: Shiklomanov (1998) © UNESCO. Retrieved from *http://webworld.unesco.org/water/ihp/publications/waterway/webpc/pag5.html*

As surface water is heated by the Sun, it evaporates to become water vapour in the atmosphere. Plants also release water to the atmosphere by evapotranspiration. As water vapour rises in the atmosphere, it cools and condenses, forming clouds. Global air currents move clouds until they release their water as precipitation, in the form of rain, hail or snow.

Water on the surface of the Earth is stored in the natural depressions of oceans and lakes, or the man-made storage facilities of reservoirs and dams. Some surface water is frozen, as occurs in polar ice caps and glaciers, and may remain in that form for millennia. Other frozen surface water regularly melts with seasonal changes.

Water running on the Earth's surface, or runoff, can come directly from precipitation or melting sources. Before flowing towards a drainage channel, precipitation can be intercepted by vegetation, buildings or small surface depressions within a catchment. Interception of rainfall allows some precipitation to soak into the ground rather than flow away. Water can infiltrate into the soil layer and be stored as soil moisture or percolate through the soil until it reaches the water table.

Beneath the Earth's surface, soil and/or rock are layered in two distinct zones. The upper zone is aerated, that is, it contains some air. Water in this zone is available to plants. In the lower, rocky zone, air pockets are saturated with water. The boundary between these zones is called the water table. The depth of the water table varies with the volume of water that is added (recharge) and/or removed (discharge). Globally, extraction of groundwater is increasing by 1% to 2% per year (WWAP, 2012).

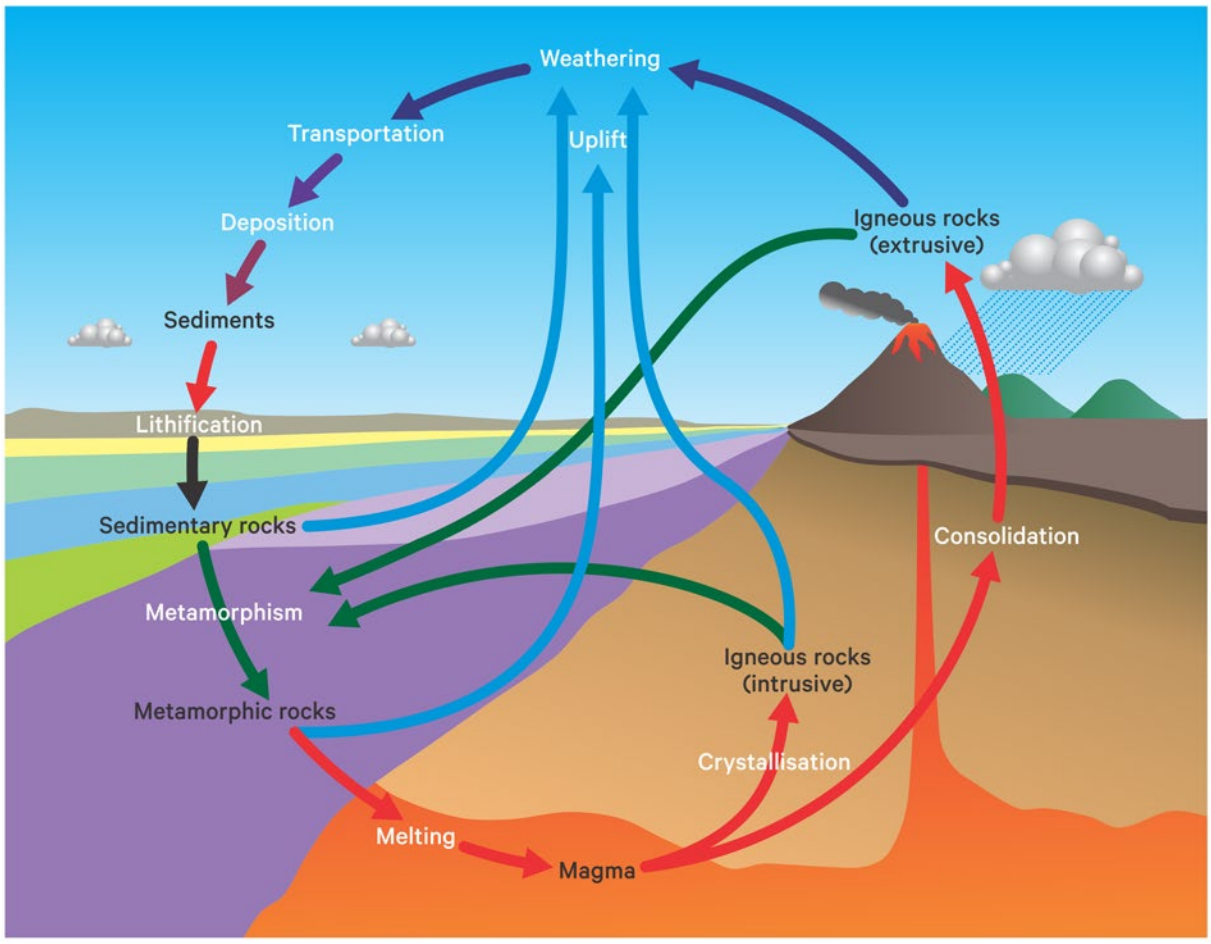
4.2.3 Earth

Just as water is transformed and moved around the planet by the hydrological cycle, so inorganic solids are recycled by the rock cycle (see Figure 4.16). This cycle explains the origins and interrelationships between the three basic rock types:

- igneous—formed by cooling and solidification of magma below or on the surface;
- sedimentary—formed by compaction of accumulated sediments that have been loosened by erosive agents of water, wind and ice; and
- metamorphic—formed from parent rock by heat and pressure deep within the Earth, and/or contact with chemically active fluids.

Figure 4.16 Rock cycle

Sedimentary, igneous and metamorphic rocks are manufactured and reconstituted in cycles.



Adapted from: Monroe and Wicander (1992) Figure 1-15

Rocks are manufactured and reconstituted in cycles. They comprise minerals, naturally occuring inorganic solids with a defined chemical composition and characteristic crystalline structure. Rocks are formed as different combinations of minerals become fused and aggregated in different ways. Although 4,000 minerals are known to exist, only a few dozen commonly occur and 98% of the Earth's crust is formed from just eight elements (O, Si, Al, Fe, Ca, Na, K, Mg). Silicates are the most commonly occurring group of minerals (Tarbuck and Lutgens, 2005).

All igneous rocks are formed from magma, molten material from the asthenosphere. When extruded onto the surface of Earth by volcanoes, magma becomes lava, which cools quickly to form rocks with fine crystals. Igneous rocks also form when magma intrudes into 'plutons' below the Earth's surface, where slower cooling produces larger crystals.

Sedimentary rocks are the result of weathering. Fragments of rocks are gradually eroded by wind, water or ice. These grains, or sediments, are transported by wind, water or gravity until they settle and solidify. Over time, sediments are compacted and/or chemically cemented together.

Metamorphic, igneous and sedimentary rocks can be transformed by heat and pressure, and/or contact with chemically active fluids to become new metamorphic rocks. Heat typically comes from contact with magma. Extremely high temperatures and pressures can re-form minerals.

The extremely slow movement of plate tectonics explains many geological processes and most changes in geology occur at the boundaries of tectonic plates (see Section 3.2). At a landscape level, the rock processes combine with tectonic activity to shape the surface of Earth:

- Surface rocks are gradually worn down by weathering and erosion, with the loosened sediments being deposited to form sedimentary rocks;
- Sediments can become buried and compressed or may be uplifted by tectonic movement. With heat and pressure they can become metamorphic rocks;

- Metamorphic rocks can be either uplifted to form new mountain ranges or can sink into the mantle to form magma;
- By internal pressure or convection, magma is forced from the mantle to the Earth's surface or into the lithosphere where it cools and solidifies to form igneous rock; and
- Movement of the mantle or crust push rocks to the surface, where they are subject to weathering.

This ongoing cycle, which has continued for millenia, creates the topography of our planet (Lutgens and Tarbuck, 1998).

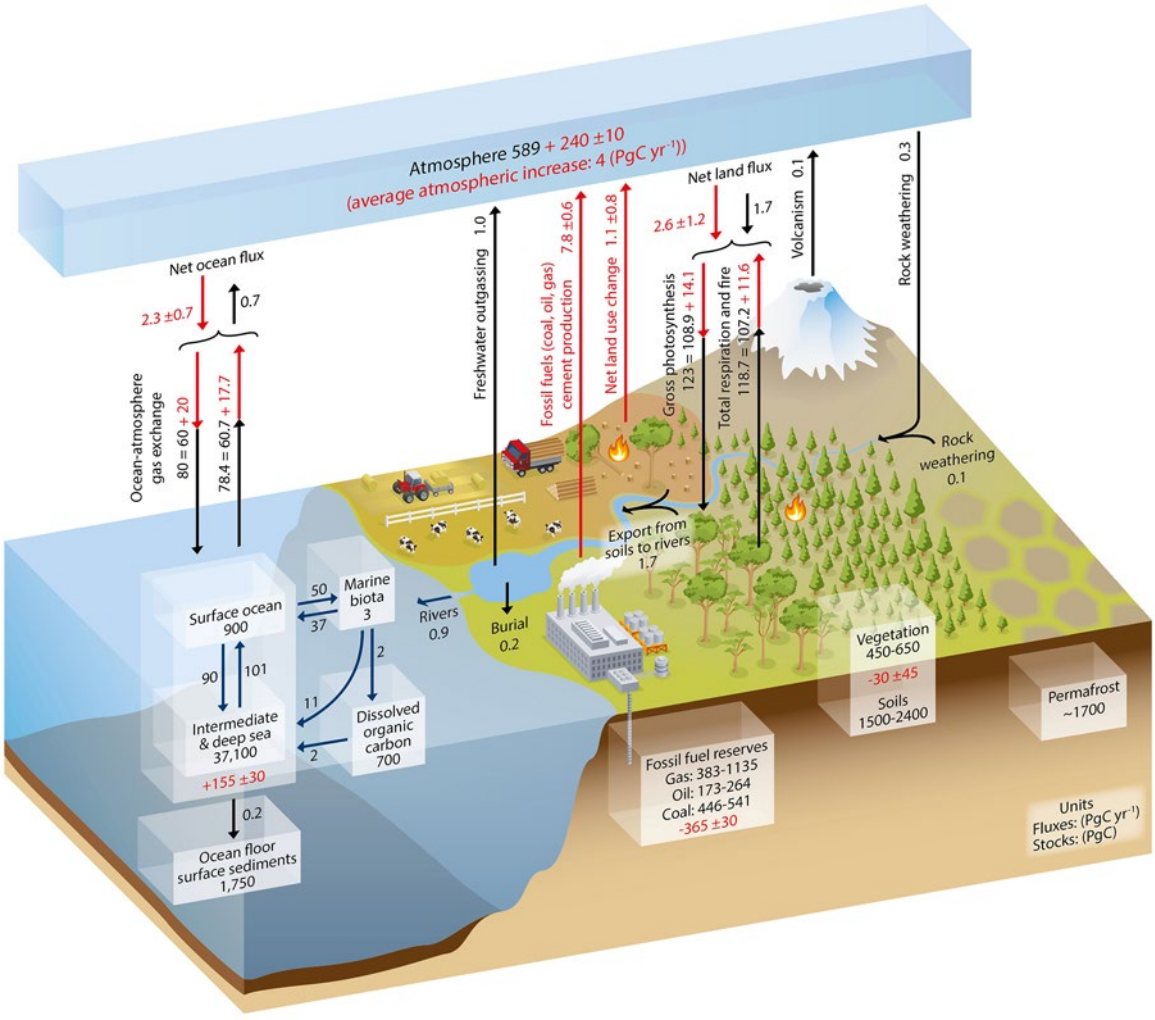
4.2.4 Carbon

An integral part of the biosphere involves the way carbon is cycled through ecosystems. The element carbon characterises all living organisms and ranks as the fourth most abundant element in the universe on the basis of mass, after hydrogen, helium and oxygen. On Earth, it exists in many forms including carbon dioxide, limestone, dolomite, graphite, diamonds, and fossil fuels, and organic compounds.

While the largest proportion of Earth's carbon is stored in rocks, it also exists in the ocean, atmosphere, vegetation, humans, animals, soil and fossil fuels. The carbon cycle describes the process of carbon flowing from one type of storage, or reservoir, to another via natural processes (see Figure 4.17).

Figure 4.17 Carbon cycle

Carbon reservoirs on Earth exchange stores in the global carbon cycle. These exchanges are called fluxes. Estimates of reservoir stores are shown in PgC (10^{15} g of elemental carbon). Pre-industrial reservoirs and fluxes are shown in black. Additonal fluxes resulting from anthropogenic activity between 2000 and 2009 are shown in red. Red numbers in reservoirs indicate the cumulative change in anthropogenic carbon from 1750 to 2011, with positive numbers indicating a gain and negative numbers indicating a loss.



Source: Figure 6.1 from Ciais *et al.* (2014) © IPCC. Retrieved from *https://www.ipcc.ch/pdf/assessment-report/ar5/wg1/WG1AR5_Chapter06_FINAL.pdf*

The slow carbon cycle, occurring over hundreds of million years, is defined as a series of processes involving chemical reactions and tectonic activity, which transfer carbon between the lithosphere, hydrosphere and atmosphere. Rain moves carbon from the atmosphere into the lithosphere in the form of carbonic acid. The process of surface weathering is aided by this weak acid to release calcium ions from rocks. These ions gradually flow into surface waters where they combine with bicarbonate ions to form calcium carbonate. Carbon is returned to the atmosphere through volcanoes as carbon dioxide.

It is estimated that around 80% of carbon in the Earth's lithosphere derives from inorganic sources. Under certain circumstances, layers of organic carbon from dead vegetation accumulate at a faster rate than they decay, forming subterranean seams of oil, coal or natural gas which together comprise the remaining 20% of carbon stores involved in the slow cycle.

The fast carbon cycle occurs much more quickly as a much smaller amount of carbon moves through various forms of life in the biosphere, particularly vegetation. Terrestrial plants and phytoplankton absorb atmospheric carbon dioxide in the process of photosynthesis. This reaction allows carbon to be stored in vegetation as carbohydrates (sugars), which provide energy. That energy can be released by:

- plants using energy to grow;
- animals eating plants for energy;
- microorganisms eating plants in the decay process; or
- fire consuming the plant as fuel.

All four mechanisms effectively reverse the photosynthetic process to release carbon dioxide back into the atmosphere. Thus, the fast carbon cycle is an important energy transfer process in all ecosystems.

The global carbon budget attempts to account for the exchange (or flux) of carbon between reservoirs (or sinks) and helps to monitor the balance of carbon in different forms (see Figure 4.17). Research has indicated that the global carbon cycle has been modified in recent centuries, particularly in terms of elevated atmospheric carbon, which is correlated with changes in climate (see Volume 3).

4.3 Further Information

Photosynthesis: *http://www.photobiology.info/Brennan.htm*

Earth Energy Balance: *http://earthobservatory.nasa.gov/Features/EnergyBalance/page1.php*

Ionosphere: *http://www.sws.bom.gov.au/HF_Systems/6/5*

Geology: *http://www.geolsoc.org.uk/heresources*

Tectonic Plates: Kious and Tilling (1996)

4.4 Reference

Anderson, D. L. (1989). Theory of the Earth (366 pages). Blackwell Publications, Boston.

Ciais, P., Sabine, C., Bala, G., Bopp, L., Brovkin, V., Canadell, J., Chhabra, A., DeFries, R., Galloway, J., Heimann, M., Jones, C., Le Quéré, C., Myneni, R. B., Piao, S., and Thornton, P. (2014). Carbon and Other Biogeochemical Cycles. Chapter 6 in 'Climate Change 2013 - The Physical Science Basis Working Group I Contribution to the Fifth Assessment Report of the Intergovernmental Panel on Climate Change' (Eds: T. F. Stocker, D. Qin, G.-K. Plattner, M. Tignor, S. K. Allen, J. Boschung, A. Nauels, Y. Xia, V. Bex, and P. M. Midgley), pp. 465-570. Cambridge University Press, Cambridge, United Kingdom.

Kious, W. J., and Tilling, R. I. (1996). This Dynamic Earth: The Story of Plate Tectonics. USGS, Washington, DC. Retrieved from *http://pubs.usgs.gov/gip/dynamic/dynamic.html*.

Lindsey, R. (2009). Climate and Earth's Energy Budget. Retrieved from *http://earthobservatory.nasa.gov/Features/EnergyBalance/*.

Lutgens, F. K., and Tarbuck, E. J. (1998). Essentials of Geology, 6th Edn. Prentice Hall, New Jersey, USA.

Monroe, J. S., and Wicander, R. (1992). Physical Geology: Exploring the Earth. West Publishing Company, St. Paul.

NOAA (2016). Space Weather Prediction Centre. Retrieved from *http://www.swpc.noaa.gov/phenomena/ionosphere*.

Robertson, E. C. (2001). The Interior of the Earth. Retrieved from *http://pubs.usgs.gov/gip/interior/*.

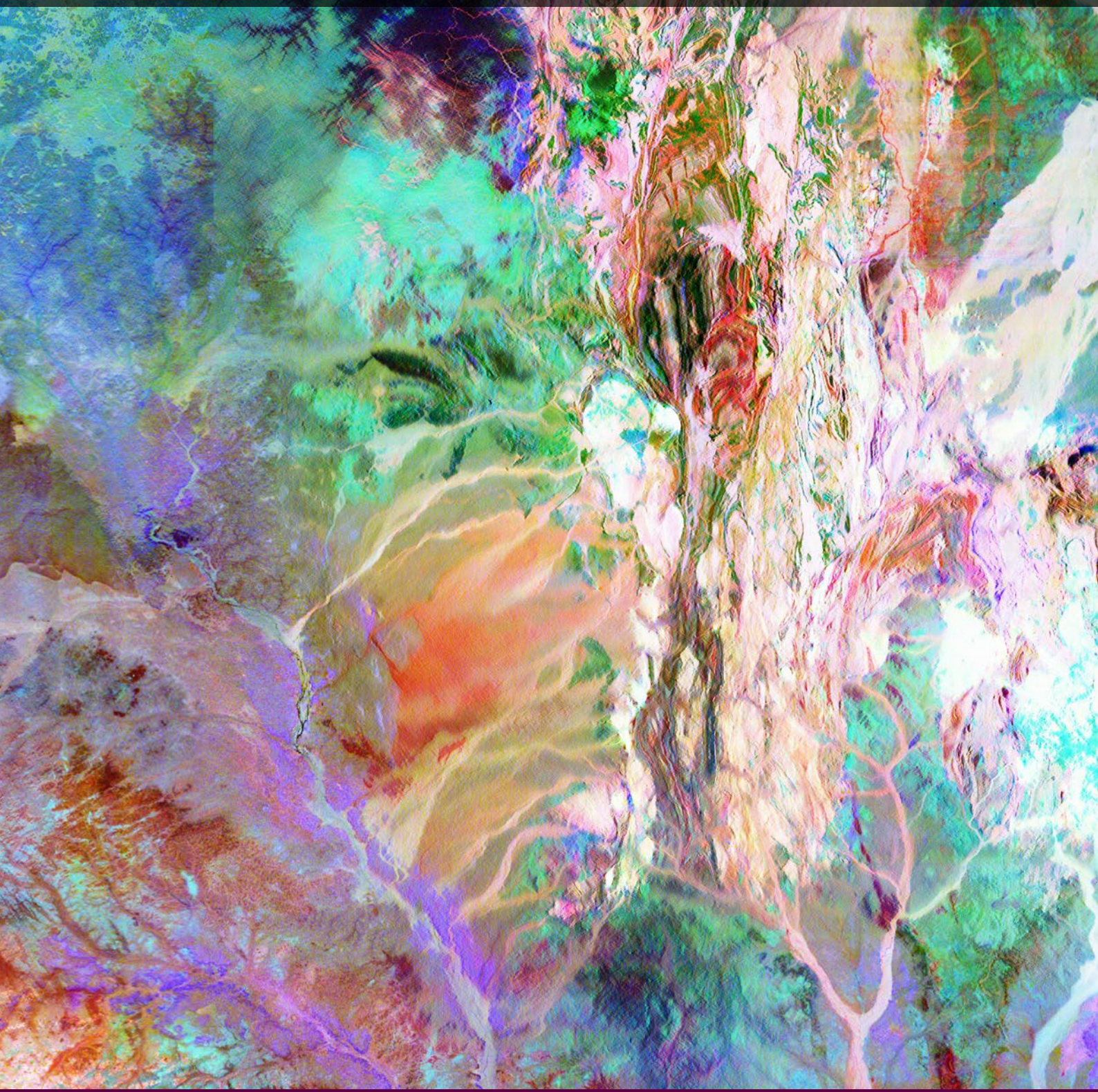
Shiklomanov, I. A. (1998). World Water Resources: A new appraisal and assessment for the 21st Century. United Nations Educational, Scientific and Cultural Organization (UNESCO), Paris, France. Retrieved from *http://webworld.unesco.org/water/ihp/publications/waterway/webpc/world_water_resources.html*.

Suess, E. (1875). Die Entstehung der Alpen (The Origin of the Alps). W. Braunmuller, Vienna.

Tarbuck, E. J., and Lutgens, F. K. (2005). Earth, 8th Edn. Prentice Hall, New Jersey, USA.

WWAP (2012). The United Nations World Water Development Report 4: Managing Water under Uncertainty and Risk. United Nations Educational, Scientific and Cultural Organization (UNESCO), Paris, France.

Energy Sources for Earth Observation



All sources of energy sensed by Earth Observation (EO) relate to the mass, composition, internal processes and/or movements of the various celestial bodies that compose our universe and the interactions that occur between them. Indeed, our understanding of the masses, compositions, movements and interactions of these bodies has been significantly extended since the advent of spaceborne remote sensing technologies.

Energy exists in many different forms, many of which can be detected remotely, that is, using sensors that are not in direct contact with the energy source. Understanding the different types of energy—how they are transmitted and how they interact with the Earth's environments—is essential for designing appropriate remote sensing instruments, and for designing algorithms to transform the resulting images into measurements of relevant environmental properties.

The following sections introduce the major energy sources detected by EO sensors:

- electromagnetic energy (see Section 5);
- radioactivity (see Section 6);
- magnetism (see Section 7);
- gravity (see Section 8); and
- vibrations (see Section 9).

Contents

5 Electromagnetic Radiation 79

6 Radioactivity 95

7 Magnetism 101

8 Gravity 111

9 Vibrations 117

Background image on previous page: Airborne radiometric image of the Mt Isa region, Queensland. Potassium is displayed as red, equivalent thorium as green and uranium as blue (see Excursus 6.1 for details). **Source**: Geoscience Australia



5 Electromagnetic Radiation

Electromagnetic (EM) radiation (EMR) is the energy form most commonly sensed by Earth remote sensing devices. EM energy is measured in defined regions of the EM spectrum, as outlined in the Section 5.1. This energy is either reflected from the Earth's surface or emitted by Earth (see Section 5.2). Known interactions between EMR and specific targets determine the most relevant spectral regions to measure. For example, the molecular structures of different minerals absorb light energy in specific and characteristic wavelengths. Similarly, the chemical chlorophyll, which drives photosynthesis in foliage, can be identified and quantified by the way EMR is reflected by vegetation. EMR spectral regions are defined in Section 5.3 and atmospheric interactions with EMR are described in Section 5.4.

5.1 The EM Spectrum

The Sun provides most of the energy that we sense as light. This energy consists of EM waves, which travel in harmonic, sinusoidal motion as shown in Figure 5.1. The electric and magnetic fields are perpendicular to each other and to the direction of travel, making EM waves a type of transverse wave (see Section 2.5), which can be characterised by wavelength (λ) and frequency (ν):

$$c = \nu \lambda$$

where

c is the speed of light in a vacuum.

The energy of these waves is not strictly continuous, but is also considered to be packaged into discrete units called photons, with the number of photons being related to the intensity of the EMR. The Planck-Einstein relation states that:

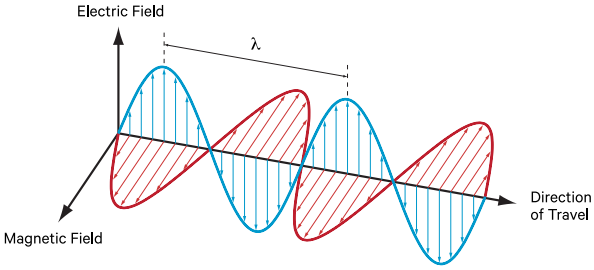
$$E = h\nu = h\frac{c}{\lambda}$$

where

E is energy of photon; and
h is Planck's constant=6.626 × 10^{-34} Joule seconds.

Figure 5.1 Electromagnetic wave

An EM wave comprises two sinusoidal waves: an electric wave (E) and a magnetic wave (H).
Each component wave is perpendicular to the other and also to the direction of travel.
Wavelength (λ) is measured as the distance between successive wave peaks or troughs.
Frequency (ν) is measured as the number of cycles per second passing a fixed point.

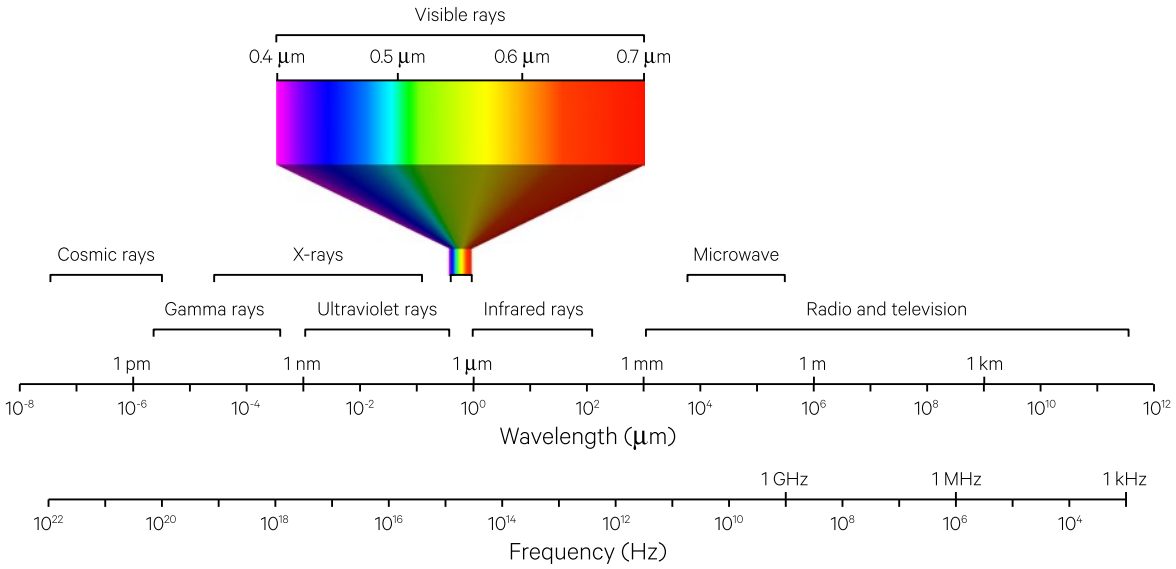


Source: Pete Harrison, Langlopress

Background image: Median mosaic of Landsat-8 image for the Gulf of Carpentaria in northwest Queensland (see Excursus 1.1). The area shown is 450 km wide. This image is displayed using bands 6, 5, 3 as RGB. Source: Norman Mueller, Geoscience Australia

Figure 5.2 Electromagnetic spectrum

Names are assigned to regions of the spectrum for convenience – there are no clearly defined divisions. Cosmic rays are high energy, charged particles that travel at close to the speed of light. They are not EMR but included for comparison. Note: scales are logarithmic



Adapted from: Harrison and Jupp (1989) Figure 2

Although all EMR travels at the same speed (3×10^8 m/s—the speed of light in a vacuum), the wavelengths (that is, the distance between consecutive troughs or crests) of the waves can and do vary. The resulting range of wavelengths gives rise to the Electromagnetic Spectrum (EM Spectrum), illustrated in Figure 5.2. The higher energy forms of EMR, such as X-rays, have short wavelengths and high frequency (since the shorter the distance per cycle, the greater the number of cycles required to achieve the same speed), while low energy forms, such as radio waves, have long wavelengths and low frequency.

The small part of the continuous EM spectrum to which the human eye is sensitive is known as 'light'. This visible portion of the spectrum approximately spans the wavelengths from 0.4–0.7 µm (10^{-6} m). For convenience, names are assigned to the various regions of the spectrum, but there are no precise division between them. The regions are generally defined by the sensing method by which they are detected. Commonly accepted ranges for EMR spectral regions are:

- visible: 0.38–0.7 µm
- infrared (IR): 0.7–1,000 µm
- microwave: > 1 mm–1 m

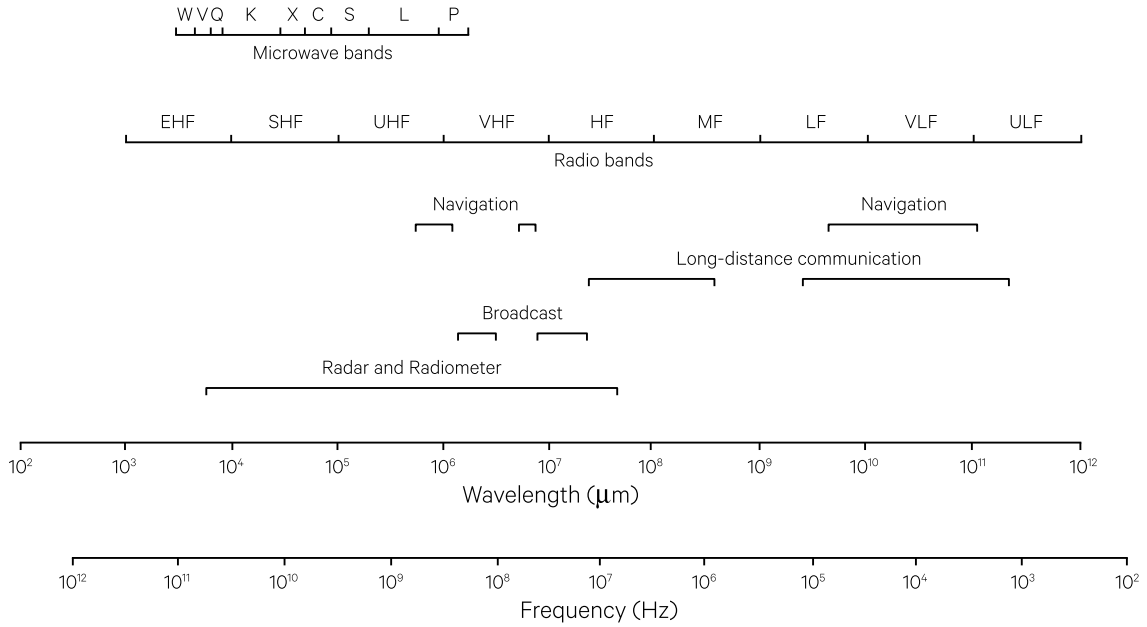
Infrared wavelengths are often sub-divided into the regions:

- near infrared (NIR): 0.7–1.3 µm
- short wave infrared (SWIR): 1.3–3 µm
- middle infrared (MIR) or mid-wavelength (or medium wave) infrared (MWIR): 3–8 µm
- thermal infrared (TIR) or long wavelength infrared (LWIR): 8–15 µm
- far infrared (FIR): 15–1,000 µm

In Earth Observation (EO), the shorter wavelengths regions denoted visible, NIR and SWIR are often collectively referenced as 'optical' (or reflective) wavelengths, and the term TIR may be used to include the wavelengths from 3–5 µm. Much of the longer wavelength energy cannot be seen or photographed but can be sensed with radiometers and scanners. The range of wavelengths in which various sensors can operate is shown in Figure 5.3. Specific remote sensors are designed to measure EMR for a defined range of wavelengths (see Sections 13 to 15).

Figure 5.3 Common remote sensing systems

Scanners and radiometers can operate outside the visible and photographic wavelength regions. Note: scale is logarithmic.



Adapted from: Harrison and Jupp (1989) Figure 4

5.2 Reflectance and Emission

All materials both reflect EMR that comes from external sources and emit EMR as a function of their temperature (see Section 2.11). Reflectance and emission from a material depend on chemical and physical characteristics of that material, and can thus be used to determine those characteristics. Remote sensors have been designed to detect both reflected and emitted EM energy from objects.

5.2.1 Reflected energy

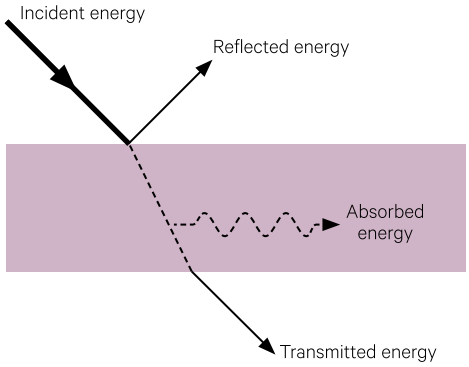
Reflected energy originates from an external energy source and is determined by the interaction of the incident energy from that energy source with the illuminated object. Matter either absorbs or transmits incoming, or incident, energy, depending on whether or not that energy excites physical processes in the matter's atoms and molecules (see Section 2.2). Excitation varies with the wavelength or frequency of the energy and the molecular composition of the matter being radiated. For example, the human body absorbs EMR in the visible, infrared and microwave wavelengths, but transmits—is transparent to—X-rays and radio waves. However, both absorption and transmission may be partial, such that some of the incident energy may also be reflected.

Thus, EM energy is selectively absorbed by materials depending on how different frequencies of EMR interact with the molecules, atoms and nuclei of the material (see Section 2.2). These fundamental components of matter are generally characterised by discrete, quantized energy levels, and transition between these levels is typically characterised by the absorption or emission of photons. Visible and ultraviolet wavelengths are primarily absorbed by a material when its electron transitions (that is the change in energy required to move from the initial state to an excited state) precisely match the quantum energy of the photon. Infrared wavelengths correspond to the range of energies that occur in molecular vibrations or chemical bonds, so tend to heat the materials that absorb them. The quantum energy of microwave photons is in the range of energies that separate the quantum states of molecular rotation and torsion[17] (see Volume 1B—Section 3 for more detail).

17. Other interactions can lower the energy of excited electrons in atoms and molecules: fluorescence happens when matter instantaneously emits a photon with lower energy and longer wavelength, while phosphorescence occurs when matter can retain the energy of excitation for a period of time then emit that energy gradually.

Figure 5.4 Incident energy components

The energy incident on a surface is reflected, transmitted or absorbed.



When the frequency of the incident EM energy does not match the energy levels required for absorption, that energy is transmitted through or reflected by the object. The transparency of an object (allowing transmission of incident radiation through the object) and its opacity (resulting in reflectance of incident radiation) are determined by the physical and chemical structure of the object, relative to the wavelength of the radiation.

Thus the relationship between an external energy source and an illuminated target can be summarised by the equation (see Figure 5.4):

incident energy = *reflected energy* + *transmitted energy* + *absorbed energy*

where

incident energy is the EM energy striking the surface of a target;
reflected energy is the energy being bounced back from the target;
transmitted energy is the energy passing through the target; and
absorbed energy is the energy penetrating into and remaining in the target.

Firstly, the proportions of reflected, transmitted and absorbed energy vary for different objects, depending on their material type and condition. Secondly, for a particular material, these proportions also vary for different wavelengths. These relationships allow remote sensors detecting radiation in the visible and near infrared regions to derive information relating to the type and condition of materials on the Earth's surface. The same principles are used to characterise chemical compounds by atomic absorption spectroscopy.

The reflectance of an object is defined as the ratio of reflected energy relative to the incident energy:

$$reflectance = \frac{reflected\,energy}{incident\,energy}$$

Similarly, absorptance and transmittance are defined as:

$$transmittance = \frac{transmitted\,energy}{incident\,energy}$$

$$absorptance = \frac{absorbed\,energy}{incident\,energy}$$

Thus, these components of incident radiation sum to one:

$$reflectance + transmittance + absorptance = 1$$

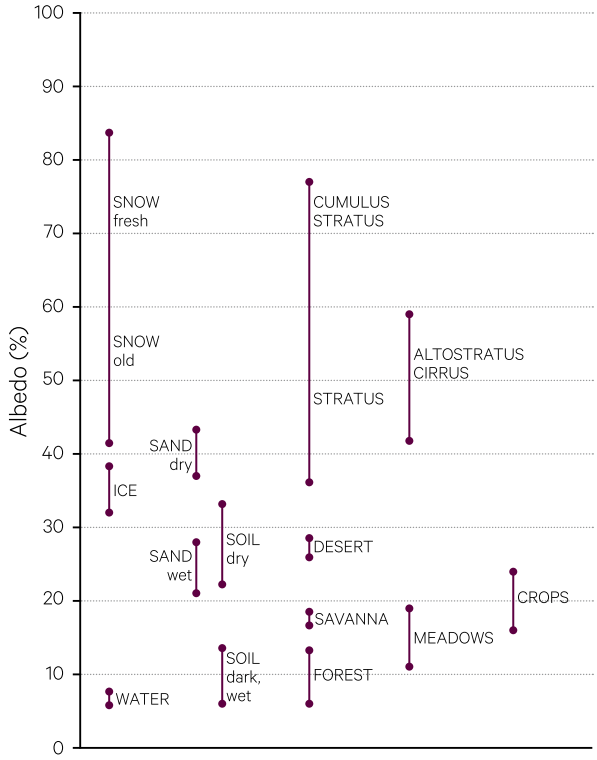
(Note that reflectance, transmittance and absorptance are sometimes computed as percentages—using the above ratios multiplied by 100—in which case they sum to 100.)

In terms of EO, the interaction of incoming radiation with surface features depends on both the spectral reflectance properties of the surface materials and the surface smoothness relative to the radiation wavelength (see Section 2.5). A relatively 'smooth' surface, which reflects energy without any scattering (that is, where the angle of incidence equals the angle of reflection), is called a 'specular' or 'mirror' reflector. 'Diffuse' or 'Lambertian' reflectance occurs when the surface is rough relative to the wavelength(s) of the incoming radiation and causes the energy to be reflected equally in all directions (see Figure 2.7). Calm water can act like a specular reflector. Most of the Earth's other surface materials are diffuse reflectors in the visible wavelengths but may display specular reflectance properties in the microwave wavelengths. Surface orientation relative to both the energy source and sensing device also affects the amount of radiation detected by the sensor. Other aspects of the interaction of EMR with the Earth's surface are discussed in Volume 1B—Sections 4 to 6.

A less precise measure of the proportion of radiation that is reflected by a surface is albedo. This is computed as the ratio of all reflected radiation (both specular and diffuse—see Section 2.5.2) to the incident radiation over a given area (see Volume 1B—Sections 6.5 and 7). This property varies with different types of material, different wavelengths of EM energy, latitudes on Earth and seasons (see Figure 5.5). Albedo measurements are used in studies related to Environmental Physics, for broad topics such as energy balance and evapotranspiration. Typical albedo values for some common materials are listed in Table 5.1.

Figure 5.5 Albedo of different materials

Albedo is the proportion of incident energy that is reflected by a material. Some materials, such as snow, reflect radiation more strongly than others.



Adapted from: Hannes Grobe (CC BY-SA 2.5) at *http://en.wikipedia.org/wiki/Albedo#/media/File:Albedo-e_hg.svg*

Table 5.1 Sample albedo values

Surface Material	Sample Albedo Values
Perfect absorber (blackbody)	0
Ocean	0.03–0.10
Forest	0.05–0.20
Bare Soil	0.05–0.40
Grass and Crops	0.1–0.25
Granite	0.30–0.35
Sand	0.15–0.45
Ice	0.20–0.50
Clouds	0.30–0.90
Snow	0.40–0.90
Perfect reflector (absolutely white surface)	1

Source: Dobos (2003); Budikova (2013)

5.2.2 Emitted energy

Emitted energy is determined by the physical properties of matter (see Section 2.10). The quantity of radiant flux emitted from an object is called its radiant temperature (T_{rad}). Generally, the kinetic temperature (T_{kin}) of an object is highly correlated with its radiant temperature (see Section 2.10).

Remote thermal infrared radiometers can be used to measure radiant temperature (see Sections 14.4, 16.1.1.1 and Volume 1B—Section 7). The physical laws introduced in Section 2.11 allow radiant temperature measurements to be converted to kinetic temperature. The variation between radiant flux from a real object compared with the radiation from a blackbody is described by a thermal property called emissivity (ε—see Section 2.11.2). Emissivity varies with EMR wavelength for all types of matter. Factors such as colour, surface texture, moisture content, and density can also change the emissivity of an object. Emissivity variations between substances at a given wavelength can be used to differentiate between them using thermal remote sensing (see Volume 1B—Section 7).

Kirchhoff's Radiation Law (see Section 2.11.2) applies to targets in 'thermodynamic equilibrium' and can be summarised as:

> *Good absorbers are good emitters and good reflectors are poor emitters.*

Thus, for a given wavelength (λ), absorptance (α) can be used to approximate emissivity (ε):

$$\alpha_\lambda \sim \varepsilon_\lambda$$

Using Kirchhoff's radiation law, and assuming minimal transmittance, absorbed energy can be replaced with emissivity to reduce the incident energy relationship to:

$$reflectance + emissivity = 1$$

so that:

$$emissivity = 1 - reflectance$$

Combining the Stefan-Boltzmann law (see Section 2.11.1) with Kirchhoff's radiation law allows us to derive a relationship between the apparent radiant temperature (T_{rad}) of an object and its true kinetic temperature (T_{kin}):

$$\sigma T_{rad}^{\ 4} = \varepsilon \sigma T_{kin}^{\ 4}$$

or

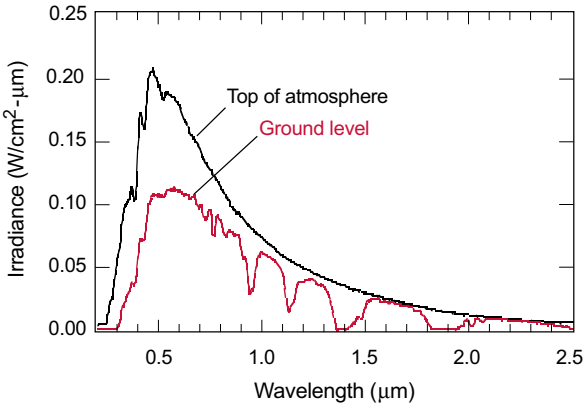
$$T_{rad} = \varepsilon^{0.25} T_{kin}$$

The Sun is not a blackbody but its radiation is similar to that of a blackbody at approximately 5800K with peak intensity being in the spectral region we detect as visible light (see Figure 2.19). Solar radiation is EMR emitted by the Sun's surface. At the top of Earth' atmosphere, the total irradiance from the Sun is approximately 1,360 W/m^2 (see Excursus 3.1). 99% of this energy is within the wavelength range 0.15–4.0 μm, with the maximum emission having the approximate wavelength 0.5 μm, which we perceive as visible green. Solar radiation is dispersed as it travels from the Sun to the Earth so that reduced energy levels are detected at the Earth compared with the theoretical curve shown in Figure 5.6. Due to the Earth's elliptical orbit around the Sun, the amount of solar radiation received at the top of the atmosphere varies throughout the year by ±3.37% (see Figure 3.3).

The Earth is not a blackbody either, but it does emit radiation in a similar way to a blackbody at 300K (or ~27°C). This temperature is the result of various interactions between the Earth's surface and the atmosphere and is determined by all the Earth's processes that produce heat. This radiation is the Earth's thermal radiation and may provide information about soil moisture status, geological properties and hot surface features such as fires (see Volume 1B—Section 7). The EMR emissions associated with Earth's temperature are in the spectral wavelength range of thermal infrared. By comparison, adult humans, with a skin temperature of approximately 33°C, emit energy in the infrared region (~100 Watts).

Figure 5.6 Solar radiation at top of atmosphere and at sea level

While the spectrum of solar radiation that reaches the top of Earth's atmosphere resembles the spectrum of a blackbody at around 5800K (Sun's temperature; see Figure 2.19), some of that radiation is absorbed by the atmosphere before it reaches sea level. As shown in the graph below, the atmosphere absorbs selected wavelengths more strongly than others.



Source: Shaw and Burke (2003). Reprinted with permission courtesy of MIT Lincoln Laboratory, Lexington, Massachusetts.

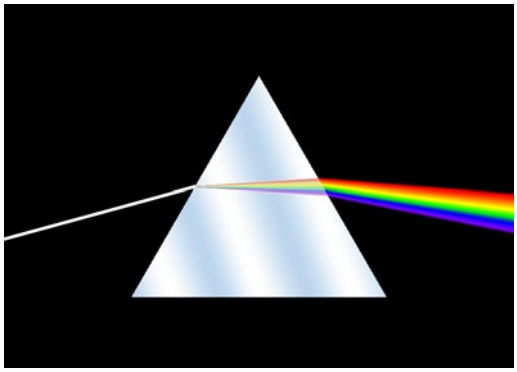
5.3 Spectral Regions

The EM spectrum describes the full range of wavelengths that have been detected for EMR. Most of the radiant energy from the Sun is within the wavelength range 0.28 to 2.8 μm, that is, those regions of the EMR spectrum described as UV, visible and NIR. This wavelength range is commonly referred to as short wave radiation. Only 15% of the Sun's energy involves wavelengths in the range 2.8 to 100 μm (SWIR and TIR), which is referred to as long wave radiation. The balance between incoming solar radiation (predominantly short wave) and outgoing radiation from the Earth (predominantly long wave) is discussed in Section 4.2.1 above.

The visible region can be sub-divided into component colours ranging from the higher energy, shorter wavelengths of violet, indigo and blue, through those of green and yellow, to the lower energy wavelengths of orange and red. What is known as 'white' light, such as sunlight, is actually a mixture of all these wavelengths and is also correctly called polychromatic light. When polychromatic light is refracted through a prism, different wavelengths are refracted by different amounts, resulting in the characteristic rainbow spectrum shown in Figure 5.7.

Figure 5.7 Refraction of polychromatic light through a prism

Transmission of light waves slows as they pass through glass. Different wavelengths of light travel at different speeds and disperse along different paths, with shorter wavelengths 'bending' more than longer ones. This mechanism is used to separate different spectral components of light into the visible light spectrum.



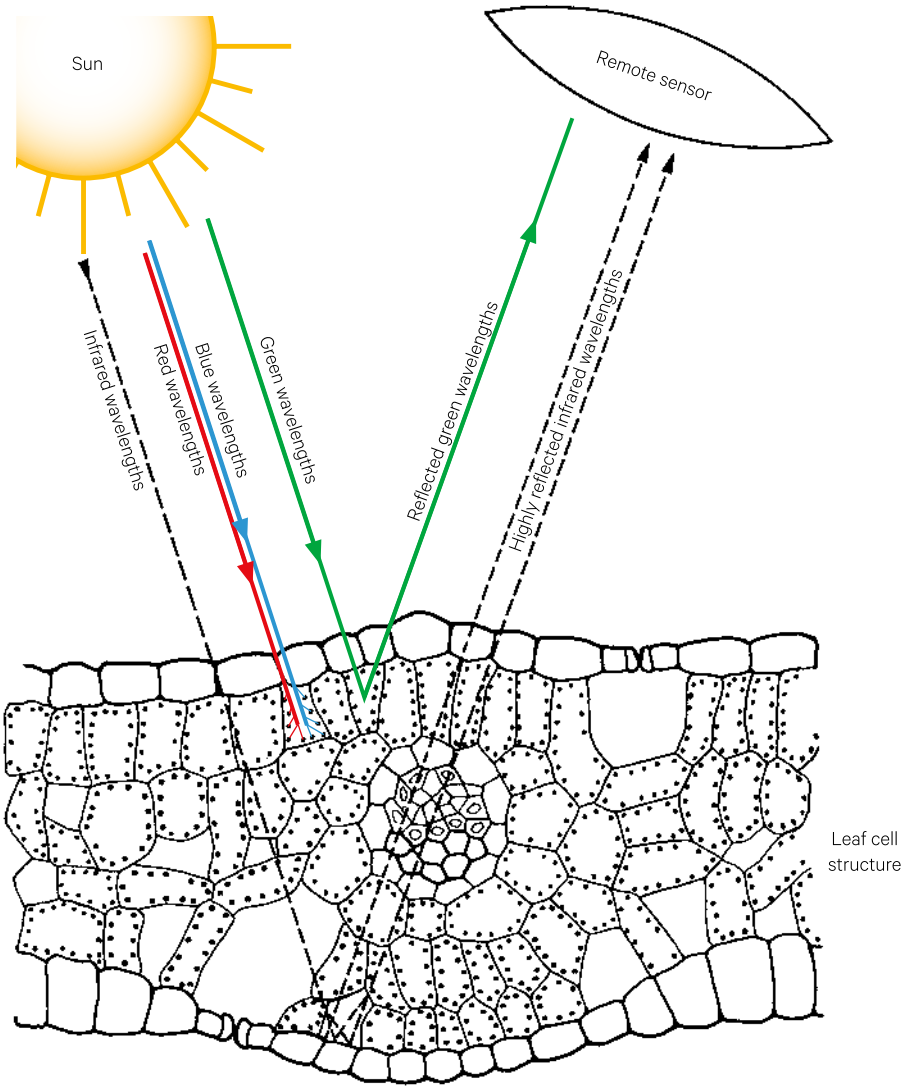
Source: Wikimedia Commons (CC BY-SA 1.0). Retrieved from *https://en.wikipedia.org/wiki/History_of_spectroscopy#/media/File:Dispersion_prism.jpg*

The feature we describe as the colour of an object is the energy not absorbed by that object. In the case of a green leaf, for example, the blue and red wavelengths of light are absorbed by the chloroplasts and used as an energy source for photosynthesis, but a greater proportion of the green wavelengths is reflected (see Figure 5.8). In this case our eyes detect this reflectance as the colour green. By a learned association of the colour green with living foliage, combined with other features such as size and shape, we identify the object and its state (living and dead). The same principle forms the basis of identifying features in remote sensing.

Different land cover features have varying, and often characteristic, reflectance in the non-visible wavelengths (such as infrared or thermal infrared). Consequently, engineered sensors, which are capable of detecting and quantifying these waves, give us more information than what we perceive as colour with which to identify an object. Figure 5.9 illustrates this for three major land cover features (vegetation, water and bare soil). Examples of using EO to identify land cover features are provided in Excursus 1.2, 1.3 and 5.1.

Figure 5.8 Reflectance characteristics of typical green leaf structure

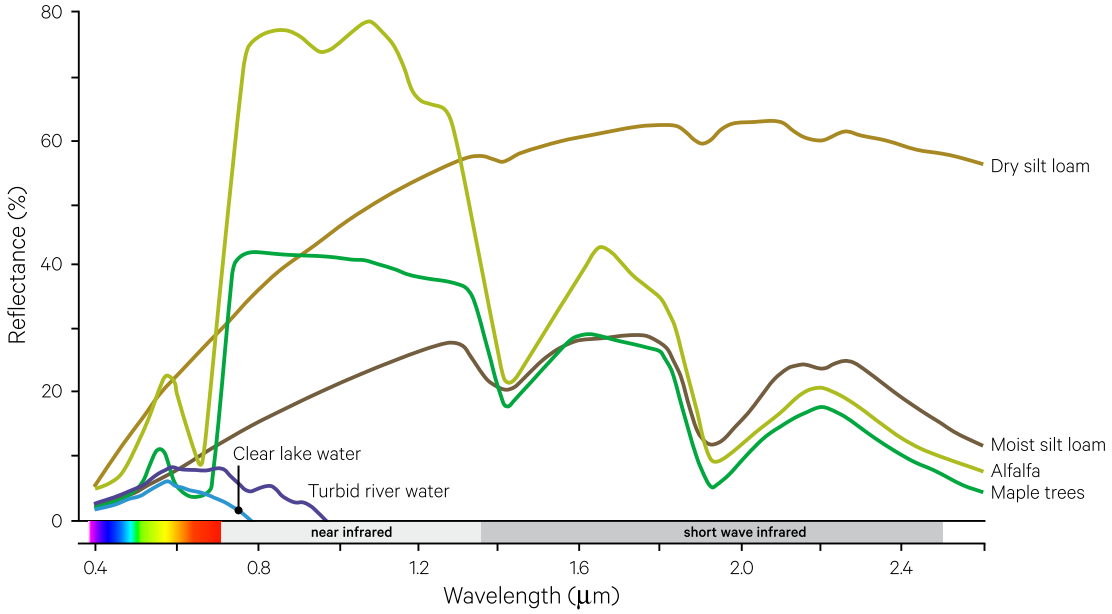
Chloroplasts reflect green wavelengths but absorb blue and red wavelengths for use in photosynthesis. Spongy mesophyll cells strongly reflect infrared wavelengths.



Source: Harrison and Jupp (1989) Figure 5

Figure 5.9 Idealised spectral reflectance curves

Reflectance from different Earth surface features varies for different wavelengths. Characteristic spectral reflectance curves can be created for different features to indicate a 'typical' shape over a particular range of wavelengths. This information can be used to differentiate between different surface features on the basis of their observed reflectance characteristics.



Source: Harrison and Jupp (1989) Figure 6

Excursus 5.1—Water Observations from Space (WOfS)

Source: Norman Mueller, Geoscience Australia
Further information: *http://www.ga.gov.au/scientific-topics/hazards/flood/wofs*, *http://www.datacube.org.au*

Following from the Natural Disaster Insurance Review in 2011, Geoscience Australia (GA) developed an access point for flood models and satellite observations in Australia—National Flood Risk Information Program (NFRIP). One of the components of NFRIP is Water Observations from Space (WOfS) which shows where water has been observed in Australia by the Landsat satellites since 1987 (see Excursus 1.1). This service provides improved understanding of water in the Australian landscape—where it is usually present, where it is seldom observed and where it occasionally floods the surface.

In conjunction with updated national guidelines for flood risk information from Engineers Australia, NFRIP aims to provide a single authoritative source of information related to floods for Australia.

How do satellites 'see' water?

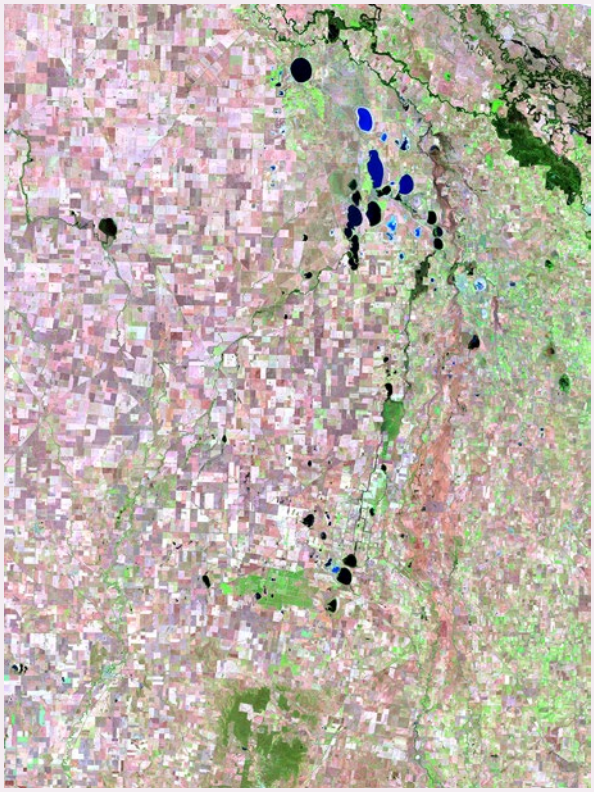
EO satellites that observe optical wavelengths measure the amount of sunlight reflected from Earth. Different materials on the Earth's surface reflect light differently. Water absorbs the infrared portion of the EMR spectrum that is not visible to human eyes. These characteristic absorption features allow us to differentiate water from other surface materials (see Figure 5.10).

Figure 5.10 Seeing water from space—Kerang, Victoria

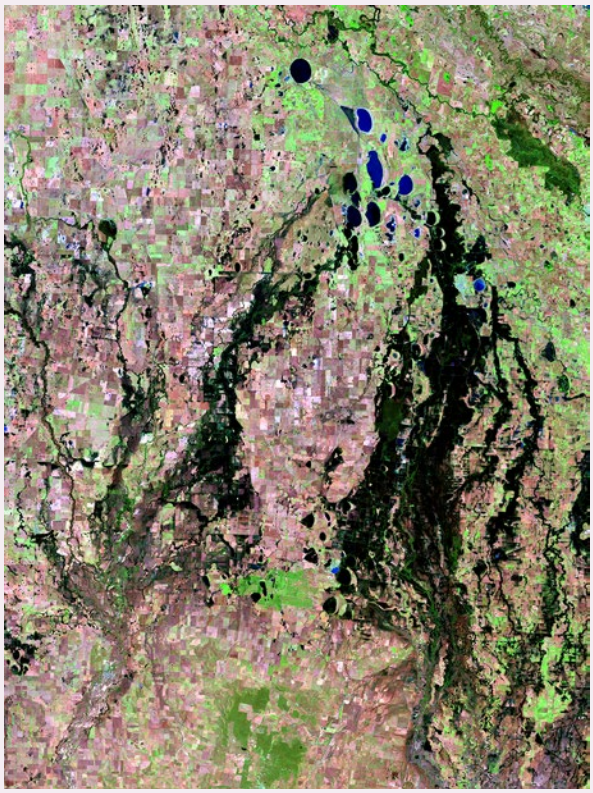
a. 4 January 2011—true colour image approximates what a human would see from space before the flood



b. 4 January 2011—False colour image highlights differences between water and vegetation before the flood (TM bands 5, 4, 2)



c. 20 January 2011—during floods the area covered by water is defined by low infrared reflectance in this false colour image (TM bands 5, 4, 2) so area of inundation appears as black



d. 20 January 2011—extent of flood is mapped from the satellite images as red overlay



Source: Norman Mueller, Geoscience Australia

Mapping permanent water

When water is mapped in every image over a given location, we can see where water occurs regularly, as in lakes and rivers, and where it only occurs occasionally, as in floods. This process was applied to Landsat imagery of the Menindee Lakes, NSW, between 1987 and 2016 (see Figure 5.11). In this image, regularly observed water is shown in shades of blue to purple, and occasional water is shown as red. Sequences of such images can be used to effectively map the process of the lakes drying out.

This analysis can be applied to every Landsat-5, -7 and -8 scene acquired over Australia since 1987 (standardised in the Australian Geoscience Data Cube: AGDC) to understand surface water over the whole continent. WOfS analyses have provided insight into:

- water cycles in braided stream networks in inland Australia;
- likely extent of flooding from permanent water bodies; and
- coastline changes such as isthmus breaches.

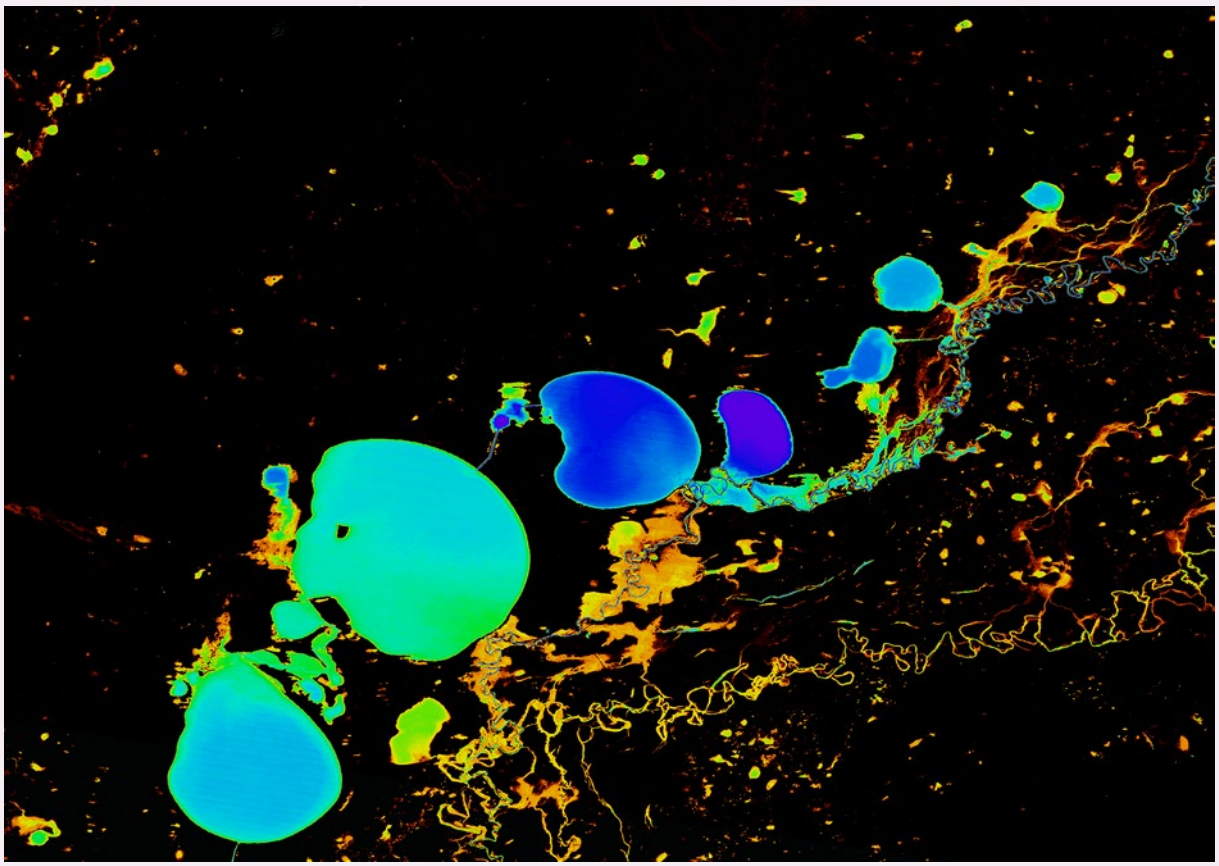
WOfS service

Results from these analyses can be viewed on the WOfS viewer*: http://www.ga.gov.au/interactive-maps/#/theme/water/map/wofs*. This service enables users to view higher resolution maps for specified locations of interest within the Australian continent and Tasmania (see Figure 5.12). From 1987 to the present, for each 25 m × 25 m grid cell WOfS displays:

- number of clear satellite observations;
- number of times water was detected;
- percentage of clear observations with water; and
- probability that water observation is correct.

Figure 5.11 Mapping permanent water

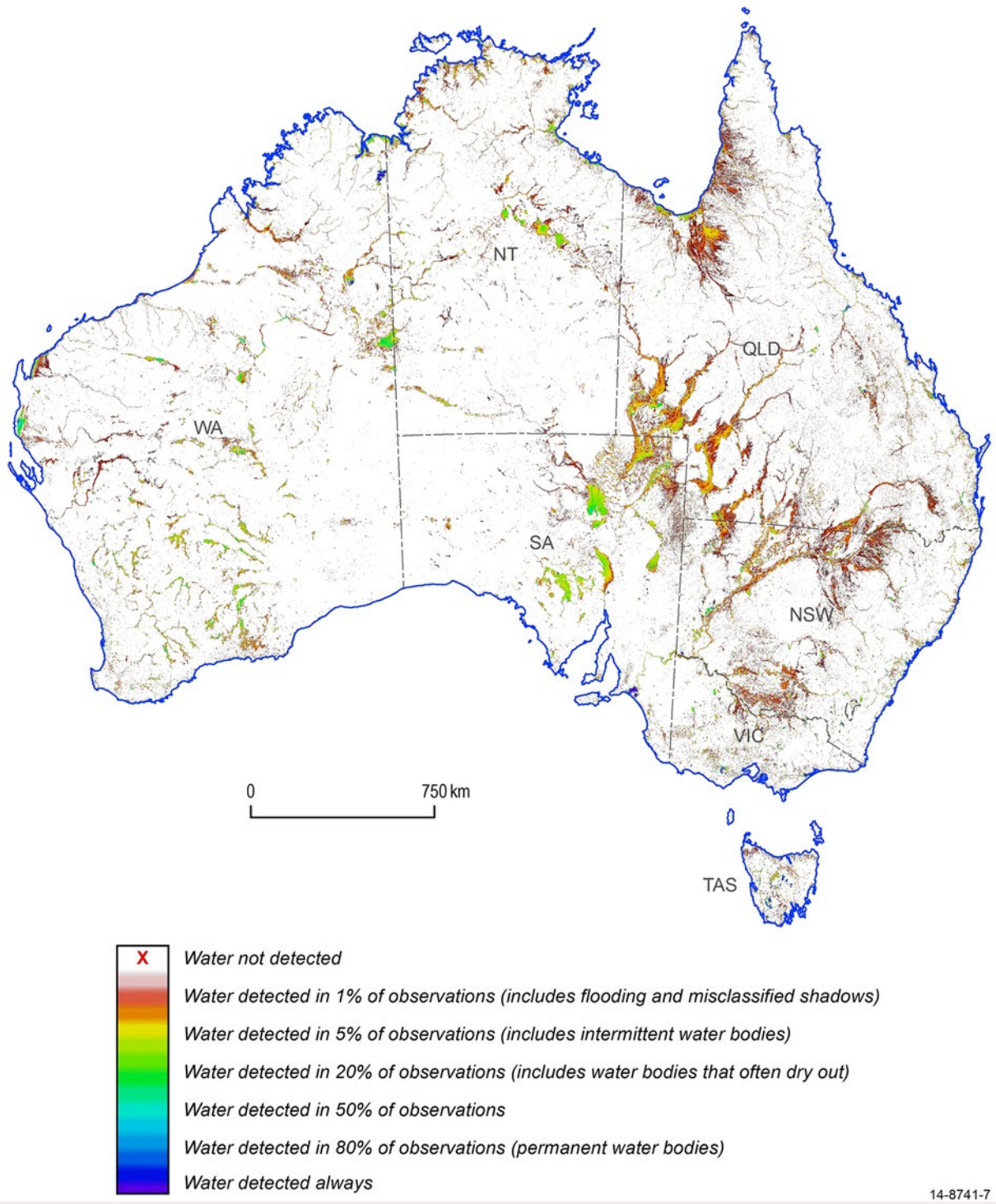
Landsat imagery of the Menindee lakes system, NSW, acquired between 1987 and 2016, was processed using WOfS to show where water was observed regularly (blue to purple) versus occasioinally (orange to red).



Source: Norman Mueller, Geoscience Australia

Figure 5.12 WOfS continental map

This continental map, produced by WOfS processing of Landsat imagery, highlights the permanence of water in the Australian landscape.



Source: Norman Mueller, Geoscience Australia

5.4 Atmospheric Interactions

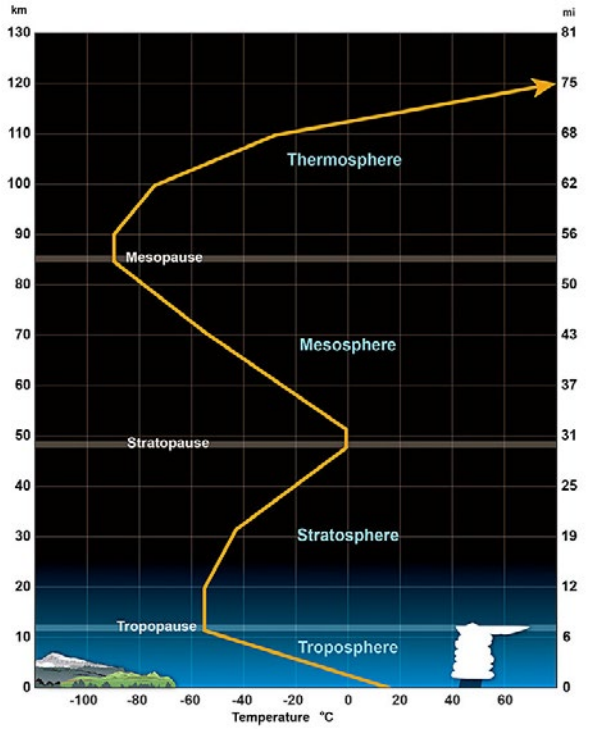
The atmosphere extends away from the Earth's surface for over 100 km. The atmosphere is 'heaviest' or most dense close to Earth, with half its mass below 5.5 km in altitude, and only 1% above 30 km altitude. While largely comprising gases, the atmosphere also contains varying concentrations of aerosols and water. Table 5.2 summarises the relevant characteristics of atmospheric layering. Each layer is bounded by abrupt changes in temperature (see Figure 5.13). These boundaries are known as pauses and inhibit vertical mixing between atmospheric layers. Most of Earth's weather and water vapour occurs in the troposphere.

Atmospheric aerosols or particulate matter comprise solid and/or liquid particles with diameters in the range 0.002—100 μm that are suspended in the air. They derive from both natural and anthropogenic sources. Natural sources include water vapour, sea spray, wind-blown dust, volcanic ash, and smoke from bushfires, while anthropogenic sources include biomass burning, various agricultural activities and industrial and domestic emissions.

Figure 5.13 Atmospheric layers

The atmospheric layers are distinguished by the way temperature changes with altitude:

- Troposphere: temperature decreases with increasing altitude;
- Stratosphere: temperature increases with increasing altitude;
- Mesosphere: temperature decreases with increasing altitude; and
- Thermosphere: temperature increases with increasing altitude.



Source: NOAA (2016). Retrieved from *http://www.srh.noaa.gov/jetstream/atmos/atmos_intro.html*

Clouds cover around 60% of the Earth's surface. As such, the presence of clouds and cloud shadows are very relevant to the interpretation of EO imagery. Thin cloud presents a particular challenge to the processing and interpretation of EO imagery since it allows the sensor to detect Earth surface radiance, but attenuates that radiance. Higher cloud cover tends to occur over oceans than over land. While some variation occurs with latitude, global averages for base heights and coverage of different types of cloud over land and ocean are summarised in Table 5.3. For detailed global information on clouds refer to Warren *et al.* (2013).

Certain regions of the EM spectrum are completely absorbed by the various gases that make up the atmosphere (particularly O_3, CO_2, H_2O), so that wavelengths in these regions cannot be used for remote sensing of the Earth's surface. The regions of the EM spectrum where radiation is not affected by the Earth's atmosphere are called 'atmospheric windows' (see Figure 5.14). Remote sensing data of the Earth's surface can only be obtained from systems operating within these regions of the EM spectrum. These windows allow detection of reflected solar energy from the Earth's surface in the visible and infrared wavelengths, Earth's emitted energy in the thermal infrared and passive microwave wavelengths, plus microwaves emitted by active sensors (see Table 5.4). Middle infrared wavelengths can originate from both reflected solar radiation and emitted EMR from the Earth's surface (Chuvieco and Huete, 2010).

I happen to have discovered a direct relation between magnetism and light, also electricity and light, and the field it opens is so large and I think rich.
(Michael Faraday, 1845)

Table 5.2 Atmospheric layers

Layer	Max Altitude[20] (km)	Depth (km)	Mass (%)	Temperature (°C)	Composition	Description
Troposphere	20	~6 at poles 9 at mid-latitudes 18–20 at equator	~80	17 to -51 (air temperature decreases with height by 6.5°C per km to altitude of 11 km unless temperature inversion exists)	Water vapour mostly < 6km Nitrogen (78%) Oxygen (21%) Aerosols	80% of atmosphere's mass
Stratosphere	50	Lower boundary is higher near equator and lower over poles	19	-60 to -15 (air temperature increases with height above 20 km altitude)	Aerosols, ozone, chlorofluorocarbons (CFCs). Very little water vapour or air movement	Contains ozone layer
Mesosphere	85	35 (average)	0.1	0 to -90 (air temperature decreases with height)	Noctilucent clouds. Sodium layer (5–10 km depth between altitudes 80–105 km)	Most meteors burn up in this layer
Thermosphere	600	~500	-	-90 to 2,000+ (air temperature increases with height above 90 km altitude)	Extremely low densities of hydrogen and helium; Contains ionosphere where sparse gases absorb high energy incoming radiation	International Space Station orbits in this layer
Exosphere	10,000	-	-	-	Atoms and molecules escape into space; satellites orbit	Fades into space

Source: NOAA (2016) at *http://www.srh.noaa.gov/jetstream/atmos/atmos_intro.html* [18]

Table 5.3 Global cloud properties

Average amount of cloud and average cloud base heights over land and ocean based on surface observations.
Data observations used for coverage estimates: land values—1971–2009; ocean values—1954–2008.
Data observations used for base heights estimates: land values—1971–1996; ocean values—1954–1997.

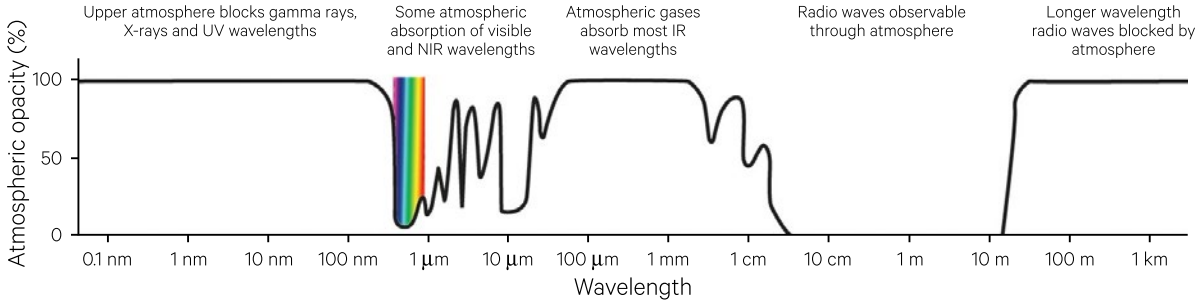
Category		Base Height (m above surface)		Average Coverage (%)	
Height Level	Type	Land	Oceans	Land	Oceans
Low	Stratus	500	400	5	13
	Stratocumulus	1000	600	12	22
	Nimbostratus	-	-	4	5
Mid	Altostratus	-	-	4	6
	Altocumulus	-	-	17	18
High	Cirriform	-	-	22	12
Vertical Development	Cumulonimbus	1000	500	5	6
	Cumulus	1100	600	5	13
	Total	-	-	54	68

Source: Eastman and Warren (2013)

18. Varies with latitude and weather.

Figure 5.14 Atmospheric opacity

Some wavelength regions of the EM spectrum are absorbed by atmospheric gases so cannot be used for remote sensing of the Earth's surface features. Note: Scale is logarithmic.



Adapted from: Wikimedia Commons at *https://commons.wikimedia.org/wiki/File:Atmospheric_electromagnetic_opacity.svg* (original source: NASA)

Table 5.4 EMR spectral regions and atmospheric windows

Energy Source	Spectral Region		Wavelengths of spectral region	Wavelengths of atmospheric window
Reflected solar radiation (plus radiation from active optical sensors, such as lidar)	Optical	Visible	0.38–0.7 µm	0.38–0.7 µm
		Near infrared	0.7–1.1 µm	0.77–0.91 µm
		Short wave infrared	1.1–3.0 µm	1.55–1.75 µm
				2.05–2.40 µm
Both reflected solar radiation and emitted by Earth's surface	Middle infrared		3.0–8.0 µm	3.0–5.0 µm
Emitted by Earth's surface	Thermal infrared		> 8.0–15 µm	8.0–9.2 µm
				10.2–12.4 µm
Emitted by Earth's surface or radar sensor	Microwave		>1 mm–1 m	7.5–11.5 mm
				> 20 mm

Within these atmospheric windows, atmospheric conditions such as haze, fog and clouds can still affect remote sensing of features on the Earth's surface through scattering of the EM waves by particles in the atmosphere. These interactions can be described in terms of three types of scattering:

- Rayleigh scattering—by gas molecules that are much smaller than the radiation wavelength;
- Mie scattering—by smoke, dust, salt and water particles which are similar size to the radiation wavelength; and
- non-selective scattering—by water droplets, ice fragments or large dust particles that are much larger than the radiation wavelength.

These various forms of scattering increase the haze level or reduce the contrast in an image and are further considered in Volume 1B—Section 4.2. Image processing methods can be applied to data obtained under such conditions to remove or reduce the effect of atmospheric 'noise' as discussed in Volume 1B—Section 5 and Volume 2A. Consideration of various sources of atmospheric 'effects' is particularly important when comparing multiple image sources. Remote sensing studies of the atmosphere itself, however, use absorption and scattering characteristics to measure atmospheric state and composition. In such studies the absorption bands, rather than atmospheric windows, are preferred and scattering effects are indicative of atmospheric condition. These are further discussed in Volume 3.

5.5 Further Information

Introduction to Electromagnetic Radiation:

EO Miners: *http://www.eo-miners.eu/earth_observation/eo_eof_rst_electrmag_remote_sensing.htm*

Natural Resources Canada: *http://www.nrcan.gc.ca/earth-sciences/geomatics/satellite-imagery-air-photos/satellite-imagery-products/educational-resources/14621*

The Atmosphere:

NOAA (2016)

Solar radiation characteristics and programs for calculating spectral irradiance:

National Renewable Energy Laboratory (NREL): *http://www.nrel.gov/rredc/solar_resource.html*

5.6 References

Budikova, D. (2013). Albedo. The Encyclopedia of Earth. Retrieved from *http://www.eoearth.org/view/article/149954*.

Chuvieco, E., and Huete, A. (2010). Fundamentals of Satellite Remote Sensing. CRC Press, Boca Raton.

Dobos, E. (2003). Albedo. 'Encyclopedia of Soil Science' (Ed: R. Lal), Vol. 1. Second Edn., pp. 64-66. Taylor & Francis Group, New York.

Eastman, R., and Warren, S. G. (2013). A 39-Yr Survey of Cloud Changes from Land Stations Worldwide 1971–2009: Long-Term Trends, Relation to Aerosols, and Expansion of the Tropical Belt. Journal of Climate, 26(4), pp. 1286-1303. doi:*http://dx.doi.org/doi:10.1175/JCLI-D-12-00280.1*.

Harrison, B. A., and Jupp, D. L. B. (1989). Introduction to Remotely Sensed Data. Part ONE of the microBRIAN Resource Manual (156 pages). CSIRO Australia, Melbourne.

NOAA (2016). National Weather Service Atmosphere Topics. Retrieved from *http://www.srh.noaa.gov/jetstream/atmos/atmos_intro.html*.

Shaw, G. A., and Burke, H. K. (2003). Spectral Imaging for Remote Sensing. Lincoln Laboratory Journal, 14(1), pp. 3-27.

Warren, S. G., Hahn, C. J., and Eastman, R. (2013). Climatic Atlas of Clouds Over Lands and Oceans. Retrieved from *http://www.atmos.washington.edu/CloudMap/*



6 Radioactivity

Radiometrics, also known as Gamma-Ray Spectrometry, measures the natural radioactivity from the Earth's surface to infer the presence of particular minerals. Radiometric surveys detect gamma-rays resulting from the natural radioactive decay of three elements (Potassium (K), Thorium (Th) and Uranium (U)) located in the upper 30-45 cm of the Earth's crust, or associated with artificial sources such as nuclear power plants. This is the most energetic form of EM energy, with very high frequencies (above 10^{19} Hz) and very short wavelengths (less than 10^{-12} m—equivalent to the nucleus of an atom).

For Earth Observation (EO) applications, radioactivity is typically measured using gamma-ray spectrometers carried by aircraft. The resultant images can be subsequently processed to indicate the relative proportions of U, Th and K in each pixel.

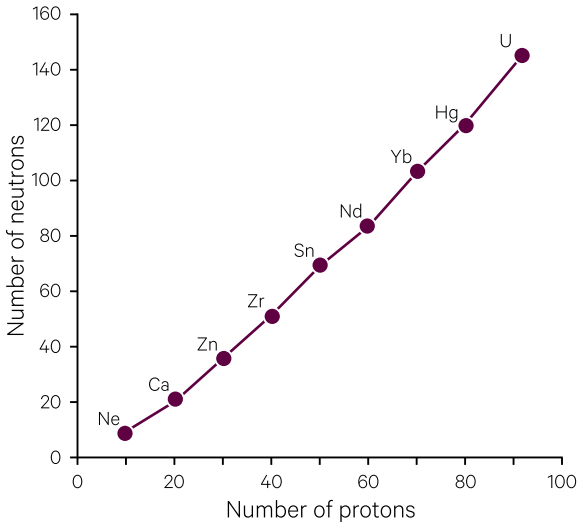
6.1 Introducing Radioactivity

Each element has a unique atomic number that indicates the number of protons contained in its nucleus. For the nucleus of an atom to be stable, the positive charge of protons needs to be balanced by an equal or greater number of neutrons. Elements with larger atomic numbers (that is, larger numbers of protons) appear to require a greater number of neutrons. Nuclei with more than 82 protons are not stable and tend to decay to regain stability (see Figure 6.1).

Radioactivity is shown to be accompanied by chemical changes in which new types of matter are being continually produced... The conclusion is drawn that these chemical changes must be sub-atomic in character. (Ernest Rutherford)

Figure 6.1 Stable nuclei

Those elements that are not on the stability line are unstable and tend to decay.



Adapted from: Andy Darvill at *http://www.darvill.clara.net/nucrad/moretypes.htm*

Background image: Airborne radiometric image of the Gulf of Carpentaria in northwest Queensland. The area shown is 450 km wide. Potassium is displayed as red, equivalent thorium as green and uranium as blue (derived from Ternary Radiometric image of Australia, Version 3, 2015; see Excursus 6.1 for details).
Source: Geoscience Australia

A nuclide is a species of atom with a specific number of protons, neutrons and energy state in its nucleus. An element can have multiple nuclides (that is, the same number of protons but different numbers of neutrons), which are called isotopes of that element. Nuclides and isotopes are referenced as:

Ename-A

or

$^{A}_{Z}X$

where

Ename is the element name;
A is the number of protons plus neutrons (or the atomic mass) of the atom;
Z is the number of protons (or the atomic number) of the atom; and
X is the element symbol (determined by the atomic number).

Since the atomic number is implied by the element name, the subscript can be, and often is, omitted. For example, the most commonly occurring form of elemental carbon has six protons and six neutrons, thus an atomic number of 12. This isotope is referenced as $^{12}_{6}C$ or ^{12}C. Radioactive carbon has an extra proton, so is referenced as $^{13}_{6}C$ or ^{13}C.

Unstable isotopes, called radioisotopes, emit ionising radiation to stabilise their nuclei. This process seeks to rebalance the ratio of protons to neutrons and often involves decreasing the number of protons in the nucleus, in which case the resulting atom becomes a different element. The process is called radioactive decay and frequently comprises a chain of decays that results in multiple intermediate (or daughter) nuclides of many elements (USEPA, 2012). These intermediate nuclides can exist for microseconds or millennia, and can be used to identify the parent isotopes.

Radioactive decay is spontaneous such that it is not possible to predict if or when an individual atom will decay. Over time, however, the frequency of decay has been observed to follow the Poisson distribution. Each radioisotope is characterised by its decay rate, such that:

$$N = N_0 e^{-\lambda t}$$

where

N_0 is the number of radionuclides at time t=0;
N is the number of radionuclides after time t; and
λ is the decay constant for the radioisotope.

The half-life of a radioisotope indicates the time required for half the nuclei to decay:

$$T_{1/2} = \frac{0.693}{\lambda}$$

The most common methods of radioactive decay produce:

- positively charged alpha particles—ejected from an unstable nucleus to reduce the number of protons; since the number of protons changes, the decaying atom becomes a new element;
- negatively charged beta particles—created when an excess neutron changes into a proton and an electron, and the new electron is expelled from the nucleus; this process also changes the original atom into a new element; or
- uncharged gamma rays—mass-less energy that is emitted by a new nucleus with an energy surplus, often following emission of an alpha or beta particle.

Alpha particles comprise two protons and two neutrons, so have mass and a discrete energy that can be used to identify the emitting isotope. They have low penetration range and are generally stopped by a few centimetres of air, whereas beta particles can travel several metres in air but are stopped by solid materials. Gamma rays are EM waves with high energy and can travel kilometres through air, 50 cm through rock and a few centimetres through lead (Minty, 1997; IAEA, 2003).

6.2 Gamma Rays

The only form of radioactivity that can be sensed remotely for EO is gamma radiation. In the Earth's crust, gamma rays result from naturally occurring radioisotopes and their intermediate decay products. They can also originate from isotopes created by the interaction of cosmic rays with our atmosphere and are occasionally generated during thunderstorms. Artificial sources of gamma rays include radioactive isotopes resulting from nuclear fission in nuclear reactors.

During radioactive decay, the radioisotopes of only three elements in the Earth's crust emit gamma radiation that can be detected remotely, namely Potassium (K), Uranium (U), and Thorium (Th). Detection of gamma rays depends on the relative abundance of the isotopes, which, in turn, is related to their half-life. While other elements have naturally occurring radioisotopes that emit gamma radiation, their levels of radiation are too low to be measured using airborne remote sensors (Minty, 1997).

Table 6.1 Isotope properties

Element			Naturally Occurring Isotopes			
Name	Symbol	Crustal Abundance (ppm)[21]	Symbol	% of Element	Half-life (years)	Gamma ray Emission
Potassium	K	2.09×10^4	^{40}K	0.012	1.3×10^9	Yes
Uranium	U	2.7	^{238}U	99.28	4.46×10^9	Only from radioactive daughter products
			^{235}U	0.72	7.13×10^8	Energy too low for remote sensing
Thorium	Th	9.6	^{232}Th	100	1.39×10^{10}	Only from radioactive daughter products

Adapted from: IAEA (2003)[19]

The occurrence of K, U and Th isotopes is summarised in Table 6.1. ^{40}K occurs as a constant proportion of K so can be used to estimate the abundance of this element. The ^{235}U isotope occurs infrequently and emits low levels of gamma radiation so is not detected by remote sensing. The total amount of U and Th can only be inferred from the gamma radiation emitted by daughter products in their radioactive decay chains, as neither ^{238}U nor ^{232}Th emit gamma rays.

Since each intermediate nuclide in a radioactive decay chain decays at its own rate, it is possible that the 'residence' time, and hence relative abundance, of each intermediate nuclide can vary and create a situation of 'disequilibrium'. When an element's abundance is being estimated from the concentration of intermediate nuclides it is essential that the radioactive decay chain is in a state of equilibrium. This situation is most relevant to estimates of U which are derived from the detected concentrations of its distant descendants after several 'generations' of radioactive decay and whose decay chain is often in disequilibrium. In this case, the estimate of Uranium is generally reported as 'equivalent Uranium' (eU) and can be erroneous. Similarly, estimates of Thorium are referenced as 'equivalent Thorium' (eTh), although its decay chain is usually in equilibrium.

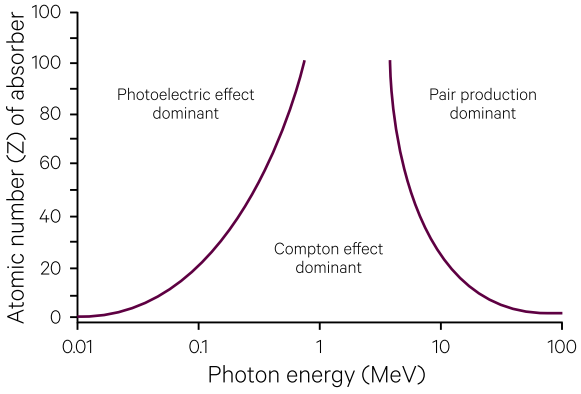
The impact of gamma rays on a material depends on its thickness, density and absorption cross-section. The energy of gamma rays determines how they ionise atoms (see Figure 6.2):

- at low energy levels, a gamma photon transfers its energy to an electron bound to an atom, resulting in emission of the electron and heating. This mechanism is called the photoelectric effect;
- at medium energy levels, a gamma photon transfers some of its energy to a bound electron as occurs in the photoelectric effect, with its remaining energy being scattered as a lower energy gamma photon. This process is referred to as Compton scattering; and
- at high energy levels, a gamma photon is absorbed by the nucleus of an atom, which quickly decays and emits as two medium energy gamma photons. This sequence is called Pair Production.

The energy of a gamma photon is characteristic of its source isotope and can be used to identify that source. Gamma radiation is usually characterised by its energy level, expressed in eV (electron volts), rather than by wavelength. Sensors which record total energy counts and/or spectra for terrestrial gamma radiation are discussed in Volume 3. Gamma spectroradiometry images are typically displayed as a colour composite using red for potassium, green for thorium and blue for uranium as illustrated in Figure 6.3 and Excursus 6.1.

Figure 6.2 Gamma ray ionisation

A photon at gamma ray energies interacts with matter in terms three principal mechanisms: the photoelectric effect, the Compton effect or via pair production. This graph shows the relative importance of these three interactions for different photon energy levels and attenuating materials (represented in terms of atomic number). Note: X-axis scale is logarithmic.

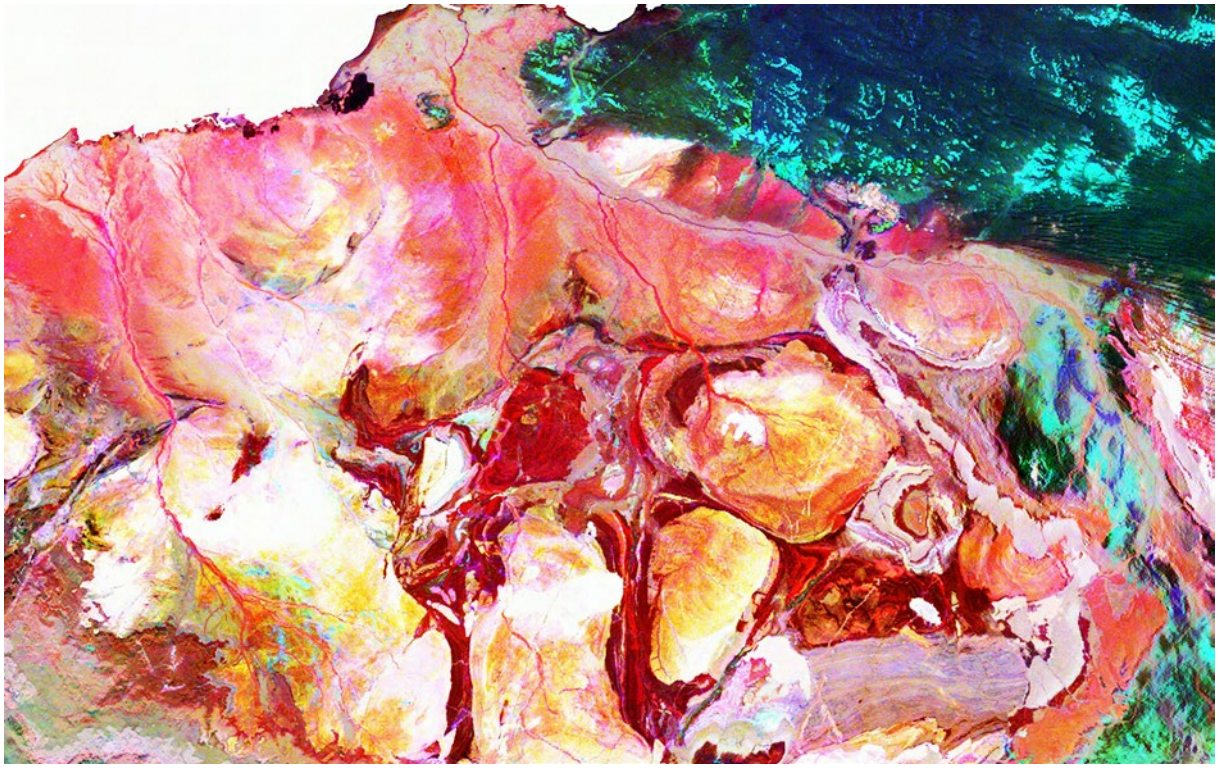


19. Lide (2008) cited in *http://www.knowledgedoor.com/2/elements_handbook/element_abundances_in_the_earth_s_crust.html*

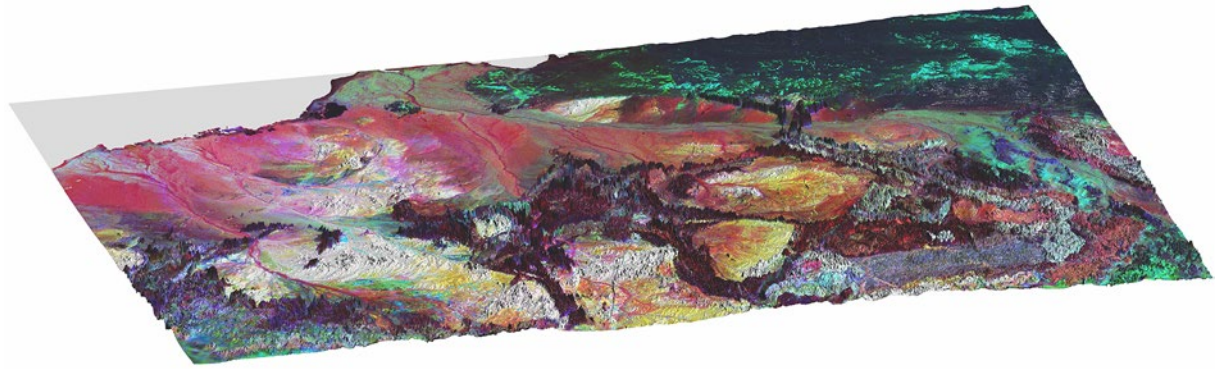
Figure 6.3 Gamma spectroradiometry

The Archaean Pilbara Craton of northwestern Western Australia consists of granitoid-greenstone terrain (3.6-2.8 Ga). Rocks include granite (white and red hues), basalts and ultra-mafics lithologies (black hues). Overlying sediments associated with the Canning Basin consist of aeolian sands, sandstone and conglomerate (east of image in black and green hues). Extensive alluvial and colluvial plains in reddish hues occur between the granitiod-reenstone terrain and the coast. This relatively well exposed province is an excellent example of how airborne gamma-ray spectrometry can be used to map bedrock types (including zonation within the granites) and structures. The image extends 210 km N-S (North to the top of the page) and 340 km E-W (East to the right of the page).

a. Two-dimensional image



b. Three-dimensional overlay of image on regional topography



Source: Geoscience Australia

Thus the radio elements formed strange and cruel families in which each member was created by spontaneous transformation of the mother substance: radium was a 'descendant' of uranium, polonium a descendant of radium.
(Eve Curie)

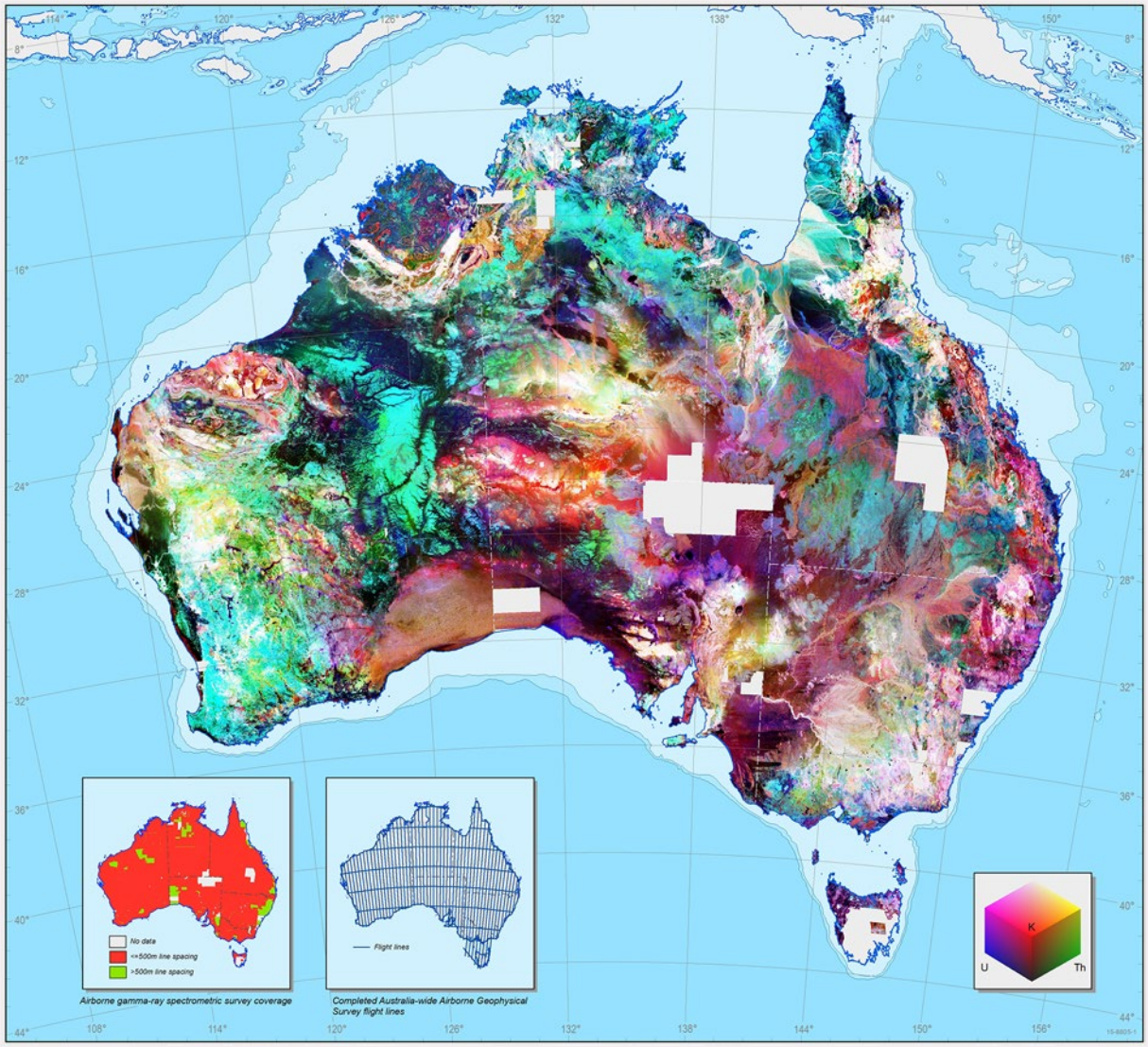
Excursus 6.1— Australian Radiometric Map

Source: Murray Richardson, Geoscience Australia
Further Information: Minty *et al.* (2008); Geoscience Australia (2016)

Geoscience Australia and the State and Northern Territory geological surveys have systematically surveyed the Australian continent for over 50 years using airborne radiometric surveys to map potassium, uranium and thorium elemental concentrations at the Earth's surface. Since the data had been collected and processed using a range of specifications, technologies and procedures over this period, the radiometric data in the national database were not all registered to the same datum. This made it difficult to combine surveys into regional compilations or to make accurate comparisons between radiometric responses over different parts of the continent, which limited the value of the database.

Figure 6.4 Radiometric map of Australia

Ternary image of Australia from the updated National Radioelement database showing equivalent uranium as blue, equivalent thorium as green and potassium as red.



Source: Geoscience Australia

In 2007 Geoscience Australia conducted an Australia-wide airborne geophysical survey (AWAGS) that covered the entire continent with north-south flight lines spaced 75 kilometres apart, and east-west tie lines spaced 400 kilometres apart (Johnson, 2006). Gamma-ray spectrometric data, acquired at an 80 m height along the flight lines during AWAGS, were processed according to international specifications, and the final estimates of the concentrations of the radioelements (potassium, uranium and thorium) comprise the new Australian radioelement datum. The national radiometric database was levelled by minimising both the differences in radioelement estimates between surveys (where these surveys overlap) and the differences between the surveys and the AWAGS traverses (where these overlap). This effectively levels the surveys to the new national datum.

A ternary image derived from the levelled national radioelement database is shown in Figure 6.4. This updated database, on a 100 m grid, will directly assist:

- uranium and thorium exploration through the ability to make quantitative comparisons between the radiometric signatures in different survey areas;
- heat flow studies and assessment of geothermal energy resources;
- geological mapping, mineral and petroleum exploration;
- geomorphological studies and environmental mapping; and
- derivation of a radiation risk map of Australia.

The improved datasets will lead to an increased understanding of the geology, structure, geochemistry and geomorphology of the continent. For example, palaeozoic granites in eastern Australia can now be quantitatively compared and assessed for areas of potential mineralisation and geothermal prospectively. These datasets are freely available from the Australian Geoscience Information Network (AUSGIN: *http://www.geoscience.gov.au*) and by accessing the Geophysical Archive Data Delivery System (GADDS).

6.3 Further Information

Radiometrics: *http://www.ga.gov.au/scientific-topics/disciplines/geophysics/radiometrics*

Gamma spectroscopy: Minty (1997)
IAEA (2003)

Gamma ray interactions: *http://www.hep.wisc.edu/~prepost/407/gamma/gamma_html.html*

Radiometric Map of Austalia: *http://www.ga.gov.au/ausgeonews/ausgeonews200812/radiometrics.jsp*

6.4 References

Geoscience Australia (2016). Geoscience Australia. Retrieved from *http://www.ga.gov.au*.

IAEA (2003). Guidelines for radioelement mapping using gamma ray spectrometry data (IAEA-TECDOC-1363). International Atomic Energy Agency, Vienna. Retrieved from *http://www-pub.iaea.org/mtcd/publications/pdf/te_1363_web.pdf*.

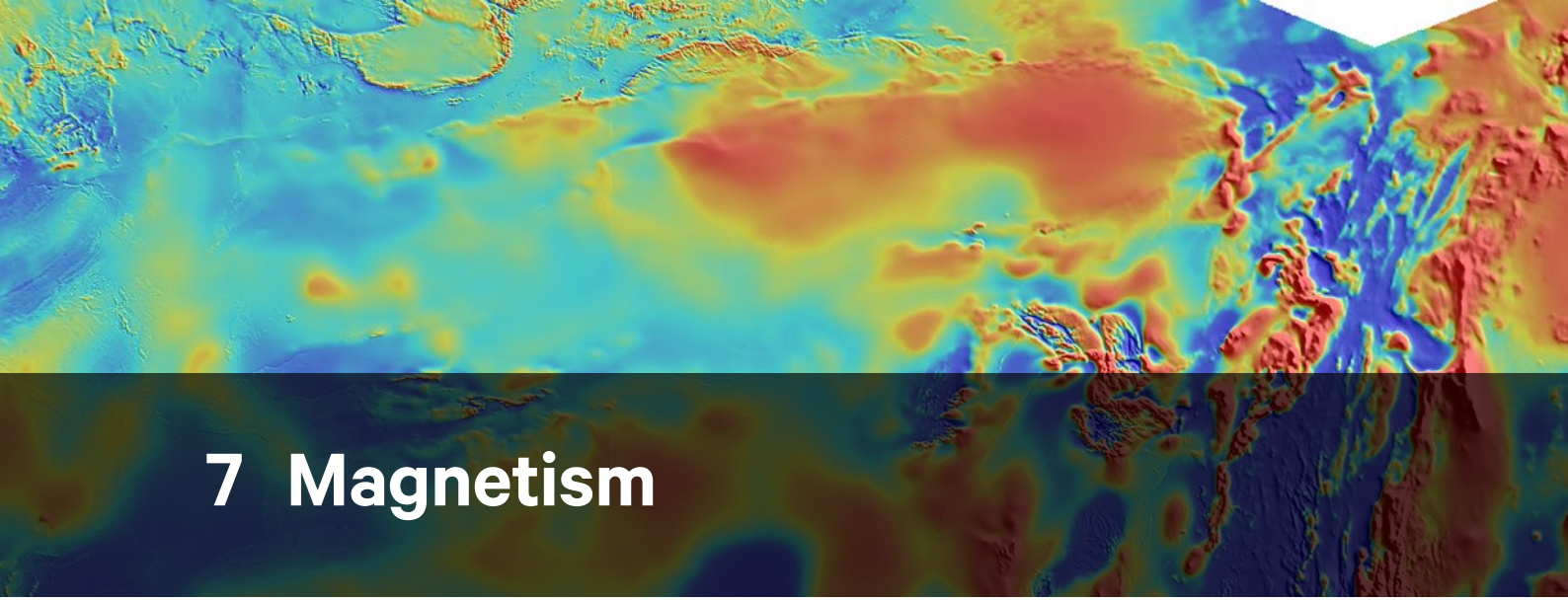
Johnson, J. (2006). Onshore Energy Security Program underway. AusGeo News, 84. Geoscience Australia, Canberra, Australia. Retrieved from *http://www.ga.gov.au/ausgeonews/ausgeonews200612/onshore.jsp*.

Lide, D. R. (2008). CRC Handbook of Chemistry and Physics, 88th Edn. Taylor & Francis Group, Boca Raton, Florida.

Minty, B. R. S. (1997). Fundamentals of airborne gamma-ray spectrometry. AGSO Journal of Australian Geology and Geophysics, 17(2), pp. 39-50.

Minty, B. R. S., Richardson, M., and Wilford, J. (2008). New Radiometric Map of Australia. AusGeo News, 92. Geoscience Australia, Canberra, Australia. Retrieved from *http://www.ga.gov.au/ausgeonews/ausgeonews200812/radiometrics.jsp*.

USEPA (2012). United States Environmental Protection Agency. Retrieved from *http://www.epa.gov/radiation/understand/index.html*.



7 Magnetism

Magnetism is a physical phenomenon that allows materials to attract or repel other materials. Certain materials called ferromagnets produce a persistent magnetic field (rather than a temporary magnetic field in response to contact with one). At an atomic level, this is due to the 'spin' of both the electrons around the nucleus and the elementary particles within the nucleus (see Section 2.2).

Magnetometers are instruments that remotely sense the magnitude and/or direction of a magnetic field. For Earth Observation (EO) studies, magnetometers can be ground-based or carried aboard aircraft or ships. The resulting measurements can be converted into maps showing the distribution and abundance of magnetic minerals, which are used for geological and mining applications.

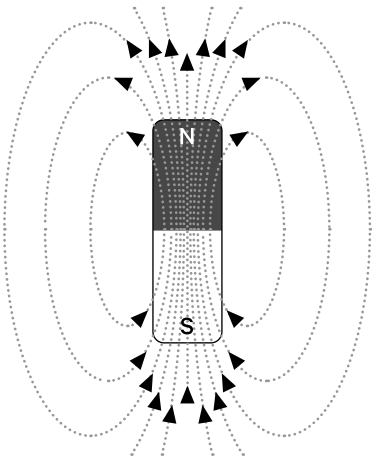
7.1 Introducing Magnetism

As introduced in Section 2.4, magnetism is fundamentally a force between two electric currents, such that two currents in the same direction attract each other and two currents in opposite directions repel each other. This principle applies whether the currents are parallel, as in bar magnets, or circular, as in an electromagnet. The region influenced by a magnet is called its magnetic field (see Figure 7.1).

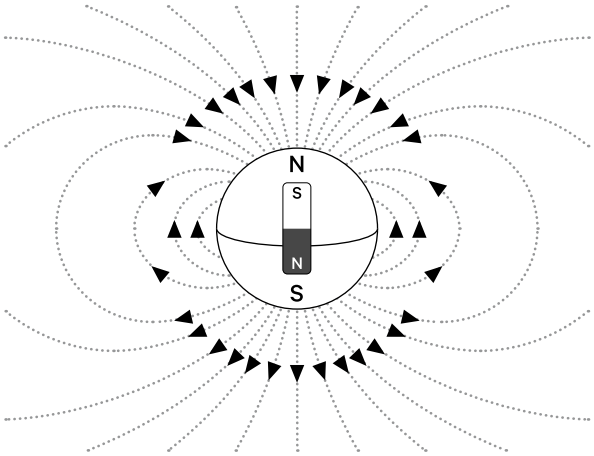
Figure 7.1 Magnetic fields

By convention, magnetic field lines are drawn in the direction of attraction from the north pole to the south pole. The magnetic field is strongest inside the magnetic material, with the strongest external magnetic fields occurring near the poles. A magnetic compass is attracted to the south pole of a bar magnet, or the North Pole of our planet.

a. Magnetic field of a bar magnet is usually drawn with the north pole at the top, and parallel magnetic field lines moving up, around and down the magnet to the south pole.



b. Earth's magnetic field resembles an electromagnet, with the equivalent of the south pole of the magnet near the North pole of the planet. Since a magnetic compass is attracted to the south pole of a bar magnet, the magnetic field lines on Earth point north.



Background image: Airborne total magnetic intensity image of the Gulf of Carpentaria, northwest, Queensland. The area shown is 450 km wide. This pseudo-colour image displays Total Magnetic Intensity as a spectrum from high values as red to low values as blue (derived from Magnetic Map of Australia, Version 6, 2015, with variable reduction to the pole; see Excursus 7.2 for details). **Source:** Geoscience Australia

While the 'spin' of any electron can produce a magnetic field, in the atoms of most materials this energy is countered by the opposite movement of other electrons, resulting in no net magnetic moment. In ferromagnetic materials, the magnetic moments of most atoms in the material are aligned. The magnetic state, or 'phase' of a material varies with temperature, pressure and external magnetic fields. Ferromagnetic materials such as nickel, iron, cobalt, gadolinium and their alloys display magnetic properties up to a particular temperature. The temperature at which a material loses its permanent magnetism is called its Curie temperature.

7.2 Magnetic Field

A magnetic field is commonly characterised by seven parameters, or magnetic elements, as summarised in Table 7.1. The relationship between these elements is illustrated in Figure 7.2.

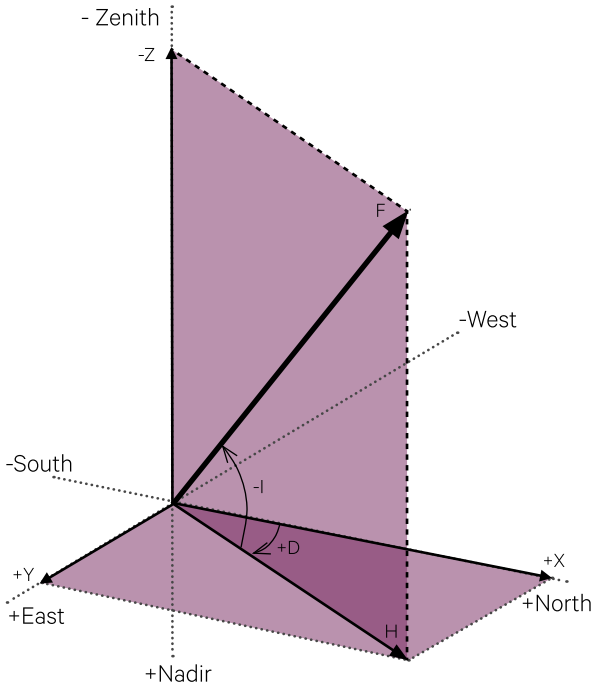
Table 7.1 Magnetic components

Element	Abbreviation	Unit	Description
Declination (or variation)	D	degrees	Difference between true and magnetic north
Inclination (or dip)	I	degrees	Angle of magnetic field above or below horizon (90° at magnetic pole)[22]
Total Intensity	F	Gauss or nanotesla (nT)	Strength of magnetic field varies between 25,000 and 65,000 nT
Horizontal Component	H	Gauss or nanotesla (nT)	Horizontal component of total intensity (direction of horizontal component is magnetic north)
North Component	X	Gauss or nanotesla (nT)	Component of total intensity in northerly direction
East Component	Y	Gauss or nanotesla (nT)	Component of total intensity in easterly direction
Vertical Component	Z	Gauss or nanotesla (nT)	Vertical component of total Intensity

Source: Geoscience Australia (2016) [20]

Figure 7.2 Magnetic vector components

In the Southern Hemisphere, Z is upwards and negative. Declination (D) is positive in most of continental Australia, except in southwest WA where it is negative.



Source: Geoscience Australia

Magnetism, you recall from Physics class, is a powerful force that causes certain items to be attracted to refrigerators.
(Dave Barry)

20. The magnetic field Is vertical at the poles and horizontal at the equator.

7.3 The Earth's Magnetic Field

The Earth essentially acts like a giant magnet surrounded by a magnetic field. Being a vector quantity, the Earth's magnetic field, which is also known as the geomagnetic field (see Figure 7.1b), has both magnitude and direction. Both the direction and intensity of Earth's magnetic field vary with time and location on the Earth, so the direction of magnetic north also varies. The Magnetic North Pole is currently offset by 11° from Earth's axis of rotation, which means that magnetic north differs from geographic (or true) north.

The configuration of the Earth's magnetic field resembles the field that would be produced if a bar magnet were buried deep within the Earth. It appears that the Earth's magnetic field is produced by the 'dynamo effect' resulting from movement of fluids within its outer core. The solid inner core can be likened to a hot iron ball (at around 6000°C) that spins inside the molten outer core. The inner core spins at a different rate to the rotation of Earth. These movements cause circulation of fluids in the outer core resulting in electric currents, which in turn create a magnetic field (Stern, 2004). The geomagnetic field is also affected by processes in the upper atmosphere and in the Earth-Sun space environment.

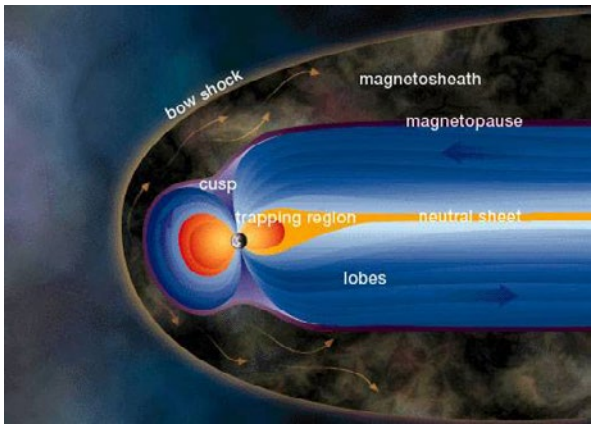
The extent of the geomagnetic field is called its magnetosphere. While the geomagnetic field is depicted with symmetrical force lines in Figure 7.1b, the actual shape is distorted by the influence of the supersonic solar wind, a stream of ionised particles released by the Sun. The speed of the solar wind effectively compresses the geomagnetic field on the Sun side of Earth, creating the magnetopause, and induces a long tail in the magnetosphere on the opposite side of Earth, which extends over 150,000 km (see Figure 7.3).

Like the Sun, the solar wind is not constant and abrupt release of plasma streams can create magnetic storms, or significant variations in the geomagnetic field, which can last for hours or days (Love, 2008; Love and Finn, 2011). Magnetic storms can result in major changes in currents, plasmas and fields in the magnetosphere, which have been known to impact satellite orbits and communication systems, disrupt radio broadcasts and power grids on Earth, and cause inaccuracies in compass readings (NOAA, 2016).

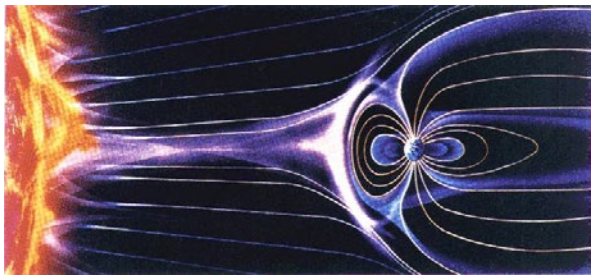
Within the magnetosphere, zones of trapped radiation were detected by the Explorer-1 satellite. These zones are called the Van Allen Belts and appear to protect the Earth from the solar wind and cosmic rays. These belts are weaker nearer the poles, which allows more particles from space to interact with the upper atmosphere and create the spectacular phenomena of aurora (see Figure 7.4).

Figure 7.3 Magnetosphere

a. Components of magnetosphere



b. Solar wind colliding with Earth's magnetosphere



Source: NASA. Retrieved from *http://ccmc.gsfc.nasa.gov/educational/MagnetosphereWebPage.php*

Figure 7.4 Southern Aurora

Photo taken by magnetic observer at Casey Station in 2010



Source: Tim Bolton, Geoscience Australia

The numerous satellites that have been launched to observe the magnetosphere have enabled mapping and modelling of the global distribution of Earth's magnetic field over time. These measurements have been supported by those made with magnetometers at approximately 200 magnetic observatories around the world. As part of this global network, in Australia GA maintains a national network of geomagnetic observatories which measure four components of the geomagnetic field (true north (X), true east (Y), vertical (Z) and the total intensity (F) every second (Hopgood (2007); see Figure 7.5). These real-time measurements (available online) show how the Earth's magnetic field continuously changes in the Australian region (see Figures 7.6 and 7.7). A range of indices have been developed to summarise the variability of Earth's magnetic field (Geoscience Australia, 2016), coordinated by the International Services of Geomagnetic Indices (ISGI).

Figure 7.5 Geomagnetic observation network for Australia

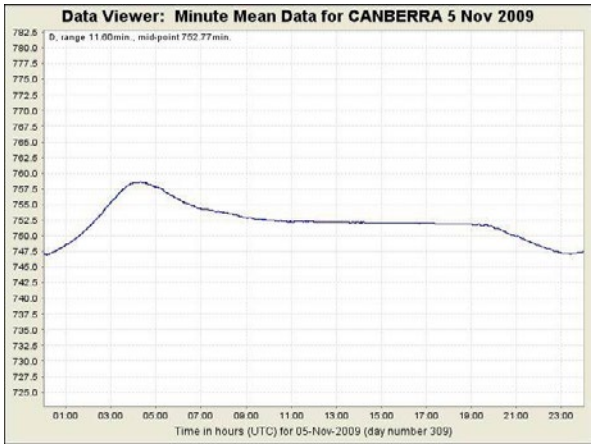


Source: Geoscience Australia

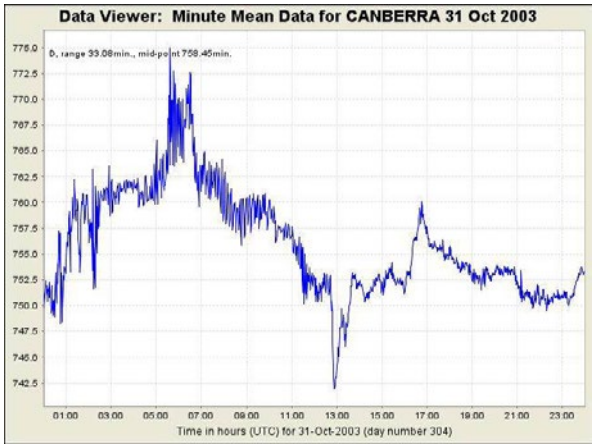
Figure 7.6 Magnetic time series

Two images of magnetic time series from the Canberra magnetic observatory show 24 hours of declination data (x-axis: time; y-axis: magnetic declination in minutes-of-arc).

a. 5 November 2009– a quiet day in terms of magnetic variation



b. 31 October 2003 — a day with magnetic disturbance



Source: Geoscience Australia

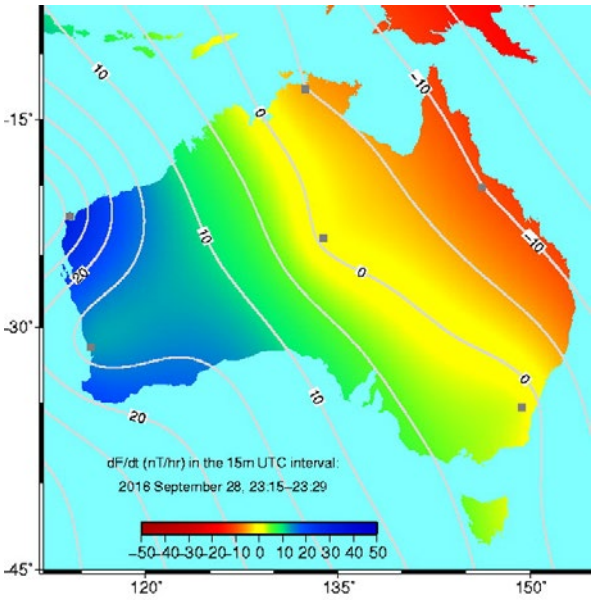
Models of the direction and intensity of Earth's magnetic field have been developed to understand how the field is changing, and these models can be used to predict future changes (see Excursus 7.1). The standard mathematical models, the International Geomagnetic Reference Field (IGRF) and the World Magnetic Model (WMM), are updated every five years and, given the variable nature of the geomagnetic field, are only valid for a five-year period. Relevant calculators, data and software are available from NOAA (2013).

The geomagnetic field is relevant to a range of applications, including navigation, mineral and resource exploration, space weather analysis, and geomagnetic hazard mitigation. A range of related products and services are provided by Geoscience Australia (2016), such as:

- compass-based navigation,
- finding magnetic direction;
- mitigating the potential hazards generated by magnetic storms; and
- calibration of compasses and magnetometers

Figure 7.7 Total intensity variability over Australia

Data recorded within a 15 minute time interval from six magnetic observatories in continental Australia are used to generate a contour display showing the rate of change in magnetic total intensity (F; in units of nanotesla per hour). This display is updated every 15 minutes. This image was generated from data recorded on 28 September 2016, 23:15–23:29. Locations of magnetic observatories are shown as grey squares.



Source: Geoscience Australia

MAGNET, n. Something acted upon by magnetism.
MAGNETISM, n. Something acting upon a magnet.
The two definitions immediately foregoing are condensed from the works of one thousand eminent scientists, who have illuminated the subject with a great white light, to the inexpressible advancement of human knowledge.
(Ambrose Bierce)

Excursus 7.1—Australian Geomagnetic Reference Field Model

Source: Andrew Lewis, Geoscience Australia
Further Information: *http://www.ga.gov.au/ausgeonews/ausgeonews201006/geomagnetic.jsp*

The Australian Geomagnetic Reference Field (AGRF) is a mathematical model of the geomagnetic field and its predicted annual changes over the Australian region, including continental Australia and nearby offshore areas, most of Papua New Guinea and parts of eastern Indonesia. The 2010 revision is a mathematical representation of the undisturbed geomagnetic main field at epoch 2010.0 and its predicted annual changes during the period 2010 to 2015 (see Figure 7.8).

The model is the sixth in the series of AGRF models and describes the field originating from internal sources using spherical cap harmonics. The main field is modelled to a nominal minimum spatial wavelength of 1500 km and the annual change to 2000 km. Extensive vector geomagnetic survey datasets were used to derive the main field model, including magnetic data from the German CHAMP satellite, high elevation airborne data, and ground based vector survey data across Australia.

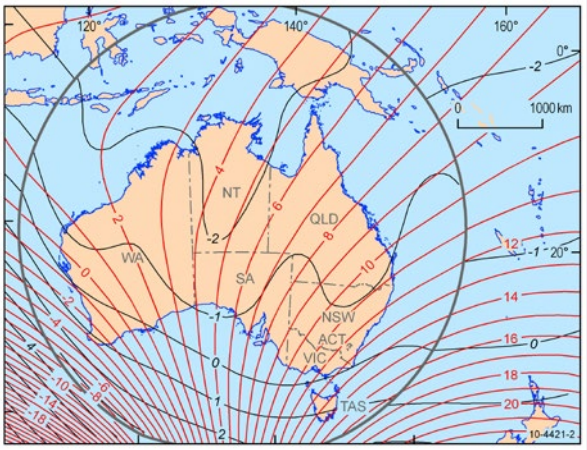
Based on knowledge of the past behaviour of the magnetic field, the secular variation model should be appropriate out to epoch 2015. The extensive regional data sets used in developing the AGRF model make it the most accurate available model for the Australian regional magnetic field for the interval 2010 to 2015.

The 2010 AGRF model is based on the recently released eleventh revision of the International Geomagnetic Reference Field (IGRF), which is a global spherical harmonic model of the geomagnetic field. The eleventh generation of the International Geomagnetic Reference Field (IGRF-11) was released by the International Association of Geomagnetism and Aeronomy (IAGA) in late December 2009. This release adds a definitive main field model for 2005.0, a new model for 2010.0 and a secular variation model for the period between 2010 and 2015.

The development of the IGRF is the result of international collaboration between magnetic field modellers and the scientific institutions and government agencies that undertake satellite magnetic surveys and operate geomagnetic observatories.

Figure 7.8 AGRF 2010 model at epoch 2010.0

Contours of magnetic declination (in degrees) are shown as red lines and annual change of declination (in minutes-of-arc per year) are shown as black lines. The limit of the ARGF model is marked as a black circle. Contours outside this circle are derived from the IGRF-11 at 2010.0.



Source: Geoscience Australia

7.4 Geomagnetics

The geomagnetic field associated with planet Earth is the sum of magnetic fields from three major sources:

- the main field derived from internal processes within the Earth's core, which accounts for more than 90% of the total intensity;
- the external field derived from electrical processes in the ionosphere and magnetosphere driven by solar activity; and
- the crustal field derived from magnetism generated in iron minerals in the Earth's crust.

While rocks comprise various minerals, their magnetic properties depend mainly on the amount of iron-rich minerals. Magnetite, for example, is a magnetic iron mineral, which occurs in small quantities in rocks. By measuring and mapping the crustal magnetic field, the general distribution of magnetic rocks and the associated subsurface geology can be mapped.

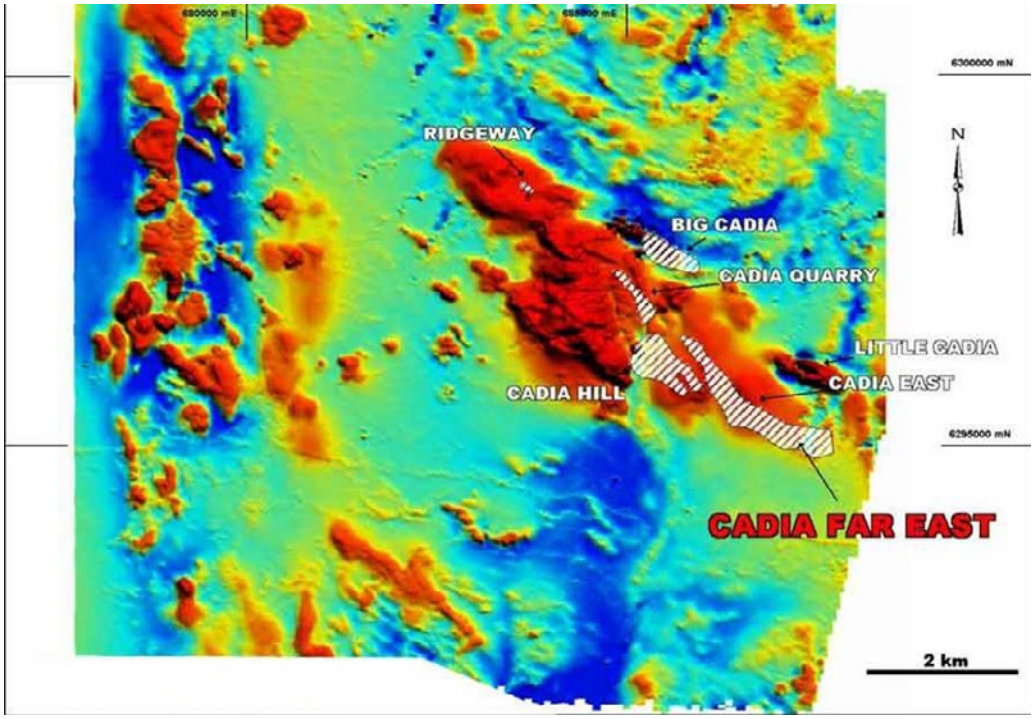
Local variations, or anomalies, in the Earth's magnetic field are generally due to variations in the chemical and magnetic properties of rocks and, thus, are valuable indicators of potentially commercial minerals, principally magnetite. Magnetic surveys use airborne, ship-borne or ground-based magnetometers to measure small changes in the intensity of the Earth's magnetic field (see Figure 7.9). These measurements

are adjusted for known variations due to global and regional magnetic variation. The resulting maps indicate the distribution and abundance of magnetic minerals and are commonly used for geological mapping, mineral exploration, archaeological surveys and locating buried ferrous objects. For example, the most recent Magnetic Anomaly Grid for Australia is shown in Excursus 7.2. Acquisition and applications of this source of EO data is further discussed in Volume 3.

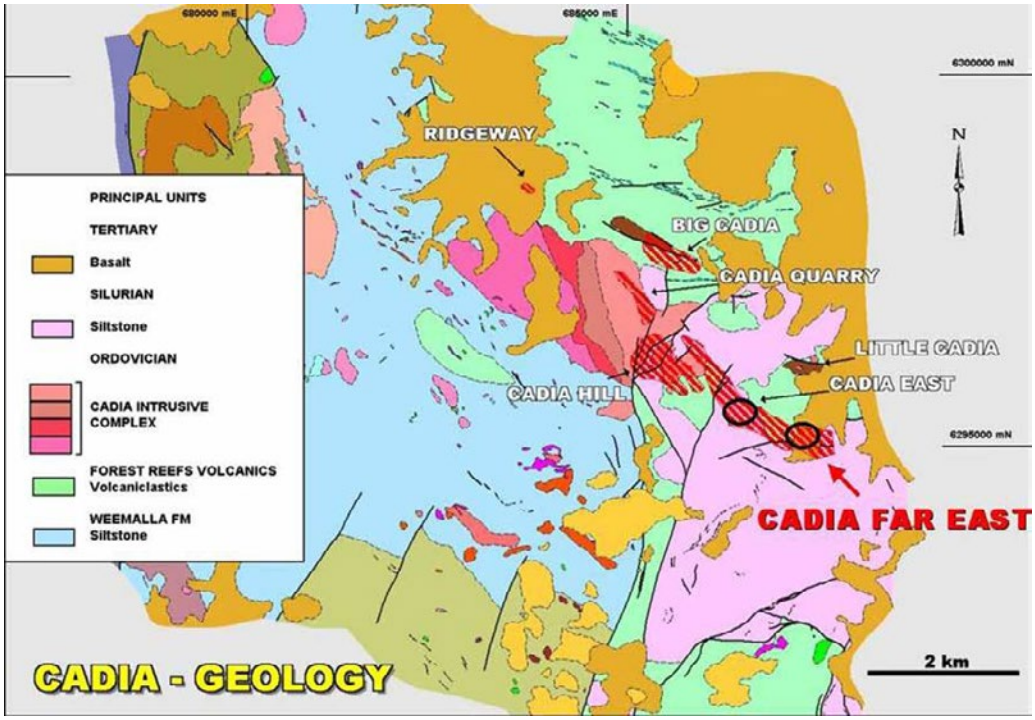
Figure 7.9 Aeromagnetic imagery

Total Magnetic Intensity (TMI or F) for Cadia-Ridgeway Mine (about 20 km south of Orange, NSW).

a. This pseudo-colour image shows TMI values as a spectrum from high values as red to low values as blue.



b. Geologic map of Cadia region. The known extent of significant ore bodies are hatched.



Source: Geoscience Australia

Excursus 7.2—Australian Magnetic Anomaly Grid

Source: Milligan *et al.* (2010)
Further information: *http://www.ga.gov.au/news-events/news/latest-news/latest-editions-of-magnetic-anomaly-grid-and-radiometric-map-released; http://www.ga.gov.au/webtemp/image_cache/GA18012.pdf*

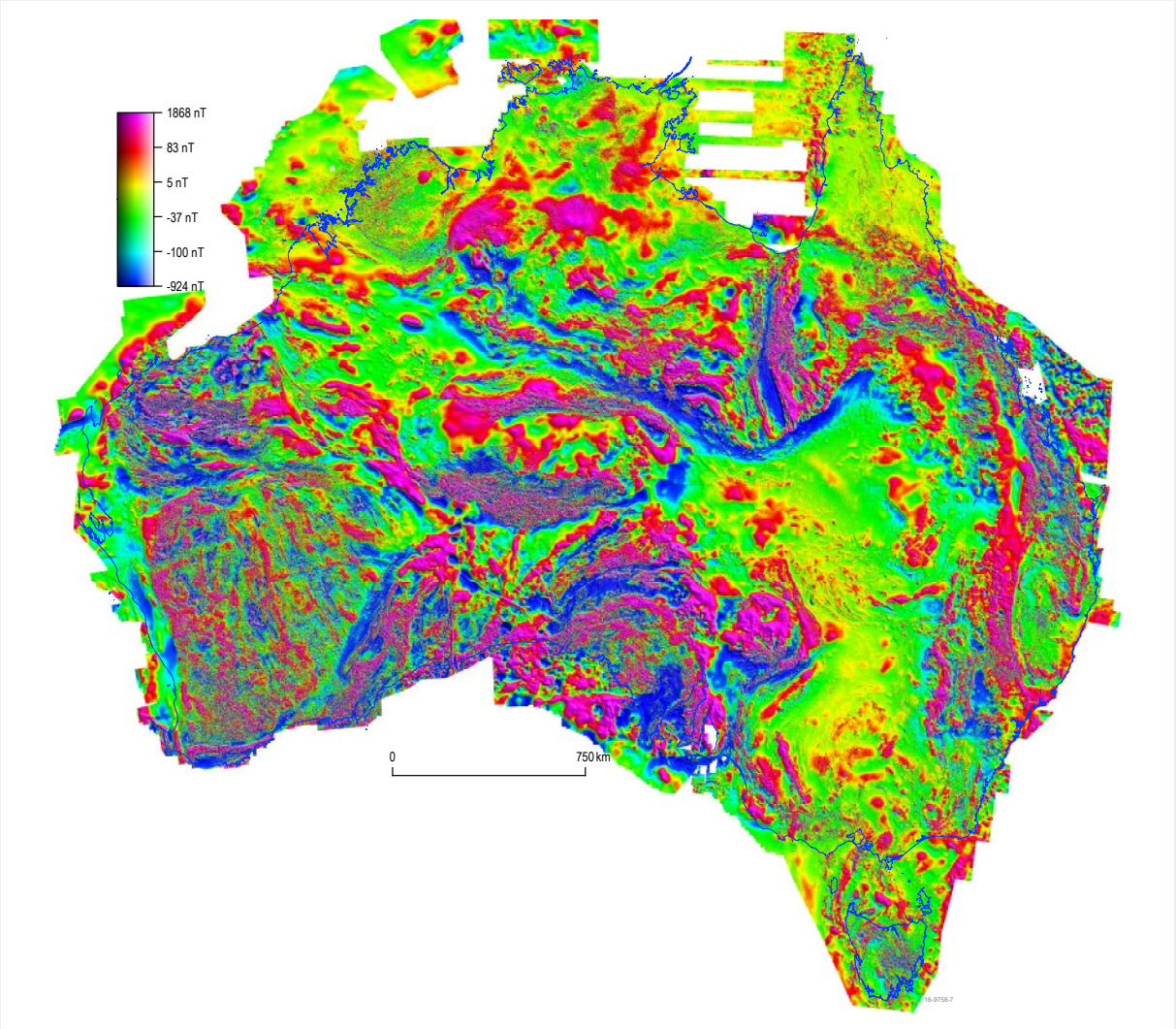
After more than 60 years of airborne surveys by state, territory and Australian Government geoscience agencies, and private companies, the Australian continent is impressively covered by a calibrated grid of magnetic data. The sixth Total Magnetic Intensity (TMI) grid of Australia is based on a cell resolution of approximately 80m (3 seconds of arc; see Figure 7.10). This grid comprises around 31.5 million line-kilometres of acquired magnetic survey data, which is 4.5 million more line-kilometres than the fifth edition released in 2010.

This grid was processed using a technique called Variable Reduction to Pole (VRTP), which makes adjustments to the location and shape of magnetic anomalies due to the variation in the inclination of the Earth's magnetic field with latitude. The VRTP process adjusts the magnetic anomalies so that simple features are mapped directly over the magnetic bodies. Without VRTP magnetic anomalies appear shifted relative to their true position.

The datasets are available for free download from the Geophysical Archive Data Delivery System (GADDS).

Figure 7.10 Australian Magnetic Anomaly Grid

Sixth edition of TMI anomaly grid for Australia was derived from more than six decades of airborne survey data with VRTP adjustments.



Source: Geoscience Australia

Australia-wide Airborne Geophysical Survey (AWAGS)

The Australia-wide Airborne Geophysical Survey (AWAGS), completed in 2008, flew the entire continent in a standardised grid at an altitude of 80 m. This grid, based on north-south flight lines 75 km apart and east-west flight lines 400 km apart, collected both magnetic and radiometric data. The consistent AWAGS dataset has allowed disparate sources of magnetic and radiometric data to be levelled and merged to a common datum (see Excursus 6.1).

7.5 Further Information

Magnetism:

Geoscience Australia: *http://www.ga.gov.au/scientific-topics/disciplines/geophysics/magnetics*

Geomagnetism:

Geoscience Australia: *http://www.ga.gov.au/oracle/geomag/agrfform.jsp*

NASA: *http://image.gsfc.nasa.gov/poetry/magnetism/magnetism.html*
http://www.nasa.gov/vision/earth/lookingatearth/29dec_magneticfield.html

Magnetosphere:

NOAA: *http://www.swpc.noaa.gov/phenomena/earths-magnetosphere*
http://www.swpc.noaa.gov/phenomena/geomagnetic-storms

Southwest Research Institute: *http://pluto.space.swri.edu/image/glossary/magnetosphere.html*

Space Weather impacts: *http://www.wmo.int/pages/prog/sat/spaceweather-intro_en.php*

Atmospheric Optics: *http://www.atoptics.co.uk/highsky/auror2.htm*

7.6 References

Geoscience Australia (2016). Geoscience Australia. Retrieved from *http://www.ga.gov.au*.

Hopgood, P. (2007). Activity of magnetic total intensity across continental Australia. Australian Society of Exploration Geophysicists, 130, pp. 18-24.

Love, J. J. (2008). Magnetic monitoring of Earth and space. Physics Today, 61(2), pp. 31-37. doi:*http://dx.doi.org/10.1063/1.2883907*.

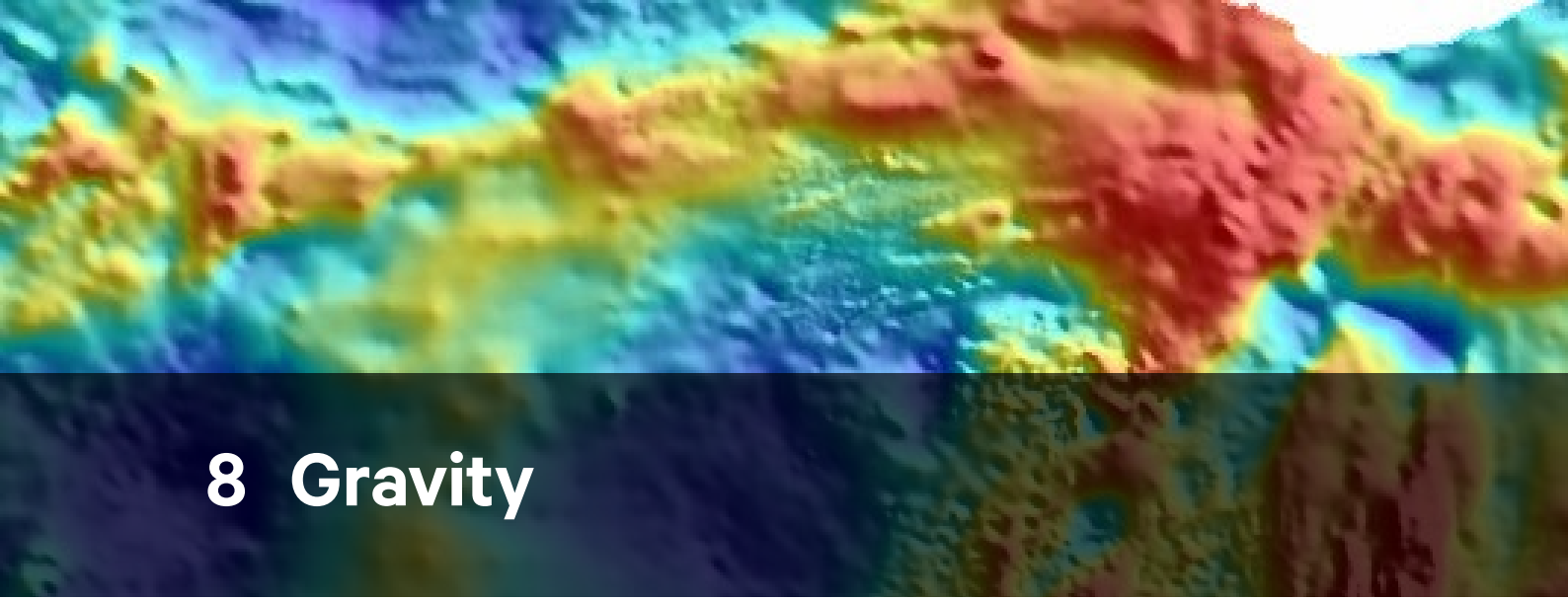
Love, J. J., and Finn, C. A. (2011). The USGS Geomagnetism Program and Its Role in Space Weather Monitoring. Space Weather-the International Journal of Research and Applications, 9. doi:*http://dx.doi.org/10.1029/2011sw000684*.

Milligan, P. R., Franklin, R., Minty, B. R. S., Richardson, L. M., and Percival, P. J. (2010). Magnetic Anomaly Map of Australia (Fifth Edition), 1:15 000 000 scale. Geoscience Australia, Canberra, Australia.

NOAA (2013). National Geophysical Data Centre. Retrieved from *http://www.ngdc.noaa.gov/geomag/*.

NOAA (2016). Space Weather Prediction Centre. Retrieved from *http://www.swpc.noaa.gov/phenomena/ionosphere*.

Stern, D. P. (2004). The Great Magnet, the Earth. *http://www.phy6.org/earthmag/dmglist.htm*.



8 Gravity

Gravitational forces exist between any two bodies in the Universe. The gravitational influence exerted by one body on another is relative to both their respective masses and the distance between the two bodies. Since changes in Earth's gravity field strength at a particular location are related to its mass at that location, Earth's gravitational field can be measured indirectly by its impact on the orbital attitude of spaceborne sensors.

The most obvious illustration of gravitational force is that objects remain on the surface of the Earth. Since the gravitational force acting on an object is directly proportional to the mass of the object, those objects with greater mass are more difficult to move away from the Earth. The gravitational force between two objects is inversely proportional to the distance between them. Objects can remain in orbit around the Earth because the Earth is still exerting some gravitational influence on them.

Newton proposed the fundamental law of gravity, which relates the masses of two bodies and the Universal Gravitational Constant (*G*):

$$F = G\left(\frac{m_1 m_2}{r^2}\right)$$

where

F is the gravitational force (in N);
$G = 6.673 \times 10^{-11}$ (in $N \cdot m^2/kg^2$);
m_1 is the mass of body 1 (in kg);
m_2 is the mass of body 2 (in kg); and
r is the distance between the centres of mass of the bodies m_1 and m_2 (in m).

Gravitational forces are not limited to forces imposed by a larger body on a smaller body as the smaller body also has an impact on the larger body. For example, the gravitational influence of the Moon on the Earth causes the movement of water in the oceans that gives rise to tides.

8.1 The Earth's Gravitational Field

Were the Earth a perfect sphere with uniform density, its gravity would be constant at all locations. However, as introduced in Section 3, neither the shape nor composition of the Earth is uniform in any sense. The structure of Earth varies both in terms of internal layering and surface topography, as well as in material type and density so that the strength of gravity varies in different locations. The interactions between the major factors shaping the Earth are illustrated in Figure 8.1.

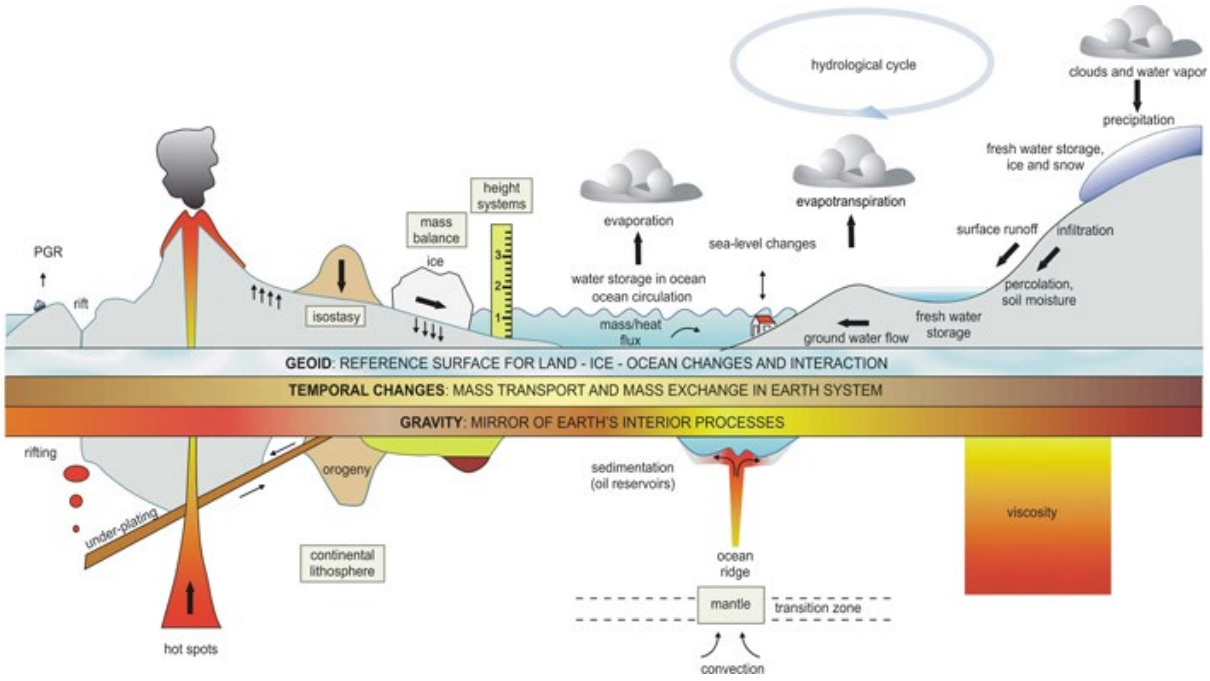
The standard gravity for Earth is accepted to be 9.81275 m/s^2. Section 3.3 introduced the geoid, a mathematical surface representing sea level equipotential, that is, where gravity would be equal to its mean sea level strength for all points on Earth. As illustrated in Figure 8.2, the shape of the geoid varies with the underlying masses so undulates relative to an ellipsoidal surface.

Our two greatest problems are gravity and paperwork.
We can lick gravity, but sometimes the paperwork is overwhelming.
(Wernher von Braun)

Background image: Isostatic residual gravity anomaly image of the Gulf of Carpentaria, northwest, Queensland. The area shown is 450 km wide. Variations in the strength of the gravity field are shown in pseudo-colour, from high values as red to low values as blue (derived from Isostatic residual gravity anomaly map for Australia, Version 2, 2016; see Excursus 8.1 for details). **Source:** Geoscience Australia

Figure 8.1 Gravity, gravity variations, mass transport and distribution

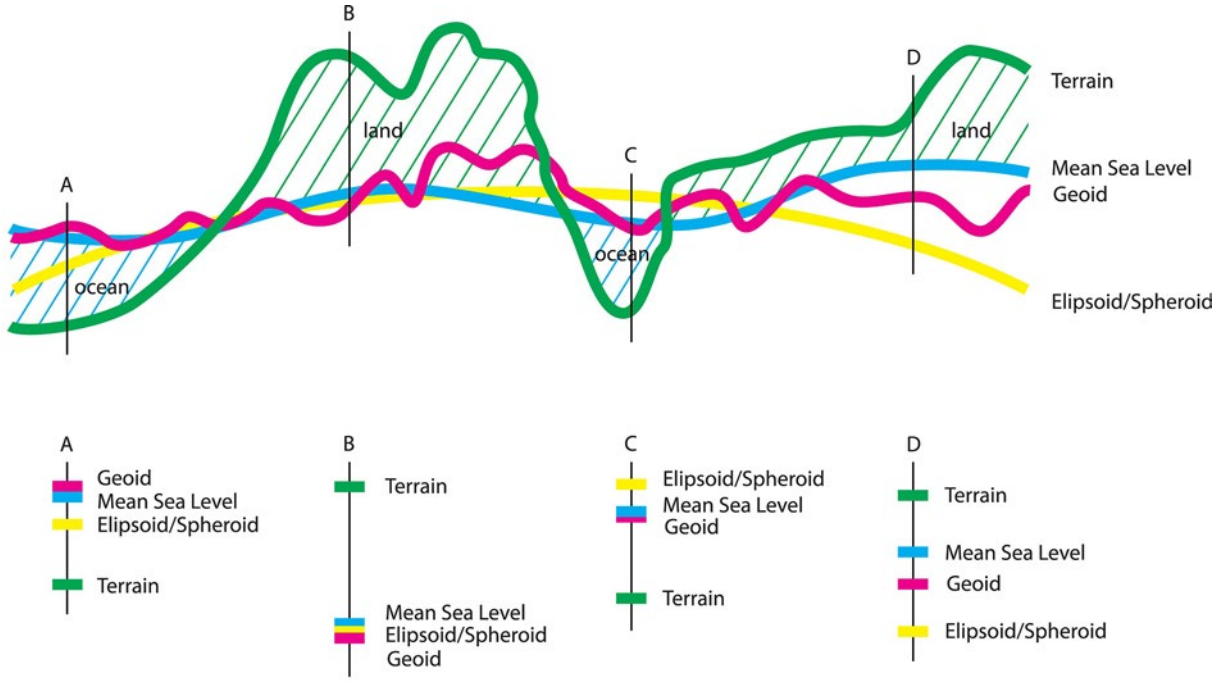
Gravity and its variations interact with the transport and distribution of masses above, on and within Earth to shape our planet.



Source: Ilk *et al.* (2005) p.4

Figure 8.2 Geoid surface

This illustration exaggerates the relationship between Earth's terrain, mean sea level, an ellipsoid/spheroid model and a geoid model. At locations A and C, Earth's terrain is below mean sea level with the geoid being close to mean sea level, so these sites would be typical of an area of surface water. At locations B and D, the terrain is higher than mean sea level, which implies land.



Source: © Commonwealth of Australia 2014 on behalf of the Intergovernmental Committee on Surveying & Mapping (ICSM). Retrieved from *http://www.icsm.gov.au/mapping/datums1.html*

8.2 Measuring Gravity

Gravimeters or pendulums are used to measure gravity on the ground. Gravimeters can be:

- relative—measure the relative difference in gravity between two locations using a calibrated spring; and
- absolute—precisely measure the acceleration of an object falling in a vacuum at a fixed location.

Relative gravimeters are portable and can be used in various vehicles.

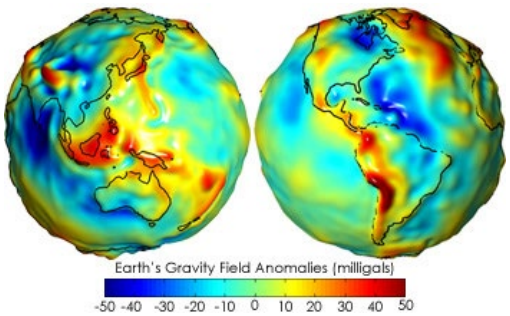
Airborne accelerometers and gradiometers have traditionally been used for continental gravity surveys, with the Global Positioning System (GPS) significantly improving the accuracy of flight line locations. These measurements can be presented as a map of gravitational 'anomalies', areas where measurements are higher or lower than the geoidal model. By convention, positive anomalies, where gravity is higher than the geoid, are coloured red, and negative anomalies, where gravity is lower than the geoid, are coloured blue (see Excursus 8.1).

Gravity anomalies often result from unusual concentrations of mass, such as a mountain range, which typically strengthen the gravitational force. Ocean trenches and land depressions can cause negative gravity anomalies (NASA, 2016). The most recent gravity anomaly map for Australia (Nakamura *et al*., 2011) is described in Excursus 8.1.

Since their orbital altitudes are influenced by Earth's gravitational field, spaceborne instruments offer another opportunity to measure gravity. Measurements of satellite orbital variations have enabled the development of regional and global geoidal models for land and seafloor surfaces (see Figure 8.3). Some of the sensors that underpin Space Geodetic Techniques are introduced in Excursus 3.2.

Figure 8.3 Global gravity field anomalies

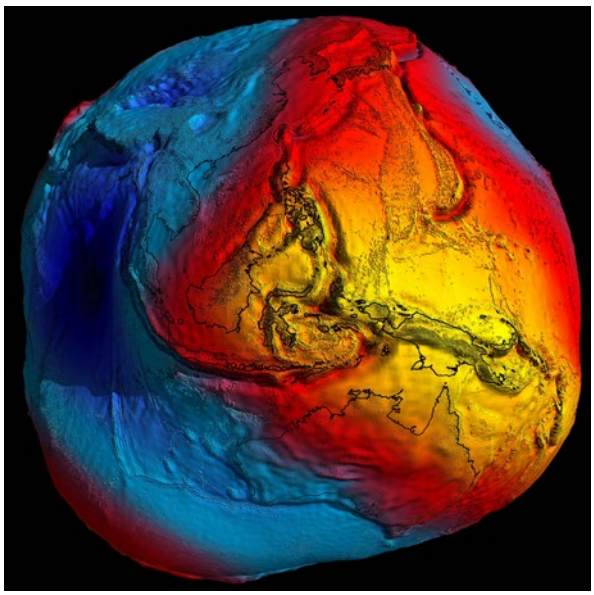
Gravity anomaly images highlight regions where gravitational force is higher or lower than the geoid. Mountainous regions typically have stronger gravitational forces than the geoid (hence have positive gravity anomalies), while ocean trenches and low-lying landmasses typically have weaker gravitional forces (or negative gravity anomalies).



Source: NASA (2016). Retrieved from *http://earthobservatory.nasa.gov/Features/GRACE/page3.php*

Figure 8.4 Global gravity derived from GOCE

This model, released on 28 March 2011, is derived from one year's data from the GOCE mission (ESA/HPF/DLR). Colours represent deviations from an ideal geoid, with blue being low values (down to -100 m) and red being high values (up to 100 m).



Source: ©ESA/HPF/DLR. Retrieved from *http://www.esa.int/spaceinimages/Images/2011/03/Best_view_yet_of_global_gravity*

Recent satellite missions have provided new means for measuring and mapping the Earth's gravity field. The Gravity Recovery and Climate Experiment (GRACE) developed a pair of satellites to precisely measure distances from Earth and each other, while the low-orbit Gravity field and steady-state Ocean Circulation Explorer (GOCE) used three pairs of accelerometers within a single satellite to measure the gravity field. Such detailed gravity measurements enable accurate mapping of the geoid (at centimetre level), and highlight geophysical features such as subduction zones at tectonic plate boundaries (see Figure 8.4).

Earth's gravity changes with rotation, surface composition and topography, water storage and movement, and interior structure. These factors necessitate ongoing monitoring of our gravity field. Continuous monitoring of the geoid has also quantified seasonal variations in gravity due to isostasy, that is, changes in the Earth's surface due to pressures such as ice cover.

Gravity measurement systems are further discussed in Volume 3.

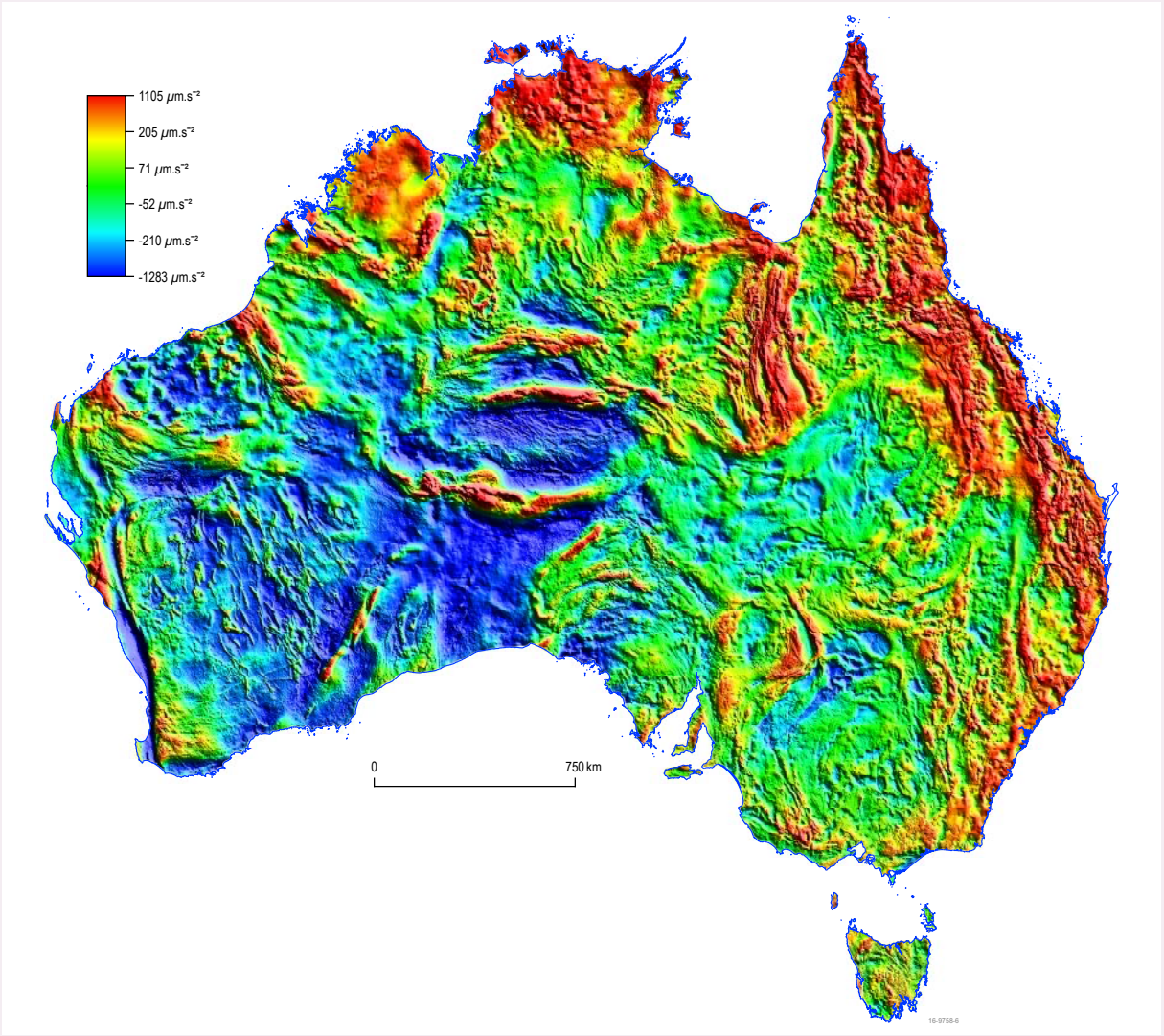
Excursus 8.1—Australian Gravity Anomaly Map

Source: Geoscience Australia AusGeo News 103, September 2011: *http://www.ga.gov.au/ausgeonews/ausgeonews201109/productnews.jsp*
Further Information: Tracey *et al.* (2008); Tracey and Nakamura (2010); Nakamura *et al.* (2011)

The most recent Isostatic Residual Gravity Anomaly Map of Australia at 1:5 million scale was released by Geoscience Australia in 2011 (see Figure 8.5). The map shows isostatic residual gravity anomalies across onshore Australia. Analysis of gravity anomaly values shows a relationship between terrain-corrected Bouguer anomaly values and the terrain height. This relationship is less evident after the isostatic correction, which improves the resolution of anomalies.

The dataset is derived from observations recorded at approximately 1,500,000 gravity stations (or reference points) held in the Australian National Gravity Database (ANGD) by Geoscience Australia. The onshore data were acquired by the federal, state and territory governments, the mining and exploration industry, universities and research organisations over the six decades since the 1950s.

Figure 8.5 Isostatic Residual Gravity Anomaly Map of Australia



Source: Geoscience Australia

And make us as Newton was, who in his garden watching
The apple falling towards England, became aware
Between himself and her of an eternal tie.
(Wystan Hugh Auden)

8.3 Gravity Applications

Given that the density of rocks in the Earth's crust affect the measured gravity at a particular location, gravity surveys can also be interpreted to remotely map the:

- distribution of rock types and rock structure;
- three-dimensional structure of sub-surface rocks to highlight potential energy or mineral resources;
- sub-surface structure for archaeological studies, urban engineering and military applications.

The Australian National Gravity Database (ANGD) is maintained by Geoscience Australia (GA). This database compiles gravity surveys in Australia undertaken by Federal, State and Territory governments, private companies and academic institutions. This data set is freely available online. The Australian Fundamental Gravity Network (AFGN), a network of permanent gravity base stations, serves as the datum for these gravity surveys (Geoscience Australia, 2016).

8.4 Further Information

Gravity: *http://www.ga.gov.au/scientific-topics/disciplines/geophysics/gravity*
http://www.ga.gov.au/about/what-we-do/projects/minerals/current/continental-geophysics/gravity

Gravity Field and Steady-State Ocean Circulation Explorer (GOCE): *http://www.esa.int/Our_Activities/Observing_the_Earth/The_Living_Planet_Programme/Earth_Explorers/GOCE/Satellite*
http://esamultimedia.esa.int/multimedia/publications/BR-285/pageflip.html

Gravity Recovery and Climate Experiment (GRACE):
ESA (2016)
NASA (2016)*http://earthobservatory.nasa.gov/Features/GRACE/*

8.5 References

ESA (2016). European Space Agency. Retrieved from *http://www.esa.int/ESA*.

Geoscience Australia (2016). Geoscience Australia. Retrieved from *http://www.ga.gov.au*.

Ilk, K. H., Flury, J., Rummel, R., Schwintzer, P., Bosch, W., Haas, C., Schröter, J., Stammer, D., Zahel, W., Miller, H., Dietrich, R., Huybrechts, P., Schmelig, H., Wolf, D., Götze, H. J., Riegger, J., Bardossy, A., Güntner, A., and Gruber, T. (2005). Mass Transport and Mass Distribution in the Earth System: Contribution of the New Generation of Satellite Gravity and Altimetry Missions to Geosciences. GOCE-Projekbüro Deutschland, Technische Universität München, GeoForschungsZentrum Potsdam, Munich, Germany. Retrieved from *http://mt.dgfi.tum.de/typo3_mt/fileadmin/Dokumente/programmschrift-Ed2.pdf*.

Nakamura, A., Bacchin, M., Milligan, P. R., Wynne, P., and Tracey, R. (2011). Isostatic Residual Gravity Anomaly Map of Onshore Australia, scale 1:5,000,000 (GEOCAT 69878). Geoscience Australia, Canberra, Australia.

NASA (2016). Gravity Recovery and Climate Experiment (GRACE). Retrieved from *http://earthobservatory.nasa.gov/Features/GRACE/page3.php*.

Tracey, R., Bacchin, M., and Wynne, P. (2008). A new absolute gravity datum for Australian gravity and new standards for the Australian National Gravity Database. Paper presented at the 19th International Geophysical Conference and Exhibition.

Tracey, R., and Nakamura, A. (2010). Complete Bouguer Anomalies for the Australian National Gravity Paper presented at the 21st International Geophysical Conference and Exhibition.



9 Vibrations

Vibrational waves are disturbances that transfer energy through different media. Sound waves (see Section 9.1) and seismic waves (see Section 9.2) are vibrations that can be sensed remotely to obtain information about the Earth.

Vibrational energy is measured using both active sensors (which emit energy and then record the echo from a target) and passive systems (which detect energy from another source). Vibrations are detected most commonly within water or solid earth. The measurements are formed into images to derive maps of surface properties, including the distance between the target and the sensor.

9.1 Sound Waves

Sound is a form of energy that is propagated as longitudinal or compression waves (see Figure 2.3a). Unlike EMR, which travels at a constant speed through a medium, and for which frequency and wavelength definitions can be used interchangeably, the speed of sound waves varies considerably with the elastic properties of the medium through which the waves are travelling. For example, in seawater, the speed of sound is a function of water density and compressibility, both of which are dependent on temperature, pressure, and salinity (see Figure 9.1):

- in deep ocean below 1500 m, the speed of sound is governed by pressure, so increases with depth;
- in upper ocean at equatorial and temperate latitudes, greater variation in temperature and some variation in salinity occurs, so the speed of sound is more variable, but tends to decrease with temperature; and
- minimum velocity occurs at the thermocline (Wells, 1986).

As a result, in ocean water the speed of sound is minimised at depths in the range 750–1,000 m. This zone of minimum speed is known as the Deep Sound Channel (DSC; formerly Sound Fixing and Ranging channel: SOFAR), and enables the guided propagation of undistorted sound for distances up to thousands of kilometres. This channel is commonly used for ocean acoustic tomography (Munk *et al.*, 1995) and submarine surveillance.

The human ear detects changes in the frequency of sound waves as changes in pitch. The range of human hearing is about 20–20,000 Hz. Sound above the human hearing range is generally known as ultrasound and that below the hearing range as infrasound. High frequency waves are heard as high pitch sounds and low frequency waves are heard as low pitch sounds.

In a spherical wave, such as a sound wave, energy propagates equally in all directions. As such, the power (P) emitted by the source is distributed evenly over a spherical surface (area = $4\pi r^2$), and assuming that there is no absorption in the medium, the intensity of the wave is given by the formulae:

$$intensity = \frac{P}{4\pi r^2}$$

Thus the intensity of a sound wave decreases with the square of the distance from the source, since the same amount of energy is spread over an increasingly larger area. The intensity of sound waves is measured in watts per square metre (W/m^{-2}). Since the human ear is capable of detecting sound levels across a very large range, however, sound intensity is usually measured using a logarithmic scale, in units of decibels (see Figure 9.2).

Background image: This seismogram shows one day's worth of aftershocks of three large earthquakes near Tennant Creek, Northern Territory in January 1988.
Source: Geoscience Australia

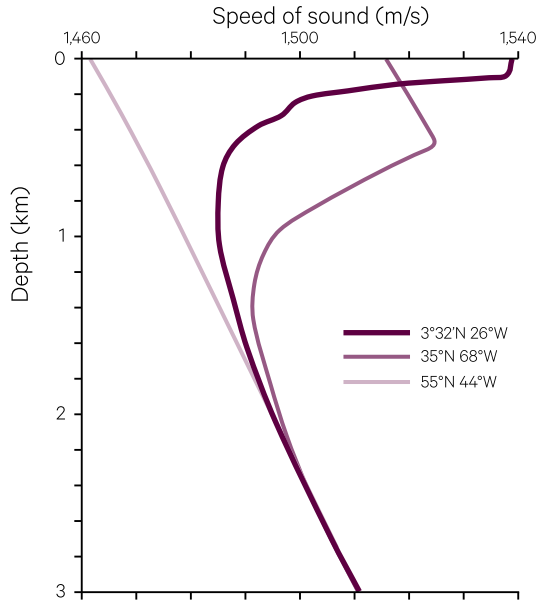
There is something very basic to the sense of listening.
The sense of hearing is the only one that operates totally from vibrations,
without other physical or chemical reactions to receive the sensations.
(Henry Reed)

Like other waves, sound waves undergo reflection, refraction and diffraction (see Section 2.5.2). The reflection of sound waves off surfaces can produce reverberations and echoes. Diffraction occurs when the wavelength of a sound wave is larger than an object it encounters, but if the wavelength is smaller than the object it tends to reflect off the object rather than diffract around it.

Figure 9.1 Speed of sound with varying water depth

In seawater, the speed of speed is mostly governed by temperatue and pressure. From the surface to 1000 m depth, the effect of temperature dominates. At depths greater than 1000 m, the effect of pressure is more dominant.

a. At equatorial latitude (3°32'N, 26°W)
b. At sub-tropical latitude (35°N, 68°W)
c. At sub-polar latitude (55°N, 44°W)



Adapted from: Wells (1986) Figure 2.4

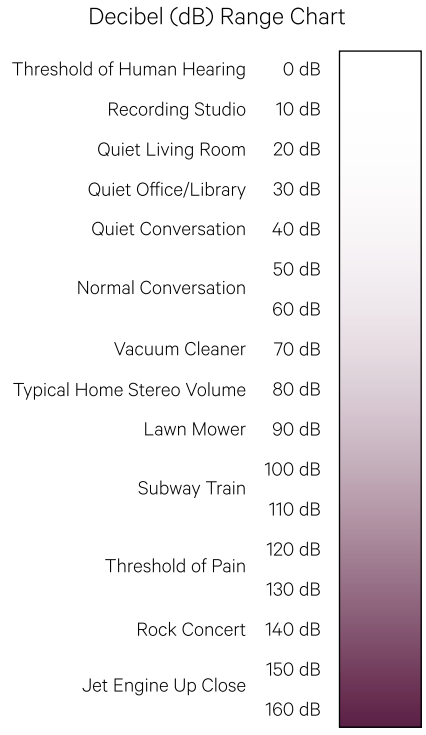
The Doppler effect (introduced in Section 2.5.4) is an observed rather than actual change in vibrational frequency. This effect is due to the relative movement of the sound source and the observer, such that when the observer and source are approaching each other the wave frequency seems higher than when they are moving apart.

When a sound source is moving at the same speed as the sound waves it is producing, a shock wave is created as the compression waves ahead of the source become 'bunched up' (see Figure 9.3a and 9.3b). Since waves are a disturbance to a medium, the shock wave can be considered to be the result of the medium not having time to compensate for the disturbance. An observer hears a shock wave as a sonic boom (see Figure 9.3c).

Sound waves may be detected by remote sensors, using both active and passive devices. Sonar (Sound Navigation and Ranging) is an active remote sensing technique for navigation, communication and detection under water. Techniques for sensing sound remotely are detailed in Volume 3.

Figure 9.2 Decibel range

Sound intensity is measured in units of decibels. Note: scale is logarithmic.



Source: Langlopress (2016)

Figure 9.3 Shock waves and sonic booms

a. Air becomes compressed ahead of a moving object, such as an aircraft. At subsonic speeds, sound is radiated in all directions. The perceived drop in pitch that occurs as an aircraft passes an observer is due to the Doppler Effect.

b. Compression of pressure waves increases with speed up to the speed of sound (Mach 1), forming a pressure cone starting at the nose of the aircraft.

c. Shock Waves are created when an object moves at, or faster than, the speed of sound. A Sonic Boom is heard when an observer's ear intersects the pressure cone from a supersonic aircraft. A vapour cloud can also occur around the aircraft as it breaks the sound barrier.



Source: Langlopress (2016)

9.2 Seismic Waves

Seismic (from) Greek, seismos meaning 'earthquake'

Seismology is the study of earthquakes and the associated propagation of seismic energy waves through the Earth. Earthquakes produce different types of seismic waves that display different characteristics in different materials. As a result, they can be used to map structures deep within the Earth.

9.2.1 What are earthquakes?

Earthquakes are the Earth's natural means of releasing stress. When the Earth's tectonic plates push against each other, the lithosphere becomes stressed and ultimately fractures or shifts, creating what is known as a fault (see Section 3). When such fractures occur, stress is released as vast quantities of energy that move through the Earth as vibrations. Tectonic plate boundaries coincide with the locations of most major earthquakes (see Figure 9.4). Intraplate earthquakes, which occur in the interior of tectonic plates, tend to be less significant and less common. Earthquakes occur rarely in Australia (mainland and Tasmania) and all are intraplate (Lewis and Collins, 2014).

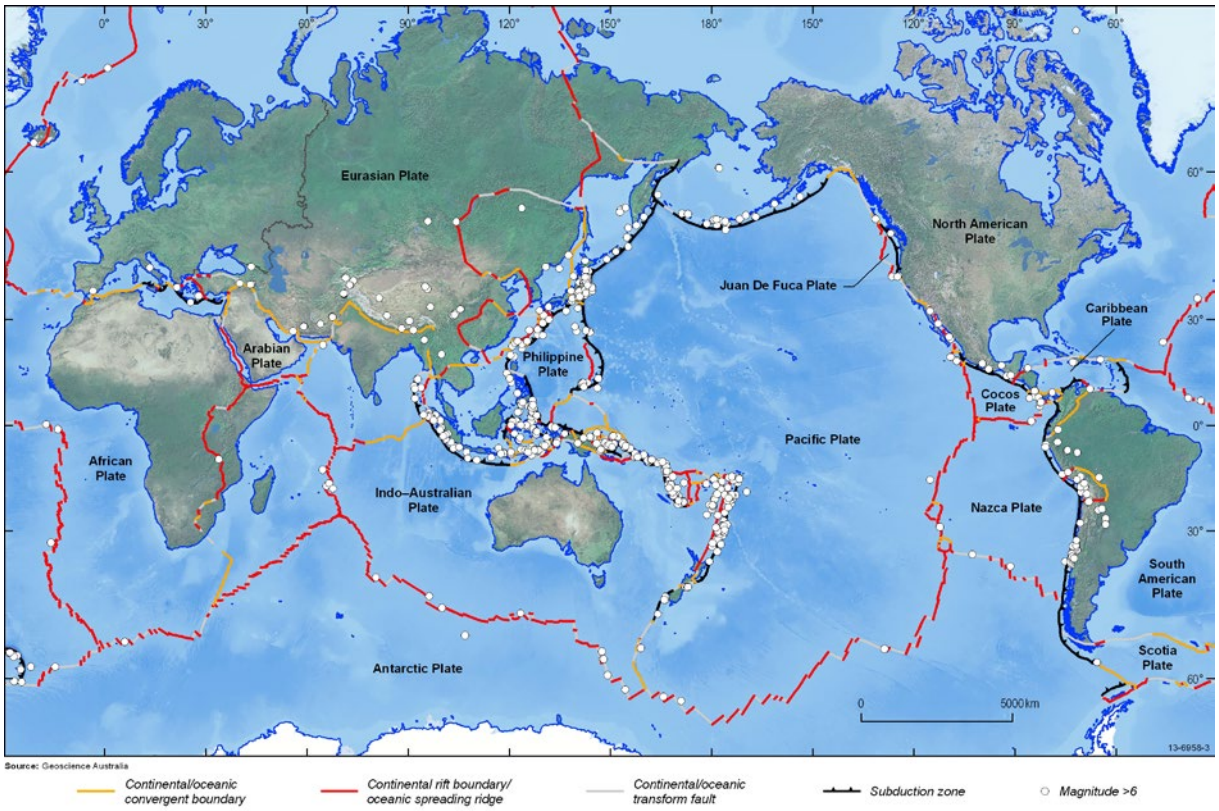
As the initial fracture in the lithosphere propagates, it releases energy along the fault, which may be up to 1,000 km long. The point of origin of an earthquake is called the focus and this may be close to the surface or many hundreds of kilometres below it. The point on the Earth's surface directly above the focus is called the epicentre (See Figure 9.5).

Earthquakes can result from both natural and human activities. Tectonic earthquakes occur when rocks in the Earth's crust break due to movement of tectonic plates (see Section 3.2). Earthquakes may also occur due to movement of magma in volcanoes, and serve as early warning of volcanic eruptions. Collapse earthquakes are associated with breakage of underground caverns and mines. Earthquakes can also result from detonation of nuclear and chemical devices, but these explosion earthquakes are characterised by different wave patterns and can thus be readily distinguished from natural events.

As seismologists gained more experience from earthquake records,
it became obvious that the problem could not be reduced to a single peak acceleration.
In fact, a full frequency of vibrations occurs.
(Charles Frances Richter)

Figure 9.4 Global earthquake occurrence

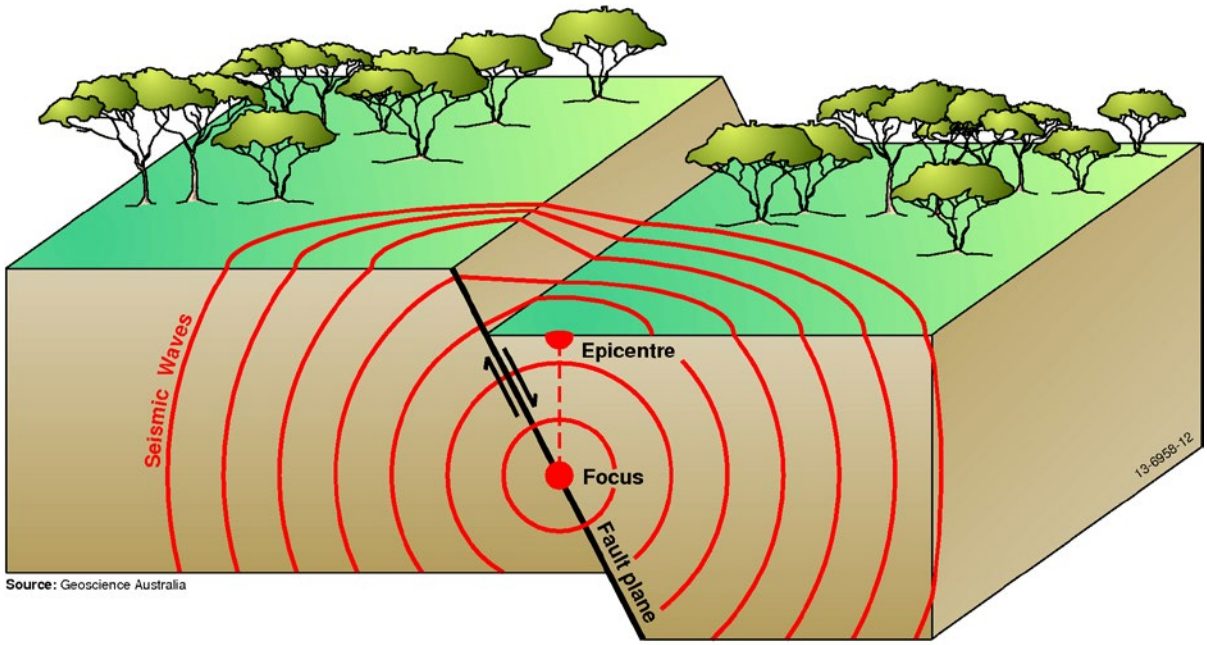
Most major earthquakes occur at tectonic plate boundaries, as a consequence of adjacent plates moving at different speeds in different directions. In Australia, most earthquakes are intraplate



Source: Lewis and Collins (2014) Figure 3

Figure 9.5 Earthquake focus and epicentre

An earthquake originates from a location known as the focus. The point on the Earth's surface that is directly above the focus is called the epicentre. This illustration shows an earthquake resulting from displacement of the Earth's crust along a fault plane. Seismic waves carry energy generated by the earthquake away from the focus in all directions.



Source Lewis and Collins (2014) Figure 12

If you want to find the secrets of the universe, think in terms of energy, frequency and vibration.
(Nikola Tesla)

9.2.2 Types of seismic waves

Two major types of seismic waves are generated by earthquakes:

- body waves—which rapidly travel through the interior of Earth (see Section 9.2.2.1); and
- surface waves—which destructively travel along the surface of Earth (see Section 9.2.2.2).

9.2.2.1 Body waves

Body waves travel more quickly that the destructive surface waves. Two forms of body waves travel through the interior of the Earth:

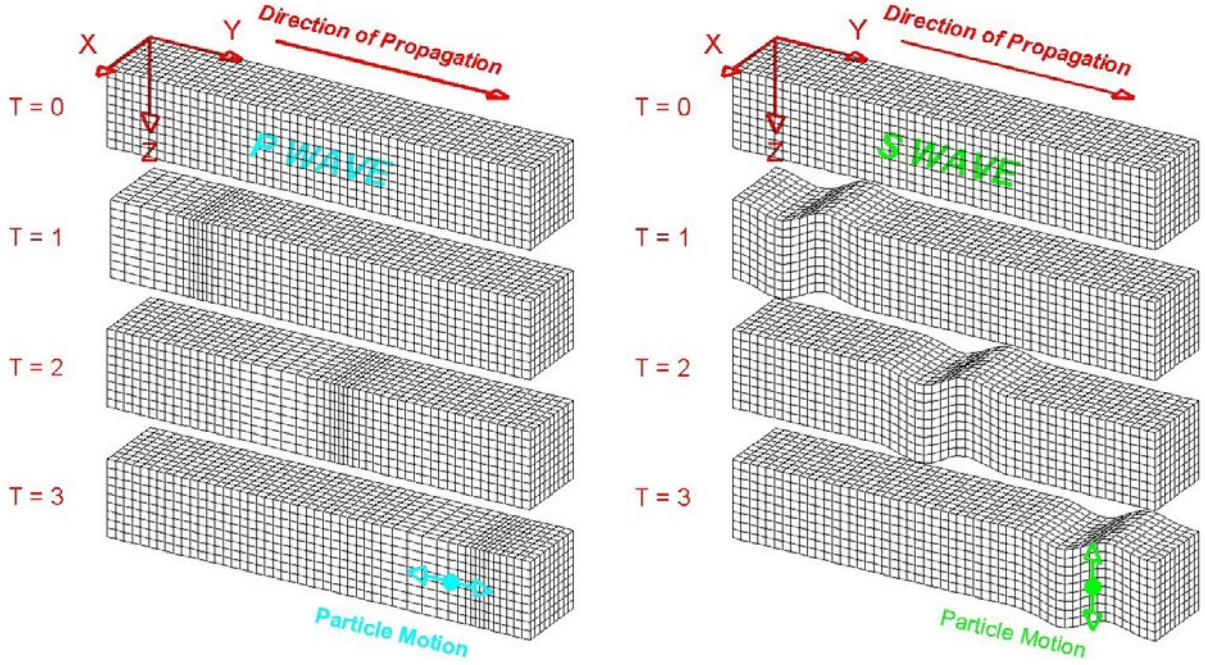
- P-waves—Primary waves are compression or longitudinal waves that propagate using a 'push-pull' motion, by alternating from compression to expansion in the direction of wave movement (see Figures 2.3a and 9.6a). P-waves travel through all types of media (solid, liquid and gas) and temporarily change its volume (Lutgens and Tarbuck, 1998). They typically travel at speeds of 8–14 km/s in the crust and mantle, generally increasing with depth to the core-mantle boundary. Being the fastest seismic waves, they are the first to be detected when an earthquake occurs; and
- S-waves—Secondary (or shear) waves are transverse waves, which only travel through solid media, and effectively 'shake' the particles of the media (see Figures 2.3b and 9.6b). These waves travel more slowly than P-waves, in the range of 4–7 km/s in the crust and mantle, generally increasing with depth to the core-mantle boundary. The lower speeds correspond to the waves in loose, unconsolidated sediment, the higher to those near the base of Earth's mantle. S-waves move rock particles in a direction that is perpendicular to the wave direction, that is, up and down or side-to-side. They are also called Shear waves because they don't change the volume of the material through which they propagate but rather shear, or fracture, it (Lutgens and Tarbuck, 1998).

Figure 9.6 Body waves

Body waves travel through Earth's interior as primary (P) or secondary (S) waves. In these diagrams, particles are represented by cubes.

a. P-waves are compression or longitudinal waves that alternate between compression and expansion in the direction of wave propagation.

b. S-waves are transverse waves that shake rock particles in direction perpendicular to wave propagation.



Source: Braille (2006) Figures 1 and 2. © L. Braille with permission granted to reproduce for non-commercial purposes

9.2.2.2 Surface waves

Surface waves, generated by the interaction of P-waves and S-waves with the surface of the Earth and with each other, only travel through the surface of Earth's crust, albeit at varying depths. They have a lower frequency than body waves, but are responsible for most of the damage associated with earthquakes.

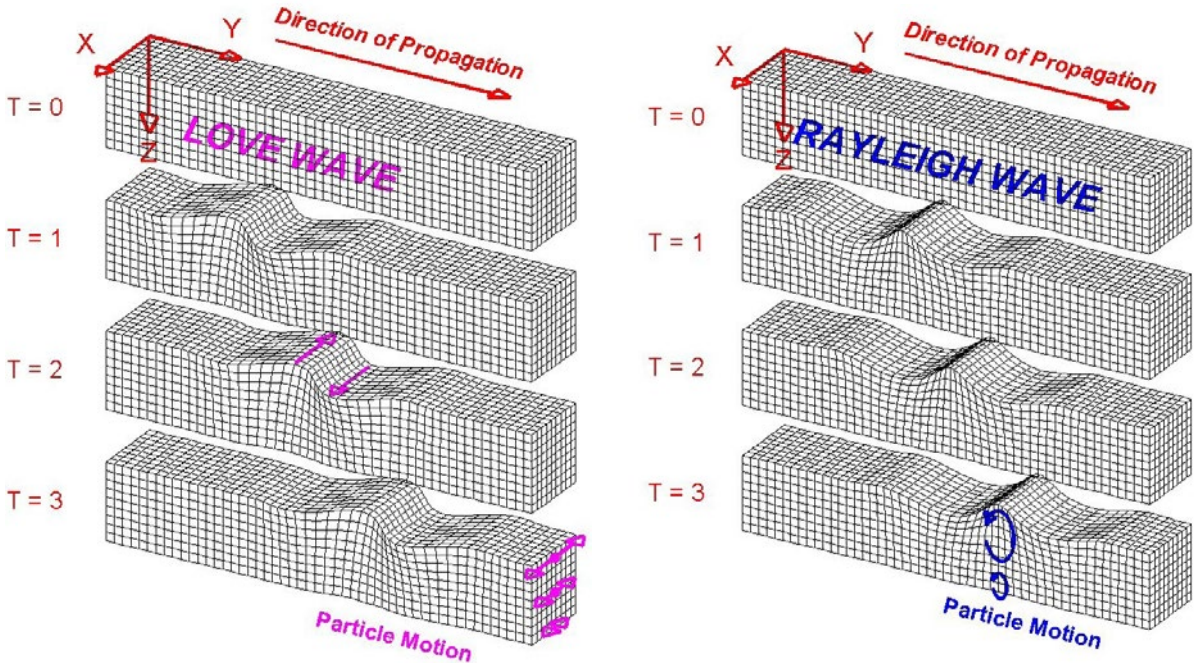
Two different types of surface waves have been observed: Love waves and Raleigh waves. Love waves result from S waves that are trapped near the surface of the Earth while Raleigh waves form when P and S waves interact with each other near the surface of the Earth. Love waves are the faster surface waves, travelling at over 4 km/s (~15,000 km/hour) and move in a horizontal plane (see Figure 9.7a), while the slower Rayleigh waves roll along the surface creating vertical movement of the Earth's crust (see Figure 9.7b).

Figure 9.7 Surface waves

Surface waves travel through the Earth's crust at different depths. In these diagrams, particles are represented by cubes.

a. Love waves travel most quickly in a horizontal plane.

b. Rayleigh waves roll along the surface, creating vertical movement of the Earth's crust.



Source: Braille (2006) Figures 3 and 4. © L. Braille with permission granted to reproduce for non-commercial purposes.

9.2.3 Using seismic waves to determine the structure of Earth

If the interior of the Earth had uniform composition and density, seismic waves would emanate from an earthquake and travel in straight paths, showing a proportional increase in time to travel greater distances and with uniform reduction in strength. However, body waves travel faster in the mantle than in the crust, which suggests that the mantle is denser. P-waves die out about 105° from the epicentre, then reappear about 140° away, and arrive much later than expected (see Figure 9.8). The region without P-waves is called the P-wave shadow zone. S-waves die out completely around 105° from the epicentre. This discrepancy implies that part of the Earth's core comprises liquid, not solid material. More recently, using improved seismographs, a solid inner core has also been distinguished.

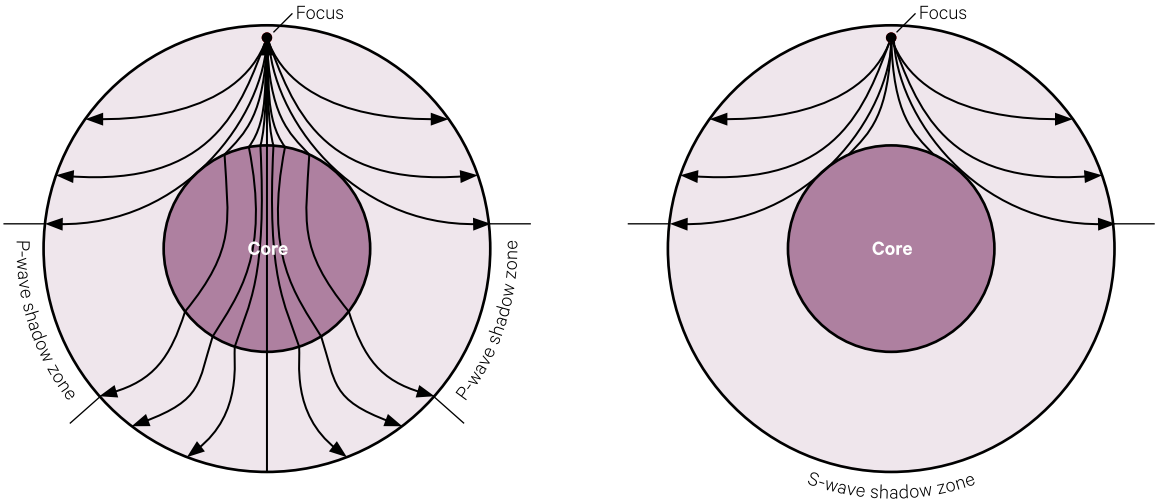
The relatively new imaging technique of seismic tomography uses seismic waves to detect very slight seismic velocity differences, which indicate variations in temperature throughout the mantle (see Section 3.2). Since waves move faster through cold material and slower through hot material, these images contribute to our understanding of the process of convection in the mantle.

Figure 9.8 Shadow zones for seismic waves

Seismic shadows are areas of the Earth, relative to the epicentre of an earthquake, where seismic waves are not detected. These are usually defined as angular distances from the epicentre on a plane through the centre of the Earth.

a. P-waves are refracted by the liquid outer core of Earth, so are not detected in two P-wave shadow zones between angular distances 105° to 140° from the epicentre.

b. S-waves do not propagate through the liquid outer core, which results in a S-wave shadow zone comprising all angular distances greater than 105° from the epicentre.



Adapted from: Earth Science Australia (CC BY NC SA 3.0) at *http://earthsci.org/index.html*

9.2.4 Detecting seismic waves

Seismographs are used to record the energy generated by earthquakes. When seismic waves are detected by a seismograph, their size and duration are recorded as a seismogram. By combining the information from several seismographic recordings, the epicentre and focus of the earthquake can be located using triangulation. More modern approaches use Earth models of seismic velocity to compare predicted and measured seismic wave arrivals. By adjusting the earthquake parameters like origin time and focal point the differences or residuals can be minimised to produce the most accurate location solution. Traditional instruments employed a pen on a pendulum-like arm that recorded ground movements on a revolving drum. Current instruments use electronic sensors connected directly to computers that can provide instant access to seismic information from locations all around the globe.

Because P-waves are the fastest seismic waves, they will typically be the first ones recorded, followed by S-waves, which, while slower, are generally larger. Surface waves travel a little slower than S-waves so they are generally recorded just after the S-waves. For shallow earthquakes, the surface waves may be the largest waves recorded by the seismograph and they are often the only ones recorded a long distance from medium-sized earthquakes.

A number of standard scales have been used to compare earthquakes. These use logarithmic scales to describe:

- magnitude—the extent of shaking caused by the earthquake; or
- intensity—the destructive power of released energy from the earthquake.

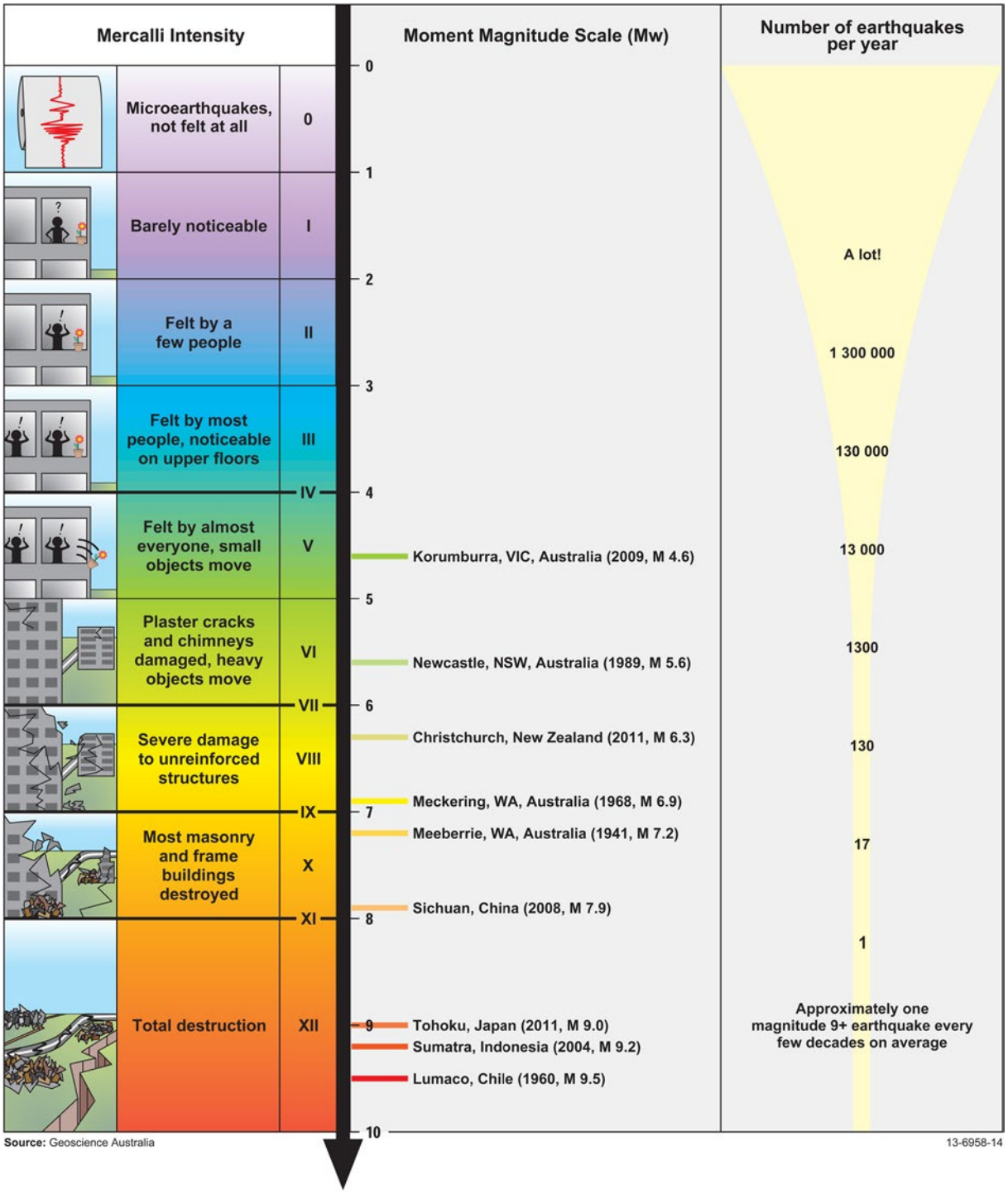
Common examples of earthquake comparison scales include:

- Richter scale (Richter, 1935), which measures magnitude in logarithmic increments;
- Modified Mercalli scale (Wood and Neumann, 1931) which describes intensity in 12 qualitative increments, expressed in roman numerals; and
- Moment magnitude scale (M_W; Hanks and Kanamori, 1979) which considers the total energy release of the earthquake, that is the distance the relevant fault or fracture actually moved during the earthquake and the force that was required to move it. The M_W generates more precise magnitudes than the Richter scale over a wider range of earthquakes, and has been the official scale used by USGS since 2002 (see Figure 9.9).

The number of seismic stations has increased from about 350 in 1931 to many thousands, which means that many more earthquakes are now being detected. The USGS estimates that, since 1900, there have been an average of 18 major earthquakes (magnitude 7.0-7.9) and one great earthquake (magnitude 8.0 or greater) per year, and that this average has been relatively stable (USGS, 2016).

Figure 9.9 Global earthquake frequency and energy

The Modified Mercalli Intensity scale is compared with the Moment Magnitude Scale for some recent earthquakes. The average global frequency of global earthquakes is shown relative to their magnitude.



Source: Lewis and Collins (2014) Figure 14

9.3 Further Information

Sonar:

http://www.nauticalcharts.noaa.gov/hsd/SSS.html

Seismology:

Australia

Geoscience Australia: *http://www.ga.gov.au/scientific-topics/hazards/earthquake*

Lewis and Collins (2014)

South Australia, Primary Industries and Resources South Australia: *http://www.pir.sa.gov.au/minerals/earthquakes/*

The University of Western Australia: *http://www.seismicity.see.uwa.edu.au*

The University of Queensland: *http://www.quakes.uq.edu.au*

Earth Science Australia: *http://earthsci.org/index.html*

Bureau of Meteorology, Australian Tsunami Warning Centre: *http://www.bom.gov.au/tsunami/about/jatwc.shtml*

USA

US Geological Survey Earthquake Hazards Program: *http://earthquake.usgs.gov/*

UPSeis: *http://www.geo.mtu.edu/UPSeis/waves.html*

Incorporated Research Institutions for Seismology (IRIS): Comprehensive site with animations of earthquakes and a live world map showing locations and magnitudes of earthquakes in real time: *http://www.iris.edu/hq*

9.4 References

Braille, L. W. (2006). Seismic Waves and the Slinky. The IRIS Consortium, Purdue University. Retrieved from *http://web.ics.purdue.edu/~braile/edumod/slinky/slinky4.htm*.

Hanks, T. C., and Kanamori, H. (1979). A moment magnitude scale. Journal of Geophysical Research: Solid Earth, 84(B5), pp. 2348-2350. doi:*http://dx.doi.org/10.1029/JB084iB05p02348*.

Langlopress (2016). Scientific Illustrations. Retrieved from *http://langlopress.net/homeeducation/resources/science/index.php?op=sciencethumbs*.

Lewis, G., and Collins, C. (2014). Earthquakes - Teacher notes and student activities (2014/06). Geoscience Australia, Canberra. Retrieved from *https://d28rz98at9flks.cloudfront.net/76611/Rec2014_006.pdf*. doi:*http://dx.doi.org/10.11636/Record.2014.006*.

Lutgens, F. K., and Tarbuck, E. J. (1998). Essentials of Geology, 6th Edn. Prentice Hall, New Jersey, USA.

Munk, W., Worcester, P., and Wunsch, C. (1995). Ocean Acoustic Tomography. Cambridge University Press.

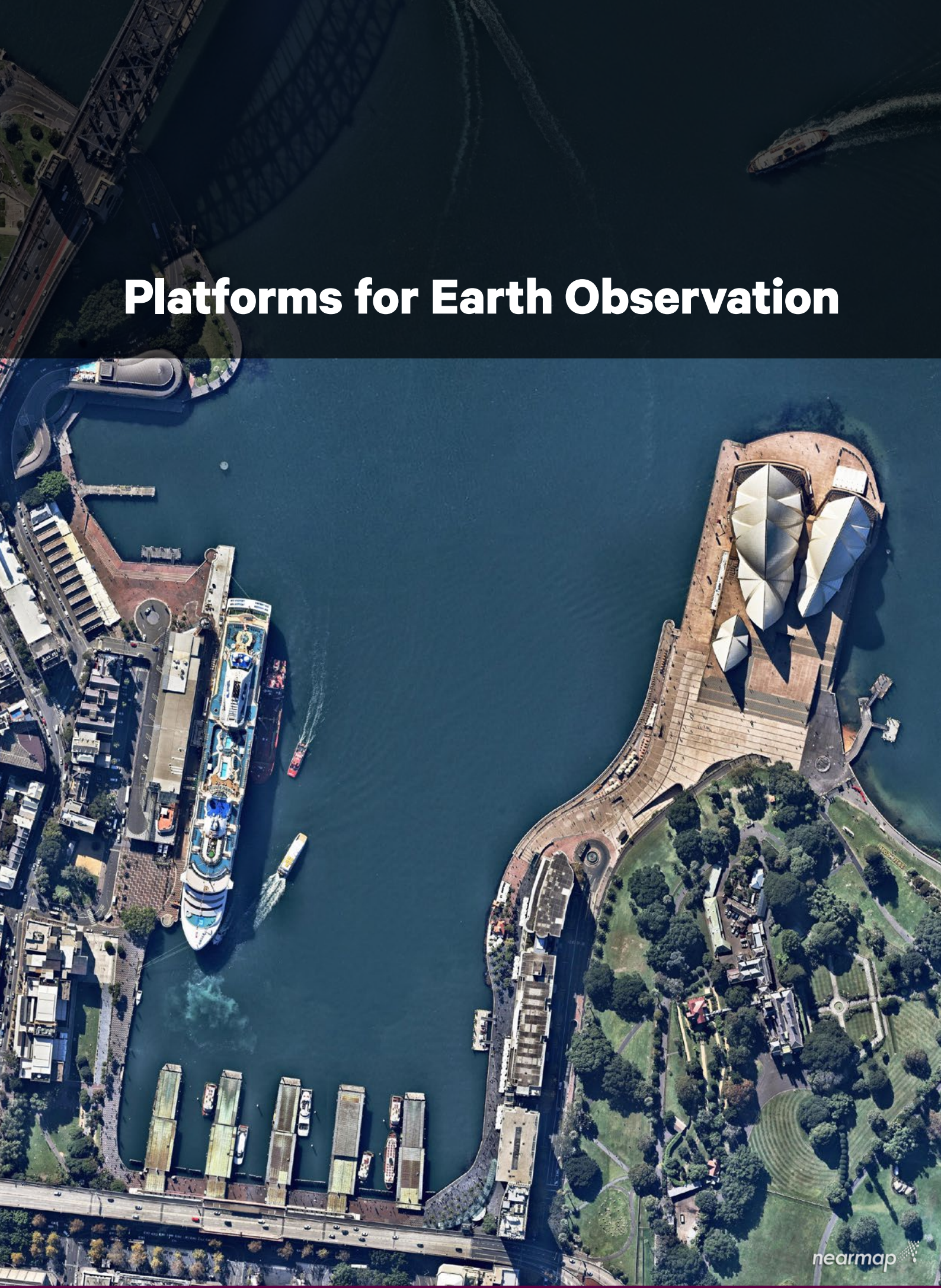
Richter, C. F. (1935). An instrumental earthquake magnitude scale. Bulletin of the Seismological Society of America, 25(1), pp. 1-32.

USGS (2016). US Geological Survey Earthquake Hazard Program. Retrieved from *http://earthquake.usgs.gov*.

Wells, N. (1986). The Atmosphere and Ocean: A Physical Introduction (347 pages). Taylor & Francis, London.

Wood, H. O., and Neumann, F. (1931). Modified Mercalli intensity scale of 1931. Bulletin of the Seismological Society of America, 21(4), pp. 277-283.

Platforms for Earth Observation



Remote sensing devices—both analogue and digital—may be operated from a variety of platforms. These can range from elevated, but ground-based, platforms such as tripods and cherry pickers, through balloons and aircraft (both manned and unmanned) at various altitudes within the Earth's atmosphere (up to about 100 km), to spacecraft, which operate outside the atmosphere. These different types of platforms provide variable performance in terms of image quality and repetitive coverage. The most commonly used platforms for remote sensing have been piloted aircraft and spacecraft, but deployment of remotely piloted or tower-mounted remote sensors is rapidly increasing.

Non spaceborne platforms such as aircraft, balloons, flux towers, hand-held instruments and ground sensors provide essential calibration and validation information for spaceborne sensor data and also offer valuable information in their own right. In addition to the use of specific sensors near the Earth, remotely sensed data has traditionally been compared with measurements and observations of ground features obtained from field surveys. This data is used to characterise specific sample locations, as points, lines or areas. Such locations or sites may be temporary or permanent, depending on the purpose of the survey, and its associated funding. There are now numerous national and international programs consistently and systematically collecting ground reference data for calibration and validation of remotely sensed data. The use of field data is further discussed in Section 10 below, Volume 1B—Section 9, and Volume 2E—Section 10.

The following sections describe the three broad types of platform used for Earth Observation (EO):

- ground-based (see Section 10);
- airborne (see Section 11); and
- spaceborne (see Section 12).

Contents

10 Ground-based Platforms 129

11 Airborne Platforms 139

12 Spaceborne Platforms 145

Background image on previous page: Nearmap high resolution airborne image acquired on 5 May 2016 over the Sydney Opera House. **Source:** © Nearmap



10 Ground-based Platforms

Ground-based observations are collected to calibrate, validate and supplement airborne and spaceborne data. These can involve the use of *in situ* or 'proximal' sensors, mobile sensors or people, including hand-held sensors, vehicle-mounted sensors, temporary ground-based sensors and measurement of atmospheric properties. Such observations require accurate knowledge of location and typically provide a direct measure of some biophysical property for a specific target. 'Close' measurements enable the spectral properties of materials to be characterised directly, without interference from the atmosphere.

Ground-based measurements allow field sites to be monitored more frequently to identify variations related to diurnal and seasonal cycles, and more flexibly to respond to specific climatic events or emergencies. The spatial density of measurements can be designed to match the distribution and density of specific features, such as individual plants, and changed and repeated as required. As less expensive and more reliable hardware has become available, the use of ground-based remote sensors has increased rapidly, and this trend is expected to continue (Wark *et al.*, 2011).

Calibration data are also necessary to accurately locate observations on the ground. These data take many forms including Global Positioning System (GPS) locations, reflective targets, satellite laser ranging (to improve knowledge of the location of the satellite; see Volume 1B—Section 9), reference images and digital elevation models (see Volume 2A—Section 3 for details of image calibration approaches).

10.1 In situ

The calibration and validation (CalVal) of Earth Observation (EO) observations, and validation of information derived from the data, are increasingly reliant on records from *in situ* or proximal sensors installed at strategically located field sites. *In situ* sensors are generally installed in a network to measure specific physical properties of landscape attributes (such as water, leaves, or soil).

Instrumentation at CalVal sites record measurements continuously, or at regular intervals, for relevant physical parameters of the Earth surface and the atmosphere. *In situ* sensors are being used to record a wide range of measurements related to vegetation and carbon dynamics, soil moisture, gravity fields, topography, bathymetry, ocean colour, water quality, sea ice, and meteorology. Examples of *in situ* sensors include:

- lidar—used to determine Leaf Area Index (LAI) and vegetation profiles (e.g. VEGNET[21], Culvenor *et al.* (2014); Portillo-Quintero *et al.* (2014); see also Volume 3A);
- IR thermometer or thermal camera—used to measure soil, water or vegetation temperature. (In vegetation, temperature variations are related to plant vigour since increased photosynthesis means increased transpiration resulting in a cooler plant.);
- solar radiometers—used to measure insolation;
- spectrometers—used to characterise vegetation, water and soil reflectance;
- video—used to identify species and/or monitor movement of plants, animals and clouds;
- audio—used to characterise sound spectrum, which has been linked to a 'naturalness index';

Background image: Intensity image created from the 1556 nm laser output of DWEL. This scan was taken in the Himalayan Cedar forest at the National Arboretum, Canberra. **Source:** Michael Schaefer, TERN AusCover/University of New England

21. *http://www.sensingsystems.com.au/public/VEGNET.pdf*

- carbon dioxide sensors—used to measure ecosystem-atmosphere exchanges in order to estimate primary productivity and carbon balances;
- soil water sensors—used to monitor the moisture available for plant growth;
- weather sensors—used to measure air temperature and pressure, precipitation, relative humidity, wind speed and direction; and
- cameras—including:
  - high spatial resolution digital images—used to characterise sample sites in detail; and
  - time-lapse photography—used to monitor phenology and temporal changes.

Figure 10.1 Dual wavelength Echidna™ LIDAR (DWEL)

DWEL is a dual wavelength, ground-based lidar which can generate three-dimensional images of ground scenes.

a. DWEL instrument in operation.



- In particular, gigapixel imagery (one billion (10^9) pixels) capture very high spatial resolution in visible and NIR wavelengths for a broad range of applications (Brown *et al*., 2012).

An example of one *in situ* sensor is the Dual Wavelength Echidna LIDAR (DWEL) illustrated in Figure 10.1, which comprises two lasers with different wavelengths that can generate precise three-dimensional images of forests and other objects, such as buildings. Such information provides a detailed record of structure at a particular time, and can be updated at selected time intervals to quantify change. VEGNET is a vegetation monitoring instrument that automatically scans the canopy on a daily basis using an upward-looking LIDAR sensor (see Figure 10.2). Operated as stand-alone instruments or as part of a distributed sensor network, this system complements the detailed three-dimensional structure measurements from Echidna by capturing the temporal variability in canopy structure (Culvenor *et al*., 2014; Portillo-Quintero *et al*., 2014; Griebel *et al*., 2015).

Calibration and validation … can be considered a process that encompasses the entire system, from remote sensing instrument to data product. The objective is to develop a quantitative understanding and characterization of the measurement system and its biases in time and space.
(National Research Council, 2007)

b. False colour scan of Tumbarumba Forest using the Dual Wavelength Echidna LiDAR (DWEL), acquired August 2014. Dark colours shown the woody fraction and green colours show the vegetation fraction. Shading is scaled by distance such that lighter shades are further away from the scanner.



Source: Michael Schaefer, TERN Auscover/University of New England.

Figure 10.2 VEGNET scanner

VEGNET is a vegetation monitoring instrument that automatically scans the canopy on a daily basis using an in situ, upward-looking LIDAR sensor. This time lapse photo of VEGNET shows a few minutes of the laser scan.



Source: Amory Culvenor and Darius Culvenor, Environmental Sensing Systems

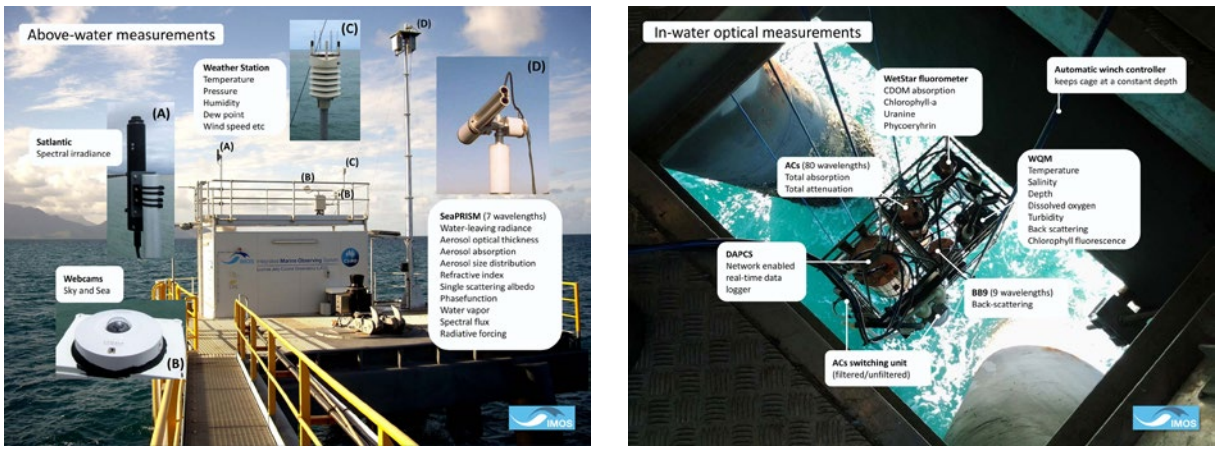
In Australia, CalVal sites are often designed to satisfy international scientific standards. Field sites enable collaboration with international EO researchers and are an important mechanism for interaction with satellite operators. Calibration sites at stable target locations ensure that the accuracy of airborne and EO data is known for specific conditions. Most developed countries now operate public data collection and sharing portals for ecosystem data, including CalVal data for remote sensing. In Australia, this capability is provided by the Terrestrial Ecosystem Research Network (TERN[22]) and the Integrated Marine Observing System (IMOS[23]), along with key agencies such as Geoscience Australia, CSIRO and the Bureau of Meteorology. For example, an observation jetty for in-water measurements that is managed by CSIRO under IMOS is illustrated in Figure 10.3.

Towers that reach above vegetation canopies are being increasingly used for proximal sensing in terrestrial landscapes (see Figure 10.4). These instrumented towers or 'flux' towers house a range of sensors to remotely sense physical and chemical characteristics of key atmospheric and ecosystem processes. An international network of over 500 flux towers has been established to provide continuous, long-term micrometeorological measurements for global ecosystem monitoring, with a focus on understanding energy, carbon and water exchange between the atmosphere and major ecosystems. Flux towers use a suite of instruments and eddy covariance methods to measure exchanges of carbon dioxide, water vapour and energy between terrestrial ecosystems and the atmosphere (see also Volume 3). In the USA, the National Ecological Observatory Network (NEON)[24] will comprise 106 terrestrial and aquatic sites, which represent a diversity of vegetation, landforms, climate and ecosystem performance. Flux towers located at NEON terrestrial sites routinely measure the physical, chemical and biological parameters listed in Figure 10.5. The TERN OzFlux[25] network performs a similar function in Australia and New Zealand, comprising over 30 sites in a variety of locations and landscapes (see Figure 10.6).

Figure 10.3 Marine in situ sensors

a. Lucinda Jetty Coastal Observatory (IMOS/CSIRO) showing instruments used for above-water measurements

b. Lucinda Jetty Coastal Observatory (IMOS/CSIRO) showing instruments used for in-water optical measurements

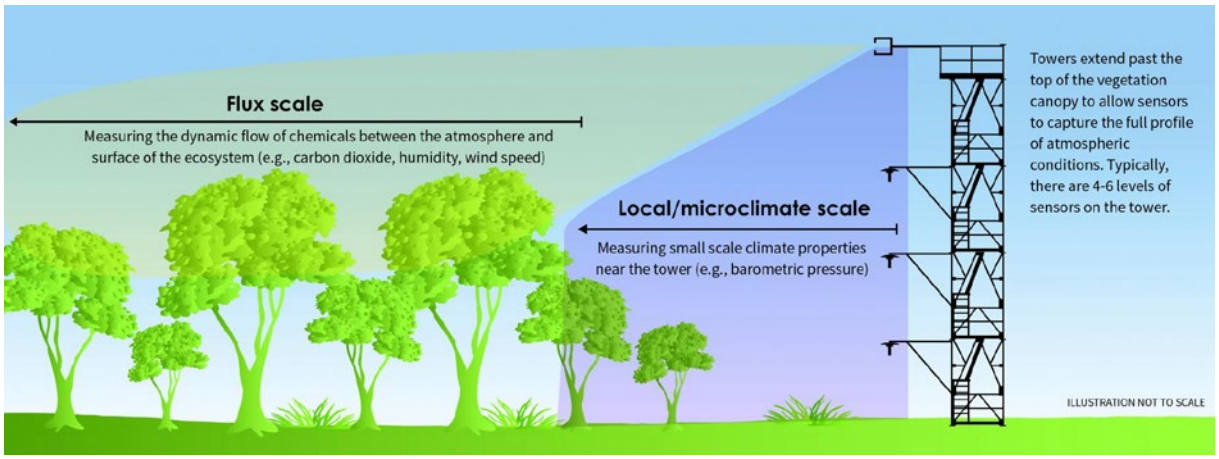


Source: Thomas Schroeder, CSIRO. IMOS (2016). Data was sourced from the Integrated Marine Observing System (IMOS), a national collaborative research infrastructure, supported by the Australian Government.

22. TERN: *http://www.tern.org.au*
23. IMOS: *http://www.imos.org.au*
24. NEON: *http://www.neonscience.org*
25. TERN OzFlux: *http://www.ozflux.org.au*

Figure 10.4 Flux Tower Function

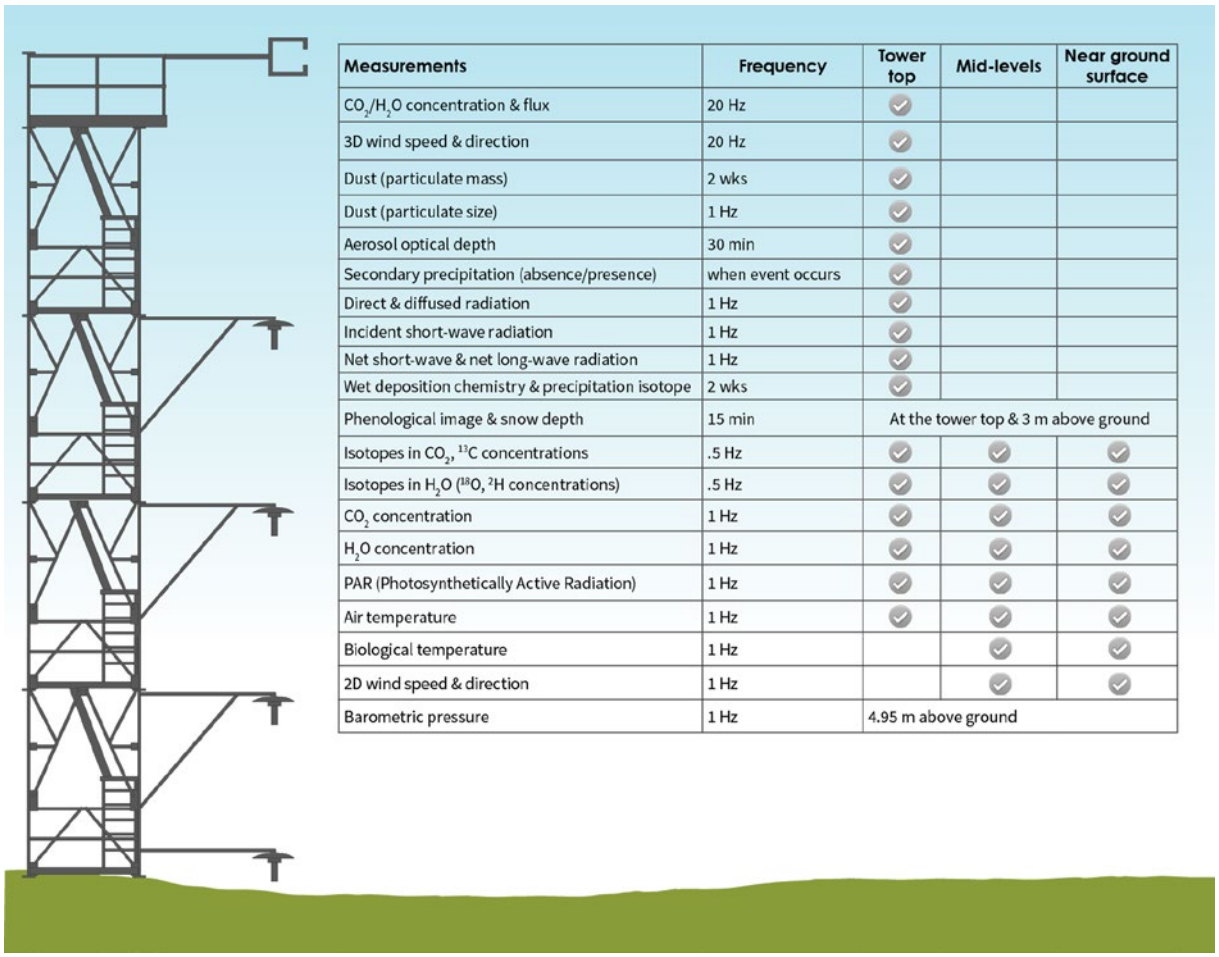
Flux towers use a suite of instruments and eddy covariance methods to measure exchanges of carbon dioxide, water vapour and energy between terrestrial ecosystems and the atmosphere.



Source: National Ecological Observatory Network, Inc (NEON). Retrieved from http://www.neoninc.org/science-design/collection-methods/flux-tower-measurements The information provided may not have been reviewed or prepared by the NEON. It is provided AS IS without any warranty of any kind, express or implied, and may not reflect NEON's views or opinions.

Figure 10.5 NEON flux tower measurements

Flux towers located at terrestrial sites in the National Ecological Observatory Network (NEON) routinely measure the parameters listed below.



Measurements	Frequency	Tower top	Mid-levels	Near ground surface
CO_2/H_2O concentration & flux	20 Hz	✓		
3D wind speed & direction	20 Hz	✓		
Dust (particulate mass)	2 wks	✓		
Dust (particulate size)	1 Hz	✓		
Aerosol optical depth	30 min	✓		
Secondary precipitation (absence/presence)	when event occurs	✓		
Direct & diffused radiation	1 Hz	✓		
Incident short-wave radiation	1 Hz	✓		
Net short-wave & net long-wave radiation	1 Hz	✓		
Wet deposition chemistry & precipitation isotope	2 wks	✓		
Phenological image & snow depth	15 min	At the tower top & 3 m above ground		
Isotopes in CO_2, ^{13}C concentrations	.5 Hz	✓	✓	✓
Isotopes in H_2O (^{18}O, ^{2}H concentrations)	.5 Hz	✓	✓	✓
CO_2 concentration	1 Hz	✓	✓	✓
H_2O concentration	1 Hz	✓	✓	✓
PAR (Photosynthetically Active Radiation)	1 Hz	✓	✓	✓
Air temperature	1 Hz	✓	✓	✓
Biological temperature	1 Hz		✓	✓
2D wind speed & direction	1 Hz		✓	✓
Barometric pressure	1 Hz	4.95 m above ground		

Source: National Ecological Observatory Network, Inc (NEON). Retrieved from http://www.neoninc.org/science-design/collection-methods/flux-tower-measurements The information provided may not have been reviewed or prepared by the NEON. It is provided AS IS without any warranty of any kind, express or implied, and may not reflect NEON's views or opinions.

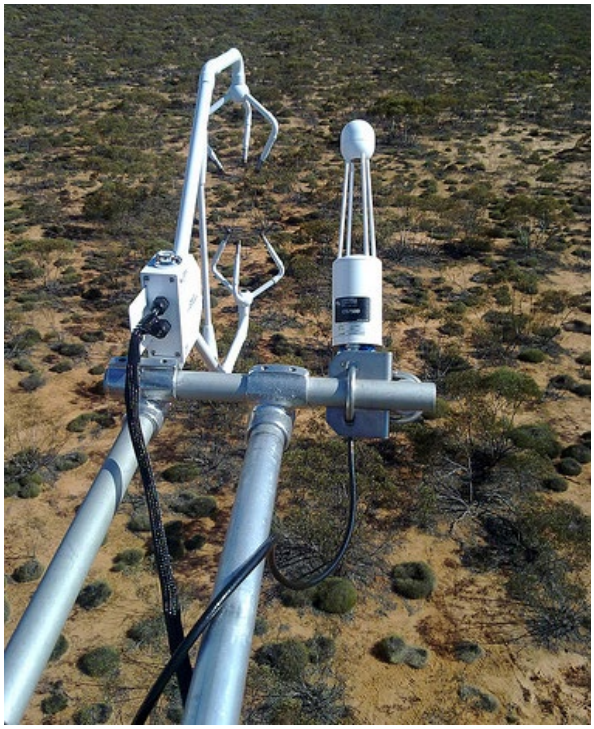
Figure 10.6 TERN OzFlux flux towers

The TERN OzFlux network in Australia and New Zealand comprises flux towers at over 30 sites in a variety of locations and landscapes.

a. 80m tower at Warra Tall Eucalypt SuperSite, Tasmania



b. Example of flux instruments on tower at Calperum Mallee Supersite, SA



Source: TERN SuperSites and TERN OzFlux (Australian and New Zealand Flux Research and Monitoring) (2016). Retrieved from a. *http://www.supersites.net.au/supersites/wrra*; b: *http://www.ozflux.org.au/monitoringsites/calperum/calperum_pictures.html*

Some of the advantages of well-designed, wireless sensor networks over traditional field surveys include:

- reduced human effort with increased data output;
- increased spatial coverage in heterogeneous environments;
- synchronous sampling across sensors;
- real-time data retrieval; and
- reduced impact on ground area.

Use of *in situ* sensors involves multiple complexities and challenges, including power requirements, battery risks, network design, data storage and communications. The maintenance of field sensors also requires consideration of the adverse impact of wildlife (of all scales—insects, birds and mammals), water penetration, temperature extremes, UV damage, natural disasters, and vandals. When observing the natural environment, it is imperative that the operation of each sensor does not change the target in any way, nor interfere with natural processes.

The time series data produced by frequent *in situ* measurements is enabling a fresh look at the dynamics of ecosystems—from plant to biome scales. Maximisation of the value of this unprecedented volume of data also demands new tools for data access and analysis. While the potential of *in situ* sensors for EO is still being realised, examples of their use are documented in Pastorello *et al.* (2011).

A number of countries are adopting standardised procedures for collecting field data using both proximal sensing instruments and quantitative sampling (such as Held *et al.*, 2015). Monitoring sites are typically instrumented, but can also require manual sampling due to the nature of the measurements and sampling schemes involved. To encourage consistency between monitoring sites, various international coordinating groups specify standards for common field measurements required for EO (such as the International Ocean Colour Coordinating Group (IOCCG)[26] for biological oceanography products, and the Group on Earth Observations (GEO)[27] and Committee on EO Satellites (CEOS)[28] Cal/Val working groups for validation of land products). For more information regarding *in situ* sensors and field surveys for EO the reader is referred to Held *et al.* (2015).

26. International Ocean Colour Coordinating Group (IOCCG): *http://www.ioccg.org*
27. Group on Earth Observation (GEO): *http://www.earthobservations.org*
28. Committee on Earth Observation Satellites (CEOS): *http://www.ceos.org*

10.2 Mobile Sensors

Mobile mapping embraces a broad range of instrumentation. Recent advances in technology have enabled the collection of high quality, geo-referenced remotely sensed data using a wide variety of devices. The availability of high definition digital cameras and other environmental sensors (such as spectrometers and laser ranging systems, and accurate, precise location (GPS) and attitudinal—inertial measurement—instruments) has extended significantly in parallel with open access software for combining environmental measurements with positional information. Many forms of mobile mapping are now employed by the general public, research institutions, governments and private industry in a range of application areas.

Mobile sensors effectively bridge the gap between terrestrial and airborne or satellite data. In most cases a measurement sensor is combined with a GPS on a mobile platform, which could be worn by an individual who is walking, diving or flying. Examples include:

- collections of digital photographs or terrestrial laser scanner data acquired from moving vehicles (such as Google Streetview, as illustrated in Figure 10.7a)—a technique that is commonly used for asset and infrastructure assessment along roads, railway lines and other utility supply corridors;
- detailed measurement of crop condition, moisture levels and/or soil properties for precision agriculture applications (Lamb *et al.*, 2008);
- tracking collars worn by livestock to monitor pasture usage and circulation patterns within paddocks (Falzon *et al.* (2013)—Figure 10.7b and Excursus 10.1); and
- hand-held sensors used in field work (see Figure 10.8).

In all cases, these measurements can be acquired at centimetre-scale pixels and tied to accurate and precise three-dimensional positioning data. Good examples of mobile sensing technologies include the Google photospheres, used to construct three-dimensional rendering of digital photographs for viewing in Google Earth, or Google Maps.

Figure 10.7 Mobile sensors for Earth Observation

a. Google street view car



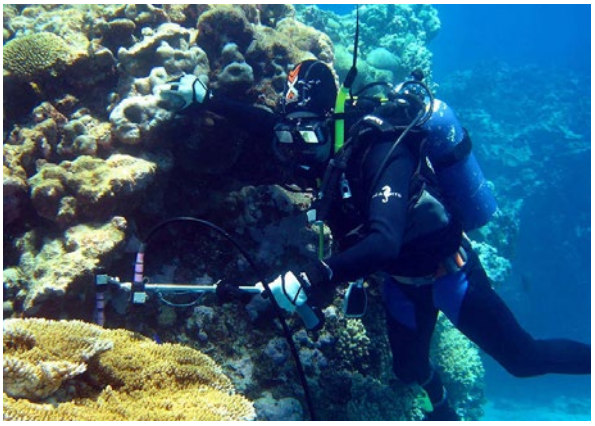
b. Tracking collar on cattle



Source: a. Google, *http://en.wikipedia.org/wiki/Mobile_mapping#mediaviewer/File:Google_Street_View_Car_in_Honolulu.jpg*); b. David Lamb, University of New England

Figure 10.8 Hand-held sensors for Earth Observation

a. Measuring underwater spectra of coral



b. Measuring vegetated canopy in arid region of South Australia



Source: a. Arnold Dekker, CSIRO; b. Megan Lewis, University of Adelaide (Photo credit: Erika Lawley)

Excursus 10.1—GPS tracking in Precision Agriculture

Source: David Lamb, UNE
Further information: *http://www.une.edu.au/parg*

Research Partners: Precision Livestock Research Alliance, UNE Precision Agriculture Research Group, CRCSI

- What is the role of different landscape systems in overall livestock production?
- Can stocking rates be better managed to optimize grazing pressure on different land systems?
- How could paddocks be better fenced to balance grazing variability?
- Space-based technologies are now being used to answer these questions.

GPS tracking

GPS tracking is being increasingly used as a research tool for monitoring livestock activity. UNETracker is a low-cost, accurate and robust GPS collar that can be deployed in large numbers for monitoring the movement of stock and other animals (see Figure 10.9). This technology is being used on grazing properties to:

- map the movement of livestock in paddocks;
- correlate paddock grazing preferences with pasture type and productivity, elevation, aspect, slope, and soil characteristics; and
- monitor diurnal activity of livestock to distinguish between preferred grazing and camping locations (see Figure 10.10).

GPS collars are also being used to track:

- guard dogs and their interactions with wild dogs;
- movements of domestic and wild horses;
- sheep and their behavioural changes under parasite burden; and
- livestock in wetland environments.

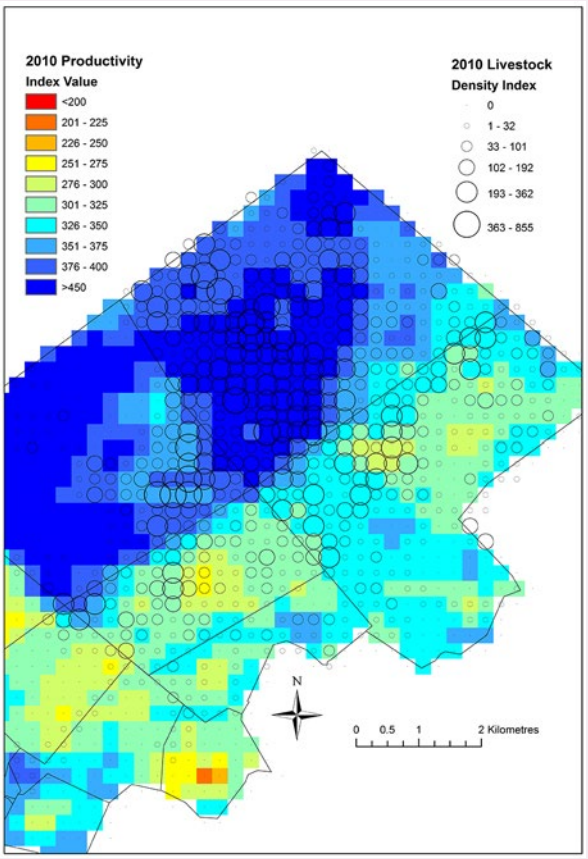
At Willoh Station, a mixed farming property near Brewarrina, NSW, cattle movement and pasture production were monitored from 2009 to 2010. *Pastures from Space* data (see Excursus 14.1) were used to map relative pasture productivity, and selected animals were tracked using GPS collars. The results from this study highlight the spatial variability in pasture utilisation, with significant under-utilisation of some areas. Farm productivity and profitability can be improved by identifying the underlying factors that determine such grazing patterns.

Figure 10.9 UNETracker



Figure 10.10 Livestock pasture usage compared with pasture productivity

In this image of Willoh Station for the period 2009 to 2010, the most productive pasture is shown as blue and least productive as red. Cattle show strong preference for some areas of pasture. Understanding the underlying reasons for this preference can help managers improve farm productivity.



10.3 Citizen Science and Crowdsourcing

An increasing number of individuals and groups are making observations and measurements of environmental conditions or events around the world. These include observing natural disasters, such as fires, floods, and earthquakes, but also more gradual environmental changes, such as pollution, vegetation extent and faunal abundance. In recent decades, the advent of portable technologies (such as cameras and GPS) in mobile phones has enabled non-scientists to make quantitative observations more frequently and more easily.

Citizen Science is defined as 'the systematic collection and analysis of data; development of technology; testing of natural phenomena; and the dissemination of these activities by researchers on a primarily avocational basis' (*http://www.openscientist.org/2011/09/finalizing-definition-of-citizen.html*). In short, this includes all people who contribute to traditional, organised science, whether officially employed to do so or not. Some Australian projects that are encouraging input from Citizen Scientists include the Atlas of Living Australia (*http://www.ala.org.au*), TeachWild (*http://www.teachwild.org.au*) and the Australian Seismometers in Schools network (*http://www.ausis.edu.au*). Each of these endeavours involves citizen input into an organised and regulated system of observations that can be cross-checked against existing knowledge.

A new category of observations about the Earth, namely crowdsourcing, is also emerging from the proliferation of mobile phones and associated devices. Crowdsourcing, 'obtaining needed services, ideas, or content by soliciting contributions from a large group of people, and especially from an online community, rather than from traditional employees or suppliers' (*http://www.merriam-webster.com/dictionary/crowdsourcing*), is similar, but not necessarily synonymous with Citizen Science. This input may provide useful information, but its unregulated nature requires that it be used with caution in scientific analyses. However, now that collection and checking standards can be applied to very large data sets, these data are used increasingly. For example, photos collected at field sites by members of the public can be uploaded and used to check various maps derived from remotely sensed imagery (see *http://www.geo-wiki.org*; in Australia: *http://www.geo-wiki.org/branches/auscover/*; see also the Atlas of Living Australia). Similarly, implementations of Volunteered Geographic Information (VGI) allow citizens to contribute local and current knowledge and images to global web-based repositories (Goodchild, 2007). Examples include the Wikimapia gazetteer (*http://www.wikimapia.org*) and OpenStreetMap (*http://www.openstreetmap.org*). These systems enable timely updates to be disseminated rapidly, which are particularly valuable during natural disaster events.

While data from Citizen Science and Crowdsourcing may be used to supplement existing data about environmental conditions and events, these sources cannot be relied upon to the same extent as other forms of ground-based remote sensing, so are not recommended to validate EO analyses. It is important that all data sources can be calibrated and verified before being used as reference data. Multiple subjective observations may provide useful contextual information, but cannot be substituted for objective measurements. Quite simply, in science, consensus is not the same as truth. The issue of 'Trust in Data' is further explored in Hudson (2015).

Anti-intellectualism has been a constant threat winding its way through our political and cultural life, nurtured by the false notion that democracy means that my ignorance is just as good as your knowledge. (Isaac Asimov)

10.4 Further Information

Research Networks:

Terrestrial Ecosystem Research Network (TERN): *http://www.tern.org.au*

Integrated Marine Observing System (IMOS): *http://www.imos.org.au*

TERN OzFlux: *http://www.ozflux.org.au*

TERN SuperSites: *http://www.supersites.net.au/*

NEON: *http://www.neoninc.org*

Ground-based Measurements:

AusCover Good Practice Guidelines (Held *et al*., 2015)

Flux towers Measurements: *http://www.neoninc.org/science-design/collection-methods/flux-tower-measurements*

International Ocean Colour Coordinating Group (IOCCG): *http://www.ioccg.org*

Dual Wavelength Echidna LIDAR (DWEL): *http://www.auscover.org.au/DWEL*

International Committees:

Group on Earth Observation (GEO): *http://www.earthobservations.org*

Committee on Earth Observation Satellites (CEOS): *http://ceos.org*

10.5 References

Brown, T., Zimmermann, C., Panneton, W., Noah, N., and Borevitz, J. (2012). High-resolution, time-lapse imaging for ecosystem-scale phenotyping in the field. Methods in molecular biology, 918, pp. 71-96. doi:*http://dx.doi.org/10.1007/978-1-61779-995-2_7*.

Culvenor, D. S., Newnham, G. J., Mellor, A., Sims, N. C., and Haywood, A. (2014). Automated In-Situ Laser Scanner for Monitoring Forest Leaf Area Index. Sensors, 14(8), pp. 14994-15008. doi:*http://dx.doi.org/10.3390/s140814994*.

Falzon, G., Trotter, M. G., Schneider, D., and Lamb, D. W. (2013). Correlating movement patterns of merino sheep to faecal egg counts using global positioning system tracking collars and functional data analysis. Small Ruminant Research, 111(1-3), pp. 171-174. doi:*http://dx.doi.org/10.1016/j.smallrumres.2012.09.001*.

Goodchild, M. F. (2007). Citizens as Sensors: The World of Volunteered Geography. GeoJournal, 69(4), pp. 221-221.

Griebel, A., Bennett, L., Culvenor, D., Newnham, G., and Arndt, S. (2015) Reliability and limitations of a novel terrestrial laser scanner for daily monitoring of forest canopy dynamics. Remote Sensing of Environment, 166(1): 205-213.

Held, A., Phinn, S. R., Soto-Berelov, M., and Jones, S. (2015). AusCover Good Practice Guidelines: A technical handbook supporting calibration and validation activities of remotely sensed data products. TERN AusCover. Retrieved from *http://www.auscover.org.au/xwiki/bin/view/Good+Practice+Handbook/WebHome*.

Hudson, D. (2015). Uptake of sensor data in emergency management. (Ph.D thesis), Fenner School, Australian National University.

IMOS (2016). Integrated Marine Observing System. Retrieved from *http://www.imos.org.au/*.

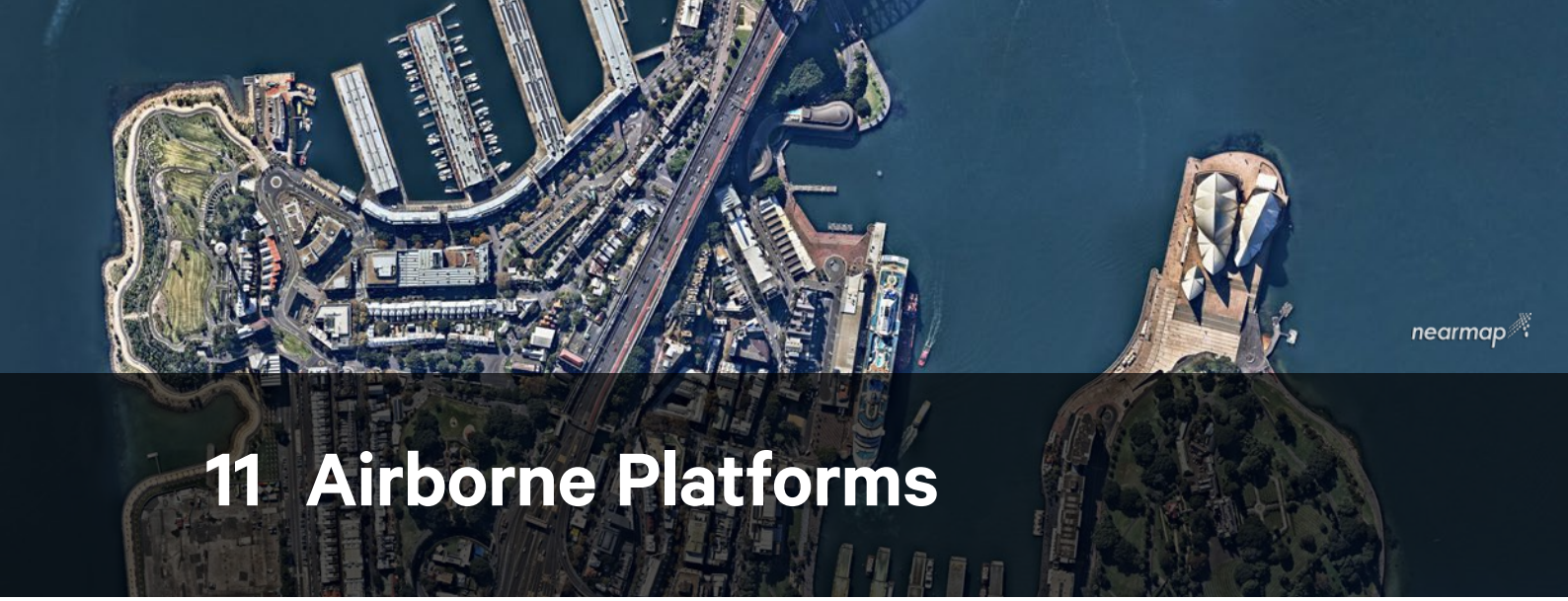
Lamb, D. W., Frazier, P., and Adams, P. (2008). Improving pathways to adoption: Putting the right P's in precision agriculture. Computers and Electronics in Agriculture, 61(1), pp. 4-9. doi:*http://dx.doi.org/10.1016/j.compag.2007.04.009*.

National Research Council (2007). Earth Science and Applications from Space: National Imperatives for the Next Decade and Beyond (454 pages). The National Academies Press, Washington, DC. doi:*http://dx.doi.org/doi:10.17226/11820*.

Pastorello, G. Z., Sanchez-Azofeifa, G. A., and Nascimento, M. A. (2011). Enviro-Net: From Networks of Ground-Based Sensor Systems to a Web Platform for Sensor Data Management. Sensors, 11(6), pp. 6454-6479. doi:*http://dx.doi.org/10.3390/s110606454*.

Portillo-Quintero, C., Sanchez-Azofeifa, A., and Culvenor, D. (2014). Using VEGNET In-Situ Monitoring LiDAR (IML) to Capture Dynamics of Plant Area Index, Structure and Phenology in Aspen Parkland Forests in Alberta, Canada. Forests, 5(5), pp. 1053-1068. doi:*http://dx.doi.org/10.3390/f5051053*.

Wark, T., O'Rourke, D., Kottege, N., Hu, W., and Moore, D. (2011). Opportunities for multimedia environmental sensor networks. IEEE COMSOC MMTC E-letter, 6(12), pp. 5-8.



11 Airborne Platforms

Various forms of Earth Observation (EO) sensors have been carried on a wide variety of airborne platforms for over a century, including balloons, blimps, unmanned aerial vehicles (UAV) and manned aircraft. Various aerial platforms are now widely used to acquire detailed imagery of Earth surface features. In this context, aerial platforms range from expensive, large, fixed wing aircraft to low-cost, remotely operated systems, which are commercially available. Airborne platforms are also used to simulate and validate satellite-borne sensors and can acquire data at times when weather may limit the utility of satellite image acquisition.

Acquiring EO data from airborne sensors has the advantage of flexibility—in timing, instrumentation and coverage. This flexibility ensures that the acquired data coincide with favourable atmospheric conditions and optimal target discrimination over the region of interest. This is particularly advantageous for natural disasters, such as bushfires or floods, where timely information is required to both direct the response effort and record the severity of the event. Timely information is also valuable for monitoring agricultural production and national security.

For remote sensing, aircraft have traditionally used photographic devices, however, these have almost been completely replaced in the past decade by metric, multispectral digital cameras. As detailed in Section 13, these sensors can record radiation over a wider spectral range than photographic devices and provide data in (multispectral) digital format.

To obtain an image swath of sufficient width, aircraft scanners generally use wider scan angles than satellite scanners. This angle is referred to as the Field of View (FOV) and may be between 70° and 90°. However, image pixel size is determined by a constant angle of view (known as the Instantaneous Field of View: IFOV). As shown in Figure 11.1, the effects of panoramic distortion become quite significant toward the edges of the FOV with the ground pixel size increasing many times across each scan line.

For image sensors that acquire data using a scanning mechanism (see Section 14.2), aircraft provide a less stable platform than spacecraft and result in imagery with significant geometric distortions (which requires subsequent correction by specific rectification processing—see Volume 2B). Frame-based digital imagery, however, which dominates the aerial sector of EO image acquisition, is captured from a central perspective (see Section 14.2) and is thus not impacted by platform instability. While the instability inherent to aerial platforms has complicated image mosaicking between adjacent flight lines acquired by scanning sensors, recent advances in camera and image processing technologies now enable production of high resolution, orthorectified image products with large area coverage (such as Nearmap imagery[29]).

Airborne platforms for EO are discussed below in terms of manned aircraft (see Section 11.1) and remotely piloted (or unmanned) aircraft (see Section 11.2).

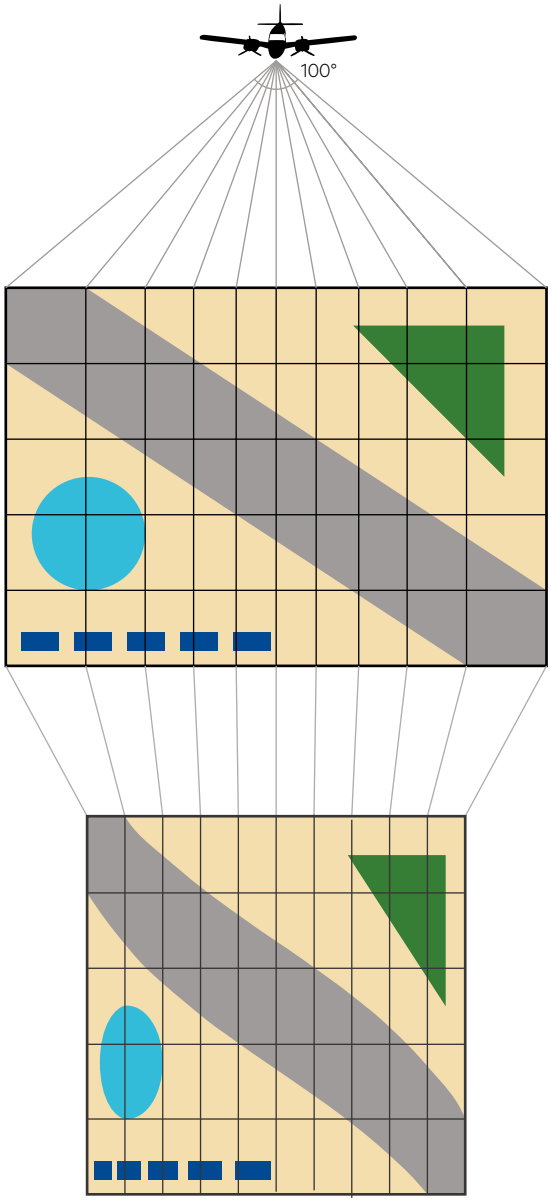
Heavier-than-air flying machines are impossible.
(Lord Kelvin, President, Royal Society, 1895)

Background image: Nearmap high resolution airborne image acquired on 5 May 2016 over the Sydney Opera House and Circular Quay. **Source:** © Nearmap

29. nearmap: *http://au.nearmap.com*

Figure 11.1 Effect of wide scan angle

a. Panoramic distortion: ground pixel width increases significantly away from a vertical view.
b. Resulting image distortions: image features have lateral distortion when displayed with a constant pixel width.



Adapted from: Harrison and Jupp (1992) Figure 18

The example of the bird
does not prove that man can fly.
Imagine the proud possessor of the aeroplane
darting through the air at a speed of
several hundred feet per second.
It is the speed alone that sustains him.
How is he ever going to stop?
(Simon Newcomb, 1903)

11.1 Manned Aircraft

Aircraft offer maximum flexibility for acquiring remotely sensed imagery in terms of mission timing, altitude and selection of spectral regions and gains. A flight may be scheduled to coincide with the best daily or seasonal conditions and avoid poor weather or cloud cover. The image spatial resolution is determined by a combination of flight altitude and sensor characteristics so flying height can be selected to best suit each application. Aircraft imagery also potentially offers much finer spatial resolution than can currently be obtained from non-military remote sensing satellites (see Figure 11.2). Airborne scanners frequently provide more spectral bands with narrower spectral bandwidth, which can be selected to detect specific targets. Similarly, the preferred view angle and direction may be specified for each flight, allowing the acquisition of stereo pairs of imagery if required. However, aircraft imaging missions are generally more expensive and more restricted in spatial coverage than satellite-derived imagery for the same area.

Figure 11.2 Nearmap imagery

This bird's eye view of Sydney's Wet'n'wild shows the water park in great detail



Source: © Nearmap

Aerial imaging can be acquired from both low and high altitude aircraft, including ultralights (Alexander, 2008) and helicopters (see Figure 11.3). Low-altitude platforms (<10 km) tend to fly more slowly, have moderate stability, can be operated from remote sites and offer limited coverage (< 1,000 km^2), whereas high-altitude platforms travel at faster speeds, with more stability and greater coverage (> 10,000 km^2), but are restricted to excursions from large airports.

While airborne EO data may be more expensive than data acquired from satellite borne sensors for some applications, recent improvements mean significant areas can be covered and processed rapidly and automatically, thereby enabling the delivery of accurate and cost-effective solutions for regional areas (for example, Nearmap[30]—see Excursus 11.1). Licensing arrangements for most airborne EO data, however, are generally more relaxed and favourable to 'creative commons' licensing than those applying to some high resolution sources of spaceborne imagery.

In some circumstances airborne sensors can replace the service provided by satellite EO capabilities, for example in high spatial resolution images of major cities. However, there are also substantial disadvantages to airborne sensors including mobilisation costs, inconsistent timing of observations, limited coverage, difficulties obtaining repeat observations, and calibration of observations.

These problems are lessening as digital camera systems are used more consistently over larger area projects. As the industry matures, these problems will be reduced but not altogether removed.

Figure 11.3 Some manned airborne platforms

a. Cessna 414—used for low to mid-altitude flights



b. Beechcraft Kingair 200T—used for mid to high altitude flights



c. Learjet—used for high altitude flights



Source: Robert Norman, Air Affairs Australia Pty Ltd

30. Nearmap: *http://au.nearmap.com*

Excursus 11.1—High resolution aerial imagery

Source: Nearmap
Further information: *http://nearmap.com.au*

High resolution aerial imagery acquired and processed by Nearmap helps organisations inspect locations remotely by seeing what is on the ground, in great detail, and how it has changed over time. This unique technology enables aerial imagery and digital elevation data to be processed and published online within days of capture. Both current and historical imagery is available for tracking change over time.

This imagery is being used by organisations across all industries for:

- business development—identifying sites with business potential or newly developed areas;
- estimating & quoting—solar panel positioning, estimate property values, estimate material needed for a job/project, measuring objects for instant quoting;
- planning and inspecting—site planning, site assessment, site measurement;
- monitoring and validating—validating data and measurements, monitor project progress, observing vegetation and seasonal changes;
- risk assessment—assessing road conditions, vegetation risk, on-site hazards, determining site accessibility; and
- communicating—including imagery in presenting, OH&S reports, emergency maps (see Figures 11.4 to 11.7).

Figure 11.4 Urban development

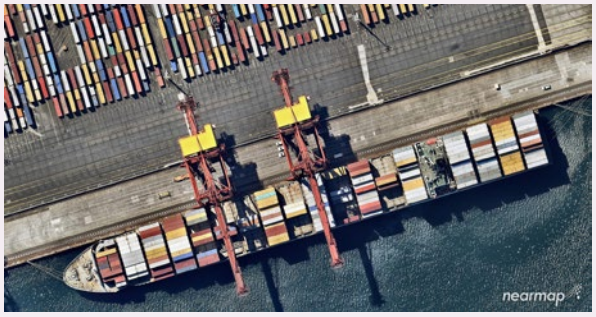
High resolution, aerial image of the man-made James Cook Island in Sylvania Waters, approximately 25km south of Sydney CBD.



Source: © Nearmap

Figure 11.5 Port operations

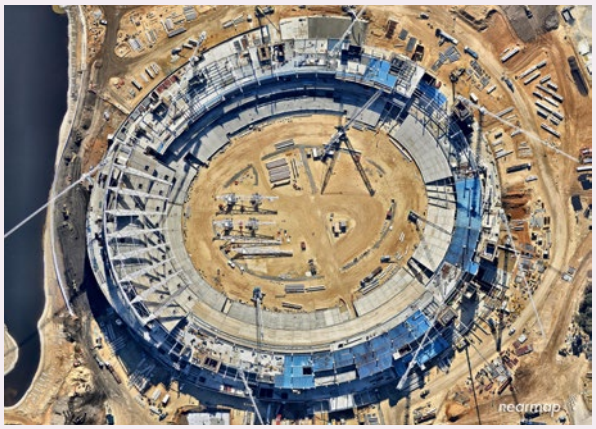
Aerial image of port operations in one of Port Botany's container terminals in Botany, NSW



Source: © Nearmap

Figure 11.6 Monitoring construction projects

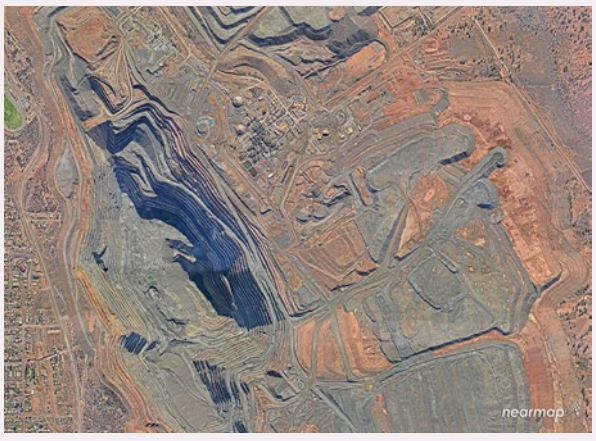
This high resolution Perth Stadium in Perth, WA is a 60,000 seat capacity facility due to be completed for the 2018 AFL season.



Source: © Nearmap

Figure 11.7 Mining operations

The Super Pit, largest open pit gold mine in Australia, located in Kalgoorlie, WA.



Source: © Nearmap

11.2 Remotely Operated Aircraft

Remotely piloted aircraft (RPA; or remotely piloted aircraft systems: RPAS) are also known as drones or unmanned aerial vehicles (UAV)[31]. As the name implies, these systems allow an airborne platform to be controlled remotely, without a pilot, and comprise an increasing range of capabilities, including:

- simple, cheap individually operated airborne systems (see Figure 11.8a);
- larger commercial grade systems with metric digital cameras or multi/hyperspectral and lidar systems, precise positioning and attitudinal measurement capabilities (see Figure 11.8b); and
- military-grade surveillance aircraft with size similar to small light aircraft (see Figure 11.8c).

In each case, both platforms and/or sensors can be pre-programmed to capture data over a certain area or be operated manually. This provides maximum flexibility in terms of user control on data acquisition, however the area being covered by these systems is limited, with smaller model aircraft, glider, and heli/octo/quad-copters covering up to 1km^2, while larger commercial systems, with bigger platforms, covering tens of square kilometres in a day. Surveillance systems operated for military purposes can cover thousands of square kilometres in a day.

The payload and on-board power that can be carried by each platform also determines its data acquisition capabilities, with the smallest systems being limited to carrying digital cameras and GPS, and commercial systems capable of carrying multi/hyperspectral or lidar sensors with a GPS and IMU. The surveillance systems can have larger and higher quality sensors and positional measurements as well as larger data storage and real-time data transmission capabilities. Currently, this is an emerging area with government agencies and private industry investing heavily in commercial grade systems to assist with fieldwork, collect highly detailed spatial data and provide detailed data for calibration/validation of satellite image data sets. For example, the Terraluma project[32] integrates unmanned aircraft systems and specialised sensors for a range of EO applications (Lucieer *et al.*, 2014b; Turner *et al.*, 2014; Wallace *et al.*, 2014). Such systems allow multispectral (optical and thermal), hyperspectral and lidar imagery to be recorded simultaneously at high spatial resolution (Lucieer *et al.*, 2014a). One of the unmanned aircraft platforms currently employed in the Terraluma project is illustrated in Figure 11.8b.

Figure 11.8 Remotely piloted aircraft systems

a. Maja UAV (1 kg payload; 20-30 minute flight)



b. Mikrokopter Oktokopter (1kg payload; 5 minute flight)



c. Military operations—Reaper, part of 39 Squadron Royal Air Force, is used for intelligence, surveillance and reconnaissance in Afghanistan. This is a medium-to-high altitude, long endurance RPAS.



Source: a: Arko Lucieer, University of Tasmania (Terraluma). Retrieved from *http://terraluma.net/platforms/fixed-wing-uavs/*
b: Arko Lucieer, University of Tasmania (Terraluma). Retrieved from *http://terraluma.net/platforms/multi-rotor-uavs/*
c: Cpl Mark Webster/MOD (OGL 1.0). Retrieved from *https://commons.wikimedia.org/wiki/File:Reaper_Remotely_Piloted_Air_System_(RPAS)_MOD_45152482.jpg*

31. Civil Aviation Safety Authority: *http://casa.gov.au*
32. Terraluma: *http://www.terraluma.net/index.html*

11.3 Further Information

Airborne Research Australia (ARA): *http://ara.es.flinders.edu.au*

AAM Group: *http://www.aamgroup.com*

Nearmap: *http://www.nearmap.com*

Spookfish: *https://www.spookfish.com*

Terraluma: *http://www.terraluma.net*

11.4 References

Alexander, D. (2008). Remote sensing and the coast: Development of advanced techniques to map nuisance macro-algae in estuaries. New Zealand Geographer, 64(2), pp. 157-161. doi:*http://dx.doi.org/10.1111/j.1745-7939.2008.00140.x*.

Harrison, B. A., and Jupp, D. L. B. (1992). Image Rectification and Registration. Part FOUR of the microBRIAN Resource Manual (draft only). MPA, Melbourne.

Lucieer, A., Malenovský, Z., Veness, T., and Wallace, L. (2014a). HyperUAS—Imaging Spectroscopy from a Multirotor Unmanned Aircraft System. Journal of Field Robotics, 31(4), pp. 571-590. doi:*http://dx.doi.org/10.1002/rob.21508*.

Lucieer, A., Turner, D., King, D. H., and Robinson, S. A. (2014b). Using an Unmanned Aerial Vehicle (UAV) to capture micro-topography of Antarctic moss beds. International Journal of Applied Earth Observation and Geoinformation, 27, pp. 53-62. doi:*http://dx.doi.org/10.1016/j.jag.2013.05.011*.

Turner, D., Lucieer, A., Malenovsky, Z., King, D. H., and Robinson, S. A. (2014). Spatial Co-Registration of Ultra-High Resolution Visible, Multispectral and Thermal Images Acquired with a Micro-UAV over Antarctic Moss Beds. Remote Sensing, 6(5), pp. 4003-4024. doi:*http://dx.doi.org/10.3390/rs6054003*.

Wallace, L., Lucieer, A., and Watson, C. S. (2014). Evaluating Tree Detection and Segmentation Routines on Very High Resolution UAV LiDAR Data. IEEE Transactions on Geoscience and Remote Sensing, 52(12), pp. 7619-7628. doi:*http://dx.doi.org/10.1109/tgrs.2014.2315649*.



12 Spaceborne Platforms

Spacecraft, both manned and unmanned, have provided platforms for a wide range of remote sensing devices since the early days of space exploration. The majority of Earth Observation (EO) data comes from satellites with imaging sensors in either polar (north-south circle around earth) or geostationary (above a fixed location) orbits. These systems are operated by national space and weather agencies, private companies, and military organisations.

Spaceborne platforms offer several advantages over lower altitude platforms, particularly:

- a synoptic viewing position for regional and global coverage of the Earth's surface;
- frequent and predictable overpasses (by most spaceborne platforms); and
- standardised imaging characteristics.

12.1 Manned Spacecraft

Various manned spacecraft have acquired large series of space photography and a number have operated scanning systems[33]. These spacecraft operate between about 60° north and south of the equator at altitudes between approximately 200–500 km to enable safe re-entry and recovery of vehicle, instrumentation, and, most importantly, crew.

The spatial resolution of space photography varies considerably, with reported image pixel size being between 5 m and 150 m. The operator-controlled nature of image collection allows selection of solar illumination angle and viewing direction. As the mode of acquisition does not yet provide for regular, repetitive coverage, the utility of the imagery is generally limited to inventory-type surveys rather than monitoring studies.

The US Mercury, Gemini and Apollo series of satellites, launched during the 1960s, provided over 1,000 normal colour photographs and some false colour infrared photographs taken from hand-held 70 mm cameras. While these images have been the subjects of considerable research, their age, oblique view and restricted coverage limit their current utility for environmental applications. The Apollo mission also tested the usefulness of multispectral imagery taken from a simultaneously triggered array of four 70 mm cameras, which were fitted with filters simulating Landsat MSS spectral bands. The positive results of this test contributed to the development of the Landsat series of unmanned satellites.

Other manned spacecraft include Skylab, in the 1970s, and the Space Shuttle series, in the 1980s. Skylab was launched in May 1973 and decommissioned in February 1975. It carried several instrument packages including the EREP (Earth Resources Experiment Package), which contained a 13-channel scanner called the S192 MSS. This scanner sampled visible, near infrared, middle infrared and thermal infrared wavelengths and produced imagery of comparable spatial resolution to the Landsat MSS.

The Space Shuttle series were reusable spacecraft, designed to commute between the Earth and space. The shuttles have carried a range of remote sensing equipment, including the Metric Camera, Large Format Camera, the first test of the Modular Optical-Electronic MSS (MOMS) and the Shuttle Imaging Radar (SIR) experiments. The latter have provided unique microwave imagery of selected regions of the Earth's surface. These have been used for research into radar applications and the development of operational, satellite-borne radar imagers. The Space Shuttle was the base platform for the most comprehensive global digital elevation mapping project completed to date, the Shuttle Radar Topography Mapping Mission (SRTM). SRTM data are publicly available as a digital elevation surface at a range of pixel sizes[34].

Background image: Southern portion of the full disk image captured by Himawari-8 geostationary satellite on 1 January 2016, displayed as natural colour composite. Source: © Bureau of Meteorology/JMA

33. NASA Astronaut photography: *http://eol.jsc.nasa.gov*
34. Shuttle Radar Topography Mapping Mission: *http://srtm.usgs.gov/index.php*

In the USSR, the major remote sensing space platforms have been manned satellites with a manned space station having been established in 1986. These platforms carried a variety of photographic equipment at an altitude of 250 km. The equivalent pixel resolution of available Russian space photography varies between 5 m and 60 m and is acquired in both multi-band and panchromatic format.

With the decommissioning of the Space Shuttle, the International Space Station (ISS) has now become a similar research and development site[35]. At present the ISS has several windows established specifically for imaging sensor payloads, the most recent example being the Hyperspectral Coastal Imager (HICO)[36].

12.2 Satellites

Data acquired by EO satellites provide numerous benefits for studying the Earth's surface and atmosphere, including:

- continuous acquisition of data over time periods suited to monitoring a range of processes;
- regular revisit capabilities, resulting in frequent and up-to-date information, from two minutes (Geostationary) to daily and weekly;
- multiple spatial scales of collection, from site specific (0.5 m pixels over 10's km^2) to continental and global (1000 m pixels over 10^6's km^2) coverage;
- range of spectral resolutions sampling several parts of the EM spectrum;
- ability to enhance or manipulate digital data with a wide range of software;
- ability to combine satellite digital data with other digital data;
- cost effective data source, much of which is freely available;
- good geo-locational accuracy;
- possibility of stereo viewing; and
- large archive of historical data.

Particular advantages offered by satellites over airborne platforms include:

- regular, repeated acquisition at predictable times;
- consistency of data in terms of spatial, spectral, radiometric and temporal characteristics;
- breadth of coverage; and
- extent and availability of archival data (Geoscience Australia, 2016).

Satellites can be differentiated in terms of several orbital characteristics as summarised in Table 12.1.

Satellite orbits are commonly classified into three groups in terms of altitude:

- low Earth orbit (LEO: 180–2,000 km)—used for polar orbiting EO satellites, the International Space Station (ISS) and the Hubble Telescope;
- medium Earth orbit (MEO: 2,000–35,780 km)—used for navigation and speciality satellites; and
- high Earth orbit (HEO: 35,780 km)—used for meteorological satellites (NASA, 2009).

A range of different orbital inclinations and shapes (or eccentricities) are used for satellites, some of which are summarised in Table 12.2 and illustrated in Figures 12.1 and 12.2. The most commonly used satellite orbits for EO are:

- geostationary—used for meteorological and communications satellites (see Section 12.2.1); and
- sun-synchronous or (near) polar—used for most other EO satellites (see Section 12.2.2).

Table 12.1 Satellite orbital characteristics

Characteristic	Description
Altitude	Height above mean sea level (km)
Inclination	Angular distance between the satellite orbital plane and Earth's equator (decimal degrees)
Eccentricity	Deviation of the orbit shape from a perfect circle
Period	Time taken to complete one overpass of Earth (minutes or orbits/day)
Repeat Cycle	Interval between overpasses at a given point (days or orbits/year)
Equatorial Crossing Time	Time satellite passes over the equator (24 hour clock in local time)

35. International Space Station sensors: *http://www.nasa.gov/mission_pages/station/research/benefits/remote_sensing.html*
36. Hyperspectral Coastal Imager: *http://hico.coas.oregonstate.edu/*

Table 12.2 Types of satellite orbits

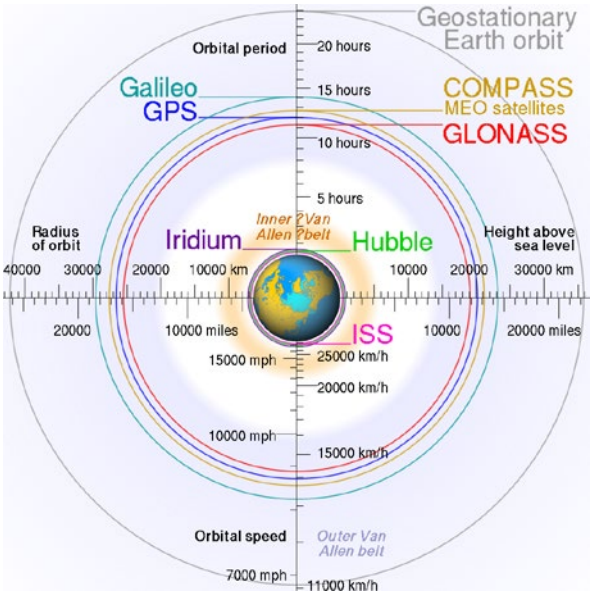
LEO: low Earth orbit; MEO: Medium Earth orbit; HEO: High Earth orbit

Characteristic	Description	Typical altitude	Advantages
Polar	Satellite that (nearly) passes from pole to pole as Earth rotates beneath it (inclination ~ 90°)	LEO	Polar coverage
Sun-synchronous, near polar	Satellite follows a near polar and near circular orbit and passes over a given point on the Earth's surface at the same local time on each overpass	LEO	Minimises surface illumination and shadowing differences, so commonly used for Earth Observation
Semi-synchronous	Satellite orbital period equals 12 hours (half the rotational period of Earth) and is near circular	MEO	Frequent coverage
Molniya	Highly elliptical orbit inclined at 63.4° (and 111.6°) with 2 revolutions of Earth per day	MEO	Optimum coverage of high northern latitudes, so used by Russian satellites
Equatorial	Satellite follows a near equatorial orbit, usually circular (inclination ± 9°)	HEO	Equatorial coverage; observing tropical weather patterns
Geostationary	Circular orbit at an average altitude of 35,786 km above the equator (inclination 0°) at a specific longitude moving with Earth's rotation such that the satellite appears to remain stationary when viewed by an observer at a particular location on Earth[39]	HEO	One hemisphere of Earth is viewed continuously, so used for communications, weather and global coverage

Source: NASA (2009)[37]

Figure 12.1 Comparison of satellite orbits

Stylised view of satellite orbits around Earth, from a perspective above the North pole.. The outer ring (~36,000 km altitude) shows the geostationary orbit, commonly used for meteorological satellites. MIddle rings are medium Earth orbits (20,000–25,000 km altitude), which are primarily used for navigation satellites. The inner rings depict the low Earth orbits (180–2,000 km) of the Hubble Space Telescope, the International Space Station (ISS) and Iridium constellation. In this graphic, all orbits have been shown on common, equatorial plane for comparison, but only the geostationary orbit is equatorial—all others are significantly inclined (see Figure 12.2). The Moon orbits at a distance around nine times further from Earth than the geostationary orbit.

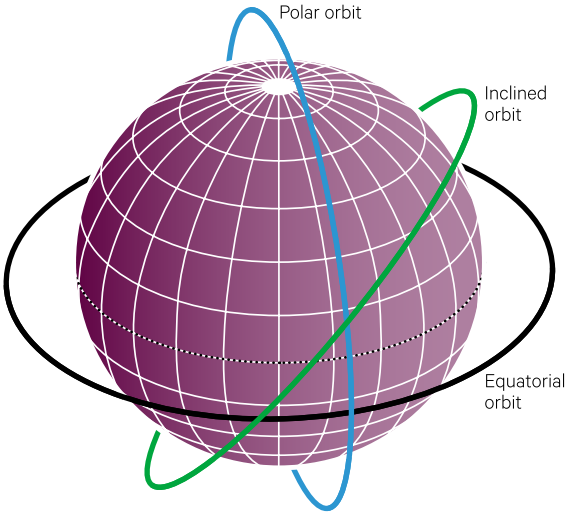


Source: Geo Swan (CC-BY-SA 3.0). Retrieved from: *https://en.wikipedia.org/wiki/Geostationary_orbit#/media/File:Comparison_satellite_navigation_orbits.svg*

It is worth noting that the number of 'objects' orbiting Earth is increasing each year, with nearly 300 launches in 2014 alone (see Volume 1B—Section 10.1.2). 70% of catalogued objects are in LEO where satellites travel at the fastest speeds, with a greater density at higher latitudes (see Figure 12.3).

Figure 12.2 Some orbital inclinations

The inclination of a satellite orbit indicates the relationship between the orbital plane and Earth's equator. The orbital inclination of many EO satellites is near polar, typically covering the latitudes 82° N and 82° S.

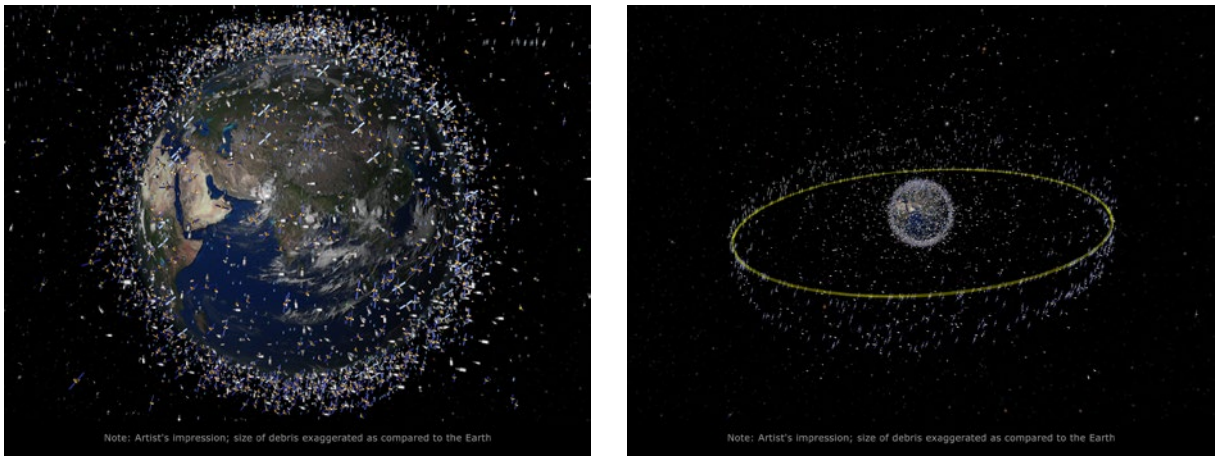


37. For example, to receive signals from geostationary communications satellites, antennae on Earth are pointed at a zenith angle equivalent to the latitude from the equator (that is, towards south for northern hemisphere locations and towards north for southern hemisphere locations) and at a fixed azimuth depending on the longitude of the satellite position.

Figure 12.3 Satellite density around Earth

a. Low Earth Orbit (LEO < 2,000 km altitude) satellites are used for most EO studies. 70% of catalogued objects are in LEO, with the spatial density of objects increasing at higher latitudes.

b. Geostationary Orbit (~36,000 km altitude) satellites are used for meteorology and telecommunications.



Source: © ESA (2016). Retrieved from a. *http://www.esa.int/spaceinimages/Images/2008/03/Debris_objects_-_mostly_debris_-_in_low_Earth_orbit_LEO_-_view_over_the_equator*; b. *http://www.esa.int/spaceinimages/Images/2008/03/The_geostationary_ring*

12.2.1 Geostationary

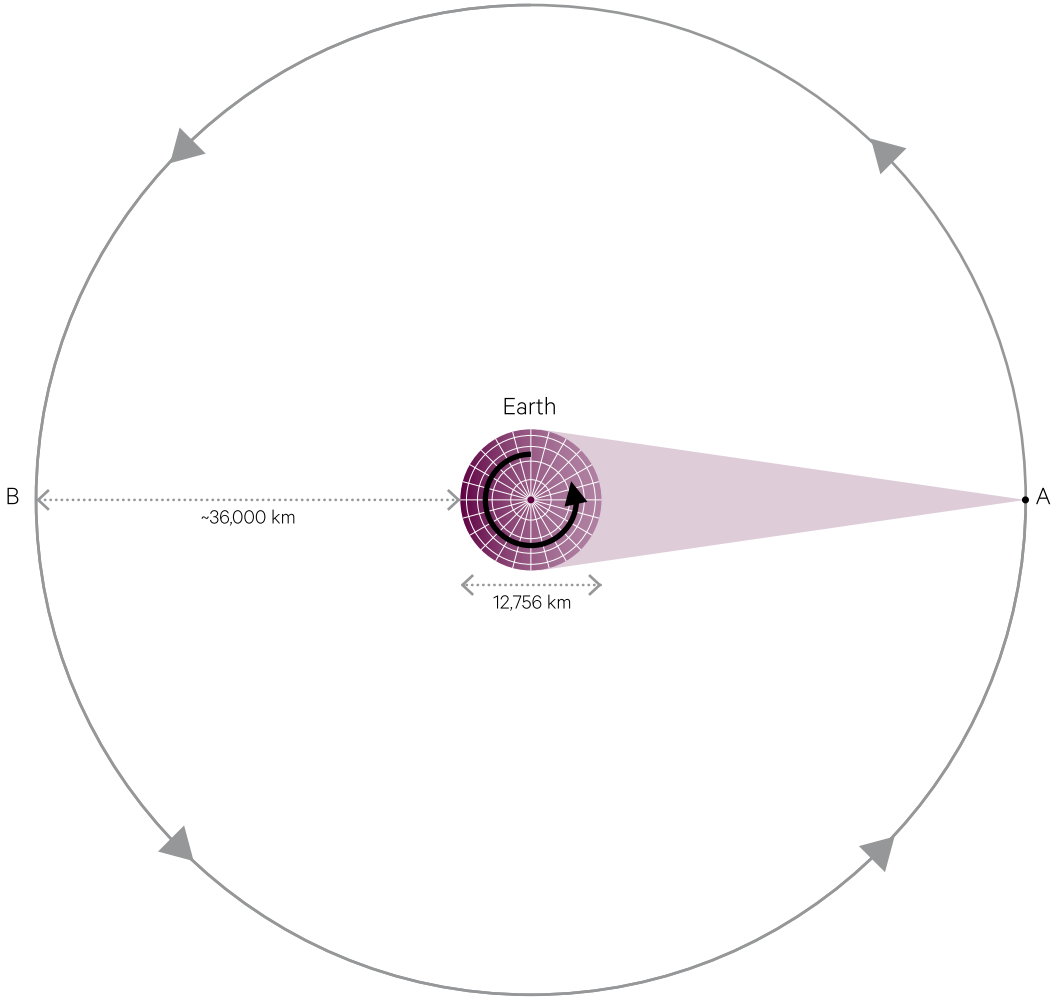
Geostationary, or geosynchronous, satellites are positioned in an orbit at an altitude of approximately 36,000 km above the equator. In this equatorial orbit they move with the same angular velocity as the Earth rotates and so remain over the same point on the Earth's surface. From this viewpoint the same region of the Earth's surface can be imaged at frequent, regular intervals by the satellite (see Figure 12.4).

The history of meteorological satellites is summarised in Excursus 12.1. More recently, a network of geostationary and LEO satellites has been established by the Coordination Group for Meteorological Satellites (CGMS), which provide global coverage for atmospheric monitoring as shown in Figure 12.5 and listed in Table 12.3.

When I arrived in Gombe 50-plus years ago, looking up at the stars, it never occurred to me that one day, we'd be relying on remote sensing—satellites circling the globe high above—to help unite communities of people and save Gombe's chimpanzees.
NASA—through its resources and data and funding—is helping us to apply the kinds of innovative solutions needed to address the complex problems people and chimpanzees face today.
(Jane Goodall)

Figure 12.4 Geostationary orbit

The geostationary orbit, at an average altitude of 35,786 km above the equator[38], allows satellites to move with the same angular velocity as the Earth's rotation. By rotating synchronously with Earth, geostationary satellites remain at their allocated longitude and continuously view the same hemisphere of Earth. Himawari-8, for example, stays at longitude 140.7°E to acquire the full disk images shown in Figures 12.6 and 12.7. In this illustration, 12 hours after the geostationary satellite is at position A, it will be at position B, but still located over the same longitude on Earth. 12 hours later it will again be at position A.

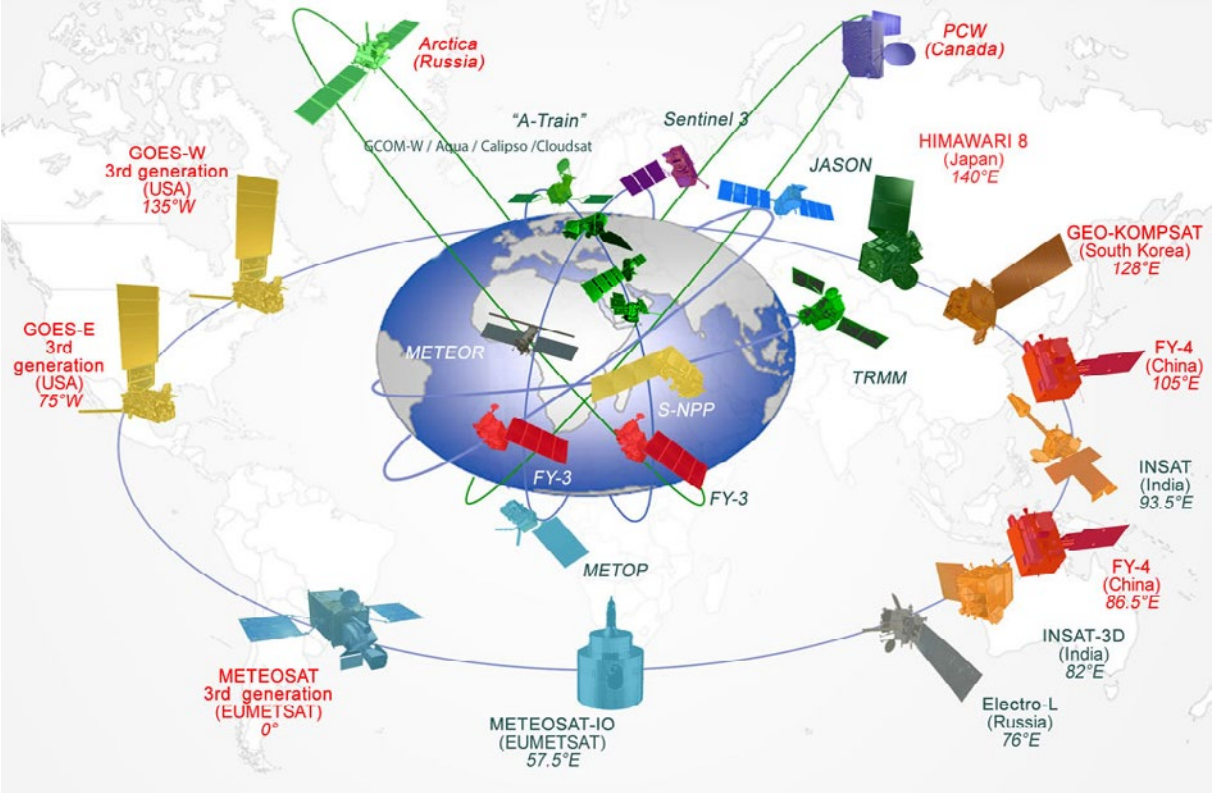


Since 1977, the Geostationary Meteorological Satellites (GMS) and Multifunctional Transport Satellites (MTSAT, renamed Himawari after launch) operated by Japan Meteorological Agency (JMA) have provided imagery for Australasia from its position around 145° E (see Figure 12.5). The principal sensor carried by MTSAT-2 (Himawari-7) is Japanese Advanced Meteorological Imager (JAMI), with five spectral channels (see Table 12.4). The replacement satellite (Himawari-8) was launched in late 2014 observes from a slightly different longitude (140.7° E). It carries the dedicated meteorological payload, Advanced Himawari Imager (AHI), to provide more frequent coverage with higher spatial and spectral resolution (see Table 12.4 for details). This sensor will enable a full disk image of Earth (as visible from 140.7° E) to be acquired every ten minutes (see Figure 12.6). Himawari-9 is scheduled for launch in late 2016, initially as a backup system, and ultimately to provide a replacement for Himawari-8.

38. EUMETSAT: *http://www.eumetsat.int/website/home/Satellites/LaunchesandOrbits/SatelliteOrbits/index.html*

Figure 12.5 Network of geostationary satellites

19 geostationary meteorological satellites are currently listed as operational or on stand-by, with an ongoing plan for replacements into the future (CGMS, 2016).



Source: © WMO (2016). Retrieved from *http://www.wmo.int/pages/prog/sat/globalplanning_en.php*

Table 12.3 Geostationary meteorological satellites

The nominal constellation includes six operational geostationary satellites to ensure full coverage between the latitudes 50° N and 50ª S, with a zenith angle below 70°.

Region	Nominal location	Nominal operator	Example Satellite
America (North, Central and South)	135° W	USA (NOAA)	GOES-15
East Pacific	75° W	USA (NOAA)	GOES-13
Europe and Africa	0°	EUMETSAT	Meteosat-10
Indian Ocean	76° E	Russian Federation (Roshydromet)	GOMS-2/Elektro-L
Asia	105° E	China (CMA)	Feng Yun-2G
West Pacific	140° E	Japan (JMA)	Himawari-8

Source: CGMS (2016); WMO (2016)

The viewpoint of a geostationary satellite is similar to that of a photographic camera, with the scanner viewing the whole image from a central perspective (see Section 14.2.3). The GMS satellites were spin-stabilised on a north-south axis so unlike the orbiting satellites, which can utilise the relative motion of the platform to separate successive scan lines in an image, these satellites used a stepping-motor to adjust the angle of view on each spin. The recent Himawari satellites are three-axis stabilised, with the view scanned relative to the platform in two directions (JMA, 2016).

Table 12.4 JMA Australasian coverage satellites

Himawari-7			Himawari-8/-9		
Channel	Spectral Range (mm)	Spatial Resolution (km)[41]	Channel	Central Wavelength (μm)	Spatial Resolution (km)[42]
			1	0.47	1
1	0.55–0.80	1	2	0.51	1
			3	0.64	0.5
			4	0.86	1
			5	1.6	2
			6	2.3	2
5	3.5–4.0	4	7	3.9	2
			8	6.2	2
4	6.5–7.0	4	9	6.9	2
			10	7.3	2
			11	8.6	2
			12	9.6	2
2	10.3–11.3	4	13	10.4	2
3	11.5–12.5	4	14	11.2	2
			15	12.4	2
			16	13.3	2

Source: JMA (2016) at *http://www.data.jma.go.jp/mscweb/en/himawari89/index.html* [39][40]

Figure 12.6 Himawari-8 disks

The Himawari-8 satellite, operated by JMA, is positioned over the equator at longitude 140.7° E. From this vantage point, full disk images covering the Asian and Australian continents are acquired every ten minutes. Five image samples from the daily sequence on 23 July 2016 are shown below using true colour channels (merged with thermal on the night side of the planet and overlaid with coastlines in white). These images were acquired at the following local times for longitude 135° E (central to Australia):

a. 6 am b. 9 am c. 12 noon d. 3 pm e. 6 pm



Source: © Bureau of Meteorology/JMA

I suppose that we shall soon travel by air-vessels; make air instead of sea voyages; and at length find our way to the Moon, in spite of the want of atmosphere.
(Lord Byron, 1822)

39. horizontal resolution in image centre
40. horizontal resolution in image centre

Excursus 12.1—Meteorological Satellites

Source: John Le Marshall, Bureau of Meteorology
Further Information: *johnlemarshall@hotmail.com, j.lemarshall@bom.gov.au*

The First Weather Satellites

The first weather satellite, TIROS 1, launched on 1 April 1960 (Figure 12.7), enabled the use of Earth Observations from Space (EOS) to help determine atmospheric state. Visible and infrared imagery became increasingly available from the early TIROS, ESSA and NIMBUS series of satellites with TIROS-8 introducing Automatic Picture Transmission (APT) capability (see Figure 12.8). APT facilitated the use of direct readout imagery around the globe for analysis, forecasting, warning and research. Before the use of satellite sounding data, these image data were used to construct mean sea level pressure charts and upper atmospheric geopotential charts over the southern hemisphere as part of operational meteorological analysis.

Here, we summarize the development and the past, current and future use of weather satellites, particularly in the southern hemisphere. Table 12.5 provides a time-referenced list indicating the development of meteorological satellite series over the last half-century.

Figure 12.7 The launch of the first weather satellite, TIROS-1, in 1960

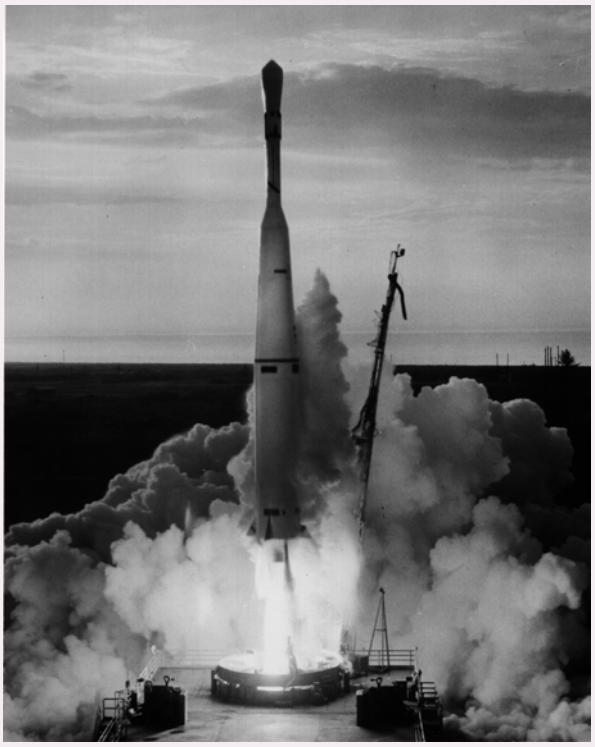
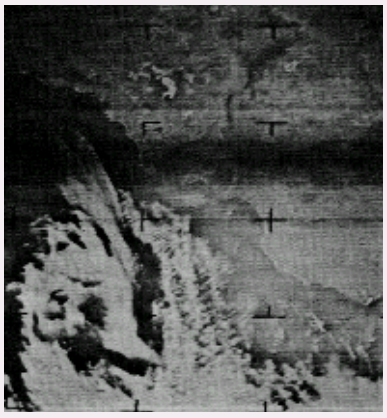


Figure 12.8 Early meteorological satellite imagery

a. First TIROS-8 image received at the Bureau of Meteorology, Melbourne, Christmas day 1963



b. NIMBUS II image Christmas day 1964, showing a cold front and low pressure system approaching south-eastern Australia, and also bushfires over southeast Australia.



c. NOAA-5 Mosaic covering much of the Pacific Ocean, received from NOAA via geostationary satellite on 8 November 1976

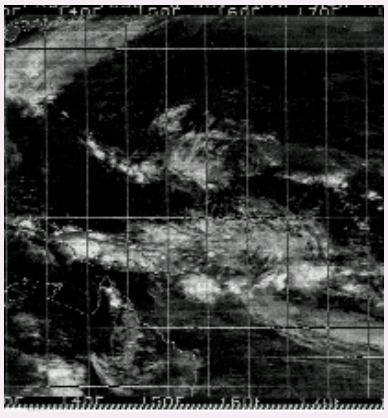


Table 12.5 Some Important Series of Weather Satellites

Satellite Series	Duration	Number of Satellites	Origin
TIROS 1 – 10	1960–1965	9	USA
DMSP (OPS)	1962–	68	USA
NIMBUS 1 – 7	1964–1978	7	USA
COSMOS 44 – 2292	1964–1994	5	USSR
OPS 8068 – 5390	1965–1979	4	USA
ESSA 1 – 9	1966–1969	9	USA
METEOR 1	1969–1977	25	USSR
ITOS-1 (TIROS-M) – ITOS-H (NOAA5)	1970–1976	8	USA
GOES 1 – 15	1975–2010	15	USA
HIMAWARI 1 – 8	1977–	8	JAPAN
METEOSAT 1 – 11	1977–2015	10	EUROPE
TIROS-N, NOAA-6 – NOAA19 (POES)	1978–2009	16	USA
INSAT	1983–2011	24	INDIA
FENGYUN 1A –1D	1988–2002	4	CHINA
GOMS	1994–	3	USSR
FENGYUN 2A– 2G,	1997–2014	7	CHINA
EOS	1997–	9	USA, GER, FR, JAP, EU
METOP A – B	2006–	2	EUROPE
FENGYUN 3A – 3C	2008–2013	3	CHINA
COMS-1	2010–	1	S.KOREA
NPP	2011–	1	USA

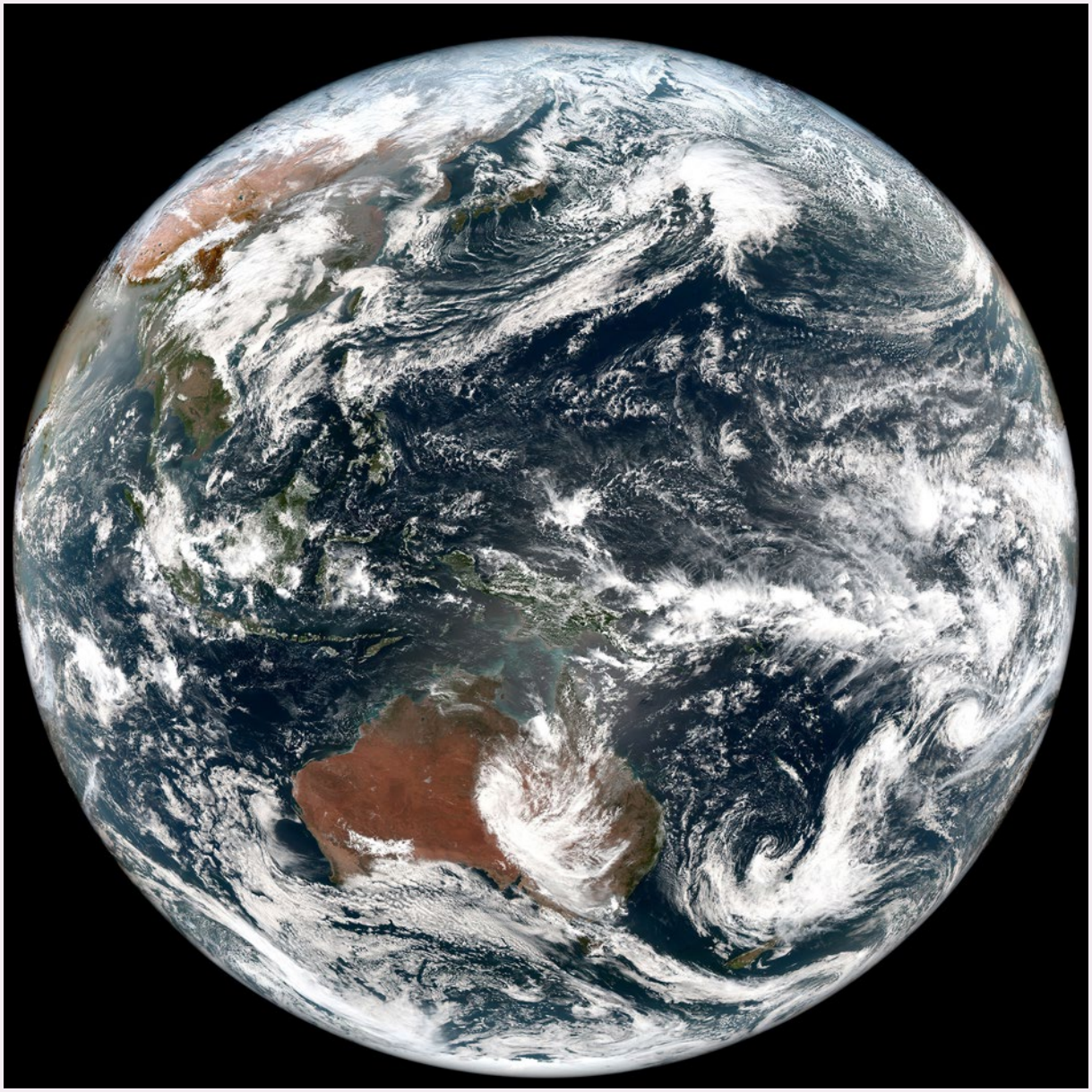
The First Geostationary Satellites

The geostationary satellite, ATS-1 was launched in 1968 and, by the 1970s, the use of sequential geostationary observations in the visible and infrared bands was well established for a number of meteorological applications, including nowcasting, forecasting, severe weather monitoring and the estimation of winds or atmospheric motion vectors (Fujita *et al.*, 1968; Young *et al.*, 1972).

The first geostationary satellite in the Australian region was GMS-1, which was provided by JMA in 1976. The most recent satellite, Himawari-8, was launched in late 2014 and was placed into geostationary orbit over the equator at 140.7° E. A colour image from Himawari-8 is seen in Figure 12.9.

Figure 12.9 A Himawari-8 colour image

This image was taken from geostationary orbit over the equator at 140.7°E on 1 January 2016.



Source: © Bureau of Meteorology/JMA

Second Generation Satellites

With the launch of TIROS-N in 1978 and the subsequent Polar Orbiting Environmental Satellites (POES) series satellites with second generation sounders (HIRS, MSU; Smith *et al.*, 1979) and, later, AMSU, real time infrared and microwave radiances and derived temperature and moisture profiles were available to the global community. The derived products (temperature and moisture profiles) were used globally for hemispheric and regional forecasting. Direct readout of the satellite data from ground stations in a number of countries was able to provide radiances which were used, first with simple statistical inversion models (Kelly *et al.*, 1983) and, later, with full physical inversion models to improve regional forecasting (such as Le Marshall *et al.*, 1989).

In many places, use of these data was facilitated by community software, such as the International TOVS Processing Package (Smith *et al.*, 1983). The resulting improvements to regional and global forecast systems from the sounding data are well documented (Kelly *et al.*, 1978; Le Marshall *et al.*, 1994; Zapotocny *et al.*, 2007, 2008) and these data have assumed an ever-increasing role in numerical analysis and prognosis.

Blowing in the wind

By the mid 1980s, water vapour imagery was used routinely to detect atmospheric movement and generate Atmospheric Motion Vectors (AMVs), which have been particularly useful for Numerical Weather Prediction (NWP; Le Marshall *et al*., 1985). During the 1980s, the ability to process digitised, sequential Global Meteorological Satellite (GMS) Special Observation imagery and generate winds was also developed in Australia. With the introduction of digital GMS Stretched-VISSR data in 1989, sequential digitised images available every hour or half-hour were processed and used to provide cloud drift winds.

The world's first, fully automatic, operational system to derive IR image-based cloud motion vectors every six hours was developed for the Australian region (Le Marshall *et al*., 1992; Le Marshall *et al*., 1993; Le Marshall *et al*., 1994). The improved spectral coverage of GMS-4 and -5 provided observations in the visible, infrared and water vapour absorption bands and these were used to provide high spatial and temporal resolution AMVs.

With the availability of hourly image data and the expansion of the number of channels, AMVs could be generated on an hourly basis, in real time, at high spatial resolution, using both visible and infrared imagery. This enabled the first operational, fully automatic generation of hourly cloud drift winds (Le Marshall *et al*., 1996a; Le Marshall *et al*., 1999) with documented benefits to operational NWP (see Excursus 16.1). Winds generated by the operational system at the Bureau of Meteorology are seen in Figure 12.10 displayed over a GMS-5 and MTSAT-2 image. In addition, in a series of studies examining tropical cyclone track and intensity predictions, significant gains were found in forecasting track accuracy, including a beneficial influence on intensity prediction, from use of these high resolution wind data (Le Marshall *et al*., 1996b; Leslie *et al*., 1998). AMVs derived from Himawari-8 imagery are shown in Figure 12.11.

In a series of studies examining tropical cyclone track and intensity predictions, significant gains were also found in forecasting track accuracy, including a beneficial influence on intensity prediction, from use of these high resolution wind data (Le Marshall *et al*., 1996b; Leslie *et al*., 1998; Le Marshall *et al*., 1999).

Figure 12.10 Wind vectors over GMS-5 image of the Tasman Sea

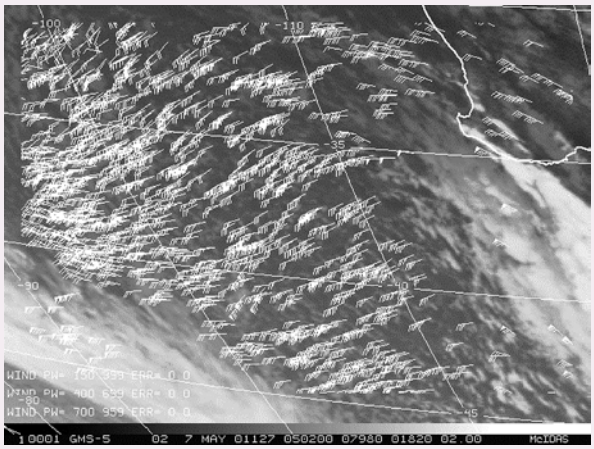
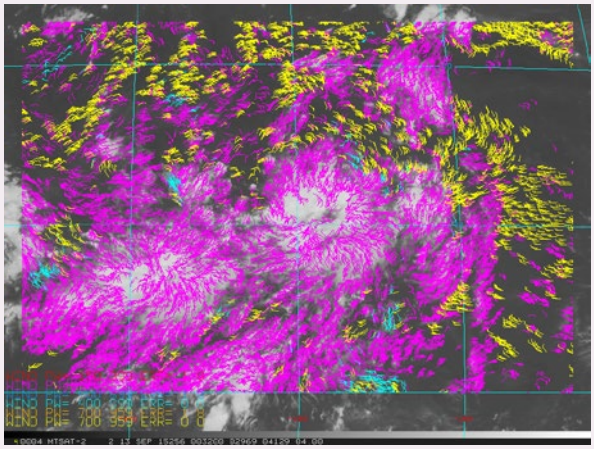


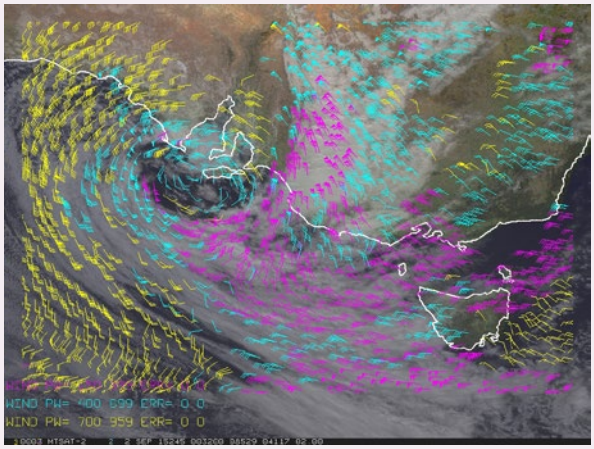
Figure 12.11 Himawari-8 Atmospheric Motion Vectors (AMVs)

Yellow vectors—low level AMV; magenta vectors—upper level AMV.

a. Over tropical storms in the equatorial Pacific north of Australia on 12 September 2015



b. Over southeast Australia



12.2.2 Polar orbiting

Polar-orbiting satellites provide imagery with a range of resolutions—spectral, spatial, radiometric and temporal (see Volume 1B—Section 1). These satellites operate in sun-synchronous orbits, that is, they always pass over given latitude at the same local solar time (see Figure 12.12). Their orbits are near polar, covering the latitudes 82° N to 82° S, with altitudes varying between 700 km and 1500 km.

A strip, or swath, of the Earth's surface is imaged with each satellite pass such that consecutive satellite paths follow a set pattern to image different ground areas. The orbital characteristics of these satellites provide near global coverage of the Earth's surface on a regular and predictable basis. The orbital track of these satellites relies on the rotation of Earth beneath the satellite. To maintain an orbit that is synchronous with the sun, the satellite orbital plane deviates slightly from a true north-south direction (see Figure 12.13).

Polar orbiting satellites are designed to collect data in either their ascending (when moving from south to north—see Figure 12.13a) or descending (moving north to south—see Figure 12.13b) mode. Local solar time necessarily varies during each orbit, but the equatorial crossing time, in terms of local solar time, is constant. Most current satellite sensors have recording facilities to allow collection of imagery in regions that are outside the range of ground stations.

Such recorded data are subsequently transmitted to Earth when the satellite is within range of an appropriate receiving station.

The Worldwide Reference System (WRS) is a global standard for cataloguing Landsat Imagery. Landsat-1, -2 and -3 followed WRS-1, while Landsat-4, -5, -7 and -8 follow WRS-2. This notation systematically subdivides continuous swaths of imagery acquired along each orbital path into discrete scenes (NASA, 2016).

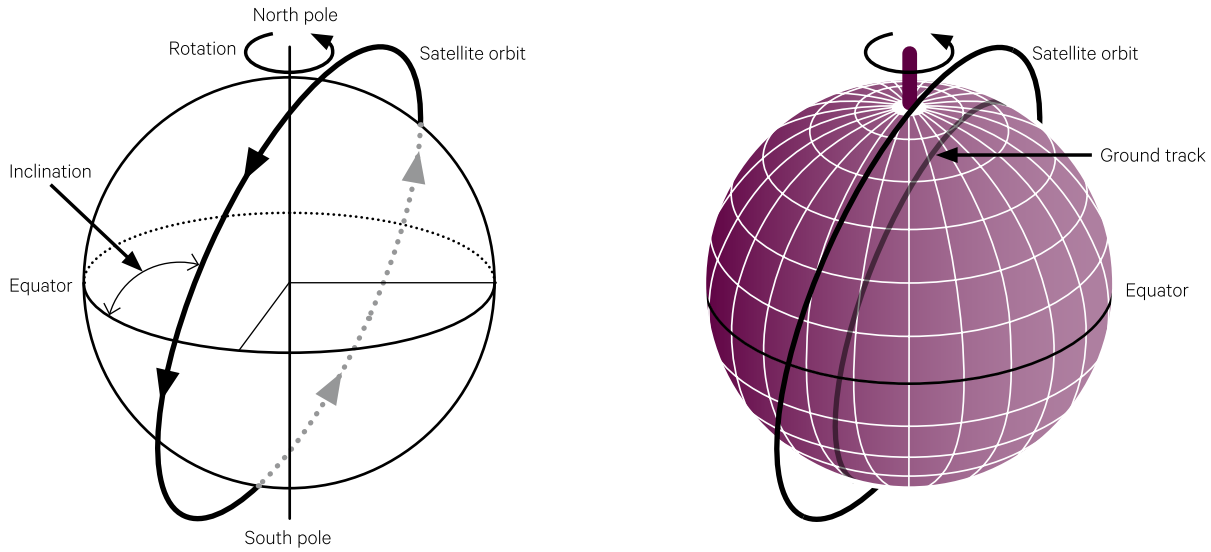
The various sensing and communications components of the venerable Landsat-5 satellite, which acquired over 2.5 million images during its 22 years of operation, are labelled in Figure 12.14a, and the Landsat-7 satellite is shown in Figure 12.14b. It is interesting to note that the body of each of these satellites could fit into the average car parking space[41].

While the Landsat series of satellites have been the best-known polar-orbiting satellites for EO, and have provided the most commonly used data, imagery is now available from a very wide range of satellite sensors. Some of these systems are illustrated in Figure 12.15 and listed in Table 12.6. (Please refer to the Glossary for full details of acronyms used in this table). A more comprehensive list of operational, non-commercial, EO satellite missions is provided in the *Earth Observation Handbook* (CEOS, 2015).

Figure 12.12 Orbit parameters

a. Spherical representation of Earth's globe showing satellite orbit relative to equator and poles. Descending node describes satellite movement from north to south and ascending node describes satellite movement from south to north.

b. Inclined view of spherical globe showing near polar orbit relative to northern latitudes



Adapted from: (Campbell, 2006)

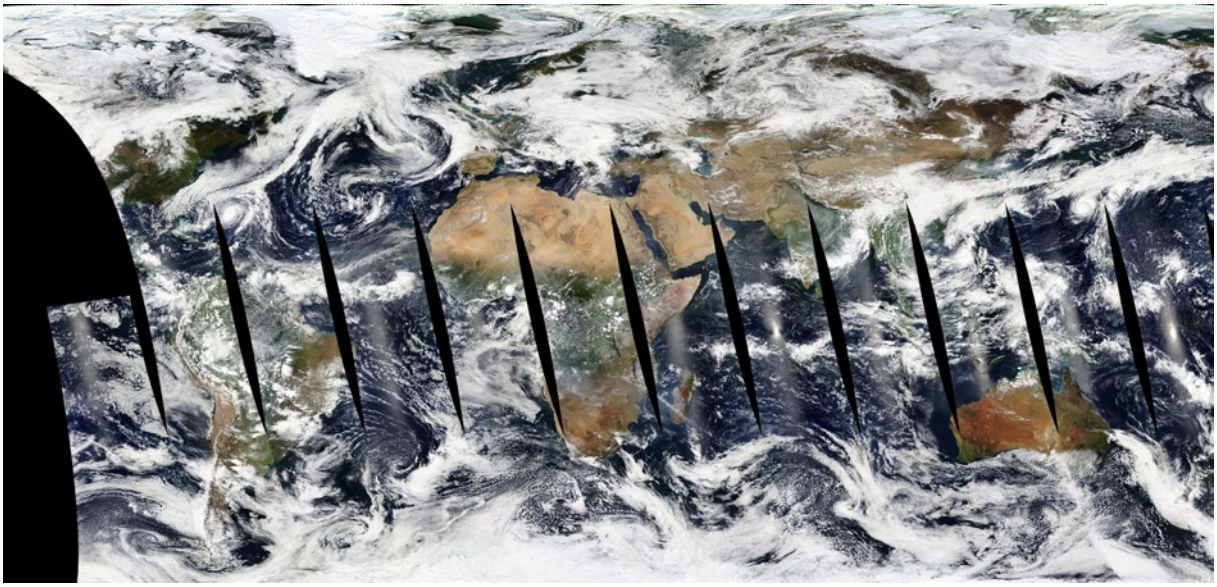
41. The bodies of Landsat-1, -2, and -3 measured 3 m in length with diameter 1.5 m; and the bodies of Landsat-7 and -8 measured 4.3 m in length with diameter 2.8 m (see Figure 12.14). Landsat-4 and -5 were of similar size to Landsat-7 (*https://directory.eoportal.org/web/eoportal/satellite-missions*).

Science has reached such a stage that...
the creation of an artificial satellite
of the Earth is a real possibility.
(A.N. Nesmeyanov, 1953)

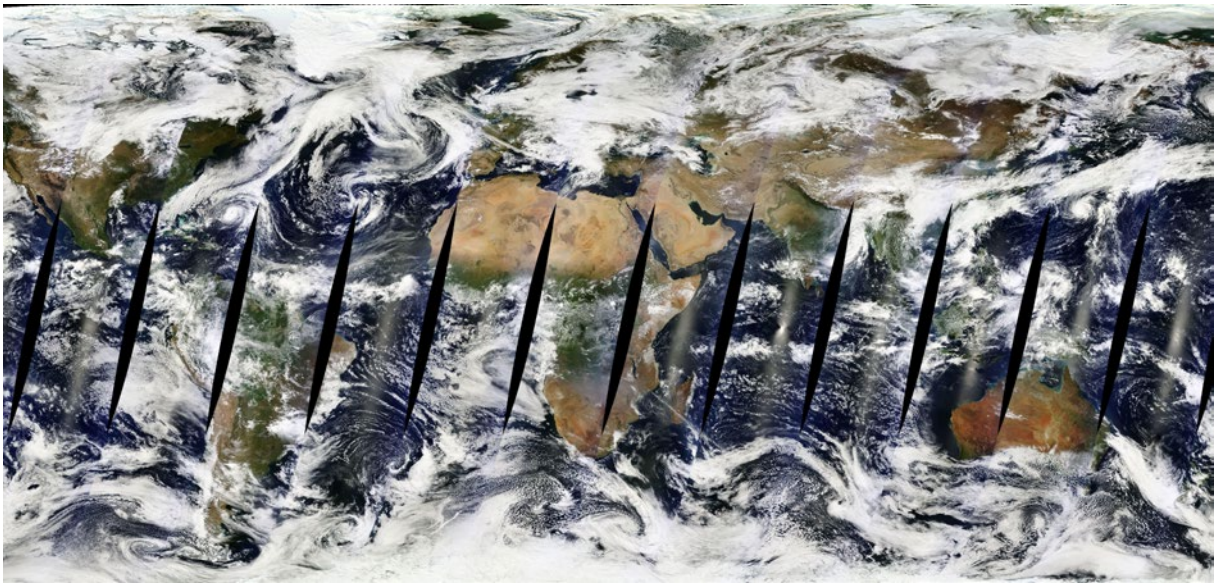
Figure 12.13 Daily acquistions for MODIS/Aqua and MODIS/Terra

These illustrations generated by NASA Worldview show the image paths acquired on 11 October 2016 by the MODIS sensor carried by the Aqua and Terra satellites (shown at 5 km resolution).

a. MODIS/Aqua collects imagery during its ascending mode so image strips are skewed in northwest/southeast direction.



b. MODIS/Terra collects imagery during its descending mode, so image strips are skewed in northeast/southwest direction.

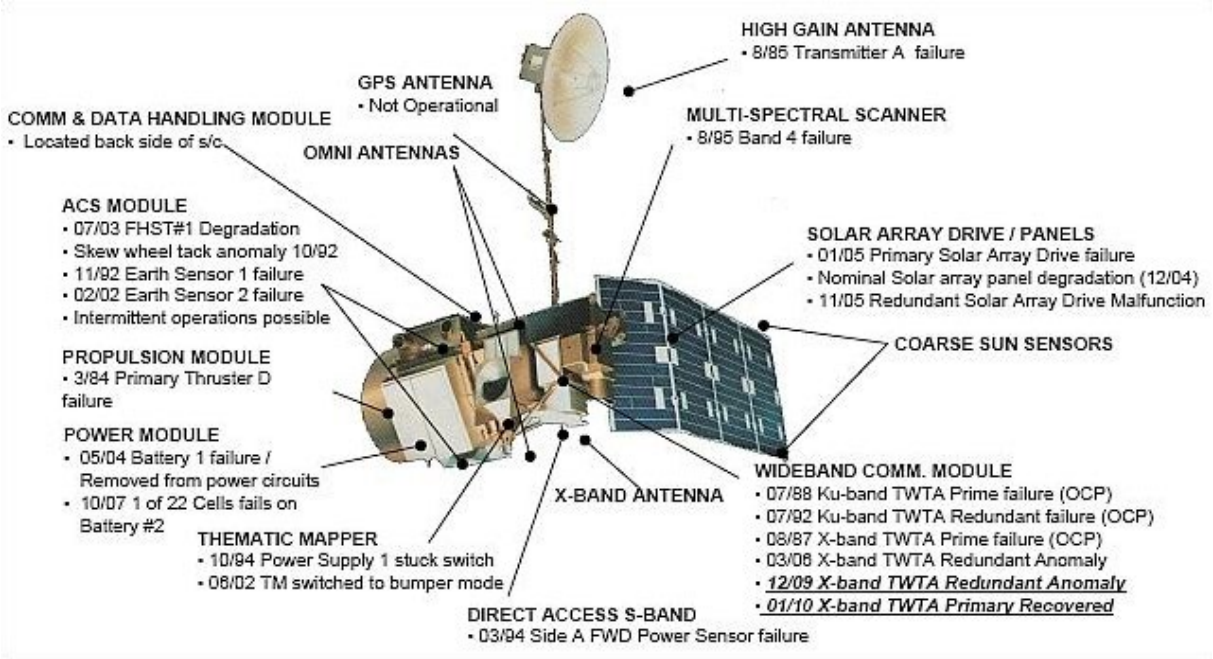


Source: NASA Worldview. Retrieved from *https://worldview.earthdata.nasa.gov*

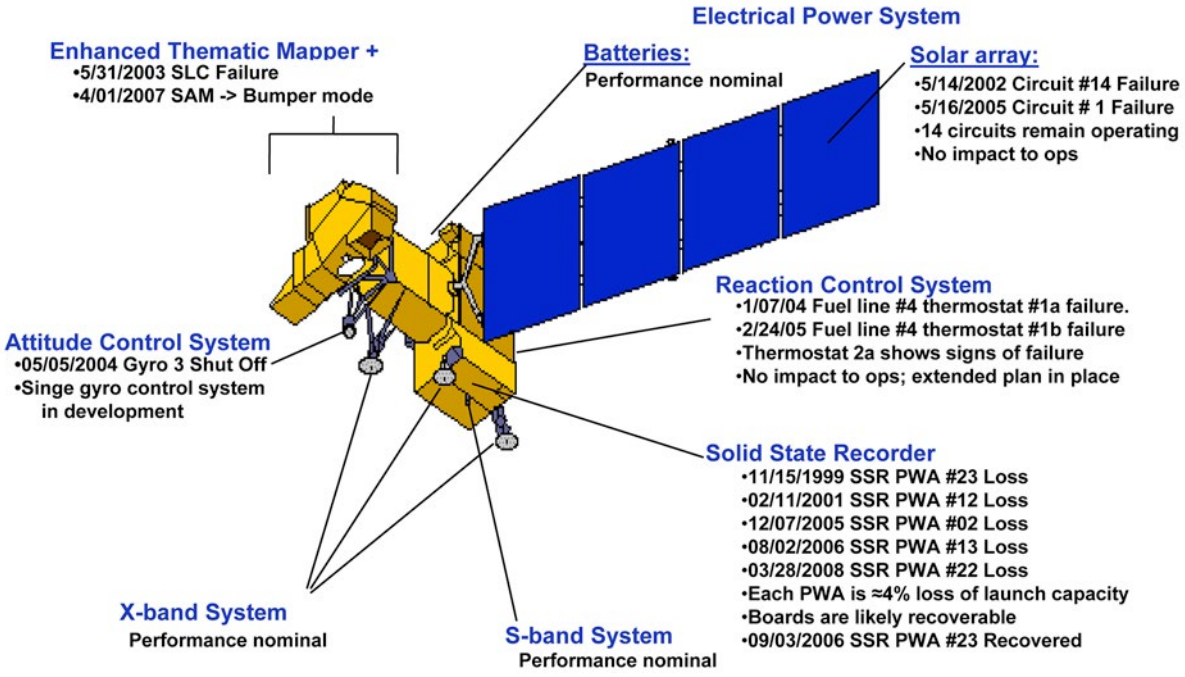
Figure 12.14 Landsat satellites

Components of Landsat satellites including malfunctions and recoveries before February 2010

a. Landsat-5 (similar body dimensions to Landsat-7)[42]



b. Landsat-7 (body length: 4.3m and diameter 2.8 m; each solar panel: 1.88 m × 2.26 m)

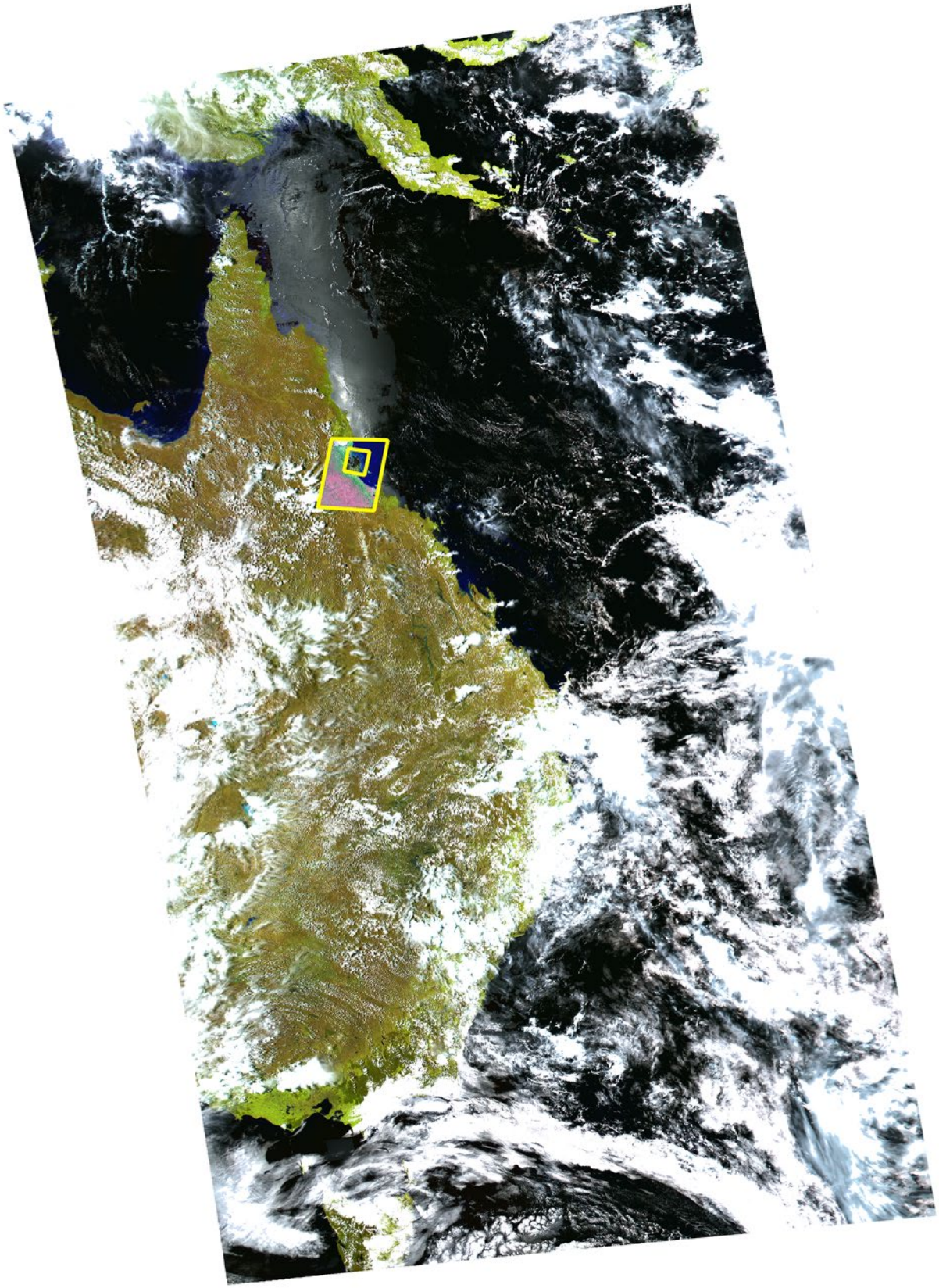


Source: Kalvelage (2010). Retrieved from *https://directory.eoportal.org/web/eoportal/satellite-missions/l/landsat-4-5*

42. Pers. Comm. Dennis Helder (USGS) and Leo Lymburner (GA)

Figure 12.15 Polar orbiting satellites provide a variety of spatial scales

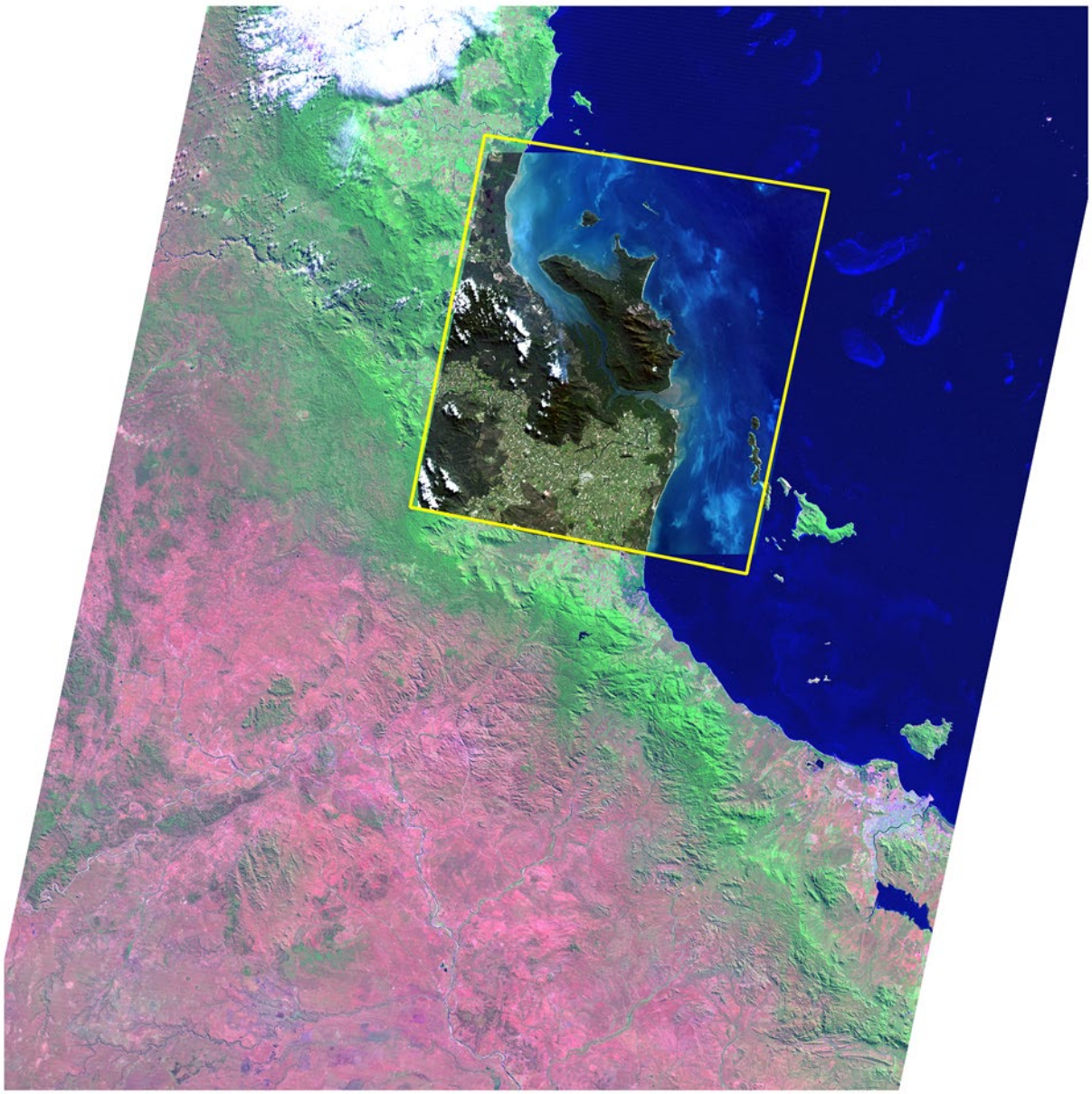
a. Full scene MODIS image showing the eastern half of Australia. Scene is 2250 km wide, acquired on 5 December 2010, and processed to 250 m spatial resolution



b. Full scene Landsat-5 TM image, showing the area around Hinchinbrook Island in Queensland. Scene is 185 km wide, acquired on the 1 June 2010, and processed to 25 m spatial resolution



c. ALOS AVNIR2 scene over the southern portion of Hinchinbrook island. Scene is 70km wide, acquired on the 12t June 2010, and processed to 10 m spatial resolution



Source: Norman Mueller, Geoscience Australia

Table 12.6 Polar orbiting satellites

For a comprehensive listing of non-commercial EO satellites and sensors visit CEOS (2016).[43][44]

Satellite (Agency)	Sensor	Number of Channels (in latest sensor)	Spectral range (in latest sensor)	Spatial Resolution (m, at nadir, in latest sensor)	Swath Width (km, at nadir, in latest sensor)	Image Archive	Radiometric Quantisation (bits)
ALOS (JAXA, Japan)	AVNIR-2	4	Optical	10	70	2006–2011	8
	PALSAR	1	L-band SAR in 3 modes with selectable polarisation	7–100	40–350	2006–2011	5
	PRISM	1	Panchromatic/ Stereo	2.5	70 (35 in triplet mode)	2006–2011	8
TIROS/ AVHRR (NOAA, USA)	AVHRR	6	Optical /thermal	1,100	~2700[45]	1978–present	10
Landsat (NASA/USGS, USA)	MSS	5	Optical /thermal	68 × 83	185	1972–1997	8
	TM/ETM+	7	Optical /thermal	30/120	185	1987–2011	8
	OLI/TIRS	11	Panchromatic/ optical /thermal	15/30/100	185	2014–present	12
Terra and Aqua (NASA, USA)	MODIS	36	Optical /thermal	250/500/ 1,000	2330	2000–present	12
Quickbird (Digital Globe, USA)	Quickbird	5	Panchromatic/ optical	0.55/2.16 (at 400 km altitude)	14.9 (at 400 km altitude)	2001–2015	11
SPOT (Airbus DS, France[46])	SPOT PAN SPOT MS	5	Panchromatic/ optical /stereo	1.5/6	60	1986–present	8–12
Geoeye	Geoimage	5	Panchromatic/ optical	0.41/1.65	15.2	2008–present	11

In Australia, the receiving station for Landsat imagery is located near Alice Springs, where Geoscience Australia (GA—and its predecessors) has been routinely receiving Landsat series data since 1979. At this central location, the station maintains contact with the satellite over the largest possible land area. The current Landsat 7 and 8 satellites take 16 days and 232 orbits to cover the measurable surface of the Earth, with each full orbit taking about 100 minutes and spanning 185 km in width. Landsat satellites 4 and 5 also followed this orbital pattern. The imaged paths are later subdivided into rows using the Worldwide Reference System (WRS-2) to form 185 km square scenes (representing 25 seconds of satellite time)[45].

Each scene can then be referenced by a path number to indicate east-west location, and a row number to define north-south position. The precise north-south location of a scene may be varied by defining a non-standard row, but obviously the east-west location is fixed by the orbital pattern. A similar system is used for other satellite imagery to define individual image scenes.

Continental scale imagery is provided by several sensors including AVHRR and MODIS. The AVHRR (Advanced Very High Resolution Radiometer) is currently carried on the NOAA 15, 16, 18 and 19 satellites. These spacecraft are part of the longest established series of low-altitude environmental satellites (TIROS/ESSA/ITOS/NOAA), TIROS–1 having been launched by the USA in April 1960. AVHRR imagery is used in two modes:

- Large Area Coverage (LAC) records spectral channels in 1.1 km pixels; while
- Global Area Coverage (GAC) sub-samples the LAC data to pixels sized 5.5 × 3.3 km.

43. Edward King (pers. comm.); see also Frulla et al. (1995)
44. Formerly Astrium/CNES
45. Image scenes for Landsat 1, 2 and 3 satellites were based on WRS-1; scenes for Landsat 4, 5, 7 and 8 are based on WRS-2. *http://landsat.usgs.gov/worldwide_reference_system_WRS.php*

While the AVHRR was designed for meteorological, hydrologic and oceanographic studies, its imagery is also useful for land-based studies. Since April 1982, NOAA has been using GAC data to compute global vegetation index (GVI) imagery, which reduces the effects of cloud cover. This imagery is produced by compositing geographically registered data sets over weekly imaging periods and has obvious application for monitoring global vegetation resources (Justice *et al*., 1985). The orbital patterns of the two NOAA satellites provide two daytime and two night-time overpasses each day for any region, with the wide swath overlap at temperate latitudes actually providing more frequent coverage. This repeat cycle offers valuable coverage of dynamic events such as flood and fire. Day/night image pairs also provide data for studies of thermal inertia. A number of organisations in Australia now receive AVHRR imagery, with large national repositories being available through GA, BoM and research stores such as IMOS and TERN[46].

A number of satellite sensors have been designed to observe ocean colour, starting with the Coastal Zone Colour Scanner (CZCS), launched in 1978. Subsequent missions include MOS, OCTS, POLDER, and SeaWiFS. As detailed in Volume 3B (Surface Waters), imagery from these sensors have been used to map chlorophyll concentration, sediment distribution and general ocean dynamics, including sea surface temperature. Details of these sensors and their calibration/validation for a range of applications are provided by IOCCG (2015).

Imagery from the Moderate Resolution Imaging Spectroradiometer (MODIS) (Justice and Townshend, 2002) has also proved valuable for mapping ocean colour. MODIS data are acquired by two NASA satellites—Terra (launched 1999) and Aqua (launched 2002)—which provide global coverage every one to two days. The frequency of MODIS imagery not only ensures up-to-date coverage of environmental change, but also allows the seasonal progression and longer-term dynamics of land cover change to be monitored and modelled (see Figure 12.13). The MODIS time series now comprises regular snapshots of Earth for over a decade, and is being increasingly exploited to understand and quantify various states and processes of the Earth's surface. Since 2000, up to four MODIS images have been acquired daily over most of Australia (see CEOS (2016) satellite and sensor details).

MODIS measures a total of 36 spectral bands, ranging from 400 nm to 14.4 μm. Two of these bands (band 1: visible red (620–670 nm) and band 2: near infrared (841–876 nm)) are imaged at 250 m spatial resolution. These bands were specifically included to detect land cover changes resulting from human activity (Townshend and Justice, 1988), and have been successfully used to map change associated with natural and anthropogenic causes (Hansen *et al*., 2000; Wessels *et al*., 2004). In addition to the MODIS spectral band data, NASA offers a range of MODIS image products, which allow improved characterisation of biophysical and biochemical characteristics of vegetation. Two of these products are 16-day composites of the standard vegetation indices, the Normalised Difference Vegetation Index (NDVI) and the Enhanced Vegetation Index (EVI; see Volumes 2 and 3A).

To avoid the problems associated with cloud cover in visible and infrared data, several northern hemisphere space agencies have developed and operate a number of microwave sensors on satellite platforms. The Canadian Radarsat series carry a C-band SAR with movable incidence angle and can acquire imagery with a range of spatial resolutions. Radarsat-2 SAR has multiple polarisation modes including a fully polarimetric mode. The ESA operated ERS-1 from 1991 to 2000, ERS-2 from 1995–2011 and launched Envisat in 2001. Each of these satellites carried an array of imaging and non-imaging devices, including C-band radar and optical/thermal radiometers and spectrometers. The JERS-1 satellite (Japan, 1992–1998), which carried an L-band SAR and optical camera, was replaced by the ALOS platform and its optical/SAR sensors (see Table 12.6). Data from these sensors have been used for numerous global applications (see Volumes 2 and 3).

46. TERN AusCover Remote Sensing Data Facility: *http://www.auscover.org.au/data/product-list*

12.3 Further Information

EO Handbook (CEOS, 2016): *http://www.eohandbook.com*

Geoscience Australia (GA): *http://www.ga.gov.au/earth-observation.html*

National Aeronautical and Space Agency (NASA): *http://www.nasa.gov*

NASA World Wind: *http://worldwind.arc.nasa.gov*

NASA Worldview: *https://worldview.earthdata.nasa.gov*

Landsat: *http://landsat.gsfc.nasa.gov* *http://landsat.usgs.gov*

MODIS: *http://modis.gsfc.nasa.gov*

NOAA Geostationary Satellite Server: *http://www.goes.noaa.gov/index.html*

World Meteorological Organisation (WMO): *http://www.wmo.int/pages/index_en.html*

Coordinating Group of Meteorological Satellites (CGMS): *http://www.cgms-info.org*

ASPRS Guide to Land Imaging Satellites (Stoney, 2008)

European Space Agency (ESA): *http://www.esa.int/ESA*

Japanese Aerospace Exploration Agency (JAXA): *http://global.jaxa.jp*

Interactive Satellite Map: *http://richiecarmichael.github.io/sat/index.html*

12.4 References

Campbell, J. B. (2006). Introduction to Remote Sensing, Fourth Edn. Guilford Press.

CEOS (2015). The Earth Observation Handbook. Committee on Earth Observation Satellites, ESA Communications, The Netherlands. Retrieved from *http://www.eohandbook.com*.

CEOS (2016). The CEOS Database. Retrieved from *http://database.eohandbook.com*.

CGMS (2016). Coordinating Group of Meteorological Satellites. Retrieved from *http://www.cgms-info.org*.

ESA (2016). European Space Agency. Retrieved from *http://www.esa.int/ESA*.

Frulla, L. A., Milovich, J. A., and Gagliardini, D. A. (1995). Illumination and Observation Geometry for NOAA-AVHRR Images. International Journal of Remote Sensing, 16(12), pp. 2233-2253.

Fujita, T. G., Bradbury, D. L., Murino, C., and Mull, L. (1968). A study of mesoscale cloud motions computed from ATS-1 and terrestrial photographs from satellite (Research Paper 71). Mesometeorological research project. Department of Geophysical Sciences, University of Chicago.

Geoscience Australia (2016). Geoscience Australia. Retrieved from *http://www.ga.gov.au*.

Hansen, M. C., Defries, R. S., Townshend, J. R. G., and Sohlberg, R. (2000). Global land cover classification at 1km spatial resolution using a classification tree approach. International Journal of Remote Sensing, 21(6-7), pp. 1331-1364. doi:*http://dx.doi.org/10.1080/014311600210209*.

JMA (2016). Japan Meteorological Agency. Retrieved from *http://www.jma.go.jp/jma/jma-eng/satellite/introduction/history.html*.

Justice, C. O., and Townshend, J. R. G. (2002). Special issue on the moderate resolution imaging spectroradiometer (MODIS): a new generation of land surface monitoring. Remote Sensing of Environment, 83(1-2), pp. 1-2. doi:*http://dx.doi.org/10.1016/s0034-4257(02)00083-4*.

Justice, C. O., Townshend, J. R. G., Holben, B. N., and Tucker, C. J. (1985). Analysis of the phenology of global vegetation using meteorological satellite data. International Journal of Remote Sensing, 6(8), pp. 1271-1318. doi:*http://dx.doi.org/10.1080/01431168508948281*.

Kalvelage, T. (2010). Landsat Project Status—Landsat Science Team Meeting 2010. United States Geological Survey. Retrieved from *http://landsat.usgs.gov/documents/Jan_2010_ScienceTeamMeeting_LandsatOverview_TomK_final_Jan19.pdf*.

Kelly, G. A., Forgan, B. W., Powers, P. E., Le Marshall, J. F., Hassett, M., and O'Connor, B. (1983). A satellite-based operational system for upper air analysis in the Australian region. Remote Sensing of Environment, 13(5), pp. 369-390. doi:*http://dx.doi.org/10.1016/0034-4257(83)90007-X*.

Kelly, G. A., Mills, G. A., and Smith, W. L. (1978). Impact of Nimbus-6 Temperature Soundings on Australian Region Forecasts. Bulletin of the American Meteorological Society, 59, pp. 393-405.

Le Marshall, J. F., C., S., and Pescod, N. (1996a). Estimation and assimilation of hourly high spatial resolution wind vectors based on GMS 5 observations. Australian Meteorological Magazine, 45, pp. 279-284.

Le Marshall, J. F., Davidson, R. E., Willmott, M. E., and Powers, P. E. (1989). A physically based operational atmospheric sounding system for TOVS data in the Australian region. Australian Meteorological Magazine, 37, pp. 193-199.

Le Marshall, J. F., Leslie, L. M., and Bennett, A. F. (1996b). Tropical Cyclone Beti - an example of the benefits of assimilating hourly satellite wind data. Australian Meteorological Magazine, 45, pp. 275-279.

Le Marshall, J. F., Pescod, N., Seaman, B., Mills, G., and Stewart, P. (1994). An Operational System for Generating Cloud Drift Winds in the Australian Region and Their Impact on Numerical Weather Prediction. Weather and Forecasting, 9(3), pp. 361-370. doi:*http://dx.doi.org/10.1175/1520-0434(1994)009%3C0361:AOSFGC%3E2.0.CO;2*.

Le Marshall, J. F., Pescod, N. R., Khaw, A., and Allen, G. (1993). The real time generation and application of cloud drift winds in the Australian region. Australian Meteorological Magazine, 42, pp. 89-103.

Le Marshall, J. F., Pescod, N. R., Mills, G. A., and Stewart, P. K. (1992). Cloud drift winds in the Australian Bureau of Meteorology. Australian Meteorological Magazine, 40, pp. 247-250.

Le Marshall, J. F., Pescod, N. R., Mills, G. A., and Stewart, P. K. (1999). Local estimation of GMS-5 water vapour motion vectors and their application to Australian region numerical weather prediction. Australian Meteorological Magazine, 48, pp. 73-77.

Le Marshall, J. F., Smith, W. L., and Callan, G. M. (1985). Hurricane Debby—An Illustration of the Complementary Nature of VAS Soundings and Cloud and Water Vapor Motion Winds. Bulletin of the American Meteorological Society, 66(3), pp. 258-263. doi:*http://dx.doi.org/doi:10.1175/1520-0477(1985)066%3C0258:HDIOTC%3E2.0.CO;2*.

Leslie, L. M., Le Marshall, J. F., Morison, R. P., Spinoso, C., Purser, R. J., Pescod, N., and Seecamp, R. (1998). Improved Hurricane Track Forecasting from the Continuous Assimilation of High Quality Satellite Wind Data. Monthly Weather Review, 126(5), pp. 1248-1258. doi:*http://dx.doi.org/10.1175/1520-0493(1998)126%3C1248:IHTFFT%3E2.0.CO;2*.

NASA (2009). Catalog of Earth Satellite Orbits. Retrieved from *http://earthobservatory.nasa.gov/Features/OrbitsCatalog/*.

NASA (2016). WRS-2 map. Retrieved from *http://landsat.gsfc.nasa.gov/wp-content/uploads/2013/01/wrs2.gif*

Smith, W. L., Woolf, H. M., Hayden, C. M., Schreiner, A. J., and Le Marshall, J. F. (1983). The Physical Retrieval TOVS Export Package. Paper presented at the First International TOVS Study Conference, Igls, Austria.

Smith, W. L., Woolf, H. M., Hayden, C. M., Wark, D., and McMillin, L. (1979). The TIROS-N operational vertical sounder. Bulletin of the American Meteorological Society, 60, pp. 1177-1187.

Stoney, W. E. (2008). ASPRS Guide to Land Imaging Satellites. Noblic Inc. Retrieved from *http://www.asprs.org/a/news/satellites/ASPRS_DATABASE_021208.pdf*.

Townshend, J. R. G., and Justice, C. O. (1988). Selecting the Spatial-Resolution of Satellite Sensors Required for Global Monitoring of Land Transformations. International Journal of Remote Sensing, 9(2), pp. 187-236.

Wessels, K. J., De Fries, R. S., Dempewolf, J., Anderson, L. O., Hansen, A. J., Powell, S. L., and Moran, E. F. (2004). Mapping regional land cover with MODIS data for biological conservation: Examples from the Greater Yellowstone Ecosystem, USA and Para State, Brazil. Remote Sensing of Environment, 92(1), pp. 67-83. doi:*http://dx.doi.org/10.1016/j.rse.2004.05.002*.

WMO (2016). World Meteorological Organisation. Retrieved from *http://wmo.int*.

Young, M. T., Doolittle, R. C., and Mace, M. (1972). Operational procedures for estimating wind vectors and geostationary satellite data (NESS 39). NOAA Technical Memorandum. National Environmental Satellite Service, National Oceanographic and Atmospheric Administration, U.S. Department of Commerce.

Zapotocny, T. H., Jung, J. A., Le Marshall, J. F., and Treadon, R. E. (2007). A Two-Season Impact Study of Satellite and In Situ Data in the NCEP Global Data Assimilation System. Weather and Forecasting, 22(4), pp. 887-909. doi:*http://dx.doi.org/10.1175/WAF1025.1*.

Zapotocny, T. H., Jung, J. A., Le Marshall, J. F., and Treadon, R. E. (2008). A Two-Season Impact Study of Four Satellite Data Types and Rawinsonde Data in the NCEP Global Data Assimilation System. Weather and Forecasting, 23(1), pp. 80-100. doi:*http://dx.doi.org/10.1175/2007WAF2007010.1*.

EMR Sensors for Earth Observation



The next three sections consider aspects of sensors that detect electromagnetic radiation (EMR) for Earth Observation (EO). Section 13 introduces the basic principles of sensing EMR, including sensor design and sensor categories. Detection systems that are used to remotely acquire EO data can be considered in terms of three broad groups:

- imaging—active and passive sensors that record radiation for a contiguous grid of locations on the Earth's surface (see Sections 14 and 15);
- non-imaging—active and passive sensors that record radiation for discrete locations on the Earth's surface (see Section 16.1); and
- sounding—active and passive sensors that record the vertical distribution of radiation within Earth's atmosphere and oceans, often at defined altitudes/depths (see Section 16.2).

Contents

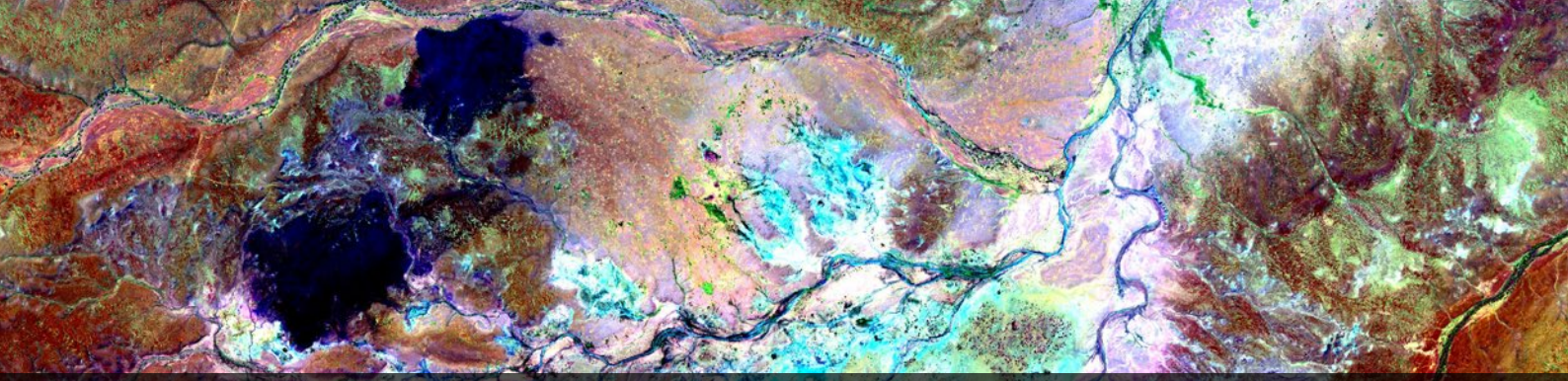
13 Sensing Electromagnetic Radiation 169

14 Passive Imaging Systems 179

15 Active Imaging Systems 203

16 Non-imaging and Sounding Systems 215

Background image on previous page: SPOT MSS image over Uluru (Ayers Rock), Northern Territory, acquired on 16 September 2013.
Source: © CNES (2016). **Distribution:** Airbus DS.



13 Sensing Electromagnetic Radiation

An overview of measuring EMR is provided in Section 13.1 below and the major types of Earth Observation (EO) sensors are introduced in Section 13.2. Aspects of EM sensor design and performance are discussed in Sections 13.3 and 13.4 respectively. CEOS categories for EO sensors are reviewed in Section 13.5.

13.1 Measuring Electromagnetic Radiation

As introduced in Section 5 above, EMR is a form of energy that can be transmitted through empty space and between objects. The EMR spectrum spans from very short wavelengths (such as gamma rays and X-rays), through the visible spectrum, to very long waves (such as microwaves and radio frequency waves). While all EMR waves travel at the speed of light (3×10^8 m sec^{-1}), the energy they carry varies with both the wavelength/frequency of radiation and its intensity. Being a wave, EMR has properties described in terms of intensity and phase as a function of wavelength. These properties are both used in various forms of remote sensing. As introduced in Section 2.5, EMR can be observed in terms of several characteristics, including:

- amplitude—maximum oscillation of wave from midpoint and proportional to the energy carried;
- wavelength or frequency—distance travelled in one full wave cycle or number of cycles per unit time, with shorter wavelength at higher frequency EMR carrying more energy;
- polarisation—orientation of electric field of EMR relative to reference vector; and
- coherence—extent to which two waves oscillate in phase; for EM waves, this characteristic describes a relationship in time (see Section 2.5.5).

EMR that is emitted by a source can be reflected, transmitted, absorbed or re-emitted by objects or surfaces (see Section 5). Most passive EO sensors detect the intensity of incoming solar energy that is reflected, transmitted (that is, scattered) or re-emitted by terrestrial materials into the field of view of the sensor. Active sensors generate their own energy source, which is radiated towards a target, and can detect range to the target using phase information of the energy backscattered from the target.

The specific geometric relationships between the sensor and target directly impact on the energy being detected by a remote sensing device. In simple terms, the energy that is observed by a sensor can be considered as falling within a viewing 'cone'. Accordingly, measured radiation needs to be quantified in terms of solid (three-dimensional) angles, which are represented units of steradians (see Figure 2.1). Specific aspects of illumination and viewing geometries are further discussed in Volume 1B—Section 3 and Volume 1X—Appendix 5.

The terminology used to quantify electromagnetic radiation (EMR) is introduced in Section 2.6. It is recommended that readers review this material in conjunction with the following sub-sections. For a more detailed treatment of these topics, readers are referred to the *Manual of Remote Sensing* (Colwell, 1983), *The Light Measurement Handbook* (Ryer, 1997), *ASPRS Manual of Remote Sensing* (Morain and Budge, 1998), or Elachi and van Zyl (2006).

Similarly, the mechanism of human colour vision and the representation of colour are introduced in Section 2.7. As detailed in Volumes 2 and 3, in order to detect and identify features in EO imagery, most image-based thematic mapping techniques attempt to mimic the processes of human vision, often using wavelengths undetected by the human visual system.

Background image: Hymap airborne hyperspectral image mosaic of Hawker Springs Complex, 80 km west of Lake Eyre, SA. It is displayed using the 2.22 μm band as red, the 0.833 μm band as green and the 0.444 μm band as blue. This region features wetlands in an arid environment, fed by Great Artesian Basin springs. This imagery was acquired by HyVista Corporation for the Allocating Water and Maintaining Springs of the Western Great Artesian Basin project in 2009.
Source: Megan Lewis, University of Adelaide

13.2 Earth Observation Sensors

By definition, a remote sensing device acquires information about a target, such as an object or surface, by detecting energy from it. Since there is no physical contact between the sensor and the target, the sensor must rely on measuring some form of energy that is being radiated by the target. In this text, we use the 'sensor' to refer to the remote sensing device or instrument and 'detector' to describe the component of a sensor which actually detects EMR.

The source of the radiation detected by a remote sensor may or may not be independent of the sensing device. Active remote sensing devices, such as radar (microwave) and lidar (optical), radiate a particular form of energy towards a target object or surface and then detect the amount of that energy which is scattered or reflected by it. Passive sensors, however, detect energy that originates from an independent source and is scattered or reflected by a target. The major source of EMR detected by passive remote sensors is the Sun, but some radiation also comes from other celestial bodies and cosmic background radiation. While the Sun is commonly assumed to be a point source of constant illumination, its energy does not emanate from a point and is not constant. The intensity of solar radiation has been shown to vary with time, and remote sensing measurements have contributed to the growing body of knowledge on the precise extent of this variation.

One category of remote sensors, polarimeters, measures polarisation, rather than radiation, characteristics of targets (see Section 2.5.3). These characteristics indicate the shape, shading and roughness of surface and atmospheric features, which are generally uncorrelated with spectral and intensity data acquired by sensors that are designed to observe the radiation reflected or emitted by surface materials (Tyo *et al.*, 2006; Snik *et al.*, 2014).

The major categories of EO sensors are grouped in terms of EMR spectral region in Table 13.1.

Table 13.1 Spectral regions observed by EO sensors

Note that, in practice, atmospheric windows restrict these ranges for observing Earth's features (see Table 5.4).

Spectral region	Wavelength	EO sensor	
		Passive	Active
Visible	0.38 to 0.7 μm	Passive radiometers Passive spectroradiometers Passive imaging spectrometers Polarimeters	Lidar
Near Infrared (NIR)	0.7 to 1.1 μm		
Short wave Infrared (SWIR)	1.1 to 3.0 μm		
Middle Infrared (MIR)	3.0 to 8.0 μm	Passive radiometers Polarimeters	
Thermal Infrared (TIR)	8.0 to 15.0 μm		
Microwave	1 mm to 1 m	Microwave radiometers Microwave spectrometers	Radar Polarimeters Scatterometers
Radio	>10 cm	Passive radiometers Sounders	Imaging radar Altimeters Sounders

We have all kinds of limitations as human beings.
I mean we can't see the whole electromagnetic spectrum;
we can't see the very small; we can't see the very far.
So we compensate for these short comings with technological scaffoldings.
(Jason Silva)

EO sensors for terrestrial, coastal and ocean monitoring (as opposed to atmospheric monitoring) primarily measure EMR that is reflected or emitted from the Earth's surface. These sensors, however, can vary considerably in terms of the resolution and extent of the data they acquire (see Volume 1B—Section 1). Since the characteristics of each sensor are designed to optimise discrimination of specific target features, EO sensors differ in terms of:

- spectral characteristics—such as the wavelength region(s) detected;
- spatial characteristics—such as the ground area 'viewed' for each observation (or pixel size in imagery);
- radiometric characteristics—such as the 'threshold' of energy required to differentiate target radiance levels; and
- temporal characteristics—such as the repeat cycle for subsequent measurements.

Sections 14, 15 and 16 provide a detailed introduction to a range of EO sensors in terms of their spectral sensitivity, operation and application areas. Here we briefly introduce three broad types of sensors in terms of instrument type and function:

- passive sensors—radiometers, spectroradiometers and spectrometers that detect reflected EMR in optical wavelengths and emitted EMR in thermal wavelengths (see Section 13.2.1);
- active sensors—lidar and radar sensors that generate their own energy source then detect its 'echo' (see Section 13.2.2); and
- sounders—active and passive sensors that acquire observations at specific water depths or atmospheric altitudes (see Section 13.2.3).

13.2.1 Passive sensors

Reflected solar energy is detected by passive remote sensing devices in the visible, near infrared and middle infrared regions, while the Earth's emitted energy may be detected in the middle infrared, thermal infrared and microwave wavelengths (see Section 5.2.2). A passive sensor actually records the 'radiance', that is the radiation within a solid angle of view, of its target (see Section 2.6.1). To account for variations in the level of incident radiation, 'reflectance' is defined as the ratio of reflected to incident radiation, that is, the proportion of energy reflected by an object. In well-designed passive remote sensing systems, material properties, which are encapsulated in reflectance, dominate (or can be extracted from) the recorded signal.

A wide range of sensors has been designed to cater for the different priorities that can be placed on potential target information. These requirements have produced three fundamental types of passive EMR remote sensing instruments:

- radiometers—measure target radiation in broad wavelength intervals (see Section 13.2.1.1);
- spectroradiometers—measure target radiation in narrow wavelength bands (see Section 13.2.1.2);
- spectrometers—measure target radiation in discrete wavelengths over a wide range to generate a spectrum for the target (see Section 13.2.1.3); and
- polarimeters—measure polarisation characteristics of targets (see Section 13.2.1.4).

13.2.1.1 Radiometers

Radiometers measure EMR from a target in defined wavelength bands. These instruments are used for sensing relatively weak signals, such as thermal infrared or passive microwave, and/or when few spectral measurements per target are required, as in panchromatic or multispectral imagery. Radiometers are often named to indicate the spectral range that they detect, such as 'microwave radiometer'. Imaging radiometers combine a scanning mechanism with one or more radiometer(s) to measure target radiance over an extended area (see Section 14.2). When measuring strong radiance signals, such as in optical wavelengths, radiometers can deliver high spatial resolution imagery (see Section 14.3.1), whereas measurement of weaker emitted radiation delivers imagery with lower spatial resolution (see Sections 14.4 and14.5).

13.2.1.2 Spectroradiometers

Spectroradiometers are advanced radiometers that measure target radiance for multiple, narrowly-defined, wavelength channels. They are principally designed to capture detailed optical information about the Earth's surface. As further discussed in Section 14.3.2, most current, satellite-borne, multispectral sensors for EO are spectroradiometers.

13.2.1.3 Spectrometers

Spectrometers are precise instruments designed to measure spectra. Imaging spectroscopy (or hyperspectral imaging) acquires imagery in numerous, narrow contiguous spectral channels such that a spectrum for imaged targets can be derived (see Section 14.3.3). Within a finite spectral range, spectrometers separate EMR from a target into a frequency spectrum that shows the constituent wavelengths.

13.2.1.4 Polarimeters

Both imaging and non-imaging passive polarimeters have been designed to measure a range of polarisation information in optical and thermal wavelengths, including specific wavelength regions (spectropolarimeters). In EO, passive polarimeters are primarily used to observe aerosols in the Earth's atmosphere, but can also provide valuable information for surveillance and military applications. Operation of passive polarimeters is beyond the scope of this volume, but interested readers are referred to Tyo *et al*. (2006).

13.2.2 Active sensors

Active remote sensing systems operate in the visible and microwave parts of the EM spectrum. The major categories of active, satellite-borne EO sensors include:

- lidar—measure the vertical distribution of features in the atmosphere, on the Earth's surface, or in shallow water, potentially using multiple polarisations in optical wavelengths (see Section 15.1);
- Synthetic Aperture Radar (SAR)—measure microwave response from surface features, potentially using multiple polarisations (see Sections 15.2);
- altimeters—based on radar or lidar to measure distance to specific features (see Sections 16.1.2.1 and 16.1.2.2);
- scatterometers—based on radar to measure surface texture (see Section 16.1.2.3); and
- polarimeters—radar instruments for observing polarisation characteristics of a target.

The operation of radar and lidar sensors is further detailed in Sections 15 and 16.

13.2.3 Sounders

A final category of EO instruments includes sounders, which can be designed as both active and passive sensors. Sounders are used to observe properties of:

- the atmosphere at particular altitudes, to derive information about air composition, temperature and movement; or
- water bodies at specified depths, to determine profiles of water depth, colour and temperature.

The types of measurements derived from sounding sensors are further discussed in Section 16.2.

13.3 Sensor Design Constraints

Remote sensing devices may record EMR directly onto photographic film or electronically code the radiation in numeric form to produce a digital image. Photographic recording of data simply requires standard film processing to obtain an image for human interpretation, but such data need to be digitised before being processed by a computer (see Volume 1X—Appendix 4.3).

A digital remote sensor observes energy that is radiated by a target then quantifies the observed energy levels as a digitised electronic signal. Since the nature of interaction between EMR and matter changes across the EMR spectrum, different techniques are required to observe energy in different wavelength regions. For example, sensors that detect optical wavelengths use lenses and optical components to observe radiation, whereas sensors detecting longer EMR wavelengths (such as microwave and radio frequencies) commonly use antennae for this purpose.

The simplest sensors incorporate components to detect and record radiation, but most also include components for focussing and separating radiation into sub-categories, such as specific wavelength or frequency ranges (known as spectral channels or bands) or polarisations, and standardising the detected and digitised levels of radiation to a reference measurement scale. Components of specific sensors are discussed in greater detail in Sections 14, 15 and 16.

While we have introduced EO sensors in generic terms, each sensor is designed for a specific purpose and only produces reliable observations when operated within defined conditions, such as the specified ranges for:

- platform speed and stability;
- target radiation levels; and
- ambient temperature and humidity.

The engineering embodied in all sensors is the result of design decisions, which have been dictated by technical and management constraints. Each sensor has a finite time to measure the radiance from a target object or surface. The time interval required for a sensor to register a valid observation is known as the dwell time. Thus, the sensor platform must travel at an appropriate speed to provide sufficient dwell time for each observation. For a given dwell time, trade-offs are necessary between both:

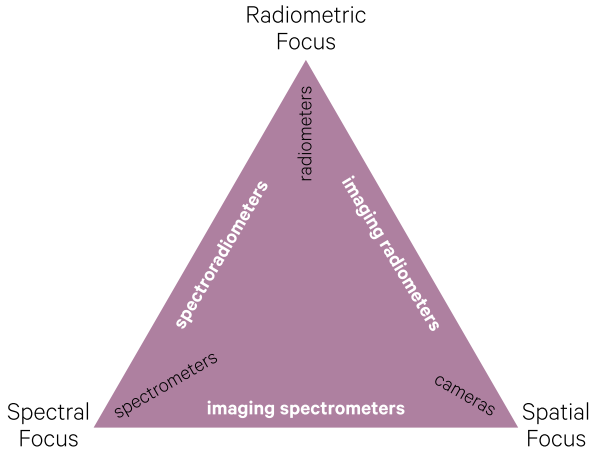
- the number of measurements of a target and the strength of the measured signal(s); and
- the number of targets measured and the strength of the measured signal(s).

As illustrated in Figure 13.1a, these relationships can be viewed as a triad in which the apexes represent focus on:

- spatial information about the target;
- spectral information about the target; and
- radiometric information about the target (Elachi and van Zyl, 2006).

Figure 13.1 Information acquired by sensors

Sensor design involves trade-offs between focussing on radiometric, spectral and spatial detail.



Adapted from: Elachi and van Zyl (2006) Figure 1-1

The design of any sensor implicitly involves assigning priorities to each type of potential information about the target object or surface. For example, in a passive imaging sensor:

- spatial focus could equate to the spatial resolution of the image (pixel size);
- spectral focus could equate to the spectral density of the image (number of spectral channels); and
- radiometric focus could equate to the radiometric resolution of the image (number of bits per pixel).

In essence, for the reasons discussed above, any given sensor cannot simultaneously acquire detailed spatial, spectral *and* radiometric information. The implications of design constraints for particular types of sensors are further considered in Volume 1B—Sections 1 and 2.

13.4 Sensor Performance Metrics

One of the primary goals in sensor design is to minimise 'noise'. In this context, noise means the acquisition of false readings that result from the sensor components rather than the target object or surface. It is also important that, for a given spectral band, the sensor response is uniform both over the detected wavelengths and over time, and linear with respect to the incident radiation (Norwood and Lansing, 1983).

The most commonly encountered metric to indicate noise levels registered by a sensor is the Signal-to-Noise Ratio (SNR or S/N). Ideally sensors register much higher levels of signal than noise, so higher SNR values are more desirable (see also Volume 1B—Section 2.1.3). Some of the other performance metrics commonly used to compare sensors are summarised in Table 13.2. These metrics are referenced in subsequent sections.

Table 13.2 Common sensor performance metrics

V_n = RMS noise voltage; A = detector area; q = electron charge; R = responsivity
f = frequency of optical signal; Δf = bandwidth; h = Planck's constant (see Section 2.11)

Performance Measure	Abbreviation	Definition	Units	Indicates
Signal-to-noise ratio	*SNR*	$\frac{P_{signal}}{P_{noise}}$	–	Strength of sensor signal relative to background noise
Quantum Efficiency	η	$\frac{signal\ electrons}{incident\ photons}$	%	Conversion efficiency of incident photons to signal electrons (wavelength-dependent)
Spectral responsivity	R_λ	$\eta\frac{q}{hf}$	A/W	Electrical output per optical input (wavelength-dependent)
Noise Equivalent Power	*NEP*	$\frac{V_n}{R}$	W	Signal power to result in SNR ratio of 1 in 1 Hz output bandwidth
Spectral Noise Equivalent Power	NEP_λ	$\frac{V_n}{R_\lambda}$	W	Wavelength-dependent NEP
Detectivity	*D*	$\frac{1}{NEP}$	W^{-1}	Smallest detectable signal (reciprocal of NEP)
Specific detectivity	*D**	$\frac{\sqrt{A\Delta f)}}{NEP}$	W^{-1} cm.sec$^{-1/2}$	Normalised measure of smallest detectable signal

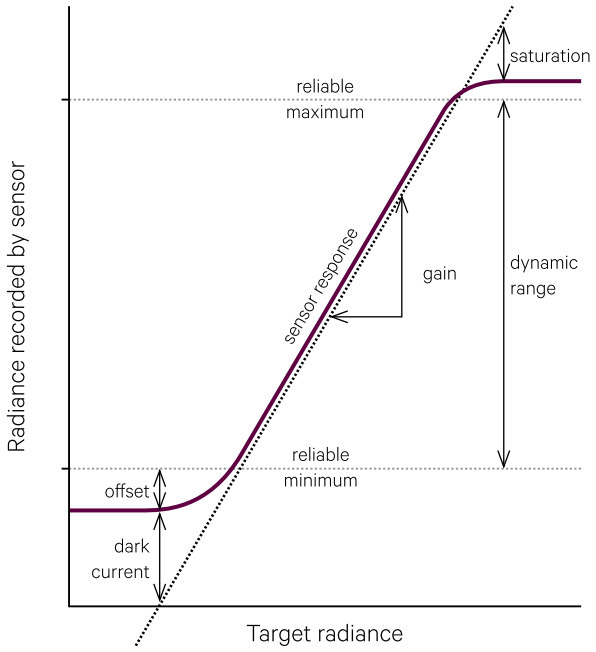
Source: Colwell (1983); Accetta and Schumaker (1993)

Each sensor band is designed to detect target radiance within a defined energy range, known as its dynamic range. As illustrated in Figure 13.2, this range conservatively lies within the actual minimum and maximum sensitivity of the sensor, with the difference between the actual minimum and the dynamic range minimum being known as the offset. Below the actual minimum sensitivity, observations are known as 'dark current', which is likely to result from the electronic components rather than target radiance. Similarly, above the actual maximum sensitivity, the sensor reaches saturation, that is, it cannot detect any additional target radiance. In image sensors, the characteristics of individual detector components can permit a saturated pixel to impact the values observed for adjacent pixels, potentially resulting in an imaging artefact that is more extensive that a single pixel (see Volume 1B—Section 2).

Within the dynamic range, sensor design aims to result in sensor readings that are confidently related to the radiance of the target object or surface. Ideally, the relationship between the target radiance and the observed radiance, or the *gain*, is linear (see Figure 13.2), in which case this relationship can be summarised as the slope of the line. For a given target object or surface, a high gain sensor would record a larger range of radiance values than one with low gain. In some sensors, the gain can be selected from pre-defined ranges to be most appropriate to the target being observed.

Figure 13.2 Sensor performance terms

Each sensor band detects radiance within a defined energy range—the dynamic range—between its actual minimum and maximum sensitivities. The relationship between input and output radiance values is known as the gain.

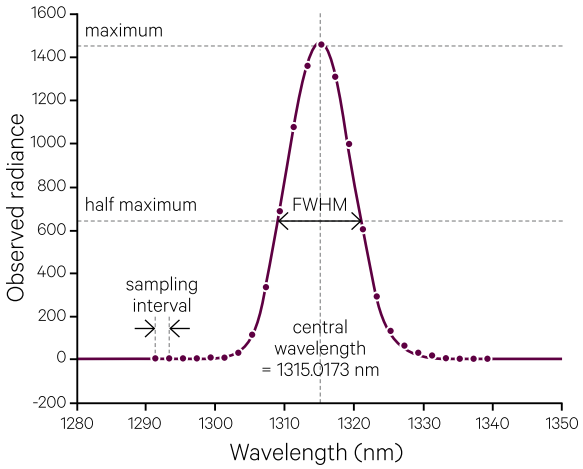


Adapted from: Campbell and Wynne (2011) Figure 4.5

Figure 13.3 Spectral response function of Hyperion SWIR band

The spectral response function of a sensor band shows the magnitude of sensor sensitivity over a range of wavelengths. This function can be characterised by the central wavelength and the Full Width Half Maximum (FWHM), where FWHM defines the wavelength range detected at half the maximum signal.

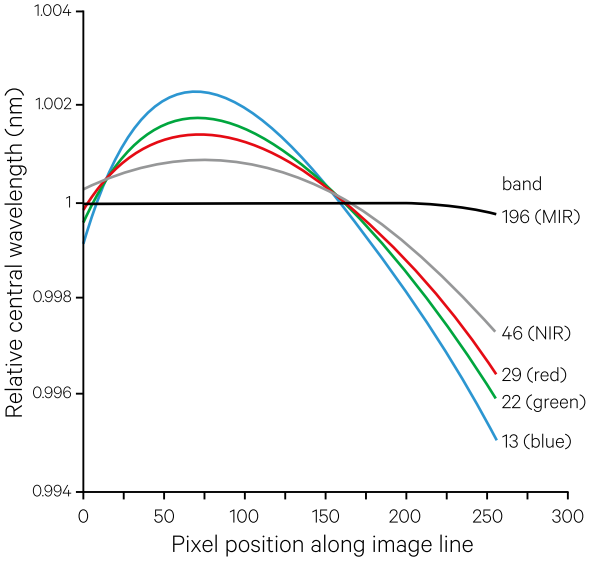
This graph shows the spectral response function of a Hyperion SWIR pixel with FWHM = 10.8335 nm.



Source: Jupp *et al.* (2004) Figure 2

Figure 13.4 Relative spectral variation across Hyperion image line

When sensor optics are not in perfect alignment, different wavelengths may be detected for different pixels across an image line. Note: Scale of y-axis is exaggerated.



Source: Jupp *et al.* (2004) Figure 3

Gains vary between different sensors and also between different bands in a single sensor. Each sensor band measures radiant energy over a range of wavelengths, with instrument sensitivity to different wavelengths varying slightly within this range. The magnitude of sensor response as a function of wavelength is called the 'spectral response function' (or 'bandpass response function'). In many cases, the response can be modelled by an analytic function, as illustrated in Figure 13.3. In this example, the response function can be conveniently characterised by the central wavelength (λ_c) and the Full Width Half Maximum (FWHM) of the spectral response function, where FWHM defines those wavelengths with half the energy of the maximum signal (Jupp *et al*., 2004).

In some sensors, both the central wavelength and FWHM can vary across a line of pixels. For example, the Hyperion sensors formed lines of image pixels by dispersing an imaged slit across the detectors of two primary arrays of the pushbroom (Barry, 2001), which can lead to a minor, non-uniform spectral response across the elements of the arrays, or the 'spectral smile' (or frown). As illustrated in Figure 13.4, this effect also varies with wavelength, in this case being most active in visible and NIR wavelengths, and virtually non-existent in SWIR.

13.5 CEOS Sensor Categories

The comprehensive publication, *The Earth Observation Handbook* (CEOS, 2015) compiles recent, current and future satellite missions and instrument sensors managed by member organisations of the Committee on Earth Observation Satellites (CEOS). The 2015 edition includes 260 satellites and 400 different instruments. This compendium does not include commercially-operated systems. In the 2015 edition, sensors are grouped into 16 categories on the basis of instrument design and function (see Table 13.3). This list demonstrates the diversity of EO sensors that currently provide information about our planet. Examples of sensors in those categories that are most commonly used for EO research and development in Australia are summarised in Table 13.4.

Table 13.3 CEOS sensor categories[47]

Instrument Type	Design Purpose	EM Wavelengths	Radiation Source	Detection System	Applications
Atmospheric chemistry instruments	Various techniques and different parts of the EM spectrum to measure atmospheric composition	UV, optical, thermal infrared, microwave	Passive	Non-imaging, Sounding	Atmospheric studies
Atmospheric temperature and humidity sounders	Measure distribution of IR or microwave radiation emitted by the atmosphere, to deliver vertical profiles of temperature and humidity through the atmosphere	Thermal Infrared, microwave	Passive (and Active)	Sounding	Atmospheric studies
Cloud profile and rain radars	Radars at cm wavelengths for rainfall, as well as very short wavelength (mm) radar (typically 94 GHz), and lidar to detect scattering from non-precipitating cloud droplets or ice particles, to deliver data on cloud characteristics such as moisture content and base height	Microwave	Active	Sounding	Weather prediction, climate studies
Earth radiation budget radiometers	Measure the radiation balance between the incoming radiation from the Sun and the outgoing reflected and scattered solar radiation, plus the thermal infrared emission to space	Optical, thermal Infrared, microwave	Passive	Imaging Sounding	Climate studies
Gravity, magnetic field and geodynamic instruments[49]	*Instruments and supporting systems used to derive information on the Earth's gravity field, magnetic field or geodynamic activity*	*Non-EM*	*Passive*	*Imaging (non-EM)*	*Geoid monitoring, ice studies, hydrology*
High Resolution Optical Imagers	Measure detailed optical radiance from the Earth's surface; generally nadir-viewing panchromatic and multispectral instruments with a horizontal spatial resolution up to 100 m and swath widths around 100 kilometres	Optical	Passive	Imaging	Land cover mapping and monitoring, geological mapping and cartography

47. Note: instruments sensing energy sources other than EMR are italicised.

Instrument Type	Design Purpose	EM Wavelengths	Radiation Source	Detection System	Applications
Hyperspectral Imagers (or imaging spectroscopy)	Measure optical reflectance from Earth's surface in many (usually 100 or more), narrow, contiguous, spectral bands	Optical	Passive	Imaging	Characterising spectral properties, especially for minerals, vegetation and coastal studies
Imaging multispectral radiometers (visible/infrared)	Measure optical and thermal infrared reflectance from the Earth's surface and atmosphere, generally with spatial resolution from 100 m to several kilometres, for broad ground swaths (thousands of km)	Optical, Thermal Infrared	Passive	Imaging, Sounding	Global and regional studies of vegetation, snow, ice and surface temperature, especially to identify and monitor biosphere and ocean processes
Imaging multispectral radiometers (passive microwave)	Measure microwave emittance (1-40 GHz and 80-100 GHz) from the Earth's surface at low spatial resolutions	Microwave	Passive	Imaging	Snow and ice mapping and monitoring soil moisture, vegetation health and ocean salinity
Imaging microwave radars (X-Band, C-Band, and L-Band)	Measure backscattered signals from transmissions in the range 1–10 GHz at spatial resolutions between 10 m and 100 m, with a swath width of 100–500 km. Includes both synthetic aperture radars (SARs) and real aperture side-looking imaging radar systems	Microwave	Active	Imaging (after processing)	Ocean waves and pollution, vegetation structure especially in tropical areas, snow and ice sheet measurements, flood monitoring, subsidence studies
Lidars	Measure radiation reflected from the Earth's surface or atmosphere when illuminated by a laser source	Optical	Active	Imaging (after processing)	Surface topography, vegetation height, atmospheric studies
Lightning Instruments	Optical sensors (~777nm) with high-speed cameras, focussed on cloud tops, detect lightning	Optical	Passive	Imaging	Weather prediction, climate studies
Multiple direction/ polarisation SAR instruments (or polarimeters)	Custom-built radar instruments for observing the direction/polarisation characteristics of the target's signature to derive geophysical information	Microwave	Active	Imaging (after processing), sounding	Surface temperature, aerosol modelling for improved Radiative transfer models and biomass estimates, soil moisture and ocean salinity estimates
Ocean colour instruments	Measure radiance from marine waters in visible and near infrared wavelengths (400-800 nm), typically with high spectral resolution and low spatial resolution	Optical	Passive	Imaging	Shallow water mapping, chlorophyll content, suspended sediment, water dynamics, marine pollution
Radar altimeters	Use the ranging capability of radar to measure the topographic profile of the Earth's surface (land and ocean) along the satellite track	Microwave	Active	Non-imaging	Topography of water surface and substratum (seafloor), sea ice, ocean wind speeds, wave height
Scatterometers	Transmit radar pulses and receives backscattered energy, the intensity of which depends on the roughness and dielectric properties of a particular target	Microwave	Active	Non-imaging	Sea surface wind speed and direction, weather and wave prediction, soil moisture, snow levels

Adapted from: Geoscience Australia (2011); CEOS (2016)

Table 13.4 EO sensors commonly used in Australia

EO Data Type	Recent, current and planned key providers (and missions)	Predominant Latency Requirement
Optical: Low Resolution	NASA (MODIS) NOAA/EUMETSAT (AVHRR/ NPP/JPSS series) JMA (Himawari series) ESA/EC (Sentinel-3 series) JAXA (GCOM-C series) CMA (FY-2 series)	Hours/Weeks
Optical: Medium Resolution	USGS (Landsat-5/7/8) ESA/EC (Sentinel-2 series)	Days/Weeks
Optical: High Resolution	USA & European commercial providers (Worldview, GeoEye, Pleiades) Airborne operators	Days/Weeks
SAR: C-band	ESA/EC (Envisat/Sentinel-1 series) CSA (Radarsat/RCM)	Weeks
SAR: L-band	CONAE-ASI (SAOCOM-1A) JAXA (ALOS-2)	Weeks
SAR: X-band	ASI (COSMO-Skymed series) DLR (TerraSAR-X series)	Weeks
Passive Microwave Radiometry	NASA (Aqua/ GPM, Aquarius, SMAP) NOAA/DOD (DMSP series) JAXA/NASA (TRMM/ GCOM-W series) ESA (SMOS) ISRO (Megha-Tropiques, RISAT-3)	Hours
Radar Altimetry	EUMETSAT-NOAA (Jason series) ESA/EC (Envisat/Sentinel-3 series)	Hours
Hyperspectral Imagery	NASA (EO-1) DLR (EnMAP) ASI (PRISMA) METI/JAXA (ALOS-3)	Weeks
Lidar	NASA (CALIPSO) ESA/JAXA (EarthCARE)	Weeks
Ocean Colour	NASA (MODIS) ISRO (OCEANSAT) ESA/EC (MERIS/Sentinel-3 series) JAXA (GCOM-C series) NOAA (NPP/JPSS series)	Hours

Adapted from: CSIRO (2012) Table 6-1

13.6 Further Information

Measurement of Light:

Ryer (1997)

Gigahertz-Optik: *http://www.light-measurement.com/tutorials-on-light-measurement/*

EO Sensors:

Colwell (1983)—see chapters 7 and 8.

EMR Basics for Remote Sensing: *http://www.usna.edu/Users/oceano/raylee/SP212/EMR/RLee_EMR_fundamentals.pdf*

NASA Earth System Science Remote Sensors: *https://earthdata.nasa.gov/data/standards-and-references/nasa-earth-system-science-remote-sensors*

CEOS (2016)

13.7 References

Accetta, J. S., and Schumaker, D. L. (1993). Electro-Optical Systems Design, Analysis, and Testing. Chapter 4 in 'The Infrared and ElectroOptical Systems Handbook' (Ed: M. C. Dudzik). Environmental Research Institute of Michigan, Ann Arbor, Michigan.

Barry, P. (2001). EO-1/Hyperion Science Data User's Guide, Level 1B (CAGE Number 11892). TRW Space, Defense and Information Systems, Redondo Beach, CA.

Campbell, J. B., and Wynne, R. H. (2011). Introduction to Remote Sensing, Fifth Edn. The Guilford Press, New York.

CEOS (2015). The Earth Observation Handbook. Committee on Earth Observation Satellites, ESA Communications, The Netherlands. Retrieved from *http://www.eohandbook.com*.

CEOS (2016). The CEOS Database. Retrieved from *http://database.eohandbook.com*.

Colwell, R. N. (1983). Manual of Remote Sensing, Second Edn. American Society of Photogrammetry, Falls Church, Virginia.

CSIRO (2012). Continuity of Earth Observation Data for Australia: Research and Development Dependencies to 2020. CSIRO, Canberra.

Elachi, C., and van Zyl, J. (2006). Introduction to the Physics and Techniques of Remote Sensing, Second Edn. Wiley Interscience, New Jersey.

Geoscience Australia (2011). Continuity of Earth Observation Data for Australia: Operational Requirements to 2015 for Lands, Coasts and Oceans. Geoscience Australia, Canberra.

Jupp, D. L. B., Datt, B., Lovell, J., Campbell, S., King, E., and others (2004). Discussions around Hyperion Data: Background Notes for the Hyperion Data Users Workshop. CSIRO Office of Space Science and Applications Earth Observation Centre, Canberra.

Morain, S. A., and Budge, A. M. (1998). Earth Observing Platforms and Sensors, Vol. 1, Third Edn., Ed: R. A. Ryerson, Manual of Remote Sensing. American Society for Photogrammetry and Remote Sensing (ASPRS); John Wiley & Sons, Inc., New York.

Norwood, V. T., and Lansing, J. C. (1983). Electro-optical Imaging Sensors. Chapter 8 in 'Manual of Remote Sensing' (Ed: R. N. Colwell). 2nd Edn. American Society of Photogrammetry, Falls Church, Virginia.

Ryer, A. (1997). Light Measurement Handbook. Retrieved from *http://www.intl-lighttech.com/services/ilt-light-measurement-handbook*.

Snik, F., Craven-Jones, J., Escuti, M., Fineschi, S., Harrington, D., de Martino, A., Mawet, D., Riedi, J., and Tyo, J. S. (2014). An Overview of Polarimetric Sensing Techniques and Technology with Applications to Different Research Fields. 'Polarization: Measurement, Analysis, and Remote Sensing Xi' (Eds: D. B. Chenault, and D. H. Goldstein), Vol. 9099.

Tyo, J. S., Goldstein, D. L., Chenault, D. B., and Shaw, J. A. (2006). Review of passive imaging polarimetry for remote sensing applications. Applied Optics, 45(22), pp. 5453-5469. doi:*http://dx.doi.org/10.1364/ao.45.005453*.



14 Passive Imaging Systems

Passive Earth Observation (EO) sensors either detect solar energy reflected by the Earth's surface in the visible to middle infrared region of the EM spectrum, or measure the thermal IR or microwave radiation emitted from the Earth. While traditional, film-based cameras have recorded countless images for EO and other purposes, the focus in this section is on current digital camera technology, which directly converts detected radiation into a digital value for each cell (pixel) in some pre-defined image grid. Relevant aspects of aerial photography acquisition and usage, and the process of digitising an image, are described in Volume 1X—Appendix 4.

In a digital image, colours are represented by numbers (see Volume 2A). A grid (or some other systematic tessellation) pattern is used to record the colours in the image, each cell being assigned one or more colour numbers. Each cell in the image grid is called a 'picture element' or pixel.

Imaging systems record a two-dimensional array of pixel values for each image channel. When an image is acquired digitally, radiance (in a specific range of wavelengths) is quantified for each pixel. This set of measurements comprises one image 'channel' or 'band'. For example, in a panchromatic image, which records a single channel, each pixel has only one value, which is commonly represented pictorially as a shade of grey (see Section 14.3.1). In a multispectral image, which records multiple channels, each pixel has multiple values, which can be viewed separately or in combination (see Section 14.3.2).

The following sub-sections will introduce passive sensors that are commonly used in EO, in the categories of:

- sensor components for optical and thermal imagery, including an overview of detector technology (see Section 14.1);
- image formation methods—electromechanical, linear array, and central perspective (see Section 14.2);
- optical—radiometers, spectroradiometers and imaging spectrometers that record visible and infrared radiance (see Section 14.3):
  - panchromatic—radiometers that record a single, very broad, channel in optical wavelengths (see Section 14.3.1);
  - multispectral—radiometers and spectroradiometers that record several broad channels in optical wavelengths (see Section 14.3.2); and
  - hyperspectral—imaging spectrometers that record numerous, narrow channels in optical wavelengths (see Section 14.3.3);
- thermal infrared—radiometers that record few broad channels in middle and thermal infrared wavelengths (see Section 14.4); and
- passive microwave—radiometers that record few broad channels in microwave wavelengths (see Section 14.5).

Background image: Landsat-8 image, acquired on 8 October 2014, of Coopers Creek, Australia's second longest inland river system (displayed using bands 5, 4, 2 as RGB). Primarily located in western Queensland, this inland river feeds into the Lake Eyre Basin. **Source:** Norman Mueller, Geoscience Australia

The implications of image sampling methods on the geometry and fidelity of the resultant imagery are further discussed in Volume 1B—Sections 1 and 2 and Volume 2A—Sections 3 and 6 respectively. It should also be noted that a given sensor may be carried on two or more concurrent platforms. A sensor being carried on multiple satellites, that follow identical orbits within a single mission series (such as the Landsat TM sensor on the Landsat 5 and Landsat 7 satellites), is specifically designed and calibrated to produce comparable image values from each satellite[48]. Some sensors are also carried by multiple satellite missions. This is the case for MODIS (Moderate Resolution Imaging Spectroradiometer), which operates on both the Terra and Aqua satellites[49]. These satellites follow different orbits to allow acquisition of MODIS data up to four times per day. Image acquisition at different times in the diurnal cycle, however, can result in image value differences that are directly attributable to changes in sun position and view angle, rather than changes in the properties of the imaged surface. Advanced correction procedures are applied to such data sets to ensure their final image values are comparable for digital analyses (see Volume 2D).

Before discussing specific passive imaging sensors, we will describe components of optical and thermal sensors and the major mechanisms that can be used to form an image.

14.1 Optical and thermal sensor components

Most optical and thermal sensors comprise some or all of a number of generic components that capture, quantify and record radiation, including:

- a collector—intercepts and directs radiation for a finite period of time known as the dwell time (see Section 13.4); in an optical sensor, the aperture size of a collector determines the maximum level of radiation that the sensor can detect;
- a focussing device—focuses intercepted radiation towards the detector, which may involve shaping and correction;
- a beam splitter—separates the focussed radiation into different wavelength bands;
- a detector—transforms EMR into another form of energy, such as chemical (for photographic film), electrical (for electronic components) or magnetic (for digital media);
- a reference—provides a standard to which the measured radiation can be precisely quantified; and
- a recording device—retains the final result for further analyses.

Specific components used by passive sensors to sense optical and thermal wavelengths are summarised in Table 14.1. Thermal infrared radiometers generally require a temperature reference, which is checked regularly to calibrate sensed observations. They also incorporate a cryocooling mechanism to maintain the detectors at an extremely low temperature to minimise dark current, which ensures that the detected temperatures are relevant to the target rather than the sensing device (see Section 13.4).

Some of the methods used by passive sensors to detect specific spectral ranges include:

- dispersing light through a prism (see Figure 5.7) or diffraction grating (see Figure 14.1);
- using thin film interference filters (such as splitting or superimposing multiple waveforms) to define a narrow range of wavelengths;
- incorporating a reference sample of gas to be identified and only detecting wavelengths that correspond to the gas absorption lines; or
- enhancing the incoming signal by mixing with a monochromatic local oscillator to produce a higher frequency signal that can be analysed more easily.

One example of a monochromatic sensor, which uses a diffraction grating to separate collected radiation, is shown in Figure 14.1. Various correction components may also be added to specific sensors to compensate for known image distortion resulting from sensor and/or platform operation. For example, to correct for platform movement, the scan line corrector component of Landsat TM 'straightens' imaged scan lines relative to the satellite path (see Volume 2B).

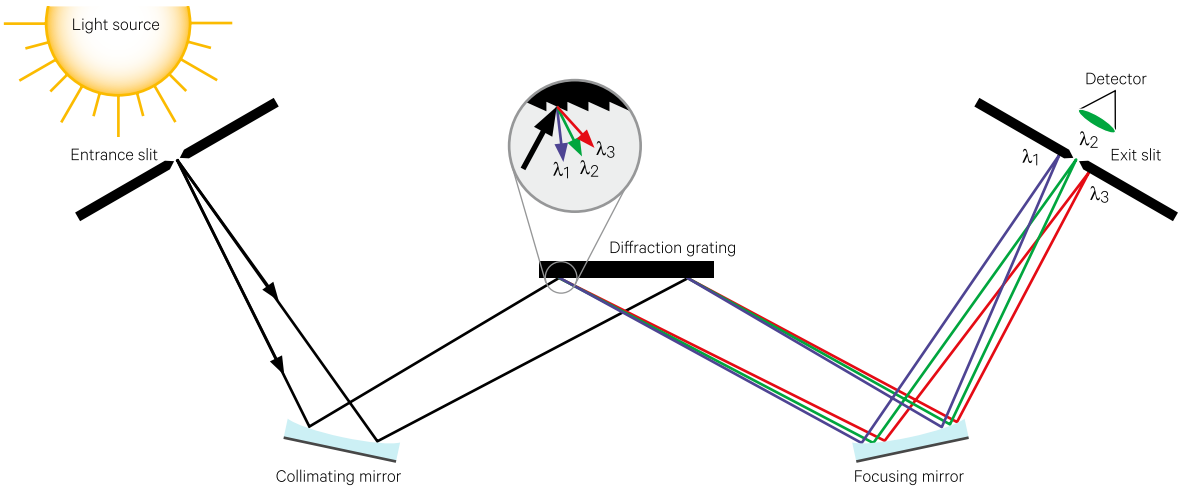
48. See *http://landsat.gsfc.nasa.gov*
49. See *http://modis.gsfc.nasa.gov*

Table 14.1 Potential components of generic passive sensor

Component	Function	EM Wavelength Region	
		Optical	Thermal
Collector	Collect incoming radiation for a finite time	aperture, telescope, scanning mirror	aperture, telescope, scanning mirror
Focussing Device	Direct collected radiation towards detector	lens, focussing mirrors, filter	lens, focussing mirrors, filter
Beam Splitter	Divide focussed radiation into sub-regions	prism, filters (interference/ dichroic), diffraction grating, Spectroscope	prism, filters (interference/ dichroic), diffraction grating, Spectroscope
Detector	Transform split radiation to different form of energy	photographic film, photoemissive device, photodiode, solid-state semiconductor (such as CCD array), CMOS	thermal infrared detectors, solid-state semiconductor (such as CCD array)
Reference	Correct detected signal against a standardised reference	reference detector solar-illuminated panel	blackbody source reference
Recording Device	Retain result for future analyses	amplifier recording device	amplifier recording device

Figure 14.1 Simple example of monochromatic sensor

Sensor components: entrance slit, collimating mirror, diffraction grating, focussing mirror, exit slit and detector. A diffraction grating uses a surface textured with parallel and equidistant grooves to separate incident polychromatic (white) light into different optical frequencies/wavelengths by the relationship d (sin a ± sin b) = ml, where a is the angle of incidence, b is the angle of diffraction, d is the distance between striations, m is the order and l is the wavelength of incident light beam.



Adapted from: David Harvey (CC BY-NC-SA) Figure 10.12 at *http://www.saylor.org/site/wp-content/uploads/2012/07/Chapter1011.pdf*

Two types of detectors, thermal and quantum, have been most commonly used to detect short wave EMR (Kinch (2000); see Table 14.2). Thermal detectors contain heat sensitive material, which is heated by incident radiation, to cause a measurable change in resistance or voltage. Thermal detectors are slower and less sensitive than quantum sensors, thus generally not used in current optical sensors. Quantum (or photon) detectors utilise photoemissive, photoconductive, or photovoltaic components, which allow the incident radiation to directly interact with the detector material to generate free-charge carriers. Quantum detectors can be designed as one-dimensional (linear) or two-dimensional (area) arrays to reduce the need for moving components to scan across the image target (see Section 14.2), and hence allow a longer dwell time to collect each signal.

Charge-Coupled Device (CCD) and Complementary Metal Oxide Semiconductor (CMOS) detectors utilise the photoelectric effect, by which photons are 'converted' to electrons after contact with a doped silicon lattice. Since CCD and CMOS devices simply respond to the number of electrons accumulated in their photodiodes, they cannot actually detect specific wavelengths, but require filters to limit the incoming radiation to the required wavelength bands. The *Quantum Efficiency* of a photoelectric detector indicates its photon-to-electron conversion efficiency, which is related to specific design aspects of sensor components, such as the illumination period, the threshold of each photodiode, and the efficiency of storing charges before measurement (see Table 13.2 in Section 13.4).

Different materials can be used to fabricate detectors, with each having unique sensitivity to different wavelengths. Some of the materials commonly used for photodiodes are summarised in Table 14.3. It should be noted that the spectral sensitivity of specific detectors often varies from these figures, depending on design requirements. The quantum efficiency of specific photodetectors also varies within and between different detector materials, depending on design criteria, ambient temperature and other components.

Table 14.2 SWIR detector categories

Characteristic	Detector Category	
	Thermal	Quantum
Operation	Radiation absorbed by thermally isolated detector material to change its temperature, which is sensed by resistivity, dielectric current, etc.	Radiation absorbed by interaction with detector material; generate free carriers which are sensed; electronic readout circuit
Spectral response	Response dependent on radiant power so independent of wavelength	Response varies with wavelength
Features	Traditionally slow, insensitive, bulky, costly, but recent advances have introduced options for mass production	High SNR; fast; generally require cooling outside the visible range
Examples	Bolometers (e.g. thermistor—measures change in electrical resistance; metal; semiconductor) Pyroelectric (measures change in internal electrical polarisation) Thermoelectric (e.g. thermopile—series of thermocouples)	Intrinsic semiconductors (absorption by detector material) Extrinsic semiconductors (absorption by impurities) Photoemissive (e.g. CCD, CMOS) Quantum Well (e.g. QWIP)

Source for data: Kinch (2000); Rogalski (2012)

Table 14.3 EMR sensitive materials

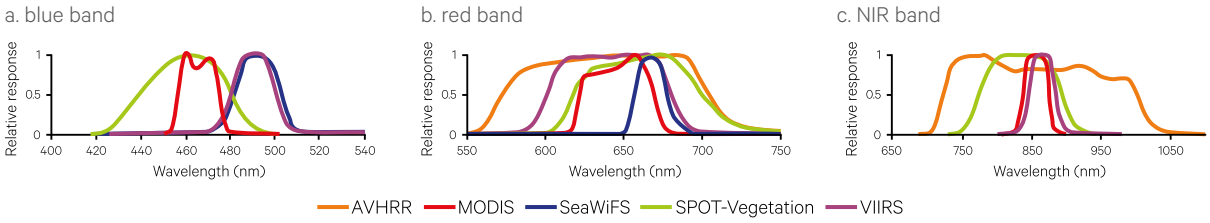
These materials are commonly used to make photodiodes to detect EMR in particular wavelength regions. The sensitivity and performance of specific photodiode products may vary from these figures.

Material	Typical EMR Sensitivity Range (μm)	Peak Sensitivity (μm)	Used for sensing
Silicon (Si)	0.2–1.1	0.9–1.0	visible and NIR
Germanium (Ge)	0.4–1.8	1.35–1.45	NIR
Indium gallium arsenide (InGaAs)	0.4–2.6	1.4–1.55	NIR
Lead sulfide (PbS)	1.0–3.5	2–3	SWIR
Indium antimonide (InSb)	1–7.5	3–4	MIR
Mercury-doped Germanium (GeHg)	2–14 μm	~10	TIR
Mercury-Cadmium-Telluride (HgCdTe)	0.6–16 μm	8–15	SWIR, MIR, TIR

Source for data: Sharma (2005), Rogalski (2012)

Figure 14.2 Spectral response functions

Normalised spectral response functions for selected EO sensors: AVHRR (orange), MODIS (red), SeaWiFS (blue), SPOT-Vegetation (green) and VIIRS (purple) for:



Adapted from: Kim *et al.* (2010) Figure 1

By virtue of detector sensitivities and other design criteria, each spectral band in optical and thermal sensors can be characterised by its sensitivities to different wavelengths, which is also known as its spectral response function or band pass function. For example, the spectral response functions for selected bands in five different EO sensors are illustrated in Figure 14.2.

The economic value of just one year of Landsat data far exceeds the multi-year total cost of building, launching, and managing Landsat satellites and sensors.
(USGS, 2015)

14.2 Image formation

EO image scanning systems can be grouped into three basic categories depending on the mechanism used by the sensors to view each pixel, namely:

- electromechanical—the sensor oscillates from side-to-side to form the image;
- linear array—an array of detectors is used to simultaneously sense the pixel values along a line; and
- central perspective or framing—the sensing device does not actually move, relative to the object being sensed, during image formation so views all pixels from the same central position in a similar way to a photographic camera (see Volume 1X—Appendix 4).

These mechanisms are illustrated in Figure 14.3.

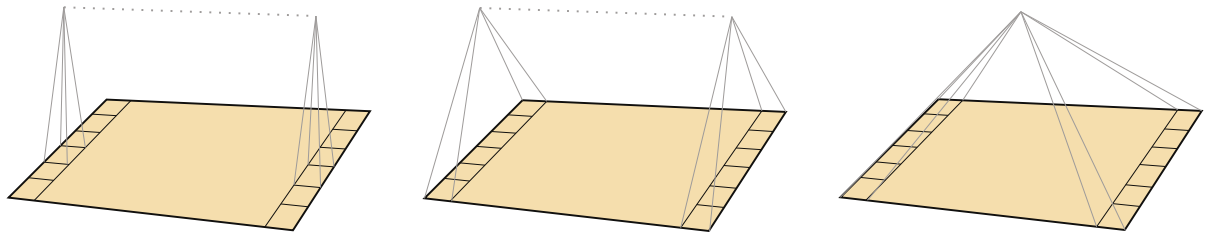
These generic mechanisms assume that the sensor is viewing the Earth's surface from a nadir position at the scene centre, that is, looking vertically downwards. Some sensors, however, can extend their area of coverage from a particular platform location by pointing the sensor to an off-nadir or side-looking position. The impact of off-nadir viewing on image geometry is discussed in Volume 2B.

Figure 14.3 Scanning mechanisms

a. Electromechanical: sensor records pixels sequentially along each line from line centre

b. Linear array: pixels recorded simultaneously along each line using an array of detectors at line centre

c. Central perspective: sensor is positioned at image centre and records lines sequentially



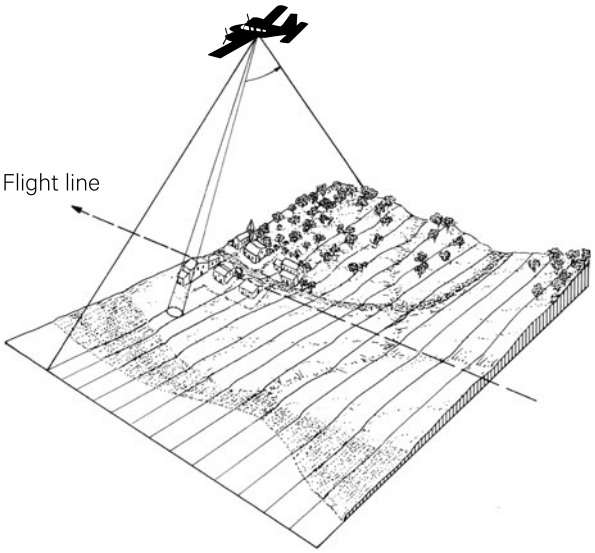
Source: Harrison and Jupp (1989) Figure 18

14.2.1 Electromechanical

As the name suggests, an electromechanical scanner comprises electronic and mechanical components. The operation of an electromechanical sensor being carried on an aircraft is illustrated in Figure 14.4, although the same principle applies to satellite-borne scanners. In this example, the image is formed by a side-to-side scanning movement as the plane travels along its path. Each line is automatically divided into pixels in the scanning process. This process is illustrated in Figure 14.5 for a multispectral scanner (MSS), with the land cover(s) within each individual pixel determining the radiation levels detected by the scanner. It should be noted that this simplistic description tends to imply that remotely sensed image pixels neatly correspond to discrete ground areas (or ground resolution elements), which is not the case. The relationship between ground resolution elements and image pixels is discussed in Volume 1B—Section 1.2 and Volume 2B.

Figure 14.4 Operation of electromechanical aircraft scanner

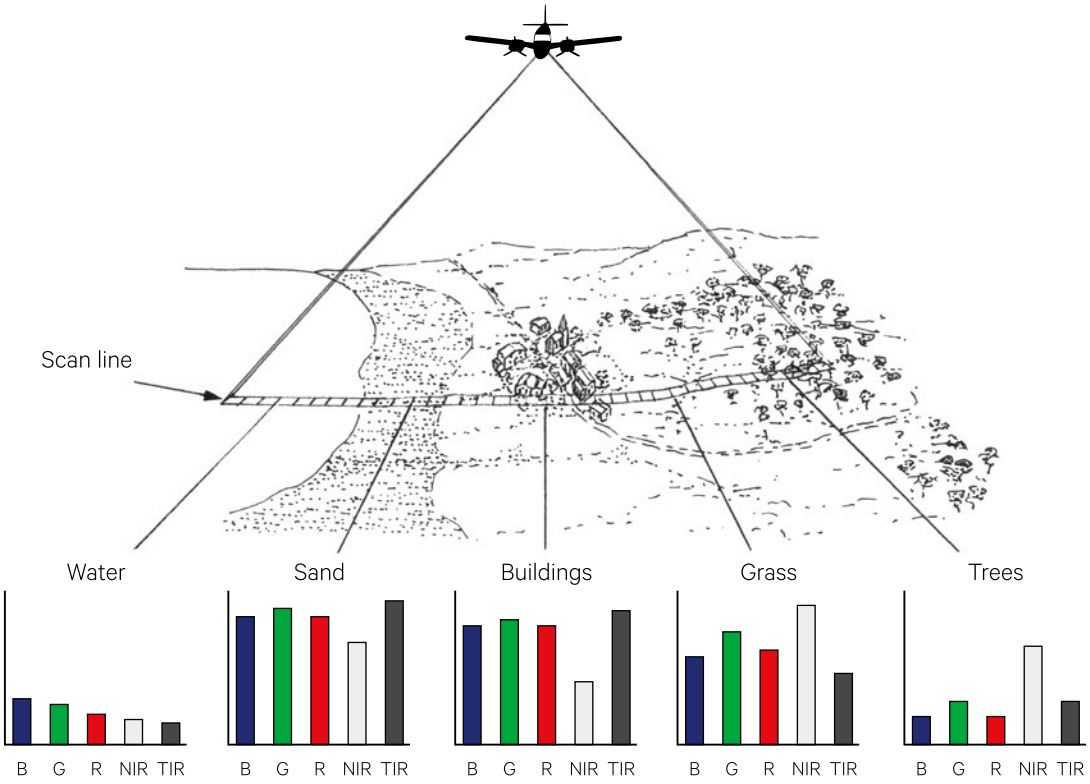
Image lines are formed sequentially by scanning side-to-side across the flight path



Source: Harrison and Jupp (1989) Figure 19

Figure 14.5 MSS measurements along one scan line

Each set of radiance readings along the line represents a pixel in the image



Source: Harrison and Jupp (1989) Figure 20

An electromechanical scanner uses an oscillating mirror to reflect incident radiation onto a relatively small number of detectors, with different types of detectors being used for different wavelengths and sensitivities (see Section 14.1). These detectors are located behind grating (or less commonly optical) filters that separate EMR into broad spectral bandwidths, which are simultaneously registered by the detector array then sequentially read as data. The detected radiation is converted into a continuous electronic signal that is then sampled at regular time intervals to give discrete measurements, or pixels, along each scan line. Sensors using this scanning mechanism are also referred to as across-track or 'whiskbroom' scanners. Examples of such sensors include Landsat MSS, TM and ETM+, and AVHRR.

The main limitation of this scanning mechanism is the restricted time available to read each detector. This generally requires that such scanners have rather broad spectral bands to achieve an adequate Signal-to-Noise Ratio (SNR; see Section 13.4 and Volume 1B—Section 2.1.4). The oscillating movement of the mirror may also result in some inconsistencies in the scanning rate, leading to geometric problems in the imagery (see Volume 2B). Moving components are also subject to wear and tear over time.

Landsat MSS and TM sensors used oscillating electromechanical scanners and the satellite's forward velocity to form imagery. Unlike the MSS, Landsat TM and ETM used a scanning mirror that collected data on both the forward and reverse scans. Landsat MSS comprised six sensors for each spectral band, so that six lines of image data were received each time the scanner moved from side-to-side. For Landsat TM/ETM+, sixteen lines of image data were collected on each scan using a 'whiskbroom' scanner. The satellite travelled from north to south as the sensing system scanned west to east. These combined movements produce the characteristic westerly skew in Landsat imagery (see Figure 12.15 and Volume 2B). Also, since each of the six (or sixteen) lines was imaged by a separate detector, slight miscalibration between the detectors led to a horizontal striping pattern in the imagery. This problem is further discussed in Volume 2.

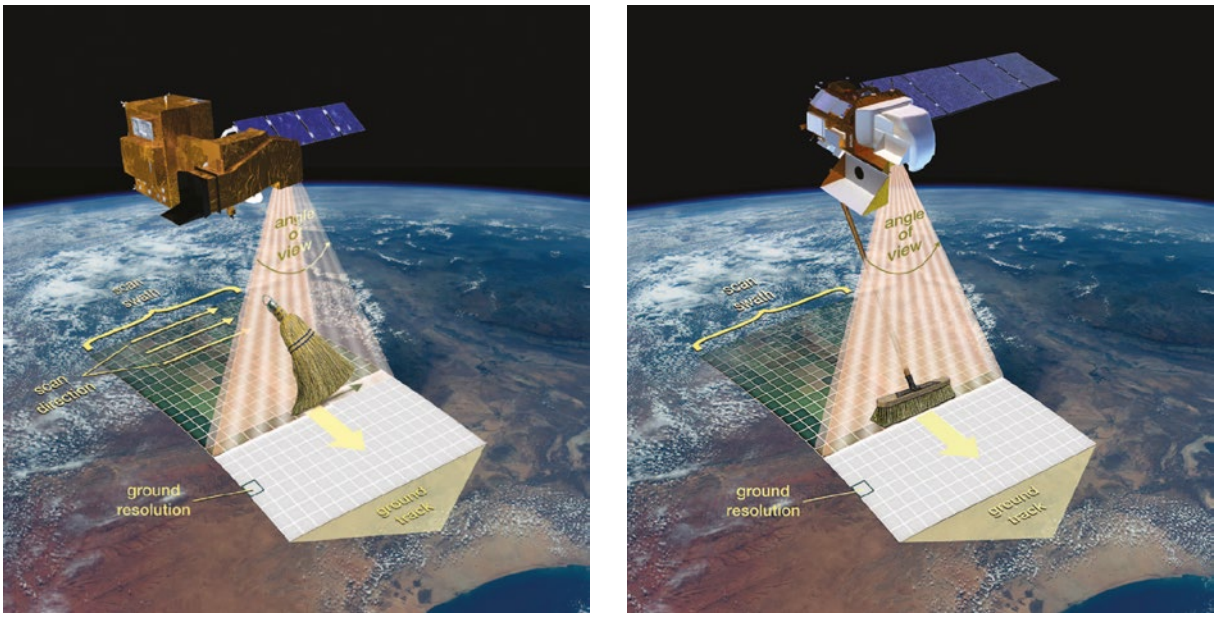
14.2.2 Linear array

A second scanner design uses a linear array of detectors (commonly CCD) to form an image line, with each detector recording the value for an individual pixel along the line (see Figure 14.3b). This design is also referred to as a 'push-broom' scanner, since the image is formed as the sensor is swept forward by the velocity of the platform. Examples of such sensors include SPOT HRV, SPOT NRVIR, SPOT-VGT, MISR, ASTER, IKONOS, IRS, OrbView, QuickBird, MOMS, MESSR, and Landsat OLI. The operation of a 'push-broom' scanner is compared with a 'whiskbroom' scanner in Figure 14.6.

Figure 14.6 Whiskbroom versus pushbroom scanners

a. A 'whiskbroom' scanner (such as Landsat-7 ETM+) relies on an oscillating mirror to scan each pixel across an image line.

b. A 'pushbroom' scanner (such as Landsat-8 OLI) utilises linear arrays of detectors to record each image line.



Source: NASA. Retrieved from *http://landsat.gsfc.nasa.gov/wp-content/uploads/2012/12/LDCM_Brochure_Dec20121.pdf*

The advantages of this design are that the scanner does not have any moving parts to cause timing inconsistencies and can allow a longer dwell time, and hence narrower spectral channels, per detector (see Section 13.4). This results in a cheaper, lighter and smaller device with lower power requirements and greater reliability as well as higher spatial and radiometric resolutions. A disadvantage however is that the larger number of detectors requires very accurate calibration to avoid vertical striping in the imagery. A further limitation is that CCD technology is not readily available for wavelengths longer than near infrared. In certain cases, due to finite detector read-out times, the number of spectral bands also needs to be limited in linear array scanners to ensure that the same ground locations are being imaged in each band.

14.2.3 Central perspective

The third category of sensors utilises an area array of CCD detectors to form an image from a central perspective (see Figure 14.3c). This sensor is used in a wide range of instruments, from mobile phones to satellite imaging scanners. The central perspective results in similar geometric distortions in an image to those that occur in photographic data, that is, distortion increases with radial distance from the focal point. In satellite-derived imagery however, radial displacement effects are barely noticeable because the field of view is so small relative to orbital altitude.

Laboratory-based scanners commonly use the central viewing perspective for image formation. The extent of distortion in the resulting image depends on the optics of the scan configuration used, including the size of the original being scanned. The early frame sensors used in vidicon cameras (such as the Return Beam Vidicon in the Landsat 1, 2 and 3 satellites) operated from a central perspective by exposing a two-dimensional array of detectors (or photosensitive tubes in the early models) for a shutter-controlled time period. Although operating with a different mechanism, imagery from the geostationary satellites (described in Section 12.2.1) is essentially formed from this perspective.

14.3 Optical

Optical sensors detect and record radiance in visible, near infrared and short wave infrared wavelengths (see Section 5.3) for either:

- one channel (panchromatic—see Section 14.3.1);
- several channels (multispectral—see Section 14.3.2); or
- numerous channels (hyperspectral—see Section 14.3.3).

As wavelengths in these regions of the spectrum are strongly affected by atmospheric scattering, the usefulness of these devices for Earth surface studies may be limited by atmospheric conditions (see Section 5.4). Optical scanners are often divided into sub-categories on the basis of their spatial resolution:

- low resolution: > 80 m;
- medium resolution: 10–80 m;
- high resolution: < 10 m; and
- very high resolution: < 1 m.

The most commonly used satellite sensors acquiring low, medium and high resolution imagery are listed in Table 14.4.

Satellite imagery can be used retrospectively, meaning that the data collected by satellites today will probably help solve issues we are not currently even aware of—an advantage which is invaluable. (Nathalie Pettorelli)

Table 14.4 Examples of satellite optical sensors

Note: Hyperion (italicised in this table) is a hyperspectral imaging system

Spatial Resolution	Instrument	Mission(s)	Agency
Low	MERIS	Envisat	ESA
	IMAGER	MTSAT-2	JMA
	GOCI	COMS	KARI
	MODIS	Aqua	NASA
	MODIS	Terra	NASA
	AVHRR/3	NOAA-15, 16, 17, 18, 19	NOAA
	VIRR	FY-3A, 3B, 3C	NRSCC (CAST)
	VIIRS	NPP	NASA
	SeaWIFS	ORBVIEW 2	Orbimage
Medium	HRVIR	SPOT-4	CNES/Astrium
	MSS	Beijing-1	DMCii
	SSTL MSS – 3 band	DMC Deimos-1	DMCii
	CHRIS	PROBA-1	ESA (BNSC)
	AwiFS	RESOURCESAT-2	ISRO
	LISS-III	RESOURCESAT-2	ISRO
	ALI	NMP EO-1	NASA
	Hyperion	*NMP EO-1*	*NASA*
	OLI	LDCM	NASA (USGS)
	NigeriaSat Med Res	NigeriaSat-1, X	NASRDA
	TM	Landsat-5	USGS (NASA)
	ETM+	Landsat-7	USGS (NASA)
High	MSS/Pan	SPOT 6, 7	Astrium
	HiRI	Pleïades-HR 1, HR 2	CNES/Astrium
	HRG/HRS	SPOT-5	CNES/Astrium
	Quickbird 2	QUICKBIRD 2	Digital Globe
	WV60	WORLDVIEW-1	Digital Globe
	WY110	WORLDVIEW-2	Digital Globe
	Multispectral	WORLDVIEW-3	Digital Globe
	MSI	RapidEye	DLR
	PAN	Beijing-1	DMCii
	GIS	GeoEye-1	GeoEye
	GeoEye-2	GeoEye-2	GeoEye
	IKONOS 2	IKONOS 2	GeoEye
	LISS-IV	RESOURCESAT-2	ISRO
	TES PAN	TES	ISRO
	NigeriaSat	NigeriaSat-2	NASRDA
	PAN	BJ-1	NRSCC (CAST)
	RSI	FORMOSAT 5, 2	NSPO/Astrium
	MSI	Sentinel-2	ESA

Adapted from: Geoscience Australia (2011) Tables F-1 to F-3

14.3.1 Panchromatic

Panchromatic scanners are imaging radiometers that record EMR in a single band, typically including all wavelengths spanning from the visible to infrared region (see Section 13.2.1.1). A single channel captures the broad contrast between features, and allows delineation of land cover transitions and boundaries. For a given volume of image data, if each pixel only has a single band value, the image can contain a greater number of pixels. Accordingly, panchromatic sensors generally deliver higher spatial resolution imagery than multispectral scanners. The design trade-offs between spectral and spatial detail in scanning systems is introduced in Section 13 and further discussed in Volume 1B—Sections 1 and 2. It should be realised that the engineering implications of increasing data volume impact not only image acquisition and recording, but also the download capacity required for remote sensors (see Volume 1B—Section 9).

Panchromatic data is typically displayed as a grey-scale image, in which pixels with lower image values appear dark and those with higher values appear bright (see Figure 14.7). For optical imagery, panchromatic channels typically record low values for water and dense vegetation and high values for urban and bare areas. As such, engineering works such as roads, mines and urban infrastructure clearly contrast with vegetation, and boundaries of waterbodies can be delineated.

Successive generations of panchromatic scanners have rendered significant advances in both spatial resolution and image quality. For example, images acquired by Landsat-7 ETM+ and Landsat-8 OLI are contrasted in Figure 14.7. While both scanners record 15 m pixels, Figure 14.7a was acquired years before Figure 14.7b, so some land surface features have changed. However, the unchanged features in these two images are cleaner and crisper in Figure 14.7b due to the higher imaging fidelity of Landsat-8 OLI, which offers greater radiometric resolution and utilises linear arrays of detectors per image scan line ('pushbroom' scanner) rather than oscillating mirrors ('whiskbroom' scanner)[50]. A more nostalgic example of the spatial 'acuity' of the Landsat-8 panchromatic channel is shown in Figure 14.8, where the decommissioned Landsat-5 satellite is visible in an image over Brazil (see Figure 12.14).

Interpretation of panchromatic imagery relies on spatial rather than spectral analysis of features. Various image processing techniques, such as rescaling, can be used to change image contrast to enhance specific features (see Volumes 2A and 2C). Transitions between adjacent pixels can be highlighted using algorithms that enhance edges or texture (see Volume 2C). Pseudo-colouring can also be applied to panchromatic images, which maps image values to selected colours (see Volumes 2A and 2E).

Panchromatic scanners often accompany multispectral scanners on satellite missions. Panchromatic imagery is not only valuable for providing crisp images of Earth features, which are invaluable for various cartographic purposes, but can also be used to visually sharpen edges in multispectral imagery (see Figure 14.9). Such techniques are detailed in Volume 2C.

Figure 14.7 Panchromatic imagery from Landsat-7 ETM+ and Landsat-8 OLI

a. Landsat-7 ETM+ 15 m pixels acquired on 25 June 2016



b. Landsat-8 OLI 15 m pixels acquired on 3 July 2016



Source: Norman Mueller, Geoscience Australia

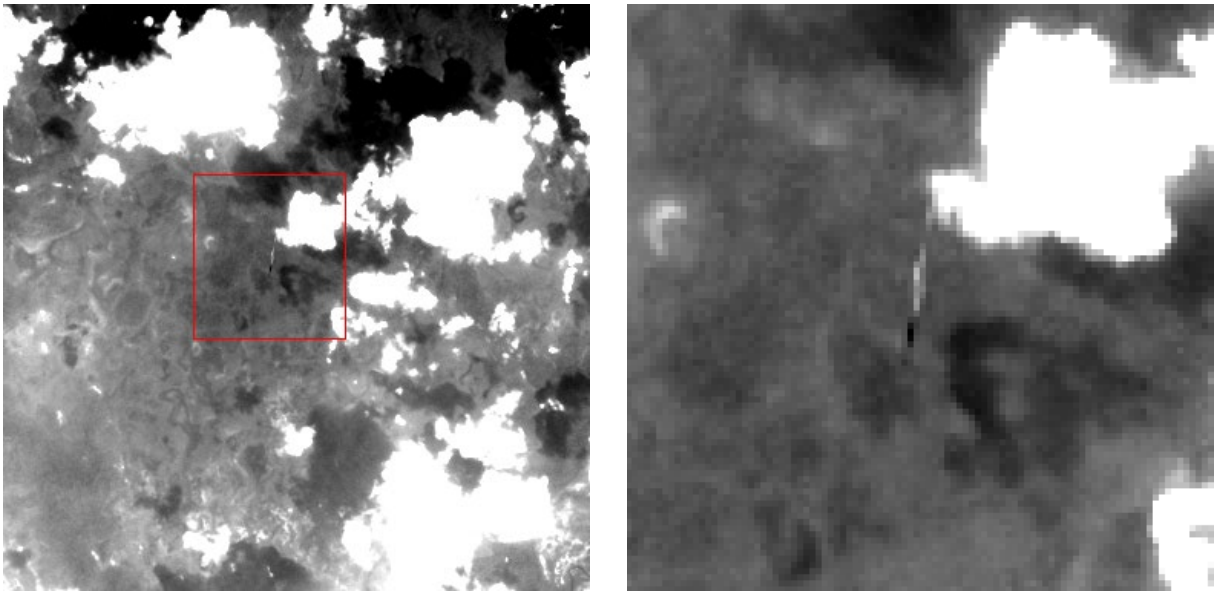
50. Please note that the spectral response functions for the Landsat 7 ETM+ and Landsat 8 OLI sensors are also different. For more details on the Landsat 8 mission and instruments visit *http://landsat.usgs.gov/documents/Landsat8DataUsersHandbook.pdf* or *https://directory.eoportal.org/web/eoportal/satellite-missions/l/landsat-8-ldcm*

Figure 14.8 Decommissioned Landsat-5 satellite visible from Landsat-8

Landsat-8 panchromatic image over northwestern Brazil on 22 November 2013 detects the decommissioned Landsat-5 satellite below its overpass (see Figure 12.14 for satellite dimensions).

a. Landsat-5 satellite appears as a streak of pixels within the red box

b. Enlarged view of red box shown in image a



Source: RIT/USGS/NASA. Retrieved from *http://landsat.gsfc.nasa.gov/?p=7849*

Figure 14.9 Image sharpening

Panchromatic imagery with high spatial resolution can be merged with multispectral imagery to create high resolution colour images.

a. Pleiades panchromatic image acquired on 15 May 2016 over Parliament House, Canberra

b. Pleiades multispectral image acquired on 15 May 2016 over Parliament House, Canberra

c. Pleiades images in a. and b. merged into sharper colour image



Source: © CNES (2016). Distribution: Airbus DS.

14.3.2 Multispectral

Multispectral scanners (MSS), as the name implies, are a particular class of remote sensing device that senses and digitally records radiation in multiple, defined wavelength regions of the visible and infrared parts of the EM spectrum using imaging radiometers or imaging spectroradiometers (see Section 13.2.1). The principle of this mode of operation is comparable to using filters on a camera to photograph limited parts of the visible spectrum. For example, when using an appropriate filter to photograph only blue light, a purely red object would appear black since only blue radiation will pass through the filter to expose the film. Thus, different information is obtained by recording the reflectance in different wavelength regions.

While the prolific MSS instrument carried by the Landsat 1 to 5 satellites (see Section 12.2.2) sensed four 'bands' of the EM spectrum for each image pixel (green: 0.5–0.6 μm; red: 0.6–0.7 μm; near infrared: 0.7–0.8 μm; and near infrared:0.8–1.1 μm), the more recent Landsat sensors, TM, ETM+ and OLI, were designed to record additional image channels (see Table 14.5). It should be noted that the spectral sensitivities (or response) of these wavelength bands do not precisely correspond to their stated wavelength ranges, as illustrated in Figure 14.2. The spectral bands of most terrestrial EO sensors are selected primarily to detect differences in land cover, and also to avoid atmospheric absorption bands (see Figure 14.10 and Section 5).

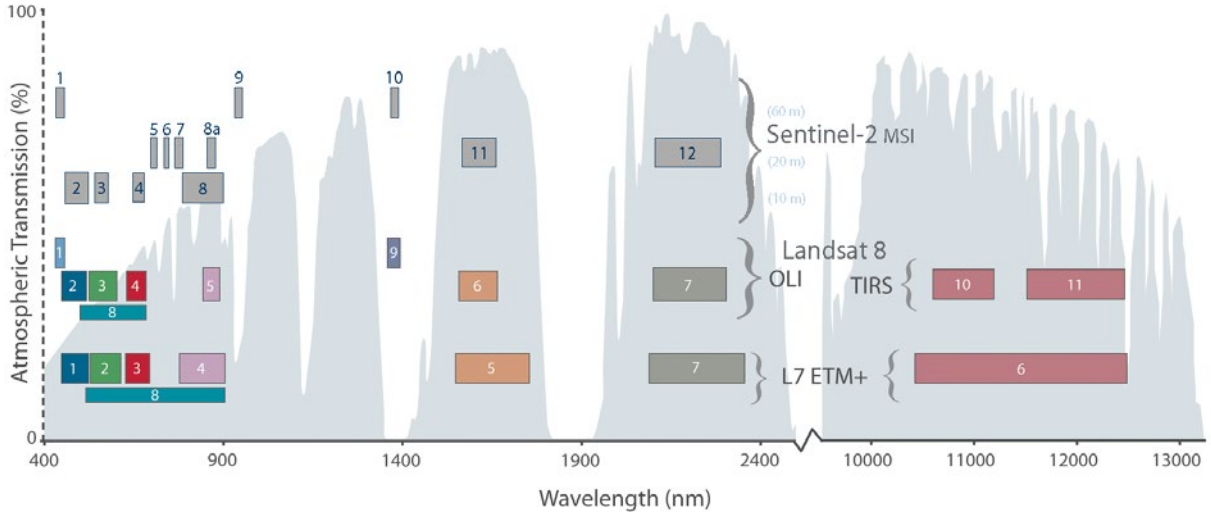
Table 14.5 Landsat TM/ETM+ channels

Landsat TM recorded the multispectral channels 1 to 7 only. Note: Band 8 is only measured by Landsat ETM+.

Band	Spectral Range (μm)	EM Region	Application	Nominal Pixel Size
1	0.45 – 0.52	Visible Blue	Coastal water mapping, vegetation versus soils	30
2	0.52 – 0.60	Visible Green	Vegetation vigour assessment	30
3	0.63 – 0.69	Visible Red	Chlorophyll absorption for vegetation differentiation	30
4	0.76 – 0.90	Near Infrared	Biomass surveys and delineation of water bodies	30
5	1.55 – 1.75	Middle Infrared	Vegetation and soil moisture; snow versus cloud	30
6	10.40- 12.50	Thermal Infrared	Thermal mapping, soil moisture, plant heat stress	120
7	2.08 – 2.35	Middle Infrared	Hydrothermal mapping	30
8 (ETM+ only)	*0.52 – 0.90 (panchromatic)*	*Green, Visible Red, Near Infrared*	*Large area mapping, urban change studies*	*15*

Figure 14.10 Comparison of bands acquired by Landsat-7, Landsat-8 and Sentinel-2

This graphic compares the bands acquired by Landsat-7 and Landsat-8 with those acquired by Sentinel-2. The wavelength regions where EMR transmission is not permanently affected by Earth's atmosphere are shaded in the background (see Section 5).



Source: NASA. Retrieved from *http://landsat.gsfc.nasa.gov/wp-content/uploads/2015/06/Landsat.v.Sentinel-2.png*

Table 14.6 Landsat OLI/TIRS channels

OLI records channels 1 to 9; TIRS records channels 10 and 11

Band	Spectral Range (μm)	EM Region	Application	Nominal Pixel Size
1	0.427–0.459	Visible blue	Ocean colour in coastal zones and aerosols	30
2	0.436–0.528	Visible blue	Pigments, atmospheric scattering, coastal monitoring	30
3	0.513–0.611	Visible green	Pigments, coastal monitoring	30
4	0.626–0.692	Visible red	Pigments, coastal monitoring	30
5	0.830–0.901	Near Infrared	Foliage, coastal monitoring	30
6	1.516–1.699	Middle Infrared	Foliage	30
7	2.038–2.356	Middle Infrared	Minerals, litter, no scattering	30
8	0.488–0.693	Panchromatic	Image sharpening	15
9	1.341–1.410	Middle Infrared	Cirrus cloud detection	30
10	10.6–11.2	Thermal Infrared	Land and ocean temperature plus atmospheric studies	100
11	11.5–12.5	Thermal Infrared	Land and ocean temperature plus atmospheric studies	100

As detailed in Table 14.5, Landsat TM recorded the multispectral bands 1 to 7 only, while Landsat ETM+ also recorded a panchromatic channel at higher spatial frequency. The channels recorded by Landsat OLI/TIRS are detailed in Table 14.6. Landsat OLI/TIRS delivers imagery with 12 bit radiometric resolution whereas Landsat 7 ETM+ provided radiometric resolution of 8 bits (selected from the best of 9 bits).

The advantage of sensing radiation in multiple spectral regions is illustrated in Figure 14.11, which shows 'typical' spectral reflectance curves (or 'signatures') for soil, dry grass and green plant material. Figure 14.11a highlights the wavelengths recorded by standard colour photography, while Figure 14.11b superimposes the optical regions detected by the Landsat TM/ETM+ sensors. Although the recorded reflectance levels in an image depend upon a wide range of factors relating to the structure and condition of a particular land cover type (see Volume 1B—Sections 3 and 6), the Landsat imagery clearly provides more spectral information than aerial photography to differentiate between different types of land cover. Note that 'signature diagrams', such as those shown in Figure 14.11, have typically been drawn from spectral reflectance data with much finer spectral resolution than those provided by the multispectral scanner bands.

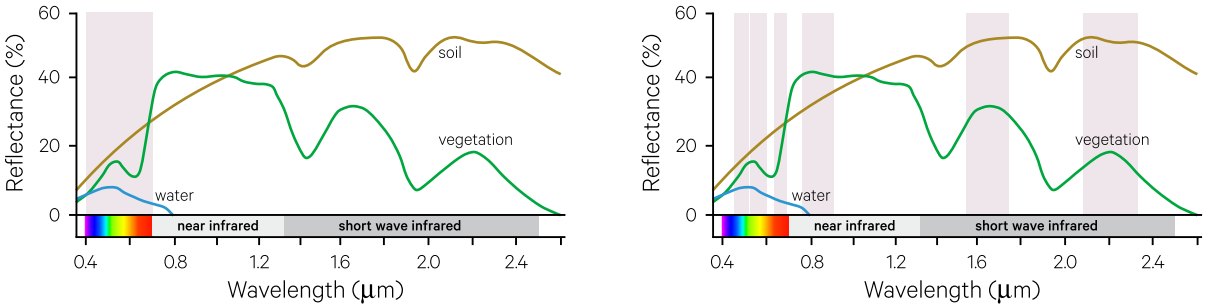
The (spatially registered) channels recorded by a MSS, such as Landsat TM, can be recombined into a single colour image using the colour additive technique described in Section 2.7. Channels representing reflected blue, green and red light can be combined to form a natural colour composite, which should resemble the colours of the imaged object (see Figure 14.12a). Different sets of channels can also be combined using the colour additive process to render false colour composites (see Figures 14.12b and 14.12c).

Figure 14.11 Differentiation within spectral regions

Wavelengths recorded by EO sensor are shaded grey against typical spectral 'signatures' for soil (brown), water (blue) and green vegetation (green).

a. Standard colour photography

b. Landsat TM/ETM+ optical bands



Adapted from: Harrison and Jupp (1989) Figure 28

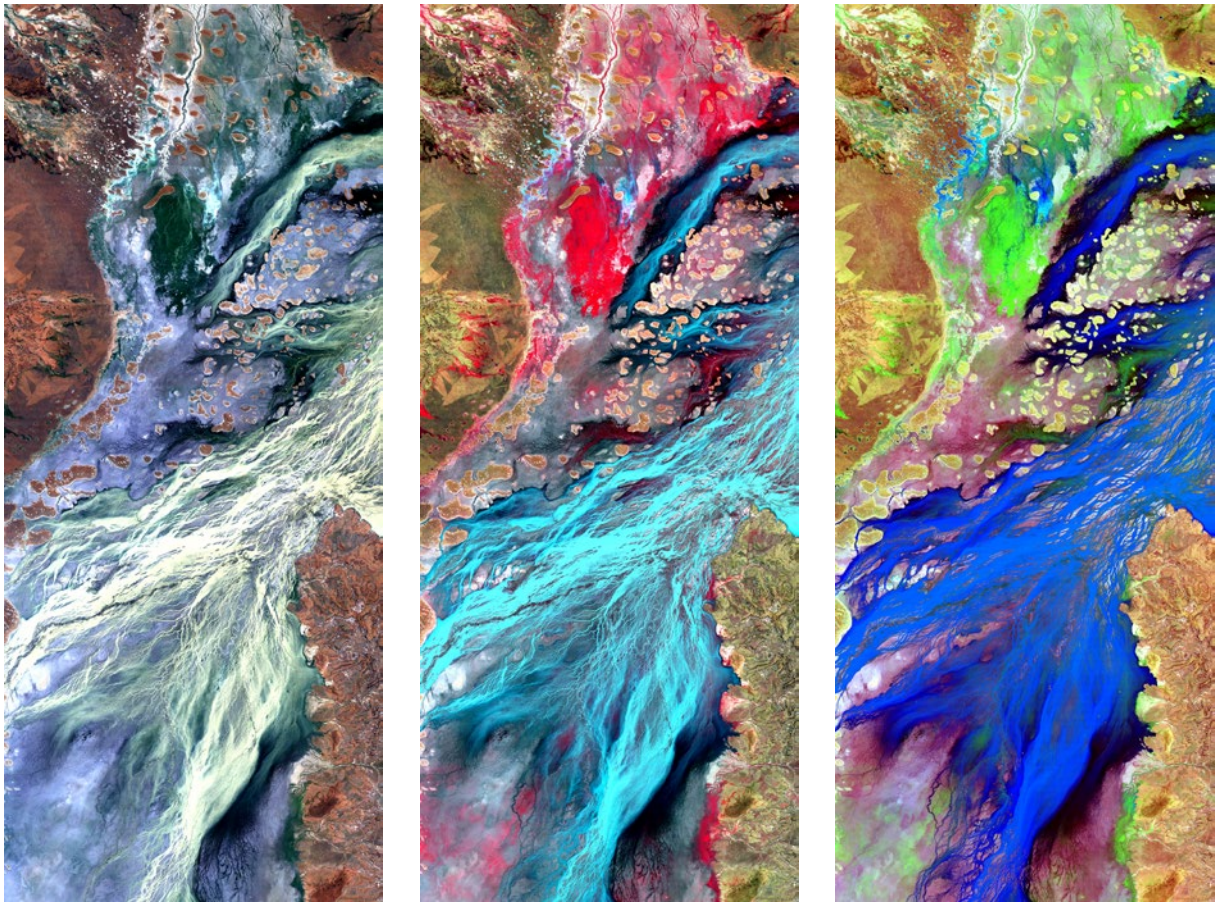
Figure 14.12 Colour composites

Landsat TM imagery acquired over Coopers Creek, near Windorah, Queensland, on 1 December 2010.

a. True colour composite—band 1 displayed blue, band 2 displayed green, band 3 displayed red

b. Standard false colour composite—band 2 displayed blue, band 3 displayed green, band 4 displayed red

c. Different false colour composite—band 2 displayed blue, band 4 displayed green, band 5 displayed red



Source: Norman Mueller, Geoscience Australia

The grey scale images corresponding to the six optical Landsat ETM+ bands are shown in Figure 14.13. The reflectance level in each of the spectral bands illustrated in Figure 14.12 tells us something about the 'object' being sensed:

- water is brightest, and more variable, in the visible blue channel (ETM band 1) and darkest in the near infrared and middle infrared channels (ETM bands 4, 5, and 7);
- urban and bare areas are brightest in the visible blue channel (ETM band 1) and darkest in the middle infrared channels (ETM bands 5 and 7); and
- vegetation is brightest in the near infrared channel (ETM band 4) and darkest in visible blue.

As introduced in Section 5, vegetation features are frequently identified by their characteristically high NIR reflectance and low red reflectance. For an image pixel containing both vegetation and background soil, the colour and visibility of the soil will modify the detected radiation levels. A light coloured soil will show a larger decrease in red radiation for increasing vegetative cover while a dark soil will cause a larger increase in the near infrared radiation. Image processing techniques of ratioing or differencing these data channels enhances the differences between them and reduces the influence of background soil colour. For example, such processes are used to monitor daily variations in pasture (see Excursus 14.1). Details of these techniques are provided in Volumes 2C and 3A. Interpretation of optical MSS imagery is further considered in Volume 1B—Sections 6.

Figure 14.13 Landsat ETM+ optical channels

Landsat ETM+ image over Adelaide, South Australia January 2000. The scene includes shallow coastal water, urban areas, forested reserves to the east and agricultural lands in the north.

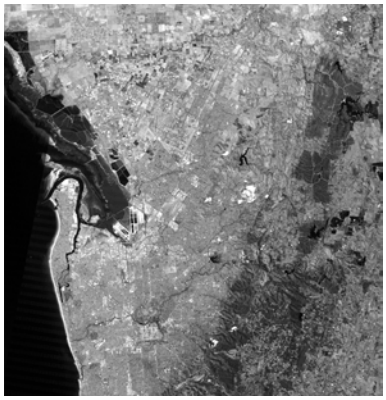
a. Band 1—visible blue (0.45–0.52 μm)



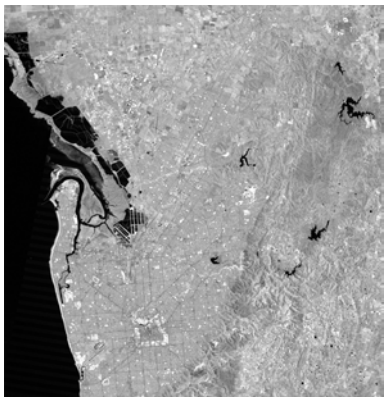
b. Band 2—visible green (0.52–0.60 μm)



c. Band 3—visible red (0.63–0.69 μm)



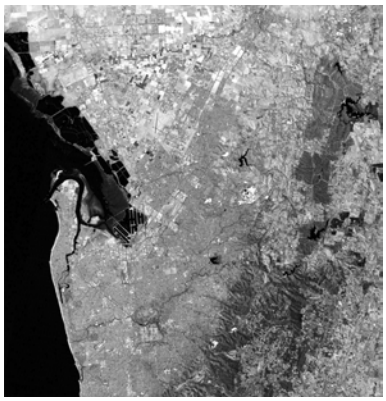
d. Band 4—near infrared (0.76–0.90 μm)



e. Band 5—middle infrared (1.55–1.75 μm)



f. Band 7—middle Infrared (2.08–2.35 μm)



g. True colour composite (bands 1, 2 and 3 as blue, green and red)



h. False colour composite (bands 2, 3 and 4, as blue, green and red)



i. Location map with broad land covers and scale bar



Source: Megan Lewis, University of Adelaide using imagery supplied by Geoscience Australia

Excursus 14.1—Pastures from Space

Source: Graham Donald, CSIRO
Further information: *www.pasturesfromspace.csiro.au*
https://www.landgate.wa.gov.au/foundationr2/channel_content.jsp?channel=farm&contentId=farmchannel-start-pasturesfromspace&source=cms&title=Pastures%20from%20Space

Australia is the largest exporter of beef, mutton, goat meat and wool in the world, and a major exporter of lamb, pork and dairy products. In 2009, Australia's livestock exports totalled nearly $1 billion.

Farm profitability is heavily dependent on the efficient use of pasture by livestock. Given the seasonal patterns of pasture growth in southern Australia, accurate and timely information is required to match total pasture production to consumption by livestock. This information has been routinely provided by satellite image analyses for over a decade.

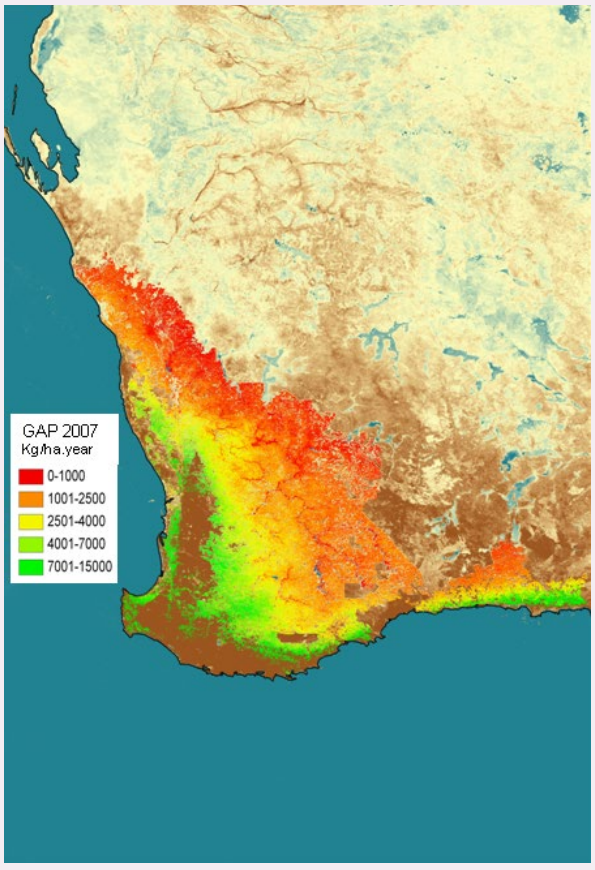
Pastures from Space uses daily satellite imagery to monitor variations in pastures, both within individual paddocks and across growing regions in southern Australia (see Figure 14.14). This information is combined with meteorological data to model plant growth. Weekly estimates of Pasture Growth Rate (PGR) are supplied to farmers via an on-line service. Current research is extending this product to Australia's eastern agricultural regions and northern rangelands.

This pasture growth information enables farmers to improve pasture utilisation and optimise the use of fertilisers. It also allows timely management of erosion, weeds, and pasture health. Over the longer term, at paddock, farm and regional scales, changes in Gross Annual Pasture Production (GAPP) can be used to assess the impact of local and regional management practices, as well as the ramifications of climatic variations.

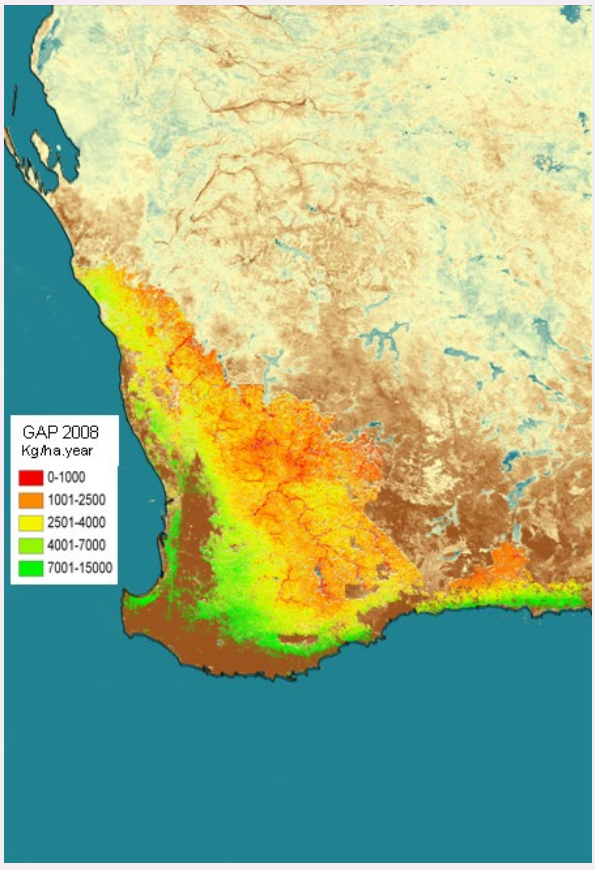
Figure 14.14 Gross Annual Pasture Production (GAPP) from 2007 to 2010 for southwestern WA

The total above ground pasture production for individual paddocks, farms and regions can be monitored over time to determine optimal management regimes and the impact of environmental changes. GAPP is derived from the Pasture Growth Rate (PGR) model and quantified as kilograms of dry matter per hectare.

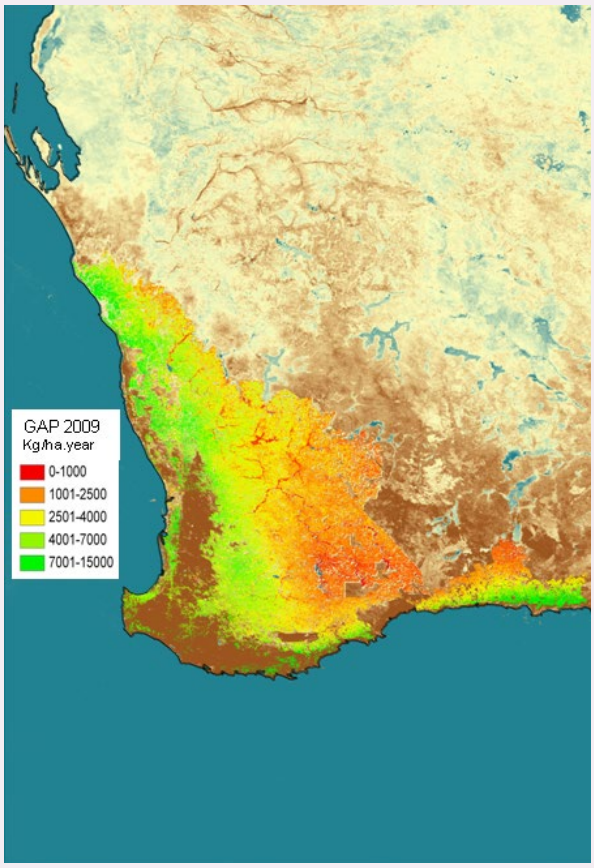
a. GAP 2007



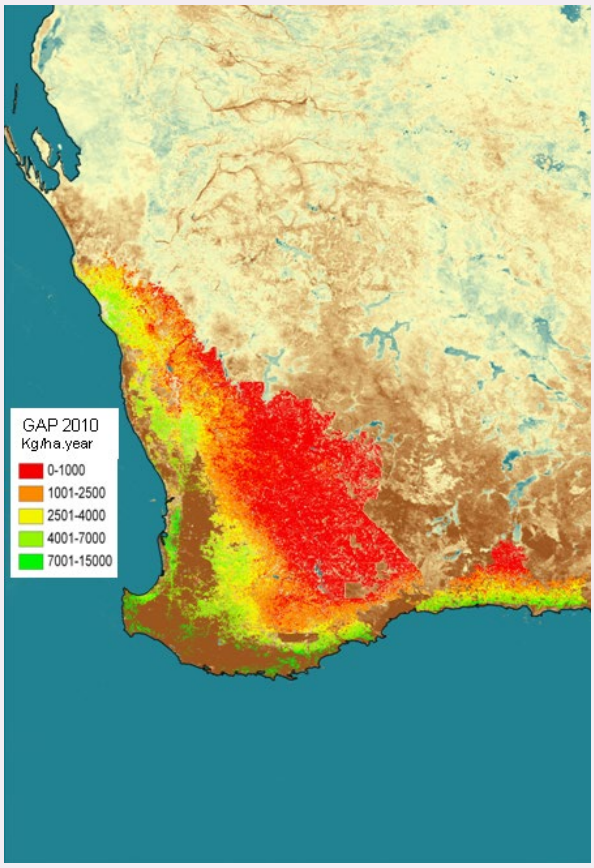
b. GAP 2008



c. GAP 2009



d. GAP 2010



14.3.3 Hyperspectral

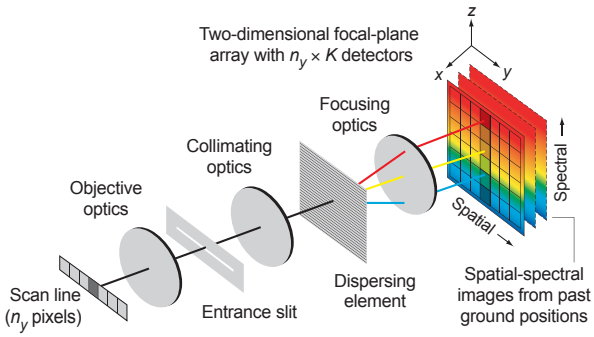
Hyperspectral scanners, or imaging spectrometers, collect image data for hundreds of spectral channels. A push-broom scanner incorporating a two-dimensional detector array records scan lines for multiple spectral bands to form a three-dimensional data cube (see Figure 14.15). This data cube can be viewed as:

- a set (size z) of two-dimensional images (x and y in Figure 14.15), one for each spectral channel; or as
- a set (size x × y) of one-dimensional spectra, one for each image pixel.

The process of image collection, data dimensions and the derived spectra are illustrated in Figure 14.16. This type of imaging allows detailed spectra for individual pixels and/or target features to be compiled (see Figure 14.16d). By comparison, a simplified form of the spectral signatures for two types of Australian vegetation and two types of bare ground that would be derived from Landsat TM optical bands is illustrated in Figure 14.17.

Figure 14.15 Compilation of hyperspectral data cube

An imaging spectrometer disperses light onto a two-dimensional array of detectors, with n_y elements in the cross-track (spatial) dimension and K elements in the spectral dimension, for a total of $N = K \times n_y$ detectors.

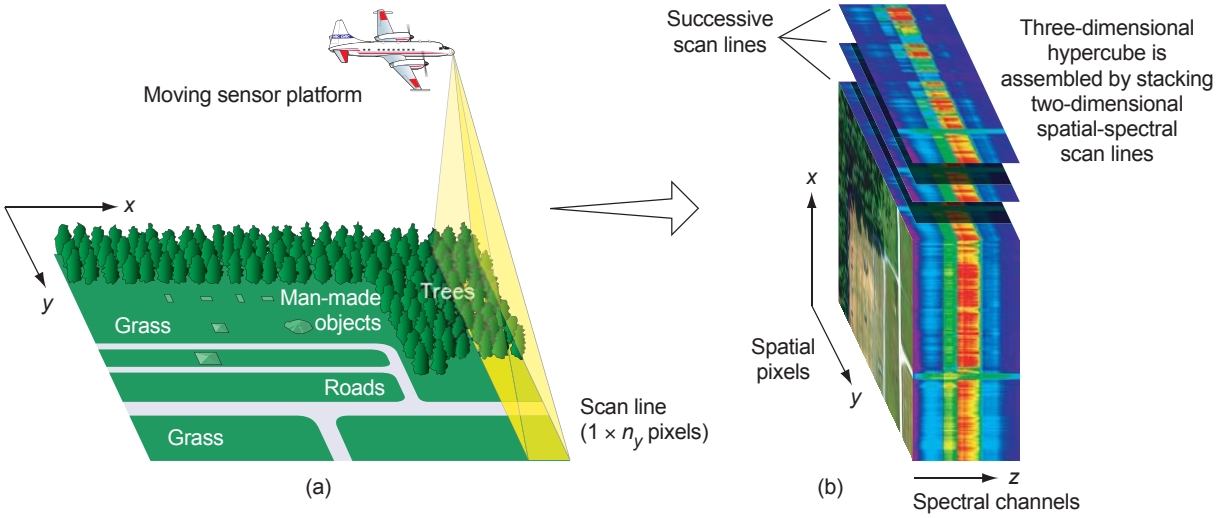


Source: Shaw and Burke (2003) Figure 3b. Reprinted with permission courtesy of MIT Lincoln Laboratory, Lexington, Massachusetts.

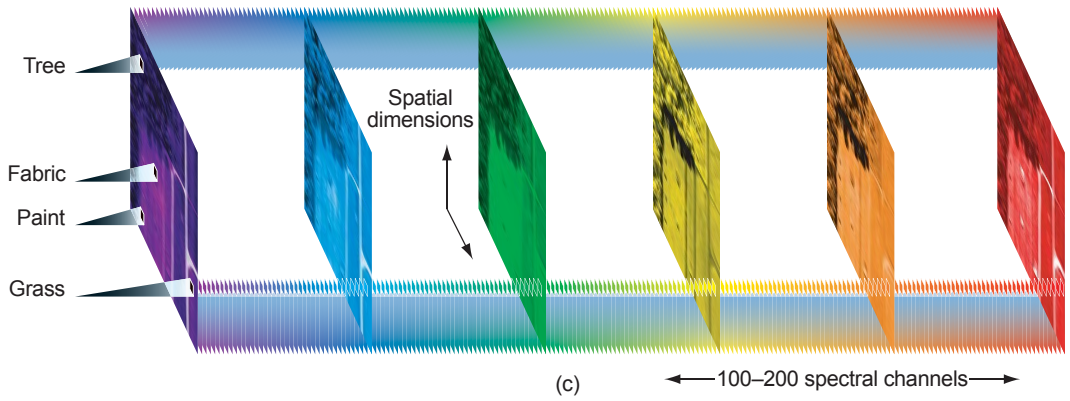
Figure 14.16 Hyperspectral image interpretation

a. Target scene is imaged line by line using a hyperspectral scanner

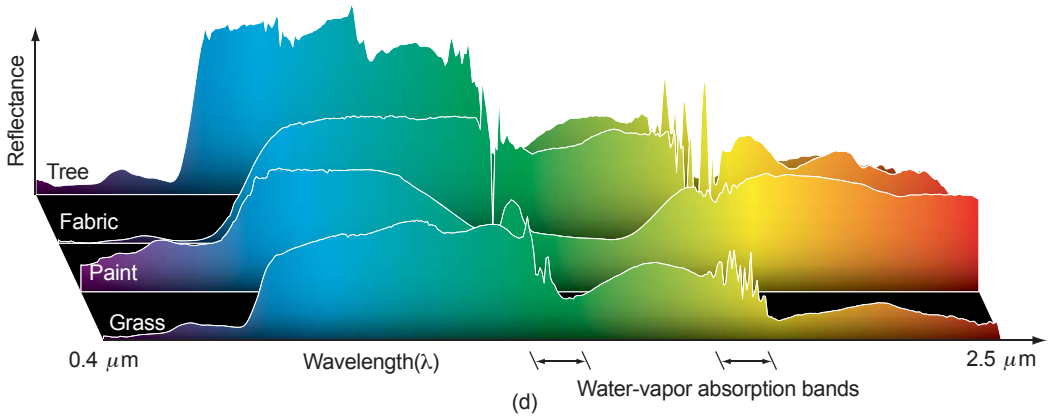
b. Multiple spectral bands for each scan line are stacked into a three-dimensional datacube



c. Each spectral channel can be viewed as a two-dimensional image



d. Detailed spectral information for individual pixels and target features can be viewed as one-dimensional spectra across all spectral bands



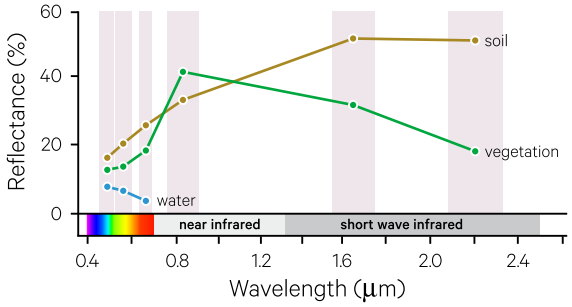
Source: Shaw and Burke (2003) Figure 4. Reprinted with permission courtesy of MIT Lincoln Laboratory, Lexington, Massachusetts.

Table 14.7 Examples of hyperspectral imagers

Sensor	Mission (Agency)	Maximum number of channels	Spectral range (μm)	Ground resolution[53] (m)
AVIRIS (Airborne Visible Infrared Imaging Spectrometer)	Airborne (JPL)	224	0.40–2.50	2.2–20
CASI-1500 (Compact Airborne Spectrographic Imager)	Airborne (iTRES)	288	0.38–1.05	0.2–1.5
HyMap	Airborne (HyVista Corp)	128	0.45–2.5	2–10
CHRIS (Compact High Resolution Imaging Spectrometer)	Proba-1 (ESA)	150[54]	0.415–1.05	17–34
HICO (Hyperspectral Imager for Coastal Ocean)	ISS (NASA)	128	0.35–1.08	90
Hyperion	EO-1 (NASA)	220	0.40–2.5	30

Figure 14.17 Simulated Landsat TM spectral signature

Simplified spectral signatures for vegetation, soil and water, based on mid-points of Landsat TM/ETM+ optical channels (see Figure 14.11b).



Hyperspectral imaging is used for an expanding range of laboratory, industrial and airborne applications, including astronomy, surveillance, food processing and biomedical research. In EO, it is especially valuable for identifying geological features, mapping surface mineral deposits and distinguishing between plant species. In particular, the narrow spectral channels of hyperspectral imagers allow the spectral feature known as the 'red-edge' (transition from low reflectance to high NIR reflectance) to be located precisely. This feature is considered as a significant indicator of plant biochemistry (see Volume 1B—Section 6 and Volume 3A), which is indicative of plant condition. Hyperspectral imagery has also been used to monitor volcanic activity and emissions from industrial plants and wildfires, as well as mapping the changing composition of coastal waters.[51][52]

Some hyperspectral imaging instruments are listed in Table 14.7. While most hyperspectral imaging for EO has been undertaken on aerial platforms, several satellite borne sensors have acquired substantial archives of hyperspectral imagery. The Hyperion sensor, for example, operated for 11 years from November, 2000. It imaged hundreds of narrow spectral channels (10 nm) over a 7.5 km swath (see Table 14.7; Pearlman *et al*., 2003), which can be used to derive detailed spectra for selected features. Examples of Hyperion data analyses have been reported by Apan *et al*. (2004), Griffin *et al*. (2005), and Zhu *et al*. (2013). Additional satellite borne hyperspectral instruments are being developed, including HyspIRI (NASA), EnMAP (Germany), PRISMA (Italy) and HISUI (Japan).

14.4 Thermal infrared

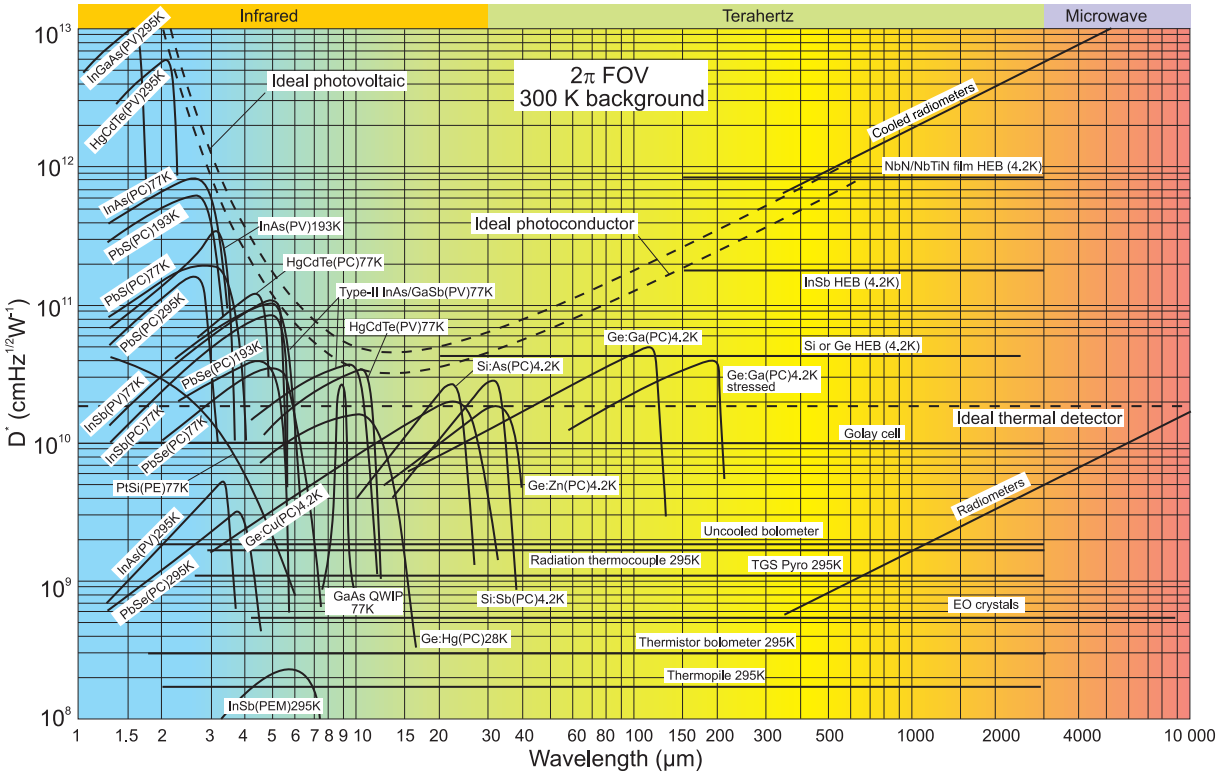
Thermal infrared emission is introduced in Sections 2.7 and 5.2.2. Thermal infrared radiometers detect energy emitted from the Earth's surface in the wavelength range 3–15 μm. It should be noted that EO thermal sensors record emittance from the upper layer of the Earth's surface, possibly as thin as 50 μm, which may or may not be characteristic of the thermal properties of the observed features (Campbell and Wynne, 2011).

A detailed account of the development of infrared detectors and their characteristics is given in Rogalski (2012). Modern thermal sensors incorporate materials that rapidly respond to thermal infrared radiation, with different detector materials responding to different thermal infrared wavelengths (see Section 14.1). For example, characteristics of the versatile and commonly used Mercury Cadmium Telluride (HgCdTe) IR detector are detailed in Rogalski (2005) and Rogalski (2010). Detectivity, which characterises the normalised signal-to-noise performance of detectors (see Table 13.2 and Volume 1B—Section 2.1), is illustrated for a range of IR detectors in Figure 14.18.

51. Ground resolution varies with flying altitude and speed.
52. The number of channels and spatial resolution vary with configuration: 17 m pixels can be imaged for 19 spectral bands or 34 m pixels can be imaged for 63 spectral bands. Spectral bands can be selected from a total of 150 available channels.

Figure 14.18 Detectivity of IR detectors

Detectivity (D*) for a range of IR detectors viewing hemisphere surrounding at 300K.
PC—photoconductive detector
PV—photovoltaic detector
PEM—photoelectromagnetic detector
HEB—hot electron bolometer



Source: Rogalski (2012) Figure 9. Used with permission.

Atmospheric gas absorption restricts thermal remote sensing for EO to two spectral windows in the thermal infrared region (see Section 5.4):

- 3–5 μm, and
- 8–14 μm.

To allow for the weaker energy levels associated with longer EM wavelengths, thermal sensors require larger IFOV and thus thermal imagery is generally only available with larger pixel sizes than optical imagery. The trade-off here is allowing sufficient integration time for a thermal observation to achieve acceptable signal fidelity without reaching saturation at the maximum design temperature (see Section 13.4). From a moving platform (aerial and spaceborne), a further consideration is ground speed, and the distance travelled during one observation. Ground speed of Landsat-8, for example, is about 7.6 km/sec[53]. With an integration time of 3.49 milliseconds per observation, one observation involves 25 m of satellite movement (Reuter *et al.*, 2015). The net result of these factors is that thermal sensors need to have lower spatial resolution to achieve high radiometric resolution (see Volume 1B—Section 1). Given the inverse-square law (that is, the intensity of detected radiation is stronger when the sensor is closer to the target—see Section 2.9.1) and to ensure that the detected signal is stronger than sensor noise, these restrictions are most significant for satellite sensors.

Since thermal sensors require large IFOV, thermal imaging scanners are generally designed to scan across a large field of view (FOV) to avoid narrow image swaths. This imaging perspective introduces characteristic geometric distortions in thermal imagery, which are more pronounced with increasing proximity to the outer edges of each swath. Distortions include:

- larger ground pixel areas—pixels at the edges of the image swath are larger than those near the centre;
- one-dimensional relief displacement—tall structures near the image edges appear to lean away from the image centre; and
- tangential scale distortions—circles near the edges of the image appear elongated (see Figure 11.1).

53. For more information, visit *http://landsat.gsfc.nasa.gov/wp-content/uploads/2012/12/LDCM_Brochure_Dec20121.pdf*

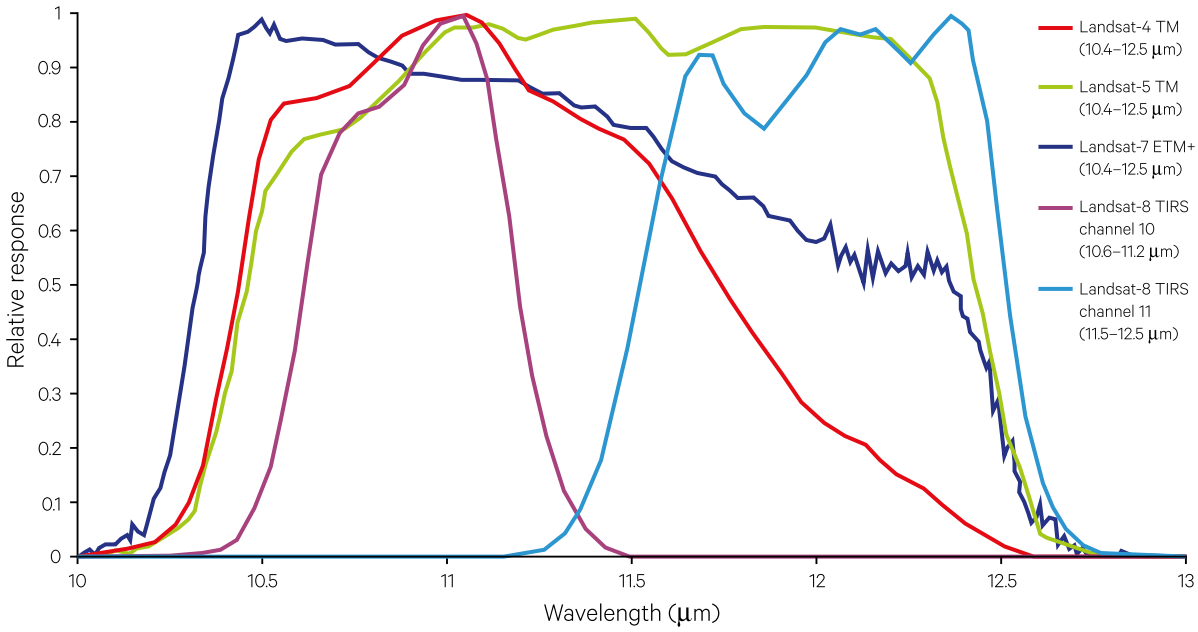
Thermal scanners have typically operated using across-track (whisk broom) scanning but recent advances have allowed development of along-track (pushbroom) thermal scanners (see Section 14.2). Landsat thermal scanners, for example, have traditionally used pushbroom, rather than whiskbroom imaging (see Section 14.2.2). Landsat-8 Thermal InfraRed Sensor (TIRS) is the first satellite-borne sensor to use Quantum Well Infrared Photodetector (QWIP[54]) arrays, with three overlapping arrays of 640 detectors scanning across each image line (Jhabvala *et al.*, 2009; Jhabvala *et al.*, 2010). Inbuilt redundancy within the array minimises the chance of missing columns of pixels due to detector failure.

Most thermal sensors used for EO rely upon inbuilt temperature references to calibrate measured temperatures. In Landsat-8 TIRS, a two-stage cryocooler maintains the QWIP arrays between 180K and 190K. Before and after imaging each orbit, the field of view (FOV) is rotated from the ground to focus on a blackbody calibrator for one minute, then into deep space for one minute, before observing the ground again. These calibration measurements verify instrument measurements and allow thermal background radiance to be removed from observations of ground targets. Additional calibration modes can be activated as required. By contrast, the thermal sensors on previous Landsat satellite needed to be calibrated twice for each image line (Reuter *et al.*, 2015).

The TIRS has been designed to capture two thermal channels with a spatial resolution of 100 m whereas the optical channels recorded by Landsat-8 OLI have spatial resolutions of 15 or 30 m. The relative spectral responses of the two Landsat-8 TIRS thermal bands compared with the thermal bands of previous Landsat satellites are illustrated in Figure 14.19. Two thermal channels allow a split-window algorithm to be used for atmospheric correction (Kerr *et al.*, 1992; Coll and Caselles, 1997) and offer feature discrimination advantages over the single thermal band acquired by the previous Landsat satellites. The TIRS pixel size is larger than the thermal channel of Landsat-7 and slightly smaller than that of Landsat-4 and Landsat-5, but deemed sufficient for imaging of centrally irrigated, circular agricultural fields, with diameters 400–800 m, which are commonly used for agriculture (Irons *et al.*, 2012).

Figure 14.19 Spectral response of Landsat thermal bands

Relative spectral response for thermal channels for:
Landsat-4 TM (10.4–12.5 μm)—red
Landsat-5 TM (10.4–12.5 μm)—green
Landsat-7 ETM+ (10.4–12.5 μm)—blue
Landsat-8 TIRS channel 10 (10.6–11.2 μm)—purple
Landsat-8 TIRS channel 11 (11.5–12.5 μm)—aqua



Adapted from: Reuter *et al.* (2015)

54. Thermal sensitivity of QWIP is based on charge-sensitive infrared phototransistors (based on Gallium arsenide (GaAs)/Aluminium Gallium Arsenide (AlGaAs) semiconductor chips)—Jhabvala *et al.* (2009); Jhabvala *et al.* (2010)

TIR imagery can be acquired at any time of the day or night. It is used for numerous EO applications, including fire mapping, military applications, and monitoring heat loss in built-up areas. Thermal remote sensing is also important for monitoring land surface and sea surface temperature, cloud temperature and other meteorological features. Handheld and laboratory-based thermal sensors are now routinely utilised in a wide range of fields, including medicine, engineering, and surveillance (see Figure 14.20). By detecting warm objects, these instruments also enable night vision.

Some commonly used thermal imaging sensors for EO are listed in Table 14.8. TIR radiometers are also used as non-imaging sensors (see Section 16.1.1.1). Interpretation of TIR imagery is considered in Volume 1B—Section 7.

Figure 14.20 Thermography

Thermal imagery is used for a wide range of applications, such as highlighting insulation problems in buildings and detecting people and motor vehicles at night.



Source: Wikimedia Commons. Retrieved from *https://upload.wikimedia.org/wikipedia/commons/thumb/c/cf/Ir_girl.png/1024px-Ir_girl.png*

Table 14.8 Commonly used thermal imaging sensors

Instrument	Mission(s)	Agency	Number of thermal bands in 3–5 μm	Number of thermal bands in 8–14 μm	Ground resolution (m)
HCMR (Heat Capacity Mapping Radiometer)	HCMM (Heat Capacity Mapping Mission)	NASA	0	1 (10.5–12.5)	600
TIMS (Thermal Infrared Multispectral scanner)	Airborne	NASA/JPL/ Daedalus	0	6 (8.2–12.2)	50 (at 20,000 m)
ATLAS (Advanced Thermal and Land Applications Sensor)	Airborne	NASA	1 (3.35–4.20)	6 (8.2–12.2)	10 (at 5,000 m)
Daedalus AMS (AA3607DS)	Airborne	Daedalus	1 (3.0 –5.4 μm)	1 (8.5–12.5)	Selectable
TM (Thematic Mapper)	Landsat-4/ Landsat-5	NASA/USGS	0	1 (10.4–12.5)	120
ETM+ (Enhanced Thematic Mapper Plus)	Landsat-7	NASA/USGS	0	1 (10.4–12.5 μm)	60
TIRS (Thermal Infrared Sensor)	Landsat-8	NASA/USGS	0	2 (10.6–11.2; 11.5–12.5)	100
ASTER (Advanced Spaceborne Thermal Emission and Reflection Radiometer)	Terra	NASA/USGS	0	5 (8.125–11.65)	90
MODIS (Moderate Resolution Imaging Spectroradiometer)	Terra/Aqua	NASA/USGS	7 (3.66–4.549)	8 (8.4–14.385)	1000
Imager	GOES	NOAA	1 (3.8–4.0)	2 (10.2–11.2; 11.5–12.5	4000 8000
AVHRR/3[57] (Advanced Very High Resolution Radiometer)	TIROS-N to NOAA-19	NOAA	1 (3.55–3.93)	2 (10.3–11.3; 11.5–12.5)	1100 (LAC) 4000 (GAC)

Adapted from: Geoscience Australia (2011) Tables F-1 and F-2 [55]

55. Earlier AVHRR instruments acquired fewer thermal channels

14.5 Passive microwave

Passive microwave radiometers operate in microwave wavelengths from 1 to 300 mm, which are shorter than radar. They rely on detecting the emissions of thermal radiation in the microwave region. The range of wavelengths detected by microwave radiometers (shown in Figure 5.3) corresponds to the very low energy end of the Earth's energy spectrum (see Figure 5.6). The intensity of passive microwave radiation depends on an object's temperature and incident radiation plus the emittance, reflectance and transmittance properties of the object. Because these sensors are detecting low energy levels, their imagery is relatively 'noisy', has lower spatial resolution and usually requires more complex interpretation.

Although a large volume of knowledge has already been obtained, the acquisition, processing and interpretation of microwave data are still largely experimental. Some aspects of microwave data interpretation are discussed in Volume 1B—Section 8. Of the available texts on the subject, Ulaby and Long (2014) offer an extensive reference on microwave remote sensing[56]. Examples of satellite-borne passive microwave sensors are listed in Table 14.9.

Table 14.9 Examples of satellite passive microwave sensors

Instrument	Mission(s)	Agency	Ground Resolution[59] at nadir (km)
AMSR-2 (Advanced Microwave Scanning Radiometer-2)	GCOM-W (Global Change Observation Mission-Water)	JAXA	5–50
Aquarius L-band radiometer	SAC-D (Satellite for Scientific Applications-D) /Aquarius	CONAE/NASA	100
MIRAS (Microwave Imaging Radiometer using Aperture Synthesis)	SMOS (Soil Moisture and Ocean Salinity)	ESA	33–50
MWRI (Microwave Radiation Imager)	FY-3A, FY–3B, FY-3C (FengYun)	NSMC, CMA	7.5x12; 51x85
SSM/I (Special Sensor Microwave Imager)	DMSP F-14, DMSP F-15 (Defence Meteorological Satellite Program)	NOAA (DoD, USA)	15.7x13.9; 68.9x44.3
TMI (TRMM Microwave Imager)	TRMM (Tropical Rainfall Measuring Mission)	NASA/JAXA	18

Adapted from: CEOS (2015)[57]

14.6 Further Information

EO Handbook (CEOS, 2015)

Photodiode detectors: (including graph of spectral responsivity for Si, Ge and In detectors): *http://course.ee.ust.hk/elec509/notes/Lect12-photodiode%20detectors.pdf*

CMOS sensors: *http://www.olympusmicro.com/primer/digitalimaging/acquisition.html*

Landsat: *http://landsat.gsfc.nasa.gov/?page_id=11*

Comparison of Landsat-7 ETM+ and Landsat-8 OLI/TIRS channels superimposed on atmospheric windows[58]: *http://landsat.gsfc.nasa.gov/?p=3186*

MODIS: *http://modis.gsfc.nasa.gov*

Introduction to Photogrammetry (Schenk, 2005)

Thermal Sensors: *http://www.temperatures.com*

56. Microwave, Radar and Radiometric Remote Sensing: *http://mrs.eecs.umich.edu*
57. Depending on frequency
58. Note that the ETM+ channels are not numbered sequentially with increasing wavelength as the decision to include thermal measurements (band 6) for geological and other applications was made after the initial design was underway.

14.7 References

Apan, A., Held, A., Phinn, S. R., and Markley, J. (2004). Detecting sugarcane 'orange rust' disease using EO-1 Hyperion hyperspectral imagery. International Journal of Remote Sensing, 25(2), pp. 489-498. doi:*http://dx.doi.org/10.1080/01431160310001618031*.

Campbell, J. B., and Wynne, R. H. (2011). Introduction to Remote Sensing, Fifth Edn. The Guilford Press, New York.

CEOS (2015). The Earth Observation Handbook. Committee on Earth Observation Satellites, ESA Communications, The Netherlands. Retrieved from *http://www.eohandbook.com*.

Coll, C., and Caselles, V. (1997). A split-window algorithm for land surface temperature from advanced very high resolution radiometer data: Validation and algorithm comparison. Journal of Geophysical Research-Atmospheres, 102(D14), pp. 16697-16713. doi:*http://dx.doi.org/10.1029/97jd00929*.

Geoscience Australia (2011). Continuity of Earth Observation Data for Australia: Operational Requirements to 2015 for Lands, Coasts and Oceans. Geoscience Australia, Canberra.

Griffin, M. K., Hsu, S. M., Burke, H. K., Orloff, S. M., and Upham, C. A. (2005). Examples of EO-1 Hyperion Data Analysis. Lincoln Laboratory Journal, 15(2), pp. 271-298.

Harrison, B. A., and Jupp, D. L. B. (1989). Introduction to Remotely Sensed Data. Part ONE of the microBRIAN Resource Manual (156 pages). CSIRO Australia, Melbourne.

Irons, J. R., Dwyer, J. L., and Barsi, J. A. (2012). The next Landsat satellite: The Landsat Data Continuity Mission. Remote Sensing of Environment, 122, pp. 11-21. doi:*http://dx.doi.org/10.1016/j.rse.2011.08.026*.

Jhabvala, M., Reuter, D., Choi, K., Jhabvala, C., and Sundaram, M. (2009). QWIP-based thermal infrared sensor for the Landsat Data Continuity Mission. Infrared Physics & Technology, 52(6), pp. 424-429. doi:*http://dx.doi.org/10.1016/j.infrared.2009.05.027*.

Jhabvala, M., Reuter, D., Choi, K., Sundaram, M., Jhabvala, C., La, A., Waczynski, A., and Bundas, J. (2010). The QWIP focal plane assembly for NASA's Landsat Data Continuity Mission. Proc. SPIE 7660 'Infrared Technology and Applications XXXVI, 76603J (May 3, 2010) doi:*10.1117/12.849305*.

Kerr, Y. H., Lagouarde, J. P., and Imbernon, J. (1992). Accurate Land Surface-Temperature Retrieval from AVHRR Data with Use of an Improved Split Window Algorithm. Remote Sensing of Environment, 41(2-3), pp. 197-209. doi:*http://dx.doi.org/10.1016/0034-4257(92)90078-x*.

Kim, Y., Huete, A. R., Miura, T., and Jiang, Z. (2010). Spectral compatibility of vegetation indices across sensors: band decomposition analysis with Hyperion data. Journal of Applied Remote Sensing, 4. doi:*http://dx.doi.org/10.1117/1.3400635*.

Kinch, M. A. (2000). Fundamental physics of infrared detector materials. Journal of Electronic Materials, 29(6), pp. 809-817. doi:*http://dx.doi.org/10.1007/s11664-000-0229-7*.

Pearlman, J. S., Barry, P. S., Segal, C. C., Shepanski, J., Beiso, D., and Carman, S. L. (2003). Hyperion, a space-based imaging spectrometer. IEEE Transactions on Geoscience and Remote Sensing, 41(6), pp. 1160-1173. doi:*http://dx.doi.org/10.1109/tgrs.2003.815018*.

Reuter, D. C., Richardson, C. M., Pellerano, F. A., Irons, J. R., Allen, R. G., Anderson, M., Jhabvala, M. D., Lunsford, A. W., Montanaro, M., Smith, R. L., Tesfaye, Z., and Thome, K. J. (2015). The Thermal Infrared Sensor (TIRS) on Landsat 8: Design Overview and Pre-Launch Characterization. Remote Sensing, 7(1), pp. 1135-1153. doi:*http://dx.doi.org/10.3390/rs70101135*.

Rogalski, A. (2005). HgCdTe infrared detector material: history, status and outlook. Reports on Progress in Physics, 68(10), pp. 2267-2336. doi:*http://dx.doi.org/10.1088/0034-4885/68/10/r01*.

Rogalski, A. (2010). Infrared Detectors, Second Edn. CRC Press, Taylor & Francis Group, Boca Raton.

Rogalski, A. (2012). History of infrared detectors. Opto-Electronics Review, 20(3), pp. 279-308. doi:*http://dx.doi.org/10.2478/s11772-012-0037-7*.

Schenk, T. (2005). Introduction to Photogrammetry. Department of Civil and Environmental Engineering and Geodetic Science, The Ohio State University, Columbus, OH. Retrieved from *http://www.mat.uc.pt/~gil/downloads/IntroPhoto.pdf*.

Sharma, D. (2005). Handbook of Spectroscopy. International Scientific, New Delhi.

Shaw, G. A., and Burke, H. K. (2003). Spectral Imaging for Remote Sensing. Lincoln Laboratory Journal, 14(1), pp. 3-27.

Ulaby, F. T., and Long, D. G. (2014). Microwave, Radar and Radiometric Remote Sensing. Retrieved from *http://mrs.eecs.umich.edu/*.

Zhu, W., Tian, Y. Q., Yu, Q., and Becker, B. L. (2013). Using Hyperion imagery to monitor the spatial and temporal distribution of colored dissolved organic matter in estuarine and coastal regions. Remote Sensing of Environment, 134, pp. 342-354. doi:*http://dx.doi.org/10.1016/j.rse.2013.03.009*.



15 Active Imaging Systems

Authors: Glenn Newnham, John Armston, Bruce C. Forster, Catherine Ticehurst[59]

The principle underlying active remote sensing devices is that they transmit energy towards a specific target, either as pulses or as a continuous signal, then measure the energy returned from the target. Two distinct categories of active imaging sensors are radar and lidar technologies:

- lidar—irradiates with pulses of selected 'optical' wavelengths (see Section 5.1) then records the range and intensities of returns or 'echoes' (see Section 15.1); and
- radar—irradiates with pulses of microwaves then records the range and intensity of 'echoes' (see Section 15.2).

Being independent of solar illumination, active sensors may be used 24 hours a day. In addition, radar sensors are less sensitive to atmospheric scattering. In many applications and geographic regions, such as the perennially cloudy tropics, these features provide a guarantee of data acquisition that is not available for passive systems operating in optical wavelengths.

While some active optical sensors (which illuminate a target with selected 'optical' wavelengths) are available (Holland *et al*., 2012), they will not be considered in detail here. Examples of these systems include CropCircle™ (Lamb *et al*., 2009) and Raptor™ (Lamb *et al*., 2011).

15.1 Lidar

Light Detection and Ranging (lidar) is a technique that uses a transmitted laser pulse to detect the presence of a target and measures the distance to the target based on the time and intensity of any reflected return pulse. Lidar is an active remote sensing technology that operates in the wavelength range from ultraviolet to near infrared. The laser directs pulsed or continuous radiation through a collimating (laser) system while a second optical system collects the returned radiation and focuses it onto a detector. Both the time for any reflected return pulses and their intensity are measured.

Lidar instruments pulse very high peak intensities of light energy within a temporally narrow and highly collimated beam. An accurate clock records the time interval (t) between transmission of the laser pulse and reception of any return to determine the range (r) from the sensor to the target:

$$r = \frac{c\,t}{2}$$

where c is the speed of light in an atmospheric medium. When this distance and the beam direction to an object are known, then the location of that object, relative to the location of the sensor, can be calculated. If the absolute location of the sensor is known, then the absolute location of the target object can also be determined.

Lidar systems exist on many different sensing platforms including satellite, airborne and ground-based systems. Airborne systems generally include an Inertial Measurement Unit (IMU), which records the platform's velocity and orientation. These are often combined with differential GPS measurements in order to determine a very accurate location and orientation of the aircraft. This location and orientation accuracy directly translates to the accuracy of derived absolute coordinates of any detected targets. Current airborne systems can deliver sub-centimetre accuracy for target positioning information.

Background image: PALSAR image, acquired on 3 January 2009 with HH polarisation, shows rivers feeding into the Gulf of Carpentaria in flood conditions. **Source:** Norman Mueller, Geoscience Australia

59. Recommended Chapter Citation: Newnham, G., Armston, J., Forster, B., and Ticehurst, C. (2016) Active Imaging Systems. Ch 15 in Volume 1A of Earth Observation: Data, Processing and Applications. CRCSI, Melbourne.

The laser light transmitted by a lidar systems can either be:

- pulsed—the system transmits short pulses of laser light, which may be intercepted by targets and scattered back towards the instrument. These return pulses are received and amplified by an optical telescope then converted to an electrical impulse by a photomultiplier; or
- continuous—the system emits a continuous stream of laser energy with modulated intensity. The phase difference between transmitted and received signals can be used to determine range. A number of different frequency modulations can be superimposed in order to overcome the possible ambiguity of receiving the same phase shift for different ranges, corresponding to different numbers of full modulation wavelengths.

Two return pulse detection systems are commonly used in Earth Observation (EO) lidar:

- discrete return—single or a small number of returns are sampled for each outgoing pulse; or
- full waveform—a digitised profile is recorded of all return intensity as a function of time (see Figure 15.1).
- Discrete return instruments can be designed to record the first return, last return or multiple returns. Each of these may be based on either pulsed or continuous phase-shift ranging techniques. However, recording of a full-waveform can only be achieved using pulsed lidar systems. Jutzi and Stilla (2005) describe how continuous intensity returns can be converted into discrete ranges, thus linking full waveform and discrete lidar technologies.

A lidar system may also scan across track to increase coverage of measurements. Scan patterns used can vary (Gatziolis and Andersen, 2008), but are commonly the saw tooth pattern, which produces an irregular pattern of irradiated points. The accumulation of returns from these irradiated points is generally referred to as a point cloud. These can be resampled into a regular grid via nearest neighbour or surface fitting, for use in image processing and GIS software packages. Imagery derived from lidar data may belie their acquisition method, and imply a greater spatial resolution than was actually present in the original measurements. Recommendations for the acquisition and validation of airborne lidar surveys are given in Quadros and Keysers (2015).

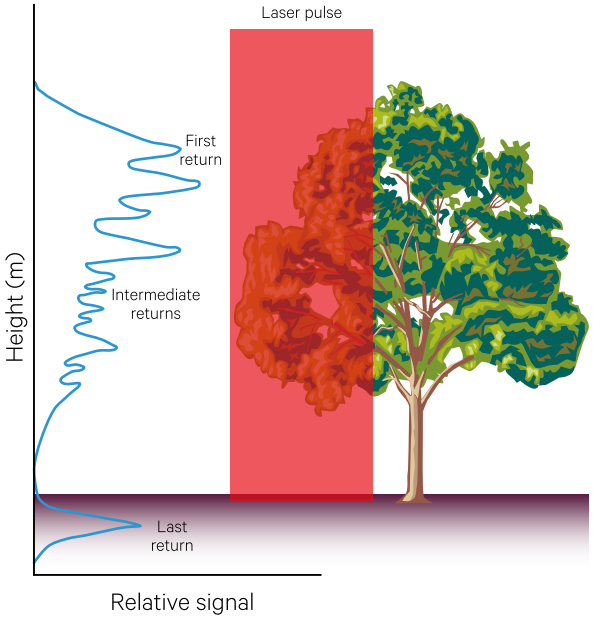
Different wavelengths of light can be used in lidar systems, as appropriate to particular applications. Blue-green wavelength (532 nm) lidar systems are used for bathymetric measurements in shallow coastal waters (see Volume 3B) and NIR lidar are used to provide topographic data, characterise vegetation canopies (see Volume 3A) and map urban environments (Lefsky *et al.*, 2002). Ground-based lidar (such as the many commercial Terrestrial Laser Scanning instruments and dedicated vegetation measurement system like the Echidna®) provides valuable verification of vegetation structure and density (see Section 10).

Lidar is only effective in clear atmospheric conditions and such devices are generally aircraft-borne or land-based. No satellite-based scanning lidar systems are currently in operation. However, the Geoscience Laser Altimeter, that was in operation on the ICESat satellite between 2003 and 2010, has been used in combination with other sensors for vegetation mapping (for example, Scarth *et al.*, 2015). The NASA Global Ecosystems Dynamics Investigation (GEDI) lidar is planned for deployment on the International Space Station in early 2019, to generate the first comprehensive high-resolution dataset of vertical forest structure at a global scale.

Airborne lidar is now ubiquitous within the global surveying industry with a primary focus on accurate and precise surface elevation and bathymetric mapping. Secondary applications focus on measurement and structural properties of vegetation (such as height and biomass), topography, built infrastructure and mine site environs (see Excursus 15.1). Other uses of lidar include spectroscopy (for air and water pollution studies) and altimetry (see Section 16).

Figure 15.1 Lidar operation

A continuous waveform sensor would record the continuous height profile shown on the left of tree. Multiple discrete return sensors record the heights of discrete targets intercepted by the laser pulse. A first-return sensor would only record the height of the first target encountered, in this case the height of the first intercepted branch. A last-return sensor would only record the distance to the last object encountered by the laser beam, so is useful for terrain mapping.



Excursus 15.1—Airborne Lidar Applications

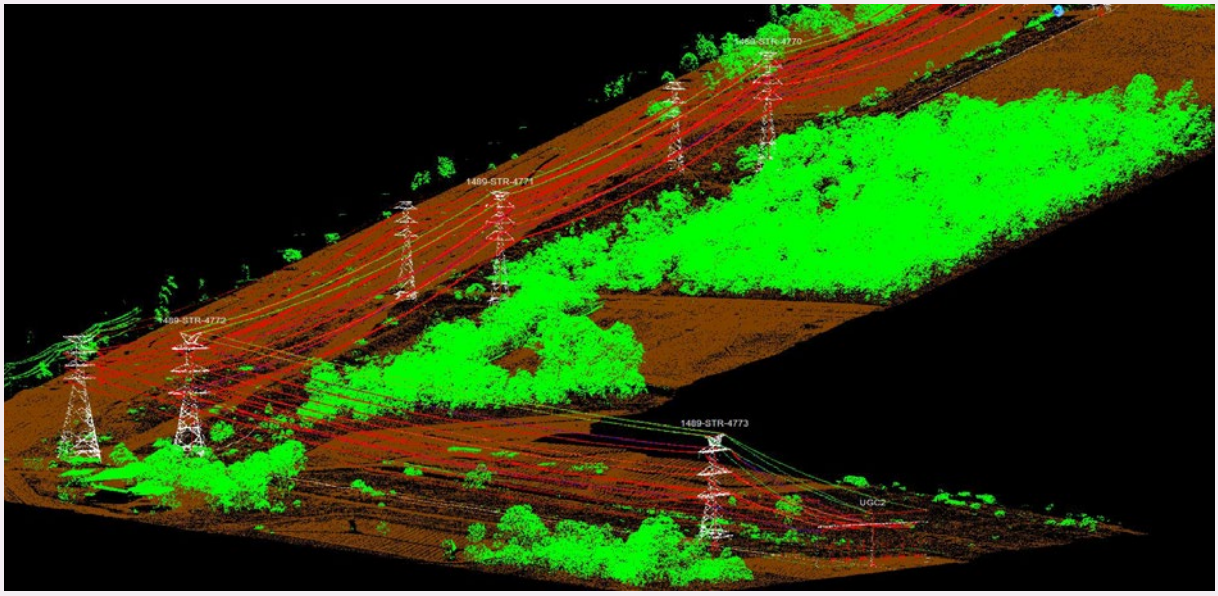
Source: AAM Group
Further information: *www.aamgroup.com*

Airborne Lidar (Light Detection And Ranging) uses laser scanner(s) mounted in an aircraft to measure the height of discrete points below the aircraft. Lidar can penetrate gaps in dense canopy, enabling the capture of both canopy and topographic heights.

Various derived products can be generated for:

- vegetation,
- built infrastructure (such as power lines, towers, buildings), and
- bathymetry.

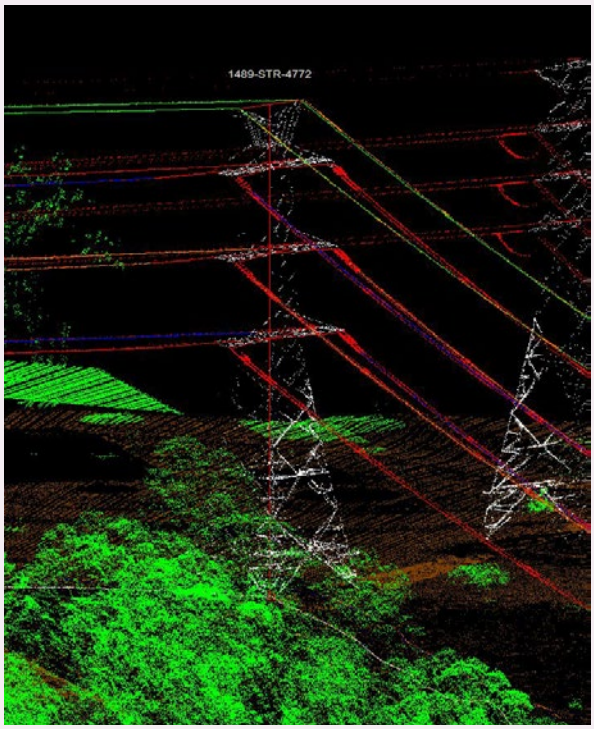
Figure 15.2 Perspective view of classified point cloud



Application 1: Power line survey

132 kV transmission lines were flown by helicopter in Brisbane at 76 kph (41 knots) in 2015. Lidar point data was acquired at 25 points/m^2, with relative accuracy better than 5 cm. Natural colour imagery (6cm resolution) was acquired simultaneously. Based on field data collected independently by surveyors, the final derived tower and power line models were accurate to 5 cm, in both vertical and horizontal measurements (see Figures 15.2 and 15.3).

Figure 15.3 Enlarged perspective view showing details of towers and power lines



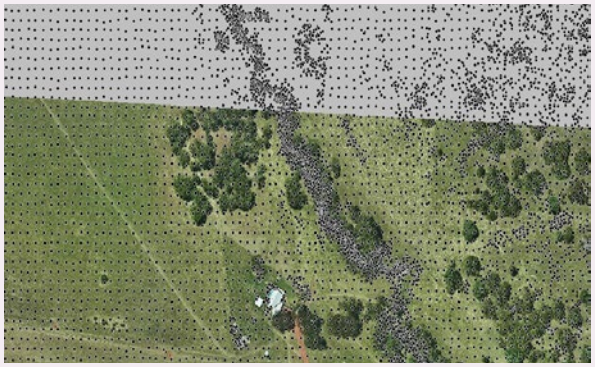
Application 2: Terrain model from topographic lidar

LIdar terrain data and imagery were captured for a recent engineering study of a potential wind farm site in NSW (220 km^2). As illustrated in Figure 15.4, these data sets were processed to deliver:

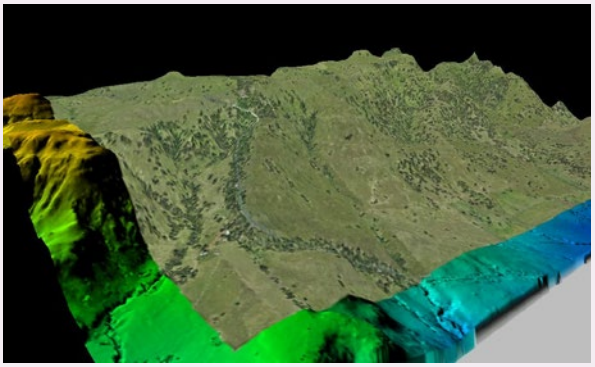
- .las point cloud (showing density of lidar points);
- terrain as 0.5 m contours (for road planning);
- 1 m ESRI grids (to generate terrain model); and
- 15 cm, three band (natural colour) ortho imagery (to provide locational context).

Figure 15.4 Terrain model

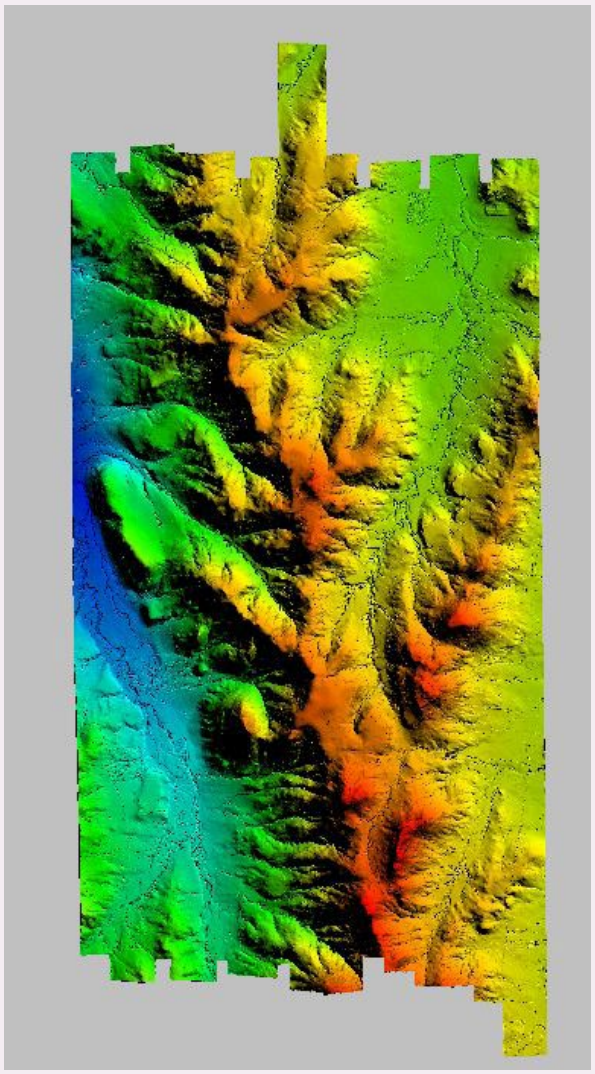
a: Laser strikes, overlaid on colour imagery to illustrate density of coverage on site



b: Mosaicked natural colour imagery draped over terrain model (mosaic spans 6 km east to west)



c: Terrain model generated from 1 m ESRI grid. Flight swaths (and overlaps) are indicated in this image. Colours range from blue for low lying areas, through green then yellow to red for higher elevations.



d: 15cm orthorectified imagery, natural colour



15.2 Radar

Radar is an acronym for RAdio Detection And Ranging, that is, using actively transmitted radio waves to detect objects and determine their position or 'range'. The principle of operation for these devices is to direct pulses of microwave (a type of radio wave with wavelengths from approximately 1 cm to 100 cm) energy at an object then record the strength, direction and sometimes polarisation of the reflected energy. As with lidar systems, microwave pulses are transmitted for a very short time period (microseconds) and alternate with recording of returns. The distance between the transmitter and the reflecting object is then determined from the return time of the signal.

Radar signals may be transmitted at a range of wavelengths/frequencies. The standard wavelengths used and their standard radar frequency letter codes are given in Table 15.1.

These ranges are illustrated in Figure 15.5 relative to the electromagnetic spectrum. The effect of atmospheric composition on transmitted signals varies with wavelength. In general, atmospheric precipitation has minimal effect on radar signals with frequency <10 GHz, which provides a distinct advantage over passive and active optical sensors for EO when cloud cover is present. Slight attenuation occurs at wavelengths less than 30 mm under clear atmospheric conditions, with attenuation increasing as wavelength decreases. Heavy precipitation will cause a strong radar echo at wavelengths of 10 mm or less (this principle being used in both ground and aircraft mounted weather detection radar systems).

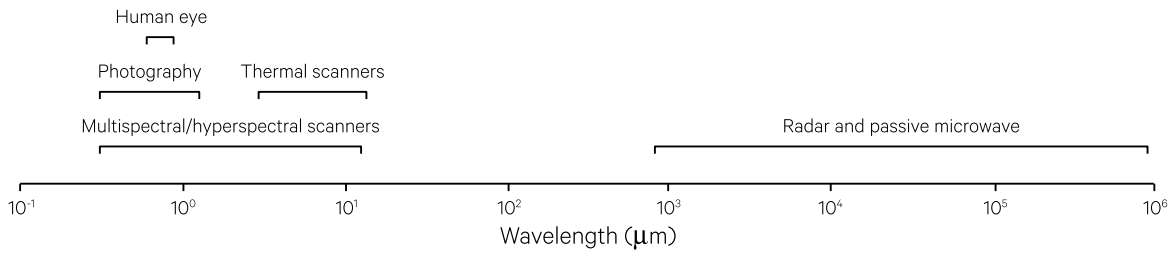
X, C and L bands are most commonly used for EO. Typical wavelengths used by airborne radars are illustrated in Figure 15.6. The interaction between these wavelengths and features on the Earth's surface is partly a function of the scale of the surface 'texture' and its dielectric properties (electrical reflectivity and conductivity; see Volume 1B—Section 8 for details). Scattered signal amplitude and polarization provides information about scattering properties and structure. Phase measurements of the return pulse are used in interferometry to reconstruct 3D topography and, more recently, vegetation height and reflectivity profiles using tomographic techniques. For vegetation canopies, the interactions depend on the size, density and orientation of elements. For example, X-band radar, with wavelengths of around 3 cm, is scattered strongly by foliage, while L-band, with wavelengths of 27 cm, is scattered more strongly by tree branches and P-bands (wavelengths around 70 cm) is predominantly scattered by tree trunks (see Figure 15.7).

Table 15.1 Standard radar frequency and wavelength letter bands.

Band	Wavelength (mm = 10^3 μm)	Frequency (GHz = 10^9 Hz)
W	2.7–4.0	75.0–110.0
V	4.0–7.5	40.0–75.0
Q	6.0–9.0	33.0–50.0
K	7.5–25.0	12.0–40.0
X	25.0–37.5	8.0–12.0
C	37.5–75.0	4.0–8.0
S	75.0–150.0	2.0–4.0
L	150.0–300.0	1.0–2.0
P	300.0–1000.0	0.3–1.0

Figure 15.5 The microwave and radio wave spectra

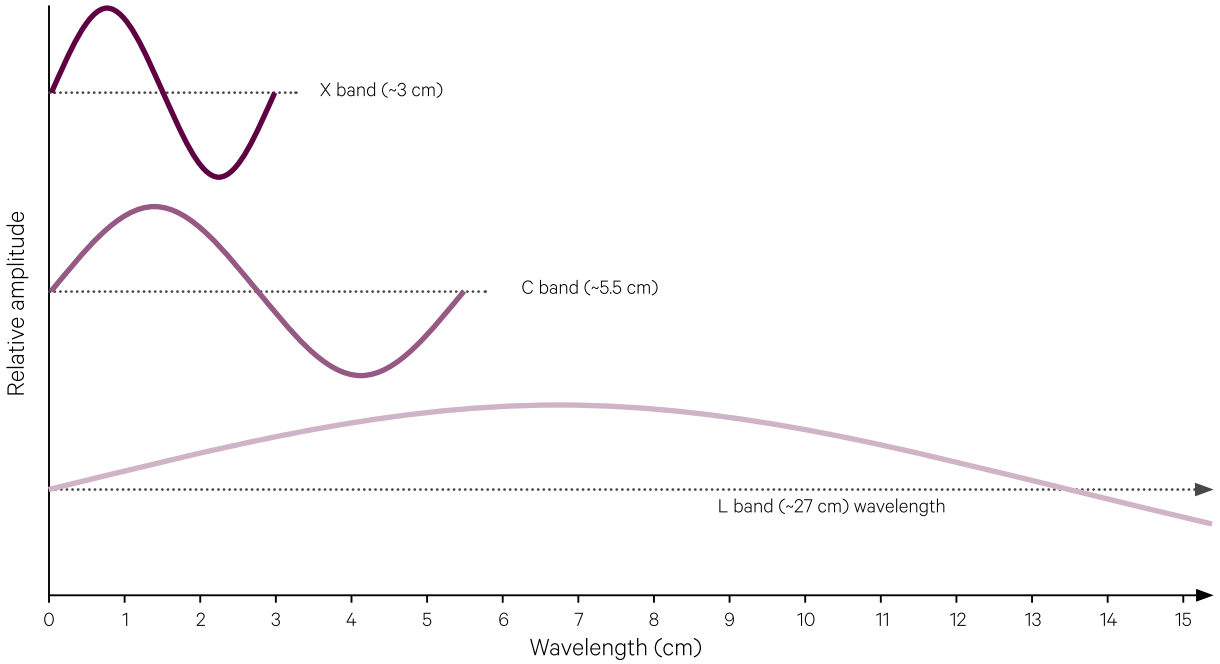
Frequencies of bands commonly referenced with long wave EMR. Note: scales are logarithmic.



Adapted from: Harrison and Jupp (1989) Figure 22

Figure 15.6 Radar wavelengths

Actual size of wavelengths for radar bands commonly used for EO



The transmitted radar signals can be generated so that the electrical wave vibrations are restricted to a single plane, that is, perpendicular to the direction of wave propagation (rather than vibrate in all directions perpendicular to that of propagation). This filtering process is referred to as polarisation. Two orthogonal modes of polarisation are used in imaging radar: these are referred to as horizontal (H) and vertical (V) and are typically transmitted separately. Interaction with features on the Earth's surface can change the polarisation of the scattered signal, so radar antennae are often designed to receive the H and V signals simultaneously. As a result, polarimetric radar detection systems can measure backscatter amplitude and phase in up to four specific polarisation modes (see Table 15.2). More recently, circular polarisation (the tip of the electric field vector is rotating in a circle as it propagates) is also used, where a circularly polarised wave is transmitted and H and V signals are received. This allows any configuration of transmit and receive to be derived (see Volume 1B—Section 8).

HH or VV images are referred to as 'co-polarised'; HV or VH are 'cross-polarised'. Radar system measurements are typically single-polarised (HH or VV or HV or VH), dual-polarised (HH and HV, VV and VH, or HH and VV), or quadrature polarised (HH, VV, HV, and VH). A quadrature polarized (that is, polarimetric) radar and some dual-polarised systems also measure the signal phase difference between the modes as well as the signal magnitude since it is important in polarimetric analysis. Differences in the structure (for example, orientation, shape) of surface features modify the polarisation of reflected microwave energy in varying degrees, with the polarisation mode affecting the scattering intensity 'echo' and thus how the objects appear in the resulting imagery.

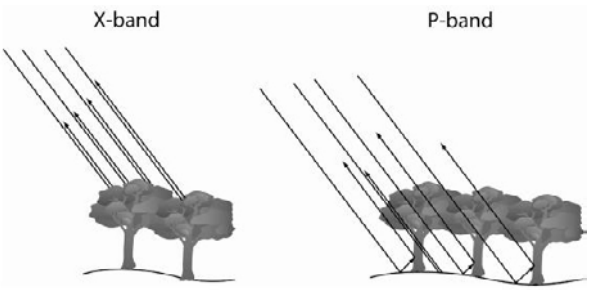
Two types of radar-based systems are commonly used for microwave imaging on aircraft and satellite platforms:

- Side-Looking Airborne Radar (SLAR) or Real Aperture Radar (RAR)—see Section 15.2.1; and
- Synthetic Aperture Radar (SAR)—see Section 15.2.2.

Figure 15.7 Interaction of radar wavelengths with vegetation

The interaction between radar wavelengths and vegetation depends on the size, density and orientation of vegetative components.

a. X-band radar, with wavelengths around 3 cm, is strongly scattered by foliage.
b. P-band radar, with wavelengths around 70 cm, is mostly scattered by tree trunks.



Adapted from: Moreira (2001). Retrieved from *http://forsys.cfr.washington.edu/JFSP06/radar_overview.htm*

Table 15.2 Polarisation options for radar signals

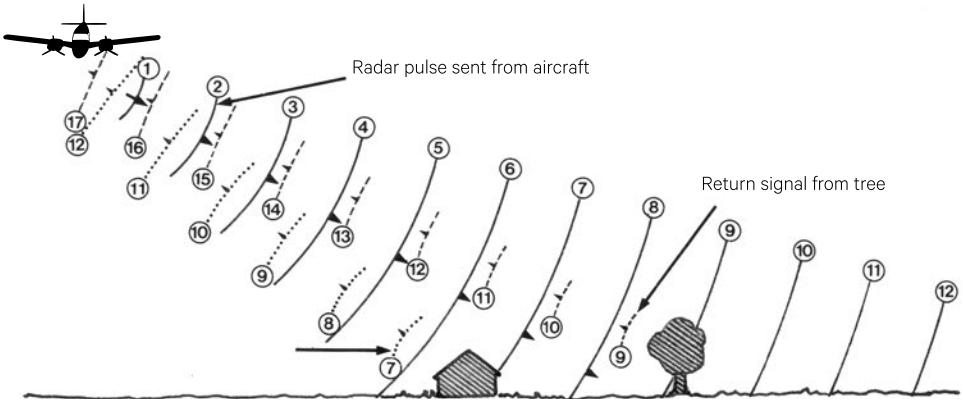
Transmitted	Received	Code	Type
H	H	HH	Co-polarised
H	V	HV	Cross-polarised
V	H	VH	Cross-polarised
V	V	VV	Co-polarised

15.2.1 Side-Looking Airborne Radar (SLAR) or Real Aperture Radar (RAR)

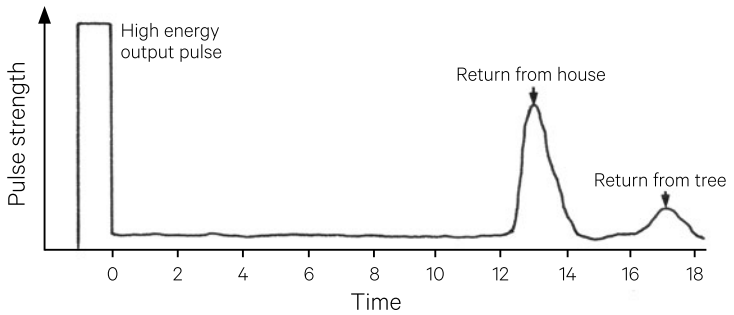
A radar pulse is transmitted off-nadir by an antenna fixed below an aircraft. This is used to image large ground areas adjacent to the flight line. The echoes are processed to produce an amplitude/time electrical signal that is then recorded as an image line, with 'brighter' pixels indicating higher scattering intensities. This procedure is illustrated in Figure 15.8.

Figure 15.8 Operation of side-looking airborne radar

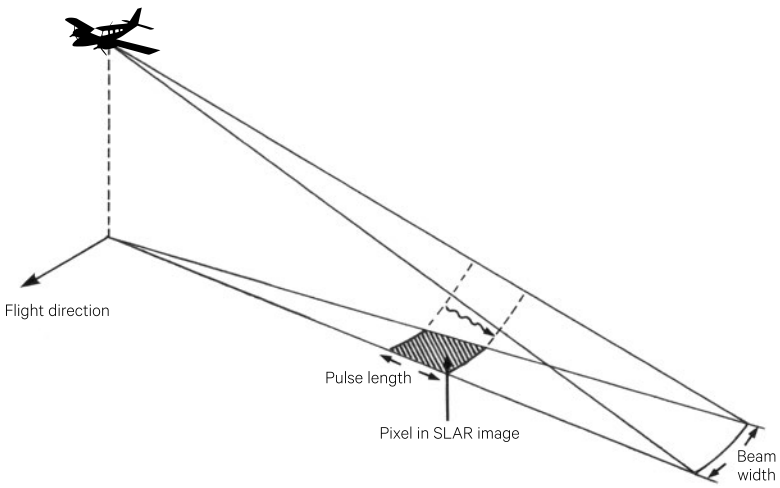
a. The propagation of one radar pulse is shown using solid lines to indicate the wavefront locations at time intervals 1 to 12. The reflected waves or echoes are shown by dashed lines beginning at time 7 for the house and time 9 for the tree. These return signals reach the antennae at times 13 and 17 respectively.



b. The antennae response graph shows a strong echo for the house at time 13 and a weaker echo for the tree at time 17. The strength of the echo depends on the way an object reflects radio waves.



c. Range resolution and azimuth resolution in SLAR imagery is determined by the time duration of the pulse and the beamwidth of the SLAR antennae.



Source: Harrison and Jupp (1989) Figure 23

The spatial resolution in such imagery is determined by the pulse time length and the beamwidth of the antenna as shown in Figure 15.8. The beamwidth of the SLAR antenna is directly proportional to the microwave signal wavelength and inversely proportional to the length of the antenna. The time duration of the pulse determines whether the signals from adjacent objects will be overlapped and hence not distinguished separately.

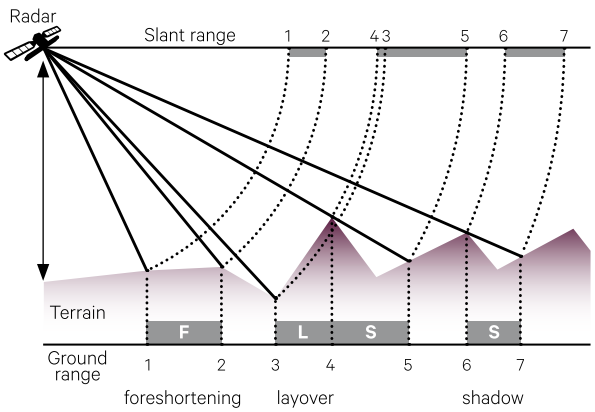
The oblique look angle used to acquire radar imagery results in characteristic geometric distortions such as radar shadows, foreshortening and layover effects (see Figure 15.9 and Volume 1B—Section 8). Foreshortening occurs when the true length of a tall feature, such as a mountain, appears compressed, while layover occurs when the radar beam reaches the top of a tall feature before it reaches the base. While these effects are more pronounced in aircraft radar images, they also occur in satellite imagery, and are more pronounced in mountainous terrain. The impact of these distortions on radar imagery is illustrated in Figure 15.10. Microwave image interpretation is discussed in greater detail in Volume 1B—Section 8.

Systems that utilise the actual antenna size, such as the SLAR systems described, are called real aperture radars (RAR). Because of the physical limitation of antenna size on aircraft, such systems are restricted to short range and low altitudes (which limit the extent of coverage) and relatively short wavelengths (which experience greater atmospheric attenuation and scattering).

Figure 15.9 Radar image distortions

Specific distortions in radar imagery resulting from its side-looing viewing geometry include:

a. Shadowing—locations shielded from the radar pulse cannot generate a return so appear as shadow.
b. Foreshortening—more elevated locations on a slope generate radar returns in a shorter time interval after lower elevations on the slope than if the points were separated horizontally.
c. Layover—where higher elevations on a slope are physically closer to the radar sensor, they will generate a return before lower elevations on that slope, which results in the top of the slope appearing to 'lay over' the base.

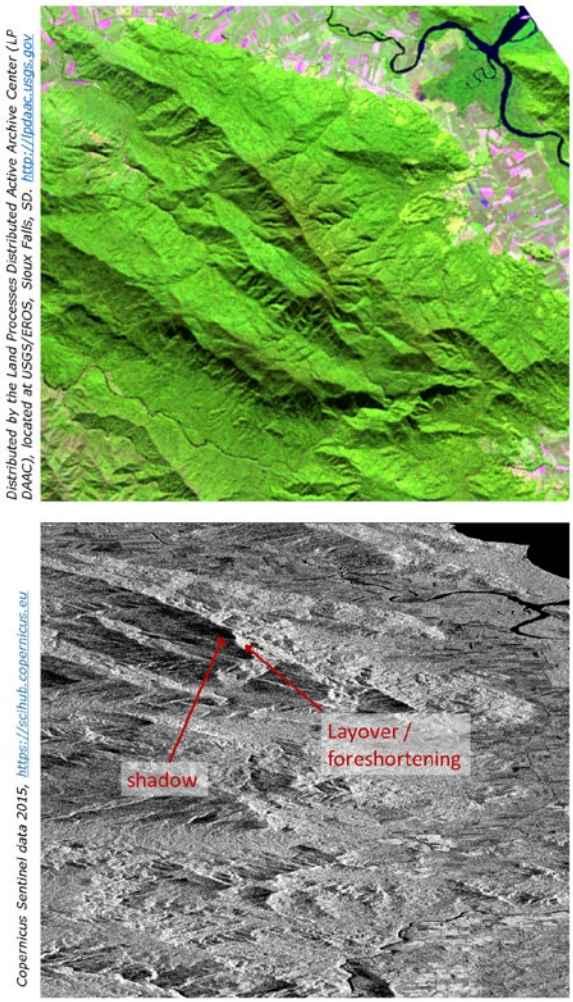


Source: Kerle *et al.* (2004). Used with permission from ITC.

Figure 15.10 Impact of radar distortions in imagery

Wooroonooran National Park, Queensland (30 km south of Cairns).

a. Landsat-8 OLI image 17 July 2015 (bands 6,5,4) showing terrain features
b. Sentinel-1 image 25 February 2015 (HV polarisation) showing different spatial relocation of terrain features due to foreshortening and layover



Source: NASA/ESA, prepared by Catherine Ticehurst, CSIRO

15.2.2 Synthetic Aperture Radar (SAR)

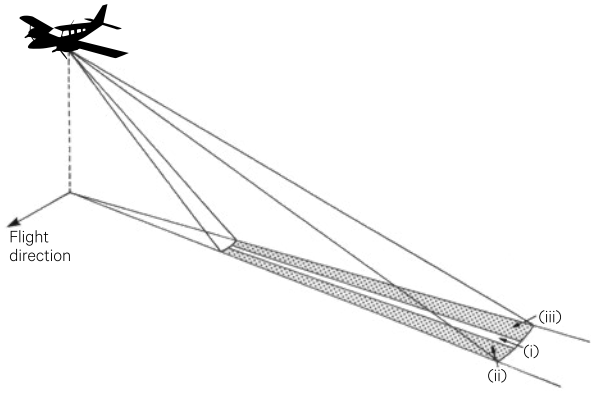
The physical antenna length may be effectively lengthened using the flight path of the radar platform by processing return signals according to their Doppler shifts (that is, a change in wave frequency as a function of the relative velocities of transmitter and receiver; see Section 2.5.4). This basic principle is used in Synthetic Aperture Radar (or SAR) as shown in Figure 15.11. This processing requires that both amplitude and phase information be recorded from objects throughout the time period in which they are within the beam of the moving antenna. The theoretical increase in the antennae length (the synthetic aperture) allows the computer-processed cross-range or azimuth resolution to be equal to half the real aperture for the whole of the range (near

range to far range). Weighted averaging of multiple returns using the platform motion and Doppler shift effects allows the signal that would have been obtained by a longer antenna to be reconstructed. The consequently larger synthetic aperture results in higher spatial resolution imagery that is constant in the along-track (azimuth) and across-track (range) directions (see Volume 1B—Section 8 for details).

An example of a SAR image acquired by Sentinel-1a is shown in Figure 15.12 over the Menindee Lakes in western NSW. This image shows the amplitude of the VV polarization data, corrected to Sigma 0. Very dark areas occur where very little of the incident microwave energy is reflected back to the sensor, and mostly correspond to open water. Very bright areas occur where a large amount of the incident energy is reflected back to the sensor. This may correspond to vegetation or very rough surfaces (where 'rough' is relative to the incident wavelength), such as a dry lake with a 'rough' lake floor. A 'double-bounce' effect occurs along the river where incident microwaves reflect off water in the river channel and then again reflect off the woody structures in the surrounding riparian vegetation. Terrain undulations and variations in vegetative cover and soil moisture change the way the incident microwaves interact with the ground and create a mottled effect. Sand dunes in the northern portion of the image introduce horizontal striping patterns due to variations in topography and soil moisture.

Figure 15.11 Operation of synthetic aperture radar

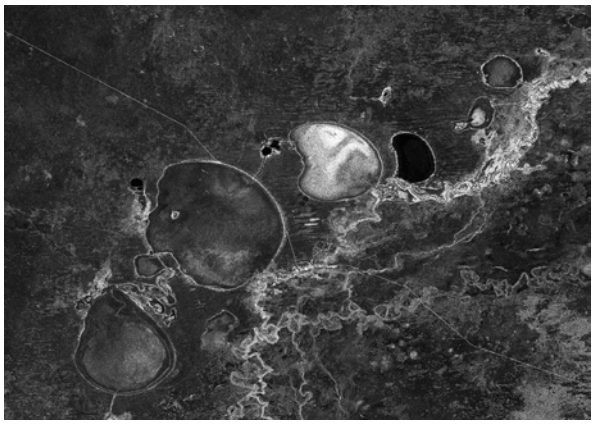
Recording the frequency as well as the amplitude of echoes allows the surface illuminated by the radar beam to be sub-divided into three regions, where the frequency of the return signal from an object will change (due to Doppler shift), which allows the position of the ground object to be more precisely located and thus greatly improves the azimuth or cross-range resolution:
(i) a narrow strip perpendicular to the flight line where the echo frequency matches the transmitted frequency,
(ii) a region ahead of the aircraft where echoes are up-shifted in frequency, and
(iii) a region behind the aircraft where echoes are down-shifted in frequency.



Source: Harrison and Jupp (1989) Figure 24

Figure 15.12 Comparing SAR and Optical imagery

a. Sentinel-1a image over the Menindee Lakes (western NSW) acquired on the 29 December 2015. This is the amplitude of the VV polarization data, corrected to Sigma 0. Very dark areas occur where very little of the incident microwave energy is being reflected back to the sensor, while very bright areas occur where a large amount of the incident energy is being reflected back to the sensor. The mottling of the landscape in general is due to undulations in terrain, vegetation and variations in soil moisture changing the way the incident microwaves interact with the ground. The intermittent, but fairly regular, horizontal stripes in the northern part of the image are caused by sand dunes, creating some topographic effects and also showing variations in soil moisture between the peaks and troughs of the dunes.



b. Landsat-8 image over Menindee Lakes, acquired on 9 January 2016, displayed as a natural colour composite (using band 2 as blue, band 3 and green and band 4 as red).



Source: ESA, prepared by Norman Mueller, Geoscience Australia

Stripmap, spotlight and scansar are different SAR acquisitions modes. Current SAR instruments acquire each mode to develop products that are suited to different applications. Scan mode involves moving the antenna in a scan pattern, and is used to capture larger areas (e.g. for flood mapping) but at the cost of lower spatial resolution. Spotlight is used to capture data over small target areas at high spatial resolution, and involves pointing the beam as the platform moves so that the target is in the beam for longer, thus making the synthetic aperture larger. Stripmap is the standard acquisition mode (fixed beam direction, no scanning) and corresponds with the SLAR described in Section 15.2.1.

TOPS (Terrain Observation by Progressive Scans) is a recent SAR mode for wide swath acquisition (the default mode of Sentinel-1), which aims at achieving the same coverage and resolution as the scan mode (besides creating scalloping-free images). Some recent SAR missions employ satellite constellations to enable single pass interferometry (e.g. TanDEM-X) and shorten revisit times.

A comprehensive list of airborne and satellite-borne SAR sensors is available in Watt *et al*. (2012). Current and future spaceborne SAR imaging sensors are detailed in CEOS (2015). Satellite SAR sensors that are currently used or planned for use in Australia are listed in Table 15.3.

Table 15.3 Examples of active and future satellite SAR sensors

Each of these sensors can have different observation modes (stripmap, spotlight and scansar) with inherently different polarisations and spatial resolutions.

Frequency Band	Launch Year	Mission(s)	Agency (Country)
C-band	2007	RADARSAT-2	CSA/MDA (Canada)
C-band	2014 2016	Sentinel-1A Sentinel-1B	EC/ESA (Europe)
X-band	2007 2007 2008 2010	COSMO-SkyMED-1 COSMO-SkyMED-2 COSMO-SkyMED-3 COSMO-SkyMED-4	ASI (Italy)
X-band	2007	TerraSAR-X	DLR/Airbus DS (Germany)
X-band	2010	TanDEM-X	DLR/Airbus DS (Germany)
X-band	2009	RISAT-2	ISRO (India)
X-band	2015 2017 2022	HY-3A WSAR Hy-3B WSAR HY-3C WSAR	NSOAS/CAST (China)
L-band	2014	ALOS-2 PALSAR-2	JAXA (Japan)
L-band	2020	NISAR	NASA/ISRO (USA/India)
L-band	2017 2018	SAOCOM-1A SAOCOM-1B	CONAE (Argentina)
P-band	2021	BIOMASS SAR	EC/ESA (Europe)

Adapted from: CEOS (2015)

15.3 Further Information

Lidar:

Terrestrial Laser Scanning Database, University of Calgary: *http://www.tlsdatabase.ucalgary.ca*

Spatial Scientific Technologies: *http://www.lidar.com.au/index.htm*

Lefsky *et al.* (2002)

Quadros and Keysers (2015)

Microwave Remote Sensing:

Natural Resources Canada website: *http://www.nrcan.gc.ca/earth-sciences/geomatics/satellite-imagery-air-photos/satellite-imagery-products/educational-resources/9371*

Radar Tutorial: *http://www.radartutorial.eu*

Christian Wolff Radar Tutorial: *http://www.radartutorial.eu/index.en.html*

Kasischke *et al.* (1997)

Richards (2009)

Toutin and Gray (2000)

Ulaby and Long (2014)

Woodhouse (2004)

Radar Animations:

Iain Woodhouse: *http://www.intro2radar.com*

SAR:

JPL Imaging radar: *http://southport.jpl.nasa.gov*

Radarsat: *http://gs.mdacorporation.com/*

Imaging Sensors and Applications:

Robust Imaging from Space (Watt *et al.*, 2012), including the following Adjunct Reference Documents:

Satellite and Airborne SAR Sensor Specifications: *http://www.crcsi.com.au/assets/Uploads/Files/Adjunct-Reference-1-SAR-Sensor-Specifications-FINAL.pdf*

SAR Application Case Studies: *http://www.crcsi.com.au/assets/Uploads/Files/Adjunct-Reference-2-SAR-Application-Case-Studies-FINAL.pdf*

Moreira (2014)

15.4 References

CEOS (2015). The Earth Observation Handbook. Committee on Earth Observation Satellites, ESA Communications, The Netherlands. Retrieved from *http://www.eohandbook.com*.

Gatziolis, D., and Andersen, H. E. (2008). A guide to LIDAR data acquisition and processing for the forests of the Pacific Northwest. Pacific Northwest Research Station, Forest Service, US Department of Agriculture.

Harrison, B. A., and Jupp, D. L. B. (1989). Introduction to Remotely Sensed Data. Part ONE of the microBRIAN Resource Manual (156 pages). CSIRO Australia, Melbourne.

Holland, K. H., Lamb, D. W., and Schepers, J. S. (2012). Radiometry of Proximal Active Optical Sensors (AOS) for Agricultural Sensing. IEEE Journal of Selected Topics in Applied Earth Observations and Remote Sensing, 5(6), pp. 1793-1802. doi:*http://dx.doi.org/10.1109/jstars.2012.2198049*.

Jutzi, B., and Stilla, U. (2005). Measuring and processing the waveform of laser pulses. Paper presented at the 7th Conference on Optical 3-D Measurement Techniques, Vienna, Austria.

Kasischke, E. S., Melack, J. M., and Dobson, M. C. (1997). The use of imaging radars for ecological applications - A review. Remote Sensing of Environment, 59(2), pp. 141-156. doi:*http://dx.doi.org/10.1016/s0034-4257(96)00148-4*.

Kerle, N., Janssen, L. F., and Huurneman, G. C. (2004). Principles of Remote Sensing, an introductory handbook. , ITC Educational textbook Series 2, 3rd edition. The international Institute for Geo-Information Science and Earth Observation (ITC), Enschede, The Netherlands.

Lamb, D. W., Schneider, D. A., Trotter, M. G., Schaefer, M. T., and Yule, I. J. (2011). Extended-altitude, aerial mapping of crop NDVI using an active optical sensor: A case study using a Raptor (TM) sensor over wheat. Computers and Electronics in Agriculture, 77(1), pp. 69-73. doi:*http://dx.doi.org/10.1016/j.compag.2011.03.009*.

Lamb, D. W., Trotter, M. G., and Schneider, D. A. (2009). Ultra low-level airborne (ULLA) sensing of crop canopy reflectance: a case study using a CropCircle TM sensor. Computers and Electronics in Agriculture, 69(1), pp. 86-91. doi:*http://dx.doi.org/10.1016/j.compag.2009.07.004*.

Lefsky, M. A., Cohen, W. B., Parker, G. G., and Harding, D. J. (2002). Lidar remote sensing for ecosystem studies. Bioscience, 52(1), pp. 19-30. doi:*http://dx.doi.org/10.1641/0006-3568(2002)052[0019:LRSFES]2.0.CO;2*.

Moreira, A. (2014). A Golden Age for Spaceborne SAR Systems. 20th International Conference on Microwaves, Radar, and Wireless Communication (MIKON). doi:*http://dx.doi.org/10.1109/MIKON.2014.6899903*.

Moreira, J., Schwabisch, M., Wimmer, C., Rombach, M., Mura, J. (2001). Surface and ground topography determination in tropical rainforest areas using airborne interferometric SAR. . 'Photogrammetric Week '01' (Ed: D. Fritsch, Spiller, R.). Herbert Wichmann Verlag, Heidelberg.

Quadros, N., and Keysers, J. (2015). Airborne LiDAR Acquisition and Validation. Chapter 15 in 'AusCover Good Practice Guidelines:A technical handbook supporting calibration and validation activities of remotely sensed data products' (Eds: A. Held, S. Phinn, M. Soto-Berelov, and S. Jones). TERN AusCover, Australia. ISBN 978-0-646-94137-0.

Richards, J. A. (2009). Remote Sensing with Imaging Radar. Springer-Verlag, Berlin.

Scarth, P., Phinn, S. R., Armston, J., and Lucas, R. (2015). Continental Scale Vegetation Structure Mapping Using Field Calibrated Landsat, ALOS Palsar and GLAS ICESat. Paper presented at the AGU Fall Meeting, San Francisco, USA.

Toutin, T., and Gray, L. (2000). State-of-the-art of elevation extraction from satellite SAR data. ISPRS Journal of Photogrammetry and Remote Sensing, 55(1), pp. 13-33. doi:*http://dx.doi.org/10.1016/s0924-2716(99)00039-8*.

Ulaby, F. T., and Long, D. G. (2014). Microwave, Radar and Radiometric Remote Sensing. Retrieved from *http://mrs.eecs.umich.edu/*.

Watt, M., Milne, T., Williams, M., and Mitchell, A. (2012). Robust Imaging from Space: Satellite SAR (Synthetic Aperture Radar). CRCSI. Retrieved from *http://www.crcsi.com.au/library/resource/robust-imaging-from-space*.

Woodhouse, I. H. (2004). Introduction to Microwave Remote Sensing. CRC Press.

16 Non-imaging and Sounding Systems

Some remote sensing devices operate in a non-imaging mode to detect information about specific locations or lines on the Earth's surface, and also to measure characteristics of either the atmosphere at selected altitudes or the oceans at nominated depths. These sensors are particularly informative for meteorological applications and have a significant impact on the accuracy of weather forecasts (see Excursus 16.1). Such systems include:

- passive non-imaging devices, which are particularly relevant to atmospheric studies—including thermal infrared sensors and passive microwave radiometers (see Section 16.1.1);
- active non-imaging altimeters or profilers—use laser or radar ranging and scattering instruments to measure detailed distances from sensor to target, which can be used to determine surface height and texture (see Section 16.1.2);
- sounding devices—measure atmospheric properties at specific altitudes or water properties at particular depths using both active and passive sensors (see Section 16.2); and
- sounding techniques, such as radio occultation, which limb sound the atmosphere by measuring the bending of EMR travelling from one satellite to another.

Excursus 16.1—Value of EO to Numerical Weather Prediction

Source: John Le Marshall, Bureau of Meteorology
Further information: Le Marshall *et al.* (2013a), Bureau of Meteorology: *http://bom.gov.au*

Numerical Weather Prediction (NWP) models combine our understanding of the physics of weather with current observations of weather conditions to predict future weather conditions. Current observations can be based on both conventional meteorological measurements (e.g. balloon-based temperature measurements) and various forms of EOS data: imaging, non-imaging and sounding. When only conventional observations are used, the accuracy of a one-day forecast is the same as the accuracy of a four-day forecast in the northern hemisphere based on both conventional and EOS data.

Observing System Experiments (OSE)

Various experiments have been conducted to test the value of EOS data in operational NWP. Two recent experiments used:

1. the ACCESS-G operational system at the Australian Bureau of Meteorology and analysed data from 28 October to 30 November 2011; and
2. the Global Forecast System (GFS) at the US National Centres for Environmental Prediction (NCEP) and analysed data from 15 August to 30 September 2010.

The correlation between the actual and predicted 500 hPa geopotential height anomaly surfaces was used to analyse these datasets. Marked differences in the rate of die-off in these curves were observed using both EOS and conventional meteorological observations compared with only using conventional data. The EOS analyses were based on the complete operational database and treated as the control.

Geopotential Height Anomalies

While geometric height is the elevation above mean sea level, the Geopotential Height adjusts this measure for gravity variations with changes in latitude and elevation. In meteorology it is used to represent the actual height of a pressure surface.

Deviations from the average geopotential height surface are called anomalies. Positive anomalies correlate with hotter than average temperatures and negative anomalies are indicative of colder temperatures. The 500 hPa geopotential height anomaly correlation between actual and predicted weather is regarded as a robust measure of forecast accuracy.

OSE Results

As can be seen in Figure 16.1, the duration of accurate numerical weather forecasts in the Southern Hemisphere is increased fourfold by the inclusion of EOS datasets. These analyses demonstrated that a 24 hour forecast without EOS data has the same accuracy as a 96 hour forecast that includes EOS data. In the Northern Hemisphere, where a higher density of conventional meteorological observations is available, the inclusion of EOS data improved forecast duration by a factor of 1.6.

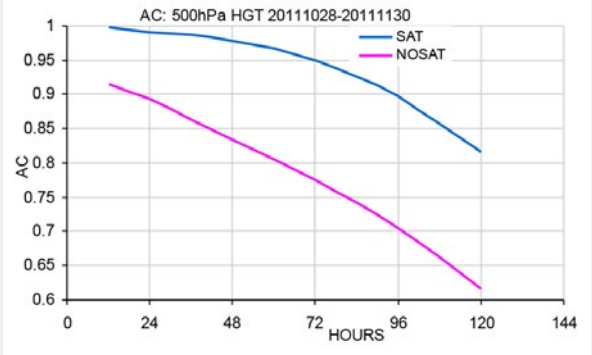
These improvements in NWP capability are also reflected in forecasting individual extreme weather events, such as cyclones. This gain in forecast skill has resulted in significant societal benefits from:

- more reliable weather forecasts;
- improved weather warnings; and
- more time to prepare for extreme weather.

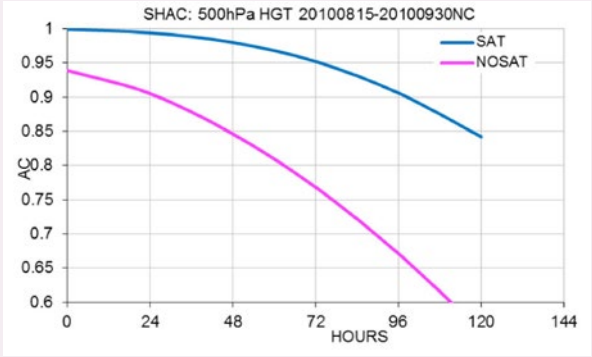
Figure 16.1 1 500 hPa height anomaly correlations

Anomaly correlations for the operational system relying on both EOS and conventional meteorological observations (blue) compared with conventional meteorological observations used without EOS (pink).

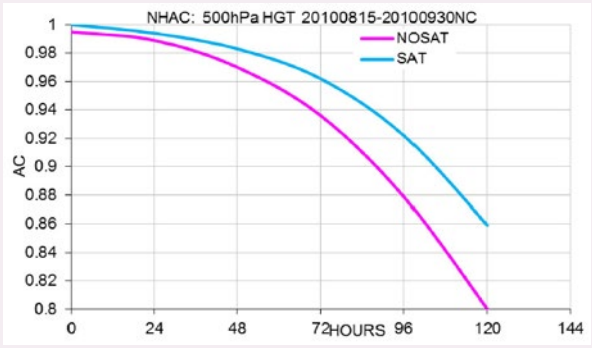
a. Southern Hemisphere ACCESS-G results 2011



b. Southern Hemisphere GFS results 2010



c. Northern Hemisphere GFS results 2010



16.1 Non-imaging systems

16.1.1 Passive

16.1.1.1 Thermal infrared

Non-imaging thermal infrared radiometers are used to measure atmospheric temperature, pressure, humidity and composition at defined locations. These measurements are particularly informative for atmospheric modelling, weather forecasting and climatic studies (see also Volume 1B—Section 7 and Volume 3).

16.1.1.2 Passive microwave

Passive microwave is used for atmospheric observations by detecting the thermal emission of broad atmospheric layers, with altitude being determined by observing at a number of frequencies. The atmospheric temperature and composition can be determined using the microwave spectrum data, with other data being used for calibration (such as infrared observations or meteorological forecasts). Non-imaging passive microwave radiometers are used to infer ocean surface wind speed, and atmospheric water content and temperature.

There are detectable differences in microwave emission intensity between water and sea-ice, the differentiation of which is important for climatic studies. Other applications include determination of:

- sea surface temperature (even in cloudy conditions) for global climate studies;
- precipitation rates; and
- characteristics (including age estimates) for ice and snow cover.

16.1.2 Active

Active non-imaging systems involve:

- ranging—recording the time interval between transmitting a signal and detecting its return; and/or
- scattering—recording the strength of the returned signal.

Some of the active non-imaging technologies used to detect radiation from Earth include:

- laser altimetry (see Section 16.1.2.1);
- radar altimetry (see Section 16.1.2.2); and
- microwave scatterometry (see Section 16.1.2.3).

16.1.2.1 Laser altimetry

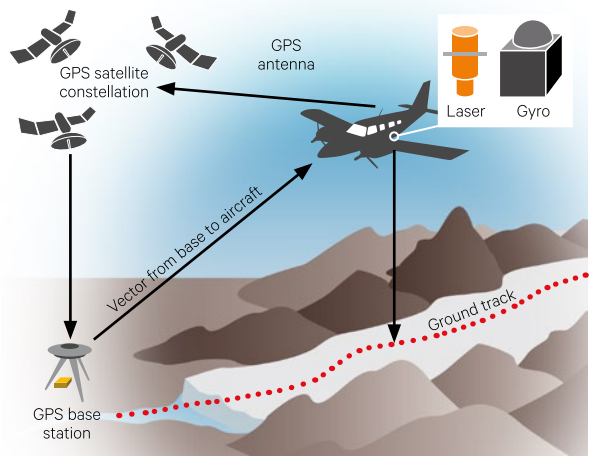
Laser imaging systems are introduced in Section 15.1. Laser altimeters or profilers transmit a light pulse towards the Earth and measure the time delay of the return to determine the distance between the target and the sensor. The pulse generally uses an infrared wavelength selected within an atmospheric window. A series of pulses allows a surface profile to be generated for the target terrain. The terrain surface is sampled by a series of point measurements along the platform direction.

Laser profilers have been carried by both aircraft and satellites. For example, the highly successful satellite laser altimetry mission, ICESat[60], has been valuable for augmenting radar altimetry data, including quantifying its accuracy (Brenner *et al.*, 2007). Figure 16.2 illustrates an airborne laser altimeter that has been used to measure the surface height of glaciers in Alaska (Valentine *et al.*, 2004). The altimetry system in this example comprises:

- a GPS receiver, which records the plane position;
- a laser, which continually measures the distance from the plane to the glacier; and
- a gyroscope, which measures the direction of the laser.

Using precise positional information for both the target and sensor, the surface profile along the laser beam can subsequently be interpolated from the points. In this case, surface profiles are used to compute long-term changes in glacier thickness by comparison with older topographic records (Arendt *et al.*, 2002).

Figure 16.2 Laser altimeter



Adapted from: Chris Larsen, University of Alaska Fairbank at *http://fairweather.alaska.edu/chris/altimetry_text.html*

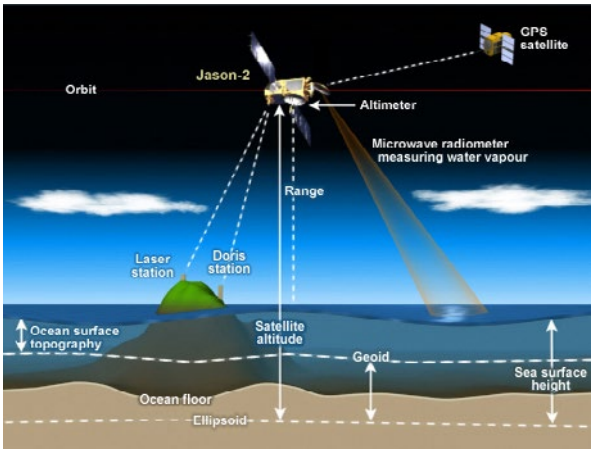
60. ICESat: *http://icesat.gsfc.nasa.gov*

A variation on this configuration is used in Satellite Laser Ranging (SLR) where a laser beam is transmitted from Earth to a reflector carried by a satellite (see Excursus 3.2). These measurements are used to track satellite orbits, monitor Earth's gravitational field, quantify movement of tectonic plates and define geodesic reference points. A growing number of satellites are now fitted with corner-cube reflectors to return the laser beams from the global network of SLR stations, allowing triangulation of both satellite and ground station positions. These activities are coordinated by the International Laser Ranging Service (ILRS)[61]. Laser Ranging data products are essential inputs to the International Terrestrial Reference Frame (ITRF)[62] (see Section 3).

16.1.2.2 Radar altimetry

Radar altimeters have been carried on several satellites, starting with Skylab in 1973, and more recently including the ERS, Jason and Cryosat platforms. This non-imaging radar detects the microwave backscattering of a surface using a narrow pulse with near normal incidence. As introduced in Section 15.2, the basic design of radar devices is to measure distance. By directing the pulse onto the Earth's surface from directly overhead (nadir) the distance being measured is the altitude of the platform above the surface. This relies on accurate knowledge of the platform position, with reference to positioning satellites and ground locating systems, such as the Doppler Orbitography and Radiopositioning Integrated by Satellite (DORIS; Guijarro *et al.*, 2000). Factors relevant to interpretation of satellite radar altimetry data are shown in Figure 16.3.

Figure 16.3 Radar altimetry

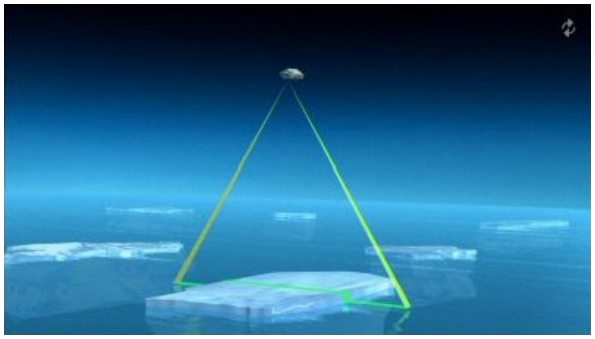


Source: © EUMETSAT. Retrieved from *https://www.eumetsat.int/jason/print.htm*

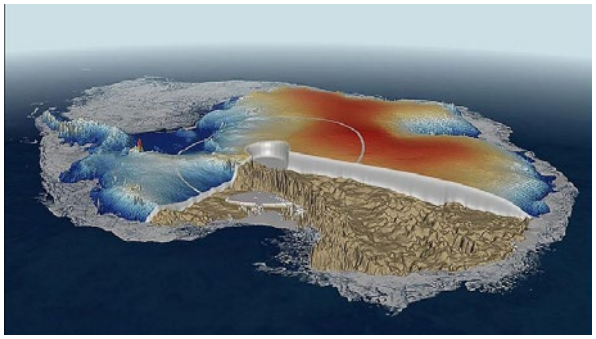
Data from these non-imaging devices can be plotted in image format, for example to map sea surface topography, if the required data volume is available. Routine observation of sea surface topography using satellite radar altimetry has been critical for monitoring sea level changes and global climatic variations (Hwang *et al.*, 2004). Over oceans, radar altimeters are also used to determine significant wave height, wind speed and mesoscale topography. The latter application has produced otherwise unattainable data describing the marine geoid, and the related sea floor topography (Vignudelli et al., 2011). Other applications include mapping land surface topography, identifying types of ice masses, monitoring sea/ice boundaries and modelling ice sheet elevation (see Figure 16.4 and Helm *et al.*, 2014).

Figure 16.4 Cryosat radar altimeter

a. Height of ice above sea level is measured by the radar altimeter carried on Cryosat-2.



b. Antarctic ice sheet: preliminary map from Cryosat-2 (ESA, UCL).



Source: © ESA, UCL. Retrieved from
a. *http://wattsupwiththat.com/2010/04/13/cryosat-passes-first-operational-tests/*
b. *https://eoportal.org/web/eoportal/satellite-missions/c-missions/cryosat-2*

61. ILRS: *http://ilrs.gsfc.nasa.gov*
62. ITRF: *http://itrf.ensg.ign.fr*

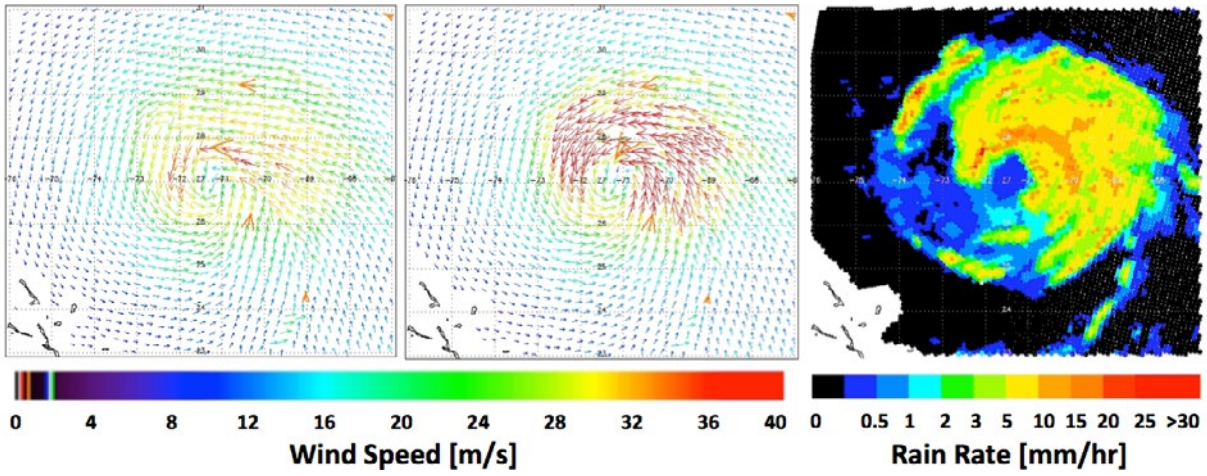
Figure 16.5 Wind estimates derived from SeaWinds observations

SeaWinds scatterometer observations of Hurricane Isabel acquired on 16 September 2003 were used to derive estimates of near-surface horizontal wind speed and direction over the ocean. Where the ocean surface is obscured by significant rain, passive microwave radiometry, when available, can be used to correct the scatterometer wind estimates.

a. Wind estimates using SeaWinds standard algorithm

b. Corrected estimates incorporating radiometer-based estimation of precipitation attenuation

c. Precipitation measured by the AMSR radiometer, illustrating that the correction is greatest in the most active parts of the storm



Source: Svetla Hristove-Veleva, Courtesy NASA/JPL-Caltech. NASA.

16.1.2.3 Microwave scatterometer

This non-imaging device measures the microwave scattering or reflective properties of surfaces and is specifically designed to measure backscattering. This requires that the sensor detect more detailed spectral information than acquired by imaging radar but with reduced spatial resolution and areal coverage. The surface is scanned in two or more directions, usually by multiple sensors using either a series of radar pulses or a continuous signal. Spaceborne microwave scatterometers have been carried on several satellite missions, using varying viewing geometries.

The primary application of microwave scatterometers is to measure wind vectors (that is, speed and direction) over the ocean surface (Barale *et al.*, 2010). This is based on the principle of ocean 'roughness' being caused by wind and resulting in a characteristic surface pattern that may be identified by its scattering properties. A mathematical model uses the reflectivity data with other sensor characteristics to determine wind speed and direction over the surface. Although radar scatterometers are non-imaging, their data may be used to construct global wind maps when collected over a sufficiently large area (see Figure 16.5). These data are also used to map soil moisture and texture, monitor vegetation and measure the extent and condition of ice and snow.

16.2 Sounding Systems

Sounding systems measure specific properties of air or water at predefined heights or depths. Such systems are primarily used to determine the vertical distribution of atmospheric parameters such as temperature, pressure, water volume, chemical composition, and wind speed and direction (see Excursus 16.2). They are also used to map water profiles of colour, depth and temperature. Sounding systems can also detect ionospheric disturbances emanating from seismic waves (Lognonné *et al.*, 2006).

16.2.1 Passive

Passive sounders measure the thermal infrared or microwave extinction, emission or scattering for atmospheric properties at particular altitudes. Gases that are uniformly mixed through the atmosphere, such as oxygen or carbon dioxide, are used as 'tracers' to estimate temperature profiles, whereas water vapour concentration is used to estimate humidity profiles. The sounding instruments are then designed to measure the EM emission of these gases. Altitude is inferred from the spectral dependence of absorption, such that the less absorbed the wavelength, the deeper the sensor 'sees' into the atmosphere.

Atmospheric sounders routinely deliver profiles of temperature and humidity for weather prediction and climate modelling. A radiosonde is the most common *in situ* passive sounding device, carried by a weather balloon, rockets, ships or aircraft. The three broad groups of passive sounders carried by aircraft or satellites are:

- multispectral radiometers—examples of selective filter radiometers are ISAMS (Improved Stratospheric and Mesospheric Sounder) and MOPITT (Measurements of Pollution in the Troposphere); AMSU (Advanced Microwave Sounding Unit) is a 15-channel microwave radiometer used to detect atmospheric water vapour and precipitation;
- hyperspectral spectrometers—for example, AIRS (Atmospheric Infrared Sounder) is a 2,378 channel grating spectrometer measuring radiance in the range 3.7–15.4 μm with nadir spatial resolution of approximately 13.5 km designed to determine atmospheric temperature and humidity; and
- laser sensors—laser heterodyne spectroscopy is used for atmospheric and astronomical observations to derive ultra-high spectral resolution measurements. This technology has enabled accurate altitude profiles for atmospheric constituents such as ozone and nitrous oxide.

16.2.2 Active

Active sounding systems use lidar or radar technologies. Pulses or continuous signals are transmitted into the atmosphere to derive information from:

- backscattering—indicating density, shape and size of scattering particles;
- absorption—indicating concentration and distribution of absorbing materials;
- polarisation—indicating shape of scattering particles, which can be used to differentiate between water droplets and snow; and
- phase change—indicating mass of particles.

16.2.2.1 Lidar

The operation of lidar systems is introduced in Section 15.1. Lidar sounding instruments measure aerosol backscatter, concentration, and temperature profiles as well as properties of winds and clouds, using:

- backscatter lidar—measures intensity and polarisation to determine properties of atmospheric layers, particularly aerosols and thin cloud, such as cirrus;
- differential absorption lidar (DIAL)—measures extinction of light at two wavelengths to derive atmospheric constituents, their densities, water vapour content and temperature profiles;
- Doppler lidar—measures phase shift from backscattering of atmospheric particles to determine wind velocity; or
- Fluorescence Lidar and Raman Lidar—both measure intensity using a pulse wavelength which differs from the measured wavelength.

The Australian Hydrographic Office uses a Laser Airborne Depth Sounder (LADS[63]) to gather hydrographic data. This system incorporates a split laser beam, comprising a green beam (which can penetrate water depths down to 70 m depending on water conditions and type of substrate) and an infrared beam (which is reflected from the water surface). The difference between the two readings is used to determine water depth. Airborne lidar measurements have also been used to locate fishing opportunities.

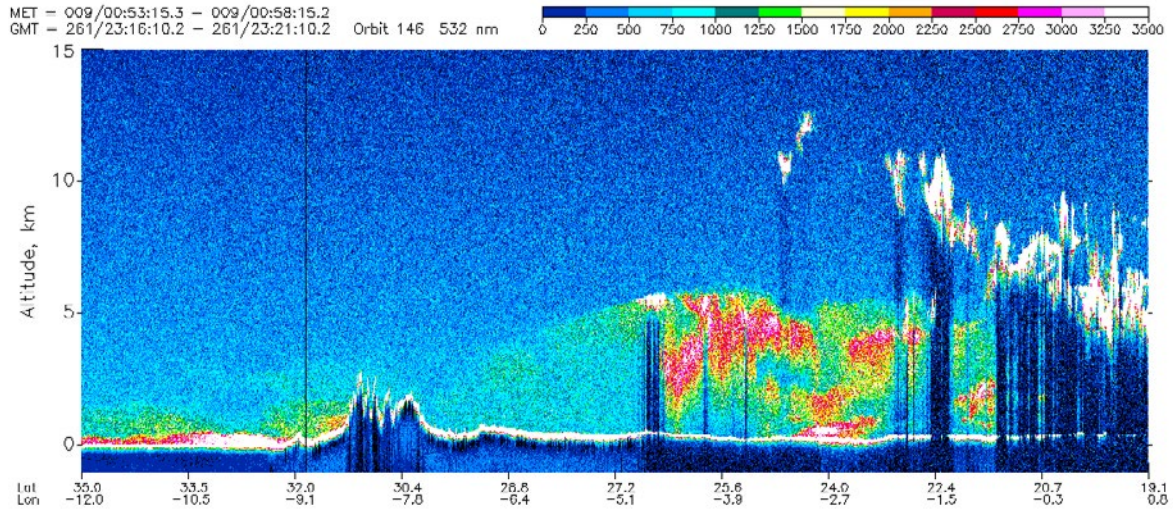
The LITE (Lidar In-Space Technology Experiment)[64] was briefly flown on the 1994 Space Shuttle for altimetry measurements. The CALIOP (Cloud-Aerosol Lidar with Orthogonal Polarisation) sensor, a dual wavelength, polarisation lidar, has been carried on the CALIPSO (Cloud-Aerosol Lidar and Infrared Pathfinder Satellite Observations) satellite since 2006, providing high-resolution profiles of clouds and aerosols. Data from both these satellites have been particularly valuable for quantifying global dust circulation and Earth's radiation budget (see Figures 16.6 and 16.7).

One look is worth a thousand words.

63. Laser Airborne Depth Sounder (LADS): *http://hydro.gov.au/aboutus/lads.htm*
64. Lidar In-space Technology Experiment (LITE): *http://lidar.jpl.nasa.gov/lite.htm*

Figure 16.6 Profile of LITE observations over Sahara Desert

LITE thumbnail image acquired over a period of 5 minutes on 18 September 1994 showing intensity of the return pulse up to 15 km altitude. The terrain profile is visible along the lower edge, with the Atlas Mountain range showing the highest elevation in this sequence. The thickness of aerosol air masses is visible, with cleaner (blue) air to the northwest (left of mountains) and an optically thick aerosol plume (about 5 km thick and coloured yellow to red with increasing density) to the southeast (right of mountains). This plume occurs over the Sahara Desert due to dust circulation. The rightmost segment of the image shows cloud coloured as white.



Source: NASA.

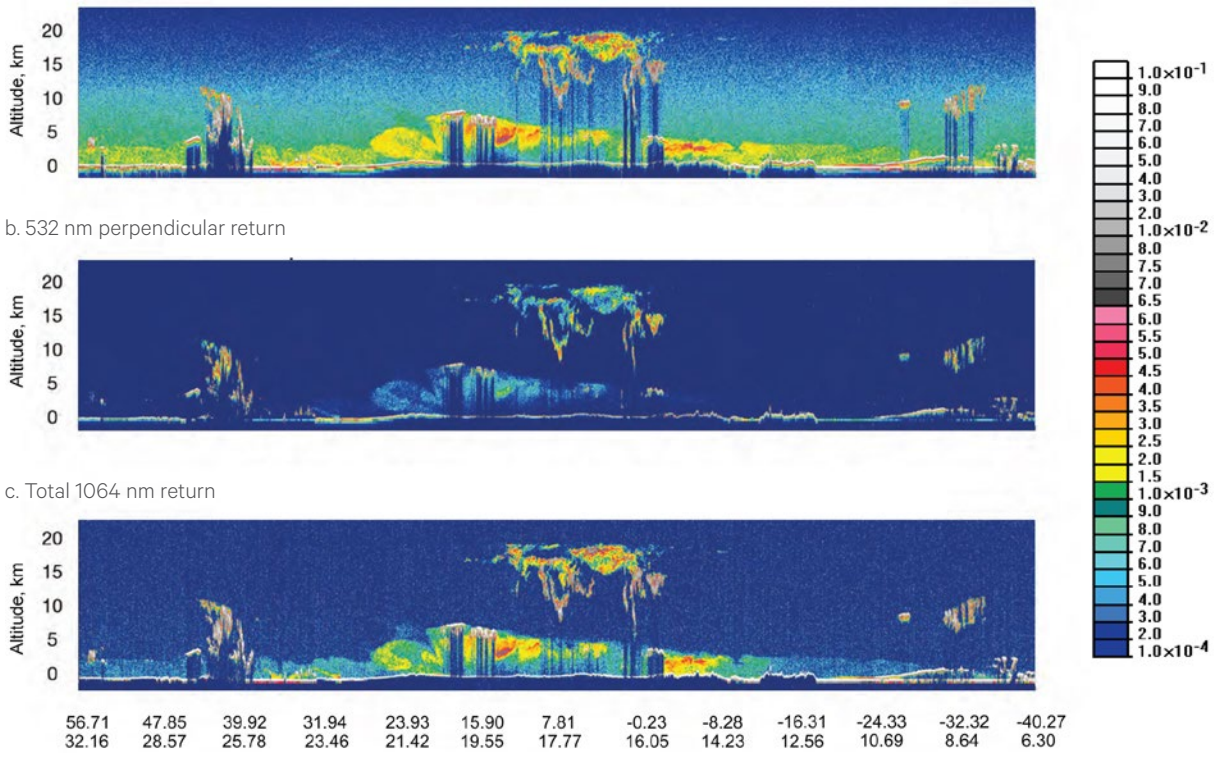
Figure 16.7 Profiles of CALIOP observations over Sahara Desert

CALIOP profiles acquired on 9 June 2006. Grey tones indicate strong returns from clouds and terrain surface. Yellow and red tones represent weak cloud and strong aerosol scattering. Green and blue tones represent molecular scattering, plus scattering from weak aerosol and cloud layers.

a. Total 532 nm return

b. 532 nm perpendicular return

c. Total 1064 nm return



Source: Winker *et al.* (2007) Figure 1. Provided by NASA Langley Research Centre.

16.2.2.2 Radar

Radar imaging sensors are introduced in Section 15.2. Radar techniques are used for sounding to determine water content:

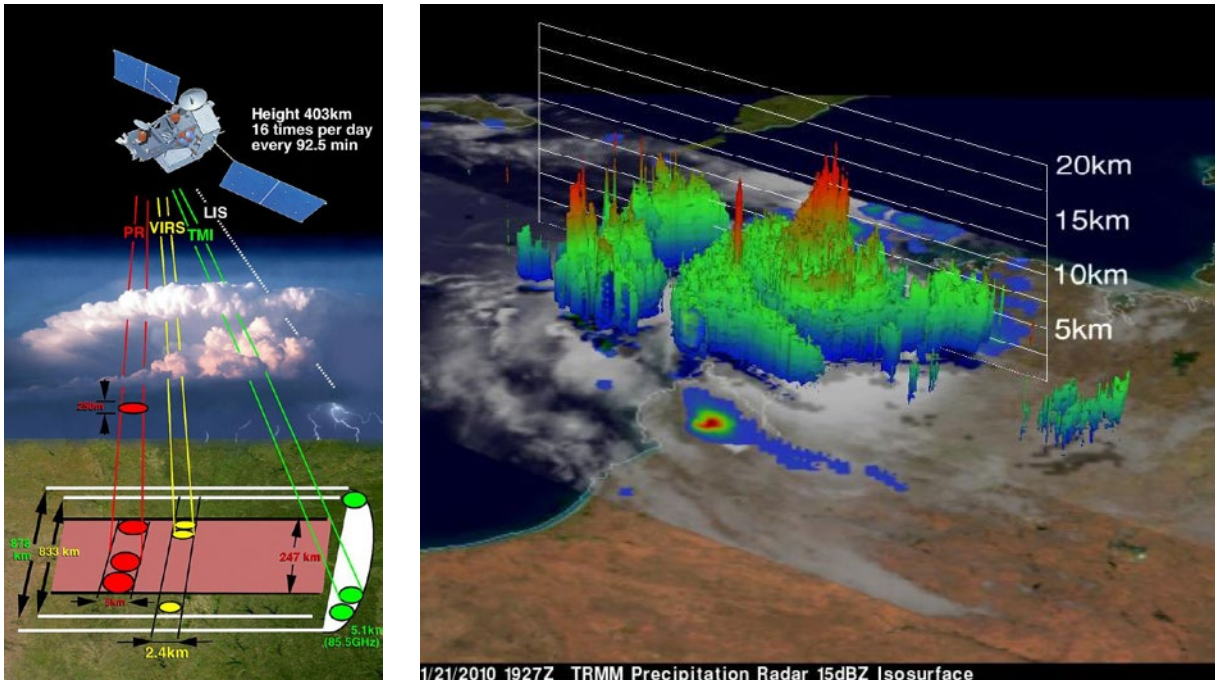
- weather radar detects precipitation in conjunction with ground-based networks; and
- Doppler radar measures wind speed and direction based on the Doppler shift between the frequencies of transmitted and returned signals (see Section 2.5.4). Doppler radars have only been carried by aircraft or used in ground-based studies.

TRMM was the first satellite-based weather radar, launched in 1997 and operated for over 17 years. Amongst other instruments, this satellite carried the first precipitation radar, which collected vertical profiles of rain and snow, extending from the Earth's surface to a height of 20 km. These data enabled modelling of three-dimensional storm structure, and delineation of the type, intensity and duration of precipitation (see Figure 16.8). Cloudsat, launched in 2006, carries a Cloud Profiling Radar (CPR). This radar sensor was designed to measure the backscatter from clouds, from which the distance from the sensor is derived. Combined with data from other sensors, this dataset allows detailed cloud and storm profiles to be created (see Figure 16.9).

Figure 16.8 TRMM Precipitation Radar

a. TRMM satellite carried a Precipitation Radar (PR), a Microwave Imager (TMI), a Visible Infrared Scanner (VIRS), a Lightning Imaging Sensor (LIS) and the Clouds and Earth's Radiant Energy System (CERES—not shown).

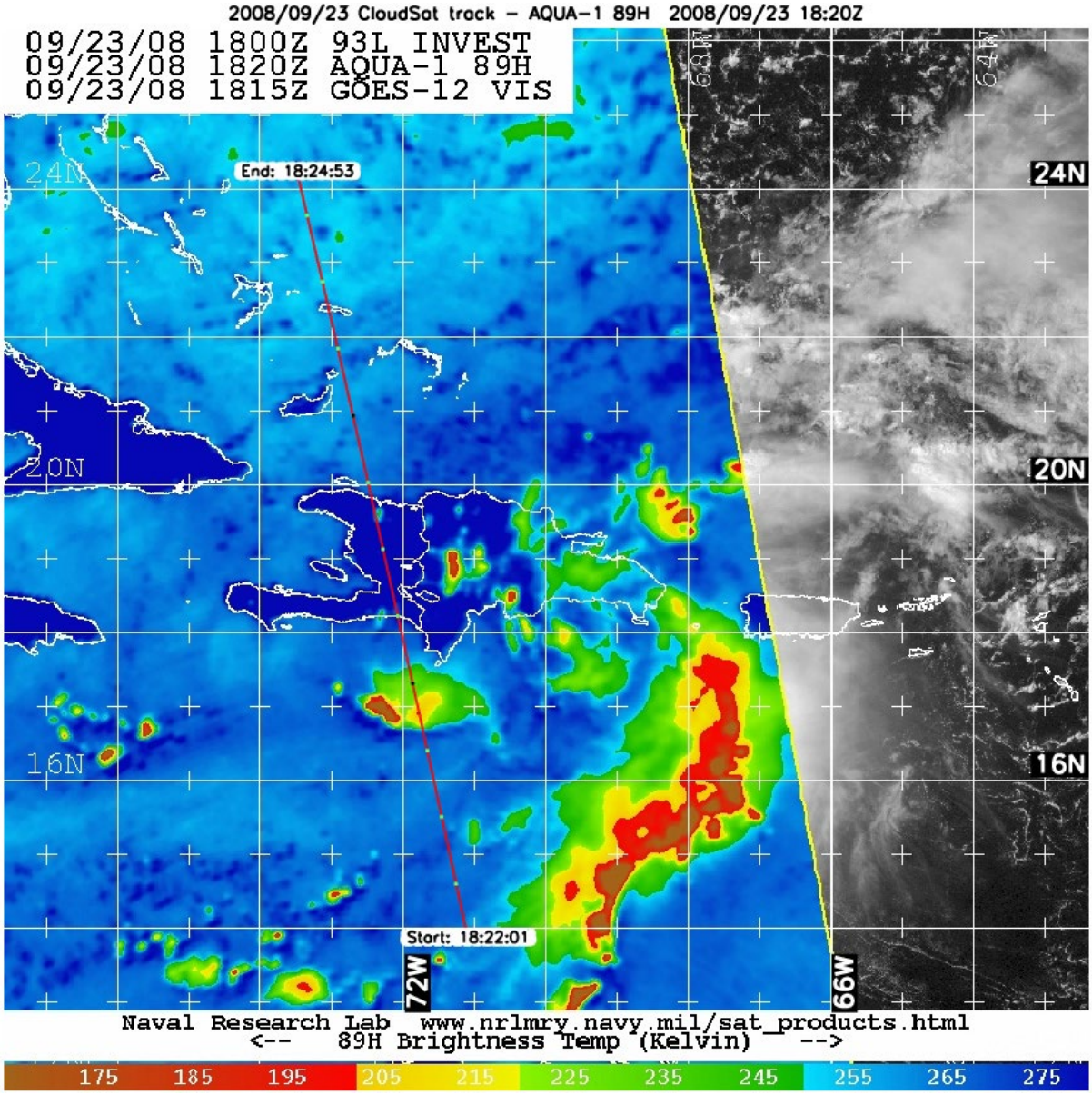
b. A three-dimensional image showing the intensity of tropical cyclone Magda approaching northwest Australia on 21 January 2010 was generated from profiles acquired by the TRMM PR and TMI sensors.



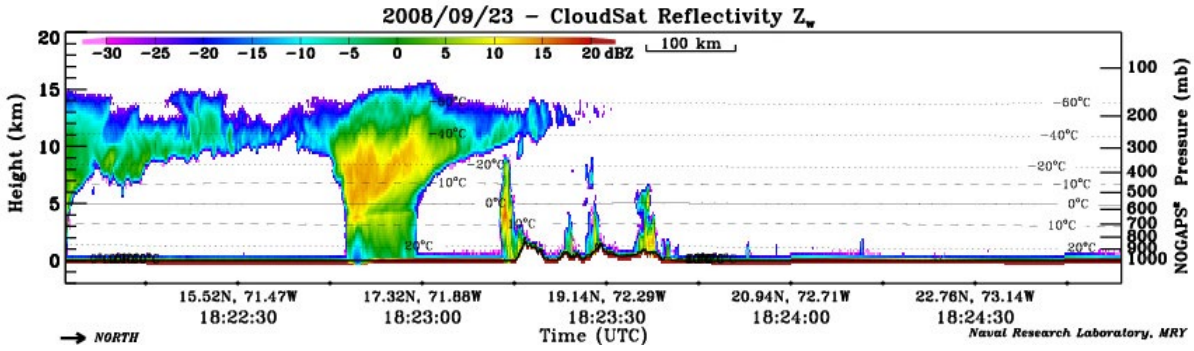
Source: NASA. Retrieved from *https://pmm.nasa.gov/image-gallery/trmm-precipitation-radar-image-magda*

Figure 16.9 Cloudsat Cloud Profiling Radar

a. Cloudsat orbit over Caribbean on 23 September 2008 shown on background of thermal imagery acquired by the Aqua satellite.



b. Cloud profile derived from Cloudsat Cloud Profiling Radar data showing height of clouds along orbital track.



Source: US Naval Research and NASA Cloudsat Project. CloudSat data courtesy CSU/CIRA.

Excursus 16.2—Meteorological Sensors and Applications

Source: John Le Marshall, Bureau of Meteorology
Further Information: *j.lemarshall@bom.gov.au, johnlemarshall@hotmail.com*

Early Applications

From the early 1960s, when imagery was first received from weather satellites, analysis and forecasting have depended heavily on these data sets. For the first time, these satellites provided information over data-sparse regions of the globe (see Excursus 12.1). Early work on satellite image interpretation was done by Vincent Oliver and others in a number of application areas, including rainfall and wind estimation (Anderson *et al.*, 1973).

The use of early images via subjective cloud picture interpretation provided the ability to position and analyse synoptic systems away from the conventional data network. Later quantitative estimates of Mean Sea Level Pressure (MSLP) and 1000–500 hPa geopotential thickness (see Excursus 16.2) were derived systematically from this imagery using methods such as those in Zillman (1968) and Guymer (1968, 1978).

Sounding the Atmosphere

By the late 1960s, sounding of the atmosphere from space for temperature and moisture using thermal infrared observations from the Satellite IR Spectrometers SIRS-A and -B had been reported (Wark and Hilleary, 1969), followed by the first example of using the soundings to improve numerical weather prediction (Smith *et al.*, 1970).

Soundings from the subsequent operational instrument, the Vertical Temperature Profile Radiometer (VTPR; McMillin *et al.*,1973) were received globally via the Global Telecommunications System (GTS) in the 1970s and used directly in operational analysis and prognosis systems. In the mid-1970s, after the utility of satellite vertical temperature profiles was established, clear column radiance (CLRAD) data (McMillin *et al.*, 1973) from the VTPR instrument (carried on the NOAA polar orbiting satellites) were distributed and used operationally at a number of places (including the National Meteorological Analysis Centre—NMAC, Australia). These sounders were followed by the TIROS Operational Vertical Sounder (TOVS) in 1979 and later the Advanced TOVS in 1998.

The New Millennium

In February 2002, the Atmospheric InfraRed Sounder (AIRS), the first new generation ultraspectral instrument able to provide operational data was launched. This instrument is able to provide radiance observations at 2378 infrared frequencies and these spectra are being used to produce temperature and moisture profiles (Chahine *et al.*, 2006). The temperature profiles have accuracies greater than 1K with moisture accuracies of the order of 15%. Temperature accuracies for the second-generation operational sounders (e.g. ATOVS) are generally 1.5K–2.0K and from 25% to 30% for moisture.

Several new hyperspectral/ultraspectral instruments are now flying, including AIRS, the Infrared Atmospheric Sounding Interferometer (IASI) and the Cross-track Infrared Scanner (CrIS), with a major impact on NWP. The increasing spectral resolution afforded by the AIRS instrument is seen in Figure 16.10 where the bandwidth of the TOVS HIRS instrument on the earlier NOAA satellites is displayed with spectra from AIRS. The improved spectral resolution shown has led to a significant increase in vertical and thermal resolution and increased accuracy in determination of concentrations of absorbers such as moisture and ozone in comparison to second generation sounders (see Table 16.1).

The first evidence of significant positive impact from higher spatial and temporal resolution ultra spectral AIRS data on global forecasts in both northern and southern hemispheres was recorded in Le Marshall et al. (2005). The improvement in forecast skill at six days for the US Global Forecast System (GFS) was equivalent to gaining an extension of forecast capability of several hours. This improvement is quite significant when compared to the rate of general forecast improvement over a decade. A several hour increase in forecast range at five or six days normally takes several years to achieve at operational weather centres.

Table 16.1 Characteristics of AIRS and HIRS sounding instruments

Characteristic	HIRS	AIRS
Spectral range	3.7–15 μm	3.7–15 μm
Spatial Resolution (sub-sat)	17.4 km	13.5 km
Number of Channels	20	2378
Spectral Resolution (Dl/l)	~1/70	~1/1000
Vertical Resolution	~3 km	~1 km
Temperature Accuracy	~1.5-2 K	<1 K in 1 km layers
Moisture Accuracy	~30%	15% in 2 km layers

Figure 16.10 Spectral resolution of HIRS/2 compared with simulated AIRS spectra

HIRS/2 = Half power Spectral Response Function

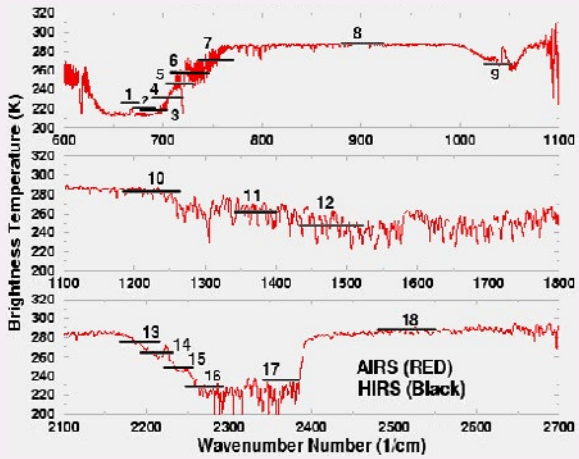


Image-based Applications

Many improvements in Earth System science, analysis and forecasting were due to the availability of imagery in the meteorological database. In particular the work of Dvorak (1972, 1975) estimating tropical cyclone intensity using satellite imagery remains important to this day (Velden *et al.*, 2006). Forecasts are often dependent on many of the image-based applications which have demonstrably benefitted from improved spatial, spectral and temporal resolution EOS, including:

- Atmospheric Motion Vectors (AMV);
- cloud top temperature/cloud height;
- cloud type and amount determination
- detection of low cloud/fog
- timing of fog clearing
- frost detection (land surface temperature)
- detection of volcanic ash
- detection of dust clouds
- detection of inversions
- rainfall estimation
- snow cover
- forest fire detection
- sea surface temperature (SST)
- NDVI estimation
- flood monitoring
- sea ice, cloud discrimination and mapping
- solar radiation
- surface albedo
- land surface temperature
- soil moisture

These improvements will continue into the future, now that the next generation Japanese geostationary satellite, Himawari-8, has replaced MTSAT-2, again providing improved spatial, temporal and spectral resolution imagery.

Recent EOS Impact Studies

In addition to the studies cited previously, data from a considerable number of other satellite instruments have been recently assimilated. These include data from the COSMIC Constellation, CHAMP, WindSat and AMSR(E).

Radio Occultation (RO) data from the COSMIC Constellation (a new remote sensing technology, Anthes *et al.* (2008) have shown significant positive impact on forecasts through the whole troposphere, particularly over the Southern Hemisphere (Healy and Thépaut, 2006; Cucurull and Derber, 2008; Le Marshall *et al.*, 2010; Le Marshall *et al.*, 2012). An important benefit of the COSMIC/GNSS system of satellites is that they provide near bias-free observations. In NWP, this helps to calibrate instruments such as the advanced sounders during tuning, resulting in analyses close to climate quality. Another important contribution from GPS RO is climate monitoring. Recently, RO data has been used to examine annual average of tropospheric temperature over the Southern Hemisphere. This use of GPS RO data has been shown to provide significant new information particularly over the data-sparse regions of the southern oceans (Le Marshall *et al.*, 2012).

WindSat data have also demonstrated a positive impact on forecasts (Le Marshall *et al.*, 2007). While WindSat covered much the same areas as QuikSCAT, it improved operational forecasts and provided an in-orbit backup covering the loss of QuikSCAT. In addition to these assimilation experiments, ASCAT, AMSR(E), SSMIS and AURA/OMI observations have also been successfully assimilated into the National Centre for Environmental Prediction's Global Forecast System (NCEP GFS). AMSR(E) and SSMIS have also been shown to improve forecasts in the Southern Hemisphere.

Considerable work has also been undertaken to enhance the use of AMV data (Holmlund, 1998; Holmlund *et al.*, 2001; Le Marshall *et al.*, 2004). The importance of these high spatial and temporal resolution vectors in NWP is seen in recent results (Le Marshall *et al.*, 2013b) where the advantage of high resolution, near-continuous data have been exploited by using 4D-Var. This approach is also being applied with the new Himawari-8 satellite where AMV are being generated operationally every 10 minutes over Australasia and Asia (see Excursus 12.1).

16.3 Further Information

Sensors:

The CEOS Database (CEOS, 2016)

Microwave Remote Sensing:

Ulaby and Long (2014)

Woodhouse (2004)

Atmospheric Research:

University Corporation for Atmospheric Research (UCAR): *http://www2.ucar.edu*

Laser Altimetry:

AAM Surveys—Local airborne laser data specialists: *http://www.aamgroup.com/services-and-technology/aerial-survey*

National Elevation Data Framework Portal: *http://nedf.ga.gov.au*

ICESAT—Ice, cloud and land elevation satellite: *http://icesat.gsfc.nasa.gov*
(also used to map vegetation height and structure across Australia: *http://www.auscover.org.au/xwiki/bin/view/Product+pages/ICESat+Vegetation+Structure*)

Radar Altimetry:

Radar Altimetry Tutorial (Rosmorduc *et al.*, 2011)

Sea Level Rise (CMAR, CSIRO): *http://www.cmar.csiro.au/sealevel/sl_meas_sat_alt.html*

Satellite Altimetry Lectures (Le Traon, 2007)

Radar Basics: *http://www.radartutorial.eu/02.basics/Altimeter.en.html*

Fu and Cazenave (2000)

DORIS system:

Guijarro *et al.* (2000)

Scatterometry:

NASA Winds: Measuring Ocean Winds from Space: *http://winds.jpl.nasa.gov/aboutscatterometry/history*

Centre for Ocean-Atmospheric Prediction Studies: *https://coaps.fsu.edu/scatterometry/about/overview.php*

Laing and Evans (2011)

Sounding:

Laing and Evans (2011)

Australian Atmospheric Sounding Information: *http://slash.dotat.org/cgi-bin/atmos*

Elachi and van Zyl (2006)

16.4 References

Anderson, R. K., Ferguson, E. W., Ashman, J. P., Farr, G. R., Isayeva, G. N., Oliver, V. J., Parmenter, F. C., Popova, T. P., Skidmore, R. W., Smith, A. H., and Veltishchev, N. F. (1973). The use of satellite pictures in weather analysis and forecasting (WMO 333). World Meteorological Organisation.

Anthes, R. A., Bernhardt, P. A., Chen, Y., Cucurull, L., Dymond, K. F., Ector, D., Healy, S. B., Ho, S.-P., Hunt, D. C., Kuo, Y.-H., Liu, H., Manning, K., McCormick, C., Meehan, T. K., Randel, W. J., Rocken, C., Schreiner, W. S., Sokolovskiy, S. V., Syndergaard, S., Thompson, D. C., Trenberth, K. E., Wee, T.-K., Yen, N. L., and Zeng, Z. (2008). The COSMIC/FORMOSAT-3 Mission: Early Results. Bulletin of the American Meteorological Society, 89, pp. 313-333.

Arendt, A. A., Echelmeyer, K. A., Harrison, W. D., Lingle, C. S., and Valentine, V. B. (2002). Rapid wastage of Alaska glaciers and their contribution to rising sea level. Science, 297(5580), pp. 382-386. doi:*http://dx.doi.org/10.1126/science.1072497*.

Barale, V., Gower, J. F. R., and Alberotanza, L. (2010). Oceanography from Space: Revisited (374 pages). doi:*http://dx.doi.org/10.1007/978-90-481-8681-5*.

Brenner, A. C., DiMarzio, J. R., and Zwally, H. J. (2007). Precision and accuracy of satellite radar and laser altimeter data over the continental ice sheets. IEEE Transactions on Geoscience and Remote Sensing, 45(2), pp. 321-331.

CEOS (2016). The CEOS Database. Retrieved from *http://database.eohandbook.com*.

Chahine, M. T., Pagano, T. S., Aumann, H. H., Atlas, R., Barnet, C., Blaisdell, J., Chen, L., Divakarla, M., Fetzer, E. J., Goldberg, M., Gautier, C., Granger, S., Hannon, S., Irion, F. W., Kakar, R., Kalnay, E., Lambrigtsen, B. H., Lee, S.-Y., Le Marshall, J. L., McMillan, W. W., McMillin, L., Olsen, E. T., Revercomb, H., Rosenkranz, P., Smith, W. L., Staelin, D., Strow, L. L., Susskind, J., Tobin, D., Wolf, W., and Zhou, L. (2006). AIRS: Improving Weather Forecasting and Providing New Data on Greenhouse Gases. Bulletin of the American Meteorological Society, 87(7), pp. 911-926. doi:*http://dx.doi.org/10.1175/BAMS-87-7-911*.

Cucurull, L., and Derber, J. C. (2008). Operational Implementation of COSMIC Observations into NCEP's Global Data Assimilation System. Weather and Forecasting, 23(4), pp. 702-711. doi:*http://dx.doi.org/10.1175/2008WAF2007070.1*.

Dvorak, V. F. (1972). A technique for the analysis and forecasting of tropical cyclone intensities from satellite pictures (NESS 36). NOAA Technical Memorandum. National Environmental Satellite Service, National Oceanographic and Atmospheric Administration, U.S. Department of Commerce.

Dvorak, V. F. (1975). Tropical Cyclone Intensity Analysis and Forecasting from Satellite Imagery. Monthly Weather Review, 103(5), pp. 420-430. doi:*http://dx.doi.org/10.1175/1520-0493(1975)103%3C0420:TCIAAF%3E2.0.CO;2*.

Elachi, C., and van Zyl, J. (2006). Introduction to the Physics and Techniques of Remote Sensing, Second Edn. Wiley Interscience, New Jersey.

Fu, L. L., and Cazenave, A. (2000). Satellite Altimetry and Earth Sciences: A Handbook of Techniques and applications. Academic Press, San Diego, London.

Guijarro, J., Auriol, A., Costes, M., Jayles, C., and Vincent, P. (2000). MWR and DORIS - Supporting Envisat's radar altimetry mission. ESA Bulletin-European Space Agency(104), pp. 41-46.

Guymer, L. B. (1968). Estimation of 1000 - 500 mb Thickness Patterns from Satellite Pictures of Convective Areas. Paper presented at the Inter-Regional Seminar on the Interpretation of Meteorological Satellite Data, Melbourne, Australia.

Guymer, L. B. (1978). Operational Application of Satellite Imagery to Synoptic Analysis in the Southern Hemisphere (Technical Report No. 29). Commonwealth Bureau of Meteorology, Melbourne, Australia.

Harrison, B. A., and Jupp, D. L. B. (1989). Introduction to Remotely Sensed Data. Part ONE of the microBRIAN Resource Manual (156 pages). CSIRO Australia, Melbourne.

Healy, S. B., and Thépaut, J. N. (2006). Assimilation experiments with CHAMP GPS radio occultation measurements. Quarterly Journal of the Royal Meteorological Society, 132(615), pp. 605-623. doi:*http://dx.doi.org/10.1256/qj.04.182*.

Helm, V., Humbert, A., and Miller, H. (2014). Elevation and elevation change of Greenland and Antarctica derived from CryoSat-2. Cryosphere, 8(4), pp. 1539-1559. doi:*http://dx.doi.org/10.5194/tc-8-1539-2014*.

Holmlund, K. (1998). The Utilization of Statistical Properties of Satellite-Derived Atmospheric Motion Vectors to Derive Quality Indicators. Weather and Forecasting, 13(4), pp. 1093-1104. doi:*http://dx.doi.org/10.1175/1520-0434(1998)013%3C1093:TUOSPO%3E2.0.CO;2*.

Holmlund, K., Velden, C. S., and Rohn, M. (2001). Enhanced Automated Quality Control Applied to High-Density Satellite-Derived Winds. Monthly Weather Review, 129(3), pp. 517-529. doi:*http://dx.doi.org/10.1175/1520-0493(2001)129%3C0517:EAQCAT%3E2.0.CO;2*.

Hwang, C., Shum, C., and Li., J. (2004). Satellite Altimetry for Geodesy, Geophysics and Oceanography. Proceedings of: International Workshop on Satellite Altimetry. Berlin Heidelberg: Springer-Verlag.

Jupp, D. L. B. (1997). Issues in Reflectance Measurement. CSIRO Earth Observation Centre, Canberra.

Laing, A., and Evans, J.-L. (2011). Introduction to Tropical Meteorology, Second Edn. The COMET Program. Retrieved from *http://www.goes-r.gov/users/comet/tropical/textbook_2nd_edition/index.htm*.

Le Marshall, J. F., Bi, L., Jung, J., Zapotocny, T., and Morgan, M. (2007). WindSat Polarimetric Microwave Observations Improve Southern Hemisphere Numerical Weather Prediction. Australian Meteorological Magazine, 56, pp. 35-40.

Le Marshall, J. F., Jung, J. D., J., Treadon, R., Lord, S., Goldberg, M., Wolf, W., Liu, H. C., Joiner, J., Woollen, J., and Todling, R. (2005). AIRS hyperspectral data improves southern hemisphere forecasts. Australian Meteorological Magazine, 54, pp. 57-60.

Le Marshall, J. F., Lee, J., Jung, J. A., and Roux, B. (2013a). The Considerable Impact of Earth Observations from Space on Numerical Weather Prediction. Australian Meteorological and Oceanographic Journal, 63(4), pp. 497-500.

Le Marshall, J. F., Rea, A., Leslie, L., Seecamp, R., and Dunn, M. (2004). Error characterization of atmospheric motion vectors. Australian Meteorological Magazine, 53, pp. 123-131.

Le Marshall, J. F., Seecamp, R., Xiao, Y., Gregory, P., Jung, J., Stienle, P., Skinner, T., Tingwell, C., and Le, T. (2013b). The Operational Generation of Continuous Winds in the Australian Region and Their Assimilation with 4DVAR. Weather and Forecasting, 28(2), pp. 504-514. doi:*http://dx.doi.org/10.1175/WAF-D-12-00018.1*.

Le Marshall, J. F., Xiao, Y., Norman, R., Zhang, K., Rea, A., Cucurull, L., Seecamp, R., Steinle, P., Puri, K., and Le, T. (2010). The Beneficial Impact of Radio Occultation Observations on Australian Region Forecasts. Australian Meteorological and Oceanographic Journal, 60, pp. 121-125.

Le Marshall, J. F., Xiao, Y., Norman, R., Zhang, K., Rea, A., Cucurull, L., Seecamp, R., Steinle, P., Puri, K., and Le, T. (2012). The Application of Radio Occultation for Climate Monitoring and Numerical Weather Prediction in Australian Region. Australian Meteorological and Oceanographic Journal, 62, pp. 323-334.

Le Traon, P.-Y. (2007). Satellite Altimetry. Lectures for ESA-MOST Dragon Programme. ESA. Retrieved from *http://earth.eo.esa.int/dragon/ocean_training/Lecture_Material/DAY5-19Oct2007/D5_L1-2_letraon_lecture1_2.pdf*.

Lognonné, P., Garcia, R., Crespon, F., Occhipinti, G., Kherani, A., and Artru-Lambin, J. (2006). Seismic waves in the ionosphere. Europhysicsnews, 37(4), pp. 11-14.

McMillin, L. M., Wark, D. Q., Siomkajlo, J. M., Abel, P. G., Werbowetzki, A., Lauritson, L. A., Pritchard, J. A., Crosby, D. S., Woolf, H. M., Luebbe, R. C., Weinreb, M. P., Fleming, H. E., Bittner, F. E., and Hayden, C. M. (1973). Satellite Infrared Soundings from NOAA Spacecraft (NESS 65). NOAA Technical Memorandum. National Environmental Satellite Service, National Oceanographic and Atmospheric Administration, U.S. Department of Commerce.

Nicodemus, F. E., Richmond, J. C., and Hsia, J. J. (1977). Geometrical considerations and nomenclature for reflectance (NBS Monograph 160). US Department of Commerce, National Bureau of Standards.

Rosmorduc, V., Benveniste, J., Bronner, E., Dinardo, S., Lauret, O., Maheu, C., Milagro, M., and Picot, N. (2011). Radar Altimetry Tutorial. Retrieved from *http://www.altimetry.info*.

Sardar, A. M. (1997). Chronology of the development of remote sensing technology. Asian-Pacific Remote Sensing and GIS Journal, 2, pp. 35-49.

Smith, W. L., Woolf, H. M., and Jacob, W. J. (1970). A Regression Method for Obtaining Real-time Temperature and Geopotential Height Profiles from Satellite Spectrometer Measurements and its Application to Nimbus-3 SIRS Observations. Monthly Weather Review, 98(8), pp. 582-603. doi:*http://dx.doi.org/10.1175/1520-0493(1970)098%3C0582:ARMFOR%3E2.3.CO;2*.

Ulaby, F. T., and Long, D. G. (2014). Microwave, Radar and Radiometric Remote Sensing. Retrieved from *http://mrs.eecs.umich.edu/*.

Valentine, V., Echelmeyer, K., Campbell, S., and Zirheld, S. (2004). Harding Icefield's Clues to Climate Change. Alaska Park Science Journal, 3(1), pp. 13-17.

Velden, C., Harper, B., Wells, F., II, J. L. B., Zehr, R., Olander, T., Mayfield, M., Guard, C. C., Lander, M., Edson, R., Avila, L., Burton, A., Turk, M., Kikuchi, A., Christian, A., Caroff, P., and McCrone, P. (2006). The Dvorak Tropical Cyclone Intensity Estimation Technique: A Satellite-Based Method that Has Endured for over 30 Years. Bulletin of the American Meteorological Society, 87(9), pp. 1195-1210. doi:*http://dx.doi.org/10.1175/BAMS-87-9-1195*.

Vignudelli, S., Kostianoy, A. G., Cipollini, P., and Benveniste, J. (2011). Coastal Altimetry. Springer-Verlag, Berlin Heidelberg.

Wark, D. Q., and Hilleary, D. T. (1969). Atmospheric Temperature: Successful Test of Remote Probing. Science, 165(3899), pp. 1256-1258. doi:*http://dx.doi.org/10.1126/science.165.3899.1256*.

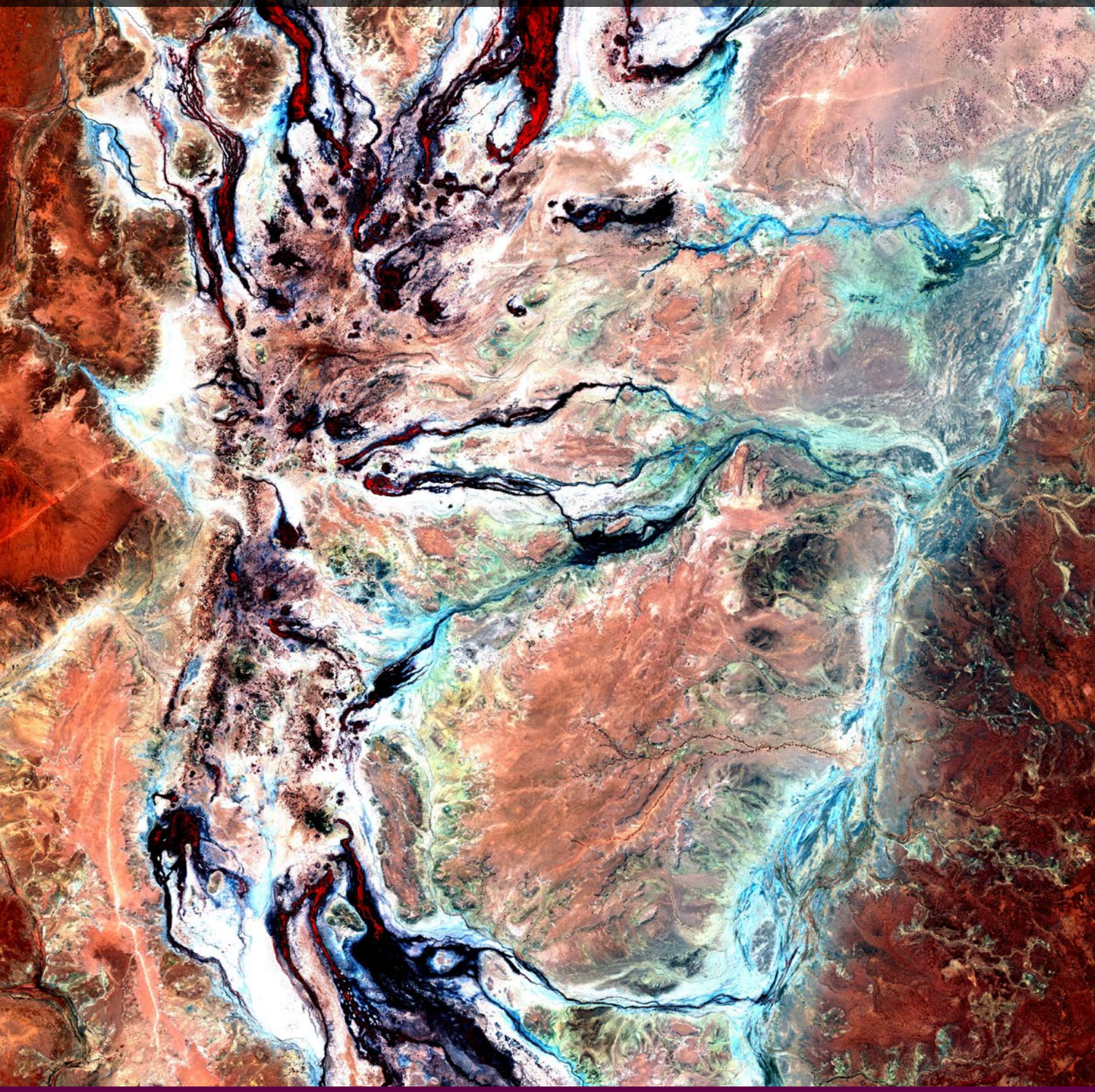
Winker, D. M., Hunt, W. H., and McGill, M. J. (2007). Initial performance assessment of CALIOP. Geophysical Research Letters, 34(19). doi:*http://dx.doi.org/10.1029/2007gl030135*.

Woodhouse, I. H. (2004). Introduction to Microwave Remote Sensing. CRC Press.

Zillman, J. W. (1968). Interpretation of satellite data over the Southern Ocean using the technique of Martin. Paper presented at the Inter-Regional Seminar on the Interpretation of Meteorological Satellite Data, Melbourne, Australia.

Earth Observation:
Data, Processing and Applications

Volume 1B: Data—Image Interpretation



This publication is available in PDF format at *eopublications.au*.
We welcome your comments regarding the readability and usefulness of this report.
To provide feedback, please email *feedback@eopublications.au*.

Publisher:
Australia and New Zealand CRC for Spatial Information

ISBN [ONLINE]:
978-0-9943019-3-2

Copyright:
All material in this publication is licensed under a Creative Commons Attribution 4.0 Australia Licence, save for content supplied by third parties, and logos. Creative Commons Attribution 4.0 Australia Licence is a standard form licence agreement that allows you to copy, distribute, transmit and adapt this publication provided you attribute the work. The full licence terms are available from *https://creativecommons.org/licenses/by/4.0/legalcode*. A summary of the licence terms is available from *https://creativecommons.org/licenses/by/4.0/*.



Disclaimer:
While every effort has been made to ensure its accuracy, the CRCSI does not offer any express or implied warranties or representations as to the accuracy or completeness of the information contained herein. The CRCSI and its employees and agents accept no liability in negligence for the information (or the use of such information) provided in this report.

Recommended Citation for Volume 1B:
CRCSI (2018) *Earth Observation: Data, Processing and Applications. Volume 1B: Data—Image Interpretation*. (Eds. Harrison, B.A., Jupp, D.L.B., Lewis, M.M., Forster, B.C., Coppa, I., Mueller, N., Hudson, D., Phinn, S., Smith, C., Anstee, J., Grant, I., Dekker, A.G., Ong, C., and Lau, I.) CRCSI, Melbourne.

Latest Revision:
October 2025

Cover Image: This HyMap airborne hyperspectral image mosaic over the Dalhousie Springs Complex, in far-northern South Australia, is displayed using the 0.833 μm band as red, the 0.666 μm band as green and the 0.559 μm band as blue. This region features extensive wetlands in an arid environment, fed by Great Artesian Basin spring flows.

This imagery was acquired by HyVista Corporation for the Allocating Water and Maintaining Springs of the Western Great Artesian Basin project in 2009.

Source: Megan Lewis, University of Adelaide

Acknowledgements

Production of this series of texts would not have been possible without the financial support of CSIRO, CRCSI, GA, BNHCRC and Digital Concepts, contributions from members of the editorial panels, direction from members of the advisory panel (Peter Woodgate, Adam Lewis, Alex Held and Arnold Dekker) and input from reviewers and contributors.

Volumes 1 and 2 of this series are based on text originally published in Harrison and Jupp (1989, 1990, 1992 and 1993)[1]. Many illustrations and some text from these publications have been reproduced with permission from CSIRO. Selected tables and text have been reproduced (with amendments) from GA (2011), GA (2013a, 2013b)[2] and CSIRO (2012)[3].

Other contributors are gratefully acknowledged:

- Chapter 8 author: Bruce Forster (In this chapter, some text and figures from Forster (2006) have been reproduced with permission from the American Society for Photogrammetry and Remote Sensing, Bethesda, Maryland, www.asprs.org);
- Chapter 10 authors: Isabel Coppa, Peter Woodgate, John Le Marshall and Alex Held;
- reviewers: Clive Fraser (Section 1), Terry Cocks (Section 2), Ross Mitchell (Section 4), Zheng-Shu Zhou and Catherine Ticehurst (Section 8); Matt Adams (Section 9), and Alfredo Huete and Laurie Chisholm (various sections);
- illustrations: Norman Mueller kindly supplied most of the lovely images; Fred Hughes permitted reproduction of his impressive photograph of a dust storm approaching Kars Station; other contributors of graphical material include: Matthew Adams, Carolyn McMillan, Megan Lewis, David Jupp, Chris Roelfsema, Fuqin Li, Yvonne Uu, Andrew Robson, Janet Anstee, Kasper Johansen, Stefan Sandmeier, Neil Flood, Andreas Hüni, Gary Shaw, Arnold Dekker, Lisa Collett, Dan Tindall, Matthew Paget, Yi Qin, Edward King, Laurie Chisholm, Stuart Phinn, Cindy Ong, Ian Lau, Carsten Laukamp, Erin Hester, Vittorio Brando, Elisabeth Botha, Andrew Buchanan, Bruce Forster, Ghislain Picard, Daniel Jaksa, Phil Tickle;
- Paul Cockram and Matej Hrcek, who 'translated' the Harrison and Jupp (1989, 1990) files from Quark Express 2.0;
- Joost Kuckartz for meticulous formatting of references and equations, plus general editing;
- Daniel Rawson (Accessible Publication & Template Design) for layout and formatting; and
- Sara Sunners-Gormley and Carl Davies (CMDphotographics) for selected graphical illustrations.

We thank all those owners of copyrighted illustrative material for permission to reproduce their work: CSIRO, CRCSI, Geoscience Australia, Aerometrix Pty Ltd, NASA, DigitalGlobe, DxOMark, Scratchapixel, and MIT Lincoln Laboratory. Credits for individual illustrations are provided below the relevant graphic.

1. Harrison, B.A., and Jupp, D.L.B. (1989) *Introduction to Remotely Sensed Data: Part ONE of the microBRIAN Resource Manual.* CSIRO, Melbourne. 156pp.
   Harrison, B.A., and Jupp, D.L.B. (1990) *Introduction to Image Processing: Part TWO of the microBRIAN Resource Manual* CSIRO, Melbourne. 256pp.
   Harrison, B.A., and Jupp, D.L.B. (1992) *Image Rectification and Registration: Part FOUR of the microBRIAN Resource Manual.* MPA, Melbourne.
   Harrison, B.A., and Jupp, D.L.B. (1993) Image Classification and Analysis: Part THREE of the microBRIAN Resource Manual. MPA, Melbourne.
2. Geoscience Australia (2011) *Continuity of Earth Observation Data for Australia: Operational Requirements to 2015 for Lands, Coasts and Oceans.* Geoscience Australia, Canberra.
   Geoscience Australia (2013a) *GA Earth Observation Product Description Framework and Templates.* Unpublished report by Barbara Harrison, February 2013.
   Geoscience Australia (2013b) *Draft Report on the National Dynamic Land Cover Dataset (Version 2).* Unpublished report by Barbara Harrison, June 2013.
3. CSIRO (2012) *Continuity of Earth Observation Data for Australia: Research and Development Dependencies to 2020.* CSIRO, Canberra.

Table of Contents

Acknowledgements i

Earth Observation Image Characteristics 1

1 Sampling Dimensions **3**
- **1.1** Spectral 4
- **1.2** Spatial 7
- **1.3** Radiometric 11
- **1.4** Temporal 13
- **1.5** Further Information 21
- **1.6** References 21

2 Imaging Artefacts **23**
- **2.1** Fidelity Measures 23
  - **2.1.1** Point source metrics 23
  - **2.1.2** Spectral sensitivity 30
  - **2.1.3** Signal-to-noise ratio 30
- **2.2** Aliasing 30
- **2.3** Scaling Parameters 33
  - **2.3.1** Geography 33
  - **2.3.2** Geostatistics 33
  - **2.3.3** Optics 33
  - **2.3.4** Linear systems 34
  - **2.3.5** Earth Observation 34
- **2.4** Upscaling and Downscaling 35
- **2.5** Further Information 36
- **2.6** References 36

EMR Interactions 37

3 EMR Interactions with Target and Sensor **39**
- **3.1** Energy of EMR 40
- **3.2** Target Type 41
- **3.3** Surface Reflectance 43
- **3.4** Volume Scattering 45
- **3.5** Illumination and Sensor Positions 47
  - **3.5.1** Basic geometry 47
  - **3.5.2** Application to EO 48
- **3.6** Surface Orientation 50
- **3.7** Anisotropy 52
  - **3.7.1** The Fresnel effect 52
  - **3.7.2** Bidirectional reflectance distribution function 54

3.8 Further Information 59
3.9 References 60

4 EMR Interactions with Atmosphere 61
4.1 Atmospheric Composition 62
4.1.1 Gas molecules 65
4.1.2 Aerosols 65
4.1.3 Water 68
4.2 Scattering Mechanisms 68
4.2.1 Rayleigh scattering 69
4.2.2 Mie scattering 71
4.2.3 Non-selective scattering 71
4.3 Absorption and Emission 71
4.4 Further Information 71
4.5 References 72

5 Radiative Transfer Modelling 73
5.1 Atmospheric Models 74
5.2 Water Models 75
5.3 Vegetation Canopy Models 78
5.4 Further Information 78
5.5 References 78

Interpreting Earth Observation Imagery 79

6 Optical Imagery 81
6.1 Optical Energy Transfer 82
6.2 Vegetation 82
6.2.1 Spectral characteristics of leaves 82
6.2.2 Foliage and canopy properties 84
6.3 Rocks and Soils 87
6.3.1 Mineralogy 87
6.3.2 Water content 90
6.3.3 Particle size 91
6.3.4 Surface coating 91
6.4 Waterbodies 92
6.4.1 Water column colour and clarity 92
6.4.2 Water column depth or bathymetry 98
6.4.3 Substratum 99
6.4.4 Water surface 101
6.5 Snow and Ice 101
6.6 Mixtures 101
6.7 Further Information 103
6.8 References 103

7 Thermal Infrared Imagery **107**
7.1 Solar Heating Cycles 108
7.2 Blackbody Concepts 109
7.3 TIR Emission Characteristics 110
7.4 TIR Signatures 112
7.5 Emissivity 114
7.6 Surface Temperature 115
7.7 Thermal Inertia 116
7.8 Further Information 121
7.9 References 121

8 Microwave Imagery **123**
8.1 Passive Microwave 123
8.1.1 Brightness temperature 124
8.1.2 Emissivity, polarisation and angle of observation 125
8.2 Imaging Radar 126
8.2.1 Overview of radar remote sensing theory 127
8.2.2 Synthetic aperture radar 130
8.2.3 Radar geometric distortions 132
8.2.4 Radar equation 135
8.2.5 Radar polarisation and polarimetric SAR 136
8.2.6 Radar backscattering mechanisms 142
8.2.7 SAR interferometry 146
8.3 Further Information 149
8.4 References 149

Using Earth Observation Imagery 151

9 From EO Images to Earth Information **153**
9.1 Satellite Image Acquisition 153
9.1.1 Radio communication 154
9.1.2 Ground stations 157
9.1.3 Tracking and data relay satellites 159
9.2 Data Volume 160
9.3 EO Data Usage 160
9.3.1 Scientific and technical workflows 160
9.3.2 Legal requirements for data collection, processing, storage and use 162
9.4 Integrated Data 162
9.5 Further Information 168
9.6 References 169

10 Looking Ahead **171**
10.1 Brave New World 171
10.1.1 Mega trends 171
10.1.2 Internet services 172

10.2 The Internet of Things 172
10.2.1 Wearable technology and implants 174
10.2.2 Brain-machine interfaces 175
10.2.3 Thinking machines 175
10.3 Location, Location, Location 176
10.3.1 Accuracy 176
10.3.2 Location-based services 177
10.3.3 National Positioning Infrastructure 177
10.4 The Data Deluge 180
10.4.1 Open data 180
10.4.2 Crowdsourcing 181
10.4.3 Secure data usage 181
10.5 Integrated 'Smart' Systems 182
10.5.1 Globes and digital Earth 183
10.5.2 Smart cities 183
10.5.3 Security 185
10.5.4 Virtual worlds 185
10.6 Developments in EO Platforms 185
10.6.1 Remotely piloted aircraft systems 185
10.6.2 Satellite Platforms 186
10.6.3 Space junk 187
10.7 The Australian Outlook 188
10.7.1 Data requirement projections 189
10.7.2 Monitoring the Australian environment 190
10.7.3 Agricultural systems 192
10.7.4 Weather and climate 195
10.8 Conclusion 196
10.9 References 197

List of Figures

Figure 1.1 Idealised spectral signatures 4

Figure 1.2 Typical green vegetation spectrum 5

Figure 1.3 Spectral resolution, density and extent of different sensors 6

Figure 1.4 Optical versus geometric pixel sizes 7

Figure 1.5 AVHRR pixel geometry 8

Figure 1.6 Spatial resolution in digitising 9

Figure 1.7 Spatial resolution and extent 10

Figure 1.8 Radiometric resolution and image contrast 12

Figure 1.9 Seasonal solar illumination variations 14

Figure 1.10 Cyclone Marcia damage in Rockhampton 15

Figure 1.11 Time series of wetlands vegetation 16

Figure 1.12 High resolution satellite imagery 17

Figure 1.13 Crop monitoring 17

Figure 1.14 Soil sampling 18

Figure 1.15 Predicted sugar yield map 18

Figure 1.16 Wallis Lake, NSW 20

Figure 2.1 Geometric versus wave optics 24

Figure 2.2 Diffraction of point source 24

Figure 2.3 Point Spread Function 25

Figure 2.4 Airy function 25

Figure 2.5 Examples of Point Spread Functions 26

Figure 2.6 Diffraction pattern 26

Figure 2.7 Separating two point sources 27

Figure 2.8 Application of Rayleigh Criterion 27

Figure 2.9 Modulation Transfer Function 29

Figure 2.10 Signal sampling and aliasing 31

Figure 2.11 Example of aliasing in imagery 31

Figure 2.12 Image sampling resolution relative to imaged objects 32

Figure 2.13 Interactions between image sampling and different land covers 32

Figure 3.1 Radiometric measurements 39

Figure 3.2 Interaction of incident light with target materials 41

Figure 3.3 Remote sensing of target 42

Figure 3.4 Example spectra for *Populus canadensis* leaf 42
Figure 3.5 Effects of surface texture on reflection 43
Figure 3.6 Surface reflectance 44
Figure 3.7 Image variations due to different observer positions 45
Figure 3.8 Effect of illumination and viewing positions 46
Figure 3.9 Zenith and azimuth 47
Figure 3.10 Geometry of illumination and viewing positions 48
Figure 3.11 Landsat-8 images acquired in four different seasons 49
Figure 3.12 Variations in image radiance due to topography 50
Figure 3.13 Impact of topographic shading in EO imagery 51
Figure 3.14 Cosine reflectance model 51
Figure 3.15 Anisotropy 52
Figure 3.16 Fresnel effect 53
Figure 3.17 Three-dimensional BRDF plots 55
Figure 3.18 BRDF plots for grass at different wavelengths 56
Figure 3.19 BRDF plots for healthy and dying watercress 57
Figure 3.20 Surface reflectance correction 58
Figure 3.21 Hotspot effect in oblique aerial photography 59
Figure 3.22 Hotspot effect in the landscape 59
Figure 4.1 Atmospheric attenuation 61
Figure 4.2 Cloud in EO imagery 63
Figure 4.3 Smoke in EO imagery 64
Figure 4.4 MODIS Precipitable Water product 64
Figure 4.5 Dust storm 65
Figure 4.6 MODIS imagery of dust storms 66
Figure 4.7 Quarterly mean aerosol optical depth 2002 to 2008 67
Figure 4.8 Monthly mean aerosol optical depth at 550 nm 68
Figure 4.9 Atmospheric interactions with EMR 69
Figure 4.10 Atmospheric scattering mechanisms 69
Figure 4.11 Rayleigh scattering 69
Figure 4.12 Rayleigh scattering impact on direct sunlight 70
Figure 4.13 Atmospheric correction 70
Figure 5.1 Radiative transfer process 73
Figure 5.2 Solar spectral irradiance 74
Figure 5.3 Simple radiative transfer model 75

Figure 5.4 Remote sensing of aquatic targets 76
Figure 5.5 Impact of water factors on incident radiation 77
Figure 6.1 Composition of green and dry vegetation 83
Figure 6.2 Vegetation reflectance and atmospheric transmittance 83
Figure 6.3 Effect of disease on vegetation reflectance 84
Figure 6.4 Red edge changes with plant vigour 84
Figure 6.5 Reflectance spectra for different *Eucalyptus/Angophora* species 85
Figure 6.6 Variations in foliage and canopy characteristics 85
Figure 6.7 Absorption mechanisms of geologic materials 88
Figure 6.8 Typical mineral spectra 88
Figure 6.9 Silica Index Map 89
Figure 6.10 Soil spectra 90
Figure 6.11 Wet and dry kaolinite spectra 90
Figure 6.12 Image differences resulting from variation in soil moisture 91
Figure 6.13 Effect of particle size on mineral spectra 91
Figure 6.14 Characteristic reflectance features of water colour constitutents 92
Figure 6.15 Reflectance from different water colours 92
Figure 6.16 Global observations of water colour 93
Figure 6.17 Simulations of water body reflectance 94
Figure 6.18 MODIS chlorophyll a concentration products 95
Figure 6.19 Seasonal trends in chlorophyll a 96
Figure 6.20 Lake Burley Griffin in 2010 97
Figure 6.21 Lake Burley Griffin, Canberra, imaged from WorldView-2 97
Figure 6.22 Water depth in remotely sensed imagery 99
Figure 6.23 Impact of water depth on substrate spectra 100
Figure 6.24 Reflectance from snow and ice 101
Figure 6.25 Simplified model of EO sensor 102
Figure 6.26 Spectral mixing of vegetation and soil 103
Figure 7.1 Diurnal variations in temperature 108
Figure 7.2 Two Landsat-7 views of Gladstone, Queensland 111
Figure 7.3 Thermal image pair 112
Figure 7.4 Christiansen feature in TIR wavelength region for minerals 113
Figure 7.5 Transmission spectra for silicates, clays and carbonates 113
Figure 7.6 Impact of emissivity on TIR emittance 114
Figure 7.7 Water surface temperature modelled from EO TIR imagery 115

Figure 7.8 Diurnal variations in thermal inertia and albedo 116
Figure 7.9 Temperature profile 117
Figure 7.10 Soil moisture saturation estimates 118
Figure 7.11 Monitoring inundation patterns 119
Figure 7.12 Flood hazard modelling 120
Figure 8.1 SSM/1 ascending orbits 125
Figure 8.2 Brightness temperature over Antarctica 125
Figure 8.3 Basic configuration of an imaging radar system 128
Figure 8.4 Concept of range resolution and ground range resolution 129
Figure 8.5 Effect of Doppler shift on the return frequency 131
Figure 8.6 Effect of change in altitude and antenna length on SAR resolution 131
Figure 8.7 Chirp pulse 132
Figure 8.8 Changing ground range resolution 132
Figure 8.9 Ground range resolution and look angle 132
Figure 8.10 Topographic relief and range compression 133
Figure 8.11 Height displacement 133
Figure 8.12 Foreshortening and elongation of slopes 133
Figure 8.13 Image distortion and layover 134
Figure 8.14 Effect of radar layover and shadows due to hilly terrain 134
Figure 8.15 Concepts of radar equation 135
Figure 8.16 Scattering coefficient 136
Figure 8.17 Vector sum of the component fields to give a resultant EM field 136
Figure 8.18 Circular polarisation 137
Figure 8.19 Agricultural area imaged in C-band HH, VV and HV 138
Figure 8.20 Radar colour composite of tropical agriculture, Malaysia 139
Figure 8.21 Radar Colour Composite of sea ice, Antarctica 139
Figure 8.22 AIRSAR colour composite of tropical vegetation, Thailand 139
Figure 8.23 Multi-date radar composite 139
Figure 8.24 Various polarisations of transmitted and received signals 140
Figure 8.25 Polarisation responses of a conducting dihedral corner reflector 140
Figure 8.26 Polarisation signatures 141
Figure 8.27 Differences in surface scattering 142
Figure 8.28 Volume scattering concept 142
Figure 8.29 Penetration for different wavelengths in multi layered volumes 143
Figure 8.30 Scattering coefficient variations 144

Figure 8.31 Bragg scattering 145
Figure 8.32 Ocean surface roughness 145
Figure 8.33 Return paths of radar for an urban corner reflector 145
Figure 8.34 Corner reflector effects 146
Figure 8.35 Repeat-pass InSAR 146
Figure 8.36 Urban application of differential across-track InSAR 147
Figure 8.37 Radar image overlaid on DEM derived from radar interferometry 147
Figure 8.38 Ocean current detection with along-track InSAR 147
Figure 8.39 Geometry for SAR Interferometry 148
Figure 8.40 Concept of phase-unwrapping 148
Figure 9.1 EOS data acquisition process 153
Figure 9.2 ACMA Radio Spectrum 156
Figure 9.3 Suomi NPP satellite communication 158
Figure 9.4 Tracking and Data Relay Satellite (TDRS) 159
Figure 9.5 TDRSS Constellation 159
Figure 9.6 Trends in EO data delivery 161
Figure 9.7 Selecting appropriate imagery 163
Figure 9.8 Scales of EO 163
Figure 9.9 Spatial and spectral scales 164
Figure 9.10 Satellite view of crop 166
Figure 9.11 Tree crop impact of Cyclone Debbie 167
Figure 10.1 Top ten transformational shifts by 2020 171
Figure 10.2 Exponential pace of disruptive technologies 172
Figure 10.3 Global internet access 172
Figure 10.4 Hype cycle for applications using the Internet of Thing 173
Figure 10.5 Distance to earthquake epicentre indicated by wearable devices 174
Figure 10.6 Summary of GNSS users. 178
Figure 10.7 Datum shift and positional accuracy comparison 179
Figure 10.8 Projected growth of the digital universe from 2010 to 2020 180
Figure 10.9 Landsat downloads since open data policy 181
Figure 10.10 System of System solutions for IoT 182
Figure 10.11 Example of smart city 184
Figure 10.12 Global RPAS market 2013-2024 185
Figure 10.13 Number of spacecraft launched 2005-2014 186
Figure 10.14 Changes in imaging satellite image spatial resolution over time 187

Figure 10.15 Catalogued space debris over time 188

Figure 10.16 Modelling of coastal risk 191

Figure 10.17 Green Precision tool 191

Figure 10.18 Components of NRM Spatial Hub 193

Figure 10.19 NRM Hub Grazing Circles 194

Figure 10.20 NRM Hub ground cover over time 194

List of Tables

Table 1.1 Sampling dimensions in remote sensing 4

Table 1.2 Quantisation levels 11

Table 2.1 Aspects of spatial data 35

Table 3.1 Effects of EMR on matter 40

Table 3.2 Wave-matter interactions relevant to EO 40

Table 3.3 Defining illumination and sensor positions 47

Table 4.1 Scattering mechanisms by atmospheric components 69

Table 4.2 Absorption and emission mechanisms 71

Table 5.1 Relevant radiometric terms 73

Table 6.1 Spectral characteristics of minerals 88

Table 7.1 Thermal and reflective properties of Earth surface materials 109

Table 7.2 Thermal behaviour of common surface materials 110

Table 7.3 Radiant temperature, kinetic temperature and emissivity 114

Table 8.1 Radar bands used for EO 127

Table 8.2 Imaging radar terminology 128

Table 8.3 Comparison of scattering components as a percentage of σ_{HH} 142

Table 9.1 Radio frequency ranges 155

Table 9.2 Satellite ground station receivers 157

Table 9.3 Standards relevant to EO data 162

Table 9.4 Time scales for monitoring Earth processes 165

Table 10.1 Connected living 173

Table 10.2 Overview of GNSS/ RNSS systems 176

Table 10.3 Spatial accuracies with established methods 177

Table 10.4 Examples of smart systems 184

Table 10.5 How many satellites? 186

Table 10.6 Instrument type performance specifications 189

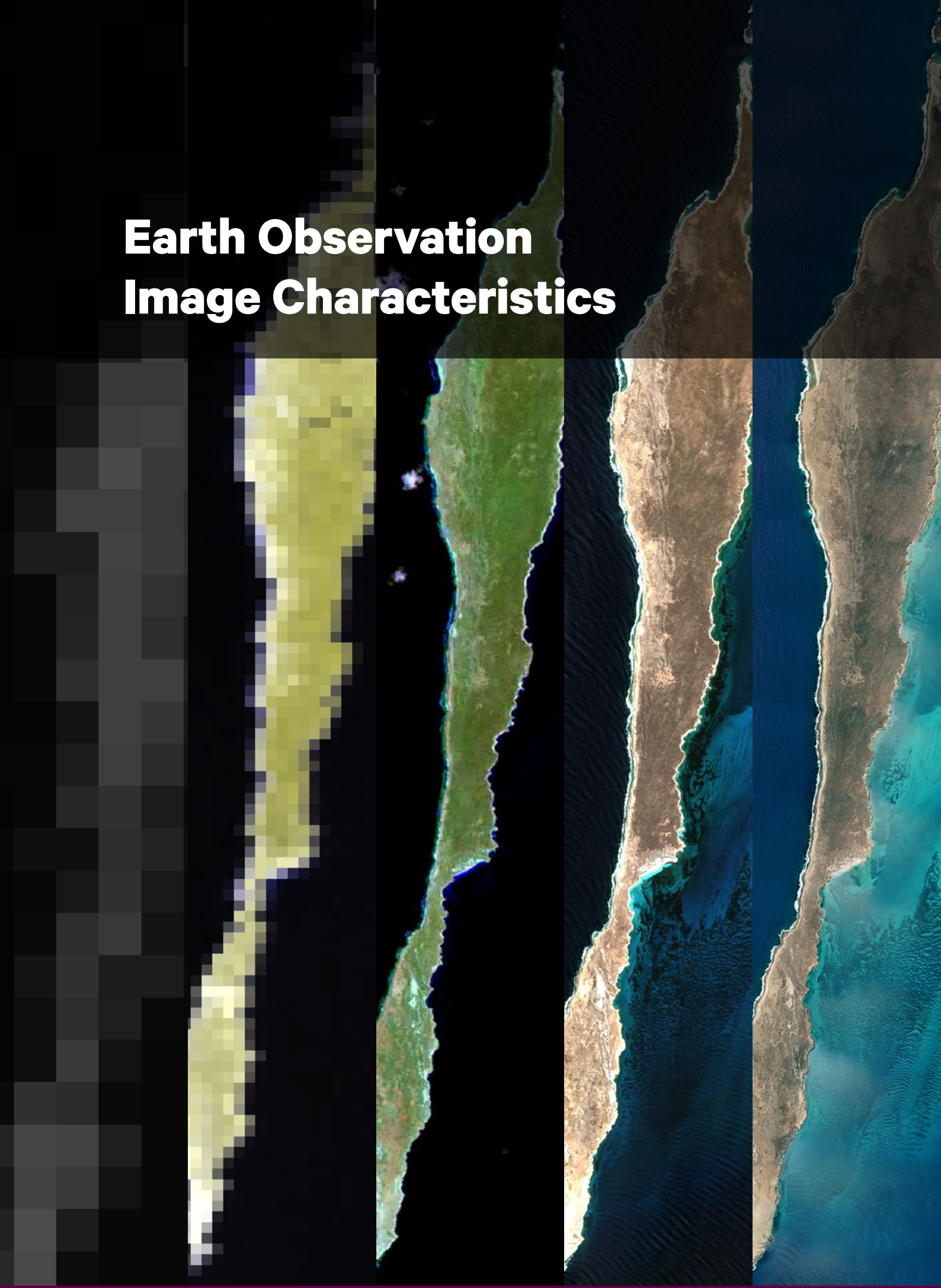
Table 10.7 Continuity risk for main instrument types 189

Table 10.8 Current and future radar satellites 190

List of Excursus

Excursus 1.1—How Much Sugar? 17
Excursus 1.2—Impact of Sea Level Changes on Estuaries 19
Excursus 4.1—Aerosol mapping from space 67
Excursus 6.1—ASTER Geoscience Maps of Australia 89
Excursus 6.2—Mapping chlorophyll concentration and ocean currents 95
Excursus 6.3—Monitoring Inland Water Quality in Australia 97
Excursus 7.1—FloodMap 118
Excursus 9.1—Crops from Space 166
Excursus 10.1—A Modern Reference Frame for Australia 178
Excursus 10.2—GEOSS 183
Excursus 10.3—NRM Spatial Hub 193

Earth Observation Image Characteristics



The first sub-volume in this series (Volume 1A—Basics and Acquisition) introduced both the fundamentals of energy sources and acquisition of Earth Observation (EO) data. This sub-volume considers a range of topics related to interpretation and analysis of EO imagery, particularly imagery based on detected electromagnetic radiation (EMR).

For convenience, names are assigned to the various regions of the electromagnetic spectrum, but there are no precise divisions between these regions—they are generally defined by the sensing method by which they are detected (see Volume 1A—Section 5). Commonly accepted ranges for EMR spectral regions most relevant to EO are:

- visible: 0.38–0.7 μm
- infrared (IR): 0.7–1,000 μm
- microwave: > 1 mm–1 m

Infrared wavelengths are often sub-divided into the regions:

- near infrared (NIR): 0.7–1.3 μm
- short wave infrared (SWIR): 1.3–3 μm
- middle infrared (MIR) or mid-wavelength (or medium wave) infrared (MWIR): 3–8 μm
- thermal infrared (TIR) or long wavelength infrared (LWIR): 8–15 μm
- far infrared (FIR): 15–1,000 μm

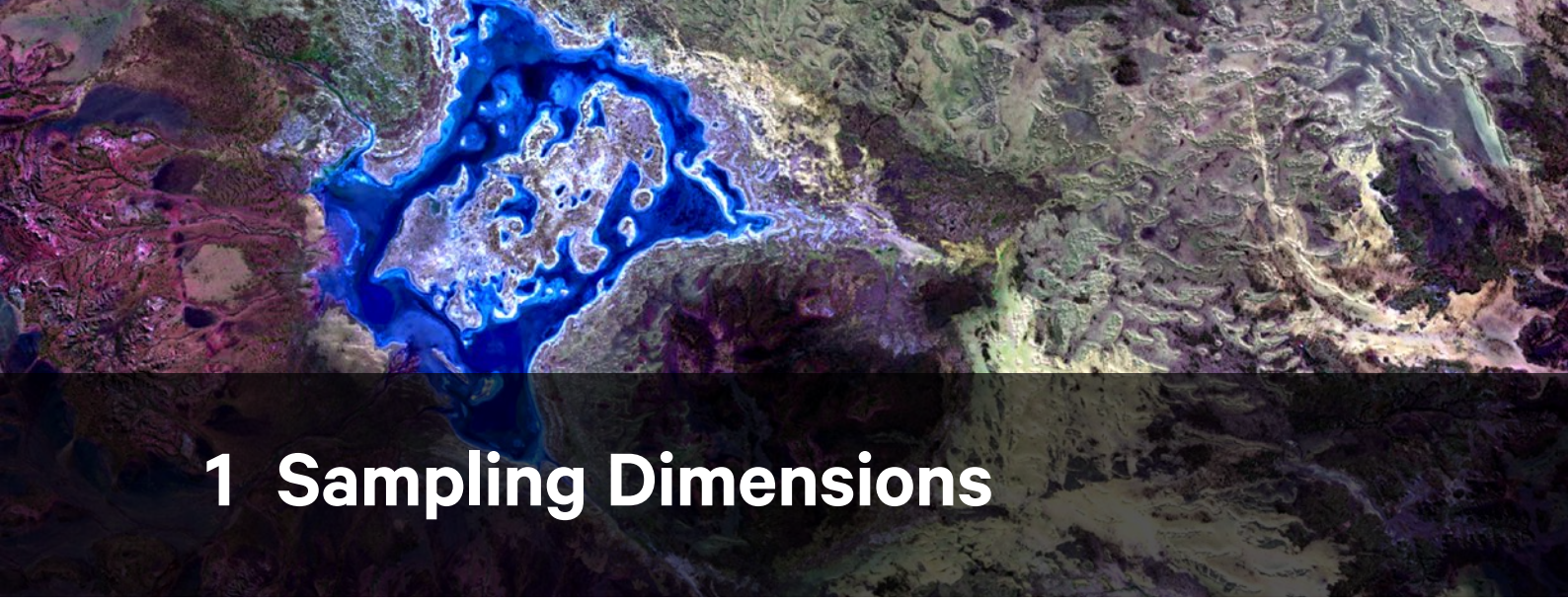
Contents

1 Sampling Dimensions 3

2 Imaging Artefacts 23

Background image on previous page: This polytych of images shows Dorre Island, located in Shark Bay, WA, as seen by five different EO sensors. From left to right image panels were acquired by NOAA AVHRR (19 March 2011; band 2), Aqua MODIS (19 March 2011; bands 2, 2, 1 as RGB), Landsat ETM+ (2002 mosaic; bands 5, 4, 3 as RGB), Sentinel 2A MSI (9 March 2016; bands 4, 3, 2 as RGB), and aerial photo (September 2007 mosaic) with pixel sizes 1 km, 250 m, 25 m, 10 m and 0.5 m respectively.

Source: Matthew Adams and Carolyn McMillan, Landgate.



1 Sampling Dimensions

Earth Observation (EO), or remotely sensed, imagery provides both a synoptic, or regional, view of the Earth's surface and the means to identify particular features of interest. Analysis techniques frequently relate particular data values in an image to certain ground features, or to attributes that identify those features.

Volume 1A introduced the concepts of observations, measurements and attributes in the context of EO datasets. These concepts, and their interrelationships, are summarised in Figure 1.4 in Volume 1A.

EO data acquisition methods implicitly involve at least one level of indirection or inference (see Volume 1A—Section 1.2). For example, a particular study may aim to determine vegetative cover and condition. Since such parameters are not directly measurable using remote sensing, they must be related to a property of vegetation that can be 'measured' remotely, namely the 'amount' of reflectance or absorption. A further limitation in EO datasets is that remotely sensed data only sample the potential range of measurements in the selected 'measurement space'.

Both observations and measurements involve interactions with some target object. An observation implicitly recognises the existence of the observed object and recognises the action of recording something about it, whereas a measurement provides a scaled record of such interactions (see Volume 1A—Section 1.6 for terminology). Image interpretation considers the consequences of observations and measurements and includes the process of moving from information to knowledge (or potential knowledge) to generate or support a hypothesis. Noise is sometimes added in the process of converting data to information or information to knowledge.

In order to relate Earth surface features or attributes to EO data, the intrinsic ability of the attributes to be resolved in the type of measurements being made must be considered together with the effectiveness of the models that relate physical processes to these measurements. The question of the structural model is too broad to consider here, but the issue of measurement is both fundamental and vital to planning EO data acquisition and its subsequent processing.

Natural vision systems and formalised image analysis exercises, such as military intelligence collection, differentiate between:

- detection—obtaining data about the existence of a target;
- recognition—gathering sufficient information about a particular target to determine its type; and
- identification—interpreting available information about a target to determine its unique identity.

Various aspects of image sampling pre-define the likelihood of being able to detect, recognise or identify targets in EO Imagery (Biberman, 2000). These include factors related to image acquisition, such as sensor characteristics (see Volume 1A—Section 13), the target scene (see Section 3), and the atmosphere (see Section 4), and also decisions related to image processing options, such as the settings selected for image display, enhancement and storage (see Section 2 and Volume 2).

The concepts of data resolution, density and extent were introduced in Volume 1A—Section 1. These can be seen to operate in four 'dimensions' of remotely sensed data acquisition as summarised in Table 1.1, namely:

- spectral (see Section 1.1);
- spatial (see Section 1.2);
- radiometric (see Section 1.3); and
- temporal (see Section 1.4).

Background image: Landsat-8 image of Baker Lake, WA (~1140 km northeast of Perth), acquired on 29 June 2013 (displayed using bands 4, 3, 2 as RGB).
Source: Norman Mueller, Geoscience Australia.

Table 1.1 Sampling dimensions in remote sensing

Dimension	Characteristic		
	Resolution	Density	Extent
Spectral	Width of each wavelength channel	Number of channels detected by sensor	Range of wavelengths covered by all channels
Spatial	Ground area imaged per optical pixel	Number of pixels and lines in image	Area covered by image
Radiometric	Smallest change in detected energy that would be represented as a different image brightness level	Number of gradations (grey levels) used to represent full range of radiances that could be detected by sensor	Actual range of radiances detected in each channel
Temporal	Time period over which each image is acquired	Frequency of successive image acquisitions	Total time period for which this imagery is available

Adapted from: Emelyanova *et al.* (2012)

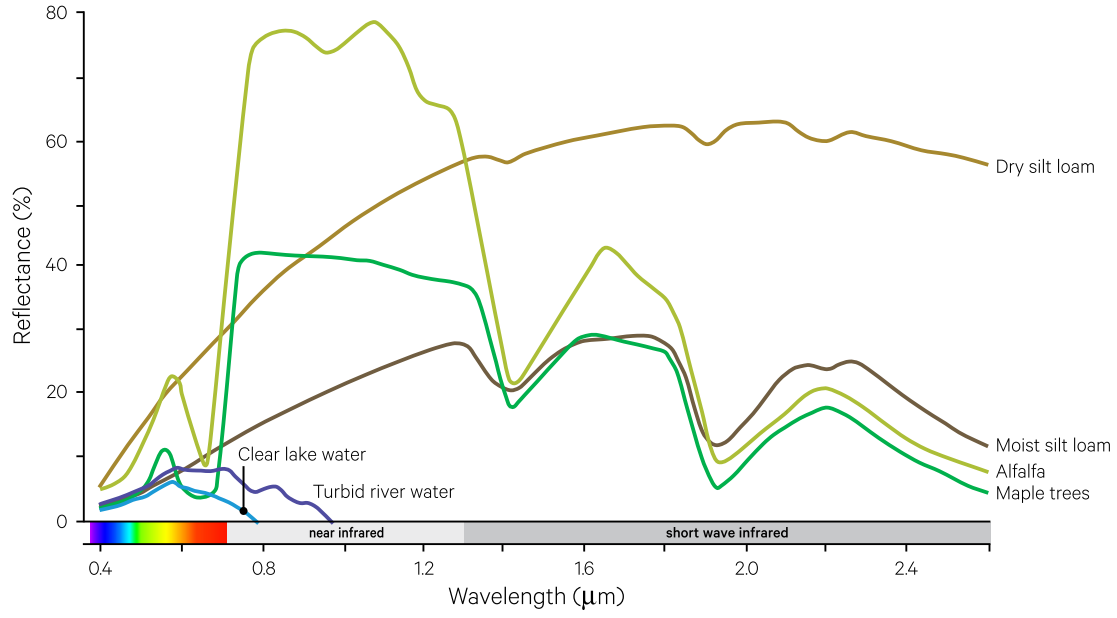
The following subsections are concerned with the measurement model that is implicit in all forms of EO data and the way in which these four dimensions of data acquisition can affect its interpretative value. The suitability of a particular EO data source to a specific application will depend on the resolution and extent of all data dimensions. Formal procedures have been developed to standardise selection of imagery and processing methods for particular applications (Roelfsema and Phinn, 2015). While the final selection of a data set is usually a compromise involving other factors such as cost and project timing, these aspects need to be carefully considered to ensure that the features to be identified can be adequately discriminated in the chosen data set.

1.1 Spectral

Different materials respond in different, and often distinctive, ways to electromagnetic radiation (EMR; see Volume 1A—Section 5). This means that a characteristic spectral reflectance curve, or spectral signature, can be determined for each material type (see Figure 1.1). Basic categories of matter (such as specific minerals) can be identified on the basis of their spectral signatures, but may require that the spectra be sufficiently detailed in terms of wavelength intervals and covers a wide spectral range. Composite categories of matter (such as soil which contains several different minerals) however, may not be uniquely identifiable on the basis of spectral data alone.

Figure 1.1 Idealised spectral signatures

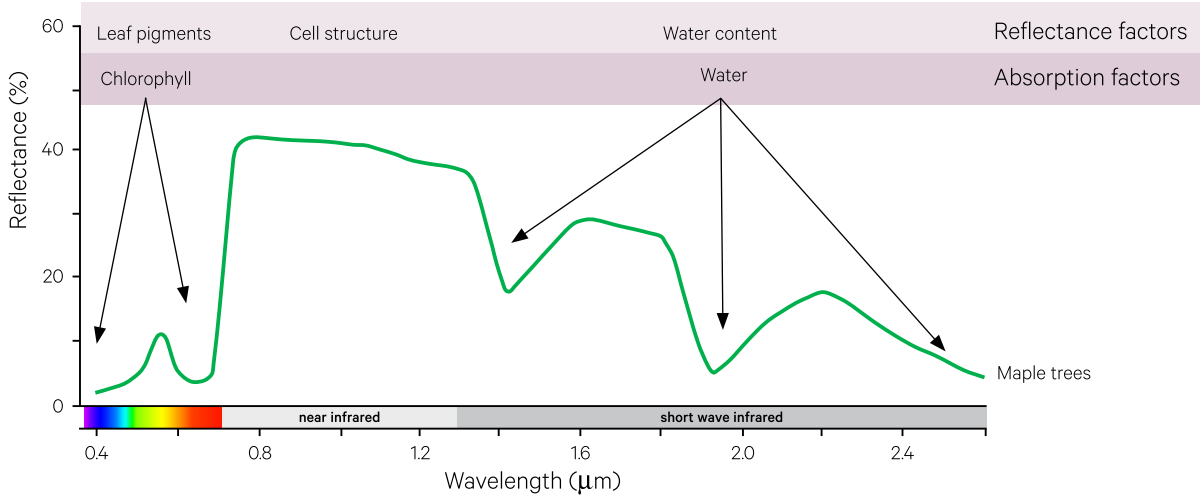
Reflectance from different Earth surface features varies for different wavelengths. Characteristic spectral reflectance curves can be created for different features to indicate a 'typical' shape over a particular range of wavelengths. This information can be used to differentiate between different surface features on the basis of their observed reflectance characteristics.



Adapted from: Harrison and Jupp (1989) Figure 6

Figure 1.2 Typical green vegetation spectrum

Reflectance properties of green vegetation primarily derive from leaf pigments in visible wavelengths, cell structure in NIR wavelengths and water content in SWIR wavelengths. Characteristic absorption features occur in visible wavelengths (due to chlorophyll) and SWIR wavelengths (due to water content).



Adapted from: Harrison and Jupp (1989) Figure 30

Those components of green vegetation that produce its spectral signature are illustrated in Figure 1.2. These spectral characteristics clearly show why changes in the condition of vegetation impact its reflectance, and also why remote sensing of appropriate wavelengths can highlight variations in vegetation vigour and stress (see also Volume 3A).

Remote sensing devices generally only sample the EM spectrum by detecting the combined radiation over a range of wavelengths (see Volume 1A—Section 13). For example, a sensor that is receptive to wavelengths in the range 0.4–0.5 µm would be sensing 'blue' light. This range is referred to as a spectral band, or channel, of data in an image. The spectral ranges that can be used for remote sensing of the Earth's surface are limited to the 'atmospheric windows' (see Volume 1A—Section 5.4).

Photographic recording devices only detect radiation within the ultra violet (UV) to near infrared (NIR) regions of the EM spectrum (depending on the type of film being used; see Volume 1X—Appendix 4). Within this range, spectral channels are defined by filters, which block out wavelengths outside the required sub-region (see Volume 1A—Sections 13 and 14). Multispectral and hyperspectral scanners, however, may also detect radiation in the middle and thermal infrared regions (see Section 6 and Section 7). Microwave radiation may be recorded using radar and passive microwave sensors (see Section 8).

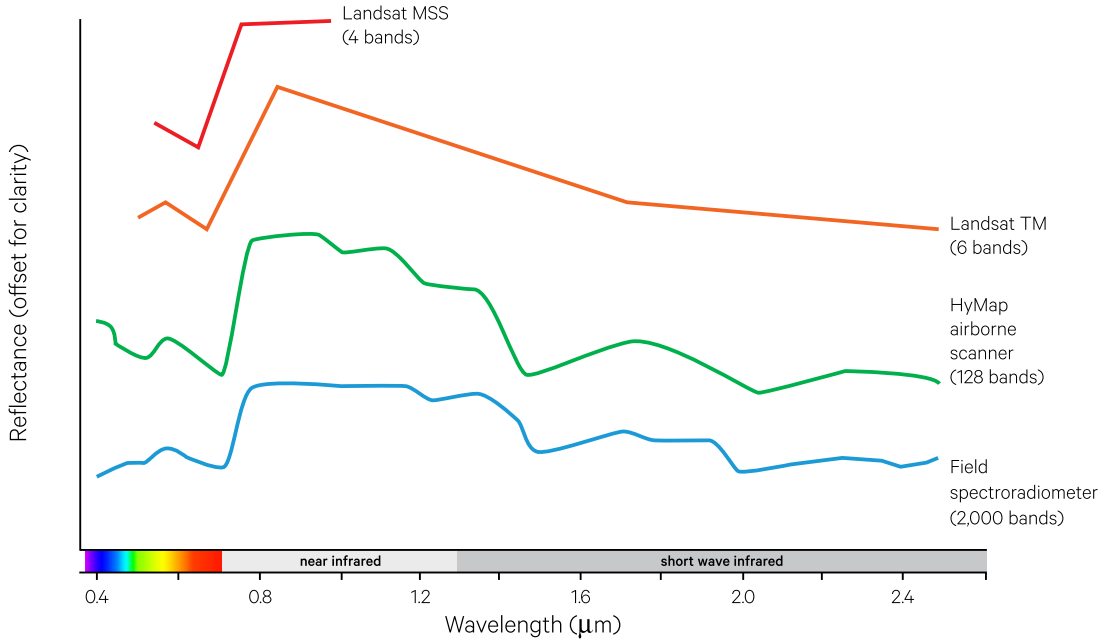
Digital imaging is as much about chemistry as it is about semiconductors.
(Antonio Perez)

Airborne scanners are typically used to provide increased spectral resolution relative to spaceborne scanners. In airborne sensors, the position, width and number of spectral channels being sensed can generally be tailored to a specific cover type, or range of covers, of interest, whereas in most satellite sensors, the channels are selected to differentiate between the major cover types. For example, since many individual minerals have diagnostic, but narrow, absorption bands at well-defined wavelengths, spectrometers can be used in the laboratory or in the field to reliably identify specific types of mineral. Airborne imaging spectrometers can detect wavelength bands as narrow as 5 nm, while satellite-borne imaging spectrometers, such as Hyperion, have bandwidths of approximately 10 nm, which still enables identification of most minerals.

The number of spectral bands being imaged is a measure of spectral density. Sensor design usually involves a trade-off between spectral and spatial dimensions (see Volume 1A—Section 13). Multispectral scanners generally image 3 to 30 bands, while hyperspectral imagers can record 100 to 300 bands (see Volume 1A—Section 14). Aperture size is a major cost factor in sensor construction, with smaller apertures (or lower spatial resolution/larger pixel sizes) resulting in less expensive sensors (Shaw and Burke, 2003). Hyperspectral sensors generally achieve a higher spectral density by reducing the spatial resolution or extent, or accepting a lower Signal-to-Noise Ratio (SNR) per detector (see Section 2.1.3).

Figure 1.3 Spectral resolution, density and extent of different sensors

A field spectroradiometer measuring 2000 spectral bands across optical wavelengths can render a detailed spectrum for specific ground features within a small target area. While the major patterns in the detailed green vegetation spectrum can be observed using a 128 band HyMap airborne scanner (which views larger ground areas than the field spectroradiometer), only the most significant changes are observed in the 6 bands of Landsat TM (for 30 m ground pixels). The four spectral bands of Landsat MSS observe ground pixels of approximately 60 m by 80 m. These bands cover a narrower spectral range than the other sensors so can only provide information about a segment of the full optical spectrum.



Source: Megan Lewis, University of Adelaide

Spectral extent describes the range of wavelengths being sensed in all channels of an image. Spectral resolution can be defined by the range of wavelengths detected by each individual channel. In many sensors, individual spectral bands vary in resolution and/or may overlap. Some may be contiguous while many will be irregularly spaced to sample specific features of interest. An increase in spectral resolution over a given spectral extent will result in a greater number of spectral channels, or spectral density. However, this additional resolution results in increased data volume with cost implications for transmission, storage and processing. The theoretically optimal spectral range and resolution for a particular cover type therefore may need to be modified with respect to the practical considerations of data collection and processing.

Different spectral signatures for vegetation are compared in Figure 1.3. These signatures were derived from four different sensors with differing spectral resolution, density and extent. Landsat MSS and TM are multispectral scanners with different spectral densities and extents, while HyMap is an airborne hyperspectral imager (see Volume 1A—Section 14). While the Landsat TM data captures the major spectral trends identified by the ground-based spectroradiometer, it misses some important transitions that can be detected in hyperspectral data.

Sampling, statisticians have told us, is a much more effective way of getting a good census.
(Rob Lowe)

1.2 Spatial

Spatial resolution defines the level of spatial detail depicted in an image. This may be described as a measure of the smallness of objects on the ground that can be distinguished as separate entities in the image, with the smallest object necessarily being larger than a single pixel. In this sense, spatial resolution is directly related to image pixel size. In terms of photographic data, an image pixel may be compared to grain size while spatial resolution is more closely related to photographic scale. Although pixels in both image space and on the ground will often be referred to here by the single term pixel, it should be recalled that in the case of image space the pixel size is constant and when the reference is to a pixel at ground scale its dimensions may vary.

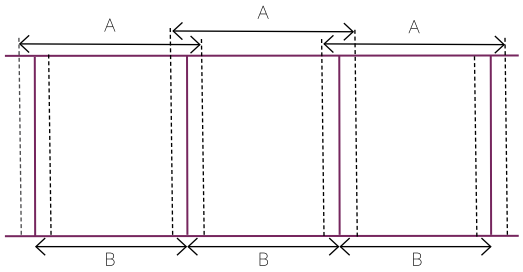
In practical terms, the 'detectability' of an object in an image involves consideration of spectral contrast as well as spatial resolution. Feature shape is also relevant to visual discrimination in an image with long, thin features such as roads being more obvious than smaller symmetrical ones. Pixel size is usually a function of both platform and sensor characteristics, while the detectability may change from place to place and time to time.

As detailed in Volume 1A—Section 14 and Volume 2B, measurements in remotely sensed imagery acquired by passive sensors are usually obtained by sampling the Earth's surface using a constant view angle. This angle is referred to as the Instantaneous Field of View (IFOV) and determines the ground area 'viewed' to form an individual pixel, or the 'optical' pixel size. The optical pixel, or spatial resolution, is generally a circular or elliptical shape and it is the combined radiation from all components within its ground area that produces the single pixel value in a given spectral channel. Along each image line, optical pixel values are sampled and recorded. The average spacing of optical pixels relative to the ground area covered is then used to determine the geometric pixel width, or spatial density, with the line spacing along the platform path being used in a similar way to derive geometric pixel depth. In most cases, the geometric pixel dimensions are referred to as the nominal image pixel size. The geometric pixel size is usually similar to the optical pixel size although there is often some overlap between adjacent optical pixels as shown in Figure 1.4. For example, Forster (1980) estimated that only 52% of the radiation recorded for a Landsat MSS pixel was derived from the area of the geometric pixel. In most applications, this does not present a problem since a pixel is likely to have a similar radiance to its neighbour. However, in urban areas with high variability of cover relative to the Landsat MSS pixel size (roughly 60 m × 80 m), this effect is significant.

Similarly, the pixel geometry for AVHRR imagery has been shown to involve significant overlap between pixels along a scan line and between rows along the satellite track, with increasing overlap with distance from the scene centre, or nadir (see Figure 1.5). For example, while the ground pixel width for AVHRR9/10 at nadir was 1,105 m, at the edge of the scan line the ground pixel width increased to 3,497 m.

Figure 1.4 Optical versus geometric pixel sizes

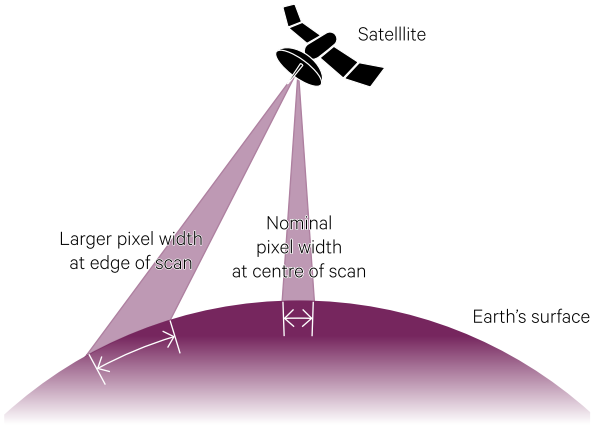
The optical pixel width (that is, the area imaged by the sensor) is labelled A, but these ground areas overlap. To account for overlapping pixels in image scaling, the geometric pixel size is given as B.



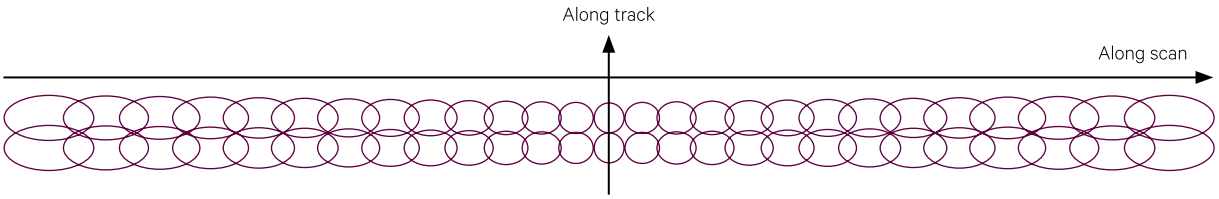
Source: Harrison and Jupp (1989) Figure 35

Figure 1.5 AVHRR pixel geometry

a. For wide scan angles, as occurs with AVHRR, pixel size increases away from the centre of an image swath. This effect is further exaggerated by Earth curvature, especially for sensors imaging wide swaths such as AVHRR.



b. When looking vertically down to Earth at the centre of each scan line (or nadir), the sensor detects radiance from a circular ground area. As the sensor looks away from the image centre (off-nadir viewing), a larger ground area is imaged in both the along-scan and along-track directions. A greater increase in imaged area occurs in the along-scan direction, resulting in the optical pixel shape changing from a circle to an ellipse. Near the edges of the image swath, the ground area being recorded as a single pixel is significantly larger than at the centre, resulting in distinct geometric distortions in such imagery (see Volume 2B). Note that there are over 2,000 pixels per line in AVHRR imagery; here the number is significantly reduced for simplicity.



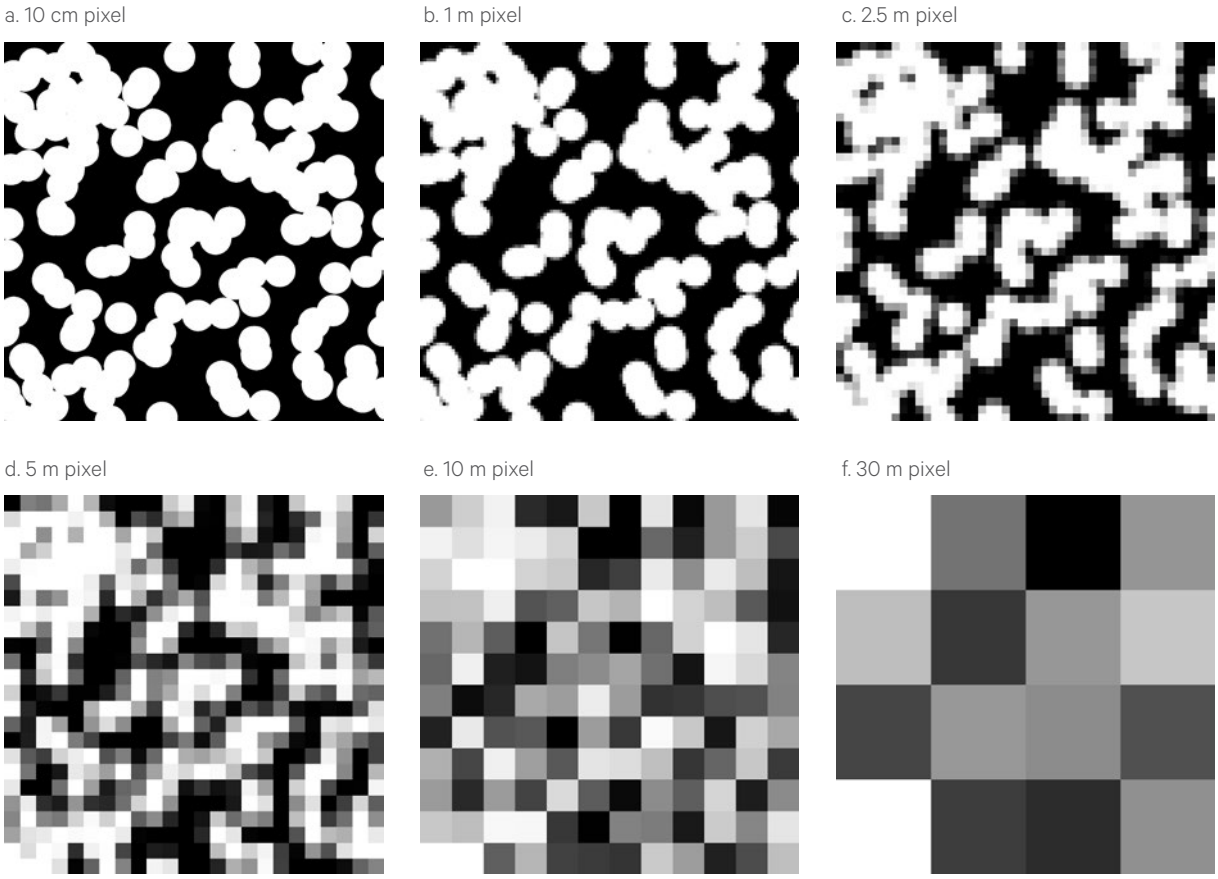
Adapted from: Breaker (1990)

The ground pixel size for airborne and satellite-borne scanners is a function of both the sensor (optics and sampling rate) and the platform (altitude and velocity). The exact placement of an image pixel grid on the Earth's surface is unpredictable for airborne and spaceborne sensors. Consequently, a pixel-sized feature that has a contrasting reflectance to its background may be imaged as a single pixel in a particular image but would more likely be imaged as a part of two or even four pixels. The combined radiation of the feature and its background are then detected as the radiance values for that group of pixels. Radiation levels of different components within a pixel combine in a complex way, with the average radiance of four pixels of 25 m square not necessarily being the same as the radiance of a 50 m square pixel covering the same area. An additional factor here is surface smoothness, since this affects the strength and direction of radiation (see Section 3.3).

These considerations are also relevant to the selection of a grid size and shape for scan digitising (see Volume 1X—Appendix 4.3). The effect of this digitising process is shown in Figure 1.6 for an artificial image. The size of individual ground features relative to the pixel size largely determines their contribution to the radiance measurement of a pixel. Object shape discrimination is severely degraded as pixel size approaches the object size, though the presence of the object may still be inferred up to this limit.

Figure 1.6 Spatial resolution in digitising

In this synthetic image, circles represent tree crowns of 10 m diameter on a contrasting background. The ground area of each image is approximately equal to 120 m x 120 m, that is, the area of 4 x 4 Landsat TM/ETM+/OLI multispectral pixels.



Source: David Jupp, CSIRO

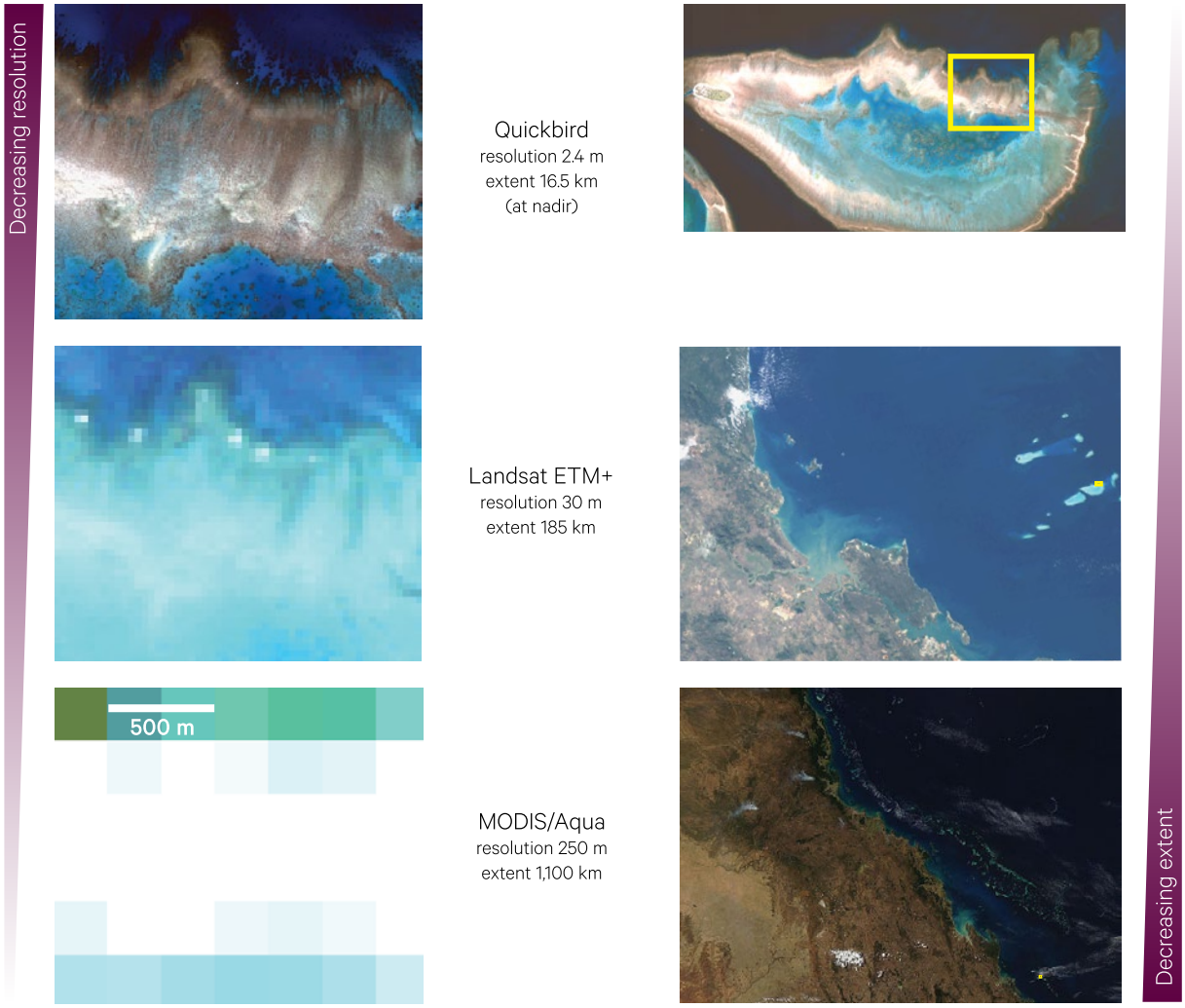
Another spatial aspect of imagery is the extent of coverage of an imaged scene. This is usually referred to as the swath width across the satellite orbit or aircraft flight path and varies with the platform altitude and the total scan angle (or Field Of View: FOV) of the sensor. Aircraft scanners typically employ a wide FOV to increase ground coverage. As illustrated in Figure 1.6 above, and Volume 1A—Figure 11.1, this results in geometric distortions in the imagery (see also Volume 2B). Continental-scale satellite data, such as MODIS and AVHRR, also use wide scanning angles and produce imagery with severe along-line distortions due to the combined effects of Earth curvature and panoramic distortion. In these cases, the nominal pixel size is usually quoted as at nadir (or the centre of an image line)[4].

Most MODIS bands have a pixel size of 1000 m × 1000 m. This imagery has good large area coverage, but poor detail for specific features. More recent satellite scanners, such as Quickbird, have smaller pixels giving fine detail for specific features, but generating too much data to be used conveniently for large area studies. Figure 1.7 demonstrates differing spatial resolutions and extents of imagery from three spaceborne platforms acquired over Heron Island Reef, Queensland.

4. By definition, the nadir of an elevated observer refers to the point directly below the observer (and diametrically opposite the zenith—see Section 3). For most EO sensors, nadir equates to the centre of an image line, however for sensors with off-nadir viewing capability, this may not be the case.

Figure 1.7 Spatial resolution and extent

Images of Heron Island Reef, Queensland, demonstrate the varying resolutions and extents in imagery acquired by different satellite sensors. In general, as image resolution increases, the image extent decreases. All subsets in the first column are shown at the same scale, but show very different spatial detail of the reef. The higher resolution images, however, cover a much smaller extent (see second column). The red box and dots in the second column of images indicate the extent and location of the subsets shown in the first column.



Source: Chris Roelsema, University of Queensland. Image credits: Quickbird—Digital Globe Inc.; Landsat—USGS/Geoscience Australia; MODIS—NASA

In multi-channel data, a slight spatial misregistration between channels also occurs due to the time required to read each sensor. In the case of Landsat TM/ETM+, with sixteen image lines being recorded in each scan, this delay causes a stepping between individual image lines, which may be visible along the sides of rectified imagery (see Volume 2B). Any intrachannel delay, however, is usually considered to be sufficiently small so that image quality is not degraded.

The required pixel size is an important consideration in any remote sensing exercise, fundamentally being a trade-off between cost, for processing time, and detail, or image resolution. The assumption that a smaller pixel size is superior for all applications is unfounded. The size of the features being studied becomes important here. Investigations of small area features such as algal blooms and river outflows will obviously require imagery with pixels somewhat smaller than the feature size. However, the broad scale patterns targeted by regional studies may be masked by the detail captured within small-area pixels, and a greater processing effort would be required to extract those patterns.

1.3 Radiometric

Radiometric resolution in EO imagery is defined as the amount of energy required to increase a pixel value by one quantisation level or 'count'. The radiometric density is the dynamic range or the maximum number of quantisation levels that may potentially be recorded by a particular sensing system, while the radiometric extent is the actual dynamic range recorded in a given image channel.

Radiometric resolution in digital imagery is comparable to the number of tones in a photographic image, with both measures being related to image contrast. Much of the early EO imagery was recorded with quantisation levels in the range 0–255, that is, the minimum 'detectable' radiation level is recorded as 0 while the 'maximum' radiation is recorded as 255. This range is also referred to as 8-bit resolution, since all values in the range may be represented by 8 bits (*b*inary dig*its*). More recent imagery tends to be recorded with more quantisation levels. For example, Landsat-8 OLI records 12-bit images whereas earlier Landsat instruments used 8-bit resolution.

Quantisation levels are frequently given in terms of the number of bits rather than the number or range of levels (see Table 1.2). These values are related by:

$$2^{\text{number of bits}} = \text{number of quantisation levels}$$

In image processing, quantisation levels are usually referred to as Digital Numbers (DN).

Table 1.2 Quantisation levels

Number of Bits	Number of Quantisation Levels	Range of Quantisation Levels
1	2	0–1
2	4	0–3
3	8	0–7
4	16	0–15
5	32	0–31
6	64	0–63
7	128	0–127
8	256	0–255
9	512	0–511
10	1024	0–1023

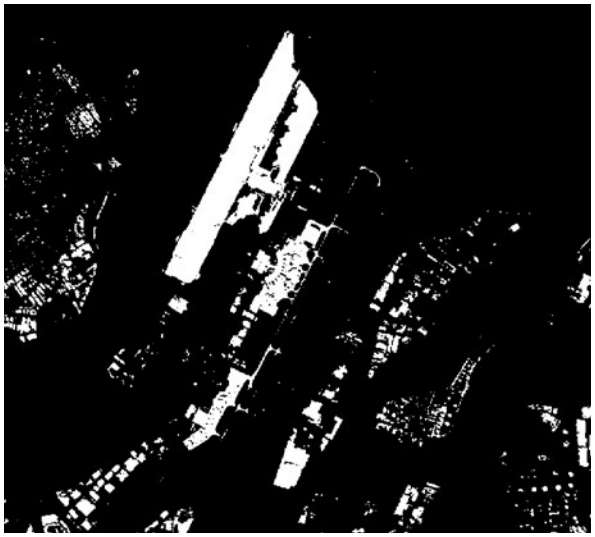
The effect of changes in radiometric resolution on image feature contrast is illustrated in Figure 1.8. As discussed in Volume 1A—Section 13.2, the human eye can only perceive 20–30 different grey levels so the additional resolution provided by images with more than about 30 levels is not visually discernible. To derive maximum discrimination from imagery with higher radiometric resolution, the sequence of images in Figure 1.8 emphasises the value of interpreting imagery using digital techniques.

The most important thing in imaging for me is the dynamic range. The dynamic range means the tones that you can capture from highlights to dark and the bits, the depth of color that you can capture. (Emmanuel Lubezki)

Figure 1.8 Radiometric resolution and image contrast

Landsat-8 panchromatic image of Brisbane airport acquired on 8 July 2016, displayed using different quantisation levels:

a. 2 (2^1 binary)



b. 4 (2^2)



c.16 (2^4)



d: 256 (2^8)



Source: Norman Mueller, Geoscience Australia

Since the radiometric resolution defines the maximum number of quantisation levels detectable by a sensor, it is most unlikely that a single remotely sensed image would actually contain data values covering the entire range. For Landsat data, for example, most imagery would only contain a maximum range of 50–100 DN (or less) in each channel. This situation is simply due to the range of objects being imaged, since the detector sensitivities are generally designed to cope with the brightest and darkest objects of interest, and a single image would rarely contain both. Atmospheric scattering and absorption effects decrease the radiometric extent of an image by reducing the discrimination between different radiation levels, especially at shorter wavelengths.

Some sensing systems have adjustable sensitivities (or gains) for imaging over surface features with markedly different radiance, such as land and water. Different gain settings may also be required to avoid sensor saturation, that is, sensing multiple, high radiance levels at the maximum detector sensitivity, but below their real values. This can occur where there is significant variation in Sun illumination in different seasons. While the sensitivity range of a detector can only be modified by engineering changes, in many sensors this range can be reduced to multiple sub-ranges or gains, with each gain setting being most appropriate for a particular ground target or condition (see Volume 1A—Section 13 and Volume 2A—Section 3).

Methods for improving contrast within an image for presentation and interpretation purposes are discussed in Volume 2A. It should be noted however, that these techniques do not improve the radiometric resolution of the data itself, as this is dependent on the scanning instrument, but only alter the visual contrast in a displayed image.

1.4 Temporal

The temporal resolution of a remotely sensed image identifies the time period over which it is acquired. Temporal density refers to the repeat cycle or interval between acquisitions of successive imagery. This cycle is fixed for spacecraft platforms by their orbital characteristics, but is quite flexible for aircraft platforms. Satellites offer repetitive coverage at reduced cost but the rigid overpass times can frequently coincide with cloud cover or poor weather. This can be a significant problem when fieldwork needs to coincide with image acquisition. While aircraft data are necessarily more expensive than satellite imagery, these data offer the advantage of user-defined flight timing, which can be modified to suit local weather conditions when necessary. The off-nadir viewing capability of some high-resolution instruments, such as Ikonos, WorldView and SPOT-HRV, introduce flexibility to the usual repeat cycle of satellite imagery by enabling acquisition areas outside of the nadir orbital path. This feature allows daily coverage of selected regions for short periods and has obvious value for monitoring dynamic events such as flood or fire.

As with the other dimensions, the 'ideal' temporal density will obviously vary considerably for different applications. Studies of thermal inertia may require two images per day (day/night pairs) but land cover monitoring projects may only require one image each year. While monitoring is cited as one of the major values of EO data, the processing and interpretation of multi-temporal imagery presents a wide range of problems (see Volumes 2D and 2E). These temporal changes can also affect interpretation of stereo pairs if the imagery were acquired in different seasons or atmospheric conditions.

The temporal dimension has special significance since we are subject to the passage of time ourselves. We are vitally interested in how things change yet are also constrained in our ability to observe these changes in an objective fashion. Temporal differences between remotely sensed imagery can occur for a number of reasons: atmospheric differences, changes in Sun position during the course of a day and during the year, and the effect of seasonal cycles in vegetation or water bodies.

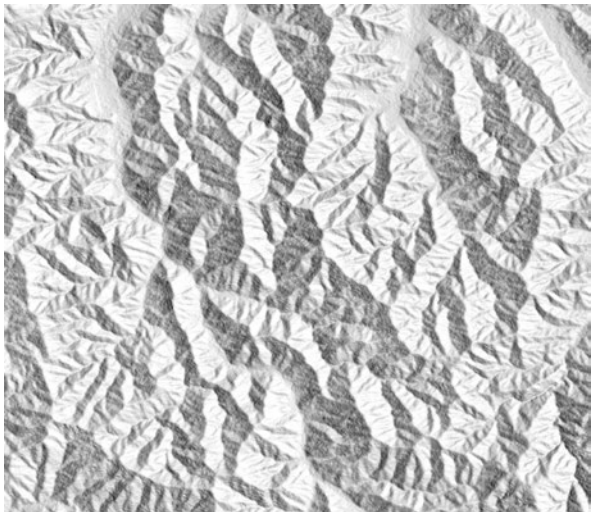
Atmospheric differences between multiple dates may alter the observed radiation levels that are actually recorded in the imagery when in fact the reflectance of surface features has not altered. Atmospheric effects are most significant in the short-wave (ultraviolet and visible) spectral regions (see Section 4 below and Volume 1A—Section 5.4). However, except for cloud, these effects are usually minor and should be minimised when comparative images are acquired at the same time of year. Digital image processing techniques that correct for these effects are considered in Volumes 2A and 2D.

As well as possible atmospheric changes with seasonal differences, both Sun position and vegetation characteristics vary significantly during the annual cycle. Figure 1.9 illustrates the differences in the extent of topographic shading in remotely sensed imagery due to changes in Sun position and irradiance in different seasons, in the Southern Hemisphere. As well as these shadowing changes, however, the reflectance of deciduous vegetation and grasslands will also vary between seasons. These relatively short-term, cyclic changes in land cover can greatly complicate the process of detecting longer term changes. The coincidence of field work and image acquisition is essential in dynamic environments such as the wet/dry tropics since grass cover can change from green to brown in less than one month at the end of the wet season. Similar rapid changes in vegetation can occur in arid zones after episodic and erratic rainfalls. A pixel containing a green grass background has a much higher level of NIR radiation than a pixel with a background of dry grass. NIR reflectance of perennial woody vegetation can also increase quickly after rain. This is especially true for many opportunistic Australian trees and shrubs (being adapted to making the most of rain in a dry environment), as the active cell division (due to both new leaves and blade expansion in old leaves) significantly increases reflectance of NIR radiation.

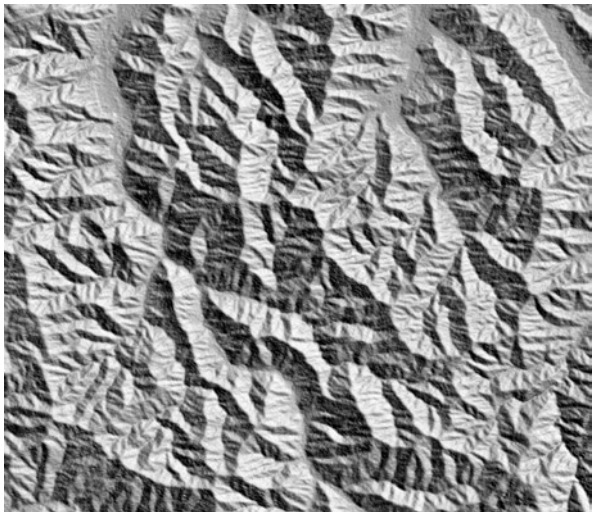
Figure 1.9 Seasonal solar illumination variations

An elevation image in the Victorian alps was used to simulate the surface shading effects for different seasonal sun positions.

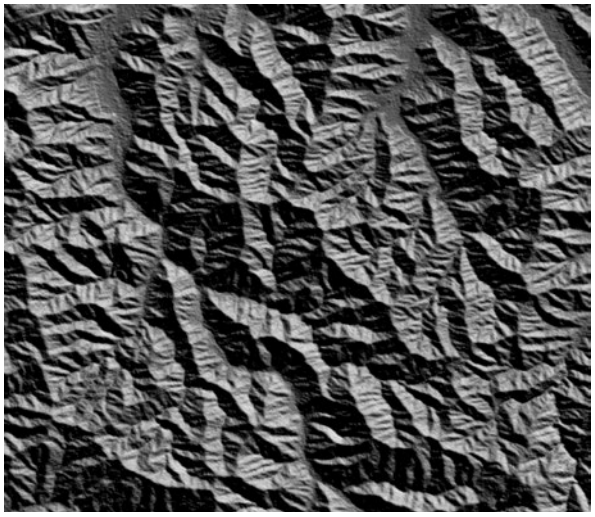
a. Summer (22 December)



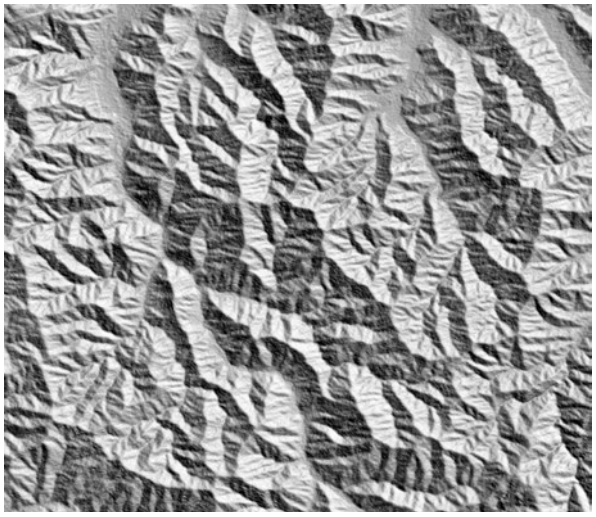
b. Autumn (22 March)



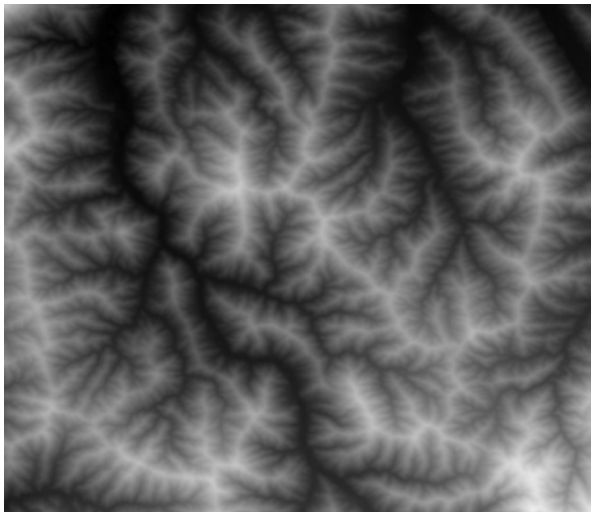
c. Winter (22 June)



d. Spring (22 September)



e. Elevation image displayed with light shades corresponding to high elevation and dark shadows indicating low elevation



Source: Fuqin Li, Geoscience Australia

Diurnal variations between imagery can also result in shadowing and atmospheric differences. These variations may occur with imagery acquired on different platforms or, in the case of aircraft data, at different times during the day. The importance of illumination and sensor positions to remote sensing cannot be over-emphasised and is further discussed in Section 3.4 and Volume 1X—Appendix 5.

Particular seasons may be optimal for remote sensing of certain features. Crop cycles will dictate the timing required for image acquisition in agriculture. In the wet/dry tropics, a mid-dry season image appears to be optimal for stratifying land cover components; an early-dry season image is too 'green' and a late-dry season image is often riddled with fire scars. Alternatively, in the temperate regions, studies relating to landform are more suited to using winter imagery when land cover differences will be minimised. Thus, acquisition date can greatly affect the utility (in terms of differentiation between objects) of EO imagery. Similarly, dates of multi-temporal imagery will influence the range and nature of features detected as 'changed' and the relative 'extent' of change between them. Acquisition dates should be selected carefully to ensure maximum information content in EO data. If the objective is to monitor change over years or decades, it is desirable to compare images acquired in similar dates and seasons, often termed 'anniversary images'. Image selection for multi-date analyses is further discussed in Volume 2D.

The temporal 'extent' of remotely sensed data could be considered as the time frame over which imagery from a particular source is available. While aerial photograph data have been available for many decades, most satellite imagery has been routinely available for less than 30 years, with exceptions such as the series of sensors on the Landsat platforms and the AVHRR series. Temporal resolution, density and extent all need consideration when selecting an EO data source for a particular application.

Frequent image acquisition is particularly valuable for mapping and monitoring the impact of natural disasters such as floods, fires and earthquakes. For example, Tropical Cyclone Marcia crossed the coast of northeast Queensland on the morning of 20 February 2015 and resulted in significant damage in several towns including Yeppoon and Rockhampton. Imagery acquired by Worldview-2 on 22 February clearly shows the extent of flooding in Rockhampton as a consequence of this cyclone (see Figure 1.10).

Figure 1.10 Cyclone Marcia damage in Rockhampton

Cyclone Marcia swept into the town of Rockhampton on the northeast coast of Queensland on 20 February 2015 and resulted in signficant storm damage and flooding. This image was captured by the WorldView-2 satellite on 22 February and provides a clear snapshot of the extent of flooding.

a. Rockhampton region inundated by brown floodwaters



b. Subset of this image showing submerged roads in southern Rockhampton



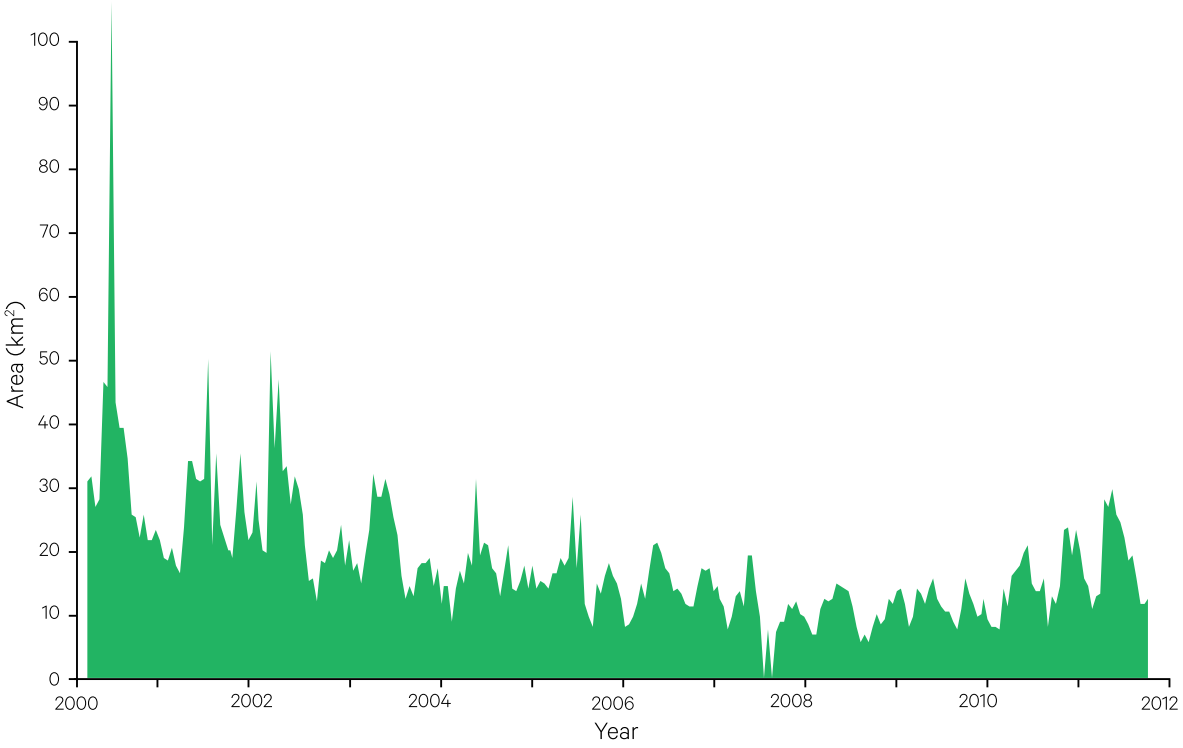
Source: Image © 2016 DigitalGlobe, Inc. Used with permission.

The growing body of EO imagery now allows time series analyses of particular features. As illustrated in Figure 1.11, such temporal trends can quantify seasonal fluctuations and longer-term changes in selected resources, and allows those changes to be correlated with other environmental variables, such as climate. Analysis of time series data is further considered in Volume 2D.

Examples of integrating EO image archives with biophysical models and other data sources include monitoring agricultural production (see Excursus 1.1) and sea level changes (see Excursus 1.2).

Figure 1.11 Time series of wetlands vegetation

Changing area of Dalhouse Springs Complex wetlands derived from MODIS Normalised Difference Vegetation Index (NDVI) 16-day composites, from 2000 to 2011 (see Volumes 2C and 3A for details of NDVI). When mapped over time, the greenness fluctuations can be separated into seasonal and climatic components.



Adapted from: Lewis *et al.* (2013)

Excursus 1.1—How Much Sugar?

Source: Andrew Robson, University of New England (UNE)
Project Sponsor: Sugar Research Australia
Project Partners: UNE and Farmacist, in collaboration with Bundaberg Sugar, ISIS Mill, Maryborough Sugar Factory, Wilmar, Tully Sugar, Sunshine Sugar, and Mackay Sugar.

Sugar is the second largest export crop in Australia. Over five million tonnes of raw sugar are produced per year, with an economic value of around $2 billion. The vast majority of Australia's sugar is grown in Queensland, where 20% of the total crop area (500,000 ha) is devoted to sugar cane.

To optimise the management of sugar cane crops, high resolution satellite imagery is being used to monitor crop area, growth, and health (see Figure 1.12). Current research is identifying the most appropriate imagery and analyses to characterise midseason variability within sugar cane crops, in terms of:

- image scale, frequency and cost;
- optimal timing for image acquisition;
- reliability of analyses;
- efficient processing and distribution; and
- costs and benefits to industry.

An accurate in-season prediction of yield is of vital importance to the Australian sugar cane industry. At a regional level, such forecasts are essential for optimising harvesting, milling, marketing and forward selling of produce. At a paddock scale, yield forecasts provide growers with an understanding of both in-crop variability and total production. By using GIS framework to extract image data from all crops within a growing region, correlations between image-based greenness maps and actual yield have been established. This correlation has been used to effectively predict regional yield as well as generate crop yield maps prior to harvest.

Variability in cane crops can occur for many reasons, including soil nutrition, plant and soil pests and diseases, irrigation deficiencies, erosion and weed infestation. By using high resolution satellite imagery to monitor crop variability during the growing season, the exact location and extent of a constraint can be identified quickly and accurately (see Figure 1.13).

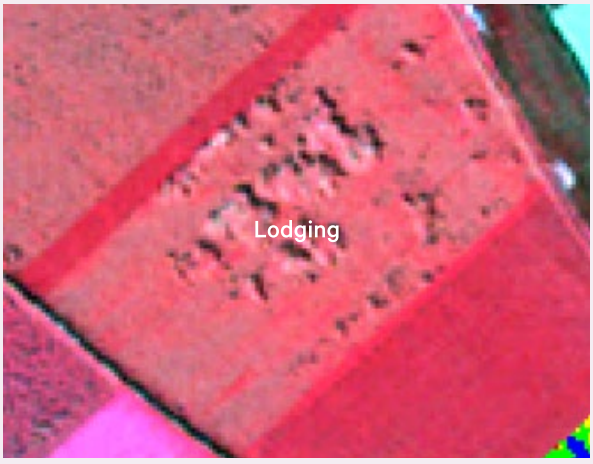
Figure 1.12 High resolution satellite imagery

This false colour composite image pair shows IKONOS data (0.8 m resolution—left) compared with SPOT imagery (10 m resolution—right).



Figure 1.13 Crop monitoring

a. Lodging



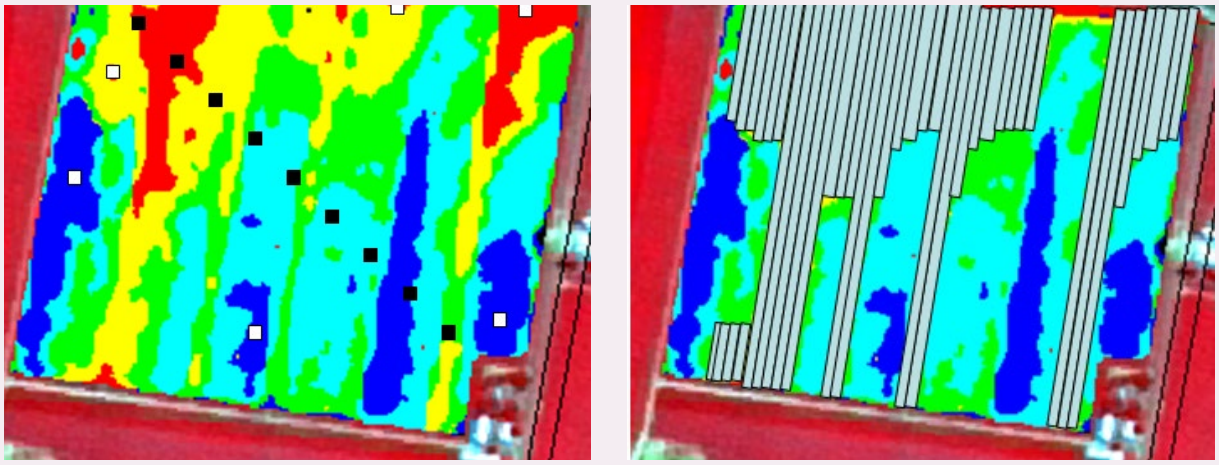
b. Weeds



Figure 1.14 Soil sampling

a. Traditional soil sampling (black dots) did not identify soil nutrient constraints, while strategic sampling based on image greenness maps (white dots) identified calcium deficiency in low vigour areas (shown as red/yellow).

b. Targeted application of lime and dolomite only required one third the volume of fertiliser, so reduced costs by more than $200/ha.

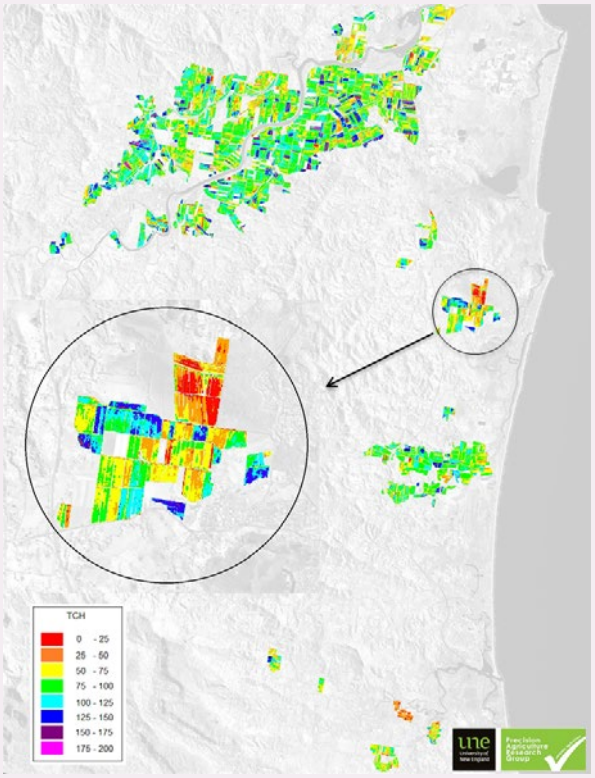


As well as allowing production to be maximised, detailed information about crop growth enables prudent use of water, fertilisers and agricultural chemicals. Monitoring crop variability over several growing seasons allows growers to better understand the inherent variability within blocks, and concentrate intensive analyses, such as soil sampling, in identified problem areas (see Figure 1.14). Production of EO-based maps of crop vigour, yield and qualitative foliar nitrogen are being automated for delivery to 95% of the Australian sugar industry.

Historic growth trends are also being incorporated into EO-based yield forecasting models as indicators of future production. These time-series yield models are tailored to each region and will allow closer monitoring of variability during the growing season (see Figure 1.15). The development of regional yield maps will provide mills with more accurate data for identifying areas of potential crop under-performance and also for scheduling harvesting operations.

Figure 1.15 Predicted sugar yield map

Classified derived yield map (tonnes of cane per ha, TCH) for the Condong growing region, southeast Queensland, based on SPOT-5 imagery acquired on 18 March 2015. Crops include those that are 1, 2 and 3 years old. The magnified section clearly shows the within-crop yield variation.



Excursus 1.2—Impact of Sea Level Changes on Estuaries

Source: Janet Anstee and Hannalee Botha, CSIRO
Further information: Anstee *et al*. (2009)

Australian estuarine ecosystems are sentinels of climate change. Estuaries, or tidal inlets of the sea, are transition zones between river and ocean environments where seawater from tidal rhythms mixes with freshwater flowing from rivers and streams. This unique environment supports a rich diversity of plants and animals, and offers shelter for fish nurseries and migratory birds.

Straddling the interface between ocean and land, estuaries are impacted by the consequences of climatic changes, such as sea level rise, storm surges and temperature-induced shifts in estuarine vegetation. Rising sea levels affect water depth, movement of sediments, and water quality, as well as the distribution and abundance of plant life, including seagrasses, saltmarshes and mangroves.

Various sources of EO imagery are now being used to monitor changes in water quality, water depth and plant life in Australian estuaries. The rate and extent of vegetation change is being established using large scale imagery, while finer scale imagery allows detailed mapping of seasonal and longer term changes in estuarine plant life.

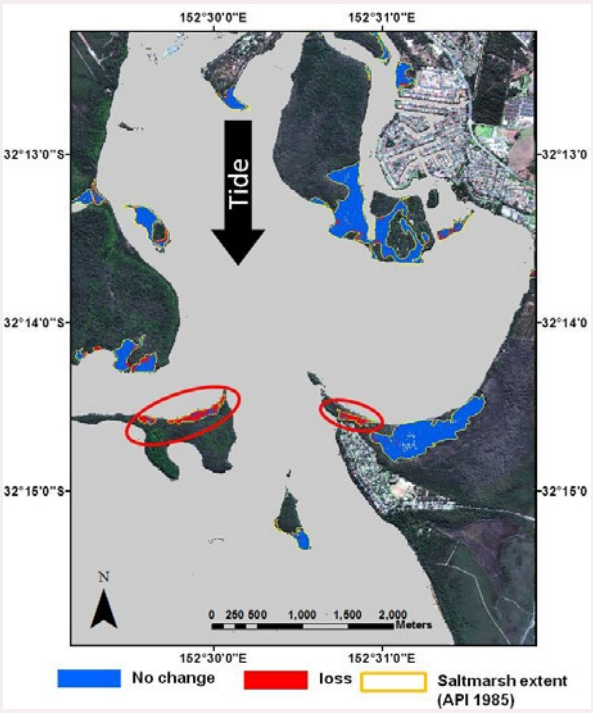
These dynamic ecosystems are among the most productive and heavily populated habitats in the world. Information being derived from EO sensors provides resource managers with insight into the potential impacts of sea level changes on estuarine health and dynamics, and the ability to monitor the effects of pollution, fishing, and other human activities (see Figure 1.16).

Figure 1.16 Wallis Lake, NSW

a. AVNIR image of Wallis Lake, NSW, acquired on 5 January 2007. Two training walls have been constructed at the entrance to this lake to stabilise the river banks and channel depth in the top right of the image. These walls have increased the tide height, thus simulating the impact of sea level rise. This situation offers an opportunity to observe and monitor potential changes in coastal habitats that could result from rising sea levels.



b. Worldview-2 image acquired in August 2010. The extent of saltmarsh was mapped from aerial photography in 1985 and is bordered by yellow in this image. When compared with the current image, the area of saltmarsh has decreased in the past 25 years, especially along north-facing shores that are most vulnerable to increased tidal inundation (see areas circled in red). Retrospective analysis of archival EO imagery can establish the extent and rate of such environmental changes.



1.5 Further Information

Image Resolution and Map Scales: *www.marinedataliteracy.org/basics/scales/scales.htm*

USGS Spectral Characteristics Viewer: *http://landsat.usgs.gov/tools_spectralViewer.php*

1.6 References

Anstee, J. M., Botha, E. J., and Dekker, A. G. (2009). *Study on the remote sensing of estuarine macrophytes and saltmarsh vegetation on Wallis Lake*. Water for a Healthy Country National Research Flagship, CSIRO.

Biberman, L. M. (2000). *Electro-optical Imaging: System Performance and Modeling*. SPIE Press, Washington.

Breaker, L. C. (1990). Estimating and removing sensor-induced correlation from advanced very high resolution radiometer satellite data. *Journal of Geophysical Research: Oceans, 95*(C6), pp. 9701-9711. doi:*http://dx.doi.org/10.1029/JC095iC06p09701*.

Emelyanova, I. V., McVicar, T. R., van Niel, T. G., Li, L. T., and van Dijk, A. I. J. M. (2012). *On blending Landsat-MODIS surface reflectances in two landscapes with contrasting spectral, spatial and temporal dynamics*. WIRADA Project 3.4: Technical Report. CSIRO Water for a Healthy Country Flagship, Australia.

Forster, B. (1980). Urban control for Landsat data. *Photogrammetric Engineering and Remote Sensing, 46*(4), pp. 539-545.

Harrison, B. A., and Jupp, D. L. B. (1989). *Introduction to Remotely Sensed Data. Part ONE of the microBRIAN Resource Manual* (156 pages). CSIRO Australia, Melbourne.

Roelfsema, C., and Phinn, S. R. (2015). *The Remote Sensing Toolkit* Retrieved from *http://ww2.gpem.uq.edu.au/CRSSIS/tools/rstoolkit_new/index.html*.

Shaw, G. A., and Burke, H. K. (2003). Spectral Imaging for Remote Sensing. *Lincoln Laboratory Journal, 14*(1), pp. 3-27.

White, D., Petus, C., and Lewis, M. M. (2013). *Temporal dynamics of Spring complexes*. In *Allocating Water and Maintaining Springs of the Western Great Artesian Basin. Volume IV. Spatial Survey and Remote Sensing of Artesian Springs of the Western Great Artesian Basin*. (Eds: M.M. Lewis, D. White, and T.G. Gotch) National Water Commission, Canberra.



2 Imaging Artefacts

The formation of imagery by passive remote sensors is introduced in Volume 1A—Sections 13 and 14 in terms of sensor design, and in Volume 2B in terms of image geometry. In this section, we consider characteristics of those imaging optics that impact imaging fidelity, namely:

- fidelity measures—how well the target object or surface is represented in the image (see Section 2.1);
- aliasing—when the sampling grid misrepresents the spatial patterns (see Section 2.2);
- scaling parameters—implications of sampling the continuous surface of Earth into an image (see Section 2.3); and
- upscaling and downscaling—impact of changing image scale (see Section 2.4).

2.1 Fidelity Measures

A range of measures is commonly used to indicate the fidelity of an imaging system, that is, how well it represents the target object or surface. The following sub-sections introduce some of the most commonly encountered metrics that are used to quantify image 'quality':

- point source metrics (see Section 2.1.1);
- spectral sensitivity—minimum level of radiation that can be detected in selected wavelengths (see Section 2.1.2); and
- signal-to-noise ratio—ratio of target signal to background noise (see Section 2.1.3).

The topic of image quality is considered in greater detail in Biberman (2000), Chapter 22.

But the work of the wise is one thing,
and the work of the merely clever is another.
(Victor Hugo)

2.1.1 Point source metrics

Imaging systems are commonly rated in terms of how they respond to a point input, that is, how well a single point of radiation in the target is imaged. When radiation is emitted from an infinitely small point source, some fraction of that radiation is collected and recorded by the sensor. In a perfect sensor the radiation source would be represented as an infinitely small point in the resulting image. Invariably, however, the detected waves of radiation are 'spread' by convergence and interference (diffraction—see Volume 1A—Section 2) at the focal point (see Figure 2.1), creating an imaged pattern of concentric rings rather than a point (see Figure 2.2). In a perfect lens, perfectly aligned with a perfectly circular aperture, these rings would be circular. However, in practice, lens distortions, complex apertures and/or poor alignment between the lens and the aperture often create asymmetric representations of the point.

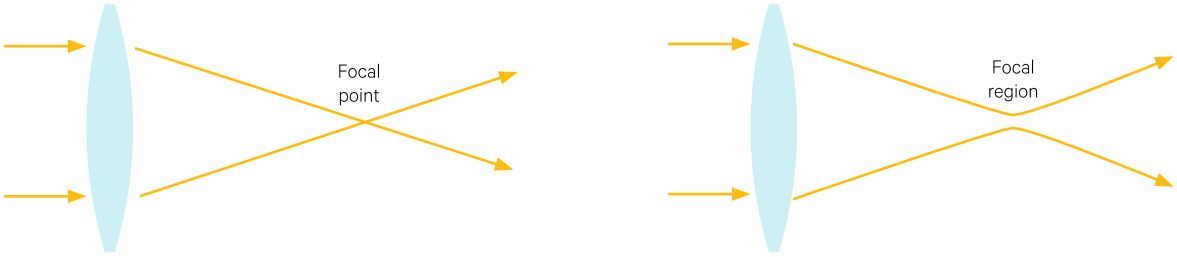
Background image: Landsat-7 image of Macquarie Marshes, in central NSW, acquired on 8 September 2016 (displayed using bands 5, 4, 2 as RGB). This image demonstrates the image striping pattern resulting from inoperation of the scan line corrector (SLC) on Landsat-7, which is more pronounced near the edges of a scene (see Volume 2A). **Source:** Norman Mueller, Geoscience Australia.

Figure 2.1 Geometric versus wave optics

Diffraction limits the width and intensity of the focal point for a beam.

a. Focus based on geometric optics only—focal point is infinitely small with very high intensity

b. Focus based on wave optics—diffraction causes focal point to spread and become a focal region



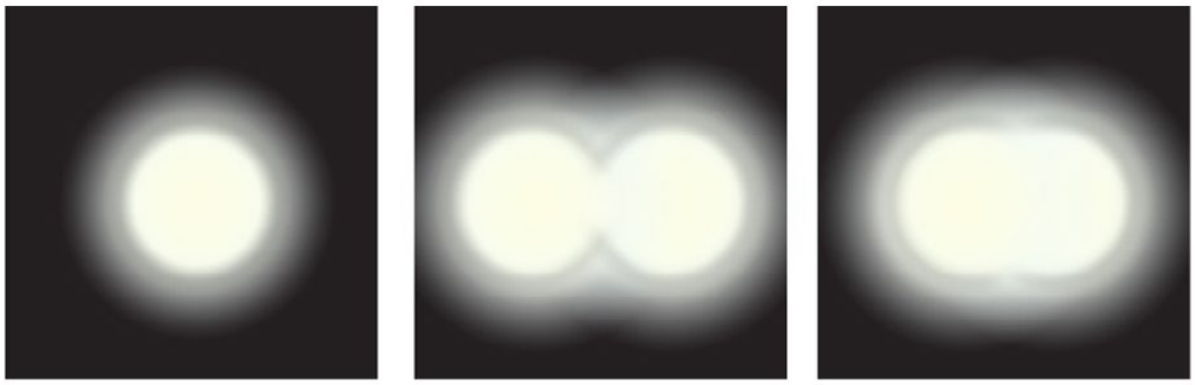
Adapted from: OpenStax, College Physics. OpenStax CNX. 11 February 2017 (CC BY AS 4.0) at: *http://cnx.org/content/m42517/latest/?collection=col11406/latest*

Figure 2.2 Diffraction of point source

a. Diffraction pattern created by light passing through small, circular aperture.

b. Overlapping, but discernible, diffraction patterns created by two, closely located point sources.

c. Diffraction patterns cannot be resolved when point sources are too close together relative to the imaging resolution.



Source: OpenStax, College Physics. OpenStax CNX. 11 February 2017 (CC BY AS 4.0). Retrieved from: *https://cnx.org/contents/9ANhisjh@5/Limits-of-Resolution-The-Rayle*

The pattern that results from imaging a point source is indicative of the way radiance measurements of other targets will be modified when they are imaged. The three most commonly encountered imaging fidelity metrics based on point source behaviour are:

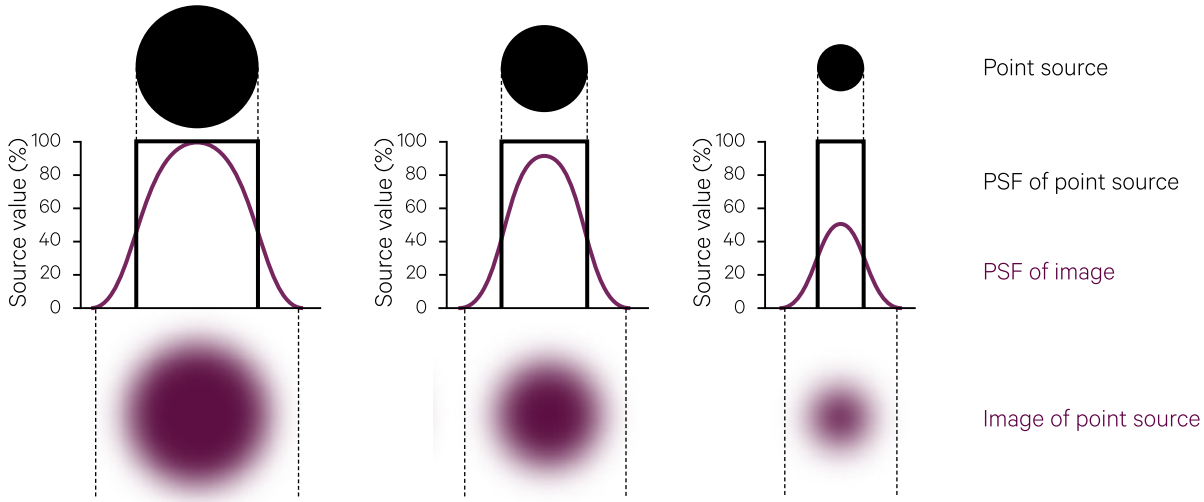
- Point Spread Function (PSF)—the image of a point source (see Section 2.1.1.1);
- Rayleigh's Criterion—minimum resolvable spatial detail (see Section 2.1.1.2); and
- Modulation Transfer Function (MTF)—frequency domain measure of image contrast (see Section 2.1.1.3).

2.1.1.1 Point Spread Function

The response of an imaging system to a point source of radiation can be summarised by the Point Spread Function (PSF), which shows how the imaged radiance is represented in the spatial (as opposed to frequency) domain. The Fourier transform of the PSF is called the Optical Transfer Function (OTF). The PSF can be simply defined as the image of a point source and is related to the spatial resolution limit of the sensor. Ideally the PSF for a defined target would result in a stepped function corresponding to the target size and density. In practice, however, target boundaries are somewhat blurred, gradually transitioning from target to background (see Figure 2.3). This measure is also used to indicate the fidelity of printing.

Figure 2.3 Point Spread Function

The Point Spread Function (PSF) quantifies the spatial representation of a point source when imaged by a sensor. Imaging systems invariably fail to represent object boundaries as clearly as they should appear, resulting in a blurred transition from object to background.



The actual shape of the PSF for a sensor depends on the design and aperture shape of its optical system. For a diffraction-limited system with a circular aperture, the PSF corresponds to the Airy function (see Figure 2.4), in which the central bright disk represents most of the detected radiance from the point source. The angular radius of this central disk can be computed as:

$$\theta = 1.22\frac{\lambda}{D}$$

where

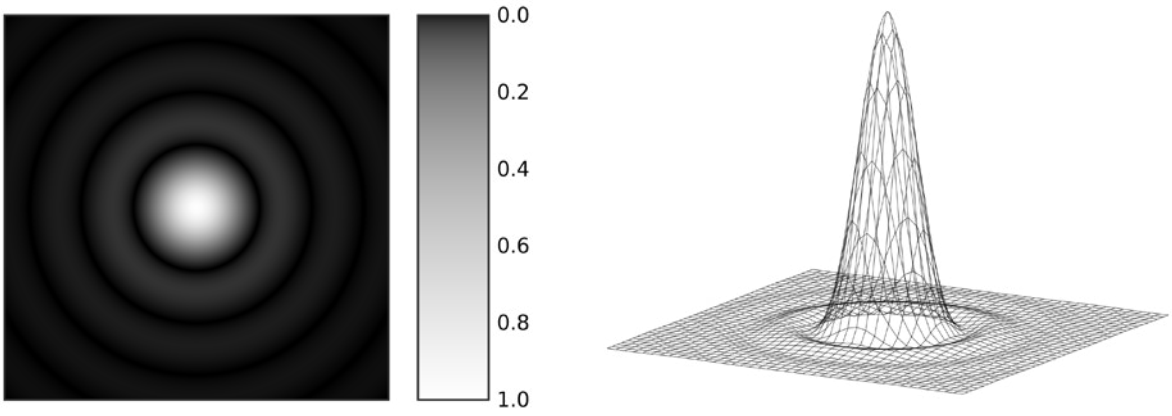
D is the imaging aperture diameter;
λ is the wavelength being imaged; and
θ is the angle of the first diffraction minimum (in radians).

In terms of EO sensors, the PSF for a single pixel would ideally form a stepped function as shown in Figure 2.5a. Figure 2.5b illustrates the modelled PSF for an AVHRR pixel. In this figure, the area representing one pixel spans from -0.5 to +0.5 on the x-axis and 0.5 to +0.5 on the y-axis. Quite clearly, a significant proportion of the radiance recorded for this single AVHRR image pixel originates from the adjacent pixels.

Figure 2.4 Airy function

a. Computer generated image of an Airy disk, with grey scale adjusted to enhance outer rings.

b. Three-dimensional representation of Airy disk pattern.

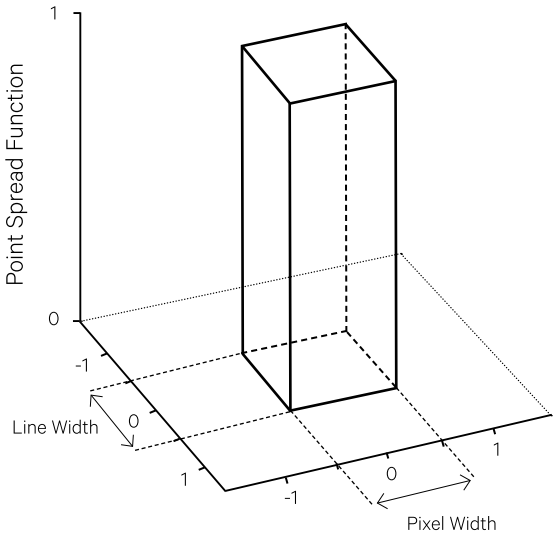


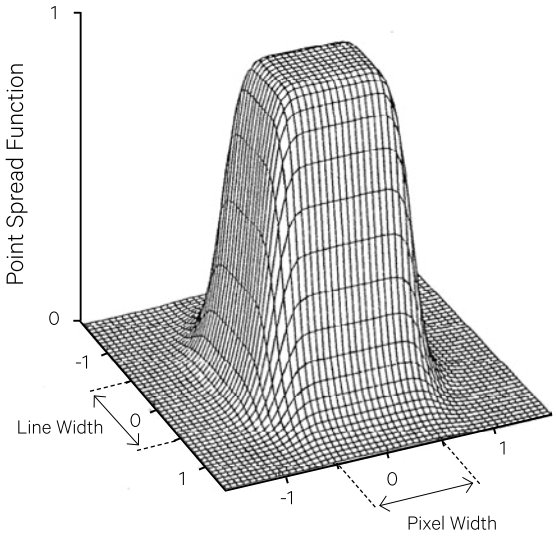
Source: Sakurambo, Wikimedia Commons. a. Retrieved from: *https://commons.wikimedia.org/wiki/File:Airy-pattern.svg.* b. Retrieved from: *https://commons.wikimedia.org/wiki/File:Airy-3d.svg*

Figure 2.5 Examples of Point Spread Functions

a. Idealised PSF—the radiance measured for a single pixel should form a stepped function (Cracknell, 1998)

b. Modelled PSF for AVHRR pixel—X and Y axes in this figure indicate the central pixel covering the area demarked by pixels -0.5 to +0.5 and lines -0.5 to +0.5. A significant proportion of the radiance recorded for this single image pixel originates from adjacent pixels.





Adapted from: a. Cracknell (1998); b. Mannstein and Gesell (1991)

2.1.1.2 Rayleigh Criterion

The term 'resolving power' was introduced by Lord Rayleigh (1842–1919) to describe the quality of optical devices and components (Rayleigh, 1879). As discussed in Section 2.1.1, light diffracts as it travels, and also as it interacts with various objects, including the aperture (see Figure 2.2). Figure 2.6 shows the diffraction patterns that result when radiation from a point source passes through an aperture. The pattern can be viewed as an image of the point source, and its intensity variations can be mapped as a sinc curve.

Assuming that the aperture is large relative to the wavelength of light (λ), the first minimum in the diffraction pattern for a circular aperture with diameter D occurs at:

$$\theta = 1.22\frac{\lambda}{D}$$

(see Section 2.1.1.1). This minimum angular separation can be used to determine the resolving power of an imaging system:

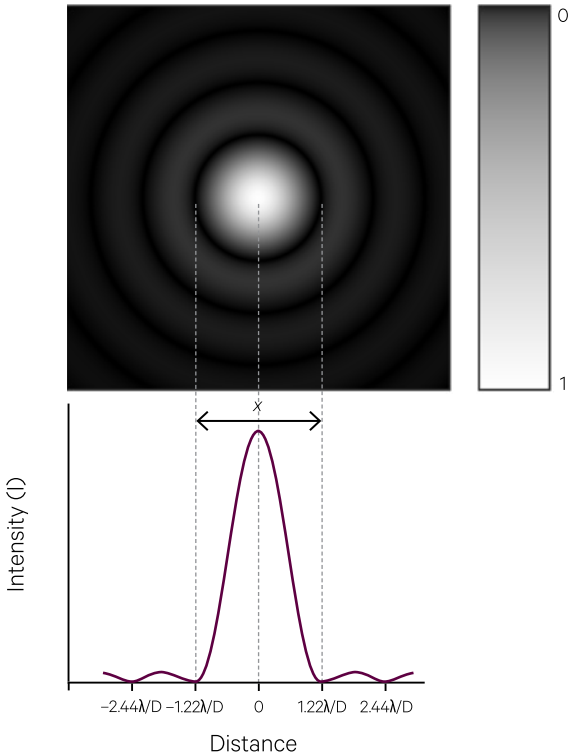
$$x = 1.22\frac{\lambda d}{D}$$

where

d is the distance from the target to the imaging lens.

Figure 2.6 Diffraction pattern

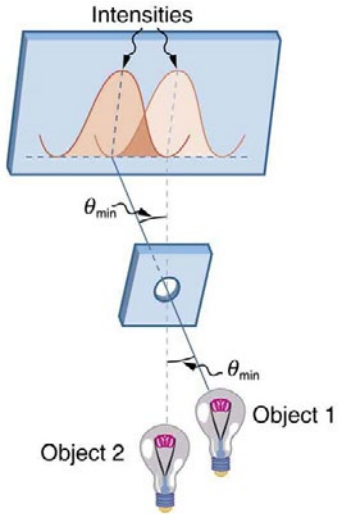
Diffraction pattern intensity graph for a circular aperture is shown. The variations in intensity across the centre of this pattern can be mapped as a sinc curve.



Source for diffraction pattern: Sakurambo, Wikimedia Commons. Retrieved from: *https://commons.wikimedia.org/wiki/File:Airy-pattern.svg*

The Rayleigh Criterion is used to determine the resolving power of imaging systems by analysing the diffraction patterns resulting from point sources. The simplest case of separating diffraction patterns from two point sources is shown in Figure 2.7. The Rayleigh Criterion identifies the point at which the first diffraction minimum of the image from one point source coincides with the image diffraction maximum from the other point source (see Figure 2.8). While the two point sources are still discernible in Figure 2.8b, their proximity in Figure 2.8c exceeds the threshold at which their individual images can be resolved. The rate of spread due to diffraction is also relevant to active remote sensors (such as laser beams or microwave signals) in terms of beam spreading for long-distance transmission.

Figure 2.7 Separating two point sources



Source: OpenStax, College Physics. OpenStax CNX. 11 February 2017 (CC BY AS 4.0). Retrieved from: *https://cnx.org/contents/9ANhisjh@5/Limits-of-Resolution-The-Rayle*

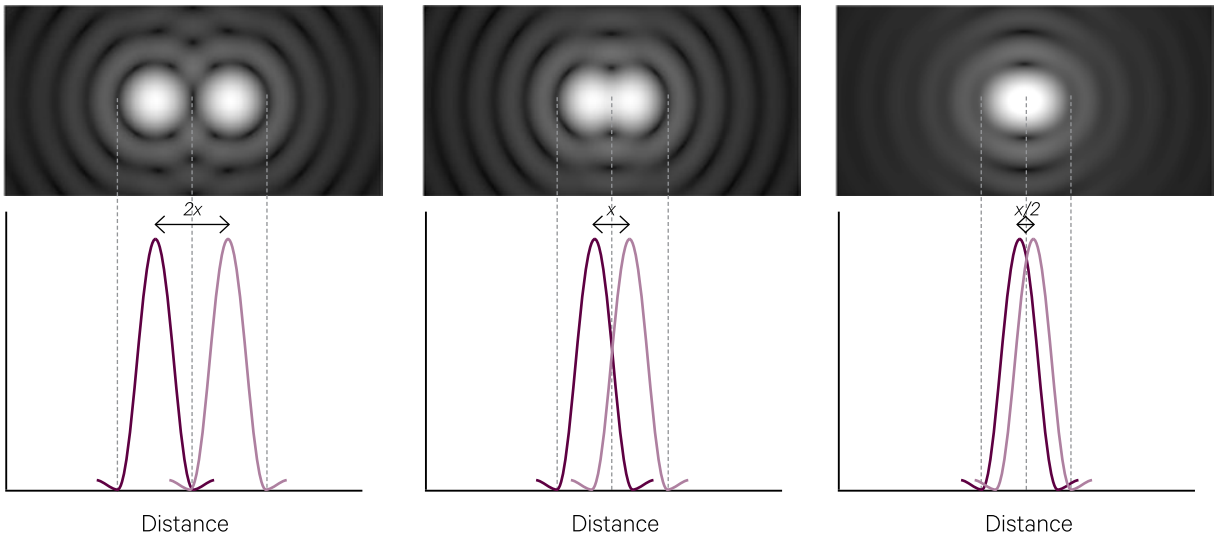
Figure 2.8 Application of Rayleigh Criterion

Two point sources are considered to be resolved by an imaging system when the first diffraction minimum for the image of point source 1 coincides with the maximum of point source 2. As point sources move closer together, relative to the resolution of the optical system, they may not be resolvable in the resulting image. The imaged patterns that result from under-sampling may introduce aliasing effects (see Section 2.2).

a. Two point sources sampled as two separated Airy disks, spaced at twice the distance to the first minimum (see Section 2.1.1.1)

b. Two point sources sampled as two Airy disks that satisfy Rayleigh Criterion for separation, spaced at exactly the distance to the first minimum

c. Two point sources sampled at a resolution that does not allow separation in the resulting image, spaced at half the distance to the first minimum



Source for diffraction patterns: Spencer Biiven, Wikimedia Commons. Retrieved from: *https://commons.wikimedia.org/wiki/File:Airy_disk_spacing_near_Rayleigh_criterion.png*

2.1.1.3 Modulation Transfer Function

The fidelity of imaging optics is most often measured in the frequency domain by the Modulation Transfer Function (MTF)[5]. This function describes how well the imaging optics transfer the contrast, or modulation, of the target into the image (see Figure 2.9). To measure how well an imaging system reproduces the spatial content of an input scene, narrow lines can be scanned to derive a Line Spread Function (LSF) or Edge Spread Function (ESF), which indicates the extent of blurring. The Fourier transform of the spread function is called the optical transfer function (OTF) and the MTF is computed as the modulus of the OTF.

The MTF value for a particular optical component indicates the highest frequency that can be detected. Thus, an image whose range of intensities exactly matches those of the imaged target would have an MTF value of 100%. However, it should be noted that, due to diffraction, even a 'perfect' optical system would not attain the theoretical maximum MTF, especially for larger apertures. This characteristic is independent of focussing errors, in which the MTF is further degraded by blurring. While theoretical MTF graphs suggest that the optical properties of lenses are symmetrical and well defined, significant variability can occur in commercial lenses with different aperture settings and view angles (Atkins, 2007).

Each component within the imaging system, namely the lens, sensor, detector and cables, has an associated MTF, which combine to define the system MTF. Platform movement also contributes to blurring of target objects during the imaging process (Slater, 1980).

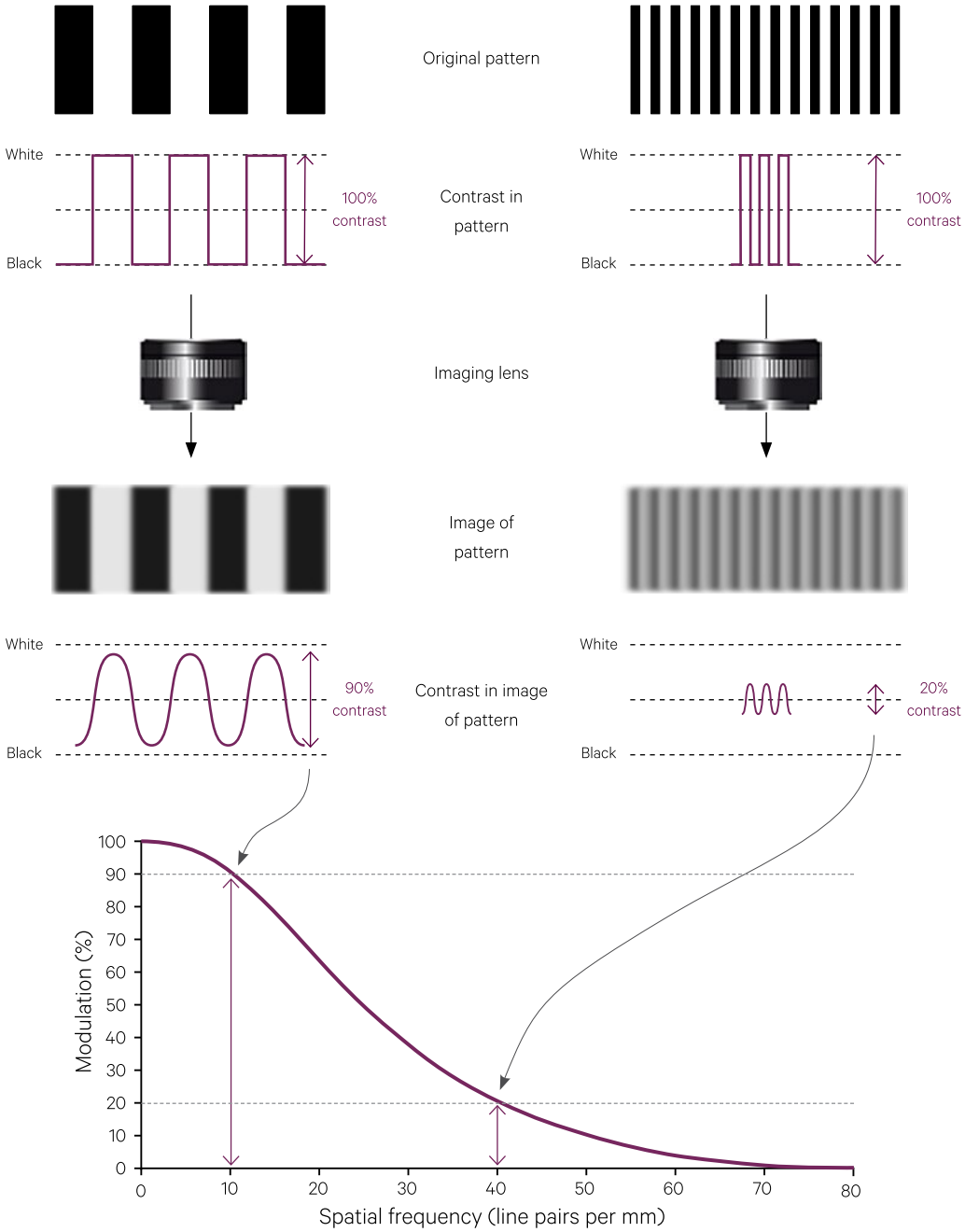
5. MTF can also be described as the square root of the power spectrum of the spread function, or 'intensity' function, with value 1.0 at zero frequency.

Figure 2.9 Modulation Transfer Function

To measure how well an imaging system reproduces the spatial content of an input scene, narrow lines can be scanned to derive a Line Spread Function (LSF) or Edge Spread Function (ESF), which indicates the extent of blurring. The Fourier transform of the spread function is called the optical transfer function (OTF) and the MTF is computed as the modulus of the OTF. The x-axis of the MTF graph shows the spatial frequency as line pairs per mm, where a line pair comprises one black line and one white line.

a. Low frequency patterns retain more contrast when imaged, resulting in a high value for the MTF.

b. High frequency patterns retain less contrast when imaged, resulting in a lower MTF value.



Source: © DxOMark; Reproduced with permission of DxO Labs. Retrieved from *http://www.dxomark.com/index.php/About/In-depth-measurements/Measurements/Sharpness*

2.1.2 Spectral sensitivity

Imaging fidelity results from the performance of multiple components that allow a sensor to quantify the detected radiance. The various components involved in sensor operation have been introduced in Volume 1A—Sections 13 and 14. Methods that quantify the precision of individual sensor components, such as PSF and MTF, have been outlined in Section 2.1.1 above.

In addition to these metrics, each component of an imaging system is designed with specific sensitivity limits, which determine the range of wavelengths that can be detected and the minimum level of radiation that can be measured. The spectral sensitivity of a sensor effectively determines the proportion of incident photons of a given wavelength that it can detect, that is, its quantum efficiency. Examples of the sensitivities of different sensors are shown in Volume 1A—Figures 14.2 and 14.19. These graphs clearly show that some wavelengths are likely to be 'measured' more often than others, potentially introducing spectral bias into the resulting imagery. In non-scanning, imaging sensors, which rely on multiple detectors to sense the radiation for different image pixels, it is also critical that sensitivity is consistent between detectors (see Section 1.3).

2.1.3 Signal-to-noise ratio

To compare the strength of a signal with any background noise, the ratio of their powers is computed by the Signal-to-Noise Ratio (SNR):

$$SNR = \frac{P_{signal}}{P_{noise}}$$

In image processing SNR is often defined as the ratio of the mean pixel value to the standard deviation of the pixel values. For most devices, the SNR increases as the strength of the signal being measured increases. Thus, for imaging devices, the SNR will be lowest in low illumination levels. Again each sensor component contributes to the system SNR.

For example, SNR values for Landsat TM varied from 46 to 60 for visible and NIR channels, and from 36 to 46 for SWIR channels. By comparison, the HyMap airborne hyperspectral sensor achieves SNR values over 500 (for 30° solar zenith angle and 50% reflectance) for all visible, NIR, SWIR and TIR channels (Cocks *et al*., 1998). This means that HyMap data provides significantly better discrimination between features with low (or similar) radiance levels.

Thermal sensors are often rated in terms of the minimum temperature difference they can detect. This rating is called the Noise Equivalent Temperature Difference (NEΔT or NEDT; Norton, 2012). Modern satellite-borne thermal sensors typically have NEDT ratings less than 0.1K (Elachi and van Zyl, 2006). However, increasing the NEDT by decreasing bandwidth (the range of temperatures that can be detected) degrades the MTF (Webb, 2000).

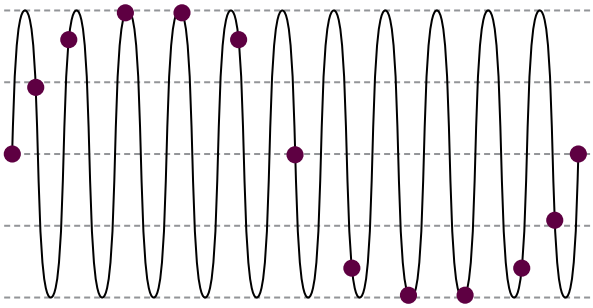
2.2 Aliasing

For all EO imagery, the process of imaging is introduced in Volume 1A—Section 14, and is further considered in Volume 2B in terms of image geometry. This process implicitly involves imposing a sampling grid onto the landscape, which may or may not match the scale of patterns in that landscape. The consequences of sampling affect both the utility of the image data and selection of the most appropriate form of processing.

The impact of sampling frequency is most easily illustrated in terms of a continuous wave pattern, such as a sound wave. When sampling the wave pattern, it is intuitive that the sampling frequency needs to match the frequency of the wave. When this is not the case, a completely different wave pattern would be detected as illustrated in Figure 2.10. In this example, a signal (black line) has been sampled at regular, but less frequent, intervals of time (purple dots). The sampled signal does not represent the frequency of the original wave—it has introduced aliasing.

Figure 2.10 Signal sampling and aliasing

When the sampling frequency (purple dots) does not match the signal frequency (black line), a different signal is detected.



Adapted from: Rick Matthews, Wake Forest University at *http://users.wfu.edu/matthews/misc/DigPhotog/alias/*

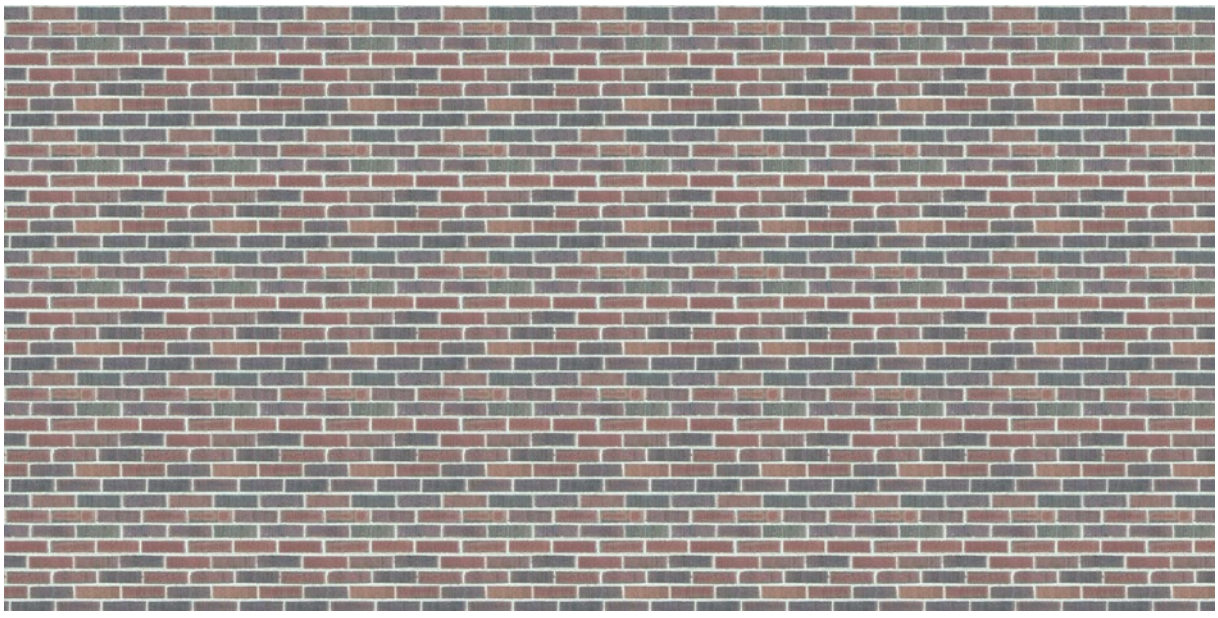
A simple spatial example of aliasing is shown in Figure 2.11 where a regular brick pattern was imaged using a sampling frequency that was not compatible with the scale of the target pattern. In Figure 2.11b, the pixel values of the original image are pre-filtered before sub-sampling (see Volume 2A). The tiny bricks are barely visible and additional periodic pattern has been introduced. Figure 2.11c shows a sub-sampled image without pre-filtering, so the resulting image retains the full range of values in the original image. In this case, the frequency of the repeating pattern no longer matches the original bricks.

To avoid common aliasing effects such as moiré patterns and jaggy edges, most current digital cameras use anti-aliasing filters, which effectively blur the subject before it is sampled. By blurring the target, anti-aliasing filters spread the dominant pattern information over a larger area and therefore increase the likelihood that pattern elements will be imaged in adjacent image pixels. In early digital cameras, pixel size was most commonly the limiting factor in the spatial resolution of imagery, but lens design has become the limiting factor in Megapixel (and Gigapixel) cameras.

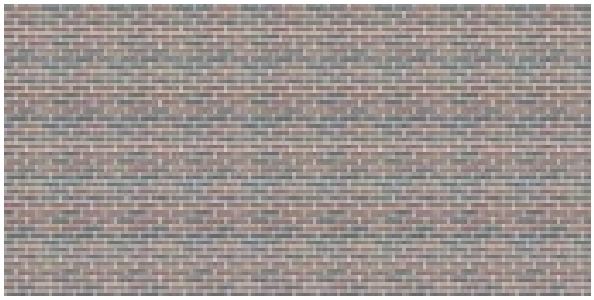
Figure 2.11 Example of aliasing in imagery

A regular brick pattern is imaged using different sampling frequencies:

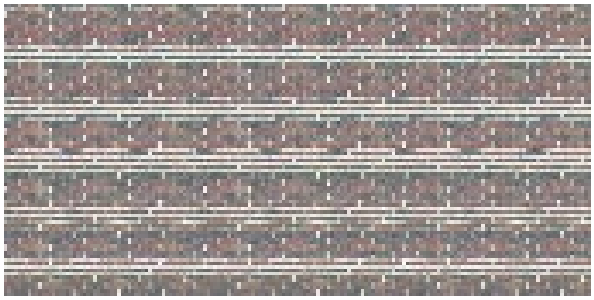
a. Original Brick Pattern



b. Sub-sampling the original image to 1/12th image size after pre-filtering reduces aliasing effects



c. Sub-sampling the original image to 1/12th image size without pre-filtering results in significant aliasing

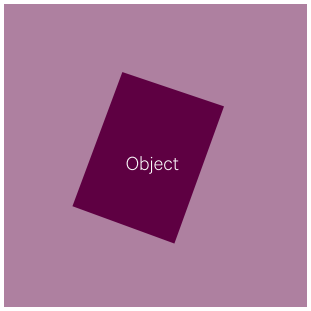


Source: Rick Matthews, Wake Forest University. Retrieved from: *http://users.wfu.edu/matthews/misc/DigPhotog/alias/*

Figure 2.12 Image sampling resolution relative to imaged objects

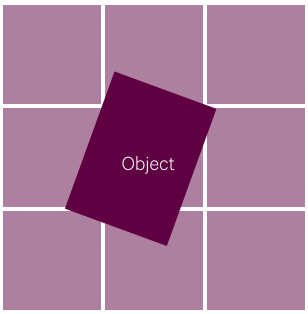
Depending on image spatial resolution, a single object can be imaged by a single pixel, several pixels or many pixels.

a. When the object being imaged is smaller than an image pixel, then sub-pixel techniques are most appropriate



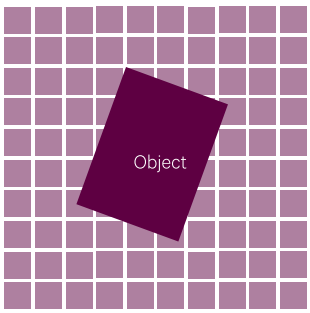
Single 30 m pixel

b. When the size of the object being imaged is similar to the pixel size, then pixel-by-pixel methods are relevant



Nine 10 m pixel

c. When the object being imaged is much larger than image pixels, object-based techniques are most appropriate



One hundred 1 m pixels

While such extreme instances of aliasing are not readily apparent in most EO imagery, the principles of image sampling that lead to aliasing are still relevant. In some cases the scale of remotely sensed imagery involves large pixels that combine several objects into a single pixel (see Figure 2.12a), while in other cases multiple image pixels cover a single object (see Figure 2.12b or Figure 2.12c). As further discussed in Volumes 2 and 3, for each of these relationships between object size and image sampling, the most appropriate scene model(s) and image processing methods will vary for different image spatial resolutions and different types of sensors.

Obviously, the scale at which these interactions occur will differ for different target objects/land covers and different sensors. The interaction between sampling rate and land cover features is demonstrated in Figure 2.13 for a range of EO image sources. These images demonstrate differences resulting from both the imaging technique (lidar, multispectral and panchromatic) and spatial sampling resolution.

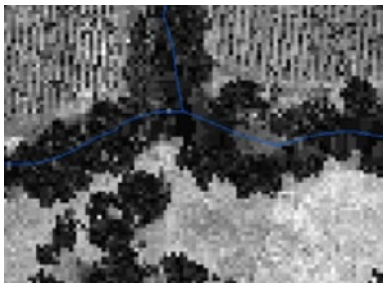
Figure 2.13 Interactions between image sampling and different land covers

Location: 3 km east of Bacchus March, Werribee Catchment, Victoria. The junction of the Lerderderg and Werribee Rivers is shown as a thin blue overlay.

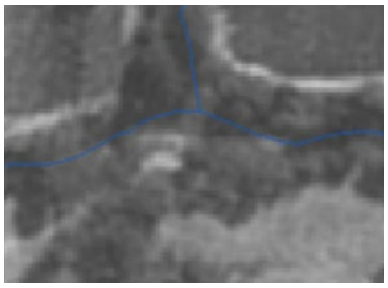
a. Ultracam image—0.25 m pixels



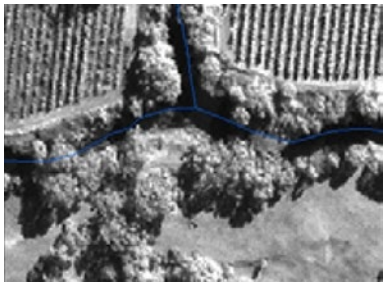
b. Lidar image—2.5 m pixels



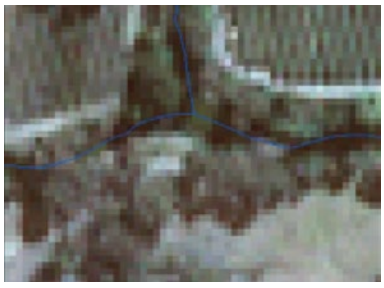
c. SPOT Panchromatic image—2.5 m pixels



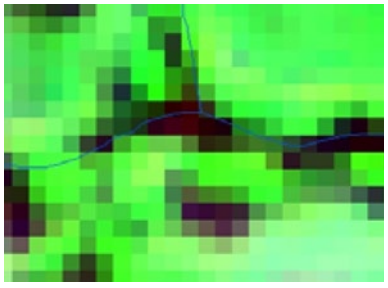
d. Ikonos Panchromatic image—1 m pixels

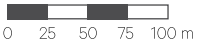


e. Ikonos MSS image—4 m pixels



f. SPOT MSS image—10 m pixels





Source: Johansen *et al.* (2009). Image data were provided by DSE, Victoria.

2.3 Scaling Parameters

One of the problems associated with discussing issues of image sampling and scaling derives from differences in terminology between different, but related, fields of study. While similar methods are used to investigate scaling, different fields emphasise different tools, or use different names for the same tools. For example, scaling issues are encountered in the following fields of study:

- geography (cartography; see Section 2.3.1);
- geostatistics (kriging; see Section 2.3.2);
- optics (remote sensing; see Section 2.3.3);
- linear systems (electronics; see Section 2.3.4); and
- Earth Observation (remote sensing; see Section 2.3.5).

Each of these disciplines acquires each dataset at a particular scale. Three fundamental aspects of spatial scale that are relevant to any dataset are the:

- area of coverage—the spatial extent of the whole dataset;
- level of detail—the area of focus for a single data sample; and
- density—the number of data samples per unit distance or area.

The following sub-sections briefly discuss the mechanisms for sampling, and the resulting scaling parameters, in each of these fields. The impact of upscaling and downscaling operations on EO imagery is specifically discussed in Section 2.4.

2.3.1 Geography

The implementation of geographic scale is strongly influenced by the historical methods used for representing detailed information on a paper map. When a mapping exercise covered a large area, the map scale generally decreased, and thus required cartographic generalisation (that is, simplification of annotation, contour lines and other spatial attributes). With the advent of digital maps, however, such simplification implicitly changes the spatial frequency of the digitised map data, and any derivative datasets.

A key question for geographical data relates to how information at one scale can be used to infer information at another (see Section 2.4). For example, how will a Digital Elevation Model (DEM) derived from a 1:100,000 contour map differ from one based on a 1:1,000,000 contour map? When DEMs are used to compute differential datasets (such as slope or curvature) or integral datasets (such as catchment areas and stream lengths) the impact of the original scale selection flows on to these products.

The distinction between 'grid systems', in which data are sampled on a grid, and 'grid cell systems', in which samples of data are integrated over the area nearest to the grid point, needs to be carefully considered in digital analyses of geographical data. Such concepts are addressed by Cliff and Ord (1981) and further discussed in Volume 2.

In terms of traditional geographic map data, the three fundamental spatial aspects equate to:

- coverage—map sheet;
- level of detail—degree of simplification; and
- density—resolution of data.

2.3.2 Geostatistics

Geostatistics uses statistical methods to understand spatial patterns in point samples for geological applications. Traditionally these methods were developed to estimate the likelihood of large ore deposits based on ore samples at discrete locations. A range of methods to interpolate irregular point samples on the basis of their spatial correlation resulted from the work of Matheron (1971). These methods are now used in a wide range of applications, including mining, hydrology, lithology, epidemiology, entomology, and forestry.

Two of the major tools used in Geostatistics are the semi-variogram (Skøien and Blöschl, 2006) and kriging (Krige, 1951), as further discussed in Volume 2. The three aspects of spatial data recognised by Geostatistics are:

- coverage—area within which samples are located;
- level of detail—the 'support' or volume in which the data apply; and
- density—the distance between samples.

2.3.3 Optics

One aspect of optics involves manipulating light through apertures, lenses and optical filters (Born and Wolf, 1963). As detailed in Volume 1A—Section 13 and Volume 1X—Appendix 4, optical data can be recorded photographically or electronically. Each recording method introduces slightly different limits on resolution. Since the grain size in photographic film is very small, its resolution is most limited by the selection of aperture, lens and focus, whereas the resolution of mega-pixel digital cameras is primarily limited by the size of the detector/sensor element (commonly, but erroneously, referred to as the pixel size) and optical focus.

Resolution in optical systems is often quantified by imaging defined lines in an input pattern then measuring their spacing in the resulting image or photograph (see Figure 2.9). The standard measures of how well an optical system retains feature contrast in an output image are the Point Spread Function (PSF—see Section 2.1.1.1) and the Modulation Transfer Function (MTF—see Section 2.1.1.3). The PSF operates in the spatial domain (that is, using the visible spatial patterns in the image) while MTF operates in the frequency domain (that is, using the frequency of patterns embedded in the image).

When the resolution of the optical system is too coarse to capture the spatial detail in the object being imaged, the resulting image will have 'aliasing' effects and the original object cannot be reconstructed from the sampled data (see Figure 2.8 and Section 2.2). Filters are often used to prevent aliasing by downscaling the data before sampling (Biberman, 2000). In this context, filters effectively change the spatial frequency of imagery and are commonly implemented using selected lens and aperture settings.

Some of the tools used by optical engineers include Fourier theory and the sampling theorem. The three spatial aspects relating to optical imagery are:

- coverage—the action of filters during imaging;
- level of detail—the resolution of an optical pixel in digital imagery or the grain size in photographic film; and
- density—the geometric pixel sampling, which may not be the same as the optical pixel size.

2.3.4 Linear systems

Linear systems theory is used to characterise the way certain systems respond to particular input signals (Brown, 1965). This is relevant to linear sequences encountered in electronics, neuroscience and signal processing. Interpolation and reconstruction of sampled time series are treated as electronic systems.

The tools of Linear Systems include Fourier and Laplace Transformation Theory, differential equations, Sampling Theorem and Shannon's Information Theory. The three aspects of spatial data in terms of Linear Systems are:

- coverage—the length of the data series;
- level of detail—the band width of the system; and
- density—the sampling rate of the system.

2.3.5 Earth Observation

EO scientists refer to the:

- Instantaneous Field of View (IFOV) of a sensor to mean the area averaged into the sensor[6]; and
- Ground Sampling Distance (GSD) to indicate the separation between these areas on the ground (see Section 1.2 and Volume 2B).

If the GSD is no larger than the IFOV then there is little aliasing, and most remote sensing systems are designed to achieve this balance.

While the IFOV is commonly cited as a measure of spatial resolution, more reliable estimates of spatial resolving power are based on the PSF (Mather, 1987; see Section 2.1.1.1). Highly contrasting objects within an optical pixel, such as rivers, roads and buildings, are often imaged as brighter or darker than their surrounding pixels in an image, and thus change the amplitude of the PSF. Such features may be discernible in EO imagery when their actual size is smaller than the IFOV. The Effective Instantaneous Field of View (EIFOV) is defined as the spatial frequency corresponding to half the maximum MTF value and has also been used to estimate the spatial resolving power of EO sensors (Townshend and Harrison, 1984; Mather, 1987). Stein *et al*. (2002) provide a good summary of tools used for spatial analysis of EO data, some of which are considered in Volume 2.

The three spatial aspects in EO data are:

- coverage—the field of view (FOV);
- level of detail—the effective instantaneous field of view (EIFOV); and
- density—the ground sampling distance (GSD).

In EO terminology, coverage of an image is more commonly referred to as its extent and the level of detail in an image is usually referred to as its spatial resolution. While the above discussion equates sampling density to the GSD, over the whole area of coverage it is directly related to the number of pixels and lines in an image. These concepts are also addressed in Section 1 above in terms of the spectral, spatial, radiometric and temporal dimensions of EO data.

6. This is sometimes specified as the solid angle used by the sensor for a single data point (see Volume 1A—Section 13).

2.4 Upscaling and Downscaling

Various geophysical studies measure parameters at one spatial scale then wish to estimate the same property at a different scale. In this context, upscaling describes the reduction of spatial data, while downscaling attempts to interpolate the data points. The three properties of spatial data discussed in Section 2.3, namely coverage, density and level of detail, define what information can be retrieved by downscaling. Where appropriate, upscaling and downscaling effectively change the density and level of detail in EO data. Extending the data coverage, however, is not a valid operation.

The equivalent terms used by each of the fields of study discussed in Section 2.3 are summarised in Table 2.1. Given these equivalences, the spatial tools developed by related fields of study have proven to be useful for analysing EO imagery (see Volume 2).

The pixel size (or density) is the property with most flexibility to change, so when applied to EO data, upscaling creates larger pixels, that is, ones that cover a larger ground area. This means that sample density is reduced and is equivalent to the display function called zooming out (see Volume 2A). Upscaling either involves aggregation of the 'original' pixels to effectively create larger ones (which may introduce blurring—see Volume 2) or sub-sampling of pixels (which may introduce aliasing—see Section 2.2). If the detail information of the original image values is retained separately (as occurs in various compression and reconstruction algorithms), then an upscaled image could be subsequently downscaled perfectly.

Conversely, downscaling results in smaller pixels, that is, ones that cover a smaller ground area, so sample density increases. This corresponds to the display function called zooming in (see Volume 2A). This process is achieved either by blocking the pixels, so that one original pixel becomes multiple downscaled pixels, or interpolating the pixel values to create pseudo measurements positioned between the original ones (see Volume 2D). However, unless care is taken, interpolation of EO data is ambiguous and can produce misleading information. The issues related to spatial resolution (see Section 1.2 above) are most relevant here.

It should be noted that mapping authorities specify standards for the appropriate scale of presentation of spatial data in terms of positional map accuracy (see Volume 2B). For example, to satisfy the Australian National Topographic Database (NTDB) assumptions for positional accuracy of base/reference material, 90% of well-defined points should be located within 0.5 mm of their true location at the scale of the base map. A comprehensive overview of map accuracy standards (MAS), including details on mapping and map production, is provided by the Intergovernmental Committee on Surveying and Mapping (ICSM)[7].

Table 2.1 Aspects of spatial data

Field of study	Coverage	Level of Detail	Density
Geography	Map Sheet	Generalisation	Resolution
Geostatistics	Extent	Support	Spacing
Optics	Aperture	IFOV, PSF, MTF	GSD
Linear Systems	Data series length	Band width	Sampling rate
Earth Observation	FOV	EIFOV	GSD

7. Intergovernmental Committee on Surveying and Mapping (ICSM): *http://www.icsm.gov.au/mapping/index.html*

2.5 Further Information

Aliasing: *http://users.wfu.edu/matthews/misc/DigPhotog/alias/*

Rayleigh Criterion (OpenStax, College Physics. OpenStax CNX): *https://cnx.org/contents/Ax2o07Ul@9.74:9ANhisjh@5/Limits-of-Resolution-The-Rayle*

National Topographic Database: *http://www.ga.gov.au/mapspecs/topographic/v6/section1.html#DataCaptureAccuracyIntegrityandExtent*

Intergovernmental Committee on Surveying and Mapping (ICSM): *http://www.icsm.gov.au*

2.6 References

Atkins, B. (2007). Modulation Transfer Function. *photo.net*.

Biberman, L. M. (2000). *Electro-optical Imaging: System Performance and Modeling*. SPIE Press, Washington.

Born, M., and Wolf, E. (1963). *Principles of Optics*, Third Edn. Pergamon, New York.

Brown, M. M. (1965). *The Mathematical Theory of Linear System*. Chapman and Hall, London.

Cliff, A. D., and Ord, J. K. (1981). *Spatial Processes: Models and Applications*. Pion, London.

Cocks, T., Jenssen, R., Stewart, A., Wilson, I., and Shields, T. (1998). *The HyMap (TM) airborne hyperspectral sensor: The system, calibration and performance*. Paper presented at the 1st Earsel Workshop on Imaging Spectroscopy, Zurich.

Cracknell, A. P. (1998). Synergy in remote sensing - what's in a pixel? *International Journal of Remote Sensing, 19*(11), pp. 2025-2047. doi:*http://dx.doi.org/10.1080/014311698214848*.

Elachi, C., and van Zyl, J. (2006). *Introduction to the Physics and Techniques of Remote Sensing*, Second Edn. Wiley Interscience, New Jersey.

Johansen, K., Arroyo, L. A., Ashcroft, E., Hewson, M., and Phinn, S. R. (2009). *Assessing the potential for remotely sensed statewide mapping of streamside zone and physical form metrics in Victoria, Australia*. Department of Sustainability and Environment, Melbourne, Victoria, Australia.

Krige, D. G. (1951). *A statistical approach to some mine valuations and allied problems at the Witwatersrand*. (Master's thesis), University of Witwatersrand.

Mannstein, H., and Gesell, G. (1991). *Deconvolution of AVHRR data*. Paper presented at the 5th AVHRR Data Users' Meeting, Tromsø, Norway.

Mather, P. M. (1987). *Computer Processing of Remotely-Sensed Images*. John Wiley and Sons, Chichester.

Matheron, G. (1971). *The Theory of Regionalised Variables and Its Applications*. Les Cahier du Centre de Morphologie Mathematique de Fontainebleu No 5. Ecole Nationale Supérieure des Mines de Paris. Retrieved from *http://cg.ensmp.fr/bibliotheque/public/MATHERON_Ouvrage_00167.pdf*.

Norton, P. (2012). Understanding the NEΔT of tactical infrared focal plane arrays. *Opto-Electronics Review, 20*(3), pp. 275-278. doi:*http://dx.doi.org/10.2478/s11772-012-0039-5*.

Rayleigh (1879). Investigations in optics, with special reference to the spectroscope. *Philosophical Magazine Series 5, 8*(49), pp. 261-274. doi:*http://dx.doi.org/10.1080/14786447908639684*.

Skøien, J. O., and Blöschl, G. (2006). Scale effects in estimating the variogram and implications for soil hydrology. *Vadose Zone Journal, 5*(1), pp. 153-167. doi:*http://dx.doi.org/10.2136/vzj2005.0069*.

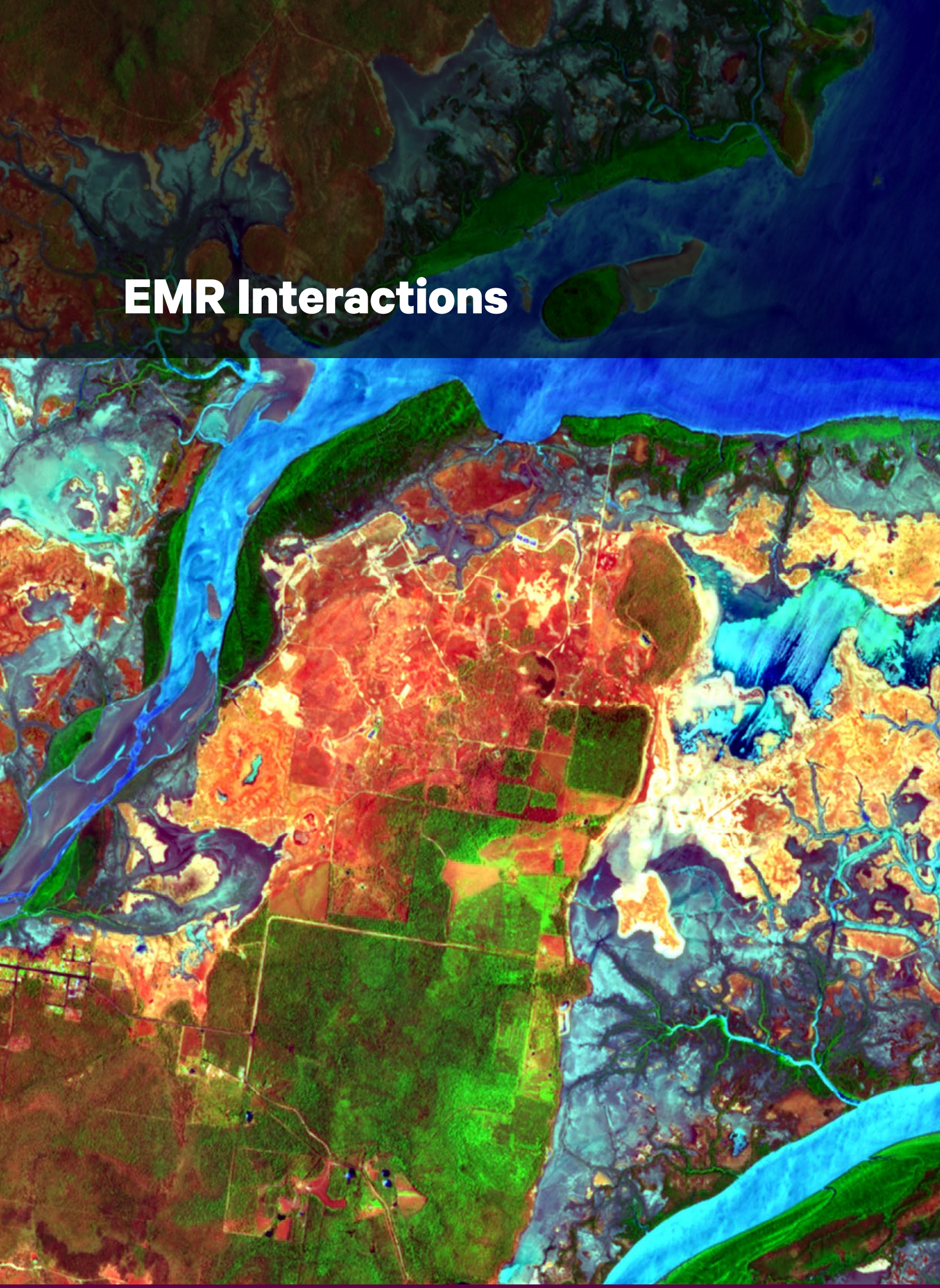
Slater, P. N. (1980). *Remote Sensing: Optics and Optical Systems* (575 pages). Addison-Wesley Publishing Co., London.

Stein, A., van der Meer, F., and Gorte, B. (2002). *Spatial Statistics for Remote Sensing, Vol. 1, Remote Sensing and Image Processing* (284 pages). Springer, Netherlands. doi:*http://dx.doi.org/10.1007/0-306-47647-9*.

Townshend, J. R. G., and Harrison, A. (1984). *Estimation of the spatial resolving power of the Thematic Mapper of Landsat 4*. Paper presented at the 10th Annual Conference of the Remote Sensing Society - Satellite Remote Sensing: Review and Preview, Reading, UK.

Webb, C. (2000). Characterisation of infrared imaging devices. Chapter 9 in 'Electro-optical Imaging: System Performance and Modeling' (Ed: L. M. Biberman). SPIE Press, Washington.

EMR Interactions



Radiance measurements from Earth Observation (EO) sensors do not directly quantify the reflectance of the Earth's surface or atmosphere. EO radiance measurements result from the interactions of EMR with both the target and the atmosphere and are modified by various factors including variations in atmospheric properties, solar properties, illumination geometry, sensor viewing geometry, surface type and surface orientation.

To derive the surface reflectance information from EO measurements, the effects of these interactions need to be removed or normalised to be minimally impacted by changing viewing and illumination geometry. Surface interactions between the illumination source and sensor are commonly considered using appropriate models of the target scene (see Section 3). Imagery can be corrected for atmospheric interactions (described in Section 4) using Radiative Transfer (RT) modelling (see Section 5). Similar models can be developed for water bodies (see Section 5.2) and vegetation canopies (see Section 5.3).

These factors are discussed in greater detail in Sections 6 to 8 for optical, thermal, and microwave imagery respectively. Once corrected, the measured reflected, absorbed or emitted energy in each spectral channel can then be used to estimate and map biophysical properties of the imaged ground features, such as vegetation, atmosphere, soil, water, snow or ice.

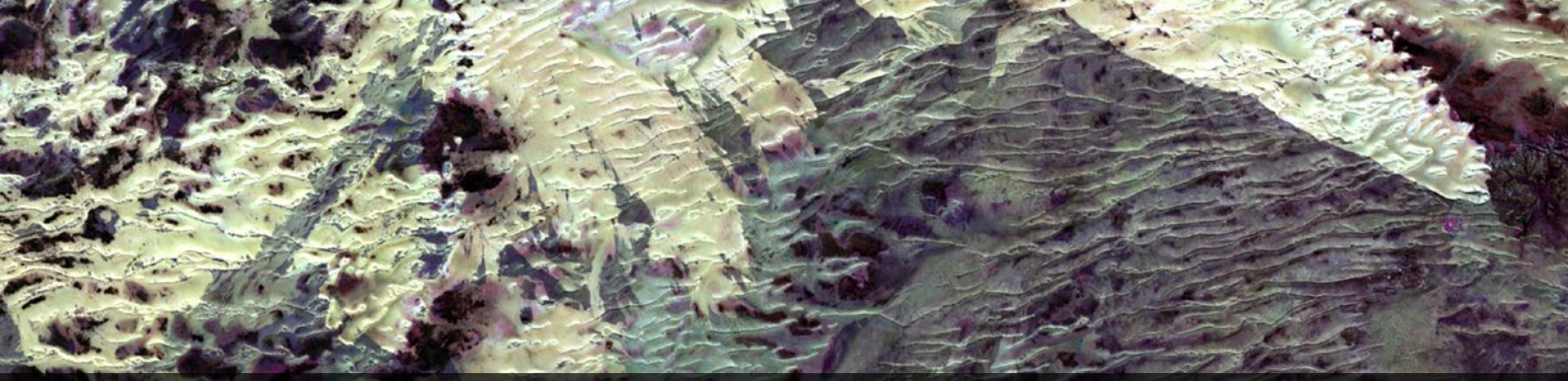
Contents

3 EMR Interactions with Target and Sensor 39

4 EMR Interactions with Atmosphere 61

5 Radiative Transfer Modelling 73

Background image on previous page: This Sentinel-2 image of the coastal town of St Lawrence, in central Queensland, was acquired on 28 November 2015 (displayed using bands 11, 8, 3 as RGB). **Source:** Norman Mueller, Geoscience Australia.



3 EMR Interactions with Target and Sensor

In the discussion below we refer to EMR using the general term 'energy'. To quantify EO observations, however, more precise quantities are required. Commonly encountered radiometric terms are reviewed in Volume 1A—Section 2.6. EO sensors typically measure energy that is reflected or emitted from a target area in a specific direction, within a defined solid angle, and within a finite time period. Accordingly, the radiometric term 'radiance' applies to EO measurements (see Figure 3.1). Radiance is defined by Colwell (1983) as:

The radiant flux per unit solid angle leaving an extended source in a given direction per unit projected source area in that direction

where radiant flux (Φ) is the radiant energy (Q) per unit time (in W).

Radiance (L) is computed in units of W/(sr.m^2) as:

$$L = \frac{\Phi / \Omega}{A \cos\theta}$$

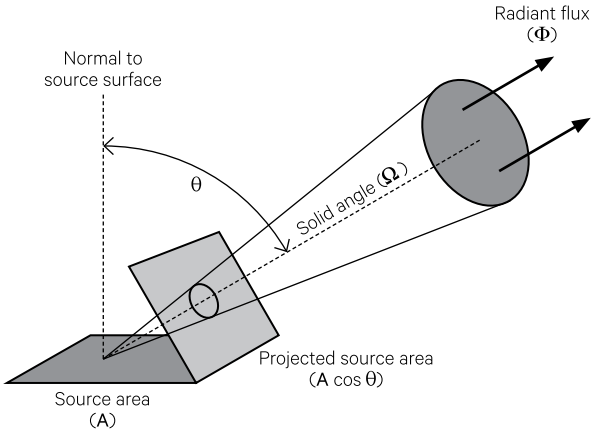
where

the solid angle $\Omega = \frac{A}{R^2}$ for surface area A at distance R (see Volume 1A—Figure 2.1); and

θ is the angle between the radiation direction and the normal to the source surface.

Figure 3.1 Radiometric measurements

The radiance (L) from a source area A is measured in terms of the radiant flux within a specified solid angle in a given direction.



Adapted from: Elachi and van Zyl (2006) Figure 2-10

Other commonly encountered radiometric terms include:

- irradiance (E)—the density of radiant flux upon a unit area of a plane surface (in W/m^2); and
- radiant emittance (or radiant exitance; M)—the density of radiant flux radiated from a unit area of a plane surface (in W/m^2).

Various interactions between incident radiation and the way the target is imaged impact the radiance measured by EO sensors. These interactions vary with the:

- energy of EMR (see Section 3.1)
- target type—land, water or air (see Section 3.2);
- surface reflectance (see Section 3.3);
- volume scattering properties of the target (see Section 3.4);
- positions of the illumination source and imaging sensor (see Section 3.5);
- orientation of the target (see Section 3.6); and
- anisotropy of the target (see Section 3.7).

The impact of atmospheric properties on EO measurements is considered in Section 4.

Background image: Landsat-8 image of fire scars on the dunes near Baker Lake, WA, acquired on 29 June 2013 (displayed using bands 6, 5, 3 as RGB).
Source: Norman Mueller, Geoscience Australia.

3.1 Energy of EMR

The physical mechanisms whereby different wavelengths of EMR interact with, and impact the structure of, matter are summarised in Table 3.1. The precise atomic and molecular interactions vary both with increasing wave energy and the structure of any matter the wave encounters. Resonant effects, such as rotations, vibrations or displacements of electrons, atoms and/or molecules primarily result from higher energy waves (gamma-rays to MIR), with the actual impact of a wave depending on its energy level(s). Non-resonant effects, such as conduction and scattering, predominantly result from lower energy waves (thermal infrared and microwave).

Higher energy waves, such as gamma rays and X-rays invoke atomic and electronic forces (see Volume 1A—Sections 2 and 6), whereas ultraviolet (UV) radiation interacts via electronic excitation and transfer mechanisms. Visible and NIR wavelengths primarily generate molecular vibrations and electronic energy transitions, which can be diagnostic of the chemical composition of matter. Middle infrared waves result in molecular vibrations and rotations (Elachi and van Zyl, 2006).

EO sensors essentially quantify the results of these interactions, such that chemical and physical properties of surface and atmospheric features are then inferred from this information. Examples of information that can be derived from observations of these wave-matter interactions are given in Table 3.2.

Table 3.1 Effects of EMR on matter

EM Spectral Region	Structural Interactions	Possible Effects
Gamma and X-rays	atomic and electronic forces	photoelectric effect Compton effect pair production effect
Ultraviolet	electronic excitation and transfer mechanisms	fluorescence ionisation
Visible and near infrared	electronic energy transitions molecular vibrations	molecular vibration ionic vibration crystal field effects charge transfer electronic conduction
Middle and thermal infrared	molecular vibrations molecular rotations	Si-O stretching vibration vibrational excitation of atmospheric gases
Microwave	molecular rotations	dielectric heating—primarily by water oxygen rotational bands

Source: Elachi and van Zyl (2006)

Table 3.2 Wave-matter interactions relevant to EO

EMR Spectral Region	Major Process(es) of Interaction	Information Derived from EO
Gamma rays X-rays	atomic	radioactive material mapping
Ultraviolet	electronic	atmospheric H and He detection
Visible and near infrared	electronic molecular vibrations	surface chemical composition
Middle infrared	molecular vibrations and rotations	surface and atmospheric chemical composition
Thermal infrared	molecular vibrations and rotations thermal emission	surface constituents surface heat capacity surface and atmospheric temperature
Microwave	molecular rotations thermal emission scattering conduction	surface physical properties surface temperature atmospheric constituents atmospheric precipitation
Radio frequencies	scattering conduction ionospheric effect	surface physical properties sub-surface sounding ionospheric sounding

Adapted from: Elachi and van Zyl (2006) Table 2-2

3.2 Target Type

EO sensors are used to acquire information about the Earth's surface and its atmosphere. As such, the imaged target can be:

- solid surfaces—land, whether bare ground, or covered by vegetation, buildings, snow or ice;
- liquid surfaces—water, both salty and fresh, with varying depth, composition and substrate; and
- gas and plasma—atmosphere, at varying heights, over different surface types.

The energy from an external source that is intercepted by a target is called incident energy (*I*; see Volume 1A—Section 5). This can be either reflected (*R*), transmitted (*T*) or absorbed (*A*) by the target:

$$I = R + T + A$$

where

incident energy (*I*) includes energy from any angle in the hemisphere above the target that is intercepted by its surface;
reflected energy (*R*) includes energy that is reflected or scattered by the surface (and other parts) of the material;
transmitted energy (*T*) simply passes through the material of the target without changing the structure or composition of the material; and
absorbed energy (*A*) may remain within the target material, changing its structure and/or composition, or be re-emitted, usually at a different wavelength.

When energy is emitted from a target, the target can be viewed as the energy source, but emission still depends on absorbed energy from an external source. In equilibrium, there is conservation of energy over all wavelengths with absorption balancing emission. Absorption can change the form of energy (usually converting it to heat) and/or the material. Thus, a photon is unchanged when reflected or transmitted, but experiences an irreversible transfer of energy when absorbed.

This energy relationship applies uniquely to each wavelength of energy and to the total energy over all wavelengths, and is based on the total amount of incident radiation intercepted by a surface. In this context, the incident energy could originate from any angle in the hemisphere above the target (see Appendix 5 for more details).

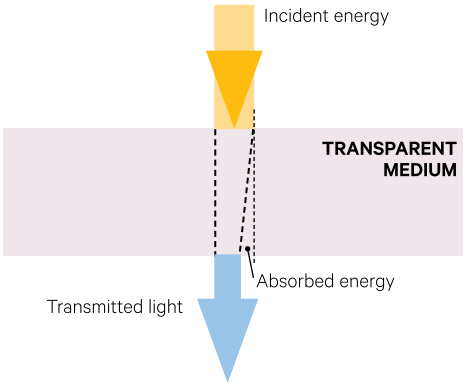
The interaction between incident energy and transparent, translucent and opaque target materials is illustrated in Figure 3.2. It should be noted that materials may appear transparent or opaque only to selected wavelength(s) of energy. Thus, for any target material that intercepts EMR, the proportion of energy that is absorbed, transmitted and reflected, will depend on characteristics of the material, with these proportions varying for different wavelengths (see Section 3.1). Typical reflectance patterns for some common Earth surface materials are illustrated in Figure 1.1.

A typical remote sensing process would involve three components:

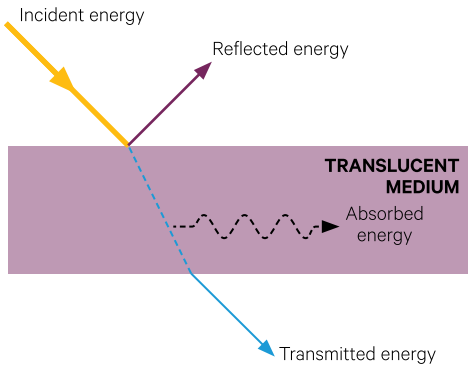
- an energy source;
- a target; and
- a sensor that observes the interactions of the incident energy with the target (see Figure 3.3).

Figure 3.2 Interaction of incident energy with target medium

a. In a transparent medium, most incident energy is transmitted but some is absorbed.



b. In a translucent medium, some incident energy is reflected, some is absorbed and some is transmitted.



c. In an opaque medium, some incident energy is reflected and some is absorbed, but none is transmitted.

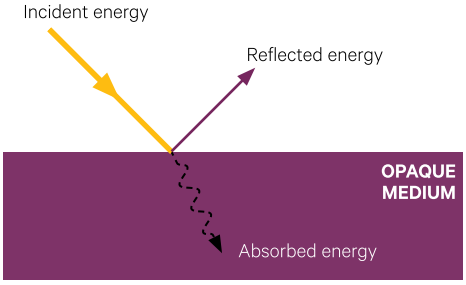


Figure 3.3 Remote sensing of target

To detect reflected energy from a target, the sensor is on same side of target as the energy source.
To detect transmitted energy, the sensor is on opposite side of the target to energy source.
Absorbed energy is inferred as the difference between reflected and transmitted energy.

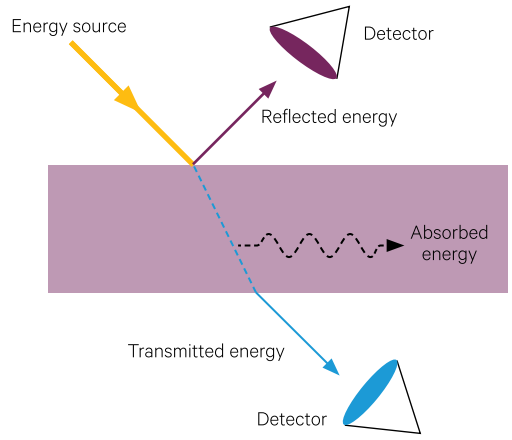
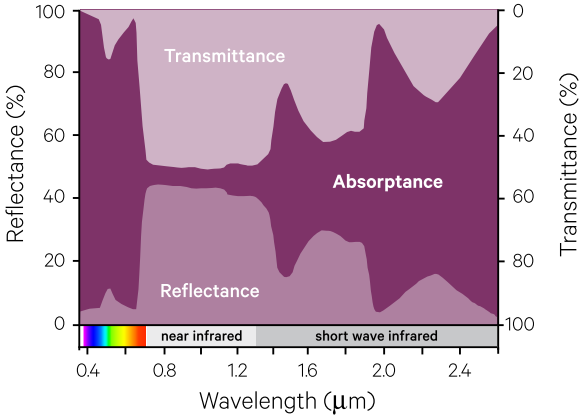


Figure 3.4 Example spectra for *Populus canadensis* leaf

Reflectance = reflected energy/ incident energy
Transmittance = transmitted energy/incident energy
Absorptance = absorbed energy/ incident energy = energy that is not reflected or transmitted



Adapted from: Jacquemoud and Ustin (2008) at *http://photobiology.info/Jacq_Ustin.html*

The interaction of material with EMR can be quantified in terms of its spectra (see Figure 3.4). Different configurations of remote sensing components (radiation source, target material and remote sensor) enable different EMR interactions to be measured:

- to measure reflected energy, the sensor needs to be located on the same side of the target as the energy source;
- to measure transmitted energy, the sensor needs to be located on the opposite side of the target to the source;
- the amount of energy absorbed can be inferred from measurements of reflected and transmitted energies subtracted from the incident energy; and
- to measure emitted energy, that is energy generated by the target material (where the material is the energy source), the sensor can be located in any position around the target.

Each of these types of spectra summarise valuable information about the way EMR interacts with different materials. If, for example, a material absorbs a particular wavelength, a peak will appear in its absorption spectra and a corresponding dip will appear in its reflectance spectra. Such changes are called spectral features and used to identify materials and their components. Absorption spectra are determined by laboratory testing of prepared samples and can be used to characterise the constituents of complex materials, such as leaves, minerals, soils and rocks. Most Earth surface materials emit EMR at wavelengths longer than the optical region.

Spectral libraries for a range of Earth surface features have been compiled to better understand spectral characteristics and the variability of component materials (e.g. USGS, 2011; Chisholm and Hueni, 2015). These libraries are used to identify the most appropriate wavelengths for discriminating between particular materials and to relate the spectral characteristics of materials to their physical properties. They also provide an essential reference standard for calibrating and analysing EO imagery (see Volume 2A—Section 3).

The physical mechanisms underlying the interaction of EMR with matter were introduced in Volume 1A—Sections 2 and 5. Within each type of molecule, specific groups of atoms called functional groups determine the characteristic chemical behaviour of the molecule, including typical patterns for absorption of EMR. The absorption characteristics of functional groups are used by chemists and other scientists, especially geologists, to identify the chemical composition of substances. These characteristics provide the basis for remote sensing. Specific interactions between EMR and target materials are introduced in Section 6, Section 7 and Section 8 for optical, thermal and microwave wavelengths respectively.

Things are not always as they seem;
the first appearance deceives many.
(Phaedrus)

3.3 Surface Reflectance

The texture and shape of a target surface, combined with the refractive index of the target material, determine how waves of EMR are reflected from the surface of a target (see Volume 1A—Sections 2.5.2 and 5.2.1). Surface texture, refractive index, and surface shape contribute to a characteristic known as 'specularity', which describes the reflective characteristics of a surface.

We know from everyday experience that some surfaces reflect more light than others. A glossy, smooth surface, for example, clearly obeys the law of reflection that states:

angle of incidence = angle of reflection

(see Volume 1A—Section 2.5.2). Each facet of a rough surface also obeys the law of reflection with the different orientations of multiple facets resulting in multiple scattering of the incident radiation (see Figure 3.5a).

Another property of a target surface that impacts its reflectance is the target shape. Again, everyday experience demonstrates that a curved shape reflects light differently to a flat surface. In this context, target shape relates to surface undulations that occur at a much greater scale than surface texture.

The final factor determining how much radiation is reflected from a surface is refraction. Depending on the composition and structure of the surface, some of the incident radiation will be refracted into the target material (see Figure 3.5b). This is most apparent for transparent materials, such as water. The relative amounts of reflection and refraction depend on the refractive index of the target material (see Volume 1A—Section 2.5.2). This dimensionless index summarises the impact of a material on the propagation of EMR through it:

$$n = \frac{c}{v}$$

where

n is the refractive index;
c is the speed of light through a vacuum; and
v is the speed of light through the material.

The refractive index of water, for example, is 1.333, which means that EMR travels 1.333 times faster through a vacuum than through water. Fresnel equations can be used to compute the proportions of EMR reflected and refracted from a target surface (Born and Wolf, 1963).

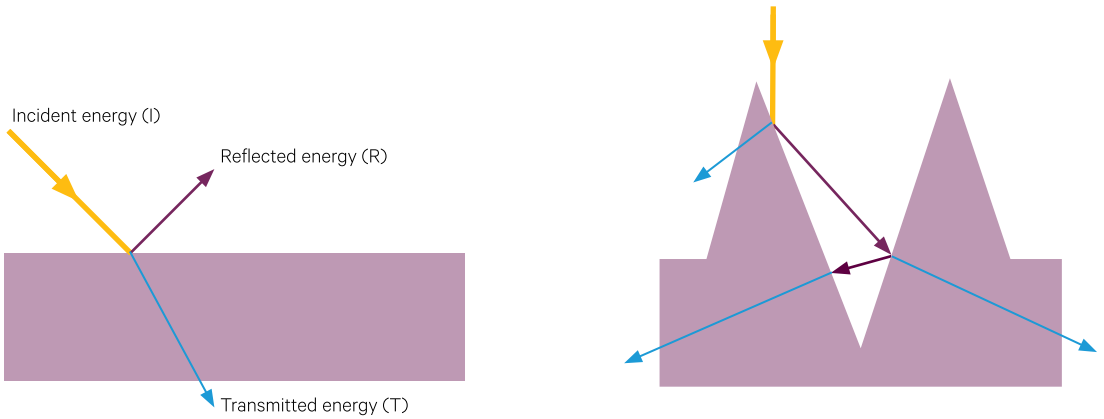
Four potential types of reflector surfaces are differentiated in Figure 3.6. Please note that these textures are relative to the wavelengths of interacting radiation, rather than relative to human vision, so can characterise small particles as well as extensive surfaces.

Figure 3.5 Effects of surface texture on reflection

Each facet of a textured surface, where surface texture is relative to wavelength, reflects incident energy, so that the varying orientations of facets on a textured surface result in multiple scattering of incident energy. Yellow lines indicate incident energy, purple lines indicate reflected energy, and blue lines indicate transmitted energy.

a. Specular reflection from a surface without 'texture'

b. Multiple reflections resulting from surface texture

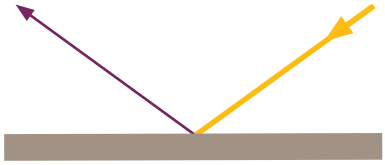


Adapted from: Brown and Arnold (2010)

Figure 3.6 Surface reflectance

Reflectance from a surface is generally not uniform, since it varies with the texture of the surface relative to the wavelengths of incident radiation. Reflectance can vary from specular (totally smooth) to diffuse (totally matt), but most surfaces display characteristics between these two extremes.

a. Specular reflector reflects incident radiation in a single direction, with angle of incidence equal to angle of reflection.



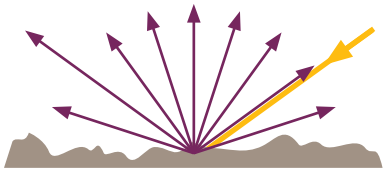
b. Diffuse or Lambertian reflector evenly reflects incident radiation in all directions.



c. Nearly specular reflector reflects incident radiation in a narrow range of directions close to the reciprocal of the angle of incidence.



d. Nearly diffuse reflector reflects incident radiation in most directions, but more strongly in the direction that is reciprocal to the angle of incidence.



A specular reflector, such as a mirror, has a totally smooth surface so that any incident radiation is reflected such that the angle of incidence equals the angle of reflection (see Volume 1A—Sections 2.5.2 and 5.2.1). There are few truly specular reflectors in nature, with most smooth surfaces behaving as 'nearly specular' reflectors. Water is an example of a 'nearly specular' reflector. The waxy coating on some Eucalypt leaves, for example, makes them strong specular reflectors.

A diffuse, or Lambertian, reflector scatters incoming radiation equally in all directions. The mechanism of diffuse reflection is based on both surface texture and absorption properties, whereby most scattered light derives from scattering beneath the surface or from microscopic roughness of the surface. Again, truly Lambertian reflectors do not occur in nature, but some non-reflective surfaces, such as plaster, behave as 'nearly diffuse' reflectors.

In this context, the texture of a surface is relative to the wavelength of EMR, with any given surface appearing smoother or rougher at different wavelengths. Specular, or near specular, reflection results from a surface whose texture or 'roughness' is much smaller than the EM wavelength, while diffuse, or nearly diffuse, reflection occurs when the surface roughness (or surface undulations) is much greater than the EM wavelength. Thus, a surface that is a 'nearly specular' reflector at selected wavelengths, can be a 'nearly diffuse' reflector at other wavelengths.

The appearance of specularity also varies with different lighting and viewing situations. Such variations are described by the Fresnel effect (see Section 3.7.1).

3.4 Volume Scattering

Unlike a simple textured surface whose reflective properties can be described in terms of specularity (see Section 3.3), a composite target scatters incident radiation both internally and externally. In this context, 'volume scattering' describes the sum total of backscattering within a volume of target material, where 'volume' is a three-dimensional space containing the total three-dimensional structure of the target. Volume scattering depends on surface structure and in vegetation it varies with leaf density, leaf angular distributions and total leaf area. Reflectance from water features combine both surface reflectance and volume scattering effects, whereas volume effects dominate reflectance from forest canopies.

As discussed in Section 3.3, the interaction of light with a Lambertian surface, or diffuse reflector, results in uniform radiance in all directions (see Figure 3.6b). Most surfaces have varying levels of texture, which introduce surface scattering and produce different radiance measurements when illuminated and viewed from different positions. For example, the variations in the appearance of mown grass that result from different camera positions are illustrated in Figure 3.7 (Sandmeier and Itten, 1999; Sandmeier, 2000).

Three examples of volume effects are shown in Figure 3.8. Two views of a black spruce forest are shown in Figure 3.8a, the first taken with the Sun behind the camera, the second taken with the Sun in front of the camera. The hotspot effect is clearly visible in the first image, with all surfaces in full illumination, while the second image shows forward scattering and increased shadowing. Similarly, Figure 3.8b shows a soybean field with backscattering when the Sun is behind the camera, and forward scattering and specular reflection on individual leaves when the Sun is in front of the camera. Corresponding differences are also visible when bare, rough soil is imaged with the Sun behind or in front of the camera (see Figure 3.8c). These variations resulting from volume effects are modelled by the bidirectional reflectance distribution function (BRDF; see Section 3.7.2).

Figure 3.7 Image variations due to different observer positions

These images of a soccer lawn (*Lolium perenne L.*) are photographed from five different viewing positions for the same Sun position of 35° (zentih angle) using a FIGOS mounted camera (settings: k = 16, t= 1/15, f = 135 mm, d = 2 m; for details see Sandmeier, 2000).

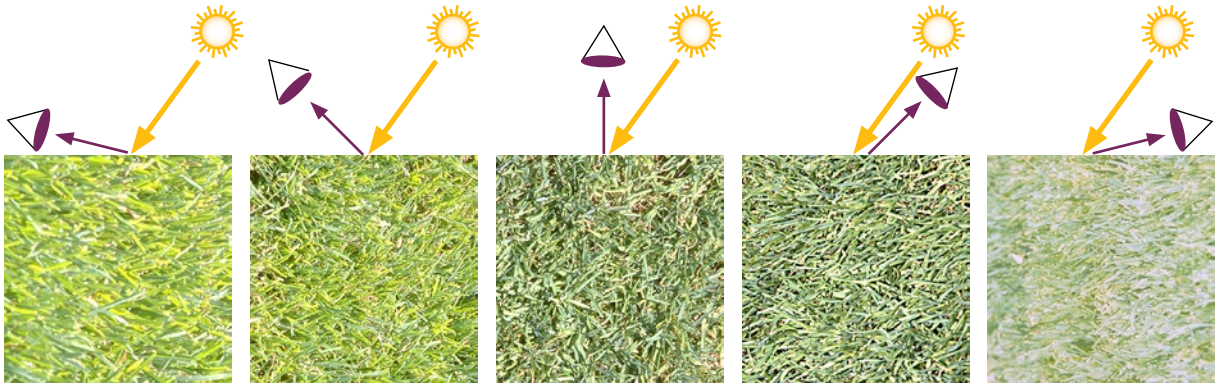
a. Camera view angle = -75° from vertical (forward scattering)

b. Camera view angle = -45° from vertical (forward scattering)

c. Camera view angle = 0° (nadir view)

d. Camera view angle = 45° from vertical (backward scattering)

e. Camera view angle = 75° from vertical (backward scattering)



Source: Stefan Sandmeier, MeteoSwiss. Used with permission.

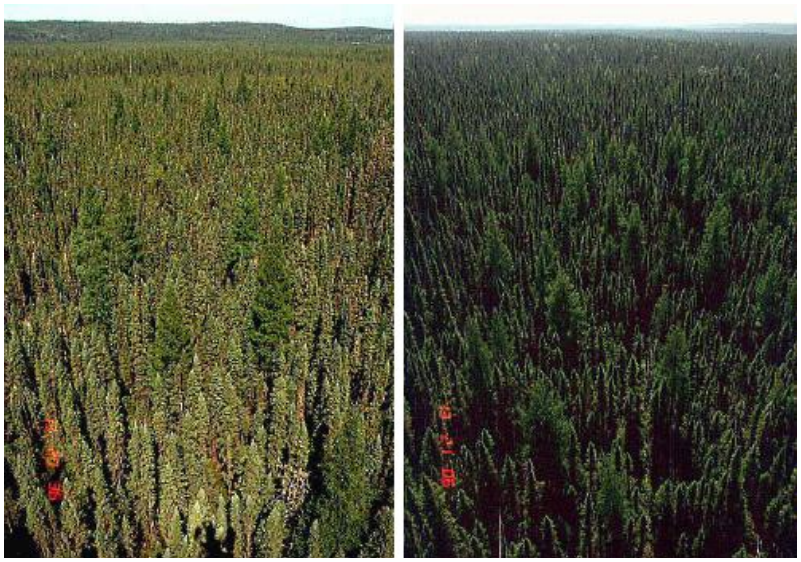
Figure 3.8 Effect of illumination and viewing positions

Left photographs: Sun behind observer—backscattering, some with hotspots
Right photographs: Sun opposite observer—forward scattering

a. Black Spruce Forest, Canada
In a forest canopy, volume effects are dominant.

Left photo (Sun behind observer) shows backscattering and hotspot in foreground where shadows are absent.

Right photo (observer facing Sun) shows forward scattering with shadowed tree centres.



b. Soybean Field

Left photo (Sun behind observer) shows backscattering with minimal specular effects.

Right photo (observer facing Sun) shows forward scattering, with specular reflection from leaves.



c. Rough Barren Field

Left photo (Sun behind observer) shows backscattering from rough texture and hotspot without shadows in the foreground.

Right photo (observer facing Sun) shows forward scattering with specular reflection.



Source: Don Deering, NASA Goddard Space Flight Centre. Retrieved from: *http://www.umb.edu/spectralmass/terra_aqua_modis/modis*

3.5 Illumination and Sensor Positions

This section introduces the basic geometry that is used to describe illumination and viewing positions in EO (see Section 3.5.1), then shows how changes in this geometry impact EO imagery (see Section 3.5.2).

3.5.1 Basic geometry

To define the three-dimensional location of a celestial body, such as the Sun, a star or a satellite, on the celestial sphere, relative to a point of observation on the Earth's surface, standard positions and angles are used. The position of any celestial body can be defined in terms of its zenith and azimuth angles (see Figure 3.9).

The zenith is the highest altitude reached by the body, and is generally equivalent to a position directly overhead the observer, whereas the nadir is the point directly below the observer. Thus, the term 'nadir-looking' implies a viewpoint looking down from the zenith towards nadir. The zenith angle measures the angle between the zenith and the body on the plane they share with the observer. Conversely, the elevation or altitude measures the angle on the same plane from the body down to the horizontal plane. Note that the zenith angle and elevation sum to 90°.

Table 3.3 Defining illumination and sensor positions

These positions and angles are used to define the location of various bodies above the Earth, such as the Sun, stars or satellites.

Position	Definition	Symbol
Zenith	Point directly above observer	Z
Zenith angle	Angle between zenith and body measured on vertical plane through zenith, observer and body	z or θ
Nadir	Point directly below observer	
Elevation or altitude	Angle between horizon and body measured on vertical plane through observer	h or α
Azimuth	Angle between reference direction (usually North) and horizontal projection of body measured clockwise from reference direction (usually North)	A or ϕ

The azimuth is the angle between a reference direction on the horizontal plane, generally North, and a line between the observer and that point on the horizontal plane directly below the body. Standard symbols used for these angles are summarised in Table 3.3.

For example, the solar azimuth is the horizontal direction of the Sun from an observer while the solar zenith angle and the solar elevation both indicate how high the Sun is positioned above the horizontal plane.

Figure 3.9 Zenith and azimuth

a. Zenith is the position directly above an observer. Nadir is the position directly below an observer, opposite the zenith. The azimuth is the angle between a reference direction on the horizontal plane, generally North, and a line between the observer and that point on the horizontal plane directly below the body.

b The zenith angle is measured from the vertical whereas elevation is measured from the horizontal.

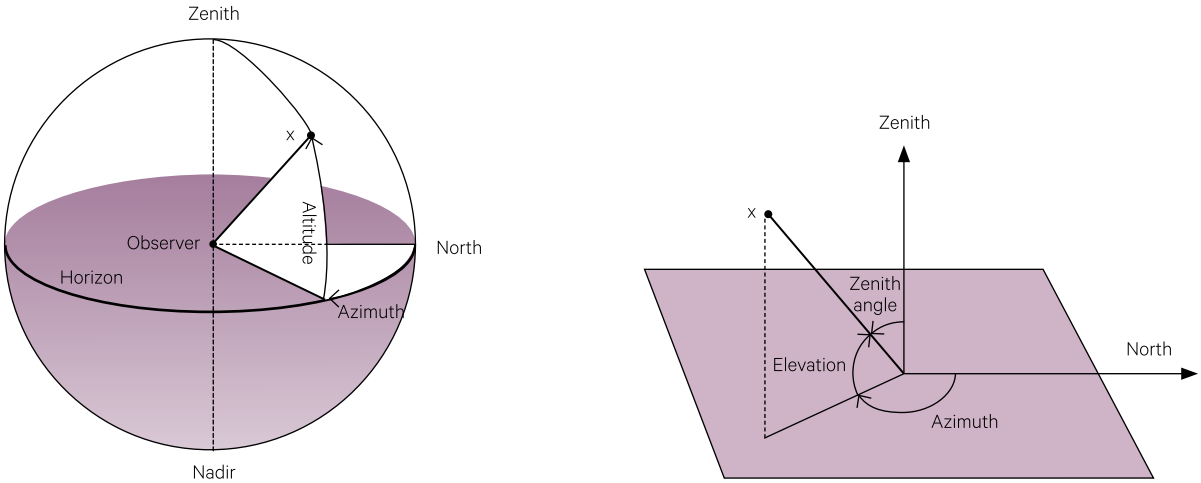
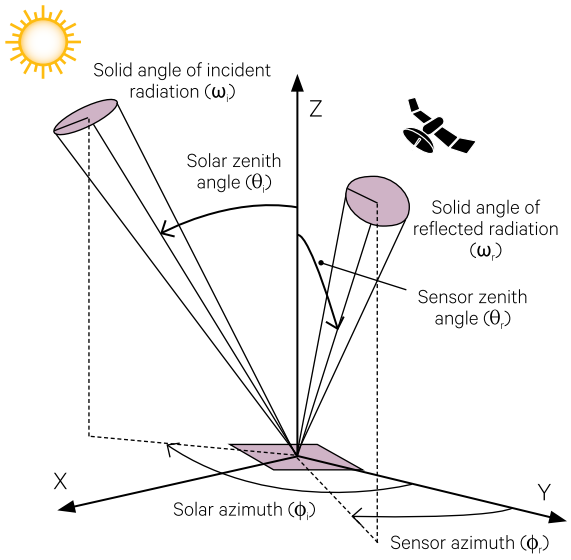


Figure 3.10 Geometry of illumination and viewing positions

The basic geometry of a passive EO sensor viewing reflected solar radiation from an illuminated target surface is shown.



These reference positions are used to define the basic geometry of illumination and viewing positions for EO as illustrated in Figure 3.10. For an illuminated target, this figure shows the angles associated with the position of the illumination source (θ_i and ϕ_i) and the viewing device (θ_r and ϕ_r) for the solid angles of incident radiation (ω_i) reaching a horizontal surface and the reflected radiation (ω_r) from that surface (see Volume 1A—Section 2.3.5).

3.5.2 Application to EO

In recent years, the importance of correcting for viewing and illumination variations in remotely sensed imagery has come into sharper focus. Since most medium resolution sensors, such as Landsat TM, scan relatively narrow swaths in a single image path, it has been traditionally assumed that the resulting imagery would display negligible variation in Sun and sensor view angles. However, the Sun and sensor view angles can vary significantly between scenes, so need to be considered when comparing imagery acquired in different seasons and geographic regions (Li *et al.*, 2012).

Accordingly, were multiple images of a particular site acquired with the same sensor, but with different illumination or observing conditions, they would not be directly comparable. This effect is most pronounced for multiple aerial images since, unlike satellite images, they are rarely acquired with identical flight paths and timetables. Satellite imagery acquired at the same time each day, however, is still affected by illumination differences as Sun angle changes through the seasonal cycles (see Figure 1.9 and Figure 3.11).

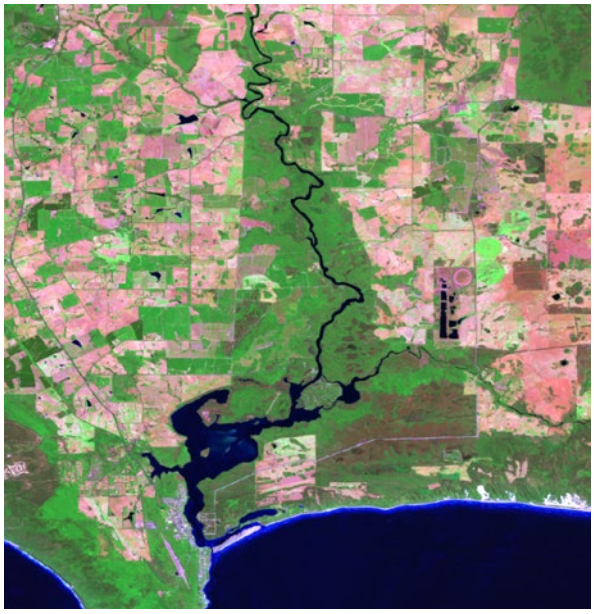
Continental scale sensors, such as MODIS, image much wider swaths in which view angle effects can be quite pronounced. Models that allow these variations to be corrected are introduced in Section 5 and detailed in Volume 1X—Appendix 5 and Volume 2 (see also Montes and Ureña, 2012).

Most EO data is acquired using a vertical (nadir) view angle. However, some satellite and airborne sensors can acquire off-nadir views, which are useful for creating stereo pairs of images, and also for obtaining a higher frequency of satellite images for a particular location (with a greater swath width). Depending on the wavelengths detected, off-nadir sensors can either view, or avoid, aerosol haze. Imagery acquired using an off-nadir view angle incurs additional distortions in terms of image geometry, measured reflectance values, and topographic shadowing. Various algorithms have been developed to account for these distortions and continue to be researched (see Volume 2).

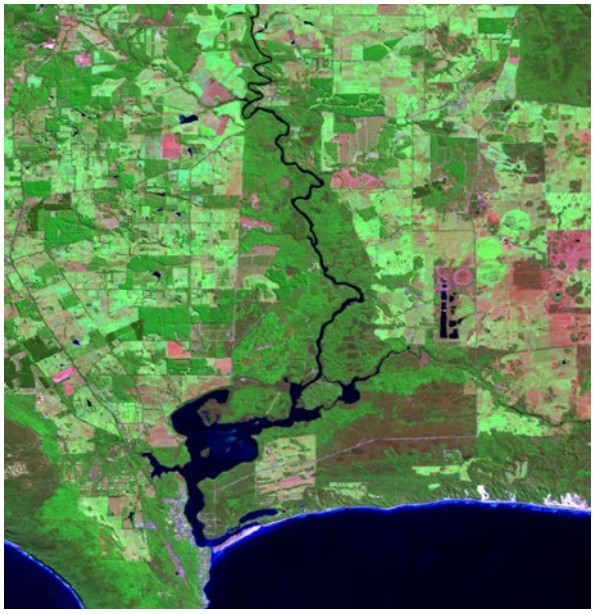
Figure 3.11 Landsat-8 images acquired in four different seasons

Landsat-8 imagery acquired over Augusta, WA, in four different seasons. Images are displayed as false colour composites, with band 6 as red, band 5 as green, and band 3 as blue.

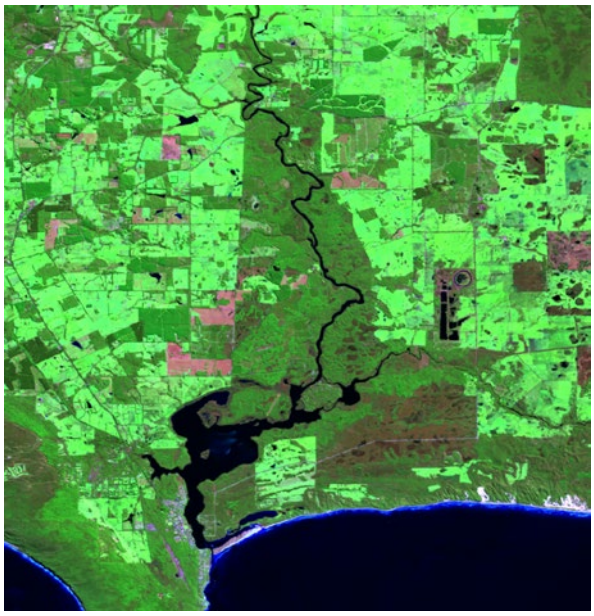
a. Summer—13 January 2015



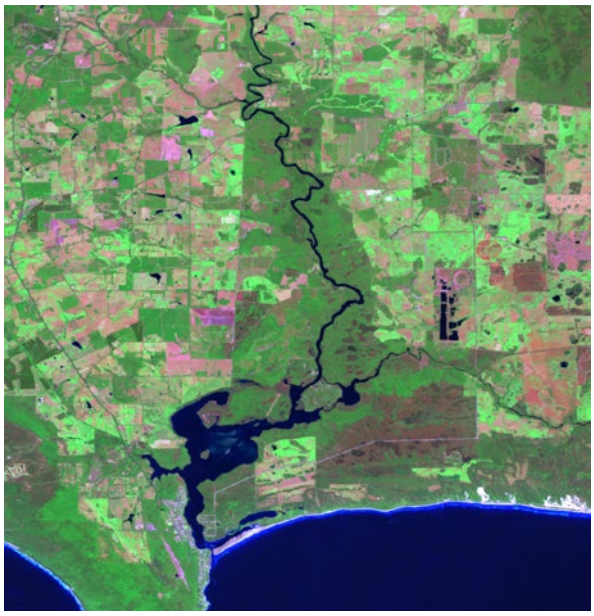
b. Autumn—19 April 2015



c. Winter—25 August 2015



d. Spring—13 November 2015



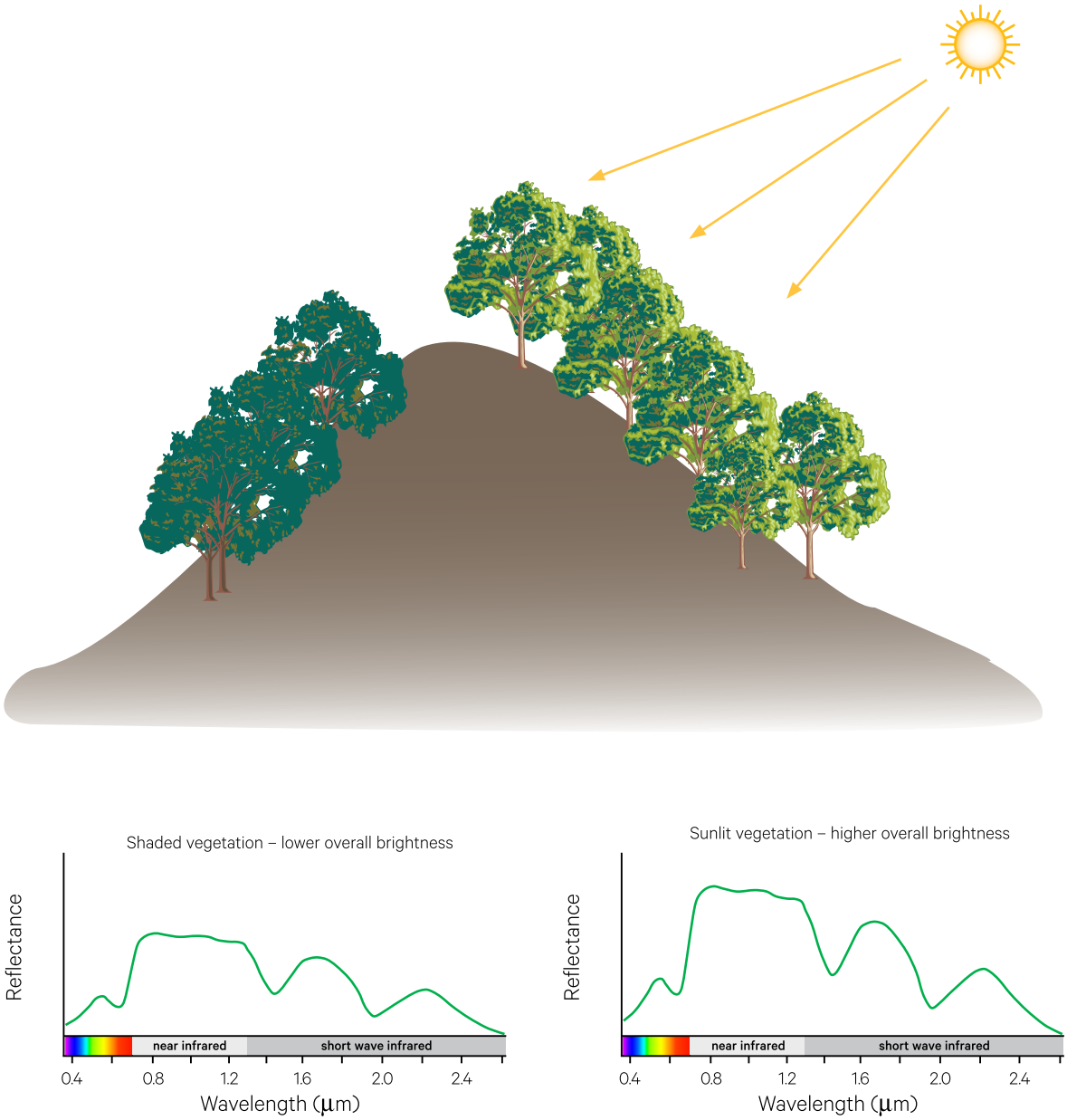
Source: Norman Mueller, Geoscience Australia

3.6 Surface Orientation

The orientation of a target surface relative to both the illumination and viewing positions will impact both the irradiance reaching the target and the radiance being reflected from it. This will impact the measured radiance for a given surface type situated in different topographic positions as illustrated in Figure 3.12. This effect is clearly visible in the Landsat image of vegetation in the Adelaide Hills shown in Figure 3.13.

Figure 3.12 Variations in image radiance due to topography

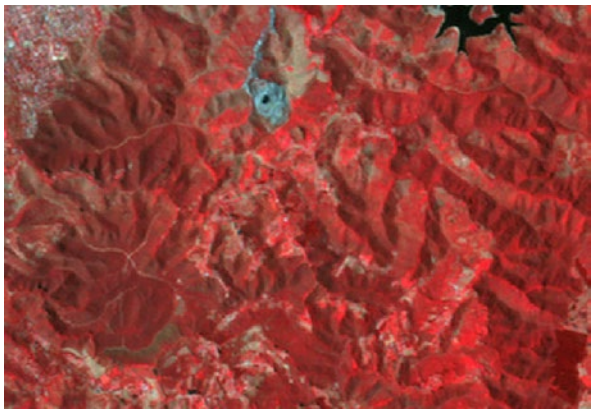
Radiance variations can occur between sunlit and shaded vegetation due to topography.



Source: Megan Lewis, University of Adelaide

Figure 3.13 Impact of topographic shading in EO imagery

This Landsat TM false colour image acquired over the Adelaide Hills in January 2001 clearly shows the difference in solar irradiance on NE and SW facing hillslopes.



Source: Megan Lewis, University of Adelaide

The term 'Sun shadowing' can be used to describe the relief shading produced on the Earth's surface by a particular Sun position. Note that the degree of shading varies both diurnally and seasonally with the changing relative Sun position (see Figure 1.9 for seasonal changes).

When topographic elevation data are registered with remotely sensed data, the Sun shadowing corresponding to the time of image acquisition can be computed to help reduce topographic shading effects in the imagery (see Volume 2). For example, the simple cosine reflectance model defines the radiance (R) of:

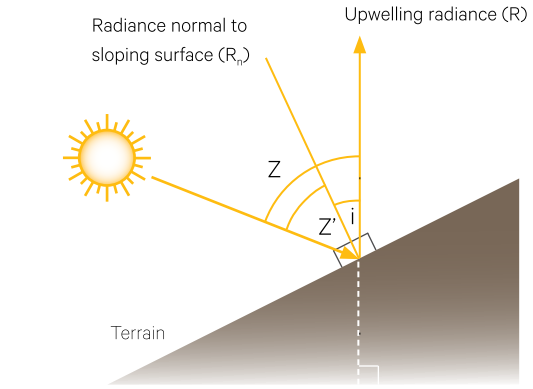
- a Lambertian surface—one with uniformly diffuse reflected radiance; and
- a direct radiation source—with no diffuse radiation as:

$$R = R_n \cos i$$

where

R is the radiance of a target surface;
R_n is radiance viewed in a direction perpendicular to the target surface; and
i is the angle between upwelling radiance and the normal to the surface as illustrated in Figure 3.14.

Figure 3.14 Cosine reflectance model



Source: Harrison and Jupp (1990) Figure 83

This effectively models the surface radiance for a Sun position that is normal (perpendicular) to the Earth's surface with a sensor positioned directly overhead. The radiance can then be modified for other Sun positions using the topographic modulation factor, which is defined as:

$$\max\left(\frac{\cos Z'}{\cos Z}, 0\right)$$

where

Z is the zenith angle of the Sun (the angle from the directly vertical position); and

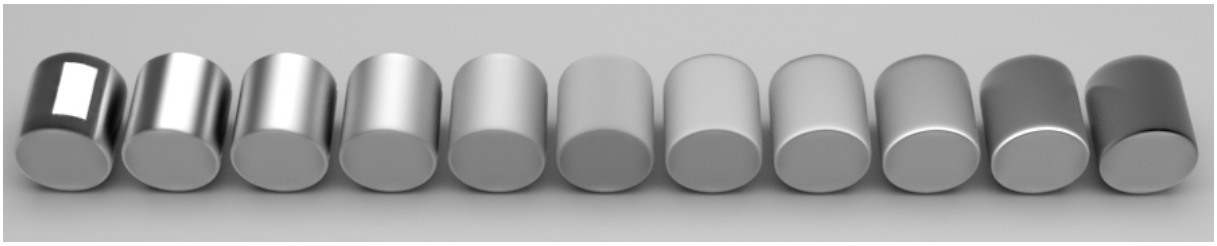
Z is the angle between the Sun vector and the normal to the slope.

The simple model applies without alteration to NIR and SWIR imagery where there is little diffuse radiation. It is not adequate, however, for visible radiance measurements. More sophisticated models which account for diffuse radiation and adjacency effects are detailed by Iqbal (1983) and discussed in Volume 1X—Appendix 5.

3.7 Anisotropy

Figure 3.15 Anisotropy

When identical metal cylinders are illuminated from a fixed light source, their appearance changes with their position relative to the viewer. This rendered image is based on the Ward Duer model, an anisotropic BRDF model for brushed metal effects (Ward, 1992; Walter, 2005) .



We have all noticed that objects can have a different appearance when viewed and illuminated from different directions. The physical and mechanical properties of some materials change with orientation. This characteristic is known as anisotropy. Many fabrics, for example, demonstrate anisotropy by changing appearance when rotated relative to a light source. A simple example of this effect is shown in Figure 3.15, where identical metal cylinders illuminated from a fixed light source all reflect the light to different extents in different positions. This example clearly shows the differences in radiance that can occur when the same object is viewed and/or illuminated from different positions. By contrast, materials with uniform properties in all directions are called 'isotropic'.

In terms of remote sensing, anisotropic surfaces result in differing radiance measurements when viewed from different positions. Anisotropy results from two major components:

- surface reflectance—due to surface roughness and shape combined with the refractive index of the surface material (see Section 3.3). The appearance of surface reflectance depends on the Fresnel effect (see Section 3.7.1); and
- volume scattering—due to radiation that is absorbed by the material (see Section 3.4), and includes hotspot and BRDF effects (see Section 3.7.2).

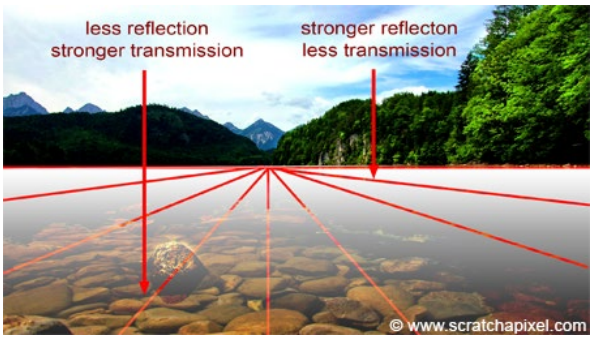
3.7.1 The Fresnel effect

Surface reflectance is governed by the 'Fresnel' effect. Auguste-Jean Fresnel, father of the wave theory of light (1788-1827), observed that the amount of light that appears to be reflected from a surface is determined by the viewing angle. The Fresnel effect describes how changes in observer position impact the perceived reflectance from a surface. This effect is illustrated in Figure 3.16, where reflection of the water surface appears to increase with distance from the observer. This effect is most pronounced when illumination angle is low and the observer is viewing the surface at a similar angle (see Figure 3.16b). These effects are visible in the photo of Cradle Mountain Lake shown in Figure 3.15c.

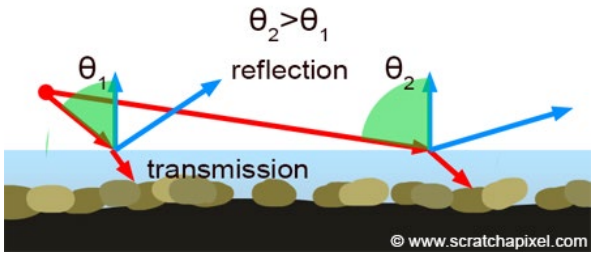
Similarly, different radiance values can be detected for the same surface feature depending on its placement relative to the positions of both the illumination source and the sensor, with the observed difference(s) varying for different illumination wavelengths.

Figure 3.16 Fresnel effect

a. While water is more transparent in the foreground, reflectance from the water surface appears to increase with distance as the effective view angle decreases.



b. The ratio of reflected to refracted light increases as the angle between the view direction and the surface normal increases.



c. Photo of Cradle Mountain Lake, Tasmania, showing a clear view through the water cover in the foreground and increasing reflectance from the water surface as the viewing angle becomes shallower into the distance.



Source: a and b. ©Scratchapixel. Used with permission. Retrieved from: *http://www.scratchapixel.com/lessons/3d-basic-rendering/introduction-to-shading/reflection-refraction-fresnel* c. Taras Vyshnya. Shutterstock image ID 215506168.

3.7.2 Bidirectional reflectance distribution function

Mathematically, the multiple interactions of incident light with any surface can be represented as a single function called the Bidirectional Reflectance Distribution Function or BRDF (Nicodemus *et al.*, 1977). The BRDF 'quantifies the geometric radiance distribution which results from light incident in any direction' (Snell, 2004), and results from anisotropy. It is a function of both the illumination and viewing positions and indicates the intensity and distribution of scattering interactions between the incident radiation and the target. Given the nature of EMR (see Volume 1A—Section 5), the BRDF varies with both the wavelength and polarisation of the incident radiation.

Bidirectional reflectance distribution measurements for a range of surface textures have been used to develop BRDF models that can be used in various applications, including computer graphics and rendering software (Montes and Ureña, 2012). Some of these models only simulate the surface reflections or the Fresnel effects, which depend on refractive index and surface roughness. In most cases encountered in remote sensing, however, Fresnel effects are small and the BRDF is defined by the scattering within the material. While the general definition of BRDF includes both situations, Fresnel effects (specularity) and volume BRDF are usually treated separately. BRDF models can also incorporate a principle of reciprocity, that is, the situation where the intensity is unchanged if illumination position and viewing position are interchanged. When this occurs, the reciprocity is maintained through all potential illumination and viewing positions.

The BRDF defines the distribution of radiance created by an irradiance (see Volume 1A—Section 2.6.1). This form, however, is not what is usually measured in experiments. Typically, in experiments the reflectance factor is the ratio of 'like' quantities such as radiance or irradiance. To distinguish this situation, the name BRF (or Bi-directional Reflectance Factor) can be used. In practice the irradiance on a target can be complicated, involving both direct (beam) radiation and diffused radiation. The nature of BRF will depend on the geometry of the illumination source and the viewing sensor. Some different BRFs will be encountered in Volume 1X—Appendix 5 but for here a simplified approach is sufficient.

Suppose a radiometer measures the radiance of a target from a viewing position, with a narrow (collimated) field of view. The incident radiance for zenith angle θ_i and azimuth ϕ_i can be denoted $L(\theta_i, \phi_i)$. For a given irradiance (Sun in a given position, possibly with some diffuse radiation) the variation of L with view direction changes as BRF. If E is the total irradiance then the reflectance measurement:

$$\rho_t(\theta_v, \phi_v) = \frac{\pi L(\theta_v, \phi_v)}{E}$$

represents the measured BRF. However, this measurement changes with E, and it is sometimes difficult to independently measure E. In practice it is usual to measure L for the target and then L for a diffuse reflectance panel covering the target and form:

$$\rho_t(\theta_v, \phi_v) = \rho_{pan} \frac{L(\theta_v, \phi_v)}{L_{pan}(\theta_v, \phi_v)}$$

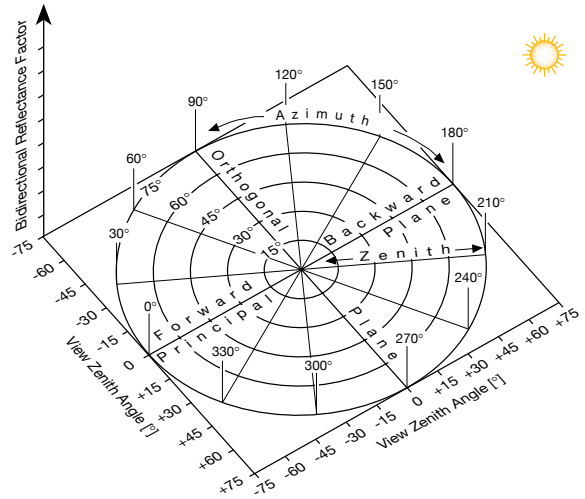
where ρ_{pan} is the reflectance of the diffuse panel. However, the measurement still changes as E changes in nature, such as the amount of Sun versus diffuse sky radiation. Some ways to handle this can be found in Volume 2X—Appendices 1 and 2 but an alternative is to take the measurements into a situation where the illumination and view are controlled and both are collimated measurements.

The collimated BRF measured in this situation represents the range of radiance measurements that result when a surface that is illuminated by a collimated beam from a given position is imaged from all possible viewing positions within a small solid angle of view. In practice the beam and view must have angular widths sufficient to illuminate and view the whole of the sample target.

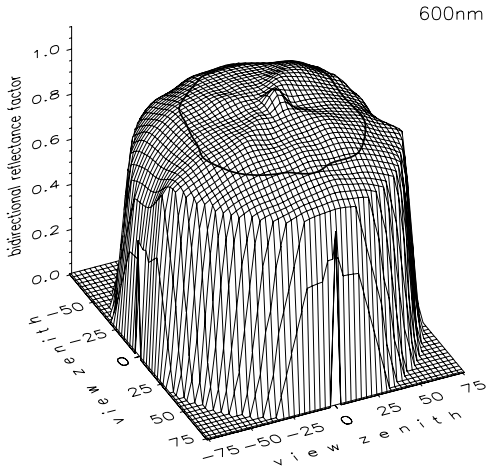
An instrument called a gonioreflectometer can be used to quantify the BRF for collimated illumination and view measurements by using a specific collimated source and measuring a dense, regular sample of viewing positions in a hemisphere above the instrument (Sandmeier *et al.*, 1998a, 1998b). For the selected illumination position and wavelength, the dome of measurements resulting from varying viewing positions can be plotted on polar coordinates (see Figure 3.17a). The three-dimensional BRF plot for a perfect Lambertian surface measured in this way would be close to a flat-topped cylinder, which can be approximated by measuring a cylinder of Spectralon (a highly diffuse surface; see Figure 3.17b). By contrast, the anisotropic nature of reflected radiation from mown grass is obvious in Figure 3.17c, with its measured radiance varying markedly with different sensor viewing positions in the BRF plot (see Figure 3.17d). As illustrated in Figure 3.18, the BRF not only varies for different target surfaces, but also varies with different wavelengths for a given surface. Alternatively, BRF measurements may be plotted as two-dimensional plots using colour to indicate the BRF value. The impact of dying vegetation on BRF plots is illustrated in Figure 3.19. In all of the BRF plots (see Figure 3.17, Figure 3.18 and Figure 3.19), there is a local peak where the view and illumination angles coincide. This point is not the specular point seen in Fresnel reflections but another that is known as the 'hotspot' point. The hotspot point can be seen from an aircraft around the shadow of the aeroplane. It will be discussed further below.

Figure 3.17 Three-dimensional BRDF plots

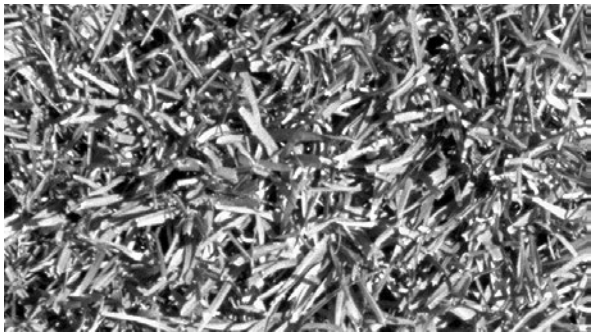
a. Polar coordinate system



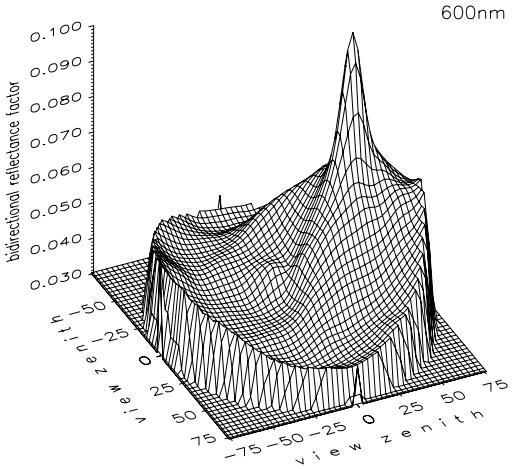
b. BRDF of Spectralon cylinder based on reflectance at 600 nm (highly diffuse surface)



c. Photo of grass surface imaged in Figure 3.17d



d. BRDF of grass surface based on reflectance at 600 nm (solar zenith angle = 35°; viewing zenith angle = 180°)

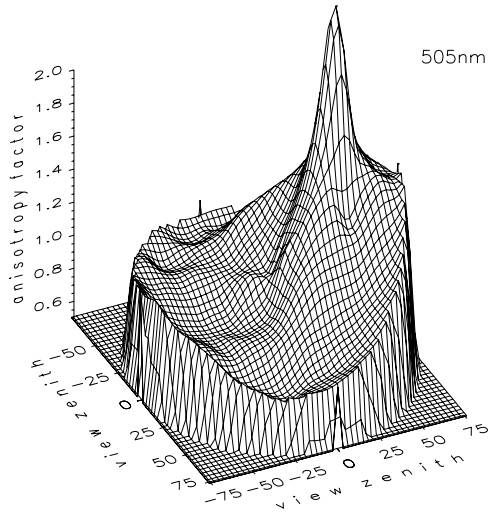


Source: Stefan Sandmeier, MeteoSwiss. Used with permission.

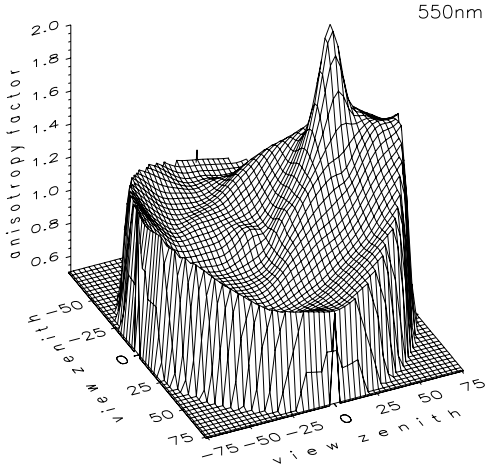
Figure 3.18 BRDF plots for grass at different wavelengths

Anisotropy factors (nadir-normalised BRDF data) for solar zenith angle of 35° and viewing zenith angle of 180° in four wavelengths (blue: 505 nm, green: 550 nm, red: 675 nm and NIR: 725 nm) over a grass canopy. High reflectance anisotropies are most evident in the blue and red wavelengths.

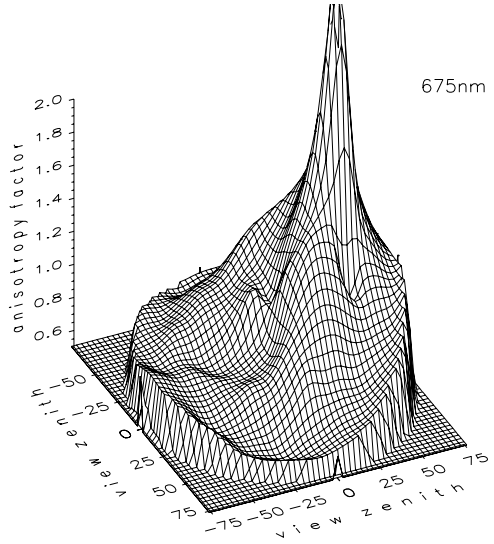
a. 505 nm (blue)



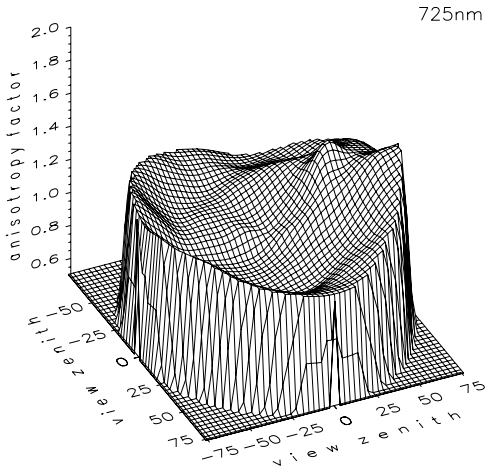
b. 550 nm (green)



c. 675 nm (red)



d. 725 nm (NIR)



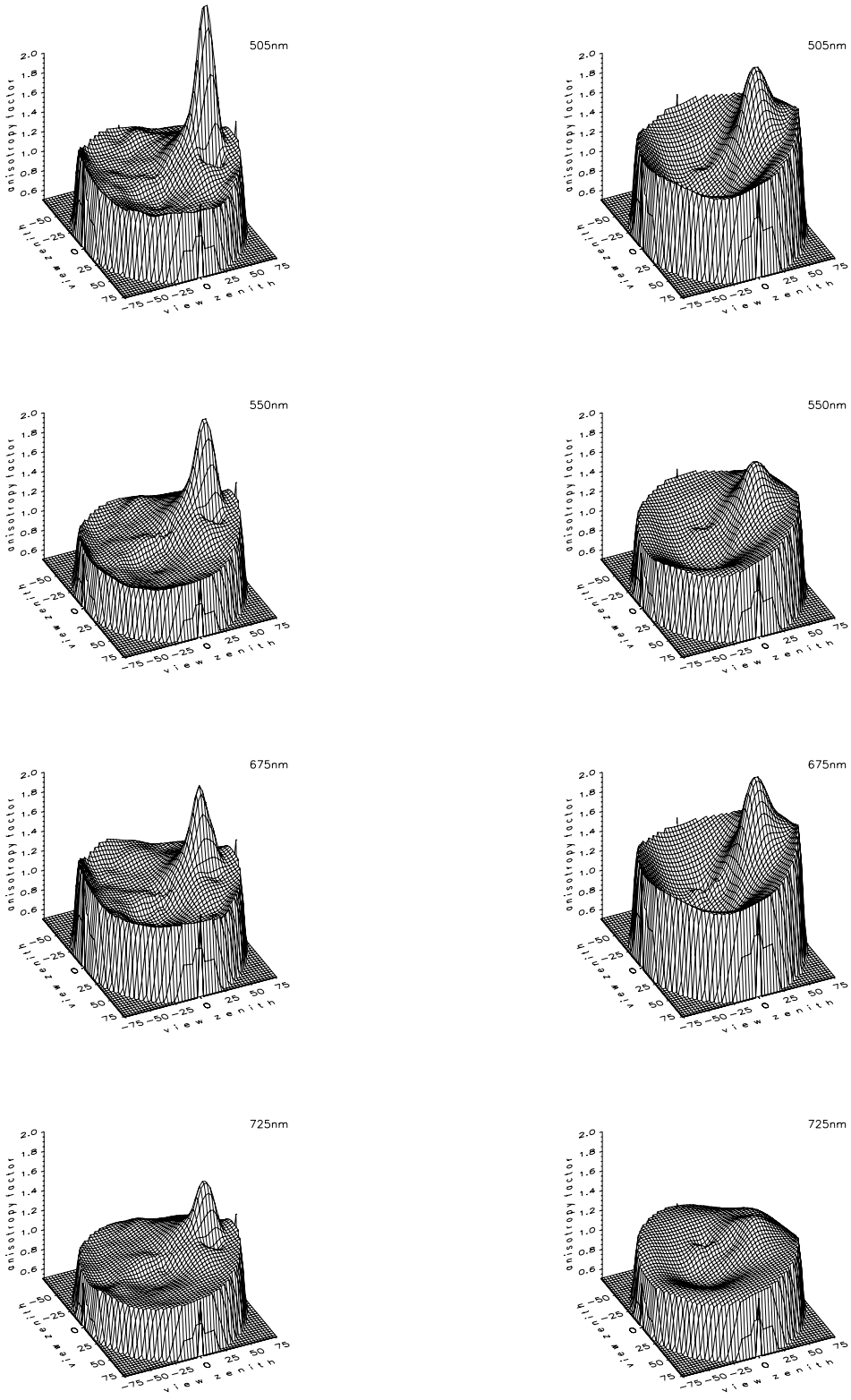
Source: Stefan Sandmeier, MeteoSwiss. Used with permission.

Figure 3.19 BRDF plots for healthy and dying watercress

Anisotropy factors (nadir-normalised BRDF data) for solar zenith angle of 35° and viewing zenith angle of 180° in four wavelengths (blue: 505 nm, green: 550 nm, red: 675 nm and NIR: 725 nm) for watercress canopies in different conditions. High reflectance anisotropies are evident in the blue and red wavelengths for both canopies.

a. Healthy watercress (high viewing angular resolution)

b. Dying Watercress (low viewing angular resolution—hence smoother)



Source: Stefan Sandmeier, MeteoSwiss. Used with permission.

The 'anisotropy factor' measures the difference between forward and backward viewing directions (or anisotropy) relative to the source direction. Sharp local peaks occur where the illumination and viewing positions are the same and are often matched by a corresponding low point when view position is complementary to the peak. The sharp local peak is known as the 'hotspot' and the low point is often referred to as the 'dark spot'. The anisotropy can be measured by the relative difference between them. Sometimes BRF models are fitted to observations such as these, and either observations or models can be used to derive BRF for different conditions, such as the complex irradiance found in practice.

As the collimated BRDF (or BRF) for remotely sensed images cannot be measured directly (Schaepman-Strub *et al.*, 2006), it is sometimes estimated by using a BRDF model and computing BRF for the type of irradiance and view geometries found in an image. The modified BRF models may be used in correction procedures that attempt to standardise radiance measurements between different images and different places such that the radiance values are what they would be for standard illumination and view angles. The impact of combined atmospheric and BRDF corrections on Landsat TM imagery is illustrated in Figure 3.20.

Anisotropy, hotspots and dark spots can be seen in EO imagery at varying scales. The hotspot effect is visible in both the oblique aerial photography shown in Figure 3.21 and in the landscape photo in Figure 3.22.

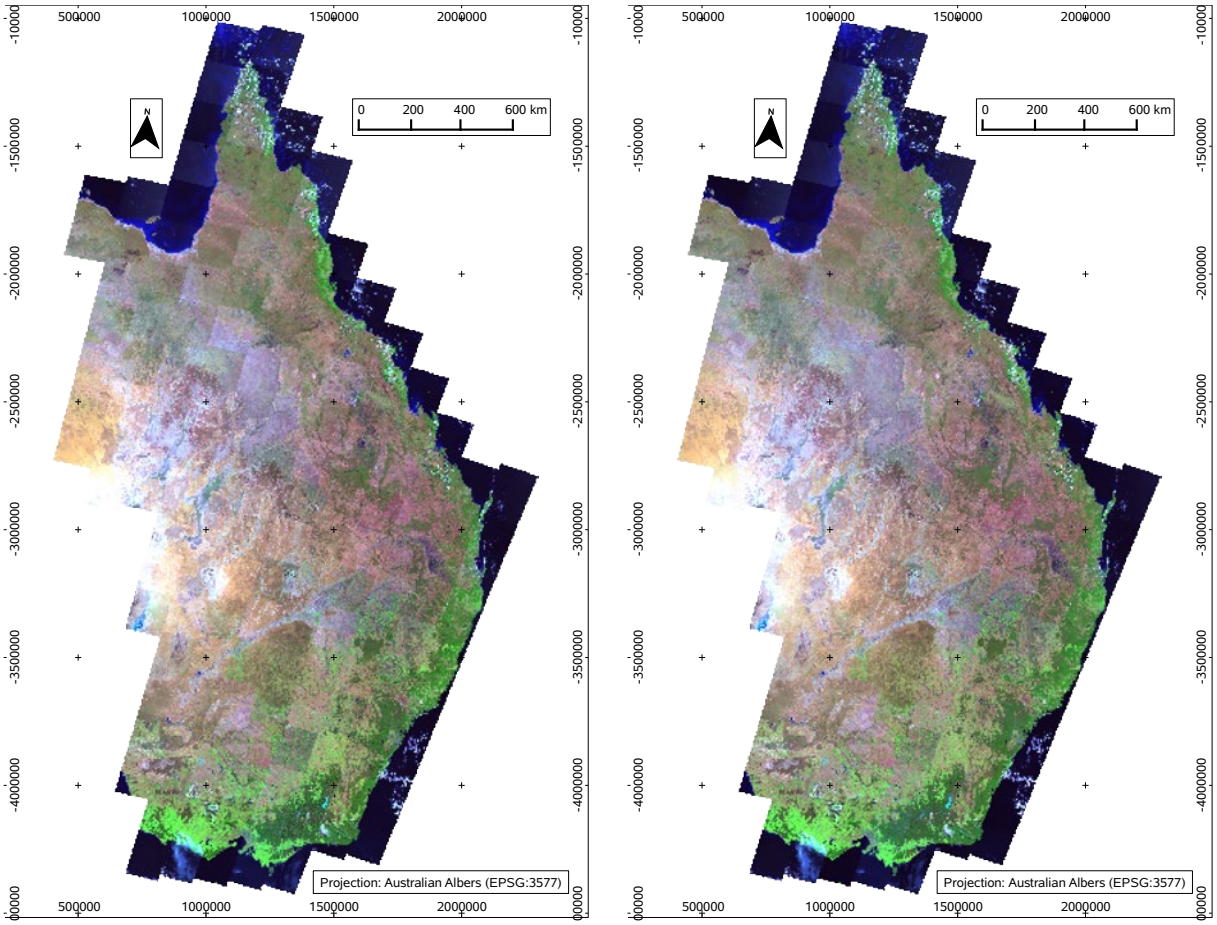
Figure 3.20 Surface reflectance correction

This example of surface reflectance correction applied to Landsat TM imagery for eastern Australia uses a method described by Flood *et al.* (2013). This method uses the 6S Radiative Transfer Model to correct for atmospheric effects and bi-directional reflectance modelling to remove the effects of topography and angular variation in reflectance. Note that some atmospheric effects remain in the corrected imagery due to limitations in input parameters. For example, aerosol modelling assumes a fixed Aerosol Optical Depth (AOD) of 0.05 which would not be valid in smoky or hazy conditions (see Section 4.1.2).

This Landsat TM mosaic of eastern Australia was compiled from imagery acquired between August and October 2006. Since these months experienced prolonged dry weather, vegetation changes were minimal.

a. Standard top-of-atmosphere reflectance

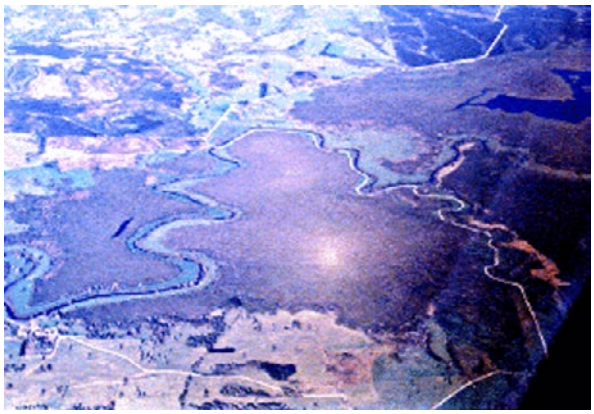
b. Corrected surface reflectance image



Source: Flood *et al.* (2013) using imagery from USGS

Figure 3.21 Hotspot effect in oblique aerial photography

The corner of the aircraft shades the lower right portion of the image, but the hotspot effect is clearly visible as a bright feature below the centre of the image.



Source: Dr J. Privette, NASA/GSFC.

Despite the name, a 'hotspot' effect does not arise in thermal imagery in the same way as in short wave data as there is no direct source/view driver. There is certainly a thermal BRDF, or more strictly BEDF (Bi-directional Emission Distribution Function), due to varying proportions of vegetation and ground elements at different temperatures with different view angles. This BEDF is strongest when the components have very different temperatures. However, what appears to be a solar 'hotspot' can occur in some thermal images (Jupp, 1998) when there is a marked thermal contrast between sunlit and shaded areas (mainly on the background), as can occur in dry woodlands at certain times during Summer (see Section 7).

Specific models for correcting for BRDF effects in EO imagery are introduced in Volume 2X—Appendices 1 and 2.

Figure 3.22 Hotspot effect in the landscape

This 180° panorama near William Creek, SA, shows the hotspot effect around the focal point of the camera, caused by the predominant backscatter of vegetation.



Source: Andreas Hüni, University of Zurich (taken on an iPhone6s)

3.8 Further Information

Specifics of EMR interactions:

Hunt (1980)

Goetz (1989)

Kirk (1986)

Elachi and van Zyl (2006)

Ryer (1977)

Calculating spectral irradiance:

National Renewable Energy Laboratory: *http://www.nrel.gov/rredc/solar_resource.html*

BRDF:

University of Massachusetts: *https://www.umb.edu/spectralmass/terra_aqua_modis/modis*

An Introduction to BRDF-based Lighting: *http://www.cs.princeton.edu/courses/archive/fall06/cos526/tmp/wynn.pdf*

Spectral libraries:

Aster (NASA): *http://speclib.jpl.nasa.gov/*

USGS: *http://speclab.cr.usgs.gov/index.html*

3.9 References

Born, M., and Wolf, E. (1963). *Principles of Optics*, Third Edn. Pergamon, New York.

Brown, M. S., and Arnold, C. B. (2010). Fundamentals of Laser-Material Interaction and Application to Multiscale Surface Modification. Chapter 4 in 'Laser Precision Microfabrication' (Ed: K. Sugioka). Springer-Verlag, Berlin.

Chisholm, L. A., and Hueni, A. (2015). The spectroscopy dataset lifecycle: good practice for exchange and dissemination. Chapter 14 in 'AusCover Good Practice Guidelines (A technical handbook supporting calibration and validation activities of remotely sensed data products)' (Eds: A. Held, S. R. Phinn, M. Soto-Berelov, and S. Jones). TERN AusCover, St Lucia, Australia.

Colwell, R. N. (1983). *Manual of Remote Sensing*, Second Edn. American Society of Photogrammetry, Falls Church, Virginia.

Elachi, C., and van Zyl, J. (2006). *Introduction to the Physics and Techniques of Remote Sensing*, Second Edn. Wiley Interscience, New Jersey.

Flood, N., Danaher, T., Gill, T., and Gillingham, S. (2013). An Operational Scheme for Deriving Standardised Surface Reflectance from Landsat TM/ETM+ and SPOT HRG Imagery for Eastern Australia. *Remote Sensing, 5*(1), pp. 83. doi:*http://dx.doi.org/10.3390/rs5010083*.

Goetz, A. H. (1989). Spectral remote sensing in geology. 'Theory and applications of optical remote sensing' (Ed: G. Asrar). John Wiley and Sons, New York.

Harrison, B. A., and Jupp, D. L. B. (1990). *Introduction to Image Processing. Part TWO of the microBRIAN Resource Manual* (256 pages). CSIRO Australia, Melbourne.

Hunt, G. R. (1980). Electromagnetic radiation: The communication link in remote sensing. 'Remote Sensing in Geology' (Eds: B. S. Siegal, and A. R. Gillespie). John Wiley and Sons, New York.

Iqbal, M. (1983). *An Introduction to Solar Ratiation*. Academic Press, Toronto.

Jacquemoud, S., and Ustin, S. L. (2008). *Modeling leaf optical properties*. Photobiological Sciences Online. Retrieved from *http://photobiology.info/Jacq_Ustin.html*.

Jupp, D. L. B. (1998). Directional radiance and emissivity measurement models for remote sensing of the surface energy balance. *Environmental Modelling & Software, 13*(3–4), pp. 341-351. doi:*http://dx.doi.org/10.1016/S1364-8152(98)00039-5*.

Kirk, J. T. O. (1986). *Light and Photosynthesis in Aquatic Ecosystems* (401 pages). Cambridge University Press, New York.

Li, F., Jupp, D. L. B., Thankappan, M., Lymburner, L., Mueller, N., Lewis, A., and Held, A. (2012). A physics-based atmospheric and BRDF correction for Landsat data over mountainous terrain. *Remote Sensing of Environment, 124,* pp. 756-770. doi:*http://dx.doi.org/10.1016/j.rse.2012.06.018*.

Montes, R., and Ureña, C. (2012). *An Overview of BRDF Models* (LSI-2012-001). University of Granada, Spain. Retrieved from *http://digibug.ugr.es/bitstream/10481/19751/1/rmontes_LSI-2012-001TR.pdf*.

Nicodemus, F. E., Richmond, J. C., and Hsia, J. J. (1977). *Geometrical considerations and nomenclature for reflectance* (NBS Monograph 160). US Department of Commerce, National Bureau of Standards.

Sandmeier, S. (2000). Acquisition of Bidirectional Reflectance Factor Data with Field Goniometers. *Remote Sensing of Environment, 73*, pp. 257–269.

Sandmeier, S., Müller, C., Hosgood, B., and Andreoli, G. (1998a). Physical mechanisms in hyperspectral BRDF data of grass and watercress. *Remote Sensing of Environment, 66*(2), pp. 222-233. doi:*http://dx.doi.org/10.1016/s0034-4257(98)00060-1*.

Sandmeier, S., Müller, C., Hosgood, B., and Andreoli, G. (1998b). Sensitivity Analysis and Quality Assessment of Laboratory BRDF Data. *Remote Sensing of Environment, 64*(2), pp. 176-191. doi:*http://dx.doi.org/10.1016/S0034-4257(97)00178-8*.

Sandmeier, S. R., and Itten, K. I. (1999). A field goniometer system (FIGOS) for acquisition of hyperspectral BRDF data. *IEEE Transactions on Geoscience and Remote Sensing, 37*(2), pp. 978-986. doi:*http://dx.doi.org/10.1109/36.752216*.

Schaepman-Strub, G., Schaepman, M. E., Painter, T. H., Dangel, S., and Martonchik, J. V. (2006). Reflectance quantities in optical remote sensing-definitions and case studies. *Remote Sensing of Environment, 103*(1), pp. 27-42. doi:*http://dx.doi.org/10.1016/j.rse.2006.03.002*.

USGS (2011). *US Geological Survey Spectroscopy Lab*. Retrieved from *http://speclab.cr.usgs.gov*.

Walter, B. (2005). *Notes on the Ward BRDF* (PCG-05-06). Cornell Program of Computer Graphics.

Ward, G. J. (1992). *Measuring and Modeling Anisotropic Reflection*. Paper presented at the SIGGRAPH 92.

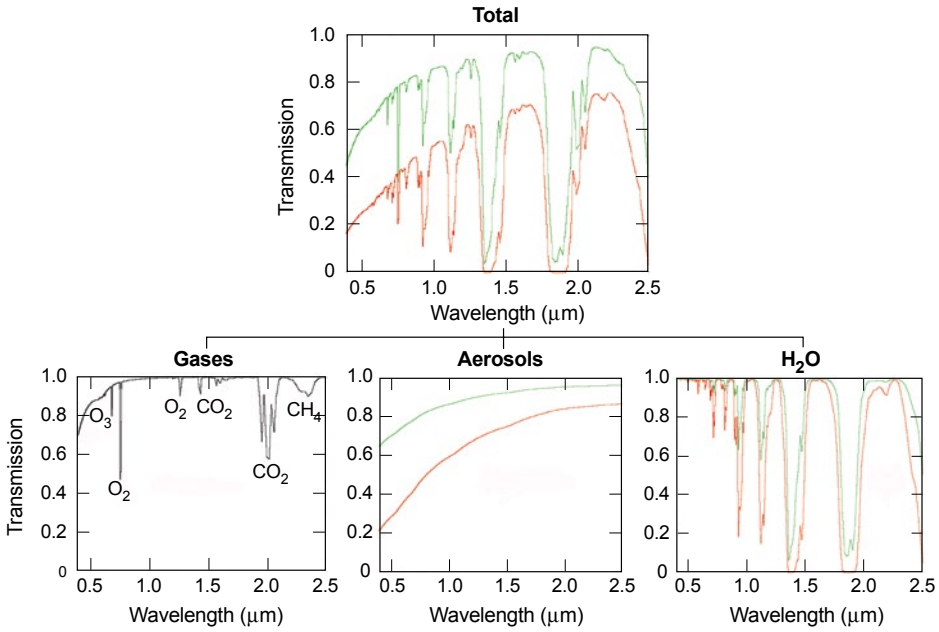


4 EMR Interactions with Atmosphere

The impact of atmospheric composition on EO imagery can be understood in terms of visibility, which is still used as a measure of atmospheric condition. On a clear day, we can see further than in hazy, dusty or smoky conditions. Atmospheric gases, aerosols and/or water vapour variously absorb and scatter solar (and other sources of) radiation as illustrated in Figure 4.1. These changes essentially reduce the strength of the source radiation, and result in lowered contrast in EO imagery. This process is also called attenuation and is further detailed in Section 4.1, Section 4.2 and Section 4.3. As well as being attenuated, solar radiation can be refracted as it passes from one atmospheric layer to another layer with different density (see Volume 1A—Section 5.4).

Figure 4.1 Atmospheric attenuation

Atmospheric components affect the amount of EMR that is transmitted through the atmosphere, with different components absorbing and scattering different wavelengths. The green line shows atmospheric composition in a rural environment with visibility of 23 km while the red line would be typical of an urban environment with visibility of 5 km.



Source: Shaw and Burke (2003) Figure 6. Reprinted with permission courtesy of MIT Lincoln Laboratory, Lexington, Massachusetts.

Background image: Landsat-7 image of fires in Namadgi National Park (southern ACT), acquired on 25 January 2003 (displayed using bands 5, 4, 2 as RGB), after devastating bushfires had swept into Canberra from nearby forests, causing severe damage in several suburbs. **Source:** Norman Mueller, Geoscience Australia.

A remote sensor is effectively 'looking' at the Earth's surface through a clear 'glass' of air. Were the contents of the glass perfectly transparent, the imaged surface would be clearly seen through the glass. The atmosphere, however, tends to be a translucent or opaque medium, rather than a transparent one. On a clear day, without clouds and aerosols, only around half the solar EMR reaching the top of Earth's atmosphere is transmitted through it to the planet's surface (Griersmith, 1991). In this case, the view of the Earth's surface through the glass would be reduced, coloured or even totally obscured.

The transfer of EMR through the atmosphere impacts the energy sensed by EO devices—in terms of both the radiation travelling from the source to the surface, then from the surface back to the sensor. Radiative Transfer (RT) models attempt to quantify the changes that occur to radiation and are introduced in Section 5.

4.1 Atmospheric Composition

Earth's atmosphere comprises varying proportions of gases, aerosols and water (as vapour, droplets and ice). Each of these constituents can absorb or scatter EMR, with the precise interaction being dependent on the relationship between the EM wavelength and the particle size (see Figure 4.1).

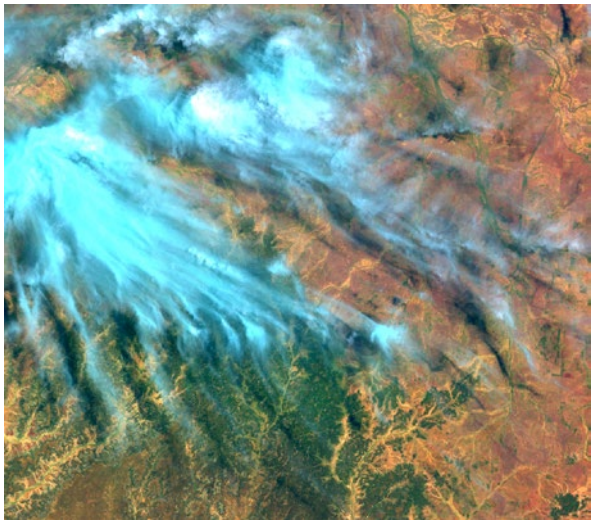
The impact of atmospheric condition(s) on EM data varies with particle abundance, distribution and size, and the wavelengths of EMR, with aerosols and gases having the greatest impact on optical wavelengths. Attenuation also increases with decreasing sun elevation (Wells, 1986). Variations in the density and form of clouds, smoke and dust can complicate image interpretation (see Figure 4.2, Figure 4.3 and Figure 4.6 respectively).

The spatial distribution of atmospheric constituents can vary significantly, both globally and regionally. Imagery acquired by the MODIS sensor is routinely used to compute a range of products that quantify atmospheric composition (King *et al*., 2003). For example, global estimates of precipitable water are generated from MODIS imagery, with typically higher concentrations of water vapour closer to the equator (see Figure 4.4).

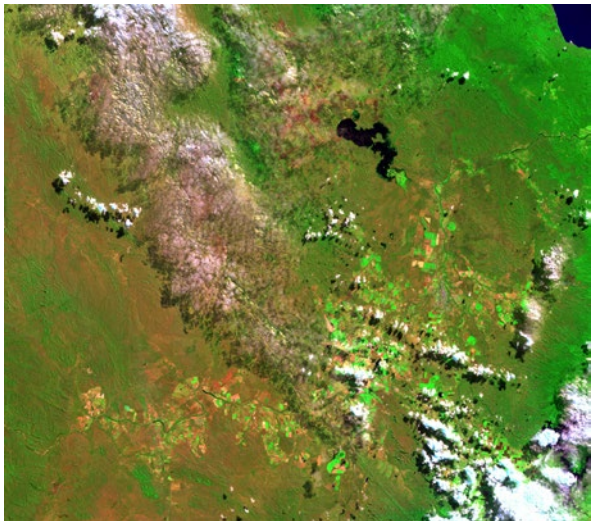
The earth's atmosphere is an imperfect window on the universe.
Electromagnetic waves in the optical part of the spectrum
(that is, waves longer than X rays and shorter than radio waves)
penetrate to the surface of the earth only in a few narrow spectral bands.
The widest of the transmitted bands corresponds roughly to the colours of visible light;
waves in the flanking ultraviolet and infrared regions of the optical spectrum
are almost totally absorbed by the atmosphere.
In addition, atmospheric turbulence blurs the images of celestial objects,
even when they are viewed through the most powerful ground-based telescopes.
(John N. Bahcall, 1977)

Figure 4.2 Cloud in EO imagery

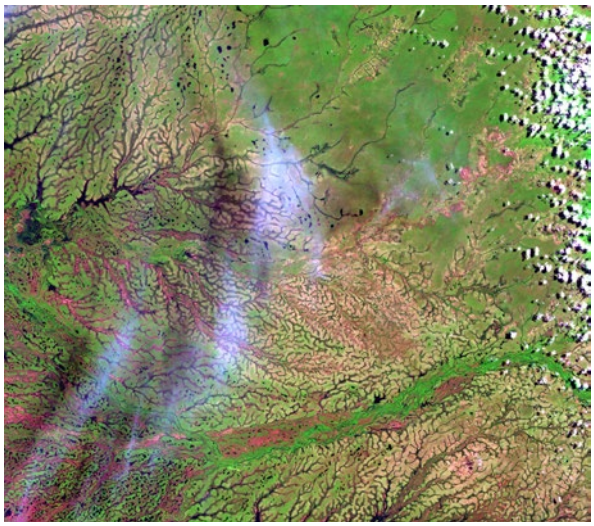
a. Landsat-7 ETM+ image acquired on 4 November 2000 showing variable cloud over Idalia National Park, 900 km west of Brisbane in southwest Queensland.



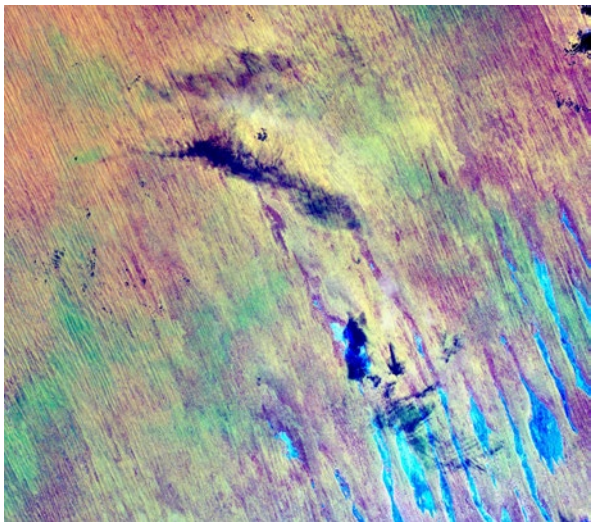
b. Landsat-5 TM image acquired on 21 June 2009 over Lake Mitchell-Mareeba, in far north Queensland, showing clouds with differing opacity and altitudes, and their associated shading effects.



c. Landsat-5 TM image acquired on 18 March 2010 showing semi-transparent, high cirrus cloud adjacent to a bank of lower level cumulus cloud (and associated surface shading) over Cape York, in far north Queensland.



d. Sentinel-2 imagery acquired on 28 April 2016 showing semi-transparent cloud (in lower right portion of image) over salt lakes and spinifex sand dunes, near Poeppel corner, southwestern Queensland.



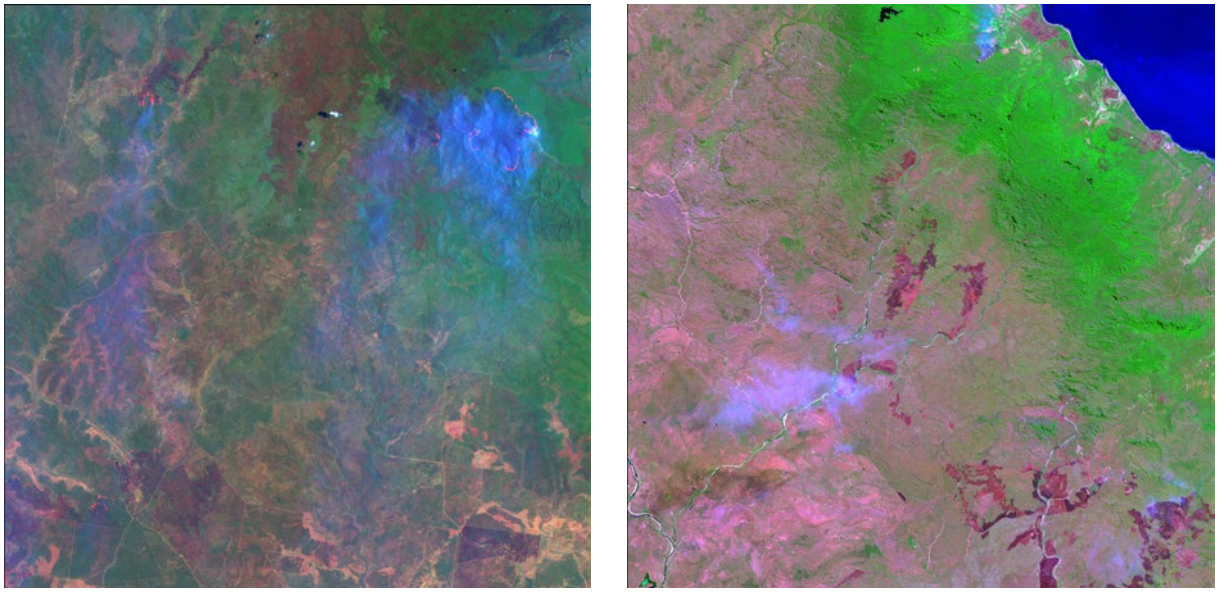
Source: Lisa Collett and Dan Tindall, Queensland Government, using imagery from USGS

Figure 4.3 Smoke in EO imagery

These Landsat TM images, processed to surface reflectance following Flood *et al.* (2013) (see Figure 3.20), are displayed using band 7 as red, band 4 as green and band 1 as blue. These Landsat TM bands are useful for highlighting fire effects on vegetation in rangeland and savanna environments. Active fires are often more evident in band 7 (SWIR) than in other bands. The inclusion of band 1 helps to identify smoke associate with fires. To reduce the visual impact of aerosols for other vegetation applications, composites of bands 5, 4, 2 or 5, 4, 3 are used.

a. Landsat-5 TM image acquired on 22 November 2009 showing smoke from wildfires burning in forests in and around Carnarvon National Park, in central Queensland.

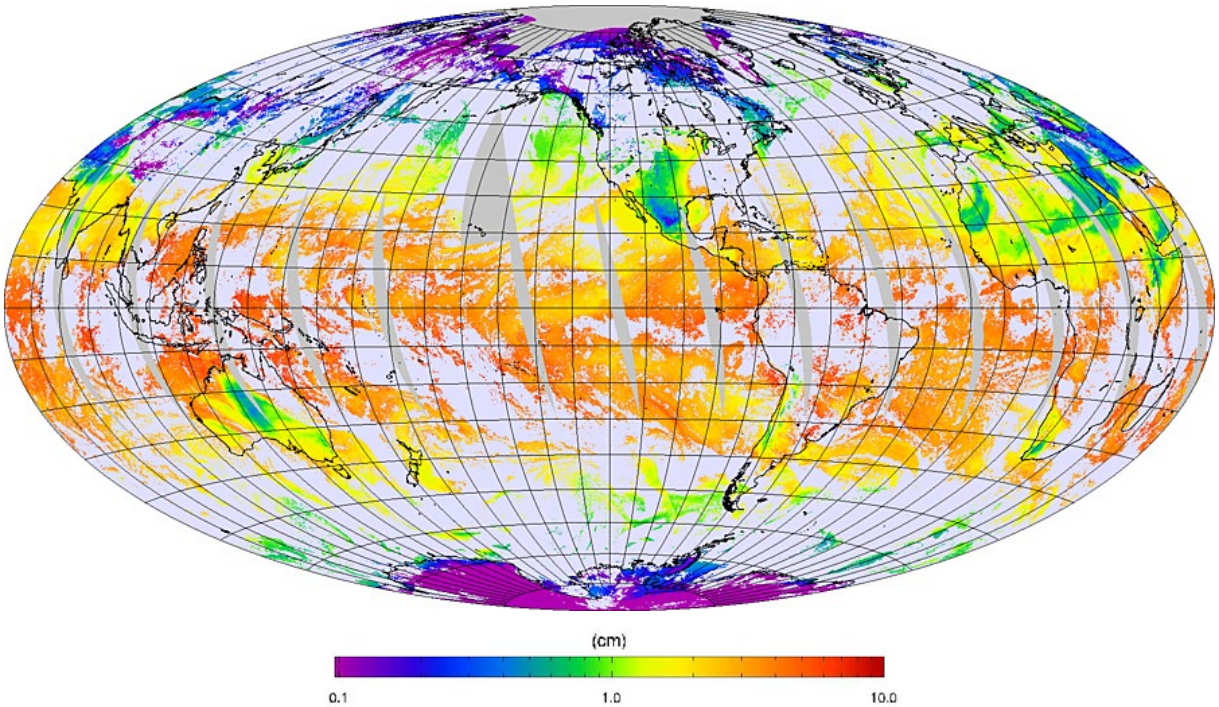
b. Landsat-5 TM image acquired on 22 July 2011 showing smoke from wildfires in savanna woodlands and grasslands near Charters Towers, in northern Queensland.



Source: Lisa Collett and Dan Tindall, Queensland Government, using imagery from USGS

Figure 4.4 MODIS Precipitable Water product

The MODIS Precipitable Water product shows the amount of water vapour in the atmosphere based on NIR reflectance. This image was generated from Aqua MODIS imagery (MYD05_L2) acquired on 21 February 2017.



Source: NASA. Retrieved from: *https://landweb.modaps.eosdis.nasa.gov/cgi-bin/ATM/ATMsingle.cgi?ver=6&date=2017059&imgProd=MYBGWIR&rotation=W*

4.1.1 Gas molecules

Gas molecules are the smallest atmospheric constituents, being approximately 10^{-4} μm. The most abundant permanent gases in the atmosphere are Nitrogen (78%), Oxygen (21%), and Argon (0.93%). The concentration of Carbon dioxide is locally more variable, with the global average being around 0.04% (NOAA, 2017).

Absorption of optical wavelengths by atmospheric gases heats the atmosphere and insulates the Earth against heat loss into space. As such, these gases are essential for life on Earth. The resulting 'windows', where EMR from the Sun can reach the Earth's surface and be reflected back to a remote sensor, are convenient for EO since they define the wavelength regions in which optical remote sensing is viable, namely:

- visible—0.3–0.75 μm;
- near infrared—0.77–0.91 μm; and
- short wave infrared—1.55–1.75 μm, 2.05–2.4 μm.

Within these windows, atmospheric conditions can significantly limit the quality of EO imagery (see Volume 1A—Section 5.4).

4.1.2 Aerosols

Suspended particles in the atmosphere, such as dust, smoke, ash, water droplets and salt, are called aerosols. Most tend to range in size from 0.1 to 1 μm. Their concentration can vary widely with weather conditions, natural disasters and anthropogenic activity. Aerosols can absorb and scatter EMR, mostly in the optical wavelengths. Aerosols can also act as cloud condensation nuclei and impact climate and energy balance on Earth.

Dust storms are a semi-regular occurrence in Australia. One extensive storm occurred on 23 September 2009 and its approach to a property in western NSW is shown in Figure 4.5. The extent of this storm is clearly depicted in satellite imagery, such as the MODIS image in Figure 4.6b. An earlier extensive dust storm is shown in Figure 4.6a.

Figure 4.5 Dust storm

This landscape view of an approaching dust storm was taken around 1pm on 23 September 2009 at Kars Station, 60 km east of Broken Hill, NSW.



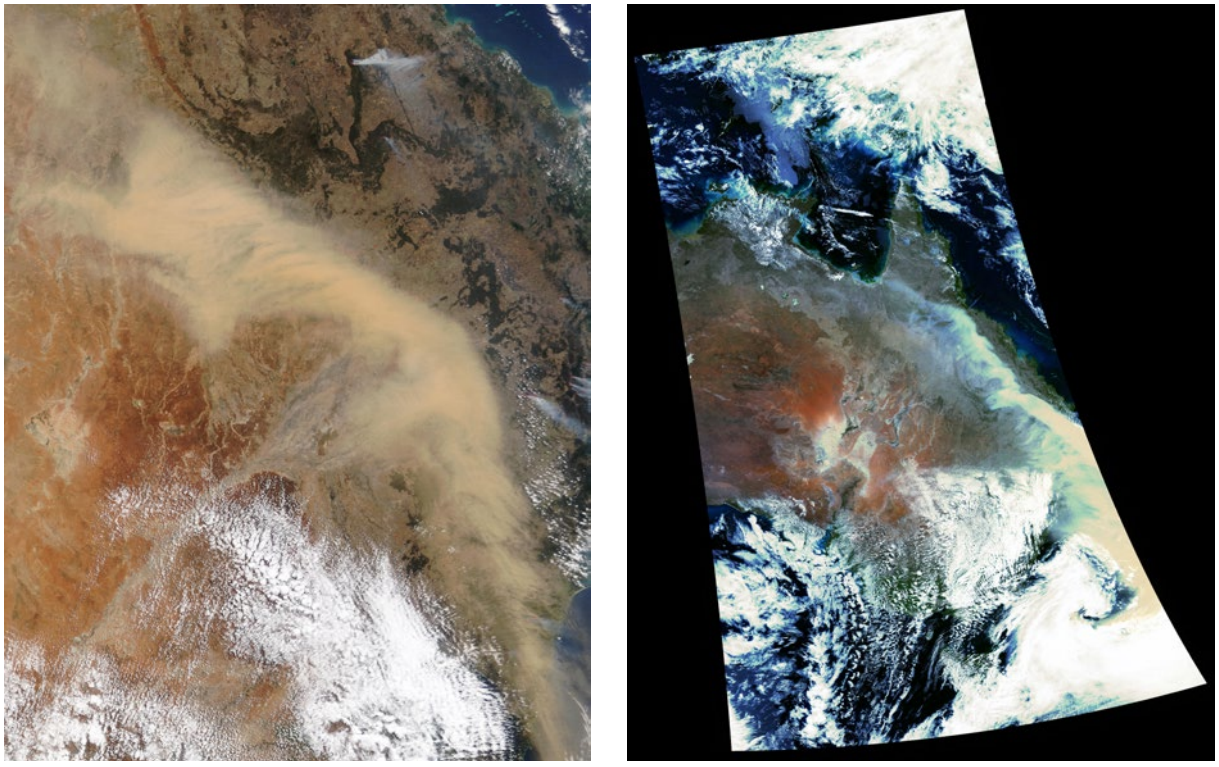
Source: Fred Hughes, Kars Station

Figure 4.6 MODIS imagery of dust storms

Continental-scale area imagery captures the extent of large scale events, such as dust storms in Australia. These MODIS images clearly indicate the significance of two recent storms.

a. On 23 October 2002 weather conditions conspired to create a blanket of dust over nearly 700,000 km^2 of eastern Australia. It is estimated that up to 5 Mt of dust, extending up to 2.5 km above the ground, was transported out to the Coral Sea in this storm. This Terra MODIS natural colour composite image shows the extent of the plume. Scattered fires are also visible in this image.

b. From 21 to 23 September 2009 another dust storm impacted central and eastern Australia. This storm covered around 840,000 km^2 with a dust load estimated between 12.1 Mt and 17.5 Mt. This Aqua MODIS mosaic, acquired at 3pm on 23 September 2009, shows the extent of the dust plume using band 5 (SWIR) as red, band 2 (NIR) as green and band 4 (green) as blue. [8]



Source: a. Jacques Descloitres, NASA/GSFC. Retrieved from: *http://visibleearth.nasa.gov/view.php?id=62540*
b. Norman Mueller, Geoscience Australia. (See also: *http://www.ga.gov.au/scientific-topics/earth-obs/basics/gallery/natural-disasters/dust-storm-australia*)

AERONET is a global network operated by NASA to investigate characteristics and impacts of aerosols. The Australian component of this network is called Aerospan[9], and comprises automated instruments, primarily sun-tracking photometers, to observe the quantity, size and type of aerosols over the Australian continent (Mitchell and Forgan, 2002; Mitchell *et al.*, 2010). AERONET and Aerospan data are used to validate satellite estimates of aerosols and apply atmospheric corrections to satellite imagery (see Excursus 4.1). Various aerosol global estimates derived from MODIS products are available from NASA (see Section 4.4).

8. For more details, visit DustWatch website: *http://www.dustwatch.edu.au/index.php/data-and-maps/historical-accounts*
9. Aerospan: *http://www.csiro.au/en/Research/OandA/Areas/Assessing-our-climate/Aerospan-aerosol-characterisation*

Excursus 4.1—Aerosol mapping from space

Airborne particles, or aerosols, rarely capture widespread attention except when events like dust storms or smoke plumes impact cities. Aerosols are one of the most important drivers of the climate system, but they are also one of the least understood. Information on the abundance and types of aerosols is fundamental to interpreting EO imagery acquired by satellites. Also, some aerosols are hazardous to human health.

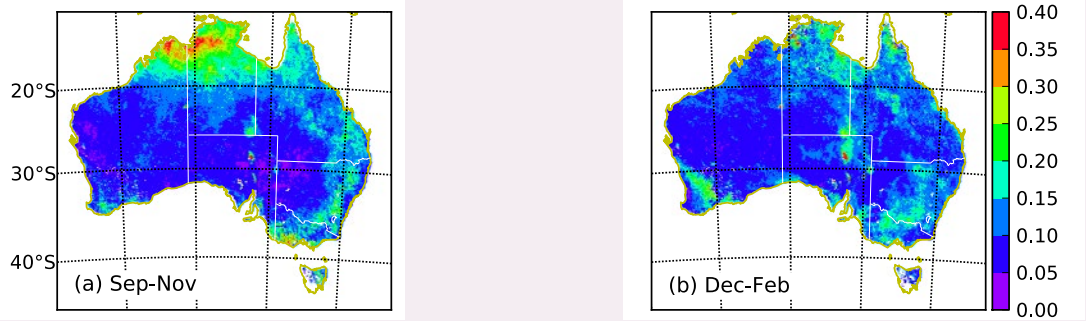
Our lack of understanding about the role of aerosols is one of the major sources of uncertainty in climate modelling. Monitoring the spatial and temporal distribution of aerosols is essential but highly challenging. Measuring aerosols using satellite data is necessary to provide continental coverage (see Figure 4.7). Over Australia, the bright land surface, coupled with low aerosol loadings, make this task particularly difficult. New methods, however, that use satellite imagery to extrapolate from the Aerospan network of ground measurements have allowed both the concentrations and types of aerosols to be mapped with unprecedented accuracy (Qin *et al.*, 2015). These mappings (see Figure 4.8) are now used to retrospectively apply atmospheric correction techniques to the archive of Landsat imagery (Li *et al.*, 2012) and assist with the development of new climate models (Rotstayn *et al.*, 2011).

Figure 4.7 Quarterly mean aerosol optical depth 2002 to 2008

Maps below show the quarterly mean aerosol optical depth (AOD)[10] at 550 nm for the period from 2002 to 2008.

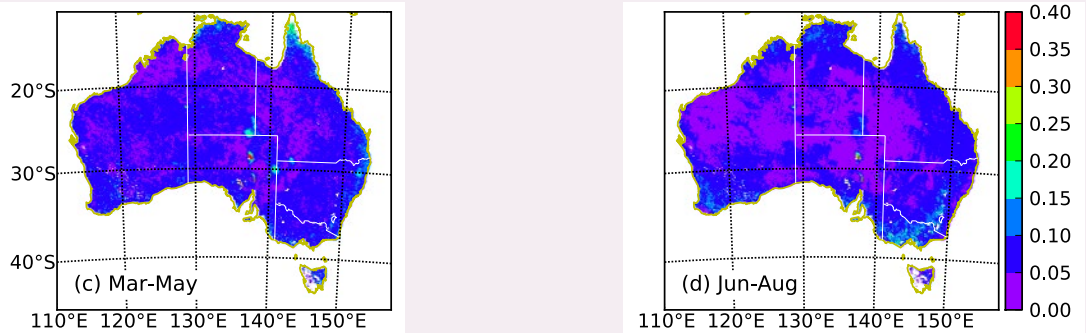
a. September to November

b. December to February



c. March to May

d. June to August

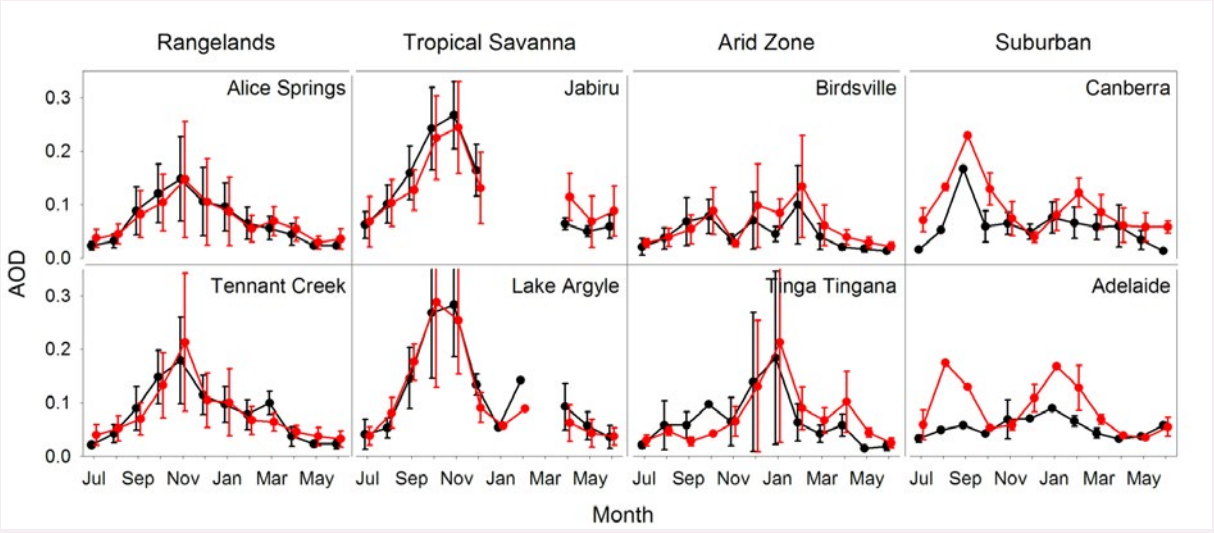


Source: Qin *et al.* (2015) Figure 14

10. Aerosol Optical Depth (AOD) is a dimensionless unit which indicates the degree to which aerosols absorb or scatter light and thus prevent transmission.

Figure 4.8 Monthly mean aerosol optical depth at 550 nm

Estimates of monthly mean aerosol optical depth (AOD) are derived by matching AATSR satellite retrievals (shown in red) to sun photometer measurements (shown in black). Standard deviation is indicated by the vertical bars (points without vertical bars were based on a single data point).



Source: Qin *et al.* (2015) Figure 10

4.1.3 Water

Water can exist in the atmosphere in the form of vapour, cloud droplets, raindrops, snow, ice crystals or hail. Water vapour concentration is strongly related to air temperature, can vary in concentration from 0 to 4%, and mostly exists in the troposphere.

Cloud droplet sizes can vary from 3–100 μm, but are mostly in the range 10–20 μm, being smaller over land than over water. Similarly, the concentration of cloud droplets ranges from 10–100 per cm^3. The typical liquid water content of clouds is in the range 0.1–0.3 g/m^3, but can vary from 0.05–3 g/m^3. Raindrops vary from 30–2500 μm, ice crystals are in the range 1–100 μm, while hail is generally less than 10 cm. Clouds scatter visible light and emit infrared and microwave wavelengths of EMR. In terms of EO imagery, clouds are generally opaque in optical wavelengths but transparent to microwaves. Heavy rain and hail can also be opaque to some microwaves.

4.2 Scattering Mechanisms

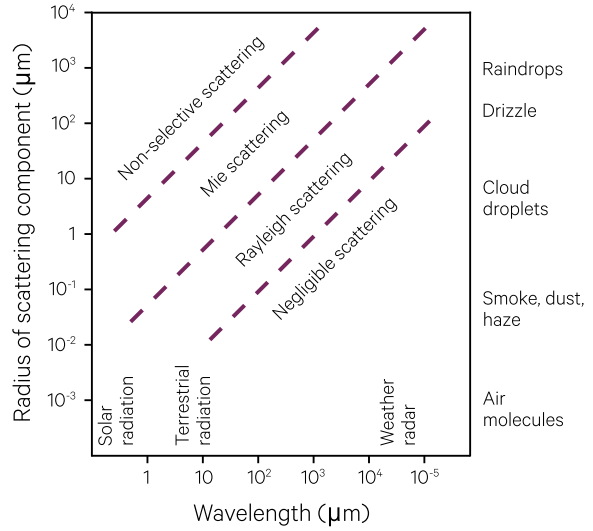
Scattering effectively redirects energy from the incoming radiation path and results in diffuse lighting. Much of the illumination on the Earth's surface is due to diffuse, rather than direct, lighting from solar radiation, especially on those topographic aspects in areas of high relief that intercept reduced levels of solar radiation.

Scattering interactions between radiation and atmospheric particles vary with wavelength relative to particle size (see Figure 4.9). These interactions result in three primary mechanisms (see Figure 4.10 and Table 4.1):

- Rayleigh scattering—radiation wavelength is much larger than the atmospheric particles (see Section 4.2.1);
- Mie scattering—radiation wavelength approximates the diameter of the atmospheric particles (see Section 4.2.2); and
- non-selective or geometric scattering—radiation wavelength is much smaller than the atmospheric particles. In this case, radiation is reflected by the particle based on geometric optics (see Section 4.2.3 and Volume 1A—Section 2).

Figure 4.9 Atmospheric interactions with EMR

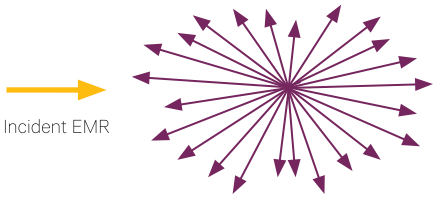
Scattering interactions between incident radiation and atmospheric particles vary with wavelength relative to particle size, resulting in three primary mechanisms: Rayleigh scattering, Mie scattering and non-selective scattering.



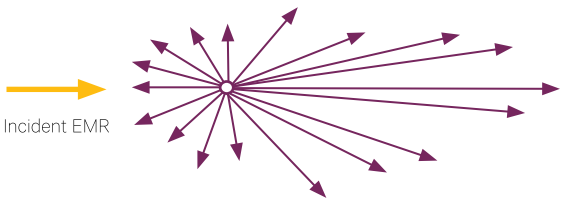
Adapted from: Wallace and Hobbs (1977) in Griersmith (1991)

Figure 4.10 Atmospheric scattering mechanisms

a. Rayleigh scattering occurs when the size of atmospheric particles is much less than the wavelength of incident EMR, so that the radiation is scattered in all directions.



b. Mie scattering occurs when particle size approximates the wavelength of incident EMR, and results in stronger forward scattering.



c. Non-selective scattering occurs when particle size is much larger than the incident EMR wavelength, resulting in much stronger, forward scattering.

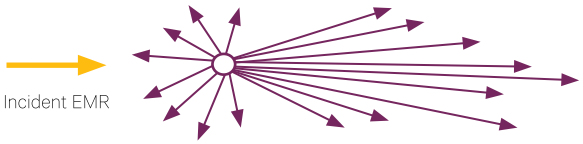


Table 4.1 Scattering mechanisms by atmospheric components

Atmospheric Component	Radius (μm)	Scattering Mechanism
Air molecules	0.001	Rayleigh
Smoke, dust, haze	0.01–1	Rayleigh, Mie
Cloud droplets, fog	1–20	Mie, Geometric
Rain droplets, drizzle	100–1000	Geometric
Snow flakes	1000–5000	Geometric

Adapted from: Awan *et al.* (2009).

4.2.1 Rayleigh scattering

When the atmospheric particles are much smaller than the wavelength of the radiation, the scattering effect is termed 'Rayleigh scattering' (see Figure 4.10a). This form of scattering is dominant in the upper 9–10 km of the atmosphere and largely results from gas molecules, so can occur in both clear and cloudy conditions. This effect is most severe with the shorter wavelengths and is the reason that the sky appears blue (the blue light is scattered to such an extent by the atmosphere that it appears to reach our eyes from all directions) and sunsets appear red (the Sun's rays follow a longer path through the atmosphere from the horizon, during which the shorter wavelengths are much scattered, leaving only the longer, orange and red, wavelengths for us to see—see Figure 4.11).

Figure 4.11 Rayleigh scattering

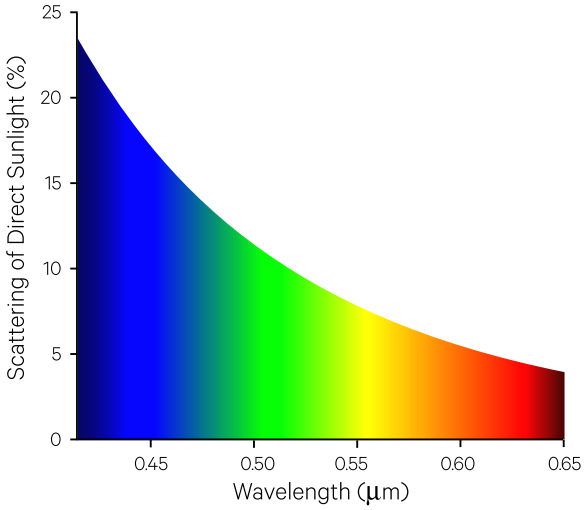
Dramatic Rayleigh scattering in the atmosphere after sunset. This picture was taken over the ocean, at 500 m altitude.



Source: Wikimedia Commons. Retrieved from: *https://commons.wikimedia.org/wiki/File:SDIM0241b.jpg*

Figure 4.12 Rayleigh scattering impact on direct sunlight

This scattering curve is calculated for sunlight passing vertically through the atmosphere based on Bucholtz (1995). Other atmospheric components, such as scattering from dust and absorption of some light by greenhouse gases, are not shown.



Source: Wikimedia Commons. CC AS 3.0. Retrieved from: *https://commons.wikimedia.org/wiki/File:Rayleigh_sunlight_scattering.png*

Scattered light reaching the Earth is called diffuse, rather than direct, radiation or 'skylight'. The radiation that has been scattered by the atmosphere and reaches the remote sensing device without contacting the Earth's surface is termed 'atmospheric path radiance'. As illustrated in Figure 4.12, this form of scattering typically reduces the radiometric extent of radiance measurements in the blue region of the EM spectrum (see Section 1.3 and Volume 1A—Section 5). Figure 4.13 shows imagery of the Queensland coast and Great Barrier Reef before and after correction for Rayleigh scattering and absorption by water vapour and ozone.

Figure 4.13 Atmospheric correction

This Aqua MODIS image, acquired on 21 June 2011, shows the impact of atmospheric correction techniques on EO imagery. In this case, atmospheric correction only accounted for Rayleigh scattering and absorption by climatological amounts of water vapour and ozone.

a. Before correction, the atmosphere is a significant source of signal at the sensor; and



b. After correction, differences in surface reflectance are enhanced.



Source: Edward King, CSIRO

4.2.2 Mie scattering

A scattering mechanism, referred to as 'Mie scattering', occurs when the particle size is comparable to the radiation wavelength (see Figure 4.10b). This effect is dominant in the lowest 5 km of the atmosphere. Particles of smoke, dust, salt and water can cause this type of scattering. For example, conditions of heavy atmospheric haze produce Mie scattering with visible and infrared wavelengths, while rain can result in Mie scattering of microwaves. Mie scattering has the greatest impact on longer wavelengths of radiation, and is most significant in overcast, dusty conditions.

4.2.3 Non-selective scattering

'Non-selective scattering' or geometric scattering is produced by water droplets, ice fragments or large dust particles, which are larger than the radiation wavelength (see Figure 4.10c). Such particles directly reflect any incident radiation, particularly in the lower atmosphere. When the particles are sufficiently dense they act as an opaque layer between the sensor and the Earth's surface. Cloudy and dust-laden atmospheres cause non-selective scattering in the visible and infrared wavelengths and thus reduce the effectiveness of data in these spectral regions for remote sensing of the Earth's surface. Fog can have a similar effect on thermal infrared wavelengths. Microwaves have much longer wavelengths so are usually only affected by very heavy rain where the size and density of water droplets is much higher.

4.3 Absorption and Emission

Solar radiation is mainly absorbed in the atmosphere by molecular oxygen, ozone, nitrogen, carbon dioxide, water vapour, atomic oxygen and nitrogen, and to a lesser extent by nitrogen oxide, carbon monoxide and methane. Most absorption occurs in the UV and IR regions of the EM spectrum, with relatively little absorption in the visible region. These absorption patterns result in 'windows' that can be used to remotely sense the Earth's surface as illustrated in Figure 5.14 in Volume 1A—Section 5.4.

Atmospheric absorption and emission involve energy exchange between gas molecules and EM energy fields, with the specific interaction being dependent on the wavelength of energy. The mechanisms involved in atmospheric absorption and emission are summarised in Table 4.2. For any wavelength, strong reflectors tend to be weak absorbers and vice versa. The Earth's emitted energy is largely absorbed by carbon dioxide, water vapour and ozone in the atmosphere, creating the 'Greenhouse Effect'.

Table 4.2 Absorption and emission mechanisms

Wavelength Region	Excitation Mechanism	Action	Atoms and Molecules
UV	Electronic	Orbital electronic change in individual atoms	Oxygen, Nitrogen, Ozone
Visible			-
NIR			-
TIR	Vibrational	Individual atoms vibrate with respect to combined molecular centre of mass	Water, Carbon dioxide, Ozone
Microwave	Rotational	Molecules rotate around their centre of mass	

4.4 Further Information

AERONET: *http://aeronet.gsfc.nasa.gov*

MODIS Atmosphere: *https://modis-atmos.gsfc.nasa.gov/index.html*

Aerospan: *http://www.csiro.au/en/Research/OandA/Areas/Assessing-our-climate/Aerospan-aerosol-characterisation*

4.5 References

Awan, M. S., Horwath, L. C., Muhammad, S. S., and Khan, M. S. (2009). Characterization of Fog and Snow Attenuations for Free-Space Optical Propagation. *Journal of Communications, 4*(8).

Bucholtz, A. (1995). Rayleigh-scattering calculations for the terrestrial atmosphere. *Applied Optics, 34*(15).

Flood, N., Danaher, T., Gill, T., and Gillingham, S. (2013). An Operational Scheme for Deriving Standardised Surface Reflectance from Landsat TM/ETM+ and SPOT HRG Imagery for Eastern Australia. *Remote Sensing, 5*(1), pp. 83. doi:*http://dx.doi.org/10.3390/rs5010083*.

Griersmith, D. C. (1991). *A review of atmospheric characteristics: general principles*. Paper presented at the 5th UN/FAO/WMO/ESA Training Course on the Use of Remote Sensing in Hydrological and Agrometeorological Applications, Canberra.

King, M. D., Menzel, W. P., Kaufman, Y. J., Tanre, D., Bo-Cai, G., Platnick, S., Ackerman, S. A., Remer, L. A., Pincus, R., and Hubanks, P. A. (2003). Cloud and aerosol properties, precipitable water, and profiles of temperature and water vapor from MODIS. *IEEE Transactions on Geoscience and Remote Sensing, 41*(2), pp. 442-458. doi:*http://dx.doi.org/10.1109/TGRS.2002.808226*.

Li, F.Q., Jupp, D.L.B., Thankappan, M., Lymburner, L., Mueller, N., Lewis, A., and Held, A. (2012). A physics-based atmospheric and BRDF correction for Landsat data over mountainous terrain. *Remote Sensing of Environment,* 124, 756–770.

Mitchell, R.M., and Forgan, B.W. (2003). Aerosol measurements in the Australian Outback: Intercomparison of sun photometers,. J. *Atmos. Oceanic Technol.*, 20, 56–66.

Mitchell, R.M., Campbell, S.K., and Qin, Y. (2010). Recent increase in aerosol loading over the Australian arid zone. *Atmos. Chem. Phys.*, 10, 1689–1699.

NOAA (2017). *Earth System Research Laboratory Global Monitoring Division Websites*. Retrieved from *https://www.esrl.noaa.gov/gmd/ccgg/trends/global.html*.

Qin, Y., Mitchell, R., and Forgan, B. W. (2015). Characterizing the Aerosol and Surface Reflectance Over Australia Using AATSR. *IEEE Transactions on Geoscience and Remote Sensing, 53*(11), pp. 6163-6182. doi:*http://dx.doi.org/10.1109/TGRS.2015.2433911*.

Rotstayn, L. D., Collier, M. A., Mitchell, R. M., Qin, Y., Campbell, S. K., and Dravitzki, S. M. (2011). Simulated enhancement of ENSO-related rainfall variability due to Australian dust. *Atmospheric Chemistry and Physics, 11*(13), pp. 6575-6592. doi:*http://dx.doi.org/10.5194/acp-11-6575-2011*.

Shaw, G. A., and Burke, H. K. (2003). Spectral Imaging for Remote Sensing. *Lincoln Laboratory Journal, 14*(1), pp. 3-27.

Wallace, J. M., and Hobbs, P. V. (1977). *Atmospheric Science - an Introductory Survey* (467 pages). Academic Press, London.

Wells, N. (1986). *The Atmosphere and Ocean: A Physical Introduction* (347 pages). Taylor & Francis, London.



5 Radiative Transfer Modelling

The transfer of energy as photons through a medium and the interactions of photons with surface materials is described by a mathematical model known as Radiative Transfer (RT) Theory. RT models account for the impact of absorption, emission and scattering on energy propagation through a medium. Figure 5.1 illustrates the processes that can affect a single beam travelling a distance of Δr through a medium.

The relationship between energy input from a source and output from a target material is:

Total Output Energy = Reflected Input Energy + Transmitted Input Energy + Absorbed Input Energy + Emitted Energy

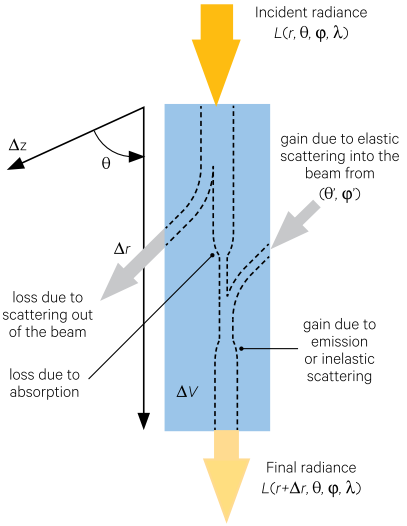
Relevant radiometric terms to define specific properties of radiant energy (Q) are listed in Table 1.1 (see also Volume 1A—Sections 2.6 and 5).

All RT modelling is tied to conservation of energy, that is, for any gain in energy in one component there must be a corresponding loss in energy in another component. As radiation passes through any medium, some energy is reflected and absorbed. RT modelling attempts to account for these energy 'losses' as energy is transmitted through the:

- atmosphere (see Section 5.1);
- water (see Section 5.2); or
- vegetation canopies (see Section 5.3).

Figure 5.1 Radiative transfer process

The energy carried by a single beam of radiation through a medium can be increased by emission and/or inelastic and elastic scattering into the beam, and decreased by scattering out of the beam and/or absorption by the medium.



Adapted from: Mobley *et al.* (2014)

Table 5.1 Relevant radiometric terms

Term	Symbol	Equation	Definition
Radiant Flux	Φ	dQ / dt	Radiant energy per unit time (rate of energy transfer)
Irradiance	E	$d\Phi / dA$	Density of radiant flux incident upon a unit area of a plane surface
Spectral irradiance	E_λ	$dE / d\lambda$	Irradiance per unit wavelength
Radiance	L	$dE / d\Omega$	Radiant flux radiated from a unit projected area per unit solid angle in a specified direction (as measured by sensor)

Background image: AVNIR-2 image of Lucinda, Queensland, acquired on 12 June 2010 (displayed as natural colour composite using bands 3, 2, 1 as RGB). **Source:** Norman Mueller, Geoscience Australia.

5.1 Atmospheric Models

Based on the discussion of atmospheric components and processes in Section 4, the atmosphere can impact the radiation detected by a remote sensor via a number of interrelated mechanisms:

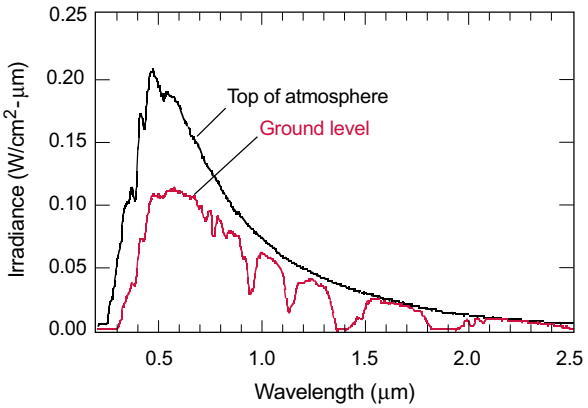
- attenuate incoming solar radiation before it reaches the Earth's surface;
- attenuate solar radiation after it is reflected by the Earth's surface;
- scatter solar radiation directly into the sensor's field of view without reaching the ground; and
- scatter shorter wavelengths to create a secondary source of diffuse radiation to illuminate shadowed targets.

The combined impact of these atmospheric processes is illustrated by comparing solar irradiance at the top of the atmosphere with that at ground level (see Figure 5.2).

RT modelling attempts to account for these effects on EO radiance measurements by removing the effects of atmospheric path radiance. This effectively converts the image radiance values to those that theoretically would occur if the Earth's surface were positioned at the top of the atmosphere (TOA).

Figure 5.2 Solar spectral irradiance

While the spectrum of solar radiation that reaches the top of Earth's atmosphere resembles the spectrum of a blackbody at around 5800K (Sun's temperature; see Volume 1A—Figure 2.19), some of that radiation is absorbed by the atmosphere before it reaches sea level. As shown in the graph below, the atmosphere absorbs selected wavelengths more strongly than others.



Source: Shaw and Burke (2003) Figure 2. Reprinted with permission courtesy of MIT Lincoln Laboratory, Lexington, Massachusetts.

The components of a simple RT model for EO image data are illustrated in Figure 5.3. The Total Irradiance (E_T) at the Earth's surface can be computed in units of W/m^2 as:

$$E_T = E_0 T(\theta_0)\cos\theta_0 + E_d$$

where

E_0 is the TOA solar irradiance modified for Sun-Earth distance;
$T(\theta_0)$ is the total transmittance (transmissivity) of the atmosphere
$\cos\theta_0$ is the cosine of solar zenith angle; and
E_d is the diffuse sky irradiance.

Then the radiance at the sensor (L_S) can be computed as:

$$L_S = L_T + L_P$$

where

L_P is the additive path radiance; and
L_T is the transmitted target radiance.

$$L_T = \left(\frac{1}{\pi} \times R \times E_T\right) \times T(\theta_S)$$

where

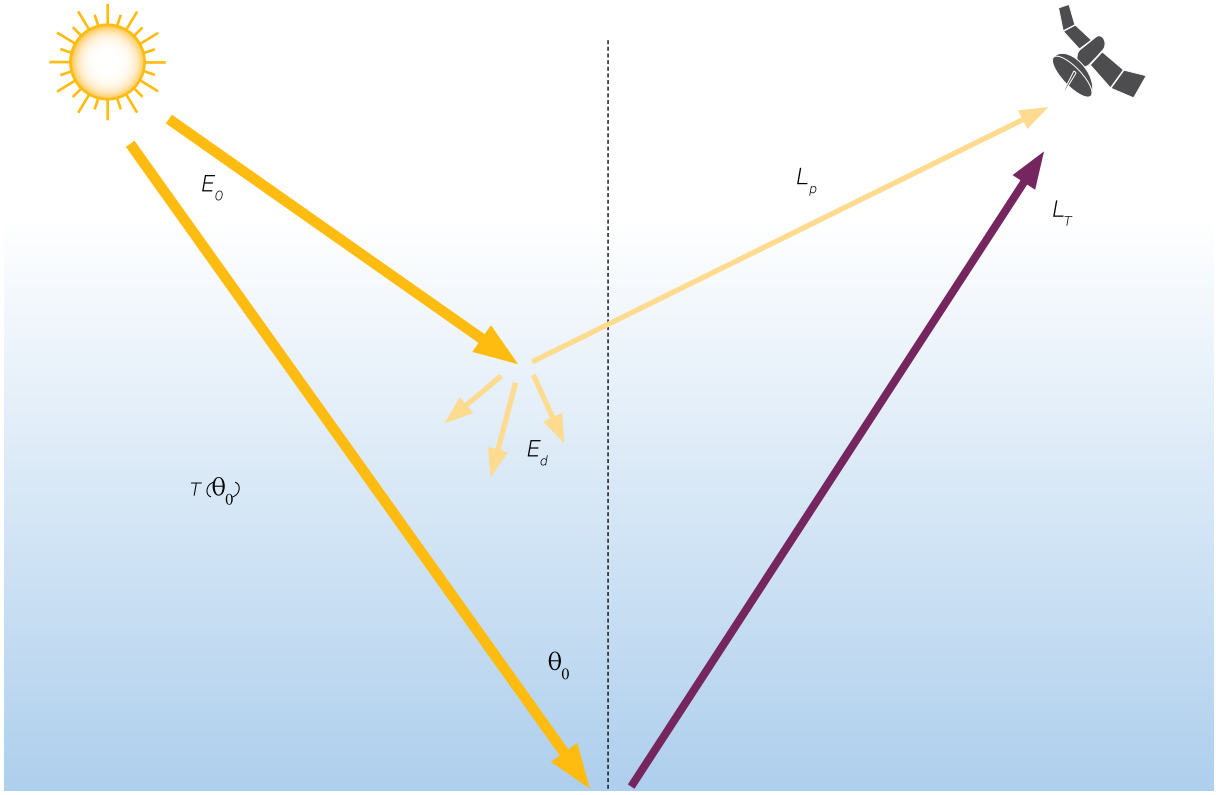
R is the composite reflectance of the target surface, which can include environmental and adjacency effects (see Volume 3); and
$T(\theta_S)$ is the atmospheric transmittance from the surface to the sensor.

When they come to model Heaven
And calculate the stars, how they will wield
The mighty frame, how build, unbuild, contrive
To save appearances, how grid the sphere
With centric and eccentric scribbled o'er
Cycle and epicycle, orb in orb.
(John Milton, Paradise Lost)

Figure 5.3 Simple radiative transfer model

a. The total irradiance (E_T) reaching the Earth's surface is computed from the solar irradiance at TOA (E_0), atmospheric transmissivity ($T(\theta_0)$), solar zenith angle (θ_0) and diffuse sky irradiance (E_d),.

b. The radiance detected by a sensor is computed from the additive path radiance (L_p), transmitted target radiance (L_T). composite surface reflectance from the target (R) and transmittance from surface to sensor ($T(\theta_S)$).



A more detailed discussion of atmospheric brightness issues is included in Volume 1X—Appendix 5. Methods to correct image values for atmospheric path radiance effects are described in Volume 2.

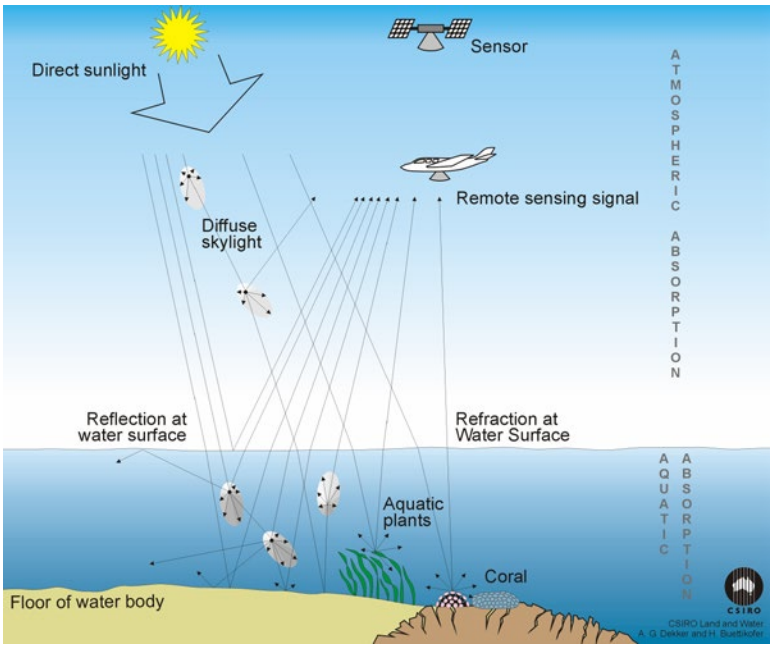
5.2 Water Models

Remote sensing of water bodies present different challenges to remote sensing of terrestrial features, such as bare ground or vegetation, since it is influenced not only by atmospheric processes, but also by:

- scattering and absorption processes within the water column;
- reflectance and refraction at the air-water interface; and
- reflectance from the substrate when it is visible at the water surface to the remote sensor (see Figure 5.4).

Figure 5.4 Remote sensing of aquatic targets

For aquatic targets, four sources can contribute to the radiance detected by a remote sensor, namely the atmosphere, the interface between air and water, constituents of the water column and, in optically shallow waters, the substrate.



Source: Arnold Dekker, CSIRO

The impact of these additional factors on incident radiation is shown in Figure 5.5. Thus, the radiation from a water surface that is recorded by a remote sensor can be resolved into four components (all variables in the following equations are spectral, but wavelength has been omitted for readability):

$$L_S = L_P + L_{AW} + L_V + L_B$$

where

L_S is total radiance recorded at sensor;
L_P is atmospheric path radiance;
L_{AW} is the radiance that just penetrates the air-water interface and is then reflected from the water;
L_V is radiance that penetrates the air-water interface, interacts with the organic/inorganic constituents in the water, and then exits the water column without encountering the bottom; and
L_B is the bottom or substrate radiance.

If atmospheric conditions are relatively consistent over a remotely sensed image, then the spatial variations in the radiance recorded by a sensor are directly proportional to the spatial changes in the radiance from the water column. Atmospheric variations within an image that are due to water surface effects, such as sunglint and skyglint, require more sophisticated correction methods (see Volume 3B).

Radiation emerging from the water column (L_W) includes effects due to:

- what is in the water—suspended sediments, chlorophyll-based materials, and coloured dissolved organic matter (CDOM; see Section 6.4);
- what is on the sea floor—the substrate: sand, mud, sea grass, coral or other macrophytes; and the
- depth of water below the surface.

Figure 5.5 Impact of water factors on incident radiation

This photo shows the journey of Sun and skylight through the atmosphere, the air-water interface, and the water column to the benthos. Note the changes in colour and intensity from the sky to the bottom of the river.



Source: Mel-nik, ©iStock photo ID 519368058.

The composite effect of these components and their behaviour in the detected radiance from the water column (L_T) can be conveniently described in terms of a simplified model (using terminology from Jupp, 1988):

$$L_T = t_W L_B + \left(1 - t_W\right) L_W$$

where

L_T is the detected radiance of the target water body;
L_W is the radiance emerging from the water column; and
t_W is the transmittance of the water column.

As transmittance in the water column varies from none (value 0) to full (value 1), the radiance measured from the water column varies from the radiance of deep water to the radiance of wet substrate. A useful approximation of water transmittance is related to water depth and absorption properties (Lyzenga, 1978, 1981):

$$t_W = \exp\left(-2Kz\right)$$

where

K is an effective attenuation coefficient for the water column; and
z is the water depth.

and

$$2K = K_d + K_u$$

where

K_d is the downwelling attenuation coefficient; and
K_u is the upwelling attenuation coefficient;

so that (cf. Doak *et al*., 1980):

$$L_T = L_W + \left(L_B - L_W\right)\exp\left(-2Kz\right)$$

While not exact models, these equations approximate the impact of water properties, substrate reflectance and water depth on the radiance leaving a water mass. In murky water, the water clarity is reduced and the attenuation coefficient will be larger and radiance from the water will be primarily determined by its composition. In clear water, the attenuation coefficient decreases so that its radiance will be closer to that of deep clear water. In this case, the substrate type will influence the upwelling radiance measurements at greater water depths.

The attenuation coefficient varies with EM wavelength as well as water composition. In clear water, blue to blue-green light penetrates to the greatest depths. In turbid waters, suspended sediments increase the attenuation coefficient due to scattering. When algal pigments are present, they can influence the attenuation coefficient by localised pigment absorption and can change the wavelengths at which light penetrates to a greater depth. Accounting for the effects due to differing absorption and scattering by components of the water mass and substrate types requires a more complex model. Implementation of appropriate RT models for analysing EO images of water is further discussed in Volumes 2 and 3B.

5.3 Vegetation Canopy Models

RT models have also been developed to describe the changes in energy propagation resulting from vegetation canopies based on descriptions of:

- canopy architecture—leaf area, orientation and size distribution, which may vary with canopy depth;
- scattering and absorption properties of the vegetation (as a function of wavelength); and
- scattering and absorption properties of the underlying surface.

Lidar measurements have enabled detailed parameterisation of the geometry and structure of forest canopies for RT modelling. Canopy RT models can then be used to retrieve biochemical and physical characteristics from optical EO imagery (Yáñez *et al.*, 2008). At a global scale, such models are being coupled with other biophysical models to simulate whole Earth processes (see Volume 3A).

5.4 Further Information

Atmospheric correction:

ESA: *http://earth.esa.int/landtraining07/D1LB2-Moreno.pdf*

Radiative Transfer in Canopies:

Prospect and SAIL Canopy Reflectance Models: *http://teledetection.ipgp.jussieu.fr/prosail/*

University College London: *http://www2.geog.ucl.ac.uk/~plewis/rnr/rtTheoryPt2v7-1.pdf*

Radiative Transfer Modeling: *http://www.ericweisstein.com/research/thesis/node40.html*

5.5 References

Doak, E., Livisay, J., Lyzenga, D. R., Ott, J., and Folcyn, F. (1980). *Evaluation of water depth extraction techniques using Landsat and aircraft data* (1359000-2-F). Defense Mapping Authority, Hydrographic/Topographic Centre, Washington.

Jupp, D. L. B. (1988). *Background and Extensions to Depth of Penetration (DOP) Mapping in Shallow Coastal Waters*. Paper presented at the International Symposium on Remote Sensing of the Coastal Zone, Gold Coast, Australia.

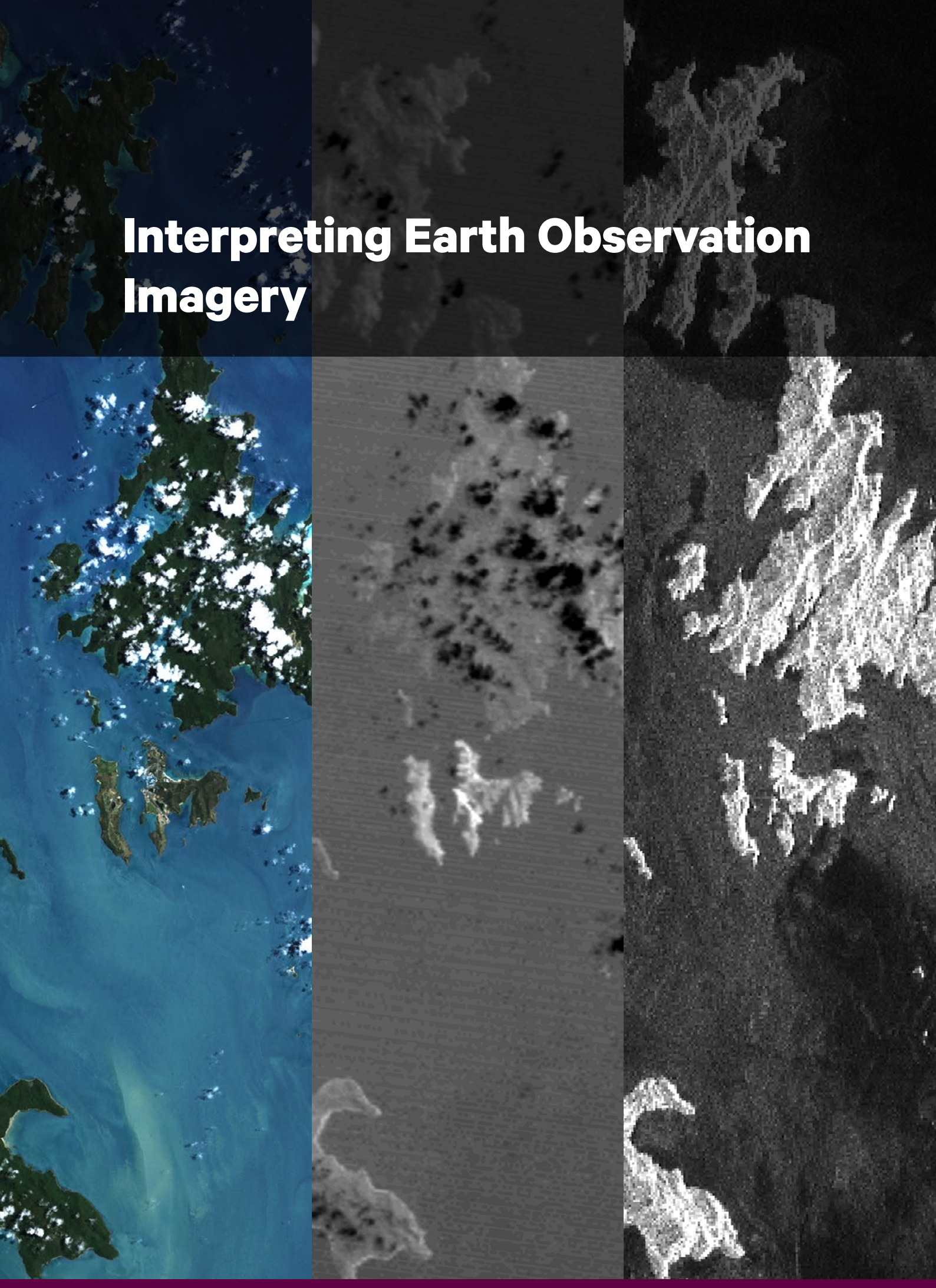
Lyzenga, D. R. (1978). Passive Remote-Sensing Techniques for Mapping Water Depth and Bottom Features. *Applied Optics, 17*(3), pp. 379-383. doi:*http://dx.doi.org/10.1364/ao.17.000379*.

Lyzenga, D. R. (1981). Remote sensing of bottom reflectance and water attenuation parameters in shallow water using aircraft and Landsat data. *International Journal of Remote Sensing, 2*(1), pp. 71-82. doi:*http://dx.doi.org/10.1080/01431168108948342*.

Mobley, C., Boss, E., and Roesler, C. (2014). *Ocean Optics Web Book*. Retrieved from *http://www.oceanopticsbook.info/*.

Shaw, G. A., and Burke, H. K. (2003). Spectral Imaging for Remote Sensing. *Lincoln Laboratory Journal, 14*(1), pp. 3-27.

Yáñez, L., Homolová, L., Malenovský, Z., and Schaepman, M. (2008). *Geometrical and Structural Parameterization of Forest Canopy Radiative Transfer by LIDAR Measurements*. Paper presented at the XXIst ISPRS Congress - Technical Commission VII, Beijing, China.



Interpreting Earth Observation Imagery

Since EO image characteristics derive from the interaction of specific EMR wavelengths with the Earth's surface and/or atmosphere, interpretation and analysis of these datasets relies on an understanding of those interactions. As detailed in previous sections, different EMR wavelengths can interact with a common target via different physical mechanisms (see Sections 3, 4 and 5). Accordingly, the most appropriate processing methods to extract relevant information from EO imagery may differ with the specific wavelength region(s) observed in the imagery.

The following sections describe interpretation and analysis of EO imagery for three broad spectral regions:

Contents

6 Optical Imagery 81

7 Thermal Infrared Imagery 107

8 Microwave Imagery 123

Background image on previous page: Triptych of Whitsunday Islands, Queensland. **Left:** Landsat-5 image acquired on 24 October 2010 (natural colour composite using bands 3, 2, 1 as RGB). **Middle:** Landsat-5 image acquired on 24 October 2010 (band 6: thermal infrared). **Right:** PALSAR image acquired on 5 December 2010 (L-band SAR). **Source:** Norman Mueller, Geoscience Australia



6 Optical Imagery

While, 'optical' implies energy that can be sensed with the human eye, in physics this term applies to those wavelengths of EMR whose behaviour is best described by ray optics, namely UV, visible, NIR, SWIR and TIR (see Volume 1A—Section 2.8). In the context of EO, however, the term 'optical imagery' most commonly refers to image data that measures reflected radiance in the following wavelengths[11]:

- visible—0.3–0.7 μm;
- near infrared (NIR)—0.7–1.3 μm; and
- short wave infrared (SWIR)—1.3–4.3 μm.

Within these theoretical regions, atmospheric absorption reduces the range of wavelengths that may be detected by EO (see Section 5 above and Volume 1A—Section 5.4). While most optical imagery is derived from passive sensors that detect reflected solar radiation (see Volume 1A—Section 14), lidar sensors detect the echo of their own active energy source using optical wavelengths (see Volume 1A—Section 15.1).

As introduced in Section 3 and Section 4 above, in addition to the actual reflectance of the target surface, the radiance measurement detected by an optical sensor depends on many factors including the:

- atmospheric conditions (such as clear or dusty);
- direction of illumination source (e.g. Sun angle varies through the daily and yearly cycle);
- scattering properties of the target (such as rough or smooth);
- orientation of the surface (resulting in topographic shadowing and/or increased radiation on undulating ground); and
- view angle of the sensor (nadir looking or off-nadir looking).

To obtain consistent and comparable measures of Earth surface reflectance from EO, such factors need to be reduced or removed from the radiance measurements (Li *et al.*, 2010). This is especially important when comparing imagery acquired in different seasons and/or geographic regions.

Section 6.1 provides an overview of energy transfer mechanisms involving optical wavelengths. Specific optical reflectance characteristics that are relevant to features of the vegetation, rocks and soils, waterbodies, and snow and ice are detailed in Section 6.2, Section 6.3, Section 6.4 and Section 6.5 below respectively. The impact of mixing different features within an EO image pixel is then briefly discussed in Section 6.6.

Of all the means of expression, photography is the only one that fixes a precise moment in time.
(Henri Cartier-Bresson)

Background image: Landsat-5 image of Whitsunday Islands, Queensland, acquired on 24 October 2010 (displayed as natural colour composite using bands 3, 2, 1 as RGB). **Source:** Norman Mueller, Geoscience Australia.

11. While ray optics can also be used to design thermal sensors, TIR imagery will be considered separately in Section 7 below.

6.1 Optical Energy Transfer

Optical imagery detects energy in the optical wavelength region that has been reflected (or scattered) towards the sensor from the Earth's surface (see Volume 1A—Sections 2 and 5). The basic interactions between EMR and target materials are introduced in Section 3, Section 4 and Section 5 above. While discussion of the precise mechanisms for energy transfer within and between molecules is beyond the scope of this text, we will briefly mention two energy excitation 'processes' that are relevant to the interaction of optical energy with solids, liquids and gases. It is currently understood that materials absorb optical wavelengths of EMR via two primary energy transitions:

- vibrational—atoms within molecules and ions can 'vibrate' at precise oscillation frequencies when activated by an external energy source (see Section 3.1). Molecular bonds have been likened to weighted springs, which allow the whole unit to vibrate. Types of vibration include stretching and asymmetric stretching of bonds and bending of the molecular structure. The frequencies at which vibrations occur are determined by a combination of the molecular structure and the wavelength(s) of the energy source, and can be diagnostic for particular molecules.
- electronic—absorption of photons causes electrons to transition to higher energy states (that is, from one quantum shell to another; see Section 3.1). Although the electronic energy level transitions in many Earth surface materials do not produce spectral 'features' in optical wavelengths, their interaction within the structure of molecules or crystals can be observed via four physical mechanisms:
  - crystal field effect— a weak electronic excitation, but the most common;
  - charge transfer—stronger absorption bands resulting from a change in electron distribution;
  - conjugate bonds—molecular orbital transitions in biological pigments (including chlorophyll and haemoglobin); and
  - conduction bands—freer movement of electrons in metals and semiconductors.

Vibrational excitation leads to different fundamental vibrational modes, or 'tones', and secondary effects, or 'overtones', for different functional groups, which principally result in spectral absorption features in SWIR and TIR wavelengths. The presence of water in various materials is often indicated by additional vibrational bands near 1450 nm and 1900 nm (SWIR). Electronic excitation occurs in response to higher energy wavelengths in the UV and visible regions and gives rise to colour. This excitation is particularly important for common elements which occur in multiple forms, such as iron and chromium (Drury, 1987). These photochemical processes are detailed in Visser and Rolinski (2014).

6.2 Vegetation

Reflectance properties of different types of vegetation vary widely with plant colour, texture, structure, density, species composition and moisture content (see Volume 3A—Terrestrial Vegetation). The interaction of these factors with radiation also varies with the incident EM wavelength(s) and illumination geometry (see Section 6.2.1 and Section 6.2.2).

6.2.1 Spectral characteristics of leaves

Some broad attributes of vegetation can be identified which contribute to the characteristic patterns in its reflectance spectra, as illustrated in Figure 1.2 above. The green colour of most vegetation corresponds to larger reflectance of green wavelengths, primarily due to the presence of chlorophyll in leaves, which strongly absorbs in blue and red wavelengths for photosynthesis. Other leaf pigments (such as carotenoids and anthocyanins) also absorb in the visible (predominantly blue) wavelengths, but are often masked by chlorophyll absorption features. Leaf coatings, such as hairs and waxes, increase reflectance across the visible wavelengths.

The cell structure of leaves reflects NIR, with healthy, green vegetation typically showing high NIR reflectances. Since plant type, vigour, maturity and water stress impact the cellular structure of vegetation, variations in these attributes will lead to variations in NIR reflectance. Since water absorbs most wavelengths in the SWIR region, changes in foliar moisture content directly affect the reflectance of SWIR radiation from vegetation.

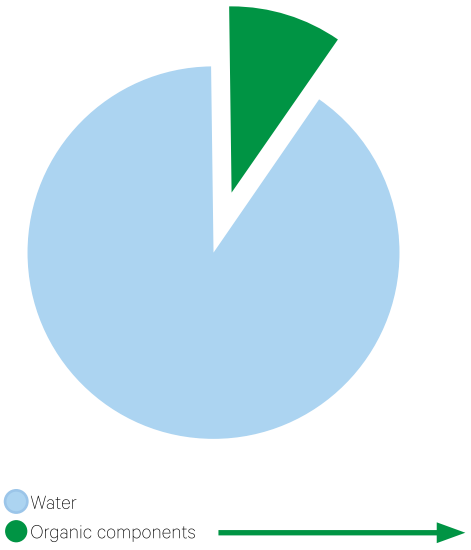
In healthy vegetation, a typical reflectance spectrum shows lower reflected energy in:

- violet and blue wavelengths due to absorption by plant pigments such as chlorophyll (coloured green), carotenoids (coloured orange) and xanophylls (coloured yellow);
- red wavelengths due to absorption by plant pigments such as chlorophyll (coloured green);
- NIR—two smaller dips due to cellular water absorption; and
- SWIR—two larger dips due to cellular water absorption.

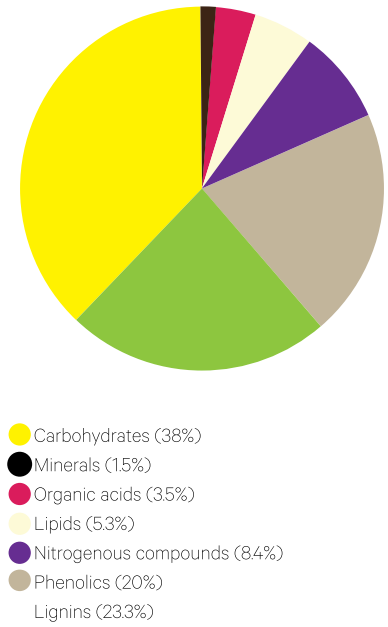
Figure 6.1 Composition of green and dry vegetation

Composition of Fresh and dry Loblolly Pine needles as a percentage of weight.

a. Water is the major component of fresh green foliage



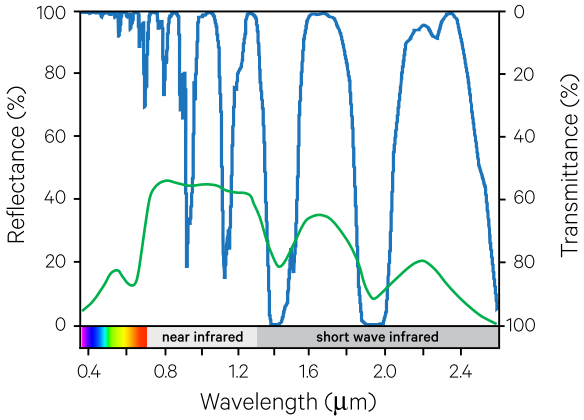
b. Proportions of various organic components in dry foliage



Data source: Chung and Barnes (1977)

Figure 6.2 Vegetation reflectance and atmospheric transmittance

Reflectance spectrum of green vegetation is compared with an atmospheric water transmission spectrum for an urban environment with visibility of 5 km (see Figure 4.1). Note the corresponding troughs in both spectra.



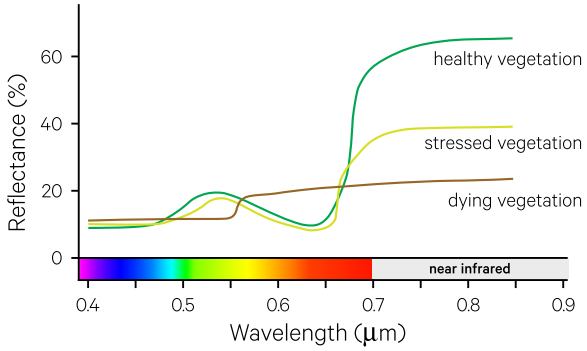
Source for spectra: Vegetation reflectance: Harrison and Jupp (1989) Figure 6; Atmospheric water transmission: Shaw and Burke (2003) Figure 6d. Reprinted with permission courtesy of MIT Lincoln Laboratory, Lexington, Massachusetts.

The most abundant component of fresh, green vegetation is water, comprising 50% to 90% of foliage and 90% to 95% of algae (Weisz and Fuller, 1962). The compositions of green and dry needles of Loblolly pine, for example, are compared in Figure 6.1. Thus, the influence of water absorption on vegetation reflectance spectra is significant as illustrated by the corresponding reflectance dips in Figure 6.2. Since water is responsible for the typical absorption features of green vegetation around 1450 nm and 1900 nm (SWIR), these features diminish as vegetation dries and the absorption patterns of biochemical components, such as cellulose, sugar, starches, waxes and lignins, become more discernible.

The distinctively high reflectance of vegetation in the 700–1200 nm region is dominated by the internal structure (cells, cell walls and intercellular spaces) of the vegetative materials. As a plant becomes stressed, senescent or diseased, however, its structure changes so its reflectance characteristics also change (see Figure 6.3).

Figure 6.3 Effect of disease on vegetation reflectance

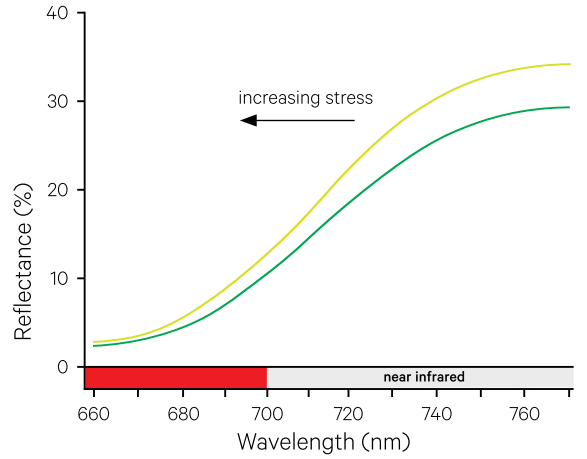
The onset of stress, senescence or disease in plants reduces reflectance in both green and NIR wavelengths and shifts the transition between red absorption and NIR reflectance. In the initial stages of disease, NIR reflectance is reduced. As disease progresses, NIR reflectance continues to decrease and the colour of foliage changes markedly.



Adapted from: Barrett and Curtis (1976)

Figure 6.4 Red edge changes with plant vigour

The term 'red edge' is used to describe the transition from the red absorption trough to the NIR reflectance peak in vegetation spectra. Increasing plant stress shifts this edge towards shorter wavelengths.



Adapted from: Cho *et al.* (2012)

Thus, healthy vegetation is characterised by low reflectance of red wavelengths and high reflectance of NIR wavelengths. In the process of vegetation drying, whether due to aging, environmental stresses or pathology, the point of transition from low reflectance of red wavelengths to high reflectance of NIR wavelengths gradually changes. This transition is called the 'red edge' and occurs between 680 nm and 750 nm (Horler *et al.*, 1983). The position and slope of the 'red edge' are indicative of vegetation vigour (see Figure 6.4).

Vegetation greenness indices rely upon highlighting the characteristically high NIR reflectance and low red reflectance of healthy, green vegetation (see Volume 2C). Reflectance values in NIR and red are differenced or ratioed to emphasise those pixels that are likely to contain a high proportion of photosynthetic material. Results may be normalised for comparison between multiple images or differenced between two images to show temporal changes in greenness.

One of the most common indices, the Normalised Difference Vegetation Index (NDVI), is based on the simple difference between NIR and red reflectances, normalised by the equation (Tucker, 1979):

$$NDVI = \frac{NIR - Red}{NIR + Red}$$

Vegetation greenness indices are used in a wide range of EO applications as detailed in Volume 3A.

6.2.2 Foliage and canopy properties

A number of leaf, canopy and stand properties affect vegetation reflectance. Some of the characteristics of individual leaves that can influence reflective properties include their:

- internal structure, chemistry and biophysical processes;
- form, shape and orientation; and
- surface coatings.

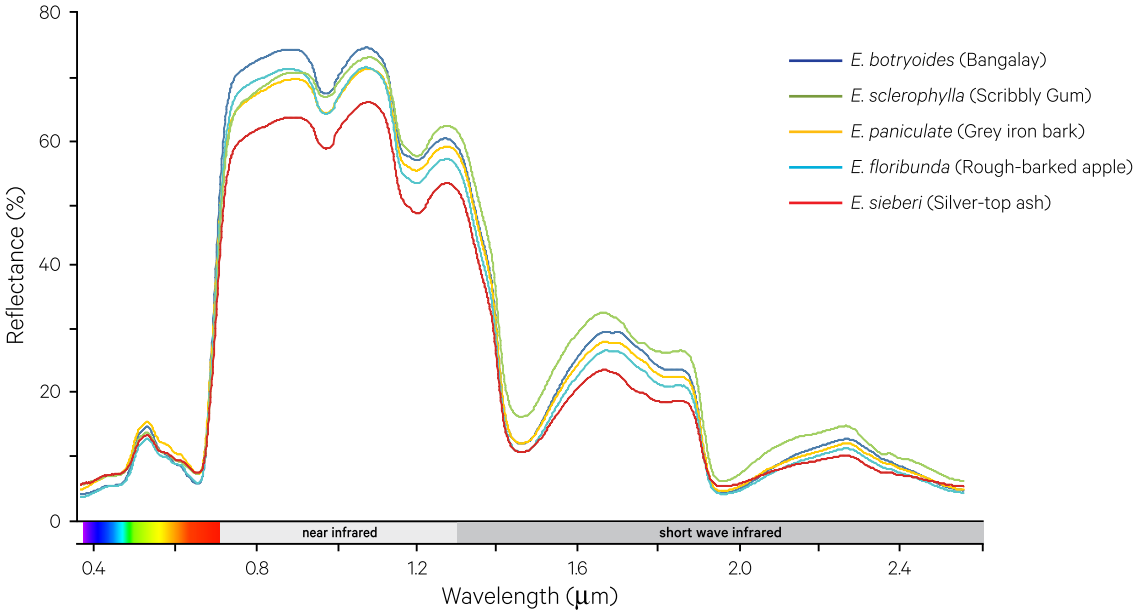
Visible wavelengths of EMR primarily interact with individual leaves in the process of photosynthesis. Plant pigments, which help to determine leaf colour, also absorb some wavelengths of visible light (see Figure 1.2).

Within a single genus, such as *Eucalyptus*, the leaves of different species can display different reflectance properties as illustrated in Figure 6.5. Various simulation models, which consider attributes such as cell size, leaf thickness, and content of chlorophyll, water, cellulose and nitrogen, have been developed to model the effects of leaf biochemical and physical composition on spectral reflectance (such as LIBERTY, Dawson *et al.*, 1998). Changes in leaf reflectance that are related to growth stages, or phenology, can also be modelled (see Volume 3A).

As well as the actual leaf colour, the surface coating can markedly modify reflectance properties. Shiny leaves will reflect light in a more specular fashion than dull, rough or glaucous leaves. Large leaves are more likely to result in specular reflectance than small leaves, and horizontal leaves are more likely to intercept, and directly reflect, solar radiation than vertical leaves (see Figure 6.6). Foliar reflectance within plant species can also change with seasonal growth, in both deciduous and evergreen vegetation, and diurnal activity.

Figure 6.5 Reflectance spectra for different *Eucalyptus/Angophora* species

Mean reflectance spectra are shown for four species of *Eucalyptus* and one species of *Angophora*.



Source: Laurie Chisholm, University of Wollongong

Figure 6.6 Variations in foliage and canopy characteristics

The colour, orientation, sheen and texture of individual leaves and plant canopies can markedly impact reflectance properties.

a. Variations in foliage texture and size impact reflectance characteristics



b. Aerial view of *Eucalyptus* forest with variations in texture and orientation



c. Aerial view of mangrove forest with relatively uniform canopy



Source: a. ©Shutterstock image ID 24807769. b. ©Shutterstock image ID 186362276. c. ©Shutterstock image ID 440199721

The density and arrangement of leaves within canopies also impacts the way EMR is scattered and absorbed. The crown form, that is, the size, shape and branching of the plant crown, obviously affects reflectance and shadowing characteristics (see Figure 6.6b). At a stand level, plant structural properties and biomass, as well as microclimates induced by topographic variations, also modify vegetation reflectance.

Radiative transfer (RT) occurs within vegetation canopies, with individual leaves and branches both scattering indirect radiation onto other leaves and preventing direct radiation reaching them. The combined impacts of scattering and shading within canopies has been simulated by canopy RT models (see Section 5.3 above).

6.3 Rocks and Soils

The spectral reflectance properties of rocks and soils vary with mineral composition and abundances, structure, texture, colour, water and organic matter content. For example, a diagnostic feature of iron oxides is the 900 nm crystal field absorption feature. The depth and geometry of this feature changes according to the abundance of iron oxide and the wavelength of the minima of this feature is diagnostic of the iron oxide composition, that is shorter wavelengths are indicative of hematitic iron oxide while longer wavelengths indicate goethite (Curtis, 1985; Morris *et al*., 1985). Additionally, the width or the location of the 'wings' of the 900 nm crystal field absorption feature is indicative of hydrated or non-hydrated minerals.

Rocks and soils comprise minerals, which in turn comprise elements. The most commonly occurring elements in rocks and minerals are oxygen, silicon and aluminium. These combine with different amounts of iron, magnesium, calcium, sodium, potassium and smaller proportions of other elements (Drury, 1987).

6.3.1 Mineralogy

Section 6.1 briefly introduced the two basic energy excitation mechanisms whereby materials absorb optical radiation, namely molecular vibrations and electronic transitions. The spectral regions that mineral spectroscopists generally use are:

- 2.0–2.5 μm (SWIR)—indicating the presence of hydroxyl ions and carbonates; and
- 8.0–11.0 μm (TIR)—indicating the presence of silicon, magnesium and aluminium.

Although, the features seen in the SWIR regions are overtones, it is commonly used because it is largely within the atmospheric windows. As in vegetation spectra (see Section 6.2.1), the presence of water is often indicated by two additional vibrational bands near 1.45 μm and 1.9 μm (SWIR).

Although the electronic energy level transitions in most common geological elements, such as silicon, aluminium or oxygen, do not produce spectral 'features' in optical wavelengths, their interaction within the structure of molecules or crystals can be observed via three physical mechanisms (Clark, 1999; Elachi and van Zyl, 2006):

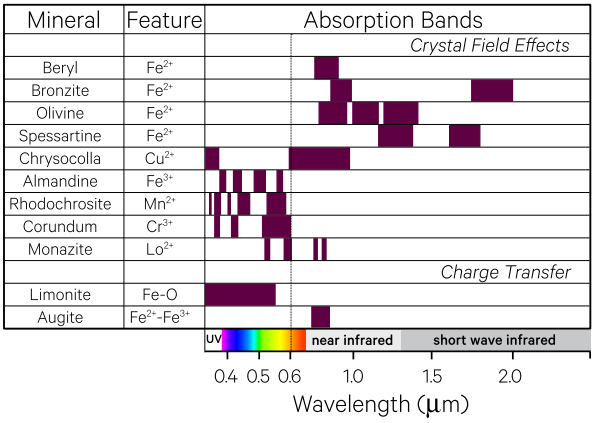
- crystal field effect—transitions in discrete ions, which occur in transition metal compounds, with key minerals displaying this effect being iron oxides and rare earth minerals. The crystal field effect enables species of iron oxide to be determined (such as hematite versus goethite) and the presence of other elements to be identified (such as zinc and lead when bonded to phosphates and sulphates);
- charge transfer—within some transition metal complexes (such as iron). This electronic transition commonly occurs from iron to oxygen at wavelengths less than 550 nm, resulting in the minerals containing iron oxide appearing yellow, orange or red; and
- conduction bands—transition of electrons from one ion to another in metals (such sulphur and cinnabar).

Electronic excitation occurs in response to higher energy wavelengths in the UV and visible regions and often gives rise to the colour of minerals. A summary of the absorption patterns resulting from these two excitations is shown in Figure 6.7.

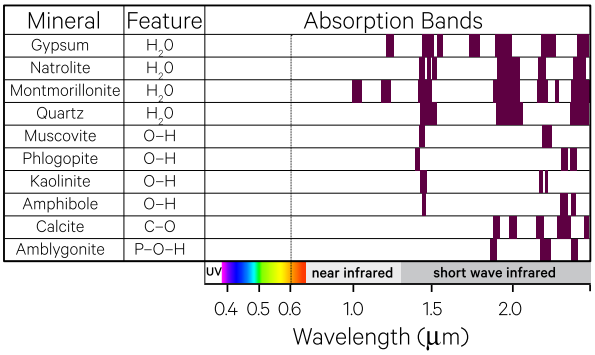
Figure 6.7 Absorption mechanisms of geologic materials

The relative widths of absorption bands for different geologic materials are indicated by the purple bars. The second column labelled 'feature' identifies the principal chemical component causing the absorption features. Note that a scale change occurs on the x-axis at 0.6 μm.

a. Electronic processes



b. Vibrational processes



Adapted from: Hunt (1977) by Cindy Ong and Carsten Laukamp, CSIRO

Diagnostic absorption features of specific minerals can be described in terms of four broad categories (see Table 6.1):

- iron oxides (e.g. hematite and goethite) have spectral features in visible and NIR wavelength regions;
- hydroxyl bearing minerals (e.g. clays, phyllosilicates, amphiboles and sulphates) have features in the SWIR wavelength region;
- carbonates have features in the SWIR, MIR and TIR wavelength regions; and
- silicates (e.g. quartz, feldspars, garnets and pyroxenes) have spectral features in the TIR wavelength region (see Excursus 6.1 and Section 7).

Some typical mineral spectra are illustrated in Figure 6.8.

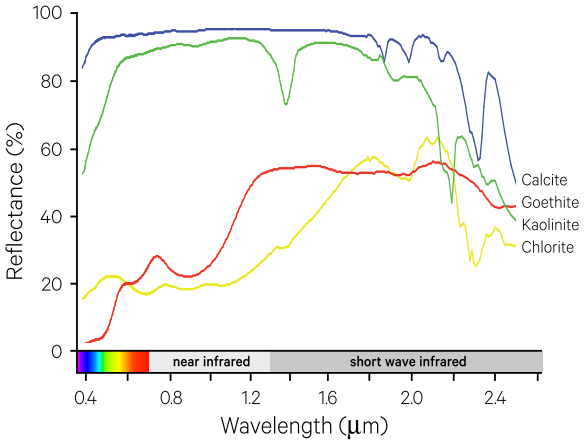
Table 6.1 Spectral characteristics of minerals

Functional Group	Mineral Group	Example Minerals	Diagnostic Absorption Features
Iron Oxides	Fe(OH)	Hematite, Goethite	<400 nm (due to charge transfer) 860–950 nm (crystal field transitions) 2700–3000 nm (OH and water)
Carbonates	CO_3	Ankerite, Siderite, Calcite, Dolomite, Magnesite	2300–2400 nm
Hydroxyl (OH)	Al(OH)	Topaz, Pyrophyllite, Kaolinite, Montmorillonite, Muscovite, Illite	2160–2220 nm
	Fe(OH)	Jarosite, Nontronite, Saponite, Hectorite Fe-rich Chlorite	2250–2300 nm
	Mg(OH)	Chlorite, Talc, Epidote, Amphibole, Antigorite, Phlogopite	2300–2400 nm
	Si(OH)	Opaline silica	2240 nm (broad)

Source: Megan Lewis, University of Adelaide

Figure 6.8 Typical mineral spectra

Reflectance spectra for selected common minerals are shown.



Source: Cindy Ong and Ian Lau, CSIRO, derived from USGS spectral library

Excursus 6.1—ASTER Geoscience Maps of Australia

Source: Cindy Ong, CSIRO
Further Information: Cudahy *et al.* (2012); *http://www.ga.gov.au/scientific-topics/earth-obs/satellites-and-sensors/aster-radiometer/national-aster-maps*

The Advanced Spaceborne Thermal Emission and Reflection Radiometer (ASTER) was launched in December 1999 aboard the Terra satellite (Yamaguchi *et al.*, 1998). The spectral band configuration of the multispectral ASTER system was designed specifically to map broad mineral groups. Features of this sensor include:

- three bands covering the visible and near infrared (VNIR: 0.52–0.86 μm), six covering the shortwave infrared (SWIR: 1.6–2.43 μm) and five in the thermal infrared (TIR: 8.125–11.65 μm) wavelength regions;
- medium spatial resolutions of 15 m, 30 m, and 90 m for each of the VNIR, SWIR and TIR ranges; and
- 60 km swath width.

These features enable ASTER imagery to provide useful information relating to mineral groups, such as clays, carbonates, quartz and iron oxides. Such specific mineralogical information had not been available from any other satellite sensors until the launch of WorldView-3 in 2014, with similar VNIR and SWIR bands to capture the iron oxide, clays and carbonates. However, WorldView-3 lacks both the bands to map quartz and the global coverage provided by ASTER imagery.

The ASTER Geoscience Maps of Australia (Cudahy *et al.*, 2012) provide mineral group abundances and composition for the entire land mass of Australia. Derived from 3,500 images, these maps were the first public, web-accessible, continental-scale geoscience maps from the ASTER Global Mapping data archive. The maps have been useful for a range of geological and environmental applications (Cudahy, 2016). For example, the silica index map (see Figure 6.9) has enabled a better understanding of surface clay loss or gain, and hence improved insights into associated erosional/depositional processes.

Figure 6.9 Silica Index Map

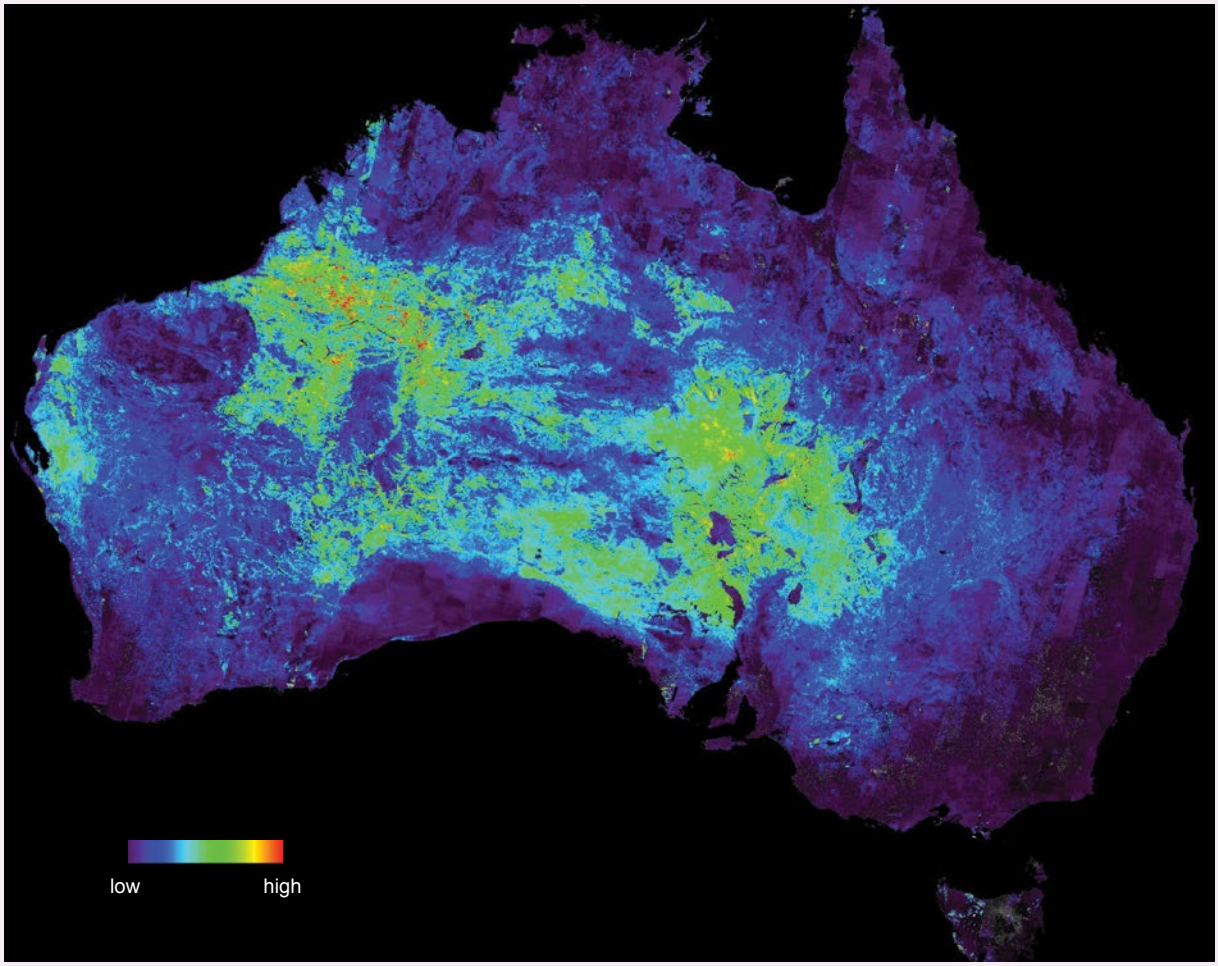
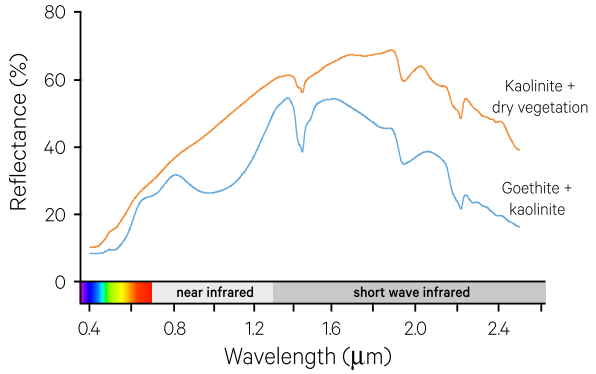


Figure 6.10 Soil spectra

Reflectance spectra acquired from soil samples collected at Wickepin, in the wheatbelt of WA. The absorption feature around 900 nm on the blue spectral line is characteristic of goethitic iron oxide, while the absorption features around 2200 nm are diagnostic of kaolinite. The absorption feature around 2080 nm on the orange spectral line is characteristic of dry plant material. Note that the soil sample shown as the orange spectral line also contains kaolinite.



Source: Cindy Ong and Ian Lau, CSIRO

Soil spectroscopy has been an active area of research in recent years. Minerals make up about half the volumes of most soils (Schulze, 2002). Accordingly, the ability to detect mineral compositions and abundances spectrally enables detection of a major component of soils. Additionally, other components of soils, such as organic matter, can be inferred spectrally. Researchers have demonstrated the ability to use spectroscopy for mapping soil components using field spectroscopy methods (Viscarra Rossel and McBratney, 2008; Summers *et al.*, 2011), as well as from remote sensing platforms (Ben Dor, 2011). Attempts have also been made to standardise laboratory measurements in order to provide more quantitative, transferable results (Ben Dor *et al.*, 2015).

Examples of spectra measured in the laboratory from soil samples acquired in the wheatbelt of WA are shown in Figure 6.10. They indicate spectrally diagnostic features of iron oxides, kaolinite and dry plant material, which are useful for characterising these soils.

6.3.2 Water content

Water content of rocks and soils varies with their structural properties and ambient environmental conditions, and occurs in a number of forms:

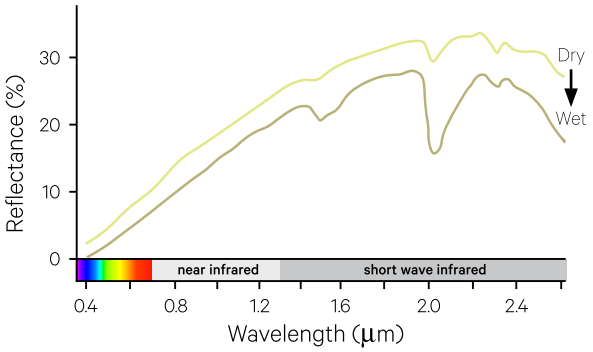
- free—moves under the effect of gravity to dissolve or precipitate constituents; or
- bound:
  - adsorbed—retained in extremely thin films on (or very close to) particles by electrical charges between the water molecules and the surface; or
  - absorbed—trapped between particles by capillary pressure.

As with vegetation, the presence of water markedly changes reflectance properties of mineral features. In the SWIR region, water reduces the overall brightness of geological samples, and hence the spectral contrast between characteristic absorption features to the extent that some absorption features can be obscured. In Figure 6.11, for example, the presence of water deepens the characteristic water absorption troughs at 1450 nm and 1900 nm (see Figure 6.2), but decreases the Kaolinite absorption feature at 2200 nm.

Soil colour is visibly darkened when moist, which is evident in EO imagery (see Figure 6.12). Moisture retention and the extent of colour darkening also vary with different soil types. The impact of variations in soil colour resulting from changes in moisture content is particularly significant for areas of sparse vegetation in optical EO imagery. Differential drying of soils changes the distribution of moisture. The surface texture (or roughness) of soil can also change with moisture content.

Figure 6.11 Wet and dry kaolinite spectra

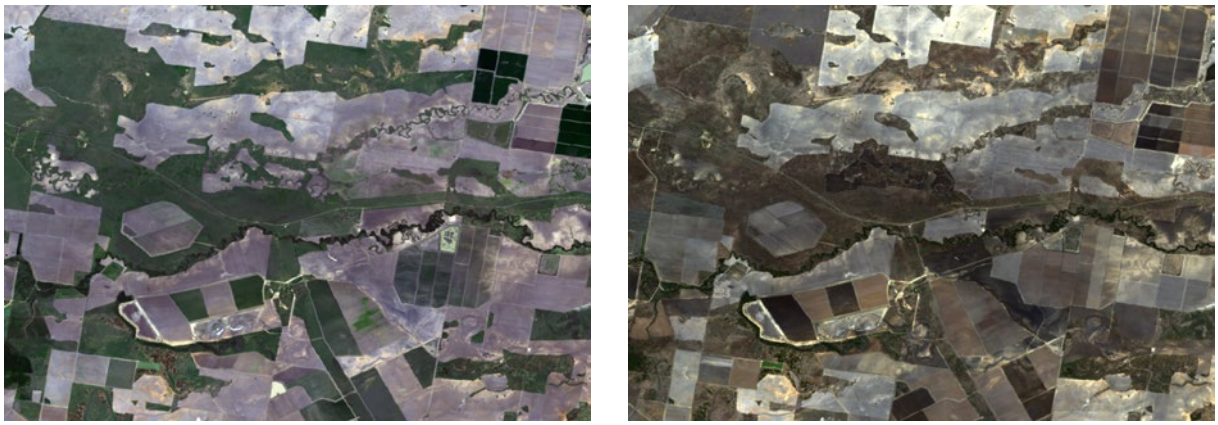
The presence of water decreases overall brightness in the kaolinite spectra. The water absorption troughs at 1450 nm and 1900 nm are further enhanced in wet kaolinite. The characteristic kaolinite absorption trough at 2200 nm, however, is smaller when water is present.



Source: Megan Lewis, University of Adelaide.

Figure 6.12 Image differences resulting from variation in soil moisture

A cotton cropping area west of Moree in northern New South Wales captured by Landsat-8 on 13 February (left) and 19 May 2016 (right). The image pair shows the variation in soil and vegetation brightness due to soil moisture. Soil moisture tends to darken soil colour, changing the observed reflectance within an image pixel. This effect needs particular consideration when mapping and monitoring sparse vegetation. The left image is generally wetter whereas significant drying has occurred in the right image, resulting in greater contrast between areas with higher and lower soil moisture.



Source: Norman Mueller, Geoscience Australia

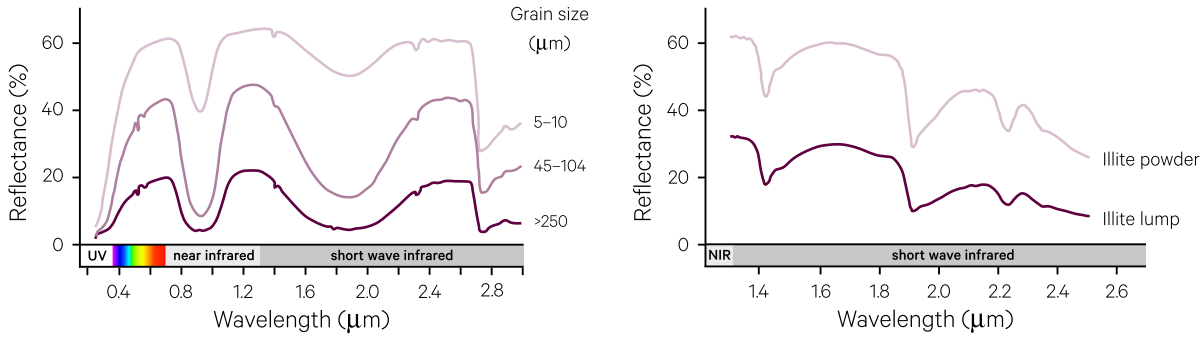
6.3.3 Particle size

The grain size, or texture, of any geological material alters the intensity of its reflectance (see Figure 6.13). For example, powders are generally more reflective than cohesive matter (see Figure 6.13b) due to their greater surface area for scattering and reflecting radiation (see Section 3.3). One exception occurs when ore samples that contain sulphides or trans-opaque minerals are crushed, resulting in darkening of the sample colour. Similarly, the structure and/or orientation of any given rock or soil type relative to the illumination source and viewing position will modify its reflective properties (see Section 3.5).

Figure 6.13 Effect of particle size on mineral spectra

a. Impact of grain size on reflectance spectra—larger grains absorb more light and reduce reflectance.

b. Powders have brighter spectra than rocks.



Adapted from: a. Clark *et al.* (1993) at *http://speclab.cr.usgs.gov/PAPERS.refl-mrs/refl4.html* b. USGS (2011)

6.3.4 Surface coating

The surface coating of rocks and soils determines the appearance of the material to a remote sensor. While laboratory samples of particular minerals may display obvious absorption features as discussed in Section 6.3.1 above, field samples can acquire various organic and/or inorganic coatings, which may significantly change their spectral properties. Encrustations of dry or photosynthetic algae, lichens and moss may mask or mix with mineral spectra of rock outcrops, and organic matter lowers soil reflectance across visible–shortwave infrared wavelengths.

6.4 Waterbodies

Most optical radiation intercepted by water surfaces is absorbed or transmitted rather than reflected (see Figure 1.1). Water bodies generally reflect 1–15% of the downwelling radiation, with most only reflecting 2–6% (Phinn and Dekker, 2004). In this context, water bodies include inland water (dams, rivers, lakes, and reservoirs) and maritime waters (estuaries, harbours, seas, and oceans). In water bodies, reflectance generally decreases with increasing water depth or decreasing particulate content, although for some substrata, such as dark seagrasses, the reverse relationship may occur. The strong absorption of NIR energy in the first few centimetres of water clearly defines land/water boundaries in EO imagery, in contrast to the high reflectance of soil and vegetation at this wavelength.

The reflectance properties of the water column (the vertical profile of water between the surface and the depth of the substrate) are determined by the water colour, the water column and the water depth. Water colour is determined by both suspended sediments and dissolved matter. These constituents can be organic (such as phytoplankton or dead and/or decaying particulate matter) or inorganic (such as minerals). In optically shallow water, the reflective properties of the substratum are also relevant to the observed reflectance from the surface of a water body. Characteristics of the water surface, such as sunglint and skyglint, can further impact observed reflectance values in EO imagery.

The following sub-sections consider reflectance properties of waterbodies in terms of:

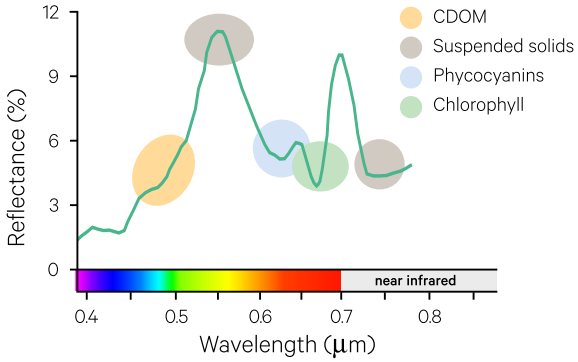
- colour and clarity of the water column (see Section 6.4.1);
- depth of the water column (see Section 6.4.2)
- substratum type (if shallow; see Section 6.4.3); and the
- texture of the water surface (see Section 6.4.4).

6.4.1 Water column colour and clarity

The main constituents that contribute to colour in the water column are suspended particles and/or dissolved organic materials. The presence of suspended particles in water is typically indicated by an increase in reflectance in visible and NIR wavelengths (depending on colour of the solids). Organic constituents, such as coloured dissolved organic matter (CDOM), chlorophyll, and phycocyanins, also display distinctive spectral absorption characteristics (see Figure 6.14).

Figure 6.14 Characteristic reflectance features of water colour constitutents

Coloured water reflectance components are shown for chlorophyll-rich water. Spectral features are exaggerated in this graph to highlight individual components. Note that the actual reflectance also varies with the density of particles in the water (see Figure 6.17). Note: CDOM = Coloured Dissolved Organic Matter.

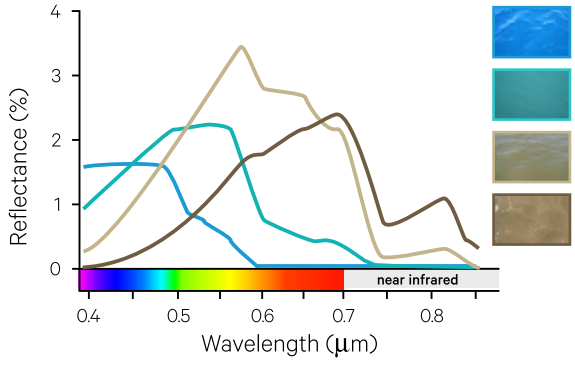


Source: Erin Hester, North Carolina State University

Both water clarity and colour impact the depth to which downwelling radiation can penetrate below the surface of a water body and determine the apparent colour of the water body. In clear, oceanic water, for example, the downwelling radiation reaching 3 m below the water surface is greatest in blue to blue-green wavelengths, with lower levels of radiation in green wavelengths, and least in red wavelengths. By contrast, in brown river water, much lower levels of radiation reach a water depth of 1 m, with maximum radiation occurring in the red-brown wavelengths. The observed reflectance spectra corresponding to four different water colours are shown in Figure 6.15.

Figure 6.15 Reflectance from different water colours

Variations in water colour result in varying spectral characteristics for water bodies. This graph shows the spectra resulting from four different water colours.



Source: Vittorio Brando, ISAC-CNR

A Secchi disk is commonly used to estimate water clarity (or turbidity) in the field. This is a flat, weighted disk (traditionally black and white for freshwater and all white for marine water), which is lowered into a water body on the end of a pole or rope until it 'just disappears'. At that point, the length of rope below the water surface is the 'Secchi depth' and provides a convenient measure of water clarity. The concept of 'just disappears', however, is hard to define objectively and can depend on water surface texture, colour and spectral contrasts, as well as the visual acuity and colour sensitivity of the observer.

Basically the Secchi depth (Z_{SD}) approximates the point when the light being reflected by the disk is no longer visible at the water surface. This observation can be used to estimate the vertical attenuation coefficient for the water (K_d), such that:

$$K_d = \frac{i}{Z_{SD}}$$

with

Z_{SD} in metres; and
i = 1.44 (Kirk, 1994). Some authors refer to a range of values for i, depending on water optical properties (Davies-Colley and Vant, 1988; Koenings and Edmundson, 1991; Gallegos *et al*., 2011).

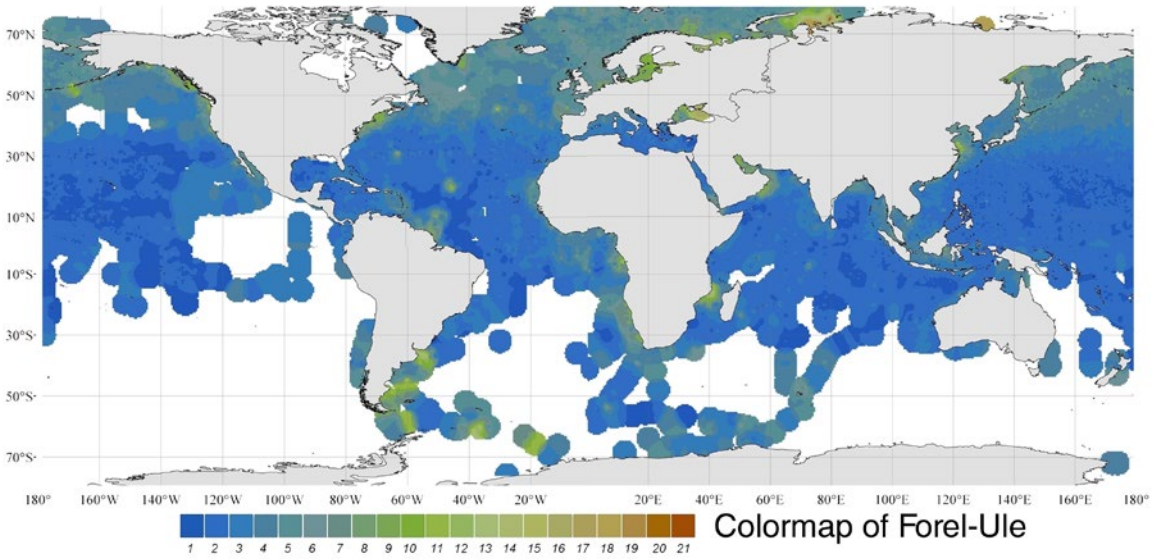
Secchi depth is determined mainly by particulate matter (algae and suspended sediments), which reduce water clarity, rather than dissolved organic materials, which change the colour of water but not necessarily its clarity.

The Z_{SD} readings can vary due to different water surface conditions, such as surface roughness or illumination conditions, but also between observations. Another common indicator of water clarity is the depth of the euphotic zone (Z_{eu}). This is defined as the depth at which, of the photosynthetically active radiation (PAR, 400 nm to 700 nm) that penetrated the water, only 1% remains. The Z_{eu} estimates are more suitable for ecological applications than the Z_{SD} estimates.

Standardised colour keys have been used to calibrate observations of water colour for over a century. The Forel Ule colour comparator scale, for example, comprises 21 colours from indigo, through blue, green, yellow and brown (Forel Ule Scale, 2017). When this colour scale is viewed simultaneously with a water sample, the colour of the sample can be matched. The Forel Ule scale is used in conjunction with a Secchi disk such that the water colour being matched corresponds to the water sample above half the Secchi depth. This system is being embraced by citizen scientists all over the world to provide valuable data to water scientists (see Figure 6.16). The Citclops project, an EU initiative, integrated observations and measurements of the colour, transparency and fluorescence of seawater that have been derived using a range of citizen science methods and low-cost sensors. This global database will greatly enhance our understanding of the dynamic nature of coastal and oceanic water bodies in both space and time (Citclops, 2017; see Volume 3B for more information).

Figure 6.16 Global observations of water colour

This global map of water colour observations is based on the Forel Ule scale.

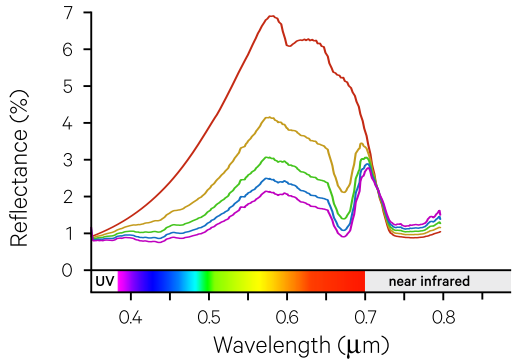


Source: Forel Ule Scale (2017). Retrieved from: *http://forel-ule-scale.com/wp-content/uploads/2014/10/Sliderfoto-2.jpg*

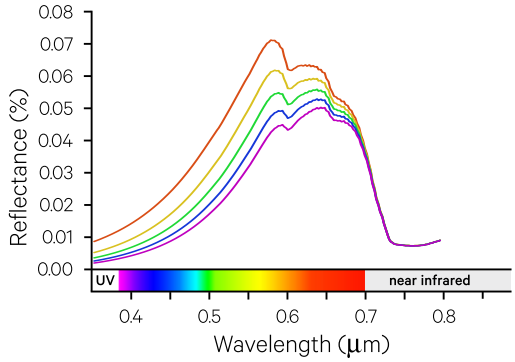
Figure 6.17 Simulations of water body reflectance

The Bio-opti model was used to generate reflectance spectra assuming a nadir view of a water body of depth 10.5 m over a sand substrate. Concentrations of three water column constitutents have been varied, with lowest concentration shown as violet through to the highest concentration as red. These simulations show the impact of these changed concentrations on reflectance spectra.

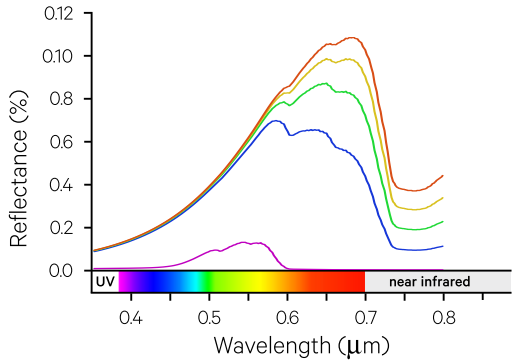
a. chlorophyll a (CHLA) 0.001–50 μg/l (with CDOM 0.25 m^{-1}, NAP 22.266 mg/l)



b. coloured dissolved organic matter (CDOM) 0.001–5 m^{-1} (with CHLA 0.001 μg/l, NAP 22.266 mg/l)



c. non-organic particles (NAP) 0.001–100 mg/l (with CHLA 0.001 μg/l, CDOM 0.25 m^{-1})



Source: Yi Qin, CSIRO

Various models have been developed to exploit the relationship between water reflectance properties and water body variables. For example, bio-optical models (such as Bio-opti, Haan *et al.*, 1999; Qin *et al.*, 2010; Gege, 2014) simulate sub-surface reflectance for water with varying depth, constituents and substrates. The impact of varying the concentrations of chlorophyll a, coloured dissolved organic matter and non-organic particles in the water column is shown in Figure 6.17.

Using EO imagery from both satellite and airborne sensors, algorithms exist for assessing the surface water concentrations of:

- chlorophyll (CHL)—indicator of phytoplankton biomass, trophic and nutrient status, and the most widely used index of water quality and nutrient status globally (see Excursus 6.1);
- cyano-phycocyanin (CPC) and cyano-phycoerythrin (CPE)—indicators of cyanobacterial biomass common in (potentially) harmful and toxic algal blooms in inland and marine waters;
- coloured dissolved organic matter (CDOM)—optically measureable component of dissolved organic matter in the water column, sometimes used as an indicator of aquatic carbon; and
- total suspended matter (TSM) and non-algal particulate matter (NAP; where NAP is defined as TSM minus phytoplankton pigments as detailed in Volume 3B)—important for assessing water quality, and a major factor controlling the light environment of aquatic environments (Dekker and Hestir, 2012).

These EO methods have been used to map water quality, create global ocean colour maps and monitor ocean productivity and are further detailed in Volume 3B. Examples of relevant applications include using EO imagery to map chlorophyll concentration and ocean currents (see Excursus 6.2) or monitor inland water quality (Excursus 6.3).

Excursus 6.2—Mapping chlorophyll concentration and ocean currents

Source: Edward King, CSIRO
Further information: IMOS OceanCurrent: *http://oceancurrent.imos.org.au*

The scattering and absorption of sunlight in near surface waters affects the apparent colour of water. By comparing the measured spectrum (colour) with chemical and particulate analysis of water samples, it is possible to establish relationships that are the basis of 'ocean colour algorithms'. These algorithms are used to map water properties by satellite sensors such as Aqua MODIS, and Sentinel-3 OLCI and, historically, CZCS, POLDER, SeaWIFS and MERIS.

A set of widely used algorithms for chlorophyll a concentration products (in mg/m^3) are commonly based on a spectral slope, typically:

$$\frac{\textit{reflectance at 490 nm}}{\textit{reflectance at 555 nm}}$$

Actual methods are more complex, depending on the spectral bands available on each sensor and the particular water types being observed.

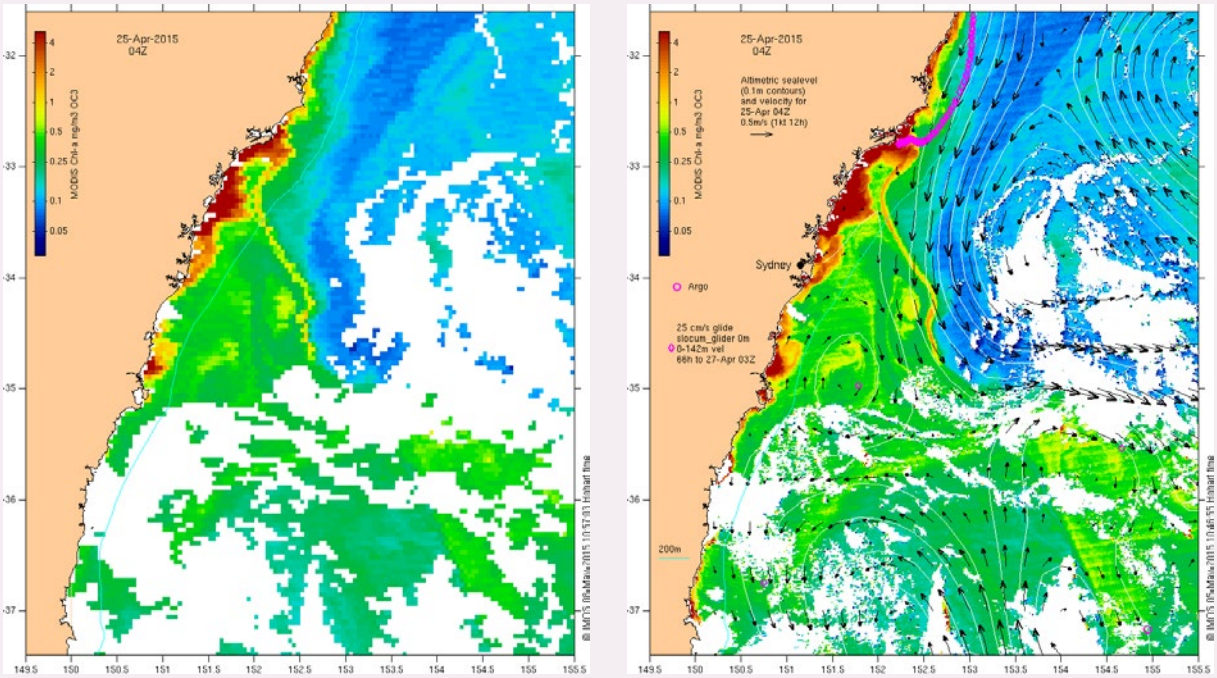
The image in Figure 6.18a is an example of a standard NASA chlorophyll product, at 4 km resolution. In this case, the algorithm is based on the assumption that chlorophyll is the only optically-active constituent affecting the spectrum. While this assumption holds for the bulk of the global ocean, near land, where there are other substances dissolved in water and also sediments flowing from rivers, the algorithm can produce misleading results. In these areas extensive fieldwork is usually required to tune the algorithms to account for the local variations of the water optical properties. When this is done ocean colour imagery can reveal a great deal of detail about the complexities of coastal waters. Figure 6.18b is the same image as Figure 6.18a, but processed at the sensor resolution of 1 km, and further enhanced with other information from satellite altimeter missions that provide the surface current field.

Figure 6.18 MODIS chlorophyll a concentration products

Major storms occurred in the Hunter region, north of Sydney, on 21–22 April 2015. On 25 April, the floodwaters appear as a yellow-orange ribbon near the centre of the images below. These MODIS chlorophyll a products highlight the interaction between floodwater from the Hunter River and both the low chlorophyll waters of the East Australian Current (coloured blue) and the more chlorophyll-rich waters of the Tasman Sea (coloured green).[12]

a. Monthly NASA product based on 4 km grid using NASA chlorophyll a algorithm (see Section 6.4.1) for 25 April at 04Z

b. The same image processed at 1 km and integrated with other datasets by IMOS OceanCurrent. Contours (at 0.1 m interval) show altimetric sea level and arrows indicate geostrophic current velocity for 25 April 2015.

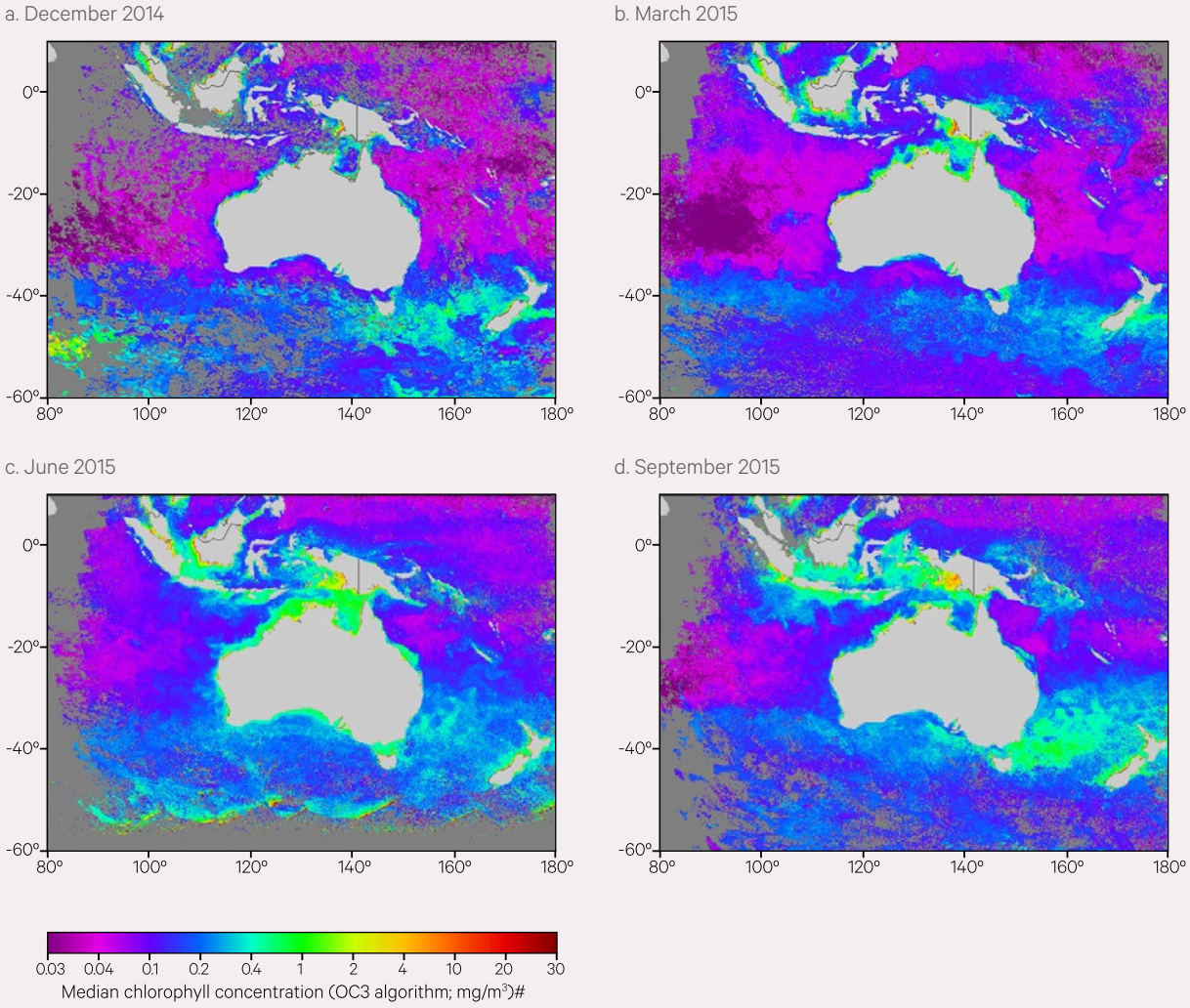


Source: Edward King, CSIRO © IMOS, based on NASA imagery.

12. For more details on this event, please visit the IMOS website: *http://imos.org.au/fileadmin/user_upload/shared/IMOS%20General/documents/newsletters/Marine_Matters_Issue_21-June-2015_WEB.pdf*

Figure 6.19 Seasonal trends in chlorophyll a

IMOS generates a range of 1 km monthly time series for the Australasian region based on imagery from Aqua MODIS. The median chlorophyll concentration (using OC3 algorithm in mg/m^3) for four different seasons are shown below.



Source: Data courtesy of CSIRO and IMOS/SRS. These datasets are available online via the IMOS portal: *http://oceancurrent.imos.org.au.*

Optical observations of water are affected by cloud, so it is usual to form composite maps from several, or many, days of imagery. Monthly image composites are also a convenient way to track seasonal variations in chlorophyll concentration. Four seasonal views of chlorophyll concentration around Australia were derived from MODIS imagery using the OC3 algorithm (see Figure 6.19). This algorithm is transferable across a range of ocean colour sensors, including Sentinel-3 or VIIRS.

Excursus 6.3—Monitoring Inland Water Quality in Australia

Source: Arnold Dekker, Janet Anstee and Elizabeth Botha, CSIRO
Further Information: Dekker and Hestir (2012)

Access to sufficient, high quality freshwater is a key national challenge for Australia. Among leading industrialised countries, water quality in Australia is ranked among the lowest. Reduced water quality affects Australia's growing population, agriculture, ecosystems, coasts and oceans. The social and economic impact of reduced water quality can be substantial, requiring significant management interventions.

Surface runoff and landscape erosion transport sediment, contaminants and nutrients through our waterways and into our reservoirs and coasts. Increased nutrients in the runoff result in (potentially) harmful algal blooms that can contaminate ecosystems and may be toxic to livestock and humans. Organic matter dispersed during floods or blackwater events can impair water clarity and lead to ecosystem stress, potentially killing fish and other aquatic life. Climate change and changing water availability may further exacerbate these water quality challenges.

Satellite imaging is a cost effective way to monitor the status and trends of optical water quality at a continental scale. Satellite remote sensing provides continental-scale coverage with rapid revisit intervals for some sensors. The sensitivity of spaceborne sensors to detect sediment, algae and organic matter in surface water make this an ideal tool for continued innovation in water management and spacecraft have long been deployed for successful global monitoring of water quality (see Volume 3B for more details).

Figure 6.20 Lake Burley Griffin in 2010

Water quality problems in Lake Burley Griffin necessitated closure of the lake in 2010.

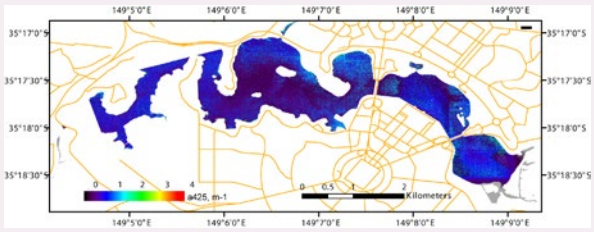


Figure 6.21 Lake Burley Griffin, Canberra, imaged from WorldView-2

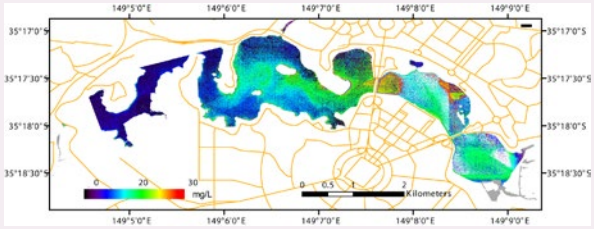
a. Lake Burley Griffin, Canberra, imaged from WorldView-2, on 17 March 2010



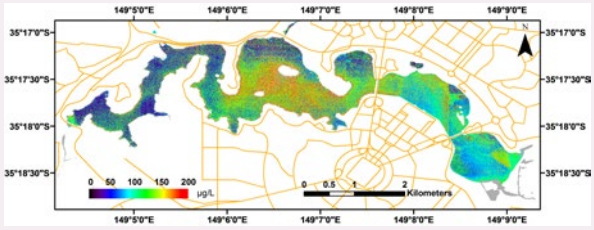
b. Derived map of coloured dissolved organic matter



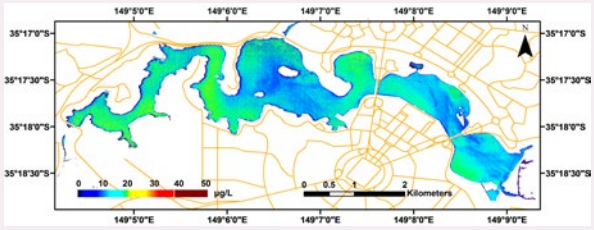
c. Derived map of non-algal particulate matter



d. Derived map of chlorophyll-a



e. Experimental derived map of cyanophycocyanin



While ocean colour satellites have the spectral sensitivity required for water quality applications, they lack the spatial resolution required to map sinuous rivers and reservoirs. As the spatial resolution of optical sensors improves, imagery with higher (but still sub-optimal) spectral resolution is being used to map inland water quality. For example, in 2010, problems with water quality in Canberra's Lake Burley Griffin required the lake to be closed (see Figure 6.20). Worldview-2 imagery of the lake (see Figure 6.21a) was used to map:

- coloured dissolved organic matter (see Figure 6.21b);
- non-algal particulate matter (see Figure 6.21c);
- chlorophyll-a (see Figure 6.21d); and
- cyanophycocyanin (see Figure 6.21e).

6.4.2 Water column depth or bathymetry

The measurement of water column depth, or bathymetry, in marine environments is valuable for monitoring and managing these systems. Accurate measurements of bathymetry provide information on sub-surface topography for navigation, as well as understanding sediment movements and budgets. As well as traditional hydrographic surveys, estimates of water depth can be derived from acoustic and EMR sensors (Goodman *et al*., 2013).

Typically bathymetry has been acquired with active sensors, which transmit energy then measure the backscattered return of energy from the target using either:

- ship-based, single beam or multi-beam acoustic devices, which emit sound waves then determine the water depth from the return time of the sound wave bouncing off the substrate and returning to the detector; or
- airborne lidar sensors, which pulse light to measure substrate depth (see Volume 1A—Section 15). Accurate bathymetry maps using airborne lidar systems (Irish and Lillycrop, 1999; Guenther *et al*., 2000) are commonly undertaken in high value areas but can be costly for large-scale applications.

In recent decades, large-area surveys of water depth have been conducted using satellite-derived bathymetry (SDB). SDB is based on passive optical sensors (see Volume 1A) and offers rapid, cost-effective coverage (Green *et al*., 2000) of large and remote areas for environmental monitoring, development planning, and exploration. SDB can be derived using:

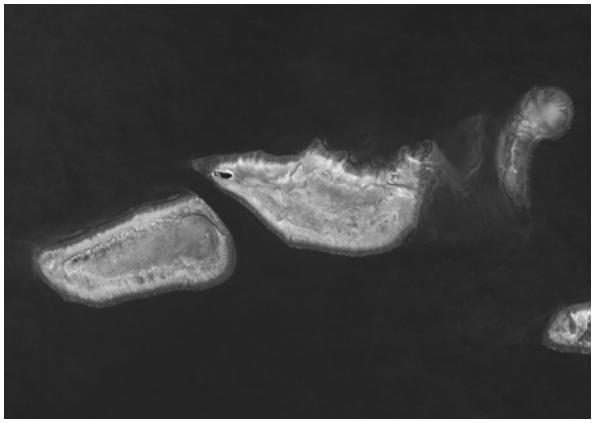
- empirical approaches, which correlate the field measured depths with the satellite image radiance or reflectance values; or
- analytical and semi-analytical approaches, which are based on RT theory and incorporate knowledge of the water column properties and benthic substrate composition. These models can be applied to create EO-based maps of water depth, water column properties and substrate cover from hyperspectral and multispectral satellite imagery.

Since different wavelengths of EMR penetrate water to different depths, these differences can be used to derive water depth maps from EO imagery. For example, in Figure 6.22, the blue band in the Landsat TM imagery is impacted by substrata down to around 25 m below the water surface, in the green band to around 15 m depth, and in the red band to around 5 m depth, whereas NIR and SWIR wavelengths are completely absorbed by very shallow water. SDB techniques are discussed in more detail in Volume 3B.

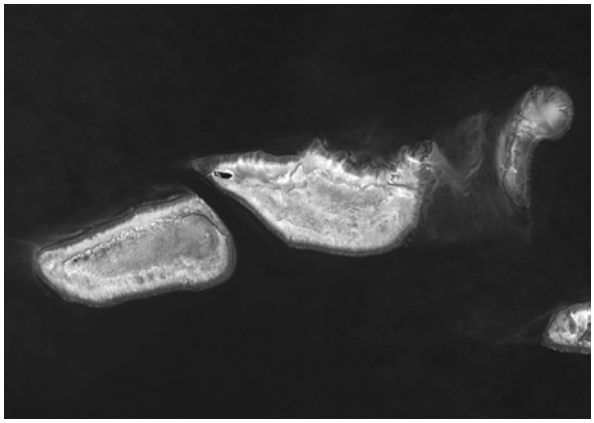
Figure 6.22 Water depth in remotely sensed imagery

Selected bands are shown from a Landsat-8 image of Heron Island reef, acquired on 6 July 2016.

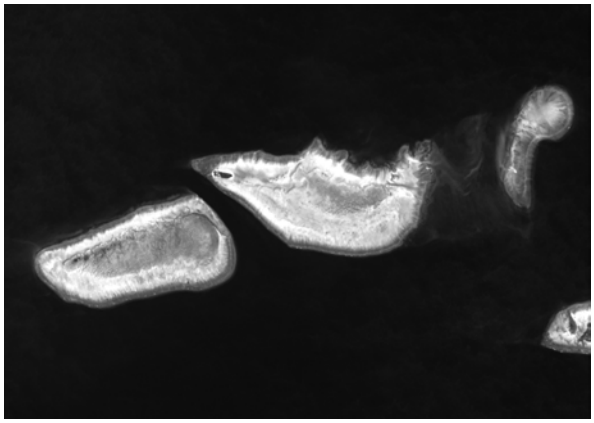
a. Band 1 (ultra blue: 0.43–0.45 μm)



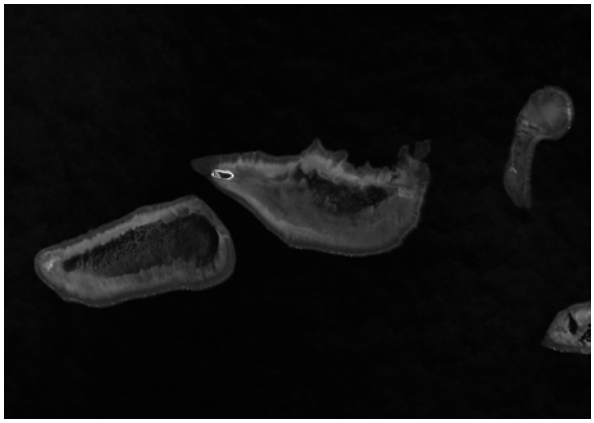
b. Band 2 (blue: 0.45–0.51 μm)



c. Band 3 (green: 0.53–0.59 μm)



d. Band 4 (red: 0.64–0.67 μm)



e. Band 5 (NIR: 0.85–0.88 μm)



f. Natural colour composite (bands 4, 3, 2 as RGB)



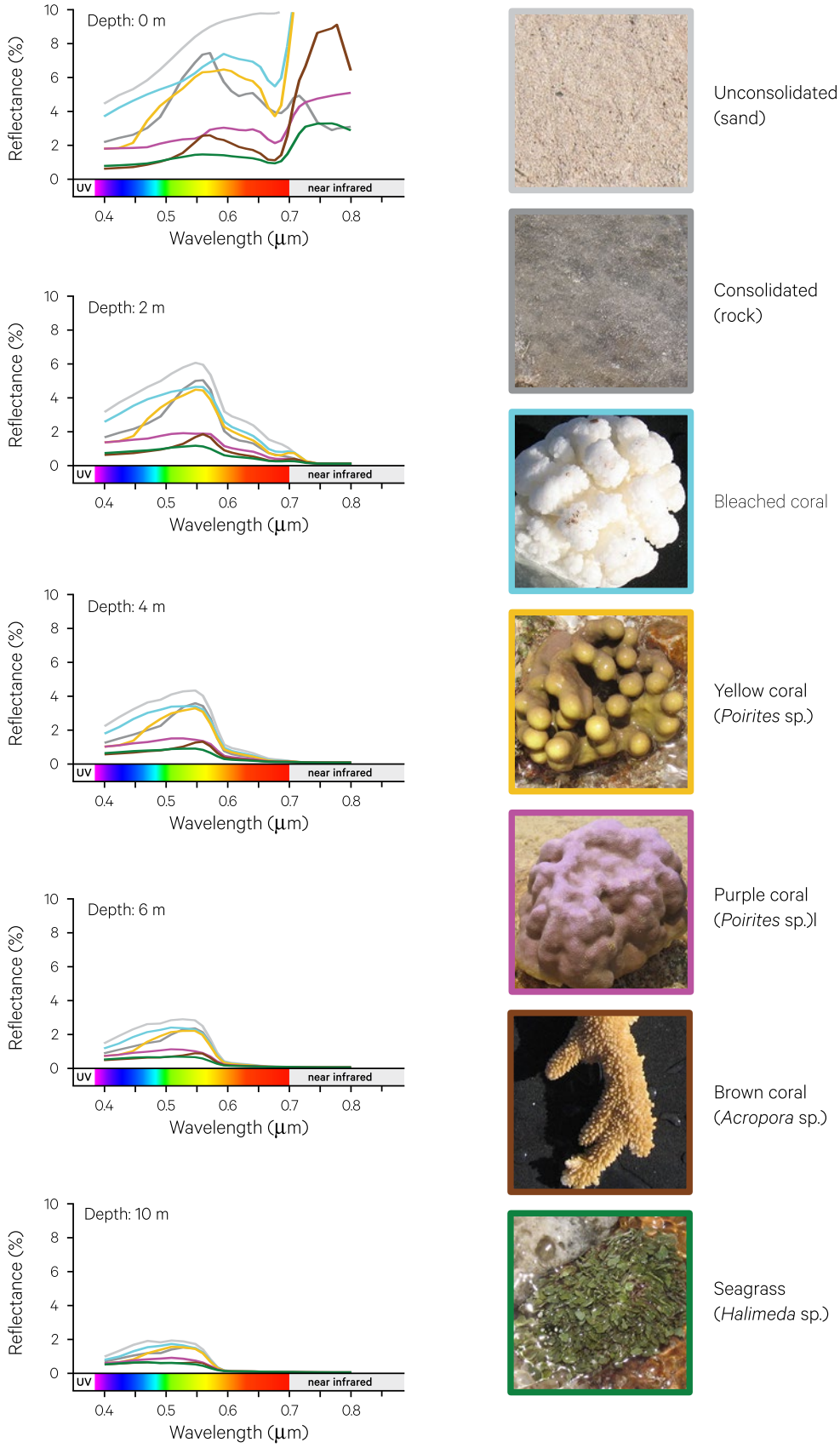
Source: Norman Mueller, Geoscience Australia

6.4.3 Substratum

In shallow water, some downwelling radiation reaches, and is reflected from, the substrate material so that it can be detected at the surface of the water. This allows different substrates, including different seagrass species, to be identified using EO imagery of clear, shallow water (see Volume 3B). Characteristic substrate reflectance spectra as observed at the water surface, however, are markedly changed by increasing water depth (see Figure 6.23) making discrimination between different substrates extremely difficult in deeper water.

Figure 6.23 Impact of water depth on substrate spectra

Reflectance spectra of a range of substrate materials are shown for different water depths. Reflected radiation across all wavelengths is signficantly diminished for most substrates as water depth increases, with the greatest impact occurring in the infrared region.



Source: Botha *et al.* (2013)

6.4.4 Water surface

Characteristics of the water surface, that is the air/water interface, also impact reflectance from water bodies. Water texture, sunglint and skyglint, floating layers (such as algal blooms and pollutants) and foam all change the spectral characteristics of surface waters. These attributes can complicate EO studies focused on the water column and substratum but are used in some applications to determine water movement and quality (see Volume 3B).

6.5 Snow and Ice

Reflectance properties of snow and ice are highly variable, depending on:

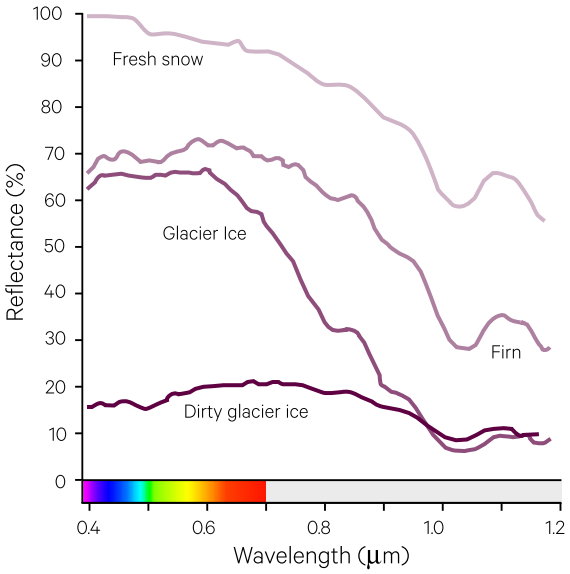
- surface colour (or purity); and
- grain size, depth and density (Dozier, 1984, 1989).

For example, fresh, clean snow reflects most incident light (albedo > 90%), whereas melting snow absorbs more incident radiation (albedo ~40%) and dirty snow absorbs most and reflects least (albedo ~20%; Hall and Martinec, 1985). Regardless of its condition, snow reflects NIR and SWIR wavelengths less strongly than visible light (see Figure 6.24). These differences, plus a more homogeneous texture, allow snow to be differentiated from clouds (Dozier, 1989).

EO imagery has been routinely used for decades to map regions covered in snow and ice around the globe and monitor changes. Given the inherent variability of snow and ice reflectance properties, albedo values are estimated on a regional basis and integrated with Global Circulation Models (Liang, 2001; Liang *et al*., 2003). Such methods are further discussed in Volume 3.

Figure 6.24 Reflectance from snow and ice

Being brighter, fresh snow reflects more radiation, in both visible and NIR wavelengths, than darker snow and ice.



Adapted from: Hall and Martinec (1985).

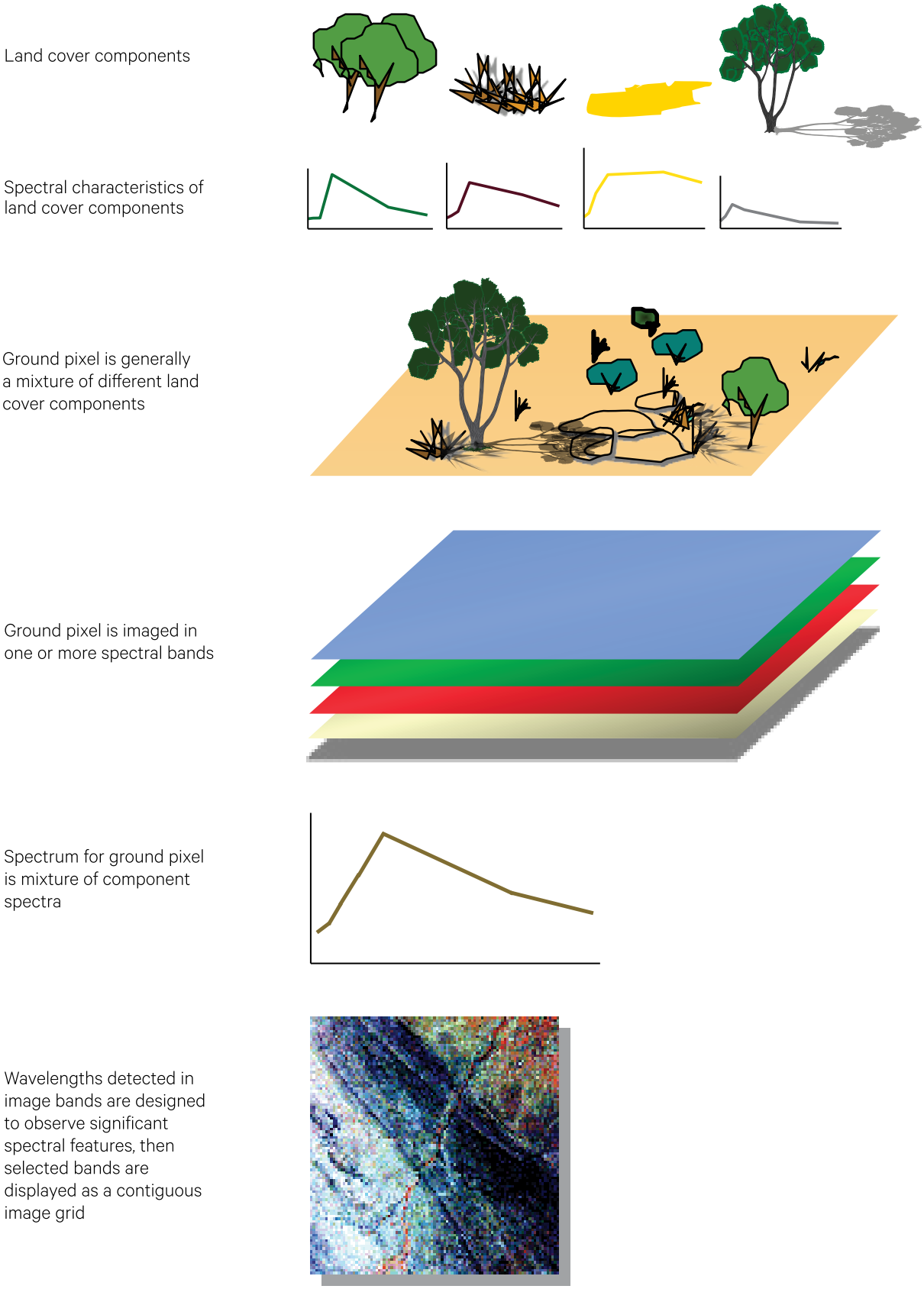
6.6 Mixtures

The spectral reflectance curves that typify a single type of target, such as vegetation, minerals or water, do not necessarily present as precisely in EO imagery as in laboratory samples. In many locations, vegetation cover is patchy and individual pixels will include a variety of surface material types, such as vegetation and bare soil. These component types can, and do, combine in myriad permutations.

The simplest model for a remote sensor is shown in Figure 6.25, in which the reflectance from a ground resolution element (represented by a single image pixel) is measured in several wavebands to produce a spectral signature. As this illustration implies, pixels encountered in EO imagery of land could represent a combination of land cover elements, such as trees, shrubs, grasses and bare ground. Comparable models have been developed for remote sensing of other fundamental states of matter, namely water and air, as detailed in Volume 3.

Figure 6.25 Simplified model of EO sensor

Each optical pixel in an EO image represents the combined spectral characteristics of the land cover components contained within the ground area corresponding to that optical pixel (see Section 1). When many land cover components are combined into a single pixel, their individual spectral characteristics combine to produce a different spectra. Contiguous optical pixels are ordered by location in grids of colour to form EO imagery.



Source: Megan Lewis, University of Adelaide

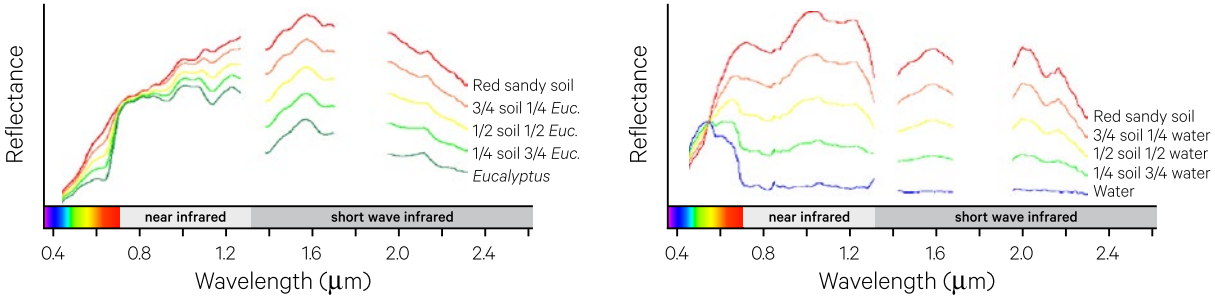
The imaged mixture is highly dependent on both the area of the ground pixel, and the proportion of that area covered by each land cover element. One example of the spectral variation resulting from different proportions of *Eucalyptus* vegetation and exposed red sandy soil within a pixel is illustrated in Figure 6.26a. Similarly, differing proportions of bare soil and water cover also yield different spectra (see Figure 6.26b).

Figure 6.26 Spectral mixing of vegetation and soil

These spectra simulate the results of mixing two land cover elements:

a. Photosynthetic vegetation and soil

b. Soil and water



Source: Megan Lewis, University of Adelaide, based on spectra from HyMap airborne imagery

6.7 Further Information

Minerals Data:

Mineral Spectroscopy Server: *http://minerals.gps.caltech.edu*

Australian Plant spectra:

Lewis (2002)

Suarez *et al.* (2015)

Marine EO products:

Citclops (2017)

Eye On Water: *https://www.workingatnioz.com/news/d.html*

EOMAP: Satellite Derived Bathymetry: *http://www.eomap.com/services/bathymetry/*

Forel Ule Scale (2017)

Hydro-international: *https://www.hydro-international.com*

Bureau of Meteorology Marine Water Quality Dashboard: *http://www.bom.gov.au/marinewaterquality/*

IMOS portal: *https://portal.aodn.org.au/*

eReefs: *https://research.csiro.au/ereefs/remote-sensing/*

CSIRO Australian-waters EO Phytoplankton-type Products Data Base: *http://aesop.csiro.au/*

NASA Aeronet-Ocean Colour: *http://aeronet.gsfc.nasa.gov/cgi-bin/type_one_station_seaprism_new?site=Lucinda&nachal=2&level=1&place_code=10*

6.8 References

Barrett, E. C., and Curtis, L. F. (1976). *Introduction to Environmental Remote Sensing* (336 pages). Chapman and Hall Ltd, London.

Ben Dor, E. (2011). Characterization of soil properties using reflectance spectroscopy. Chapter 22 in 'Hyperspectral Remote Sensing of Vegetation' (Eds: P. S. Thenkabail, J. G. Lyon, and A. Huete), pp. 704. Taylor and Francis, Boca Raton, Florida.

Ben Dor, E., Ong, C., and Lau, I. C. (2015). Reflectance measurements of soils in the laboratory: Standards and Protocols. Geoderma, . *Geoderma, 245–246*, pp. 112–124. doi:*http://dx.doi.org/10.1016/j.geoderma.2015.01.002*.

Botha, E. J., Brando, V. E., Anstee, J. M., Dekker, A. G., and Sagar, S. (2013). Increased spectral resolution enhances coral detection under varying water conditions. *Remote Sensing of Environment, 131*, pp. 247-261. doi:*http://dx.doi.org/10.1016/j.rse.2012.12.021*.

Cho, M. A., Debba, P., Mutanga, O., Dudeni-Tlhone, N., Magadla, T., and Khuluse, S. A. (2012). Potential utility of the spectral red-edge region of SumbandilaSat imagery for assessing indigenous forest structure and health. *International Journal of Applied Earth Observation and Geoinformation, 16*, pp. 85-93. doi:*http://dx.doi.org/10.1016/j.jag.2011.12.005*.

Chung, H.-H., and Barnes, R. L. (1977). Photosynthate allocation in Pinustaeda. I. Substrate requirements for synthesis of shoot biomass. *Canadian Journal of Forest Research, 7*(1), pp. 106-111. doi:*http://dx.doi.org/10.1139/x77-015*.

Citclops (2017). *Citizens' Observatory for Coast and Ocean Optical Monitoring*. Retrieved from *http://www.citclops.eu/*.

Clark, R. N. (1999). Spectroscopy of Rocks and Minerals, and Principles of Spectroscopy. Chapter 1 in 'Manual of Remote Sensing. Volume 3: Remote Sensing for the Earth Sciences' (Ed: A. N. Rencz), pp. 3–58. John Wiley and Sons, New York.

Clark, R. N., Swayze, G. A., and Gallagher, A. (1993). Mapping Minerals with Imaging Spectroscopy. *U.S. Geological Survey, Office of Mineral Resources Bulletin, 2039*, pp. 141-150.

Cudahy, T., Caccetta, M., Lau, I., Rodger, A., Laukamp, C., Ong, C., Mauger, A., Close, D., Tyler, I., Chia, J., Vote, J., J, ones, M., Thomas, M., Abrams, M., Warren, P., Woodcock, R., Fraser, R., Collings, S., and Rankine, T. (2012). *Satellite ASTER Geoscience Map of Australia*. Retrieved from *http://dx.doi.org/10.4225/08/51400D6F7B335*.

Cudahy, T., Caccetta, M., Thomas, M., Hewson, R., Abrams, M., Kato, M., Kashimura, O., Ninomiya, Y., Yamaguchi, Y., Collings, S., Laukamp, C., Ong, C., Lau, I., Rodger, A., Chia, J., Warren, P., Woodcock, R., Fraser, R., Rankine, T., Vote, J., de Caritat, P., English, P., Meyer, D., Doescher, C., Fu, B., Shi, P., Mitchell, R. (2016). Satellite-derived mineral mapping and monitoring of weathering, deposition and erosion. *Scientific Reports, 6*(23702). doi:*http://dx.doi.org/*10.1038/srep23702.

Curtis, B. (1985). *Evaluation of the physical properties of naturally occurring oxyhydroxides on rock surfaces in arid and semi-arid regions using visible and near infrared spectroscopy*. (PhD thesis), University of Washington, Seattle.

Davies-Colley, R.J., and Vant, W.N. (1988). Estimation of optical properties of water from Secchi disk depths. *J. Amer. Water Res. Assoc.*, 24, 1329–1335.

Dawson, T. P., Curran, P. J., and Plummer, S. E. (1998). LIBERTY - Modeling the effects of leaf biochemical concentration on reflectance spectra. *Remote Sensing of Environment, 65*(1), pp. 50-60. doi:*http://dx.doi.org/10.1016/s0034-4257(98)00007-8*.

Dekker, A. G., and Hestir, E. L. (2012). *Evaluating the Feasibility of Systematic Inland Water Quality Monitoring with Satellite Remote Sensing*. CSIRO: Water for a Healthy Country National Research Flagship.

Dozier, J. (1984). Snow Reflectance from Landsat-4 Thematic Mapper. *IEEE Transactions on Geoscience and Remote Sensing, 22*(3), pp. 323-328. doi:*http://dx.doi.org/10.1109/tgrs.1984.350628*.

Dozier, J. (1989). Spectral reflectance of alpine snow cover from Landsat Thematic Mapper. *Remote Sensing of Environment, 28*, pp. 9-22.

Drury, S. A. (1987). *Image Interpretation in Geology*. Allen and Unwin, London.

Elachi, C., and van Zyl, J. (2006). *Introduction to the Physics and Techniques of Remote Sensing*, Second Edn. Wiley Interscience, New Jersey.

Forel Ule Scale (2017). *Forel Ule Scale: Toolkit for Coast and Ocean Optical Monitoring* Retrieved from *http://forel-ule-scale.com*.

Gallegos, C.L., Werdell, P.J., and McClain, C.R. (2011). Long-term changes in light scattering in Chesapeake Bay inferred from Secchi depth, light attenuation, and remote sensing measurements. *J. Geophys. Res.*, 116, C00H08.

Gege, P. (2014). WASI-2D: A software tool for regionally optimized analysis of imaging spectrometer data from deep and shallow waters. *Computers and Geosciences,* 62, 208–215.

Goodman, J. A., Purkis, S. J., and Phinn, S. R. (2013). *Coral Reef Remote Sensing: A Guide for Mapping, Monitoring and Management*. Springer, Dordrecht.

Green, E. P., Mumby, P. J., Edwards, A. J., and Clark, C. D. (2000). *Remote sensing handbook for tropical coastal management*. UNESCO, Paris.

Guenther, G. C., A.G., C., LaRocque, P. E., and Reid, D. J. (2000). *Meeting the accuracy challenge in airborne lidar bathymetry*. Paper presented at the 20th EARSeL Symposium: Workshop on Lidar Remote Sensing of Land and Sea, Dresden, Germany.

Haan, d., J.F., Kokke, J. M. M., Dekker, A. G., and Rijkeboer, M. (1999). *Remote sensing algorithm development, TOOLKIT for water quality continued. Operationalisation of tools for the analysis and processing of remote sensing data of coastal and inland waters* (NRSP report 98-12). Begeleidingscommissie Remote Sensing, Delft, Netherlands.

Hall, D. K., and Martinec, J. (1985). *Remote sensing of ice and snow* (189 pages). Chapman and Hall, New York.

Harrison, B. A., and Jupp, D. L. B. (1989). *Introduction to Remotely Sensed Data. Part ONE of the microBRIAN Resource Manual* (156 pages). CSIRO Australia, Melbourne.

Horler, D. N. H., Dockray, M., and Barber, J. (1983). The Red Edge of Plan Leaf Reflectance. *International Journal of Remote Sensing, 4*(2), pp. 273-288.

Hunt, G. R. (1977). Spectral signatures of particulate minerals in the visible and near infrared. *Geophysics, 42*(3), pp. 501. doi:*http://dx.doi.org/10.1190/1.1440721*.

Irish, J. L., and Lillycrop, W. J. (1999). Scanning laser mapping of the coastal zone: the SHOALS system. *ISPRS Journal of Photogrammetry and Remote Sensing, 54*(2–3), pp. 123-129. doi:*http://dx.doi.org/10.1016/S0924-2716(99)00003-9*.

Kirk, J.T.O. (1994) *Light and Photosynthesis in Aquatic Ecosystems*. Cambridge University Press, 509 pp.

Koenings, J.P., and Edmundson, J.A. (1991) Secchi disk and photometer estimates of light regimes in Alaskan lakes: Effects of yellow color and turbidity. *Limnology and Oceanography*, 36.91–105.

Lewis, M. M. (2002). Spectral characterization of Australian arid zone plants. *Canadian Journal of Remote Sensing, 28*(2), pp. 219-230. doi:*http://dx.doi.org/10.5589/m02-023*.

Li, F., Jupp, D. L. B., Reddy, S., Lymburner, L., Mueller, N., Tan, P., and Islam, A. (2010). An Evaluation of the Use of Atmospheric and BRDF Correction to Standardize Landsat Data. *IEEE Journal of Selected Topics in Applied Earth Observations and Remote Sensing, 3*(3), pp. 257-270. doi:*http://dx.doi.org/10.1109/jstars.2010.2042281*.

Liang, S. L. (2001). Narrowband to broadband conversions of land surface albedo: I. Algorithms. *Remote Sensing of Environment, 76*(2), pp. 213-238. doi:*http://dx.doi.org/10.1016/s0034-4257(00)00205-4*.

Liang, S. L., Shuey, C. J., Russ, A. L., Fang, H. L., Chen, M. Z., Walthall, C. L., Daughtry, C. S. T., and Hunt, R. (2003). Narrowband to broadband conversions of land surface albedo: II. Validation. *Remote Sensing of Environment, 84*(1), pp. 25-41. doi:*http://dx.doi.org/10.1016/s0034-4257(02)00068-8*.

Morris, R. V., Lauer Jr, H. V., Lawson, C. A., Gibson Jr, E. K., Nace, G. A., and Stewart, C. (1985). Spectral and other physicochemical properties of submicron powders of hematite, maghemite, magnetite, goethite and lepidocrocite. *Journal of Geophysical Research, 90*(84), pp. 3126–3144.

Phinn, S. R., and Dekker, A. G. (2004). *An Integrated Remote Sensing Approach for Adaptive Management of Complex Coastal Waters. The Moreton Bay Case Study*. Moreton Bay Remote Sensing Tasks (MR2). CRC for Coastal Zone, Estuary and Waterway Management, Brisbane.

Qin, Y., Brando, V., Dekker, A. G., Schroeder, T., and Park, Y.-J. (2010). *Bio-opti Toolkit, Version 2.1 (unpublished)*. Environmental Remote Sensing Group, CSIRO Land and Water.

Schulze, D. G. (2002). An Introduction to Soil Mineralogy. Chapter 1 in 'Soil Mineralogy with Environmental Applications' (Eds: J. B. Dixon, and D. G. Schulze), pp. 1–36. Soil Science Society of America, Inc., Madison, Wisconsin.

Shaw, G. A., and Burke, H. K. (2003). Spectral Imaging for Remote Sensing. *Lincoln Laboratory Journal, 14*(1), pp. 3-27.

Suarez, L., Restrepo-Coupe, N., Hueni, A., and Chisholm, L. A. (2015). Vegetation spectroscopy. Chapter 13 in 'AusCover Good Practice Guidelines (A technical handbook supporting calibration and validation activities of remotely sensed data products)' (Eds: A. Held, S. R. Phinn, M. Soto-Berelov, and S. Jones). TERN AusCover, St Lucia, Australia.

Summers, D., Lewis, M. M., and Ostendorf, B. (2011). Visible near-infrared reflectance spectroscopy as a predictive indicator of soil properties. *Ecological Indicators, 11*, pp. 123–131.

Tucker, C. J. (1979). Red and Photographic Infrared Linear Combinations for Monitoring Vegetation. *Remote Sensing of Environment, 8*(2), pp. 127-150. doi:*http://dx.doi.org/10.1016/0034-4257(79)90013-0*.

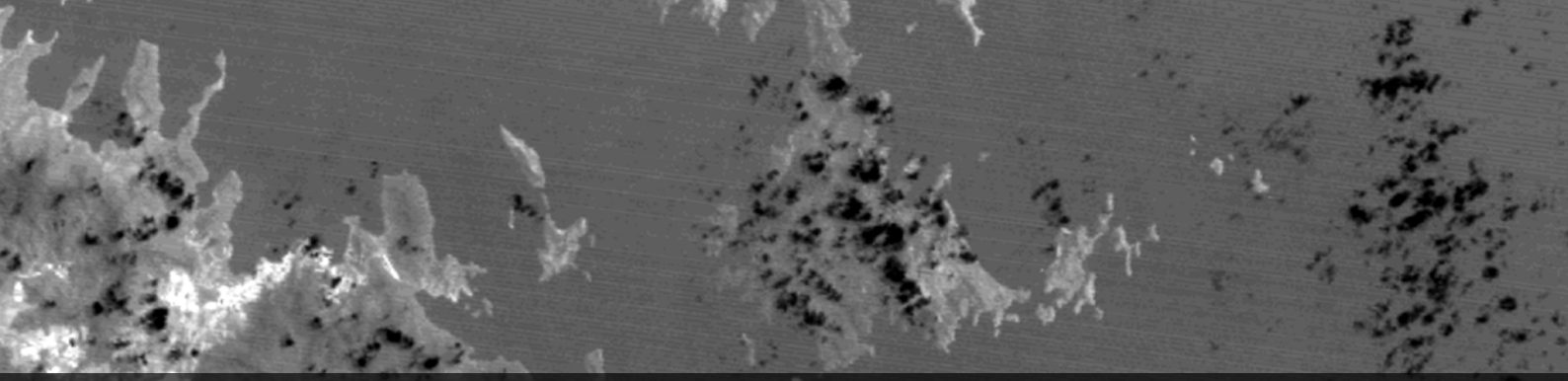
USGS (2011). *US Geological Survey Spectroscopy Lab*. Retrieved from *http://speclab.cr.usgs.gov*.

Viscarra Rossel, R. A., and McBratney, A. B. (2008). Diffuse reflectance spectroscopy as a tool for digital soil mapping. Chapter 13 in 'Digital Soil Mapping with Limited Data: Developments in Soil Science Series' (Eds: A. B. Hartemink, A. B. McBratney, and L. Mendonca-Santos). Elsevier Science, Amsterdam.

Visser, A. J. W. G., and Rolinski, O. J. (2014). *Basic Photophysics*. Photobiological Sciences Online. Retrieved from *http://www.photobiology.info*.

Weisz, P. B., and Fuller, M. S. (1962). *The Science of Botany* (562 pages). McGraw-Hill, Tokyo.

Yamaguchi, Y., Kahle, A. B., Tsu, H., Kawakami, T., and Pniel, M. (1998). Overview of Advanced Spaceborne Thermal Emission and Reflection Radiometer (ASTER). *IEEE Transactions on Geoscience and Remote Sensing, 36*, pp. 1062_1071.



7 Thermal Infrared Imagery

Thermal sensors record thermal infrared (TIR) emissions from objects (see Volume 1A—Section 14.4). In the context of EO, thermal scanners primarily measure the thermal energy being radiated by the Earth's surface although some emission from the atmosphere is included in the data. This energy can be derived from various sources, principally:

- geo-thermal features;
- man-made thermal features (such as power stations);
- fires; and
- emitted TIR energy, resulting from absorbed solar energy.

The environmental context of the thermal or long wave part of the spectrum of Earth has been encountered already in Volume 1A—Section 5.2, with underlying radiation concepts being discussed in Volume 1A—Sections 2.10 and 2.11. In summary:

- the Sun is very hot (near 6000K);
- peak intensity of incoming solar radiation is between 500 nm and 600 nm;
- outside the shortwave region (250–2500 nm) there is little radiation incoming to Earth from the Sun;
- interactions between the Sun's radiation and Earth's atmosphere and surface occur in the shortwave region;
- despite the distance from the Sun to Earth, its radiation heats the atmosphere and surface of Earth;
- for Earth materials at roughly 300K (a typical value), the peak intensity of emitted radiation is around 10 μm (10,000 nm) with little radiation emitted outside the long wave or thermal region (8–15 μm);
- the balance of radiation between the short and long wave regions is very important in the Earth's environment (see Volume 1A—Excursus 4.1).
- in the short wave region the dominant property being sensed is reflectance; and
- in the complementary long wave (thermal) region the dominant properties being sensed are emittance and temperature.

Two parts of the thermal infrared wavelength region, which correspond to atmospheric windows, may be used for remote sensing: 3–5 μm and 8–14 μm (see Volume 1A—Section 5.4). The shorter wavelength region (3–5 μm) is predominantly used for sensing emission from very hot objects, such as fires, man-made thermal features and geo-thermal activity although it also includes some small amounts of reflected solar radiation. The 8–14 μm region coincides with the peak energy emission for the Earth, so is used for monitoring ocean temperature and land surface temperature (LST; see Section 7.6 and Volume 3).

Those thermal properties that are most relevant to the interpretation of TIR imagery are:

- heat capacity (*C*)—the heat required to raise the temperature of an object, which indicates how well it can store heat;
- thermal conductivity (*K*)—the rate at which heat can transfer through an object;
- thermal inertia (*P*)—the resistance of an object to changing its temperature to match the temperature of its surroundings; and
- emissivity (ε)—the effectiveness with which the surface of an object emits TIR energy.

When you can't make them see the light, make them feel the heat.
(Ronald Reagan)

Background image: Landsat-5 image of Whitsunday Islands, Queensland, acquired on 24 October 2010 (displayed using band 6: thermal infrared).
Source: Norman Mueller, Geoscience Australia

TIR imagery is used for a wide range of engineering and environmental applications, including assessment of heat loss, thermal efficiency, and insulation effectiveness in residential, commercial and industrial buildings; thermal water pollution; dam seepage and fire hotspots. Since thermal emissions are closely related to moisture content, TIR imagery is also valuable for mapping soil moisture, evapotranspiration, surface temperature and vegetation stress. TIR remote sensing has particular value for a variety of geological applications, including aeolian sediment transport, volcanic landform interpretation, lithological mapping and surface roughness (Ramsey, 2004; Carter *et al.*, 2009; see also Volume 3). Finally, at a global scale, thermal imagery also provides valuable insights into the global energy budget (see Volume 1A—Section 4, and Volume 3).

The following sections address various aspects of TIR energy in the context of EO imagery:

- solar heating of Earth surface materials (see Section 7.1);
- blackbody concepts (see Section 7.2);
- TIR signatures (see Section 7.3);
- thermal emission characteristics of common materials (see Section 7.4);
- emissivity (see Section 7.5);
- surface temperature—for both waterbodies and land (see Section 7.6); and
- thermal inertia (see Section 7.7).

7.1 Solar Heating Cycles

The response of different materials to solar heating largely depends on the heat conduction property of their surface layer, that is, how they absorb heat to generate a change in physical temperature. Planck's law (see Volume 1A—Section 2.11.4) states that objects with a surface temperature greater than 0K will emit some heat as EMR. It is this emission of EMR, resulting from an object's kinetic temperature, which is measured by TIR sensors (see Volume 1A—Sections 2.10, 2.11 and 5.2.2). This is the reason that hot objects, such as fires, can be sensed by satellite scanners some 700 km away, and not felt by people until in much closer proximity. The thermal scanners measure radiance, whereas people sense absorbed energy due to the EMR emission resulting from the temperature of a fire (Mobley, 1994).

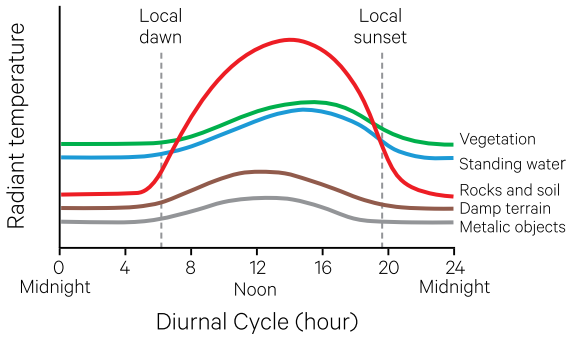
Earth's daily rotation on its own axis, combined with its annual revolution around the Sun, result in cyclic variations in solar heating of the Earth's surface (see Volume 1A—Sections 3 and 4). Both axes of movement change the intensity of solar radiation reaching the Earth's surface at different locations. Temperature changes related to Earth's rotation are experienced as the daily temperature cycles between cooler nights and warmer days, while the annual revolution of Earth around the Sun following an elliptical orbit (which modifies the Earth to Sun distance, see Volume 1A—Section 3.1) manifests as seasonal temperature changes throughout the year. Variations in solar heating on the Earth are also related to distance from the equator (see Volume 1A—Section 4), with more radiation per unit area reaching the Earth's surface at the equator than at the poles. Furthermore, the response of objects to solar heating cycles can vary markedly for different materials, coatings, compositions and orientations.

As illustrated in Figure 7.1, the mechanism behind TIR emission from an object as a consequence of solar heating involves a time lag, with peak radiant input to the surface occurring prior to the object's peak surface temperature response. While reflected optical properties reach a maximum at solar noon, when the solar radiation is at maximum intensity, emitted TIR reaches a maximum around 2 hours later. For example, the peak solar flux occurs at solar noon when the Sun is at zenith, but surface soil temperatures peak around 2 pm.

Clouds reduce the solar radiation reaching the Earth's surface, and thus reduce the amount of solar heating. Heavy cloud cover also baffles emissions from the surface, resulting in lower remote measurement of TIR emissions and, consequently, lowered contrast in thermal imagery. Shadowing from terrain features and vegetation also reduces the solar radiation that can reach the surface.

Figure 7.1 Diurnal variations in temperature

Different materials respond differently to diurnal temperature variations, and some such as water and vegetation only change by small amounts, while rocks and soil experience a large change in temperature. Note: time axis is relative to solar day.



Adapted from: Sabins (1987)

The diurnal cycle of radiant temperature has important implications for the timing of thermal data acquisition (Drury, 1987). Many applications aspire to distinguish between different surface materials, so require thermal data to be acquired when differences in their radiant temperatures are emphasised. Generally, 'cross-over' times, near dawn and sunset (when rocks and soils have similar radiant temperature to vegetation and waterbodies) are avoided in thermal image acquisition for those applications that aim to delineate these land covers (see also Figure 7.8 below). To assess seasonal differences, image pairs with similar solar illumination conditions are recommended, such as mid-Autumn and mid-Spring (see Volume 2D).

7.2 Blackbody Concepts

While the thermal properties relating to heat, temperature and blackbody radiation are introduced in Volume 1A—Sections 2.10 and 2.11, some key concepts are reviewed here in the context of TIR imagery. A blackbody is a theoretical concept in which a body absorbs all radiation it receives over all wavelengths. According to theory, blackbodies would demonstrate the most efficient conversion of heat energy into EMR (and vice versa) for all wavelengths. While cavity radiators can come close to the ideal, most materials do not. The efficiency with which these real-world objects convert heat energy into EMR can be rated by comparison with blackbody behaviour at wavelength λ using a ratio called emissivity (ε) (see Volume 1A—Section 2.11.2):

$$\varepsilon(\lambda) = \frac{\textit{emitted radiance at } \lambda}{\textit{blackbody radiance at } \lambda}$$

Using this equation, it follows that:

- blackbody: $\varepsilon(\lambda) = 1$;
- greybody: $\varepsilon(\lambda) = x$ where $x < 1$; and
- selective radiator: $\varepsilon(\lambda)$ varies with λ.

Real world objects are selective radiators, that is, their emissivities vary with wavelength. Some materials can act like blackbody radiators at specific wavelengths. Emissivity can also vary with the direction of emission (θ), so it is often written as $\varepsilon(\lambda,\theta)$. Planet Earth has peak emissivity at the wavelengths 9.18 μm, 9.66 μm and 12.4 μm. Emissivity characteristics of common materials are summarised in Table 7.1 and further discussed in Section 7.5.

Table 7.1 Thermal and reflective properties of Earth surface materials

Note that actual thermal properties of sea water vary with temperature and salinity (see Sharqawy *et al.* (2010) for detailed analyses) and that higher albedo values apply to fresh, clean snow or ice (see Section 6.5).

Surface Material	Thermal Properties				Reflective Properties
	Specific heat capacity (J/(kg·°C))	Thermal conductivity (W/(m·K))	Thermal inertia ($J \cdot m^{-2} \cdot K^{-1} \cdot s^{-1/2}$)	Emissivity	Albedo
Sea water	4180	0.572–0.678	0.038	0.99	0.01–0.1
Ice/Snow	2090	0.59	low	0.80–0.98	0.25–0.9
Sand	800–1600	0.15–0.25 (dry) 2–4 (saturated)	0.024 (sandy soil)	0.94–0.96	0.2–0.4
Granite	794	1.7–4.0	0.56	0.90	0.3–0.35
Concrete	880	0.4–0.7 (medium) 1.0–1.8 (dense)	high	0.85	0.2–0.3 (aged) 0.4–0.55 (new)
Steel	120	16–21 (stainless) 25–51 (mild steel)	0.168 (stainless)	0.07 (polished) 0.79 (oxidised)	0.24 (galvanised)

Sources for data: *http://www.engineeringtoolbox.com*; Jensen (2007); Sharqawy *et al.* (2010); Alnefaie and Abu-Hamdeh (2013)

Thermal inertia (P) describes the ability of an object to change temperature (see Section 7.7). In response to input radiation, the thermal inertia of a surface impacts its temperature and TIR emission.

Another important thermal property is diffusivity, which measures how a material conducts heat relative to how it stores heat. Thermal diffusivity (k) is computed from thermal conductivity (K), density (ρ) and specific heat capacity (c), as:

$$k = \frac{K}{\rho c}$$

This term is used in the heat conduction equation, which describes the temperature distribution in an object or region over time:

$$\nabla^2 T - \frac{1}{k}\frac{\partial T}{\partial t} = 0$$

However, if a surface is covered by a thin layer of material with low diffusivity, the underlying surface will be barely affected by variations in surface cover temperature (Elachi and van Zyl, 2006).

7.3 TIR Emission Characteristics

Different surface materials can vary markedly in terms of their thermal behaviour (see Table 7.2). Water, for example, retains heat, cools slowly at night and warms slowly during the day, whereas rocks and soils absorb heat quickly during the day and release heat rapidly at night. The thermal behaviour of Earth surface materials is influenced by many factors including Sun angle variations, topography, rainfall, climatic conditions, and the composition, texture and density of each material (see Volume 1A—Sections 3 and 4).

As a general rule, materials with high albedo (that is high reflectance—see Volume 1A) have low absorption, and therefore a lower temperature. Accordingly, albedo (α), the reflecting power of an object's surface, often contrasts with thermal properties (see Volume 1A—Section 5). Some materials, however, vary in terms of their short and long wave properties. Snow, for example, is highly reflective in optical wavelengths and also has high TIR emission (Elachi and van Zyl, 2006). Examples of thermal and albedo characteristics for selected Earth surface materials are listed in Table 7.1 above.

In Figure 7.2, two Landsat-7 images of Gladstone, Queensland, acquired in May 2001, illustrate the differences between visible and TIR imagery. The true colour image (see Figure 7.2a) indicates the visible colours of surface features, whereas the thermal channel (see Figure 7.2b) shows their relative temperature. Typically in TIR imagery, features with cooler temperatures appear as dark shades while higher temperatures appear brighter.

Table 7.2 Thermal behaviour of common surface materials

Surface Material	Interaction with Incident Radiation	Thermal Emission Increased by	Temperature Decreased by
Bare soil	More absorbed than reflected, not transmitted	Greater surface area due to small particles (roughness)	shadowing cloud cover vegetation cover moisture
Vegetation	More reflected than absorbed, some transmitted	Greater surface area	shadowing cloud cover vegetation cover moisture
Water	More absorbed than reflected, little transmitted	Surface roughness (wave height and wind speed)	shadowing cloud cover vegetation cover Increasing water depth
Metal	Much more reflected, little absorbed or transmitted	Greater surface area (Oxidation, coatings, roughness)	shadowing cloud cover
Urban Infrastructure	More reflected than absorbed or transmitted	Greater surface area (roughness, coatings)	shadowing cloud cover vegetation cover insulation

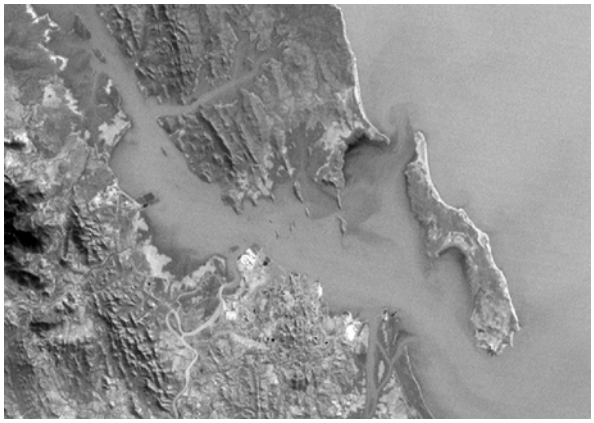
Figure 7.2 Two Landsat-7 views of Gladstone, Queensland

Comparison of images showing reflected (a) and emitted (b) radiation acquired by Landsat-7 on 31 May 2000.

a. True colour composite (bands 3, 2, 1 as RGB)—colours indicate visible colour of surface features



b. Thermal channel—grey shades indicate surface temperature: darker shades are cooler and brighter shades are warmer



Source: Norman Mueller, Geoscience Australia

Unlike reflected solar energy, TIR emissions may also be detected at night (see Volume 1A—Sections 14.4 and 16.1.1.1). Several satellite-borne thermal scanners, such as AVHRR, acquire data during both day and night overpasses, which enables day/night pairs of TIR imagery to be obtained for a given area. Day/night TIR image pairs are frequently used to study properties such as thermal inertia. While TIR images acquired during the day can be affected by cloud cover and shadows (of various origins), they generally provide greater thermal contrast between surface features than is offered by nighttime images.

For example, a pair of thermal airborne images, acquired before dawn and during the day, is shown in Figure 7.3. The daytime image offers better contrast between warmer urban areas and cooler vegetation and water. In the pre-dawn image, while road networks and the urban heat island are more clearly delineated, both vegetation and standing water are warmer and thus have lowered contrast with other warm surface features. TIR imagery acquired during the daytime in the wavelength range 3–5 μm, however, may record both reflected and emitted radiation, as well as thermal variations resulting from cloud and topographic shadowing.

TIR imagery is noisier than optical imagery, due to both sensor operation and terrain features. Thermal emission signals are weaker than reflected signals, so thermal sensors need larger fields-of-view (FOV) than optical sensors (see Volume 1A—Section 14.4). An increasing number of sensors acquiring thermal data also incorporate optical bands, which allows thermal emission information to supplement optical analyses. In broad terms, TIR imagery is most commonly used to indicate:

- type of material—based on thermal emission characteristics; and
- temporal changes—based on changes in thermal properties, which are possibly related to the presence of water.

Figure 7.3 Thermal image pair

Airborne thermal images acquired by Advanced Thermal and Land Applications Sensor (ATLAS) over central Atlanta, GA, on May 11 and 12, 1997.

a. Daytime image—warmer urban areas contrast with cooler vegetated surfaces and waterbodies.

b. Dawn image—relatively warm asphalt roadways outline the road network while vegetation is warmer and waterbodies are much warmer compared with the daytime image. The urban heat island is also delineated.



Source: NASA. Retrieved from: *https://weather.msfc.nasa.gov/atlanta/*

7.4 TIR Signatures

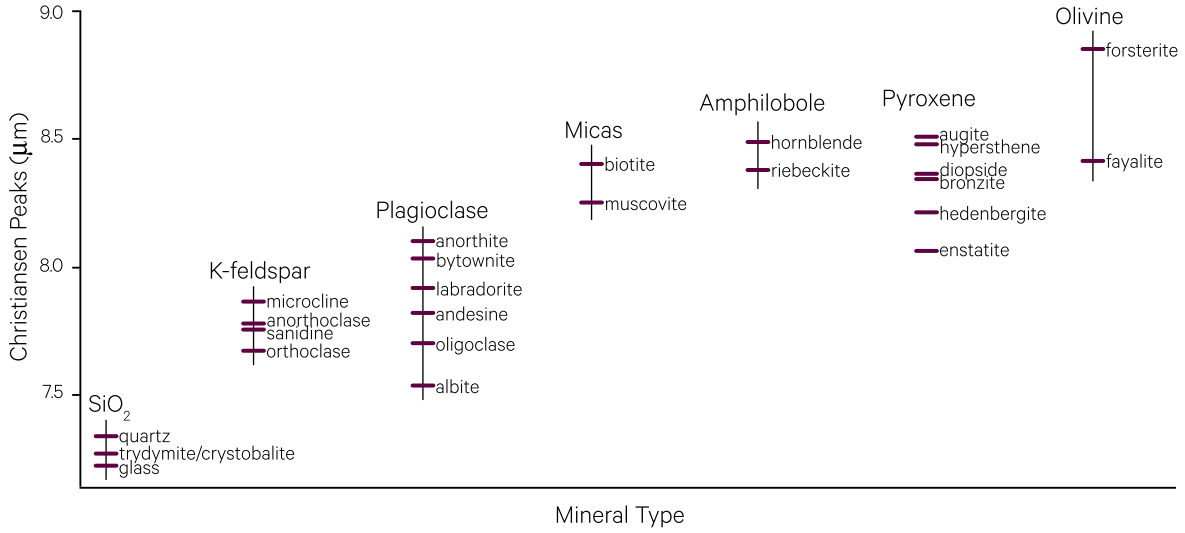
The TIR region can be viewed in the same way as the optical part of the EMR spectrum with different materials displaying characteristic spectral features. Vibrational processes are responsible for most spectral features in TIR spectral regions (see Section 6.1). For geological applications, as a general rule, TIR signatures are indicative of rock composition, whereas optical signatures indicate alteration products (Hecker *et al*., 2013). In particular, silicates (quartz, feldspars, olivines and pyroxenes), which do not display optical spectral features, have diagnostic absorption features in TIR wavelengths (van der Meer *et al*., 2012).

Relying on the Stefan-Boltzmann and Wien's laws (see Volume 1A—Section 2.11), the wavelength of peak emittance for an object is indicative of its temperature. As the temperature of an object increases, the wavelength of peak radiant emittance decreases.

The minima in TIR spectra indicate opaque surfaces, that is, these surfaces totally reflect incident solar radiation. With no absorption, there is no emission. This TIR spectral minima feature is called the Restrahlen effect and is used to identify the presence of silicates and other minerals. While rock spectra are more complicated that mineral spectra, felsic rocks tend to display the Reststrahlen effect at shorter wavelengths than mafic rocks (Lyon, 1964).

Figure 7.4 Christiansen feature in TIR wavelength region for minerals

For silicate minerals, the wavelength of the Christiansen features shift to shorter wavelengths with increasing SiO_2 content.



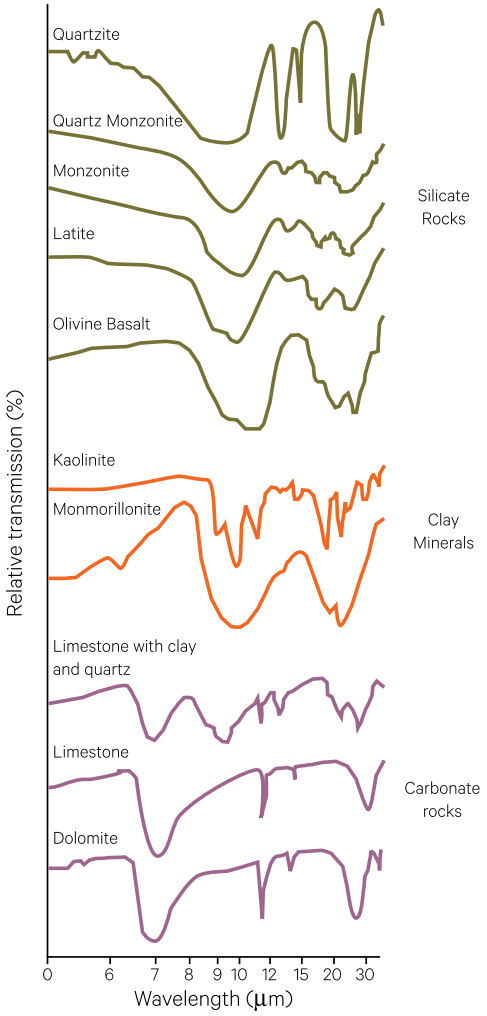
Source: Cudahy (2002)

The TIR spectral signatures for many materials also show emittance maxima, corresponding to the wavelength(s) where the refractive index is close to 1, that is, there is little scattering of incident radiation. When this effect occurs away from absorption bands, most energy is re-emitted, resulting in a strong TIR signal, typically around 7.5 µm and 12.0 µm. These regions are called Christiansen frequencies and can be diagnostic of particular materials (Elachi and van Zyl, 2006).

Some geological materials that can be identified by TIR spectral features (see Figure 7.4) include:

- silicates (see Figure 7.5):
  - emittance minima due to the Restrahlen effect and fundamental vibration of Si-O near 10 µm;
  - emittance maxima due to Christiansen frequency near 8 µm;
- clays (see Figure 7.5): absorption bands due to Si-O stretching and H-O-Al bending near 11 µm; and
- carbonates (see Figure 7.5): vibrations of CO_3^2 result in an asymmetric stretch near 7 µm and a planar bend near 11.5 µm and 14.5 µm (Elachi and van Zyl, 2006).

Figure 7.5 Transmission spectra for silicates, clays and carbonates



Adapted from: Kahle (1984)

7.5 Emissivity

Emissivity is defined as the effectiveness with which objects emit TIR energy. Kirchoff's law (see Volume 1A—Section 2.11.2) can be summarised as:

> 'Good absorbers are good emitters and good reflectors are poor emitters.'

Accordingly, materials with strong energy emission generally also absorb energy strongly, and vice versa. Typical emissivity values of some common materials are summarised in Table 7.1 above.

Metals and glass tend to have low emissivity, that is, they reflect, rather than absorb, incident energy. Their emissivity decreases with polished surfaces (higher reflectance and less absorption of energy) and increases with temperature and oxide coating (lower reflectance and more absorption of energy). Non-metals have high emissivity values, generally over 0.8, which decrease with increasing temperature. In the wavelength range 8–14 μm, emissivity of distilled water is around 1, that is, for TIR wavelengths it behaves nearly as efficiently as a blackbody in converting heat energy into EMR.

Several factors affect the amount of energy that is absorbed and re-emitted by a surface, and hence the emissivity of an object, including:

- colour—dark colours tend to have higher emissivity than lighter colours, that is, they absorb and re-emit more energy;
- surface roughness and compaction—rough or loose surfaces tend to have higher emissivity than smoother ones;
- moisture content—moist surfaces tend to have higher emissivity than drier ones; and
- viewing position—both the orientation of the viewing instrument and the area being viewed will impact emissivity measurements.

Both surface cover and structure of terrain components, such as snow, ice and vegetation, impact emissivity. In particular, vegetation can markedly change the temperature and emissivity of soils. The impacts of these factors on common surface features of Earth are summarised in Table 7.2.

As introduced in Volume 1A—Section 2.11, for any object, the emitted TIR radiation (W) is related to both kinetic temperature (T_{kin}) and emissivity (ε) as:

$$W = \sigma \varepsilon T_{kin}^{4}$$

where

σ is the Stefan-Boltzmann constant (see Volume 1A—Section 2.11); and
T_{kin} is measured in K.

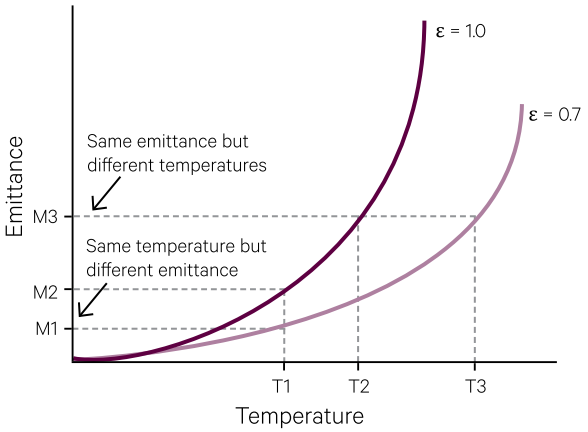
Thus, the TIR radiation emitted by an object depends on both its kinetic temperature and its emissivity, such that a change in one of these factors would change the TIR emissions observed by a remote thermal sensor. For example, a lowered emissivity would result in reduced TIR emissions, without any change in the kinetic temperature of an object (see Figure 7.6).

When emissivity is close to one, radiant temperature (T_{rad}) is related to kinetic temperature (T_{kin}) by:

$$T_{rad} = \varepsilon^{0.25} T_{kin}$$

Figure 7.6 Impact of emissivity on TIR emittance

Different emissivities cause changes in emitted TIR radiation for the same surface temperature, and surfaces with different temperatures can have the same TIR emission.



Adapted from: Forster (2006)

Table 7.3 Radiant temperature, kinetic temperature and emissivity

When emissivity is close to one, radiant temperature is related to kinetic temperature by $T_{rad} = \varepsilon^{0.25} T_{kin}$

Material at 27°C (300K)	Emissivity (ε)	Radiant Temperature (T_{rad})	
Blackbody	1	300K	27°C
Distilled Water	0.99	299.2K	26.2°C
Rough Basalt	0.95	296.2K	23.2°C
Vegetation (closed canopy)	0.98	298.5K	25.5°C
Dry Loam	0.92	293.8K	20.8°C
Stainless steel	0.16	–	–
Polished Aluminium	0.08	–	–

Adapted from: Jensen (2007) Table 8-2

Most natural materials have emissivity values between 0.8 and 0.98 (see Table 7.1). A detailed analysis of emissivity characteristics for a range of natural Earth surface materials in the 8–14 μm atmospheric window is reported in Salisbury and Daria (1992). Where surfaces are characterised by high and homogeneous emissivity values, the relationship between kinetic temperature and TIR emissions is close to linear. Ocean surfaces, for example, exhibit uniform emissivity, so TIR imagery of such areas can be reliably used to derive maps of water temperature. Materials with both high and uniform emissivity values enable reliable estimates of kinetic temperature to be derived from TIR imaging (see Table 7.3). For materials with low emissivity values, however, such as metals and glass, TIR emissions will not be closely related to kinetic temperature.

If appropriate assumptions are made about surface characteristics and atmospheric radiance, emissivity can be estimated from TIR imagery (Gillespie *et al.*, 1998; Dash *et al.*, 2002). In general, highly reflective materials, such as metals, are poorly modelled by emissivity retrieval methods that assume high emissivity (Payan and Royer, 2004) and TIR emissions are not closely correlated with kinetic temperature.

7.6 Surface Temperature

The thermal wavelengths that can be used to estimate surface temperature are limited by atmospheric absorption to two ranges:

- 3–5 μm—measures peak emissions from bushfires, mine fires, and power stations at 3–4 μm; and
- 8–14 μm—measures peak emissions from land, waterbodies (including thermal water pollution), and urban infrastructure at 9–10 μm.

Airborne thermal sensors can detect these full atmospheric windows, whereas satellite-borne thermal sensors are further restricted by the ozone layer in the stratosphere which absorbs radiation in the wavelength range 9.2–10.8 μm (see Volume 1A—Section 14.4). Some care is needed in the 3-5 μm region since, for bright land surfaces, there can be some residual reflected solar radiation present.

A number of processing methods have been developed to calibrate TIR data to indicate apparent surface temperature (see Volume 3). This technique is commonly used for:

- inland water temperature (see Figure 7.7);
- sea surface temperature (SST) mapping (where actual temperature of the sea surface 'skin' can be measured to within 0.15°C[13]; see Volume 3B);
- land surface temperature (LST); and
- meteorological applications (see Volume 3).

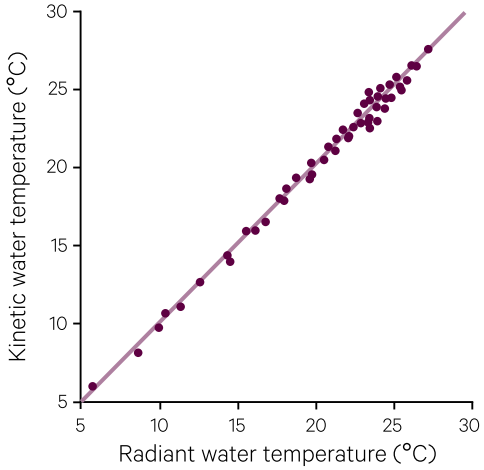
The sensitivity of current thermal sensors also allows industrial and illegal thermal water pollution to be detected.

LST has been defined as 'the result of the equilibrium thermodynamic state dictated by the energy balance between the atmosphere, surface and sub-surface soil and the efficiency by which the surface transmits radiant energy into the atmosphere' (surface emissivity; Schmugge *et al.*, 2002). Diurnal variations in LST can be modelled from satellite TIR imagery for different land covers (e.g. Duan *et al.*, 2014). Several EO agencies routinely derive LST data products from satellite imagery on a global basis (such as MOD11—Land Surface Temperature and Emissivity product; Wan, 2008). A range of methods used to retrieve LST from thermal satellite sensors are reviewed by Li *et al.* (2013).

Many urban surface features demonstrate similar TIR emissivity values, allowing TIR imagery to be used to highlight and monitor energy usage and insulation efficiency. In particular, the contrast between urban surfaces (with high heat capacities, more heat traps and warmer night temperatures) and surrounding rural areas (with fewer compacted surfaces, more vegetation and cooler night temperatures) creates the phenomenon known as the 'urban heat island' (Lo *et al.*, 1997). Airborne thermal sensors can be used to identify priority areas for implementing heat island mitigation strategies, such as green infrastructure (Harris and Coutts, 2011). Imagery from satellite-borne TIR sensors have also been used to estimate the relationship between LST and vegetation abundance for urban studies (Weng *et al.*, 2004).

Figure 7.7 Water surface temperature modelled from EO TIR imagery

Airborne TIR data is used to model inland water temperature.



Adapted from: Torgersen *et al.* (2001) Figure 4

13. This assumes that at least two TIR bands are required to compensate for atmospheric effects.

Variations in LST derived from satellite thermal imagery may also be used in land areas to indicate differences in soil moisture (such as with irrigated crops) and monitor drought (McVicar and Jupp, 1998), or estimate changes in evapotranspiration and/or vegetative cover. Soil moisture is a significant factor both in the water cycle and for global energy balance (see Volume 3). Even small amounts of water can impact thermal properties of geological materials, making TIR useful for mapping water movement (Schmugge *et al.*, 2002).

Estimation and modelling of surface temperature at global scales is relevant to a wide range of climate and environmental studies (Running *et al.*, 1994; see also Volume 1A—Section 4). In particular, LST products derived from various sources of satellite thermal imagery are routinely used to validate and refine predictive global meteorological models (Wan *et al.*, 2004; Wan, 2008; Guedj *et al.*, 2011; Fang *et al.*, 2014). EO methods for deriving global estimates of surface temperature and the Earth's energy balance are detailed in Volume 3.

7.7 Thermal Inertia

Thermal inertia, the resistance of a material to changing its temperature to match its surroundings, is a thermal property that is used to differentiate between surface materials (see Table 7.1 above). Materials with large differences in temperature during the day and night have low thermal inertia, and conversely, materials with small differences between day and night temperatures have high thermal inertia. Diurnal temperature changes of Earth surface materials result from the response of each material to the incident solar illumination. Day/night temperature differences strongly depend on thermal inertia and only weakly depend on albedo or emissivity (see Figure 7.8).

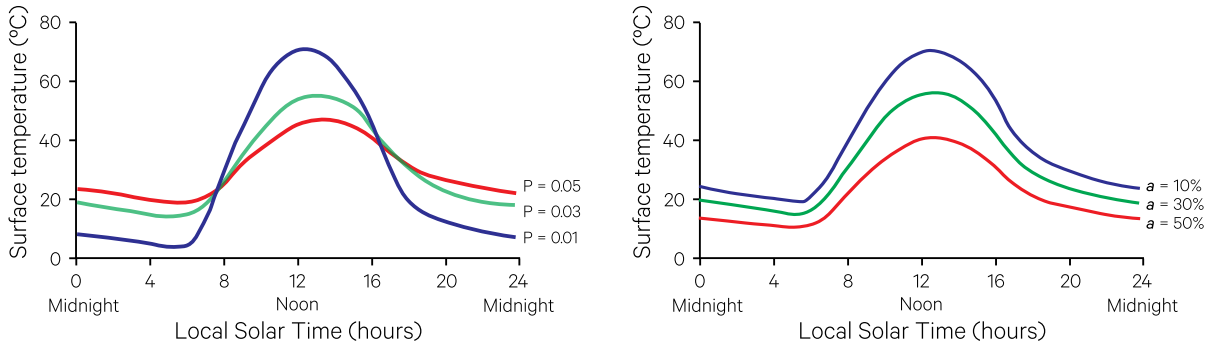
TIR image pairs acquired at 2 am and 2 pm are ideal to observe differences in the thermal inertia of different materials (Elachi and van Zyl, 2006). For example, dolomite, limestone, quartzite and granite have high thermal inertia (a large difference between their temperature during the day and night) whereas young alluvium has low thermal inertia.

The depth of the surface heating resulting from insolation varies with material structure, composition, moisture content and time of day. During the day, solar heating on the Earth's surface is conducted down into sub-surface layers. As solar heat wanes during the afternoon the surface of Earth starts to cool and the stored sub-surface heat moves back to the surface (Drury, 1987). The precise local times corresponding to surface heating and cooling cycles vary with both latitude and season.

Figure 7.8 Diurnal variations in thermal inertia and albedo

a. Thermal Inertia—with other heating factors constant, clear crossover points occur in thermal inertia values (*P*) at dawn and dusk. For *P* >>0.05 (e.g. metals), near linear diurnal curves pass through the crossover points.

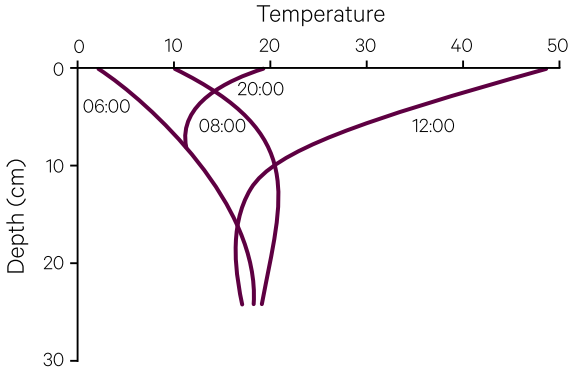
b. Albedo—higher albedo values result from increasing the proportion of reflected radiation relative to incident radiation, with dark surfaces having low albedo and light-coloured surfaces having high albedo. Darker surfaces with low albedo display consistently higher surface temperature than lighter surfaces with high albedo. Thus, both minimum and maximum daily temperature values decrease with increasing reflectance of solar radiation.



Adapted from: Watson (1975). **Note:** These graphs have been derived from mathematical models, not measurements

Figure 7.9 Temperature profile

Modelled extreme rates of heating and cooling are shown for low density soil (ρ=1.05) with very low thermal inertia (P=0.2).



Adapted from: Kahle (1980)

One modelled example of a temperature profile in a 25 cm layer below the Earth's surface is shown in Figure 7.9. In this example, the greatest variation in temperature occurs in the topmost 10 cm. For some soils and rocks, however, changes in surface temperature can impact sub-surface materials to a maximum depth of 30–50 cm, at which point the geothermal gradient dominates. The transfer of heat from the surface to sub-surface layers effectively forms a heat reservoir, which together with the amount of insolation determine the diurnal maximum and minimum temperatures of the surface. The extent to which materials absorb, transfer and retain heat will vary with their thermal properties, especially thermal conductivity, and also specific heat and density (Drury, 1987).

The specific heat of a material, that is its capacity to store heat, limits the variation that can occur between daily temperature extremes. Thermal inertia varies between materials with changes in mineralogy, particle size, compactness, and the extent of unconsolidated material (Campbell and Wynne, 2011). As with other thermal properties, however, a number of factors can induce variations in thermal inertia for a given material, such as:

- density or porosity—porous materials with spaces filled by air or water have higher thermal inertia and less variation between day and night temperatures; for example, igneous rocks with a larger number of interstitial air pockets have higher thermal inertia than other rock types;
- topography (slope and aspect)—terrain shadowing and surfaces oriented away from incident radiation limit the energy reaching the surface, and can thus introduce temperature variations in a particular surface material;
- thermal conductivity—as more heat is transferred to greater depths, temperature extremes at the surface will be reduced; and
- moisture content—since water warms and cools slowly, the presence of moisture stabilises temperature changes and reduces thermal inertia (see the difference between diurnal temperature variation for typical rocks and soils versus damp terrain in Figure 7.1).

Since the moisture content in soils changes their thermal properties (with moist soils tending to be cooler than dry soils), various studies have demonstrated a unique relationship between soil moisture, vegetation greenness (NDVI) and land surface temperature (LST) within a given region (Carlson *et al.*, 1994; Piles *et al.*, 2010). Such relationships allow soil moisture and evapotranspiration maps to be routinely derived from thermal imagery (see Volume 3). Apparent thermal inertia (ATI) is computed from TIR imagery based on the temperature difference between day/night image pairs (Jensen, 2007). ATI can be used to estimate soil moisture saturation and has been valuable for modelling flood hazards (see Excursus 7.1). Methods for mapping thermal inertia are detailed in subsequent volumes.

Excursus 7.1—FloodMap

Source: Andrew Buchanan and Adrian Allen, Landgate
Further information: *http://floodmap.landgate.wa.gov.au*

Large portions of rural and remote Australia lack the basic survey and meteorological information required to predict and respond to flood events. In these regions, flash floods can disrupt traffic routes, and isolate and endanger indigenous and mining communities. Detailed mapping of floods greatly assists emergency services during evacuation activities and subsequent administration of compensation claims.

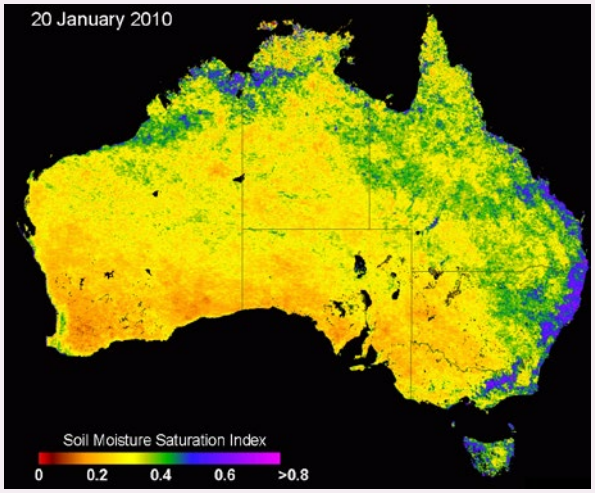
FloodMap offers an online service that integrates satellite imagery (from MODIS, MTSAT, Landsat and SAR) with other available data to provide timely flood intelligence and forecasting in these areas. Across Australia, on a daily basis and in near real-time, MODIS imagery is used to automatically map surface water daily at 250 m resolution. Soil moisture has been mapped at 4 km resolution from MTSAT, and will transition to Himawari-8 at 2 km resolution (see Figure 7.10). A flood risk model is also available. This information is not only valuable for natural disaster mitigation and hydrological modelling, but also delineates areas of standing water that could spread waterborne diseases, thus safeguarding the health of remote communities.

Surface water archives can be used to map catchment inundation over time (see Figure 7.11). This data source is particularly valuable for remote catchments that are not monitored by ground-based gauges. In the longer term, models based on these archives will improve our understanding of the conditions and consequences of natural disasters, enabling more efficient management of these inevitable events. One example of a flood hazard model based on topography and drainage that was been calibrated using FloodMap is shown in Figure 7.12.

Figure 7.10 Soil moisture saturation estimates

Soil Moisture Saturation estimates derived from satellite imagery show the impact of floods on soil moisture. Apparent Thermal Inertia (ATI) is derived from satellite measurements at 4 km resolution. The Soil Moisture Saturation Index (SMSI) is based on ATI over 60 days and is scaled between 0 (minimum water in soil) and 1 (saturated soil).

a. 20 January 2010



b. 20 March 2010

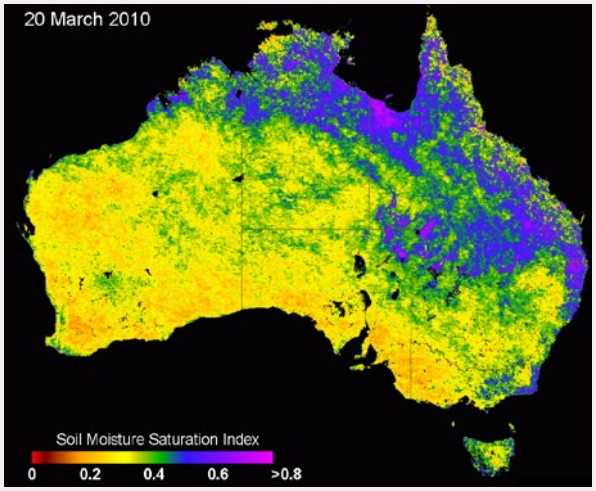


Figure 7.11 Monitoring inundation patterns

Extent of inundation in Australia's main internal drainage channels from 2006 to 2011 is shown as blue. Surface water across Australia has been archived daily since 2006.

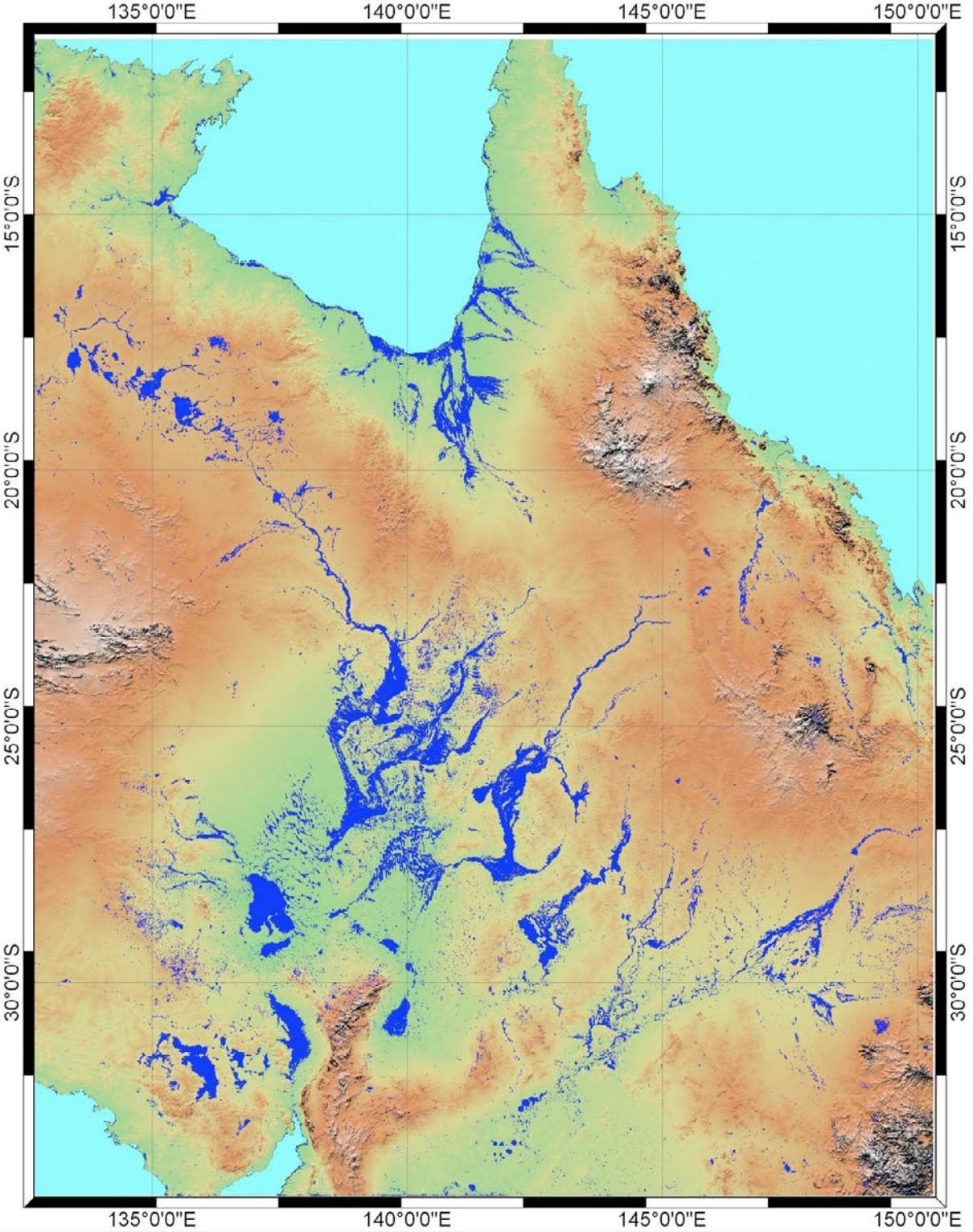
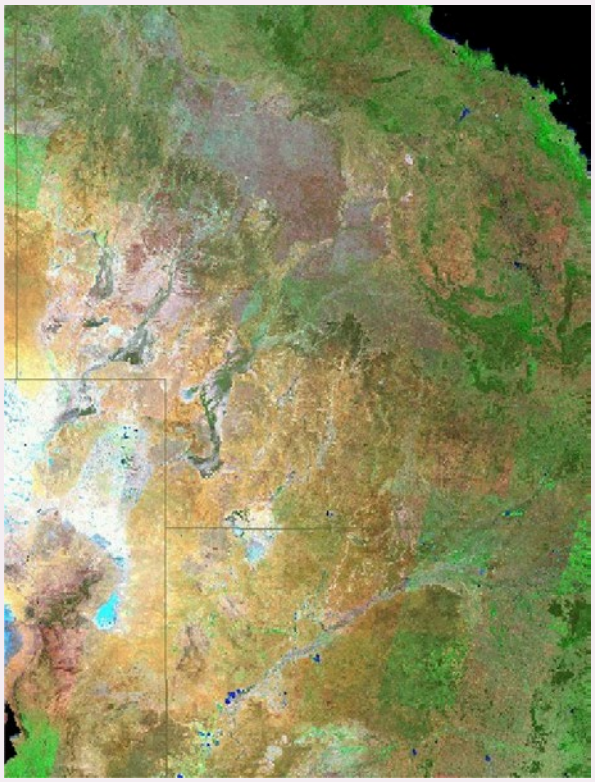


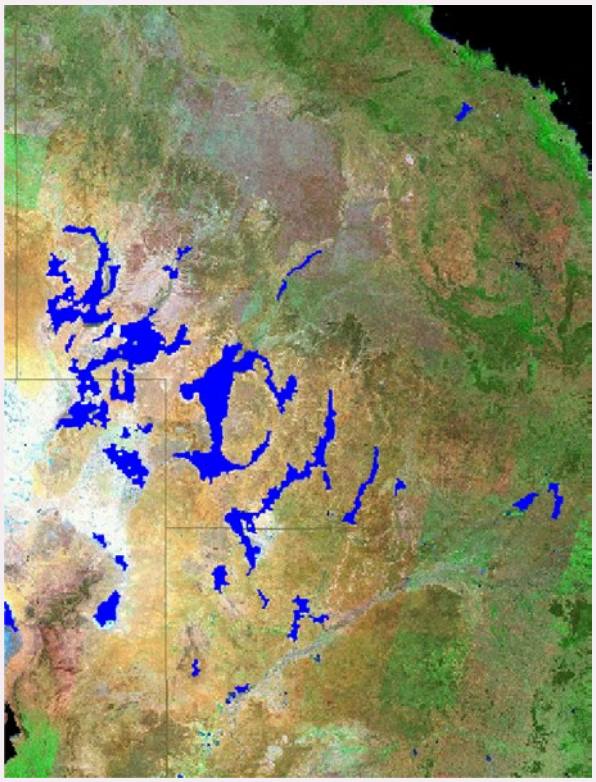
Figure 7.12 Flood hazard modelling

Between 10 February and 9 March 2010, flooding occurred in the Thomson, Bulloo, Barco, and Diamantina rivers in southern Queensland.

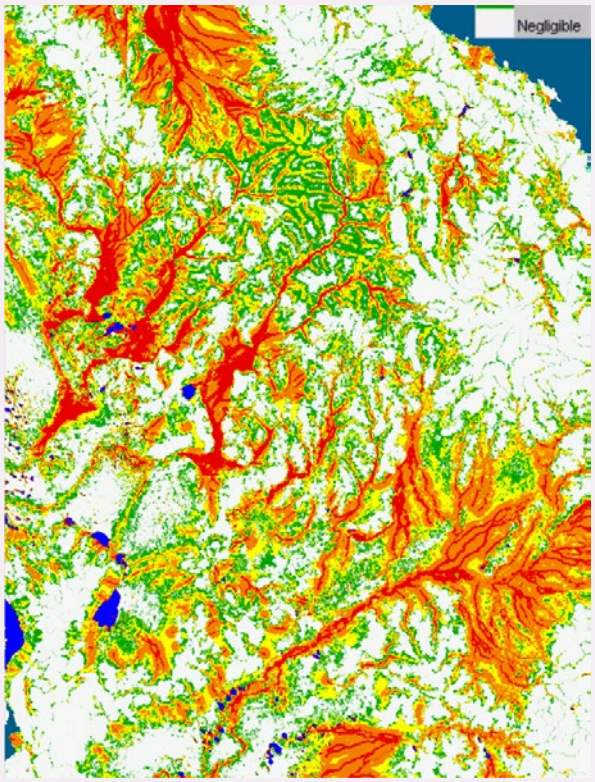
a. Landsat TM composite showing dry river systems



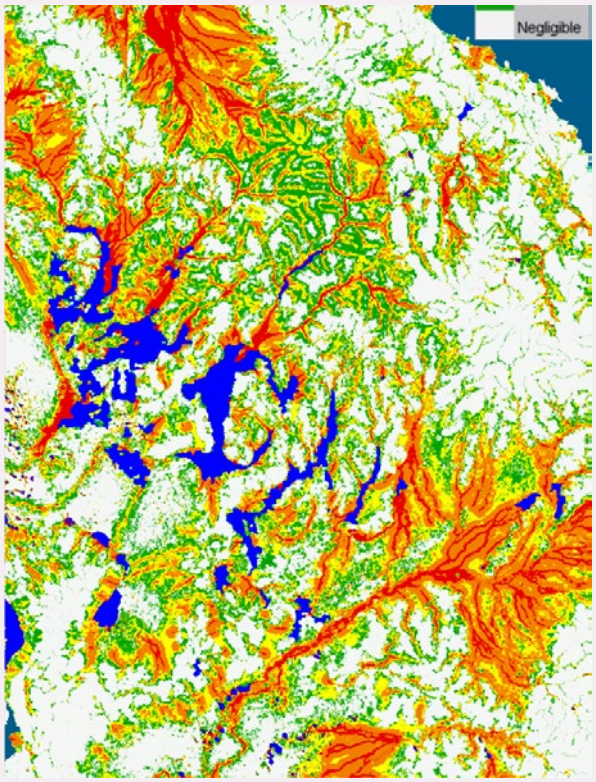
b. FloodMap presentation of flood extent is shown in blue (estimated at 80,000 km^2)



c. Flood hazard model based on topography and drainage has been calibrated using FloodMap estimates from 2001 to 2010.



d. FloodMap estimates of flood extent are overlaid on the flood hazard model, demonstrating strong correlation between them.



7.8 Further Information

Sea Surface Temperature

IMOS Ocean Current: *http://oceancurrent.imos.org.au/sst.php*

Reef Temp: *http://www.bom.gov.au/environment/activities/reeftemp/reeftemp.shtml*

Heat Transfer and Thermal Radiation Modelling:

Isidoro Martinez: *http://webserver.dmt.upm.es/~isidoro/tc3/Heat%20transfer%20and%20thermal%20radiation%20modelling.pdf*

7.9 References

Alnefaie, K. A., and Abu-Hamdeh, N. H. (2013). *Specific Heat and Volumetric Heat Capacity of some Saudian soils as affected by moisture and density*. Paper presented at the International Conference on Mechanics, Fluids, Heat, Elasticity and Electromagnetic Fields, Venice, Italy. *http://www.europment.org/library/2013/venice/bypaper/MFHEEF/MFHEEF-21.pdf*.

Campbell, J. B., and Wynne, R. H. (2011). *Introduction to Remote Sensing*, Fifth Edn. The Guilford Press, New York.

Carlson, T. N., Gillies, R. R., and Perry, E. M. (1994). A method to make use of thermal infrared temperature and NDVI measurements to infer surface soil water content and fractional vegetation cover. *Remote Sensing Reviews, 9*(1-2), pp. 161-173. doi:*http://dx.doi.org/10.1080/02757259409532220*.

Carter, A. J., Ramsey, M. S., Durant, A. J., Skilling, I. P., and Wolfe, A. (2009). Micron-scale roughness of volcanic surfaces from thermal infrared spectroscopy and scanning electron microscopy. *Journal of Geophysical Research-Solid Earth, 114*. doi:*http://dx.doi.org/10.1029/2008jb005632*.

Cudahy, T. (2002) *Thermal Infrared Mineral Mapping*. Open Industry Workshop, 24 June 2002, Toronto.

Dash, P., Gottsche, F. M., Olesen, F. S., and Fischer, H. (2002). Land surface temperature and emissivity estimation from passive sensor data: theory and practice-current trends. *International Journal of Remote Sensing, 23*(13), pp. 2563-2594. doi:*http://dx.doi.org/10.1080/01431160110115041*.

Drury, S. A. (1987). Image Interpretation in Geology. Allen and Unwin, London.

Duan, S.-B., Li, Z.-L., Tang, B.-H., Wu, H., Tang, R., Bi, Y., and Zhou, G. (2014). Estimation of Diurnal Cycle of Land Surface Temperature at High Temporal and Spatial Resolution from Clear-Sky MODIS Data. *Remote Sensing, 6*(4), pp. 3247-3262. doi:*http://dx.doi.org/10.3390/rs6043247*.

Elachi, C., and van Zyl, J. (2006). *Introduction to the Physics and Techniques of Remote Sensing*, Second Edn. Wiley Interscience, New Jersey.

Fang, L., Yu, Y., Xu, H., and Sun, D. (2014). New Retrieval Algorithm for Deriving Land Surface Temperature from Geostationary Orbiting Satellite Observations. *IEEE Transactions on Geoscience and Remote Sensing, 52*(2), pp. 819-828. doi:*http://dx.doi.org/10.1109/tgrs.2013.2244213*.

Forster, B. C. (2006). Principles and Tools for Remote Sensing of Human Settlements. Chapter 2 in 'Remote Sensing of Human Settlements' (Eds: M. K. Ridd, and J. D. Hipple). ASPRS, Bethesda.

Gillespie, A., Rokugawa, S., Matsunaga, T., Cothern, J. S., Hook, S., and Kahle, A. B. (1998). A temperature and emissivity separation algorithm for Advanced Spaceborne Thermal Emission and Reflection Radiometer (ASTER) images. *IEEE Transactions on Geoscience and Remote Sensing, 36*(4), pp. 1113-1126. doi:*http://dx.doi.org/10.1109/36.700995*.

Guedj, S., Karbou, F., and Rabier, F. (2011). Land surface temperature estimation to improve the assimilation of SEVIRI radiances over land. *Journal of Geophysical Research-Atmospheres, 116*. doi:*http://dx.doi.org/10.1029/2011jd015776*.

Harris, R., and Coutts, A. (2011). *Airborne Thermal Remote Sensing for Analysis of the Urban Heat Island*. Victoria Centre for Climate Change Adaptation Research, Melbourne.

Hecker, C., Smith, T. E. L., Ribeiro da Luz, B., and Wooster, M. J. (2013). Thermal Infrared Spectroscopy in the Laboratory and Field in Support of Land Surface Remote Sensing. 'Thermal Infrared Remote Sensing' (Eds: C. Kuenzer, and S. Dech). Springer, Netherlands.

Hunt, G. R. (1982). Spectroscopic properties of rocks and minerals. 'Handbook of Physical Properties of Rocks,' (Ed: R. S. Carmichael), Vol. 1, pp. 295-385. CRC Press, Boca Raton.

Jensen, J. R. (2007). *Remote Sensing of the Environment: An Earth Resource Perspective*, Second Edn. (592 pages). Pearson Prentice Hall, New Jersey.

Kahle, A. B. (1980). Surface Thermal Properties. 'Remote Sensing in Geology' (Eds: B. S. Siegal, and A. R. Gillespie). John Wiley and Sons, New York.

Kahle, A. B. (1984). Measuring spectra of arid lands. Chapter 11 in 'Deserts and arid lands' (Ed: F. El-Baz), pp. 195-217. Martinus Nijhoff Publishers, The Hague, Netherlands.

Li, Z.-L., Tang, B.-H., Wu, H., Ren, H., Yan, G., Wan, Z., Trigo, I. F., and Sobrino, J. A. (2013). Satellite-derived land surface temperature: Current status and perspectives. *Remote Sensing of Environment, 131*, pp. 14–37. doi:*http://dx.doi.org/10.1016/j.rse.2012.12.008*.

Lo, C. P., Quattrochi, D. A., and Luvall, J. C. (1997). Application of high-resolution thermal infrared remote sensing and GIS to assess the urban heat island effect. *International Journal of Remote Sensing, 18*(2), pp. 287-304. doi:*http://dx.doi.org/10.1080/014311697219079*.

Lyon, R.J.P. (1964). Evaluation of Infrared *Spectrophotometry for Compositional Analysis of Lunar and Planetary Soils*. Final Report PSU-3943. SRI, Menlo Park, California. 278pp.

McVicar, T. R., and Jupp, D. L. B. (1998). The current and potential operational uses of remote sensing to aid decisions on drought exceptional circumstances in Australia: a review. *Agricultural Systems, 57*(3), pp. 399-468. doi:*http://dx.doi.org/10.1016/s0308-521x(98)00026-2*.

Mobley, C. D. (1994). *Light and water: radiative transfer in natural waters*. Academic Press. , San Diego.

Payan, V., and Royer, A. (2004). Analysis of Temperature Emissivity Separation (TES) algorithm applicability and sensitivity. *International Journal of Remote Sensing, 25*(1), pp. 15-37. doi:*http://dx.doi.org/10.1080/0143116031000115274*.

Piles, M., Camps, A., Vall-llossera, M., Sánchez, N., Martínez-Fernández, J., Monerris, A., Baroncini-Turricchia, G., Pérez-Gutiérrez, C., Aguasca, A., Acevo, R., and Bosch-Lluís, X. (2010). *Soil moisture downscaling activities at the REMEDHUS Cal/Val site and its application to SMOS*. Paper presented at the 11th Specialist Meeting on Microwave Radiometry and Remote Sensing of the Environment (MicroRad).

Ramsey, M. S. (2004). *Quantitative geological surface processes extracted from infrared spectroscopy and remote sensing*. Paper presented at the Mineralogical Association of Canada Thermal Infrared Spectroscopy Workshop, London, Ontario, Canada. *http://www.pitt.edu/~mramsey/papers/GAC1.pdf*.

Sabins, F. F. (1987). *Remote Sensing: Principles and Interpretation*, Second Edn. Freeman, New York.

Salisbury, J. W., and Daria, D. M. (1992). Emissivity of Terrestrial Materials in the 8-14 μm Atmospheric Window. *Remote Sensing of Environment, 42*(2), pp. 83-106. doi:*http://dx.doi.org/10.1016/0034-4257(92)90092-x*.

Schmugge, T. J., Kustas, W. P., Ritchie, J. C., Jackson, T. J., and Rango, A. (2002). Remote sensing in hydrology. *Advances in Water Resources, 25*(8-12), pp. 1367-1385. doi:*http://dx.doi.org/10.1016/s0309-1708(02)00065-9*.

Sharqawy, M. H., Lienhard, J. H. V., and Zubair, S. M. (2010). Thermophysical properties of seawater: a review of existing correlations and data. *Desalination and Water Treatment, 16*(1-3), pp. 354-380. doi:*http://dx.doi.org/10.5004/dwt.2010.1079*.

Torgersen, C. E., Faux, R. N., McIntosh, B. A., Poage, N. J., and Norton, D. J. (2001). Airborne thermal remote sensing for water temperature assessment in rivers and streams. *Remote Sensing of Environment, 76*(3), pp. 386-398. doi:*http://dx.doi.org/10.1016/s0034-4257(01)00186-9*.

USGS (2011). *US Geological Survey Spectroscopy Lab*. Retrieved from *http://speclab.cr.usgs.gov*.

Wan, Z. (2008). New refinements and validation of the MODIS Land-Surface Temperature/Emissivity products. *Remote Sensing of Environment, 112*(1), pp. 59-74. doi:*http://dx.doi.org/10.1016/j.rse.2006.06.026*.

Wan, Z., Zhang, Y., Zhang, Q., and Li, Z. L. (2004). Quality assessment and validation of the MODIS global land surface temperature. *International Journal of Remote Sensing, 25*(1), pp. 261-274. doi:*http://dx.doi.org/10.1080/0143116031000116417*.

Watson, K. (1975). Geologic applications of thermal infrared images. *Proceedings of the IEEE, 63*(1), pp. 128-137. doi:*http://dx.doi.org/10.1109/PROC.1975.9712*.

Weng, Q. H., Lu, D. S., and Schubring, J. (2004). Estimation of land surface temperature-vegetation abundance relationship for urban heat island studies. *Remote Sensing of Environment, 89*(4), pp. 467-483. doi:*http://dx.doi.org/10.1016/j.rse.2003.11.005*.



8 Microwave Imagery

Author: Bruce C. Forster[14]

Microwave sensors operate between the wavelengths of approximately 1–1000 mm (see Volume 1A). Passive microwave sensors rely upon the natural radio emission of the Earth, and its effects on Earth and atmospheric constituents, to sense a variety of geophysical parameters (see Section 8.1). Section 8.2 provides an overview of radar theory, data characteristics and applications. Active microwave sensors, such as radar, are independent of solar illumination and hence may be used 24 hours a day. In many applications and geographic regions, such as the perennially cloudy tropics, these features provide a guarantee of data acquisition that is not available for systems operating in visible and infrared wavelengths.

Microwave remote sensing systems, whether active or passive, have important implications for global climatic and weather system studies. Their data have already been used for numerous applications in meteorology, oceanography, and land studies.

Remote sensing in the microwave wavelengths offers the opportunity of selecting bands which are unaffected by cloud cover and most weather conditions.

8.1 Passive Microwave

Passive microwave sensing is similar in concept to thermal remote sensing (see Section 7) but detects longer wavelengths using radiometers or scanners. For Earth surfaces at a temperature of 300K (27°C) maximum emission occurs at wavelengths centred approximately on 10 μm, which is in the thermal infrared (TIR) range. However, Planck's Law shows that exitance (in W/m^2) is inversely proportional to wavelength (λ^5), so that, for an object at Earth's temperature (300K), the emission at a microwave wavelength of 1 cm would be very many times less. Thus, while all objects emit microwave energy, the amounts are generally very small, so the bandwidth and the spatial resolution of the sensor must be large to allow acquisition of sufficient measurable radiation. A passive microwave sensor detects this naturally emitted microwave energy within its field of view. The emitted energy is related to the temperature and moisture content of the emitting object or surface. Surface roughness can also increase the measured radiation from an object or surface because rough texture (such as with ocean waves) increases the surface area of emission per unit area viewed.

Applications of passive microwave remote sensing include meteorology, hydrology, and oceanography. Depending on the wavelength being detected, meteorologists can use passive microwaves to measure atmospheric profiles and determine water and ozone content in the atmosphere. Hydrologists can use passive microwaves to measure soil moisture, which influences natural microwave emission, while oceanographic applications include mapping sea ice, currents, and surface winds, as well as detecting marine pollutants such as oil slicks. Passive microwave sensors are typically designed to sense the Earth and the atmosphere in two different regions of the spectrum. Imaging systems operate at wavelengths which can see through the atmosphere to the surface of the Earth, while sounders operate at wavelengths that record the energy from various vertical levels in the atmosphere and not from the Earth's surface.

Background image: PALSAR image of Whitsunday Islands, Queensland, acquired on 5 December 2010 (L-band SAR). **Source:** Norman Mueller, Geoscience Australia

14. Recommended Chapter Citation: Forster, B.C. (2017). Microwave Imagery. Ch 8 in Volume 1B of Earth Observation: Data, Processing and Applications. CRCSI, Melbourne. *In this chapter, some text and figures from Forster (2006) have been reproduced with permission from the American Society for Photogrammetry and Remote Sensing, Bethesda, Maryland, www.asprs.org*

8.1.1 Brightness temperature

Passive microwave sensors measure the emitted spectral radiance received, L_λ. This is called the brightness temperature, T_B, and it is linearly related to the kinetic energy of the surface (see Section 7 and Volume 1A). The amount of energy emanating from an object at a given wavelength is related to a number of physical properties. In the microwave portion of the spectrum, the two most important properties are the physical temperature (T) of the object and its radiating efficiency or emissivity (ε). Emissivity is the ratio of emitted radiation at a particular wavelength of a real surface to the equivalent radiation from a blackbody at the same temperature and wavelength (see Volume 1A—Section 2.11).

The Rayleigh-Jeans approximation provides a simple linear relationship between measured spectral radiance temperature and emissivity and is valid for wavelengths greater than approximately 3 mm at surface temperatures of 300K:

$$L_\lambda = \frac{\varepsilon 2kcT}{\lambda^4}$$

where

k is Planck's constant;
c is the velocity of EMR (speed of light);
ε is emissivity; and
T is kinetic energy.

Since $2kc$ in this equation is a constant, spectral radiance is a linear function of kinetic energy for the same wavelength.

Brightness temperature, T_B, is equal to the product of the kinetic energy of the surface or object (T), and its emissivity, thus:

$$T_B = \frac{\lambda^4}{2kc} L_\lambda$$

And so brightness temperature can be related to kinetic energy through the emissivity of the material:

$$T_B = \varepsilon T$$

Brightness temperature can therefore be used to monitor temperature as well as properties related to emissivity. In the microwave region, surface materials can have large variations in emissivity. For example, land surfaces can have emissivity of the order of 0.9 while water is of the order of 0.5, although emissivity differences will be less at shorter wavelengths (higher frequencies). Thus, the difference in brightness temperature between land and water at the same kinetic temperature will be largely due to the large difference in their emissivities. Over oceans, the contribution of the atmosphere is greater relative to the surface contribution, whereas over land the atmospheric contribution, although similar in magnitude to that over ocean surfaces, is less relative to the land surface contribution. For the same atmosphere, emissivity of land of 0.9 and of water 0.5, then for a surface temperature of 300K, the brightness temperature of the land would be 275.7K compared to water of 178.5K. The atmospheric contribution to the signal is approximately 12% over the land surface and approximately 25% over the ocean. It should be noted that ice or snow surfaces and clouds and rain can modify these results (Ferraro *et al.*, 1998).

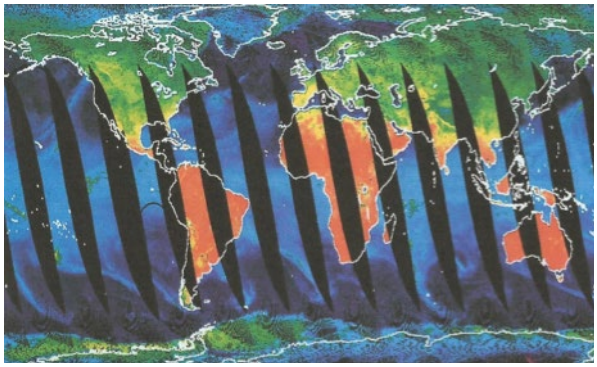
Examples of SSM/I images (TRMM Special Sensor Microwave/Imager) are shown in Figure 8.1 (Ferraro *et al.*, 1998) for measurements taken at 19 GHz and 85 GHz (1.58 cm and 0.35 cm wavelengths) using vertical polarisation. These images show large brightness temperature differences between land and oceans, particularly at 19 GHz. This is due to the lower emissivity of water compared to land. The difference between land and water is not as large in the 85 GHz image since the emissivity differences are not as large at this frequency. Over the oceans, various cloud band features are apparent, as well as changes in brightness temperature due to the presence of sea ice. Over land, very cold regions are evident on the 85 GHz image, which are associated with the scattering properties of convective rainfall and snow cover.

The only technology that can 'see' beneath the ground is radar imagery. But satellite imagery also allows scientists to map short- and long-term changes to the Earth's surface. Buried archaeological remains affect the overlying vegetation, soils and even water in different ways, depending on the landscapes you're examining. (Sarah Parcak)

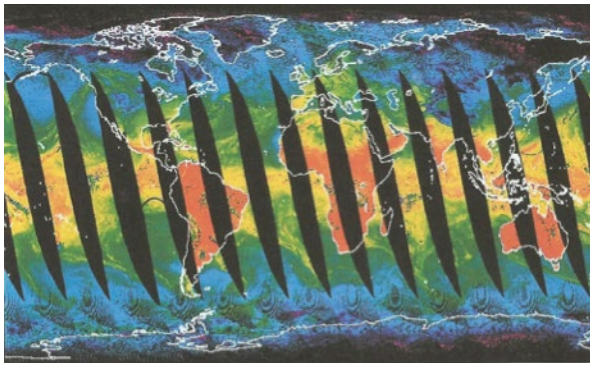
Figure 8.1 SSM/1 ascending orbits

Images acquired 11 December 1997, in vertical polarisation, with brightness temperature ranging from 160 K (purple) to 290 K (red)

a. 19 GHz



b. 85 GHz



Source: Ferraro *et al.* (1998)

8.1.2 Emissivity, polarisation and angle of observation

The basic expression for emissivity (as a function of θ, the angle of observation from the nadir) can be given by:

$$e_p(\theta) = 1 - r_p(\theta)$$

where

$e_p(\theta)$ is the emissivity of the surface layer;
p is the polarisation, either vertical or horizontal; and
$r_p(\theta)$ is the reflectivity coefficient.

This assumes that all radiation that is not reflected is absorbed, and then re-radiated as emitted radiation. In the case of a smooth surface over a homogeneous medium, the reflectivity coefficient can be obtained from the Fresnel reflection coefficient $R_p(\theta)$ as:

$$r_p(\theta) = \left| R_p(\theta) \right|^2$$

The Fresnel coefficient for horizontal polarisation is:

$$R_{pH}(\theta) = \frac{\cos\theta - \sqrt{\varepsilon_r - \sin^2\theta}}{\cos\theta + \sqrt{\varepsilon_r - \sin^2\theta}}$$

where

ε_r is the dielectric constant of the surface interface (air to surface).

And for vertical polarisation:

$$R_{pV}(\theta) = \frac{\varepsilon_r \cos\theta - \sqrt{\varepsilon_r - \sin^2\theta}}{\varepsilon_r \cos\theta + \sqrt{\varepsilon_r - \sin^2\theta}}$$

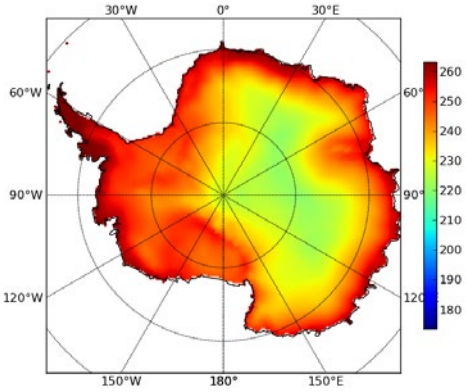
where

ε_r is the dielectric constant of the material.

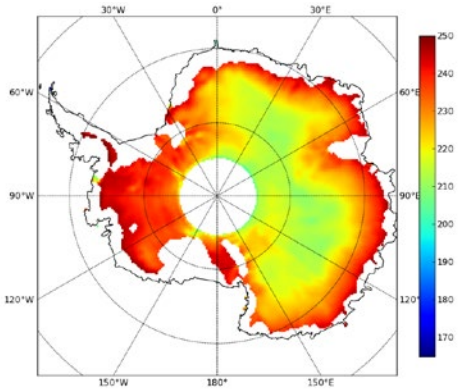
Figure 8.2 Brightness temperature over Antarctica

SMOS L-band (1.4 GHz) vertical polarisation with viewing angle of 55° processed to brightness temperature compared with physical temperature. Note that the colour scales in these two images are slightly different.

a. Spatial variations of L-band T_B show two different zones—a warmer, wet zone with low emissivity (coloured red and orange) and a colder, dry zone with high emissivity (coloured yellow and green).



b. ERA-Interim annual mean air temperature shows similar temperature mappings, especially for the dry zone.



Source: Ghislain Picard, Université Grenoble Alpes from Picard *et al.* (2011)

When θ is equal to 0°, R_{pH}^2 and R_{pV}^2 are equal. If ε_r is equal to 4 (dry soil), then r_p is 0.11 (11%) and so emissivity will be 0.89. That is, 89% of the absorbed radiation will also be emitted.

For both horizontal and vertical polarisation as θ approaches 90°, r_p approaches 1.00 and thus emissivity approaches zero—all incident radiation is reflected, therefore no absorption, and thus no emission. However, some simple trigonometry shows, for vertical polarisation, that at a certain viewing angle (called the Brewster angle) the emissivity is 1.00, that is, all the radiation is absorbed and re-radiated. Theoretically the Brewster angle can be given by the following relationship:

$$\tan\theta = \sqrt{\varepsilon_r}$$

For ε_r equal to 4, $\tan\theta = 2$, so θ equals 63°. Optimum observation of passive radiation occurs at the Brewster angle, where brightness temperature is close to the value of the physical temperature. In Figure 8.2, for example, SMOS multi-date, multi-polarisation imagery over Antarctica was processed into a data cube (Picard *et al.*, 2011), in which individual pixel temperatures are represented as:

$$T_B\left(x,y,t,\theta,p\right)$$

where

x,y indicate location;
t indicates time;
θ indicates incidence angle; and
p indicates polarisation.

For L-band imagery (0.39–1.55 GHz; see Volume 1A—Section 15.2):

- coarse surfaces (ice or coarse snow grains) scatter microwaves strongly so emissivity is low;
- dry snow scatters weakly, so emissivity is higher; and
- wet snow absorbs strongly, so emissivity is close to 1.

Picard *et al.* (2011) conclude that brightness temperature is reliably correlated with snow temperature for dry snow with incidence angles 50–55° using L-band imagery with V-polarisation.

8.2 Imaging Radar

In addition to passive microwave sensors, active sensors such as radar are used to generate and detect stronger backscattering microwave signals from the Earth's surface. The formation of imagery using radar sensors was introduced in Volume 1A—Section 15. Numerous characteristics of terrain determine the intensity of returns for a given wavelength and polarisation of radar signals. Imaging radar also has the potential to operate at longer wavelengths where Earth surface features become partly translucent and returns are received from subterranean features. The major factors influencing an object's return signal intensity are considered to be relief, surface roughness and electrical properties. The great advantages of imaging radar systems is that they can acquire imagery both during the day and at night, and penetrate through cloud and rain (although rain shadows can occur when using shorter wavelengths—3 cm or less).

The side-looking nature of imaging radar devices records relief characteristics with higher returns from sensor-facing slopes, and lower or no returns from away-facing slopes or radar shadow areas, in much the same way as an off-nadir Sun position differentially illuminates a landscape with varying relief. Depending on an object's height, and radar signal characteristics, relief displacement can occur in radar imagery, with the return from the top of an object (such as a hill or building) being recorded before the return from its base. This produces a characteristic layover effect, which is maximized at near range. At far ranges, a foreshortening effect can occur with the size of a sloping surface facing the antenna being compressed in the image.

Surfaces with local relief variations that are greater than the wavelength of the radar signal will scatter the signal in all directions (diffuse reflectors) and thus return a small, but measurable, portion of the signal to the sensor (see Volume 1A—Section 15). Smooth surfaces, with surface roughness much less than the wavelength of the radar signal, tend to reflect most of the energy away from the sensor (specular reflectors) thus producing a low return signal. However, the actual response will obviously depend on surface orientation relative to the sensor, so that if the surface is perpendicular to the transmitted signal, the returned signal will be directed back toward the sensor. Similarly, a corner reflector (adjacent smooth surfaces which doubly reflect (double bounce) the signal) can result in a high radar return. More surfaces tend to be specular reflectors for microwave wavelengths than in the visible and infrared wavelengths, with some objects that appear rough in optical imagery, such as roadways, appearing smooth in radar imagery.

Materials differ in terms of their electrical reflectivity and conductivity. One measure of these characteristics is called the 'complex dielectric constant'. For most dry natural materials, the magnitude of this constant has relatively low values

(3–8) in the microwave region of the EM spectrum. Water, however, has a value of approximately 80. Thus, water, or moisture in soil or vegetation, significantly increases radar backscatter from vegetation and rough soil surfaces. Metal objects also have characteristically high dielectric constant values.

Vegetation cover can scatter radar signals in a number of ways such as volume scattering by leaves or grass, scattering from stems, corner reflection from trunks, and returns from the ground layer through gaps in the vegetation layers. The relative strengths of these effects depend on the radar frequency. At X- and C-band frequencies, a moderate cover of grass or trees can completely mask the soil effect and volume scattering dominates. When there is little vegetation cover, the soil micro-relief dominates the X-band signal, followed in strength of effect by the moisture content of the soil surface crust.

The local slope and aspect modify the backscattered radar signal by decreasing or increasing the local angle of incidence. Slopes towards the aircraft or space-borne platform are enhanced and slopes away are darkened. This effect explains the use of radar to map landform and geological structure. At X-band, the effect of the vegetation is strong, while P-band will be better for structural mapping in densely vegetated areas. The use of different wavelengths and polarisations allows 'multispectral' radar imaging, which can indicate both structure and properties of the Earth's surface and near surface soil and vegetation layers.

In view of the above factors, the orientation and position of the flight line directly affects the resulting radar image. The side-looking nature of radar sensors can also result in slant range scale distortions in the imagery (since the slant distance does not vary consistently with respect to the ground distance), which requires subsequent geometric rectification to be able to relate image features to a map base (see Volume 2C). However, if an object is imaged from two different flight lines, the relief displacements cause image parallax, which allow the imagery to be viewed stereoscopically. As pairs of imagery which are produced by viewing terrain features from opposite sides will have reversed side-lighting effects, stereo pairs are usually produced from flights along the same path at different altitudes, the lower image having the greater extent of shadow. This altitude parallax characteristic may also be used to determine approximate heights of image features. Height determination using radar interferometry is discussed in Section 8.2.7.

8.2.1 Overview of radar remote sensing theory

To adequately interpret radar images, it is necessary to have a good understanding of radar theory as the images are acquired in a completely different way to centrally-projected images derived in the optical wavelength regions. Radar remote sensing uses microwave EMR, emitted by an antenna carried on an aircraft or spacecraft platform, to irradiate the Earth's surface and measure the amount of returning radiation reflected from surfaces (called backscatter) within the resolution elements of the system. The radiation is transmitted in a fan-shaped beam as a series of pulses of very short length. The time taken for each pulse (travelling at the 'speed of light') to be reflected and returned to the antenna determines the distance of that portion of the Earth's surface from the antenna.

The amount of the original signal backscattered to the antenna will depend on the characteristics of the Earth surface, such as material, shape and orientation. The wavelength of the transmitted radiation ranges from 1 cm to 1 m, with an equivalent range in frequency between 30 Gigahertz (GHz) and 0.3 GHz. As a simple rule, 30 divided by the frequency in Gigahertz will give wavelength in centimetres, and vice versa. In the following, wavelength rather than frequency will mainly be used to describe the radiation, as it is easier to compare wavelength with Earth surface roughness and the size of surface feature elements such as leaves. The wavelengths and frequencies of radar bands used to acquire EO imagery are summarised in Table 8.1, with X-, C-, and L-bands being the most commonly used.

Table 8.1 Radar bands used for EO

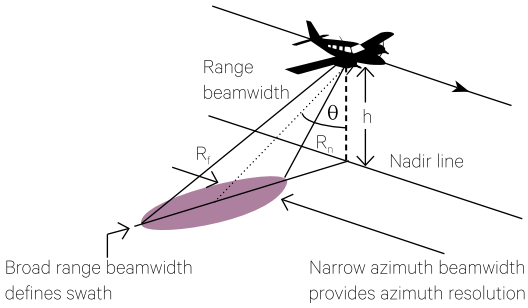
Code	Wavelength (mm = 10^3 μm)	Frequency (GHz = 10^9 Hz)	EO Example
K	7.5–24.0	12.5–40.0	Early airborne systems
X	24.0–37.5	8.0–12.5	Military reconnaissance, terrain mapping, surveillance
C	37.5–75.0	4.0–8.0	Sea-ice surveillance (limited penetration of solids or vegetation)
S	75.0–150.0	2.0–4.0	Medium-range meteorological applications, such as rainfall measurement, airport surveillance
L	150.0–300.0	1.0–2.0	Ice sheet monitoring, glacier dynamics, penetrates vegetation
P	300.0–1000.0	0.3–1.0	Experimental—penetrates vegetation, sea ice, soil, glaciers

Source for descriptive details: Parker (2012)

The amount and nature of backscattered EMR can provide information about the size, shape, configuration and electrical properties of the surfaces and objects irradiated. In general, the return signal is a function of the surface roughness compared with the wavelength of the radiation and the dielectric properties of the material, which are approximately related to its moisture content. The moisture content will determine how deeply the radiation penetrates into the material, as high water content allows for little penetration. For surfaces that are smooth relative to the wavelength, a mirror-like reflection will occur and little or no radiation will be returned to the sensor, whereas if the surface is rough, a significant amount of the transmitted signal will be backscattered to the radar antenna. In addition, hard targets such as metal objects can have a very strong return signal if they are oriented towards the antenna. The amplitude, polarisation and phase of the return signal can also be measured, although the simplest systems only record the amplitude.

Figure 8.3 Basic configuration of an imaging radar system

Range and resolution are shown with respect to flight path.



Source: Forster (2006) Figure 2-42

Most imaging radar systems are side-looking, and early systems were called side-looking airborne radars (SLAR). They have a rectangular antenna with the long side oriented in the direction of motion of the sensor platform, and the antenna beam pointing to one side of the platform as illustrated in Figure 8.3. Basic terms relating to imaging radar systems are listed in Table 8.2.

Table 8.2 Imaging radar terminology

Term	Symbol	Definition
Speed of radar beam	c	Speed of light (see Volume 1A)
Wavelength of radar	λ	Distance between successive peaks or troughs in EMR (see Volume 1A)
Height	h	Altitude of radar platform
Pulse length	τ	Duration of transmitted pulse (also called pulse width or transmit time)
Total pulse time	T	Time interval from transmission of pulse to detection of returned signal
Length of antenna	l	Longest dimension of effective aperture for transmitting antenna (generally across-track)
Width of antenna	w	For non-circular apertures, effective width of transmitting antenna (generally along-track)
Near range	R_n	Side of irradiated ground nearest antenna
Far range	R_f	Side of irradiated ground furthest from antenna
Horizontal beam width of antenna	b_H [c]	Effective angular width of radar beam in horizontal plane
Vertical beam width of antenna	b_V [c]	Effective angular width of radar beam in vertical plane
Range of antenna	R	Distance of antenna from surface along beam projection (also called slant range distance)
Look angle of beam	θ	Elevation angle of centre of beam
Azimuth direction	az	Direction parallel to platform travel
Range direction	r	Direction parallel to side-looking radar beam (hence perpendicular to platform travel)
Azimuth resolution	r_{az}	Smallest element that can be recorded in the azimuth direction (also called along-track resolution)
Range resolution	r_r	Smallest element that can be recorded in the range direction (also called across-track resolution)
Ground range resolution	r_g	Range resolution divided by sine of incidence angle

The direction parallel to the platform travel direction is called the azimuth direction, while at right angles and in the direction of the beam is called the range direction. The side of the irradiated area (or image) nearest the antenna is called the near range, R_n, while the side furthest away is called the far range, R_f. The horizontal beam width of the antenna, b_H^c, is the effective angular width of the radiation beam in radians, in the horizontal plane, while the vertical beam width, b_V^c, is the angular width of the beam in the vertical plane, producing a fan-shaped beam. The projection of the beam onto the Earth's surface effectively defines the area of irradiation, which will increase as the altitude of the antenna above the surface increases. R is the range (or distance) of the antenna from the surface along the projection of the beam, and $2 \times R$ defines the distance that the radiation has to travel at a velocity of c (the speed of light) to reach the target and return to the antenna, while θ is the look angle at the centre of the radiation beam (or the elevation angle with respect to the vertical). The beam widths in radians can be approximately given by:

$$b_H^c = \frac{\lambda}{l}$$

$$b_V^c = \frac{\lambda}{w}$$

where

l and w are the respective length and width of the antenna;

λ is the wavelength of the radar signal; and the equivalent ground dimensions of the beam widths can be obtained by multiplying by R, the range.

The limited size of the antenna (of the order of metres) leads to illuminated areas on the Earth's surface with range-direction dimensions of the order of kilometres and azimuth dimensions of tens of metres for aircraft platforms, which would be very much greater for satellite or spaceborne platforms. The azimuth resolution, r_{az} (the smallest element that can be recorded in the azimuth direction), is given by:

$$R_{az} = R b_H^c = \frac{R\lambda}{l}$$

and since

$$R = h / \cos\theta$$

then

$$r_{az} = h\lambda / l\cos\theta$$

The range resolution of the system is solved by the transmission of short pulses of time t, (or it can be visualized as a pulse of length $t \times c$), that allows the discrete time of the return signal to be determined and thus the total return distance from the antenna to the target and back. The slant range distance, R, to a target can be given by:

$$R = c\frac{T}{2}$$

where

c is the velocity of EMR; and

T is the total time from when the discrete pulse leaves the antenna to when it returns (with its amplitude, polarisation and phase modified by the surface it has irradiated).

The range resolution of the system will be determined by the pulse length, τ. The front of the pulse can be pictured as first striking the surface and then wrapping back on itself towards the antenna, with the balance of the pulse continuing to strike the surface until the back of the pulse finally reaches it. The position of the surface feature within the pulse length that is causing the changes to the incoming radiation can only be determined to half the pulse length, and thus the range resolution, r_r (that is, the smallest element from which a unique return signal is emanating) can be given by:

$$r_r = c\frac{\tau}{2}$$

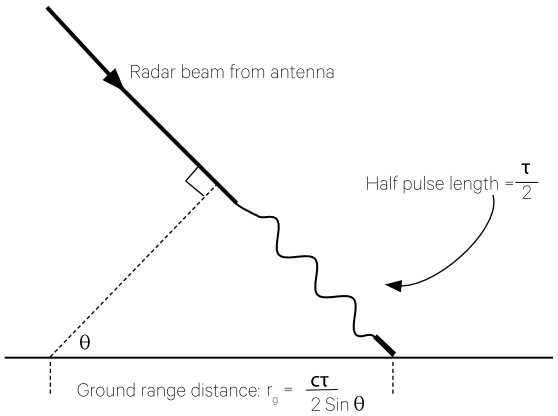
This can be converted to an equivalent ground range resolution by dividing by sin θ to give:

$$r_g = c\frac{\tau}{2\sin\theta}$$

as illustrated in Figure 8.4.

Figure 8.4 Concept of range resolution and ground range resolution

Range resolution remains constant while ground range resolution increases with θ



Source: Forster (2006) Figure 2-43

Azimuth resolution is improved for smaller wavelengths and smaller look angles (θ—that is, in the near range), and for lower altitudes and larger antenna length, while ground range resolution improves as θ becomes larger (that is, in the far range) and as pulse length (τ) becomes smaller. The look angle θ therefore has the opposite effect on azimuth and ground range resolutions. However, there are technical limitations as to how small τ can be while still having sufficient power to reach the ground surface and return, without dramatically increasing the amplitude (and thus power) of the emitted radiation. There are also limitations on how large the antenna length (l) can be and still be carried on an aircraft or satellite platform. Reducing the wavelength increases the potential interference from rain, when the raindrops are of the same order of size as the wavelength. This would negate one of the benefits of radar remote sensing, that of all-weather capacity. From the ground range equation it is clear that these systems cannot provide good azimuthal resolution at satellite altitudes. For example, for a 10 m azimuth resolution to be achieved with 3 cm wavelength radar at a range of 400 km, the antenna would need to be approximately 1.2 km in length, which effectively is impossible.

Radar systems that use antenna beam width and pulse width for azimuth and range resolution are called real aperture radars (RAR). Synthetic aperture radar (SAR) is a more recently developed system (see Volume 1A—Section 15.2.2 and Figure 15.7) that uses a long synthetic antenna (the equivalent of an array of short real antennae) and a modified pulse with a small linear variation in frequency over the pulse length (as compared to an RAR that has a constant frequency or wavelength). These modifications allow both the azimuth and range resolutions to be improved. For both SAR and RAR, the image produced occurs as a result of the motion of the airborne or space-borne platform over the area being covered. A short pulse of energy is transmitted which strikes the ground and is partially backscattered. The time that elapses between the initial transmission and its return gives the range, with the return from the closest strip occurring first, and the return from the farthest strip occurring last. Other features of RAR, which also apply to SAR (except for azimuth resolution), include:

- grazing and normal angles should be excluded, as grazing rays will cause excessive shadow in other than flat terrain, while normal angles (that is, the radar beam has a look angle of zero and is incident on a horizontal surface at right angles) will cause the range resolution to be indeterminate (that is, the range resolution cannot be resolved);
- range resolution is poorer in the near range;
- azimuth resolution becomes poorer with increasing range because of the absolute increase in the beam width;
- for aircraft use, the wavelength, λ, generally ranges from 3.0–0.8 cm (10–37.5 GHz) to maintain a reasonable azimuth resolution;
- signal power from a small target decreases inversely as the fourth power of the range. The signal gain (that is, a factor used to multiply the signal strength) must be varied with the range so that similar surfaces are uniformly displayed;
- range of the maximum to minimum signal strength returning to the antenna is very wide, with diffuse natural surfaces ranging from 100 to 1, that is, a range of 20 dB, while specular-built surfaces, particularly corner reflectors, can range from 10^6 to 1 or 60 dB; and
- high frequencies (shorter λ) are discouraged by power and weather difficulties. The peak power is more difficult to generate at shorter wavelengths and greater power is needed, while shorter wavelengths are more sensitive to water particles as their size approaches half a wavelength.

8.2.2 Synthetic aperture radar

Synthetic aperture radar (SAR) creates the equivalent of a long antenna by synthesizing a long linear array of short real antenna apertures. A single short aperture (real) antenna fulfils the function of a long antenna by recording the amplitude and phase of the return signal as it moves from one end of the hypothetical array to the other, due to the platform motion. A single short antenna will have a large horizontal beam width so that the azimuth resolution will also be large. As an object in front of the beam will have a relative velocity towards the antenna, the return frequency of the emitted signal will be larger than that emitted due to the Doppler shift (see Volume 1A—Section 2.5.4). When the object has moved to the centre of the beam due to the forward motion of the platform, there will be no relative velocity between the antenna and the ground and thus no change in frequency of the signal, whereas when the object is in the back of the beam there will be a relative velocity away from the antenna and the frequency of the return signal will be less. This effect is exactly the same as the sound of a vehicle approaching and then passing by, that is, a high frequency sound changes to a lower frequency sound.

Thus, the frequency of the return signal of a specific object on the ground will change over the period it is in the radar beam. The history of this change, which will be different for objects separated in the azimuth direction, allows the determination of the object's position with much greater accuracy than for a single antenna alone, with a consequent substantial improvement in the azimuth resolution. The change in return frequency due to Doppler shift is illustrated in Figure 8.5. When the relative velocity of the radar

sensor to the target is much less than c (velocity of EMR) then the change in frequency, Δf, is given by:

$$\Delta f = \frac{Fu\cos\theta}{c}$$

where

F is the central frequency of radar signal;
u is the relative velocity between source and receiver; and
θ is the angle between direction of motion of the energy source and a line connecting the source and the observer.

Note that, from antenna to ground and return, the frequency change is twice the Doppler shift of one direction—that is, f in Figure 8.5 is equal to $2\times\Delta f$.

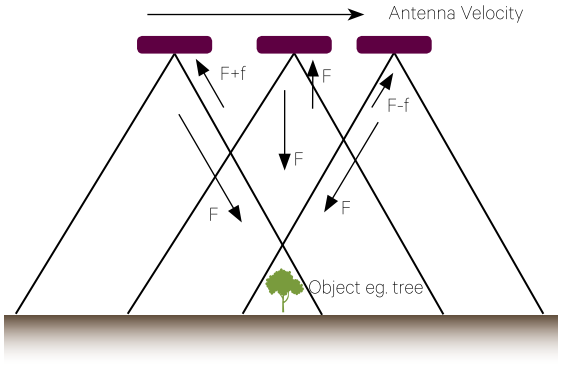
It can be shown that azimuth resolution (r_{az}) for SAR is approximately given by:

$$r_{az} = \frac{l}{2}$$

that is, azimuth resolution is half the length of the antenna (l). Thus, the azimuth resolution for SAR is independent of the operating range, R (or altitude, h), the look angle, θ, and the wavelength, λ, and reduces as the length of the real aperture (antenna) reduces. A schematic illustration of why this occurs for different altitudes and antenna lengths is given in Figure 8.6, which shows that while the azimuth resolution of a RAR would be poorer for a smaller antenna (Figure 8.6b), the ground object will remain in the view of a SAR for a longer period, increasing the number of observations of the return signal and thus improving the frequency history and azimuth resolution, which counteracts the effect of the shorter antenna. The same principle applies for an antenna at a higher altitude (Figure 8.6a), Although the range distance increases, the azimuth resolution remains the same, and is independent of altitude. Thus, by making the antenna smaller, the azimuth resolution can be increasingly improved.

Figure 8.5 Effect of Doppler shift on the return frequency

Frequency increases moving towards object and decreases moving away.



Source: Forster (2006) Figure 2-44

However, when the wavelength (λ) is constant, radar complexity, accuracy requirements, and storage and processor requirements will increase with range (R) or altitude (h). Radar complexity and accuracy requirements also increase with increasing wavelength while the radiated power requirements increase sharply as the length of the antenna is decreased. Thus, there is a technical limit to how small an antenna can be for effective use.

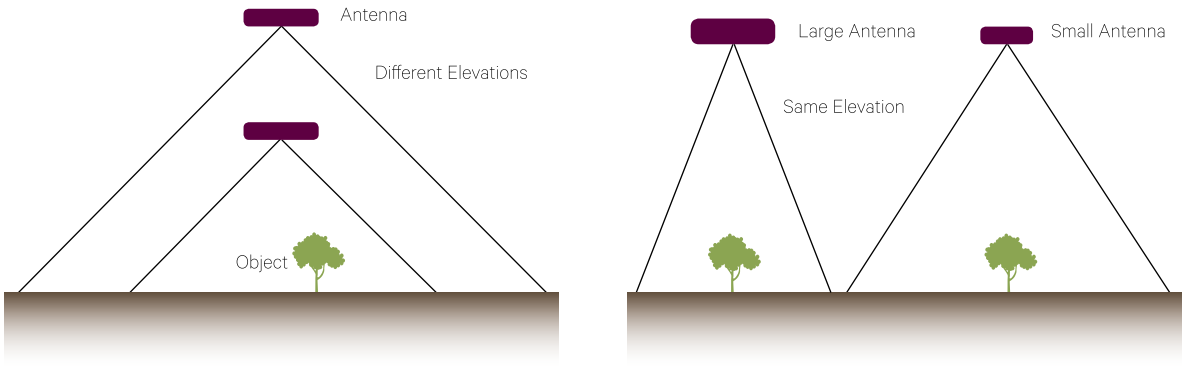
In the range direction, the resolution is limited by the radar pulse length: the shorter the pulse, the greater the power (square of the amplitude) requirement, which also introduces limitations. To overcome this, the antenna sends a 'chirp' pulse (a linearly frequency modulated signal) instead of a constant frequency, which can be much longer and have a much smaller amplitude as shown in Figure 8.7. The return signal can then be 'matched' to the outgoing signal to allow range estimation to fractions of a wavelength. For older SAR systems, in particular airborne systems, the range resolution can be larger than the azimuth resolution, however for most modern systems the range and azimuth resolution is normally similar.

Figure 8.6 Effect of change in altitude and antenna length on SAR resolution

Resolution for different altitudes and constant antenna length are compared to the same altitude for different antenna lengths.

a. Smaller antenna

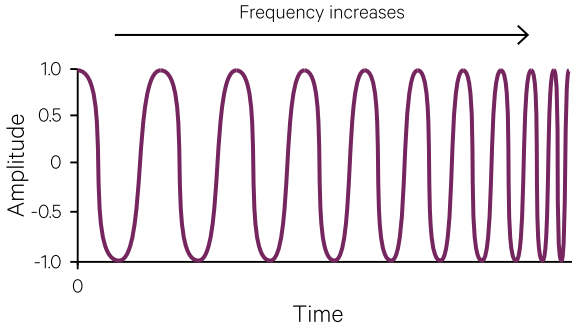
b. Larger antenna



Source: Forster (2006) Figure 2-45

Figure 8.7 Chirp pulse

A constant amplitude waveform is shown with increasing frequency over the length of the pulse.



Source: Bruce Forster and Linlin Ge, University of New South Wales

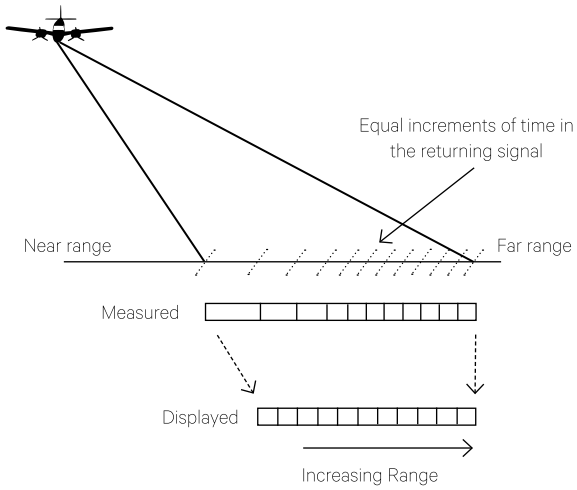
As radar is monochromatic, that is, only one wavelength, the return signals coming from spatially close objects within a resolution element will be coherent, that is, will be highly correlated, causing reinforcement or negation of the signal depending on the phase difference between these return signals. This will give a speckled appearance to the image as bright areas of in-phase reinforcing signals contrast with dark out-of-phase negating signals. To reduce speckle, SAR imagery is often processed to average a number of resolution elements in the azimuth direction, or 'azimuth looks', thus degrading the resolution. Many space-borne SAR systems (for example, ERS-1) average four azimuth looks, degrading the azimuth resolution by a factor of four, while JERS-1 used a factor of three and some airborne systems use a factor of seven. Thus, while the real azimuth resolution is half the antenna length, the actual resolution will be greater, as a function of the number of averaged looks. The ground range resolution is usually engineered to be approximately the same as this degraded azimuth resolution so that the image pixel element is approximately square, although this will depend on the look angle used and other factors.

8.2.3 Radar geometric distortions

Both RAR and SAR images (that is, a square raster-based output of the measured backscatter as an image) will suffer a number of geometric distortions because of the side-viewing nature of the system. Ground range distortions will be related to the look angle, that is, the vertical angle measured from the nadir. As the look angle increases, the ground range resolution will improve, as shown in Figure 8.8. However, these increasingly shorter resolution elements will be displayed as the same size in the radar image, thus creating a distorted image, shown schematically in Figure 8.8.

Figure 8.8 Changing ground range resolution

The effect of change in ground range resolution on the displayed radar image is shown below.



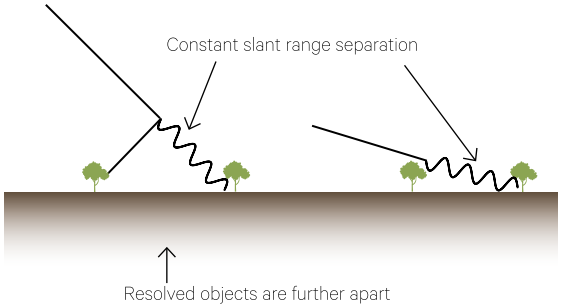
Source: Forster (2006) Figure 2-46

When the look angle of the radar system is very large (approaching a grazing ray), the ground range resolution will become smaller and will approach the range resolution. Thus, objects that are resolved can be closer together, as shown in Figure 8.9.

When the look angle is small, that is, a near-normal or near-vertical beam, then the range is sensitive to changes in topographic relief and the horizontal separation of points at different elevations can be significantly compressed, as illustrated in Figure 8.10. The image of elevated points will be displaced towards the radar antenna. This is a similar effect to height displacement in central projection optical systems (see Volume 1A—Section 14) except that the displacement is in the opposite direction and is equal to $h / \tan\theta$ as shown in Figure 8.11.

Figure 8.9 Ground range resolution and look angle

Ground range resolution improves with increasing look angle.

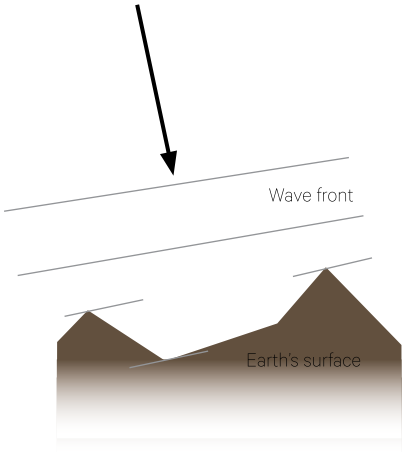


Source: Forster (2006) Figure 2-47

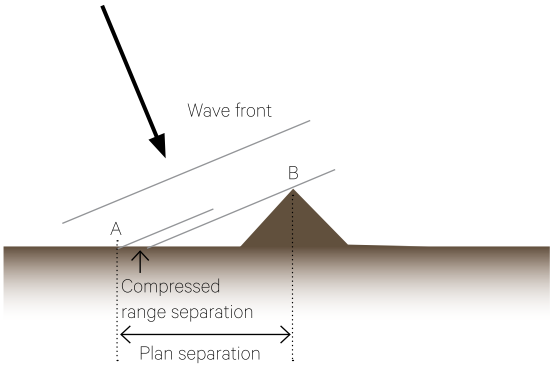
Figure 8.10 Topographic relief and range compression

Sensitivity to topographic relief and range compression is shown for a near vertical radar beam.

a. Range is dependent on elevation



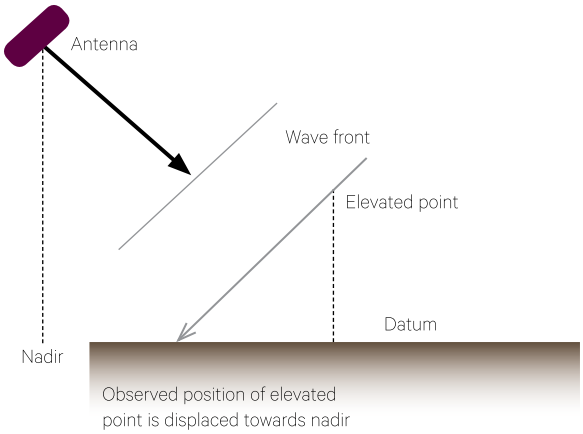
b. Range separation is compressed



Source: Forster (2006) Figure 2-4

Figure 8.11 Height displacement

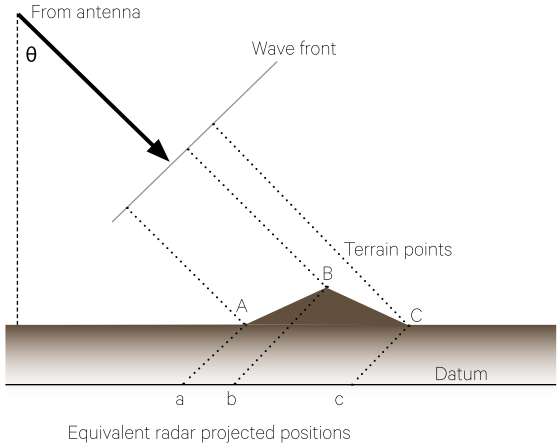
Height displacement of an elevated point occurs towards the nadir of the radar antenna.



Source: Forster (2006) Figure 2-49

Figure 8.12 Foreshortening and elongation of slopes

Foreshortening and elongation of slopes facing towards and away from the radar antenna are shown.



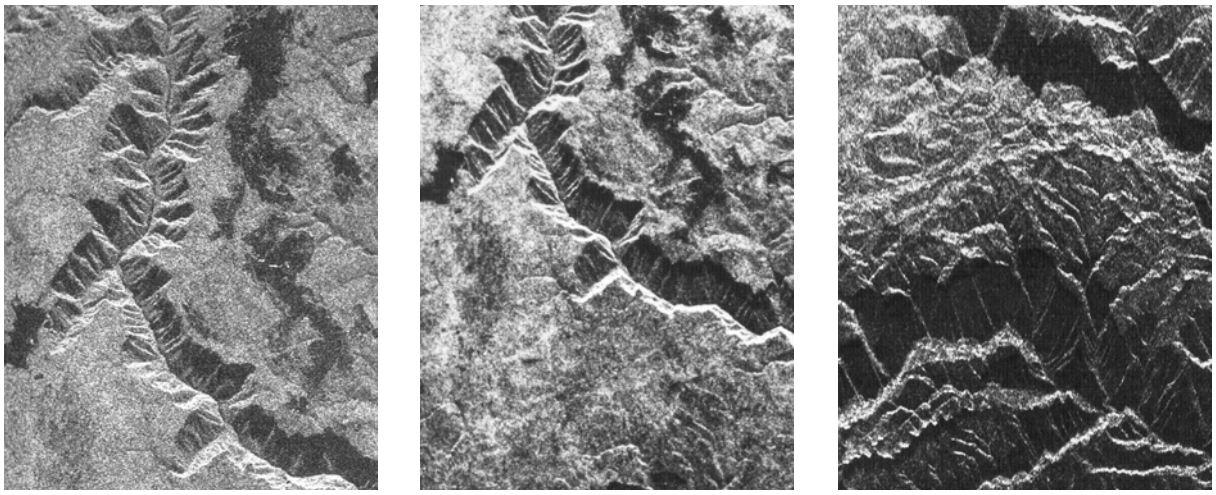
Source: Forster (2006) Figure 2-50

As a consequence of the effect of height displacement, terrain slopes facing toward the radar antenna will appear foreshortened and slopes facing away will appear elongated on the displayed radar image (see Figure 8.12). This can cause severe distortion of a radar image when the angle of terrain slopes approaches the look angle of the radar system. This is more likely to occur when the look angle is small (25° or less).

Figure 8.13 shows the effect of three different look angles on L-band HH, SIR-B images over the same valley feature to the south of Sydney. Image distortion and layover increase as look angle reduces from left to right.

Figure 8.13 Image distortion and layover

Three SIR-B images (L-band, HH) acquired over undulating terrain south of Sydney show increasing image distortion and layover as the look angle decreases from left to right. The common valley is near the lower edge of the left image, near the centre of the middle image, and near the top edge of the right image. Each image strip spans approximately 10 km.



Source: NASA JPL

The effect of foreshortening is translated into terrain layover when terrain slopes become normal to, or greater than, the direction of propagation (that is, when the look angle θ is less than the terrain slope α). Thus, the terrain points A and B (Figure 8.14) will be imaged as A' and B' but in the reverse location relative to the antenna nadir, and with respect to their plan positions, a and b. Therefore, all backscattered radiation returning to the antenna from all of the Earth surfaces from A to B, and from B to a' (that is, the projection of the wave front through A onto the back slope) will be imaged between B' and A', so no useful information about the nature of the surfaces will be extractable from the image data.

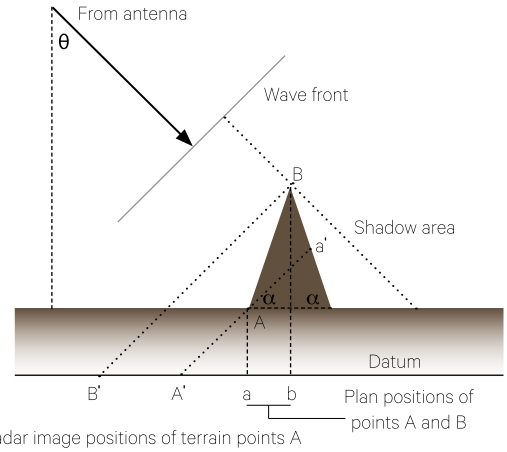
In a similar manner radar shadow areas are created when the angle 90°–θ is less than the terrain slope α. Because radar wavelengths are very much larger than atmospheric molecules, such as water vapour and pollution particles, the radiation will not be scattered by the atmosphere (or only very slightly scattered at shorter wavelengths), as is the case for visible solar radiation. Thus no scattered radiation will be available to irradiate the shadow area and no signal will return to the antenna; therefore, the imaged area will be completely black and no Earth details will be available to be interpreted. Such shadowing will also occur when buildings block the radar beam.

The effect of layover and shadowing are also illustrated in Figure 8.14. Similar, but reverse, effects would occur in valleys, where the shadowing would impact the valley face closest to the antenna, and the layover would occur on the valley face furthest from the antenna (for example, see the valley in radar images shown in Figure 8.13). As an aside, radar images (in fact all EO images) should be viewed so that the source of the radiation is towards the observer. If viewed in the opposite direction, valleys will appear as ridges and vice versa—pseudo topography. This can be confirmed by viewing the images in Figure 8.13 turned 'upside down', in which case the valley will appear as a ridge.

Unscheduled platform motion can also cause geometric distortions resulting from short-term or long-term motion. 'Short-term' motions are rapid movements of the platform that cause relative geometric error between individual pixels or a few lines, whereas 'long-term' motion affects a significant portion of the image. These effects are more likely to occur on aircraft platforms that are more prone to unscheduled movement as opposed to the very stable orbit path of a space platform.

Figure 8.14 Effect of radar layover and shadows due to hilly terrain

Layover is inversely proportional to θ, while shadow length is directly proportional to it.



Radar image positions of terrain points A and B have layover, or are reversed, with respect to the plan positions a and b.

Source: Forster (2006) Figure 2-51

8.2.4 Radar equation

To understand the return signal measured at the antenna, it is first necessary to briefly examine the radar equation. This equation describes the performance of a radar system, and relates the received return power at the antenna to the target parameters and the parameters of the radar. The equation is as follows:

$$P_R = \frac{P_\tau G_\tau}{4\pi R^2}\sigma\frac{A_R G_R}{4\pi R^2}$$

where

P_R is the received power (W);

P_τ is the transmitted power (W);

G_τ is the gain of the transmitting antenna in the direction of the target;

σ is the radar cross-section or effective backscatter area of the target (m^2);

A_R is the effective antenna area (m^2);

G_R is the gain of the receiving antenna in the direction of the antenna; and

R is the range (m).

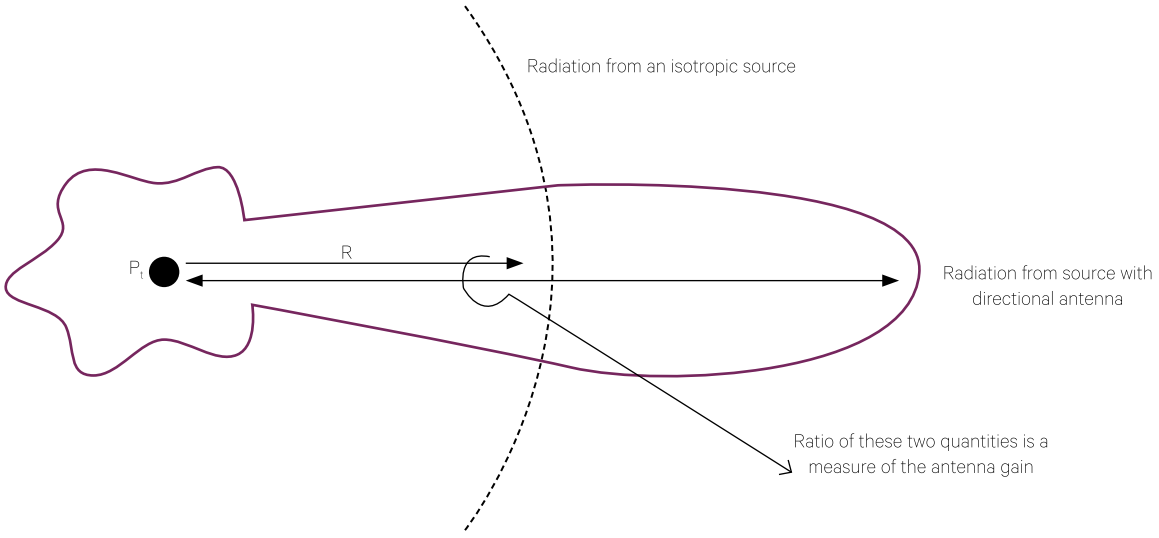
The concepts behind the radar equation can be explained by the graphics in Figure 8.15. Radiation from an isotropic source, that is, one radiating equally in all directions, will be incident on a target at a distance R, the range, from the antenna. At this distance the radiation will be equally distributed over a sphere of surface area equal to $4\pi R^2$, and the amount reaching the target will be the transmitted power, divided by the surface area of the sphere, giving the units W/m^2. This is then multiplied by the effective backscatter area of the target, to give incident power on the target (in W). The target could be of any shape and have reflectance, absorption and transmission characteristics quite different to a fully conducting metal sphere, which is taken as the reference target. However, the radar cross-section of a target is taken to be the equivalent cross-sectional area of a metal sphere with the same backscatter. That is, the return power reflected or backscattered from the target is the same as that which would have been received had the target been replaced by a metal sphere of cross-sectional area equal to σ.

Rather than having the power radiated isotropically, which is inefficient, the radiation is concentrated in a particular direction by a directional antenna (in the same way as a flashlight concentrates the light from an isotropically emitting globe into a beam of one direction) as shown in Figure 8.15. Thus, the power in the direction is increased, and the 'gain' is the measure of the proportional increase.

The target is now acting as the source of the radiation returning to the antenna. By the time this backscattered radiation (measured in W) reaches the antenna it will also be theoretically spread over an equivalent sphere of surface area $4\pi R^2$, and so will need to be divided by this area to give the power (in W/m^2) incident on the antenna. By multiplying this value by the surface area of the antenna (length×width), the received power (in W) can then be determined. To increase the strength of the return signal (which is inversely proportional to the fourth power of the range and is therefore quite weak), a receiving gain, G_R, is also applied.

Figure 8.15 Concepts of radar equation

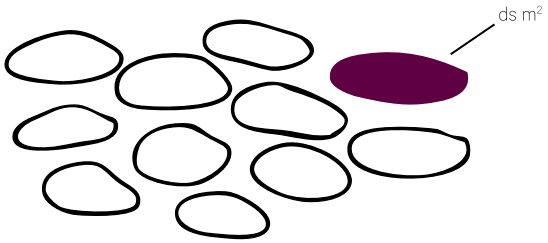
Concepts of radiation from an isotropic source and from a directional antenna are shown.



Source: Forster (2006) Figure 2-52

Figure 8.16 Scattering coefficient

The scattering coefficient is equal to $\sum ds\, m^2$ where *ds* is the radar cross-section of an individual scattering element divided by the unit area.



Source: Forster (2006) Figure 2-53

However, most applications involve extended targets, and the overall scattering coefficient, σ^0, is defined as the average radar cross-section per unit area of the individual scattering elements, where the unit area is usually the area of the resolution element (ratio of the scattering cross-section to the physical cross-section of the illuminated area). The return power is then taken as the average return power from these elements. Note that the scattering coefficient is a normalized, unitless value (compared with the radar cross-section in m^2), and is similar to the concept of reflectance in the optical wavelength region. This is illustrated in Figure 8.16.

The response usually varies over several orders of magnitude, and can have differences of up to a million to one, particularly from urban regions, where targets range from very low scattering to very high scattering. These could be smooth surfaces that scatter the radiation away from the antenna, such as a road surface, and metal targets facing towards the antenna, such as a sloping metal roof, that strongly scatter towards the antenna. To reduce the dynamic range, the scattering coefficient is usually expressed in decibels (dB):

$$\sigma^0(dB) = 10\log\sigma^0$$

Most radars use either the same or identical antennae for both transmitting and receiving, and gain can be related to the receiving aperture (the effective area of the antenna) by the following relationship:

$$G = G_\tau = G_R = \frac{4\pi A_R}{\lambda^2}$$

and so the received power can also be expressed as

$$P_R = \frac{P_\tau G^2 \lambda \sigma^0}{4\pi^3 R^4}$$

Apart from σ^0, all quantities are either system or propagation parameters. Thus, the differences in the received power from adjacent resolution elements are entirely due to corresponding differences in the magnitudes of their scattering coefficients. When displayed in an image form, these differences will appear as contrast differences.

8.2.5 Radar polarisation and polarimetric SAR

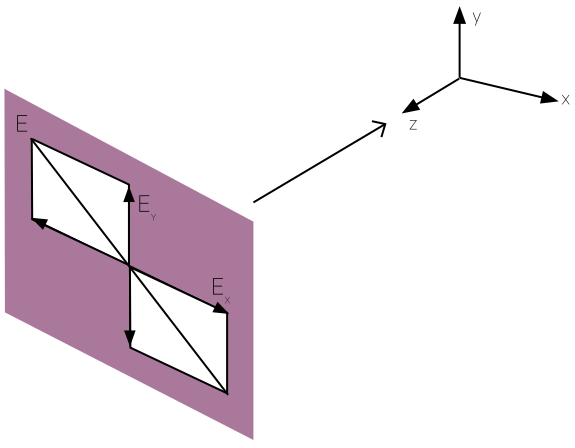
Imaging radars can operate in one or more of the following polarisation modes:

- HH—transmitted signal is horizontally polarised, and only the horizontal component of the return signal is measured;
- HV—transmitted signal is horizontally polarised, and only the vertical component of the return signal is measured;
- VV—transmitted signal is vertically polarised, and only the vertical component of the return signal is measured; and
- VH—transmitted signal is vertically polarised, and only the horizontal component of the return signal is measured.

When the return signal is the same polarisation as the one that was transmitted, the signal is said to be *co-polarised* (HH and VV), and when the transmitted and return signals have different polarisation it is said to be *cross-polarised* (HV and VH). A single target area can therefore have different backscattering coefficients depending on the polarisation mode, and these coefficients are shown as σ^0_{hh}, σ^0_{hv}, σ^0_{vv} and σ^0_{vh}. Normally σ^0_{hv} is considered equal to σ^0_{vh}. The direction of the electric field is conventionally used to define the direction of wave polarisation. If the electric field has a fixed direction, then the field is said to be plane-polarised. EMR of the same frequency and direction will give a resultant electric field, which is the vector sum of the two component fields, as shown in Figure 8.17.

Figure 8.17 Vector sum of the component fields to give a resultant EM field

Polarisation is in the direction of the resultant field.

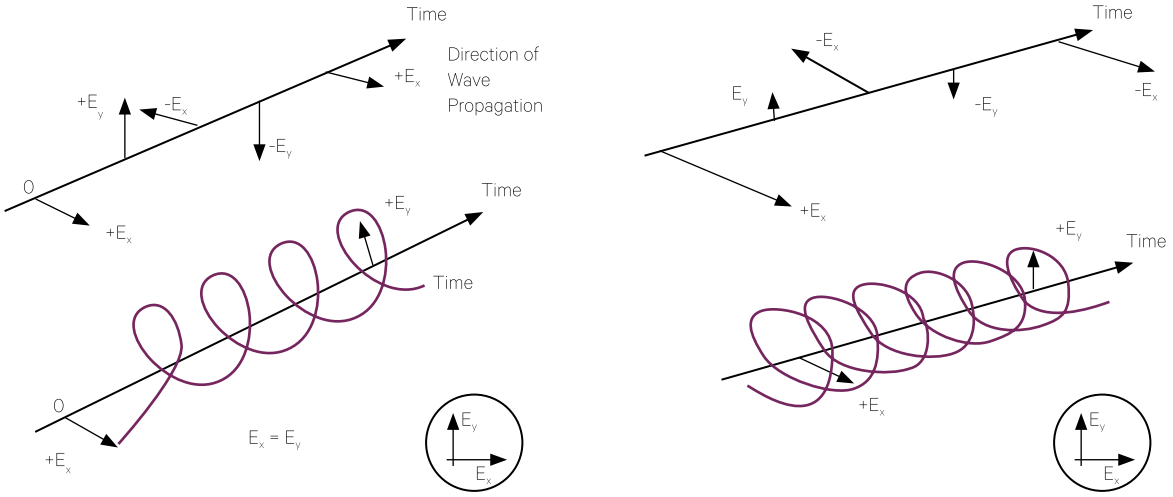


Source: Forster (2006) Figure 2-54

Figure 8.18 Circular polarisation

a. E_x and E_y are equal and the phase difference is 90°.

b. E_x and E_y are not equal and the phase difference is 90°.



Source: Forster (2006) Figures 2-55 and 2-56

Polarisation will be in the direction of the resultant field as illustrated in Figure 8.18. In addition, with *quad-polarised* radars (recording HH, HV, VV and VH on the one system), circularly-polarised radiation is transmitted, and all components of the return signal are measured. With circularly-polarised radiation the direction of the electric vector changes in a circular manner as the wavefront travels through space. It can be pictured as a 'corkscrew-like' motion and can be either left-handed or right-handed, indicating the direction of apparent rotation of the electric vector. The radiation backscattered to the antenna can also be circularly-polarised, and can be co-polarised or cross-polarised depending on whether the return has the same or different polarisation from the transmitted signal.

Both plane and circular polarisation are special cases of elliptical polarisation. All polarised radiation can be said to have two component parts, E_x and E_y polarised at right angles to each other, and the nature of the resultant polarisation will depend on the amplitude and phase difference of the parts. If the amplitudes are the same, that is, $E_x = E_y$ and the phase difference is 90°, then the radiation will be circularly-polarised as illustrated in Figure 8.18a. If the phase difference is 0°, and E_x may be equal to E_y then the radiation is plane-polarised. Elliptical polarisation is the general form of polarisation, where the phase difference is 90° and E_x does not equal E_y, as illustrated in Figure 8.18b.

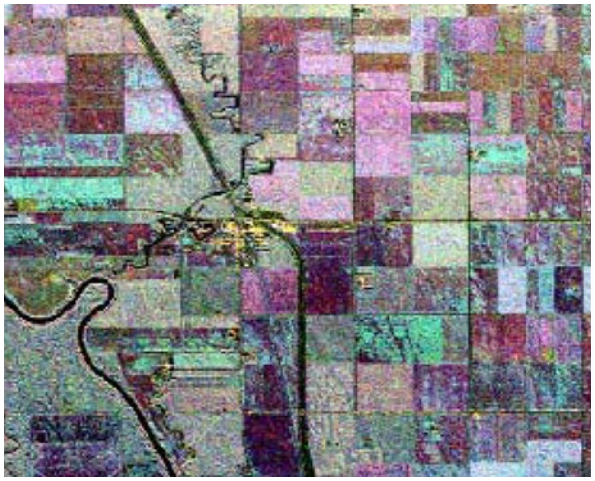
When plane-polarised radiation is incident upon a surface, the surface will reflect (backscatter) in different amounts depending upon the direction of the polarisation relative to the surface. Randomly-oriented surfaces can cause the polarised radiation field to be depolarised, so that the return signal has no specific polarisation. Horizontal and vertical polarisations are used to describe the direction of the two component parts in microwave radar terminology. The 'vertical' component is not strictly vertical, but is mutually orthogonal to the horizontal component and the direction of propagation. For optical wavelengths, the terms parallel and perpendicular polarisation are used to describe the two components, which use a different reference plane to that of microwave radiation. As solar radiation (the primary energy source for optical remote sensing) is randomly polarised, the effects of polarisation are generally not an important factor. However, this is not the case in the microwave region of the spectrum.

Various classes of terrain will depolarise the reflected signal to varying degrees and the reflected signal will have both V and H polarised components. For scattering from a rough surface, the amount of depolarisation is a function of the surface roughness and wavelength, as well as the dielectric constant and the conductivity of the surface. Volume scattering will cause the return signal to be depolarised, as the radiation suffers multiple reflection or scattering. Figure 8.19 shows an agricultural area imaged in C-band HH, VV and HV polarisations, and with a colour composite of all three displayed as red, green and blue respectively. Clear differences can be seen between the different fields depending on crop type, crop stage and bare soil for the three polarisations.

Figure 8.19 Agricultural area imaged in C-band HH, VV and HV

Airborne CV-580 SAR data was acquired on 26 July 1995 over Altona, Manitoba, Canada.

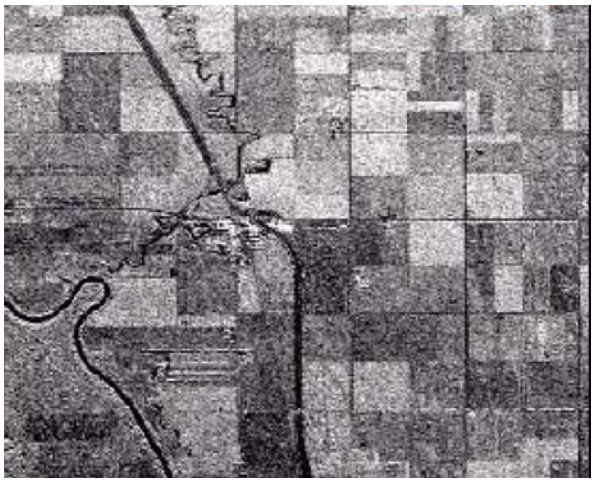
a. Colour composite of C-band HH as red, C-band VV as green and C-band HV as blue



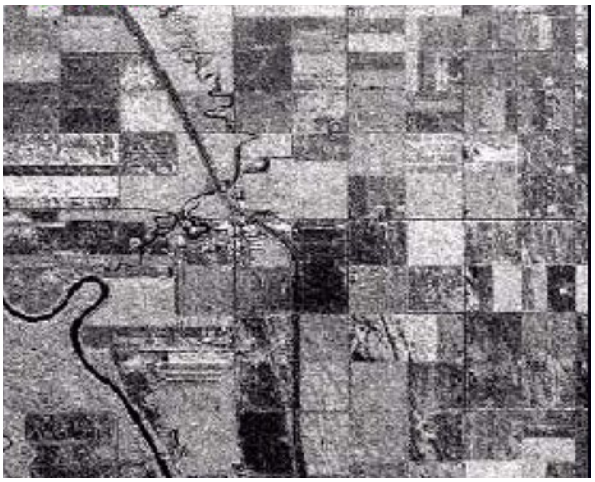
b. C-band HV



c. C-band HH



d. C-band VV



Source: GlobeSAR Agricultural Applications/CCRS

Since leaves have a high dielectric constant due to their high moisture content, where the leaves of a tree tend to align or hang in a particular direction, the return signal will tend to have a polarity parallel to the orientation of the leaves. For example, for leaves hanging vertically with an incoming signal horizontally-polarised, the return signal would be predominantly vertically-polarised. This will be particularly evident when the length of the leaves is a multiple of half the wavelength, in which case a dipole effect will be created. In eucalypt forests, and with other plant species, the alignment of the leaves can change during the day due to the Sun's orientation, resulting in differing polarities of the return signal with different acquisition times. A similar effect will be found for other oriented materials embedded in a material with different dielectric properties, such as gravel in soil (for leaves, the surrounding air has a very low dielectric constant, approaching a value of 1).

Images can be displayed as a colour composite using any combination of wavelengths and polarisation to highlight particular ground features (see Volume 2A). Figure 8.20 shows an agricultural area in Malaysia that has a range of surface features including urban, airport, mangroves, water, plantations, crops and bare soil, using two different microwave wavelengths and three polarisations. In Figure 8.21, an image generated from three different polarisations of one wavelength (C-band) highlights differences in ice due to age, salt content and surface roughness. Figure 8.22 shows an AIRSAR composite image, which clearly delineates mangrove and forest vegetation.

Figure 8.20 Radar colour composite of tropical agriculture, Malaysia

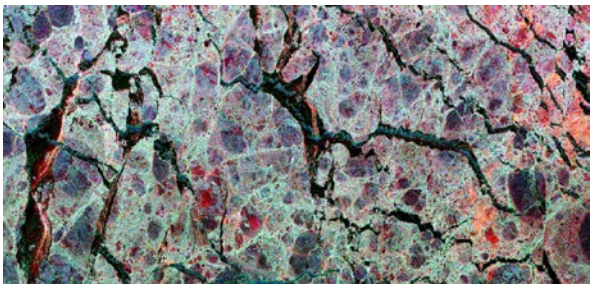
POLSAR imagery (AIRSAR: C-band HH, L-band VV and C-band HV displayed as red, green and blue respectively) covering 9.5 km × 7.9 km agricultural area in northwest Kedah, northwest Malaysian Peninsula. Patterns of agricultural development are clearly visible.



Source: NASA JPL

Figure 8.21 Radar Colour Composite of sea ice, Antarctica

Shuttle SIR-C/X SAR (C-band HH, L-band HV and L-band HH displayed as red, green, blue respectively) for central location 58.2°S and 21.6°E covering an area 45 km x 18 km. Colours indicate ice thickness, which is related to ice growth stages:
• darker lines of open water and smooth ice (< 0.7 cm thick) including
 - blue lines (open water in new fractures) and
 - bright red lines (new ice growth <0.5 m thick);
• undeformed floes as blue-grey (~0.7 m thick); and
• red-tinged deformed ice pieces (< 2 m thick).



Source: CCRS. Retrieved from: *http://www.indiana.edu/~geol105/images/gaia_chapter_2/antarctic_sea.htm*

Radar can also be used for temporal monitoring of land use and land use change, and biomass estimation. Three acquisitions of radar imagery are illustrated as a colour composite in Figure 8.23, which allows the different stages of rice crop planting to be monitored. Other applications of using C-band and P-band HV image data include mapping biomass and tree density (Proisy *et al.*, 2001).

Figure 8.22 AIRSAR colour composite of tropical vegetation, Thailand

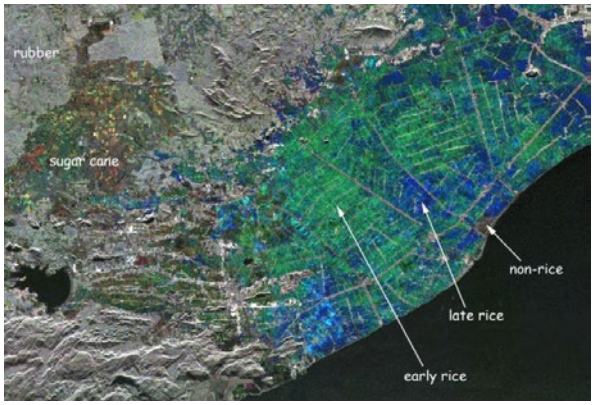
A colour composite of AIRSAR bands (C-VV as red, L-HH green, and P-HV as blue) shows clear boundary between mangroves (green) and forest vegetation (red and blue).



Source: NASA JPL

Figure 8.23 Multi-date radar composite

Classification of different stages of rice planting and forest vegetation using JERS-1 multitemporal L-band HH radar images from three time periods over Thailand using 27 May image as red, 10 July image as green and 23 August image as blue.



Source: JAXA

Polarimetry is the science of using measurements of the full polarisation scattering matrix to infer physical properties of the Earth's surface. On transmission, the two orthogonal polarisations (H and V) are alternated on successive pulses, which can be considered as circular polarisation. On reception, the two polarisations are received simultaneously, leading to four channels of received data as discussed at the beginning of this section. For example, on odd pulses, HH and HV may be measured, then on even pulses, VV and VH may be measured. The Stokes Vector describes the amplitude and phase of the transmitted or received EM field. Polarimetric SAR or POLSAR is used to describe a synthetic aperture radar where the complete electromagnetic wave information of both amplitude and phase of the transmitted signal is known and of the return signal is measured. Any combination of the transmit and received signal can be synthesised from the amplitude and phase, as illustrated in Figure 8.24, and shown as polarisation

signatures in Figure 8.25 and Figure 8.26. However only the HH, HV, VV and VH modes are generally made available and are commonly termed quad-polarised data. Polarisation phase differences can be caused by scattering and the observed phase difference can reveal the nature of the scattering event.

The relationship between a completely polarised incident and scattered wave is described by the Mueller (Scattering) Matrix:

$$Received = \frac{1}{R^2}\left[Scattering\,Matrix \right] Transmitted$$

where

R is the slant range distance to the ground object.

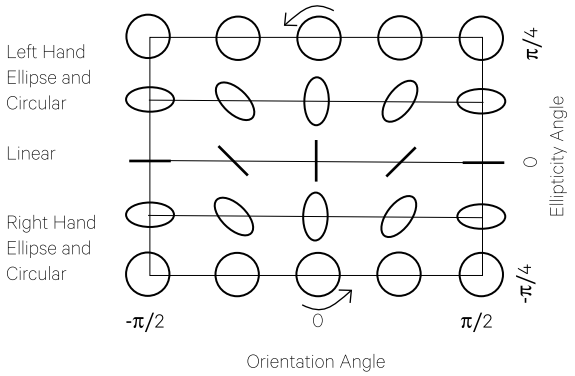
The scattered and incident vectors are Stokes Vectors and describe the amplitude and phase of the H and V transmitted and received signals. The effect of scattering is shown by a polarisation signature, which shows returns with the same polarity as transmitted (co-polarised) and opposite polarity (cross-polarised). The full range of returns for circularly polarised radar is illustrated in Figure 8.24.

The polarised signals are classified in terms of their orientation and ellipticity angles. Plane-polarised radar will have an ellipticity angle of zero but an orientation angle ranging from -90° to +90°. As the ellipticity angle changes from -45° through 0° to +45°, the polarisation will change from left-hand circular, through elliptical and plane polarised to elliptical and right-hand polarised.

The range of cross-polarised and co-polarised signals are represented by a polarisation signature, as shown in Figure 8.25 for a corner reflector (double bounce). It can be seen from the diagram that the co-polarised response of HH (orientation +/- 90° and ellipticity of 0°) and VV (orientation of 0° and ellipticity of 0°) is high with a normalized backscatter (σ) of 1, while the equivalent cross-polarised, HV and VH, are zero.

Figure 8.24 Various polarisations of transmitted and received signals

Polarisation is a function of orientation angle and ellipticity.

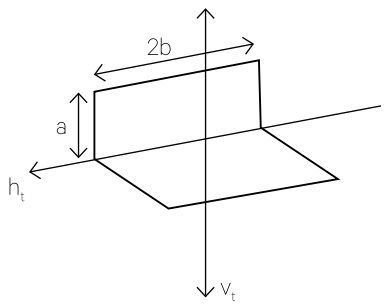


Source: Bruce Forster and Linlin Ge, Course Notes, UNSW

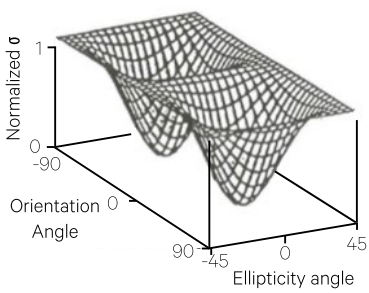
Polarisation signatures for a theoretical single bounce scattering are shown in Figure 8.26b. In comparison to the double bounce signature (see Figure 8.25), the response is high for all plane, co-polarised return signals (orientation -45° to +45° and ellipticity angle 0°), while all cross-polarised return signals are zero. Figure 8.26a shows the polarisation signatures from a residential area using P-band radar. It can be seen that the signature approximates the theoretical single bounce signature, which is assumed to be due to the orientation of sloping metal and metal insulated roofs being approximately normal to the incoming 30° incidence angle radar. Because P-band is used, the attenuating effects of vegetation surrounding the residential buildings will be lessened. It will be noted that the co-polarised signature does not commence until a normalized cross-section (δ) of approximately 0.3 is reached. This is a measure of the amount of backscattered un-polarised radiation, caused by volume scattering in the target area. This un-polarised plateau is termed the pedestal.

Figure 8.25 Polarisation responses of a conducting dihedral corner reflector

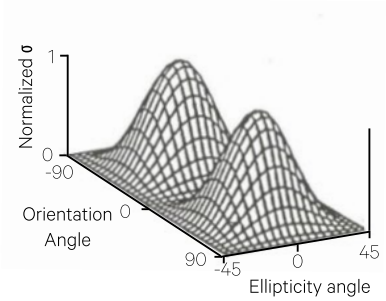
a. Underlying geometry



b. Co-polarised signal (HH/VV)



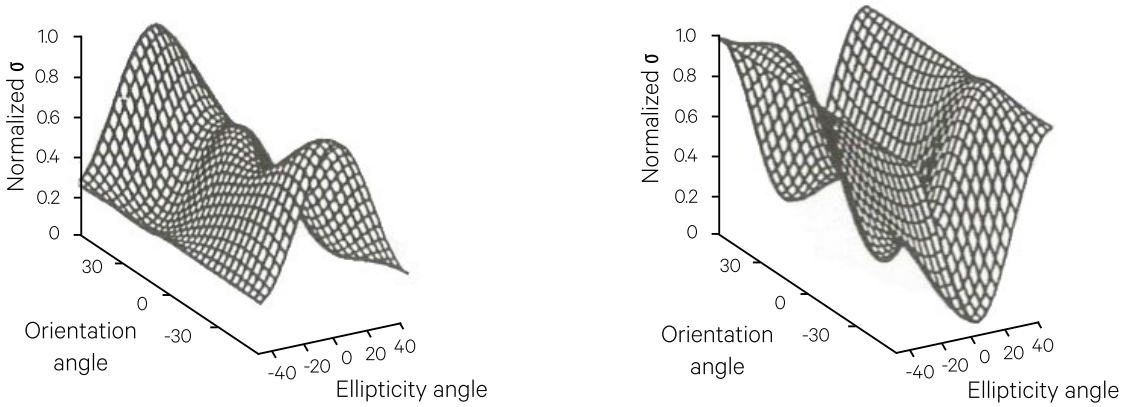
c. Cross-polarised signal (HV/VH)



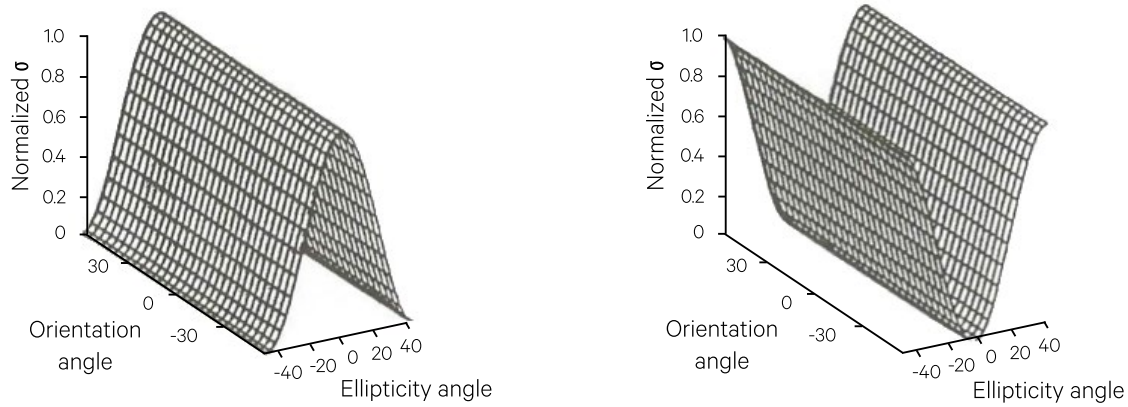
Source: Dong *et al.* (1997)

Figure 8.26 Polarisation signatures

a. Co-polarisation (left) and cross-polarisation (right) signatures from residential buildings (P-band, incidence angle = 30°) are dominated by single bounce scattering.



b. Theoretical co-polarisation (left) and cross-polarisation (right) signatures of single bounce scattering are shown.



Source: Dong *et al.* (1997)

Quad-polarisation ('quad-pol') data can be transformed into four main scattering types:

- single bounce;
- double bounce;
- volume (or cross-polarisation—'cross-pol'); and
- Bragg scattering (caused by surfaces that have a periodic structure, which resonates well with the radar wavelength).

The proportion of each type of scattering will depend on the surface feature and the wavelength. Any three of these can be displayed as a colour composite image where the colours will then have physical meaning.

Table 8.3 provides a comparison of the scattering from different urban and rural surface features (in Sydney and surrounding areas), derived from P-, L-, and C-band quad-pol data. Note that this table only shows the percentage of the total backscattered radar signal for each scattering type, not their absolute values. It can be seen from the table that tall commercial buildings with a good percentage of metal material, and with very little surrounding vegetation, will have high double bounce for all wavelengths, whereas for residential buildings and shorter wavelengths, the single bounce increases, mainly derived from sloping metal or metal-lined roofs. P-band double bounce is high for eucalypts, as it penetrates to the forest floor and then double bounces from tree trunks, while shorter wavelength C-band has higher single and volume scattering because it is scattered from the leaves, twigs and branches. For grass, both double bounce and volume scattering is greatest because it is of a similar order of size to C-band wavelengths, namely about 8 cm.

Table 8.3 Comparison of scattering components as a percentage of σ_{HH}

Comparison of scattering components as a percentage of σ_{HH}, with single, double and volume scattering adding to 100%

Surface Feature	Band	Scattering (%)			
		Single bounce	Double bounce	Volume	Bragg
Commercial	P	16	83	1	3
	L	14	86	0	2
	C	0	94	6	5
Residential	P	32	68	0	10
	L	34	66	0	11
	C	42	58	0	10
Eucalypt forest	P	17	77	6	14
	L	24	67	10	20
	C	47	44	9	23
Grasses	P	53	33	14	7
	L	63	27	10	10
	C	43	42	15	20

Source: Dong *et al.* (1996, 1998)

8.2.6 Radar backscattering mechanisms

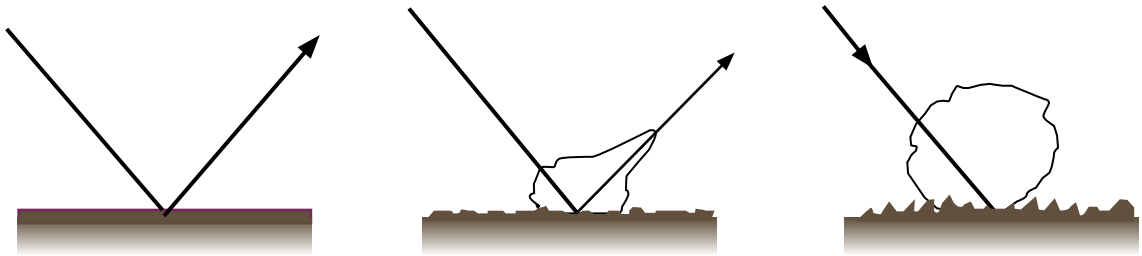
Radar backscatter can be caused by the following three primary mechanisms:

- Surface scattering—either specular or diffuse scattering, or intermediate levels of both, depending on the wavelength and surface roughness. As the surface becomes rougher with respect to the wavelength, the greater the proportion of diffuse scattering. Totally specular surfaces will appear dark, as there is no backscattered return to the antenna. This is illustrated in Figure 8.27 (see also Volume 1A—Section 2.5.2).
- Volume scattering—when the radar is able to penetrate the surface and the backscattering is due to scattering from the underlying material or volume. Volume scattering will not occur if the material has constant dielectric properties, but will occur if there is spatial heterogeneity at scales that are comparable to the radar wavelength. Typical examples of volume scatterers are the leaves and twigs of trees, or gravel, clay nodules or stones in soil. The concept is illustrated in Figure 8.28.
- Hard target and corner reflectors—where the metallic nature of the material or its orientation can cause extremely strong returns.

Figure 8.27 Differences in surface scattering

Diffuse scattering increases with surface roughness, where roughness is relative to wavelength.

a. Specular dark . Slightly rough c. Very rough



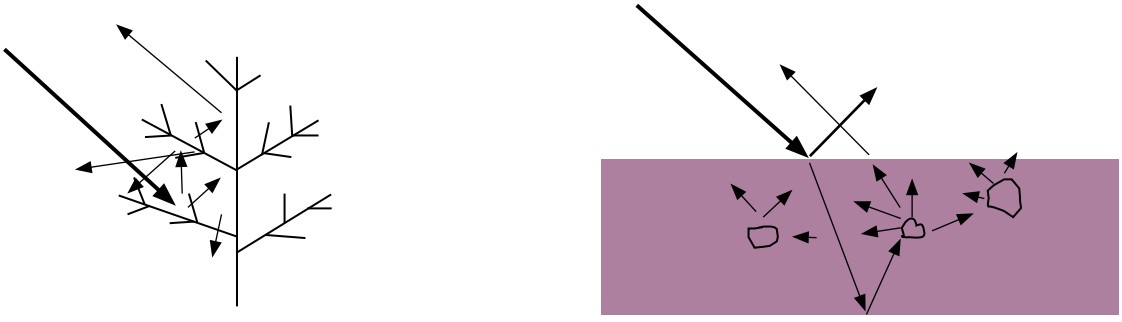
Source: Forster (2006) Figure 2-57

Figure 8.28 Volume scattering concept

Depolarisation by objects with different dielectric properties to the surrounding volume

a. Volumetric scattering in a tree

b. Volumetric scattering under a surface with inhomogeneous dielectric properties

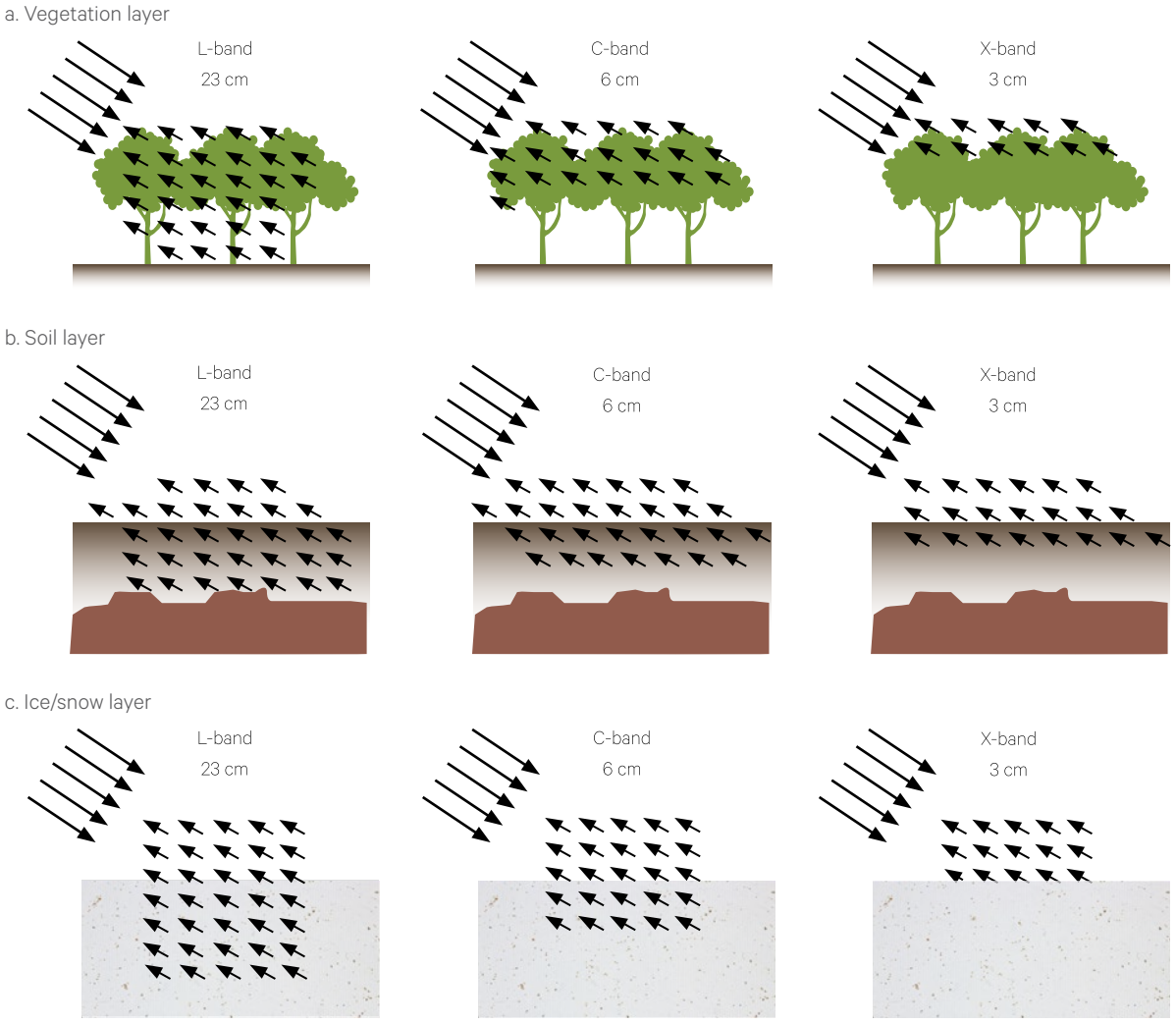


Source: ESA (2007) Figure 1.7

The depth to which the radiation will penetrate is defined as the penetration depth, *dp*. This is not the actual depth of penetration, as the radiation will continue until the energy is totally dissipated, but is the depth below the surface at which the magnitude of the power of the transmission wave is equal to 1/*e* (where *e*, the exponential constant, equals 2.7183). Penetration depth is dependent on the wavelength and the water content of the volume material (more strictly speaking it is dependent on the dielectric properties of the material which are strongly related to the water content). Longer wavelength radiation will penetrate further than shorter wavelength radiation. For dry materials, *dp* is at least a few wavelengths long and usually many wavelengths long. For multi-layered media, such as snow over ground or vegetation over soil, short wavelengths are needed to investigate the upper layer, while long wavelengths are needed for examination of the underlying properties. An illustration of the penetration of various wavelengths into forest, soil and ice/snow is shown in Figure 8.29.

The amount of diffuse and specular scattering will also depend on the angle of incidence and the surface roughness. Surface roughness is based on two parameters, the standard deviation of the surface height and the surface correlation length. The latter can be considered as the distance at which the surface roughness pattern repeats itself. Changes in backscatter or scattering coefficient as a function of the incidence angle θ are illustrated in Figure 8.30.

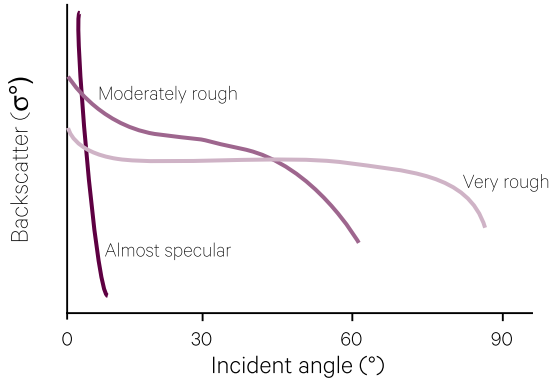
Figure 8.29 Penetration for different wavelengths in multi layered volumes



Source: Bruce Forster and Linlin Ge, Course Notes, UNSW

Figure 8.30 Scattering coefficient variations

Variations in the scattering coefficient as a function of the angle of incidence, θ, for varying surface roughness. Note that, for very rough or very smooth (specular) surfaces, at low values of θ, σ^0 is approximately independent of the surface roughness.



Source: Forster (2006) Figure 2-59

The bounding surface roughness condition (H_B) between diffuse and specular reflection can be approximately given by Rayleigh's formula:

$$H_B = \frac{\lambda}{8\cos\theta}$$

For example, for θ equal to 60° and λ equal to 24 cm (L-band), H_B will equal 6 cm. Where the actual surface roughness is less than 6 cm, the scattering will tend towards specular, with an increasing amount being reflected away from the antenna. Where the surface roughness is greater than 6 cm, the scattering will tend towards diffuse (that is, equal scattering in all directions), and a significant amount will be backscattered to the antenna. For a given surface roughness, the likelihood of specular reflection will increase as θ approaches 90°, that is, a grazing ray. Intermediate type scattering will occur for surface roughness at or near the bounding surface roughness condition. Field-sampled estimates of surface roughness can be made visually or by the use of simple devices.

However, while the surface roughness determines the scattering mechanism at the surface, it is the dielectric constant, ε_r, that determines how much radiation is available at the surface interface. The percentage of reflection at a surface interface (such as between air and soil) is a function of the difference in dielectric constant, which is approximately proportional to the surface water content. It is made up of two parts—the reflectance and absorption or loss factor—reflectance being at the surface and absorption being below the surface.

If $\varepsilon_r = 1$, then the interface is equivalent to free space and there is 100% transmission with no absorption. The Earth's atmosphere can be considered to approximate free space. When $\varepsilon_r = 3$ (air/dry sandy soil interface at L-band wavelength) then 7% is reflected at the surface and 93% is transmitted and gradually absorbed at depth. For $\varepsilon_r = 81$ (air/water interface at L-band wavelength) then 64% is reflected and the balance is absorbed within the first few centimetres. Thus the degree or amount of reflection is strongly dependent on the dielectric constant or difference, but is also dependent on the wavelength.

For a smooth, dry soil surface, the 7% reflected at L-band wavelengths will be specularly scattered away from the antenna and no backscattered signal will be recorded. If the surface is rough with respect to the wavelength, then the 7% surface reflectance will be scattered diffusely and a small backscattered signal will be recorded. If the soil is smooth and wet, the same specular surface scattering applies as for dry soil and, while much larger, again there will be no backscattered signal recorded. In this case very little radiation will penetrate into the soil. However, if the wet soil is rough, then the large surface reflection will be scattered diffusely and a large backscattered signal will be recorded showing as bright pixels in the image. Thus, the recorded radar signal can be viewed as a measure of soil moisture content.

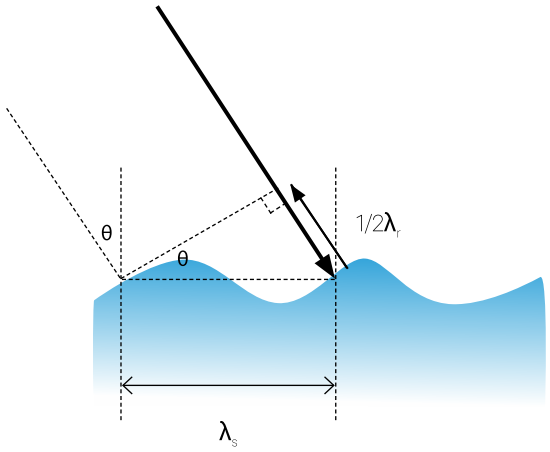
A further scattering mechanism is termed Bragg Scattering or Bragg Resonance. It has been used to describe scattering from the ocean in terms of resonance with the tiny capillary and short gravity waves, even when these waves have a height measured in tenths of a millimetre, and ride on waves that are metres high. The short Bragg-scale waves are formed in response to wind stress. If the sea surface is rippled by a light breeze with no long waves present, the radar backscatter is due to the component of the wave spectrum that resonates with the radar wavelength. The Bragg equation defines the ocean wavelengths for Bragg scattering to occur, as a function of radar wavelength (λ_r) and incidence angle (θ; see Figure 8.31) as follows:

$$\lambda_s = \frac{\lambda_r}{2\sin\theta}$$

Using different wavelengths and polarisations, scattering from ocean surfaces of different wave heights can be highlighted as illustrated in Figure 8.32. Scattering due to ocean roughness and Bragg scattering are more apparent in VV polarised images. In Figure 8.32 ocean surface roughness increases from red, through green to blue, as the wavelength increases from C-band to L-band and P-band.

Figure 8.31 Bragg scattering

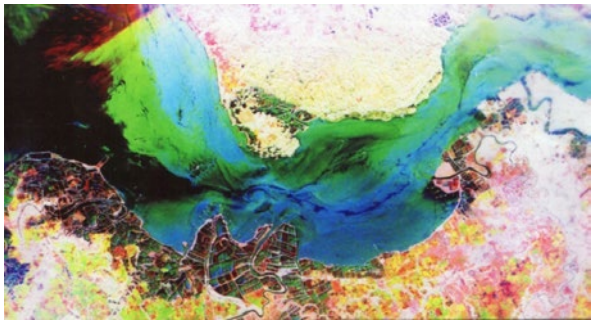
Bragg scattering relationship is shown for an ocean wavelength of λ_s and incoming radiation of λ_r wavelength.



Source: Bruce Forster and Linlin Ge, Course Notes, UNSW

Figure 8.32 Ocean surface roughness

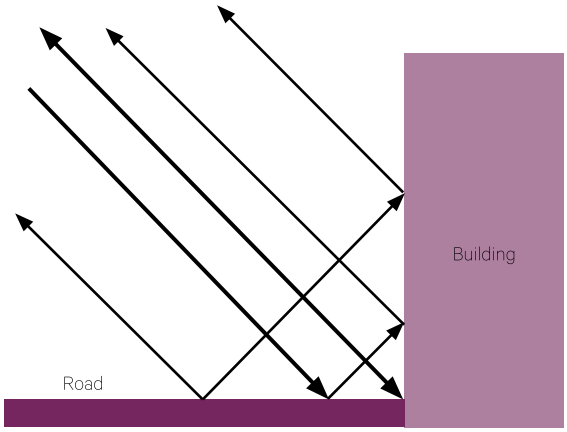
Ocean surface roughness highlighted using POLSAR (fully polarised) AIRSAR VV images of increasing wavelength to form a colour composite (C-band as red, L-band as green and P-band as blue) for Coastal Panay, Philippines.



Source: NASA JPL

Figure 8.33 Return paths of radar for an urban corner reflector

Return distance is the same for all paths entering at 45º, and will appear to return from the same point.



Source: Forster (2006) Figure 2-60

The look direction of the incoming radiation (that is, the azimuth or bearing of the radar beam) can also have a significant effect on the returned signal when the surface features have a defined orientation. This can occur for natural features such as river banks or ridge lines, but can also occur with regularly planted crops or built features such as an urban street and building alignments, as illustrated in Figure 8.33. Three paths of the wavefront are shown, from antenna to road to wall and returning to the antenna, and each of these also occurs in the reverse direction.

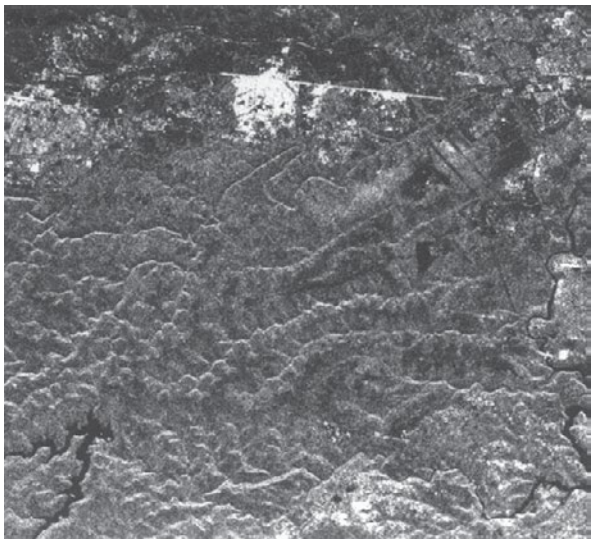
An examination of the geometry of the diagram will show that the distance travelled by the radiation from transmission to return to the antenna, over all paths, will be the same distance (when θ is 45°). As the imaging radar determines the relative distance of features from each other by the time taken for the signal to leave and return to the antenna, then the backscatter from every return path will be recorded as being from the line of intersection of the building and the road. The amount of backscatter will depend on the surface roughness and the dielectric properties of the material. If the corner is made of materials that are very smooth and with a high dielectric constant, then the return will approach 100% of the incoming radiation and appear to originate from the road/building intersection.

Figure 8.34 uses an L-band SIR-B radar image to show corner reflector effects and some hard target scattering from part of a railway line on the edge of the city of Sydney. Such corner reflector returns will be a feature of many radar images of urban areas. The magnitude of the backscattered return will, in part, be a function of the height and width of the building(s) facing the antenna, so significantly higher returns can be expected from large multi-story buildings compared to smaller single-story buildings. Also, larger buildings are built of materials that contain more metal than smaller buildings, including reinforced concrete, metal frameworks, and metal pipes, guttering and windows, which will increase their return signal.

Hard targets in urban areas, such as motor vehicles or transmission towers, can also cause strong backscattered returns to the antenna. Similar effects can occur from the banks of rivers facing the antenna where the signal reflects from water to bank (and vice versa) and returns to the antenna, and from tree trunks on the edge of a forest (particularly when vegetation has regular planting patterns as occur in a plantation).

Figure 8.34 Corner reflector effects

SIR-B radar image (L-Band) showing some corner reflector effects—large white area at top is due to building and street patterns and hard target scattering from railway line (linear white feature near top of image) at right angles to incoming radar (direction from top to bottom of image). Also notice foreshortening and highlighting of topographic slopes facing the antenna.



Source: NASA/JPL-Caltech

Scattering summary:

- backscatter is very high when the incoming radiation is at right angles to the feature;
- amount of backscatter will depend on the surface roughness and the dielectric properties of the material;
- if the corner is made of material that is very smooth and has a high dielectric constant then the return will approach 100% of the incoming radiation;
- penetration depth, *dp*, increases with increasing radar wavelength;
- scale of roughness necessary for diffuse reflection decreases with decreasing wavelength and there is a weaker dependence for scattering on the angle of incidence;
- with decreasing wavelength, the volume scattering component of the backscatter will become more important;
- at any given wavelength the relative contribution of volume scattering increases with increasing angle of incidence due to the increased slant depth; and
- volume scattering will cause the return signal to be depolarised (for example, the alignment and high moisture content of tree leaves). This will be particularly evident when the length of the objects is a multiple of half the wavelength.

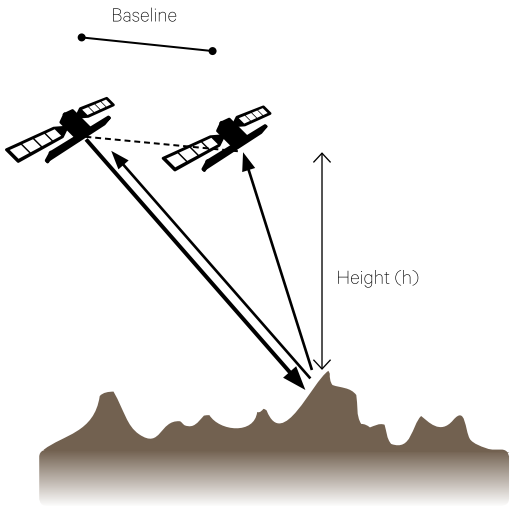
8.2.7 SAR interferometry

In airborne or spaceborne SAR, radiation is actively transmitted to illuminate the terrain, and the backscattered radiation from the various surfaces is collected. An image of the scene is produced after processing the return signals. Each picture element (pixel) comprises both amplitude and phase information. A conventional SAR image displays the amplitude or power (the square of the amplitude) information. However, interferometric SAR (InSAR) exploits the phase information as well as the amplitude. In this technique two images are acquired for the same scene using two separated antennae. After registering the two images and resampling one image to overlay the other, the phases corresponding to each pixel are calculated and differenced, resulting in a phase difference image called an interferogram. The antennae may be on the same platform (single-pass InSAR) or the same antenna may be flown twice over the same scene areas (repeat-pass InSAR) as shown in Figure 8.35.

Repeat-pass InSAR allows for differential radar interferometry before and after an event, such as an earthquake. The phase difference between the two dates is related to the height change and measurements of the order of a few millimetres can be detected. If the antennae are separated parallel to the line of flight, in the azimuth (along-track) direction, the motion of the sea surface and the radial velocity of the ground moving target can be measured, whereas if the antennae are separated perpendicular to the line of flight, in the range (across-track) direction, altitude information can be derived. Applications of differential InSAR and along-track InSAR are shown in Figure 8.36, Figure 8.37 and Figure 8.38.

Figure 8.35 Repeat-pass InSAR

Difference in phase of the return signals allows altitude determination.

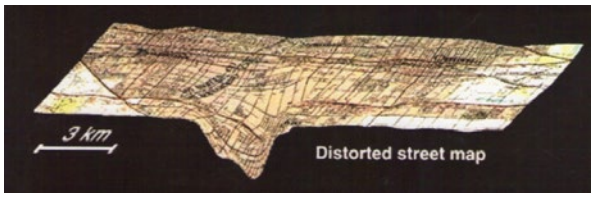


Source: Bruce Forster and Linlin Ge, University of NSW

Figure 8.36 Urban application of differential across-track InSAR

Coverage of Pomona, California between 20 October 1993 and 22 December 1995 showing subsidence monitoring using the PS technique.

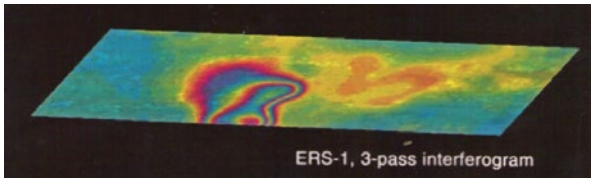
a. Street map showing location and extent of ground distortion



b. Shaded view of phase field (with vertical exaggeration factor of ~ 20,000)



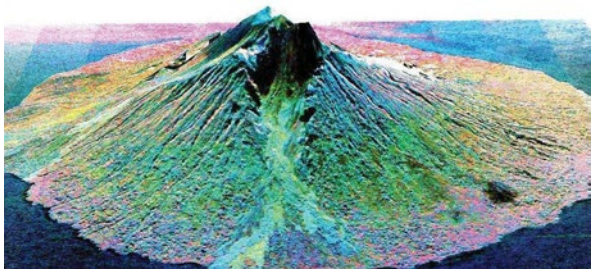
c. Three pass interferogram derived from ERS-1 imagery



Source: Politecnico of Milan (2005)

Figure 8.37 Radar image overlaid on DEM derived from radar interferometry

AIRSAR (operating in TOPSAR mode) image of Manam Island, Papua New Guinea, shows active lava flows.



Source: NASA JPL

Figure 8.39 illustrates the geometry for obtaining height information. The distance between the two antennae is referred to as the baseline. Consider two radar antennae A_1 and A_2 simultaneously viewing the same region, with a baseline of *B*. The range distance between A_1 and an illuminated point on the ground is *r*, while $r + \delta r$ is the distance between A_2 and the same point. In this example the radiation is transmitted from antenna A_1 then, after interaction with the terrain, the backscattered return is recorded by both antennae A_1 and A_2. The signals are then processed to make complex SAR images of the same scene. The two images are spatially registered, and the phase measured in each is differenced on a pixel-by-pixel basis. The phase difference is sensitive to both viewing geometry and the height of the illuminated point, *P*, with respect to the reference or datum surface. From the imaging geometry shown in Figure 8.39 the height *h* is given by:

$$h = H - r\cos\theta$$

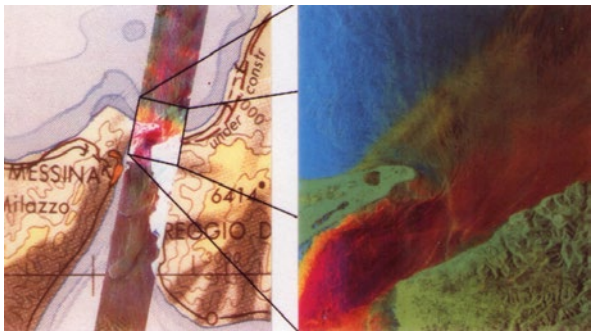
where θ is the look angle of the radar, with wavelength λ. The phase difference between the two return signals can be modelled as the corresponding distance δr in wavelengths, which (expressed in radiance) is:

$$f = \frac{2\pi\delta r}{\lambda}$$

Figure 8.38 Ocean current detection with along-track InSAR

POLSAR and Along Track Interferometry (ATI) images of the Straits of Messina, Italy

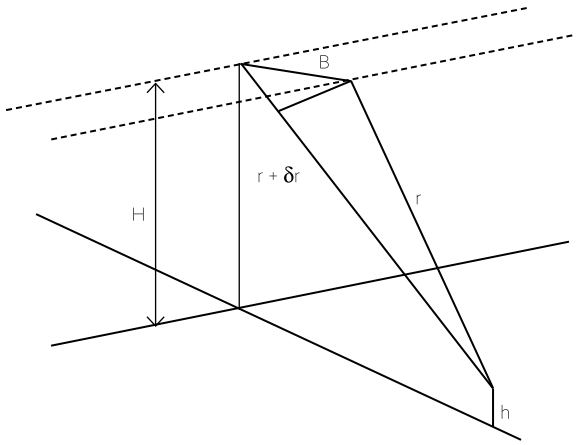
a. Three frequency POLSAR image (left) registered to topographic map
b. L-band ATI image (right) —change in colour relates to varying current velocities



Source: NASA JPL (AIRSAR 1991)

Figure 8.39 Geometry for SAR Interferometry

Phase difference between two return signals separated by base, *B*, on the same platform, allows determination of altitude for an illuminated point.



Source: Forster (2006) Figure 2-62

However, in repeat-pass interferometric SAR, since on each pass the antenna acts as both transmitter and receiver, the total path difference for each observation to the illuminated point on the ground is twice what would be expected in single-pass imaging geometry. The equation for repeat-pass geometry differs from the single pass by a factor of two, that is, a multiplier of 4 in the previous equation instead of 2. Some difficulties arise in repeat-pass InSAR because the scattering surfaces can change between observations (for example, wind effects on branches and leaves). However, this decorrelation can also be used as a means to classify vegetated areas.

The path difference δr is related to the baseline and the look angle by:

$$\delta r = B_x \sin\theta - B_y \cos\theta$$

where B_x and B_y are components of the baseline. The fractional phase difference (value 0–2π radians) leads to an ambiguity in range. This can be solved by phase-unwrapping techniques and then converted to an image displaying variations in height, providing the viewing accuracy is known to sufficient accuracy. The concept of phase-unwrapping is shown in Figure 8.40.

For along-track interferometry, two antennas are located front and rear of an aircraft. The rear antenna sends and the front antenna receives. These are separated by a known base distance, *B*. In time *T* the radar platform moves a distance of *B* and so the velocity of the platform is $v = B/T$. In the same time the ground surface (such as an ocean or river surface) moves a distance of uT, where u is the surface velocity at right angles to the flight direction. The surface velocity (u) can then be calculated from:

$$u = \frac{v\lambda\Phi}{4\pi B}$$

where

Φ is phase difference over time *T*.

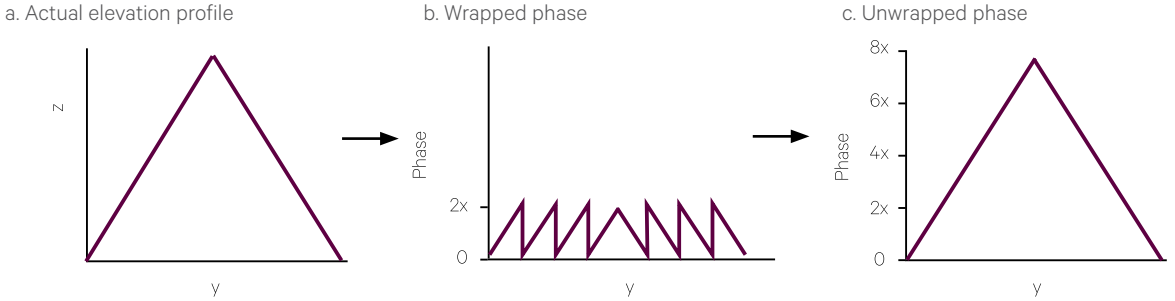
Some applications of InSAR include:

- digital elevation models (across-track interferometry);
- ocean current (along-track interferometry);
- ground moving target indication (GMTI; also based on along-track interferometry);
- change detection (differential interferometry); and
- surface classification (coherence images).

Different wavelengths can provide top of forest canopy height and building height, in addition to ground heights. Methods for processing radar images are detailed in Volumes 2 and 3.

Figure 8.40 Concept of phase-unwrapping

Multiple, wavelength-dependent phase differences, add together to obtain overall height change.



Source: Bruce Forster and Linlin Ge, Course Notes, UNSW

8.3 Further Information

Radar Tutorials:

http://www.radartutorial.eu/druck/Book1.pdf

http://www.radartutorial.eu/index.en.html

http://www.nrcan.gc.ca/earth-sciences/geomatics/satellite-imagery-air-photos/satellite-imagery-products/educational-resources/9341

http://nature.berkeley.edu/~penggong/textbook/chapter3/html/sect35.htm

8.4 References

Dong, Y., Forster, B., and Ticehurst, C. (1996). Decomposition and interpretation of radar polarisation signatures. In *IGARSS: International Geoscience and Remote Sensing Symposium*, Lincoln, Nebraska, 27–31 May, 1996.

Dong, Y., Forster, B., and Ticehurst, C. (1998). A new decomposition of radar polarisation signatures. *IEEE Trans. Geoscience and Remote Sensing, 36*(3), pp. 933–939.

ESA (2007). *ASAR Product Handbook*. European Space Agency. Retrieved from *https://earth.esa.int/pub/ESA_DOC/ENVISAT/ASAR/asar.ProductHandbook.2_2.pdf*.

Ferraro, R. R., Kusselson, S. J., and Colton, M. (1998). An introduction to passive microwave remote sensing and its application to meteorological analysis and forecasting. *National Weather Digest, 22*(3), pp. 11-23.

Forster, B. C. (2006). Principles and Tools for Remote Sensing of Human Settlements. Chapter 2 in 'Remote Sensing of Human Settlements' (Eds: M. K. Ridd, and J. D. Hipple). ASPRS, Bethesda.

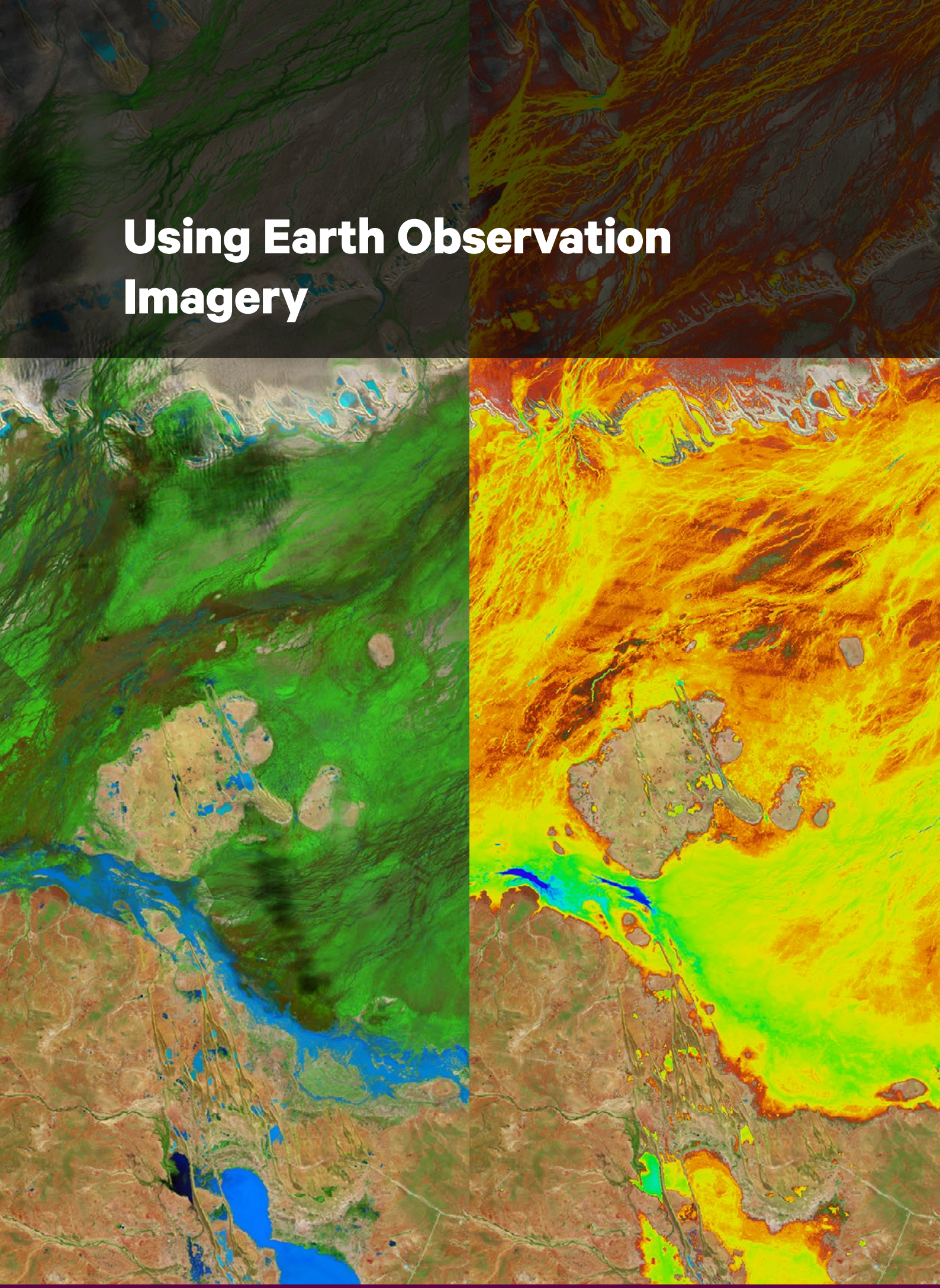
Parker, W. V. (2012). Discover the Benefits of Radar Imaging. *Earth Imaging Journal*. Retrieved from *http://www.intelligence-airbusds.com/files/pmedia/edited/r15796_9_eij_radarimagery_finalarticle.pdf*.

Picard, G., Kerr, Y., Macelloni, G., Champollion, N., Fily, M., Cabot, F., Richaume, P., and Brogioni, M. (2011). *Spatial variations of L-band emissivity in Antarctica, first results from the SMOS mission*. Paper presented at the IGARSS, Vancouver, Canada.

Politecnico of Milan (2005). *Synthetic Aperture Radar Processing Group*. Retrieved from *http://home.deib.polimi.it/monti/sar/*.

Proisy, C., Mougin, E., and Fromard, F. (2001). *Radar remote sensing of mangroves: Results and perspectives*. Paper presented at the IGARSS 2001: Scanning the Present and Resolving the Future.

Using Earth Observation Imagery



While EO images are used for a wide variety of purposes, some characteristics of these datasets are poorly understood, which limits their potential benefits. The following sections consider the process of transforming EO data to Earth information (see Section 9) and the changes anticipated in this area in the future (see Section 10).

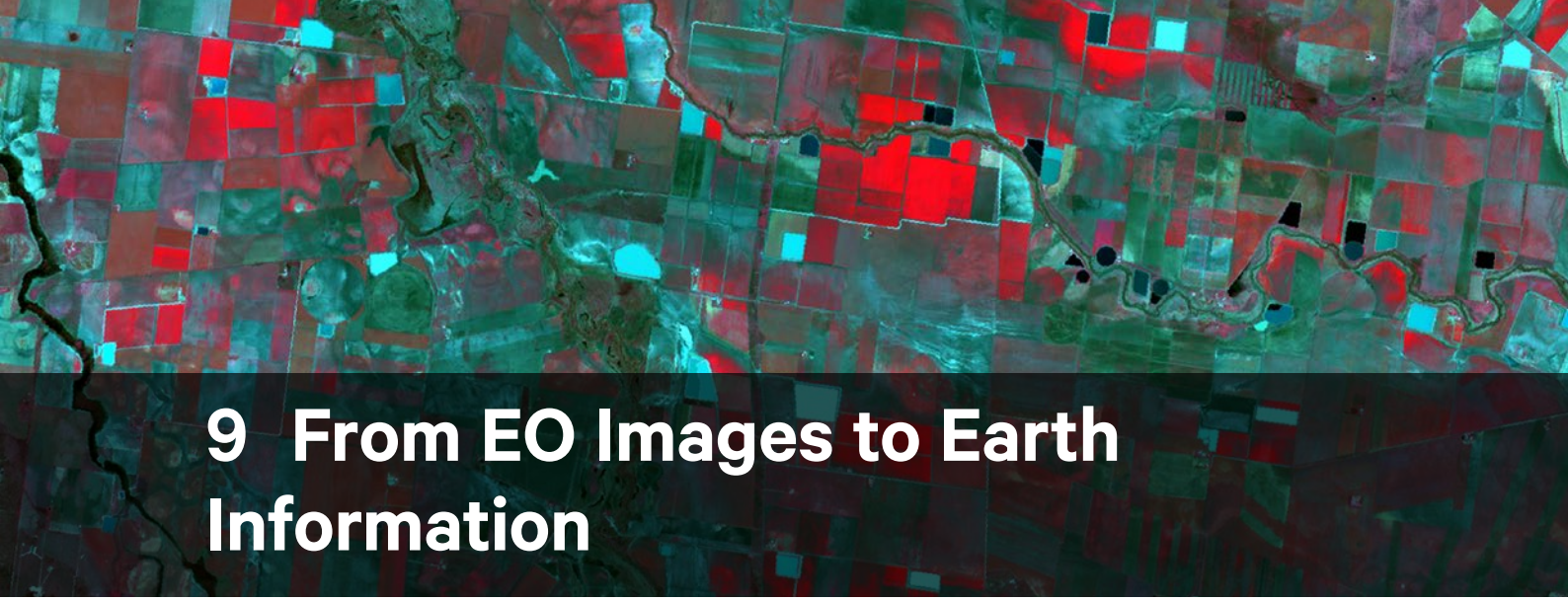
Subsequent volumes in this series detail image processing methods commonly applied to EO imagery (see Volume 2) and a range of applications areas that rely on EO datasets (see Volume 3).

Contents

9 From EO Images to Earth Information 153

10 Looking Ahead 171

Background image on previous page: Leftmost panel shows a Landsat-8 image of the Diamantina River system (southeast Queensland) acquired on 21 May 2016 (displayed using bands 6, 5, 3 as RGB). The rightmost panel shows the results of processing decades of imagery for this region using the WOfS (Water Observations from Space) system to highlight the permanence of water in this braided stream network (see Volume 1A—Excursus 5.1 for details).
Source: Norman Mueller, Geoscience Australia



9 From EO Images to Earth Information

This Section presents pratical approaches for selecting and processing image data to deliver accurate information.

Selection of the most suitable image dataset will vary for different applications, in different situations. Some EOS data, such as measurements of visible and infrared wavelengths, are affected by atmospheric conditions, including clouds, rain and dust (see Section 4), while others, such as measurements in the microwave regions, are mostly unaffected by weather conditions (see Section 8).

The designed resolution and extent of a sensor on a given platform contribute to the quality of data it can collect (see Section 1 above and Volume 1A—Section 13). Other factors that impact data quality are instrument maintenance, preprocessing, calibration, and validation. Some agencies supplying data also offer more reliable acquisition and distribution procedures than others.

Specific uses of EOS are generally adapted to the characteristics of particular sensors. While other sensors may offer similar characteristics in terms of both resolution and extent, the use of substitute sensors generally requires changes to data processing procedures and may impact the continuity of ongoing monitoring programs (Geoscience Australia, 2011).

Selection of optimal EO data, in terms of appropriate spectral, spatial, radiometric and temporal resolutions (see Section 1), for a specific environment and mapping or monitoring purpose, has been the subject of extensive research (Phinn, 1998; Roelfsema and Phinn, 2015).

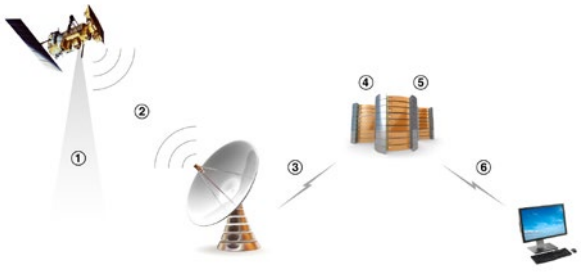
9.1 Satellite Image Acquisition

Acquisition of satellite image data generally involves multiple steps that are critically dependent on appropriate infrastructure. As illustrated in Figure 9.1, the generic process includes the following sequence:

- satellite-borne sensor scans Earth's surface;
- scanned measurements are transmitted to a satellite dish at a receiving station as telemetry data;
- telemetry data are transmitted by high speed communications link to a processing facility;
- telemetry data are decoded and calibrated to create a raw data image
- the raw data image is further processed to create an image product; and
- the image product is transmitted to the user by a communication link or digital media.

Figure 9.1 EOS data acquisition process

Satellite measurements (1) are transmitted to Earth via telemetry (2) then transmitted to processing facility (3), where telemetry is processed to raw data image (4). The raw data image is processed into an image product (5) then the product is transmitted to the user (6).



Source: Geoscience Australia (2011) Figure 1-1. Copyright credits: Computer workstation: Dmitry Rukhlenko, *http://www.shutterstock.com;* 3D Servers: Konstantinos Kokkinis, *http://www.shutterstock.com*; Satellite dish 3D: Maxx-Studio, *http://www.shutterstock.com*

Background image: ASTER image of cropping along the Condamine River, in southern Queensland, acquired on 24 January 2011 (displayed in false colour using bands 3, 2, 1 as RGB). **Source:** Norman Mueller, Geoscience Australia

There are several critical infrastructure components in this sequence, all of which need to be fully operational to ensure timely delivery of EOS products to users:

- receiving station needs appropriate technology to continuously acquire the transmitted format, volume and frequency of telemetry data;
- high speed communications link must have adequate capacity to continuously transmit the necessary volume of acquired data without delay;
- processing facility needs ample storage capacity to record and archive telemetry data, raw data imagery and image products;
- processing facility needs to have agreed processing capacity to accommodate expected volume of raw data imagery and process image products without delay; and
- communication link with users requires sufficient capacity to distribute required volume of data in a timely manner.

Each component in this sequence must operate continuously, or services based on EOS data are compromised. Additionally, an archive of raw and processed imagery must be maintained to supply future data requirements. Efficient access to this archive also requires ongoing management of data storage facilities and distribution networks.

The following sub-sections outline how the data acquired by satellites are communicated to ground receiving stations, processed and delivered for use.

9.1.1 Radio communication

Artificially generated radio waves are used for various forms of domestic communications, navigation systems, and communication with satellites. The established ranges used to describe radio frequencies are summarised in Table 9.1 and illustrated in Figure 9.2. Use of artificial radio waves is tightly regulated to avoid interference and ensure availability of required frequencies for essential services. An International Telecommunications Framework is managed by the International Telecommunications Union (ITU), and local implementations of this framework are determined by national bodies. For example, the Australian Communications and Media Authority (ACMA) allocates frequency bands for radio communication services in Australia according to the Australian Radiofrequency Spectrum Plan. A more recent allocation of radar frequency bands for military electronic countermeasures (ECM) systems has been defined by NATO, which designates band names in alphabetical order with increasing band frequency.

Man is the best computer we can put aboard a spacecraft...
and the only one that can be mass produced with unskilled labour.
(Wernher von Braun)

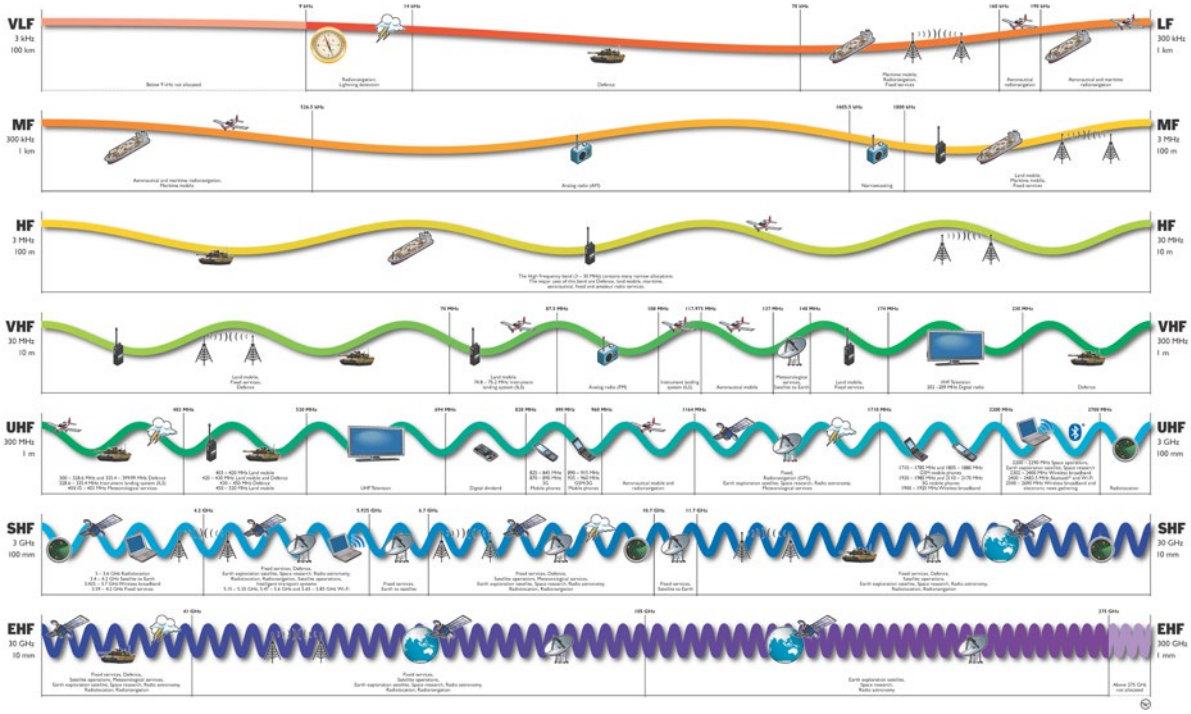
Table 9.1 Radio frequency ranges[15]

ITU Radio Band					Used for	IEEE Radar Frequency Codes		
No.	Abbr.	Name	Frequency	Wavelength		Name		Frequency
1	ELF (ELF1)	Extremely Low Frequency	3 to 30 Hz	100,000 to 10,000 km	Submarine communications			
2	SLF (ELF2)	Super Low Frequency	30 to 300 Hz	10,000 to 1,000 km				
3	ULF (ELF3)	Ultra Low Frequency	300 Hz to 3 kHz	1,000 to 100 km	Submarine and intra-mine communications			
4	VLF	Very Low Frequency	3 to 30 kHz	100 to 10 km	Radionavigation, lightning detection time signals, submarine communication			
5	LF	Low Frequency	30 to 300 kHz	10 to 1 km	Radionavigation, clock time signals, analogue radio (AM), amateur radio			
6	MF	Medium Frequency	300 to 3000 kHz (or 3 MHz)	1 km to 100 m	Radionavigation, AM broadcasts, amateur radio, avalanche beacons			
7	HF	High Frequency	3 to 30 MHz	100 to 10 m	Over-the-horizon radar and aviation communications, marine and mobile radio telephony			
8	VHF	Very High Frequency	30 to 300 MHz	10 to 1m	Analogue radio (FM), television broadcasts, weather radio, line-of-sight aviation communications			
9	UHF	Ultra High Frequency	300 to 3000 MHz	1 m to 100 mm	UHF Television broadcasts, microwave ovens, radio astronomy, mobile phones, EO satellites	L-band	Long wave	1 to 2 GHz
						S band	Short wave	2 to 4 GHz
10	SHF	Super High Frequency	3 to 30 GHz	100 to 10 mm	Communications and EO satellites, modern radars, microwave communication devices	C-band	Compromise between S-and X-band	4 to 8 GHz
						X-band	Used in WW II for fire control (X for cross, as in crosshair)	8 to 12 GHz
						Ku-band	Kurz-under	12 to 18 GHz
						K-band	German Kurz (short)	18 to 27 GHz
						Ka-band	Kurz-above	27 to 40 GHz
11	EHF	Extremely High Frequency	30 to 300 GHz	10 to 1 mm	Microwave remote sensing, radio astronomy, directed-energy weapons	V-band	Very high	40 to 75 GHz
						W-band	W comes after V	75 to 110 GHz
						mm	Millimeter (or G-band)	110 to 300 GHz
12	THF	Tremendously High Frequency	300 to 3,000 GHz	1 mm to 100 μm	Terahertz communications, remote sensing, amateur radio			

Source: IEEE (2002); Elert (2015); ITU (2015)

15. For space radiocommunications the symbol K_a is often used to refer to both K- and Ka-bands (ITU, 2015).

Figure 9.2 ACMA Radio Spectrum



Source: ACMA Spectrum Illustrated (ACMA, 2016)

Radio waves are the longest form of EMR, with wavelengths ranging from 100μm (3,000 GHz—Tremendously High Frequency: THF—also called terahertz waves or submillimetre radiation) to 100,000 km (3 Hz—Extremely Low Frequency: ELF). Given this large range, radio waves are generally described in terms of standardised frequency bands (and sub-bands) rather than wavelengths (see Table 9.1). Note that, as wavelength increases, frequency decreases, so low frequency waves are longer than high frequency waves.

Like all EMR, radio waves travel at the speed of light (299,792,458 m/s; see Volume 1A—Section 2.4). Accordingly, a theoretical 1 Hz EMR wave (which equates to one full wave cycle per second) would have a wavelength of 299,792,458 m or around 300,000 km—over three-quarters of the distance from Earth to our moon. However, radio waves with frequencies greater than 300 GHz (that is, wavelengths less than 1 mm) are absorbed by the atmosphere, so are generally not used for EO or communications. An ELF wave of 3 Hz therefore equates to a wavelength of 100,000 km, or 2.5 times the circumference of Earth.

Radio waves are generated by a transmitter and interpreted by a receiver. To transmit digital data via radio signals requires that the data be 'modulated' into a radio frequency by the transmitter and then transformed back to a digital signal by the receiver.

Radio signals can be either narrowband, which as the name implies uses a narrow range of radio frequencies, or broadband (also called wideband). Narrowband radio signals provide reliable communication for long range, low power applications, but wideband signals offer greater speed for higher data volumes. The volume of data being transmitted by most satellite communication links necessitates using wideband transmission.

Digital data quantity is measured in bits (binary digits) and the transmission speed of digital data is often cited as bits per second (bit/s). For digital data transmission, the speed of transfer is also measured in terms of the radio frequencies used to transport the data (and measured in Hz).

9.1.2 Ground stations

Once EO data have been acquired by satellite sensors, it is transmitted to satellite reception ground stations on Earth via specific radio frequencies. Ground stations are also used to track satellite position and attitude, and send tasking information, such as when and where imagery should be acquired. This 'housekeeping' information is known as Telemetry, Tracking and Command data, or TT&C.

To transmit data from one location to another, it must be converted from digital format into a radio frequency modulated signal. To uplink data, that is send it from a ground station on Earth to a satellite in space, a digital signal of TT&C data is converted to radio frequency using a modulator. Conversely, to send data from the satellite to a ground station (downlink), the radio frequency modulated signal is converted into an input signal using a demodulator.

While some satellites, such as geostationary satellites used for meteorology and communications, remain in a single location relative to a ground station on Earth, most EO satellites do not. For this reason, many ground stations must be capable of 'tracking' satellites (mostly polar orbiting) as they move in and out of view. Since geographic features such as high mountains can obstruct the line of sight between ground stations and satellites, in order to track most polar orbiting EO satellites a satellite reception ground station requires a reception area which can be approximately calculated by a 2400 km circle around the station, which equates to approximately 3° above the horizon on the ground.

The ground and communications infrastructure comprising satellite reception systems includes:

- antennas and data ingest systems;
- on-site processing systems;
- communications links from ground stations to central data storage and processing infrastructure
- scheduling systems to control data acquisition for operational and research purposes;
- data uplink systems; and
- calibration and validation infrastructure.

Spacecraft launched in the 1960s communicated with ground stations using S-band frequencies. However, as data download volumes increased, X-band became more commonly used. Many spacecraft communicate via dual frequencies (using a lower frequency for uplink of ground to satellite communications and a higher frequency for downlink of data from satellite to ground station), such as S/X and more recently X/Ka. Increasing data volumes are likely to necessitate the use of higher frequency bands for future satellites, with potential data rates over 1.5 Gbit/s. NASA's Deep Space Network (DSN), which relies on three ground stations (in Goldstone, California; Tidbinbilla, near Canberra; and Madrid, Spain), also communicates with more distant spacecraft using S-, X- and Ka-bands. High frequency communications with spacecraft enables greater bandwidth, improved tracking, reduced ionospheric effects and better pointing accuracy.

Different types of EO ground station receivers exist in Australia with different tracking, transmission and reception capabilities as summarised in Table 9.2. Reliable high-speed communications infrastructure is required to link ground stations with national EOS operating agencies and international EOS data providers. This is particularly critical for the transmission of the rapidly increasing data volumes used for applications with a time sensitive nature, such as weather forecasts and warnings, and emergency response.

Table 9.2 Satellite ground station receivers

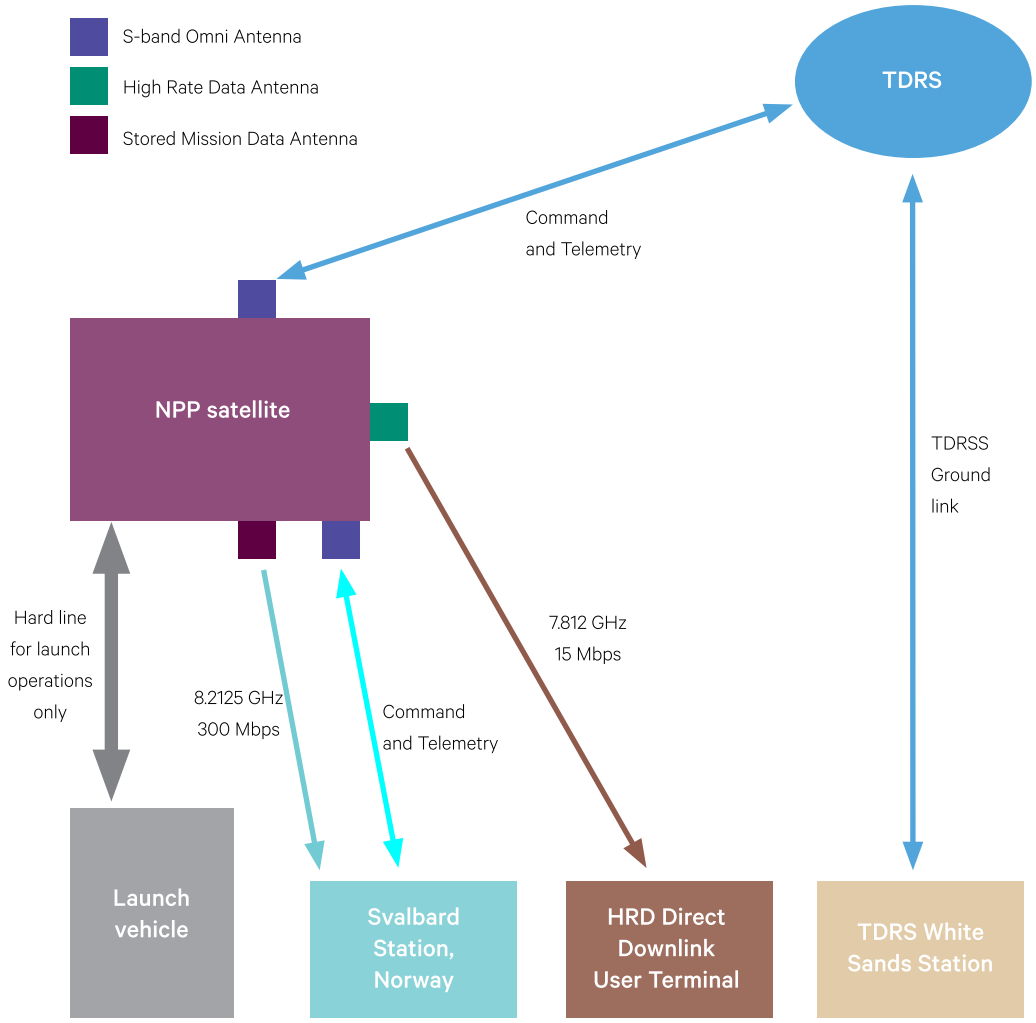
Note: Antenna sizes: Large > 10 m; Medium to large > 8 m; Small < 3 m

Requirement	Tier 1	Tier 2	Tier 3	Tier 4
Tracking	Yes	Yes	Yes	No
Elevation masks	< 3˚	< 3˚	< 5˚	Line of sight to geostationary satellite
Antenna size	Large	Medium to large	Small	Small
Standard frequency band(s) for downlink	X, Ku, Ka	X	X, L	C, L, S
Standard frequency band(s) for uplink	S	–	–	S
Standard communications link bandwidth	≥ 1 Gbit/s – 100 Mbit/s	≥ 100 Mbit/s	≥ 100 Mbit/s	≥ 10 Mbit/s

Source: David Hudson, Geoscience Australia

Figure 9.3 Suomi NPP satellite communication

Overview of Suomi NPP (previously NPOESS) satellite communication with ground segment. Command communication rate between the NPP spacecraft and both the TDRS (see Figure 9.4) and the Svalbard station is 2067.270833 MHz, while the telemetry rate is 2247.5 MHz.



Adapted from: Wilczynski (2005)

A typical example of a satellite reception arrangement is the one used by the Suomi National Polar-orbiting Partnership (NPP) satellite mission managed by NASA (see Figure 9.3). In addition to its onboard imaging instruments, this satellite carries three control subsystems:

- Attitude Determination and Control Subsystem (ADCS)—stabilises attitude and reports on position and attitude;
- Electrical Power Subsystem (EPS)— orients satellite and drives instruments using solar powered engine; and
- Command and Data Handling Subsystem (C&DHS)—collects and stores instrument data for subsequent transmission to ground station.

Science data from this satellite is generated at 12.5 MB/s and downlinked at 300 Mbit/s to a small receiving station in Svalbard in Norway, comprising a 13 m antenna dish. The high latitude of this location (78.216°N) enables the antenna to track all 14 orbits of this satellite each day. Up to 280 Gbits of stored data is downlinked at 300 Mbit/s (using 8.2125 GHz—X-band) once per orbit when the satellite is over the ground station. The Stored Mission Data (SMD; capacity 280 Gbit) is then transmitted immediately to the USA via fibre-optic cable. In the USA, the Raw Data Records (RDR) are processed into Sensor Data Records (SDR) and Environmental Data Records (EDR), within three hours of acquisition.

As well as the SMD, the mission records housekeeping telemetry and High Rate Data (HRD). The latter includes instrument science, calibration and engineering information. These datasets are also merged and transmitted in real time to direct broadcast users at 15 Mbit/s.

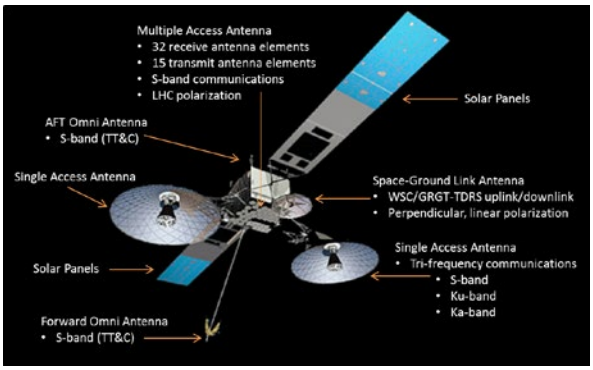
9.1.3 Tracking and data relay satellites

A specialised network of communication satellites, called the Tracking and Data Relay Satellite System (TDRSS), has been established by NASA to track and communicate with a range of space platforms, including various EO satellites, the International Space Station (ISS) and the Hubble Space Telescope. Three current TDRSS ground stations for command and control of these satellites are located in the White Sands Complex in New Mexico (WSC), Guam Remote Ground Terminal (GRGT) and Network Control Centre (NCC) in Maryland). A new station is being built at Blossom Point (BPRS), Marylands. The TDRSS satellites (see Figure 9.4) follow a geostationary orbit at an altitude of 35,786 km (see Figure 9.5). Deactivated satellites are placed in the 'Super-sync' orbit (350 km higher—also called the disposal or graveyard orbit) to avoid collisions with operational satellites.

The TDRSS network is designed to relay signals from spacecraft to ground stations and thus extend the period of contact with numerous space missions. This network now provides nearly continuous, high bandwidth (S-, Ku- and Ka-band) telecommunications with a wide range of EO platforms and has significantly increased the volume of data being transferred to ground stations.

Figure 9.4 Tracking and Data Relay Satellite (TDRS)

Capabilities of the third generation TDRS are shown in this illustration.

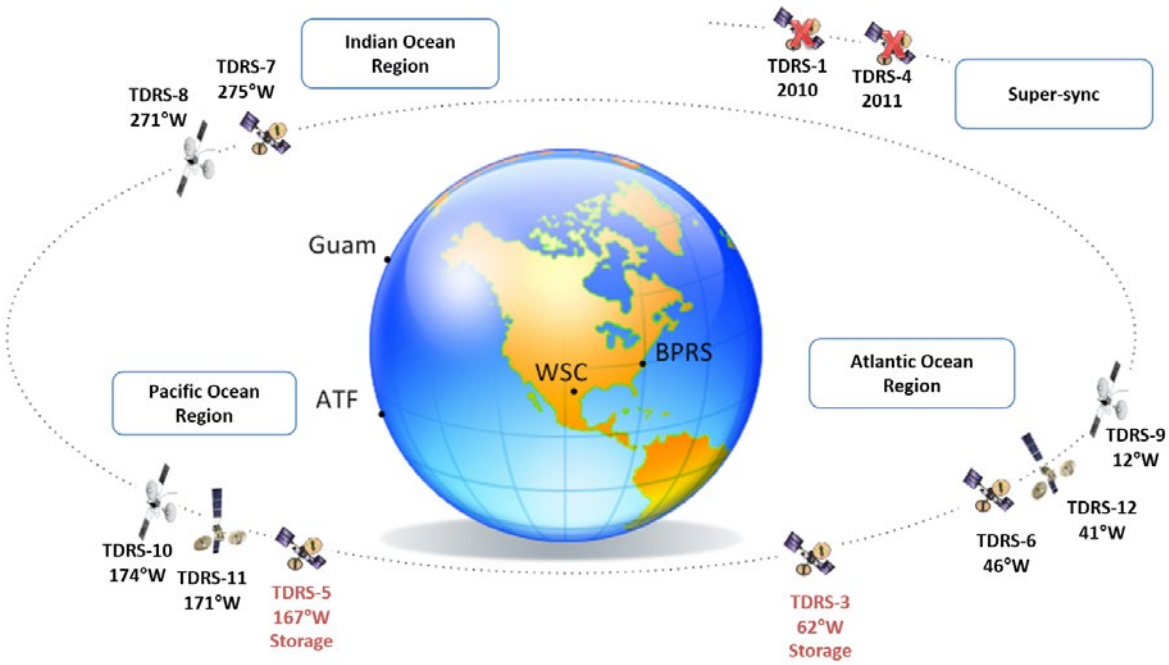


Source: NASA. Retrieved from: *https://www.nasa.gov/directorates/heo/scan/services/networks/txt_tdrs_gen3.html*

The TDRSS forms the space component of NASA's Space Network (SN), which continuously supports telecommunications, tracking and clock calibration, and testing and analysis of spacecraft. Other components of the SN are ground facilities, ground systems that relay information between satellites, and satellites in Low Earth Orbit (LEO: 180–2,000 km altitude).

Figure 9.5 TDRSS Constellation

TDRSS configuration on 1 June 2015 comprised nine 'working' satellites: six operational, two in storage, and one under evaluation. Current ground stations are located at WSC (White Sands Complex, New Mexico), GRGT (Guam Remote Ground Terminal), and Network Control Centre (Marylands). BPRS (Blossom Point Relay Station, Marylands) will become the fourth ground station. ATF is the Australian TDRSS Facility, located at Tidbinbilla (near Canberra).



Source: NASA. Retrieved from: *http://www.nasa.gov/directorates/heo/scan/services/networks/txt_tdrs_fleet.html*

9.2 Data Volume

Raster imagery generates huge volumes of data that need to be stored, processed and delivered. For example, the total archive of raw data imagery, from 1979 to 2010, that is being maintained by Geoscience Australia (GA) comprises approximately 500 TB. Nearly half of this archive was acquired from the Landsat series of satellites. By early 2017, the total volume of imagery at GA amounted to around 2 PB.

Raw EOS data are typically processed multiple times to correct for radiometric and geometric distortions. A conservative estimate of the storage required to process raw EOS data is three times the raw data volume. For example, before distribution to users, most satellite imagery acquired by GA has been processed three to five times, with each processing stage requiring access to additional data storage. Between July 2009 and June 2010, approximately 19 TB of raw EOS data were acquired by GA from 11 sensors carried by eight satellites. The current annual data volume acquired from all EOS sources in Australia is estimated at 20 TB. This volume of data would require 60 TB of storage to allow conversion of the raw data into standard image products. Full global archives of corrected data from the Landsat satellite sensors (MSS, TM, ETM, OLI), plus global coverages from several other satellites, are now available via public-good sectors of international data stores (such as Google and Amazon; see Section 9.5).

The volume of available EOS data is expected to increase dramatically in future decades. For climate models alone, Overpeck *et al.* (2011) estimated more than a fiftyfold increase in the volume of EOS data from 2010 to 2020, with a 150 times increase expected by 2030. Ongoing strategic planning is essential to ensure that the necessary infrastructure is in place to support the anticipated future volume of EOS data (see Section 10).

640K ought to be enough for anybody.
(Bill Gates, 1981)

9.3 EO Data Usage

9.3.1 Scientific and technical workflows

The collection and processing of satellite and airborne image data to derive spatial data products for biophysical, infrastructure and socio-economic uses extends across multiple disciplines and professions. These data provide standardised products in:

- a wide range of environmental monitoring and management applications, including:
  - meteorological and oceanographic products for temperature, rainfall, solar radiation, and ocean surface wind and waves;
  - vegetation type, structure, biomass and condition; and
  - topography and bathymetry; and also in
- asset and infrastructure planning and monitoring—inventory and assessment of roads, pipelines, powerlines, buildings and other structures.

In each case the derived spatial data must meet specific requirements in terms of:

- documented, positional accuracy and precision;
- accuracy of estimated biophysical quantity or thematic map classes; and
- inclusion of standard metadata.

To enable commercial tendering and ensure product consistency and utility, standards are often set by government agencies for the collection of EO data and generation of derived products. As a result, common standards now exist for data collection, and also for delivery of specific products via defined workflows. In the context of scientific and government data sets, raw data, metadata, processing workflow and derived products are increasingly available in the public domain through data portals operated by government agencies and environmental data infrastructure programs. In Australia, several data portals deliver a wide range of image-based data, including:

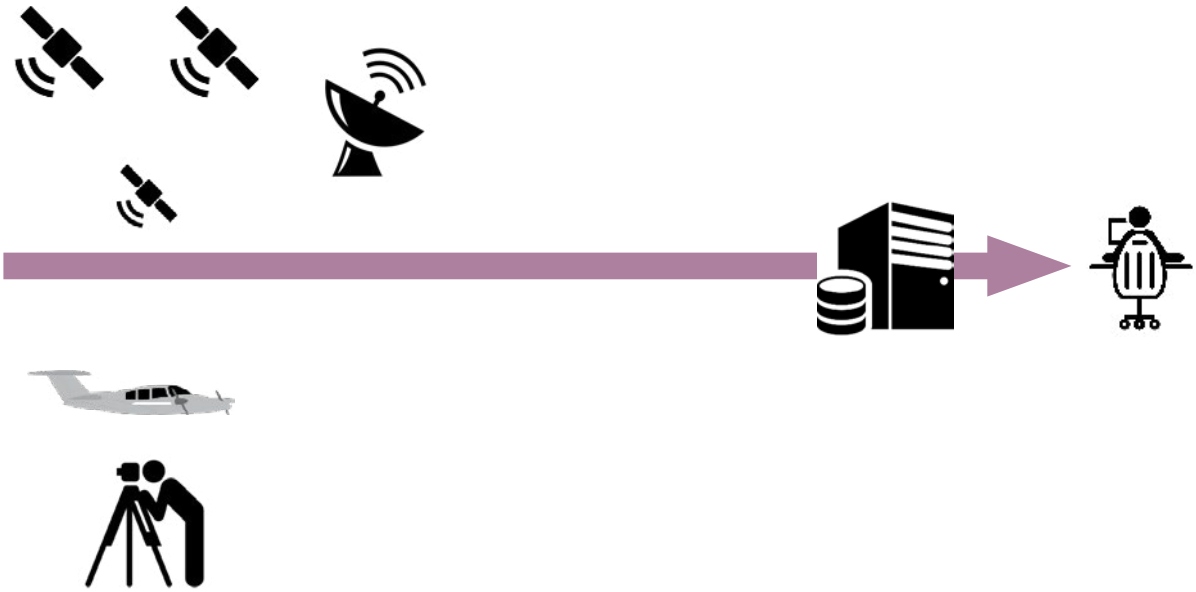
- TERN AusCover;
- Integrated Marine Observing System (IMOS);
- Australian Urban Research Infrastructure Network (AURIN);
- Atlas of Living Australia (ALA); and
- National Computational Infrastructure (NCI; repository for NOAA, MODIS, sentinel, Landsat and VIIRS imagery).

Internationally, national space agencies such as NASA, ESA and JAXA provide ready access to an extensive range of EO products, including their raw data, metadata and processing workflows (see Section 9.5). Satellite image processing is moving towards integrating multiple, cloud-based image archives with online processing and product delivery (see Figure 9.6).

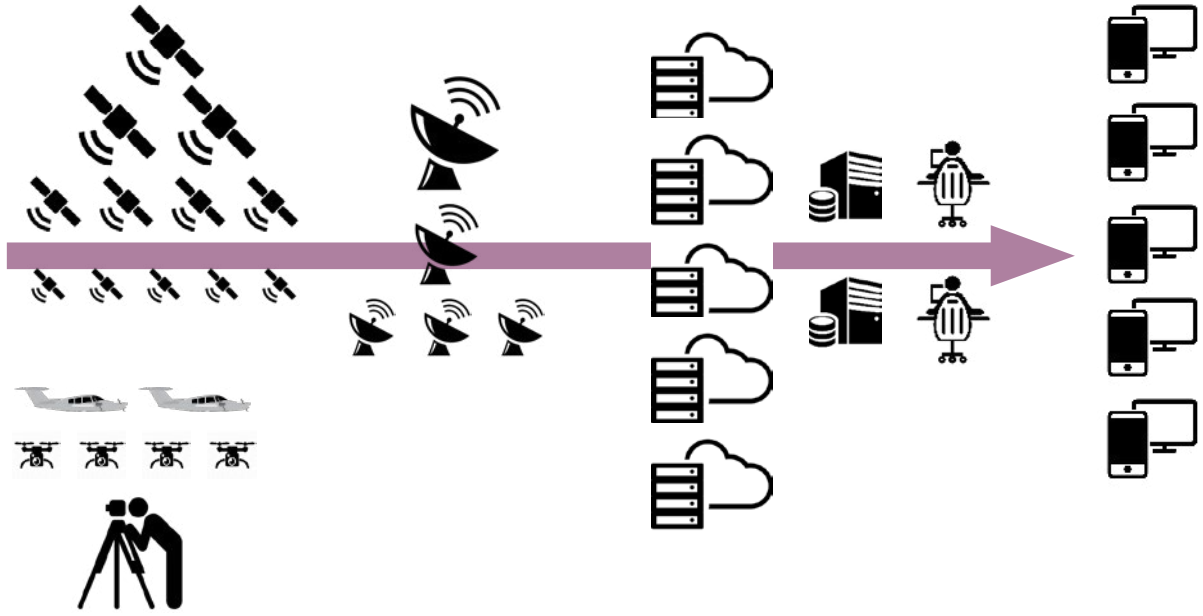
Figure 9.6 Trends in EO data delivery

Satellite image processing is moving towards the use of software that works with multiple, extensive, online (cloud-based) image archives as web data services, then processing the data online, and delivering output images, image products or analyses that show changes in an environmental attribute over time (see Excursus 10.3).

a. Schematic of traditional, localised approach to EO data processing and delivery



b. Usage of EO data increasingly embraces online storage, processing and delivery opportunities



Source: Stuart Phinn, University of Queensland

9.3.2 Legal requirements for data collection, processing, storage and use

The processing workflows outlined above build on a number of standards, which have evolved across a range of remote sensing applications, and predominantly derive from:

- government airborne data acquisition programs—images and lidar data;
- international science programs—satellite image products, lidar and terrestrial laser scanners; and
- specific environmental applications/scientific communities—such as ocean colour, atmospheric chemistry, and land-cover.

The list in Table 9.3 is not exhaustive but outlines the main standards that are now being employed in remote sensing applications as this area of science moves to become more transparent. Ideally, transparency would include open and freely accessible data and algorithms resulting from publicly funded research and applications. EO-based data is increasingly used for legislated monitoring and management and, more recently, as legally admissible evidence (Purdy, 2010a, 2010b, 2011, 2012). Accordingly, appropriate standards are required for data collection, processing, storage and use of all EO products, including those provided by:

- research organisations—such TERN Auscover, NASA, or ESA;
- government agencies—such as GA, Landgate or USGS;
- international coordinating bodies—such as CEOS working groups, ISPRS Commissions, IEEE-GRSS; and
- private industry—such as chartered image acquisitions and customised processing methods.

Finally, cartographic standards for EO products need to be clearly defined. By convention, all maps include a number of well-defined elements, including title, scale, projection, datum, coordinate system, north point, map production date, legend, author and copyright. Additionally, EO image maps should specify additional relevant factors such as:

- provenance—sensor type (and orbit details for satellite sensors—path/row and heading), plus image acquisition date and time;
- geometric accuracy of final product and viewing perspective of sensor (nadir or oblique);
- image spectral bands used to display product (if relevant); and
- processing history.

Current standards for EO image products are not comprehensive or consistent, but need to become so. International templates for sensor data, such as the Generic Earth Observation Metadata Standard (GEOMS; Retscher *et al.*, 2011), are being developed. An overview of recent developments in standards-based systems for processing, archiving and managing EO data is provided by Di and Ramapriyan (2010).

Table 9.3 Standards relevant to EO data

Standards	Type	Examples
Data	Image without metadata	JPEG2000, GeoTIFF
	Standalone metadata	XML
	Image with metadata	NetCDF, HDF
Metadata	International standards	ISO 19115 *Geographic Information—Metadata* (from ISO/TC 211) Climate and Forecast (CF) conventions in NetCDF
	National standards	ANZLIC National Nested Grid guideline (draft only)
Licencing	Creative Commons Attribution (CC-BY)	GA-CC-BY-4.0
	Creative Commons Attribution ShareAlike (CC BY-SA)	TERN-BY-SA-NC
	End User Licence Agreement	Customised licences

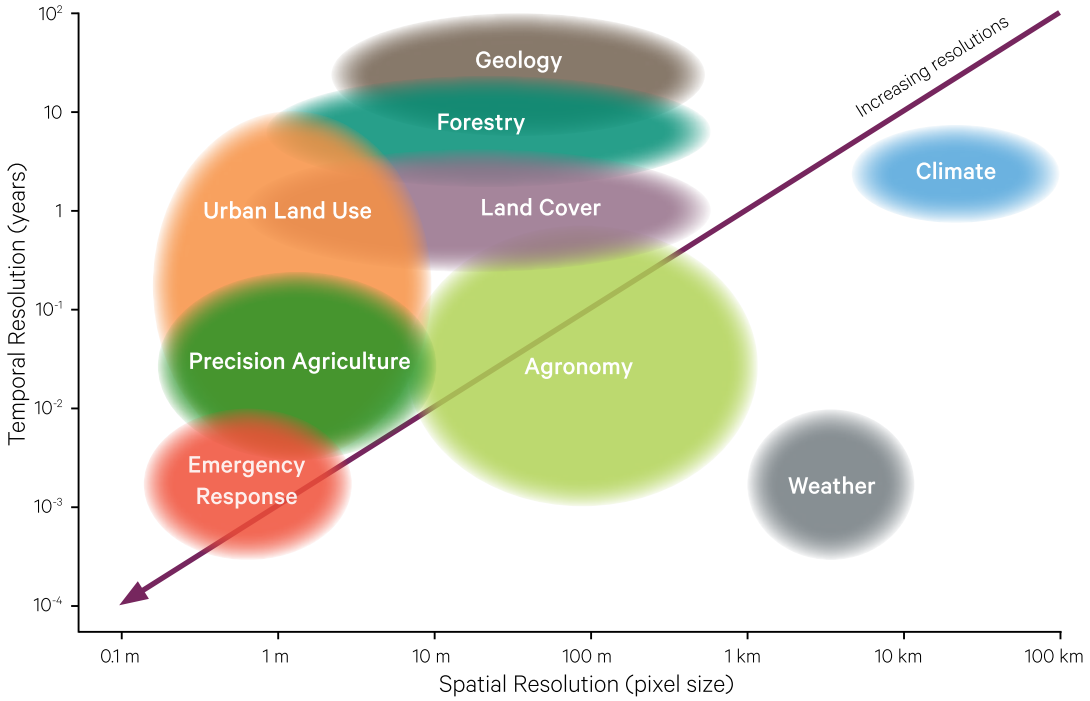
9.4 Integrated Data

One of the greatest opportunities and challenges offered by EO datasets is data integration—blending different datasets to achieve better understanding of spatial and temporal changes. Given the enormous range of EO data available, reliable results and efficient processing both depend on using the most relevant data.

Selection of the most appropriate imagery for a particular application involves consideration of the spatial, spectral and temporal nature of the phenomenon to be characterised in relation to the spectral, spatial, temporal and radiometric dimensions of potential sources of imagery. Of particular importance are the size and extent of features, the time frames over which they vary and the extent to which relevant variations can be detected with EO data. Figure 9.7 illustrates the interactions between temporal and spatial scales for several EO data sources.

Figure 9.7 Selecting appropriate imagery

Image selection can be considered in terms of spatial and temporal resolution and extent. This schematic illustrates typical ranges of spatial and temporal scales for different EO applications.



Adapted from: Jensen (2007) Colour plate 1.1

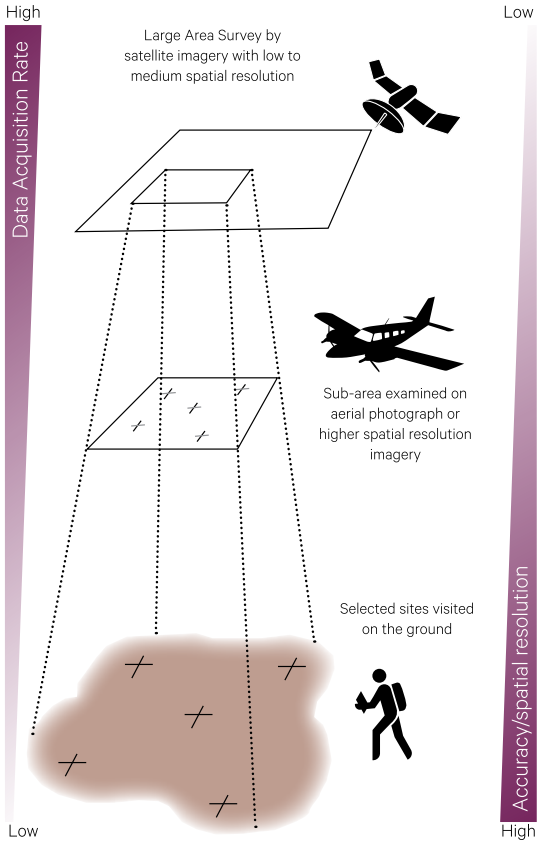
A complete remote sensing exercise usually involves integrating imagery at several different spatial resolutions with other spatial data sources. Within a large region represented in a medium resolution satellite image, certain areas are usually selected for checking with high resolution imagery, some of which would be visited in the field. In such an exercise, using medium resolution imagery has reduced the alternative cost of requiring high resolution imagery, or field checking, over the whole study area. This concept of a multi-level approach is illustrated in Figure 9.8. In this context, coarser resolution data can also be considered to act as a checksum on finer resolution data sources.

Once consistent and comparable measures of surface reflectance have been retrieved from EO data, it is possible to quantify changes in Earth surface features through time. This process is further simplified when the surface reflectance data conforms to a sensor agnostic nested grid.

Such integrated products can be viewed as a data cube, with time as an additional dimension. Data for each imaged date and time can be stacked in chronological order, with relevant data sources being interleaved as appropriate to their acquisition time. Interrogation of this data cube allows the time series for individual grid cells, as well as their heritage and data quality, to be extracted and compared (see Volume 2A).

Figure 9.8 Scales of EO

Analysis of low and medium resolution imagery can be more easily related to ground data through high resolution imagery.



Adapted from: Harrison and Jupp (1989) Figure 39

As illustrated in Figure 9.9, one example of using multiple types of imagery to provide complementary information about groundwater-fed wetlands in the Australian Great Artesian Basin (Lewis and White, 2013) incorporated:

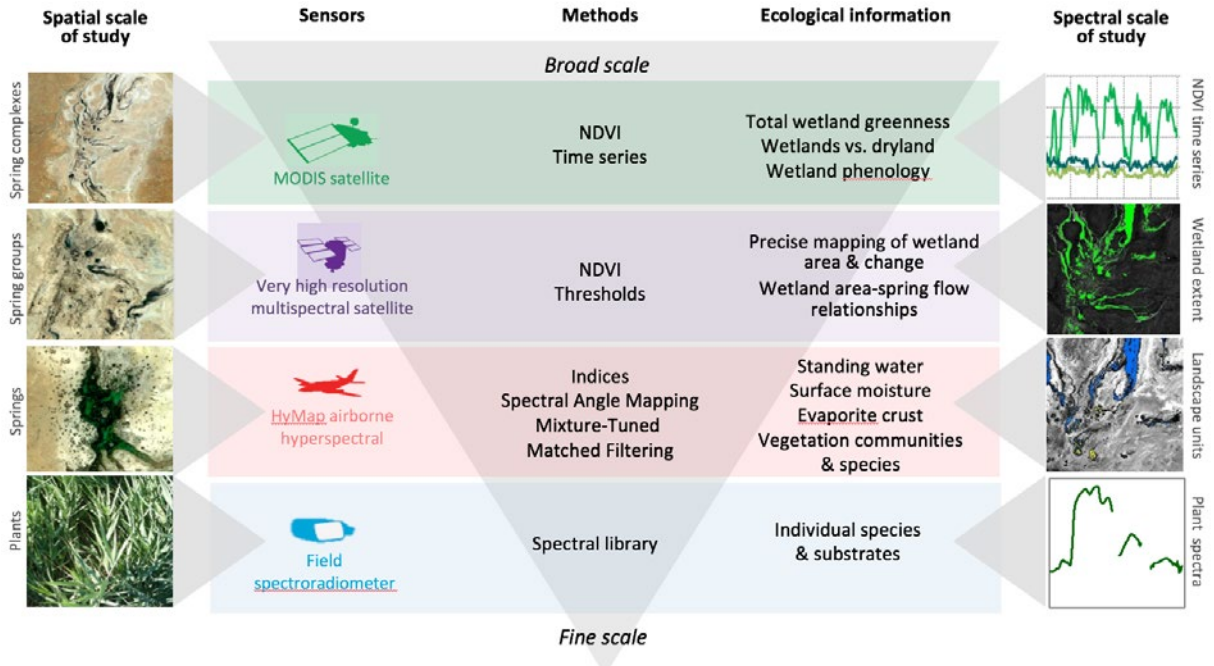
- a ten-year series of MODIS 16-day NDVI composites—to provide information about intra and inter-annual variation in wetland greenness over broad areas;
- very high resolution multispectral satellite imagery—to more precisely delineate selected wetlands at a few specific intervals;
- airborne hyperspectral imagery—to provide high-resolution mapping of vegetation species, surface minerals, water and soil moisture at key representative sites; and
- in-situ measurements of reflectance with a narrow-band spectroradiometer—to characterise spectral signatures for plants and soils and to calibrate and interpret the hyperspectral imagery.

Similarly, when attempting to model Earth processes, the time scale of the process needs to be matched with the frequency of observations. The most appropriate frequency to monitor relevant processes can vary from minutes to centuries. Some ecological processes being modelled using EO data are summarised in Table 9.4 with their relevant time scales. Such processes are further considered in Volume 3.

Figure 9.9 Spatial and spectral scales

Multi-sensor, multi-scale approach to characterising environmental phenomena is illustrated by a study of Great Artesian Basin mound springs in arid South Australia (Lewis and White, 2013).

1. High temporal frequency, low spatial resolution series of MODIS NDVI were used to monitor intra and inter-annual changes in wetland greenness for large spring complexes;
2. Selected dates of very high resolution multispectral satellite imagery were used to more precisely map wetland area and localised changes for smaller spring groups;
3. Airborne hyperspectral imagery was analysed with a variety of methods to characterise surface water, minerals and vegetation composition at selected springs and groups; and
4. In-situ measurements with a portable spectroradiometer were used to characterise species and surfaces, assess spectral differences and provide references for hyperspectral image analysis.



Adapted from: Lewis and White. (2013)

Table 9.4 Time scales for monitoring Earth processes

Process	Time Scale	Value of EO Monitoring
Photosynthesis/ leaf respiration	Minutes to months	Stomata responds to variability in environmental conditions and CO_2 concentration when coupling between photosynthesis and stomatal conductance is explicitly modelled
Growth respiration and stem root maintenance respiration	Minutes to months	Estimating respiration allows us to model NPP and GPP
Phenology	Daily to monthly	The timing of leaf onset and offset can be modelled rather than prescribed
Allocation	Daily to annual	Biomass allocated to leaves determines LAI, which varies with changes in climatic conditions from year to year. This allows seasonal LAI cycle to be simulated from EO rather than prescribed.
Nitrogen cycle	Monthly to annual	Explicitly modelling N cycle and plant N uptake implies that N availability does not have to be assumed constant. The effect of variability in N availability on plant productivity can thus be modelled.
Competition between plant functional types (PFT)	Decades to centuries	Vegetation reacts to long term changes in climate. PFTs that are best suited for a given region and climate are the ones that succeed.

Adapted from: Moreno (2007)

An example of integrating a variety of EO imagery to track crop production 'from paddock to plate' is described in Excursus 9.1.

All parts should go together without forcing. You must remember that the parts you are reassembling were disassembled by you. Therefore, if you can't get them together again, there must be a reason. By all means, do not use a hammer.
(IBM Manual, 1925)

Excursus 9.1—Crops from Space

Source: Andrew Robson, University of New England

The commercial value of crops can be reduced by sub-optimal timing of harvest, soil pathogens, pests, inadequate nutrition and other growing constraints. To identify and predict such constraints, a range of high resolution imagery from satellite and airborne sources has been used commercially to:

- identify crop variability both within and between growing seasons;
- predict variation in maturity and quality within a crop to enable harvest segregation;
- predict high risk areas for soil pathogens, pests, disease, and biosecurity outbreaks;
- predict regional and crop yield;
- track produce from 'paddock to plate'; and
- monitor the impact of natural disasters.

The spatial and temporal variability in crop vigour across an individual field or across a growing region can be measured by an EO image, often expressed as a vegetation index (VI; see Volume 2). By establishing the relationship between the VI and actual crop yields, there is the opportunity to predict average yield as well as derive surrogate yield maps (see Figure 9.10). It is, however, important to ensure that the relationship remains constant across growing regions, seasons and cultivars.

EO imagery is being used to forecast yield and monitor a number of Australian crops, including sugar, peanut and grains. Research currently being undertaken in tree crops is identifying a strong relationship between yield and fruit size achieved by an individual tree (avocado, mango and macadamia) to the VI derived from the reflectance properties of the corresponding tree canopy. Using this relationship, accurate predictions of total yield are being achieved as well as derived maps of yield and fruit size for avocado (Robson *et al*., 2016). Yield estimation in avocado orchards currently involves visual counting of a small sample of trees. In the absence of a commercial yield monitor, EO-based yield maps offer significant benefit to growers for improving orchard management, harvest scheduling and forward selling decisions. Additionally, the ability to map fruit size prior to harvest allows growers to focus on areas of the orchard that are producing larger fruit, thus ensuring maximum payment when prices are high and miniming labour costs.

Following the lead of the Australian sugar industry (see Excursus 1.1), monitoring individual tree health in commercial orchards will provide accurate information about grower demographics and introduce new levels of efficiency in the supply chain for crops such as banana, avocado, mango and macadamia. At the industry scale, the establishment of a GIS database that holds the locations and associated attribute information of every commercial orchard provides growers and their respective industry bodies with a better understanding of grower demographics (such as area of cultivar, yield variability, or disease spread). The mapping of the crop extents alone offers significant benefit by supporting the industry-wide generation and distribution of imagery products, such as tree vigour, yield, and fruit quality.

Figure 9.10 Satellite view of crop

a. QuickBird image of a peanut crop (2.4 m spatial resolution)

b. Greenness map derived from QuickBird imagery identify high and low growth regions

c. Classified yield map generated from greenness map with 97% accuracy)

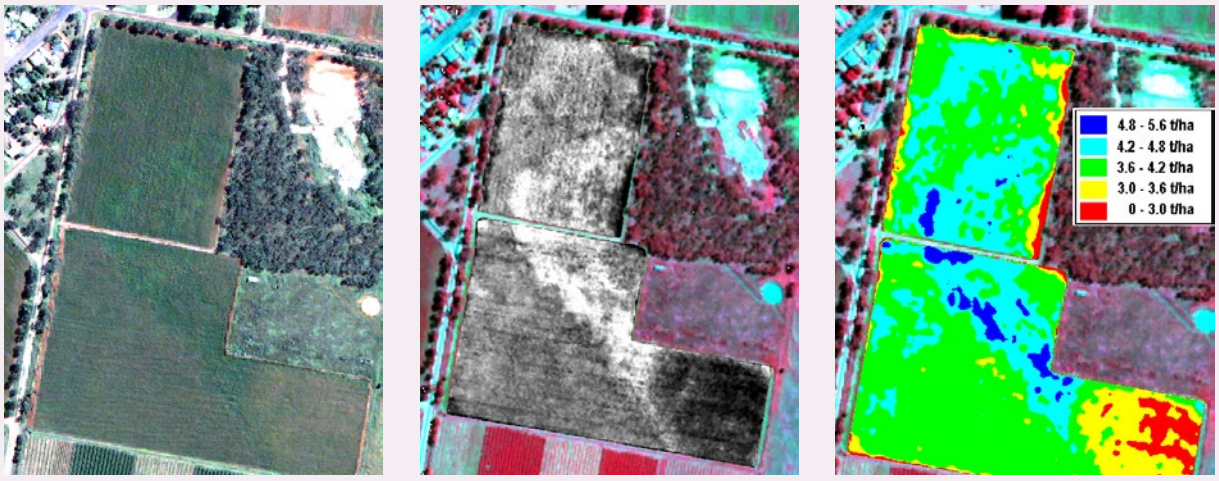
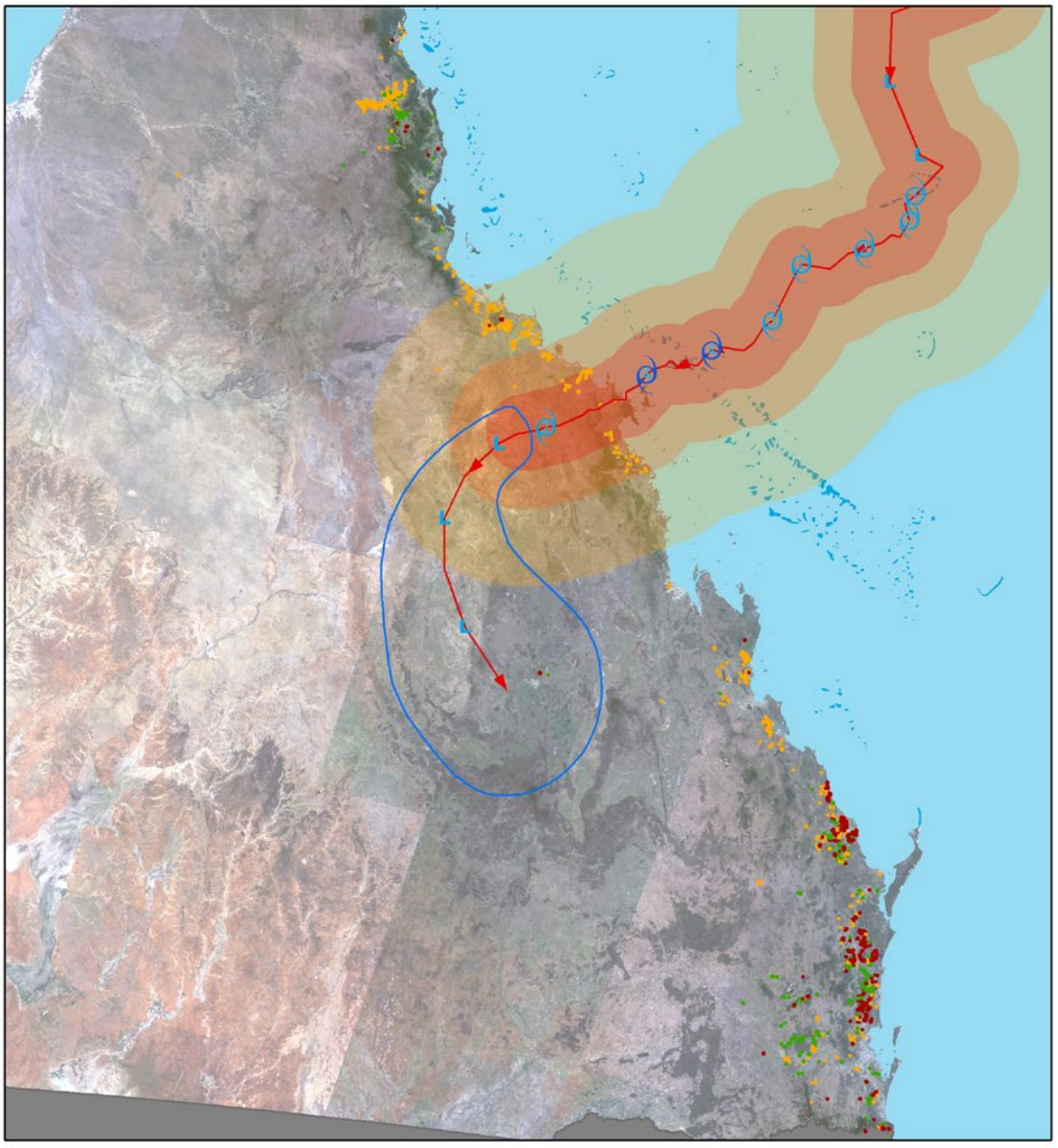


Figure 9.11 Tree crop impact of Cyclone Debbie

In March 2017, Cyclone Debbie swept onto the central Queensland coast leaving a trail of destruction in towns and agricultural areas. Data from the Bureau of Meteorology was used to locate the cyclone's track, points and predicted path. Buffer zones map impact at 50 km, 100 km and 200 km away.



EO imagery has also proved useful for mapping the impact of extreme weather events on crops, providing rapid assessment of the extent of damage and enabling faster support for those affected. For example, a range of satellite and airborne imagery were analysed in conjunction with on-ground data from an industry app to produce a map of avocado, macadamia and mango orchards affected by Cyclone Debbie in March 2017 (see Figure 9.11). A web map was developed that displayed the destructive track of the cyclone in three severity classes and distributed in a format that could be viewed on any browser or smart device. By combining the destructive cyclone path with the extent of each orchard, a rapid estimation of affected orchards could be made and provided to industry. This information is vital for post-disaster response, estimating lost production, and crop insurance. The accuracy of this mapping exercise is being improved by ongoing measurements from a range of ground, air, and satellite-based remote sensing platforms, and citizen scientists.

9.5 Further Information

Australian Data Portals:

TERN Auscover: *http://www.auscover.org.au/data*

Integrated Marine Observing System (IMOS): *https://imos.aodn.org.au/imos123/*

Australian Urban Research Infrastructure Network (AURIN): *http://aurin.org.au/*

Atlas of Living Australia (ALA): *https://www.ala.org.au/*

International Data Portals:

National Aeronautical and Space Agency (NASA): *https://data.nasa.gov* and *https://open.nasa.gov/open-data/*

European Space Agency (ESA): *https://earth.esa.int/web/guest/data-access/browse-data-products*

Japanese Aerospace Exploration Agency (JAXA): *https://gcom-w1.jaxa.jp/auth.html* *https://www.gportal.jaxa.jp/gp/top.html*

Amazon Webservices Public Datasets: *https://aws.amazon.com/public-datasets/*

Google Earth Engine Datasets: *https://earthengine.google.com/datasets/*

Legal Issues:

http://www.brill.com/evidence-earth-observation-satellites

http://www.space-evidence.net/about-us-publications-in-the-field/

http://www.ecocentric-consulting.com/our-publications/

Virtual Globes:

Butler (2006)

Australian Geoscience Data Cube:

http://www.ga.gov.au/about/what-we-do/projects/earth-observation-and-satellite-imagery/australian-geoscience-data-cube

Telecommunications:

ITU (2015)

Elert (2015)

Tracking and Relay Satellites:

http://www.nasa.gov/directorates/heo/scan/services/networks/txt_tdrs.html

Standards:

Di and Ramapriyan (2010)

GEOMS: Retscher *et al.* (2011)

Open Geospatial Consortium (OPG) Standards: *http://www.opengeospatial.org/standards*

9.6 References

ACMA (2016). *Australian Communications and Media Authority*. Retrieved from *http://www.acma.gov.au*.

Butler, D. (2006). The web-wide world. *Nature, 439*(7078), pp. 776-778. doi:*http://dx.doi.org/10.1038/439776a*.

Di, L., and Ramapriyan, H. K. (2010). *Standard-Based Data and Information Systems for Earth Observation, Lecture Notes in Geoinformation and Cartography*. Springer-Verlag, Berlin Heidelberg. doi:*http://dx.doi.org/10.1007/978-3-540-88264-0*.

Elert, G. (2015). *The Physics Hypertextbook*. Retrieved from *http://physics.info/em-spectrum/*.

Harrison, B. A., and Jupp, D. L. B. (1989). *Introduction to Remotely Sensed Data. Part ONE of the microBRIAN Resource Manual* (156 pages). CSIRO Australia, Melbourne.

IEEE (2002). *IEEE Standard Letter Designations for Radar-Frequency Bands* (IEEE Standard 521–2002). Retrieved from *http://standards.ieee.org/findstds/standard/521-2002.html*.

ITU (2015). *Nomenclature of the frequency and wavelength bands used in telecommunications* (Recommendation ITU-R V.431-8). V Series: Vocabulary and related subjects. ITU-R: Radiocommunication Sector of ITU. Retrieved from *http://www.itu.int/dms_pubrec/itu-r/rec/v/R-REC-V.431-8-201508-I!!PDF-E.pdf*.

Lewis, M. M., and White, D., (2013). *Evaluation of remote sensing approaches*. In *Allocating Water and Maintaining Springs of the Western Great Artesian Basin. Volume IV. Spatial Survey and Remote Sensing of Artesian Springs of the Western Great Artesian Basin*. (Eds: M.M. Lewis, D. White, and T.G. Gotch) National Water Commission, Canberra.

Moreno, J. (2007). *Optical Theory Basics - 2. Atmospheric corrections and parameter retrieval*. Lecture D1Lb2 in Advanced Training Course on Land Remote Sensing. ESA. Retrieved from *http://earth.esa.int/landtraining07/D1LB2-Moreno.pdf*.

Overpeck, J. T., Meehl, G. A., Bony, S., and Easterling, D. R. (2011). Climate Data Challenges in the 21st Century. *Science, 331*(6018), pp. 700-702. doi:*http://dx.doi.org/10.1126/science.1197869*.

Phinn, S.R. (1998). A Framework for Selecting Appropriate Remotely Sensed Data Dimensions For Environmental Monitoring and Management. *International Journal of Remote Sensing*, 19(17), 3457-3463.

Retscher, C., de Maziere, M., Meijer, Y., Vik, A. F., Boyd, I., Niemeijer, S., Koopman, R. M., and Bojkov, B. (2011). *The Generic Earth Observation Metadata Standard (GEOMS), Version 1.0*. Retrieved from *http://avdc.gsfc.nasa.gov/PDF/GEOMS/geoms-1.0.pdf*.

Robson, A., Rahman, M.M., Muir, J., Saint, A., Simpson, C., and Searle, C. (2016). Evaluating satellite remote sensing as a method for measuring yield variability in Avocado and Macadamia tree crops. *Proc. Australian Society of Sugar Cane Technologies 38*, 27-29 April 2016, Mackay, Queensland.

Roelfsema, C., and Phinn, S. R. (2015). *The Remote Sensing Toolkit*. Retrieved from *http://ww2.gpem.uq.edu.au/CRSSIS/tools/rstoolkit_new/index.html*

Wilczynski, P. A. (2005). *NPOESS Preparatory Project (NPP)*. Paper presented at the 14th International TOVS Study Conference, Beijing, China. *http://cimss.ssec.wisc.edu/itwg/itsc/itsc14/presentations/session5/5_2_wilczynski.pdf*.



10 Looking Ahead

Authors: Isabel Coppa, Peter Woodgate, John Le Marshall and Alex Held[16]

10.1 Brave New World

This section introduces the major developments that are likely to impact EO:

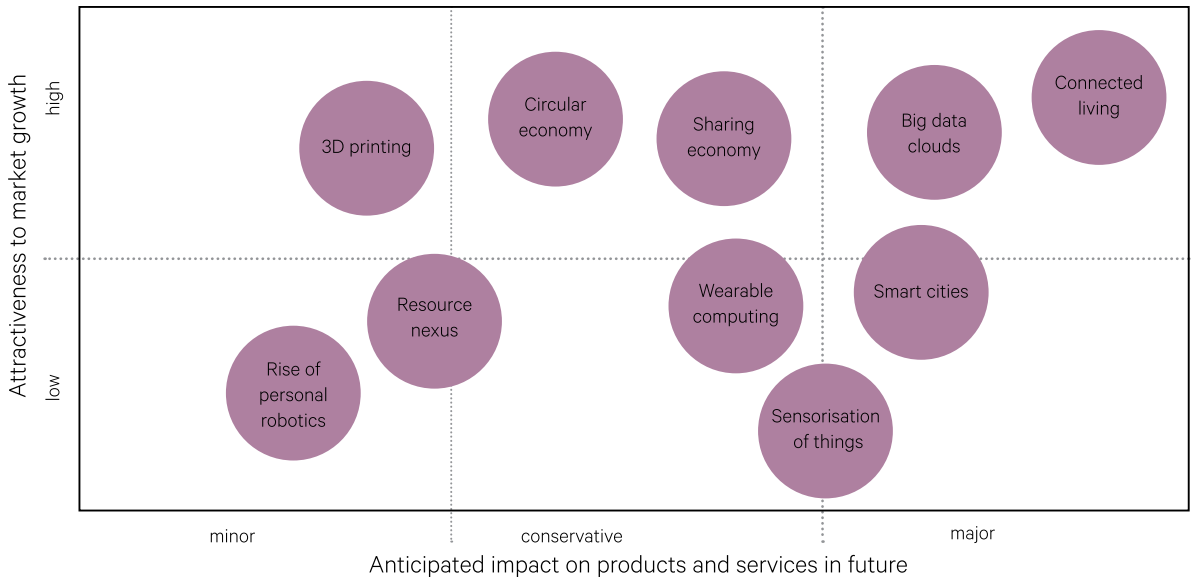
- mega trends in technology that are changing how we live and work (see Section 10.1.1); and
- internet services that are planned to reach all residents on Earth (see Section 10.1.2).

10.1.1 Mega trends

We are currently experiencing rapidly converging technologies. While a few decades ago record players, cameras, calculators, flashlights, Dictaphones, address Rolodexes, daily newspapers, televisions and telephones (just to name a few devices) were in common usage, all of these capabilities are now combined in a small smart phone. Smart phones and the internet are examples of 'disruptive technologies' with the potential to rapidly revolutionise the way we work and live. Disruptive technologies are making many well-established industries obsolete almost overnight. For example, Figure 10.1 shows areas of projected game-changing technologies, and their likely growth and impact on future products and services.

Figure 10.1 Top ten transformational shifts by 2020

'Connected Living' is the most significant trend, supported by convergence.



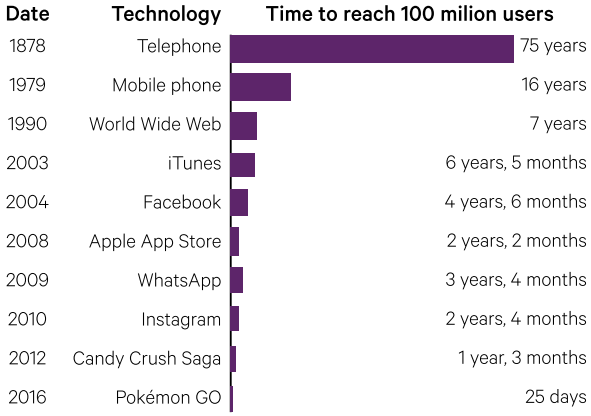
Adapted from: Jawad (2014)

Background image: Dreamstime stock photo: *http://www.dreamstime.com/stock-illustration-man-futuristic-d-glasses-sensors-people-technology-future-progress-microchip-implant-over-blue-background-image56098520*

16. Recommended Chapter Citation: Coppa, I., Woodgate, P. Le Marshall, J., and Held, A.A. (2017) *Looking Ahead. Ch 10 in Volume 1B of Earth Observation: Data, Processing and Applications.* CRCSI, Melbourne.

Figure 10.2 Exponential pace of disruptive technologies

Compared with inventions launched nearly 150 years ago, today's innovations reach millions of users significantly more quickly. Original sources in footnote.



Adapted from: Dreischmeier *et al.* (2015)[17]

Looking at history, the pace of disruption has increased exponentially (Dreischmeier *et al.*, 2015). While it took the telephone 75 years to reach 100 million users worldwide (starting in 1878), Instagram took less than two and a half years to reach the same size audience (by 2010), and in 2016 the location-enabled game 'Pokemon Go' achieved the same number of users in just 25 days (see Figure 10.2). Technological advances and adoption take place at a staggering speed; however, ethical research and legal frameworks are lagging behind, and systematic efforts, often demanding global collaboration, are needed to catch up with technological capabilities (see Section 10.4.3).

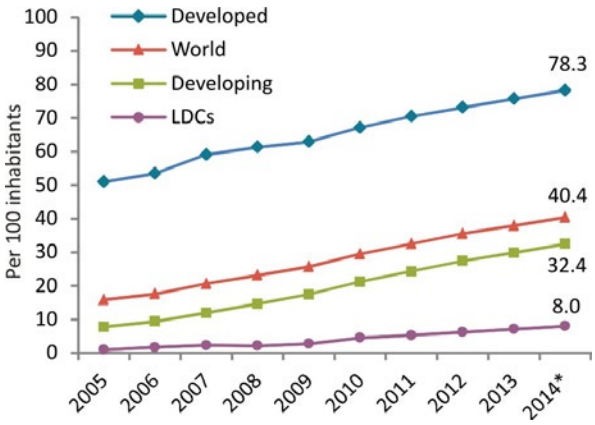
10.1.2 Internet services

Internet connectivity is becoming increasingly important for IoT (Internet of Things)/M2M (machine to machine) communications. Of the almost 7.5 billion residents on Earth, nearly half (3.4 billion) are connected to the Internet today (see Figure 10.3). The current, keen competition between industry giants to connect all global residents to the internet (and widen their customer base) has been aptly called the 'second' Space Race. The average mobile user data cost decreased 99% between 2005 and 2013, while mobile data transmission speeds have skyrocketed—4G networks now being 12,000 times faster than 2G networks (Bezerra *et al.*, 2015). Similarly, the volume of data downloaded via the internet continues to grow rapidly, with 53% growth in data traffic reported for the 12 months between the first quarter of 2014 and the first quarter of 2015 (Ericsson, 2015).

The global telecommunication industry has declared connecting the remaining world's population to the Internet to be one of the most urgent issues (and opportunities). The major focus is on the continent of Africa, with a population of 1.1 billion people. Since traditional Internet delivery, such as laying underground fibre cables, is often impractical and expensive, satellite broadband seems to be the preferred option. Big names, and large companies (such as Facebook, Avanti, Google, O3B, SpaceX, OneWeb) are participating in this 'second space race'. Connection options range from solar-powered Remotely Piloted Aircraft Systems (RPAS), satellite consortia, to helium balloons (Coppa *et al.*, 2016). Satellite phones provide (slow) internet connection where conventional networks are not available and, like other technologies, are becoming smaller, faster and cheaper and even modular (e.g. Iridium Go).

Figure 10.3 Global internet access

Globally, the percentage of individuals using the Internet has more than doubled in the last decade. (LDC = Least Developed Countries)



Source: ITU (2014)

10.2 The Internet of Things

The number one Mega Trend is considered to be 'connected living' (see Figure 1), a concept defined by connectivity and convergence. Jawad (2014) defines connected living as: *A world in which consumers use many different devices to experience compelling new services, that integrate video, voice and data services to provide access and ubiquitous connectivity anytime and anywhere.*

17. Original sources: ITU; Statista; BCG research. Telephone: ITU; Mobile phone: ITU (base year considered as start of first cellular network), mobilephonehistory.co.uk; World Wide Web: Scientific American, Internet Live Stats; iTunes: number of accounts, Fortune; Facebook: active monthly users, Facebook; Apple App Store: number of accounts, OS X Daily, VentureBeat; WhatsApp: active users, Wired, Digital Quarterly; Instagram: monthly users, TechCrunch; Candy Crush Saga: Facebook users only, AppMtr.com; Pokémon Go: Perez (2016).

Table 10.1 Connected living

	Home	Work	City
% connected living total market	31	15	54
Specific areas of impact	automation energy health entertainment	mobile communications, mobile working, enterprise social networking	eGovernance, ecitizens, Smart transportation, elearning, mobile banking

Adapted from: Jawad (2014)

Three important aspects of connected living are 'home', 'work', and 'city' (see Table 10.1).

The Internet of Things (IoT) connects devices, people, processes and data in an integrated global network. It is anticipated that, by 2020, the Internet of Things will comprise more than 50 billion interconnected devices—each of which may comprise multiple sensors—effectively creating a trillion sensor ecosystem (LeHong and Velosa, 2014). In effect it will be possible to build a 'Planetary Nervous System' that will assist individual decision-making, enable self-organizing 'smart' systems and create a collective intelligence (Helbing, 2014). However, to achieve an economy of scale and interworking of the IoT, interoperable global standards are absolutely essential (Vermesan and Friess, 2013).

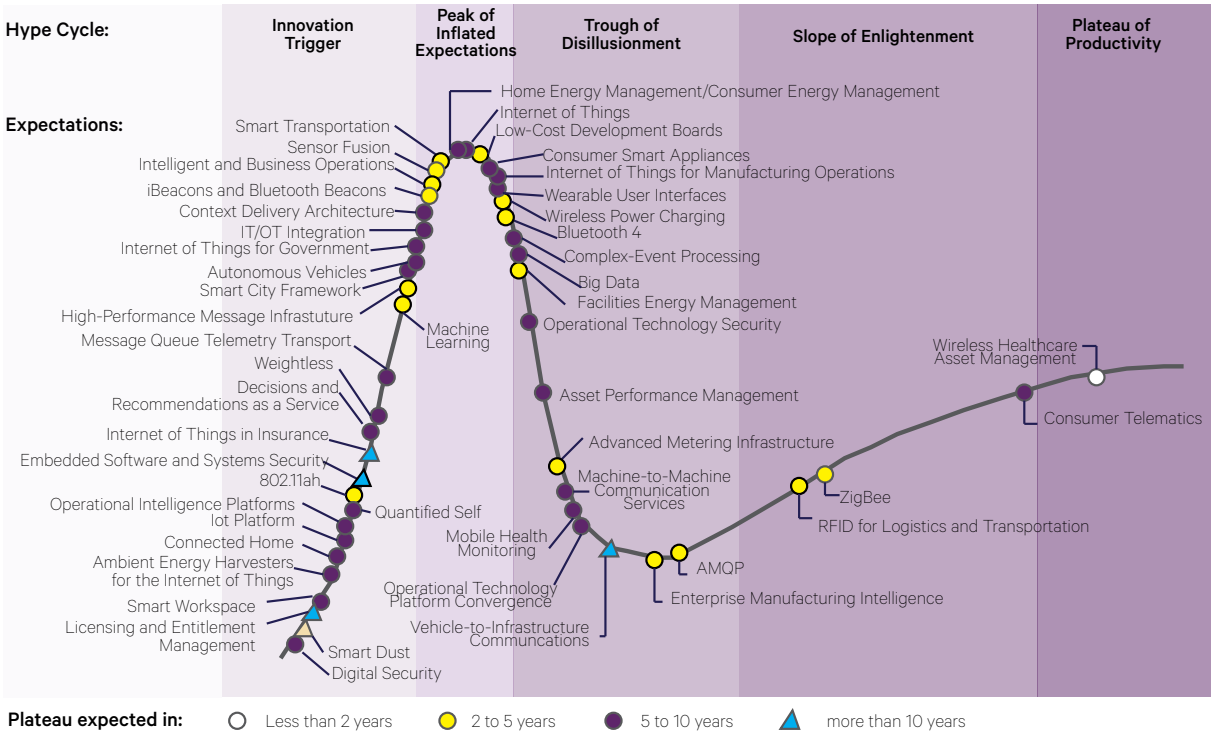
It is difficult to say what is impossible,
for the dream of yesterday is the hope of today
and the reality of tomorrow.
(Robert Hutchings Goddard)

This market has been estimated to be worth US $19 trillion[18] over the next 10 years, with about 75% of investments being in the private sector and about 25% in the public sector (created by initiatives such as smart cities and infrastructure; LeHong and Velosa, 2014). Current implementations of the IoT are reporting an average of 28% in cost savings and productivity and efficiency gains of 29% (Telsyte, 2015). Over a third of organisations that have implemented IoT report that revenues have risen by an average of 33% after deployment, this increase being attributed to improved and accelerated decision-making, and better customer service (Telsyte, 2015).

Figure 10.4 shows the 'Hype Cycle'—from innovation triggers to the plateau of productivity—for a variety of applications using the IoT. As can be seen, most IoT applications are at an early stage and many are not yet fully commercially. However, the IoT is expected to develop rapidly over the next few years, with rates of adoption that may surprise many observers.

Figure 10.4 Hype cycle for applications using the Internet of Thing

In July 2014, the Internet of Things reached maximum position in Gartner's hype cycle for new technologies.



Adapted from: Gartner (2014)

18. 1 trillion = 1 million × 1 million

10.2.1 Wearable technology and implants

Embedded sensors in 'wearable' devices typically measure parameters relevant to the fitness, medical and security sectors. One example of wearable technologies is a wristband to track human activity (from a range of manufacturers, including Jawbone UP, Fitbit, or Garmin). The variety of wearable technologies on the market is so extensive that a database of options is maintained (Vandrico, 2016). Sensor data are usually uploaded via smartphone to the Cloud for analysis, and results are communicated via smart phone display. The majority of surveyed experts (Anderson and Rainie, 2014) expect a widespread and beneficial effect of wearable sensors to the general public by 2025; it is thought that wearable connected devices will become less visible, even 'unobtrusive to the naked eye' (LeHong and Velosa, 2014) or embedded as implants (Anderson and Rainie, 2014).

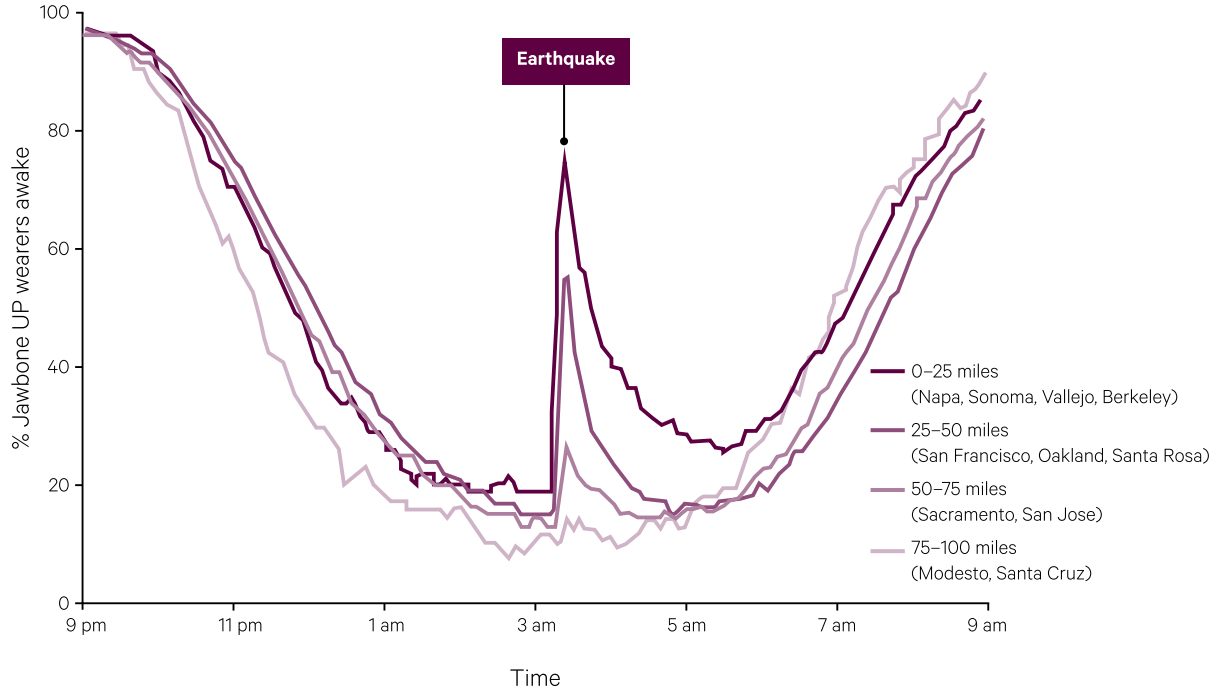
Computers in the future may weigh no more than 1.5 tons (Popular Mechanics, 1949)

This expected advance is aligned with developments in the health care industry. Medical companies envision implantable devices will shift medicine from reactive, symptom-based diagnosis, to proactive, early detection and prevention (Strickland, 2014). Examples include monitoring blood sugar levels using a 'smart contact lens' and smart contact lenses with build-in cameras, which naturally follows the wearer's gaze. Future applications of such technology could include being part of a bionic eye system for the blind, or providing 'superhuman' powers, such as night vision, infrared vision, digital zoom, and/or colliding object alerts.

Wearable technology is already monitoring incidents for which it was never designed. For example, at 3:20 am on 24 August 2014, a 6.0 earthquake hit the Southern Napa Valley in California. In cities less than 15 miles from the epicentre, 93% of people wearing the Jawbone Up fitness monitor suddenly woke up—45% of whom did not go back to sleep that night. As can be seen in Figure 10.5, the location of the earthquake epicentre and areas where the earthquake could be felt can be mapped by its impact on the sleep of monitor wearers (Mandel, 2014). In effect the wearable fitness monitor turned into a 'perceived earthquake intensity' sensor, and collective data could be used to create a map of the disturbance.

Figure 10.5 Distance to earthquake epicentre indicated by wearable devices

Wearable devices assist seismic Earth Observations after a 6.0 earthquake occurred in Southern Napa Valley, California at 3:20 am on 24 August 2014. As distance from the epicentre increased, fewer wearers of the Jawbone Up fitness monitor were woken from sleep.



Adapted from: Mandel (2014) at *https://jawbone.com/blog/napa-earthquake-effect-on-sleep/*

Such involuntarily crowdsourced maps, by-products of wearable technology big data sets, offer amazing new methods for EO. However, they also raise the concern about data privacy. Android Apps frequently track and share location information about users (subject to the App used, approximately every three minutes, Storm, 2015) leading to growing concerns over the implications of location data being shared unknowingly via social media posts. To provide greater protection for individual privacy, calls are being made for a code of ethics to guide the use of personal information with a location component (Barrett *et al*., 2013; Carpenter and Snell, 2013).

10.2.2 Brain-machine interfaces

Another major change in how we operate as humans and as a society is on the horizon, namely connecting brains together with sophisticated developments in brain-machine interfaces. These developments are fuelled by advanced understanding of the brain, the use of transcranial magnetic stimulations, or optogenetically enhanced cells (Grau *et al*., 2014; Hewitt, 2014).

Researchers reported successful conscious communication between two humans via the Internet, enabling telepathy via a computer-to-brain interface (Grau *et al*., 2014). It is anticipated that in the not too distant future machines will routinely communicate directly and fluently with brains. This could change many aspects of life, such as:

- thought-controlled planes and possibly missiles, as was demonstrated (in a flight simulator) by TU Munich and TU Berlin;
- with the App 'MindRDR', Google Glass, together with a Neurosky Mindwave sensor (EEG monitor) allows people to take photos using pure thought (brain signals) and to post them on social media;
- 'Braingate', an implant to wirelessly connect the brains of paralysed people with computers, offers the potential to move robotic arms and wheelchairs. Open robotic platforms (such as ROS), together with off-the-shelf modular robotic hardware, are dramatically accelerating these developments and allowing customised applications (Woodgate *et al*., 2014); or
- the first bionic eye has been fitted to a sufferer of one of the most common forms of blindness, Age-related Macular Degeneration (AMD). Using this technology, video images are beamed directly to the brain, bypassing damaged photoreceptors in his eyes. The success of this trial offers hope to millions of other patients with this condition.

10.2.3 Thinking machines

Expectations are that, in the near future, machines will know more and think faster than humans. Cognitive computing, using big analytics engines, is forecast to reshape the world we know and the way we live and work in entirely unexpected and unprecedented ways. Futurist Kurzweil predicts that by 2020 smartphones might rival the human mind in terms of storage and processing capability, although it is likely that it will take until 2029 for 'brain software' to be completely functional.

However, concern has been voiced by a large group of thinkers and innovators saying that artificial intelligence (AI) could become an existential threat to humans, although possibly not for several decades. An open letter of concern has been signed by many well-known personalities in the field (Future of Life Institute, 2016) asking for focus on research priorities that ensure AI systems be robust and beneficial (Russell *et al*., 2015).

Cognitive computing is the most significant disruption in the evolution of computing since the advent of the Internet. It helps extract patterns and insights from data sources that are almost totally opaque today, what is sometimes known as 'dark data'. Examples include extracting disease insights from healthcare records and social feeds, or finding financial fraud or opportunities from discrete geopolitical, social, and business events.
(Manoj Saxena, former IBM Watson project lead)

10.3 Location, Location, Location

From 2015 to 2019 the global real-time location system market is expected to grow at a Compound Annual Growth Rate (CAGR) of 37.41% (Technavio, 2015). In the USA alone, the Global Positioning System (GPS) conservatively contributed around $68 billion to the economy in 2013, comprising (Divis, 2015b):

- about 38 % related to vehicle location services;
- 20 % for precision farming;
- 18 % for fleet vehicle telematics;
- 17% for surveying; and
- 7 % for GPS-based guidance of earth moving equipment.

10.3.1 Accuracy

Integration of JAXA QZSS GNSS signals with the US GPS system has improved positioning accuracy to around 5 cm, which enables remote robot tractor operation (Chester, 2015). Signal augmentation of multiple GNSS systems shows promise to further boost location accuracy. Apart from GPS, alternative GNSS systems are operated by several nations (see Table 10.2).

While national space-based Positioning, Navigation and Timing (PNT) is deemed a critical infrastructure by the US Department of Homeland Security, the GPS constellation is not (Divis, 2015a). The Defence Advanced Research Projects Agency (DARPA), with its Spatial, Temporal and Orientation Information in Contested environments program (STOIC), is working on a brand new global PNT system that is resistant to jamming and does not depend on satellites. Using miniaturization, quantum physics, and pulsed lasers, they are looking at novel inertial measurement devices with cold-atom interferometry and affordable chip scale self-calibrating devices (including gyroscopes, accelerometers, and clocks; Lendino, 2015).

An Australian innovation by Locata has the potential to replace or augment GNSS signals and overcome the challenge posed by signal loss in both indoor and urban environments, and deep open-cut mines, as well as both intended and unintended RFI (Radio Frequency Interference). The Locata synchronized transceivers form a network that enables single point positioning to centimetre accuracy using phase measurements without using differential techniques (Rizos, 2013; Rizos *et al*., 2014). Locata's V-Ray antenna has been tested at US White Sands Missile Range and delivered location information with 6 cm horizontal, and 15 cm vertical accuracy to an aircraft flying at 25,000 ft altitude and at speeds of 550 mph (Locata, 2013). Consequently, Locata has been selected as the core positioning technology for UAV research at the NASA Langley Research Center in Hampton, Virginia (Wallace, 2015a). As listed in Table 10.3, the accuracies achieved are far superior to traditional location methods.

Table 10.2 Overview of GNSS/ RNSS systems

Note that some constellations were not complete when this table was compiled.

System	Owner	Coding	Constellation Size	Frequencies
GPS	United States	CDMA	32 (at least 24 by design)	1.57542 GHz (L1 signal) 1.2276 GHz (L2 signal)
GLONASS	Russian Federation	FDMA/CDMA	28 (at least 24 by design)	Around 1.602 GHz (SP) Around 1.246 GHz (SP)
BeiDou	China	CDMA	35 (5 GEO, 30 MEO)	1.561098 GHz (B1) 1.20714 GHz (B2) 1.26852 GHz (B3)
Galileo	European Union	CDMA	30	1.164–1.215 GHz (E5a and E5b) 1.260–1.300 GHz (E6) 1.559–1.592 GHz (E2-L1-E11)
NAVIC	India	CDMA	7	1,176.45 MHz (L5) 2,492.028 MHz (SPS)
QZSS	Japan	CDMA	4 (7 in future)	L1 (1575.42 MHz) L2 (1227.6 MHz) L5 (1176.45 MHz) LEX (1278.75 MHz) compatible with E6

Source: ICG (2010); GPS (2016); IACPNT (2016); UCS (2016)

Table 10.3 Spatial accuracies with established methods

Location Method	Example System	Accuracy (m)
Network-based	Cell ID	200–5000
	Cell Tower Triangulation	50–1000
GNSS	GPS	10-20
Wifi	Hotspot triangulation/'Fingerprinting'	3–10 20–50
Beacons	Bluetooth Low Energy (BLE)	3–50

Adapted from: Buczkowski (2012)

10.3.2 Location-based services

LBS (Location Based Services) use location-enabled devices to track users and determine visitor patterns, and many developers are working on innovative ways to use this information. For example, Google introduced 'visit monitoring', a feature that collects information about places visited in the day-to-day life of users. Mobile advertising is a driving force behind this research, with studies showing that LBS yield vastly superior sales results compared with advertising via non-mobile devices such as desktop computers (Urbanski, 2015). In 2016, advertisers in the USA are expected to more than double their spending—to over $40 billion—to reach mobile users via phones, tablets etc. This follows the strong trend towards using mobile devices (in 2014 *en par* with desktop and laptop usage time). LBS is expected to grow significantly and enable much more targeted advertising campaigns (Telsyte, 2015).

Apart from advertising, the current LBS market includes tracking, navigation (indoor and outdoor), infotainment, analytics, recreation and fitness (Technavio, 2015). For example, one form of LBS is geo-fencing, which relies on GPS and/or local radio frequency networks to create virtual boundaries around a defined location. This technology can be used for a variety of purposes, such as:

- retailers could notify potential, nearby shoppers of transient bargains and local events;
- users could set location-aware triggers to be reminded when they are in the vicinity of something on their 'to do' list;
- appropriate sensors could automatically turn off security systems and/or turn on lights when you arrive home;
- companies could track their vehicle movements away from a defined zone; or
- livestock managers could be alerted if animal herds moved away from their designed area.

It is predicted that 400 million BLE (Bluetooth Low Energy) beacons will be shipped by 2020 (ABI Research, 2015a). Many large-scale installations (comprising thousands of beacons) are already completed.

LBS are essential for enabling the Internet of Things (IoT), giving everyday objects location-smarts with enterprise grade stickers and beacons. The M8 motion coprocessor since iPhone 6 includes a barometer (in addition to its compass, gyroscope and accelerometer), which senses air pressure to a degree of accuracy that enables a phone to be located at a specific building floor level. Many other technologies, such as WifiSLAM, are making ubiquitous indoor navigation a reality.

10.3.3 National Positioning Infrastructure

Positioning technologies have become an assumed, but essential, component of both traditional and innovative enterprises worldwide. GNSS techologies have revolutionised navigation and positioning methods (see Section 10.3.1). In all weather conditions (other than severe space weather), they continuously deliver accurate information on three-dimensional position, velocity of travel, and time, for users on land, on the sea and in the air.

The value of accurate positioning information is especially valuable in a sparsely populated country like Australia, and we are fortunate to be one of the countries positioned to receive signals from all GNSS satellite systems (see Table 10.2). The increasing accuracy, however, necessitates changes to traditional mapping methods. The National Positioning Infrastructure (NPI) project, led by Geoscience Australia, will ensure a seamless transition from traditional mapping frameworks to the opportunities that will be accessible with future positioning systems. The background and scope of this project are summarised in Excursus 10.1.

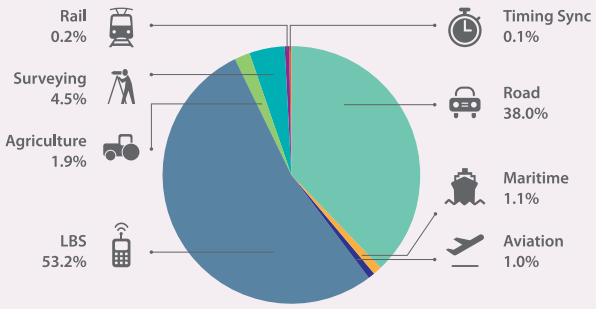
Excursus 10.1—A Modern Reference Frame for Australia

Source: Daniel Jaksa, Geoscience Australia
Further information: Geoscience Australia: *http://www.ga.gov.au/scientific-topics/positioning-navigation/national-positioning-infrastructure*. ICSM: *http://www.icsm.gov.au/gda2020/*

Once only the domain of experienced navigators, surveyors and mappers, the ability for anyone to simply and quickly determine precise position is fast becoming a reality. Aided by Australia's National Positioning Infrastructure, along with the rapid uptake of smartphones with built-in Global Navigation Satellite Systems (GNSS), users will be able to position features in Australia's built and natural environment to within 3 cm by the year 2020. The projected economic value of accurate positioning capabilities to a variety of GNSS users is summarised in Figure 10.6.

Figure 10.6 Summary of GNSS users.

Expected Cumulative Core Revenue of GNSS chipsets from 2013 to 2023 are shown.



Source: European GNSS Agency (2015). Retrieved from: *http://www.gsa.europa.eu/market/market-report*

Looking back

A horizontal datum is used to provide a coherent geometric structure to spatial information and is the basis for coordinate reference systems used in surveying and mapping. They define the physical location of where to place the geographic graticule and map grid on paper and digital maps. It gives rise to defining the geographic coordinates of features and hence the distances and directions between them. Similarly, a vertical datum allows for the change in height between features to be determined and supports the development of digital elevation models. Where a common datum is used, all spatially-referenced data can be confidently integrated, thus broadening the application and utility of various datasets.

In Australia the first national horizontal datum was the Australian Geodetic Datum of 1966 (AGD66) and used the Australian National Spheroid for geodetic computations. It was based on coordinates derived from classical triangulation, traversing and astrogeodetic and aero observations. The final coordinates were obtained from a national least squares adjustment of azimuths and distances holding the coordinate of the Johnston Geodetic Station in the centre of the country fixed. With advances in aero and space-based geodetic techniques, such as Doppler satellite measurements, Very Long Baseline Interferometry and Satellite Laser Ranging during the 1970's and early 1980's, a further refinement to the datum was made with the release of the Australian Geodetic Datum of 1984 (AGD84).

With the introduction of the Global Positioning System by the United States Air Force from the late 1970's, Australia's map makers were under pressure to move to an Earth-centred, geocentric system used by GPS. This required moving away from the Australian National Spheroid and onto the more internationally accepted reference ellipsoid, the Geodetic Reference System 1980 (GRS80). GRS80 was adopted at the XVII General Assembly of the International Union of Geodesy and Geophysics in Canberra, Australia in 1979. The new Geocentric Datum of Australia 1994 (GDA94) was thus realised by fixing the coordinates of 21 Australian Fiducial Network geodetic stations referred to the GRS80 ellipsoid determined within the International Terrestrial Reference Frame 1992 at the epoch 1994.0.

Looking ahead

GDA94 and all past Australian horizontal datums can be described as *plate-fixed*, where the coordinates that define points in Australia remain the same over time, regardless of Australia's tectonic plate movement of about 7 cm per year to the north-north-east. The horizontal datum used by GNSS devices are described as *Earth-fixed*, where coordinates can change over time and recognises tectonic movements. Consequently, if 3 cm global positions are to be achieved, the horizontal datum used to reference location by defining geographic coordinates will need to take account of the movement of the Earth's tectonic plates.

Recognising the growing need for positioning information that is readily accessible, reliable and interoperable for every user, not just the spatially literate, the Australian Government is leading the development of a National Positioning Infrastructure (NPI) Capability. The NPI Capability has the objective to provide instantaneous, reliable and fit-for-purpose positioning and timing services anywhere, anytime across the Australian landscape and its maritime jurisdictions. This is addressing the need for infrastructure, data access and good governance to improve datum accuracy and accessibility. The spatial community, in partnership with a growing user base from non-spatial sectors, are key stakeholders that can support and champion the benefits of producing and implementing position, navigation and timing data connected to Australia's NPI.

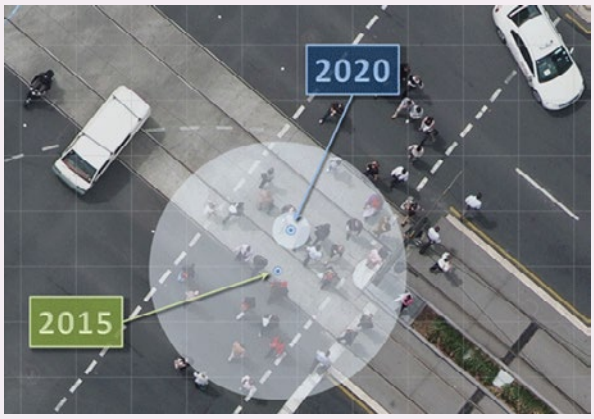
To assist in the transition to a modern Australian horizontal datum, a two-stage approach is planned:

- Stage 1 will deliver a new and more homogenous conventional plate-fixed datum with the defining coordinates projected forward to a reference date of 1 January 2020. The new datum will be known as GDA2020.
- In Stage 2, a time-dependent reference frame will commence implementation in January 2020, and nominally conclude in 2023. It will be an Earth-fixed system and highly accurate with respect to international systems utilised by GNSS, meaning Australian spatial information and GNSS measurements will be directly interoperable.

GDA2020 will continue to operate in conjunction with the time-dependent reference frame until it is no longer required. The datum shift of 1.8 m and the positional accuracy available in 2015 and expected in 2020 are compared in Figure 10.7.

Figure 10.7 Datum shift and positional accuracy comparison

Comparison of the datum shift of 1.8 metres and the positional accuracy available in 2015 (larger circle) compared with that expected in 2020 (smaller circle). The background image is a very high resolution aerial photo of Adelaide at 25 mm taken in March 2009.



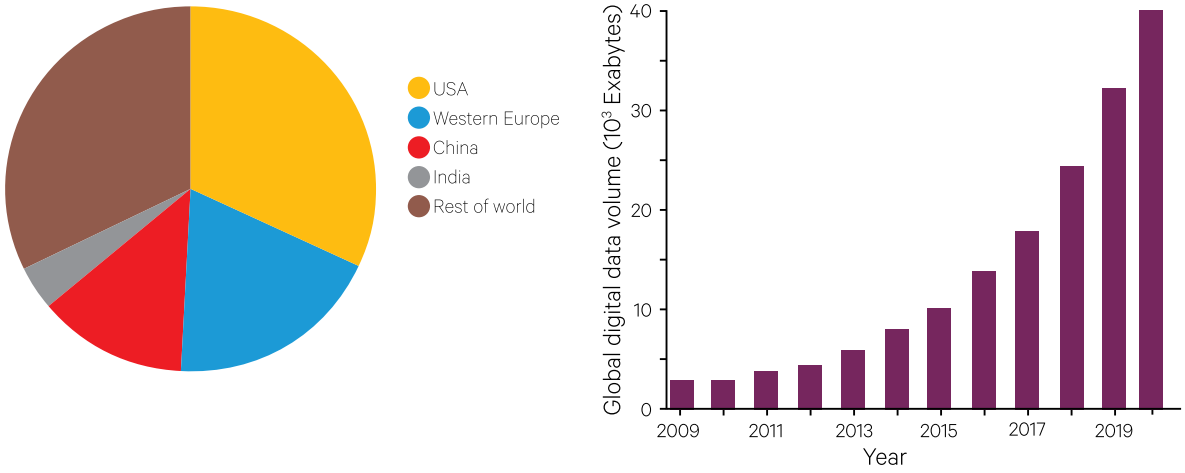
Source: Background image courtesy of Aerometrex Pty Ltd. Used with permission.

10.4 The Data Deluge

Figure 10.8 Projected growth of the digital universe from 2010 to 2020

a. There has been a 50-fold growth in the digital world during the decade from 2010 to 2020.

b. Global distribution of the digital universe in 2012 is shown.



Adapted from: McLellan (2013)

A data deluge is rising on Planet Earth. This decade alone a 50-fold growth in data is expected to reach a global volume of 40,000 EB (exabytes) by 2020 (Figure 10.8). Western civilisations dominated the creation and use of digital data but it is now expected that Asia will assume the dominate position (McLellan, 2013) so that by 2020 the emerging markets will account for 62% of the digital Universe (China alone being 21%). It is estimated that 60 to 80% of this data will have a spatial component (Dempsey, 2012).

10.4.1 Open data

Governments have realized the value of open data, and are actively pursuing ways to enable easy access (Department of the Prime Minister and Cabinet, 2015). In this ongoing trend of opening up data to the public, the massive archive of Landsat satellite imagery (including atmospherically-corrected imagery) is now freely available, with these datasets being supported by a number of private concerns such as Amazon S3, Mapbox and Planetlabs (see Figure 10.9). Several Australian states have reported a steady increase in geospatial data requests via their open Globe platforms, with as many as 200 million hits per month in Queensland (Coppa *et al*., 2016).

A key component of improved data access for EO imagery is the compilation of different datasets into a 'sensor-agnostic' grid (see Section 9 and Volume 2A). The Australia Geoscience Data Cube (AGDC) was developed as a collaborative project between Geoscience Australia, CSIRO, and NCI (AGDC, 2016). AGDCv2 carefully massages decades of image data from Landsat satellites and imagery from the MODIS sensors onto a common geometric and radiometric framework. This enormous data cube simplifies access to big data sets from disparate sources and enables systematic analyses of continental changes over time. The AGDCv2 is a working prototype of a framework for large-scale multidimensional data management for geoscientific data.

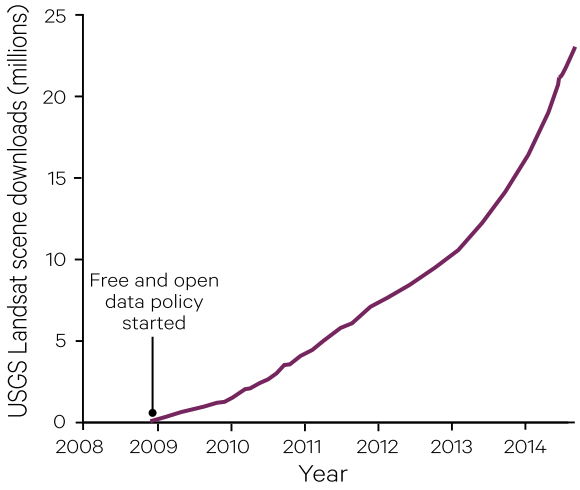
Google Earth Engine allows users to utilize cloud storage and computing: it is a planetary scale platform to analyze 40 years of EO datasets. Earth Engine gives easy access to the Landsat satellite archives, MODIS datasets, Sentinel-1 data, precipitation data, elevation data, sea surface temperature, NAIP, and CHIRPS climate data (Google, 2016).

With over 100 government programs and hundreds of researchers, Australia is globally one of the largest users of EO data (Wallace, 2015b). It is therefore imperative to adequately plan for sufficient funding to build robust data infrastructures in Australia that can handle the upcoming deluge of spatial data, especially from satellites.

The rapid growth in public-good and commercial EO systems, plus the increasing variety of sensors and associated data volumes, provides more opportunities to the remote sensing research community, however it is also posing major problems to developing countries trying to access and use such data to map and monitor their environments, or to fulfil international treaty obligations. The AGDC technology aims to help in part overcome such challenges by providing open access to large 'stacks' of pre-processed 'analysis-ready data' via regional data cubes that are being implemented through CEOS (see Section 10.6.2).

Figure 10.9 Landsat downloads since open data policy

Cumulative Landsat scenes downloaded from USGS EROS Centre since the advent of the public good data policy.



Source: USGS

10.4.2 Crowdsourcing

Crowdsourced information from the public—very often with a spatial component—has also become an important source of information, particularly for crisis management. For example, the earthquake in Nepal in April 2015 demonstrated the usefulness of geospatial tools for emergency management. A global network of IT volunteers (or 'digital humanitarians') assisted with vital information to help emergency workers on the ground, including:

- information gleaned from Twitter tweets with embedded locational data, or accumulated by active crowd volunteering on relevant platforms (such as Tomnod, and the Humanitarian Open Street Map Team: HOT);
- Mapbox helped with information on road conditions, and building damage analysis;
- Shakeslide (University of Cardiff) mapped landslide risks;
- ESRI offered smart maps to visualize impact maps; and
- Facebook and Google helped with locating loved ones in the crisis region.

In Australia, volunteer GIS professionals are coordinated by the Mapping and Planning Support (MAPS) group to support emergency services organisations during emergencies (MAPS, 2016). Tools for remote mapping efforts have increased in sophistication in recent years. Since Cyclone Pam (Vanuatu, March 2015) RPAS were added to the mapping toolkit box since oblique (off-nadir) imagery from RPAS provides better assessment of damage than traditional nadir-viewing satellite imagery (see Section 3). The Red Cross flagged the need to map the entire globe prior to disasters, and launched the 'Missing Maps' project in the fall of 2014.

10.4.3 Secure data usage

A 2014 study by the US President's National Security Telecommunications Advisory Committee gives a three to five year window to adopt the IoT in such a way that maximizes security and minimizes risk. Failure to do so will see the country dealing with the consequences for generations (NSTAC, 2014). For example, it is conceivable to hack wireless medical equipment like insulin pumps and pacemakers. Sitting on a sofa several kilometres away, hackers took control of a moving car and crashed it into a ditch (Curtis, 2015). Similarly, a hacker overwrote code on a large commercial aeroplane's thrust management computer via the inflight entertainment system, which made the plane climb and briefly change course (Zetter, 2015). The hacker, a security researcher with One World Labs, reported on his 'experiment' at a conference and was subsequently interviewed by the FBI (Hurley, 2015).

The conflict between security needs and privacy rights will not go away, but is likely to intensify in the near future as citizens become more and more aware of what technology and analytics can do. Data about individuals are being collected and meshed together at unprecedented rates. As the IoT advances, connected devices, such as smart watches, often 'invisible' (in clothing or implants), will collect massive amounts of personal data. As an example, if data collected by sensors on acute stress levels in individuals could be hacked, it might give unfair advantage to one party during sensitive business negotiations. Some experts consider that no data is truely secure, and the potential misuse of data collected by wearable technology could be 'terrifying'. The average user has no idea which organization collects what data and how the data are used, as it is typically too confusing and time-consuming to view this information. Data are often hosted internationally and privacy laws vary vastly within different jurisdictions. A public debate on this topic is needed and globally enforceable laws are one useful option.

10.5 Integrated 'Smart' Systems

In the near future it is envisioned that the integrated global internet of things (IoT) network will be feeding 'big data' into advanced analytics to create actionable intelligence with predictive algorithms to program automated 'smart' systems with improved efficiencies. In this scenario, ubiquitous cameras, scanners, and sensors will feed smart systems in every sphere of life—cities, energy, transport, agriculture, natural resource management, health and more will benefit from integrated smart systems. Sensor data and smart algorithms will merge to create the most futuristic applications (see Figure 10.10).

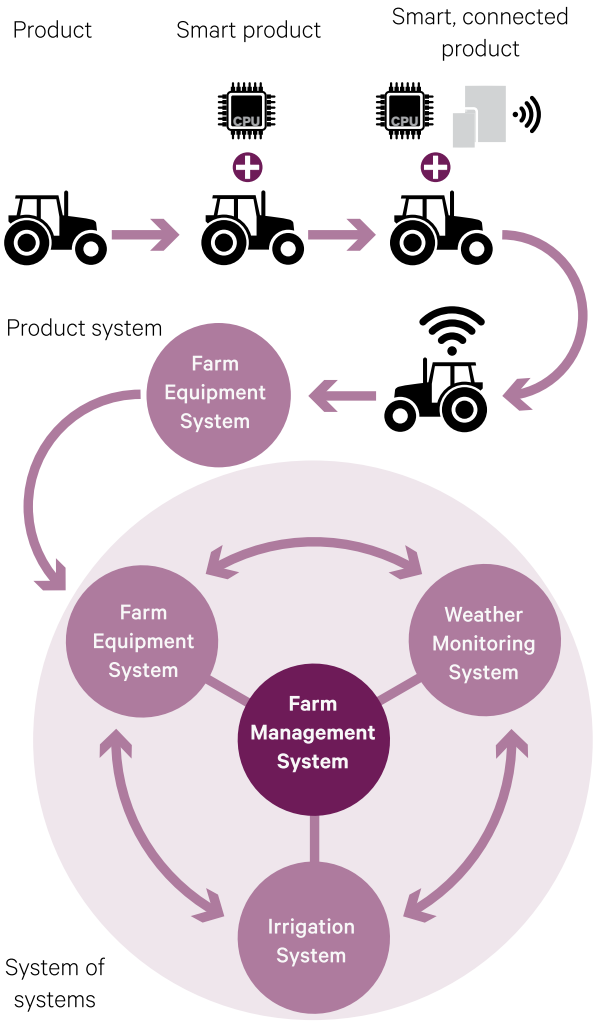
There is also a convergence in systems that manipulate spatial data, such as Building Information Modelling (BIM), Computer Aided Design (CAD) and Geographic Information Systems (GIS), allowing seamless transition from the outdoor virtual world to indoor virtual models. Seamless models give greater interoperability, broader access, and integrated data and tools. Standards and consolidated systems are important for both virtual and augmented-reality visualisations of spatial data.

A national program of built and natural environment 3D modelling is underway by the PSMA (Public Sector Mapping Agencies) Australia Ltd. Intended to cover the whole of Australia, all buildings, trees, roads, natural land cover and water bodies will be mapped and then updated periodically. Buildings will be captured at accuracies as good as 1 m. The data will be linked to property address and cadastre. High resolution satellite imagery will be one of the input datasets.

Access to EO datasets are being streamlined by integrated systems such the Global Earth Observation System of Systems (GEOSS), which is being developed by the intergovernmental Group on Earth Observation (GEO; see Excursus 10.2). GEO membership currently includes 102 nations, the European Commission (EC) and 108 participating international organisations with a mandate in EO.

Figure 10.10 System of System solutions for IoT

An example of a 'smart' system for agriculture shows the incremental integraton of technology to assist farming. Starting with a tractor, the addition of computer control creates a smart product. Wireless control of smart equipment delivers a smart, connected product. The integration of multiple smart, connected products, such as harvesters, tillers and planters, produces a farm equipment system. Similar integration applied to other farm inputs, such as weather data and irrigation, results in a farm management system.



Adapted from: Porter and Heppelmann (2014)

Excursus 10.2—GEOSS

Source: *http://www.earthobservations.org/geoss.php*

A central part of the mission for the Group on Earth Observation (GEO) is to build the Global Earth Observation System of Systems (GEOSS; see Volume 1A—Section 1.5.1). GEOSS is a set of coordinated, independent systems that interact and provide access to diverse information for a broad range of users in both public and private sectors. GEOSS links EO, information and processing systems for improved monitoring of Earth by:

- facilitating the sharing of environmental data and information collected from the large array of observing systems that have been contributed by countries and organizations within GEO; and
- ensuring that these data are accessible, of identified quality and provenance, and interoperable to support the development of tools and the delivery of information services.

This framework:

- provides access to data, information and knowledge to a wide variety of users;
- increases our understanding of Earth processes;
- enhances predictive capabilities that underpin sound decision-making;
- supports the need for the development of new systems where gaps currently exist; and
- promotes common technical standards so that data from the thousands of different instruments can be combined into coherent data sets.

The *GEOSS Portal* offers a single internet access point for users seeking data, imagery and analytical software packages relevant to all parts of the globe. It connects users to existing databases and portals, and provides reliable, up-to-date and user-friendly information, which is vital for the work of decision makers, planners and emergency managers. For users with limited or no access to the internet, similar information is available via the 'GEONETCast' network of telecommunication satellites.

10.5.1 Globes and digital Earth

The role of globes was foreshadowed by Al Gore in his 1998 speech on virtual globes predicting the world's citizens would one day be able to interact with virtual globes depicting scientific and cultural information (Goodchild *et al.*, 2012). Globe technologies include Google Earth, Bing Maps 3D Platform, Cesium (AGI), Bhuvan 3D (India), QLD Cube Globe, NASA World Wind, WebGL Earth 2 (Klokan Technologies), Marble (KDE), Skyline Globe, ESRI ArcGlobe, EV Globe, SuperMap GIS, Digital Earth Science Platform, and osgEarth (Keysers, 2015). The potential of free access and exchange of spatial information, and the spatial visualisation thereof, was demonstrated with the Queensland Globe during the G20 Leaders' Summit in Brisbane in 2014 (Open Digital Earth Foundation, 2015). The globe allows users to explore the trade relationships between Queensland and the other G20 nations showing the nature, volume and direction of trade through the use of maps, imagery and other data. Building on the concept of virtual globes, the International Society for Digital Earth was formed in 2006 in Beijing to foster the vision of a Digital Earth.

10.5.2 Smart cities

Smart systems optimise efficiencies by self-regulating through feedback loops based on actionable intelligence from expert systems. A 'Smart City' benefits residents, businesses and visitors by integrating human, physical and digital systems on the basis of location. 'Smart Cities' pose huge business opportunities in building, health care, transportation, infrastructure, governance, security, energy and education (Jawad, 2014).

Over half the world's population live in cities. To achieve optimal benefits from the available urban information technologies, standards are required for communication and interoperability. Guidelines for planning and implementing urban spatial intelligence systems based on open standards have been developed by the Open Geospatial Consortium (OGC, 2012), including deployment of:

- mobile location information;
- 3D urban models;
- building information models;
- indoor navigation;
- augmented reality; and
- sensor webs (OGC, 2015).

Some examples of cities and regions using smart systems are listed in Table 10.4.

Table 10.4 Examples of smart systems

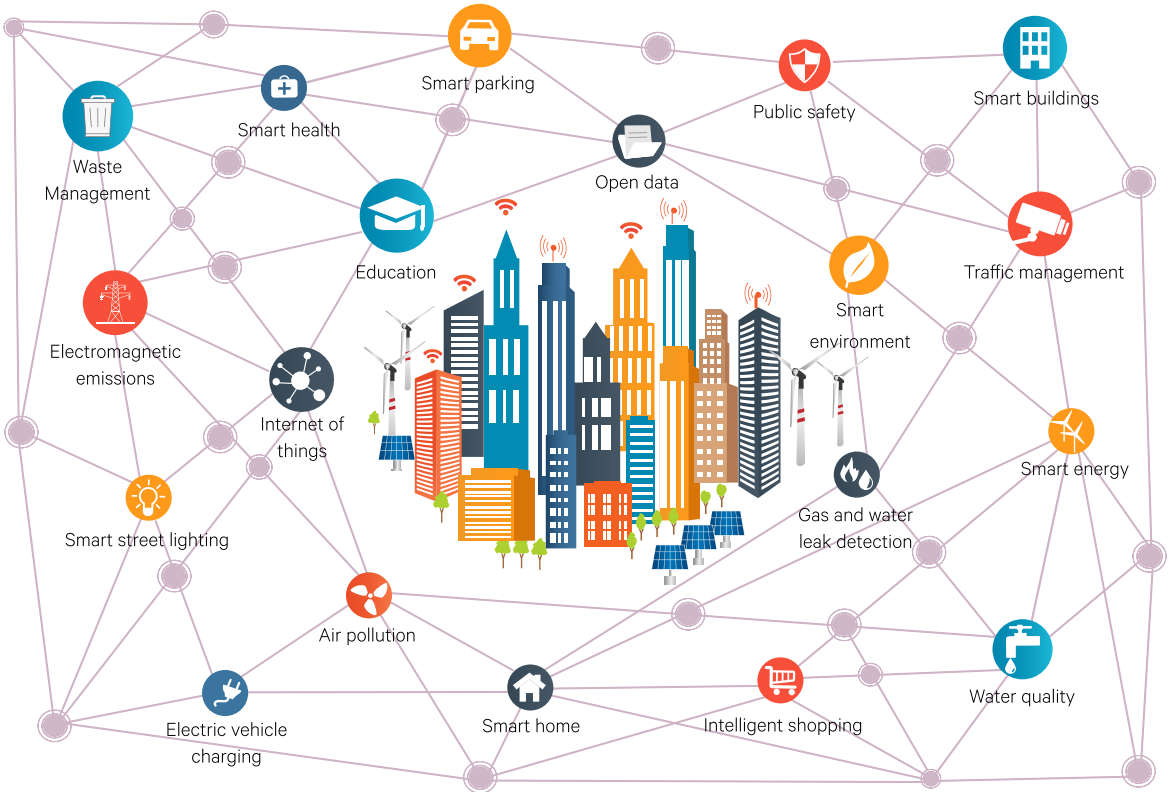
Transport		Energy		Water, Waste and Social	
City	Technology	Region	Technology	City	Technology
Hong Kong	Large-scale traffic management	California	Roll-out of smart meters since 2006, being used by >90% of households	Toronto	Large roll-out of smart water meters improving metering accuracy and billing efficiency
Singapore	Time-based urban road pricing to reduce congestion	France	Staged introduction of obligatory charging stations in new-buildings and offices	São Paulo	Digital water management, real-time system control, automatic leaks warning
San Francisco	Sensors report available parking spaces and prices are adjusted on demand	Ontario	'Peaksaver' programme to switch off home devices during peak hours	Boston	Telepresence robots, observing out-patient recovery after discharge from hospital
Singapore	Inter-modal journey planners and real-time information systems	Lower Saxony	Piloting of dynamic distribution transformers	Rio de Janeiro	Real-time city monitoring and control of municipal services

Source: Rothballer *et al.* (2014)

For example, the Spanish city of Santander is a large-scale living lab for smart cities. It aims to create a unique European experimental test facility (Sanchez *et al.*, 2014) for research and experimentation with different IT architectures, key enabling technologies and services and applications for the IoT. A wireless sensor network using a distributed network of intelligent sensor nodes, or 'motes', assists in efficient city management (see Figure 10.11). Parameters such as noise, temperature, carbon monoxide concentrations, ambient light levels and the locations of available parking spaces could be monitored for the benefit of citizens.

Figure 10.11 Example of smart city

An urban environment can be automated using a range of wireless sensors related to public safety, essential services and environmental monitoring.



Adapted from: Shutterstock image ID 570741217

10.5.3 Security

Ten million identities are digitally pickpocketed each year. Since online behaviour can differ between users, security can be enhanced when behavioural biometrics are used to identify users. For example, using Biocatch, the behavioural information about a user could be checked during a financial transaction on a bank's website: when the cursor disappears, some users scan the corners of the screen, while others wiggle the mouse in circles to retrieve the cursor. While it is easy to use a stolen user ID and password for access, it is much more difficult to misrepresent behavioural biometrics.

Location data can be used as an extra layer of security. For example:

- location data of bank clients' transactions can be used as an added security layer to combat fraud (McGrath, 2014);
- geofencing combined with mobile device management software ensures that visitors cannot take pictures in secure areas (Korolov, 2015); and
- the smart system 'Predpol' has successfully reduced crime by merging big data with analytical algorithms.

10.5.4 Virtual worlds

Technological advances are rapidly changing the world we live in. Virtual worlds are being built for gaming, automation and modelling 'what-if' scenarios. Augmented reality allows us to combine the virtual world with the real world, with information flowing both ways—we receive information in the real world from the virtual world and adjust our decision-making with the given information overlays. Spatially-enabled wearable sensor technologies allow data from our daily lives to be constantly fed back into the virtual world. In combination with advanced visualisation techniques (such as virtual reality glasses, contact lenses or bionic vision implants), and telepresence through holograms users will live in a much 'smarter' world. As the seamless integration and accuracy of indoor and outdoor navigation rapidly improve over the next few years, so will the virtual worlds that we can access (Woodgate *et al.*, 2014).

10.6 Developments in EO Platforms

The EO sector is a growing market. Over 50 countries now invest in EO programs, with India and China striving towards data self-sufficiency. Top priorities remain environmental and climate change monitoring (see Section 10.7).

10.6.1 Remotely piloted aircraft systems

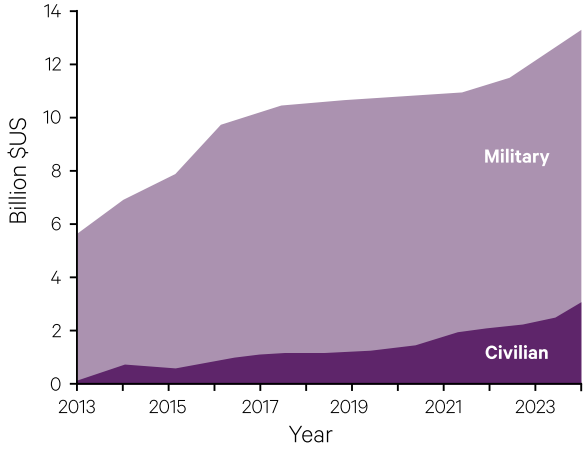
The market for remotely piloted aircraft systems (RPAS; or unmanned aerial vehicles (UAV), see Volume 1A—Section 11.2), is expected to grow by 51% before 2020, with growth anticipated in both military and civilian usage (see Figure 10.12). This market is currently most buoyant in the USA.

It is anticipated that key industry drivers will not be hardware and platforms, but rather industry-specific applications and data, as well as operator and modelling services (ABI Research, 2015b; Ballve, 2015). For example, apps are being developed which enable a smartphone, incorporating integrated sensors such as accelerometer, GPS, compass and camera, to effectively generate spatial data, including EO imagery (Anderson *et al.*, 2016). When carried by readily available aerial platforms, such as RPAS or kites, this capability promises to bring sophisticated mapping opportunities into the hands of communities and individuals.

Given their decreasing costs, flexible manoeuvrability, and rapid deployment, potential users of real-time imagery acquired by RPAS are increasing. For example, these systems are now being used routinely to assess subsidence in open pit mines, provide 'situational awareness' in a range of emergency situations, and monitor agricultural and urban boundaries and assets.

Figure 10.12 Global RPAS market 2013-2024

The size of both civilian and military markets for RPAS are growing rapidly.



Adapted from: Teal Group, Business Intelligence

Where they exist, regulations applicable to small RPAS vary hugely from country to country, even from State to State. Small RPAS are readily available for purchase from shops and online, yet it is often unclear where they can be flown legally. For example, the same RPAS flown recreationally on the weekend by a family may be subject to different laws when flown Monday morning by the same adult in a professional income-earning context (RPAS, 2016). A number of emerging Apps (such as RPAS Logger and AirMap) help users to locate spaces where RPAS can be flown legally. The integration of small RPAS with the existing air traffic control systems still needs clarification. In an effort to minimize collisions between RPAS and manned aircrafts, some (such as China-manufactured DJI RPA) have added geo-fenced 'no fly zones', which block them from operating in the vicinity of 350 airports around the world.

10.6.2 Satellite Platforms

CEOS manage a dynamic database of all key civilian EO platforms in space, or planned for launch in the next five years (CEOS, 2016). According to data from the Union of Concerned Scientists (UCS), as of 31 December 2015 there were 1,381 active satellites in orbit (see Table 10.5; UCS, 2016). These satellites are primarily used for communication, positioning, and EO. Figure 10.13 shows categories of spacecraft launches over the last decade, and highlights an increasing number of launches in recent years by commercial enterprises. This trend is being fuelled by miniaturisation and inexpensive off-the-shelf systems for satellites, making these platforms increasingly cheaper to build, launch and maintain.

Table 10.5 How many satellites?

By the end of 2015, a total of 1381 satellites were orbiting Earth in four different types of orbit: Low Earth Orbit (LEO), Medium Earth Orbit (MEO), Geostationary Earth Orbit (GEO) or Elliptical orbit.

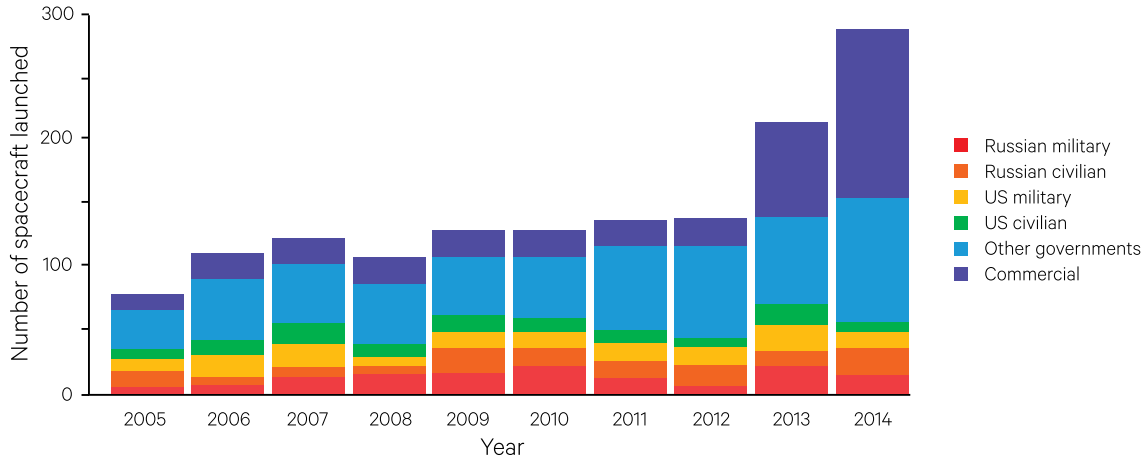
Satellite Ownership		
Nation	**Category**	**Number of Satellites**
USA	Commercial	273
	Military	149
	Government	131
	Civil	15
	Total	568
China		177
Russia		133
Other		503
Satellite Orbit		
LEO		759
GEO		493
MEO		92
Elliptical		37

Source: UCS (2016)

As can be seen from Figure 10.14, the spatial resolution of both civilian and military satellite imagery has steadily improved over the past few decades. Until February 2015, the best commercially-available spatial resolution from satellite imagery was 50 cm, but since then the US Government relaxed that restriction allowing access to 30 cm imagery (DigitalGlobe, 2015).

Figure 10.13 Number of spacecraft launched 2005-2014

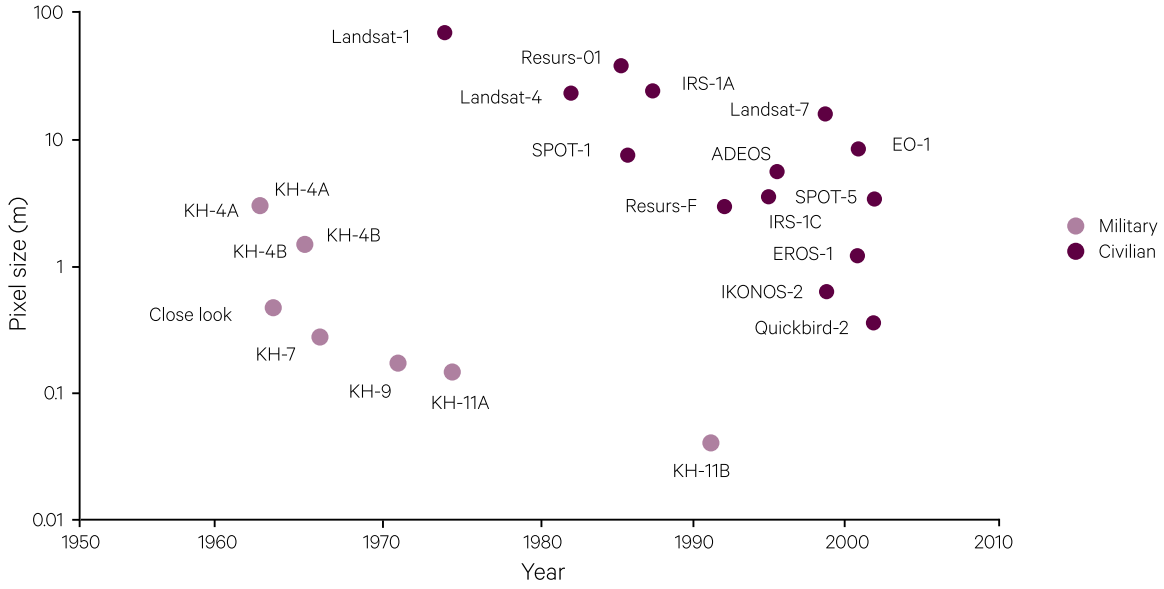
The number of civilian and military spacecraft launched between 2005 and 2014 are shown by nation and sector.



Adapted from: Lafleur (2015)

Figure 10.14 Changes in imaging satellite image spatial resolution over time

KH=Keyhole (designates several US DoD reconnaissance satellite series, such as CORONA, ARGON, LANYARD, and LACROSSE)



Adapted from: Kramer (2002)

As costs to build and launch decrease, satellite image aquisition operated by private companies is also rapidly expanding. For example:

- CubeSats—measure about 10 cm, weigh 1.3 kg, use smartphone components and give much of the performance provided by traditional technologies for a fraction the cost (see Volume 1A—Figure 1.9).
  - in November 2014, Orbital Science launched 29 CubeSats in a LEO orbit from Virginia, USA (a record at the time);
  - within days the Russian joint-venture Kosmostras deployed 32 CubeSats into a similar orbit;
  - STRaND-1 was the first 'phonesat' to go into orbit, built by Surrey Satellite Technology (SST: part of the Airbus group) from a Google Nexus One smartphone and a three unit cubesat; and
  - QB50 is a network that will launch 50 CubeSates together in 2016 in a string-of-pearl configuration. Participant UNSW will test the Namuru Space GPS, amongst other objectives for their CubeSat (ACSER, 2016).
- Planetlabs, who builds its nanosats in 'clean-enough' rooms in San Franciso, now has 113 operational satellites, and plans to launch 150 nanosats into orbit before the end of 2017. Planetlabs has also used the NanoRacks CubeSat Deployer on the International Space Station (ISS);
- UrtheCast broadcasts live imagery from the ISS, and aims to be its largest commercial user; and
- Airbus Defence, with its Pleiades and SPOT satellites, has formed a partnership with Hexagon Geospatial to provide access to high-resolution satellite data in 'smart' applications, as well as planning future access to TerraSAR-X radar data and digital elevation models.

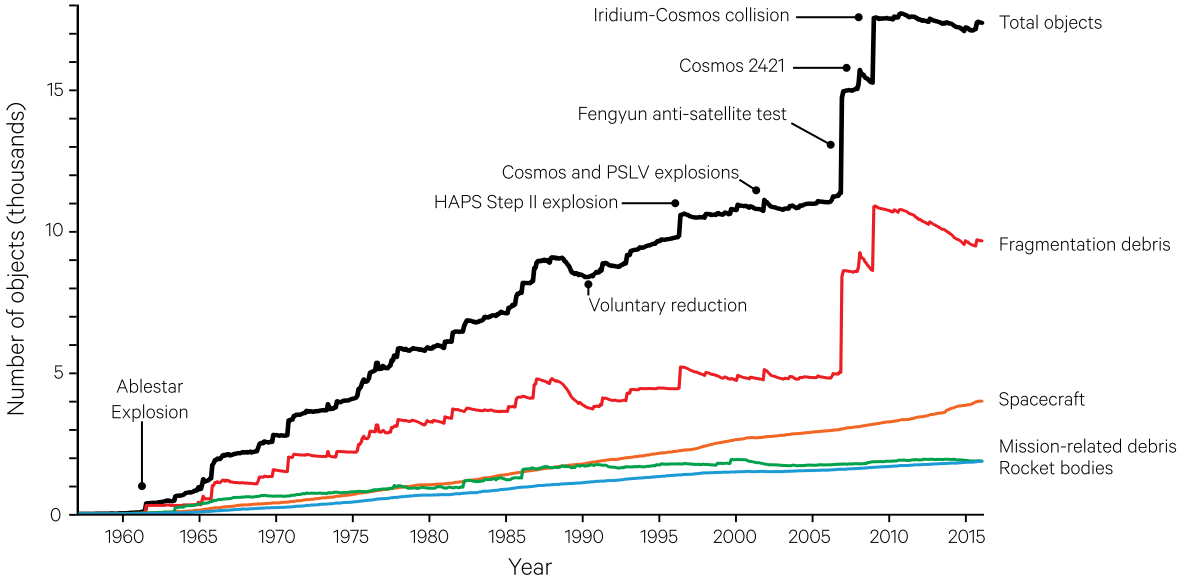
10.6.3 Space junk

Space assets are worth about AUD$900 billion. These investments are at serious risk from over 300,000 items of space debris in orbit (see Figure 10.15). Only 10% of space debris is larger than 5 mm and can be monitored (SERC, 2016). Archives of NASA's Orbital Debris Quarterly document the history of space junk:

- in 1961 the first major accident happened in space, when an explosion of the Ablestar launch vehicle created nearly 300 debris fragments (two-thirds were still in orbit in 2002);
- for two decades (1963 onwards), the Soviet Union and US demonstrated an array of ASAT systems, blowing up their own satellites in the act of deliberate anti-satellite tests;
- in 2007 the Chinese tested their anti-satellite system by firing a ballistic interceptor missile at their retired meteorological satellite Fengyun-1C, creating more than 1,600 debris fragments in the process; and
- in 2009 the communication satellite Iridium 33 (USA) collided with the decommissioned communication satellite Cosmos 2251 (Russia).

Figure 10.15 Catalogued space debris over time

The monthly number of objects in Earth orbit by object types is shown.



Adapted from: NASA, McKinnon (2014)

The Low Earth Orbit (LEO—up to 2,000 km altitude) contains the highest concentration of orbital debris. Based on NASA data, McKinnon (2014) reported there were 10,000 objects greater than 10 cm and 100,000 objects sized between 1 and 10 cm. A breakdown of composition yielded the following statistics:

- rocket bodies—17%;
- mission-related debris—19%;
- non-functional spacecraft—22%; and
- fragmentation debris such as fuel, paint flakes, batteries—42%.

Once space junk exists, it presents a danger to other spacecraft and satellites in a colliding orbit. Collisions give rise to more space debris, and the worst-case scenario is a run-away chain reaction (Kessler Effect) rendering earth orbits unusable for centuries. DARPA/ NASA launched an Orbital debris removal request (Ansdell, 2010) in 2009. In Australia, the CRC for Space Environment Management, managed by the Space Environment Research Centre (SERC) builds on Australian and international expertise in measurement, monitoring, analysis and management of space debris to develop technologies to preserve the space environment (SERC, 2016).

The following solutions have been proposed to remove space debris:

- laser cannons on ISS in 2017 (Ackerman, 2015a);
- Pac-Man satellite (Swiss) launch in 2018 (Ackerman, 2015b);
- in-orbit servicing and recycling (that is, modular satlets, DARPA Phoenix Program; Henry, 2015);
- SpaDE-Space debris elimination in lower LEO orbits using gravity wave perturbations (Gregory *et al.*, 2012);
- EDDE Electrodynamic Debris Eliminator—a propellant-less spacecraft for debris removal (Pearson *et al.*, 2010);
- a debris engine that is fuelled by space waste (Lan *et al.*, 2015); and
- e.deorbit: ESA's Space clean up concept (arm or net) for debris removal in 800–1000 km near-polar orbits (to be launched in 2021; ESA, 2016a).

10.7 The Australian Outlook

The technological changes described in the preceding sub-sections will impact the volume and type of data available for EO, its locational accuracy and the ways it can be integrated with other information. Integrated systems, such as GEOSS (see Excursus 10.2), will simplify access to the increasing number of EO data sources, and streamline the integration of EO data with other geographic datasets. Section 10.7.1 reviews data needs and risks that have been identified for Australia. Section 10.7.2, Section 10.7.3 and Section 10.7.4 consider some application areas in which EO datasets have already been integrated with 'smart' systems in Australia. Other applications of EO are detailed in Volume 3.

10.7.1 Data requirement projections

A comprehensive report by Symbios summarises current satellite capabilities available to Australia, and assesses the risk associated with data discontinuity (Symbios, 2015). Table 10.6 shows the performance specifications for selected instrument categories, while Table 10.7 assesses their continuity risk.

The report identified the supply of L-Band SAR as having the highest risk of being disrupted (Table 10.7). The rationale for this assessment is the high uncertainty of the future Japanese EOS missions, in particular the continuity planning for ALOS.

Table 10.6 Instrument type performance specifications

Instrument Characteristics		Instrument type				
		Low resolution optical	Medium resolution optical	High resolution optical	Very high resolution optical	SAR
Spatial resolution	Minimal	250 m	20 m	10 m	1 m	30 m
	Optimal	100 m	10 m	<10 m	50 cm	30 m
Spectral bands	Minimal	22 (optical–TIR; e.g. VIIRS)	8 (optical–TIR; e.g. Landsat ETM+)	optical	visible	C-band L-band X-band
	Optimal	36 (optical–TIR; e.g. MODIS)	> 8 (optical–TIR)	optical–TIR	optical	
Coverage	Minimal	Land: full national Oceans: global	full state	sub-state selected sites	selected site	selected site
	Optimal	Land: full national Oceans: global	full national	sub-state selected sites /regions	multiple sites	full national
Coverage Frequency	Minimal	Land: twice daily Oceans: daily	weekly	every five years	daily to monthly	weekly
	Optimal	Land: multiple daily Oceans: hourly (continous)	daily	daily	daily	hours
Latency	Minimal	30 mins	24 hours	weeks	weeks	weeks
	Optimal	10 mins	2–3 hours	weeks	hourly during flooding	hours

Adapted from: Symbios (2015)

Table 10.7 Continuity risk for main instrument types

Green: meets or exceeds the most demanding optimal requirement
Yellow: meets or exceeds the most demanding minimal requirement
Red: does not meet the most demanding minimal requirement

Instrument type	Risk		
	Technical continuity	Programmatic	Political/policy
Low resolution optical	Low	Medium (JPSS delays, Sentinel ground segment, GCOM-C continuity, MODIS failure)	Low
Medium resolution optical	Low	Low	Low
High resolution optical	Low	Low	Low
C-band SAR	Low	Low	Low
L-band SAR	Medium (One operational mission)	High (ALOS continuity unclear, SAOCOM unproven at global scale)	High (Japanese space policies uncertain)
X-band SAR	Low	Low	Low
C-band SAR	Low	Low	Low

Source: Symbios (2015)

Table 10.8 Current and future radar satellites

Instrument	Band	Supplier	Commercial	Country	Current / Future (year)
RADARSAT-2	C-band	CSA/MDA	Yes	Canada	Current (to 2015+)
Sentinel-1	C-band	EC/ESA	No	Europe	Current (to 2023+)
RADARSAT Constellation	C-band	CSA	No (projected)	Canada	Future (2018 – 2025)
COSMO-SkyMED	X-band	ASI	Yes	Italy	Current (to 2017+)
TerraSAR-X	X-band	Airbus DS	Yes	Europe	Current (to 2015+)
TanDEM-X	X-band	Airbus DS	Yes	Europe	Current (to 2015+)
RISAT-2	X-band	ISRO	No	India	Current (to 2015)
Meteor-M-N1 and N2	X-band	ROSHYDROMET	No	Russia	Current (to 2020+)
WSAR (HY-3A – 3C)	X-band	NSOAS	No	China	Current (to 2027)
PAZ	X-band	CDTI	No	Spain	Future (2015–2020)
LOTUSat 1 and 2	X-band	VAST	No	Vietnam	Future (2017–2023)
SCLP	X-band	NASA	No	U.S.A.	Future Concept (2030+)
ALOS-2	L-band	JAXA / RESTEC	Yes	Japan	Current (to 2019)
SAOCOM	L-band	CONAE	No (projected)	Argentina	Future (2016–2025)
NISAR	L-band / S-band	NASA / ISRO	No	U.S. A./ India	Future (2020–2025)
NovaSAR	S-band	SSTL/Airbus	Yes	U.K.	Future (2016+)
BIOMASS	P-band	ESA	No	Europe	Future (2020–2025)

Source: Symbios (2015)

For each instrument type, the publication gives an overview of current and future satellites/instruments as demonstrated in Table 10.8 for Imaging Radar/ Synthetic Aperture Radar (SAR). There is demand in Australia for training additional specialists familiar with radar data analysis. To this end, the Radar Research Facility at the CRCSI (CRCSI, 2016b) has developed a road map for Australia to examine SAR applications of national significance.

In June 2015 CSIRO signed an agreement with the European Space Agency (ESA) that will provide Australia with better access to data from European satellites. In return, Australia will share its scientific expertise. ESA is launching a range of Sentinel satellites to address the needs of the Copernicus programme (Copernicus, 2016; ESA, 2016b) and access to these data sets provides exciting opportunities to the Australian research communities.

10.7.2 Monitoring the Australian environment

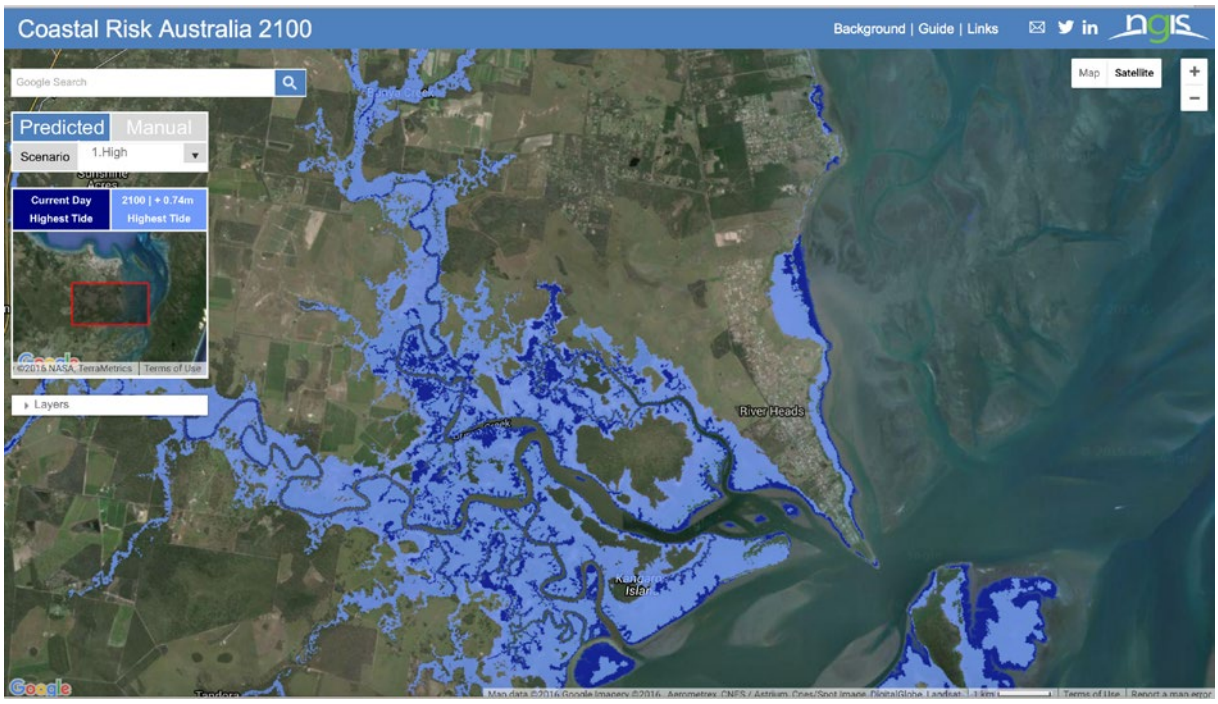
Most environmental monitoring programs look for changes from a baseline then estimate whether these changes are within normal fluctuations. Multiple data sets can be merged to improve model forecasts. Using time series analysis, changes can be detected with respect to specific outcomes, such as land degradation, urban development, or climatic and oceanic changes.

In the AGDC project (see Section 10.4.1), 27 years of archived Landsat imagery over Australia have been converted into a 'data cube' for monitoring changes in land and water patterns (see also Volume 2A and Volume 2D). This time series has provided unique information for flood risk and ecosystem management (Mueller *et al.*, 2016). Excursus 5.1 in Volume 1A, for example, shows Landsat imagery of the Menindee Lake system, which has been mapped to indicate the permanence of lake water in the landscape.

Satellite archives and modelling tools are now becoming more accessible to the general public. For example, interactive modelling tools based on coastal lidar data (see Volume 1A—Section 15; CRA, 2016) and built on the Google Earth Engine, allow users to set different scenarios for sea level rise up to the year 2100 around selected coastal areas of Australia (Figure 10.16 and Volume 3B). Another Australian website, the Green Precision tool (GreenPrecision, 2016; see Figure 10.17), provides interactive access to remotely sensed vegetation greenness for selected locations and time periods. Such information is valuable to farmers and land managers to monitor and compare changes in vegetation cover and condition.

Figure 10.16 Modelling of coastal risk

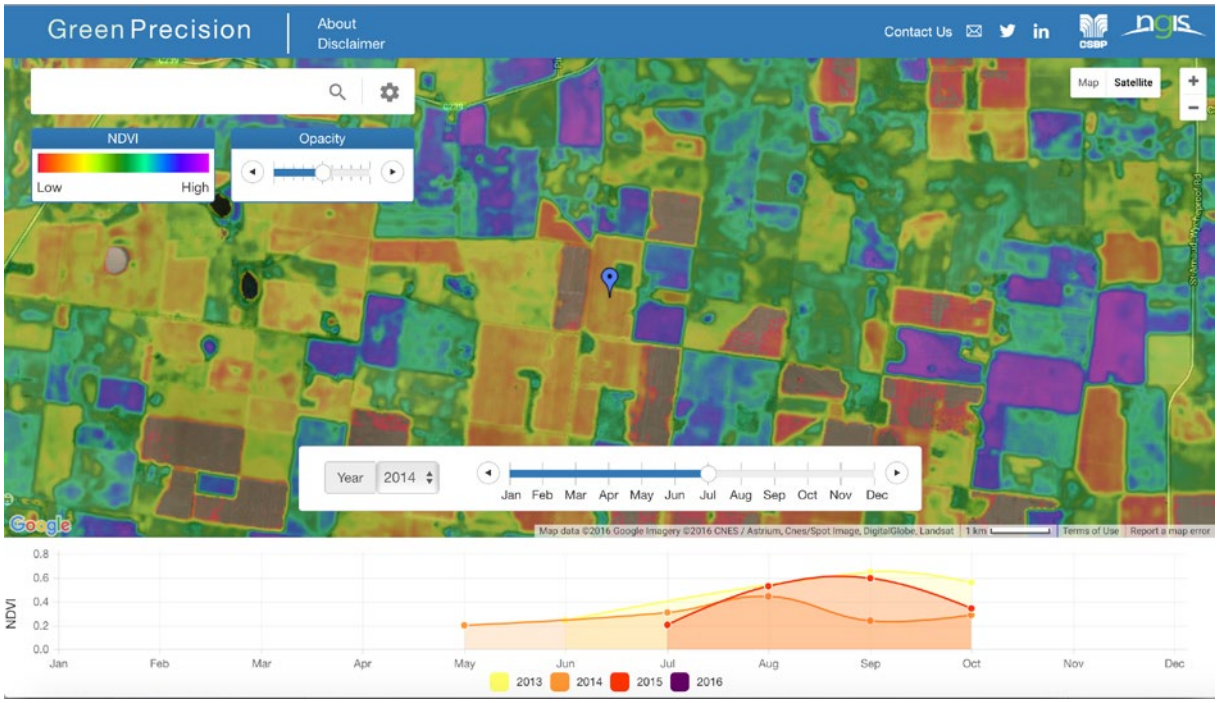
Date visualisation of coastal risk for Rivers Heads Area, Queeensland. Blue areas indicate coastal areas at risk of flooding with highest tides in 2100.



Source: CRA (2016)

Figure 10.17 Green Precision tool

Interactive screen from Green Precision tool showing NDVI image and greenness trends over time.



Source: GreenPrecision (2016)

Australia's iconic Great Barrier Reef is impacted by tourism, agriculture, and fishing, plus 12 busy ports servicing the resource industry. eReefs is a collaborative project started in 2012 to protect and preserve the unique environment of the Reef by building a comprehensive coastal information system (eReefs, 2016). The programme conducts research and promises to deliver powerful visualisation and reporting tools for decision support.

Currently about 10,000 ships frequent these ports near the Reef, with projections of 35,000 ships by 2032 (Pearce, 2016). This volume will increase the risk of maritime accidents, such as oil spills. The key to minimising Reef damage from such incidents is rapid response; however to date, it has been difficult (and expensive) to detect oil spills. Oil has a different conductivity than salt water, and its surface also has different viscosity characteristics, so appears darker in radar imagery. For example, when marshes were affected by the Deepwater Horizon oil spill in the Gulf of Mexico in 2010, the contamination was successfully mapped by NASA's Uninhabited Aerial Vehicle Synthetic Aperture Radar (UAVSAR) using fully polarimetic L-band data (Ramsey *et al.*, 2011). CSIRO is working on methods to automatically detect oil spills on the Reef using SAR imagery acquired by the Sentinel-1 satellite (Pearce, 2016).

10.7.3 Agricultural systems

Smart systems have the possibility of transforming entire supply chains in agriculture. New systems are emerging and are in the early stages of industry adoption. Some of the current systems include:

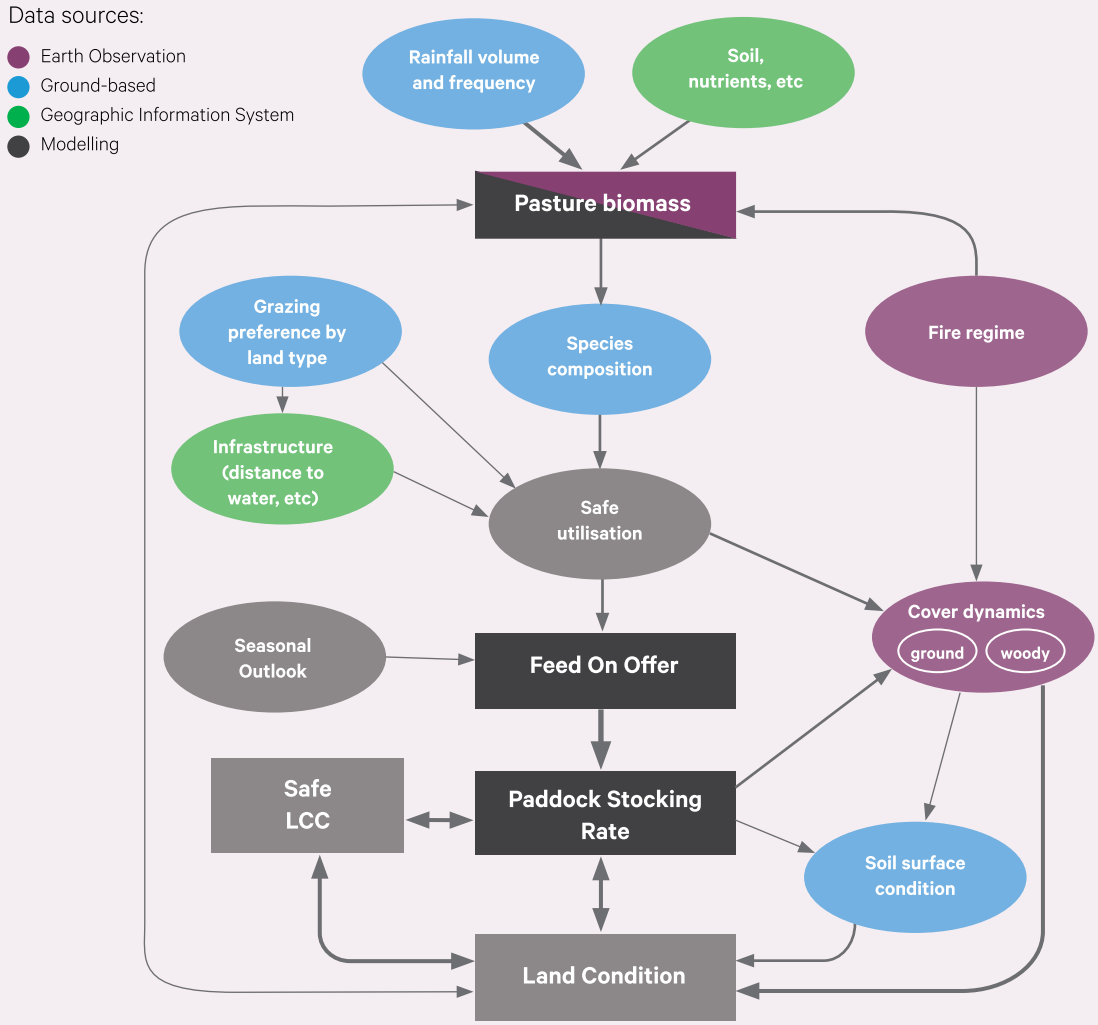
- The Pastures from Space system—uses satellite data to quantitatively estimate pasture biomass or FOO (food on offer) and, combined with soil and climate data, estimates pasture growth rates (CSIRO, 2014; see Excursus 14.1 in Volume 1A);
- The Precision Pastoral Management System—incorporates remote livestock management, such as automated weighing and drafting, telemetry, satellite land and pasture observation, water management and cloud-based analytics (Ninti One, 2015). This integrated system has been shown to improve farm and livestock productivity, increase sustainability and protect vegetation and wildlife in arid rangelands and savannahs;
- The NRM Spatial Hub—helps farms optimize infrastructure developments and maintain sustainable grazing regimes. Information is extracted from satellite imagery and provided to farmers as digital farm maps (CRCSI, 2016a; see Excursus 10.3).

Excursus 10.3—NRM Spatial Hub

Source: Phil Tickle, CRCSI
Further Information: NRM Hub (2016) *http://www.nrmhub.com.au*

Figure 10.18 Components of NRM Spatial Hub

Stylized representation of the inter-related components determining paddock stocking rate and land condition. Components within boxes or ellipses with darker shades represent 'fast' variables and are more commonly associated with tactical decision making. Corresponding shapes with lighter shades indicate slower variables and strategic decisions. The thickness of arrowed lines indicates the strength of linkages.



Adapted from: Bastin *et al.* (2016) Figure 1.1

The Natural Resource Management (NRM) Spatial Hub is an online planning and information system designed to map existing infrastructure, planning of proposed infrastructure (including fences, water points and lines, roads, gates, grids, buildings and yards), and monitor land condition over the short, medium and long term. The relationships between NRM Spatial Hub components is illustrated in Figure 10.18.

Spatial Hub is a valuable tool to assist in the management of grazing lands and their livestock, including:

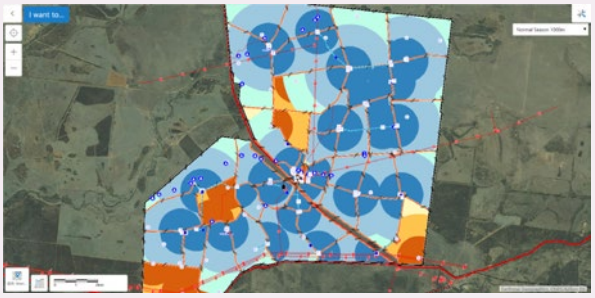
- determining areas of paddocks;
- determining the area of paddocks effectively grazed (see Figure 10.19);
- determining the ideal placement of new infrastructure;
- assisting in the costing of development capital (such as the length of proposed pipelines);

- assisting in budgeting (such as determining the distances and cost of grading required each year);
- mapping ground cover to highlight areas that require close attention on the ground and prioritise management intervention (such as areas that are consistently bare and possibly overgrazed, or consistently green, possibly indicating woody weed encroachment);
- planning infrastructure development and management strategies in conjunction with all stakeholders; and
- developing a team approach to management through joint management planning, thus creating a sense of all stakeholders working towards the same goals and outcomes.

For example, using the NRM Spatial Hub, Figure 10.20 plots the development of a paddock over time, with respect to ground cover. Farmers can estimate optimal stocking rates and compare the performance of their paddocks to other paddocks in their neighbourhood. Future capabilities will include 'virtual fencing', where actual fences will not be needed to subdivide paddocks. Instead, a digital fence would be created by the farm manager, and farm animals trained to stay within its boundaries using GPS location-tracking and cueing (Whan *et al*., 2010).

Figure 10.19 NRM Hub Grazing Circles

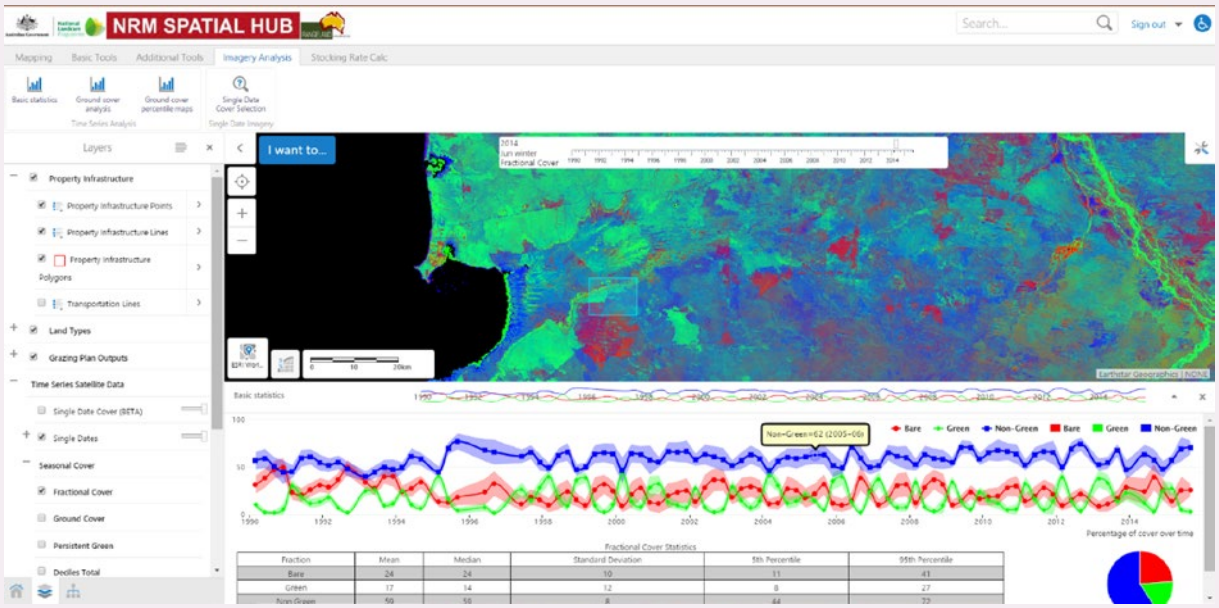
Grazing Circle analysis shows perennial (blue) and ephermal (orange) paddock grazing patterns, plus the estimated paddock usage.



Companies such as John Deere and AGCO are beginning to connect farm machinery, irrigation systems, weather reports, and soil and nutrient data with crop and commodities futures to optimize overall farm performance. The total system performance will become more and more important, and companies that address this market requirement are in the best position to drive this process and gain competitive advantage (Porter and Heppelmann, 2014).

Figure 10.20 NRM Hub ground cover over time

The graph from the online system shows the seasonal fractional ground cover for the selected paddock over time. Over the past 30 years, the percentage of bare ground (depicted in red) is typically below 50% and the percentage of green cover varies strongly based on seasonality. On a regional basis this information helps identify paddocks requiring urgent management intervention (such as strategic resting from grazing over several wet seasons to facilitate recovery and lightening of the pressure from feral animals).



Source: CRCSI (2016a)

10.7.4 Weather and climate

The first polar orbiting weather satellites, launched in the early 1960s provided imagery that allowed detailed synoptic analysis over the whole globe, including areas that previously had sparse data coverage, especially the southern oceans (see Volume 1A—Excursus 12.1). This imagery was used for forecasting and weather warnings, particularly forecasting significant weather such as tropical cyclones. Later it was also used for quantitative analysis and input into Numerical Weather Prediction (NWP) through systematic cloud picture interpretation. The images were also used for myriad meteorological and general scientific applications.

From the late 1960s, sequential images from geostationary satellites were used to estimate wind, and observations taken by polar orbiting sounders were used to estimate temperature and moisture profiles. Winds are now produced at least hourly from global satellite observations, and advanced sounders measure temperature to within a degree as well as the concentration of a large number of atmospheric constituents such as water vapour, on average, every four hours. In addition, many new observation types such as those from scatterometers, polarimetric microwave radiometers and satellite constellations observing radio occultation are making significant contributions to meteorology (see Volume 1A—Section 16).

The growing value and importance of these Earth Observation from Space (EOS) observations, with their increasing temporal, spatial and spectral resolution, is demonstrated in Volume 1A—Excursus 16.1. The applications that provide warnings for fog, volcanic ash and tropical cyclones, for example, are becoming more important. In relation to NWP, recent experiments show that, in the southern hemisphere, the accuracy of 24 hour (one day) forecast without satellite data is of the same accuracy, on average, as a 96 hour (four day) forecast with satellite data, when forecasts were verified against the control (all data used) analysis (see Volume 1A—Excursus 16.2). These results attest to the great importance of EOS particularly in the southern hemisphere, their significant benefit to forecast and warning systems and climate monitoring, their significant economic impact, and their great societal benefits.

10.7.4.1 Challenges

The major challenges for satellite meteorology include the:

- large number of diverse instruments providing data that need to be assimilated;
- radiative transfer calculations associated with the use of many of the instrument observations; and
- the complexity of modern data assimilation systems.

These challenges have required both intra-national and international collaboration to allow the international NWP centres to successfully exploit the observations from the current spacebased systems, and provide considerable benefit from the investment in these systems. This collaboration has been aided by groups such as The International TOVS Working Group and the International Winds Workshop, which provide advice, recommendations and software to the international community. Into the future, effective collaboration and cooperation amongst the international community will remain an important component for the effective exploitation of EOS.

Preparation for the Joint Polar Satellite System (JPSS) and the next-generation US satellite GOES-R, and improved exploitation of current operational and experimental data, remain high priorities for most NWP centres, which have, to date, assimilated data from well over forty instruments into their forecast systems. In addition, preparations for, and exploitation of, data from experimental satellites such as CloudSat/Calipso, ADM Aeolus and SATMOS are advancing.

In recent years, significant progress has been made by global data assimilation centres in using advanced satellite data. This has been vital, as the strength of global satellite data assimilation is central to the quality of future operational weather, climate and environmental analysis and forecasting around the globe. Considerable benefits are yet to be accrued by the southern hemisphere and international community from the use of these data.

In addition to the benefits from the assimilation of these data in NWP, a wide range of of applications, have greatly benefitted from meteorological EOS (see Volume 1A—Excursus 16.1). Typical examples of these applications are detecting volcanic ash for the aviation industry using MODIS and AVHRR data, generating vegetation indices, and locating wildfires using these instruments. The accuracy of many of these applications will improve into the future and be further extended to provide new products as EOS advances.

10.7.4.2 Prospects

From the time of the launch of the first weather satellite on 1 April 1960, increasing EOS data resolution have led to improved characterisation of atmospheric state and greater accuracy of prediction. The first weather satellites provided television images in visible and IR (11 μm) wavelengths, allowing cloud picture interpretation to provide quantitative analyses in areas where there was otherwise no data (see Volume 1A—Excursus 12.1). Analyses and forecasts were substantially improved by the provision of sounding data in the thermal IR and microwave (see Volume 1A—Excursus 16.1).

Improvements have also been made through increases in the spatial and spectral resolutions associated with the ATOVS instrument (HIRS and AMSU) on NOAA-15 and subsequent POES satellites. These improvements in temperature and moisture sounding have been accompanied by the use of sequential imagery with increasing spatial, temporal and spectral resolutions to produce high resolution wind vectors, which have also contributed to increased forecast accuracy. The observational capability was also supported by instruments such as AATSR (to observe sea surface temperature), QuikScat, SSMI, SSMIS, WindSat, ASCAT, MODIS, AVHRR and the GNSS observing constellations.

The improvement in observational capacity was further expanded with the launch of the Advanced Infrared Sounder (AIRS), followed by the Infrared Atmospheric Sounding Interferometer (IASI) and the Cross-track Infrared Sounder (CrIS). These third generation ultraspectral IR sounders provide sounding accuracies greater than 1K and estimates of humidity to within 15%. The benefits of this improved observational capacity, enhanced by improving data assimilation methods such as 4D variational assimilation and the availability of burgeoning computer power have already led to significantly improved forecast accuracy.

In addition to these hyperspectral observations from polar orbiting satellites, it is anticipated that the new Geostationary Sounders similar in design to the Geostationary Imaging Fourier Transform Spectrometer (GIFTS; Smith *et al*., 2000) will provide these data on a nearcontinuous basis, resulting in further significant improvement in analysis and forecast accuracy. The benefits from these instruments will be realized through both increased temperature and moisture sounding capability, thousands of channels for use by image-based applications, and also in the vastly improved ability to generate wind fields.

In the near future, there are considerable prospects for improved specification of atmospheric state (namely, improved analyses) and the related improvement in forecast capability, as well as improved climate monitoring. This points to the next decade being one of significant improvement in our observational capacity, and substantial benefits from its exploitation.

10.8 Conclusion

The power of big data in the cloud, combined with access to supercomputers by just about anyone with mobile devices, is immense. We are gaining knowledge with relative ease compared to what would have been involved just a few years ago. Vast silos of data reach back over several decades, enabling unprecedented opportunities for modelling and learning.

Technological advances such as connectedness, wide sensor networks (IoT; see Section 10.2) and cloud computing, result in smart systems with wide-reaching ramifications to society. They will disrupt the way we live, work, and play. Many technological advances will need ethical frameworks and global legal modifications. Ultimately a virtual world will mirror the real world, and solutions need to be found to manage huge data volumes, ensure data integrity and facilitate access and usage rights.

Most future developments will be built with location as a key component and identifier, thereby making spatial innovation vital to the advancement of these technologies. Key developments are likely to share these common elements (Woodgate *et al*., 2014):

- high precision location accuracy;
- the 'always on' phenomenon (ubiquitous streaming and continuous analysis);
- real time response to requests for information;
- a sentient presence (making us, and the world around us, 'smart'); and
- universal accessibility, irrespective of skill level, language, location or socio-demographic circumstances.

There are unprecedented opportunities (and challenges) in the next decade and beyond in all technologies, including EO.

I think there is a world market for maybe five computers.
(Thomas Watson, Chairman of IBM, 1943)

10.9 References

ABI Research (2015a). *BLE Beacons*. Retrieved from *https://www.abiresearch.com/pages/ble-beacons/*.

ABI Research (2015b). Small Unmanned Aerial Systems Market Exceeds US$8.4 Billion by 2019, Dominated by the Commercial Sector and Driven by Commercial Applications.

Ackerman, E. (2015a). Proposal Would Put Laser Cannon on ISS to Blast Space Junk. *IEEE Spectrum*. Retrieved from *http://spectrum.ieee.org/tech-talk/aerospace/space-flight/proposal-would-put-laser-cannon-on-iss-to-blast-space-junk*.

Ackerman, E. (2015b). Swiss 'Pac-Man' Satellite to Gobble Up Space Junk in 2018. *IEEE Spectrum*. Retrieved from *http://spectrum.ieee.org/tech-talk/aerospace/satellites/swiss-pacman-satellite-to-gobble-up-space-junk-in-2018*.

ACSER (2016). *The UNSW-EC0 QB50 CubeSat*. The Australian Centre for Space Engineering Research (ACSER). Retrieved from *http://www.acser.unsw.edu.au/QB50*.

AGDC (2016). *Australian Geoscience Data Cube*. Retrieved from *http://www.datacube.org.au*.

Anderson, J., and Rainie, L. (2014). *The Internet of Things Will Thrive by 2025*. Pew Research Center. Retrieved from *http://www.pewinternet.org/2014/05/14/internet-of-things/*.

Anderson, K., Griffiths, D., DeBell, L., Hancock, S., Duffy, J. P., Shutler, J. D., Reinhardt, W. J., and Griffiths, A. (2016). A Grassroots Remote Sensing Toolkit Using Live Coding, Smartphones, Kites and Lightweight Drones. *Plos One, 11*(5), pp. e0151564. doi:*http://dx.doi.org/10.1371/journal.pone.0151564*.

Ansdell, M. (2010). Active Space Debris Removal: Needs, Implications and recommendations for today's Geopolitical Environment. *Journal of Public and International Affairs, 21*, pp. 1-16.

Ballve, M. (2015). *Commercial drones have leapt far ahead of regulators and are already entrenched in a handful of massive industries*. Business Insider. Retrieved from *http://www.businessinsider.co.id/uav-or-commercial-drone-market-forecast-2015-2/-PtIAahRypJeIU8j3.97*.

Barrett, P., Berrill, A., Gale, G., Jones, K., Leger, N., Lonergan, D., Warner, J., Woodgate, P., and Ziobrowski, M. (2013). *Location Data Privacy: Guidelines, Assessmet & Recommendations (Version 2)*. Location Forum.

Bastin, G., Carter, J., Tickle, P., Stone, G., Trevithick, R., O'Reagain, P., Phelps, D., Cowley, R., Pringle, M., Scanlan, J., and Hoffman, M. (2016). Remotely sensed and modelled pasture biomass, land condition and the potential to improve grazing-management decision tools across the Australian rangelands. Unpublished report to Meat and Livestock Australia.

Bezerra, J., Bock, W., Candelon, F., Chai, S., Choi, E., Corwin, J., DiGrande, S., Gulshan, R., Michael, D. C., and Varas, A. (2015). *The Mobile Revolution: How Mobile Technologies Drive a Trillion-Dollar Impact*. Retrieved from *https://www.bcgperspectives.com/content/articles/telecommunications_technology_business_transformation_mobile_revolution/*.

Buczkowski, A. (2012). *Location-Based Services – Technologies*. Retrieved from *http://geoawesomeness.com/knowledge-base/location-based-services/location-based-services-technologies/*.

Carpenter, J., and Snell, J. (2013). *Future trends in geospatial information management: the five to ten year vision*. United Nations Initiative on Global Geospatial Information Management (UN-GGIM).

CEOS (2016). *The CEOS Database*. Retrieved from *http://database.eohandbook.com*.

Chester, S. (2015). *Japan's QZSS GNSS to benefit Australia*. Retrieved from *http://www.spatialsource.com.au/2015/04/14/japans-qzss-gnss-to-benefit-australia/*.

Copernicus (2016). *Sentinels*. Retrieved from *http://www.copernicus.eu/main/sentinels*.

Coppa, I., Woodgate, P., and Mohamed-Ghouse, Z. (2016). *Global Outlook 2016: Spatial Information Industry*. Australia and New Zealand Cooperative Research Centre for Spatial Information. Retrieved from *https://www.crcsi.com.au/assets/Resources/CRCSI-Global-Outlook-Report-November-2016.pdf*.

CRA (2016). *Coastal Risk Australia*. Retrieved from *http://coastalrisk.com.au*.

CRCSI (2016a). *NRM Spatial Information Hub*. Retrieved from *http://www.crcsi.com.au/research/commissioned-research/nrm-spatial-information-hub/*.

CRCSI (2016b). *Radar Research Facility*. Retrieved from *http://www.crcsi.com.au/research/radar-research-facility/*.

CSIRO (2014). *Pastures from Space*. Retrieved from *http://www.pasturesfromspace.csiro.au*.

Curtis, S. (2015). *Security experts hack into moving Jeep and seize control of car*. Retrieved from *http://www.smh.com.au/digital-life/consumer-security/security-experts-hack-into-moving-jeep-and-seize-control-of-car-20150721-gihmn3.html*.

Dempsey, C. (2012). *Where is the Phrase "80% of Data is Geographic" From?* Retrieved from *https://www.gislounge.com/80-percent-data-is-geographic/*.

Department of the Prime Minister and Cabinet (2015). *Public Sector Data Management*. Australian Government, Canberra, Australia.

DigitalGlobe (2015). *A Detailed View of the Ground with 30-centimeter Satellite Imagery*. Retrieved from *http://spacenews.com/a-detailed-view-of-the-ground-with-30-centimeter-satellite-imagery/*.

Divis, D. A. (2015a). PNT Advisory Board Debates Critical Infrastructure Designation for GPS. *Inside GNSS*. Retrieved from *http://www.insidegnss.com/node/4536*.

Divis, D. A. (2015b). Study: GPS Contributed More Than $68 Billion to the U.S. Economy. *Inside GNSS*. Retrieved from *http://www.insidegnss.com/node/4535*.

Dreischmeier, R., Close, K., and Trichet, P. (2015). *The Digital Imperative*. Retrieved from *https://www.bcgperspectives.com/content/articles/digital_economy_technology_strategy_digital_imperative/*.

eReefs (2016). *About eReefs*. Retrieved from *http://ereefs.org.au/ereefs/about*.

Ericsson (2015). *Erricsson Mobility Report on the Pulse of the Networked Society*. Retrieved from *http://www.ericsson.com/res/docs/2015/ericsson-mobility-report-june-2015.pdf*.

ESA (2016a). *e.deorbit*. Retrieved from *http://www.esa.int/Our_Activities/Space_Engineering_Technology/Clean_Space/e.Deorbit*.

ESA (2016b). *Sentinel*. Retrieved from *https://sentinel.esa.int/web/sentinel/missions*.

Future of Life Institute (2016). *An Open Letter: Research Priorities for Robust and Beneficial Artificial Intelligence*. Retrieved from *http://futureoflife.org/ai-open-letter/*.

Gartner (2014). *Gartner's 2014 Hype Cycle for Emerging Technologies Maps the Journey to Digital Business. Newsroom Press Release*. Retrieved from *http://www.gartner.com/newsroom/id/2819918?_ga=1.51071721.1904172021.1401730474*.

Goodchild, M. F., Guo, H., Annoni, A., Bian, L., de Bie, K., Campbell, F., Craglia, M., Ehlers, M., Genderen, J. v., Jackson, D., Lewis, A. J., Pesaresi, M., Remetey-Fülöpp, G., Simpson, R., Skidmore, A., Wang, C., and Woodgate, P. (2012). Next-generation Digital Earth. *Proceedings of the National Academy of Sciences of the United States of America, 209*(28), pp. 11088-11094.

Google (2016). *A planetary-scale platform for Earth science data & analysis*. Retrieved from *https://earthengine.google.com*.

GPS (2016). *Current and Future Satellite Generations*. Retrieved from *http://www.gps.gov/systems/gps/space/*.

Grau, C., Ginhoux, R., Riera, A., Thanh Lam, N., Chauvat, H., Berg, M., Amengual, J. L., Pascual-Leone, A., and Ruffini, G. (2014). Conscious Brain-to-Brain Communication in Humans Using Non-Invasive Technologies. *Plos One, 9*(8). doi:*http://dx.doi.org/10.1371/journal.pone.0105225*.

GreenPrecision (2016). *GreenPrecision powered by CSBP and NGIS*. Retrieved from *http://www.greenprecision.com.au*.

Gregory, D., Mergen, J. F., and Ridley, A. (2012). *Space Debris Elimination (SpaDE) Phase I Final Report* (NASA NIAC -- 11- 11NIAC-0241). Raytheon BBN Technologies.

Helbing, D. (2014). *The Digital Society: A Summary*. Social Science Research Network. Retrieved from *http://ssrn.com/abstract=2541331*.

Henry, C. (2015). *DARPA Revamps Phoenix In-Orbit Servicing Program*. Retrieved from *http://www.satellitetoday.com/regional/2015/06/02/darpa-revamps-phoenix-in-orbit-servicing-program/*.

Hewitt, J. (2014). *The first thought-activated implant is an exciting hint of things to come*. Retrieved from *http://www.extremetech.com/extreme/193990-the-first-thought-activated-brain-implant-is-an-exciting-hint-of-things-to-come*.

Hurley, M. S. (2015). *Application for a Search Warrant* (5:15-mj-00154-ATB). Federal Bureau of Investigation. Retrieved from *http://www.wired.com/wp-content/uploads/2015/05/Chris-Roberts-Application-for-Search-Warrant.pdf*.

IACPNT (2016). *Information and Analysis Center for Positioning, Navigation and Timing*. Retrieved from *https://www.glonass-iac.ru/en/GLONASS/*.

ICG (2010). *Current and Planned Global and Regional Navigation Satellite Systems and Satellite-based Augmentations Systems*. International Committee on Global Navigation Satellite Systems, UN Office for Outer Space Affairs, New York, USA. Retrieved from *http://www.unoosa.org/pdf/publications/icg_ebook.pdf*.

ITU (2014). *Measuring the Information Society Report 2014*. International Telecommunication Union, Geneva, Switzerland. Retrieved from *http://www.itu.int/en/ITU-D/Statistics/Pages/publications/mis2014.aspx*.

Jawad, I. (2014). *World's Top Global Mega Trends To 2025 and Implications to Business, Society and Cultures*. Paper presented at the Baltic Sea Region IPA Forum, Helsinki. *http://www.investinbsr.com/ipaforum/wp-content/uploads/Iain-Jawad-IPA-Forum-2014-Presentation.pdf*.

Keysers, J. (2015). *Review of Digital Globes 2015*. Australia and New Zealand Cooperative Research Centre for Spatial Information. Retrieved from *http://www.crcsi.com.au/assets/Uploads/Globe-review-paper-March-2015.pdf*.

Korolov, M. (2015). *Geofencing could add security layer for mobile devices*. Retrieved from *http://www.csoonline.com/article/2891834/mobile-security/geofencing-could-add-security-layer-for-mobile-devices.html*.

Kramer, H. J. (2002). *Observation of the Earth and its Environment: Survey of Missions and Sensors*. Springer-Verlag, Berlin Heidelberg.

Lafleur, C. (2015). *Spacecraft Encyclopedia: A Comprehensive Census of All Spacecraft Ever Launched*. Retrieved from *http://claudelafleur.qc.ca/Spacecrafts-index.html*.

Lan, L., Li, J., and Baoyin, H. (2015). Debris Engine: A Potential Thruster for Space Debris Removal. *arXiv*(1511.07246).

LeHong, H., and Velosa, A. (2014). *Hype Cycle for the Internet of Things, 2014*. Retrieved from *https://www.gartner.com/doc/2804217/hype-cycle-internet-things-*.

Lendino, J. (2015). *DARPA to re-invent GPS navigation without the use of satellites*. Retrieved from *http://www.extremetech.com/extreme/202111-darpa-to-re-invent-gps-navigation-without-satellites*.

Locata (2013). *White Sands Missile Range LocataNet*. Retrieved from *http://www.locata.com/article/white-sands-missile-range-locatanet-new/*.

Mandel, E. (2014). *How the Napa earthquake affected bay area sleepers*. Retrieved from *https://jawbone.com/blog/napa-earthquake-effect-on-sleep/*.

MAPS (2016). *Mapping and Planning Support*. Retrieved from *http://www.maps-group.org/about_us*.

McGrath, D. (2014). *Geo-location to Combat Fraud*. Retrieved from *http://blogs.unisys.com/financialindustryinsights/geo-location-to-combat-fraud/*.

McKinnon, M. (2014). *A History of Garbage in Space*. Retrieved from *http://space.gizmodo.com/a-history-of-garbage-in-space-1572783046*.

McLellan, C. (2013). *Big data: An overview*. Retrieved from *http://www.zdnet.com/article/big-data-an-overview/*.

Mueller, N., Lewis, A., Roberts, D., Ring, S., Melrose, R., Sixsmith, J., Lymburner, L., McIntyre, A., Tan, P., Curnow, S., and Ip, A. (2016). Water observations from space: Mapping surface water from 25 years of Landsat imagery across Australia. *Remote Sensing of Environment, 174*, pp. 341-352. doi:*http://dx.doi.org/10.1016/j.rse.2015.11.003*.

Ninti One (2015). *Managing Australian cattle stations from space*. CRC Remote Economic Participation. Retrieved from *http://scinews.com.au/releases/988/view*.

NRM Hub (2016). *NRM Hub: Providing rangeland managers with quality information to make better decisions*. Retrieved from *http://www.nrmhub.com.au/*.

NSTAC (2014). *NSTAC Report to the President on the Internet of Things*. The President's National Security Telecommunications Advisory Committee.

OGC (2012). *Earth Observation Metadata profile of Observations and Measurements* (OGC 10-157r3) (J. Gasperi, F. Houbie, A. Woolf, and S. Smolders Eds.). Open Geospactial Consortium.

OGC (2015). *OGC Smart Cities Spatial Information Framework*. Open Geospatial Consortium. Retrieved from *https://portal.opengeospatial.org/files/?artifact_id=61188*.

Open Digital Earth Foundation (2015). *Queensland G20 Globe*. Retrieved from *https://digitalearthglobe.org/home/news-2/*.

Pearce, K. (2016). *Eye in the sky on reef pollution*. Retrieved from *https://blogs.csiro.au/ecos/eye-sky-reef-pollution/*.

Pearson, J., Levin, E., Oldson, J., and Carroll, J. (2010). *ElectroDynamic Debris Eliminator (EDDE): Design, Operation, and Ground Support*. Paper presented at the Advanced Maui Optical and Space Surveillance Technologies Conference, Wailea, Maui, Hawaii.

Perez, S. (2016). *Pokémon Go passed 100 million installs over the weekend*. Retrieved from *https://techcrunch.com/2016/08/01/pokemon-go-passed-100-million-installs-over-the-weekend/*.

Porter, M. E., and Heppelmann, J. E. (2014). How Smart, Connected Products Are Transforming Competition. *Harvard Business Review*.

Ramsey, E., Rangoonwala, A., Suzuoki, Y., and Jones, C. E. (2011). Oil Detection in a Coastal Marsh with Polarimetric Synthetic Aperture Radar (SAR). *Remote Sensing, 3*(12), pp. 2630-2662. doi:*http://dx.doi.org/10.3390/rs3122630*.

Rizos, C. (2013). Synchronized Ground Networks Usher in Next-Gen GNSS: Locata Fills Satellite Availability Holes in Obstructed Environments. *GPS World*, 36-42. Retrieved from *http://gpsworld.com/synchronized-ground-networks-usher-in-next-gen-gnss/*.

Rizos, C., Kealy, A., Li, B., Choudhury, M., Choy, S., and Feng, Y. (2014). *Locata's VRay™ Antenna Technology – Multipath Mitigation for Indoor Positioning*. Paper presented at the 27th International Technical Meeting of The Satellite Division of the Institute of Navigation (ION GNSS+ 2014), Tampa, Florida.

Rothballer, C., Lam-Frendo, M., Kim, H., and others (2014). *Strategic Infrastructure: Steps to Operate and Maintain Infrastructure Efficiently and Effectively*. World Economic Forum.

RPAS (2016). *Drone Laws in Australia - We explain CASA CASR 101 laws for RPAS in Australia*. Retrieved from *https://www.rpastraining.com.au/casr-101-uav-drone-legal-or-illegal*.

Russell, S., Dewey, D., and Tegmark, M. (2015). *Research Priorities for Robust and Beneficial Artificial Intelligence*, Future of Life Institute. Retrieved from *http://futureoflife.org/data/documents/research_priorities.pdf*.

Sanchez, L., Munoz, L., Antonio Galache, J., Sotres, P., Santana, J. R., Gutierrez, V., Ramdhany, R., Gluhak, A., Krco, S., Theodoridis, E., and Pfisterer, D. (2014). SmartSantander: IoT experimentation over a smart city testbed. *Computer Networks, 61*, pp. 217-238. doi:*http://dx.doi.org/10.1016/j.bjp.2013.12.020*.

SERC (2016). *The Space Environment Research Centre Limited - Research Programs*. Retrieved from *http://www.serc.org.au/research/*.

Smith, W. L., Harrison, F. W., Revercomb, H. E., Bingham, G. A., Huang, H. L., and Le Marshall, J. F. (2000). *The Geostationary Imaging Fourier Transform Spectrometer*. Paper presented at the Technical Proceedings of the Eleventh International TOVS Study Conference, Budapest, Hungary.

Storm, D. (2015). *Wearing GPS ankle monitor is a search, yet apps track your location every 3 minutes*. Retrieved from *http://www.computerworld.com/article/2904833/wearing-gps-ankle-monitor-is-a-search-yet-apps-track-your-location-every-3-minutes.html*.

Strickland (2014). Medtronic Wants to Implant Sensors in Everyone. *IEEE Spectrum*. Retrieved from *http://spectrum.ieee.org/tech-talk/biomedical/devices/medtronic-wants-to-implant-sensors-in-everyone*.

Symbios (2015). *Risks of Data Supply of Earth Observations from Space for Australia*. Australia and New Zealand Cooperative Research Centre for Spatial Information. Retrieved from *http://www.crcsi.com.au/assets/Program-2/Risks-of-Data-Supply-of-Earth-Observations-from-Space-for-Australia-Symbios-Communications-Final.pdf*.

Technavio (2015). *Global Real-time Location System (RTLS) market 2015-2019*. Retrieved from *http://www.technavio.com/report/global-real-time-location-system-rtls-market-2015-2019*.

Telsyte (2015). *Cut through: How the Internet of Things is sharpening Australia's competitive edge*. Retrieved from *http://download.microsoft.com/documents/australia/server-cloud/Microsoft_IoT_Whitepaper_Final.pdf*.

UCS (2016). *UCS Satellite Database*. Retrieved from *http://www.ucsusa.org/nuclear-weapons/space-weapons/satellite-database*.

Urbanski, A. (2015). *Mobile Campaigns Drive Twice the Sales of Desktop* Retrieved from *http://www.dmnews.com/mobile-marketing/study-mobile-campaigns-drive-twice-the-sales-of-desktop/article/413941/*.

Vandrico (2016). *Wearable Technology Database*. Retrieved from *http://vandrico.com/wearables/*.

Vermesan, O., and Friess, P. (2013). *Internet of Things: Converging Technologies for Smart Environments and Integrated Ecosystems*. River Publishers, Aalborg, Denmark.

Wallace, A. (2015a). *Australia's Locata to direct NASA's UAV tests* Retrieved from *http://www.spatialsource.com.au/latest-news/australias-locata-to-direct-nasas-uav-tests*.

Wallace, A. (2015b). *CSIRO signs cooperative agreement with ESA*. Retrieved from *http://www.spatialsource.com.au/latest-news/csiro-signs-cooperative-agreement-with-esa*.

Whan, I., Chudleigh, P., and Petty, S. (2010). *The business case for Precision Livestock Management technologies and applications*. Meat & Livestock Australia Limited (MLA), Sydney, Australia.

Woodgate, P., Coppa, I., and Hart, N. (2014). *Global Outlook 2014: Spatial Information Industry.* Australia and New Zealand Cooperative Research Centre for Spatial Information. Retrieved from *http://www.crcsi.com.au/assets/Resources/Global-Outlook-Report-November-2014.pdf*.

Zetter, K. (2015). *Feds Say That Banned Researcher Commandeered a Plane*. Retrieved from *https://www.wired.com/2015/05/feds-say-banned-researcher-commandeered-plane/*.

Earth Observation:
Data, Processing and Applications

Volume 1X: Data—Appendices



This publication is available in PDF format at *eopublications.au*.
We welcome your comments regarding the readability and usefulness of this report.
To provide feedback, please email *feedback@eopublications.au*.

Publisher:
Australia and New Zealand CRC for Spatial Information

ISBN [ONLINE]:
978-0-9943019-6-3

Copyright:
All material in this publication is licensed under a Creative Commons Attribution 4.0 Australia Licence, save for content supplied by third parties, and logos. Creative Commons Attribution 4.0 Australia Licence is a standard form licence agreement that allows you to copy, distribute, transmit and adapt this publication provided you attribute the work. The full licence terms are available from *https://creativecommons.org/licenses/by/4.0/legalcode*. A summary of the licence terms is available from *https://creativecommons.org/licenses/by/4.0/*.



Disclaimer:
While every effort has been made to ensure its accuracy, the CRCSI does not offer any express or implied warranties or representations as to the accuracy or completeness of the information contained herein. The CRCSI and its employees and agents accept no liability in negligence for the information (or the use of such information) provided in this report.

Recommended Citation for Volume 1X:
CRCSI (2018) *Earth Observation: Data, Processing and Applications. Volume 1X: Data—Appendices*. (Eds: Harrison, B.A., Jupp, D.L.B., Lewis, M.M., Forster, B.C., Mueller, N., Smith, C., Phinn, S., Hudson, D., Grant, I., Coppa, I.) CRCSI, Melbourne.

Latest Revision:
October 2025

Background image on previous page: This HyMap airborne hyperspectral image mosaic over the Dalhousie Springs Complex, in far-northern South Australia. It is displayed using the 0. 0.636 μm band as red, the 0.544 μm band as green and the 0.467 μm band as blue. This region features extensive wetlands in an arid environment, fed by Great Artesian Basin spring flows. This imagery was acquired by HyVista Corporation for the *Allocating Water and Maintaining Springs of the Western Great Artesian Basin* project in 2009. **Source:** Megan Lewis, University of Adelaide

Table of Contents

Appendix 1 Recommended Reading **1**
- **A1.1** Professional Journals 1
- **A1.2** Textbooks 1

Appendix 2 Professional Societies **3**

Appendix 3 EO Data and Information Sources **5**
- **A3.1** Australian 5
- **A3.2** International 6
- **A3.3** USA 6
- **A3.4** Canada 7
- **A3.5** Europe 7
- **A3.6** Asia 7

Appendix 4 Photographic Products **9**
- **A4.1** Photographic Film 9
- **A4.2** Aerial Photography 11
- **A4.3** The Digitising Process 12
- **A4.4** Further Information 12
- **A4.5** References 12

Appendix 5 Measuring Reflectance **13**
- **A5.1** Radiance and Irradiance 13
- **A5.2** Reflectance 14
- **A5.3** BRDF and reflectance functions 15
  - **A5.3.1** Directional reflectance factor 15
  - **A5.3.2** Irradiance reflectance 15
  - **A5.3.3** Summary of special cases 16
- **A5.4** Natural Radiation Measurements 17
- **A5.5** Measuring Reflectance in the Field 18
  - **A5.5.1** Establishing K-factor panels 19
  - **A5.5.2** Measuring diffuse radiation 20
- **A5.6** Summary 21
- **A5.7** References 21

List of Figures

Figure A4.1 Spectral sensitivities of panchromatic film 10

Figure A4.2 Spectral sensitivities of visible colour and colour infrared film 10

Figure A4.3 Photographic scale 11

Figure A4.4 A digital image 12



Appendix 1
Recommended Reading

A1.1 Professional Journals

- Asian Journal of Remote Sensing
- Canadian Journal of Remote Sensing
- Geocarto International
- IEEE Transactions on Geoscience and Remote Sensing
- International Journal of Digital Earth
- International Journal of Geographical Information Systems
- International Journal of Remote Sensing
- Journal of Applied Meteorology
- Journal of Geophysical Research
- Journal of Ocean Engineering
- Marine Geodesy
- Photogrammetria
- Photogrammetric Engineering and Remote Sensing
- Remote Sensing
- Remote Sensing in Ecology and Conservation
- Remote Sensing of Environment
- Sensors
- Space Technology: Industrial and Commercial Applications

A1.2 Textbooks

ASPRS: *Manual of Remote Sensing*. 3rd edn (Ed: Rencz, A.N.) John Wiley and Sons.
Volume 1—*Earth Observing Platforms and Sensors* (Eds: Morain, S.A., Budge, A.M.)
Volume 2—*Principles of Imaging Radar* (Eds: Henderson, F.M., and Lewis, A.J.)
Volume 3—Remote Sensing for the Earth Sciences (Ed: Rencz, A.)
Volume 4—Remote Sensing for Natural Resource Management and Environmental Monitoring (Ed: Ustin, S.L.)
Volume 5—*Remote Sensing of Human Settlement* (Eds: Ridd, M.R., and Hipple, J.D.)

Campbell, J.B., and Wynne, R.H. (2011) *Introduction to Remote Sensing*. 5th edn. Guilford Press, New York.

Castleman, K.R. (1996) *Digital Image Processing*. Prentice Hall.

Chuvieco, E., and Huete, A. (2010) *Fundamentals of Satellite Remote Sensing*. CRC Press, Boca Raton.

Cracknell, A. (2007) *Introduction to Remote Sensing*. 2nd edn. Taylor and Francis.

Curran, P.J. (1985) *Principles of Remote Sensing*. Longman.

Drury, S.A. (2001) *Image Interpretation in Geology* 3rd edn. Blackwell Science.

Elachi, C., and van Zyl, J. (2006) *Introduction to the Physics and Techniques of Remote Sensing*. 2nd edn. John Wiley and Sons.

Gibson, P.J. and Power, C. H. (2000) *Introductory Remote Sensing Principles and Concepts*. London, Routledge.

Gonzalez, R.C., and Woods, R.E. (2018) *Digital Image Processing*. Pearson Educational Inc., New York.

Jensen, J.R. (1986) *Introductory Digital Image Processing*. 2nd edn. Prentice Hall.

Jensen, J.R. (2007) *Remote Sensing of the Environment*: An Earth Resource Perspective. 2nd edn. Prentice Hall.

Lillesand, T.M. and Kiefer, R.W. (2000) *Remote Sensing and Image Interpretation*. 4th edn. John Wiley and Sons, New York.

Richards, J. (2009) *Remote sensing with imaging radar*. Springer, Heidelberg.

Richards, J.A. and Xiuping, J. (2006) *Remote Sensing Digital Image Analysis: An Introduction*. 4th edn. Springer.

Background image: Landsat-5 image, acquired on 29 April 2011 over Shark Bay, WA, displayed as true colour (using bands 3, 2, 1 as RGB).
Source: Norman Mueller, Geoscience Australia



Appendix 2
Professional Societies

International Society for Photogrammetry and Remote Sensing (ISPRS): *http://www.isprs.org/*

National societies that are members of the ISPRS are listed here: *http://www.isprs.org/links/members.aspx*
They include:
American Society for Photogrammetry and Remote Sensing (ASPRS): *http://www.asprs.org/*
The Remote Sensing and Photogrammetry Society (RSPSoc): *http://www.rspsoc.org.uk/*
IEEE Geoscience and Remote Sensing Society (GRSS): *http://www.grss-ieee.org/*
Canadian Aeronautics and Space Institude (CASI): *http://www.casi.ca*

Earth Observation Australia: : http://www.eoa.org.au

The Colour Society of Australia is concerned with various aspects of colour measurement and perception and thus has relevance to remote sensing and image processing: *http://www.coloursociety.org.au*

Background image: Sentinel-2 image of Port Alma, Queensland, acquired on 24 January 2016, showing saltpans and mangroves in Fitzroy River delta (displayed using bands 11, 8, 3 as RGB). **Source:** Norman Mueller, Geoscience Australia



Appendix 3
EO Data and Information Sources

A3.1 Australian

Government

Geoscience Australia (GA): *http://www.ga.gov.au/scientific-topics/earth-observation.html*

Introduces remote sensing concepts and provides information on data sources. Includes a catalogue of satellite images that may be downloaded or purchased, plus facts and examples for different types of images.

Regional Copernicus Data Hub: *http://www.copernicus.gov.au/*

Serves Sentinel satellite data.

Commonwealth Scientific and Industrial Research Organisation (CSIRO):

Australian-waters Earth Observation Phytoplankton-type Products Data Base: *http://aesop.csiro.au/*

Serves marine in-situ optical data.

Landgate: *https://www.landgate.wa.gov.au/maps-and-imagery*

Bureau of Meteorology: *http://bom.gov.au*

Marine Water Quality Dashboard: *http://www.bom.gov.au/marinewaterquality/*

Serves satellite derived water quality information and data.

Reef Temp: *http://www.bom.gov.au/environment/activities/reeftemp/reeftemp.shtml*

Serves satellite information on coral bleaching risk.

Academia

Terrestrial Ecosystem Research Network (TERN): *http://www.tern.org.au*

TERN Auscover Remote Sensing Data Facility: *http://www.auscover.org.au*

TERN SuperSites: *http://www.supersites.net.au*

TERN OzFlux: *http://www.ozflux.org.au*

Integrated Marine Observing System (IMOS): *http://www.imos.org.au*

Australian Ocean Data Network (AODN): *https://portal.aodn.org.au/*

Serves marine in-situ and satellite observations made under IMOS.

IMOS Ocean Current: *http://oceancurrent.imos.org.au/*

Serves satellite observations of currents and sea surface temperature.

University of Queensland—Remote Sensing Toolkit: *Http//www.sees-rsrc.science..uq.edu.au/cser-rstoolkit*

KEJOYCE.COM .

http://www.kejoyce.com/education.html

Flinders University:

Airborne Research Australia (ARA): *http://www. airborneresearch.org.au*

Background image: Landsat-5 image of Australia's most devastating bushfires, known as the Black Saturday Fires, in Victoria, which ignited on 7 February 2009. This image was acquired on 17 February and shows the extensive areas impacted by the fires as brown scars in the centre of the image. These fires have been rated as the world's worst fire event, involving 173 deaths, destruction of over 2,000 houses, and burning of over 400,000 ha. This image is displayed using bands 5, 4, 2 as RGB. **Source:** Norman Mueller, Geoscience Australia

Private Companies

AirAffairs: *http://www.airaffairs.com.au*

An Australian company providing specialised airborne and engineering services, including bushfire mapping.l

Airbus Defence and Space: *https://airbusdefenceandspace.com*

An international company developing both military aircraft and space systems, including a comprehensive range of EO satellites systems, as well as communications, intelligence and security systems.

Digital Globe: *https://www.digitalglobe.com*

An international company operating constellations of high spatial resolution satellites.

Geoimage: *http://www.geoimage.com.au/media/brochures*

An Australian company distributing imagery. Informative web site and brochures on remote sensing principles, applications and image types.

Nearmap: *http://au.nearmap.com*

An Australian company with a proprietary technology platform that combines aerial camera systems, rapid image processing and data visualisation applications, enabling it to regularly capture and publish high resolution aerial surveys.

Spookfish: *https://www.spookfish.com*

An Australian company using a dynamic motion camera to capture high resolution imagery across the continent to deliver two- and three-dimensional datasets.

Fugro Spatial Solutions: *http://www.fugrospatial.com.au*

Australia's largest aerial survey company.

Hyvista Corporation: *http://www.hyvista.com*

An Australian company specialising in the supply of airborne hyperspectral remote sensing data, large format digital imagery and value-added information products.

AAM Group: *http://www.aamgroup.com*

An Australian company specialsing in the collection, analysis, presentation and delivery of geospatial information.

A3.2 International

Committee on Earth Observation Satellites (CEOS): *http://www.ceos.org*

International committee coordinating civil spaceborne observations of the Earth.

EO Handbook: *http://www.eohandbook.com*

A3.3 USA

Government

National Aeronautical and Space Agency (NASA): *http://www.nasa.gov*

Landsat Science—Education: *http://landsat.gsfc.nasa.gov/education/*

A very comprehensive website covering remote sensing theory and history, image processing, applications and specialist forms of remote sensing.

NASA World Wind: *http://worldwind.arc.nasa.gov*

Viewing of images from several sensors for the world.

NASA Goddard Space Flight Centre: *http://imagine.gsfc.nasa.gov/docs/sats_n_data/sats_n_data.html*

Aster Spectral Library: *http://speclib.jpl.nasa.gov*

NASA Aeronet-Ocean Colour: *http://aeronet.gsfc.nasa.gov/cgi-bin/type_one_station_seaprism_new?site=Lucinda&nachal=2&level=1&place_code=10*

Serves a few of the Lucinda above-water measurements (IMOS; see Section 10).

United States Geological Survey (USGS): *http://www.usgs.gov*

USGS Global Visualization Viewer: *http://glovis.usgs.gov*

GloVis allows you to visually search, download and order various satellite data including Landsat.

USGS Spectroscopy: *http://speclab.cr.usgs.gov/PAPERS.refl-mrs/refl4.html#section1.1*

Chapter 1 from Volume 3 in Manual of Remote Sensing, includes detailed background information relating to spectroscopy of rocks and minerals.

USGS Spectral Library: *http://speclab.cr.usgs.gov/index.html*

National Oceanic and Atmospheric Administration (NOAA): *http://www.noaa.gov*

Academia

The Pennsylvania State University: *https://www.e-education.psu.edu/geog883/*

University of Colorado at Boulder

The Geographer's Craft: *http://www.colorado.edu/geography/gcraft/contents.html*

National Earth Science Teachers Association

Windows to the Universe: *http://www.windows2universe.org*

Federation of American Scientists

Remote Sensing Tutorial (Nicholas Short): *http://www.fas.org/irp/imint/docs/rst/Front/overview.html*

Private Companies:

The Light Measurement handbook: *http://www.intl-lighttech.com/services/light-measurement-handbook*

TNT Mips

Introduction to Remote Sensing of the Environment: *http://www.microimages.com/documentation/Tutorials/introrse.pdf*

ERDAS/ERmapper: *http://www.erdas.com*

A3.4 Canada

Canada Centre for Remote Sensing, Natural Resources Canada: *http://www.nrcan.gc.ca/earth-sciences/geomatics/satellite-imagery-air-photos/satellite-imagery-products/educational-resources/9309*

A3.5 Europe

European Space Agency (ESA): *http://www.esa.int/ESA*

Science Education through Earth Observation for High Schools (SEOS, ESA/ESRIN): *http://www.seos-project.eu/modules/remotesensing/remotesensing-c00-p01.html*

eLearning tutorials

Advanced Training Course on Land Remote Sensing: *http://earth.esa.int/landtraining07/*

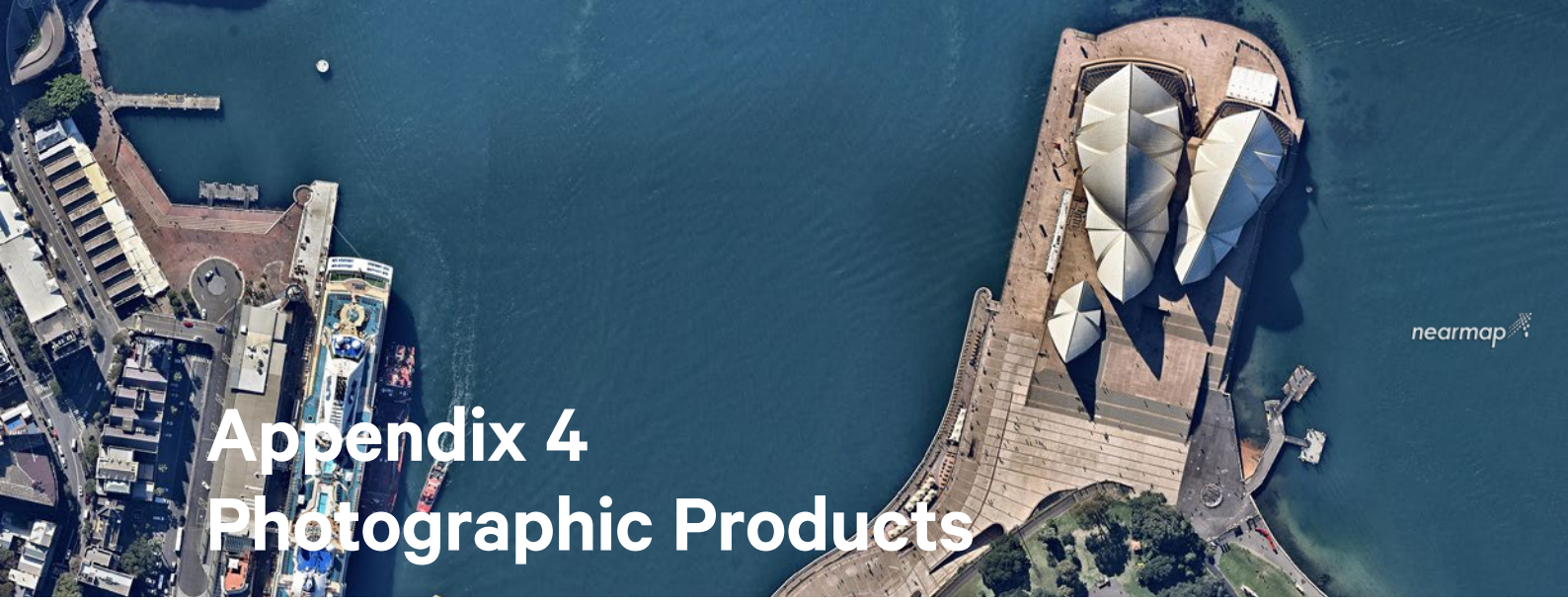
University College London: *http://www2.geog.ucl.ac.uk/~mdisney/teaching/PPRS/PPRS_5/principles5.pdf*

A3.6 Asia

Japanese Aerospace Exploration Agency (JAXA): *http://global.jaxa.jp*

Centre for Remote Imaging, Sensing and Processing

Principles of Remote Sensing (S.C. Liew): *http://www.crisp.nus.edu.sg/~research/tutorial/rsmain.htm*



Appendix 4
Photographic Products

The first remote sensors were aerial cameras recording images onto light-sensitive film (see Sardar (1997), for a summary of the historical development of remote sensing). A major advantage of photographic imagery is its technical simplicity in terms of processing and interpretation. An important disadvantage, however, is that the utility of photographic products are controlled by the quality of acquisition and processing, especially for monitoring applications where multiple photographs acquired on different dates or for different areas need to be compared.

A4.1 Photographic Film

The range of wavelengths that may be detected by traditional (film-based) photographic devices is limited by the sensitivities of the film and filter(s) being used in the camera. The spectral sensitivity of photographic film can range from ultraviolet to near infrared wavelengths. Filters may be used in conjunction with different film types to restrict the wavelengths being recorded or reduce the effect of atmospheric haze. Multi-band cameras, which simultaneously record multiple photographic impressions of an object, may be used to simulate a multi-spectral image. Such cameras use varying film and filter combinations to record different spectral regions in each photograph.

Photographic film may be sensitive to wavelengths over a single range (such as single layer black and white film) or in three wavelength ranges (such as three-layer colour film). The four types of film that may be used for aerial photography are:

- black and white visible, or 'panchromatic' (sensitive to wavelengths in the range 0.3–0.7 μm)
- black and white near infrared
- colour visible
- false colour near infrared

There are two types of panchromatic film:

- 'mapping' film which has roughly equal sensitivity to all visible wavelengths. This is the most commonly used film for aerial photography. It may be used in conjunction with a 'minus-blue' (blue absorbing) filter to reduce the effects of atmospheric scattering and haze in the blue end of the EM spectrum; and
- 'reconnaissance' film which is less sensitive in the blue wavelength region to reduce the effect of atmospheric scattering.

Panchromatic film is sensitive to visible wavelengths in the range 0.3–0.7 μm (see Figure A4.1). The spectral sensitivity of black and white infrared film extends to about 0.9 μm in the near infrared region (see Figure A4.1). It can be used with a dark red absorption filter to record near infrared radiation only, or with appropriate filters to record selected regions in both visible and near infrared wavelengths.

As colour film is designed to mimic human vision, its three emulsion layers are sensitive to the three wavelength regions of blue, green and red.

The spectral sensitivity of colour infrared film differs from normal colour film. Colour infrared film is used in conjunction with a yellow (blue absorbing) filter to record green, red and infrared radiation onto its three emulsion layers. This relationship produces false colour imagery with characteristic colours for different land covers:

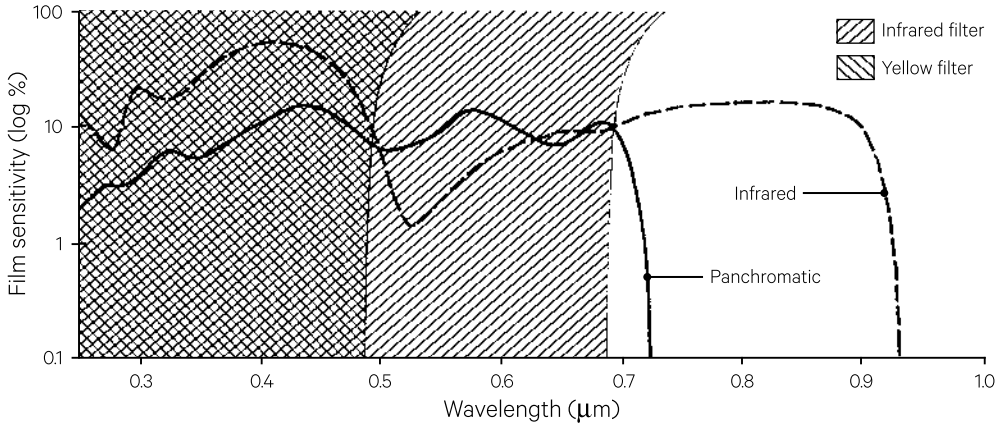
- green vegetation appears red;
- deep clear water is dark blue;
- turbid water is bright blue;
- red soil appears green; and
- bright urban areas appear pale blue.

The concepts of colour and colour mixing are introduced in Volume 1A and further discussed in Volume 2. The sensitivities of colour and colour infrared films are illustrated in Figure A4.2.

Background image: High resolution airborne image acquired by Nearmap on 5 May 2016, showing Opera House and Circular Quay in Sydney. **Source:** © Nearmap

Figure A4.1 Spectral sensitivities of panchromatic film

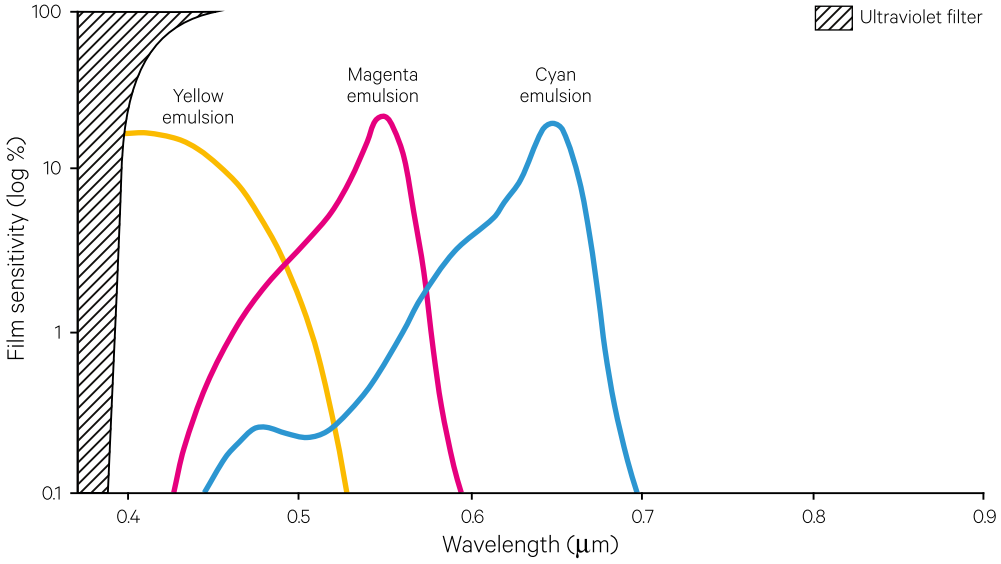
This graph compares the spectral sensitivity of panchromatic 'visible' film and 'infrared' film. It also shows the spectral impact of using a yellow filter.



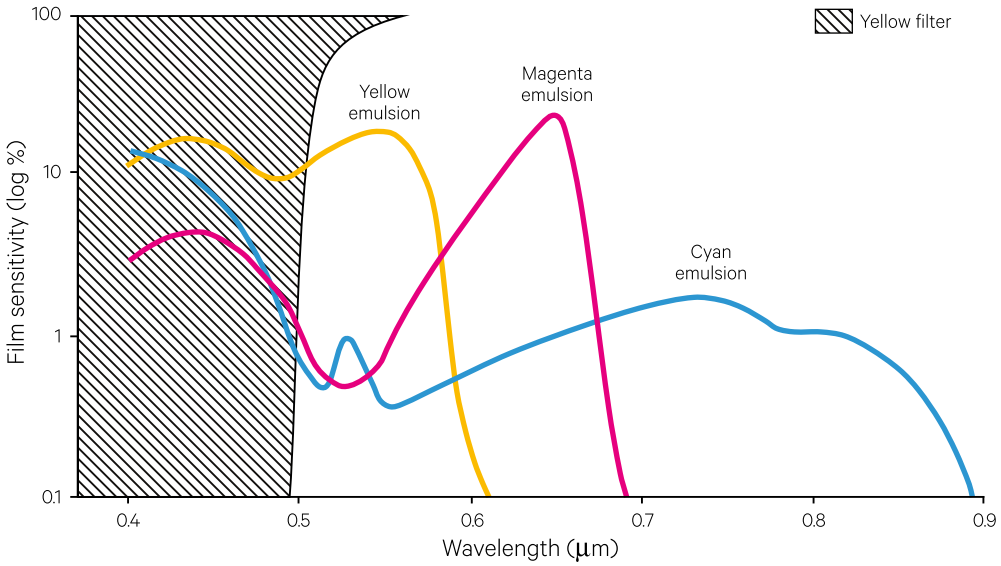
Source: Harrison and Jupp (1989) Figure 13

Figure A4.2 Spectral sensitivities of visible colour and colour infrared film

a. Colour Film



b. Colour Infrared Film



Source: Harrison and Jupp (1989) Figure 14

A4.2 Aerial Photography

The spatial resolution of aerial photography is determined by the combined effects of film grain, camera optics and flying height. The scale of aerial photography may be determined by dividing the focal length of the camera by the vertical height of the lens above ground level (see Figure A4.3):

$$S = \frac{f}{H - h}$$

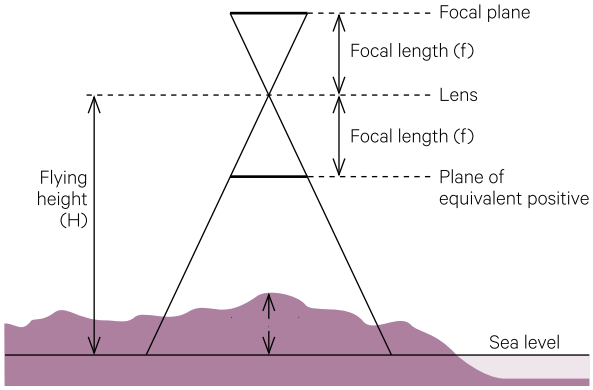
where

S is the scale;
f is the focal length;
H is the flying height; and
h is the terrain elevation.

If these parameters are unknown, the scale may also be computed by dividing the distance between two points on the photograph by the ground distance separating them. In either case, the units used to measure these parameter pairs must be consistent. The resulting scale is generally referenced as a fraction (e.g. 1/25,000) or ratio (e.g. 1:25,000).

Since photographic devices can only directly detect radiation in the visible and near infrared range of the EM spectrum, the resulting data are affected by cloud cover. Photographic imagery may also be produced for other wavelength regions using film-recording techniques after the radiation has been initially recorded by appropriate sensors. The range of processing options available for photographic imagery (without digitising) is greatly reduced compared with the range for digital imagery.

Figure A4.3 Photographic scale



Remote sensing devices that record data photographically require that the film be recoverable for processing. Such devices have been carried by manned and unmanned aircraft, or retrievable spacecraft (such as the Space Shuttle). Examples of data collected this way include traditional aerial photography, the Large Format Space Camera imagery and Shuttle Imaging Radar scenes.

Interpretation of photographic imagery has traditionally relied heavily on the skills and time of a trained human interpreter. Tools for photointerpretation include colour or tone, texture, patterns, shapes, shadows, as well as feature size and situation. Photographic data may be converted into a digital image via the digitising process described in Appendix 4.3.

More recently, digital cameras are used in preference to film cameras. These ubiquitous devices are becoming ever cheaper, smaller and more powerful. At the top end of the range, gigapixel cameras acquire very high spatial resolution imagery for a range of applications, including Earth Observation (EO).

A4.3 The Digitising Process

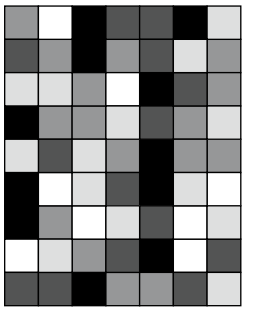
Any picture, photograph or map can be digitised. Automatic scanning devices, which operate in a similar manner to the satellite scanning systems, can be used to convert coloured or black and white maps, pictures or photographs, into digital images for processing by computer.

The conversion of an image from pictorial to 'raster' format is called scan digitising (as opposed to line digitising), and involves two basic processes:

- Sub-divide the image using a grid (or some other systematic tessellation) pattern into small cells called picture elements or pixels. Obviously, a finer digitising grid will produce a digital image with greater spatial detail but also with a larger number of pixels.
- Assign a single numeric value to each pixel to represent its overall brightness level. When a number has been assigned to every pixel, the image is represented by a two-dimensional integer array as shown in Figure A4.4.

Figure A4.4 A digital image

The 'colour' of each grid cell is represented by a number



3	5	1	2	2	1	4
2	3	1	3	2	4	3
4	4	3	5	1	2	3
1	3	3	4	2	3	4
4	2	4	3	1	3	3
1	5	4	2	1	4	5
1	3	5	4	2	5	4
5	4	3	2	1	5	2
2	2	1	3	3	2	4

Source: Harrison and Jupp (1989) Figure 15

A colour image is scanned into three channels, with each channel representing one of the primary colours: blue, green and red. It is possible to recombine several (usually three) registered image channels through a colour additive technique (see Figure 13.2) to generate a colour composite image. The specific colours thus regenerated depend on the grey level patterns in each individual image channel and on the colour filters used in the additive process. Those colour renditions that simulate the original scene colours are called natural colour images; those consisting of significantly different colours to the original scene are referred to as false colour images. The digital image and its processing is further discussed in Volume 2. While the scan digitising process is usually automated, with the grid size being quite small and very subtle changes in colour being recorded as different digital values, the process could be simulated manually for simplified maps.

A4.4 Further Information

Digital Photography Fundamentals: *https://manuals.info.apple.com/MANUALS/0/MA123/en_US/Aperture_Photography_Fundamentals.pdf*

A4.5 References

Harrison, B.A., and Jupp, D.L.B. (1989). Introduction to Remotely Sensed data. Part ONE of the microBRIAN Resource Manual. CSIRO Australia, Melbourne.

Sardar, A.M. (1997) Chronology of the development of remote sensing technology. *Asian-Pacific Remote Sensing and GIS Journal* 2, 35–49.



Appendix 5
Measuring Reflectance

Source: Jupp (1997) *Issues in Reflectance Measurement. CSIRO Earth Observation Centre, Canberra.*

Remote sensors and field instruments used to calibrate and/or validate remotely sensed data measure spectral bands of radiation entering across the field of view of one of a number of instruments. In order that there be a fundamental consistency between such measurements it is important that the instruments be cross calibrated when they are measuring similar information and that enough information be collected for the data to be interpretable and relatable to the eventual application taking them serves.

The measurements are of three basic types:

- radiance;
- irradiance; and
- reflectance.

Provided that basic measurements are consistent and the relationships between radiance and irradiance taken into account, the most important area of concern for us will be the consistent definition and derivation of reflectance factors. It is important to realise that, in practice, there will be a number of ways of defining these, that they will normally not be independent of the conditions under which they are measured and the inter-relationship between different measurements will be complex. Many of these differences arise from the geometry of reflectance measurements and Nicodemus *et al.* (1977) contains probably the most extensive classification of possible geometries.

A5.1 Radiance and Irradiance

The radiance of a source or target is the radiant flux per unit solid angle per unit area normal to the source. It is denoted L and is the quantity to which a narrow angle radiometer is calibrated. Laboratory calibration consists of reading a target of known radiance characteristics as the calibration. However, in practice, calibration in a field setting is also usually needed as the object of the exercise is field measurement.

The reason that the laboratory source is not enough is that when instruments read in a broad band and over a finite Instantaneous Field of View (IFOV) the calibration depends on the wavelength distribution and heterogeneity of the incident source. Hence, calibration in the field setting allows the types of irradiance relevant to the application to be sampled as well as standard laboratory sources.

Irradiance is the total hemispherical radiant flux per unit area and for a radiance distribution, $L(\mu)$, at a specific wavelength irradiating a flat target surface, the resulting irradiance, E, is:

$$E = \int_{2\pi} L(\mu)\cos\theta \, d\omega$$

$$= \int_{0}^{2\pi}\int_{0}^{\frac{\pi}{2}} L(\mu)\cos\theta\sin\theta \, d\theta \, d\phi$$

where

- θ, ϕ are the coordinates (zenith, azimuth) of the radiance;
- μ is a symbol denoting the direction cosines of the direction vector;
- ω is solid angle (steradians).

Background image: This Landsat-5 image of Eyre Creek, about 100 km north of Lake Eyre, was acquired on 28 March 2011. Lake Eyre, located in northern SA, is the largest, driest and lowest salt lake in Australia. This image (displayed using bands 2, 4, 5 as RGB) captures this arid region after a rare rainfall event.
Source: Norman Mueller, Geoscience Australia

If the irradiance distribution (such as a sky distribution) were a constant radiance at all points of the hemisphere (L) independent of angle, it would follow that:

$$E = L\int_{2\pi}\cos\theta\, d\omega$$
$$= L\int_{0}^{2\pi}\int_{0}^{\frac{\pi}{2}}\cos\theta\sin\theta\, d\theta\, d\phi$$
$$= \pi L$$

Later, another irradiance definition will be briefly mentioned. It is the scalar irradiance which measures the total incident radiant flux rather than the normal incident radiant flux. It will be denoted here as S and is:

$$S = \int_{2\pi} L(\mu)\, d\omega$$
$$= \int_{0}^{2\pi}\int_{0}^{\frac{\pi}{2}} L(\mu)\sin\theta\, d\theta\, d\phi$$

For a constant radiance distribution (L) it follows that:

$$S = L\int_{2\pi} d\omega$$
$$= L\int_{0}^{2\pi}\int_{0}^{\frac{\pi}{2}}\sin\theta\, d\theta\, d\phi$$
$$= 2\pi L$$

The ratio of the normal irradiance to the scalar irradiance is a measure of the angular distribution of the radiance. It is sometimes called the 'average cosine' of the field.

$$\overline{\mu} = \frac{E}{S} = \frac{\int_{2\pi} L(\mu)\cos\theta\, d\omega}{\int_{2\pi} L(\mu)\, d\omega}$$
$$= \frac{\int_{0}^{2\pi}\int_{0}^{\frac{\pi}{2}} L(\mu)\cos\theta\sin\theta\, d\theta\, d\phi}{\int_{0}^{2\pi}\int_{0}^{\frac{\pi}{2}} L(\mu)\sin\theta\, d\theta\, d\phi}$$

For a uniform distribution of radiance the value of $\overline{\mu}$ is 0.5.

A5.2 Reflectance

The reflectance factor we measure in the laboratory and field is generally one of two types. There is the directional reflectance factor, ρ_t:

$$\rho_t = \frac{\pi L_t(\mu_r)}{E_d}$$

This measurement is the target radiance recorded by the observer in the 'reflected' direction (μ_r) multiplied by π and divided by the total irradiance on the target (E_d). The directional reflectance factor is the factor closest to what is normally produced by atmospheric correction of remotely sensed data and measured in the field with a narrow IFOV radiometer.

A second measured reflectance factor is the irradiance reflectance:

$$R = \frac{E_u}{E_d}$$

This is the ratio of upwelling irradiance to downwelling irradiance and it is the reflectance factor obtained with an integrating sphere or from the ratio of data taken by cosine collecting diffusers in field experiments. It is sometimes called the spectral 'albedo' (Strahler *et al.*, 1995) although the above definition is for a particular wavelength and the albedo of energy balance studies is the ratio of total irradiances over all (shortwave) bands. The irradiance reflectance is measured by a LI-COR instrument in water studies and by an integrating sphere in the laboratory.

There are two complications to be taken into account in practice which will be revisited later. The definitions so far relate to radiances in specific directions in elements of solid angle $d\omega$ and at a single wavelength. All of the instruments we are concerned with measure over finite wavebands and over finite solid angles and the broader these bands and angles are, the further the resulting reflectance factors will diverge from the ones we have so far defined.

A5.3 BRDF and reflectance functions

The BRDF, or Bidirectional Reflectance Distribution Function, $f\left(\mu_r,\mu_i\right)$, is not a reflectance but a 'kernel' or 'phase function' relating incoming and outgoing radiance. The (reflected) radiance observed in the observer direction, $L_r\left(\mu_r\right)$, is the composite of radiances derived from the incident (sky and Sun for field measurements) radiance distribution, $L_i\left(\mu_i\right)$:

$$L_r\left(\mu_r\right)=\int_{2\pi} f\left(\mu_r,\mu_i\right)L_i\left(\mu_i\right)\cos\theta_i\, d\omega_i$$
$$=\int_0^{2\pi}\int_0^{\frac{\pi}{2}} f\left(\mu_r,\mu_i\right)L_i\left(\mu_i\right)\cos\theta_i\sin\theta_i\, d\theta_i\, d\phi_i$$

The BRDF is generally taken as the material property on which the various reflectance factors and other measures can be based.

A5.3.1 Directional reflectance factor

The reflectance measured as the directional reflectance factor, ρ_t, is therefore expressed in terms of the BRDF as:

$$\rho_t=\frac{\pi L_r\left(\mu_r\right)}{E_d}$$
$$=\pi\frac{\int_0^{2\pi}\int_0^{\frac{\pi}{2}} f\left(\mu_r,\mu_i\right)L_i\left(\mu_i\right)\cos\theta_i\sin\theta_i\, d\theta_i\, d\phi_i}{\int_0^{2\pi}\int_0^{\frac{\pi}{2}} L_i\left(\mu_i\right)\cos\theta_i\sin\theta_i\, d\theta_i\, d\phi_i}$$
$$=\pi\overline{f}\left(\mu_r;E_d\right)$$

where $\overline{f}$ is the BRDF and is an irradiance weighted average BRDF which depends on the irradiance angular distribution of E_d as well as the view direction.

For a uniform radiance distribution (L_i a constant for all directions) the measured reflectance factor would be:

$$\rho_t=\pi\overline{f}\left(\mu_r,2\pi\right)$$
$$=\int_0^{2\pi}\int_0^{\frac{\pi}{2}} f\left(\mu_r,\mu_i\right)\cos\theta_i\sin\theta_i\, d\theta_i\, d\phi_i$$
$$=\overline{\rho}\left(\mu_r,2\pi\right)$$

Where $\overline{\rho}\left(\mu_r,2\pi\right)$ is the directional reflectance factor for a uniform distribution and is a function of the material surface being measured.

For a direct beam irradiance from direction μ_s the measured reflectance factor would be:

$$\rho_t=\pi f\left(\mu_r,\mu_s\right)$$
$$=\overline{\rho}\left(\mu_r,\mu_s\right)$$

where $\overline{\rho}\left(\mu_r,\mu_s\right)$ is often called the BRF or Bidirectional Reflectance Factor for direct beam irradiance. It is also a property of the material and is obviously the BRDF up to the factor π.

A5.3.2 Irradiance reflectance

The irradiance reflectance can also be expressed in terms of the BRDF as:

$$R_t=\frac{E_u}{E_d}$$
$$=\frac{\pi\int_0^{2\pi}\int_0^{\frac{\pi}{2}}\overline{f}\left(2\pi,\mu_i\right)L\left(\mu_i\right)\cos\theta_i\sin\theta_i\, d\theta_i\, d\phi_i}{\int_0^{2\pi}\int_0^{\frac{\pi}{2}} L\left(\mu_i\right)\cos\theta_i\sin\theta_i\, d\theta_i\, d\phi_i}$$
$$=\pi\overline{f}\left(2\pi,E_d\right)$$
$$=\overline{\rho}\left(2\pi,E_d\right)$$

where:

$$\overline{f}\left(2\pi,\mu\right)=\frac{\int_0^{2\pi}\int_0^{\frac{\pi}{2}} f\left(\mu_r,\mu\right)\cos\theta_r\sin\theta\, d\theta_r\, d\phi}{\int_0^{2\pi}\int_0^{\frac{\pi}{2}}\cos\theta_r\sin\theta_r\, d\theta\, d\phi_i}$$
$$=\frac{1}{\pi}\int_0^{2\pi}\int_0^{\frac{\pi}{2}} f\left(\mu_r,\mu\right)\cos\theta_r\sin\theta_r\, d\theta_r\, d\phi_r$$

For a uniform irradiance, it follows that:

$$R_t = \frac{\pi \int_0^{2\pi}\int_0^{\frac{\pi}{2}} \overline{f}\left(2\pi,\mu_i\right)\cos\theta_i \sin\theta_i \, d\theta_i \, d\phi_i}{\int_0^{2\pi}\int_0^{\frac{\pi}{2}} \cos\theta_i \sin\theta_i \, d\theta_i \, d\phi_i}$$
$$= \pi\overline{f}\left(2\pi,2\pi\right)$$
$$= \overline{\rho}\left(2\pi,2\pi\right)$$

This 'Bi-hemispherical Reflectance Factor' (Nicodemus *et al.*, 1977) is another material property directly derived from the BRDF. It is close to the measurement made in the laboratory with an integrating sphere.

In addition, if the irradiance is beam irradiance from direction μ_s it follows that:

$$\overline{\rho}\left(2\pi,\mu_s\right) = \pi\overline{f}\left(2\pi,\mu_s\right)$$

Without pursuing the discussion here, the 'reciprocity' principle implies that:

$$\overline{f}\left(\mu,2\pi\right) = \overline{f}\left(2\pi,\mu\right)$$

hence

$$\overline{\rho}\left(\mu,2\pi\right) = \overline{\rho}\left(2\pi,\mu\right)$$

The objective of processing remotely sensed data to 'reflectances' and measuring 'reflectances' is to establish a property of the materials rather than the environmental conditions. The BRDF is not always only a property of the material but the assumption is normally made that it is 'close' to a material property independent of the radiation environment. The BRDF is also the source for the reciprocity relations. Moreover, the measurable reflectance factors have complex geometrical relationships and depend on the environmental conditions. That is, there can really be no 'spectral library' without a clear record of the measurement geometry, the environmental conditions and sensor all being specified. They are part of the spectrum and the only means by which the different measurements can eventually be compared.

The laboratory based integrating sphere irradiance reflectance and the field directional reflectance factors are different measurements and they depend on the irradiating source and the measurement conditions. However, it is our objective to attempt to get standard measurements and material properties. One way towards this is to define a directional quantity:

$$\gamma\left(\mu_r,\mu_s\right) = \frac{\overline{\rho}\left(\mu_r,\mu_s\right)}{\overline{\rho}\left(2\pi,2\pi\right)}$$

This quantity is a material property and contains essentially the directional behaviour.

A5.3.3 Summary of special cases

The BRF is the reflectance measured by the radiance radiometer when there is only incident beam (e.g. Sun) radiation. To summarise the factors arising from the uniform irradiance distribution case in terms of the BRF:

$$\overline{\rho}\left(\mu_r,2\pi\right) = \frac{1}{\pi}\int_0^{2\pi}\int_0^{\frac{\pi}{2}} \overline{\rho}\left(\mu_r,\mu_i\right)\cos\theta_i \sin\theta_i \, d\theta_i \, d\phi_i$$

$$\overline{\rho}\left(2\pi,\mu_i\right) = \frac{1}{\pi}\int_0^{2\pi}\int_0^{\frac{\pi}{2}} \overline{\rho}\left(\mu_r,\mu_i\right)\cos\theta_r \sin\theta_r \, d\theta_r \, d\phi_r$$
$$= \overline{\rho}\left(\mu_i,2\pi\right)$$

$$\overline{\rho}\left(2\pi,2\pi\right) = \frac{1}{\pi}\int_0^{2\pi}\int_0^{\frac{\pi}{2}} \overline{\rho}\left(2\pi,\mu_i\right)\cos\theta_i \sin\theta_i \, d\theta_i \, d\phi_i$$
$$= \frac{1}{\pi}\int_0^{2\pi}\int_0^{\frac{\pi}{2}} \overline{\rho}\left(\mu_r,2\pi\right)\cos\theta_r \sin\theta_r \, d\theta_r \, d\phi_r$$

In Strahler *et al.* (1995), $\overline{\rho}\left(2\pi,\mu_i\right)$ is called the 'Black Sky' Albedo and $\overline{\rho}\left(2\pi,2\pi\right)$ is called the 'White Sky' Albedo. Estimates of these quantities will be standard products from MODIS expressed as polynomial functions. Some simplification of these expressions is also possible if it is assumed the BRDF is symmetrical relative to the Principal Plane and the integrations with respect to ϕ changed to azimuthal difference.

A5.4 Natural Radiation Measurements

The natural light irradiance that is measured by a well calibrated device with a good cosine response has a primary atmospheric component (E_d) that can be expressed as:

$$E_d = E_0' \cos\theta_s t_s + \int_0^{2\pi}\int_0^{\frac{\pi}{2}} L_{sky}\left(\mu_i\right)\cos\theta\sin\theta\, d\theta\, d\phi$$
$$= E_{dir} + E_{diff}$$

where

E_0' is the exoatmospheric normal irradiance (corrected for Sun-Earth geometry);
t_s is the beam transmittance;
L_{sky} is the sky radiance distribution from the upper hemisphere;
E_{dir} is the direct irradiance; and
E_{diff} is the diffuse irradiance.

The ratio of the diffuse term E_{diff} to the total E_d is the fraction of diffuse radiation:

$$f_d = \frac{E_{diff}}{E_d}$$

Strictly, these expressions are for a 'black' Earth but in practice, there are interactions between the Earth and sky which are greatest when the diffuse fraction is high. Radiation reflected back into the atmosphere from the Earth is again reflected back to the surface by an atmospheric reflectance(s). This means that the measured irradiance can be expressed as:

$$E_d^* = \frac{E_d}{1 - s\rho^*}$$

where ρ^* is the local background reflectance near the target which is approximately an average over an area of about 200 metres radius under some conditions and s depends on the atmospheric turbidity. The effects due to s are smallest for clear skies (when the diffuse radiation is low) and highest when the atmospheric turbidity is high (when the diffuse radiation is high).

In practice, the increase in irradiance can be regarded as a component of the (even more diffuse) diffuse sky distribution.

$$E_d^* = E_{dir} + E_{diff}^*$$
$$= E_{dir} + \frac{s\rho^* E_{dir} + E_{diff}}{1 - s\rho^*}$$

and

$$f_d^* = f_d + \left(1 - f_d\right)s\rho^*$$

It is important to recognise the presence of the background effect (which becomes most significant in atmospheric correction) by always assessing and (if possible) measuring the background as part of a target field survey. Because of this extra term, it is often not possible to neglect the effect of the diffuse fraction outlined here, especially in the near infra-red when the background is green.

If the irradiance distribution is modelled simply as a beam term (the direct radiation) and a uniformly diffuse irradiance term (assuming a uniform sky radiance distribution), it follows that the measured reflectance factors will be:

$$\rho_t = \left(1 - f_d\right)\overline{\rho}\left(\mu_r, \mu_s\right) + f_d\,\overline{\rho}\left(\mu_r, 2\pi\right)$$
$$R_t = \left(1 - f_d\right)\overline{\rho}\left(2\pi, \mu_s\right) + f_d\,\overline{\rho}\left(2\pi, 2\pi\right)$$

In this expression there are the three special case material property measures and the fraction of diffuse radiation at the wavelength being measured. This gives a lead as to how field measurements may be done to estimate the BRDF. A range of measurements could taken under natural conditions (where diffuse and direct irradiance terms are measured) with (possibly) both directional and irradiance reflectances measured. If the BRDF is modelled with a parametric model, the parameters could be chosen to fit the data.

Using the directional term defined previously, these equations may be written:

$$\rho_t = \overline{\rho}\left(2\pi, 2\pi\right)\left(\left(1 - f_d\right)\gamma\left(\mu_r, \mu_s\right) + f_d\,\gamma\left(\mu_r, 2\pi\right)\right)$$
$$R_t = \overline{\rho}\left(2\pi, 2\pi\right)\left(\left(1 - f_d\right)\gamma\left(2\pi, \mu_s\right) + f_d\right)$$

It would be ideal if from such field data and other sources (such as airborne data) some relatively consistent γ functions were found for classes of land cover. It may be necessary to use different functions (that is, 'kernels') for the different covers but the key is to have some consistency in the γ functions.

A5.5 Measuring Reflectance in the Field

In principle, if a calibrated instrument measured the radiance and another the irradiance the reflectance could be computed simply as:

$$L_t = \frac{1}{\pi}\rho_t E_d^*$$

$$\rho_t = \frac{\pi L_t}{E_d^*}$$

This is the paired radiometer approach and the operation of atmospheric correction of remotely sensed data effectively works in this same way.

However, in the field there is an alternative and very convenient way to measure the reflectance without separately measuring the irradiance which uses a *reflectance standard*. It can easily be carried out with a single instrument plus a panel rather than two instruments.

A reflectance standard is a panel of known total and directional reflectance properties. If the target radiance (L_t) is measured by a radiance radiometer and the standard radiance (L_s) is also measured under the same geometrical and environmental conditions with the same instrument then, if ρ_s is the known reflectance of the standard it follows that:

$$\rho_t\left(\mu_r, E_d\right) = \frac{\pi L_t\left(\mu_r\right)}{E_d}$$

$$\rho_s\left(\mu_r, E_d\right) = \frac{\pi L_s\left(\mu_r\right)}{E_d}$$

$$\rho_t\left(\mu_r, E_d\right) = \rho_s\left(\mu_r, E_d\right)\frac{L_t\left(\mu_r\right)}{L_s\left(\mu_r\right)}$$

Moreover, suppose the calibration relation between volts measured by the instrument measuring the radiance (with dark current effect removed) and radiance is linear and can be written as:

$$L = c_L V$$

it then follows that the reflectance of the target (t) can be obtained without knowing c as:

$$\rho_t\left(\mu_r, E_d\right) = \rho_s\left(\mu_r, E_d\right)\frac{V_t}{V_s}$$

In this expression, only the properties of the standard must be known other than the uncalibrated target and standard readings.

Note that in the case of the paired radiometers it follows that:

$$\rho_t = \frac{\pi c_L}{c_E}\frac{V_t}{V_d}$$

That is, the ratio of the instrument calibration factors must be known and be stable. However, for expensive instruments the use of paired radiometers is often not an option and only the panel method is feasible.

It is convenient to write the reflectance of the standard panel in the form:

$$\rho_t\left(\mu_r, E_d\right) = R_s K_s\left(\mu_r, \mu_s, f_d; \lambda\right)$$

where R_s is the Bi-hemispherical reflectance of the panel (as measured, for example by an integrating sphere) and K_s is the panel K-factor. It is shown as a function of observer position, Sun position, fraction of diffuse irradiance and wavelength as all of these can affect it.

In terms of modelling the panel BRDF it is useful to consider the simplified irradiance model of direct plus uniform diffuse for which:

$$\begin{aligned}\rho_s\left(\mu_r, E_d\right) &= \left(1-f_d\right)\bar{\rho}\left(\mu_r, \mu_s\right) + f_d\,\bar{\rho}\left(\mu_r, 2\pi\right)\\ &= \bar{\rho}\left(2\pi, 2\pi\right)\left(\left(1-f_d\right)\gamma\left(\mu_r, \mu_s\right) + f_d\,\gamma\left(\mu_r, 2\pi\right)\right)\\ &= R_s K_s\left(\mu_r, \mu_s, f_d; \lambda\right)\end{aligned}$$

That is, the panel could be characterised by its directional function and its Bi-hemispherical Reflectance Factor and K obviously depends on both the Sun and observer positions as well as f_d in the field if there is a significant BRDF variation.

At this point, without going too far with the (very wide) discussion, it is necessary to remember that the panel method discussed here assumes that the panel essentially 'replaces' the target to get the reference measurement. If the target and standard are separated then the measured reflectance factor will be different again from the ones being considered. There are many cases where panel and target are in quite different situations. These provide us with equally different 'reflectance' measurements.

A5.5.1 Establishing K-factor panels

A considerable amount of attention is normally given to making a standard panel close to a 'Lambertian' target. A Lambertian target is perfectly diffusing and has uniform BRDF over the outgoing hemisphere. For a truly Lambertian panel, therefore K_s is 1.0 and only R_s needs to be known. Since a Lambertian panel is difficult to approximate, the panel K-factor must be carefully assessed. Low Sun, specular panel effects and diffuse conditions will create problems if K_s is ignored.

Normally, considerable work is expended on a basic standard panel or money expended to buy a standard panel for the laboratory. These are often quite small and not field-robust. For field missions, the panels normally need to be large and robust as well as able to be cleaned. These requirements often mean they do not have ideal Lambertian behaviour and may change with use. Hence, establishing the panel K-factor and monitoring it is a basic step in field procedure.

The first factor needed is R_s which can be measured using an integrating sphere acting on a piece of the panel. This may only need to be done once - it is a normalising factor.

The panel directional factor could be established in the laboratory by physical measurement. Some investigations of this are needed for the larger field standards but this would be normally the way the 'Lambertian' panel is checked. In the past, people have also attempted to carry out some K-factor estimation of a field panel using the near 'Lambertian' panel and natural light as follows:

- assume that the Laboratory panel is Lambertian and has a spectral reflectance which is a constant R_s in the visible NIR range.
- monitor the radiance of the Laboratory standard and the field panel with a narrow FOV radiance sensor at the same time as monitoring the irradiance using a calibrated irradiance sensor with high spectral resolution.
- monitor the diffuse radiation well as total irradiance.
- collect the data over a number of days, with as wide a variation in Sun positions and view angles as possible.

A set of measurements of this type can be used in a number of ways. One important use is to establish Calibration Consistency. That is, if the sensor being used is calibrated then the following equation needs to be consistent when the Laboratory standard is being measured:

$$L_s\left(\mu_r\right)=\frac{1}{\pi}R_s E_d$$

Since the Lambertian panel reflectance (R_s) is assumed known and E_d is measured, this provides a consistency check on the (inter-)calibrations over a wide range of conditions. Departures from a simple calibration can be expected and this will provide an average 'field' corrected calibration of considerable usefulness.

The field (or 'alternate') panel K-factors can be estimated from the data (assuming the Laboratory panel's K-factor is known and the alternate panel Bi-hemispherical Reflectance Factor has been measured using an integrating sphere) by:

$$K_{alt}\left(\mu_r,\mu_s,f_d;\lambda\right)=\frac{\rho_s}{R_{alt}}\frac{V_{alt}}{V_s}$$
$$=\frac{R_s}{R_{alt}}\frac{V_{alt}}{V_s}K_s\left(\mu_r,\mu_s,f_d;\lambda\right)$$

In this way, the estimated K_{alt} will be measured over many conditions of Sun and observer position and environmental conditions if K_s is known. It is very important to measure the azimuthal variation fully to establish specular effects.

However, even with considerable work, the range of measurements is likely to be limited and not cover the range expected in the field. To overcome this, the best strategy would seem to be to fit the K-factor by a parametric function (which is likely to be much simpler for a panel than a natural surface!). For example, a good candidate might be the 'Walthall model' (Walthall *et al.*, 1985; Strahler *et al.*, 1995).

$$\overline{\rho}\left(\mu_r,\mu_i\right)=p_0\left(\theta_r^{\,2}+\theta_i^{\,2}\right)+p_1\theta_r^{\,2}\theta_i^{\,2}+p_2\theta_r\theta_i\cos\phi+p_3$$

The simplifying assumption of uniformly diffuse sky radiation can additionally be used to provide the model for K (since the γ functions will be computable as rational functions of the parameters):

$$K_s\left(\mu_r,\mu_s,f_d;\lambda\right)=\left(1-f_d\right)\gamma\left(\mu_r,\mu_s\right)+f_d\gamma\left(\mu_r,2\pi\right)$$

In this way, a fairly robust panel 'calibration' would be available that can be used under a wide range of conditions.

If such K-factors are established for the panels and tested relative to good laboratory standards then they can then also provide field checks of radiometer calibration against field robust but accurately calibrated irradiance devices. That is if the panel is read and converted to radiance and the irradiance taken at the same time, the following consistency equation should hold:

$$L_s\left(\mu_r\right)=\frac{1}{\pi}R_s K_s\left(\mu_r,\mu_s,f_d;\lambda\right)E_d$$

Readings under a number of conditions with panel radiance, total irradiance and diffuse irradiance measured can supply a constant check of instrument and/or panel behaviour.

In the field, if a panel model of this kind has been developed, the Sun and view positions as well as the fraction of diffuse at the wavelengths used are necessary data in the measurement set as well as the two target and panel readings and data on sky conditions, surrounding area reflectance ideally should be recorded as well.

A5.5.2 Measuring diffuse radiation

Separating diffuse and direct components of the irradiance is essential in most modelling. At very least, the fraction of diffuse should be established when BRDF effects are strong. Diffuse radiation is generated by many sources. Scattering by air and aerosols is a primary source but high objects on the land surface and clouds generate scattered radiation as well and the sky re-reflects radiation leaving the land back into the diffuse term. Clouds are an especially difficult source to model and take into account in corrections.

Therefore, diffuse radiation measurements should be accompanied by descriptions of the site (trees, buildings etc) and the sky (cloud type and amount) for reference. Given such data, the field crew could obtain diffuse data from two setups:

- shadow band instrument; and
- Sun disk shading a LI-COR irradiance sensor or a Spectron with diffuser.

To get diffuse readings using a Sun disk, the procedure is as follows:

1. Have a Sun disk 10 cm diameter and blackened on a thin stick about 50 cm length.
2. Person using disk should stand on the opposite side of the instrument from the Sun and hold the disk 1 m from the sensor head with the shadow centred on the sensor.
3. Take four readings (the Qin Yi method). One reading with no disk and no person, one reading with person in place but disk not used, one reading with person in place and shading the sensor head and lastly one with no person and no disk to see that there has not been significant change.

The person shading the sensor should wear matt clothes which are not too reflective. Note, denim is bright in the near infrared!

If the four readings in 3. above are denoted $\left[E_1,E_2,E_3,E_4\right]$ then the quantities needed are derived as:

$$E_d^* = E_1$$
$$E_{dir} = E_2 - E_3$$
$$E_{diff}^* = E_d^* - E_{dir}$$
$$E_4 \approx E_1$$

The shadow band method is automatic and much better in principle than the Sun disk. However, the current YES MFR instrument that CL&W and CAR use only records in a relatively few (6) bands and does not therefore provide a complete irradiance description. It may be possible to fit an atmospheric model to the MFR data and predict the irradiance and the fraction of diffuse for the full spectrum. This needs some testing.

To provide some measure of the uniformity of the sky distribution, it may be useful to consider the benefit of taking scalar irradiance data (*S*) as well as cosine irradiance data (*E*). If the Sun disk is used so that the diffuse and direct fraction are know it follows that the average cosine of the complete Sun and sky distribution would be:

$$\overline{\mu}=\frac{E}{S}$$

For no diffuse irradiance:

$$\overline{\mu}=\cos\theta_s$$

If there were significant diffuse radiation but not completely diffuse conditions, a Sun-corrected average cosine for the sky distribution would be:

$$\overline{\mu}_{diff}=\frac{E_{diff}}{S_{diff}}$$
$$=\frac{E-E_{dir}}{S-E_{dir}/\cos\theta_s}$$
$$=\frac{f_d\overline{\mu}}{1-\left(1-f_d\right)\overline{\mu}\cos\theta_s}$$

This can be used to assess the usefulness of the simplified irradiance assumption (that diffuse irradiance is uniform) and also provides useful (phase) data for an atmospheric model when conditions are relatively clear.

A5.6 Summary

This brief outline of the issues needing to be addressed in measurement and modelling of image 'reflectance' given the fact of BRDF and the variety of possible choices for reflectance factors has assumed a single wavelength and that the radiance measurements are done with a narrow Field of View instrument. If either of these assumptions is changed the nature of the measurement also changes.

Provided, however, that the BRDF characteristics of targets or panels are relatively the same over the wavebands of interest and that the targets are relatively homogeneous over the FOV (which should at least be less than or equal to 5° in field measurements) the method and ideas discussed here can be retained. However, any data taken must be augmented with waveband and FOV information.

Given this, the main outcome of the discussion is to suggest that field panels need to be modelled and their K-factors assessed regularly. This is as important as cross calibrating instruments. In addition, if no account is taken of BRDF then there will be wide variations between field and image estimates of reflectance. Spectral libraries may not be possible. Even if very standard viewing geometry is used, the variation of the data with Sun position may be very large.

The issues discussed have ramifications for correction for BRDF in both Atmospheric Correction and field studies. A possible option is to use the simple model:

$$\rho_t = \bar{\rho}\left(2\pi,2\pi\right)\left(\left(1-f_d\right)\gamma\left(\mu_r,\mu_s\right)+f_d\gamma\left(\mu_r,2\pi\right)\right)$$
$$= \bar{\rho}\left(2\pi,2\pi\right)\Gamma\left(\mu_r,\mu_s,f_d\right)$$

Since, if a simple parametric form is available for the BRDF and the diffuse fraction is known it follows that Γ is known and it could be proposed that all measurements be normalised to an apparent Bi-hemispherical Reflectance Factor:

$$\bar{\rho}\left(2\pi,2\pi\right) = \frac{\rho_t}{\Gamma\left(\mu_r,\mu_s,f_d\right)}$$

If the BRDF directional behaviour parameters are defined for a given land cover it may be possible, provided f_d is measured or modelled, to normalise reflectances to the Bi-hemispherical Reflectance Factor in both field situations and in atmospheric correction.

Following from this is a specification for the structure of an adequate Spectral Library. A 'library' entry would include:

1. Waveband and FOV:
   - 1.1 ρ_t (the actual data)
   - 1.2 $\bar{\rho}\left(2\pi,2\pi\right)$
   - 1.3 $\gamma\left(\mu_r,\mu_s\right)$ as a parametric function or land cover 'type'
2. μ_r,μ_s,f_d at the time of the measurement
3. Panel/Target geometry
   - 3.1 ρ^* and other environmental information

Since this allows the original data to be reconstructed, the entry should also include the error of re-construction via the model.

A5.7 References

Jupp, D.L.B. (1997) *Issues in Reflectance Measurement*. CSIRO Earth Observation Centre, Canberra.

Nicodemus, F.E., Richmond, J.C. and Hsia, J.J. (1977). *Geometrical considerations and nomenclature for reflectance*. NBS Monograph 160, US Department of Commerce, National Bureau of Standards, 52p.

Strahler, A.H., Barnsley, M.J., d'Entremont, R., Hu, B., Lewis, P., Li, X., Muller, J-P., Barker Schaaf, Wanner, W. and Zhang, B. (1995). *MODIS BRDF/Albedo Product: Algorithm Theoretical Basis Document Version 3.2*. NASA EOS, May 1995.

Walthall, C.L., Norman, J.M., Welles, J.M., Campbell, G. and Blad, B.L. (1985). Simple equation to approximate the bidirectional reflectance from vegetation canopies and bare soil surfaces. *Appl. Optics*, *24*, 383-387.






Australian Government
Geoscience Australia

bushfire&natural
HAZARDSCRC